textiles

# New Research Trends for Textiles

Edited by
Laurent Dufossé

Printed Edition of the Special Issue Published in *Textiles*

www.mdpi.com/journal/textiles

MDPI

# New Research Trends for Textiles

# New Research Trends for Textiles

Editor

**Laurent Dufossé**

MDPI • Basel • Beijing • Wuhan • Barcelona • Belgrade • Manchester • Tokyo • Cluj • Tianjin

*Editor*
Laurent Dufossé
ESIROI & CHEMBIOPRO
Université de La Réunion
Saint-Denis
France

*Editorial Office*
MDPI
St. Alban-Anlage 66
4052 Basel, Switzerland

This is a reprint of articles from the Special Issue published online in the open access journal *Textiles* (ISSN 2673-7248) (available at: www.mdpi.com/journal/textiles/special_issues/trends_textiles).

For citation purposes, cite each article independently as indicated on the article page online and as indicated below:

LastName, A.A.; LastName, B.B.; LastName, C.C. Article Title. *Journal Name* **Year**, *Volume Number*, Page Range.

**ISBN 978-3-0365-6082-3 (Hbk)**
**ISBN 978-3-0365-6081-6 (PDF)**

# Contents

# About the Editor

**Laurent Dufossé**

Laurent Dufossé has held the position of Professor of Food Science and Biotechnology since 2006, at Reunion Island University, which is located on a volcanic island in the Indian Ocean, near Madagascar and Mauritius. The island is one of France's overseas territories, with almost one million inhabitants, and the university has 19,000 students. Previously, Professor Dufossé was a researcher and senior lecturer at the Université de Bretagne Occidentale, Quimper, Brittany, France. He attended the University of Burgundy, Dijon, France, where he received his PhD in Food Science in 1993, and has been involved in the field of the biotechnology of food ingredients for more than 30 years. His main research interests over the last 20 years have mainly been the microbial production of pigments and the study of aryl carotenoids, such as isorenieratene, C50 carotenoids, azaphilones and anthraquinones. These studies have relevance for applications in science and technology, in areas such as the supplying of sustainable components in many industrial sectors and the development of biobased pigments and dyeing agents for the textile industry.

# Preface to ”New Research Trends for Textiles”

The *Textiles* journal is a peer-reviewed, open-access journal, officially launched in 2020. It concerns research and innovation in the field of textile materials. This field is very broad and covers many topics. Textile materials composed of fibers linked by weaving, braiding, knitting, or sewing constitute a wide range of materials and are essential for many applications. They are both ancestral materials used since antiquity and in advanced applications, such as composites in aeronautics or the medical industry.

*Textiles*, an open-access international journal by *MDPI* (Basel, Switzerland), focuses on the broad field of textile materials and topics including, but not limited to, the following: fibers and yarns for textiles, properties, and microstructures; advances in weaving, braiding, and knitting technologies; 3D textiles; nonwovens; structure and properties of high-performance textiles; characterization and testing of textiles; fatigue, damage, and failure of textile; friction in textile materials; simulation in textiles; textile and clothing science; sustainable fibers and textiles; dyeing textiles; microbial and plant pigments for the textile industry; microbial enzymes in the textile industry; bio-polishing; bioconversion of waste fabric; microbial wastewater treatment; microbial silk; bacterial cellulose; recycling in textiles; fashion and apparel design; textile composite; preform and prepreg draping; medical textile materials; textile materials for civil engineering applications; geo-textiles; smart textiles; protective and thermal protective textiles; textile history and archeology.

In order to demonstrate the huge impact of textile research and technology in the world, the publisher, the Editorial Board, and myself decided to invite contributions, feature papers, from key world-class researchers, which were collected in a single Special Issue entitled ‘New World Research Trends for Textiles’, from May 2021 to May 2022.

In total, 36 papers were submitted. These 24 papers can be roughly subdivided into four parts: functional textiles; process and modelling; control; and consumers and behavior.

I, as Editor, trust that all readers of this Special Issue reprint will enjoy the contents, and I would like to deeply thank all the wonderful authors who contributed; Prof. Philippe Boisse, Editor-in-Chief of *Textiles*; the numerous reviewers; and the whole team at *MDPI* (editing, production, website, etc.).

**Laurent Dufossé**
*Editor*

*textiles*

*Editorial*

# New Research Trends for Textiles

**Laurent Dufossé**

CHEMBIOPRO Laboratoire de Chimie et Biotechnologie des Produits Naturels, ESIROI Agroalimentaire, Université de La Réunion, 15 Avenue René Cassin, F-97400 Saint-Denis, Ile de La Réunion, France; laurent.dufosse@univ-reunion.fr; Tel.: +262-692402400

The *Textiles* journal is a peer-reviewed, open-access journal, officially launched in 2020. It concerns research and innovation in the field of textile materials. This field is very broad and covers many topics. Textile materials composed of fibers linked by weaving, braiding, knitting, or sewing constitute a wide range of materials and are essential for many applications. They are both ancestral materials used since antiquity and in advanced applications, such as composites in aeronautics or the medical industry [1].

*Textiles*, an open-access international journal by MDPI (Basel, Switzerland), focuses on the broad field of textile materials and topics including, but not limited to, the following: fibers and yarns for textiles, properties, and microstructures; advances in weaving, braiding, and knitting technologies; 3D textiles; nonwovens; structure and properties of high-performance textiles; characterization and testing of textiles; fatigue, damage, and failure of textile; friction in textile materials; simulation in textiles; textile and clothing science; sustainable fibers and textiles; dyeing textiles; microbial [2,3] and plant pigments for the textile industry; microbial enzymes in the textile industry; bio-polishing; bioconversion of waste fabric; microbial wastewater treatment; microbial silk; bacterial cellulose; recycling in textiles; fashion and apparel design; textile composite; preform and prepreg draping; medical textile materials; textile materials for civil engineering applications; geotextiles; smart textiles; protective and thermal protective textiles; textile history and archeology [1].

To date, *Textiles* has published articles that can be found here: https://www.mdpi.com/search?q=&journal=textiles&sort=pubdate&page_count=50.

In order to demonstrate the huge impact of textile research and technology in the world, the Publisher, the Editorial Board, and myself decided to invite contributions, feature papers, from key world-class researchers which were collected in a single Special Issue entitled 'New world research trends for textiles', from May 2021 to May 2022.

In total, 36 papers were submitted. These 24 papers can be roughly subdivided into four parts: functional textiles; process and modelling; control; consumers and behavior.

## 1. Functional Textiles

Photochromic Textiles Based upon Aqueous Blends of Oxygen-Deficient WO3-x and TiO2 Nanocrystals. by Roberto Giannuzzi, Vitantonio Primiceri, Riccardo Scarfiello, Marco Pugliese, Fabrizio Mariano, Antonio Maggiore, Carmela Tania Prontera, Sonia Carallo, Cristian De Vito, Luigi Carbone and Vincenzo Maiorano. Textiles 2022, 2(3), 382–394; https://doi.org/10.3390/textiles2030021.

50/60 Hz Power Grid Noise as a Skin Contact Measure of Textile ECG Electrodes. by Khorolsuren Tuvshinbayar, Guido Ehrmann and Andrea Ehrmann. Textiles 2022, 2(2), 265–274; https://doi.org/10.3390/textiles2020014.

Characterizing Steam Penetration through Thermal Protective Fabric Materials. by Sumit Mandal and Guowen Song. Textiles 2022, 2(1), 16–28; https://doi.org/10.3390/textiles2010002.

Stretchable Textile Yarn Based on UHF RFID Helical Tag. by Sofia Benouakta, Florin Doru Hutu and Yvan Duroc. Textiles 2021, 1(3), 547–557; https://doi.org/10.3390/textiles1030029.

**Citation:** Dufossé, L. New Research Trends for Textiles. *Textiles* **2022**, *2*, 579–581. https://doi.org/10.3390/textiles2040033

Received: 29 October 2022
Accepted: 10 November 2022
Published: 16 November 2022

Fibers and Textiles for Personal Protective Equipment: Review of Recent Progress and Perspectives on Future Developments. by Patricia I. Dolez, Sabrina Marsha and Rachel H. McQueen. Textiles 2022, 2(2), 349–381; https://doi.org/10.3390/textiles2020020.

Textile-Based Sound Sensors (TSS): New Opportunities for Sound Monitoring in Smart Buildings. by Andrea Giglio, Karsten Neuwerk, Michael Haupt, Giovanni Maria Conti and Ingrid Paoletti. Textiles 2022, 2(2), 296–306; https://doi.org/10.3390/textiles2020016.

High-Performance and Functional Fiber Materials—A Review of Properties, Scanning Electron Microscopy SEM and Electron Dispersive Spectroscopy EDS. by Boris Mahltig and Thomas Grethe. Textiles 2022, 2(2), 209–251; https://doi.org/10.3390/textiles2020012.

Geotextiles—A Versatile Tool for Environmental Sensitive Applications in Geotechnical Engineering. by Fulga Tanasă, Mărioara Nechifor, Mauruşa-Elena Ignat and Carmen-Alice Teacă. Textiles 2022, 2(2), 189–208; https://doi.org/10.3390/textiles2020011.

Review of Fiber- or Yarn-Based Wearable Resistive Strain Sensors: Structural Design, Fabrication Technologies and Applications. by Fei Huang, Jiyong Hu and Xiong Yan. Textiles 2022, 2(1), 81–111; https://doi.org/10.3390/textiles2010005.

Wearable Actuators: An Overview. by Yu Chen, Yiduo Yang, Mengjiao Li, Erdong Chen, Weilei Mu, Rosie Fisher and Rong Yin. Textiles 2021, 1(2), 283–321; https://doi.org/10.3390/textiles1020015.

Bacterial Secondary Metabolites as Biopigments for Textile Dyeing. by Ana Kramar and Mirjana M. Kostic. Textiles 2022, 2(2), 252–264; https://doi.org/10.3390/textiles2020013.

**2. Process and Modelling**

Loop Order Analysis of Weft-Knitted Textiles. by Levi Kapllani, Chelsea Amanatides, Genevieve Dion and David E. Breen. Textiles 2022, 2(2), 275–295; https://doi.org/10.3390/textiles2020015.

New Geometrical Modelling for 2D Fabric and 2.5D Interlock Composites. by Mohamad Abbas Kaddaha, Rafic Younes and Pascal Lafon. Textiles 2022, 2(1), 142–161; https://doi.org/10.3390/textiles2010008.

Meso-Macro Simulations of the Forming of 3D Non-Crimp Woven Fabrics. by Jie Wang, Peng Wang, Nahiene Hamila and Philippe Boisse. Textiles 2022, 2(1), 112–123; https://doi.org/10.3390/textiles2010006.

Continuous Yarn Electrospinning. by Shakir Zainuddin and Thomas Scheibel. Textiles 2022, 2(1), 124–141; https://doi.org/10.3390/textiles2010007.

A Review on Tough Soft Composites at Different Length Scales. by Wei Cui and Ruijie Zhu. Textiles 2021, 1(3), 513–533; https://doi.org/10.3390/textiles1030027.

Textile Branch and Main Breakthroughs of the Czech Republic in the Field of Textile Machinery: An Illustrated Review. by Jiří Militký, Dana Křemenáková, Miroslav Václavík, Václav Klička and Stanislav Dídek. Textiles 2021, 1(3), 466–482; https://doi.org/10.3390/textiles1030024.

Recent Efforts in Modeling and Simulation of Textiles. by Julia Orlik, Maxime Krier, David Neusius, Kathrin Pietsch, Olena Sivak and Konrad Steiner. Textiles 2021, 1(2), 322–336; https://doi.org/10.3390/textiles1020016.

**3. Control**

A Comparison of Two Different Light Booths for Measuring Color Difference of Metameric Pairs. by Azmary Akter Mukthy, Michal Vik and Martina Viková. Textiles 2021, 1(3), 558–570; https://doi.org/10.3390/textiles1030030.

Effect of Textile Characteristics on the AR-Glass Fabric Efficiency. by Marco Carlo Rampini, Giulio Zani, Louis Schouler, Matteo Colombo and Marco di Prisco. Textiles 2021, 1(2), 387–404; https://doi.org/10.3390/textiles1020020.

Dielectric Properties of Textile Materials: Analytical Approximations and Experimental Measurements—A Review. by Yusuke Yamada. Textiles 2022, 2(1), 50–80; https://doi.org/10.3390/textiles2010004.

### 4. Consumers and Behavior

Development of a Consumer-Based Quality Scale for Artisan Textiles: A Study with Scarves/Shawls. by Denis Richard Seninde, Edgar Chambers IV, Delores H. Chambers and Edgar Chambers V. Textiles 2021, 1(3), 483–503; https://doi.org/10.3390/textiles1030025.

Organic Cotton Clothing Purchase Behavior: A Comparative Study of Consumers in the United States and Bangladesh. by Md Nakib Ul Hasan, Chuanlan Liu and Bulbul Ahmed. Textiles 2021, 1(2), 376–386; https://doi.org/10.3390/textiles1020019.

A Review on Textile Recycling Practices and Challenges. by Jeanger P. Juanga-Labayen, Ildefonso V. Labayen and Qiuyan Yuan. Textiles 2022, 2(1), 174–188; https://doi.org/10.3390/textiles2010010.

I, as Guest Editor, trust all readers of this Special Issue enjoy the contents and I would like to deeply thank all the wonderful authors who contributed; Prof. Philippe Boisse, Editor-in-Chief of *Textiles*; the numerous reviewers; and the whole team at MDPI (editing, production, website, etc.).

**Conflicts of Interest:** The author declares no conflict of interest.

## References

1. Boisse, P. Editorial. Textiles: Multidisciplinary Open Access Journal in Research and Innovation of Textiles. *Textiles* **2021**, *1*, 1. [CrossRef]
2. Venil, C.K.; Velmurugan, P.; Dufossé, L.; Devi, P.R.; Ravi, A.V. Fungal pigments: Potential coloring compounds for wide ranging applications in textile dyeing. *J. Fungi* **2020**, *6*, 68. [CrossRef] [PubMed]
3. Venil, C.K.; Dufossé, L.; Velmurugan, P.; Malathi, M.; Lakshmanaperumalsamy, P. Extraction and Application of Pigment from *Serratia marcescens* SB08, an Insect Enteric Gut Bacterium, for Textile Dyeing. *Textiles* **2021**, *1*, 21–36. [CrossRef]

*textiles*

MDPI

*Article*

# Photochromic Textiles Based upon Aqueous Blends of Oxygen-Deficient $WO_{3-x}$ and $TiO_2$ Nanocrystals

**Roberto Giannuzzi [1,2], Vitantonio Primiceri [1,2], Riccardo Scarfiello [1,*], Marco Pugliese [1], Fabrizio Mariano [1], Antonio Maggiore [1], Carmela Tania Prontera [1,3,*], Sonia Carallo [1], Cristian De Vito [1], Luigi Carbone [1] and Vincenzo Maiorano [1]**

[1] CNR NANOTEC—Institute of Nanotechnology c/o Campus Ecotekne, University of Salento, Via Monteroni, 73100 Lecce, Italy; roberto.giannuzzi@nanotec.cnr.it (R.G.); vitantonio.primiceri@unisalento.it (V.P.); marco.pugliese@nanotec.cnr.it (M.P.); fabrizio.mariano79@gmail.com (F.M.); antonio.maggiore@nanotec.cnr.it (A.M.); sonia.carallo@nano.cnr.it (S.C.); cristian.devito@nanotec.cnr.it (C.D.V.); luigi.carbone@nanotec.cnr.it (L.C.); vincenzo.maiorano@nanotec.cnr.it (V.M.)

[2] Department of Mathematics and Physics "Ennio De Giorgi", University of Salento, 73100 Lecce, Italy

[3] Istituto per la Microelettronica e Microsistemi (IMM)—CNR, Via Monteroni, 73100 Lecce, Italy

* Correspondence: riccardo.scarfiello@nanotec.cnr.it (R.S.); tania.prontera@nanotec.cnr.it (C.T.P.)

**Abstract:** With the main objective being to develop photochromic smart textiles, in this paper, we studied the photochromic behavior of $WO_{3-x}$ nanocrystals (NCs) cooperatively interacting with variable amounts of $TiO_2$ NCs. We tested several blends of $WO_{3-x}$:$TiO_2$ NCs, admixed in different compositions (relative molar ratio of 4:0, 3:1, 2:2, 1:3, 0:4) and electrostatically interfacing because of opposite values of Z-potential, for photo-induced chromogenic textiles. We further monitored the photochromic sensitivity of NC-impregnated textiles after exposure to a few solvents (i.e., methanol, ethanol, and isopropanol) or when over-coated with different polymeric matrices such as natural cellulose or ionic conductive Nafion. The optimization of the compositions of the $WO_{3-x}$:$TiO_2$ blends embedded in polymeric matrices, allowed the nanostructured photochromic textiles to show rapid and tunable coloration (<5 min) and bleaching kinetics (~5 in at 75 °C or 6 h at room temperature) along with good recovery and cycling stability. This study features a simple strategy for the widespread application of $WO_{3-x}$:$TiO_2$-based photochromic smart textiles.

**Keywords:** smart textile; photochromism; inorganic nanoparticles

**Citation:** Giannuzzi, R.; Primiceri, V.; Scarfiello, R.; Pugliese, M.; Mariano, F.; Maggiore, A.; Prontera, C.T.; Carallo, S.; De Vito, C.; Carbone, L.; et al. Photochromic Textiles Based upon Aqueous Blends of Oxygen-Deficient $WO_{3-x}$ and $TiO_2$ Nanocrystals. *Textiles* **2022**, *2*, 382–394. https://doi.org/10.3390/textiles2030021

Academic Editor: Laurent Dufossé

Received: 28 April 2022
Accepted: 17 June 2022
Published: 1 July 2022



## 1. Introduction

The term 'smart textiles' is used to describe those fabrics that, thanks to the integration of specific digital tools, devices, and sensors, show supplementary features which make them sensitive to environmental conditions and/or able to interact with the end-user [1–5]. These technologies are recently receiving growing interest for extensive applications in different fields spanning from the safety industry to the healthcare and fashion industry [6]. A specific class of materials used for the fabrication of smart textiles is chromogenic materials, whereby the change of their color is reversibly induced as a response to an environmental stimulus, which can be thermal, optical, mechanical, electrical, etc. [7]. In particular, photochromism is a photo-induced modification of the electronic state of the material and it is a phenomenon already used in various commercial products such as sunglasses, packaging, cosmetics, memories, sensors, and displays [8]. Thus, we saw a potential interest for textile applications to open perspectives towards the development of UV protective and sensing clothes that can find considerable implications in the safety and military industries [7,9,10]. Disparate examples of photochromic fabrics were obtained by using several organic dyes, such as spirooxazines, spiropyrans and naphthopyrans, employed with different kinds of integration processes [11–18]. Traditional and innovative

dyeing techniques based on supercritical $CO_2$ were used for the production of photochromic textiles by using organic molecules [16,17]. An alternative approach is based on electrospinning, Zheng et al. reported electrospun polycaprolactone fibers doped with photochromic dyes and their subsequent embroidering into commercial fabrics for the development of wearable UV indicators [14]. Printing techniques such as inkjet and screen printing were also widely used for the development of photochromic textile, by incorporating the dyes into polymeric matrices to obtain printable inks [11–13]. The electrostatic layer-by-layer self-assembly method of photochromic microcapsules was also reported for the preparation of photochromic cotton fabric [15].

Despite this, organic materials are at the same time largely affected by external environmental conditions such as oxygen and pH, hence, microencapsulation processes are usually required to ensure long-time service [13,15,18]. Nevertheless, embedding photochromic dyes into a rigid polymeric matrix often reduces the molecular mobility and therefore slows down the reversible modification responsible for the photochromism in organic molecules. Immobilization of photochromic dyes onto inorganic matrices, before their combination with textiles, might partially overcome those drawbacks and possibly induce enhanced color-exchange properties, stability and comfort [19–21].

Inorganic materials represent a valid alternative to organic molecules since they usually report better stability and for that have recently been under investigation for photochromic textiles fabrication [8,22–25]. Fang et al. reported the preparation of cellulose fibers with the incorporation of hackmanite micro-particles for the development of wearable UV sensors [24]. A photochromic cellulosic fabric was also obtained by screen printing of strontium aluminate pigment and aqueous binder [8]. Photochromic properties of tungsten-based materials were also exploited for the development of smart chromogenic textiles [22,23,25,26].

Bao et al. obtained photochromic textiles by a simple hydrogen bonding self-assembly of polyacrylic acid and sodium deca-tungstate [25]. Wang et al. reported waterborne tungsten-based polyvinyl alcohol (PVA) coating by simply dipping the fiber into a mixture of $Na_2WO_4$ and PVA and the obtained fibers showed an instantaneous color response after UV irradiation [23]. Another approach based on dip coating was developed by Ling et al. starting from $WO_3$ nanomaterials and PVA, obtaining photochromic fibers with a fast and reversible color switch [22]. Electrospinning is another valid technique employed to obtain fibrous substrates and it was employed by Wei et al. to fabricate fibrous photochromic membranes starting from polyvinylpyrrolidone and $WO_3$ [26].

Although different specific mechanisms were proposed in the literature (tungsten bronze formation where the optical transition is associated with the intervalence-charge transfer mechanism or where absorption arises from free or trapped charge carriers) [27], the photochromic performance in tungsten-based materials is determined by the behavior of optically excited electron-hole pairs [28]. Thus, by controlling the lifetime and the optical paths of these free charge carriers, the coloration performances can be controlled. For this purpose, it was reported that the photochromic properties of tungsten oxide can be improved by mixing/coupling it with other metal oxides such as $TiO_2$. Nowadays, consistent experimental pieces of evidence demonstrated the advantages of mixed $WO_{3-x}TiO_2$ materials for photochromic applications [29–32]. Such performance enhancement can be understood by evaluating the energy levels of the two materials and the formation of a junction at the $WO_{3-x}$-$TiO_2$ interface. In other words, the enhanced photochromic response is a consequence of reduced recombination paths of photogenerated carriers which result in more electrons trapped within the bandgap of the $WO_{3-x}$ domain, contributing to the coloration process. Additionally, for tungsten oxide-based nanocomposites, polymeric matrix encapsulation proved to be a valid strategy for influencing both coloration and bleaching processes, which depend on concentrations of proton available in the nanocomposites–polymer matrix and on the diffusion rate achievable of generated proton via hydrogen bonding into the matrix [33]. However, the stronger the interaction between tungsten oxide and the matrix is, the higher and faster the coloration process could be, and the slower

the bleaching process would be. Thus, it is a big challenge to make a proper balance and compatibility between the matrix and inorganic nanoparticles to achieve a consistent coloration process followed by rapid bleaching recovery, thus achieving a suitable compromise necessary for any specific practical application.

In this context, we used for the first time, a mixture of $WO_{3-x}$ and $TiO_2$ nanomaterials to obtain photochromic textiles with improved performances compared to bare $WO_{3-x}$. In particular, we report a low-cost and industrially suitable procedure to functionalize common textiles, through a simple impregnation method, with nanostructured active inks obtained by mixing $WO_{3-x}$ and $TiO_2$ nanocrystals. A systematic study of the effect of the addition of $TiO_2$ nanoparticles on the photochromic response of $WO_{3-x}$ coating textiles was achieved by simply mixing the nanocrystal solutions of the two photoactive materials. Different photochromic performances resulted from variable compositions of photoactive inks used for textile impregnation. Moreover, the photochromic response of the $WO_{3-x}$:$TiO_2$ blend-coated textile was evaluated in the presence of selected organic solvent and/or embedded in polymeric matrices. Coloration kinetics, operational stability toward environmental chemicals (water and oxygen), and physical stresses of the nanofunctionalized and –structured smart textile were also investigated.

## 2. Materials and Methods

### *2.1. Materials*

All chemicals were used as received without further purification. The following chemicals were purchased from Sigma-Aldrich (Burlington, MA, USA): methanol (MeOH, 99.9%), ethanol (EtOH, 95%), 2-propanol (i-PrOH, 95.5%), hydroxyethylcellulose (HEC, average molecular weight: 380 kDa), starch from corn. Nafion alcoholic solution (D2021CS isopropanol-based 1100 EW at 20% *w*/*w*) was provided by Ion Power. Fabrics were provided by our industrial partner Klopman SRL made by cotton–polyester 50/50 blend, 270 g/m$^3$. Water-dispersed sub-stoichiometric $WO_{3-x}$ nanocrystals (NCs) were synthesized as reported elsewhere [34]; water-dispersible $TiO_2$ NCs were prepared according to a previously reported procedure, with minor changes [35]. A more detailed synthetic procedure of the latter will be exhaustively reported elsewhere. Representative TEM pictures and XRD diffraction patterns of $TiO_2$ and $WO_{3-x}$ nanocrystals are reported in Figure S1a–d, respectively.

### *2.2. Preparation of Samples and Analysis Method*

Textile samples were prepared by cutting samples as 1.0 × 2.0 cm in size. NC impregnation was performed by soaking samples in a proper blend of NC solution made by different $WO_{3-x}$:$TiO_2$ ratio content (relative molar compositions of 4:0, 3:1, 2:2, 1:3, 0:4 expressed in $WO_{3-x}$% named hereafter, 100%, 75%, 50%, 25% and 0%), for 3 s and then dried on hot plate at 80 °C for 3 min. This process was repeated 10 times for each sample to ensure an adequate loading of nanostructures. The manufacturing of textiles NC functionalization is sketched in Figure 1. The photochromic properties were evaluated by irradiating samples at 320–400 nm lamp with Bromograph MF 1030 (Nuova Delta Electronica) with different time exposure. Reflectance measurements were performed soon after UV (ultraviolet) exposure with PerkinElmer Lambda 1050 UV/Vis (visible)/NIR (near-infrared) spectrophotometer in a wavelength range between 250 nm and 1000 nm. For optical properties measurements, we evaluated a negligible transmittance (data not shown), thus we acquired reflectance (R) information that can be eventually converted into absorption (Abs) as follow Abs = 1-R. For photochromic measurements with different solvents exposure, 300 µL of solvent were cast on each sample and then exposed to UV radiation. Reflectance spectrum was suddenly recorded ensuring that the textile was still wetted during the measurement. The solvent impregnation process was repeated for each exposure time investigated. Photochromic measurements with starch and HEC were performed as follows: polymers were stirred in hot distilled water (80 °C) until complete powder gelation (concentration 0.05 mg/mL) before being uniformly deposited on samples by spin coating 1 mL of solutions (2000 rpm for

60 s); then, a further step of 5 min at 80 °C was adopted to ensuring complete evaporation of water. Nafion solution was spin-coated (2000 rpm for 60 s) as received without further dilutions, and dried onto the hot plate (80 °C for 5 min). Samples were then exposed to UV irradiation at different time scales and reflectance spectra were suddenly acquired.

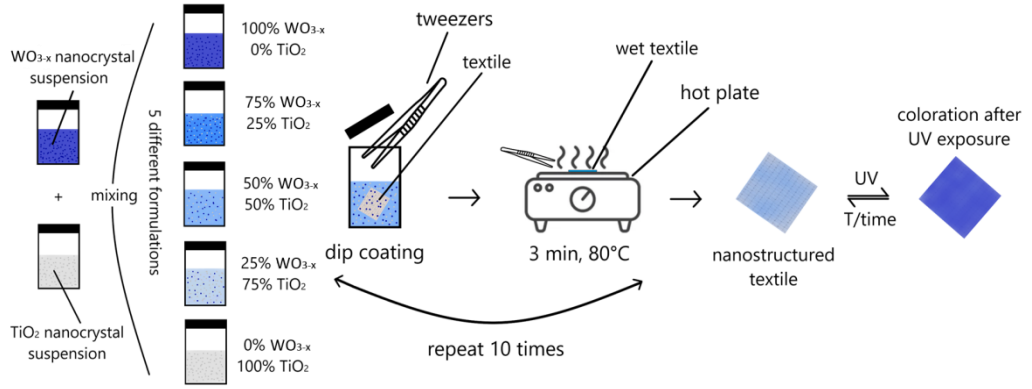


**Figure 1.** Schematic illustration of textile's sample functionalization with different $TiO_2$ and $WO_{3-x}$ nanoparticle solution compositions.

SEM morphological investigations were carried out on NC-decorated textiles without any further treatment, with FE-SEM Zeiss Merlin (Oberkochen, Germany) equipped with a GEMINI2 column, Schottky-type electron gun and secondary electron/Inlens detectors; images were recorded at 5 kV.

TEM images of $WO_{3-x}$ and $TiO_2$ nanocrystals were recorded on a JEOL JEM 1011 microscope (Peabody, MA, USA), equipped with a W filament source operating at 100 kV. Samples for TEM analysis were prepared by drop-casting a few drops of dilute nanocrystal solutions onto standard carbon-coated Cu grids, then allowing the solvent to evaporate. The as-dried sample grids were stored at 50 °C overnight before being transferred into the microscope for imaging.

XRD spectra were collected at room temperature using a Bruker D8 Discover diffractometer (Billerica, MA, USA) (operating conditions 40 kV, 40 mA) equipped with a Goebel mirror for copper radiation ($\lambda K\alpha 1$ = 1.540 56 Å, $\lambda K\alpha 2$ = 1.544 39 Å), and a scintillator detector. Samples were deposited onto a silicon zero background substrate. Data were collected in a reflection geometry at a fixed incidence angle of $\omega = 3°$ while moving the detector between 5° and 120° with a step size of 0.05°.

CAM 200 (KSV Instruments Ltd., Helsinki Finland) instrument was used to allow static contact angle measurements of all the samples by the sessile drop method (water drop volume—10 µL, time between frames—16 ms).

## 3. Results

For the functionalization of the hydrophilic component of textiles, with the idea of defining a process extendible to various commercially available fabrics, proper water-dispersible NC solutions were adopted. In the view of industrially accessible processability, scalability, and greener chemistry, water-dispersible inorganic NC solutions of $TiO_2$ and $WO_{3-x}$ were properly synthesized and processed. The chemical synthesis was performed within a hydroalcoholic environment and heated through microwave irradiation, which allows faster and in-core homogeneous heating rates. Both individual inorganic nanocomponents were generated without the need for the NC surface of a specific organic capping layer that would hinder the direct interaction either between the inorganic NCs with polymeric matrices or with other chemical environments.

The commonly accepted mechanism for tungsten oxide photochromism claims the formation of $H_xW^{6+}{}_{1-x}W^{5+}{}_xO_3$ is responsible for the blue color observed upon irradiation [27]. The combination with $TiO_2$ would clearly emphasize the coloration mechanism,

but to ensure an efficient and homogeneous photochromic behavior an intimate contact between $TiO_2$ and $WO_{3-x}$ is a critical issue and, for that, high surface contact between both nanostructured building blocks needs to be guaranteed. The nanocrystalline colloids exhibit opposite surface charges (−39 mV for $TiO_2$ and +2.8 mV for $WO_{3-x}$ related to Z-potential measurements performed on individual NC water solutions), which allows an electrostatic attraction between nanosized building blocks, and mutual interaction, therefore, when admixed in the same solution. When fabric samples were dipped into different NC solutions, the expressed photochromism reflects on photochromic textiles. Figure 2a reports a gallery of different pictures recorded on different samples impregnated with different $WO_{3-x}$:$TiO_2$ content (as reported by vertical annotations) and compared with only $TiO_2$ and $WO_{3-x}$ impregnation. The relative elemental amounts were characterized and controlled by inductively coupled plasma optical emission spectrometry (ICP-OES, data not shown) to keep constant the overall inorganic amounts deposited on each textile. A first qualitative outcome of the different $TiO_2$ content on photochromic textiles can be appreciated with distinctive blue intensities obtained at different UV exposure times (as reported by horizontal annotations).

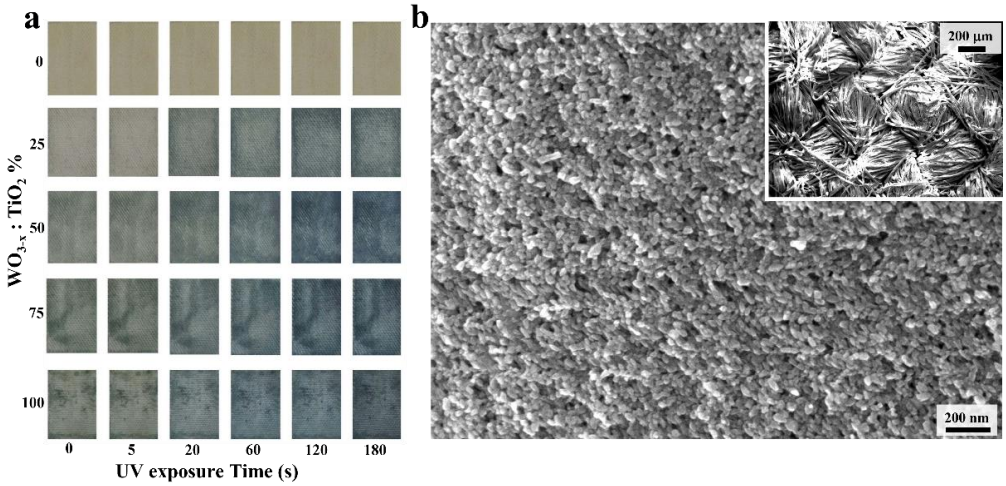


**Figure 2.** (**a**) Pictures recorded on textile samples functionalized via NC solution impregnation with different $WO_{3-x}$:$TiO_2$ contents; different degrees of blue are obtained with different UV exposure times for each composition. (**b**) Lower (inset) and higher magnification SEM micrograph of textiles functionalized with NC solution prepared with $WO_{3-x}$:$TiO_2$ ratio of 1:3 or 25%.

The nanostructured texture covering the pristine textile manufacture was characterized by SEM microscopy.

Figure 2b and Figure S1e report SEM images recorded on textile functionalized with NC solutions prepared with a $WO_{3-x}$:$TiO_2$ ratio of 25% after hotplate drying, without any other washing step. In particular, the inset of Figure 2b shows the fabric texture after NC impregnation and the higher magnification SEM images show complete and homogenous nanocrystalline coverage along the fibers (Figure 2b). In the Supporting Information, the SEM picture of one single fiber before and after NC impregnation is reported (Figure S1e,f). The pristine fiber is characterized by a fibrous motif/pattern (Figure S1f), which is not any more visible after impregnation (Figure S1e).

To investigate the photochromic textile performances with different $WO_{3-x}$:$TiO_2$ contents and compare them with two bare oxides on coloration and bleaching kinetics, detailed reflectance spectra were measured by a UV/Vis/NIR spectrometer. Figure 3a shows the reflectance changing values of NC-based photochromic fabrics of discrete compositions, at different UV exposure times and obtained at the two characteristic wavelengths of 550 nm and 830 nm. The individual reflectance spectra variations for each NC-functionalized photochromic fabric to different compositions are reported in Figure S2. The reflectance decreased within the initial 30 s and the changing rate became gradually slower with an

exponential trend, reaching a plateau (becoming saturated) within 5 min of UV exposure. It is worth underlying that a strong absorption in the IR and Vis regions already within 5 s of UV exposure was achieved only for the $WO_{3-x}$:$TiO_2$ mixture, compared with both pure oxide-coated textiles ($TiO_2$ alone does not show any photochromic behavior at the irradiate wavelength). The comparison of differences in reflectance between the no-exposure state and different times of UV exposure (ΔR) for all NC compositions are reported in Figure 3b (solid line for λ = 550 nm and dashed line for λ = 830 nm). It becomes clearer that the presence of $TiO_2$ increases the coloring kinetics for all mixture compositions compared with pure $WO_{3-x}$. Moreover, as the greatest ΔR values were achieved with a $WO_{3-x}$:$TiO_2$ ratio of 1:3 for both wavelengths, we selected this composition for further characterizations, as reported below. The after effect of $TiO_2$ blending (content) on the bleaching kinetics of the photochromic textiles was evaluated by monitoring, immediately after 5 min of UV exposure, the reflectance decay as a function of time. The representative reflectance values during the bleaching process of $WO_{3-x}$:$TiO_2$ functionalized textiles are reported in Figure 3c. All samples showed good reversible photochromic properties and $TiO_2$ blending was also revealed to be beneficial for photochromic recovery. Indeed, fabric samples containing $TiO_2$ blended with $WO_{3-x}$ NCs showed a recovery of 80–100% (for λ = 550 nm) and 75–85% (for λ = 830 nm) values unlike samples functionalized with only $WO_{3-x}$, which recovered only the 75% and 70% of pristine reflectance values for Vis and IR, respectively (see Table 1 for specific values). All samples returned to their original bleached state after being stored in the dark (in the air) for about 6 h. Representative reflectance values are summarized in Table 1 for a more immediate comparison.

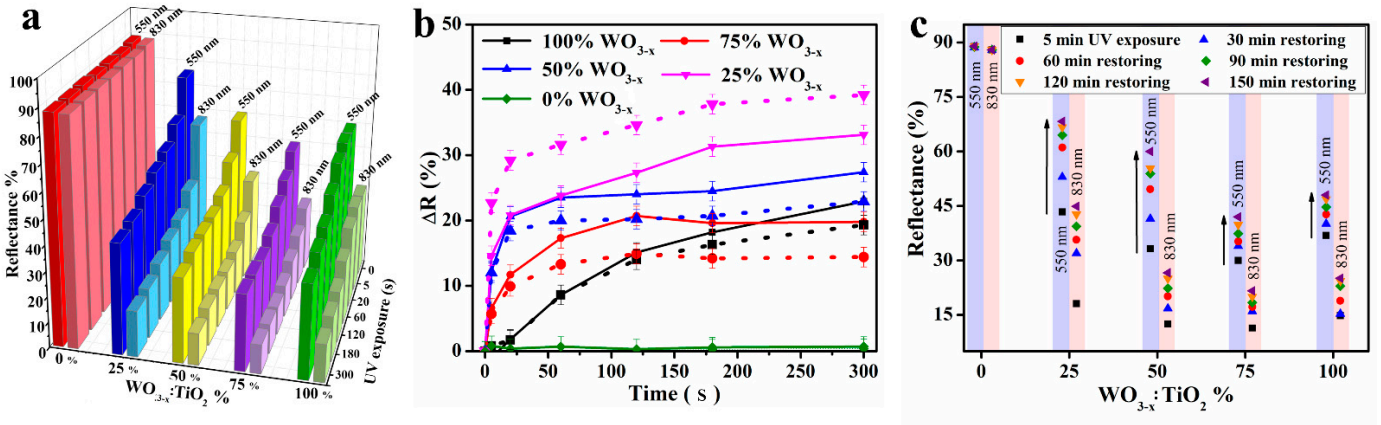


**Figure 3.** (**a**) Representative reflectance values at λ = 550 nm and λ = 830 nm of nanocrystalline-coated textile with different $WO_{3-x}$:$TiO_2$ compositions exposed to different UV irradiation times. (**b**) ΔR (difference between reflectance value after 5 min of UV exposure and no-exposed samples) variation at different UV exposure; solid lines are related to λ = 550 nm and dashed lines are related to λ = 830 nm. (**c**) Reflectance values during the bleaching process were carried out after 5 min of UV irradiation and recorded at different time intervals.

**Table 1.** $WO_{3-x}$:$TiO_2$ % related to different $WO_{3-x}$ percentage content into NCs mixture for textile coating; $R_{UV = 0 (550 nm)}$ and $R_{UV = 0 (830 nm)}$ Reflectance percentage at 550 nm and 830 nm, respectively, of NC-functionalized samples with no UV exposure; $R_{UV = 5 min (550 nm)}$ and $R_{UV = 5 min (830 nm)}$ Reflectance percentage at 550 nm and 830 nm, respectively, of NC-functionalized samples with 5 min of UV exposure; $\Delta R_{550 nm}$ and $\Delta R_{830 nm}$ related to the difference between $R_{UV = 5 min (550 nm)}$−$R_{UV = 0 (550 nm)}$ and $R_{UV = 5 min (830 nm)}$−$R_{UV = 0 (830 nm)}$, respectively; $R_{rec (550 nm)}$ and $R_{rec (830 nm)}$ related to recovered reflectance percentage at 550 nm and 830 nm, respectively, of air-exposed samples kept 150 min in the dark; $\%rec_{(550 nm)}$ and $\%rec^{(830 nm)}$ related to percentage $R_{rec (550 nm)}$ and $R_{rec (830 nm)}$ compared to initial $R_{UV = 0 (550 nm)}$ and $R_{UV = 0 (830 nm)}$.

| $WO_{3-x}$:$TiO_2$ % | $R_{UV = 0}$ (550 nm) | $R_{UV = 0 (830 nm)}$ | $R_{UV = 5 min (550 nm)}$ | $R_{UV = 5 min (830 nm)}$ | $\Delta R_{550 nm}$ | $\Delta R_{830 nm}$ | $R_{rec (550 nm)}$ | $R_{rec (830 nm)}$ | %rec (550 nm) | %rec (830 nm) |
|---|---|---|---|---|---|---|---|---|---|---|
| 0 | 88 | 88 | 88 | 88 | 0 | 0 | 0 | 0 | - | - |
| 25 | 75 | 55 | 42 | 15 | 33 | 40 | 68 | 45 | 90 | 82 |
| 50 | 60 | 35 | 34 | 15 | 26 | 20 | 60 | 28 | 100 | 80 |
| 75 | 50 | 25 | 30 | 12 | 20 | 13 | 40 | 21 | 80 | 84 |
| 100 | 60 | 33 | 38 | 15 | 22 | 18 | 47 | 25 | 78 | 75 |

The photochromic responses of the mixed oxide-functionalized textiles were tested in different alcoholic environments. Different photochromic responses or coloration intensities observed were compared in Figure 4a, while individual reflectance spectra variation recorded on 25% $WO_{3-x}$ impregnated textiles soaked with different solvents were reported in Figure S3. For that aim, we selected the textile sample functionalized with $WO_{3-x}$:$TiO_2$ (25% $WO_{3-x}$) because of its greater ΔR observed without any additive. We monitored the reflectance as a function of UV time exposure after soaking each sample with 300 μL of selected organic solvent (see experimental details). The largest optical response in the Vis as well as in the NIR was achieved with MeOH, followed by EtOH and i-PrOH, which show also an improvement in coloration sensitivity for both wavelengths compared with pristine samples (NC-coated textile with no alcohol impregnation) (Figure 4b). Moreover, we used acetone for comparison which did not show any coloration improvement (data not shown). Our interpretation of the increased modulation relates to the protic nature of alcohols compared with the aprotic habit of acetone, while the observed modulation trend (MeOH > EtOH~i-PrOH) could be attributed to the greater acidity of MeOH compared with EtOH and i-PrOH (pKa MeOH ~ 15.5; pKa EtOH ~ 16; pKa i-PrOH ~ 17) or to their intrinsic hole scavenger nature (see Discussion below for a more exhaustive analysis).

Based upon this solvent effect, the following measurements were conducted with a suitable polymeric medium in order to mimic the solvent behavior in a solid-state. As the presence of hydroxyl groups increases the photochromic efficiency [28] we selected hydroxyl-rich, cheap, non-toxic, and naturally abundant materials as a polymeric matrix. For this purpose we over-coated the NC-functionalized textile with two alternative polysaccharides, taking advantage of structural –OH moieties present in their chemical structures. More specifically, we compared corn starch and hydroxyethylcellulose (HEC). Both of them underwent a gelation process (rather than a full dissolution) when stirred in hot (80 °C) water, while they became badly water-soluble at room temperature, materials suitable in view of greener chemistry since no organic solvents were adopted for polymer overcoating. It is worth saying that HEC displays easier solubility and processability at higher concentrations, which is a not negligible detail in the view of the industrial scalability process. Pictures of different photochromic responses recorded on as described samples are reported in Figure 4a. The reflectance variations as a function of UV exposure times are compared in Figure 4b, while individual reflectance spectra variation recorded on 25% $WO_{3-x}$-impregnated textiles over-coated with different polymers are reported in Figure S4. The HEC-coated photochromic textile reported faster and stronger exponential modulation sensitivity than pristine samples as well as compared with EtOH and i-PrOH soaked samples, while slightly reduced compared with MeOH both in the Vis and NIR window with comparable UV exposure time. The starch-coated photochromic textile re-

ported similar behavior as the EtOH and i-PrOH treated textiles. The bleaching kinetics, reported in Figure 4c, remain mainly influenced by the $TiO_2$ presence in the inorganic NCs blend and was not substantially inferred by any further over-coating, besides Nafion (see below). To investigate the coloring–bleaching cycles stability, specific experiments were carried out with the HEC over-coated $WO_{3-x}$:$TiO_2$ (25%) textile, by exposing a sample to repeated cycles of 5 min UV irradiation and then keeping it at 75 °C under air on a hot plate to accelerate the bleaching condition. We stressed the sample with 100 cycles and the results are reported in Figure 4d. The initial reflectance (in the colored state) of each cycle raises by increasing the number of irradiation cycles, ascribable this to a little decline in photochromism. For comparison, we over-coated the NC-functionalized textile with Nafion. Samples reported an extremely fast and intense, though irreversible, modulation for Vis (λ = 550) and NIR (λ = 830) wavelengths. We suppose this to be due to the intrinsic high acidity of sulfonic moieties in the Nafion chemical structure, which could stabilize the chemical structure responsible for the colored state.

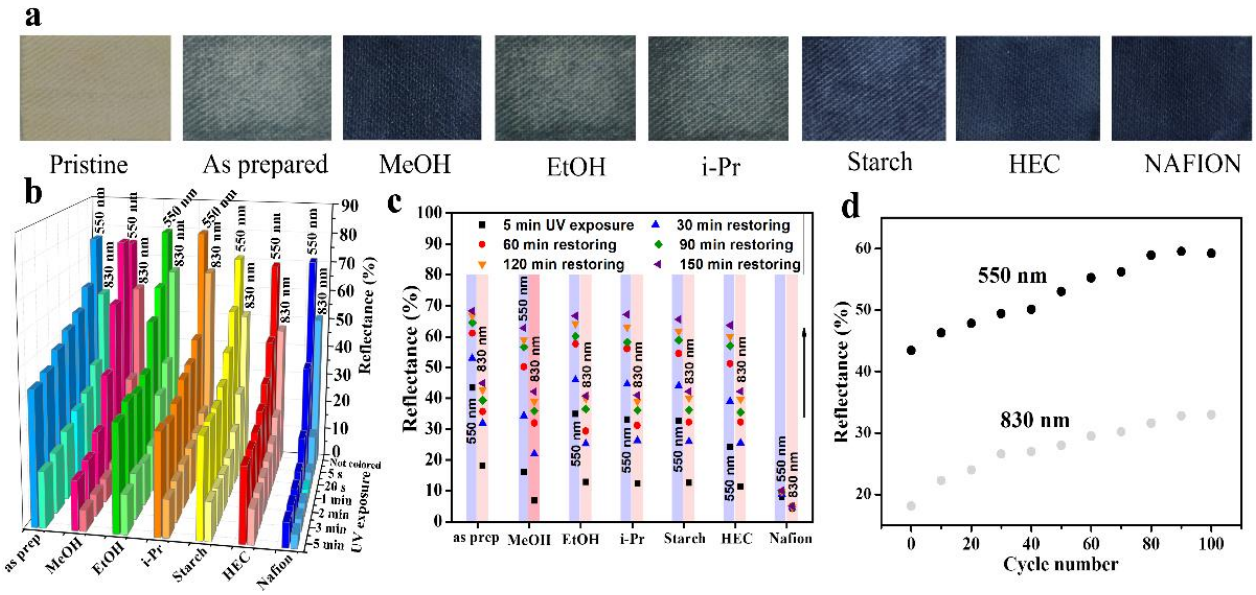


**Figure 4.** (**a**) Pictures of soaked or over-coated textile sample previously functionalized with NC solution of $WO_{3-x}$:$TiO_2$ (25% $WO_{3-x}$) and UV irradiated for 5 min. (**b**) Representative reflectance values during coloring process with different UV exposure and (**c**) and bleaching process carried out after 5 min of UV irradiation and recorded at different time intervals for λ = 550 nm and λ = 830 nm on soaked or over-coated textile's sample previously functionalized with NC solution containing $WO_{3-x}$:$TiO_2$ (1:3). (**d**) Cycling property of HEC over-coated $WO_{3-x}$:$TiO_2$ (25% $WO_{3-x}$) textile exposed to 100 cycles of 5 min UV irradiation followed by 5 min heated at 75 °C.

Contact angle measurements were performed to evaluate functionalized fabrics' wettability (Figure S5). All functionalized fabrics (except the one treated with Nafion) showed high wettability and the water drops were rapidly adsorbed within a few hundred ms. For this reason, it was not possible to evaluate the contact angle. In the case of fabrics coated with starch and HEC, the hydrophilic nature of the two polymers led to an absorption of the drop-in times very similar to those of the pristine fabric. In the case of fabrics treated with nanocrystals only (100% $TiO_2$ or 100% $WO_{3-x}$), the adsorption of the drop is even faster, occurring in less than 100 ms. Only fabric coated with Nafion, a fluorinated polymer, acquired good hydrophobicity, with slightly asymmetrical left–right contact angles due to the surface morphology of the fabric (113° left, 120° right).

To demonstrate the proof of concept of a free-standing membrane, a prototype was fabricated following the identical experimental procedures described in this study. For that, $WO_{3-x}$ and $TiO_2$ solutions (25% $WO_{3-x}$) were dispersed in an HEC solution (50 mg/mL),

cast onto a hydrophobic substrate, and then dried at 70 °C for 2 h. The as-deposited film could be detached from the substrate and used as a free-standing photochromic membrane. This lab-scale prototype has a dimension of about 3 cm × 3 cm and shows a good color change modulation. Pictures of the bleached and colored states are shown in Figure 5. This represented just a proof of concept for developing a sticky photochromic membrane to be eventually attached and detached onto any kind of already fabricated textiles.

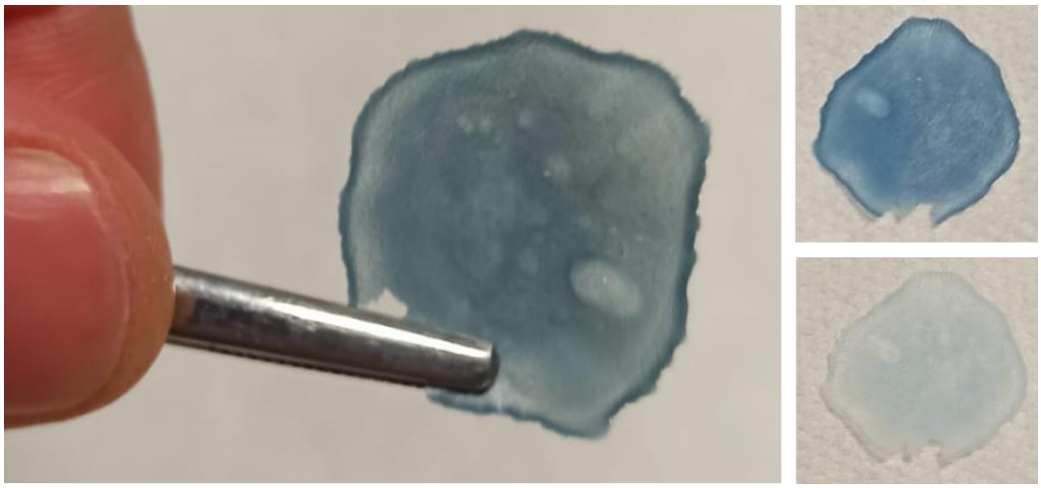

**Figure 5.** Pictures of photochromic freestanding membrane both in bleached and colored states.

## 4. Discussion

The commonly accepted photo-induced coloration mechanism for tungsten oxide, which represents the photo-active optical material for our purpose, can be roughly summarized as follows:

Coloration process:

$$WO_3 + h\nu \rightarrow WO_3^* + e^- + h^+ \quad (1)$$

$$2h^+ + H_2O \rightarrow 2H + O \quad (2)$$

$$WO_3 + xH^+ + xe^- \rightarrow H_xW^{6+}{}_{1-x}W^{5+}{}_xO_3 \quad (3)$$

Bleaching process:

$$H_xW^{6+}{}_{1-x}W^{5+}{}_xO_3 + {}^x/_4\ O_2 \rightarrow WO_3 + {}^x/_2\ H_2O$$

The irradiation of $WO_3$ with UV-light induces the excitation of electrons to the conduction band and the formation of holes in the valence band (Reaction 1). The photogenerated holes can interact with absorbed water molecules, thus inducing the decomposition into protons and oxygen radicals (Reaction 2). Finally, photogenerated electrons react with protons and $WO_3$ with the formation of hydrogen tungsten bronze responsible for the blue color (Reaction 3).

In comparison with pure $WO_3$ (as well as for its substoichiometric counterpart $WO_{3-x}$), as for other reported oxide samples such as $MoO_3$ (into $CdS/WO_3$ bi-layers and for $MoO_3/TiO_2$ composites), the suddenly reported photochromic mechanism for $WO_3$ is maximized by the presence of $TiO_2$. Thus, $WO_{3-x}$:$TiO_2$ blends exhibited much stronger photochromic properties to date, an effect mainly ascribable to hetero-interface formation between the two oxides [28,36]. $WO_{3-x}$ and $TiO_2$ are both n-type semiconductors and can both be excited by UV light, generating holes and electrons (reaction 1). Because of the staggered alignment of the energetics bands, the photogenerated holes can be transferred from the $WO_{3-x}$ valence band to the $TiO_2$ valence band and the electrons can transfer from the $TiO_2$ conduction band to the $WO_{3-x}$ conduction band. The segregation of photoexcited carriers into two different materials would consequently increase the electron-hole lifetime.

The photo-produced hole can weaken the H−O bond of adsorbed water molecules, or other H-O-containing species, and causes the water molecules decomposition into a proton and highly reactive oxygen radicals (reaction 2). While protons diffuse into the lattice, the photogenerated electrons injected into the conduction band of $WO_{3-x}$, balanced by proper counterions (i.e., protons), react inducing the reduction of W(VI) to W(V) and generate $H_xW^{6+}{}_{1-x}W^{5+}{}_xO_3$, (hydrogen tungsten bronze) (reaction 3). Moreover, it was suggested that the coloration in $WO_{3-x}$ could also be due to electrons trapped at energy levels within the forbidden gap, which can lead to a broad absorption in the IR region when they are excited into higher energy levels [28]. A representative scheme of photochromism in the $WO_{3-x}$:$TiO_2$ systems is shown in Figure 6.

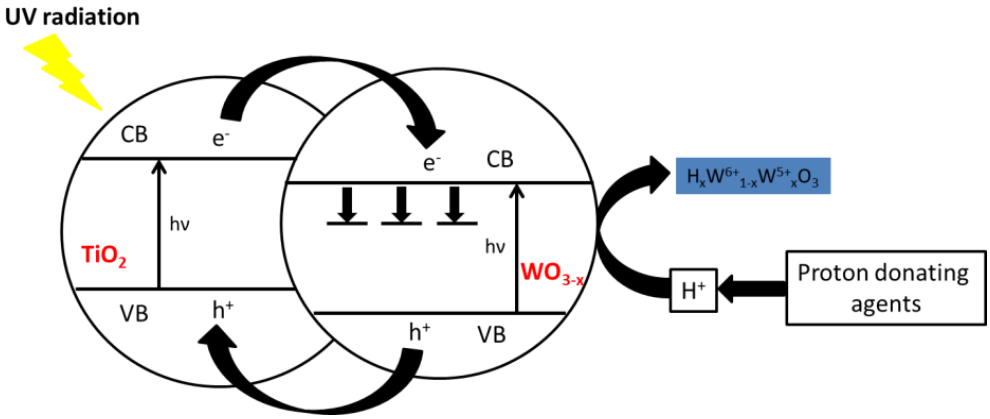


**Figure 6.** Scheme of photochromism mechanism in $WO_{3-x}$:$TiO_2$ systems.

Therefore, the photogenerated carriers in $WO_{3-x}$:$TiO_2$ blends are more effectively separated with respect to pure $WO_3$ and result in improved coloration performances because of the effective interfacial interaction. In particular, the more protons diffuse into the lattice, the more hydrogen tungsten bronze will be formed, and faster and stronger polaronic absorption will be obtained.

The number of available protons depends on the amount and nature of the surface adsorbed solvents such as $H_2O$, or alcohols. Alcohol can form protons easier because of its greater proton acidity compared to water, therefore, $WO_{3-x}$-$TiO_2$ alcohol-wetted fabrics showed larger photochromic efficiency than as-prepared samples (i.e., only NC-functionalized) where the photochromism is most probably powered by atmospheric water [35]. Moreover, alcohols (particularly MEOH) are largely used in photocatalytic similar systems for their prerogative of acting as an efficient hole scavenger or, in other words, used as a sacrificial electron donor for the depletion of photogenerated holes, thus they would partially inhibit intrinsic charges quenching.

Therefore, methanol represents the best solvent for improving the performance of the photochromic fabrics, both in terms of acidity and hole scavenger properties.

The nanoscale dimensions of inorganic colloids play also a fundamental role for two main reasons: (i) they decrease the distance of charges transfer, thus increasing the rate of coloration and decreasing the time of de-coloration; (ii) they maximize the surface-assisted hetero-interface interaction between oxides contributing to the higher charge transfer and ion intercalation kinetics, favoring the overall photochromic efficiency.

In the examples of over-coating with polymeric matrices, the –OH moieties in their chemical structure can enhance the number of available protons thus inducing an improvement of photochromic performances (as observed for alcohol impregnated samples), while the polymeric chain and the presence of hydrogen bonds would facilitate the migration of produced $H^+$ and electrons.

Polymers with this prerogative, with an adequate viscosity that would guarantee enough ionic mobility and eventually could show interesting foil-forming potential, would

be of great interest for accelerating coloration and bleaching behavior of the tungsten oxide-based hybrid photochromic foil with outstanding cycling stability.

## 5. Conclusions

In this work, photo-sensitive chromogenic smart textiles were realized with a straightforward industrially practicable approach potentially extendible over a broad range of every hydrophilic fabric. For that, commercial fabrics were functionalized with mixtures of $WO_{3-x}$ and $TiO_2$ nanocrystalline breeds to produce photochromic textiles. Because of nanometric particle size and their peculiar opposite surface charges, high specific surface areas with rich interfacial sites for charge transfer were created and hetero-interfaces were designed through strong electrostatic interactions. Indeed, an enhanced and reversible optical response both in the visible ($\lambda$ = 550 nm) and infrared ($\lambda$ = 830 nm) ranges was obtained. Moreover, the photochromic behaviors of nano-functionalized textiles exposed to different solvents and dispersed in several matrices were studied. Analyses of the different coloring and bleaching efficiencies were performed to reach an optimal balance between coloration and discoloration behavior along with consistent cycling stability. Furthermore, by using hydroxyl-rich water-dispersible polysaccharides over-coating the nano-functionalized textiles, an interesting enhancement of the overall photochromic response was generated. Those substrates furnish non-toxic, unpolluted, moldable rigidity, strong adhesion, and solvent resistance platforms for different practical useful textile applications or even photochromic freestanding foils. The high UV sensitivity and the filmogenic nature of the resulting hybrid materials make them important candidates for application in practical UV sensing devices and light-activated smart textiles.

**Supplementary Materials:** The following supporting information can be downloaded at: https://www.mdpi.com/article/10.3390/textiles2030021/s1, Figure S1: TEM, SEM images and XRD diffraction pattern. Figure S2: Reflectance spectra of NCs impregnated textiles in the bleached state and for different UV irradiation times. Figure S3: Reflectance spectra of $WO_3$-x:$TiO_2$ (1:3) (25% $WO_{3-x}$) impregnated textiles soaked with different solvents. Figure S4: Reflectance spectra of $WO_{3-x}$:$TiO_2$ (1:3) (25% $WO_{3-x}$) impregnated textiles over-coated with different polymeric matrices. Figure S5. Contact angle measurements on functionalized fabrics.

**Author Contributions:** Conceptualization: R.S., M.P. and R.G. Methodology: R.S., V.P., S.C., and C.D.V. Software: F.M. and A.M. Formal analysis: R.S. and V.P.; Investigation, Data curation, Writing—original draft preparation: R.S. Reviewing: L.C. and C.T.P. Editing: R.S. Founding acquisition: V.M. All authors have read and agreed to the published version of the manuscript.

**Funding:** This research was funded by "ECO-sustainable and intelligent fibers and fabrics for TEChnic clothing (ECOTEC)", PON «R&I» 2014–2020, project N° ARS01_00951, CUP B66C18000300005—COR 577006, Azione II—OS 1.b—D.D. Prot. N. 2055 del 02/08/2018.

**Data Availability Statement:** The data presented in this study are available on request from the corresponding author.

**Acknowledgments:** The authors appreciate the technical support and fabrics provided by Klopman Srl.

**Conflicts of Interest:** The authors declare no conflict of interest.

## References

1. Stoppa, M.; Chiolerio, A. Wearable Electronics and Smart Textiles: A Critical Review. *Sensors* **2014**, *14*, 11957–11992. [CrossRef] [PubMed]
2. Shah, M.A.; Pirzada, B.M.; Price, G.; Shibiru, A.L.; Qurashi, A. Applications of Nanotechnology in Smart Textile Industry: A Critical Review. *J. Adv. Res.* **2022**, *38*, 55–75. [CrossRef] [PubMed]
3. Cinquino, M.; Prontera, C.; Pugliese, M.; Giannuzzi, R.; Taurino, D.; Gigli, G.; Maiorano, V. Light-Emitting Textiles: Device Architectures, Working Principles, and Applications. *Micromachines* **2021**, *12*, 652. [CrossRef] [PubMed]
4. Ojha, G.P.; Pant, B.; Acharya, J.; Park, M. Prussian Red Anions Immobilized Freestanding Three-Dimensional Porous Carbonaceous Networks: A New Avenue to Attain Capacitor- and Faradic-Type Electrodes in a Single Frame for 2.0 v Hybrid Supercapacitors. *ACS Sustain. Chem. Eng.* **2022**, *10*, 2994–3006. [CrossRef]

5. Pant, B.; Ojha, G.P.; Kuk, Y.S.; Kwon, O.H.; Wan Park, Y.; Park, M. Synthesis and Characterization of Zno-Tio2/Carbon Fiber Composite with Enhanced Photocatalytic Properties. *Nanomaterials* **1960**, *10*, 960. [CrossRef]
6. Dang, T.; Zhao, M. The Application of Smart Fibers and Smart Textiles. *J. Phys. Conf. Ser.* **2021**, *1790*, 12084. [CrossRef]
7. Ferrara, M.; Bengisu, M. *Materials That Change Color: Smart Materials, Intelligent Design*; Springer Briefs in Applied Sciences and Technology; Springer: Cham, Switzerland, 2013; ISBN 3319002899.
8. Khattab, T.A.; Rehan, M.; Hamouda, T. Smart Textile Framework: Photochromic and Fluorescent Cellulosic Fabric Printed by Strontium Aluminate Pigment. *Carbohydr. Polym.* **2018**, *195*, 143–152. [CrossRef]
9. Bashari, A.; Shakeri, M.; Shirvan, A.R. *UV-Protective Textiles*; Elsevier Ltd.: Amsterdam, The Netherlands, 2018; ISBN 9780081024911.
10. Karpagam, K.R.; Saranya, K.S.; Gopinathan, J.; Bhattacharyya, A. Development of Smart Clothing for Military Applications Using Thermochromic Colorants. *J. Text. Inst.* **2017**, *108*, 1122–1127. [CrossRef]
11. Seipel, S.; Yu, J.; Viková, M.; Vik, M.; Koldinská, M.; Havelka, A.; Nierstrasz, V.A. Color Performance, Durability and Handle of Inkjet-Printed and UV-Cured Photochromic Textiles for Multi-Colored Applications. *Fibers Polym.* **2019**, *20*, 1424–1435. [CrossRef]
12. Seipel, S.; Yu, J.; Periyasamy, A.P.; Viková, M.; Vik, M.; Nierstrasz, V.A. Inkjet Printing and UV-LED Curing of Photochromic Dyes for Functional and Smart Textile Applications. *RSC Adv.* **2018**, *8*, 28395–28404. [CrossRef]
13. Wu, S.; Fan, J.; Wang, W.; Yu, D. Smart Screen-Printed Photochromic Fabrics with Fast Color Switching Performance and High Fatigue Resistance for Energy Storage Applications. *Colloids Surf. A Physicochem. Eng. Asp.* **2022**, *632*, 127760. [CrossRef]
14. Zheng, Y.; Panatdasirisuk, W.; Liu, J.; Tong, A.; Xiang, Y.; Yang, S. Patterned, Wearable UV Indicators from Electrospun Photochromic Fibers and Yarns. *Adv. Mater. Technol.* **2020**, *5*, 2000564. [CrossRef]
15. He, Z.; Wang, W.; Fan, J.; Bao, B.; Qin, X.; Yu, D. Photochromic Microcapsules Anchored on Cotton Fabric by Layer-by-Layer Self-Assembly Method with Erasable Property. *React. Funct. Polym.* **2020**, *157*, 104762. [CrossRef]
16. Abate, M.T.; Seipel, S.; Yu, J.; Viková, M.; Vik, M.; Ferri, A.; Guan, J.; Chen, G.; Nierstrasz, V. Supercritical $CO_2$ Dyeing of Polyester Fabric with Photochromic Dyes to Fabricate UV Sensing Smart Textiles. *Dye. Pigment.* **2020**, *183*, 108671. [CrossRef]
17. Billah, S.M.R.; Christie, R.M.; Shamey, R. Direct Coloration of Textiles with Photochromic Dyes. Part 3: Dyeing of Wool with Photochromic Acid Dyes. *Color. Technol.* **2012**, *128*, 488–492. [CrossRef]
18. He, Z.; Bao, B.; Fan, J.; Wang, W.; Yu, D. Photochromic Cotton Fabric Based on Microcapsule Technology with Anti-Fouling Properties. *Colloids Surf. A Physicochem. Eng. Asp.* **2020**, *594*, 124661. [CrossRef]
19. Liu, X.; Cheng, T.; Parhizkar, M.; Wang, X.; Lin, T. Photochromic Textiles from Hybrid Silica Coating with Improved Photostability. *Res. J. Text. Appar.* **2010**, *14*, 1–8. [CrossRef]
20. Parhizkar, M.; Zhao, Y.; Wang, X.; Lin, T. Photostability and Durability Properties of Photochromic Organosilica Coating on Fabric. *J. Eng. Fibers Fabr.* **2014**, *9*, 155892501400900320. [CrossRef]
21. Pinto, T.V.; Costa, P.; Sousa, C.M.; Sousa, C.A.D.; Pereira, C.; Silva, C.J.S.M.; Pereira, M.F.R.; Coelho, P.J.; Freire, C. Screen-Printed Photochromic Textiles through New Inks Based on $SiO_2$@naphthopyran Nanoparticles. *ACS Appl. Mater. Interfaces* **2016**, *8*, 28935–28945. [CrossRef]
22. Ling, Z.; Liu, K.; Zou, Q.; Li, Q.; Zhang, K.-Q.; Cui, Z.; Yuan, W.; Liu, Y. Continuous and Rapid Fabrication of Photochromic Fibers by Facilely Coating Tungsten Oxide/Polyvinyl Alcohol Composites. *RSC Adv.* **2018**, *8*, 28581–28587. [CrossRef]
23. Wang, X.; Wang, W.; Li, Y.; Wang, Y. Preparation of Tungsten-Based Polyvinyl Alcohol Waterborne Coating and Development of Photochromic Composite Fabric. *Macromol. Mater. Eng.* **2021**, *306*, 2100540. [CrossRef]
24. Fang, W.; Sairanen, E.; Vuori, S.; Rissanen, M.; Norrbo, I.; Lastusaari, M.; Sixta, H. UV-Sensing Cellulose Fibers Manufactured by Direct Incorporation of Photochromic Minerals. *ACS Sustain. Chem. Eng.* **2021**, *9*, 16338–16346. [CrossRef]
25. Bao, B.; Fan, J.; Wang, Z.; Wang, Y.; Wang, W.; Qin, X.; Yu, D. Sodium Deca-Tungstate/Polyacrylic Acid Self-Assembled Flexible Wearable Photochromic Composite Fabric for Solar UV Detector. *Compos. Part B Eng.* **2020**, *202*, 108464. [CrossRef]
26. Wei, J.; Jiao, X.; Wang, T.; Chen, D. Electrospun Photochromic Hybrid Membranes for Flexible Rewritable Media. *ACS Appl. Mater. Interfaces* **2016**, *8*, 29713–29720. [CrossRef] [PubMed]
27. He, T.; Yao, J.N. Photochromism in Transition-Metal Oxides. *Res. Chem. Intermed.* **2004**, *30*, 459–488. [CrossRef]
28. He, T.; Yao, J. Photochromism in Composite and Hybrid Materials Based on Transition-Metal Oxides and Polyoxometalates. *Prog. Mater. Sci.* **2006**, *51*, 810–879. [CrossRef]
29. He, T.; Ma, Y.; Cao, Y.; Hu, X.; Liu, H.; Zhang, G.; Yang, W.; Yao, J. Photochromism of $WO_3$ Colloids Combined with $TiO_2$ Nanoparticles. *J. Phys. Chem. B* **2002**, *106*, 12670–12676. [CrossRef]
30. Li, H.; Wu, H.; Xiao, J.; Su, Y.; Robichaud, J.; Brüning, R.; Djaoued, Y. A Hierarchically Porous Anatase $TiO_2$ Coated-$WO_3$ 2D IO Bilayer Film and Its Photochromic Properties. *Chem. Commun.* **2016**, *52*, 892–895. [CrossRef]
31. Radhika, T.; Ramalingam, R.J.; Aneesha, V.; Albaqami, M.D. Synthesis and Characterization of Photochromic Inkless Coating Based on $WO_3$-Titania Nanocomposite under Sun Light and Solar Simulation Condition. *Optik* **2021**, *228*, 166145. [CrossRef]
32. Djaoued, Y.; Balaji, S.; Beaudoin, N. Sol–Gel Synthesis of Mesoporous $WO_3$–$TiO_2$ Composite Thin Films for Photochromic Devices. *J. Sol-Gel Sci. Technol.* **2013**, *65*, 374–383. [CrossRef]
33. Li, R.; Zhou, Y.; Shao, Z.; Zhao, S.; Chang, T.; Huang, A.; Li, N.; Ji, S.; Jin, P. Enhanced Coloration/Bleaching Photochromic Performance of WO3 Based on PVP/PU Composite Matrix. *ChemistrySelect* **2019**, *4*, 9817–9821. [CrossRef]

34. Scarfiello, R.; Prontera, C.T.; Pugliese, M.; Bianco, G.V.; Bruno, G.; Nobile, C.; Carallo, S.; Fiore, A.; Sibillano, T.; Giannini, C.; et al. Electrochromic Evaluation of Airbrushed Water-Dispersible $W_{18}O_{49}$ Nanorods Obtained by Microwave-Assisted Synthesis. *Nanotechnology* **2021**, *32*, 215709. [CrossRef] [PubMed]
35. Yao, J.N.; Loo, B.H.; Hashimoto, K.; Fujishima, A. Photochromic Characteristics of Mixed $WO_3$–$MoO_3$ Thin Films in Alcohol Vapors. *Ber. Der Bunsenges. Für Phys. Chem.* **1991**, *95*, 554–556. [CrossRef]
36. Tatsuma, T.; Saitoh, S.; Ngaotrakanwiwat, P.; Ohko, Y.; Fujishima, A. Energy Storage of $TiO_2$-$WO_3$ Photocatalysis Systems in the Gas Phase. *Langmuir* **2002**, *18*, 7777–7779. [CrossRef]

*textiles*

MDPI

*Communication*

# 50/60 Hz Power Grid Noise as a Skin Contact Measure of Textile ECG Electrodes

**Khorolsuren Tuvshinbayar [1], Guido Ehrmann [2] and Andrea Ehrmann [1,*]**

[1] Faculty of Engineering and Mathematics, Bielefeld University of Applied Sciences, 33619 Bielefeld, Germany; khorolsuren.tuvshinbayar@fh-bielefeld.de
[2] Virtual Institute of Applied Research on Advanced Materials (VIARAM); guido.ehrmann@gmx.de
* Correspondence: andrea.ehrmann@fh-bielefeld.de

**Abstract:** The electrocardiogram (ECG) is one of the most commonly measured biosignals. In particular, textile electrodes allow for the measuring of long-term ECG without skin irritation or other discomforts for the patient. Such textile electrodes, however, usually suffer from insufficient or unreliable skin contact. Thus, developing textile electrodes is impeded by the often-complicated differentiation between signal artifacts due to moving and breathing and artifacts related to unreliable skin contact. Here, we suggest a simple method of using 50/60 Hz power grid noise to evaluate the skin contact of different textile electrodes in comparison with commercial glued electrodes. We use this method to show the drying of wetted skin under an embroidered electrode as well as sweating of the originally dry skin under a coated electrode with high water vapor resistance.

**Keywords:** electrocardiogram (ECG); Arduino; electrodes; conductive coating; conductive yarn; sensor

**Citation:** Tuvshinbayar, K.; Ehrmann, G.; Ehrmann, A. 50/60 Hz Power Grid Noise as a Skin Contact Measure of Textile ECG Electrodes. *Textiles* **2022**, *2*, 265–274. https://doi.org/10.3390/textiles2020014

Academic Editors: Laurent Dufossé and Philippe Boisse

Received: 28 March 2022
Accepted: 18 April 2022
Published: 1 May 2022



## 1. Introduction

Cardiac diseases are among the most frequent causes of death in the US [1] and many other countries worldwide [2]. Measuring the electrocardiogram (ECG) of a person is thus one of the procedures often applied in patients with heart-related health issues.

The 12-lead ECG contains six precordial leads according to Wilson, three limb leads according to Einthoven, and three augmented limb leads according to Goldberger and allows full observation of all electrical processes in the heart because of the large number of different measurement directions across the heart [3,4]. For long-term observations, common glued gel electrodes can cause skin irritation and reduce the comfort of the patient. This is why several research projects have aimed at developing textile ECG electrodes [5–10].

The main problem with such textile ECG electrodes is related to skin contact. While commercial gel electrodes create contact between uneven skin and a small metal electrode via a conductive gel, which is soft enough to follow the skin structure, more rigid materials necessitate a certain pressure to enable sufficient contact [11–15]. Moreover, the structure of the textile fabric significantly influences the signal quality [16–19]. In addition, conductive coatings can not only improve skin contact but also result in a thin sweat film, which also improves electric contact [20–23].

In addition, noise from movements, breathing, muscle tonus, and other body-based signals or from the typical power supply of the 50/60 Hz interference has to be canceled, such as by wavelet transform [24–26], adaptive filters [25,27,28], and many others [29–32].

Currently, many approaches to measuring biosignals are based on single-circuit boards, such as Arduino or Raspberry, or even smaller solutions to enable full textile integration [33,34], which may be insufficient for highly sophisticated, real-time filtering methods.

Here, we report on an investigation of textile ECG electrodes with an inexpensive sensor module and an Arduino Uno and without additional filtering. Instead, the 50 Hz noise from the local power grid was used to evaluate the signal quality. Open-circuit noise, which is known to occur in open circuits [35], can, in some cases, be used to investigate

the circuit itself [36]. Here, insufficient skin contact has a similar effect. It is known that 50 Hz noise occurs in ECG measurements because of magnetically induced interference, interference currents in the body, and interference currents in the electrode leads [37], and the real part of the impedance between the skin and the electrode generates so-called Johnson noise [38]. However, applying the 50/60 Hz noise as a qualitative measure of the skin–electrode contact has not been reported in the literature yet.

Our measurements show that this simple approach is highly suitable for unambiguously investigating the skin contact of textile and other electrodes and can thus be applied for electrode optimization in future studies before the filtered signals are depicted.

## 2. Materials and Methods

Measurements were performed using an AD8232 (Analog Devices) ECG sensor module, available from Sparkfun [39] and others. This chip is often used for the research of ECG measurements with textile electrodes [40–43]. The instrumentation amplifier typically has a common-mode rejection ratio from DC to 60 Hz of 86 dB [44]. An Arduino Uno, based on the ATmega328P, was used to read and display the ECG real-time signals on the serial plotter and the monitor of the Arduino IDE, respectively, using the sketch suggested by Sparkfun [45]. The three electrodes were also placed on the chest of a proband as suggested in [39], according to Einthoven. Precisely, one electrode was placed above the left breast, the second electrode was placed above the right breast, and the third one was placed on the lowest rip on the right side of the body. Figure 1a depicts a possible connection of the AD8232 (larger red board) to an Arduino (shown here as an Arduino Nano) and three electrode clips with commercial glued electrodes, while Figure 1b shows possible electrode positions on a human, of which the right one was chosen in this study [39].

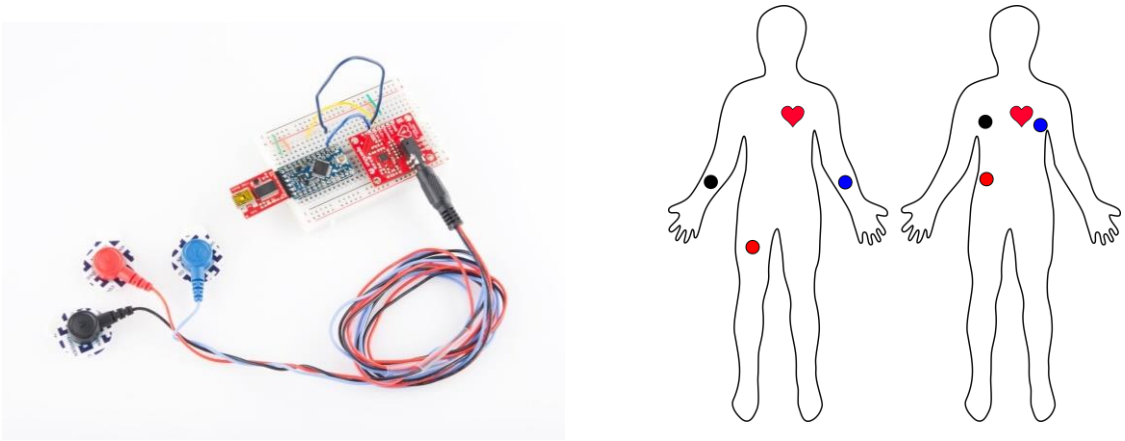

(**a**) (**b**)

**Figure 1.** (**a**) Connection of ECG electrodes to the AD8232, which is connected to an Arduino board on the other side; (**b**) typical electrode positions. From [39], originally published under a CC-BY-SA 4.0 license.

Textile electrodes were produced with areas of approx. 1–2 $cm^2$. The electrodes under investigation were as follows (cf. Figure 2):

- Commercial glued gel electrodes;
- Moss-embroidered electrode from silver-coated yarn Shieldex 235/34 dtex 2-ply HC+B, as also used in [46], named "electrode 8" (Figure 2a);
- Electrode with Shieldex backstitch and elastic blind stitch on jeans, named "electrode 4.3" (from [46], Figure 2b);
- Electrode with Shieldex backstitch and elastic blind stitch on jeans, coated by Powersil (20 mg/$cm^2$, applied in two layers by a squeegee and hardened for 4 h at 60 °C), named "electrode 4.2" (from [46], Figure 2c);

- Powersil coating on cotton without conductive yarn (Figure 2d);
- Ripstop Silver Fabric (Less EMF, NY, USA; Figure 2e);
- Shieldit Super (Less EMF; Figure 2f);
- Hand-sewn Shieldex yarn on Hansaplast Sensitive Fixation plaster (band-aid, Figure 2g);
- Poly(3,4-ethylenedioxythiophene) polystyrene sulfonate (PEDOT:PSS) double-coated woven fabric (Figure 2h);
- Tubicoat ELH [47] coated woven fabric (Figure 2i);
- Graphite foil, also used in [48] (Figure 2j).

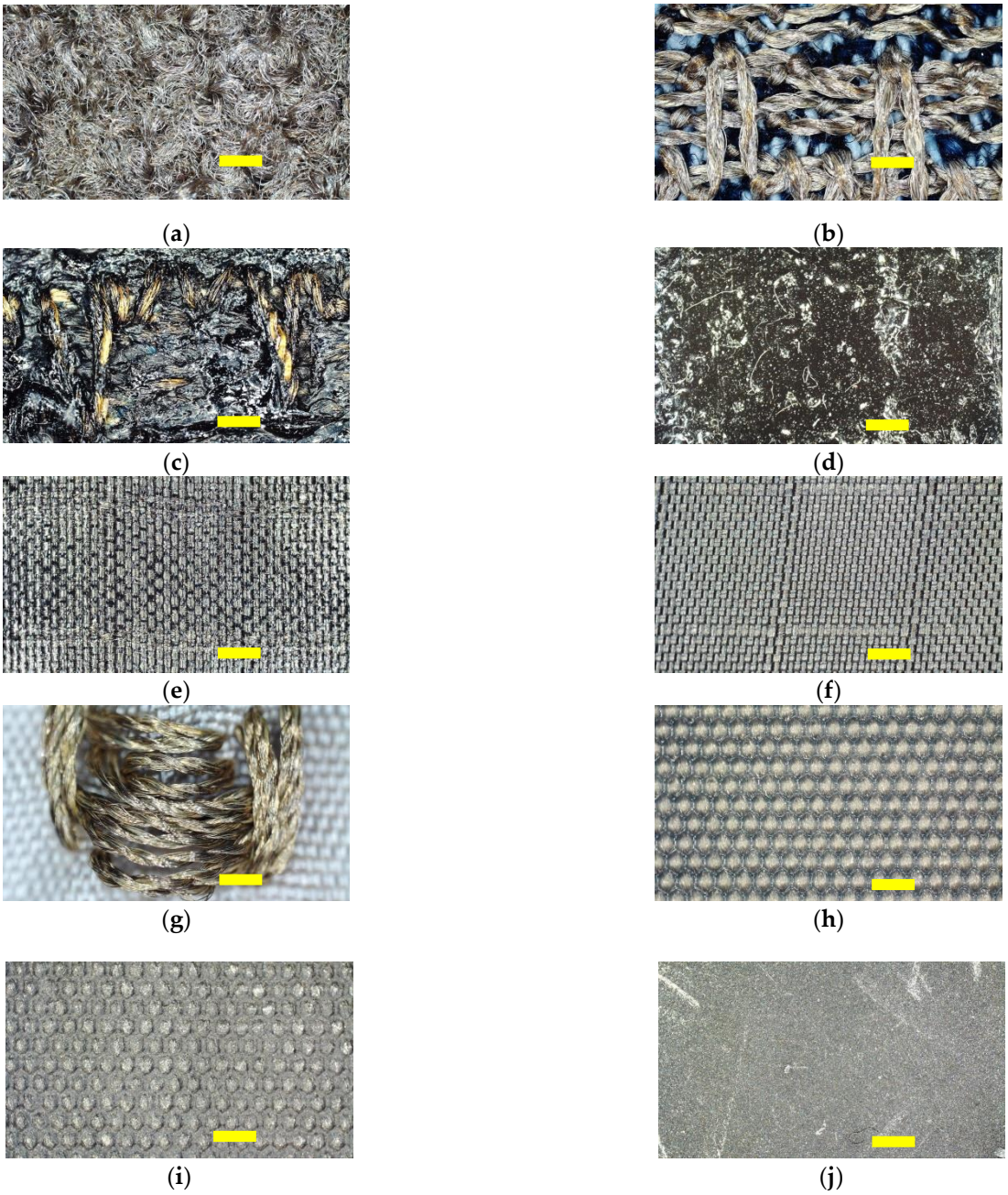


**Figure 2.** Textile electrodes used in this study: (**a**) electrode 8; (**b**) electrode 4.3; (**c**) electrode 4.2; (**d**) Powersil on cotton; (**e**) Ripstop Silver; (**f**) Shieldit Super; (**g**) sewn Shieldex; (**h**) PEDOT:PSS coating; (**i**) Tubicoat coating; (**j**) non-textile graphite foil. Yellow scale bars depict 1 mm.

The moss-embroidered electrode 8 and the stitched electrodes 4.3 and 4.2 were re-used since they were found to be best suited for bioimpedance measurements [46], suggesting that they may also be suitable for ECG measurements.

All electrodes besides the glued gel electrodes were fixed to the skin using Hansaplast Sensitive. While the electrode–skin contact of commercial glued gel electrodes is typically in the range of 1 kΩ to 20 kΩ [37], the skin contact of dry textile electrodes is typically a few hundred kΩ [49]. It is well-known that increased humidity below the electrode reduces skin contact significantly [4,6]; thus, here, additional tests are shown with wetted electrodes as well as with water vapor-resistant electrodes (e.g., graphite foil and electrode 4.2) under which the proband started sweating after a short time.

To investigate the impact of the power grid noise, the setups displayed in Figure 3 were chosen. In one setup, a pure laptop without a connection to the power grid was chosen (upper process), while in the other, the laptop was connected to the power grid by a USB-C docking station, over which the signal from the Arduino was also transferred to the laptop. The first setup was thus expected to show nearly no 50 Hz noise, while in the second setup, the 50 Hz noise from the power grid could influence the signal more strongly.

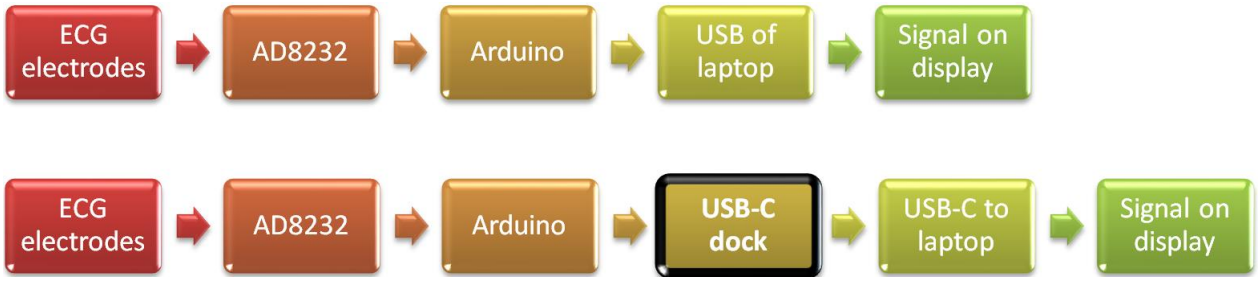


**Figure 3.** ECG measurement with a laptop working in battery mode (**upper process**) or with a laptop connected to the power grid by a common USB-C docking station (**lower process**).

## 3. Results and Discussion

As a reference, Figure 4 shows a measurement with glued electrodes. Data were taken via the serial monitor while the Arduino was attached to a laptop via a docking station, i.e., connected with the grid, in this case working at 50 Hz.

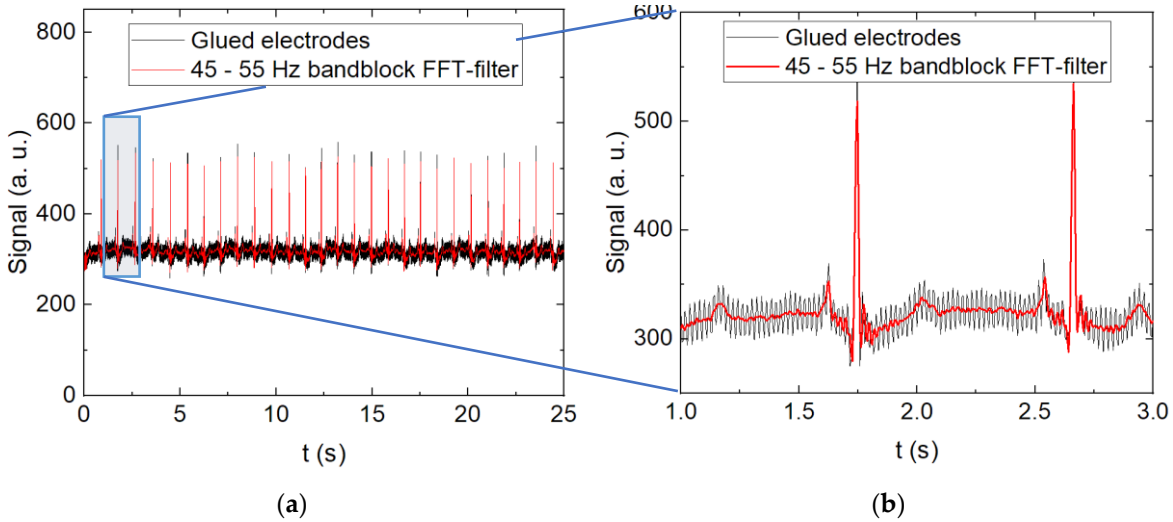


**Figure 4.** ECG measurement with glued electrodes: (**a**) complete measurement; (**b**) magnified excerpt of the area marked in (**a**).

At first glance, Figure 4a shows a noisy measurement with several spikes. Zooming in, Figure 4b reveals that the noise is a 50 Hz interference from the power grid. Apparently, the common-mode rejection—which is used to reduce mains hum—is not sufficient if the Arduino is coupled in the way described here. Further reduction of the 50 Hz noise was performed by a 45–55 Hz bandblock FFT filter applied in Origin 2021 (OriginLab, Northampton, MA, USA). Afterward, a clear ECG signal was visible, with the "spikes" depicting the QRS complexes due to the rapid depolarization of the left and right ventricles (the lower heart chambers), the small P-waves before the QRS complexes showing the depolarization of the atria (the upper heart chambers), and the broader T-waves after the QRS complexes depicting the repolarization of the ventricles.

De-noising the signal using this software filter worked for the complete ECG, as visible in Figure 4a, as well as in all other ECGs that were collected in this study. However, the next tests were performed with the Arduino attached to the pure laptop without a connection to the power grid. The residual 50 Hz noise was very well-filtered by the AD8232 in the case of glued electrodes (not shown here) and for textile electrodes, as depicted in Figure 5.

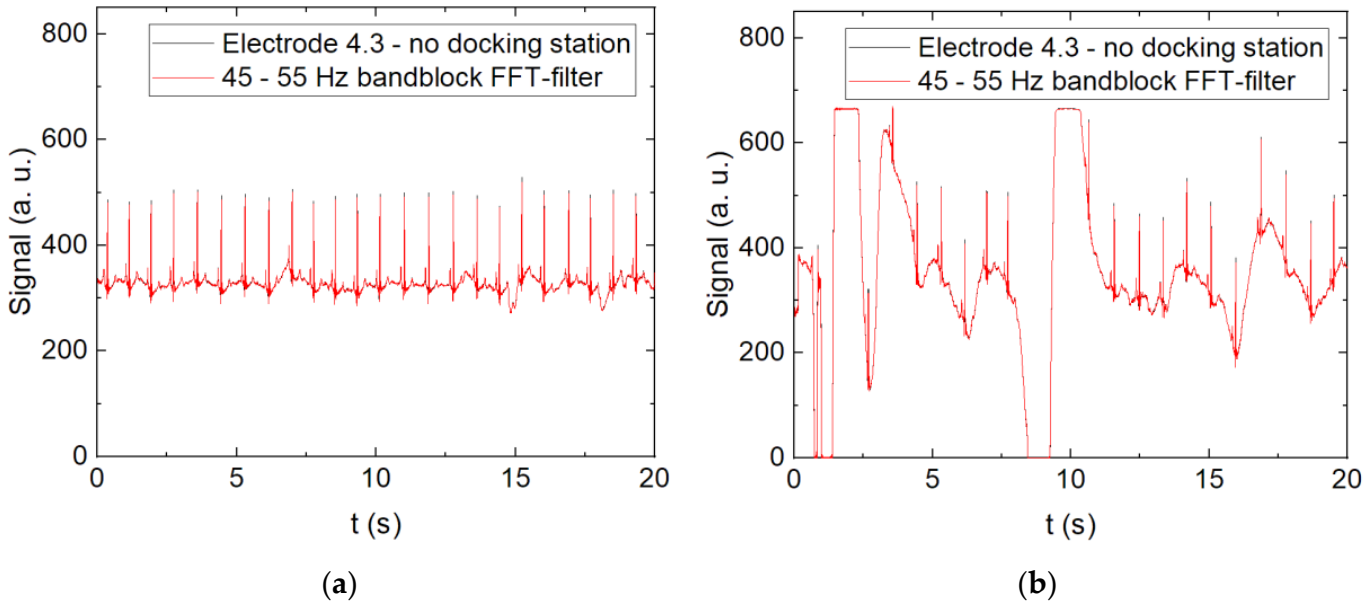


**Figure 5.** ECG measurement with textile electrode 4.3: (**a**) sitting without movement; (**b**) slightly moving.

Figure 5a shows an ECG measurement using textile electrode 4.3 (sewn, without coating) with the proband sitting still. The red (filtered) curve is nearly identical to the black (raw) signal, showing that without direct connection to the power grid, the AD8232 blocked additional 50 Hz noise very well (the same electrode with connection to the docking station is visible in Figure 6b). Nevertheless, a deeper look revealed that the baseline was not flat but showed additional irregular noise. This effect was much more pronounced if the proband moved slightly (Figure 5b), resulting partly in the saturation of the signal and generally in a highly irregular baseline, which makes evaluation of the complete ECG signal quite complicated and nearly impossible as long as no additional high-pass filter suppresses these baseline fluctuations.

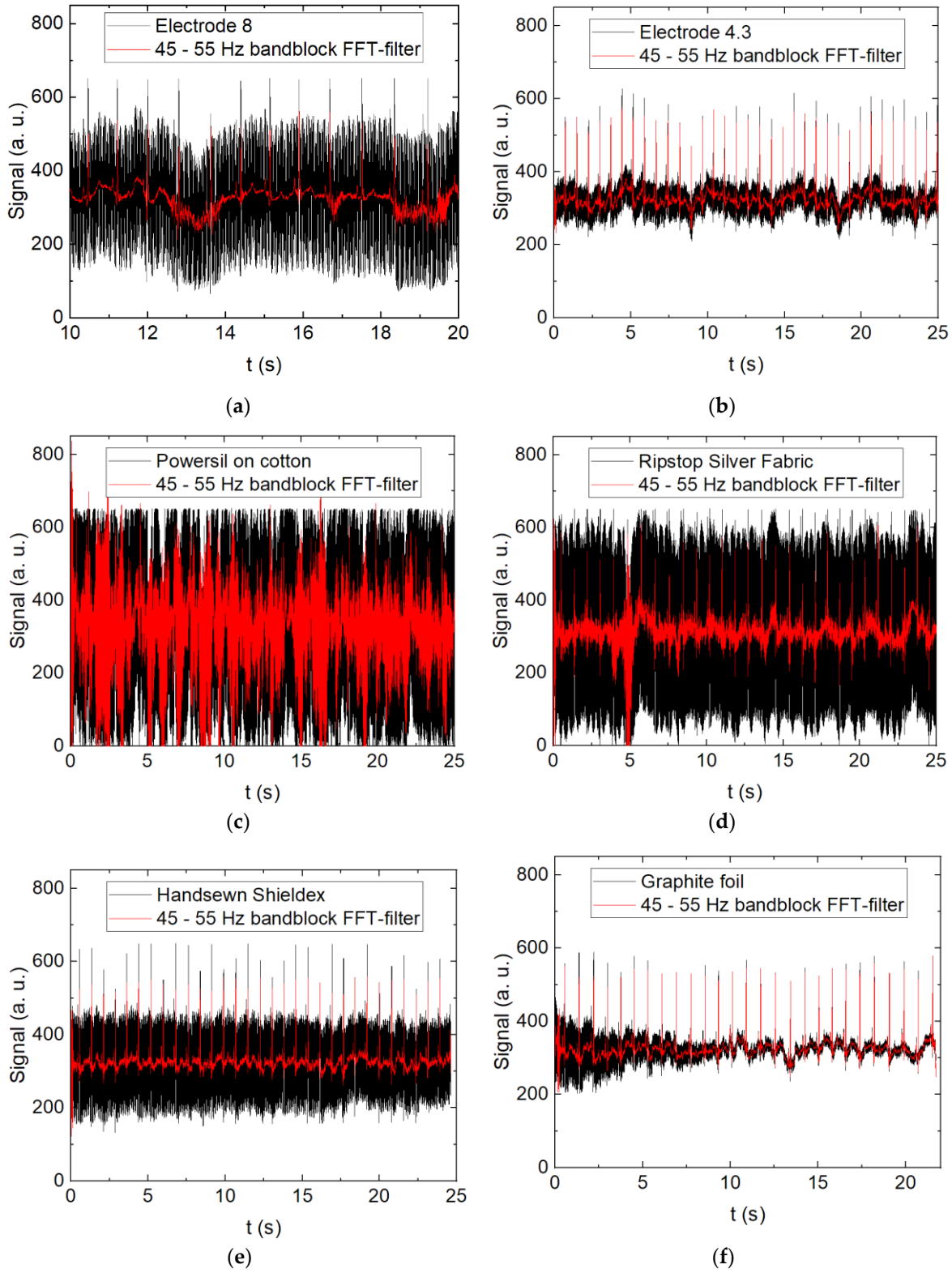


**Figure 6.** ECG measurement with textile electrodes with the laptop attached to the power grid: (**a**) electrode 8; (**b**) electrode 4.3; (**c**) Powersil on cotton; (**d**) Ripstop Silver Fabric; (**e**) handsewn Shieldex yarn; (**f**) non-textile graphite foil.

Comparing Figure 5a,b shows the difficulty in evaluating the quality of a textile electrode—while Figure 5a looks nearly sufficient besides some outliers, Figure 5b shows significant problems with the electrodes. It must be mentioned that only quite small

movements were performed during this measurement, i.e., bending the back more or less and sitting up straight or not, without large movements of the arms for which such disturbed signals could be expected even in the case of glued electrodes.

This finding suggests using the normally undesired 50 Hz noise as a measure of the skin–electrode contact. It is well known that 50 Hz noise occurs especially because of poor contact between skin and electrodes [13]. This is also the case for the baseline drift; however, since the latter is also strongly influenced by breathing and moving, the baseline drift is not a reliable measure of the skin contact with the electrodes under investigation. Figure 6 depicts several measurements over 20–25 s taken with the Arduino attached to the laptop via a docking station, i.e., connected to the grid.

In all cases, only the upper left electrode (left arm) was exchanged for a textile electrode, while both other electrodes were glued electrodes to avoid changes in the position as much as possible. The textile electrode was slightly attached to the skin without applying much pressure to reach full skin contact when the tape buckled slightly.

Comparing these measurements, electrode 8 showed high noise with the QRS complexes visible even in the raw signal and T- and P-waves partly visible in the filtered signal. Electrode 4.3 performed much better but still showed a noisy baseline after filtering. Powersil on cotton did not show any signal, not even the pulse (QRS complex). Similarly, no signals could be detected by Shieldit Super, PEDOT:PSS-coated, and Tubicoat-coated fabrics (not shown here). Ripstop Silver performed slightly better but still showed very high 50 Hz noise, and only the QRS complexes were visible after de-noising, while none of the other features could be extracted from the signal. Interestingly, the simple hand-sewn Shieldex electrode also showed a better signal, but it was still worse than the machine-sewn sample 4.3, most likely since the latter has a denser and more fixed yarn distribution (cf. Figure 2). Finally, the graphite foil, a non-textile reference, showed interesting behavior, starting with an average noise that was clearly reduced after some measurement time.

The latter can be explained by the proband's skin starting to sweat below the air-impermeable foil. As mentioned before, this trick is often used to prepare well-working textile ECG electrodes. In Figure 7, the influence of humidity on the skin is clearly visible. Here, no pressure was exerted onto the textile electrodes so that only very narrow skin contact occurred.

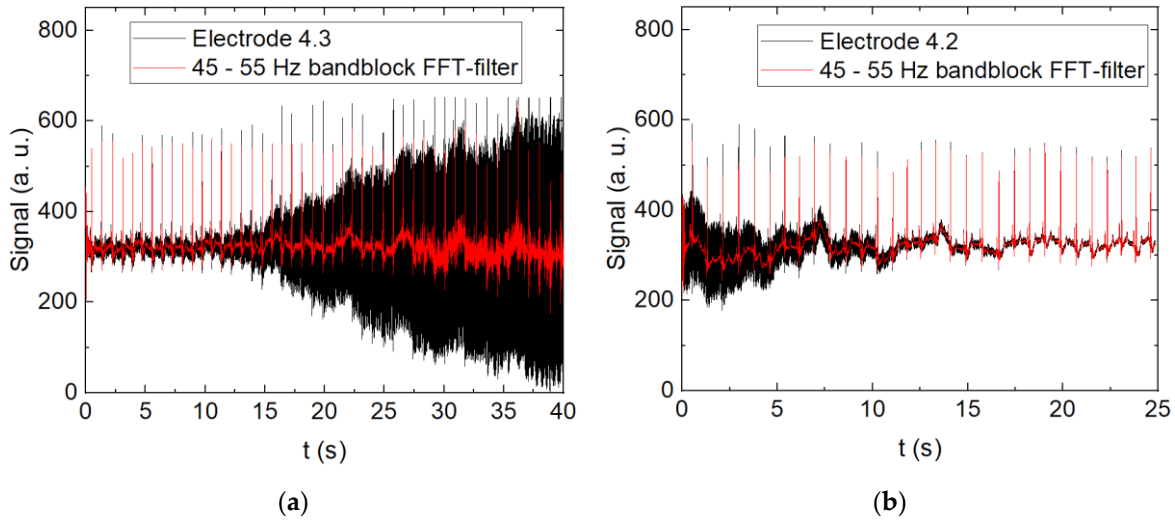


(**a**) (**b**)

**Figure 7.** ECG measurement with textile electrodes: (**a**) electrode 4.3 on pre-wetted skin during drying; (**b**) electrode 4.2.

In the case of the sewn electrode 4.3, the skin was slightly wetted before the measurement by putting a few drops of tap water using the fingers at the respective position. Figure 7a shows that the 50 Hz noise started increasing after approx. 10 s when the skin

dried again by evaporation through the electrode. This process was also visible—on different time scales—for all other textile electrodes without a water-vapor blocking coating, such as Powersil.

On the other hand, electrode 4.2, which was Powersil-coated after sewing, showed the opposite time dependence. Here, the 50 Hz noise was clearly reduced after approx. 20 s since the skin started sweating slightly under this air-impermeable electrode. In both cases, the noise of the textile electrodes on slightly wet skin was comparable to the noise of the commercial glued gel electrodes.

As these examples show, the undesired 50 Hz noise can be used as a simple tool to evaluate the skin contact of textile electrodes.

## 4. Conclusions

Several textile ECG electrodes were evaluated with respect to their skin contact compared with commercial glued gel electrodes. Measurements were performed with an inexpensive ECG module based on the AD8232 chip. The inevitable 50 Hz noise, visible in all measurements in which the laptop for data acquisition was connected to the power grid, was used to evaluate the skin–electrode contact. This simple method is suggested as a possibility to rate the skin contact of textile electrodes in future developments.

Regarding the choice of textile ECG electrodes, none of the tested ones worked well on dry skin. Electrode 4.2, containing a Powersil coating under which the proband started sweating slightly, gave the best results. This indicates that, if the electrodes are not meant for sports but for daily use, a coating that supports sweating is indispensable for textile ECG electrodes.

**Author Contributions:** Conceptualization, G.E. and A.E.; formal analysis, A.E.; investigation, K.T. and A.E.; writing—original draft preparation, A.E.; writing—review and editing, K.T. and G.E.; visualization, A.E. All authors have read and agreed to the published version of the manuscript.

**Funding:** This research was partly funded by the German Federal Ministry of Education and Research (BMBF), grant number 13GW0202C.

**Institutional Review Board Statement:** Not applicable.

**Informed Consent Statement:** Informed consent was obtained from all subjects involved in the study.

**Data Availability Statement:** All obtained data are shown in the paper.

**Conflicts of Interest:** The authors declare no conflict of interest. The funders had no role in the design of the study; in the collection, analyses, or interpretation of data; in the writing of the manuscript; or in the decision to publish the results.

## References

1. Ahmad, F.B.; Anderson, R.N. The leading causes of death in the US for 2020. *JAMA* **2021**, *325*, 1829–1830. [CrossRef]
2. Ritchie, H.; Roser, M. Causes of Death. *Our World in Data* **2018**. Available online: https://ourworldindata.org/causes-of-death (accessed on 7 January 2022).
3. Armstrong, W.F.; Jordan, J.W. Prevalence and magnitude of ST-segment and T wave abnormalities in men during continuous ambulatory electrocardiography. *Am. J. Cardiol.* **1981**, *49*, 249–251.
4. Trummer, S.; Ehrmann, A.; Büsgen, A. Development of underwear with integrated 12 channel ECG for men and women. *AUTEX Res. J.* **2017**, *17*, 344–349. [CrossRef]
5. Coosemans, J.; Hermans, B.; Puers, R. Integrating wireless ECG monitoring in textiles. *Sens. Actuators A Phys.* **2006**, *130–131*, 48–53. [CrossRef]
6. Aumann, S.; Trummer, S.; Brücken, A.; Ehrmann, A.; Büsgen, A. Conceptual design of a sensory shirt for fire-fighters. *Text. Res. J.* **2014**, *84*, 1661–1665. [CrossRef]
7. Lee, E.; Kim, H.; Liu, H.; Cho, G. Exploration of AgNW/PU nanoweb as ECG textile electrodes and comparison with Ag/AgCl electrodes. *Fibers Polym.* **2017**, *18*, 1749–1753. [CrossRef]
8. Matsouka, D.; Vassiliadis, S.; Tao, X.; Koncar, V.; Bahadir, S.K.; Kalaoglu, F.; Jevsnik, S. Electrical connection issues on wearable electronics. *IOP Conf. Ser. Mater. Sci. Eng.* **2018**, *459*, 012017. [CrossRef]
9. An, X.; Stylios, G.K. A hybrid textile electrode for electrocardiogram (ECG) measurement and motion tracking. *Materials* **2018**, *11*, 1887. [CrossRef]

10. Ehrmann, G.; Ehrmann, A. Electronic textiles. *Encyclopedia* **2021**, *1*, 115–130. [CrossRef]
11. Pani, D.; Achilli, A.; Bonfiglio, A. Survey on Textile Electrode Technologies for Electrocardiographic (ECG) Monitoring, from Metal Wires to Polymers. *Adv. Mater. Technol.* **2018**, *3*, 1800008. [CrossRef]
12. An, X.; Tangsirinaruenart, O.; Stylios, G.K. Investigating the performance of dry textile electrodes for wearable end-uses. *J. Text. Inst.* **2019**, *110*, 151–158. [CrossRef]
13. Takeshita, T.; Yoshida, M.; Takei, Y.; Ouchi, A.; Hinoki, A.; Uchida, H.; Kobayashi, T. Relationship between Contact Pressure and Motion Artifacts in ECG Measurement with Electrostatic Flocked Electrodes Fabricated on Textile. *Sci. Rep.* **2019**, *9*, 5897. [CrossRef] [PubMed]
14. Nigusse, A.B.; Malengier, B.; Mengistie, D.A.; Tseghai, G.B.; van Langenhove, L. Development of Washable Silver Printed Textile Electrodes for Long-Term ECG Monitoring. *Sensors* **2020**, *20*, 6233. [CrossRef]
15. Euler, L.; Guo, L.; Persson, N.-K. Textile Electrodes: Influence of Knitting Construction and Pressure on the Contact Impedance. *Sensors* **2021**, *21*, 1578. [CrossRef]
16. Acar, G.; Ozturk, O.; Golparvar, A.J.; Elboshra, T.A.; Böhringer, K.; Yapici, M.K. Wearable and Flexible Textile Electrodes for Biopotential Signal Monitoring: A review. *Electronics* **2019**, *8*, 479. [CrossRef]
17. Zhang, X.; Zhong, Y.Q. Development of woven textile electrodes with enhanced moisture-wicking properties. *J. Text. Inst.* **2021**, *112*, 983–995. [CrossRef]
18. Terada, T.; Toyoura, M.; Sato, T.; Mao, X.Y. Noise-Reducing Fabric Electrode for ECG Measurement. *Sensors* **2021**, *21*, 4305. [CrossRef]
19. Uz Zaman, S.; Tao, X.Y.; Cochrane, C.; Koncar, V. Smart E-Textile Systems: A Review for Healthcare Applications. *Electronics* **2022**, *11*, 99. [CrossRef]
20. Schäl, P.; Juhász Junger, I.; Grimmelsmann, N.; Ehrmann, A. Development of graphite-based conductive textile coatings. *J. Coat. Technol. Res.* **2018**, *15*, 875–883. [CrossRef]
21. Ankhili, A.; Tao, X.Y.; Cochrane, C.; Koncar, V.; Coulon, D.; Tarlet, J.-M. Ambulatory Evaluation of ECG Signals Obtained Using Washable Textile-Based Electrodes Made with Chemically Modified PEDOT:PSS. *Sensors* **2019**, *19*, 416. [CrossRef]
22. Shathi, M.A.; Chen, M.Z.; Khoso, N.A.; Rahman, M.T.; Thattacharjee, B. Graphene coated textile based highly flexible and washable sports bra for human health monitoring. *Mater. Des.* **2020**, *193*, 108792. [CrossRef]
23. Tseghai, G.B.; Melengier, B.; Fante, K.A.; Nigusse, A.B.; Etana, B.B.; van Langenhove, L. PEDOT:PSS/PDMS-Coated Cotton Fabric for ECG Electrode. In Proceedings of the 2020 IEEE International Conference on Flexible and Printable Sensors and Systems (FLEPS), Manchester, UK, 16–19 August 2020; pp. 1–4.
24. Xu, X.W.; Liang, Y.; He, P.; Yang, J.L. Adaptive Motion Artifact Reduction Based on Empirical Wavelet Transform and Wavelet Thresholding for the Non-Contact ECG Monitoring Systems. *Sensors* **2019**, *19*, 2916. [CrossRef]
25. Xiong, F.; Chen, D.Y.; Huang, M. A Wavelet Adaptive Cancellation Algorithm Based on Multi-Inertial Sensors for the Reduction of Motion Artifacts in Ambulatory ECGs. *Sensors* **2020**, *20*, 970. [CrossRef]
26. An, X.; Stylios, G.K. Comparison of Motion Artefact Reduction Methods and the Implementation of Adaptive Motion Artefact Reduction in Wearable Electrocardiogram Monitoring. *Sensors* **2020**, *20*, 1468. [CrossRef]
27. Xiong, F.; Chen, D.Y.; Chen, Z.H.; Dai, S.M. Cancellation of motion artifacts in ambulatory ECG signals using TD-LMS adaptive filtering techniques. *J. Vis. Commun. Image Represent.* **2019**, *58*, 606–618. [CrossRef]
28. Huang, M.; Chen, D.Y.; Xiong, F. An Effective Adaptive Filter to Reduce Motion Artifacts from ECG Signals Using Accelerometer. In Proceedings of the 2019 9th International Conference on Biomedical Engineering and Technology, Tokyo, Japan, 28–30 March 2019; pp. 83–88.
29. Suchetha, M.; Kumaravel, N.; Jagannath, M.; Jaganathan, S.K. A comparative analysis of EMD based filtering methods for 50 Hz noise cancellation in ECG signal. *Inform. Med. Unlocked* **2017**, *8*, 54–59. [CrossRef]
30. Babusiak, B.; Borik, S.; Balogova, L. Textile electrodes in capacitive signal sensing applications. *Measurement* **2018**, *114*, 69–77. [CrossRef]
31. Fink, P.L.; Sayem, A.S.M.; Teay, S.H.; Ahmad, F.; Shahariar, H.; Albarbar, A. Development and wearer trial of ECG-garment with textile-based dry electrodes. *Sens. Actuators A Phys.* **2021**, *328*, 112784. [CrossRef]
32. Nikolova, E.; Ganev, B.; Gieva, E. Wearable Intelligent Textile Suits for Telemetry Monitoring in Pediatrics. In Proceedings of the 2021 XXX International Scientific Conference Electronics (ET), Sozopol, Bulgaria, 15–17 September 2021; pp. 1–6.
33. Ehrmann, G.; Ehrmann, A. Suitability of common single circuit boards for sensing and actuating in smart textiles. *CDATP* **2020**, *1*, 170–179. [CrossRef]
34. Ehrmann, G.; Blachowicz, T.; Homburg, S.V.; Ehrmann, A. Measuring biosignals with single circuit boards. *Bioengineering* **2020**, *9*, 84. [CrossRef]
35. Searson, P.C.; Dawson, J.L. Analysis of electrochemical noise generated by corroding electrodes under open-circuit conditions. *J. Electrochem. Soc.* **1988**, *135*, 1908. [CrossRef]
36. Rothenhagen, K.; Fuchs, F.W. Performance of Diagnosis Methods for IGBT Open Circuit Faults in Voltage Source Active Rectifiers. In Proceedings of the 2004 IEEE 35th Annual Power Electronics Specialists Conference, Aachen, Germany, 20–25 June 2004; pp. 4348–4354.
37. Wan, S.W.S.; Nguyen, H.T. 50 Hz interference and noise in ECG recordings—A review. *Australas. Phys. Eng. Sci. Med.* **1994**, *17*, 108–115.

38. Fernandez, M.; Pallas-Areny, R. Electrode Contact Noise in Surface Biopotential Measurements. In Proceedings of the 14th Annual International Conference of the IEEE in Medicine and Biology Society, Paris, France, 29 October–1 November 1992; pp. 123–124.
39. Sparkfun. AD8232 Heart Rate Monitor Hookup Guide. Available online: https://learn.sparkfun.com/tutorials/ad8232-heart-rate-monitor-hookup-guide/all (accessed on 7 January 2022).
40. Prasad, A.S.; Kavanashree, N. ECG Monitoring System Using AD8232 Sensor. In Proceedings of the 2019 International Conference on Communication and Electronics Systems (ICCES), Coimbatore, India, 17–19 July 2019; pp. 976–980.
41. Wu, T.Y.; Redouté, J.-M.; Yuce, M. AWearable, Low-Power, Real-Time ECG Monitor for Smart T-shirt and IoT Healthcare Applications. In *Advances in Body Area Networks I*; Fortino, H., Wang, Z., Eds.; Internet of Things; Springer: Cham, Switzerland, 2019; pp. 165–173.
42. Simanjuntak, J.E.S.; Khodra, M.L.; Manullang, M.C.T. Design Methods of Detecting Atrial Fibrillation Using the Recurrent Neural Network Algorithm on the Arduino AD8232 ECG Module. *IOP Conf. Ser. Earth Environ. Sci.* **2019**, *537*, 012022. [CrossRef]
43. Malek, A.S.; Elnahrawy, A.; Anwar, H.; Naeem, M. From fabric to smart T-shirt: Fine tuning an improved robust system to detect arrhythmia. *Textile Res. J.* **2021**. *online first*. [CrossRef]
44. Analog Devices. Single-Lead, Heart Rate Monitor Front End AD8232 Data Sheet. Available online: https://www.analog.com/media/en/technical-documentation/data-sheets/ad8232.pdf (accessed on 7 January 2022).
45. Sparkfun/AD8232_Heart_Rate_Monitor. Available online: https://github.com/sparkfun/AD8232_Heart_Rate_Monitor (accessed on 7 January 2022).
46. Meding, J.T.; Tuvshinbayar, K.; Döpke, C.; Tamoue, F. Textile electrodes for bioimpedance measuring. *Commun. Dev. Assem. Text. Prod.* **2021**, *2*, 49–60. [CrossRef]
47. Graßmann, C.; Mann, M.; van Langenhove, L.; Schwarz-Pfeiffer, A. Textile Based Electrochromic Cells Prepared with PEDOT: PSS and Gelled Electrolyte. *Sensors* **2020**, *20*, 5691. [CrossRef]
48. Hellert, C.; Wortmann, M.; Frese, N.; Grötsch, G.; Cornelißen, C.; Ehrmann, A. Adhesion of Electrospun Poly(acrylonitrile) Nanofibers on Conductive and Isolating Foil Substrates. *Coatings* **2021**, *11*, 249. [CrossRef]
49. Popovic-Maneski, L.; Ivanovic, M.D.; Atanasoski, V.; Miletic, M.; Zdolsek, S.; Bojovic, B.; Hadzievski, L. Properties of different types of dry electrodes for wearable smart monitoring devices. *Biomed. Eng.* **2020**, *65*, 405–415. [CrossRef]

*textiles*

MDPI

*Article*

# Characterizing Steam Penetration through Thermal Protective Fabric Materials

**Sumit Mandal [1,*] and Guowen Song [2]**

[1] Department of Design, Housing and Merchandising, Oklahoma State University, Stillwater, OK 74078, USA
[2] Department of AESHM, Iowa State University, Ames, IA 50010, USA; gwsong@iastate.edu
* Correspondence: sumit.mandal@okstate.edu

**Abstract:** This study performs an analysis of steam penetration through thermal protective fabric materials. Different, multilayered thermal protective fabrics were selected and tested in a laboratory-simulated steam exposure, and their steam protective performance (SPP) was measured in terms of the time required to generate second-degree burns on the bodies of wearers. Additionally, the total transmitted thermal energy (TTTE) through the fabrics during testing was measured. Through statistical analysis, it was established that fabric properties, namely air permeability and thickness, are the key factors that affect the SPP and TTTE; the relationship among the fabric properties, SPP, and TTTE is also summarized. Theoretically, it has been found that heat and mass (steam) transfer occur through fabrics in the course of steam exposure, which mainly affect the SPP and TTTE. This study could help textile/materials engineers to develop high performance thermal protective fabrics for the increased occupational health and safety of firefighters and industrial workers.

**Keywords:** thermal protective fabrics; steam exposure; fabric properties; heat and mass transfer; burn injuries

**Citation:** Mandal, S.; Song, G. Characterizing Steam Penetration through Thermal Protective Fabric Materials. *Textiles* **2022**, *2*, 16–28. https://doi.org/10.3390/textiles2010002

Academic Editor: Laurent Dufossé

Received: 23 November 2021
Accepted: 26 December 2021
Published: 3 January 2022



## 1. Introduction

Firefighters and industrial workers often incur burn injuries when they encounter hazardous thermal exposures while performing their job duties [1–3]. Contextually, it has been identified that water used by firefighters to put out a fire may convert into steam, which may reach the firefighters [4–8]. Additionally, upstream oil and gas industry workers are often exposed to steam while extracting bitumen from oil sands and producing heavy oil [9,10]. As the performance of thermal protective clothing worn by firefighters and industrial workers depends upon the various thermal exposures these workers face in their occupations [11–17], it can be inferred that steam has a significant impact on the thermal protective performance of clothing [4–8]. In steam exposure, a significant amount of thermal energy transfer occurs through clothing, which causes burns to workers in these occupations.

In considering thermal protection and steam exposure, many researchers studied the SPP of fabric materials used in thermal protective clothing [4–8,18–21]. Keiser et al. (2008), Keiser and Rossi (2008), Keiser et al. (2010), Mandal et al. (2013), and Shoda et al. (1998) suggested that imposed high-pressurized steam enters into the fabric structure and gradually condenses [4–8]. After the condensation phase, the steam converts into hot water. This hot water generates burn injuries when it comes into contact with the human body. These researchers identified that a permeable fabric allows more steam transfer toward wearers than an impermeable fabric. As a result, they suggested that thermal protective fabrics should be steam impermeable in nature to provide effective protection from steam exposure. Mandal et al. (2013) further found that the air permeability of the outer layer (shell fabric) is crucial for the SPP of a multilayered thermal protective fabric system (i.e., an assembly of shell fabric, moisture barrier, and/or thermal liner) [7]. They recommended that it

is essential to place a moisture barrier with zero air permeability in the outer layer of multilayered fabric systems in order to achieve a high SPP. This air-impermeable moisture barrier will immediately stop the steam penetration through the fabric system, which will considerably decrease the chances of burns on the bodies of wearers [7,18–24]. Along with air permeability, Desruelle et al. (2002) indicated that the thickness of the fabric systems has a considerable impact on its steam protective performance [25]. Recently, Su et al. (2018) found that fabric thickness insignificantly improves the steam protective performance in comparison to the air permeability of the fabrics [26].

Although previous researchers extensively studied steam penetration through fabrics by evaluating the SPP, only a few studies focused considerably on the TTTE through fabrics in steam exposure of a certain duration [4–10,18–26]. This paper studied experimentally both the SPP and TTTE and identified fabric features affecting both. The SPP is also compared with the flame and radiant heat protective performance of fabrics. Steam penetration through fabric systems was studied based on the theory of heat and mass transfer. This paper will contribute to understanding the mechanisms associated with the heat and mass transfer in fabric systems, and the results obtained could help textile/material engineers to develop fabrics for high performance thermal protective clothing.

## 2. Materials and Methods

In this study, multiple thermal protective fabrics (A–F) were selected for testing (Table 1). These fabrics are commercially available and commonly used in the clothing of firefighters and industrial workers. These fabrics were assembled to produce multilayered fabric systems; these configured fabric systems were A (Fabric-A), B (Fabric-B), AC (Fabric-A + Fabric-C), AE (Fabric-A + Fabric-E), AF (Fabric-A + Fabric-F), FA (Fabric-F + Fabric-A), AFC (Fabric-A + Fabric-F + Fabric-C), AFD (Fabric-A + Fabric-F + Fabric-D), AFE (Fabric-A + Fabric-F + Fabric-E), and FAD (Fabric-F + Fabric-A + Fabric-D). The constructional attributes and physical properties of these fabric systems were measured using the American Society for Testing and Materials (ASTM) standards (Table 2) [27–30]. In this context, it is notable that porosity (the ratio of pore volume to the total volume of the fabrics depending upon the open and closed porosity) is an important fabric property that could affect the steam penetration through fabrics. However, it is difficult to accurately characterize the pore volume because the pore system within a fabric typically forms a very complicated pore surface that is geometrically irregular; in fact, it is also not accurate to define the pore size in terms of the diameter considering the different structures of pores existing in the fabric [31–33]. Considering this situation, although porosity and air permeability are not the same thing, air permeability is measured as an indirect measurement of porosity and is used for explaining the SPP.

Three specimens (200 mm $\times$ 200 mm) of each fabric system were conditioned in a standard atmosphere (21 °C temp. and 65% relative humidity) for 24 h. To understand the steam penetration parameters of the fabric systems, these specimens were tested under steam exposure using the instrument shown in Figure 1. In this test, a specimen of the fabric system was placed on a Teflon-plated specimen holder embedded with a skin simulant sensor. Steam was generated at 150 °C using a 3 kW boiler, and the steam generated was administered at 200 kPa from 50 mm above the specimen through a 4.6 mm nozzle. The skin simulant sensor was used to measure the heat flux, and this heat flux was applied using burn prediction software (programmed according to Henrique's Burn Integral algorithm) to calculate the time required to generate second-degree skin burns [34]. The skin simulant sensor was developed by the University of Alberta in Canada using inorganic material called 'colorceron', which is a mixture of calcium, aluminum, silicate, asbestos fibers, and a binder; and this sensor was calibrated using the standardized Schmidt–Boelter water-cooled sensor [34]. The predicted mean burn time obtained from the three specimens was interpreted as the SPP of the fabric system. The TTTE of the fabric system specimen during (30 s) and after (10 s) of steam exposure was also measured. Subsequently, the fabric properties, SPP, and TTTE values were normalized statistically, and a *t*-test was carried

out using STATCRUNCH software (developed by West of Texas A&M University, USA). The association among the fabric properties, SPP and/or TTTE was inferred based on the sign (+ or −) of the T-stat value obtained from the *t*-test. *p*-values obtained from the *t*-test for all fabric properties were also analyzed. If the *p*-value for any property was less than 0.05, this property was identified as the key property affecting the SPP/TTTE. Relationship plots were developed among the fabric properties, SPP, and/or TTTE; and the coefficient of determination ($R^2$) of the plots developed was calculated. A $R^2$ value with proximity to 1 was inferred as a strong association among the fabric properties, SPP, and/or TTTE. Inference tests (hypothesis test (*p*-value) and a 95% confidence interval (upper and lower limits)) were carried out to understand the differences in the SPP/TTTE of various sets of fabric systems.

**Table 1.** Thermal protective fabrics.

| Constructional Attributes | Fabric Types | | | | | |
|---|---|---|---|---|---|---|
| | **A (Shell Fabric)** | **B (Shell Fabric)** | **C (Thermal Liner)** | **D (Thermal Liner)** | **E (Thermal Liner)** | **F (Moisture Barrier)** |
| **Fiber Content** | Kevlar®-PBI | Fire-retardant cotton fabric with Water Repellent Finish | Nomex® (100%) | Nomex® (100%) | Nomex® (100%) | Nomex®-III (100%) with Polyurethane Coating |
| **Weave Structures** | Plain weave, rip-stop woven | Plain weave with finished surface | Plain weave Nomex® layer quilted to two thin Nomex® oriented webs | Plain weave Nomex® layer quilted to Nomex® needle-felted batt | Plain weave Nomex layer quilted to Nomex scrim, needle-felted batt and scrim | Plain weave Nomex backcoated with polyurethene film |
| **Thickness(mm)** [a] | 0.46 | 0.67 | 1.08 | 2.07 | 3.57 | 1.10 |
| **Weight (g/m$^2$)** [b] | 211.5 | 412.5 | 170.6 | 301.5 | 332.7 | 185.5 |

[a] Measured by the ASTM D 1777: 1996; [b] Measured by the ASTM D 3776: 2009 [27,28].

**Table 2.** Assembled fabric systems.

| Fabric Properties | Fabric Systems | | | | | | | | | |
|---|---|---|---|---|---|---|---|---|---|---|
| | **Single-Layered** | | **Double-Layered** | | | | **Triple-Layered** | | | |
| | **A** | **B** | **AC** | **AE** | **AF** | **FA** | **AFC** | **AFD** | **AFE** | **FAD** |
| **Thickness(mm)** [a] | 0.46 | 0.67 | 1.54 | 4.03 | 1.56 | 1.56 | 2.64 | 3.63 | 5.13 | 3.63 |
| **Weight (g/m$^2$)** | 211.5 | 412.5 | 382.1 | 544.2 | 207 | 207 | 567.6 | 698.5 | 729.7 | 698.5 |
| **Thermal Resistance (Km$^2$/W)** [b] | 0.07 | 0.08 | 0.12 | 0.17 | 0.09 | 0.09 | 0.13 | 0.15 | 0.18 | 0.15 |
| **Air Permeability (cm$^3$/cm$^2$/s)** [c] | 17.1 | 0 | 13.9 | 12.5 | 0 | 0 | 0 | 0 | 0 | 0 |

[a] Measured by the ASTM D 1777; [b] Measured by the ASTM D 1518: 2011; [c] Measured by the ASTM D 737: 2004 [27,29,30].

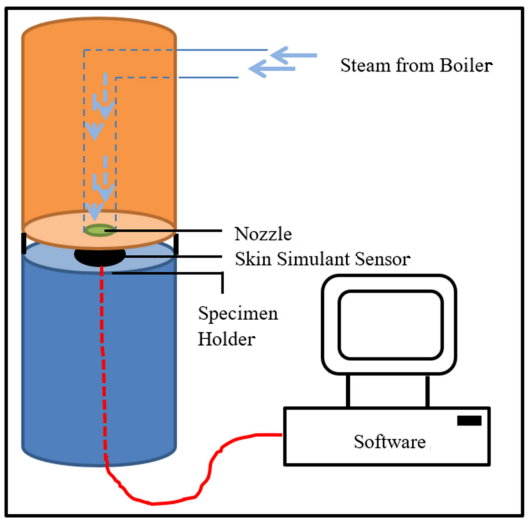


**Figure 1.** Steam exposure test.

## 3. Results and Discussion

The parameters for steam penetration (SPP and TTTE) through the selected fabric systems (obtained from the steam exposure test) are shown in Table 3. The SPP per unit thickness of each fabric system is also calculated and presented in Table 3. Based on the data shown in Table 3, a relationship plot between the SPP and TTTE is displayed in Figure 2. According to Figure 2, the trend line of the plot is negative, and the $R^2$ value is close to 1; hence, a strong negative relationship exists between the SPP and TTTE. From this, it can be inferred that the TTTE through a fabric system is generally low if the fabric system possesses a high SPP. Mandal et al. (2013) previously evaluated the flame and radiant heat protective performance of the same set of fabric systems mentioned in Table 3, which firefighters often encounter in flame and radiant heat exposures [7]. A comparison of these previous results (Table 4) with the SPP values of Table 3 clearly shows that the protective performances of air-permeable fabric systems are significantly lower in steam exposure. This is because flame and radiant heat exposures mainly involve a heat transfer through the fabric systems toward the bodies of wearers [35]; however, in steam exposure, a hot mass transfer mainly occurs through fabric systems. As the mode of thermal energy transfer differs in these exposures, the performance of the fabric systems lowers under steam exposure. In the following section, the effect of fabric features on the SPP/TTTE is established to characterize the steam penetration through the fabric system.

**Table 3.** Steam penetration parameters of fabric systems.

| Steam Penetration Parameters | Fabric Systems | | | | | | | | | |
|---|---|---|---|---|---|---|---|---|---|---|
| | Single-Layered | | Double-Layered | | | | Triple-Layered | | | |
| | A | B | AC | AE | AF | FA | AFC | AFD | AFE | FAD |
| SPP (Second-degree Burn Time in Seconds) | 0.34 | 2.26 | 0.59 | 0.71 | 7.95 | 10.35 | 11.44 | 19.27 | 22.2 | 25.55 |
| TTTE (kJ/m$^2$) | 610.6 | 526.5 | 581.3 | 533.9 | 416.3 | 216.2 | 375.5 | 249.6 | 240.2 | 221.2 |
| SPP/Thickness (Second-degree Burn Time in Seconds/mm) | 0.74 | 3.37 | 0.38 | 0.18 | 5.10 | 6.63 | 4.33 | 5.31 | 4.33 | 7.04 |

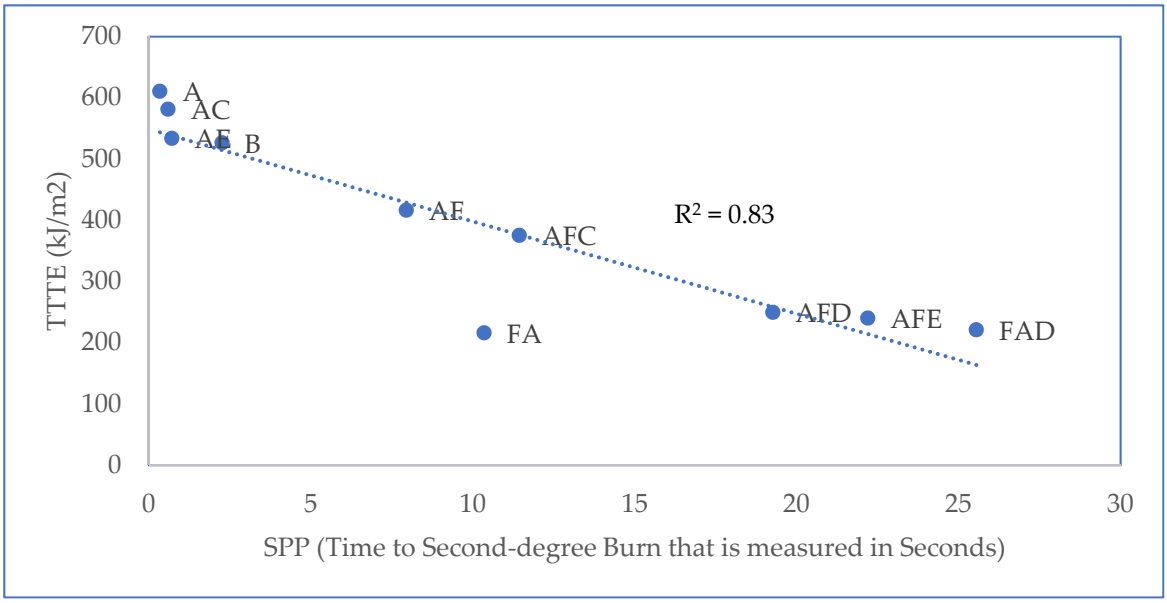


**Figure 2.** Relationship plot between SPP and TTTE.

**Table 4.** Flame and radiant heat protective performance of selected fabric systems [adapted from Mandal, et al. (2013)] [7].

| Protective Performance | | Fabric Systems | | | | | | | | | |
|---|---|---|---|---|---|---|---|---|---|---|---|
| | | Single-Layered | | Double-Layered | | | | Triple-Layered | | | |
| | | A | B | AC | AE | AF | FA | AFC | AFD | AFE | FAD |
| Second-degree Burn Time in Seconds | Flame | 2.87 | 12.3 | 12.0 | 16.5 | 9.01 | 5.18 | 11.5 | 15.8 | 20.6 | 15.4 |
| | Radiant Heat | 4.49 | 7.62 | 11.5 | 24.2 | 9.89 | 7.90 | 17.3 | 23.3 | 28.7 | 20.6 |

*Effect of Fabric Features on SPP/TTTE*

Table 3 shows that the SPP of triple-layered fabric systems is much higher than for single- or double-layered fabric systems. This is because a triple-layered fabric system including a moisture barrier can trap higher amounts of dead air than single- or double-layered fabric systems [36–40]. Consequently, triple-layered fabric systems prove to be more thermally insulated and can provide better protection against steam exposure [7]. In this context, it is necessary to mention that the SPP per unit thickness of a double-layered fabric system incorporating a moisture barrier (e.g., AF or FA) is equivalent or sometimes even higher to triple-layered fabric systems; however, the SPP per unit thickness of a double-layered fabric system not comprising a moisture barrier (e.g., AC or AE) is much lower than triple-layered fabric systems (Table 3). This finding could help to establish that structural differences, such as the presence or absence of moisture barriers in fabric systems, are crucial to the SPP. In fact, only the presence of a moisture barrier in combination with a shell fabric (e.g., FA) could give better protection than a few high thickness triple-layered fabric systems (e.g., AFC, AFD, and AFE). Furthermore, it is evident from Table 3 that the TTTE through triple-layered fabric systems is lower than for single- or double-layered fabric systems. This is because triple-layered fabric systems have increased amounts of empty space (among their constituent shell fabrics (SF), moisture barriers (MB), and thermal liners (TL)), and these empty spaces can store steam within the fabric systems [21]. As the stored steam inside the triple-layered fabric system remains high, the transferred steam or the TTTE through the fabric system is low (Figure 3).

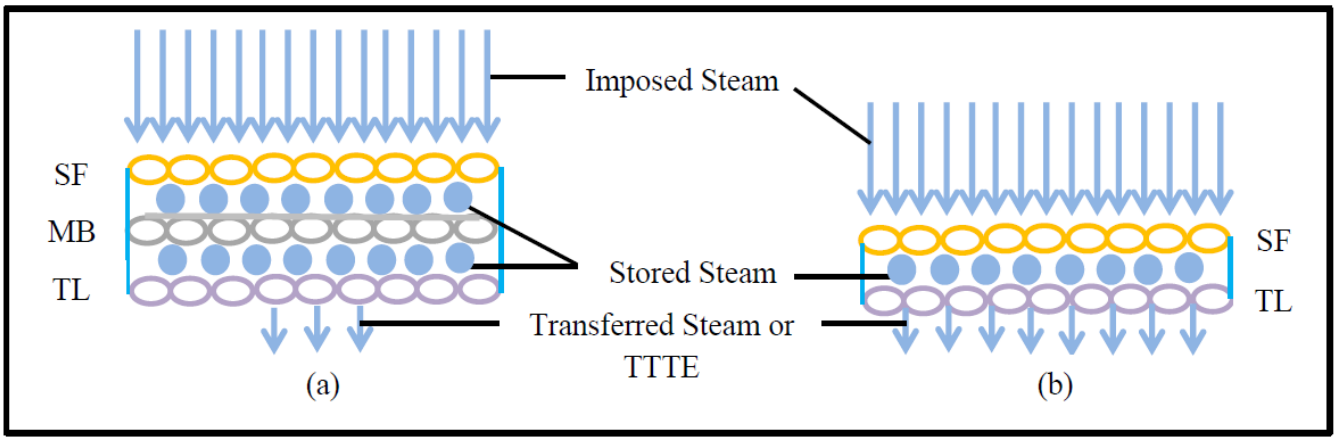


**Figure 3.** TTTE through (**a**) triple-layered and (**b**) double-layered fabric systems.

Furthermore, the results of the *t*-test (T-stat and P-value) between normalized values of the fabric system properties (Table 2) and SPP/TTTE (Table 3) are shown in Table 5. In Table 5, the T-stat values of thickness, weight, and thermal resistance with SPP are positive, whereas the T-stat values of these properties with TTTE are negative. This indicates that these properties possess a positive and negative relationship with the SPP and TTTE, respectively. The relationship plots of these properties with SPP and TTTE, shown in Figures 4–6, suggest that a moderate relationship exists between each of them

and the SPP/TTTE. These relationships can be further explained by the theory of heat transfer through fabric systems [14,18,20]. In a high-pressurized steam exposure, intimate contact occurs between fabric systems and the skin of the wearers (skin simulant sensor) (Figure 7). Consequently, a conductive thermal energy transfer proceeds from the fabric systems toward the skin. In this situation, a fabric with high weight and thickness can trap more insulative dead air, which can augment the thermal resistance of the fabric. This highly thermally insulated and resistive fabric can enhance the SPP by slowly transferring conductive thermal energy and generating slower burns on the bodies of wearers. Turning our attention to Figure 7, Equations (1) and (2) represent in analytical and mathematical terms the conservation of conductive thermal energy for a one-dimensional rectangular coordinate, X and Y coordinates-based fabric system [41]. Based on Equation (2), it can be inferred that the behavior of the TTTE through a fabric system is dependent upon the area of the fabric system (A in $cm^2$), gradient of temperature along the x direction of the fabric system ($\delta T/\delta x$ in °C/cm), rate of energy generation per unit volume of the fabric system ($q_g$ in $W/cm^3$), density of the fabric system ($\rho$ in $g/cm^3$), thickness of the fabric system ($dx$ in cm), specific heat of the fabric system ($C_p$ in J/gm. °C), total steam exposure time ($t$ in s), and thermal conductivity of the fabric system ($k_f$ in W/m.K).

Thermal energy conduction into the fabric system + Thermal energy generation inside the fabric system = Thermal energy conduction out of the fabric system + Thermal energy storage inside the fabric system (1)

$$-k.A.\frac{\delta T}{\delta x}\Big|_x + q_g.A.dx = -k.A.\frac{\delta T}{\delta x}\Big|_{x+\delta x} + \rho.A.dx.C_p.\frac{\delta T(x+dx/2,t)}{\delta t} \quad (2)$$

**Table 5.** Results of *t*-test.

| Fabric Properties | SPP | | TTTE | |
|---|---|---|---|---|
| | T-Stat | *p*-Value | T-Stat | *p*-Value |
| **Thickness** | 2.60 | 0.03 | −1.95 | 0.08 |
| **Weight** | 2.71 | 0.02 | −1.52 | 0.17 |
| **Thermal Resistance** | 1.90 | 0.09 | −1.31 | 0.2 |
| **Air Permeability** | −2.65 | 0.001 | 3.56 | 0.007 |

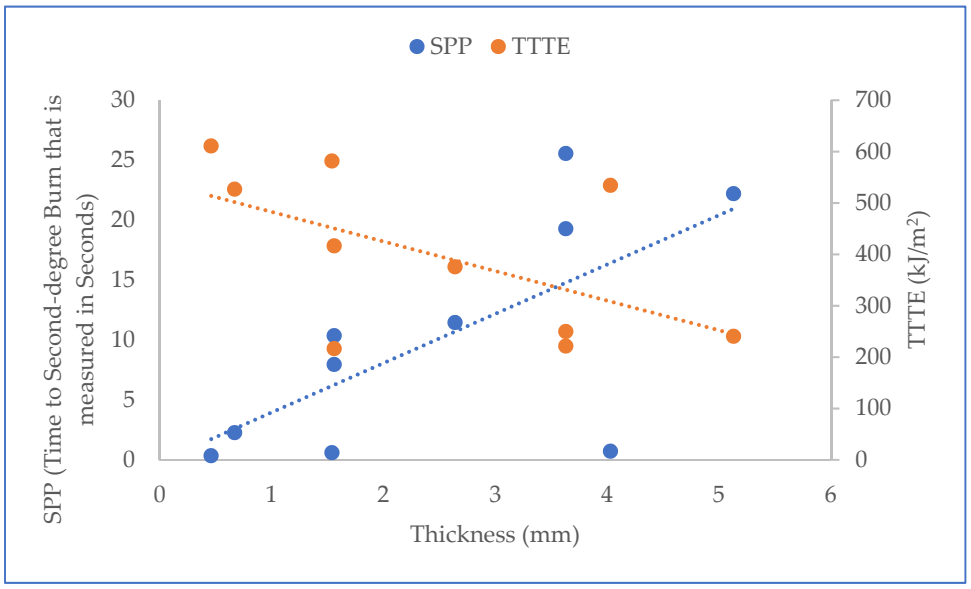


**Figure 4.** Relationship plot of thickness with SPP and TTTE.

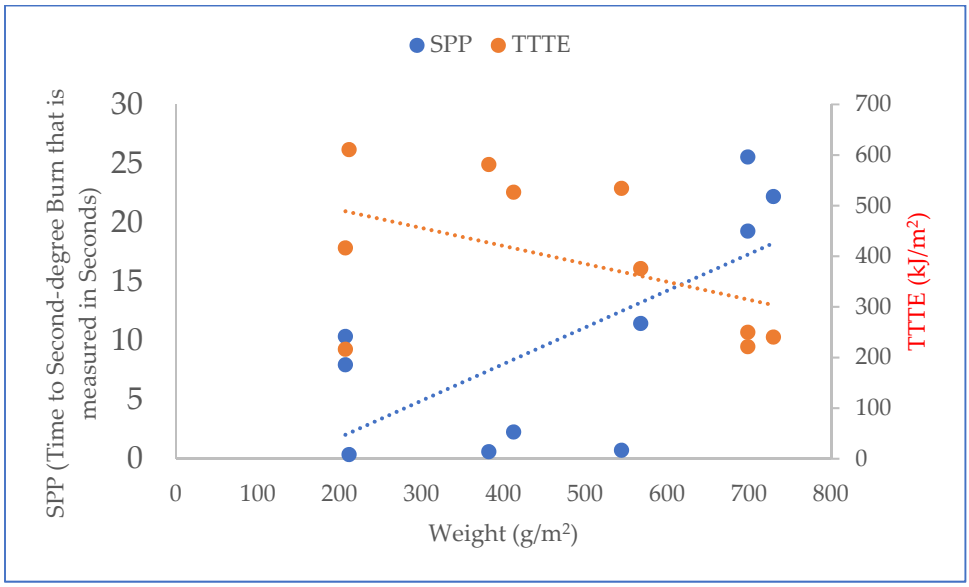


**Figure 5.** Relationship plot of weight with SPP and TTTE.

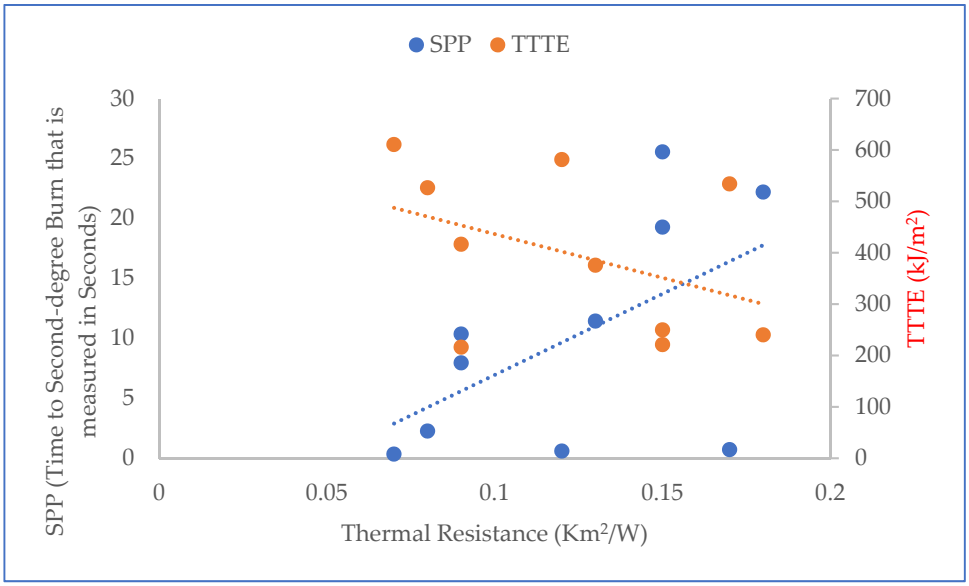


**Figure 6.** Relationship plot of thermal resistance with SPP and TTTE.

Moreover, Table 5 shows that the T-stat value of air permeability is negative with respect to the SPP; however, the T-stat value of air permeability is positive with respect to the TTTE. This implies that air permeability has a negative and positive relationship with the SPP and TTTE, respectively (Figures 8 and 9). In addition, the *p*-values (0.001 and 0.007) of air permeability are least among all fabric properties and are below 0.05. This means that air permeability is the most important and significant property to understand the SPP of or the TTTE through fabric systems. This finding can be explained comprehensively by the theory of mass (steam) transfer through fabric systems [11–15]. In this context, it is notable that a regular fabric is a multiphase, porous media, which comprises both solid fiber and gaseous air phases (Figure 10); and Darcy's law states that the mass transfer through porous media depends upon the permeability of that media (Equation (3). According to this law, a fabric with high air permeability can quickly transfer thermal energy in the form of convective steam jets through its air phase; eventually, the SPP and TTTE become low and high, respectively. Here, steam that has entered the fabric system gradually condenses and produces a mixture of steam and hot water; this hot water mainly transfers

through the fabric system toward the bodies of wearers and generates burns (Figure 10). In the steam condensation process, a considerable amount of thermal energy is released, which also causes burns on the bodies of wearers [34,37]. Through inference testing (hypothesis and a 95% confidence interval) of the dataset shown in Table 3, it has been found that a significant difference exists between the TTTE of air-impermeable and air-permeable fabrics ($p$-value < 0.05), and this difference always remains negative. This demonstrates that the TTTE through an air-impermeable fabric is much lower than an air-permeable fabric, because air-impermeable fabrics do not allow a steam transfer, lowering the TTTE [42,43]. In the case of multilayered, impermeable fabric systems (shown in Table 3), a fabric system including a moisture barrier in its outer layer has less TTTE (or high SPP) than a fabric system including a moisture barrier in its inner (middle) layer. This is because the presence of a polyurethane-coated (smooth surfaced) moisture barrier in its outer layer can immediately stop the steam transfer through the fabric system during exposure; as a result, the TTTE becomes lower, or the SPP enhances (Figure 11). This immediate stop of the steam transfer is less prominent in a fabric system with a moisture barrier in its inner layer. In this context, it is also notable that Fabric-B (in Table 3) is an air-impermeable, single-layered fabric (without any moisture barrier) that possesses a moderately acceptable SPP. This is because Fabric-B has encapsulated fiber finishing that did not allow a transfer of steam through its structure; as a consequence, the SPP enhances (Figure 12).

$$Q = \frac{-KA(P_b - P_a)}{\mu L} \tag{3}$$

where $Q$ = the total discharge of steam per unit time ($m^3/s$), $K$ = fabric permeability ($m^2$), $A$ = cross sectional area of mass flow ($m^2$), $P_a$ = pressure of the steam jet (Pa), $P_b$ = pressure of steam jet after passing through the fabric system (Pa), $\mu$ = viscosity (Pa·s), and $L$ = thickness of the fabric systems (m).

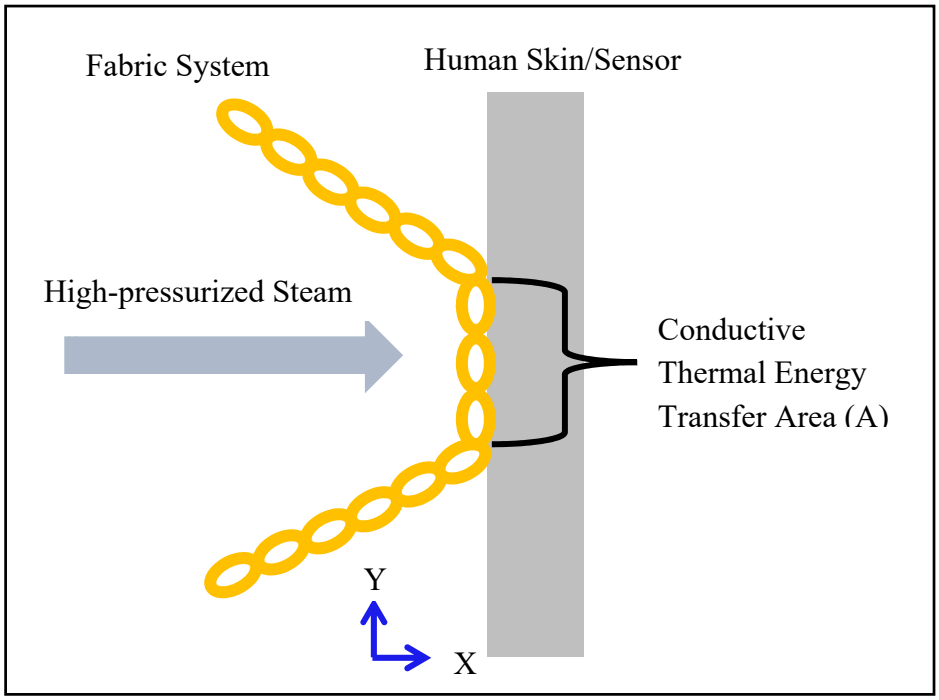


**Figure 7.** Conductive thermal energy transfer through a fabric system under steam exposure.

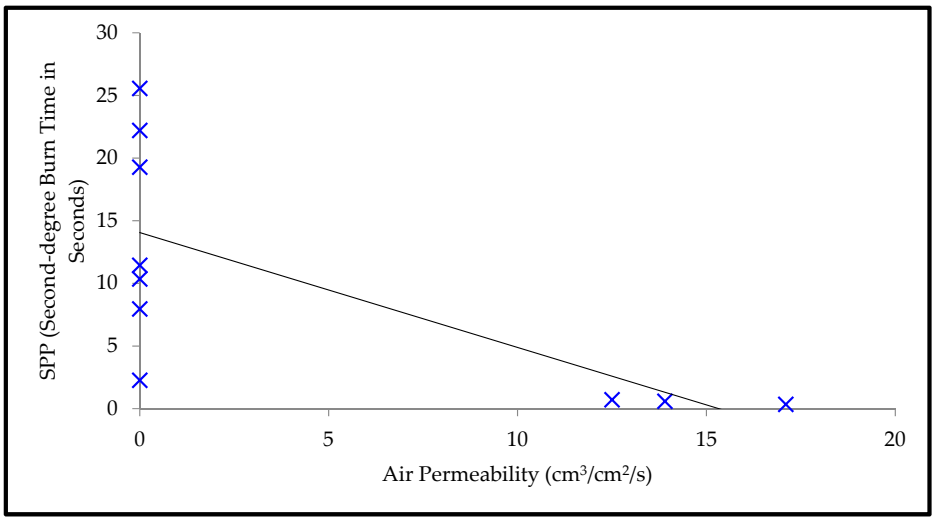


**Figure 8.** Relationship plot of air permeability and SPP.

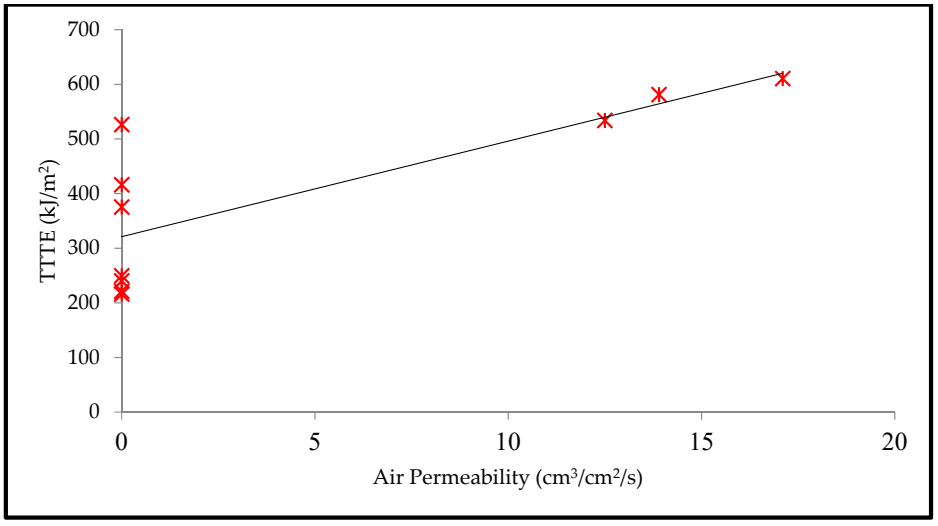


**Figure 9.** Relationship plot of air permeability and TTTE.

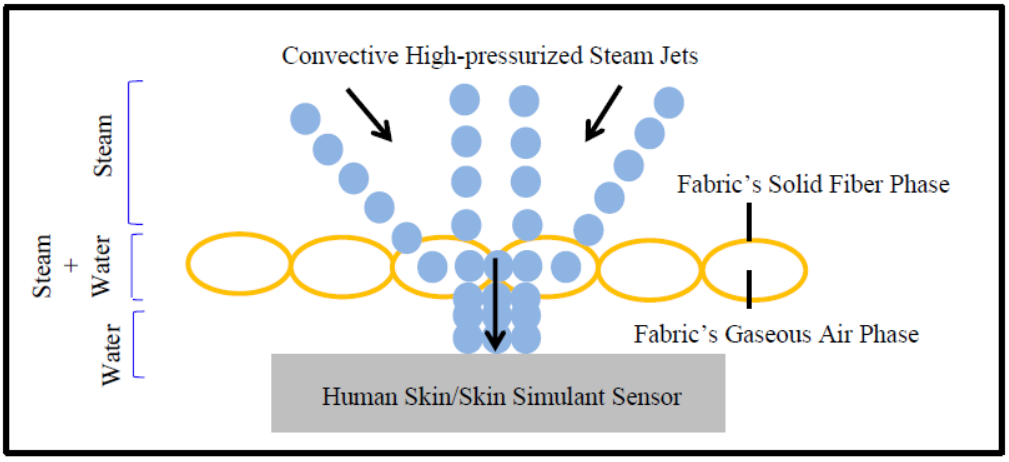


**Figure 10.** Steam transfer mechanisms through regular fabrics.

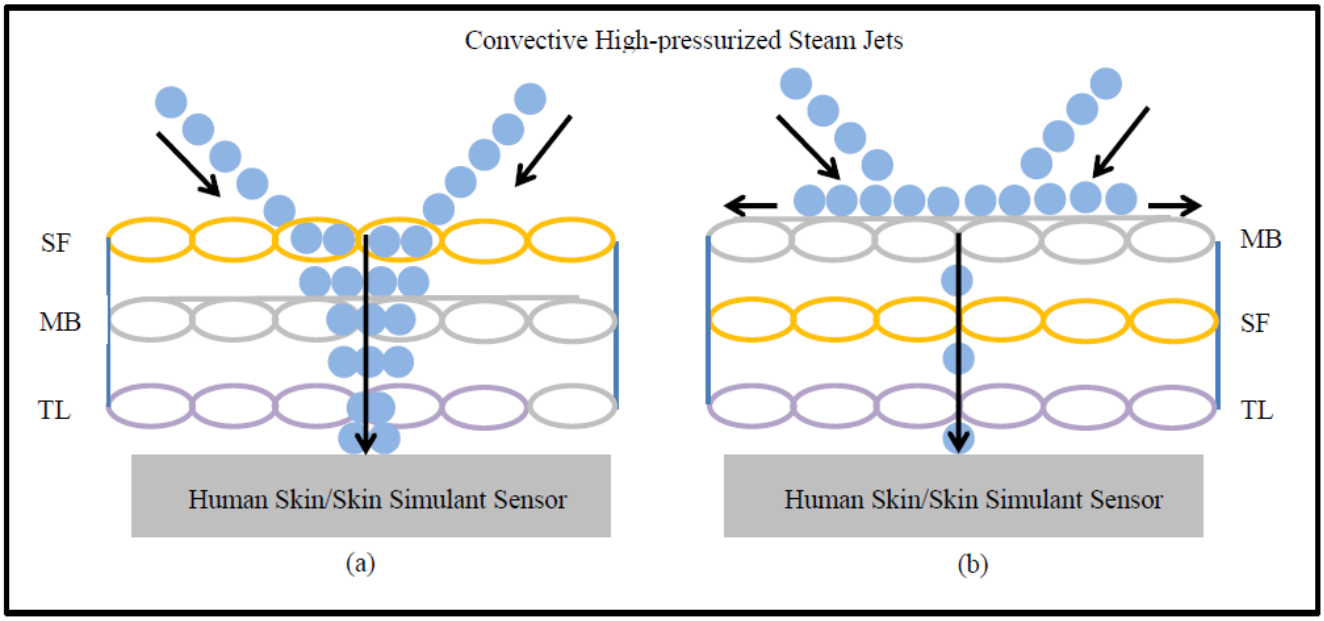


**Figure 11.** High-pressurized steam transfer through (**a**) a triple-layered fabric with SF in the outer layer, and (**b**) a triple-layered fabric with MB in the outer layer.

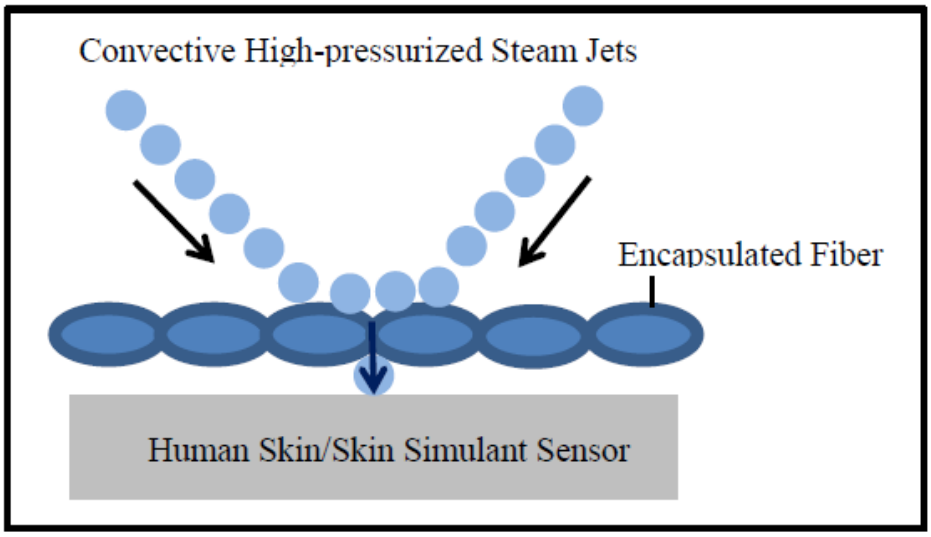


**Figure 12.** High-pressurized steam transfer through a single-layered encapsulated fiber finished fabric.

## 4. Summary and Conclusions

In this study, it has been found that a fabric system with a low total transmitted thermal energy (TTTE) generally possesses high steam protective performance (SPP). The SPP/TTTE are mainly dependent upon the constructional attributes and physical properties of fabric systems. Usually, multilayered fabric systems comprising a moisture barrier are highly thermally insulated due to higher amounts of dead air trapped in their structures, and they can store steam in the empty spaces present among their constituent layers. Consequently, multilayered fabric systems have a high SPP and a low TTTE. It can also be concluded from this study that moisture barriers present in fabric structures play a crucial role in achieving a high SPP and low TTTE, by minimizing mass transfer through fabric systems toward the bodies of wearers. Altogether, it can be suggested that designing a thermal protective fabric system comprising a moisture barrier and considerable empty space may be useful to provide adequate protection against steam.

Furthermore, it was found that intimate contact occurs between fabric systems and the bodies of wearers in high-pressurized steam exposure; as a result, conductive thermal energy transfers through fabric systems toward the bodies of wearers. In this case, a thick, weighty, and thermally resistive fabric system can reduce the conductive thermal energy transfer, lower the TTTE, and enhance the SPP. Along with the physical properties of fabrics (e.g., weight and thickness), thermal properties (thermal conductivity, specific heat, and density) also contribute equally to the TTTE/SPP. Sometimes, thermophysical properties (e.g., weight, thickness, thermal conductivity, specific heat, and density) of fabric systems may change due to the compression exerted on them by high-pressurized steam; this situation can lower the SPP. Thus, it is expected that anticompression-based fabric systems could provide better protection from steam by achieving a high SPP. Furthermore, it can be concluded that the air permeability of a fabric is the most important property that affects the SPP/TTTE. As fabric is a porous medium comprising both solid fibers and gaseous air phases, a highly air-permeable fabric can transfer steam quickly in its air phase, resulting in a lower SPP. Generally, an air-impermeable fabric system can be used effectively to achieve a high SPP or a low TTTE. In the case of multilayered, impermeable fabric systems, it is suggested to place a moisture barrier in their outer layers. This configuration can effectively reduce the overall air permeability of these fabric systems; eventually, their mass transfer may decline and result in a lower TTTE and a higher SPP.

Overall, the findings obtained from this study can be useful for textile/material engineers to develop high performance thermal protective fabrics that increase the occupational health and safety of firefighters and industrial workers. This study can be further extended by analyzing the heat flux profile through fabric systems in the steam exposure of a certain duration.

**Author Contributions:** S.M., conceptualization, designing and performing experiments, writing, and data analysis; G.S., conceptualization. All authors have read and agreed to the published version of the manuscript.

**Funding:** This work was supported by the University of Alberta, Canada, by an Izaak Walton Killam Memorial Scholarship to Sumit Mandal and Oklahoma State University, USA, by a start-up grant to Sumit Mandal.

**Data Availability Statement:** Not applicable.

**Acknowledgments:** The authors appreciate technical support from Mark Ackerman (Adjunct Professor, Department of Mechanical Engineering, University of Alberta, Canada) and Stephen Paskaluk (Research Engineer, Department of Human Ecology, University of Alberta, Canada).

**Conflicts of Interest:** The authors declare no conflict of interest.

## References

1. Karter, M.J.; Molis, J.L. *U.S. Firefighter Injuries—2011*; National Fire Protection Association (NFPA): Quincy, MA, USA, 2012. Available online: http://www.tkolb.net/firereports/2012/2011ff_injuries.pdf (accessed on 5 July 2013).
2. Fahy, R.F.; LeBlanc, P.R.; Molis, J.L. *Firefighter Fatalities in the United States—2011*; National Fire Protection Association (NFPA): Quincy, MA, USA, 2012. Available online: https://kstp.com/kstpImages/repository/cs/files/FirefighterFatalities.pdf (accessed on 5 July 2013).
3. Mian, M.A.H.; Mullins, R.F.; Alam, B.; Brandigi, C.; Friedman, B.C.; Shaver, J.R.; Hassan, Z. Workplace-related burns. *Ann. Burns. Fire. Disasters* **2011**, *24*, 89–93.
4. Keiser, C.; Becker, C.; Rossi, R.M. Moisture Transport and Absorption in Multilayer Protective Clothing Fabrics. *Text. Res. J.* **2008**, *78*, 604–613. [CrossRef]
5. Keiser, C.; Rossi, R.M. Temperature Analysis for the Prediction of Steam Formation and Transfer in Multilayer Thermal Protective Clothing at Low Level Thermal Radiation. *Text. Res. J.* **2008**, *78*, 1025–1035. [CrossRef]
6. Keiser, C, Wyss, P, Rossi, RM. Analysis of steam formation and migration in firefighters' protective clothing using x-ray radiography. *Int. J. Occup. Saf. Ergon.* **2010**, *16*, 217–229. [CrossRef] [PubMed]
7. Mandal, S.; Song, G.; Ackerman, M.; Paskaluk, S.; Gholamreza, F. Characterization of textile fabrics under various thermal exposures. *Text. Res. J.* **2013**, *83*, 1005–1019. [CrossRef]
8. Shoda, A.; Wang, C.Y.; Cheng, P. Simulation of constant pressure steam injection in a porous medium. *Int. Commun. Heat. Mass.* **1998**, *25*, 753–762. [CrossRef]

9. Jalbani, S.; Ackerman, M.; Crown, E.; Keulen, M.; Song, G. *Performance of Protective Clothing and Equipment: Emerging Issues and Technologies STP-1544*; ASTM International: West Conshohocken, PA, USA, 2012; Volume 9, p. 329.
10. Sarma, B.P. Epidemiology and man-days loss in burn injuries amongst workers in an oil industry. *Burns* **2001**, *27*, 475–480. [CrossRef]
11. Kahn, S.A.; Patel, J.H.; Lentz, C.W.; Bell, D.E. Firefighter Burn Injuries: Predictable Patterns Influenced by Turnout Gear. *J. Burn. Care. Res.* **2012**, *33*, 152–156. [CrossRef]
12. Rossi, R. Fire fighting and its influence on the body. *Ergonomics.* **2003**, *46*, 1017–1033. [CrossRef] [PubMed]
13. Shalev, I.; Barker, R.L. Analysis of Heat Transfer Characteristits of Fabrics in an Open Flame Exposure. *Text. Res. J.* **1983**, *53*, 475–482. [CrossRef]
14. Song, G.; Paskaluk, S.; Sati, R.; Crown, E.M.; Dale, D.J.; Ackerman, M. Thermal protective performance of protective clothing used for low radiant heat protection. *Text. Res. J.* **2011**, *81*, 311–323. [CrossRef]
15. Mandal, S.; Song, G. An Empirical Analysis of Thermal Protective Performance of Fabrics Used in Protective Clothing. *Ann. Occup. Hyg.* **2014**, *58*, 1065–1077. [PubMed]
16. Sun, G.; Yoo, H.S.; Zhang, X.S.; Pan, N. Radiant Protective and Transport Properties of Fabrics Used by Wildland Firefighters. *Text. Res. J.* **2000**, *70*, 567–573. [CrossRef]
17. Mandal, S.; Song, G.; Gholamreza, F. A novel protocol to characterize the thermal protective performance of fabrics in hot-water exposure. *J. Ind. Text.* **2016**, *46*, 279–291. [CrossRef]
18. Mandal, S.; Song, G. Characterization of protective textile material for thermal hazard. In Proceedings of the Fiber Society Spring Conference, Hung Hum, Hong Kong, 23–25 May 2011.
19. Mandal, S.; Lu, Y.; Song, G. Characterization of thermal protective clothing under hot-water and pressurized steam exposure. In Proceedings of the The 2013 Herman and Myrtle Goldstein Student Paper Competition organized by American Association of Textile Chemists and Colorists (AATCC), Greenville, SC, USA, 9–11 April 2013.
20. Rossi, R.; Indelicato, E.; Bolli, W. Hot Steam Transfer Through Heat Protective Clothing Layers. *Int. J. Occup. Saf. Ergon.* **2004**, *10*, 239–245. [CrossRef]
21. Mandal, S.; Lu, Y.; Wang, F.; Song, G. Characterization of Thermal Protective Clothing under Hot Water and Pressurized Steam Exposure. *AATCC J. Res.* **2014**, *1*, 7–16. [CrossRef]
22. Su, Y.; Li, R.; Song, G.; Dong, H. *Thermal Protective Performance of Membrane material Used in Protective Clothing against Hot Water and Steam*; Iowa State University Digital Press: Ames, IA, USA, 2017; Volume 74, p. 1.
23. He, J.; Lu, Y.; Yang, J. Quantification of the energy storage caused dual performance of thermal protective clothing containing with moisture exposed to hot steam. *Energy Sci. Eng.* **2019**, *7*, 2585–2595. [CrossRef]
24. He, J.; Sun, L.; Lu, Y. Effects of Radiant Heat and Frictional Abrasion on Thermal Protective Performance of Clothing Against High Pressurized Steam. *Cloth. Text. Res. J.* **2021**, 1–14. [CrossRef]
25. Desruelle, A.; Schmid, B.; Montmayeur, A. Technical Report. 2002. Available online: https://apps.dtic.mil/sti/citations/ADP012415 (accessed on 20 November 2021).
26. Su, Y.; Li, R.; Song, G.; Li, J.; Xiang, C. Modeling steam heat transfer in thermal protective clothing under hot steam exposure. *Int. J. Heat Mass Transf.* **2018**, *120*, 818–829. [CrossRef]
27. *ASTM D 1777*; Standard Test Method for Thickness of Textile Materials. ASTM International: West Conshohocken, PA, USA, 1996.
28. *ASTM D 3776*; Standard Test Method for Mass per Unit Area (Weight) of Fabric. ASTM International: West Conshohocken, PA, USA, 2009.
29. *ASTM D 1518*; Standard Test Method for Thermal Resistance of Batting Systems Using A Hot Plate. ASTM International: West Conshohocken, PA, USA, 2011.
30. *ASTM D 737*; Standard Test Method for Air Permeability of Textile Fabrics. ASTM International: West Conshohocken, PA, USA, 2004.
31. Epps, H.H.; Leonas, K.K. Pore Size and Air Permeability of Four Nonwoven Fabrics. *Int. Nonwovens J.* **2020**. [CrossRef]
32. Maisel, E. The Three P's: Porosity, Permeability and Permeance. Available online: https://thefiberwire.com/2016/04/07/the-three-ps-porosity-permeability-and-permeance/ (accessed on 20 November 2021).
33. Scheidegger, A.L. *The Physics of Flow Through Porous Media*; University of Toronto Press: Toronto, ON, USA, 1974.
34. Mandal, S.; Song, G. Thermal sensors for performance evaluation of protective clothing against heat and fire: A review. *Text. Res. J.* **2015**, *85*, 101–112. [CrossRef]
35. Mandal, S.; Camenzind, M.; Annaheim, S.; Rossi, R.M. Evaluation of heat and flame protective performance of clothing using manikins. In *Manikins Textile Evaluation*; Woodhead Publishing: Sawston, UK, 2017. [CrossRef]
36. Guan, M.; Annaheim, S.; Camenzind, M.; Li, J.; Mandal, S.; Psikuta, A.; Rossi, R.M. Moisture transfer of the clothing–human body system during continuous sweating under radiant heat. *Text. Res. J.* **2019**, *89*, 4537–4553. [CrossRef]
37. Mandal, S.; Annaheim, S.; Camenzind, M.; Rossi, R.M. Characterization and modelling of thermal protective performance of fabrics under different levels of radiant-heat exposures. *J. Ind. Text.* **2018**, *48*, 1184–1205. [CrossRef]
38. Guan, M.; Psikuta, A.; Camenzind, M.; Li, J.; Mandal, S.; Michel Rossi, R.; Annaheim, S. Effect of perspired moisture and material properties on evaporative cooling and thermal protection of the clothed human body exposed to radiant heat. *Text. Res. J.* **2019**, *89*, 3663–3676. [CrossRef]

39. Mandal, S.; Annaheim, S.; Capt, A.; Greve, J.; Camenzind, M.; Rossi, R.M. A categorization tool for fabric systems used in firefighters' clothing based on their thermal protective and thermo-physiological comfort performances. *Text. Res. J.* **2018**, *89*, 3244–3259. [CrossRef]
40. Keiser, C. Steam Burns Moisture Management in Firefighter Protective Clothing. Ph.D. Thesis, Swiss Federal Institute of Technology ETH, Zurich, Switzerland, 2007.
41. Lienhard, J.H.; Lienhard, J.H. *A Heat Transfer Textbook*, 4th ed.; Dover Publication: New York, NY, USA, 2011; pp. 111–152.
42. Rossi, R.; Traugott, Z. Influence of humidity on the radiant, convective and contact heat transmission through protective clothing materials. In Proceedings of the Fifth International Symposium on Performance of Protective Clothing: Improvement through Innovation, San Francisco, CA, USA, 25–27 January 1994.
43. Murtaza, G.; Batcheller, J.; Crown, E.M.; Ackerman, M.Y. Development of thermal protective fabrics for steam and hot water protection. In Proceedings of the 108th Institute of Textile Science Scientific Session, Qubec, QC, Canada, 21 November 2011.

textiles

MDPI

*Article*

# Stretchable Textile Yarn Based on UHF RFID Helical Tag

**Sofia Benouakta [1,*], Florin Doru Hutu [2] and Yvan Duroc [1]**

[1] Univ Lyon, Université Claude Bernard Lyon 1, INSA Lyon, Ecole Centrale de Lyon, CNRS, Ampère, UMR5005, 69622 Villeurbanne, France; yvan.duroc@univ-lyon1.fr
[2] Univ Lyon, INSA Lyon, Inria, CITI, EA3720, 69621 Villeurbanne, France; florin-doru.hutu@insa-lyon.fr
* Correspondence: sofia.benouakta@univ-lyon1.fr

**Abstract:** In the context of wearable technology, several techniques have been used for the fabrication of radio frequency identification (RFID) tags such as 3D printing, inkjet printing, and even embroidery. In contrast to these methods where the tag is attached to the object by using sewing or simple sticking, the E-Thread® technology is a novel assembling method allowing for the integration of the RFID tag into a textile yarn and thus makes it embeddable into the object at the fabrication stage. The current E-Thread® yarn uses a RFID tag in which the antenna is a straight half-wave dipole that makes the solution vulnerable to mechanical strains (i.e., elongation). In this paper, we propose an alternative to the current RFID yarn solution with the use of an antenna having a helical geometry that answers to the mechanical issues and keeps quite similar electrical and radiative properties with respect to the present solution. The RFID helical tag was designed and simulated taking into consideration the constraints of the manufacturing process. The helical RFID tag was then fabricated using the E-Thread® technology and experimental characterization showed that the obtained structure exhibited good performance with 10.6 m of read range in the ultra high frequency (UHF) RFID band and 10% of tolerance in terms of elongation.

**Keywords:** helical RFID tag; helical antenna; RFID; textile yarn; wearable

**Citation:** Benouakta, S.; Hutu, F.D.; Duroc, Y. Stretchable Textile Yarn Based on UHF RFID Helical Tag. *Textiles* **2021**, *1*, 547–557. https://doi.org/10.3390/textiles1030029

Academic Editor: Laurent Dufossé

Received: 22 October 2021
Accepted: 19 November 2021
Published: 22 November 2021



## 1. Introduction

Radio frequency identification (RFID) is a very popular standardized technology that is mainly employed for the identification purposes of objects or people. More precisely, an object associated with a RFID tag is remotely identified by the means of a RFID reader. The communication principle is based on the tag's load modulation of the backscattered electromagnetic wave [1–3], which implies that in most of the cases, the RFID tag is passive (i.e., it uses the transmitted energy from the reader without the need for any additional energy source). RFID is a very interesting concept that contributes to the Internet of Things (IoT) development and, more generally, it is considered as a key technology for humanity [4,5]. The advantages that are offered by RFID tags such as communication without line of sight, low cost, small size, and unique identification have made them an essential candidate for a wide range of applications, for example, logistics, retail, access and identity cards as well as wireless payment systems.

Recently, the emergence of electronic devices that can be worn in, on, or near the body called "wearables" has allowed for the possibility of recovering various physiological information from a human body and transmitting it wirelessly to a processing unit or even to a smartphone [6]. The information obtained from a wearable device can be very useful in a wide range of applications, especially in the health care sector and one of the required operations is the unique identification of the device. For this purpose, in the last years, many efforts have been undertaken in order to develop wearable RFID tags that can be associated with clothing or an accessory in a way that is non-invasive, comfortable, and invisible for the wearer. Popular considerations during the design of wearable RFID tags are usually the impact of deformation on the RFID tag's performance,

the effect of the human body's proximity to the tag's electrical and radiative properties or the tag's washability [7–11]. However, in the encountered studies, the RFID tag's topology is often kept unchanged from the conventional one (i.e., planar antenna on a substrate with properties that are specific to the application). In fact, the link between a RFID tag and the object it is associated to, is often neglected and the concept of integrating the tag into the object since the manufacturing phase is part of the "Industry 4.0" era.

One of the technologies that supports this idea is E-Thread®, in which the RFID tag's form factor is reinvented as a RFID textile yarn. The patented technique [12] consists of an automated assembling process during which the RFID chip is associated with a half-wave dipole antenna in a repeated operation. The obtained cascaded RFID tags are then wrapped by a textile material to constitute a spool of textile RFID yarns. When isolated from the spool, one RFID yarn operates in the European Ultra High Frequency (UHF) band $(865.5 - 867.5)$ MHz and exhibits a reading range of 12 m [13]. The current E-Thread® RFID yarn constitutes a very interesting solution as it can be integrated within an object during the fabrication stage and offers great advantages with its slender configuration such as invisibility and comfortable for the user. However, a RFID wearable tag has to be robust to any kind of mechanical constraints such as the elongation, which is lacking in the actual RFID yarn.

In this paper, we propose an alternative solution that consists of using for the tag's antenna, a helical geometry that has similar mechanical properties to a string. A helical antenna is mainly fabricated by winding a conductive material and its geometrical parameters have an important impact on its electromagnetic properties in terms of input impedance and radiation pattern. Usually, these helical antenna properties are exploited for several scenarios such as phased antenna arrays for millimeter waves and wireless power transfer applications [14,15], wireless sensor nodes in smart agriculture [16] as well as biomedical applications [17–19]. However, to the authors' knowledge, in the literature, very few examples can be found where a helical antenna has been used in a RFID tag. For example, the study in [20] focused on the development of a helical RFID tag to be integrated into a vehicle tire. In this case, the impedance matching between the antenna and the chip was achieved using a transmission line. Meanwhile, in the study presented in [21], a helical antenna was developed for and RFID tag in which the impedance matching was achieved by tuning the geometrical parameters of the antenna.

In a previous work [22], the latter method was employed in order to design a helical antenna for the RFID tag yarn without the use of any additional elements in order to perform the impedance matching. The RFID helical tag exhibited a maximum read range at 1040 MHz, which is higher than the frequency of interest and 1 m of read range in the European UHF RFID band. As explained, the observed result is due to manufacturing process constraints and one of the given improvement solutions was to design a helical antenna with a spacing between turns that is higher while increasing the antenna's half-length $h$.

In this paper, the new UHF RFID helical tag-based textile yarn includes two significant improvements: (i) the helical RFID tag was designed while taking into consideration the manufacturing constraints (the nature of the employed materials and the physical dimensions' limits), and (ii) the integration of a stretchable core material as a support for the elongation. Compared to the previous version of the helical RFID tag, the suggested methodology design also allows for a manufactured structure to be obtained for which the dimensions and the electromagnetic characteristics are close to the simulated ones. This is possible through a more accurate modeling of the materials' characteristics in the design process. The rest of this paper is organized as follows. In Section 2, the topology of the helical antenna when integrated into a textile yarn is presented together with the design methodology including electrical and manufacturing specifications. Moreover, criteria for the helical RFID tag characterization using simulation and experiments are given. Section 3 highlights the simulation results in terms of reflection coefficient and radiation pattern.

Moreover, the fabricated prototypes as well as the experimental characterization's results are presented. Finally, conclusions and future work are drawn in Section 4.

## 2. Materials and Methods

### *2.1. Topology of the RFID Textile Yarn Integrating a Helical Antenna*

In free space, the helical antenna is characterized by its geometrical parameters, which are the diameter $D$; the half-length $h$; the turns number $N$; the pitch $s$; and the wire radius $a$, as shown in Figure 1a. As stated, these parameters impact the electromagnetic properties as follows: the diameter $D$ and the pitch $s$ mainly have an impact on the impedance matching while the half-length $h$ and turns number $N$ mainly modify the resonance frequency. Moreover, a helical antenna with a diameter much smaller than the wavelength allows a radiation pattern to be maintained with a normal mode similar to the dipole antenna of the current solution [23].

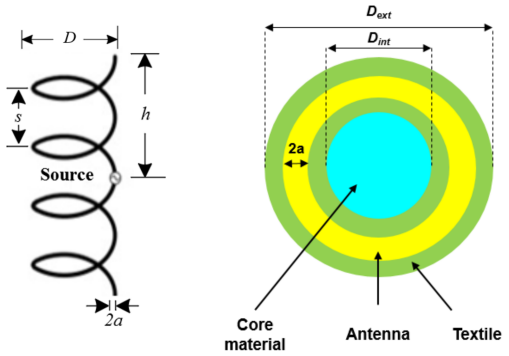


**Figure 1.** (**a**) Helical antenna configuration; (**b**) Cross section of the RFID textile yarn integrating the helical antenna.

The RFID helical tags presented in this paper were fabricated using the E-Thread® technology. The E-Thread technology consists of an automated assembling process where a dipole antenna is associated with a RFID chip for which the package was modified beforehand. On the RFID chip edges, two grooves receive two copper wires that form the tag's antenna [12]. This technique allows for several cascaded RFID tags to be obtained that can have a textile finishing during a wrapping process [13]. Furthermore, in order to obtain the helical shape, an additional step is required. This step consists of wrapping the textile material containing the cascaded RFID tags around a core material giving the helical aspect; here, a stretchable material is employed as the core of the helical antenna offering elongation capabilities. Details on the practical fabrication are given in [22]. Preliminary parametric simulations testing different dielectric constants for the used core material has allowed us to conclude that when the dielectric constant of the core increases, the impedance matching frequency shifts toward the low frequencies. Thus, it is important to identify and characterize the nature of the used material as the core during the antenna design. Indeed, any change after the manufacturing process is very difficult and may strongly deteriorate the RFID yarn.

For the simulation purpose, the textile material used for wrapping and the core material were modeled simply as dielectric materials characterized by their permittivity constant provided by the industrial partner. The dielectric constants for the employed *nylon* and *lycra* are $\varepsilon_r = 3.6$ and $\varepsilon_r = 1.5$, respectively. A cross section of the helical RFID textile yarn is shown in Figure 1b: $D_{ext}$ is the external diameter of the helical tag integrated in the textile; $D_{int}$ is the diameter of the cylindrical core material; and $2a$ is the helical antenna wire's diameter.

### *2.2. Design Specifications*

In order to design a helical antenna for the RFID textile yarn, electrical specifications have to be guaranteed. In addition to these conditions, manufacturing constraints in terms of dimensioning are imposed by the manufacturing process.

#### 2.2.1. Electrical Specifications

- The helical RFID tag has to operate, here (but without loss of generality on the concept), within the European UHF RFID band $(865.5 - 867.5)$ MHz; and
- The considered RFID integrated circuit (IC) is the Monza R6 [24] and its impedance is $Z_{chip} = 15 - j150\ \Omega$ at 865 MHz. This RFID IC is used by the industrial partner for the current commercialized solution. However, the design methodology is independent from the IC choice.

#### 2.2.2. Manufacturing Constraints

In order for the RFID helical tag design to be compatible with the E-Thread® manufacturing process, some of the helical antenna's geometrical parameters have to respect certain limitations (which for the most part are therefore fixed according to manufacturing constraints):

- The helical antenna's pitch has to be higher than 0.7 mm. As explained in [22], the value of this parameter depends on the rotation speed of the conductive filament around the core material. Consequently, the value that meets the manufacturing process and employed for our design methodology was $s = 1.2$ mm;
- The core material around which the copper conductive wire was wound had a diameter of 1 mm. A lower diameter strongly alters the impedance matching while a high value leads to a complex winding process. Consequently, this condition allows us to make a compromise between the manufacturing process and the helical RFID tag's performance;
- The external diameter $D_{ext}$, which depends on the textile material thickness, is provided by the industrial partner as $D_{ext} = 1.35$ mm; and
- The conductive wire diameter was fixed to $2a = 0.1$ mm and corresponded to the copper's diameter used in the E-Thread® process.

Hence, the geometrical parameters of the helical antenna that can be varied in order to design a helical RFID tag while meeting the specifications are: the half-length $h$ and the turns number $N$. Table 1 summarizes the variable and the fixed geometrical parameters.

**Table 1.** Geometrical parameters of the helical antenna integrated into a textile yarn.

| Geometrical Parameters | Value [mm] |
|---|---|
| $D_{ext}$ | 1.35 |
| $D_{int}$ | 1 |
| $s$ | 1.2 |
| $a$ | 0.05 |
| $h$ | Varied |
| $N$ | Varied |

### *2.3. Helical Antenna's Simulated Structure*

All the presented simulations were performed using CST Microwave Studio 2018, electromagnetic simulation commercial software.

The described helical RFID tag was configured in 3D and a full view is shown in Figure 2a. In addition, a vertical cross section is illustrated in Figure 2b. The pitch $s$ and the diameter $D$ that strongly impact the impedance matching of the helical antenna have been fixed for manufacturing constraints and thus, only the resonance frequency can be

modified. For this purpose, the number of turns $N$ and the half-height $h$ are simultaneously varied in order to obtain a resonance frequency in the UHF RFID band.

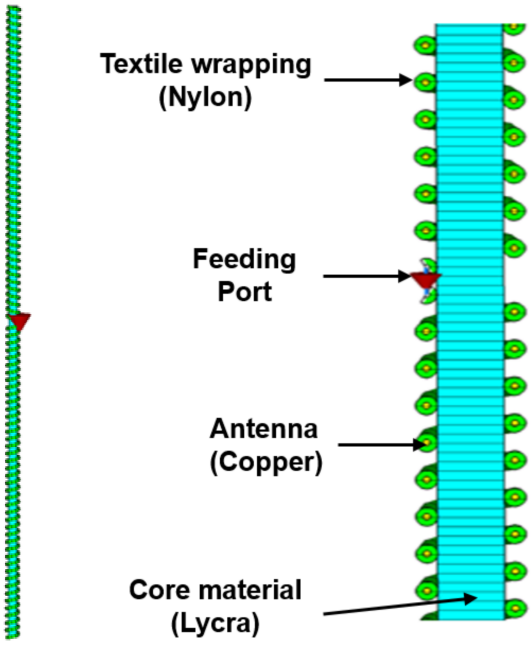


(**a**) (**b**)

**Figure 2.** Helical antenna in 3D. (**a**) Full view of the structure. (**b**) Vertical cross section of the structure.

*2.4. Characterization of the Helical RFID Tag*

Here, the designed helical RFID tag was characterized in two ways. First, by simulation, and more precisely by evaluating its impedance matching and its radiation pattern. Second, the tag was evaluated by experimental tests through the measurements of the read range and by estimating its robustness to stretching.

2.4.1. Helical RFID Tag's Impedance Matching

Unlike other RF scenarios in which the antenna's impedance has to be matched to 50 Ω, in RFID, the antenna's impedance has to be matched with the IC's impedance. The impedance matching is evaluated through the complex power wave reflection coefficient Γ, which can be expressed as in Equation (1):

$$\Gamma = \frac{Z_{chip} - Z_{ant}*}{Z_{chip} + Z_{ant}} \quad (1)$$

where $Z_{ant}$ is the helical antenna's input impedance.

2.4.2. Helical RFID Tag's Read Range

In most applicative contexts of UHF RFID, the read range is a very important criterion to describe the performance. In order to compare the experimental result to the one obtained by simulation, the read range can be calculated using the theoretical expression obtained from the Friis transmission equation:

$$R = (\lambda/4\pi) \cdot \sqrt{\frac{P_t G_t G_r \chi \tau}{P_{th}}} \quad (2)$$

where $\lambda$ is the wavelength; $P_t$ is the power transmitted by the reader; $G_t$ is the reader's antenna gain; $G_r$ is the tag's antenna gain; $\chi$ is the polarization loss; $P_{th}$ is the tag's activation

threshold that represents the power needed for the IC to start operating; and $\tau$ is the power transmission coefficient defined as:

$$\tau = 1 - |\Gamma|^2 \quad (3)$$

It is worth noting that the quantity $P_t G_t$ represents the equivalent isotropic radiated power (EIRP). Its maximum value depends on the geographical location, for instance, the value imposed by the European Telecommunications Standards Institute (ETSI) is 3.28 W, whereas the tag's activation threshold is specific to the chosen IC.

In the presented work, the Voyantic Tagformance commercial test bench [25] was used to measure the read range.

#### 2.4.3. Helical RFID Tag's Robustness in Terms of Stretching

In order to measure the helical RFID tag's tolerance to elongation, the Voyantic Bench test was also used after performing some modifications in order to correspond to our application. More precisely, both the antenna extremities are attached to a basic textile filament that is wound around two spools. As shown in Figure 3, the spools' rotation, clockwise and counter clockwise, allows for the application of an elongation on the tag. The read range is then measured for each considered elongation.

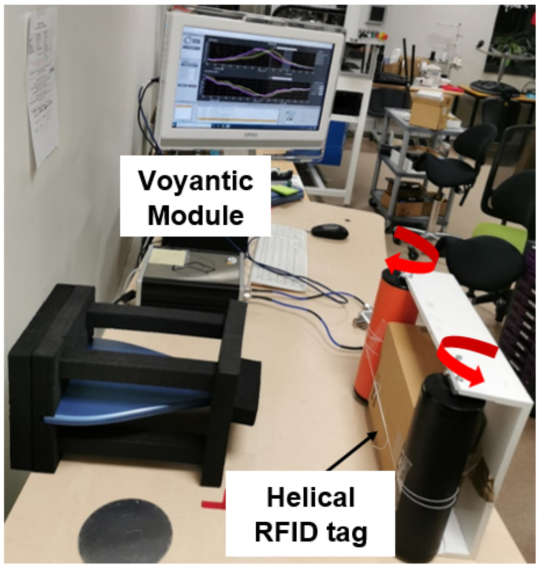


**Figure 3.** Modified Voyantic test bench for the measurement of the helical RFID tag's reading range when elongation efforts are applied.

## 3. Discussion of the Simulation and Measurement Results

### *3.1. Helical RFID Tag's Reflection Coefficient* $\Gamma$ *and Its Radiation Pattern*

After optimization, the helical RFID tag's geometrical parameters were: $h$ = 50 mm; $N = 42$, in addition to the fixed ones given in Table 1. The reflection coefficient obtained from simulation is shown in Figure 4. It can be observed that the tag's antenna exhibited a minimum value of the reflection coefficient $\Gamma$ of $-6.27$ dB at 865 MHz.

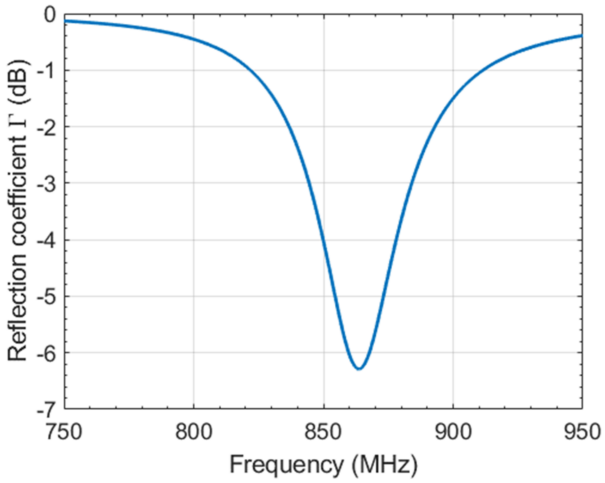


**Figure 4.** Reflection coefficient Γ obtained by simulation at the antenna feed point.

The radiation pattern obtained by simulation is shown in Figure 5, where the antenna is positioned along the z-axis and has a maximum gain of 1.27 dB. It can be seen that the radiation pattern was omnidirectional in the *xoy* plan, which is identical to a half-wave's dipole radiation pattern. Moreover, through the obtained axial ratio (AR) as shown in (Figure 6), defined as $\frac{E_\theta}{E_\varphi} = 35.8$ dB for the main lobe ($E_\theta$ and $E_\varphi$ being the orthogonal components of the radiated electric field), the antenna is elliptically polarized with a vertical major axis [23].

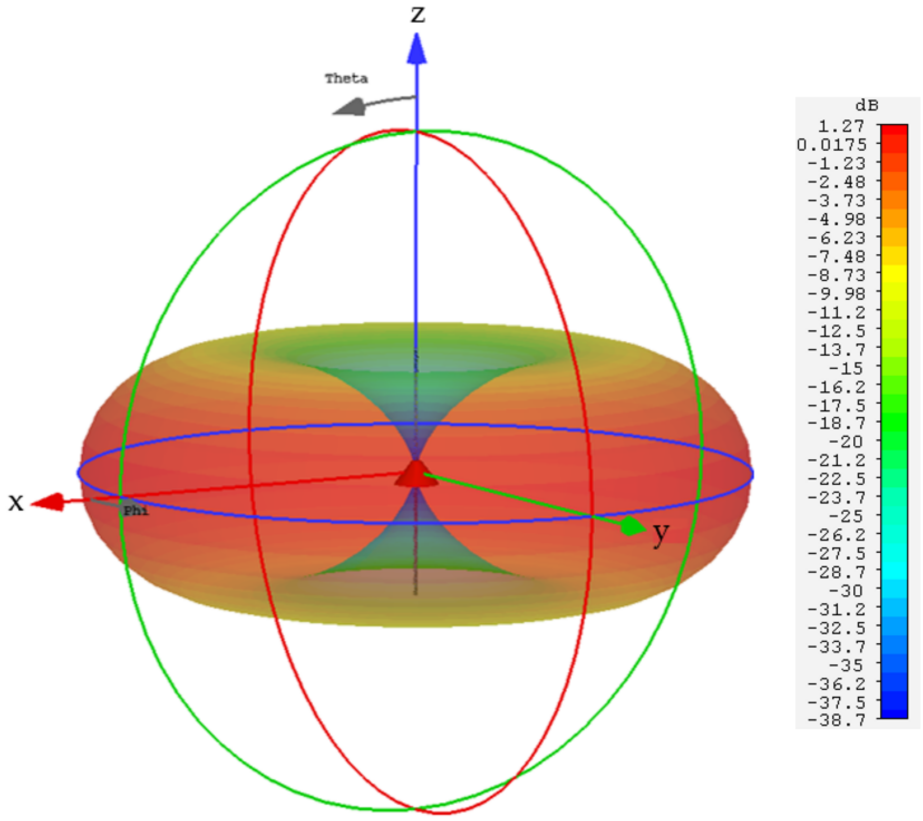


**Figure 5.** Helical RFID antenna's radiation pattern.

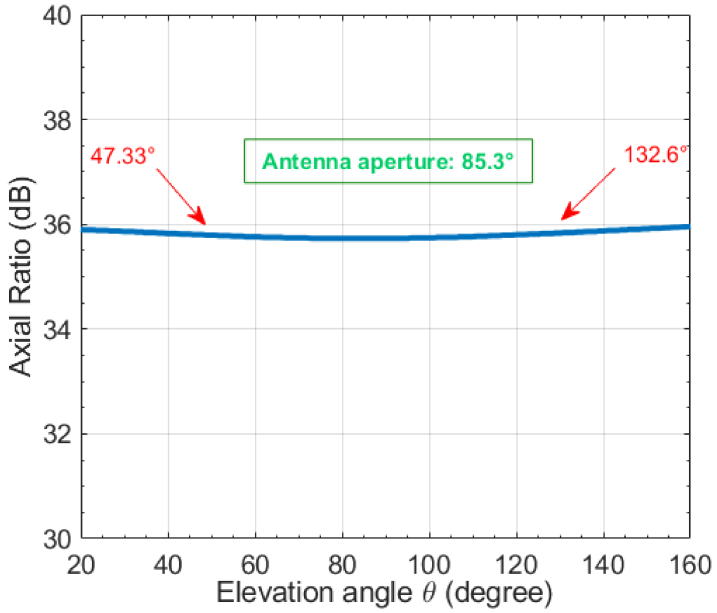


**Figure 6.** Helical antenna's axial ratio for an azimuth angle $\varphi = 90°$. The axial ratio is independent of the azimuth angle.

### *3.2. Helical RFID Tag's Experimental Characterization*

#### 3.2.1. Fabricated Prototypes

Figure 7a presents the fabricated textile yarn obtained from the modified E-Thread® assembling process. The spool of the textile filament is composed of helical RFID tags, which are cascaded. Note that in practice, each tag can be cut at the appropriate length in order to be operational at the desired frequency. One helical RFID tag was isolated from the spool by cutting at the length that allowed it to have a resonance frequency in the UHF RFID band.

(**a**) (**b**)

**Figure 7.** Fabricated helical RFID tags. (**a**) Spool of cascaded helical RFID tags. (**b**) RFID helical tag after isolation from the spool.

The obtained RFID helical tag is shown is Figure 7b and has the following geometrical parameters: $h$ = 47.5 mm; $N = 40$, in addition to the ones given in Table 1. An error of 5% can be observed regarding the height, which is due to the fact that in the simulation, the material properties are known with a certain imprecision and the pitch $s$ is not ideal. Thus, the helical tag's length has to be adjusted after fabrication.

3.2.2. Measured Read Range of the Helical RFID Tag

Considering that the RFID reader has an EIRP of 3.28 W and the IC has a threshold power $P_{th} = -20$ dBm, the measured read range and the one deduced from the simulation using Equation (2) are shown in Figure 8. It was shown that the helical RFID tag exhibited a maximum measured read range of 10.6 m at the frequency of 865 MHz. Moreover, the RFID helical tag exhibited a wide band behavior as it can be operational in the U.S. UHF RFID band $(902 - 928)$ MHz with a read range of 9 m. The measured result is coherent with respect to the simulation as the maximum read range obtained by the simulation was 11.3 m at 865 MHz. It is also worth remarking that the gain value of the antenna helped to compensate for the transmission coefficient and allowed a read range to be obtained closer to that of the current E-Thread solution (12 m).

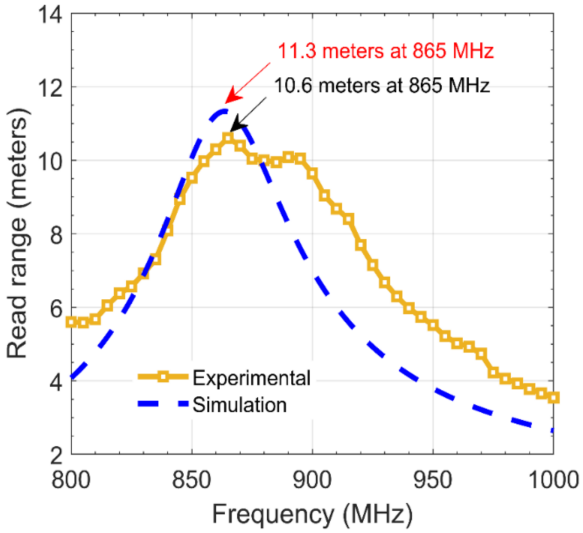


**Figure 8.** Helical RFID tag's read range obtained by simulation and by experimental measurement.

Moreover, it can be remarked that compared to the simulation, a wider frequency bandwidth was obtained in the experiment, which is very advantageous for an applicative scenario. The difference in the results may be explained by the manufacturing process (some inaccuracies in the dimensions and the permittivity values of materials), which does not allow for an exact fit with the dimensions employed in the simulation.

*3.3. Evaluation of the Helical RFID Tag's Robustness in Terms of Stretching*

The impact of the tag's elongation on the read range was measured and the results are presented in Figure 9. At the initial state (without elongation) for an antenna having the total length of 9.5 cm, the maximum read range was 11 m at 865 MHz, which is higher than the previously shown result. This small difference may be attributed to the fact that in the previous measurement, the antenna was slightly bent; this also shows the impact that the curvature will have for a tag in wire form. It can also be observed that up to a length of 10 cm, the helical RFID tag's read range is maintained at the frequency of interest. However, beyond this length, the resonance frequency is shifted to lower frequencies, which is coherent with the increase in the length of an antenna. At the maximum considered length of 10.6 cm, the tag was still readable at a range of 9 m (18% of loss) at the frequency of interest.

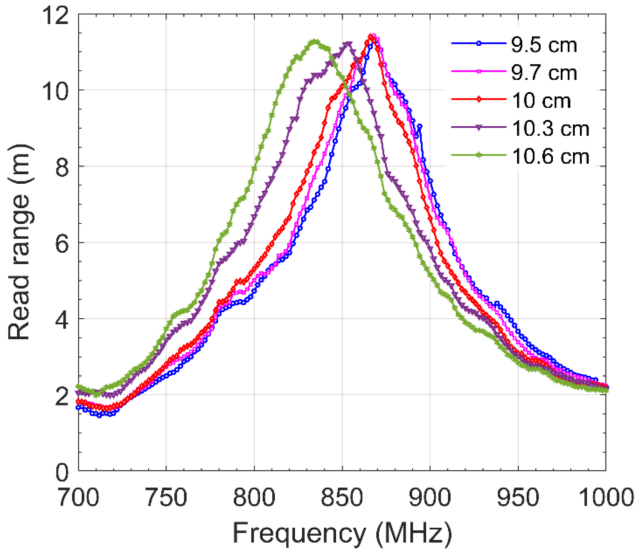


**Figure 9.** Impact of the stretching on the helical RFID tag's read range, obtained by experimental measurements.

From these measurements, the robustness of the proposed antenna was confirmed in terms of the read range performance as well as the structural aspect of the textile material.

## 4. Conclusions

In this paper, a helical RFID tag was designed to be integrated into a textile yarn using the E-Thread® technology. The simulation results showed that fixing the parameters such as the pitch $s$ and the diameter $D$ made a complex impedance matching process due to the strong impact these parameters have on the helical antenna input impedance. However, the tag's read range maybe improved to reach a value close to the one obtained in the current solution by ensuring an antenna gain that enables compensating the reflection coefficient $\Gamma$. Another improvement solution might be adding lumped elements to achieve an impedance matching with the inconvenience of a complex manufacturing process. From the experimental measurements, the helical RFID tag exhibited a read range of 10.6 m, which is an improvement considering the previous work [15]. Compared to the current solution of the RFID yarn using a half-wave dipole that has a read range of 12 m, the helical RFID tag offers a close read range with the advantage of being robust to elongation. Indeed, as the experiments have demonstrated, up to an elongation of 10% from the initial length, the helical RFID tag is still readable at 9 m.

The presented helical RFID tag may be used in a wide range of applications. The capabilities of the helical RFID tag could also be expanded beyond the classical identification purposes to some other functionalities, for example, using the antenna elasticity in order to measure strain deformation and thus the textile helical RFID tag becomes a sensor.

**Author Contributions:** Conceptualization, S.B.; methodology, S.B., F.D.H. and Y.D.; software, S.B.; validation, S.B., F.D.H. and Y.D.; formal analysis, S.B.; investigation, S.B., F.D.H. and Y.D.; writing—original draft preparation, S.B.; writing—review and editing, F.D.H. and Y.D.; supervision, F.D.H. and Y.D.; funding acquisition, Y.D. All authors have read and agreed to the published version of the manuscript.

**Funding:** This research was funded by the "La Région Auvergne Rhône-Alpes" Lyon, France, through the "Pack Ambition Recherche 2017" program.

**Data Availability Statement:** Not applicable.

**Acknowledgments:** The authors would like to thank the company Primo1D for their help during the manufacturing process and the experimental characterization.

**Conflicts of Interest:** The authors declare no conflict of interest.

## References


1. Nikitin, P.V.; Rao, K.V.S. Antennas and Propagation in UHF RFID Systems. In Proceedings of the IEEE International Conference on RFID, Las Vegas, NV, USA, 16–17 April 2008; pp. 277–288.
2. Keehr, E.A.; Lasser, G. Making a low-cost software-defined UHF RFID reader. *IEEE Microw. Mag.* **2021**, *22*, 25–45. [CrossRef]
3. Athauda, T.; Karmakar, N. Chipped versus chipless RF identification: A comprehensive review. *IEEE Microw. Mag.* **2019**, *20*, 47–57. [CrossRef]
4. Duroc, Y.; Tedjini, S. RFID: A key technology for humanity. *Comptes Rendus Phys.* **2018**, *19*, 64–71. [CrossRef]
5. Zannas, K.; Matbouly, H.E.; Duroc, Y.; Tedjini, S. From identification to sensing. In *Wireless Power Transmission for Sustainable Electronics*; Wiley: Hoboken, NJ, USA, 2020.
6. Fernández-Caramés, T.M.; Fraga-Lamas, P. Towards the internet of smart clothing: A review on IoT wearables and garments for creating intelligent connected E-Textiles. *Electronics* **2018**, *7*, 405. [CrossRef]
7. Bakkali, M.E.; Martinez-Estrada, M.; Fernandez-Garcia, R.; Gil, O.; Mrabet, E. Effect of Bending on a Textile UHF-RFID Tag Antenna. In Proceedings of the 14th European Conference on Antennas and Propagation, Copenhagen, Denmark, 15–20 March 2020.
8. Koski, K.; Lohan, E.S.; Sydanheimo, L.; Ukkonen, L.; Rahmat-Samii, Y. Electro-Textile UHF RFID Patch Antennas for Positioning and Localization Applications. In Proceedings of the IEEE RFID Technology and Applications Conference (RFID-TA), Tampere, Finland, 8–9 September 2014; pp. 246–250.
9. Björninen, T.; Virkki, J.; Sydanheimo, L.; Ukkonen, L. Impact of Recurrent Washing on the Performance of Electro-Textile UHF RFID tags. In Proceedings of the IEEE RFID Technology and Applications Conference (RFID-TA), Tampere, Finland, 8–9 September 2014; pp. 251–255.
10. Corchia, L.; Monti, G.; Tarricone, L. Wearable antennas: Nontextile versus fully textile solutions. *IEEE Antennas Propag. Mag.* **2019**, *61*, 71–83. [CrossRef]
11. Kiourti, A. RFID antennas for body-area applications: From wearables to implants. *IEEE Antennas Propag. Mag.* **2018**, *60*, 14–25. [CrossRef]
12. Vicard, D.; Brun, J. Cap for a Chip Device Having a Groove, Device Provided with Said Cap, Assembly Consisting of the Device and a Wire Element, and Manufacturing METHOD thereof. U.S. Patent App. 14,428,254, 13 August 2015.
13. Andia, G. Slenderly and Conformable Passive UHF RFID Yarn. In Proceedings of the IEEE International Conference on RFID, Phoenix, AZ, USA, 9–11 May 2017; pp. 130–136.
14. Song, Z.; Li, Y.; Zheng, H.; Li, Y.; Li, E. Design of an Electronically Steerable Dielectric Helical Antenna Phased Array for Millimeter Wave Applications. In Proceedings of the Global Symposium on Millimeter-Waves & Terahertz (GSMM), Nanjing, China, 23–26 May 2021; pp. 1–3.
15. Mardani, H.; Buchanan, N.; Fusco, V.; Naeem, U. Increasing the Wireless Power Transfer (WPT) Link Efficiency by High Gain Helices. In Proceedings of the IEEE Texas Symposium on Wireless and Microwave Circuits and Systems (WMCS), Waco, TX, USA, 18–20 May 2021; pp. 1–4.
16. Okada, N.; Koshimizu, S.; Shimasaki, H. Helical Antennas in 920-MHz Band for Wireless Sensor Nodes under the Ground. In Proceedings of the International Symposium on Antennas and Propagation (ISAP), Osaka, Japan, 25–28 January 2021; pp. 325–326.
17. Mizuno, H.; Takahashi, M.; Saito, K.; Ito, K. Design of a Helical Folded Dipole Antenna for Biomedical Implants. In Proceedings of the 5th European Conference on Antennas and Propagation (EUCAP), Rome, Italy, 11–15 April 2011; pp. 3484–3487.
18. Karnaushenko, D.D.; Karnaushenko, D.; Makarov, D.; Schmidt, O.G. Compact helical antenna for smart implant applications. *NPG Asia Mater.* **2015**, *7*, e188. [CrossRef]
19. Binti Mohd Baharin, R.H.; Yamada, Y.; Kamardin, K.; Michishita, N. Changes of Electric Current on a Normal-Mode Helical Antenna Inside a Human Body. In Proceedings of the IEEE Conference on Antenna Measurements & Applications (CAMA), Tsukuba, Japan, 4–6 December 2017; pp. 403–406.
20. Yamada, Y.; Hong, W.G.; Jung, W.H.; Michishita, N. High Gain Design of a Very Small Normal Mode Helical Antenna for RFID Tags. In Proceedings of the TENCON IEEE Region 10 Conference, Taipei, Taiwan, 30 October–2 November 2007; pp. 1–4.
21. Liao, Y.; Zhang, K.; Cai, K.; Liang, Z. Impedance Matching Design of Small Normal Mode Helical Antennas for RFID Tags. In Proceedings of the International Symposium on Antennas and Propagation, Nanjing, China, 23–25 October 2013; pp. 1150–1153.
22. Benouakta, S.; Hutu, F.; Sette, D.; Duroc, Y. UHF RFID elastic textile yarn. *Microw. Opt. Technol. Lett.* **2020**, *62*, 3186–3194. [CrossRef]
23. Kraus, J.D. The helical antenna. *Proc. IRE* **1949**, *37*, 263–272. [CrossRef]
24. Impinj. Monza 6 Product Brief. Available online: https://support.impinj.com/hc/en-us/articles/202765328-Monza-R6-Product-Brief-Datasheet (accessed on 15 March 2021).
25. Voyantic. Tagformance Pro. Available online: https://voyantic.com/products/tagformance-pro (accessed on 2 January 2021).

*textiles*

MDPI

*Review*

# Fibers and Textiles for Personal Protective Equipment: Review of Recent Progress and Perspectives on Future Developments

**Patricia I. Dolez *, Sabrina Marsha and Rachel H. McQueen**

Department of Human Ecology, University of Alberta, Edmonton, AB T6G 2R3, Canada; smarsha@ualberta.ca (S.M.); rachel.mcqueen@ualberta.ca (R.H.M.)
* Correspondence: pdolez@ualberta.ca

**Abstract:** This article reviews recent developments in fibers and textiles for Personal Protective Equipment (PPE) applications. Fibers are grouped into six categories: highly extensible elastomeric fibers, cellulose-based fibers, commodity synthetic fibers, high strength inorganic materials, and high performance polymer fibers. New developments with highly extensible elastomeric fibers include polyester-based elastic fibers and shape memory polyurethane. In the case of cellulose-based fibers, environmentally friendly processes and nanotechnology-enabling treatments are developed for natural fibers where attempts are made to transfer interesting attributes of the feedstock to regenerated cellulose fibers. Commodity synthetic fibers comprise polyolefins, polyester, and polyamide; they have seen recent developments in terms of surface functionalization and the formation of structures at the nanoscale. In terms of high strength inorganic materials, basalt fibers and carbonaceous materials have found increased use in PPE. Boron is also generating considerable interest for fibers and coatings. Research on high-performance polymer fibers includes further improving their short- and long-term performance, moving to the nanoscale for new functionalities, and exploring their recyclability. An additional section describes a series of special textile structures relevant to PPE involving 3D textile structures, auxetic textile structures, shear thickening fabrics, nanoporous structures, phase change materials, and some specially designed textile-based composite structures for improved protection against mechanical hazards. The article ends with some perspectives on promising avenues for further developments.

**Keywords:** fibers; textiles; personal protective equipment; protective clothing; high-performance fibers; special textile structures

**Citation:** Dolez, P.I.; Marsha, S.; McQueen, R.H. Fibers and Textiles for Personal Protective Equipment: Review of Recent Progress and Perspectives on Future Developments. *Textiles* **2022**, *2*, 349–381. https://doi.org/10.3390/textiles2020020

Academic Editor: Laurent Dufossé

Received: 18 April 2022
Accepted: 6 June 2022
Published: 13 June 2022



## 1. Introduction

According to the US Occupational Safety and Health Administration (OSHA), Personal Protective Equipment (PPE) are "equipment worn to minimize exposure to hazards that cause serious workplace injuries and illnesses" [1]. Hazards can be of various natures: mechanical, chemical, biological, thermal, electrical, radiological, and nuclear. PPE can also provide protection against vibrations, insufficient visibility, drowning, and falls for instance. In addition, they can be used for activities that are not work related, e.g., sports and domestic chores.

PPE are part of the toolbox for risk management along with engineering controls and administrative measures [2]. The PPE selection process can be organized into seven steps (Figure 1):

- Analyze the risks and identify those that cannot be avoided through engineering controls and administrative measures;
- Determine the requirements for PPE based on the risks involved, including those resulting from wearing the PPE, and considerations related to the activity to be performed and the environment;
- Assess and compare the characteristics of commercially available PPE;

- Select the optimal PPE based on the protection and functionality requirements as well as other aspects, such as cost and durability;
- Initiate and train users to properly wear the PPE;
- Establish a procedure for the PPE inspection and care;
- Perform a periodic review of the choice of PPE to verify that they still meet requirements and that the level of risk has not changed.

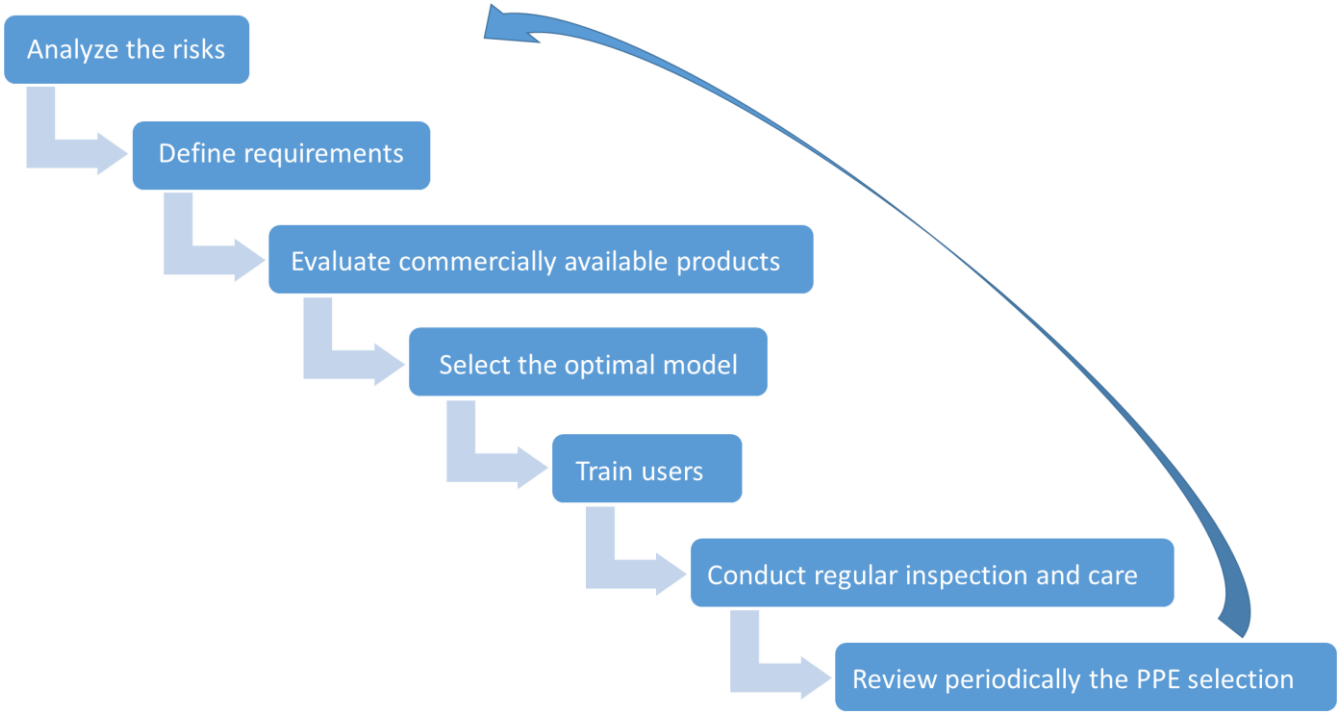


**Figure 1.** PPE selection process in seven steps [2].

Different types of PPE are used depending on the hazards present and the body part or function at risk. One subset of PPE is protective clothing. It is designed to isolate the whole body or different body parts from the one or more hazards one may be exposed to [3]. Protective clothing can be categorized according to the part of the body they protect. A first category comprises bunker suits, lab coats, coveralls, gowns, lifejackets, bulletproof vests, safety harnesses, and aprons for instance, which cover the whole body or the torso. Protection to the legs and feet can be offered by pants, chaps, gaiters, booties, and boots. Gloves and arm guards can be used to protect the arms and hands, while hoods and balaclavas serve for the head. Other types of PPE aside from protective clothing include respirators, goggles, face shields, helmets, and earmuffs.

PPE have been used for thousands of years. In the case of body armor, materials included animal hides with the first examples dated as early as 5000 B.C. [4,5], metal plates introduced by the Egyptians circa 1500 B.C. [6], and silk used in Japan in the Middle Ages [5]. Leather has also been used for protection against thorns [7] and to manufacture blacksmiths' aprons [8]. With its resistance to flame, wool was the preferred material for firefighter protective clothing until World War II [9].

A major change came with the introduction of synthetic polymers in the middle of the 20th century. Commodity polymers, such as polyethylene, polypropylene, polyester, and polyamide, provided durability at low cost [10]. From the 1960's, high performance polymers revolutionized protective clothing with exceptional mechanical performance and/or inherent heat/flame resistance combined with low weight [11]. These high performance fibers include aramids, polybenzimidazoles (PBI), polybenzoxazoles (PBO), and ultra-high molecular weight polyethylene [11,12].

Regulations for protective clothing and PPE were established around the same period with, for instance, the Occupational Safety and Health Act of 1970 [13]. Standardization organizations have also been developing test methods and specifications for protective clothing and PPE since the early 1990s, with, e.g., the Technical Committee TC 94 on Protective Clothing and Equipment of the International Organization for Standardization (ISO) [14] and the Committee F23 on Personal Protective Clothing and Equipment of the American Society for Testing and Materials (ASTM) [15].

Technical advances in polymer science, textiles, and materials engineering as well as new technologies, such as nanotechnologies and smart textiles, have allowed improvements to the high-performance materials and structures used in PPE to provide better performance and enhanced comfort while being aware of environmental sustainability during manufacture and use. The purpose of this article is to review recent developments in fibers and textiles for protective clothing and PPE applications. The review considers six categories of fibers—highly extensible elastomeric fibers, cellulose-based fibers, commodity synthetic fibers, high strength inorganic materials, and high performance polymer fibers—as well as special textile structures relevant to PPE. It concludes with some perspectives on promising avenues for further developments in fibers and textiles for PPE.

## 2. Highly Extensible Elastomeric Fibers

Elastomeric fibers are highly extensible fibers. They are a key component for improved garment fit in protective clothing. Elastomeric fibers are also used as part of the securing system for many PPE.

Spandex (elastane) fibers are a segmented copolymer of polyurethane cross-linked rigid segments with polyester or polyether flexible segments (Figure 2a). Some variants aimed at specific applications have been developed; for instance a highly hygroscopic spandex for moisture management, a soft spandex with a greater stretch, and a chlorine-resistant spandex [16]. Despite a patent from 1978 describing different strategies to prepare flame resistant (FR) polyurethane elastomeric fibers [17], no such product appears to be commercially available. The solution used to produce FR elastic textile products is thought to involve wrapping the elastic core with a flame resistant fiber, such as the meta-aramids using the core-spun technique as described in the patent by Aldridge [18]. Core-spinning is a common method for preparing spandex-blend fabrics as spandex fibers are always used in conjunction with another fiber. This technique, which can be implemented using ring, friction, rotor, and air-jet spinning, has traditionally been used in the textile industry to cover elastic fibers with a cotton yarn to improve the touch aspect [19].

Polyester-based elastic fibers have recently been developed [16]. They include polybutylene terephthalate (PBT) (Figure 2b) and polytrimethylene terephthalate (PTT) (Figure 2c). PTT offers the possibility of being bio-based, with for instance the Sorona fiber from Dupont using corn as a raw material. The fiber cross-section can also be shaped with a specific profile to improve its moisture-wicking performance. An olefin-based elastic fiber, named XLA, has also been developed, with a good resistance to chemicals, heat and UV light. Bicomponent stretch fibers, such as T400, combine two fibers with different stretch properties.

The latest trend in highly extensible elastomeric fibers involves the use of shape memory polyurethane. Recent works include the preparation of shape memory polyurethane fibers by melt spinning [20], melt-blowing [21], and electrospinning [22] for instance. The possibility to switch between the two programmed configurations they offer provides a solution to the challenge of donning and doffing tight-fitted garments [16].

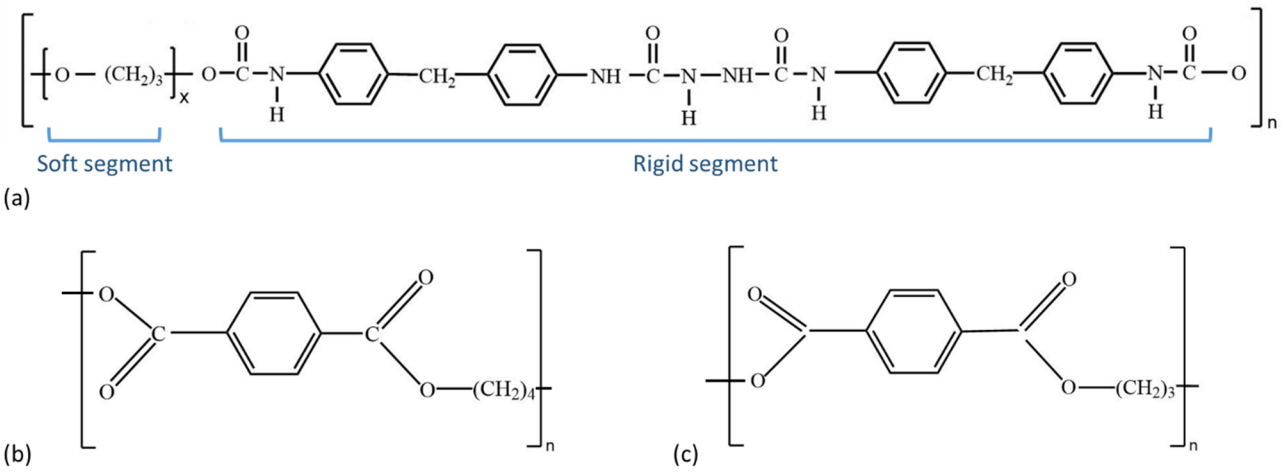


**Figure 2.** Chemical formula of: (**a**) Elastane [23]; (**b**) Polybutylene terephthalate; (**c**) Polytrimethy lene terephthalate.

## 3. Cellulose-Based Fibers

Cellulose-based fibers used in PPE include natural fibers and regenerated cellulose fibers. Although they have largely been replaced by synthetic fibers for many high performance applications, cellulose-based fibers have maintained a presence in the field. Their continued presence is in large part due to tactile comfort considerations as well as cost for some applications. For instance, FR treated cotton and FR viscose are still a major component of FR coveralls used in the oil and gas industry and other applications with low to medium risk of heat and flame exposure [24,25]. FR treated cotton performs well also for arc flash and is the most common fabric used in arc rated protective clothing [26].

### *3.1. Natural Fibers*

One of the trends observed with natural fibers is the search for plants with a lower environmental footprint than cotton, such as hemp. For instance, attempts have been made to blend hemp fibers with softer fibers to increase its tactile comfort [27] and UV protection rating [28] while benefiting from the hemp fiber strength and thermal performance. Promising developments in the area of FR finishes for cellulose fibers involve taking advantage of the synergetic effect of environmentally friendly multi-element systems, for instance phosphorous–nitrogen [29]. This eco trend also includes the potential for improvements to the recyclability of FR treated fabrics [25]. This will depend on the ability to remove finishes and additives after the PPE has reached the end of their life so that the fibers can have a second life or be composted.

Another development with natural fibers involves taking advantage of nanotechnologies to improve their performance with a surface treatment without impacting their tactile comfort and weight. For instance, cotton fabrics with electromagnetic interference shielding functionality were prepared by layer-by-layer self-assembly to form alternating layers of chitosan graphene and poly(sodium 4-styrenesulfonate) (PSS) [30]. With a 10-layer coating, the fabric shielding effectiveness reached more than 30 db and its electrical conductivity $1.67 \times 10^3$ S m$^{-1}$. Other applications include silver and copper oxide nanoparticle coatings on cotton for antibacterial properties, zinc oxide nanorods and titanium dioxide ($TiO_2$) nanoparticles grown on jute fibers to make the fibers superhydrophobic after a fatty acid treatment (Figure 3), and a treatment of cotton fabrics with $TiO_2$ nanoparticles to improve the efficiency of the anti-wrinkle compounds for instance [31].

Attempts have also been made recently to use natural fibers as a cheaper alternative to high-performance fibers. For instance, a multilayered armor system was developed where the intermediate layer of aramid fabric epoxy laminate was replaced by an epoxy composite reinforced with ramie fibers [32]. A decrease in performance was observed with

the ramie fibers but the product still met the standard requirements. The ramie structure was much less expensive than its aramid counterpart. Ramie has also been recognized as being an environmentally sustainable fiber [33].

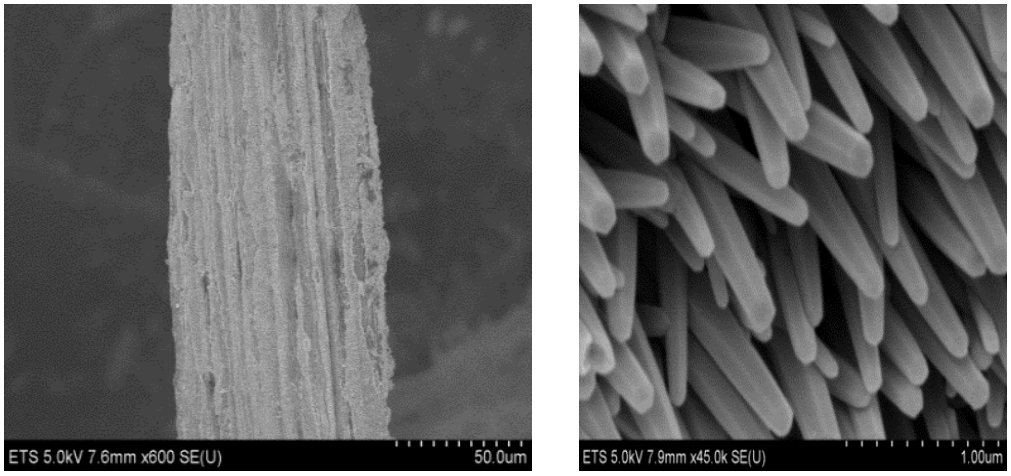


(**a**) (**b**)

**Figure 3.** Images by Field Emission Scanning Electron Microscopy (FE-SEM) of zinc oxide nanorods grown on jute fibers by a hydrothermal process: (**a**) 600 magnification; (**b**) 40K magnification (Reprinted with permission from Ref. [34]. Copyright 2017, Elsevier).

### *3.2. Regenerated Cellulose Fibers*

In the case of regenerated cellulose, researchers are exploring the possibility of taking advantage of some natural attributes of the feedstock. For instance, it was shown that the activity of bamboo's natural antimicrobial agent, bamboo kun, is maintained after it has gone through the cellulose dissolution process [35]. Although, other researchers have found that fabrics made from regenerated bamboo fibers do not exhibit antibacterial properties [36]. Another characteristic of cellulose that researchers have recently worked to harness is its nanostructures. For instance, cellulose nanocrystals have been used to help functionalize a polyvinyl alcohol–polyethylene copolymer (PVA-co-PE) nanofibrous membrane with the anthraquinone-2-carboxylic acid photo-catalyst for use in protective clothing [37]. The resulting membrane combined antibacterial, aerosol filtration, and chemical detoxifying functions. In another study, a flame resistant thermally insulating lightweight aerogel was prepared with cellulose nanofibrils, N-methylol dimethylphosphonopropionamide, and 1,2,3,4-butanetetracarboxylic acid [38]. The thermal conductivity was 0.03258 W/(m.K), which opens an interesting perspective for thermal protective equipment for firefighters for instance. Other applications of cellulose nanostructures relevant to PPE include lightweight materials for ballistic protection [39].

## 4. Commodity Synthetic Fibers

Since polymers became commercially available in the 1950's, synthetic fibers made with commodity polymers (polyolefins, polyester, polyamide) have been widely used in PPE because of their low price and durability. In addition, these synthetic fibers can easily have their shape and dimensions modified for enhanced performance properties. For instance, hollow fibers have been manufactured with polyester, polyamide, and polypropylene to provide improved thermal insulation [40]. Fibers with a serrated or multilobal cross-section offer better liquid transportation along their length, and thus improve the wicking performance [41].

### *4.1. Polyolefin Fibers*

Polyolefins offer a low-cost solution for protective clothing, e.g., for protection against splashes of liquid chemicals [42]. For instance, polypropylene (PP) displayed a much longer breakthrough time compared with a polymer blend typically used for manufacturing CBN (chemical, biological, nuclear) protective garments, as well as a higher tensile strength. Polyolefins are also heavily used for air and liquid filtration because of their good resistance to abrasion, strength retention in the wet state, good resistance to chemicals, excellent resistance to micro-organisms, dimensional stability, and low cost [43].

PP fibers currently dominate the market of disposable respirators and respirator filtration media. They are formed into a three-layer nonwoven structure [44]; the filtering function is provided by the melt-blown middle layer, while the spun-bond outer and inner layers provide strength and give the product a specific shape. Researchers recently proposed the use of 3D printing to prepare N95 masks and other medical PPE [45]. Other recent developments with polyolefins include functionalizing the nonwoven fibers to improve their efficiency and/or comfort. For instance, Okrasa et al. added alkyl substituted octaisobutyl polyhedral oligomeric silsesquioxane (POSS) as a filler to PP before producing nonwoven samples by melt-blowing to improve the electrostatic performance retention of the electret filter [46]. They also explored the possibility of incorporating particles of super-absorbing polymers into the PP nonwoven structure to favor the absorption of moisture in the mask and improve the user's comfort.

In another study, a core-sheath filament was prepared by melt extrusion and drawing for the controlled release of insect repellents [47]. High-density polyethylene (HDPE) was used as the sheath, while the core was made of poly(ethylene-co-vinyl acetate) (EVA) containing the insecticide N,N-Diethyl-m-toluamide (DEET). A strategy explored to provide an antibacterial function to PP nonwovens for shoe insole relied on using magnesium monoperoxyphthalate as an additive during the fiber formation melt-blown process [48]. The study also looked at modifying polycarbonate and polyamide nonwovens in a similar way. A N–halamine compound, 1-chloro-2,2,5,5-tetramethyl-4-imidazolidinone, was also coated on a PP melt-blown nonwoven to provide it with antimicrobial capabilities [49].

Another interesting recent finding in the area of PPE relates to the risk of slipping in cold environments. It was shown that a PP footwear sole offered better slip resistance on ice between $-1$ and $-15$ °C compared to vulcanized and polyurethane rubber [50]. A last area of research is related to the challenge in dyeing PP fibers. For instance, Elmaaty et al. have come up with an environmentally friendly process involving disperse dyes and supercritical carbon dioxide [51]. Others have explored the use of nanoclay as a filler to increase the dyeability of PP [52].

### *4.2. Polyester and Polyamide Fibers*

In the case of recent developments with polyester and polyamide fibers, efforts have involved surface functionalization using nanotechnologies [31]. Applications include antibacterial activity, chemical detoxification, superhydrophobicity, UV protection, flame retardancy, abrasion resistance, antistatic, photonics, and electronics. For instance, graphene has been put forward as a coating on polyester and polyamide fibers for protective clothing applications [53]. An example of a clothing product already on the market takes advantage of graphene thermal conductivity for improved heat management [54]. A nanocomposite coating comprised of silica nanoparticles in a fluoropolymer matrix was applied on a polyester fabric using a dip–pad–cure process [55]. The treated fabric showed a high acid repellency. In addition, its strength was only minimally affected after being immersed for 5 min in 80% sulfuric acid. Other researchers have worked with polyamide 6 to develop a new type of FR intumescent nanocomposite electrospun fibers using nanoclay [56]. These low-cost inherently FR fibers have been blended with PBI and Lenzing FR regenerated cellulose fibers to identify the best combination of performance at the lowest cost.

An environmentally friendly strategy to impart fabrics with both oil- and water-repellency was developed using a perfluorocarbon-free oleophobic finish based on a thin

polydimethylsiloxane coating with a specific texture at a smaller length scale [57]. The principle was tested with a woven polyamide fabric. Good repellency was obtained against canola, olive and castor oil, synthetic sweat, and water. This environmentally friendly oleophobic solution can be applied to other types of fibers.

Finally, polyester and polyamide fibers and filaments are also used in the area of smart textiles, where they can be coated or plated with silver to create electrically conductive yarns or blended with silver fibers to prepare a heating nonwoven [58]. Wearing a garment made with polyamide fibers coated with silver has also been proposed as a way to reduce exposure to electromagnetic fields [59].

### *4.3. Modacrylic Fibers*

Modacrylic fibers are used in the area of heat and flame protection [60]. They are generally blended with cotton, although they can also be found in blends with regenerated cellulose and synthetic fibers. A potential issue of the release of hydrogen chloride and cyanide in the event of the combustion of modacrylic fabric was raised a few years ago [61]. However, it does not appear as critical as initially thought because the concentrations observed were not estimated to be a significant risk to health nor do they limit the ability to escape or survive a fire [62]. Regarding the release of particulate antimony, the same group mentioned that the concentrations observed were well below anything considered hazardous. Efforts have also been dedicated by fiber manufacturers to develop low antimony or antimony-free modacrylic, for instance the Protex® Q fiber by Kaneka Corporation [63].

### *4.4. Nanofibers*

Nanofibers produced by electrospinning with different polymers are increasingly being used in air filtration as they offer a higher aerosol collection efficiency with a lower pressure drop compared to their microscale counterparts [64]. They include PP [65], polyurethane [66], polyacrylonitrile (PAN) [67], and polyvinylidene fluoride [68] as well as cellulose acetate [69] and polylactic acid (PLA) [70] biopolymers. Electrospun nanofibers are also being considered for protective clothing to provide higher breathability (i.e., water vapor transport) and filtration while being lightweight [71,72]. For instance, polyamide 6 (PA6) nanofibers were deposited on the surface of fabrics typically used in protective clothing [73]. An increase in thermal insulation was obtained.

Nanofibrous mats can further be functionalized by grafting photoactive species, such as benzophenones and polyphenols [74], N-halamines [75], or silver nanoparticles [76], for antibacterial activity for instance. Nanocomposite nanofibers can also be prepared by adding nanoparticles in the electrospinning solution. Recent works include PAN and PAN-co-polyacrylate nanocomposite nanofiber membranes incorporating titanium dioxide nanoparticles for improved particulate matter adhesion [77], polyethersulfone/barium titanate nanofibrous membranes deposited on a nonwoven polypropylene substrate for improved mask filtration and comfort [78], silica aerogel/PAN nanocomposite nanofibers for adsorption of volatile organic compounds [79], and PAN nanofibers containing a compound combining silver and lipid vesicles for antibacterial activity [80].

Some researchers have also developed multifunctional nanocomposite nanofibers mats. One strategy involved preparing chitosan–poly (vinyl alcohol) nanocomposite nanofibers loaded with silica nanoparticles, and then coating the nanofibers with silver nanoparticles formed by the UV reduction of silver nitrate on the fiber surface [81]. Another strategy was based on the use of dual electrospinning, which allows combining non-compatible active nanoparticles [82]. Nanocomposite mats containing a blend of silver nanoparticle-containing PAN nanofibers and magnesium oxide nanoparticle-containing PAN nanofibers were electrospun using two separate syringes subjected to a translational motion. The membrane was developed for chemical and biological detoxifying applications. Analysis by energy dispersive X-ray (EDX) spectrophotometry showed the absence of contamination of each type of nanofibers by the nanoparticles of the other type of nanofibers in the comingled electrospun mat (Figure 4).

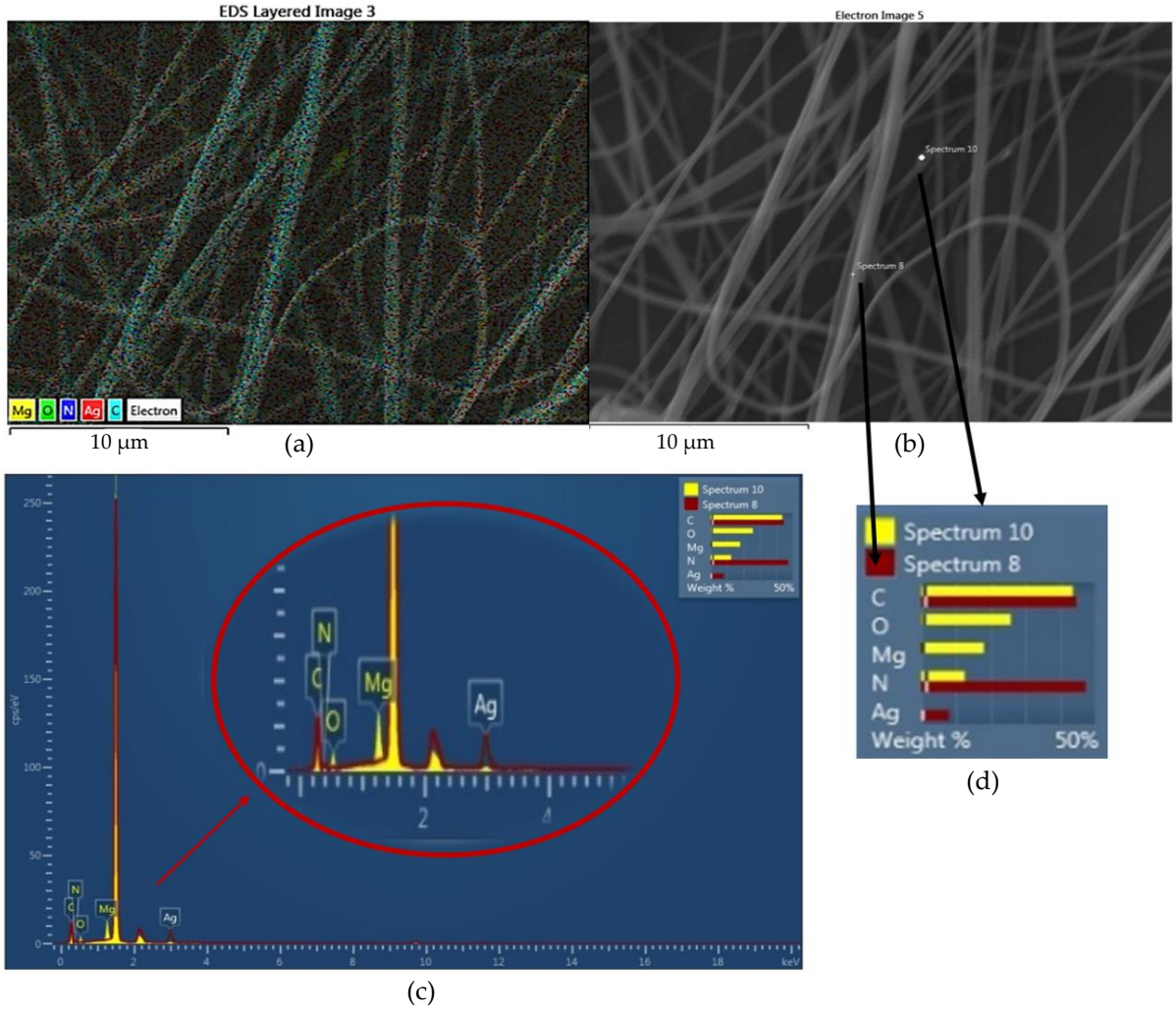


**Figure 4.** Multifunctional nanocomposite nanofibrous mat combining silver nanoparticle-containing PAN nanofibers and magnesium oxide nanoparticle-containing PAN nanofibers produced by dual-electrospinning: (**a**) EDX layered image; (**b**) Electron scanning microscopy image; (**c**) Superimposed spectra corresponding to two different fibers; (**d**) Details of the chemical content of the two different fibers showing the absence of contamination by the nanoparticles between the different types of nanocomposite fibers [82].

An interesting strategy involves 3D printing struts on nanofiber mats using PLA polymer to form a transparent hierarchical structure [83]. This technique can make masks less visually obtrusive, therefore, increasing their adoption by the public. A transparent mask will also enable facial expressions to be viewed, which is critical for efficient communication. Another new concept for masks combines an electrospun nanofibrous mat with a triboelectric nanogenerator driven by respiration to maintain and reinforce the electrostatic aerosol capture mechanism [84]. A filtration efficiency of more than 85% was obtained after the mask was continuously worn for 4 h as well as after a 30-day interval.

## 5. High-Strength Inorganic Materials

Various inorganic materials have found a place in PPE due to their high strength as well as other interesting characteristics. This includes glass, basalt, carbon, metal, and boron fibers. These fibers have found applications in flame protection, puncture and cut resistance, and thermal protection from cold and hot hazards for instance. Inorganic materials are also key components for wearable electronics and smart textiles.

### *5.1. Basalt Fibers*

In the area of heat and flame protection, fire shelters used by firefighters and protective clothing for foundry workers for instance have traditionally been manufactured with a glass fiber fabric coated with a layer of aluminum on the outside to reflect the incident radiant heat. However, researchers have explored the possibility of replacing the glass fibers by basalt fibers, which are not only less expensive but also offer higher strength and better thermal resistance [85]. They compared the performance of an aluminized glass fiber protective clothing for foundry workers with an aluminized basalt fiber protective clothing using a thermal manikin. Better clo values were measured for the aluminized basalt clothing. Promising results with aluminized basalt fabrics have also been obtained for protective gloves [86]. Improvements in the contact resistance at 100 °C, heat transfer, and thermal resistance were obtained for a basalt fabric coated with a layer of chromium or zirconium oxide compared to the uncoated fabric [87]. The fabric also displayed static-dissipation properties.

In addition, basalt fabrics have been explored as an alternative to glass fibers for composite manufacturing [88], which is used in different types of PPE, such as for puncture-resistant plates for boots, ballistic plates, or helmets. One of the advantages of basalt fibers over glass fibers in composites is their higher resistance to high temperature [89]. This can allow thermal recycling at the end of the composite life as the matrix would thermally degrade while the basalt fibers remain unaffected. Basalt fabrics can be used as a reinforcement on their own or be combined with other high performance fibers, such as aramids [90] and carbon fibers [91]. A graphene coating has also been used to increase the interfacial adhesion between basalt fibers and the polymer matrix such as polyamide 6 (Figure 5) [92].

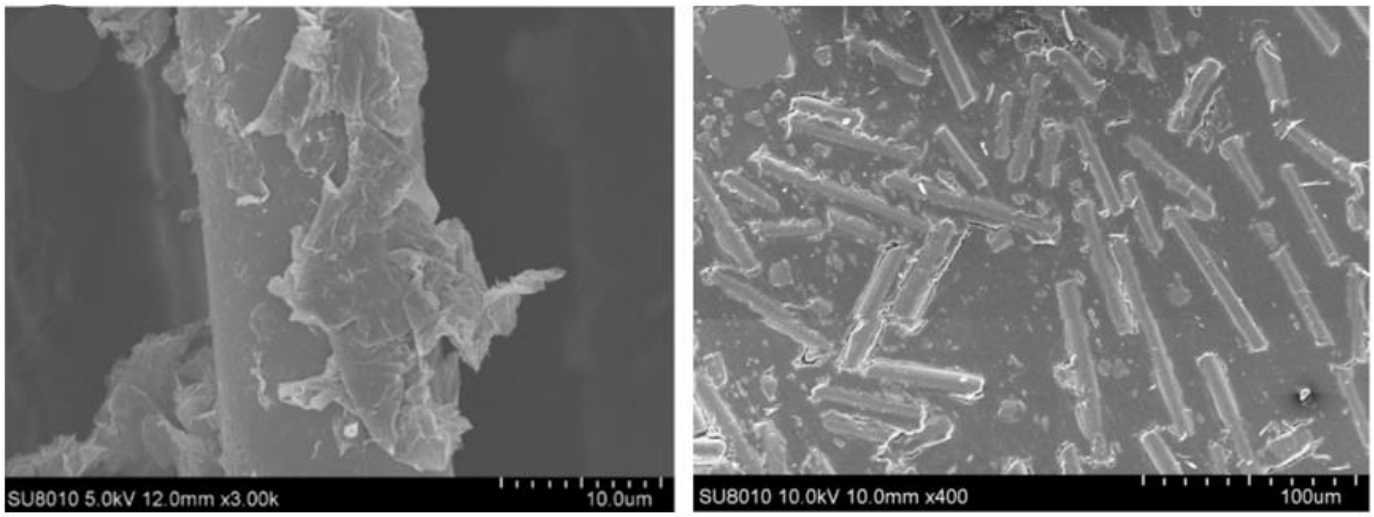


**Figure 5.** SEM images: (**a**) Basalt fibers coated with graphene; (**b**) Abraded surface of polyamide 6 composite sample containing the graphene-coated basalt fibers (Reprinted with permission from Ref. [92]. Copyright 2018, Elsevier).

### *5.2. Carbon Fibers, Carbon Nanofibers, and Other Carbonaceous Nanomaterials*

Carbonaceous materials have found increased use in PPE. For instance, carbon fibers can be used in combination with aramid fibers to manufacture soft body armor materials [93]. A combination of carbon and para-aramid fibers in an epoxy matrix was also explored as a potential replacement for acrylonitrile butadiene styrene (ABS) in safety helmets [94]. Better impact energy absorption, flexural and tensile strength, and heat resistance were obtained compared to ABS. Another PPE product where the use of carbon fibers could improve people's safety is air cylinders that are part of the breathing apparatus used by firefighters [95]. An

improvement in balance and gait performance was observed with the lighter carbon fiber air cylinders compared with the heavier aluminum air cylinders most often used. Carbon fibers have also shown a potential for producing radio-absorbing materials used in protective clothing [96]). They were dispersed at different concentrations in polyester nonwovens and porous PVC films stacked in multilayer structures. The results obtained in terms of the reflection coefficient as a function of the radiation frequency point towards a strategy based on concentration gradients in carbon fibers to maximize the radiation protection offered.

Carbon-based materials have also found applications in PPE at the nanoscale. For instance, activated carbon nanofiber mats containing alumina and magnesium oxide nanoparticles were prepared for the destructive adsorption of diazinon pesticide [97]. The addition of the nanoparticles improved the adsorption rate of the pesticide, which was converted into a less toxic product by chemical reaction with the metal oxide nanoparticles. The optimal carbonization conditions for the preparation of nanofiber mats from PAN nanofibers were investigated by Storck et al. [98]. Using silicon substrates to sandwich the PAN mats during the high temperature carbonization provided the best results in terms of preservation of the nanofiber morphology, whereas using titanium substrates allowed the carbonization temperature to be increased to 1200 °C and produced the highest degree of carbonization and crystallinity. Moreover, carbon nanotubes can be used to form a breathable membrane [99]. The selective water vapor transport through the carbon nanotube channels provides breathability to the membrane while ensuring protection against chemical and biological hazards. Graphene can also be applied as a coating on polymer fibers and improve their performance for application in protective clothing [53]. This includes improved mechanical strength, flame resistance, heat management, UV resistance, antibacterial activity, and electrical conductivity.

### *5.3. Metal Fibers and Structures*

Cut protection is another area where inorganic fibers have found applications [100]. The use of steel fibers can achieve very high levels of cut resistance; this is particularly beneficial in knitted structures for protective gloves. As these fibers are not very comfortable to the skin, inorganic filaments are usually wrapped by polymer or cellulose-based fibers in a core-sheath structure [101]. Researchers are still working to develop the core-spinning technique that will ensure the best cover factor [102]. Chainmail with stainless steel rings are used when the highest protection is needed, for instance in meat transformation and metal working industries as well as when diving around sharks [103]. A new development in this area by the National Aeronautics and Space Administration (NASA) involves chainmail with small metal squares 3D printed on each ring [104].

### *5.4. Boron Fibers and Other Boron-Containing Materials*

Boron offers various interesting perspectives for PPE. First, as a fiber, it combines high strength and high elastic modulus [105]. For instance, boron and silicon carbide fibers are used as reinforcements in polymer composites for ballistic protection [106]. The stab resistance of para-aramid and PA6 fabrics has also been improved by coating the fabrics with boron carbide using a laboratory knife coater [107]. However, the coating affected the comfort performance of the fabrics with a decrease in air permeability and an increase in water vapor and thermal resistance. Boron nitride nanosheets have been shown to increase the flame resistance of cotton when applied as a coating [108]. Shielding can also be achieved using boron-based compounds. For instance, boron and nitrogen co-doped reduced graphene oxide provided an EMI shielding of $-42$ dB in the 12.8–18 GHz frequency range [109]. Good gamma ray and neutron shielding can be obtained using boron-doped glass, opening the door for applications in radiology facilities [110].

### *5.5. Components for Wearable Electronics and Smart Textiles*

Wearable electronics and smart textiles' penetration in the PPE market is still quite limited but wearable sensors and actuators are expected to be a game changer for PPE once

they have overcome the remaining challenges they still face [111]. Inorganic materials play a large role into these developments, for instance for power and data transmission, as a sensor, or as a heating element [58]. The metals used are mostly silver, stainless steel, and copper. Yarn configurations include metal monofilament yarns, metal and metal/polymer blend multifilament yarns, metal and metal/polymer blend fiber spun yarn, and metal-plated polymer fiber and filament yarns. Conductive yarns are also manufactured using carbon-based materials such as carbon fibers, carbon nanotubes, carbon black, and graphene. Silver and carbon-based compounds are used in the form of conductive inks as well. Optic fibers and fiber grating provide an interesting solution for data transmission and sensing functions in environments with electromagnetic radiations. However, the poor flexibility and brittleness of glass fibers is a challenge for textile integration, and research is moving towards the development of polymer-based optical systems instead [112].

## 6. High-Performance Polymer Fibers

A series of high-performance polymer fibers have been developed between the 1960s and the 1990s and have contributed to make PPE more performant and more comfortable at the same time. Aramids, polyamide imide, polybenzimidazole, polyphenylene benzobisoxazole, melamine, oxidized poly(acrylonitrile), polypyridobisimidazole, polyimide, novoloid, ultra-high molecular weight polyethylene, and liquid crystal polyester are the most commonly used polymers. The first nine families of fibers listed are inherently flame resistant. Several of them are rigid-rod polymers and exhibit extremely high strength. Para-aramid and ultra-high molecular weight polyethylene fibers are used for cut-resistant and ballistic PPE.

### *6.1. Para-Aramid Fibers*

Recent developments regarding para-aramid fibers have mostly aimed at improving their mechanical performance. For instance, subjecting para-aramids to different levels of a microwave electromagnetic field has led to a strong increase in the strength of filaments due to a reduction in the fiber stratification [113] and an increase in interfiber bonding [114]. It generated an increase in the ballistic performance when tested as a fabric/resin armor package [115]. Other researchers have explored different strategies to increase the friction coefficient of the para-aramid yarn and improve stab performance. A first result is that high yarn crimp leads to a reduction in knife penetration [116]. The coating of para-aramid fabrics with multiwall carbon nanotubes increased both the static and kinetic friction coefficients of the yarns, as well as their modulus [117]. It translated into a 50% increase in the ballistic limit of the fabric. Other researchers have used coatings of silica [118], graphene oxide [119], and alumina/titania with an aluminum or a copper bond coat [120] to improve the stab or ballistic performance of para-aramid fabrics.

Work has also been done to improve the stab resistance of composite structures. It was shown that inserting a layer of aramid woven fabric as a core between two layers of thermoplastic resin-impregnated aramid woven fabrics improves the resistance to stabbing [121]. Another type of sandwich structure was prepared using a nonwoven fabric combining polyamide, recycled para-aramid, and low-melting-point polyester fibers as the skin and either high-strength polyester filaments randomly organized or high-strength polyester staple fibers needle punched into a nonwoven as the core [122]. The best stab resistance was obtained with the high-strength polyester staple fiber nonwoven core. Carbon fiber/aramid hybrid composite structures have also been investigated for the stab-resistant materials used in riot shields [123]. The addition of the aramid fibers made the failure mechanism change from brittle to ductile. Depending on the stacking sequence of the carbon and aramid layers, it was possible to obtain an increase in the stab resistance for the hybrid structure. Finally, a technique was developed to prepare para-aramid aerogel fiber sheets with the goal of simultaneously providing mechanical and thermal protection [124]. The aerogel fiber sheets offered a similar fragment projectile penetration resistance compared to commercial para-aramid fibers while their thermal insulation was increased 20 times.

### *6.2. Meta-Aramid Fibers*

Efforts have been made over the last years to prepare meta-aramid nanofibrous mats as a way to filter smoke particulates emitted during fires, which have been linked to the increased cancer numbers reported for firefighters [125]. For instance, meta-aramid nanofibers were successfully produced using a wire-based needleless electrospinning setup [126]. The polymer was dissolved in a polar aprotic solvent. The selection of optimal conditions allowed producing nanofibers with an average diameter between 80 and 90 nm. An investigation of the effect of the nanofiber diameter showed that the particle collection efficiency increases when the nanofiber diameter decreases [127]. However, the pressure drop of the filter also increased when the nanofiber diameter decreased. The authors reported that the nanofibrous filters retained their mechanical and chemical durability up to 200 °C. In an attempt to improve the stability of the meta-aramid nanofibrous mats, which is affected by the fact that the crystallinity is lost during the electrospinning process, the electrospun nanofibers were washed to remove the LiCl salt added to dissolve the meta-aramid to prepare the electrospinning solution, then heat-treated at 250 and 300 °C for 10 min [128]. This allowed the restoring the meta-aramid crystalline structure, which enhanced the nanofibrous mat mechanical and chemical stability. The authors also treated the mats with silane to make them hydrophobic and superoleophobic. An alternative strategy to restore the crystalline structure of the meta-aramid nanofibers using a lower heat treatment temperature involved immersing the nanofibrous mat in a solvent mixture of N,N-dimethylacetamide, and ethylene glycol in water followed by a 30 min heat treatment at 120 °C [129]. A strong increase in mechanical strength and chemical stability was obtained in comparison with the 300 °C/10 min heat treatment.

A meta-aramid nanofibrous mat functionalized with 2-{3-[2-(2-hydroxy-4-methoxy-phenyl)-vinyl]-5,5-dimethyl-cyclohex-2-enylidene}-malononitrile (dye 3) was prepared for ammonia gas detection [130]. The sensing mat exhibited a sensitivity of 1–10 ppm with a response time of 10 s. Research on meta-aramid has also led to an increase in the heat resistance using a honeycomb structure [131]. A reduction in 2nd and 3rd degree burn injury was obtained in flash fire testing.

An interesting initiative to recycle used meta-aramid coveralls has successfully produced FR-rated protective clothing of a similar performance to what is available on the market using the recycled meta-aramid fibers [132]. Recently, they explored the possibility of extending the application to arc-rated clothing [133]. The results showed that the weighted average glass transition temperature of FR fabrics can be used as a prediction of their arc rating performance. In addition, they demonstrate that the recycled nature of aramid fibers does not affect the arc rating performance of the corresponding fabrics.

### *6.3. Other Rigid-Rod Polymer Fibers*

Polyamide-imide is another inherently FR polymer that is sometimes classified as an aramid. Recent developments involved the synthesis of a new polyamide-imide series with good thermal stability [134]. The temperatures at 10% weight loss in nitrogen were around 489–501 °C, which is a little higher than what has been reported for Kermel fibers currently used in protective clothing. Other recent research on polyamide-imide dealt with high performance membranes for water filtration [135].

Polybenzimidazole (PBI) is also used in FR protective clothing due to its excellent thermal behavior [136]. In addition, recent work involved the production of electrospun PBI nanofibrous mats for respirator applications [137]. A threefold reduction in the pressure drop was obtained compared to commercial masks with a similar filtration efficiency. In addition, it was possible to clean and reuse the filter medium after contamination by organic and inorganic ultrafine particles due to PBI's high mechanical, thermal, and chemical resistance. A strategy developed to provide a PBI-based nanofibrous filter medium with high UV resistance and chemical and thermal durability uses benzophenone (PB), a UV absorber, as an additive in the electrospinning solution [138]. The performance of the PBI–

PB filter was retained after 30 days of UVA exposure. In addition, the damage sustained was much less than that of commercial filters when exposed to UVC light.

Polyphenylene benzobisoxazole (PBO) has the highest modulus and tensile strength of all commercial polymeric fibers [139]. It was excluded from ballistic protective clothing application a few years ago because of the failure of a bullet-proof vest, which was attributed to premature aging due to moisture among others and resulted in a major loss in the fabric strength [140]. However, recent results involving repeated washing/drying cycles of various fabrics used as an outer shell in firefighter bunker suits showed a very limited decrease in tear strength of a fabric blend containing PBO after 50 washing/drying cycles [141]. It was shown with PBO films that the chain scission of o-hydroxy amide bonds dominates the initial stage of PBO hydrolytic degradation [142]. These o-hydroxy amide bonds may result from the incomplete polymerization of the PBO molecule. Therefore, it is possible that a satisfactory resistance of PBO to environmental aging can be achieved with a high level of polymerization of the PBO fibers. Other researchers have explored the use of titanium dioxide ($TiO_2$) nanoparticles as an additive in the PBO fibers to improve their UV resistance [143]. The $TiO_2$ nanoparticle concentration has to remain below 3% to provide the protective effect. Above this value, an acceleration of UV aging is observed. Taking advantage of the high mechanical performance of PBO, researchers have examined various knitted structures for protection against stabbing [144]. Better results were obtained with PBO multifilament spacer fabrics compared with para-aramid. An interesting performance was also observed with a PBO structure using para-aramid tucks.

### *6.4. Ultra-High Molecular Weight Polyethylene*

Ultra-high molecular weight polyethylene (UHMWPE) fibers have raised large interest in recent years due to their excellent mechanical performance. Compared to para-aramid, they have higher tenacity, better abrasion and fatigue resistance, and a comparably high modulus [145]. They are also extremely resistant to chemical and biological attack. As a result, they now occupy a central place in ballistic PPE [146]. Recent developments have involved extending the use of UHMWPE to protection against spike, knife, and needle puncture by coating the fabric with silica nanoparticles dispersed in polyurethane [147]. The coated fabric in a multilayer configuration provided a large increase in the resistance to puncture by spike and hypodermic needle while remaining more flexible compared to a multi-layer stack of uncoated fabrics of the same surface density.

Another recent development involving UHMWPE fibers deals with the preparation of single-polymer reinforced composites. Self-reinforced UHMWPE composite samples had a threefold increase in tensile strength and Young's modulus compared to unfilled UHMWPE [148]. When prepared by hot compaction, an efficient load transfer was obtained when only a small amount of the UHMWPE fibers were incorporated to form the composite matrix [149]. A very interesting avenue explored by other researchers in Canada involves the use of crosslinkers to further improve the mechanical performance of UHMWPE [150]. Fabrics impregnated with the developed bis-diazirine crosslinker molecule exhibited a marked improvement in resistance to drop-tower impact and tear due to additional crosslinking of the C–H bonds. UHMWPE was also explored as the matrix of X-ray protective composites using tungsten and boron carbide particles as fillers [151].

Attempts have also been made to combine UHMWPE fibers with other high performance polymer fibers. For instance, Ertekin & Erhan Kirtay prepared hybrid core-spun yarns with different types of filaments as the core [152]. The sheath was composed of staple para-aramid fibers. The best performance in terms of cut, abstraction, and puncture resistance of fabrics woven using these yarns was obtained with the UHMWPE core compared to glass fiber, polyamide, and polyester for instance. In another study, the ballistic performance of composite structures combining UHMWPE laminates and aramid fabrics was assessed [153]. Composites with 75% UHMWPE and 25% aramid provided the best results.

### *6.5. Other High-Performance Polymer Fibers*

Melamine formaldehyde is an efficient flame retardant and can also be made into a fiber. Kocer et al. used melamine formaldehyde fibers to prepare an N-halamine antibacterial nonwoven [154]. The fibers were first hydrolyzed with sulfuric acid and then chlorinated with household bleach. The treated fabric preserved more than 70% of its N–Cl bonds after 2 weeks of exposure under UV light. It also displayed detoxifying efficacy against paraoxon, a chemical warfare agent.

The flammability performance of polyimide fibers was recently explored [155]. Compared to meta-aramid, polyimide fibers perform better in terms of ability to resist ignition but have a higher heat release. Research was also conducted to prepare polyimide nanofibrous mats. A hybrid membrane was prepared by coating a Kevlar® fabric with electrospun polyimide nanofibers [156]. Further annealing of the modified fabric at 260 °C allowed a strong increase in its water resistance. There was no significant effect of the polyimide nanofibrous coating on the membrane water vapor permeability while it decreased its air permeability. Further refinement allowed the production of polyimide nanofibrous mats with reasonable mechanical strength, excellent thermal stability, and a filtration efficiency of 90% [157]. Other developments in the area of composite manufacturing led to an improved compatibility between polyimide fibers and epoxy matrices by pretreating the fibers with oxygen plasma [158].

A relatively newcomer in the area of high performance fibers is liquid crystal polyester (LCP). Its physical performance is similar to that of aramids [159]. However, it has a better resistance to creep, cyclic thermal, flex–fatigue, and abrasion, and chemical/dimensional stability. Composite fibers were prepared by electrospinning by combining LCP fibers dissolved in a solution of chloroform and pentafluorophenol with polyurethane [160]. An increase in strength, toughness, and elastic modulus was obtained for fibers of random orientation when the amount of LCP increased. Balagna et al. developed an antibacterial coating for LCP fabrics using silver nanoclusters embedded in a silica matrix [161]. The mechanical properties of the fabric were preserved but the resistance of the coating to laundering was relatively limited.

Nature has also been a source of inspiration for the development of new high-performance fibers. For instance, researchers have manufactured artificial silk fibers that are stronger than steel with a mean ultimate tensile strength of close to 1 GPa and tougher than Kevlar® with a mean toughness of 161 MJ/m$^3$ [162]. These fibers are made of amyloid proteins and were synthesized by engineered bacteria and produced by wet spinning. The same group has also been working on fibers made of titin, which is the protein found in muscles [163]. The titin polymer was synthesized using engineered *Escherichia coli* bacteria and had a molecular weight of more than 2.4 MDa. Monofilaments of 10 μm diameter were then produced by wet spun and post-spin drawing. They exhibit a high damping capacity of 80% at 30% strain as well as high values of strength (378 MPa), modulus (4.2 GPa), extensibility (47%), and toughness (130 MJ/m$^3$). These fibers offer interesting perspectives for ballistic protection for instance.

### *6.6. Aging of High-Performance Polymer Fibers*

A number of high-performance polymer fibers have been discussed in the above sections. If these fibers offer exceptional characteristics when new, several of them are sensitive to environmental and service aging. For instance, a series of testing campaigns performed on used firefighter protective garments, some retired and some not, revealed significant losses of some properties, in particular mechanical performance and resistance to water penetration [164]. Accelerated aging tests performed on fabrics used in firefighter protective clothing, made of blends of high-performance polymer fibers, confirmed the degradation experienced when exposed to heat [165], laundering [141], moisture [166,167], and UV [168] for instance. A strategy explored by researchers at the University of Alberta consists in graphene-based end-of-life sensors positioned on the outer surface of the protective clothing [169]. The condition of the garment while in use, is monitored by measuring

the residual conductivity of the graphene tracks. Results showed that conductive tracks prepared on a meta-aramid woven fabric using reduced graphene oxide (Figure 6) resisted water immersion and the equivalent of 10 domestic launderings, while the conductivity was progressively lost as a result of abrasion [170]. Potential sacrificial polymers were successfully identified for thermal [171] and moisture [172] end-of-life sensors.

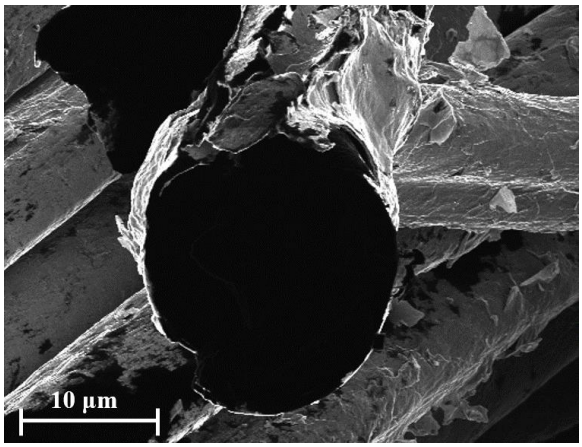


**Figure 6.** Image by helium-ion microscopy (HIM) of reduced graphene oxide flakes wrapped around individual meta-aramid fibers. (Reprinted with permission from Ref. [170]. Copyright 2021, Sage).

## 7. Special Textile Structures

This section describes a series of special textile structures that have been developed or can be used for PPE applications. They include three-dimensional textiles, auxetic textiles, shear thickening fabrics, nanoporous structures, phase change materials, Janus textiles, and textile-based composite structures for protection against cut and puncture.

### *7.1. Three-Dimensional Textiles*

Three-dimensional (3D) textile structures have been explored for impact/ballistic protection. For instance, tests performed with 3D woven aramid and PBO fabrics showed that 3D woven fabrics exhibit higher ballistic performance in terms of breaking load and energy absorption compared to 2D woven fabrics [173]. The results of a knife penetration test are also better. Efforts were dedicated as well to better understand the behavior of 3D woven fabrics under ballistic impact through analytical and numerical modelling [174] and analyze the effect of local and global localization on the failure phenomenon [175]. The use of 3D warp interlock fabric structures was explored with para-aramid for the manufacture of female soft body armors [176]. The 3D warp interlock fabric structure showed a better moldability and less wrinkles. With a 66.6% binding and 33.3% stuffer warp yarn ratio, 3D warp interlock fabric panels achieved a lower back face signature depth and higher energy absorbing capacity compared to the 2D fabric with the same type of yarns [177]. Seamless female body armor vests were also designed using 3D knitting [178]. The thermophysiological comfort of loose and tight fitting versions were assessed using a thermal manikin. A warp-knitted spacer fabric was also evaluated as an interlining to improve the thermophysiological comfort of a ballistic armor vest made with a Kevlar®-woven fabric [179]. A three-plied warp-knitted polyester spacer fabric performed better in terms of moisture vapor and heat transfer compared to single- and five-plied spacer fabrics. Moreover, 3D knitted structures are also considered for impact absorption in sportswear [180]. They can provide a similar protection against impacts to the closed cell foam pads currently available to rugby players but with improved flexibility and comfort.

Aside from the traditional textile manufacturing processes, 3D printing has also been considered for the preparation of 3D textile structures. This technique allows producing complex structures using a computer-controlled layer-by-layer process and has been proposed for the rapid manufacturing of N95 masks and other medical PPE, when in high

demand, such as during the COVID-19 pandemic [45]. Researchers have explored the possibility of using inexpensive 3D-printed polymers for applications at high temperatures [181]. Among the polymers tested, stereolithography resins showed the best thermal stability to 185 °C and the best mechanical properties upon UV post-treatment. This may open some possibilities for protective clothing and PPE used in high-temperature environments.

### *7.2. Auxetic Textiles*

As an alternative strategy to using auxetic materials to prepare auxetic textiles, Ugbolue et al. identified how to engineer yarn and fabric structures so that auxetic textiles are made using non-auxetic materials [182]. They developed several auxetic warp knitted structures by using filling yarn inlays in the repeating units. This has led to the development of 3D auxetic spacer fabrics [183]. These structures offer a better formability compared to regular spacer fabrics [184]. Auxetic textiles have also been constructed using high performance fibers [185]. With small loop lengths, a negative Poisson ratio of $-0.713$ was achieved using para-aramid yarns. The smaller loop length also gave the higher strength. Using para-aramid fibers, Sun et al. designed a stab-resistant auxetic weft-knitted fabric [186]. It had a higher peak load and energy absorption capacity than a plain knitted fabric made with the same yarns. Auxetic textiles also offer a promising perspective for wearables and medical applications with an improved comfort and increased piezoresistive sensitivity [187]. Auxetic fabrics have also been investigated as a reinforcement for composite parts [188].

Auxetic textiles have been prepared using woven structures as well. Lolaki & Shanbeh prepared 30 auxetic woven fabrics with different weave designs, fabric counts, and yarn linear density using helical auxetic weft yarns [189]. They concluded that the auxetic behavior of the fabrics did not depend only on weave design, but also on the yarn linear density and fabric count in the warp direction. Other researchers developed a highly elastic auxetic woven fabric using a zigzag configuration for the warp and weft yarns [190].

### *7.3. Shear Thickening Fabrics*

Shear thickening fabrics are another recent development for PPE, especially for impact protection. For instance, para-aramid fabrics were impregnated with a shear thickening fluid made of silica nanoparticles dispersed in polypropylene glycol [191] and polyethylene glycol [192]. An increase in the load at penetration compared with untreated fabrics was achieved with spiked and rounded impactors. The addition of a silane coupling agent further improved the stab performance of shear thickening fluid-treated para-aramid fabrics [193]. Work also involved impregnating UHMWPE fabrics with silica/polyethylene glycol shear thickening fluid [194]. Experiments conducted with both para-aramid and UHMWPE fabrics showed that impregnation with the shear thickening fluid strongly increased the force of yarn pull-out taking place at impact [195]. A correlation between the energy absorption and the yarn pull-out force was observed for low-velocity impacts. Shear thickening fluid impregnation has been shown to increase the shock wave mitigation provided by the high-performance fabrics too [196]. A positive effect of impregnation by shear thickening fluid was also observed with a spacer fabric [197]. If the performance was similar to the foam used in football helmets at low kinetic energy impacts, a strong improvement in energy absorption was measured for impact energies larger than 15J. A damping effect on the shock wave was obtained too with polyurea foam impregnated with shear thickening fluid [198].

Other researchers investigated the effect of shear thickening fluid on the sound absorption of textiles. Li et al. showed that a concentration of at least 30% of silica nanoparticles in the polyethylene glycol-based shear thickening fluid was necessary to measure an improvement in sound insulation of knitted fabrics [199]. Researchers also used a mixture of ZnO whiskers, silica nanoparticles, and polyethylene glycol as shear thickening fluid to prepare a sound-insulating glass fiber fabric [200]. Shear thickening fluid was also explored

as a strategy to increase the cut and puncture resistance of a thermal micrometeoroid garment [201].

Work has been conducted to look at the effect of the silica nanoparticle morphology (spherical or irregular) on the efficiency of the shear thickening fluid of aramid fabrics against stabbing [202]. The best results were obtained with spherical nanoparticles. Attempts were also made to combine two different sizes of silica particles, one size at the microscale and one at the nanoscale [203]. An improvement was obtained compared to the mono-sized specimens. An improvement in ballistic performance was also achieved by adding carbide particles to the silica nanoparticles in the shear thickening fluid, showing interesting perspectives for multi-phase systems [204].

The shear thickening fluid technology has also been combined with some of the special fabric structures described earlier in this section. It was shown to improve the ballistic performance of 3D woven aramid fabric structures [205] and the low-velocity impact resistance of an auxetic warp-knitted spacer fabric [206]. A similar shear thickening behavior was recently obtained by creating 3D printed chain mail-structured fabrics (Figure 7) using selective laser sintering [207]. The three-dimensional octahedral particles are organized into layers. The chain mail sheets can freely bend and drape curved objects, even when two layers are stacked on top of each other. However, when a pressure of 93 kPa is applied, the stiffness of the two sheets increases by more than 25 times as the octahedral particles interlock between and within the sheets.

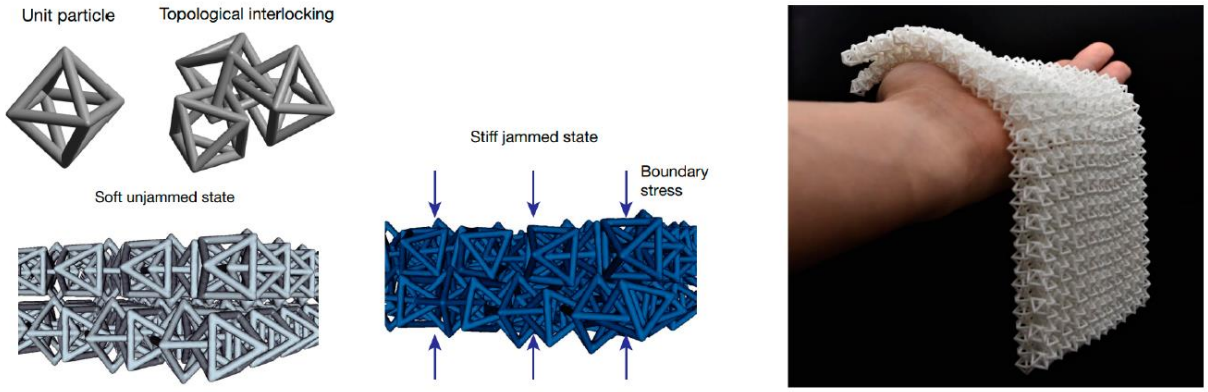


**Figure 7.** Schematic representations of the unit particle, topological interlocking, soft unjammed state and stiff jammed state and picture of a 3D printed chain mail structured fabric. (Reprinted with permission from Ref. [207]. Copyright 2021, Springer Nature).

### *7.4. Nanoporous Structures*

Nanoporous structures using aerogels can be applied to textiles to provide exceptional thermal insulation. To circumvent the issue of brittleness with silica aerogels, they can be chemically crosslinked or reinforced with fibers [208]. The advantage of fiber reinforcement is that a reduction in the material density can be obtained, which is critical for PPE comfort. The use of organic fibers, either natural or synthetic, also provides flexibility. Cellulose has been explored as a raw material for aerogels. Diverse strategies have been used to overcome the challenge associated with cellulose flammability, which would prevent the application of cellulose-based aerogels for insulation from heat. For instance, Han et al. used magnesium hydroxide nanoparticles, which were synthesized in situ in the nanostructured cellulose gel prepared from waste cotton, to make the aerogel flame resistant while preserving most of its excellent heat insulation performance [209].

Aerogel structures can also be obtained from high-performance fiber polymers. For instance, para-aramid aerogel filaments were prepared by spinning, solvent exchange, and freeze drying [210]. The inherently FR filaments were strong and flexible enough to be woven into a fabric; they also displayed an excellent thermal insulation between −196 and +300 °C. Polyimide aerogel fibers were manufactured by freeze spinning [211]. The polar

bear hair-inspired fiber combined thermal insulation, temperature resistance, and flame retardancy with strength and high stretch. Polyimide aerogels have also been explored as filter materials. By adding polyvinylidene fluoride to the crosslinked polyimide aerogel, researchers were able to control the porosity of the hybrid nanoporous material to improve its air permeability while maintaining a very good aerosol filtration efficiency [212]. The polyvinylidene fluoride also improved the hydrophobicity of the polyimide aerogel so that it maintains its integrity and performance in humid environments.

In addition, nanoporous structures have been proposed as an alternative strategy for the manufacture of liquid-tight yet breathable membranes. An example uses electrospun nanofibrous polyurethane mats to prepare such a membrane [213]. Better water resistance, air permeability, and water vapor transmission rate were obtained compared to a commercially available waterproof breathable fabric based on flash-spun polyethylene (Tyvek®). The use of para-aramid to prepare an electrospun nanofibrous mat allowed adding heat and flame resistance to the liquid-tight breathable membrane [214]. It showed a higher water vapor permeability compared to commercial expanded polytetrafluoroethylene (ePTFE) membranes currently used in FR protective clothing.

### *7.5. Phase Change Materials and Janus Textiles*

Phase change materials (PCMs) can be incorporated into fibers/filaments or applied as coating on fabrics [215]. They have found numerous applications for thermo-regulating purposes in protective clothing [216]. Recent developments include the preparation of ultrafine phase change fibers by emulsion electrospinning [217]. Poly(meta-phenylene isophthalamide) was used as the matrix to encapsulate the fatty acid ester active compound. The resulting fibers displayed a phase change in the 30–40 °C range, very high enthalpies, and a good shape stability. Other researchers have worked on bio-based PCM textiles. For instance, Saraç et al. tested coconut oil as a PCM to functionalize cellulosic fabrics [218]. Microcapsules of coconut oil in melamine formaldehyde/poly (methyl methacrylate) polymer shells were applied by knife-coating on cotton fabrics. Thermoregulating performance between 6.7 and 14.9 J/g in terms of latent heat were achieved. To overcome the issues of solid–liquid PCMs in terms of poor shape stability and low thermal conductivity, Sheng et al. used carbon scaffolds prepared through the direct carbonization of cotton cloth [219]. A heat capacity of 170 J/g was obtained for carbon scaffold/paraffin wax PCMs. The thermal conductivity increased by a factor of three to four depending on the scaffold direction compared to pure paraffin wax. Another solution to the shape stability issue associated with liquid PCMs is based on solid–solid PCMs. For instance, polyoxyethylene (2) hexadecyl ether was grafted as a functional side chain on a cellulose benzoate skeleton [220]. A solid-solid phase transition was observed in the 25–30 °C physiological temperature range. Phase change nanofiber hollow yarns have been prepared to provide both thermoregulation and thermal insulation [221]. Poly(meta-phenylene isophthalamide)/fatty acid ester PCM nanofibers were simultaneously electrospun and wrapped around a rotating polyvinyl alcohol (PVA) yarn using a twisting funnel. The PVA core was then dissolved in hot water. The resulting nanofiber hollow yarns have a high enough strength to sustain weaving and displayed a heat storage capacity of 30–40 J/g. PCMs have also been used to functionalize para-aramid aerogel filaments [210]. The polyethylene glycol active ingredient was driven into the nanoporous structure by capillary force. High energy storage was obtained with a phase change enthalpy of 162 J/g.

Interesting thermal management solutions have also been proposed using the so-called Janus textiles, which can provide both passive radiative heating and cooling by flipping the garment inside out [222]. This dual-mode textile is based on a membrane of infrared (IR) radiation-transparent nanoporous polyethylene membrane, in which a low emissivity/high emissivity bilayer is embedded in an asymmetrical manner. The researchers obtained a 6.5 °C temperature difference between the heating and cooling modes. All the layers are porous, which allows maintaining some level of breathability. To further increase the breathability which maintaining the dual cooling-heating function, other researchers have

come up with a double side fabric design using Janus yarns [223]. The low emissivity side is made of woven metal fibers while the high emissivity layer is composed of dielectric fibers. Their simulations pointed to a 13 °C comfort range.

### *7.6. Textile-Based Composite Structures for Protection against Cut and Puncture*

Textile-based composite structures have also been developed to provide improved protection against knives, needles, and other sharp/cutting impactors while preserving as much dexterity and range of motion as possible [224]. This is especially critical for protective gloves. A strategy developed is based on small guard plates screen-printed on a fabric surface [225]. These guard plates are made of a hard polymer [226]. When protection against very pointed objects such as hypodermic needles is needed, several layers of this material are superimposed with the assumption that the space between two adjacent guard plates in one layer will be covered by a guard plate in the next layer (Figure 8) [227]. This technology has recently been refined to precisely control the location of the guard plates in one layer vs. the next one [228].

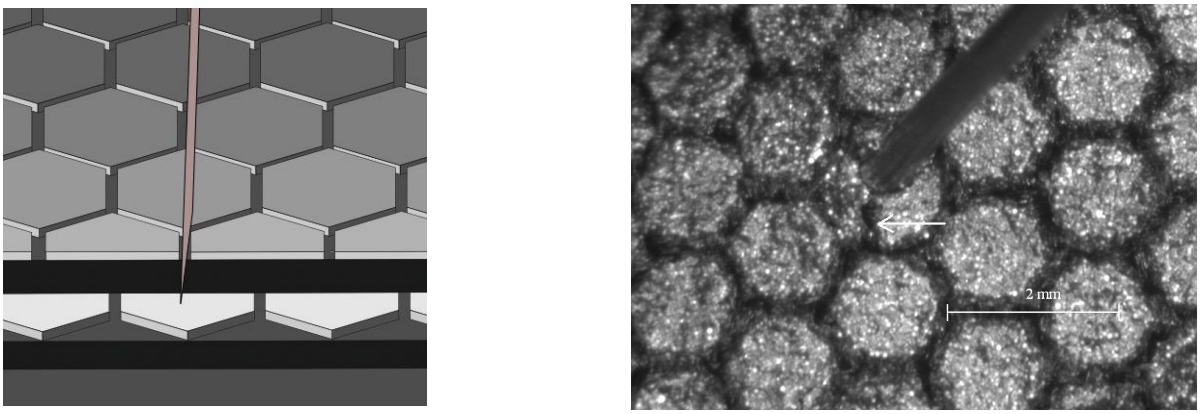


(**a**) (**b**)

**Figure 8.** (**a**) Schematic representation of the resistance to pointed objects provided by the superposition of small hard guard plates secured on a support fabric; (**b**) Optical microscopy image showing a broken guard plate (identified with a white arrow) at the site of a hypothermic needle puncture (Reprinted with permission from Ref. [229]. Copyright 2012, IRSST).

This material also provides resistance to abrasion. Another product named TurtleSkin® involves tightly woven cut-resistant fibers, such as para-aramid [230]. A thin coating of polymer can be applied to increase the puncture resistance but with a reduction in flexibility. This technology was used with LCP fibers to improve the International Space Station Extravehicular Activity Phase VI glove design [231]. These two types of strategies (hard guard plates and tightly woven cut-resistant fibers) offered a good resistance to puncture when tested with hypodermic needles in conditions simulating use in protective gloves [232,233].

Another solution recently proposed for elastomer gloves used by workers exposed to needle stick injuries in the healthcare, service, and hospitality sectors involves dispersing hard particles, such as colloidal silica and silicon carbide nanoparticles, into polydimethylsiloxane [234]. When applied on a high-density polyethylene woven fabric, the coating allowed an increase in the penetration force of hypodermic needles by 90% with only silica particles and by 110% with combined silica/silicon carbide particles. Abrasion resistance and thermal protection can also be brought to textiles with small-printed plates of inorganic or metal particles dispersed in a hard polymer [235] or ceramics [236,237].

## 8. Perspectives on Promising Avenues of Further Development

If large progress has been made and is still being made in fibers, fabrics, and textile structures for application in protective clothing and other types of PPE, areas of improvement remain, especially considering the seemingly irreconcilable nature of protection and comfort. This section describes strategies that can be used for further development in the area: measuring comfort, adopting new technologies, enhancing sustainability, and taking an interdisciplinary approach.

### *8.1. Measuring Comfort*

In terms of comfort, a major challenge lies in its multifaceted and highly subjective nature [238]. Test methods have been developed to assess the four aspects of clothing comfort—thermophysiological, skin sensorial, ergonomic, and psychological [239]. Requirements in terms of comfort are also gradually taken into considerations in standard specifications for protective clothing and PPE. They have been included in some standards; there is now a minimum level of evaporative heat transfer required for firefighter protective clothing in NFPA 1971 [240]. However, in many instances, the assessment of clothing comfort involves wear trials using human subjects, e.g., to assess the thermophysiological effect of firefighter protective garments [241] or the comfort and fit of chemical protective ensembles [242]. These tests involving human subjects are time-intensive and expensive, which may be a limitation.

As an alternative, it may be possible to develop bench-scale laboratory test protocols that describe the impact of protective clothing and PPE on the wearer's comfort. For instance, bench-scale laboratory test methods to assess glove stiffness and grip have been developed [243,244]. In both instances, an excellent correlation with biomechanical measurements and/or psychophysical evaluation test results were obtained. These two test methods, which rely on simple laboratory equipment, could be used to assess glove dexterity, which has been shown to be controlled by three parameters: glove flexibility, friction between the glove and the object, and snugness of fit with the hand [245]. Similar strategies could be attempted for other aspects of protective clothing and PPE comfort, enabling manufacturers to more easily characterize the comfort performance of their products and improve them, and end-users to be able to take into account comfort when selecting protective clothing and PPE.

### *8.2. Adopting New Technologies*

A second very promising avenue of further development relies on the adoption of new technologies in protective clothing and PPE products. If many examples of recent progress using nanotechnologies have been identified in this review (Table 1), the nano-enabled commercial products of protective clothing and PPE are still rare. One example of such a product is fabrics impregnated with a shear-thickening fluid containing silica nanoparticles dispersed in polyethylene glycol that are used in soft body armor and other PPE for impact, stab, and ballistic protection [246]. Several clothing and other textile items have also been made antibacterial using silver nanoparticles, either applied as a coating or dispersed in the fiber polymer [31,247]. Products involving nano-enabled superhydrophobicity and stain-resistance have also reached the market [31]. As nano-based solutions for fibers and textiles become more durable, including to the severe environments to which protective clothing and PPE products may be exposed to in service, and more affordable due to improvement in production processes and larger produced volumes, they are expected to bring large improvements in protective clothing and PPE, in particular by enabling reductions in weight and bulkiness.

**Table 1.** Promising technology-based innovations for protective clothing and PPE.

| Fiber/Textile Category | Strategy Used | Applications/Improvements |
|---|---|---|
| Highly extensible elastomeric fibers | Polyester-based elastic fibers [16]<br>Olefin-based elastic fibers [16]<br>Bicomponent fibers [16]<br>Shape-memory polyurethane, e.g., [20] | Enhanced sustainability<br>Improved resistance to chemicals and UV<br>Switchable tightness |
| Cellulose-based fibers | Hemp as an alternative to cotton, e.g., [27]<br>Ramie as alternative to high-performance fibers [32]<br>Recycling of used products [25]<br>Nano-enabled coating, e.g., [31]<br>Cellulose nanostructures, e.g., [37] | Enhanced sustainability<br>Electromagnetic shielding<br>Antibacterial activity<br>Chemical detoxification<br>Thermal protection<br>Lower cost |
| Commodity synthetic fibers | Surface functionalization [31]<br>Nano-enabled coatings, e.g., [81]<br>Core-sheath structures [47]<br>Nanocomposite structures, e.g., [56]<br>3D printing [83]<br>Nanofibers, e.g., [73]<br>Dual electrospinning [82]<br>Environmentally friendly processes, e.g., [51] | Improved filtration efficiency<br>Biological and chemical activity<br>Superhydro/oleo-phobicity<br>UV protection<br>Heat and flame protection<br>Abrasion resistance<br>Electrical properties<br>Multifunctionality<br>Improved comfort<br>Enhanced sustainability |
| High-strength inorganic materials | Basalt as an alternative to glass fibers, e.g., [85]<br>Carbon and boron fibers as a reinforcement for composites, e.g., [106]<br>Carbon and boron nanomaterials as coating and additive, e.g., [53]<br>Nano-enabled coatings, e.g., [92]<br>Nanofibers, e.g., [97]<br>Conductive inks [111]<br>Conductive yarns [111]<br>Recycling of composite products [89] | Heat and flame protection<br>Radiation protection<br>Improved strength<br>Impact protection<br>Chemical detoxification<br>Enhanced sustainability<br>Lower weight<br>Lower cost<br>Power and data transmission<br>Sensors and actuators |
| High-performance polymer fibers | Electromagnetic radiation treatment, e.g., [113]<br>Nano-enabled coatings, e.g., [117]<br>Sandwich/hybrid structures, e.g., [121]<br>Crosslinkers [150]<br>Nanocomposite fibers, e.g., [143]<br>Nanofibers, e.g., [126]<br>Biomimetics, e.g., [162]<br>End-of-life sensors [169]<br>Recycling of used garments [132] | Improved strength<br>Increased impact resistance<br>Thermal protection<br>Heat and flame resistance<br>Antibacterial activity<br>UV resistance<br>FR filter media<br>Improved comfort<br>Degradation monitoring during use<br>Enhanced sustainability |
| Special textile structures | 3D weaving/knitting, e.g., [176]<br>3D printing, e.g., [181]<br>Auxetic woven/knitted textiles, e.g., [190]<br>Shear thickening fabrics, e.g., [193]<br>Polymer and cellulose aerogels, e.g., [211]<br>Nanofibrous membranes, e.g., [214]<br>Nanocomposite coatings, e.g., [234]<br>Solid–solid PCMs, e.g., [220]<br>Janus textiles, e.g., [223] | Increased impact resistance<br>Resistance to needle puncture<br>Thermal protection<br>Improved thermophysiological comfort |

Another type of very promising new technology for protective clothing and PPE is smart textiles and materials (Table 1). However, even if the sensing, reacting, and adapting capability they offer would provide a response to several of the current needs in occupational health and safety, their adoption in the field is still very limited [111].

Products of protective clothing and PPE using smart textiles and materials identified by Dolez et al. [111] include smart shirts collecting vital signs for firefighters, athletes, and astronauts; protective gloves detecting toxic chemicals in the air; smart trousers making a chain saw switch off when in close proximity; surgical gowns that adjust their water vapor permeability based on the user's temperature; antibacterial medical clothing based on N-halamine that are recharged with chlorine bleach; and a vest for caregivers that monitors and supports movements when lifting heavy loads. However, many of their products are only at the prototype stage and have not reached the market yet. Several issues currently limiting their adoption in protective clothing and PPE have been identified [111]: the limited maturity of technologies associated with smart textiles; worries about potential impacts on health and safety; potential interference with communication systems and other electronic systems; issues of compatible with other PPE requirements; knowledge gaps and lack of standards and test methods; high cost of the product and the accessories necessary for its operation; challenges related to power supplies and resistance to care procedures; need to demonstrate the benefit for the user; and issues related to the end of life of the products. Luckily, researchers are dedicating large efforts to solving the weaknesses of smart textiles and materials so that they can benefit protective clothing and PPE.

A major issue that e-textiles can help solving in occupational health and safety relates to the power that is required for all the electronic devices that people have to carry with them to perform their tasks. For instance, about 20% of the carry-on load of soldiers on a mission is made of batteries [248]. There is a large interest in developing textile-based solutions for power generation and storage. In terms of power generation, energy can be harvested from the body and external sources such as the sun using protective clothing and PPE as a substrate [249]. The latest developments include a flexible photovoltaic film 15 times thinner than paper [250], soft and flexible magnetoelastic generators harvesting body movements [251], and carbon nanotube fiber thermoelectric generators woven into a cotton fabric [252]. Researchers are also working to develop flexible and thin batteries that may ultimately resist care and use conditions. For instance, a flexible lithium-ion fiber battery of 140 m long has been produced using solid-state electrolytes and thermal drawing [253]. Other researchers have designed a 0.4 mm thick biodegradable zinc battery, which powered a small fan for 45 min [254].

### *8.3. Enhancing Sustainability*

Another important avenue of development relates to sustainability. The COVID-19 pandemic has revealed to the face of the world that protective clothing and PPE have a major end-of-life issue [255]. Most of these products are made of petroleum-based polymers and take very long to decompose in landfills. However, solutions exist to implement to protective clothing and PPE the four R's towards environmental sustainability [256]. In terms of reducing our consumption, smart technologies can be used to dispose of items only when they are contaminated, for instance with chemical protective clothing and PPE that show with a change in color when they have been exposed to chemicals [257], and textile end-of-life sensors that allow replacing items only when needed [169]. Protective clothing and PPE can also be reused to extend their lifetime, for example by subjecting them to a decontamination treatment using ultraviolet germicidal irradiation [258], by including a self-detoxifying finish against biological agents based on N-halamine, silver, or quaternary ammonium [247] or by embedding chemically and biologically active nanoparticles in nanofibers forming a breathable membrane [82].

PPE can also be recycled to make new products. For example, the company TerraCycle in Canada collects used PPE and reprocesses them into hard plastic lumber, which can be used to make park benches and boardwalks (www.terracycle.com, accessed on 7 June 2022). Another Canadian company collects used FR aramid coveralls used in the oil and gas industry and through a mechanical recycling process, turns them into new FR aramid coveralls [132]. Research has shown that the recycling process does not affect the arc rating

of the FR aramid coveralls, which offer the same FR performance and electric arc protection as FR coveralls made of 100% virgin fibers [133].

Finally, biodegradable protective clothing and PPE can be produced to cater to the last R—recover, for example by using bio-based polymers and natural fibers or by adding compounds to otherwise non-biodegradable polymers so that enzymes are produced that depolymerise the polymer [256]. These different solutions will ultimately reduce the environmental footprint of protective clothing and PPE so that the ability of future generations to meet their own needs is preserved.

### *8.4. Taking an Interdisciplinary Approach*

Protective clothing and PPE are complex systems and the challenges faced for their development are multidisciplinary. Therefore, a truly interdisciplinary approach is required to achieve meaningful progress. It needs to bring together the different expertise relevant to protective clothing and PPE, including textiles and clothing, health and safety, design, materials, different fields of engineering, manufacturing, and human factors. A holistic, human-centered perspective that starts with the users' needs and considers the industry capacity is key to finding sustainable solutions to the remaining challenges in protective clothing and PPE.

## 9. Conclusions

As this review, one of the very few of its kind on this very important topic, has shown, large progress in fibers and textiles for protective clothing and PPE has been made over the last 50 years. In terms of highly extensible elastomeric fibers, which are critical for fitted garments and securing systems, new developments include polyester-based elastic fibers and shape memory polyurethane. Cellulose-based fibers, which were a main component of original PPE and still play a major role in their modern day counterparts, are now benefitting from environmentally friendly processes and nanotechnology-enabling treatments. Commodity synthetic fibers are also taking advantage of new technologies, e.g., with surface functionalization and formation of structures at the nanoscale, to offer improved performance and new functionalities. High strength inorganic materials, such as basalt, carbon, and boron, are generating considerable interest in PPE, both as fibers and coatings. For their part, high-performance polymer fibers, which brought breakthrough changes to the world of PPE 60 years ago, are seeing improvements in their short and long-term performance. They are also moving to the nanoscale for new functionalities as well as becoming recyclable. Finally, special textile structures have been developed with large opportunities for PPE: 3D textile structures, auxetic textile structures, shear thickening fabrics, nanoporous structures, phase change materials, and some specially designed textile-based composite structures for improved protection against mechanical hazards.

However, many challenges remain in PPE, in particular due to the fact that protection and comfort are often at odds with each other. Yet, promising avenues of further progress can be identified: (1) the development of bench-scale laboratory test methods to assess the different aspects of PPE comfort as felt by the user; (2) nano-based solutions for fibers and textiles to become more durable and affordable; (3) the adoption of smart textiles and materials, including for energy generation and storage; (4) the implementation of strategies towards PPE sustainability; and (5) a truly interdisciplinary approach involving a holistic, human-centered perspective that starts with the users' needs and considers the industry capacity. Protective clothing and PPE is a complex, yet rewarding topic; solving the challenge of improving protection without reducing comfort can save people's lives.

**Author Contributions:** Writing—Original Draft Preparation, P.I.D., S.M.; Writing—Review and Editing, R.H.M. All authors have read and agreed to the published version of the manuscript.

**Funding:** This research was funded by The National Research Council of Canada, contract number 947309.

**Institutional Review Board Statement:** Not applicable.

**Informed Consent Statement:** Not applicable.

**Data Availability Statement:** As this is a review paper, data is available in the articles cited.

**Acknowledgments:** The authors wish to thank Ajibola Anifowose for his help with the chemical drawings.

**Conflicts of Interest:** The authors declare no conflict of interest.

## References

1. OSHA. Personal Protective Equipment. Occupational Safety and Health Administration. 2022. Available online: https://www.osha.gov/personal-protective-equipment (accessed on 21 February 2022).
2. Dolez, P.; Soulati, K.; Gauvin, C.; Lara, J.; Vu-Khanh, T. *Information Document for Selecting Gloves for Protection against Mechanical Hazards*; Publications IRSST, RG-738: Montreal, QC, Canada, 2012; 61p.
3. *ISO 11610*; Protective Clothing—Vocabulary. International Organization for Standardization: Geneva, Switzerland, 2004; 93p.
4. Thomsen, A. History of Body Armour. Timetoast Timelines. Available online: https://www.timetoast.com/timelines/history-of-body-armour (accessed on 21 February 2022).
5. Risteski, S.; Srebrenkoska, V. Appearance of Protective Clothing over the Centuries. *Tekst. Ind.* **2020**, *4*, 38–48. [CrossRef]
6. Watkins, S.M. Development of Protective Clothing. LoveToKnow Media. Available online: https://fashion-history.lovetoknow.com/alphabetical-index-fashion-clothing-history/protective-clothing (accessed on 21 February 2022).
7. Blümner, H.; Zimmern, A. *The Home Life of the Ancient Greeks*; Cassell and Company Limited: London, UK; Paris, France; Melbourne, Australia, 1893; 548p.
8. Medieval Blacksmith Clothing. Working the Flame. 2019. Available online: https://workingtheflame.com/medieval-blacksmith-clothing/ (accessed on 27 February 2022).
9. Lee, A.; Meyer, R. Escape through Time. NOVA. 2000. Available online: https://www.pbs.org/wgbh/nova/escape/timefire.html (accessed on 27 February 2022).
10. Feldman, D. Polymer History. *Des. Monomers Polym.* **2008**, *11*, 1–15. [CrossRef]
11. Bourbigot, S.; Flambard, X. Heat resistance and flammability of high performance fibres: A review. *Fire Mater.* **2002**, *26*, 155–168. [CrossRef]
12. Kelly, J.M. Ultra-High Molecular Weight Polyethylene. *J. Macromol. Sci. Part C* **2002**, *42*, 355–371. [CrossRef]
13. MacLaury, J. The Job Safety Law of 1970: Its Passage Was Perilous. *Mon. Labor Rev.* **1981**, *104*, 18–24.
14. ISO/TC 94 Personal Safety—Personal Protective Equipment. International Organization for Standardization. Available online: https://www.iso.org/committee/50580.html (accessed on 27 February 2022).
15. Committee F23 on Personal Protective Clothing and Equipment. ASTM International. Available online: https://www.astm.org/get-involved/technical-committees/committee-f23 (accessed on 27 February 2022).
16. Hu, J.; Lu, J. Recent developments in elastic fibers and yarns for sportswear. *Text. Sportsw.* **2015**, 53–76. [CrossRef]
17. Fletcher, J.C.; Howarth, J.T.; Sheth, S.; Sidman, K.R.; Massucco, A.A. Flame Retardant Spandex Type Polyurethanes. U.S. Patent 4,069,212, 17 January 1978.
18. Aldridge, D. Limited-Stretch, Permanently Fire-Resistant Suspenders. U.S. Patent 5,448,779, 12 September 1995.
19. Tausif, M.; Cassidy, T.; Butcher, I. Yarn and thread manufacturing methods for high-performance apparel. In *High-Performance Apparel*; McLoughlin, J., Sabir, T., Eds.; Woodhead Publishing: Duxford, UK; Cambridge, MA, USA; Kidlington, UK, 2018; pp. 33–73.
20. Sáenz-Pérez, M.; Bashir, T.; Laza, J.M.; García-Barrasa, J.; Vilas, J.L.; Skrifvars, M.; León, L.M. Novel shape-memory polyurethane fibers for textile applications. *Text. Res. J.* **2019**, *89*, 1027–1037. [CrossRef]
21. Safranski, D.L.; Boothby, J.M.; Kelly, C.N.; Beatty, K.; Lakhera, N.; Frick, C.P.; Lin, A.; Guldberg, R.E.; Griffis, J.C. Thermomechanical behavior and structure of melt blown shape-memory polyurethane nonwovens. *J. Mech. Behav. Biomed. Mater.* **2016**, *62*, 545–555. [CrossRef]
22. Banikazemi, S.; Rezaei, M.; Rezaei, P.; Babaie, A.; Eyvazzadeh-Kalajahi, A. Preparation of electrospun shape memory polyurethane fibers in optimized electrospinning conditions via response surface methodology. *Polym. Adv. Technol.* **2020**, *31*, 2199–2208. [CrossRef]
23. Otaigbes, J.U.; Madbouly, A. 11-The processing, structure and properties of elastomeric fibers. In *Handbook of Textile Fibre Structure*; Eichhorn, S.J., Hearle, J.W.S., Jaffe, M., Kikutani, T., Eds.; Woodhead Publishing: Cambridge, UK, 2009; Volume 1, pp. 325–351.
24. Crown, E.M.; Batcheller, J.C. Technical textiles for personal thermal protection. In *Handbook of Technical Textiles*, 2nd ed.; Horrocks, A.R., Anand, S.C., Eds.; Woodhead Publishing: Duxford, UK; Cambridge, MA, USA; Kidlington, UK, 2016; Volume 2, pp. 271–285. [CrossRef]
25. Horrocks, A.R. Technical fibres for heat and flame protection. In *Handbook of Technical Textiles*, 2nd ed.; Horrocks, A.R., Anand, S.C., Eds.; Woodhead Publishing: Duxford, UK; Cambridge, MA, USA; Kidlington, UK, 2016; Volume 2, pp. 237–270. [CrossRef]
26. Hoagland, H. Flame resistant textiles for electric arc flash hazards. In *Handbook of Fire Resistant Textiles*; Kilinc, Ed.; Woodhead Publishing: Cambridge, UK; Philadelphia, PA, USA; New Delhi, India, 2013; pp. 549–580.

27. Novaković, M.; Popović, D.M.; Mladenović, N.; Poparić, G.B.; Stanković, S.B. Development of comfortable and eco-friendly cellulose based textiles with improved sustainability. *J. Clean. Prod.* **2020**, *267*, 122154. [CrossRef]
28. Kocić, A.; Bizjak, M.; Popović, D.; Poparić, G.B.; Stanković, S.B. UV protection afforded by textile fabrics made of natural and regenerated cellulose fibres. *J. Clean. Prod.* **2019**, *228*, 1229–1237. [CrossRef]
29. Liang, S.; Neisius, N.M.; Gaan, S. Recent developments in flame retardant polymeric coatings. *Prog. Org. Coat.* **2013**, *76*, 1642–1665. [CrossRef]
30. Tian, M.; Du, M.; Qu, L.; Chen, S.; Zhu, S.; Han, G. Electromagnetic interference shielding cotton fabrics with high electrical conductivity and electrical heating behavior via layer-by-layer self-assembly route. *R. Soc. Chem. Adv.* **2017**, *7*, 42641–42652. [CrossRef]
31. Dolez, P.I. Application of nanomaterials in textile coatings and finishes. In *Nanomaterials-Based Coatings: Fundamentals and Applications*; Nguyen-Tri, R., Plamondon, O., Eds.; Elsevier: Amsterdam, The Netherlands; Oxford, UK; Waltham, MA, USA, 2019; pp. 139–169.
32. Braga, F.D.O.; Milanezi, T.L.; Monteiro, S.N.; Louro, L.H.L.; Gomes, A.V.; Lima, É.P. Ballistic comparison between epoxy-ramie and epoxy-aramid composites in multilayered armor systems. *J. Mater. Res. Technol.* **2018**, *7*, 541–549. [CrossRef]
33. Venkatesan, H.; Periyasamy, A.P. Eco-fibers in the Textile Industry. In *Handbook of Ecomaterials*; Martinez, L.M.T., Ed.; Springer International Publishing: Cham, Switzerland, 2019; pp. 1413–1433.
34. Arfaoui, M.A.; Dolez, P.I.; Dubé, M.; David, É. Development and characterization of a hydrophobic treatment for jute fibres based on zinc oxide nanoparticles and a fatty acid. *Appl. Surf. Sci.* **2017**, *397*, 19–29. [CrossRef]
35. Arafa Badr, A. Anti-microbial and durability characteristics of socks made of cotton and regenerated cellulosic fibers. *Alex. Eng. J.* **2018**, *57*, 3367–3373. [CrossRef]
36. Hardin, I.R.; Wilson, S.S.; Dhandapani, R.; Dhende, V. An assessment of the validity of claims for "Bamboo" fibers. *AATCC Rev.* **2009**, *9*, 33–36.
37. Zhu, Q.; Jin, Y.; Sun, G.; Yan, K.; Wang, D. AQC functionalized CNCs/PVA-co-PE composite nanofibrous membrane with flower-like microstructures for photo-induced multi-functional protective clothing. *Cellulose* **2018**, *25*, 4819–4830. [CrossRef]
38. Guo, L.; Chen, Z.; Lyu, S.; Fu, F.; Wang, S. Highly flexible cross-linked cellulose nanofibril sponge-like aerogels with improved mechanical property and enhanced flame retardancy. *Carbohydr. Polym.* **2018**, *179*, 333–340. [CrossRef]
39. Sharma, A.; Thakur, M.; Bhattacharya, M.; Mandal, T.; Goswami, S. Commercial application of cellulose nano-composites—A review. *Biotechnol. Rep.* **2019**, *21*, e00316. [CrossRef]
40. Tessier, D. Testing thermal properties of textiles. In *Advanced Characterization and Testing of Textiles*; Dolez, V.I., Ed.; Elsevier: Amsterdam, The Netherlands, 2017; pp. 71–92.
41. Sabir, T. Fibers used for high performance apparel. In *High-Performance Apparel*; McLoughlin, J., Sabir, T., Eds.; Woodhead Publishing: Duxford, UK; Cambridge, MA, USA; Kidlington, UK, 2018; pp. 7–32.
42. Lefakane, T.E.; Ndibewu, P.P.; Netshiozwi, T.E. Characterization, chemical phase identification, and performance evaluation of omnipotent, polymers used in the manufacturing of personal protective garments. *Polym. Res. J.* **2015**, *9*, 2530.
43. Kim, Y.K. The use of polyolefins in industrial and medical applications. In *Polyolefin Fibres: Structure, Properties and Industrial Applications*, 2nd ed.; Woodhead Publishing: Duxford, UK; Cambridge, MA, USA; Kidlington, UK, 2017; pp. 135–155. [CrossRef]
44. Purchas, D.B.; Sutherland, K. *Handbook of Filter Media*; Elsevier: Amsterdam, The Netherlands, 2002.
45. Ishack, S.; Lipner, S.R. Applications of 3D Printing Technology to Address COVID-19−Related Supply Shortages. *Am. J. Med.* **2020**, *133*, 771–773. [CrossRef] [PubMed]
46. Okrasa, M.; Brochocka, A.; Majchrzycka, K. Electret filtering nonwovens with enhanced protective and comfort properties for human protection in heavy working conditions. In *International Textile Conference*; National Research Institute: Łódź, Poland, 2016; pp. 24–25.
47. Sibanda, M.; Leuteritz, A.; Brünig, H.; Focke, W. Development of polyolefin bicomponent filaments as controlled release devices of volatile repellents for use in malaria vector control. *AIP Conf. Proc.* **2019**, *2055*, 060007. [CrossRef]
48. Irzmańska, E.; Brochocka, A. Modified polymer materials for use in selected personal protective equipment products. *Autex Res. J.* **2017**, *17*, 35–47. [CrossRef]
49. Demir, B.; Cerkez, I.; Worley, S.D.; Broughton, R.M.; Huang, T.-S. N-Halamine-Modified Antimicrobial Polypropylene Nonwoven Fabrics for Use against Airborne Bacteria. *ACS Appl. Mater. Interfaces* **2015**, *7*, 1752–1757. [CrossRef]
50. Crăciun, N.; Trifu, A. Reducing the risk of slipping on ice by selecting appropriate protective footwear. *Qual.-Access Success* **2019**, *20*, 147–152.
51. Elmaaty, A.T.; Sofan, M.; Elsisi, H.; Kosbar, T.; Negm, E.; Hirogaki, K.; Tabata, I.; Hori, T. Optimization of an eco-friendly dyeing process in both laboratory scale and pilot scale supercritical carbon dioxide unit for polypropylene fabrics with special new disperse dyes. *J. CO2 Util.* **2019**, *33*, 365–371. [CrossRef]
52. Razafimahefa, L.; Chlebicki, S.; Vroman, I.; Devaux, E. Effect of nanoclays on the dyeability of polypropylene nanocomposite fibres. *Coloration Technol.* **2008**, *124*, 86–91. [CrossRef]
53. Bhattacharjee, S.; Joshi, R.; Chughtai, A.A.; Macintyre, C.R. Graphene modified multifunctional personal protective clothing. *Adv. Mater. Interfaces* **2019**, *6*, 1–27. [CrossRef]

54. Lomazzo Directa Plus and Alfredo Grassi to Develop Graphene-Enhanced Workwear. Innovation in Textiles. 2017. Available online: https://www.innovationintextiles.com/directa-plus-and-alfredo-grassi-to-develop-grapheneenhanced-workwear/ (accessed on 15 April 2022).
55. Wang, H.; Xu, L.; Song, X.; Cai, Z. Facile preparation of acid-resistant polyester fabrics with organic/inorganic nanocomposites. *Cloth. Text. Res. J.* **2017**, *35*, 98–110. [CrossRef]
56. Yao, L.; Wu, L.; Wu, H.; Koo, J.H.; Krifa, M. Design and characterization of flame resistant blended nondrip PA6/Lenzing FR®/PBI fiber nonwoven fabrics. *Flame Retard. Therm. Stab. Mater.* **2019**, *2*, 49–59. [CrossRef]
57. Shabanian, S.; Khatir, B.; Nisar, A.; Golovin, K. Rational design of perfluorocarbon-free oleophobic textiles. *Nat. Sustain.* **2020**, *3*, 1059–1066. [CrossRef]
58. Decaens, J.; Vermeersch, O. Wearable technologies for personal protective equipment: Embedded textile monitoring sensors, power and data transmission, end-life indicators. In *Smart Textiles and Their Applications*; Woodhead Publishing: Duxford, UK; Cambridge, MA, USA; Kidlington, UK, 2016; pp. 519–537. [CrossRef]
59. Korpinen, L.; Pirkkalainen, H.; Heiskanen, T.; Pääkkönen, R. The possibility of decreasing 50-HZ electric field exposure near 400-kV power lines with arc flash personal protective equipment. *Int. J. Environ. Res. Public Health* **2016**, *13*, 942. [CrossRef]
60. Grgac, S.F.; Bischof, S.; Pušić, T.; Petrinić, I.; Luxbacher, T. Analytical assessment of the thermal decomposition of cotton-modacryl knitted fabrics. *Fibres Text. East. Eur.* **2017**, *25*, 59–67. [CrossRef]
61. Ackerman, M.Y. Thermal Decomposition of Selected Flame Resistant Clothing Materials. *AATCC Rev.* **2011**, *11*, 35–43.
62. Mackay, C.E.; Reinhardt, T.E.; Vivanco, S.N.; McClure, S.; Vercellone, J. Real-Time Monitoring and Assessment of Thermal and Toxicological Risk Associated with Fire Retardant Textiles in a Full-Size Simulation of an Engulfment Flash Fire. *Fire Technol.* **2015**, *51*, 1167–1193. [CrossRef]
63. Waxman, R.; Seward, P. Flame Resistant Blends. U.S. Patent Application US 2013/0212790 A1, 22 August 2013.
64. Zhu, M.; Han, J.; Wang, F.; Shao, W.; Xiong, R.; Zhang, Q.; Pan, H.; Yang, Y.; Samal, S.K.; Zhang, F.; et al. Electrospun nanofibers membranes for effective air filtration. *Macromol. Mater. Eng.* **2017**, *302*, 1–27. [CrossRef]
65. Nayak, R. *Polypropylene Nanofibers-Melt Electrospinning Versus Meltblowing*; Springer International Publishing: Cham, Switzerland, 2017.
66. Mohraz, M.H.; Golbabaei, F.; Yu, I.J.; Ghahri, A. Optimization of the electrospinning process of polyurethane nanofibers and their filtration performance for use in respiratory protection mask filters. *J. Mil. Med.* **2019**, *21*, 195–204.
67. Kao, T.H.; Su, S.K.; Su, C.I.; Lee, A.W.; Chen, J.K. Polyacrylonitrile microscaffolds assembled from mesh structures of aligned electrospun nanofibers as high-efficiency particulate air filters. *Aerosol Sci. Technol.* **2016**, *50*, 615–625. [CrossRef]
68. Lolla, D.; Lolla, M.; Abutaleb, A.; Shin, H.U.; Reneker, D.H.; Chase, G.G. Fabrication, polarization of electrospun polyvinylidene fluoride electret fibers and effect on capturing nanoscale solid aerosols. *Materials* **2016**, *9*, 671. [CrossRef]
69. Akduman, C. Cellulose acetate and polyvinylidene fluoride nanofiber mats for N95 respirators. *J. Ind. Text.* **2019**, *50*, 1239–1261. [CrossRef]
70. Zhang, J.; Gong, S.; Wang, C.; Jeong, D.Y.; Wang, Z.L.; Ren, K. Biodegradable electrospun poly(lactic acid) nanofibers for effective PM 2.5 removal. *Macromol. Mater. Eng.* **2019**, *304*, 1900259. [CrossRef]
71. Gorji, M.; Bagherzadeh, R.; Fashandi, H. Electrospun nanofibers in protective clothing. In *Electrospun Nanofibers*; Woodhead Publishing: Duxford, UK; Cambridge, MA, USA; Kidlington, UK, 2017; pp. 571–598. [CrossRef]
72. Sheng, J.; Zhao, J.; Yu, X.; Liu, L.; Yu, J.; Ding, B. Electrospun nanofibers for waterproof and breathable clothing. In *Electrospinning: Nanofabrication and Applications*; Elsevier: Amsterdam, The Netherlands, 2018; pp. 543–570. [CrossRef]
73. Akshat, T.M.; Misra, S.; Gudiyawar, M.Y.; Salacova, J.; Petru, M. Effect of electrospun nanofiber deposition on thermo-physiology of functional clothing. *Fibers Polym.* **2019**, *20*, 991–1002. [CrossRef]
74. Si, Y.; Zhang, Z.; Wu, W.; Fu, Q.; Huang, K.; Nitin, N.; Ding, B.; Sun, G. Daylight-driven rechargeable antibacterial and antiviral nanofibrous membranes for bioprotective applications. *Sci. Adv.* **2018**, *4*, eaar5931. [CrossRef]
75. Wang, R.; Li, Y.; Si, Y.; Wang, F.; Liu, Y.; Ma, Y.; Yu, J.; Yin, X.; Ding, B. Rechargeable polyamide-based: N -halamine nanofibrous membranes for renewable, high-efficiency, and antibacterial respirators. *Nanoscale Adv.* **2019**, *1*, 1948–1956. [CrossRef]
76. Kharaghani, D.; Kee Jo, Y.; Khan, M.Q.; Jeong, Y.; Cha, H.J.; Kim, I.S. Electrospun antibacterial polyacrylonitrile nanofiber membranes functionalized with silver nanoparticles by a facile wetting method. *Eur. Polym. J.* **2018**, *108*, 69–75. [CrossRef]
77. Ruan, D.; Qin, L.; Chen, R.; Xu, G.; Su, Z.; Cheng, J.; Xie, S.; Cheng, F.; Ko, F. Transparent PAN:$TiO_2$ and PAN-co-PMA:$TiO^2$ nanofiber composite membranes with high efficiency in particulate matter pollutants filtration. *Nanoscale Res. Lett.* **2020**, *15*, 7. [CrossRef]
78. Wang, N.; Cai, M.; Yang, X.; Yang, Y. Electret nanofibrous membrane with enhanced filtration performance and wearing comfortability for face mask. *J. Colloid Interface Sci.* **2018**, *530*, 695–703. [CrossRef]
79. Yu, Y.; Ma, Q.; Zhang, J.B.; Liu, G.B. Electrospun $SiO_2$ aerogel/polyacrylonitrile composited nanofibers with enhanced adsorption performance of volatile organic compounds. *Appl. Surf. Sci.* **2020**, *512*, 145697. [CrossRef]
80. Hussain, M.; Salam, A.; Arain, M.F.; Ullah, A.; Dao, A.-T.; Vu-Manh, H.; Phan, D.-N.; Ansari, A.S.; Khan, M.Q.; Javed, Z.; et al. Polyacrylonitrile Nanofibers Containing Viroblock as Promising Material for Protective Clothing. *Appl. Sci.* **2021**, *11*, 11469. [CrossRef]
81. Zhu, M.; Xiong, R.; Huang, C. Bio-based and photocrosslinked electrospun antibacterial nanofibrous membranes for air filtration. *Carbohydr. Polym.* **2019**, *205*, 55–62. [CrossRef] [PubMed]

82. Kalantari, M.; Ayranci, C.; Dolez, P.I. Multifunctionalized dual-electrospun nano-fibrous webs for protection against chemical and biological hazards. In Proceedings of the 5th International Congress on Soldiers' Physical Performance–ICSPP 2020, Quebec City, QC, Canada, 11–14 February 2020.
83. He, H.; Gao, M.; Illés, B.; Molnar, K. 3D printed and electrospun, transparent, hierarchical polylactic acid mask nanoporous filter. *Int. J. Bioprint* **2020**, *6*, 278. [CrossRef] [PubMed]
84. Liu, G.; Nie, J.; Han, C.; Jiang, T.; Yang, Z.; Pang, Y.; Xu, L.; Guo, T.; Bu, T.; Zhang, C.; et al. Self-powered electrostatic adsorption face mask based on a triboelectric nanogenerator. *ACS Appl. Mater. Interfaces* **2018**, *10*, 7126–7133. [CrossRef] [PubMed]
85. Frydrych, I.; Cichocka, A.; Gilewicz, P.; Dominiak, J. Thermal Manikin Measurements of Protective Clothing Assemblies. *Fibres Text. East. Eur.* **2018**, *26*, 126–133. [CrossRef]
86. Hrynyk, R.; Frydrych, I. Study on textile assemblies with aluminized basalt fabrics destined for protective gloves. *Int. J. Cloth. Sci. Technol.* **2015**, *27*, 705–719. [CrossRef]
87. Miśkiewicz, P.; Frydrych, I.; Tokarska, M.; Pawlak, W. Study on Some Thermal and Electrical Properties of Basalt Fabric Modified with Metal and Ceramics as a Result of Magnetron Sputtering. *Polymers* **2019**, *11*, 2087. [CrossRef]
88. Fiore, V.; Scalici, T.; Di Bella, G.; Valenza, A. A review on basalt fibre and its composites. *Compos. Part B Eng.* **2015**, *74*, 74–94. [CrossRef]
89. Pucci, M.F.; Seghini, M.C.; Liotier, P.J.; Sarasini, F.; Tirilló, J.; Drapier, S. Surface characterisation and wetting properties of single basalt fibres. *Compos. Part B Eng.* **2017**, *109*, 72–81. [CrossRef]
90. Sarasini, F.; Tirillò, J.; Valente, M.; Ferrante, L.; Cioffi, S.; Iannace, S.; Sorrentino, L. Hybrid composites based on aramid and basalt woven fabrics: Impact damage modes and residual flexural properties. *Mater. Des.* **2013**, *49*, 290–302. [CrossRef]
91. Sun, G.; Tong, S.; Chen, D.; Gong, Z.; Li, Q. Mechanical properties of hybrid composites reinforced by carbon and basalt fibers. *Int. J. Mech. Sci.* **2018**, *148*, 636–651. [CrossRef]
92. Zhou, S.; Wang, J.; Wang, S.; Ma, X.; Huang, J.; Zhao, G.; Liu, Y. Facile preparation of multiscale graphene-basalt fiber reinforcements and their enhanced mechanical and tribological properties for polyamide 6 composites. *Mater. Chem. Phys.* **2018**, *217*, 315–322. [CrossRef]
93. Purnomo, H.; Widananto, H.; Sulistio, J. The optimization of soft body armor materials made from carbon-aramid fiber using the Taguchi method. *AIP Conf. Proc.* **2018**, *1977*, 020003. [CrossRef]
94. Kim, S.; Lee, J.; Roh, C.; Eun, J.; Kang, C. Evaluation of carbon fiber and p-aramid composite for industrial helmet using simple cross-ply for protecting human heads. *Mech. Mater.* **2019**, *139*, 103203. [CrossRef]
95. Rosengren, K.S.; Hsiao-Wecksler, E.T.; Horn, G. Fighting fires without falling: Effects of equipment design and fatigue on firefighter's balance and gait. *Ecol. Psychol.* **2014**, *26*, 167–175. [CrossRef]
96. Devina, E.A.; Bokova, E.S.; Devin, K.L.; Evsyukova, N.V.; Abramova, A.B. Effect of Fibrous-Porous Composite Composition on its Radiophysical Characteristics. *Fibre Chem.* **2017**, *48*, 487–490. [CrossRef]
97. Behnam, R.; Morshed, M.; Tavanai, H.; Ghiaci, M. Destructive adsorption of diazinon pesticide by activated carbon nanofibers containing A12O3 and MgO nanoparticles. *Bull. Environ. Contam. Toxicol.* **2013**, *91*, 475–480. [CrossRef]
98. Storck, J.L.; Wortmann, M.; Brockhagen, B.; Frese, N.; Diestelhorst, E.; Grothe, T.; Hellert, C.; Ehrmann, A. Comparative Study of Metal Substrates for Improved Carbonization of Electrospun PAN Nanofibers. *Polymers* **2022**, *14*, 721. [CrossRef]
99. Fornasiero, F. Water vapor transport in carbon nanotube membranes and application in breathable and protective fabrics. *Curr. Opin. Chem. Eng.* **2017**, *16*, 1–8. [CrossRef]
100. Rebouillat, S.; Steffenino, B.; Miret-Casas, A. Aramid, steel, and glass: Characterization via cut performance testing, of composite knitted fabrics and their constituent yarns, with a review of the art. *J. Mater. Sci.* **2010**, *45*, 5378–5392. [CrossRef]
101. Guevel, J.; Bontemps, G. Cut-Resistant Yarn Intended Especially for the Production Of Protective Garments. U.S. Patent 7,065,949, 27 June 2006.
102. Mofarah, H.M.; Najar, S.S.; Etrati, S.M. Mechanical properties of copper/cotton core-spun yarns produced by siro and ring spinning methods. *Indian J. Fibre Text. Res.* **2019**, *44*, 431–436.
103. Koren, M. Chainmail, Metal Spikes and Unbreakable Material: Can We Design a 'Shark-Proof' Wetsuit? *Smithson. Mag.* **2013**. Available online: https://www.smithsonianmag.com/arts-culture/chainmail-metal-spikes-and-unbreakable-material-can-we-design-a-shark-proof-wetsuit-27310741/ (accessed on 10 June 2022).
104. Landau, E. 'Space Fabric' Links Fashion and Engineering. *Space Tech.* Available online: https://www.nasa.gov/feature/jpl/space-fabric-links-fashion-and-engineering (accessed on 18 April 2017).
105. Bernard, S.; Chassagneux, F.; Berthet, M.-P.; Vincent, H.; Bouix, J. Structural and mechanical properties of a high-performance BN fibre. *J. Eur. Ceram. Soc.* **2002**, *22*, 2047–2059. [CrossRef]
106. Tam, T.; Bhatnagar, A. High-performance ballistic fibers and tapes. In *Lightweight Ballistic Composites: Military and Law-Enforcement Applications*, 2nd ed.; Woodhead Publishing: Duxford, UK; Cambridge, MA, USA; Kidlington, UK, 2016; pp. 1–39. [CrossRef]
107. Nayak, R.; Kanesalingam, S.; Wang, L.; Padhye, R. Stab resistance and thermophysiological comfort properties of boron carbide coated aramid and ballistic nylon fabrics. *J. Text. Inst.* **2019**, *110*, 1159–1168. [CrossRef]
108. Liu, H.; Du, Y.; Lei, S.; Liu, Z. Flame-retardant activity of modified boron nitride nanosheets to cotton. *Text. Res. J.* **2020**, *90*, 512–522. [CrossRef]

109. Umrao, S.; Gupta, T.K.; Kumar, S.; Singh, V.K.; Sultania, M.K.; Jung, J.H.; Oh, I.-K.; Srivastava, A. Microwave-Assisted Synthesis of Boron and Nitrogen co-doped Reduced Graphene Oxide for the Protection of Electromagnetic Radiation in Ku-Band. *ACS Appl. Mater. Interfaces* **2015**, *7*, 19831–19842. [CrossRef]
110. Tekin, H.O.; Altunsoy, E.E.; Kavaz, E.; Sayyed, M.I.; Agar, O.; Kamislioglu, M. Photon and neutron shielding performance of boron phosphate glasses for diagnostic radiology facilities. *Results Phys.* **2019**, *12*, 1457–1464. [CrossRef]
111. Dolez, P.I.; Decaens, J.; Buns, T.; Lachapelle, D.; Vermeersch, O. Applications of smart textiles in occupational health and safety. *IOP Conf. Ser. Mater. Sci. Eng* **2020**, *827*, 012014. [CrossRef]
112. Min, R.; Ortega, B.; Marques, C. Latest Achievements in Polymer Optical Fiber Gratings: Fabrication and Applications. *Photonics* **2019**, *6*, 36. [CrossRef]
113. Zlobina, I.V.; Bekrenev, N.V. Influence of microwave radiation on the strength of aramid filaments. *AIP Conf. Proc.* **2018**, *2053*, 040107. [CrossRef]
114. Zlobina, I.V.; Bekrenev, N.V. Study of the microstructure of aramid fabrics for structural and protective organoplastics modified in a microwave electromagnetic field. *IOP Conf. Ser. Mater. Sci. Eng.* **2019**, *511*, 012033. [CrossRef]
115. Zlobina, I.V.; Bekrenev, N.V. Study of mechanical and protective characteristics of composite materials based on aramid fabrics modified in a microwave electromagnetic field. *IOP Conf. Ser. Mater. Sci. Eng.* **2019**, *511*, 012031. [CrossRef]
116. Safonov, P.E.; Yukhin, S.S. Deformation of aramid fabrics with different structures during low-speed penetration by an indenter. Review. *Fibre Chem.* **2017**, *48*, 478–486. [CrossRef]
117. LaBarre, E.D.; Calderon-Colon, X.; Morris, M.; Tiffany, J.; Wetzel, E.; Merkle, A.; Trexler, M. Effect of a carbon nanotube coating on friction and impact performance of Kevlar. *J. Mater. Sci.* **2015**, *50*, 5431–5442. [CrossRef]
118. Usman Javaid, M.; Militký, J.; Wiener, J.; Jabbar, A.; Salačová, J.; Umair, M. Effect of surface modification and knife penetration angle on the Quasi-Static Knife Penetration Resistance of para-aramid fabrics. *J. Text. Inst.* **2019**, *110*, 590–599. [CrossRef]
119. da Silva, A.O.; Weber, R.P.; Monteiro, S.N.; Lima, A.M.; Faria, G.S.; da Silva, W.O.; Oliveira, S.D.S.A.; Monsores, K.; Pinheiro, W.A. Effect of graphene oxide coating on the ballistic performance of aramid fabric. *J. Mater. Res. Technol.* **2020**, *9*, 2267–2278. [CrossRef]
120. Manaee, P.; Valefi, Z.; Goodarz, M. The effect of bond coat type on the stab resistance of $Al_2O_3$–13 wt% $TiO_2$ plasma sprayed ceramic coating on aramid fabrics. *Surf. Interfaces* **2020**, *18*, 100432. [CrossRef]
121. Rodríguez-Millán, M.; Álvarez-Díaz, A.; Aranda-Ruiz, J.; Álvarez-Díaz, J.; Loya, J.A. Experimental analysis for stabbing resistance of different aramid composite architectures. *Compos. Struct.* **2019**, *208*, 525–534. [CrossRef]
122. Lin, T.R.; Lin, T.A.; Lin, M.C.; Lin, Y.Y.; Lou, C.W.; Lin, J.H. Impact resistance of fiber reinforced sandwich-structured nonwoven composites: Reinforcing effect of different fiber length. *Mater. Today Commun.* **2020**, *24*, 101345. [CrossRef]
123. Cheon, J.; Lee, M.; Kim, M. Study on the stab resistance mechanism and performance of the carbon, glass and aramid fiber reinforced polymer and hybrid composites. *Compos. Struct.* **2020**, *234*, 111690. [CrossRef]
124. Gonzalez, G.M.; Ward, J.; Song, J.; Swana, K.; Fossey, S.A.; Palmer, J.L.; Zhang, F.W.; Lucian, V.M.; Cera, L.; Zimmerman, J.F.; et al. Para-aramid fiber sheets for simultaneous mechanical and thermal protection in extreme environments. *Matter* **2020**, *3*, 742–758. [CrossRef]
125. Levit, N.V.; Young, R.H. Flame Resistant Thermal Liner, Composite Fabric, and Garment. U.S. Patent 9,913,504, 13 March 2018.
126. Oertel, A.; Khenoussi, N.; Schacher, L.; Adolphe, D.C.; Graftieaux, H. Optimization of meta-aramid electrospun nanofibers productivity through wire-based electrospinning setup scale up. *J. Ind. Text.* **2018**, *48*, 236–254.
127. Kim, H.B.; Lee, W.J.; Choi, S.C.; Lee, K.B.; Lee, M.-H. Dependence of the fiber diameter on quality factor of filters fabricated with meta-aramid nanofibers. *Sep. Purif. Technol.* **2019**, *222*, 332–341. [CrossRef]
128. Ryu, S.-Y.; Chung, J.W.; Kwak, S.-Y. Amphiphobic meta-aramid nanofiber mat with improved chemical stability and mechanical properties. *Eur. Polym. J.* **2017**, *91*, 111–120. [CrossRef]
129. Chung, J.; Kwak, S.-Y. Solvent-assisted heat treatment for enhanced chemical stability and mechanical strength of meta-aramid nanofibers. *Eur. Polym. J.* **2018**, *107*, 46–53. [CrossRef]
130. Oh, H.J.; Yeang, B.J.; Park, Y.K.; Choi, H.J.; Kim, J.H.; Kang, Y.S.; Bae, Y.; Kim, J.Y.; Lim, S.J.; Lee, W.; et al. Washable Colorimetric Nanofiber Nonwoven for Ammonia Gas Detection. *Polymers* **2020**, *12*, 1585. [CrossRef]
131. Jung, J.-Y.; Ku, P.; Kim, D.H.; Kwon, M.-J.; Kang, S.; Choi, J.-Y.; Lee, J.-Y. Development of firefighters' personal protective clothing with Nomex honeycomb fabric and its protective and comfort evaluation. *Fash. Text. Res. J.* **2019**, *21*, 606–617. [CrossRef]
132. Kasper, D. Aramid recycling. In Proceedings of the 116th Scientific Session, Institute of Textile Science, Montreal, QC, Canada; Edmonton, AB, Canada, 3 April 2017.
133. Dolez, P.; Breton, H.; Paskaluk, S.; Batcheller, J. Predicting the Arc Rating of Fire-Resistant Fabrics Containing Recycled Aramid Fibers. In Proceedings of the Fiber Society Conference, Hong Kong, China, 21–23 May 2019.
134. Mushtaq, N.; Wang, Q.; Chen, G.; Lao, H.; Zhang, Y.; Sidra, L.R.; Fang, X.; Bashir, B. Synthesis of polyamide-imides with different monomer sequence and effect on transparency and thermal properties. *Polymer* **2020**, *190*, 122218. [CrossRef]
135. Helali, N.; Rastgar, M.; Farhad Ismail, M.; Sadrzadeh, M. Development of underwater superoleophobic polyamide-imide (PAI) microfiltration membranes for oil/water emulsion separation. *Sep. Purif. Technol.* **2020**, *238*, 116451. [CrossRef]
136. Dawkins, B.G.; Qin, F.; Gruender, M.; Copeland, G.S. Polybenzimidazole (PBI) high temperature polymers and blends. *High Temp. Polym. Blends* **2014**, 174–212. [CrossRef]
137. Lee, S.; Cho, A.R.; Park, D.; Kim, J.K.; Han, K.S.; Yoon, I.-J.; Lee, M.H.; Nah, J. Resuable polybenzimidazole nanofiber membrane filter for highly breathable PM2.5 dust proof mask. *ACS Appl. Mater. Interfaces* **2019**, *11*, 2750–2757. [CrossRef]

138. Lee, S.; Han, K.S.; Kim, M.; Kim, M.C.; Anh, C.V.; Nah, J. Polybenzimidazole-benzophenone composite nanofiber window air filter with superb UV resistance and high chemical and thermal durability. *ACS Appl. Mater. Interfaces* **2020**, *12*, 23914–23922. [CrossRef]
139. Chen, X.; Zhou, Y. Technical textiles for ballistic protection. In *Handbook of Technical Textiles-V2: Technical Textile Applications*; Woodhead Publishing: Duxford, UK, 2016; pp. 169–192.
140. Hart, S.V. *Third Status Report to the Attorney General on Body Armor Safety Initiative Testing and Activities*; National Institute of Justice: Washington, DC, USA, 2005.
141. Dolez, P.; Malajati, Y. Resistance of Fire Protective Fabrics to Repeated Launderings. In *Performance of Protective Clothing and Equipment: Innovative Solutions to Evolving Challenges*; (STP 1624); ASTM International: West Conshohocken, PA, USA, 2020; 14p.
142. Fu, Q.; Zhang, H.; Song, B.; Liu, X.; Zhuang, Q.; Han, Z. Mechanism of Degradation of Poly(P-Phenylene Benzobisoxazole) under Hydrolytic Conditions. *J. Appl. Polym. Sci.* **2011**, *121*, 1734–1739. [CrossRef]
143. Liu, J.; Liu, X.; Wang, D.; Wang, H. An important factor affecting the UV aging resistance of PBO fiber foped with nano-$TiO^2$: The number of amorphous regions. *Polymers* **2019**, *11*, 869. [CrossRef] [PubMed]
144. Obermann, M.; Aumann, S.; Heimlich, F.; Weber, M.O.; Schwarz-Pfeiffer, A. Comparison of flat-knitted structures made of poly(P-phenylene-2,6-benzobisoxazole) and para-aramid referring to their stab resistance. *IOP Conf. Ser. Mater. Sci. Eng.* **2016**, *141*, 012004. [CrossRef]
145. Vlasblom, M.P.; Van Dingenen, J.L.J. The manufacture, properties and applications of high strength, high modulus polyethylene fibers. In *Handbook of Tensile Properties of Textile and Technical Fibres*; Bunsell, A.R., Ed.; Woodhead Publishing: Cambridge, UK; New Delhi, India; Boca Raton, FL, USA, 2009; pp. 437–485.
146. Van Der Werff, H.; Heisserer, U. High-performance ballistic fibers: Ultra-high molecular weight polyethylene (UHMWPE). In *Advanced Fibrous Composite Materials for Ballistic Protection*; Woodhead Publishing: Duxford, UK; Cambridge, MA, USA; Kidlington, UK, 2016; pp. 71–107. [CrossRef]
147. Firouzi, D.; Ching, C.Y.; Rizvi, S.N.; Selvaganapathy, P.R. Development of oxygen-plasma-surface-treated UHMWPE fabric coated with a mixture of SiC/polyurethane for protection against puncture and needle threats. *Fibers* **2019**, *7*, 46. [CrossRef]
148. Chukov, D.I.; Kharitonov, A.P.; Tcherdyntsev, V.V.; Zherebtsov, D.D.; Maksimkin, A.V. Structure and mechanical properties of self-reinforced ultra-high molecular weight polyethylene. *J. Compos. Mater.* **2018**, *52*, 1689–1698. [CrossRef]
149. Zherebtsov, D.; Chukov, D.; Torokhov, V.; Statnik, E. Manufacturing of single-polymer composite materials based on ultra-high molecular weight polyethylene fibers by hot compaction. *J. Mater. Eng. Perform.* **2020**, *29*, 1522–1527. [CrossRef]
150. Lepage, M.L.; Simhadri, S.; Liu, C.; Takaffoli, M.; Bi, L.; Crawford, B.; Milani, A.S.; Wulff, J.E. A broadly applicable cross-linker for aliphatic polymers containing C–H bonds. *Science* **2019**, *366*, 875–878. [CrossRef]
151. Ivanov, S.; Kuznetsov, S.; Volkov, A.; Terekhin, P.; Dmitriev, S.; Tcherdyntsev, V.; Gorshenkov, M.; Boykov, A. Photons transport through ultra-high molecular weight polyethylene based composite containing tungsten and boron carbide fillers. *J. Alloy. Compd.* **2014**, *586* (Suppl. 1), 2012–2015. [CrossRef]
152. Ertekin, M.; Erhan Kirtay, H. Cut resistance of hybrid para-aramid fabrics for protective gloves. *J. Text. Inst.* **2016**, *107*, 1276–1283. [CrossRef]
153. da Silva, L.F.; Lavoratti, A.; Pereira, I.M.; Dias, R.R.; Amico, S.C.; Zattera, A.J. Development of multilaminar composites for vehicular ballistic protection using ultra-high molecular weight polyethylene laminates and aramid fabrics. *J. Compos. Mater.* **2019**, *53*, 1907–1916. [CrossRef]
154. Kocer, H.B.; Ozkan, F.; Broughton, R.M.; Worley, S.D. Treatment of melamine formaldehyde fibers for decontaminating biological and chemical warfare agents. *J. Appl. Polym. Sci.* **2015**, *132*, 42799. [CrossRef]
155. Zhu, F.; Xu, Y.; Feng, Q.; Yang, Q. Thermal kinetics study and flammability evaluation of polyimide fiber material. *J. Therm. Anal. Calorim.* **2018**, *131*, 2579–2587. [CrossRef]
156. Serbezeanu, D.; Popa, A.M.; Stelzig, T.; Sava, I.; Rossi, R.M.; Fortunato, G. Preparation and characterization of thermally stable polyimide membranes by electrospinning for protective clothing applications. *Text. Res. J.* **2015**, *85*, 1763–1775. [CrossRef]
157. Yi, B.; Zhao, Y.; Tian, E.; Li, J.; Ren, Y. High-performance polyimide nanofiber membranes prepared by electrospinning. *High Perform. Polym.* **2019**, *31*, 438–448. [CrossRef]
158. Wen, Y.; Meng, X.; Wang, Z.; Yan, J. Surface modification of high-performance polyimide fibers by oxygen plasma treatment. *High Perform. Polym.* **2017**, *29*, 1083–1089. [CrossRef]
159. Sloan, F. Liquid crystal aromatic polyester-arylate (LCP) fibers: Structure, properties, and applications. In *Structure and Properties of High-Performance Fibers*; Woodhead Publishing: Duxford, UK; Cambridge, MA, USA; Kidlington, UK, 2017; pp. 113–140. [CrossRef]
160. Bertocchi, M.J.; Simbana, R.A.; Wynne, J.H.; Lundin, J.G. Electrospinning of Tough and Elastic Liquid Crystalline Polymer–Polyurethane Composite Fibers: Mechanical Properties and Fiber Alignment. *Macromol. Mater. Eng.* **2019**, *304*, 1900186. [CrossRef]
161. Balagna, C.; Irfan, M.; Perero, S.; Miola, M.; Maina, G.; Crosera, M.; Santella, D.; Simone, A.; Ferraris, M. Antibacterial nanostructured composite coating on high performance Vectran™ fabric for aerospace structures. *Surf. Coat. Technol.* **2019**, *373*, 47–55. [CrossRef]
162. Li, J.; Zhu, Y.; Yu, H.; Dai, B.; Jun, Y.-S.; Zhang, F. Microbially Synthesized Polymeric Amyloid Fiber Promotes β-Nanocrystal Formation and Displays Gigapascal Tensile Strength. *ACS Nano* **2021**, *15*, 11843–11853. [CrossRef]

163. Bowen, C.H.; Sargent, C.J.; Wang, A.; Zhu, Y.; Chang, X.; Li, J.; Mu, X.; Galazka, J.M.; Jun, Y.-S.; Keten, S.; et al. Microbial production of megadalton titin yields fibers with advantageous mechanical properties. *Nat. Commun.* **2021**, *12*, 5182. [CrossRef]
164. McQuerry, M.; Klausing, S.; Cotterill, D.; Easter, E. A Post-use Evaluation of Turnout Gear Using NFPA 1971 Standard on Protective Ensembles for Structural Fire Fighting and NFPA 1851 on Selection, Care and Maintenance. *Fire Technol.* **2015**, *51*, 1149–1166. [CrossRef]
165. Dolez, P.I.; Tomer, N.S.; Malajati, Y. A quantitative method to compare the effect of thermal aging on the mechanical performance of fire protective fabrics. *J. Appl. Polym. Sc.* **2018**, *135*, 47045. [CrossRef]
166. Arrieta, C.; David, E.; Dolez, P.; Vu-Khanh, T. Hydrolytic and photochemical aging studies of a Kevlar-PBI blend. *Polym. Degrad. Stab.* **2011**, *96*, 1411–1419. [CrossRef]
167. Hoque, M.S.; Saha, A.; Chung, H.-J.; Dolez, P.I. Hydrothermal aging of fire-protective fabrics. *J. Appl. Polym. Sci.* **2022**, e52666. [CrossRef]
168. Dolez, P.I.; Tomer, N.S.; Malajati, Y. Aging of aramid fabrics: Effect of exposure to high temperature, UV, and laundering on mechanical performance. In Proceedings of the 5th International Congress on Soldiers' Physical Performance—ICSPP, Quebec City, QC, Canada, 11–14 February 2020.
169. Dolez, P.; Chung, H.-J.; Cho, C. End-of-Life Sensors for Fabrics. PCT International Patent Application PCT/CA2022/000006, 3 March 2022.
170. Cho, C.; Elias, A.; Batcheller, J.; Dolez, P.; Chung, H.-J. Electrical conduction of reduced graphene oxide coated meta-aramid textile and its evolution under aging conditions. *J. Ind. Text.* **2021**, *50*, 1330–1347. [CrossRef]
171. Cho, C.; Nam, S.L.; de la Mata, P.A.; Harynuk, J.J.; Elias, A.; Chung, H.-J.; Dolez, P.I. Investigation of the accelerated thermal aging behavior of polyetherimide and lifetime prediction at elevated temperature. *J. Appl. Polym. Sci.* **2021**, *139*, e51955. [CrossRef]
172. Braun, C.; Nam, S.L.; de la Mata, P.A.; Harynuk, J.J.; Chung, H.-J.; Dolez, P.I. Hydrothermal Aging of Polyimide Film. *J. Appl. Polym. Sci.* **2022**, *139*, e52183. [CrossRef]
173. Behera, B.K.; Dash, B.P. An experimental investigation into structure and properties of 3D-woven aramid and PBO fabrics. *J. Text. Inst.* **2013**, *104*, 1337–1344. [CrossRef]
174. Gu, B. Modelling of 3D woven fabrics for ballistic protection. In *Advanced Fibrous Composite Materials for Ballistic Protection*; Woodhead Publishing: Duxford, UK; Cambridge, MA, USA; Kidlington, UK, 2016; pp. 145–197. [CrossRef]
175. Chu, T.L.; Ha-Minh, C.; Imad, A. Analysis of local and global localizations on the failure phenomenon of 3D interlock woven fabrics under ballistic impact. *Compos. Struct.* **2017**, *159*, 267–277. [CrossRef]
176. Abtew, M.A.; Boussu, F.; Bruniaux, P.; Loghin, C.; Cristian, I. Engineering of 3D warp interlock p-aramid fabric structure and its energy absorption capabilities against ballistic impact for body armour applications. *Compos. Struct.* **2019**, *225*, 111179. [CrossRef]
177. Abtew, M.A.; Boussu, F.; Bruniaux, P.; Loghin, C.; Cristian, I. Enhancing the ballistic performances of 3D warp interlock fabric through internal structure as new material for seamless female soft body armor development. *Appl. Sci.* **2020**, *10*, 4873. [CrossRef]
178. Mahbub, R.; Nayak, R.; Wang, L.; Arnold, L. Comfort properties of 3D-knitted seamless female body armour vests. *J. Text. Inst.* **2017**, *108*, 1997–2005. [CrossRef]
179. Palani Rajan, T.; Ramakrishnan, G.; Kandhavadivu, P. Permeability and impact properties of warp-knitted spacer fabrics for protective application. *J. Text. Inst.* **2016**, *107*, 1079–1088. [CrossRef]
180. Nayak, R.; Kanesalingam, S.; Vijayan, A.; Wang, L.; Padhye, R.; Arnold, L. Design of 3D knitted structures for impact absorption in sportswear. *KnE Eng.* **2017**, *2*, 127. [CrossRef]
181. Storck, J.L.; Ehrmann, G.; Uthoff, J.; Diestelhorst, E.; Blachowicz, T.; Ehrmann, A. Investigating inexpensive polymeric 3D printed materials under extreme thermal conditions. *Mater. Futures* **2022**, *1*, 015001. [CrossRef]
182. Ugbolue, S.C.; Kim, Y.K.; Warner, S.B.; Fan, Q.; Yang, C.-L.; Feng, Y.; Kyzymchuk, O. Formation and Performance of Auxetic Textiles. *Natl. Text. Cent. Annu. Rep.* **2008**, *101*, 660–667. [CrossRef]
183. Wang, Z.; Hu, H.; Xiao, X. Deformation behaviors of three-dimensional auxetic spacer fabrics. *Text. Res. J.* **2014**, *84*, 1361–1372. [CrossRef]
184. Wang, Z.; Hu, H. Tensile and forming properties of auxetic warp-knitted spacer fabrics. *Text. Res. J.* **2017**, *87*, 1925–1937. [CrossRef]
185. Steffens, F.; Rana, S.; Fangueiro, R. Development of novel auxetic textile structures using high performance fibres. *Mater. Des.* **2016**, *106*, 81–89. [CrossRef]
186. Sun, Y.; Xu, W.; Wei, W.; Ma, P.; Xia, F. Stab-resistance of auxetic weft-knitted fabric with Kevlar fibers at quasi-static loading. *J. Ind. Text.* **2019**, *50*, 1384–1396. [CrossRef]
187. Ali, M.; Zeeshan, M.; Ahmed, S.; Qadir, B.; Nawab, Y.; Anjum, A.S.; Riaz, R. Development and comfort characterization of 2D-woven auxetic fabric for wearable and medical textile applications. *Cloth. Text. Res. J.* **2018**, *36*, 199–214. [CrossRef]
188. Goncalves, C.; Magalhaes, R.; Rana, S.; Fangueiro, R.; Nunes, J.; Dias, G. Novel high performance auxetic fibrous structures for composite reinforcement. *IOP Conf. Ser. Mater. Sci. Eng.* **2018**, *406*, 012046. [CrossRef]
189. Lolaki, A.; Shanbeh, M. Variation of Poisson's ratio of fabrics woven with helical composite auxetic weft yarns in relation to fabric structural parameters. *J. Ind. Text.* **2019**, *50*, 149–169. [CrossRef]
190. Chen, J.; Du, Z.; Li, T. Structural design and characterization of highly elastic woven fabric containing helical auxetic yarns. *Text. Res. J.* **2020**, *90*, 809–823. [CrossRef]

191. Zielinska, D.; Delczyk-Olejniczak, B.; Wierzbicki, L.; Wilbik-Hałgas, B.; Struszczyk, M.H.; Leonowicz, M. Investigation of the effect of para-aramid fabric impregnation with shear thickening fluid on quasi-static stab resistance. *Text. Res. J.* **2014**, *84*, 1569–1577. [CrossRef]
192. Baharvandi, H.R.; Alebooyeh, M.; Alizadeh, M.; Khaksari, P.; Kordani, N. Effect of silica weight fraction on rheological and quasi-static puncture characteristics of shear thickening fluid-treated Twaron®composite. *J. Ind. Text.* **2016**, *46*, 473–494. [CrossRef]
193. Santos, T.F.; Santos, C.M.S.; Aquino, M.S.; Ionesi, D.; Medeiros, J.I. Influence of silane coupling agent on shear thickening fluids (STF) for personal protection. *J. Mater. Res. Technol.* **2019**, *8*, 4032–4039. [CrossRef]
194. Li, W.; Xiong, D.; Zhao, X.; Sun, L.; Liu, J. Dynamic stab resistance of ultra-high molecular weight polyethylene fabric impregnated with shear thickening fluid. *Mater. Des.* **2016**, *102*, 162–167. [CrossRef]
195. Majumdar, A.; Laha, A. Effects of fabric construction and shear thickening fluid on yarn pull-out from high-performance fabrics. *Text. Res. J.* **2016**, *86*, 2056–2066. [CrossRef]
196. Haris, A.; Lee, H.P.; Tay, T.E.; Tan, V.B.C. Shear thickening fluid impregnated ballistic fabric composites for shock wave mitigation. *Int. J. Impact Eng.* **2015**, *80*, 143–151. [CrossRef]
197. Fowler, J.N.; Pallanta, A.A.; Swanik, C.B.; Wagner, N.J. The use of shear thickening nanocomposites in impact resistant materials. *J. Biomech. Eng.* **2015**, *137*, 054504. [CrossRef]
198. Haris, A.; Lee, H.P.; Tan, V.B.C. An experimental study on shock wave mitigation capability of polyurea and shear thickening fluid based suspension pads. *Def. Technol.* **2018**, *14*, 12–18. [CrossRef]
199. Li, S.; Wang, Y.; Ding, J.; Wu, H.; Fu, Y. Effect of shear thickening fluid on the sound insulation properties of textiles. *Text. Res. J.* **2014**, *84*, 897–902. [CrossRef]
200. Wang, Y.; Zhu, Y.; Fu, X.; Fu, Y. Effect of TW-ZnO/$SiO^2$-compounded shear thickening fluid on the sound insulation property of glass fiber fabric. *Text. Res. J.* **2015**, *85*, 980–986. [CrossRef]
201. Cwalina, C.D.; McCutcheon, C.M.; Dombrowski, R.D.; Wagner, N.J. Engineering enhanced cut and puncture resistance into the thermal micrometeoroid garment (TMG) using shear thickening fluid (STF)-ArmorTM absorber layers. *Compos. Sci. Technol.* **2016**, *131*, 61–66. [CrossRef]
202. Wei, R.; Dong, B.; Wang, F.; Yang, J.; Jiang, Y.; Zhai, W.; Li, H. Effects of silica morphology on the shear-thickening behavior of shear thickening fluids and stabbing resistance of fabric composites. *J. Appl. Polym. Sci.* **2020**, *137*, 1–7. [CrossRef]
203. Zhang, X.; Li, T.T.; Peng, H.K.; Wang, Z.; Huo, J.; Lou, C.W.; Lin, J.H. Effects of bi-particle-sized shear thickening fluid on rheological behaviors and stab resistance of Kevlar fabrics. *J. Ind. Text.* **2020**, 1–16. [CrossRef]
204. Gürgen, S. Numerical modeling of fabrics treated with multi-phase shear thickening fluids under high velocity impacts. *Thin-Walled Struct.* **2020**, *148*, 106573. [CrossRef]
205. Majumdar, A.; Laha, A.; Bhattacharjee, D.; Biswas, I. Tuning the structure of 3D woven aramid fabrics reinforced with shear thickening fluid for developing soft body armour. *Compos. Struct.* **2017**, *178*, 415–425. [CrossRef]
206. Xu, W.; Yan, B.; Hu, D.; Ma, P. Preparation of auxetic warp-knitted spacer fabric impregnated with shear thickening fluid for low-velocity impact resistance. *J. Ind. Text.* **2020**. [CrossRef]
207. Wang, Y.; Li, L.; Hofmann, D.; Andrade, J.E.; Daraio, C. Structured fabrics with tunable mechanical properties. *Nature* **2021**, *596*, 238–243. [CrossRef]
208. Linhares, T.; Pessoa de Amorim, M.T.; Durães, L. Silica aerogel composites with embedded fibres: A review on their preparation, properties and applications. *J. Mater. Chem. A* **2019**, *7*, 22768–22802. [CrossRef]
209. Han, Y.; Zhang, X.; Wu, X.; Lu, C. Flame retardant, heat insulating cellulose aerogels from waste cotton fabrics by in situ formation of magnesium hydroxide nanoparticles in cellulose gel nanostructures. *ACS Sustain. Chem. Eng.* **2015**, *3*, 1853–1859. [CrossRef]
210. Liu, Z.; Lyu, J.; Fang, D.; Zhang, X. Nanofibrous kevlar aerogel threads for thermal insulation in harsh environments. *ACS Nano* **2019**, *13*, 5703–5711. [CrossRef]
211. Wang, Y.; Cui, Y.; Shao, Z.; Gao, W.; Bai, H.; Fan, W.; Liu, T. Multifunctional polyimide aerogel textile inspired by polar bear hair for thermoregulation in extreme environments. *Chem. Eng. J.* **2020**, *390*, 124623. [CrossRef]
212. Qiao, S.; Zhang, H.; Kang, S.; Quan, J.; Hu, Z.; Yu, J.; Wang, Y.; Zhu, J. Hydrophobic, Pore-Tunable Polyimide/Polyvinylidene Fluoride Composite Aerogels for Effective Airborne Particle Filtration. *Macromol. Metarials Eng.* **2020**, *305*, 2000129. [CrossRef]
213. Maksoud, F.J.; Lameh, M.; Fayyad, S.; Ismail, N.; Tehrani-Bagha, A.R.; Ghaddar, N.; Ghali, K. Electrospun waterproof breathable membrane with a high level of aerosol filtration. *J. Appl. Polym. Sci.* **2018**, *135*, 45660. [CrossRef]
214. Park, Y.S.; Lee, J.W.; Nam, Y.S.; Park, W.H. Breathable properties of m-Aramid nanofibrous membrane with high thermal resistance. *J. Appl. Polym. Sci.* **2015**, *132*, 41515. [CrossRef]
215. Iqbal, K.; Khan, A.; Sun, D.; Ashraf, M.; Rehman, A.; Safdar, F.; Basit, A.; Maqsood, H.S. Phase change materials, their synthesis and application in textiles—a review. *J. Text. Inst.* **2019**, *110*, 625–638. [CrossRef]
216. Gao, C. Phase-change materials (PCMs) for warming or cooling in protective clothing. In *Protective Clothing: Managing Thermal Stress*; Woodhead Publishing: Cambridge, MA, USA; Waltham, MA, USA; Kidlington, UK, 2014; pp. 227–249.
217. Chen, W.; Ni, S.; Weng, W.; Fu, M. The preparation and characterization of ultrafine fatty acid ester/poly(meta-phenylene isophthalamide) phase change fibers designed for thermo-regulating protective clothing. *Fibers Polym.* **2018**, *19*, 498–506. [CrossRef]
218. Saraç, E.G.; Öner, E.; Kahraman, M.V. Microencapsulated organic coconut oil as a natural phase change material for thermo-regulating cellulosic fabrics. *Cellulose* **2019**, *26*, 8939–8950. [CrossRef]

219. Sheng, N.; Rao, Z.; Zhu, C.; Habazaki, H. Enhanced thermal performance of phase change material stabilized with textile-structured carbon scaffolds. *Sol. Energy Mater. Sol. Cells* **2020**, *205*, 110241. [CrossRef]
220. Han, N.; Zhang, W.; Wang, X.; Zhang, X.; Li, W.; Yu, W. Preparation and properties of shape-stabilized phase change material cellulose benzoate-g-polyoxyethylene (2) hexadecyl ether with potential for thermal energy storage. *Text. Res. J.* **2019**, *89*, 1512–1521. [CrossRef]
221. Chen, W.; Fu, M.; Weng, W. Electrospinning of continuous nanofiber hollow yarns for thermal storage and insulation by a multi-step twisting method. *Text. Res. J.* **2020**, *90*, 1045–1056. [CrossRef]
222. Hsu, P.-C.; Liu, C.; Song, A.Y.; Zhang, Z.; Peng, Y.; Xie, J.; Liu, K.; Wu, C.-L.; Catrysse, P.B.; Cai, L.; et al. A dual-mode textile for human body radiative heating and cooling. *Sci. Adv.* **2017**, *3*, e170089. [CrossRef]
223. Abebe, M.G.; De Corte, A.; Rosolen, G.; Maes, B. Janus-Yarn Fabric for Dual-Mode Radiative Heat Management. *Phys. Rev. Appl.* **2021**, *16*, 054013. [CrossRef]
224. Koohestani, A.S.; Bashari, A. Advanced bulletproof and stab-and spike-resistant textiles. In *Advances in Functional and Protective Textiles*; Woodhead Publishing: Duxford, UK; Cambridge, MA, USA; Kidlington, UK, 2020; pp. 261–289. [CrossRef]
225. Kim, Y.H.; Smith, N.; Ji, H. Penetration Resistant Fabric with Multiple Layer Guard Plate Assemblies and Method of Making the Same. U.S. Patent 7,018,692; United States Patent Office, 28 March 2006.
226. SuperFabric®A Cut Above. HexArmor. 2020. Available online: https://www.hexarmor.com/technologies/superfabric (accessed on 10 June 2022).
227. Dolez, P.I.; Nguyen, C.T.; Guero, G.; Gauvin, C.; Lara, J. Influence of medical needle characteristics on the resistance to puncture of protective glove materials. *J. ASTM Int.* **2008**, *5*, 12.
228. Boorsma, J.; Smith, N. Cut, Abrasion and/or Puncture Resistant Knitted Gloves. U.S. Patent 10,455,875; United States Patent Office, 29 October 2019.
229. Vu-Khanh, T.; Dolez, P.; Nguyen, C.T.; Gauvin, C.; Lara, J. *Needlestick Resistance of Protective Gloves-Development of a Test Method*; Publications IRSST: Montréal, QC, Canada, 2012; ISBN 978-2-89631-638-0.
230. Howland, C.A.; Hannigan, M.A. Protective Garment and Glove Construction and Method for Making Same. U.S. Patent 7,007,308; United States Patent Office, 7 March 2006.
231. Jones, R.J.; Linsner, A.; Wyatt, S.; Scheir, C.; Muller, G.; Sung, J.; Hewes, L.; Graziosi, D. Enhancements to the ISS Phase VI Glove Design. In Proceedings of the 44th International Conference on Environmental Systems, Tucson, AZ, USA, 13–17 July 2014; pp. 1–11.
232. Nguyen, C.; Dolez, P.; Vu-Khanh, T.; Gauvin, C.; Lara, J. Resistance of protective gloves materials to puncture by medical needles. *J. ASTM Int.* **2010**, *7*, 1–16.
233. Nguyen, C.T.; Dolez, P.I.; Vu-Khanh, T.; Gauvin, C.; Lara, J. Effect of protective glove use conditions on their resistance to needle puncture. *Plast. Rubber Compos.* **2013**, *42*, 187–193. [CrossRef]
234. Firouzi, D.; Russel, M.K.; Rizvi, S.N.; Ching, C.Y.; Selvaganapathy, P.R. Development of flexible particle-laden elastomeric textiles with improved penetration resistance to hypodermic needles. *Mater. Des.* **2018**, *156*, 419–428. [CrossRef]
235. Gartmann, V.; Lottenbach, R.; Hibner, H.J. Textiles Having a Protective Function Against Abrasion and Contact Heat. Patent Application US 2014/0255664 A1; United States Patent Office, 11 September 2014.
236. Optimum Protection from Abrasion. Schoeller Textiles. 2020. Available online: https://www.schoeller-textiles.com/en/technologies/ceramic-coating (accessed on 10 June 2022).
237. Blakely, K.S. Apparel with Heat Retention Layer and Method of Making the Same. U.S. Patent 9,719,206; United States Patent Office, 1 August 2017.
238. Das, A.; Alagirusamy, R. *Science in Clothing Comfort*; Woodhead Publishing: New Delhi, India; Cambridge, UK; Oxford, UK, 2010.
239. Classen, E. Comfort testing of textiles. In *Advanced Characterization and Testing of Textiles*; Elsevier: Amsterdam, The Netherlands, 2017; pp. 59–69.
240. *NFPA 1971*; Standard on Protective Ensembles for Structural Fire Fighting and Proximity Fire Fighting. National Fire Protection Association: Quincy, MA, USA, 2018.
241. Wang, F. Udayraj Human Wear Trials for Assessing Comfort Performance of Firefighter Protective Clothing. In *Firefighters' Clothing and Equipment*; Song, G., Wang, F., Eds.; CRC Press: Boca Raton, FL, USA, 2018; pp. 217–268.
242. *ASTM F1154-11*; Standard Practices for Qualitatively Evaluating the Comfort, Fit, Function, and Durability of Protective Ensembles and Ensemble Components. ASTM International: West Conshohocken, PA, USA, 2018; 7p.
243. Harrabi, L.; Dolez, P.I.; Vu-Khanh, T.; Lara, J.; Tremblay, G.; Nadeau, S.; Larivière, C. Characterization of protective gloves stiffness: Development of a multidirectional deformation test method. *Saf. Sci.* **2008**, *46*, 1025–1036. [CrossRef]
244. Gauvin, C.; Airoldi, A.; Proulx-Croteau, S.; Dolez, P.I.; Lara, J. A new test method to characterize the adherence of protective glove materials. In *Performance of Protective Clothing and Equipment: Emerging Issues and Technologies*; Shepherd, A.M., Ed.; ASTM International: West Conshohocken, PA, USA, 2012; pp. 392–406.
245. Bradley, J.V. Glove characteristics influencing control manipulability. *Hum. Factors* **1969**, *11*, 21–35. [CrossRef]
246. Dolez, P.; Mlynarek, J. Smart Materials for PPE: Tendencies and Recent Developments. In *Smart Textiles and their Applications*; Koncar, V., Ed.; Elsevier: Amsterdam, The Netherlands, 2016; pp. 497–517.
247. Dolez, P. Smart barrier membranes for protective clothing. In *Smart Textiles for Protection*; Chapman, R., Ed.; Woodhead Publishing Ltd.: Cambridge, UK, 2012; pp. 148–189.

248. Hambling, D. The Overloaded Soldier: Why, U.S. Infantry Now Carry More Weight than Ever. Hearst Magazine Media. 26 December 2018. Available online: https://www.popularmechanics.com/military/research/a25644619/soldier-weight/ (accessed on 24 July 2021).
249. Dolez, P.I. Energy Harvesting Materials and Structures for Smart Textile Applications: Recent Progress and Path Forward. *Sensors* **2021**, *21*, 6297. [CrossRef] [PubMed]
250. Nazif, K.N.; Daus, A.; Hong, J.; Lee, N.; Vaziri, S.; Kumar, A.; Nitta, F.; Chen, M.E.; Kananian, S.; Islam, R.; et al. Cambridge High-specific-power flexible transition metal dichalcogenide solar cells. *Nat. Commun.* **2021**, *12*, 7034. [CrossRef] [PubMed]
251. Zhou, Y.; Zhao, X.; Xu, J.; Fang, Y.; Chen, G.; Song, Y.; Li, S.; Chen, J. Giant magnetoelastic effect in soft systems for bioelectronics. *Nat. Mater.* **2021**, *20*, 1670–1676. [CrossRef]
252. Komatsu, N.; Ichinose, Y.; Dewey, O.S.; Taylor, L.W.; Trafford, M.A.; Yomogida, Y.; Wehmeyer, G.; Pasquali, M.; Yanagi, K.; Kono, J. Macroscopic weavable fibers of carbon nanotubes with giant thermoelectric power factor. *Nat. Commun.* **2021**, *12*, 4931. [CrossRef] [PubMed]
253. Khudiyev, T.; Grena, B.; Loke, G.; Hou, C.; Jang, H.; Lee, J.; Lee, J.T. Thermally drawn rechargeable battery fiber enables pervasive power. *Mater. Today* **2022**, *52*, 80–89. [CrossRef]
254. Yang, P.; Li, J.; Lee, S.W.; Fan, H.J. Printed Zinc Paper Batteries. *Adv. Sci.* **2022**, *9*, 2103894. [CrossRef]
255. Ammendolia, J.; Saturno, J.; Jacobs, S. *Environmental Concern Emerges from COVID-19 Pandemic: PPE Waste by the Public*; Canadian Science Policy Centre: Richmond Hill, ON, Canada, 2020.
256. Dolez, P.I. When Protective Clothing and PPE Become Sustainable. In Proceedings of the International e-Conference on Sustainable Growth in Textiles (SGT-2021), Kanpur, India, 19–21 August 2021.
257. Trupp, S. Colour-changing gloves for toxic-substance detection. *Smart Text. Nanotechnol.* **2013**, *9*, 11.
258. COVID-19–What We Know So Far about ... Reuse of Personal Protective Equipment. Ontario Agency for Health Protection and Promotion. Public Health Ontario, Toronto, ON: Queens's Printer for Ontario. 2020. 10p. Available online: https://www.publichealthontario.ca/-/media/documents/ncov/covid-wwksf/what-we-know-reuse-of-personal-protective-equipment.pdf?la=en (accessed on 16 April 2022).

*textiles*

MDPI

*Review*

# Textile-Based Sound Sensors (TSS): New Opportunities for Sound Monitoring in Smart Buildings

**Andrea Giglio [1,*], Karsten Neuwerk [2], Michael Haupt [2], Giovanni Maria Conti [1] and Ingrid Paoletti [1]**

[1] Department of Architecture, Built Environment and Construction Engineering, Politecnico di Milano, 20133 Milan, Italy; giovanni.conti@polimi.it (G.M.C.); ingrid.paoletti@polimi.it (I.P.)
[2] DITF Denkendorf, German Institutes of Textile and Fibre Research Denkendorf, 73770 Denkendorf, Germany; karsten.neuwerk@ditf.de (K.N.); michael.haupt@ditf.de (M.H.)
* Correspondence: andrea.giglio@polimi.it

**Abstract:** Persistent poor acoustic conditions can imbalance humans' psychophysical capabilities. A good acoustic project starts with either correct measurements of the existing acoustic parameters or with the correct hypothesis of new sound conditions. International standards define invasive measurement conditions and procedures that can disturb user activities. For this reason, alternative methodologies have been developed by mounting real-time sound-monitoring devices. Most of the research on these aims to decrease their dimensions in order to be placed in the tight service spaces of modern architecture and to reduce their aesthetic impact on interiors design. In this perspective, this article explores the features and potentialities of textile-based sound sensors (TSS) as they can not only fulfill these needs but can also be used as architectural ornaments by partially wrapping interiors. The ubiquitous of e-textiles for wearable applications has led to increasing the performance of TSS. Therefore, a comparison of the sensitivity values, signal-to-noise ratio and noise floor of sound TSS with sound sensors is presented, which is still missing in the literature. The paper demonstrates how these can be exploited for sound monitoring and can provide valid opportunities for new smart acoustic textiles.

**Keywords:** e-textiles; textile-based sound sensors; sound monitoring; smart building

**Citation:** Giglio, A.; Neuwerk, K.; Haupt, M.; Conti, G.M.; Paoletti, I. Textile-Based Sound Sensors (TSS): New Opportunities for Sound Monitoring in Smart Buildings. *Textiles* **2022**, 2, 296–306. https://doi.org/10.3390/textiles2020016

Academic Editor: Laurent Dufossé

Received: 29 March 2022
Accepted: 11 May 2022
Published: 19 May 2022



## 1. Introduction

Sound conditions can have physiological and psychological effects on people in either a positive or negative way. Studies have demonstrated effects in educational spaces [1], working spaces [2], restaurants [3], canteens [4] and outdoor spaces [5]. Negative conditions can cause permanent hearing damage, increased stress [6], reduced efficiency at work [7], disturbance of sleep patterns [8] and interference in communications [9] as well as cardiovascular illnesses [10].

Therefore, it is increasingly compelling to embed sound condition considerations starting in the first stages of the design process. International standards indeed provide the requirements for running considerations at the design stage of new programs [11], and for existing functions, international standards give the terms, definitions, measurement conditions, procedures and evaluation methodologies [12–14]. Nonetheless, most of these conditions are invasive and concern the use of annoying sources that can affect normal user activities. For this reason, non-invasive sound-monitoring devices have been developed to provide real-time sound-data gathering.

These systems are framed in the consolidated trends of monitoring systems that help to maximise the energy savings, comfort and safety for the occupants [15]. The most commonly used sensing systems detect real-time information on the temperature and air quality and enable building environmental control systems, such as heating, ventilation, and air conditioning systems if the gathered data does not fulfill the fixed benchmarks.

Indoor environmental quality influences occupant productivity and health; therefore, its management is crucial, and sound has a prominent role. Sound-monitoring devices find applications in urban contexts [16] with low-cost [17] wireless sensor networks [18] embedding spatial statistical analysis [19], through considering indexes that embed subjective measures [20], in detecting noise levels while being powered by energy harvesting [21] and through the development of sensor nodes for accurate indoor sound-level measurements [22].

This article intends to compare the performances of sound sensors of the aforementioned cases with textile-based sound sensors (TSS). The combination of electronics and textiles is increasingly achieving important results in the trend for common computing. The rapid advancements of science and technologies keep revolutionizing traditional textiles and achieving new applications; smart textiles have more functions, including tactile sensing [23], displays [24], communicating [25], self-charging [26] and regulating body temperature [27] and humidity [28].

In the last decades, important advances have been achieved in sound sensors as well. They can measure correlation between the subjective assessment of perceived sound quality and the cardiac activity of the listeners [20], they can be embedded in gloves [29] and used for sound-direction detection, acoustic communications and heart-sound auscultation [30]. Their applications are mostly in wearable fabrics. Greinke used piezo electric films for sound measurement by sticking the film into fabric and sewing a conductive path with conductive yarn [31].

Nakad et al. designed and implemented a large-scale e-textile that functions as an acoustic beamforming array [32]. The prototype aims to find the location of a passing vehicle based upon the vehicle's acoustic emissions through a system that combines multiple lines-of-bearing to the vehicle's traffic. These lines-of-bearing are computed using an acoustic beamforming algorithm under the assumption that the vehicle is in the far field and lies in the same plane as the e-textile. They concluded that, at the physical scale, robust connectors are necessary for attaching electronic components, in order to insulate conductive elements in the fabric. At the system scale, the communication is energy-efficient and fault-tolerant and can serve a wide range of e-textile applications.

Comparisons between the performances of sound sensors have already been presented in the literature; however, a deep comparison of sound sensors for monitoring systems and TSS is still missing. This article intends to fill this gap.

## 2. Research Methodology

The article intends to compare the microphones embedded in sound-monitoring systems with TSSs. Only case studies published in scientific journals or accredited conference are reported.

An imperfect selection of materials, transducer modes and processing circuity can lead poor acoustic functionalities by decreasing the values of the signal-to-noise ratio (SNR) [33–35]. The SNR depends on the sensitivity and noise measured at a given acoustic pressure. The sensitivity is the converted sensing signal arising from the mechanical vibration with respect to the applied acoustic pressure. Therefore, the higher the value is, the better the performance. Furthermore, when the energy conversion takes place, an electrical noise—in form of a voltage/current—is also introduced followed by the thermal-mechanical or Johnson noise [33,34,36]. As a consequence, the signal-to-noise ratio (SNR), sensitivity and noise floor (plotted in Table 1 with the related unit) are the parameters used for the comparison.

**Table 1.** The main parameters and relative units for acoustic sensor performance.

| Parameters | Unit |
|---|---|
| Sensitivity at 1 kHz | mV/Pa, or dB |
| Signal-to-noise ratio (SNR) | dB |
| Noise floor | dB |
| Sensitivity Resonance | Hz |

## 3. Methods to Embed Sound Sensors in Textile

One of the most critical aspects for electronic textiles is the power supply. All electronic components require an energy supply in order to be employed as a stand-alone component. Avoiding conventional batteries important since it makes the garment similar to an ordinary one. Batteries are very bulky to add into the fabric, and they can limit the characteristics of the textile itself. Alternatives are given by flexible solar cells (Silicon Solar Inc, Bainbridge, New York, USA.) and micro fuel cells (Enfucell, Vantaa, Finland) since they can be used as a power supply for electronic devices. Other options are given by materials that are able to transform changing pressures (such as body motions or sound pressures in electric power [35]) using piezo electric materials [36]. The piezoelectricity is the generation of electrical polarization in a material under applied mechanical stresses. When a deformation occurs, it generates an electric charge. Vice versa, under applied charge, the material would deform in response [37].

Piezoelectric material-based sensors offer two main advantages: (1) there is no specific requirement for the input power and (2) a broad dynamic range. For these reasons, most of the cases considered for the purpose of this article are piezoelectric-based acoustic sensors (from here on PAS) and micro-electrotechnical systems (from here on MEMS).

Two methods are mainly used to embed sound sensors in textiles: 1. by attaching external sensors to the textile structures and 2. by embroidering piezo electric threads to create the fabric circuits. The two methodologies are described in the next paragraphs.

### *3.1. Piezoelectric Acoustic Sensors (PAS) Films*

According to the plane in which the sensing phase is placed, the energy conversions in piezoelectricity takes place in two transducing modes (Figure 1). In the case where it occurs in plane 31, we consider the D31 mode. If it occurs in direction 3, it is the D33 mode.

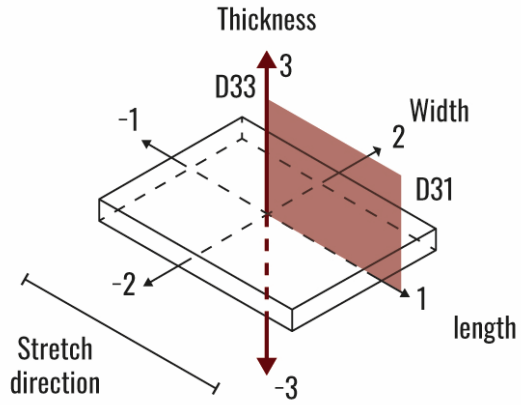


**Figure 1.** Definition of the planes where the sensing phases can be placed.

Upon an application of the acoustic pressure, the induced voltage (V) is defined as [34],

$$V = E \times s \quad (1)$$

where E is the induced electric field and *s* is the electrode spacing. The electrode spacing (s) can be "t" or "d" (as shown in Figure 2), depending on the transducer mode. In D31

mode, the "3-1" refers to the induced polarization in direction 3 with respect to the per unit stress applied in direction 1 (Figure 2a) [35]. Thus, the thickness (t) limits the sensing signal. The improvement of the SNR in order to fit it with new technology demands has been achieved by incorporating different piezoelectric materials with different thicknesses, such as aluminium nitride (AlN) and D31 mode [36], sputtered zinc oxide (ZnO) and D31 mode [38] as well as lead zirconate titanate (PZT) and D31 mode [39].

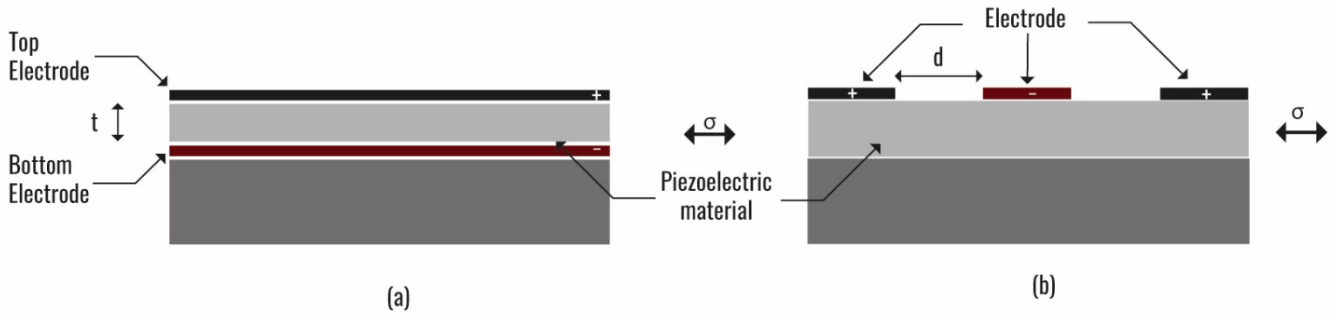


**Figure 2.** Piezoelectric acoustic sensor (PAS) with (**a**) D31 mode where t is the film thickness and (**b**) D33 mode where d is the electrode spacing [40].

The highest thickness values can increase the induced voltage; however, at the same time, it makes the sensor bulky and generates higher noise followed by mass and gravitational acceleration. For instance, Wang et al. reported a 60 dB SNR and a 34 dB noise floor by utilizing 0.7 μm thick PZT [39]; whereas, the reported sensitivity was only 0.49 mV/Pa, which is still a challenge for further signal processing. Therefore, an increase in film thickness is not a favourable solution to enhance the SNR.

For this reason, the D33 mode, where the stress and strain take place in the "3-3" directions (Figure 2b), has been developed. In this mode, the design focuses on the electrode spacing because this mode is not related to the film thickness [40]. Shen et al. incorporated inter-digitated electrodes (D33 mode) to enhance the sensitivity of the piezo electric sensors (PAS) [40]. However, they did not obtain substantial improvement on sensitivity using 250 μm electrode spacing as the reported sensitivity was 0.126 mV/Pa which is far behind than what Wang et al. achieved using D31 mode [39]. The main drawback of the Shen et al.'s PAS is the material selection.

The zirconate titanate (PZT) is good for energy scavenging due to its high piezoelectric constant when compared to other piezoelectric materials [41]. However, the incorporation of zirconate titanate (PZT) requires a special attention during the fabrication, i.e., for the poling process [42]. This is an additional drawback of zirconate titanate (PZT) because it shows the de-poling effect at higher electrode spacing starting from 16 μm which is 4 μm less than the nominal spacing of AlN, i.e., 20 μm [38,43,44].

As a result, the electric field as well as the sensing signal is lower at higher electrode spacing [43]. When compared to the PZT and D33, the combination AlN and D33 can be the better option for acoustic sensors. This combination does not show the de-poling effect since it depends on the lattice orientation [42]. Table 2 categorizes the previous studies by thickness, material, typology, sensitivity, SNR, noise floor and sensitivity peak. Others cases studies are plotted in Table 2 such as [44–47] for piezoelectric acoustic sensors in D31 mode. [48,49] refer to piezoelectric acoustic sensors in D33 mode and are plotted in Table 2.

**Table 2.** References on D31 and D33 piezo acoustic sensors and the relative achieved values. NR: Not reported.

| Reference | PAS Thickness [μm] | PAS Material | Sensitivity mV/Pa at 1 kHz | SNR dB at 1 kHz | Noise Floor | Sensitivity Peak kHz |
|---|---|---|---|---|---|---|
| **D31 mode** | | | | | | |
| [36] | 3 | AlN (Aluminium nitride) | 1.82 | 57 | 37 in dB(A) (A-weighted decibels expresses the relative loudness of sounds in air as perceived by the human ear) | NR |
| [40] | 127 | PZT (lead zirconate-titanate) | 0.12 | NR | NR | 13.71 |
| [44] | 3.5 | ZnO (Zinc oxide) | 0.92 | 37 | 57 Hz (resonance frequency) | 18 |
| [45] | 2.14 | AlN (Aluminium nitride) | 0.039 | 54 | 40 in dB SPL | 20 |
| [46] | 0.267 | PZT (lead zirconate-titanate) | 0.00166 | 58.3 | 35.7 in dB SPL (Sound pressure level measured in decibel) | 59 |
| [47] | 0.2 | AlN (Aluminium nitride) | 0.68 | NR | NR | 11.2 |
| **D33 mode** | | | | | | |
| [48] | 26 | PP (polypropylene) | 2 | 57 | 37 in dB SPL | NR |
| [49] | 0.5 | AlN (Aluminium nitride) | 4.49 | 67 | 27.3 in dB SPL | 10.18 |

### *3.2. Piezoelectric Acoustic Sensors (PAS) Yarns*

The studies on piezoelectric yarns aim at overcoming their inability to control changing properties over a wide range of frequencies [50]. This has led to the breach of new applications fields, such as energy harvesting [51] and conformal acoustics [52].

The development of fabrication methods that facilitate multi-functional and multi-material yarns enable several attractive properties for new applications. The preform-based thermal drawing process offers a scalable means of producing kilometre-long fibre devices with sub millimetric cross-sectional dimensions [53]. These long and flexible fibres can easily be assembled into fabrics [54]. Furthermore, the integration of electrodes into the fibre enables the straightforward electrical connection of the device to an external electrical circuit [55].

The latest advancements in this field have led to the development of piezoelectric fibres (based on polyvinylidene fluoride (PVDF) and its copolymer, polyvinylidene fluoride-trifluoroethylene, (PVDF-TrFE)), which are capable of emitting and detecting sound waves over a broad range of frequencies [50]. While the small cross-sectional area of these fibres enables both miniaturization and flexibility, it seemingly involves an equally small active area that potentially limits the fibre performance [52]. The research of Yan et al. overcame the traditional use of acoustic fabrics by introducing a fabric that operates as a sensitive audible microphone while retaining the traditional qualities of fabrics, such as machine washability and draping [30].

Key to the fibre sensitivity is an elastomeric cladding that concentrates the mechanical stress in a piezocomposite layer with a high piezoelectric charge coefficient, of approximately 46 picocoulombs per newton, due to the thermal drawing process [56]. With the fibre subsuming less than 0.1% of the fabric by volume, a single fibre draw enables tens of square metres of fabric microphone. The measured sensitivity of the fibre-on-membrane is 19.6 mV (at 94 dB and 1 kHz, making it comparable to that of off-the-shelf condenser and dynamic microphones [30].

## 4. Sound Sensors Typologies in Monitoring System

The advancements in low-power computing, microphone technology and networking have allowed to move from very expensive static acoustic sensors to low-cost easy-to-use ones. Dedicated stations have been upgraded with real-time data transmission capabilities, but the most important advancements have been achieved in elaborating more flexible sensor node that can perform advanced digital signal processing.

Mydlarz et al. identified three general categories by relating sensor functionality and cost [16]. For the purposes of this article, we considered their sound performance related to the dimensions. When the transfer factor is not specified, the following formula is used to calculate it from sensitivity values in dB re. V/Pa (decibel relative to 1 volt per 1 pascal:

$$\text{transfer factor } = 10^{\left(\frac{\text{sensitivity}}{20}\right)\times 1000} \tag{2}$$

If only the transfer factor is presented, the sensitivity is calculated with the following equation:

$$\text{sensitivity} = 20 \times \log_{10}\left(\frac{\text{transfer factor}}{1000}\right) \tag{3}$$

Table 3 categorizes the case studies according with the typology, application field (Indoor or outdoor), sensitivity, transfer factor, signal-to-noise ratio and thickness. It shows that for sound-monitoring system in free field several typologies of microphone have been tested: from Microelectromechanical system (MEMS) to condenser microphones. In these cases, the sensitivity range from −38to −42.04 dB re. 1 V/Pa with a thickness between 1700 to 17,600 µm. Since the monitoring of noise pollution is more topical in socio-political debate about the comfort of our cities, there are more explorations on open air applications.

**Table 3.** Comparison of sound sensors typologies, thickness, and relative acoustic performances in monitoring systems.

| Reference Source | Sound Sensors Typology | Application | Sensitivity at 1 kHz, dB re. 1 V/Pa | Transfer Factor mV/Pa at 1 kHz | SNR | Thickness [µm] |
|---|---|---|---|---|---|---|
| [16] | MEMS | Outdoor | −38 | 12.59 | 63 dBA | 11,000 |
| [17] | Monacor MCE-400 | Outdoor | −42.04 | 7.9 | 58 dB | 6700 |
| [18] | Tmote-Invent | Outdoor | −35 | 17.78 | NR | 86,000 |
| [19] | Condenser microphone $\frac{1}{2}$" C-130 Cesva | Outdoor | −35.14 | 17.5 | NR | 17,600 |
| [20] | ADMP401 MEMS | Outdoor | −42 | 7.94 | 62 dBA | 10,000 |
| [21] | Knowles SPU0410LR5H-QB analog MEMS | Indoor | −41 | 8.91 | 94 dBA | 1700 |

Devices which embed all the hardware has adopted with a sensitivity higher than the previous examples at −41 V/Pa at 1 kHz [13]. The high performance represents an opportunity for furthermore applications, but the high volume represents a limitation respect with the necessity to save the net area of use of interiors from services spaces, such as false ceiling and false walls.

## 5. Comparison of Textile-Based Sound Sensors and Other Microphones

The sound sensors in current monitoring systems range between 1700 and 86,000 µm. The sensitivity coefficients cover a broad range between 7.9 to 17.78 mV/Pa re. at 1 kHz. It can be observed that the typologies of microphone in this case are mainly for environmental measurements except for [13]. In this latter, the low thickness is combined with middle low sensitivity respect to the other (Figure 3). These studies are identified in Figure 3 in gradient of green.

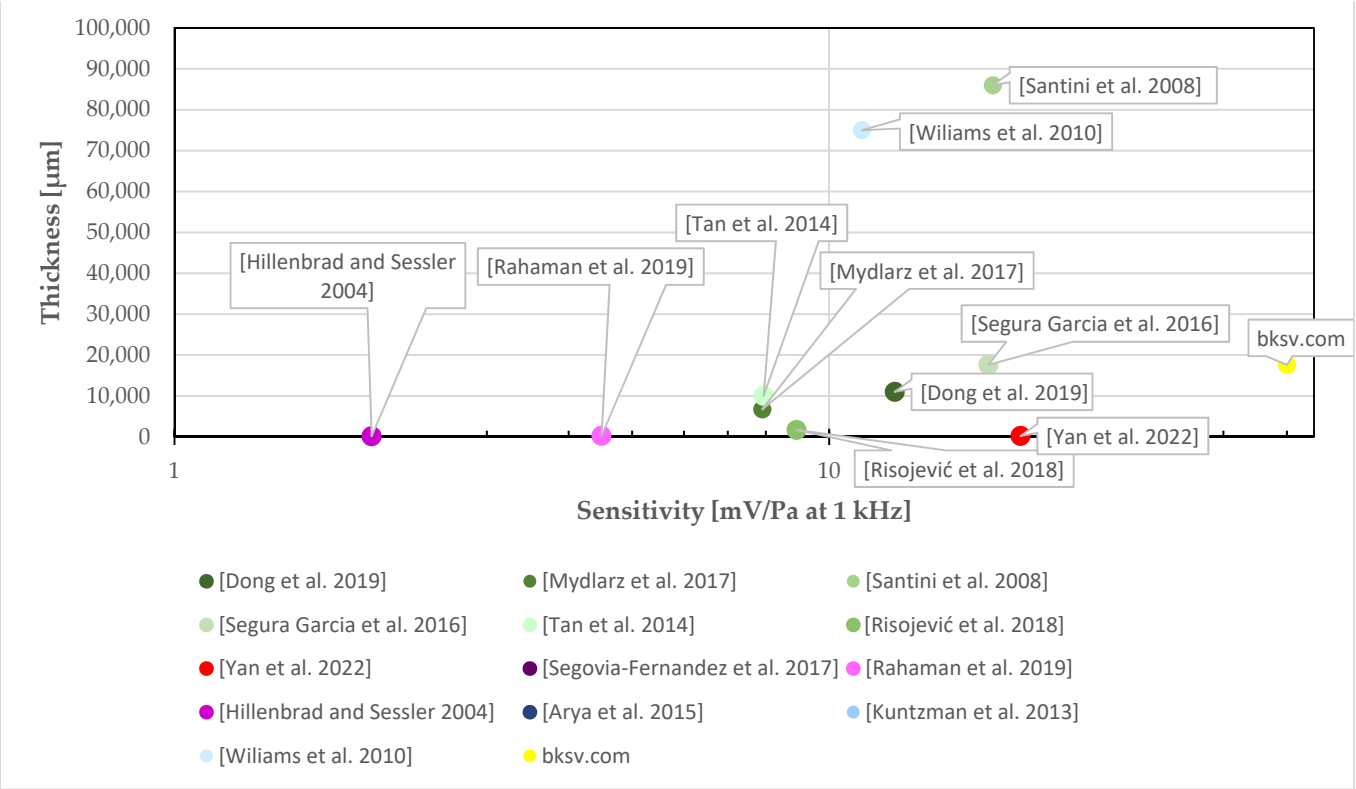


**Figure 3.** Relationship between the thickness and sensitivity of the literature. The sensors of current monitoring systems are in the gradient of green ([Dong et al. 2019] [15], [Mydlarz et al. 2017] [16], [Santini et al. 2008] [18], [Segura Garcia et al. 2016] [19], [Tan et al. 2014] [20], [Risojević et al. 2018] [21]). The PAS yarn is red ([Yan et al. 2022] [30]). The PAS film in D33 mode is the gradient of violet ([Segovia-Fernandez et al. 2017] [47], [Hillenbrad and Sessler 2004] [48], [Rahaman et al. 2019] [49]. The MEMs are in gradient of blue [57], [Arya et al. 2015] [58], [Kuntzman et al. 2013] [59], [Wiliams et al. 2010] [60]) and reference microphone is yellow ([bksv.com] [61]).

Apart from the reference microphones, which have the higher value of sensitivity (in yellow in Figure 3) [61], the studied microphones or sound sensors do not exceed the 19.6 mV/Pa in Yan et al. [30]. This value is achieved by a piezo electric acoustic sensors yarn [30] (identified with red color in the Figure 3). The PAS films remain in a low thickness range since the higher value does not exceed the 240 µm with a sensitivity of 4.49 mV/Pa [39]. They are represented in gradient of violet in the Figure 3.

The MEMS cover a broad range of sensitivity from 0.61 [57] to 11.22 mV/Pa [59] at 1 kHz. Their thickness is proportional to their sensitivity. It has to be considered that the thickness measure does not take in consideration the dimensions of all the other hardware that monitoring systems require. Amplifier, pre-amplifier, add more volume and consequently weight and mass and are an issue in mounting phase when service spaces, such as false ceiling or false wall, are tight. The TSS balanced the acoustic performance with the possibility to be adapted in aforementioned spaces.

## 6. Conclusions

The article aims to compare the sound performance of sound sensors applied in sound-monitoring systems with textile-based sound sensors. The necessity to provide a continuously informed systems to monitor the sound conditions in a space has led to assessing several typologies of microphones aiming to reduce the dimensions and increase the performance. These are requirements that can be fulfilled by the TSSs in both the film and yarn configurations. Table 4 presents how the sensitivity of textile-based sensors is comparable with MEMS, and in some cases, they even have higher performance. This is

more so apparent, when considering the volume of all the hardware that MEMs require to complete a monitoring system. Figure 4 demonstrates that they would increase it considerably.

**Table 4.** Comparison of parameters between Pas D31, Pas D33, Acoustics MEMs and microphones.

| References Source | Sensitivity mV/Pa at 1 kHz | SNR dBA at 1 kHz | Noise Floor | Thickness µm |
|---|---|---|---|---|
| Sound sensors in current monitoring system | | | | |
| [15] | 12.59 | 63 | NR | 11,000 |
| [16] | 7.9 | 58 | NR | 6700 |
| [18] | 17.78 | NR | NR | 860,000 |
| [19] | 17.5 | NR | NR | 17,600 |
| [20] | 7.94 | 62 | NR | 10,000 |
| [21] | 8.912 | −41 | NR | 1700 |
| PAS (Piezo acoustic sensors) yarn | | | | |
| [30] | 19.6 | 30 | NR | 200 |
| PAS (Piezo acoustic sensors) film D33 mode | | | | |
| [48] | 2 | 57 | 37 in dB SPL | 26 |
| [49] | 4.49 | 67 | 27.3 in dB SPL | 0.5 |
| MEMS | | | | |
| [57] | 1 | NR | 16 in (kHz) | 2.0 |
| [58] | 0.0966–0.1266 | NR | 85 in (kHz) | 15 |
| [59] | 0.61 | NR | 13 in (kHz) | 29 |
| [60] | 11.22 | NR | 176 in (kHz) | 150,000 |
| [48] | 2 | 57 | 37 | 125 |
| Conventional microphone | | | | |
| [61] | 50 | NR | 15 dBA | 17,600 |

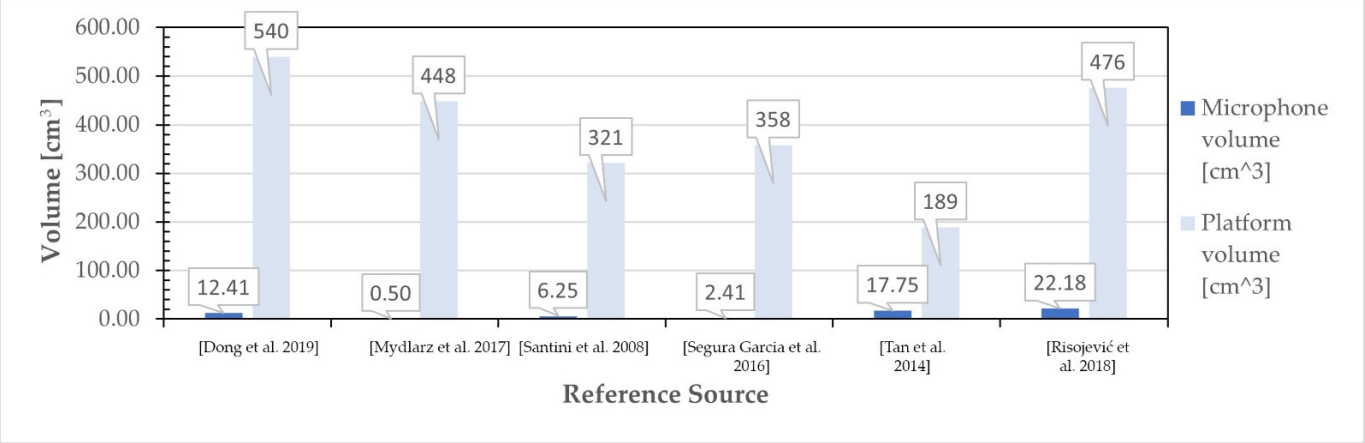


**Figure 4.** The relations between the volume of the MEMS microphones themselves and with the hardware of the monitoring system. ([Dong et al. 2019] [15], [Mydlarz et al. 2017] [16], [Santini et al. 2008], [18], [Segura Garcia et al. 2016] [19], [Tan et al. 2014] [21], [Risojević et al. 2018] [22]).

The low thickness of TSSs can facilitate use in tight service spaces, such as false ceilings and false walls, in order to reduce the aesthetic impact on the space design. Therefore, one of main requests for these systems is either the reduction of their shapes or a high degree of adaptability. Moreover, due to the aesthetic characteristics of the textile itself, in future works it could be interesting to demonstrate how they can be used to combine aesthetic features with sound-monitoring ones.

This feature can enable sound smartness in fabrics with active absorption behaviours to improve sound conditions in real time, thereby, opening new scenarios for the development of acoustic textiles.

**Author Contributions:** Conceptualization, investigation, writing—original draft preparation, A.G.; writing—review and editing, K.N.; supervision, M.H., G.M.C., I.P. All authors have read and agreed to the published version of the manuscript.

**Funding:** This research received no external funding.

**Data Availability Statement:** The data presented in this study are available in the article.

**Conflicts of Interest:** The authors declare no conflict of interest.

## References

1. Astolfi, A.; Puglisi, G.E.; Murgia, S.; Minelli, G.; Pellerey, F.; Prato, A.; Sacco, T. Influence of Classroom Acoustics on Noise Disturbance and Well-Being for First Graders. *Front. Psychol.* **2019**, *10*, 2736. [CrossRef] [PubMed]
2. Mikulski, W. Acoustic Conditions in Open Plan Offices. *Med. Pract.* **2018**, *69*, 153–166.
3. Poncetti, N.F.; Soares, P.F. An analytical model for calculating the minimum space between restaurant tables in order to attenuate the Lombard effect. *Appl. Acoust.* **2022**, *194*, 108771. [CrossRef]
4. Marsico, G.; Brambilla, G.; Curcuruto, S.; Clapiz, M.; Betti, R.; Riccardi, M. Acoustic Climate inside a Canteen and Mitigation Solutions. *J. Acoust. Soc. Am.* **2008**, *123*, 3354. [CrossRef]
5. de Paiva Vianna, K.M.; Alves Cardoso, M.R.; Rodrigues, R.M.C. Noise Pollution and Annoyance: An Urban Soundscapes Study. *Noise Health* **2015**, *17*, 125–133. [CrossRef]
6. Westman, J.C.; Walters, J.R. Noise and Stress: A Comprehensive Approach. *Environ. Health Perspect.* **1981**, *41*, 291–309. [CrossRef]
7. Seddigh, A.; Berntson, E.; Jönsson, F.; Danielson, C.B.; Westerlund, H. The Effect of Noise Absorption Variation in Open-Plan Offices: A Field Study with a Cross-over Design. *J. Environ. Psychol.* **2015**, *44*, 34–44. [CrossRef]
8. Griefahn, B.; Spreng, M. Disturbed Sleep Patterns and Limitation of Noise. *Noise Health* **2004**, *6*, 27.
9. Noise Interference with Oral Communication | SpringerLink. Available online: https://link.springer.com/article/10.1007/BF03053765 (accessed on 28 April 2022).
10. Hahad, O.; Kröller-Schön, S.; Daiber, A.; Münzel, T. The Cardiovascular Effects of Noise. *Dtsch. Arztebl. Int.* **2019**, *116*, 245–250. [CrossRef]
11. *UNI EN ISO 16283-1:2018*; Building Acoustics—Estimation of Acoustic Performance of Buildings from the Performance of lements—Part 1: Airborne Sound Insulation between Rooms. International Standard Organization: Geneva, Switzerland, 2018.
12. *ISO 3382-1:2009*; Acoustics—Measurement of Room Acoustic Parameters—Part 1: Performance Spaces. International Standard Organization: Geneva, Switzerland, 2009.
13. *ISO 3382-2:2008*; Acoustics—Measurement of Room Acoustic Parameters—Part 2: Reverberation Time in Ordinary Rooms. International Standard Organization: Geneva, Switzerland, 2008.
14. *ISO 3382-3:2012*; Acoustics—Measurement of Room Acoustic Parameters—Part 3: Open Plan Offices. International Standard Organization: Geneva, Switzerland, 2012.
15. Dong, B.; Prakash, V.; Feng, F.; O'Neill, Z. A Review of Smart Building Sensing System for Better Indoor Environment Control. *Energy Build.* **2019**, *199*, 29–46. [CrossRef]
16. Mydlarz, C.; Salamon, J.; Bello, J.P. The Implementation of Low-Cost Urban Acoustic Monitoring Devices. *Appl. Acoust.* **2017**, *117*, 207–218. [CrossRef]
17. Hakala, I.; Kivelä, I.; Ihalainen, J.; Luomala, J.; Gao, C. Design of Low-Cost Noise Measurement Sensor Network: Sensor Function Design. In Proceedings of the 2010 First International Conference on Sensor Device Technologies and Applications, Venice, Italy, 18–25 July 2010; pp. 172–179.
18. Santini, S.; Ostermaier, B.; Vitaletti, A. First Experiences Using Wireless Sensor Networks for Noise Pollution Monitoring. In Proceedings of the Workshop on Real-World Wireless Sensor Networks; Association for Computing Machinery: New York, NY, USA, 2008; pp. 61–65.
19. Segura Garcia, J.; Pérez Solano, J.J.; Cobos Serrano, M.; Navarro Camba, E.A.; Felici Castell, S.; Soriano Asensi, A.; Montes Suay, F. Spatial Statistical Analysis of Urban Noise Data from a WASN Gathered by an IoT System: Application to a Small City. *Appl. Sci.* **2016**, *6*, 380. [CrossRef]
20. Dourou, N.; Poli, A.; Terenzi, A.; Cecchi, S.; Spinsante, S. IoT-Enabled Analysis of Subjective Sound Quality Perception Based on Out-of-Lab Physiological Measurements. In *IoT Technologies for Health Care. HealthyIoT 2021*; Spinsante, S., Silva, B., Goleva, R., Eds.; Lecture Notes of the Institute for Computer Sciences, Social Informatics and Telecommunications Engineering, 2022; Springer: Cham, Switzerland, 2021; Volume 432, pp. 153–165. [CrossRef]
21. Tan, W.M.; Jarvis, S.A. On the Design of an Energy-Harvesting Noise-Sensing WSN Mote. *EURASIP J. Wirel. Commun. Netw.* **2014**, *2014*, 167. [CrossRef]

22. Risojević, V.; Rozman, R.; Pilipović, R.; Češnovar, R.; Bulić, P. Accurate Indoor Sound Level Measurement on a Low-Power and Low-Cost Wireless Sensor Node. *Sensors* **2018**, *18*, 2351. [CrossRef]
23. Jinno, H.; Fukuda, K.; Xu, X.; Park, S.; Suzuki, Y.; Koizumi, M.; Yokota, T.; Osaka, I.; Takimiya, K.; Someya, T. Stretchable and Waterproof Elastomer-Coated Organic Photovoltaics for Washable Electronic Textile Applications. *Nat. Energy* **2017**, *2*, 780–785. [CrossRef]
24. Zhang, Z.; Cui, L.; Shi, X.; Tian, X.; Wang, D.; Gu, C.; Chen, E.; Cheng, X.; Xu, Y.; Hu, Y.; et al. Textile Display for Electronic and Brain-Interfaced Communications. *Adv. Mater.* **2018**, *30*, 1800323. [CrossRef]
25. Takamatsu, S.; Lonjaret, T.; Ismailova, E.; Masuda, A.; Itoh, T.; Malliaras, G.G. Wearable Keyboard Using Conducting Polymer Electrodes on Textiles. *Adv. Mater.* **2016**, *28*, 4485–4488. [CrossRef]
26. Dong, K.; Wang, Y.-C.; Deng, J.; Dai, Y.; Zhang, S.L.; Zou, H.; Gu, B.; Sun, B.; Wang, Z.L. A Highly Stretchable and Washable All-Yarn-Based Self-Charging Knitting Power Textile Composed of Fiber Triboelectric Nanogenerators and Supercapacitors. *ACS Nano* **2017**, *11*, 9490–9499. [CrossRef]
27. Hsu, P.-C.; Song, A.Y.; Catrysse, P.B.; Liu, C.; Peng, Y.; Xie, J.; Fan, S.; Cui, Y. Radiative Human Body Cooling by Nanoporous Polyethylene Textile. *Science* **2016**, *353*, 1019–1023. [CrossRef]
28. Zhou, G.; Byun, J.-H.; Oh, Y.; Jung, B.-M.; Cha, H.-J.; Seong, D.-G.; Um, M.-K.; Hyun, S.; Chou, T.-W. Highly Sensitive Wearable Textile-Based Humidity Sensor Made of High-Strength, Single-Walled Carbon Nanotube/Poly (Vinyl Alcohol) Filaments. *ACS Appl. Mater. Interfaces* **2017**, *9*, 4788–4797. [CrossRef]
29. Edmison, J.; Jones, M.; Nakad, Z.; Martin, T. Using Piezoelectric Materials for Wearable Electronic Textiles. In Proceedings of the Sixth International Symposium on Wearable Computers, Seattle, WA, USA, 10 October 2002; pp. 41–48.
30. Yan, W.; Noel, G.; Loke, G.; Meiklejohn, E.; Khudiyev, T.; Marion, J.; Rui, G.; Lin, J.; Cherston, J.; Sahasrabudhe, A.; et al. Single Fibre Enables Acoustic Fabrics via Nanometre-Scale Vibrations. *Nature* **2022**, *603*, 616–623. [CrossRef] [PubMed]
31. Greinke, B. *Culture Lab. Advanced Placement Project "Twiddletone"*; Queens Mary. University of London: London, UK, 2011.
32. Nakad, Z.; Jones, M.; Martin, T.; Shenoy, R. Using Electronic Textiles to Implement an Acoustic Beamforming Array: A Case Study. *Pervasive Mob. Comput.* **2007**, *3*, 581–606. [CrossRef]
33. Gabrielson, T.B. Mechanical-Thermal Noise in Micromachined Acoustic and Vibration Sensors. *IEEE Trans. Electron Devices* **1993**, *40*, 903–909. [CrossRef]
34. Littrell, R.J. High Performance Piezoelectric MEMS Microphones. Ph.D. Thesis, University of Michigan, Ann Arbor, MI, USA, 2010.
35. Priya, S.; Song, H.-C.; Zhou, Y.; Varghese, R.; Chopra, A.; Kim, S.-G.; Kanno, I.; Wu, L.; Ha, D.S.; Ryu, J.; et al. A Review on Piezoelectric Energy Harvesting: Materials, Methods, and Circuits. *Energy Harvest. Syst.* **2019**, *4*, 3–39. [CrossRef]
36. Littrell, R.; Grosh, K. Noise Minimization in Micromachined Piezoelectric Microphones. *Proc. Mtgs. Acoust.* **2013**, *19*, 030041. [CrossRef]
37. Tuncay, A. Development of Piezoelectric PVDF Integrated Textile Yarn. Ph.D Thesis, The University of Manchester, Manchester, UK, 2014.
38. Baumgartel, L.; Vafanejad, A.; Chen, S.-J.; Kim, E.S. Resonance-Enhanced Piezoelectric Microphone Array for Broadband or Prefiltered Acoustic Sensing. *J. Microelectromech. Syst.* **2013**, *22*, 107–114. [CrossRef]
39. Wang, Z.; Wang, C.; Liu, L. Design and Analysis of a PZT-Based Micromachined Acoustic Sensor with Increased Sensitivity. *IEEE Trans. Ultrason. Ferroelectr. Freq. Control* **2005**, *52*, 1840–1850. [CrossRef]
40. Shen, Z.; Lu, J.; Tan, C.W.; Miao, J.; Wang, Z. D33 Mode Piezoelectric Diaphragm Based Acoustic Transducer with High Sensitivity. *Sens. Actuators A Phys.* **2013**, *189*, 93–99. [CrossRef]
41. Al Ahmad, M.; Plana, R. Piezoelectric Coefficients of Thin Film Aluminum Nitride Characterizations Using Capacitance Measurements. *IEEE Microw. Wirel. Compon. Lett.* **2009**, *19*, 140–142. [CrossRef]
42. Kim, D.; Hewa-Kasakarage, N.N.; Hall, N.A. A Theoretical and Experimental Comparison of 3-3 and 3-1 Mode Piezoelectric Microelectromechanical Systems (MEMS). *Sens. Actuators A Phys.* **2014**, *219*, 112–122. [CrossRef]
43. Kim, S.-B.; Park, J.-H.; Kim, S.-H.; Ahn, H.; Wikle, H.C.; Kim, D.-J. Modeling and Evaluation Ofd33mode Piezoelectric Energy Harvesters. *J. Micromech. Microeng.* **2012**, *22*, 105013. [CrossRef]
44. Ried, R.P.; Kim, E.S.; Hong, D.M.; Muller, R.S. Piezoelectric Microphone with On-Chip CMOS Circuits. *J. Microelectromech. Syst.* **1993**, *2*, 111–120. [CrossRef]
45. Williams, M.D.; Griffin, B.A.; Reagan, T.N.; Underbrink, J.R.; Sheplak, M. An AlN MEMS Piezoelectric Microphone for Aeroacoustic Applications. *J. Microelectromech. Syst.* **2012**, *21*, 270–283. [CrossRef]
46. Horowitz, S.; Nishida, T.; Cattafesta, L.; Sheplak, M. Development of a Micromachined Piezoelectric Microphone for Aeroacoustics Applications. *J. Acoust. Soc. Am.* **2007**, *122*, 3428–3436. [CrossRef] [PubMed]
47. Segovia-Fernandez, J.; Sonmezoglu, S.; Block, S.T.; Kusano, Y.; Tsai, J.M.; Amirtharajah, R.; Horsley, D.A. Monolithic Piezoelectric Aluminum Nitride MEMS-CMOS Microphone. In Proceedings of the 2017 19th International Conference on Solid-State Sensors, Actuators and Microsystems (TRANSDUCERS), Kaohsiung, Taiwan, 18–22 June 2017; pp. 414–417.
48. Hillenbrand, J.; Sessler, G.M. High-Sensitivity Piezoelectric Microphones Based on Stacked Cellular Polymer Films (L). *J. Acoust. Soc. Am.* **2004**, *116*, 3267–3270. [CrossRef]
49. Rahaman, A.; Park, C.H.; Kim, B. Design and Characterization of a MEMS Piezoelectric Acoustic Sensor with the Enhanced Signal-to-Noise Ratio. *Sens. Actuators A Phys.* **2020**, *311*, 112087. [CrossRef]

50. Egusa, S.; Wang, Z.; Chocat, N.; Ruff, Z.M.; Stolyarov, A.M.; Shemuly, D.; Sorin, F.; Rakich, P.T.; Joannopoulos, J.D.; Fink, Y. Multimaterial Piezoelectric Fibres. *Nat. Mater.* **2010**, *9*, 643–648. [CrossRef]
51. Zaarour, B.; Zhu, L.; Huang, C.; Jin, X.; Alghafari, H.; Fang, J.; Lin, T. A Review on Piezoelectric Fibers and Nanowires for Energy Harvesting. *J. Ind. Text.* **2021**, *51*, 297–340. [CrossRef]
52. Chocat, N.; Lestoquoy, G.; Wang, Z.; Rodgers, D.M.; Joannopoulos, J.D.; Fink, Y. Piezoelectric Fibers for Conformal Acoustics. *Adv. Mater.* **2012**, *24*, 5327–5332. [CrossRef]
53. Chen, J. Capacitive Micromachined Ultrasonic Transducer Arrays for Minimally Invasive Medical Ultrasound. *J. Micromech. Microeng.* **2010**, *20*, 023001. [CrossRef]
54. Abouraddy, A.F.; Shapira, O.; Bayindir, M.; Arnold, J.; Sorin, F.; Hinczewski, D.S.; Joannopoulos, J.D.; Fink, Y. Large-Scale Optical-Field Measurements with Geometric Fibre Constructs. *Nat. Mater.* **2006**, *5*, 532–536. [CrossRef] [PubMed]
55. Abouraddy, A.F.; Bayindir, M.; Benoit, G.; Hart, S.D.; Kuriki, K.; Orf, N.; Shapira, O.; Sorin, F.; Temelkuran, B.; Fink, Y. Towards Multimaterial Multifunctional Fibres That See, Hear, Sense and Communicate. *Nat. Mater.* **2007**, *6*, 336–347. [CrossRef] [PubMed]
56. Brown, L.F. Design Considerations for Piezoelectric Polymer Ultrasound Transducers. *IEEE Trans. Ultrason. Ferroelectr. Freq. Control* **2000**, *47*, 1377–1396. [CrossRef] [PubMed]
57. Kim, E.S.; Kim, J.R.; Muller, R.S. Improved IC-Compatible Piezoelectric Microphone and CMOS Process. In Proceedings of the TRANSDUCERS '91: 1991 International Conference on Solid-State Sensors and Actuators. Digest of Technical Papers, San Francisco, CA, USA, 24–27 June 1991; pp. 270–273.
58. Arya, D.S.; Prasad, M.; Tripathi, C.C. Design and Modeling of a ZnO-Based MEMS Acoustic Sensor for Aeroacoustic and Audio Applications. In Proceedings of the 2015 2nd International Symposium on Physics and Technology of Sensors (ISPTS), Pune, India, 7–10 March 2015; pp. 278–282.
59. Kuntzman, M.L.; Gloria Lee, J.; Hewa-Kasakarage, N.N.; Kim, D.; Hall, N.A. Micromachined Piezoelectric Microphones with In-Plane Directivity. *Appl. Phys. Lett.* **2013**, *102*, 054109. [CrossRef] [PubMed]
60. Williams, M.D.; Griffin, B.A.; Meloy, J.; Sheplak, M. A Microelectromechanical Systems-based Piezoelectric Microphone for Aeroacoustic Measurements. *J. Acoust. Soc. Am.* **2010**, *128*, 2444. [CrossRef]
61. Type 4190 $\frac{1}{2}$-Inch Free-Field Microphone | Brüel & Kjær. Available online: https://www.bksv.com/en/transducers/acoustic/microphones/microphone-cartridges/4190 (accessed on 28 April 2022).

*textiles*

MDPI

*Review*

# High-Performance and Functional Fiber Materials—A Review of Properties, Scanning Electron Microscopy SEM and Electron Dispersive Spectroscopy EDS

**Boris Mahltig * and Thomas Grethe**

Hochschule Niederrhein, Faculty of Textile and Clothing Technology, University of Applied Sciences Niederrhein, Webschulstraße 31, 41065 Mönchengladbach, Germany; thomas.grethe@hs-niederrhein.de

* Correspondence: boris.mahltig@hs-niederrhein.de; Tel.: +49-2161-186-6128

**Abstract:** This review supports an overview of selected high-performance fibers and functional fiber materials. A review of several properties and applications is given. For fiber materials and fabrics, microscopic images taken by scanning electron microscopy (SEM) are presented. As well as this, electron dispersive spectroscopy (EDS) is performed on the fiber materials and an overview of EDS spectra is presented. The features of SEM images and EDS spectra are discussed, especially with the aim of supporting people who are working in the field of fiber analytics. To support a complete view of both analytic methods—SEM and EDS—challenges and typical mistakes for SEM measurements on textiles are also described. Altogether, this review supports a useful overview of interesting high technology fiber materials and their investigation using the analytical methods SEM and EDS. Using these, material properties and their composition are presented and discussed. The composition of industrial fiber materials is investigated and discussed, as well as fiber treatments for the realization of functional fiber properties. Furthermore, it aims to support a helpful tool for fiber and textile analytics and identification.

**Keywords:** high-performance fibers; functional textiles; metallized textiles; inorganic fibers; Scanning Electron Microscopy (SEM); Electron Dispersive Spectroscopy (EDS)

**Citation:** Mahltig, B.; Grethe, T. High-Performance and Functional Fiber Materials—A Review of Properties, Scanning Electron Microscopy SEM and Electron Dispersive Spectroscopy EDS. *Textiles* **2022**, 2, 209–251. https://doi.org/10.3390/textiles2020012

Academic Editor: Laurent Dufossé

Received: 2 March 2022
Accepted: 12 April 2022
Published: 15 April 2022



## 1. Introduction

High-performance fibers and functional fiber materials are innovative high-tech materials [1,2]. A high-performance fiber is made from synthetic polymers or inorganic materials, and has at least one extraordinary property, going far beyond the properties of conventional fibers, such as polyester (PET), nylon, and cotton. These extraordinary properties are related to resistance to various chemicals, light exposure, high temperature, and fire. Furthermore, high-strength fiber materials are counted as part of the group of high-performance fibers [1–6].

Functional fiber materials—also called functional textile fabrics—can be realized by the use of high-performance fibers. Alternatively, functional fabrics can be also realized by wet chemical processes, e.g., finishing processes or sol-gel processes, applied to conventional textile materials [7–10]. A good example is a flame-retardant fabric, which can be realized either by using flame-retardant fibers (e.g., meta-aramid), or by the treatment of conventional cotton with flame-retardant finishing agents [11,12].

Compared to conventional fibers, the market share of high-performance fibers is quite small at less than 1% [13]. The main reason for this small amount is probably the high cost of high-performance fibers. Because of the high price, high-performance fibers are only used for applications where their extraordinary properties are demanded and the customer is willing to accept the costs. A good example in this area can be given with high-strength ropes for sport and sailing purposes, made from high-performance fibers. For example, a rope made from high-performance fibers (PBO and HPPE) is available with a price

range of around 20 to 50 EUR/meter. In comparison, ropes offered by the same supplier based on conventional materials such as polyester, polypropylene, or hemp are offered in a price range of around 0.2 to 3 EUR/meter [14]. However, because of these special applications, high-performance fibers are important and can generate special benefits. They could also lead to special profit for the supplier of the fiber. The same statement is, in a similar way, valid for functional textiles, where based on a certain function, a significantly higher price can be realized for the final product. A very prominent example can be given with antimicrobial functionalized clothes offered for persons with atopic dermatitis. For products in this category—even for a simple shirt—prices in the range of EUR 100 to EUR 200 can be realized [15].

With this background, the aim of this review is to give an overview of the main categories of high-performance fibers and functional fiber materials. Material properties and applications are summarized. However, each high-performance fibers also exhibit few disadvantageous properties—some of these are mentioned also. For this, this review can be a helpful tool for the decision of what type of high-performance fiber is useful for a certain application and what application should be avoided. Of course, it is nearly impossible to report on every fiber material and property, so a selection for this presentation has to be made. This selection is mainly done according to the availability on the market for these fibers and products containing them. Additional to the report on selected properties and applications, scanning electron microscopic (SEM) investigations and electron dispersive spectroscopy (EDS) measurements are supported for the fibers presented and for the functional textiles. Both SEM and EDS are well established methods in material science and analytics [16]. In addition, sensitive objects such as microorganisms can be investigated by those methods [17]. In this area, the development of field-emission scanning electron microscopy (FESEM) for investigation on biological surfaces should particularly be mentioned [18,19].

The working principle of an electron microscope is quite old and was initially realized by Ruska and Knoll in the year 1932 [20]. In an electron microscope, a focused electron beam is generated by a glow filament, of which the emitted electrons are accelerated towards the sample. When the electrons collide with the sample, the electrons are scattered back. The amount of these scattered electrons is measured by a detector. For each point on the sample, a measurement of the number of electrons scattered back from this point is recorded. Each of these points then corresponds to a pixel in the microscopic image; the brightness of each pixel codes for the number of detected electrons. An electron microscope image is therefore always a grayscale image. Since heavier chemical elements scatter electrons more efficiently than lighter ones, such elements result in larger detector signals and therefore brighter pixels. Consequently, electron microscopy differs from light microscopy; not only in its resolution, but also in its contrast behavior. This renders it a useful tool for textile analytics, since contrasts can be detected which would otherwise be invisible to the eye. However, the lack of electrical conductance of textile materials and their constitution of lighter chemical elements lead to difficulties investigating such samples in SEM, so replication techniques were used [21]. Due to the necessity of very low operating pressures in early devices, textile materials also needed special drying steps before observation [22]. Furthermore, the working principle of EDS is developed early on. Historically, the EDS measurement is based on electron beam microanalysis, which was introduced by Castaing and Guinier in 1949 [23,24]. A good review on the development of electron beam microanalysis is given by C. Colliex [25]. It was not until 1966 that both techniques SEM and EDS were combined with a predecessor of most modern SEM-EDS devices, which was commercialized in 1967 [26,27].

Often, environmental scanning electron microscopy (ESEM) is also used for the investigation of textile materials [28]. ESEM devices are equipped with a sample chamber containing only a low vacuum [29]. The remaining gas in the sample chamber can avoid the electrical charging of the textile samples. Moreover, the swelling behavior of hydrophilic cellulosic fibers in the presence of humidity can be investigated by ESEM [28–31].

In the current paper, both techniques—SEM and EDS—are used to investigate conventional and industrial fiber products with high-performance and functional properties. These investigated textile samples are industrial products prepared and offered for specific customer applications. The shown fiber-based products are gained from completely different areas, such as technical filter materials from high-performance fibers, inorganic fiber materials for heat resistance applications, carbon fibers used in the production of fiber-reinforced composited, or flame-retardant textiles for clothing applications. The detection of composition is discussed, as well as fiber treatment for the realization of functional fiber properties. With this, it is aimed to support a broad overview of successful industrial textile products and to provide a helpful tool for fiber and textile analytics and identification.

## 2. Analytical Methods and Challenges for SEM and EDS Measurements on Textiles

This review paper reports on functional fiber materials and gives a special view of these materials by using scanning electron microscopy (SEM) and electron dispersive spectroscopy (EDS) [16]. All presented measurement results are exclusively recorded for this review paper. The investigated samples are typical industrial fiber-based products, prepared and offered for specific customer applications. Among others, these are advanced filter materials from high-performance fibers, textiles for flame-retardant clothes, or metalized textile fabrics offered for the shielding of electrosmog. The used microscopes are a Tabletop TM3000 and a Tabletop TM4000, both from Hitachi High-Tech Corp., which are equipped with EDS units from Bruker. In the following, some typical measurement errors for SEM and EDS, if they are applied on textile and fiber samples, are presented. An overview of typical measurement errors is offered as a useful tool to improve measurement skills for students and scientists, starting with the application of this microscopic technique and its application on textile- and fiber-based samples. Of course, the shown measurement errors do not occur during every microscopic investigation, and they can be avoided by improving the measurement procedure, the sample preparation, or by using an advanced electron microscope.

Compared to former times, nowadays it is quite simple to work with a scanning electron microscope (SEM) and to record images. For example, the currently used Tabletop microscope can be successfully used by students only after a short introduction of around 30 min. Nevertheless, there are still challenges in optimizing SEM measurements—especially on textile and polymer samples [32]. These issues often lead to misleading pictures or limited magnification, which are significantly below the magnification theoretically possible for SEM measurements. It is a general issue of SEM measurements that the measured samples are exposed to an electron beam. This electron beam causes an energy impact and an electron contribution to the measured sample. If the image is recorded in high magnification, this impact of energy and electrons is concentrated on a smaller area of the sample surface. For this reason, measurements in higher magnification have a higher tendency to cause sample damages by energy impact, or to show charging effects. The occurrence of charging effects while measuring a textile fiber can be described by view on the SEM images shown in Figure 1. Here, a polyester filament fiber is measured. For this measurement, the polyester fiber is placed on a conductive sticker containing graphite. This conductive sticker is not charged by exposure to the electron beam, because of its electric conductivity. Different behavior is shown by the polyester fiber, which is not electrically conductive. In the case of higher magnification, the number of up-taken electrons is high, and for this, the fiber appears brighter in the SEM image. This brightness covers the sample topography, so topography details cannot be detected, because of charging effects. For the shown example, with low magnification of $\times 100$, charging effects have no influence on the quality of recorded SEM images (Figure 1). A different result is gained for the higher magnification of $\times 500$.

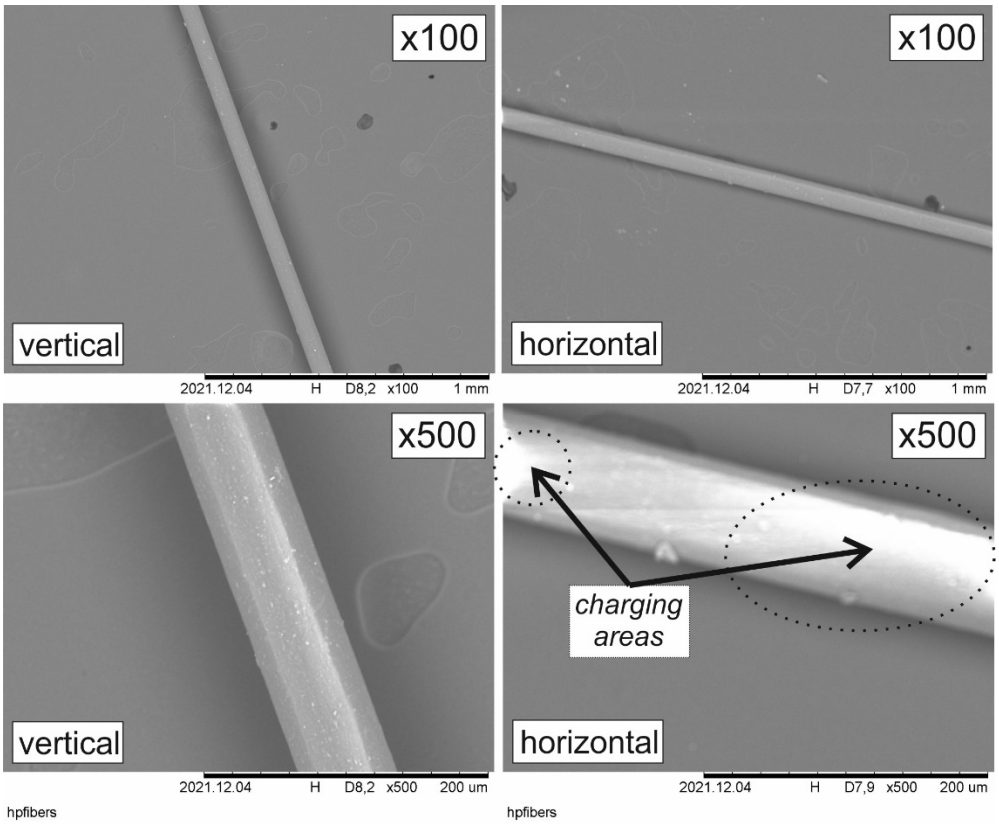


**Figure 1.** SEM images of a polyester filament fiber. The SEM images are recorded with two different magnifications ($\times$100 or $\times$500) and with two different fiber arrangements on the sample holder (horizontal or vertical).

However, it makes a significant difference if the fiber is placed vertically or horizontally on the sample holder (Figure 1). Especially for the horizontal arrangement, charged areas occur, influencing the quality of the recorded images. The reason for this is the horizontal direction of the moving electron beam during the sample scan. At the turning points of the beam at the left and right edges of the image area, the impact of electrons is high. In case the polyester fiber is placed vertically on the sample holder, the turn-point areas of the electron beam are not hitting the polyester fiber. Here, only the conductive sample holder is affected, so the influence on the image quality of the fiber is lower [32].

For this, the recommendation for SEM measurements on single fibers is to place the fiber vertically on the sample holder. This is quite a simple method to improve the quality of SEM images. However, unwished-for charging effects can also be avoided by other methods. First, this is the coating of the non-conductive samples by a thin conductive layer, e.g., from gold, copper, or graphite. However, using such coatings, the surface topography may also change. Furthermore, the detection of chemicals on textile surfaces by EDS measurements can be hindered by such coatings. Second, a special measurement method called "charge-up-reduction-mode" can be used for SEM recording [33]. In that case, only a moderate vacuum is present in the measurement chamber. By the ionization of remaining gas molecules in the measurement chamber, up-taken charges can be conducted away from the sample surface into the surrounding gas phase. In addition, by use of an environmental scanning electron microscope (ESEM), such charging effects can be avoided [28,30].

Other than the described charging effects, the energy impact of the applied electron beam can simply damage sensitive polymer materials (Figure 2). Figure 2 shows a typical vertical damaging feature caused by a former SEM measurement in higher magnification. Such vertical lines are typical damages occurring at the turn-point of the electron beam. In this area, the energy impact is higher compared to other sample areas, so the sensitive polymer substrate is damaged. By the use of advanced SEM techniques, such as ESEM or

FESEM, such damages to sensitive samples can be minimized [28,34,35]. Furthermore, with conventional SEM devices (like the Hitachi TM3000 or TM4000), such sample damages occur only in the case of sensitive organic samples. Figure 2, is given as an example of one possible measurement error which can eventually occur, but of course, does not occur during every measurement with the used SEM device.

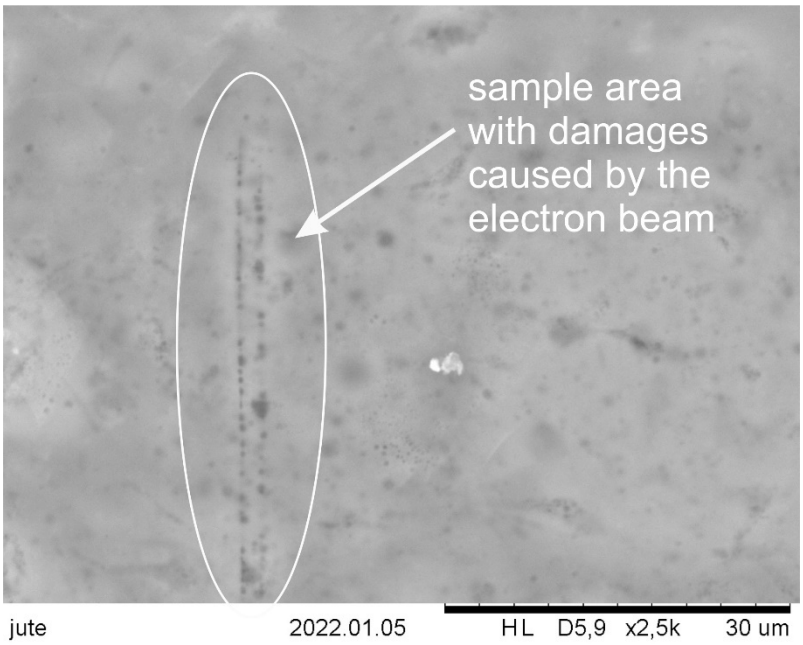


**Figure 2.** SEM image of a polybag with jute fibers; shown as an example for damaging the sample surface using the electron beam during SEM measurements.

Additional to the simple damaging of the sample surface by exposure to the electron beam, other more sophisticated influences on the sample surface are also possible. A special feature is, e.g., the movement of particles on the sample surface during the measurement, as shown in Figure 3. In this example, glass fiber fabric with deposited vermiculite particles is investigated. This glass fiber fabric is an industrial product supplied for high temperature application. The vermiculite particles are processed by the industrial supplier in between the fibers building up the fabric structure. However, few vermiculite particles are only deposited on the fabric surface and not fixed in between the fabric structure. During this measurement, one vermiculite particle on the fabric surface is charged and changes its position on the sample surface. Such features are usually not recorded for single SEM measurements with a short record time. Instead, they are more likely to occur during EDS measurements, which normally have a duration of several minutes. Of course, a sample treatment done before could eventually avoid such a position change, e.g., a sputtered gold layer on the sample could fix the loosely attached particles. In addition, by the use of the ESEM technique, such phenomena could be avoided. It should be clear that Figure 3 is given as an example of one possible measurement error which can potentially occur, but of course does not occur necessarily during every measurement with an SEM device.

For EDS measurements, there is a specific feature often leading to measurement mistakes. This is the shadowing; impressively shown in Figure 4. In this example, a fabric made from silver-coated yarn placed on the graphite-containing sample holder is presented. Here, the chemical elements—silver for the fiber and carbon for the sample holder—can be clearly detected by EDS mapping (Figure 4). However, there are also areas wherein no element is detected. These black areas can also be named shadow areas. From these areas, no x-radiation is reaching the EDS detector, so no element can be determined from them. The reason for this feature is the non-symmetric arrangement of the EDS detector in the measurement chamber of this microscope. With this, the silver fibers in front are covering a certain area of the sample holder behind. As a result, a shadow image of the

knitted fabric can be found on the sample holder. This non-symmetric arrangement is of course a feature related to the set-up of the sample chamber of the used SEM/EDS devices TM3000 and TM4000 from Hitachi. However, also for other scanning electron microscopes containing an EDS unit, effects related to the non-symmetric arrangement of detectors can be expected, because several detectors for primary electrons, secondary electrons, and the emitted X-rays have to be placed in the sample chamber of the microscope. It should be remarked that there is quite a simple method to minimize the shown "shadowing". This is done by increasing the distance of the sample holder to the detectors.

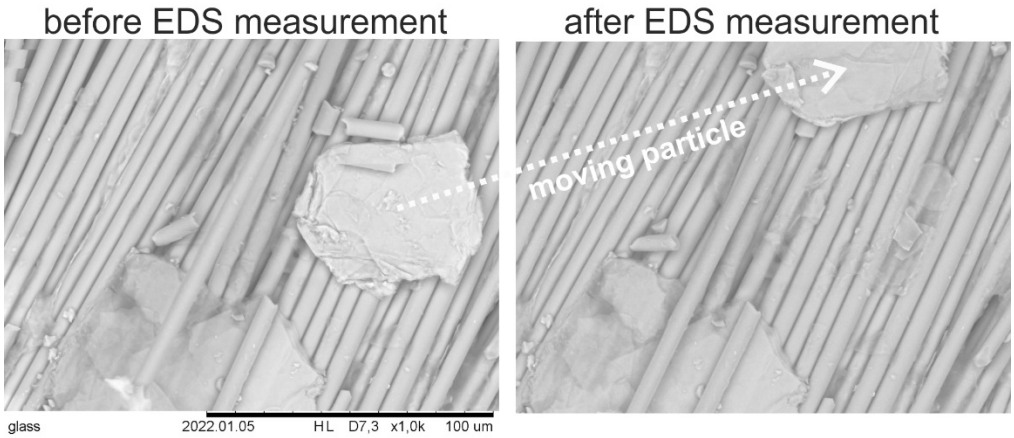


**Figure 3.** Two SEM images taken from a glass fiber fabric modified with vermiculite particles. The images are taken on the same sample position before and after an EDS measurement. Especially indicated is the movement of one vermiculite particle during this measurement.

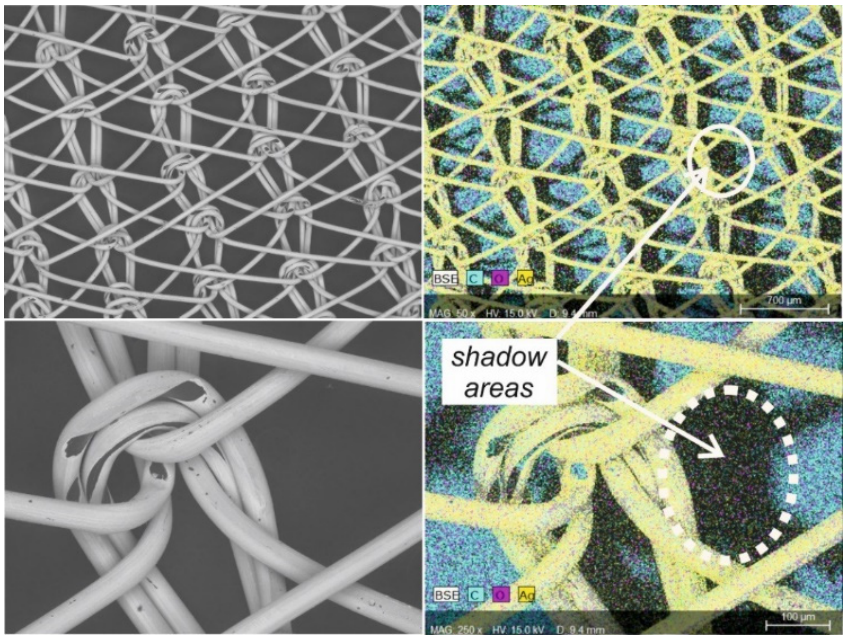


**Figure 4.** SEM images and related EDS images from a silver-coated yarn. Example for shadowing during EDS measurements.

## 3. High-strength Fibers

High-strength fibers exhibit extraordinary strength compared to conventional synthetic fibers and are, for this, used in applications, e.g., high-strength ropes, and cut-resistant textiles, for ballistic protection and for the realization of fiber-reinforced composite materials [36–44]. A selection of properties of four high-strength fibers is given in Table 1. Here, a comparison with the properties of the two conventional fibers nylon (polyamide 6.6) and

PET (polyester) is also supported. The shown parameter—tensile strength—is related to the mechanical strength of the fibers. Additionally, the density, the LOI value, and the maximum temperature of usage are mentioned to support a broader view of fiber advantages and disadvantages. The LOI value is a parameter describing the flame-retardant properties of a fiber material [45,46]. The abbreviation LOI stands for limited oxygen index. This value gives the minimum oxygen content in the atmosphere which is necessary to set a fiber material on fire. An increased LOI value corresponds to the increased fire stability of the fiber. Due to the oxygen content of 21% in standard air, fibers with LOI values of 21 or less can be easily set on fire. Fibers with LOI values > 21 are usually determined to have a certain flame resistance. Fibers with LOI > 28 are usually described as fire-resistant. In Table 1, for some fibers, two different LOI values or a range for the LOI value are given. Here, these numbers are taken from different references, reporting a variation of LOI values. As a further parameter, the maximum temperature of usage $T_{max}$ is given in Table 1. This parameter is not a clear material parameter of fiber materials. This $T_{max}$ should be better taken as a recommendation to the user of the fiber. At temperatures below $T_{max}$, the main fiber properties can be guaranteed for dedicated usage. $T_{max}$ is often related to a temperature causing fiber decomposition (pyrolysis) or the changing of mechanical properties due to reaching the temperature area around the glass temperature $T_G$ or the melting temperature $T_M$. Additional to these numbers in Table 1 selected related fiber properties are also summarized, which are often mentioned in relation to the fiber. Table 2 summarizes all investigated high-strength fibers and other later discussed fibers with their sum formula of the polymer repeating unit. Furthermore, the content of chemical elements of the related polymer is given to support a discussion of EDS measurements. Because the chemical element hydrogen cannot be detected by EDS, hydrogen is not mentioned in Table 2. In Table 2, the mentioned chemical compositions of the fibers are determined by calculation from the composition of the monomer units of the polymers building up the fibers. In fact, these are theoretically values on the basis that the fibers are built up by pure polymers. However, the fibers are industrial products often containing pure polymers, as well as additives, surface treatments, copolymers, and polymer end groups. All these further components can influence the chemical compositions of real fiber products.

As high-strength fibers, four types are selected for presentation—high-performance polyethylene HPPE, para-aramid, aromatic polyester, and polyphenylenebisoxazol (PBO). This selection is done based on the economic relevance and availability of these fibers. The chemical structures of the polymers building up these four fibers are presented in Figure 5, together with the sum formulas. By view on the chemical structure, the fundamental difference between HPPE compared to the other three high-strength fibers is clear. These three high-strength fibers are built up by aromatic ring systems which are conjugated over the entire polymer chain. By this, a stiff polymer chain is given—also named a rigid rod-like polymer [44]. This structure leads naturally to a parallel orientation of the polymer chains in the fiber, and by this to a high degree of crystallinity. Here, the chemical structure of the polymer building up the fiber is directly responsible for the high strength of the fiber. Additional to the aromatic stiff polymer chain, its linear parallel orientation is necessary for the high strength of those polymer fibers. In comparison, Nomex fibers built up from meta-aramid consist also of aromatic polymer chains, but due to the meta conformation, are not in a linear structure, so that no linear orientation is possible, and crystallinity is greatly decreased. As a consequence, Nomex fibers exhibit weaker mechanical properties.

**Table 1.** Comparison of properties of some high-strength fibers.

| Fiber | Tensile Strength [cN/tex] | Density [g/cm$^3$] | LOI [%] | Maximum Temperature of Usage $T_{max}$ [°C] | Selected Properties | References |
|---|---|---|---|---|---|---|
| Polyethylene HPPE, (Dyneema) | 280/330 | 0.95/0.97 | 18 | 90 | High strength, high elastic modulus | [47–49] |
| Para-Aramid, (Kevlar) | 232/235 | 1.44 | 28–30 | 190/200 | Extraordinary mechanical properties, stability against contact heat | [11,47,48,50–52] |
| Aromatic polyester, (Vectran) | 200–250 | 1.4 | 28/30 | 195 | High strength and modulus, thermoplastic | [1,53–55] |
| Phenylene Benzobisoxazol, PBO (Zylon) | 327/370 | 1.56 | 56–68 | 310/350 | Extraordinary mechanical properties, stability against contact heat | [11,47,48,51,52] |
| Polyamide, Nylon | 40–60 | 1.13–1.16 | 24 | 110/115 | Mechanically stable, stable against abrasion | [47,48,56–59] |
| Polyester, PET | 35–56 | 1.38–1.41 | 21–22 | 150 | Low cost | [47,56–59] |

**Table 2.** Summary of chemical composition of currently investigated high-performance fiber. Listed is the sum formula of the polymer repeating unit and the content containing chemical elements in at-% without the chemical element hydrogen, because hydrogen cannot be detected by EDS method.

| Fiber | Sum Formula of Repeating Unit | Content of Chemical Elements [at-%] | | | | |
|---|---|---|---|---|---|---|
| | | Carbon | Nitrogen | Oxygen | Fluorine | Sulfur |
| Polyethylene HPPE (Dyneema) | $(C_2H_4)_x$ | 100 | — | — | — | — |
| Para-Aramid (Kevlar) | $(C_{14}H_{10}N_2O_2)_x$ | 77.8 | 11.1 | 11.1 | — | — |
| Meta-Aramid (Nomex) | $(C_{14}H_{10}N_2O_2)_x$ | 77.8 | 11.1 | 11.1 | — | — |
| Aromatic polyester (Vectran) | $(C_{18}H_{10}O_4)_x$ | 81.8 | — | 18.2 | — | — |
| Phenylene Benzobisoxazol, PBO (Zylon) | $(C_{14}H_6N_2O_2)_x$ | 77.8 | 11.1 | 11.1 | — | — |
| Polyamide, PA6.6 (Nylon) | $(C_{12}H_{22}N_2O_2)_x$ | 75.0 | 12.5 | 12.5 | — | — |
| Polyester, PET | $(C_{10}H_8O_4)_x$ | 71.4 | — | 28.6 | — | — |
| Polytetrafluoroethylene PTFE (Teflon) | $(C_2F_4)_x$ | 33.3 | — | — | 66.7 | |
| PAN-homopolymer, polyacrylonitrile | $(C_3H_3N)_x$ | 75.0 | — | 25.0 | — | — |
| Polyphenylene sulfide, PPS | $(C_6H_4S)_x$ | 85.7 | — | — | — | 14.3 |
| Polyamideimide, PAI (Kermel) | $(C_{22}H_{14}N_2O_3)_x$ | 81.5 | 7.4 | 11.1 | — | — |
| Polyimide, PI (P84) | $(C_{30}H_{16}N_2O_5)_x$ | 81.1 | 5.4 | 13.5 | — | — |

In contrast to the fibers built up by aromatic polymers, the chemical structure of the monomer unit of HPPE is the same as for conventional PE, which is known to be a quite soft polymer material used, e.g., for the production of polybags. The high strength of HPPE fibers is the result of several parameters and influences. At first, there is a high molecular weight of HPPE with values of more than 1 million g/mol. For this, HPPE is often also called ultra-high molecular weight polyethylene UHMWPE. In comparison, conventional low-density polyethylene LDPE contains a molecular weight in the range of 30,000 to 50,000 g/mol. For conventional high-density polyethylene HDPE, a molecular weight of around 60,000 to 100,000 g/mol is given. For this, HPPE fibers are built up by PE containing 10 to 100 times higher molecular weight compared to other conventional PE types. From UHMWPE as a polymer material, the HPPE fibers are produced by using a special gel spinning process. In comparison to the spinning with molten polymers, the gel spinning process has the advantage that polymer loops can be solved easier during fiber formation [60,61]. By this, the parallel orientation of the polymer chains by drawing is promoted and a high degree of crystallinity can be reached. These parallel orientations and crystallinity are the result of the fiber production parameters and are not naturally given by the chemical structure of PE [60,61]. This issue is one main difference between fibers made from rigid rod-like polymers.

HPPE fibers are often also called Dyneema fibers, in relation to the brand name Dyneema belonging to the Dutch company DSM. This company supplies different types of

HPPE fibers with a variation in molecular weight and degree of crystallinity. Of course, there are also other companies supplying HPPE fibers under different brand names, such as, for example, Spectra Fiber (Honeywell), Exceed (ExxonMobil) or TYZ UHMWPE Fiber (Tongylzhong, China) [1,62–65]. For this, several different types of HPPE fibers are available on the market. Other than the high strength of the HPPE fibers, their second outstanding property is the low density with values < 1 g/cm$^3$. Such a low density is typical for polyolefins such as polyethylene PE or polypropylene PP. Compared to other fibers based on polyester or polyamide structures, HPPE fibers exhibit a good stability against acidic or alkaline chemicals [66]. The simple chemical structure of HPPE does not contain any functional group which can easily react and be cleaved under acidic or alkaline conditions. Furthermore, the stability against exposure to sunlight and weathering is significantly better compared to the aromatic high-strength fibers. The simple aliphatic chemical structure of HPPE fibers supports no absorption of UV-A and UV-B light, which is part of the sunlight. From this, a certain light stability results. Nevertheless, in view of Table 1, the disadvantageous properties of HPPE are clear. HPPE fibers are absolutely not fire-resistant, and quite temperature-sensitive, with a low $T_{max}$ < 100 °C.

In comparison, the other three presented high-strength fibers are fire-resistant and exhibit extraordinary temperature stability. In particular, the PBO fiber shows extraordinary properties, with a high LOI value around 60, and $T_{max}$ higher than 300 °C, even in the presence of air. For usage in an inert gas atmosphere for PBO fibers, even higher temperatures of usage are reported [11,67]. Nevertheless, their sensitivity to exposure to sunlight is advantageous. Due to their aromatic structure, these high-strength fibers exhibit a high absorbance for UV light. The absorbed UV light can start photochemical reactions, leading to the destruction of the fiber materials.

For EDS investigations of high-strength fibers, different samples from typical products are taken. PBO fibers (Zylon fibers) and HPPE fibers are taken from a high-strength rope offered for the sport market. This two-component rope (tradename: LIROS Runner PBO-XTR) is made up of a core of braided HPPE fibers and an outer layer made from braided PBO fibers. From the EDS spectrum of the PBO fibers, the three chemical elements carbon, oxygen, and nitrogen building up the fiber can be detected (Figure 6). The detected concentration of these elements is nearly in the ratio which can be expected from the chemical sum formula of the PBO polymer (Table 2). It should be remarked that the element hydrogen cannot be detected by EDS, and the sensitivity of the EDS method for the element nitrogen is quite low. For this, the nitrogen-related EDS signal is nearly negligible in comparison to the oxygen signal in the same EDS spectrum—even if both elements are present in PBO in the same content. In the literature for PBO fibers a significantly lower content of nitrogen compared to determined oxygen is also reported. However, due to the chemical composition of the PBO polymer, both chemical elements—oxygen and nitrogen—should occur in the same amount in PBO fibers [68].

The EDS spectrum of HPPE fibers taken from the core rope is also shown in Figure 6. Here, a clear signal related to carbon is recorded. Surprisingly, a signal for oxygen with a related surface concentration of 6.9 at-% is also detected. Oxygen is not a part of the chemical structure of HPPE, and the samples are not further treated before the EDS measurements are done. For this, the appearance of oxygen is probably caused by fiber treatment or finishing done on this industrial product. Furthermore, this is after plasma treatment oxygen can be detected on the surface of HPPE fibers [69]. The grey coloration of the investigated HPPE rope can be a hint for such a fiber treatment, because naturally polyethylene materials are uncolored. Often, ropes from HPPE fibers exhibit a grey coloration. This coloration is also supported for marketing reasons. The grey coloration should remind the customer of conventionally used steel ropes and the related slogan "Dyneema fiber is stronger than steel" [70].

The EDS spectra from para-aramid fabric (Kevlar) and an aromatic polyester (Vectran line) are presented in Figure 7 The aromatic polyester is gained from a line made from Vectran fibers. Vectra is a co-polyester formed from the monomers 2.6-hydroxynaphthoic

acid and para-hydroxybenzoic acid [71]. The chemical elements that are present in the structures of the related polymers can also be detected by EDS (compare Figures 5 and 7, Table 2). The EDS spectrum of the Vectran material shows only signals according to carbon and oxygen in a ratio that is expected from the chemical structure of the polymer. The EDS spectrum of the Kevlar fabric additionally exhibits the weak signal related to nitrogen. Even if this nitrogen signal is quite small, due to the low sensitivity of the EDS method for this element, it stands nearly for the same amount of detected nitrogen compared to the detected amount of oxygen. This measurement is in good accordance with the chemical structure of the para-aramid, which exhibits the elements oxygen and nitrogen in a ratio of 1:1 (Figure 5). The determined amounts of nitrogen and oxygen are a little higher compared to their theoretical content calculated from the chemical structure of the polymer p-aramid (compare Table 2). A report from earlier measurement shows that the contents of nitrogen and oxygen are below the theoretical values [72]. Such low values are probably related to measurement or data evaluation mistakes. In contrast, the actual reported higher values can be explained by the occurrence of polymer end groups containing higher contents of nitrogen and oxygen.

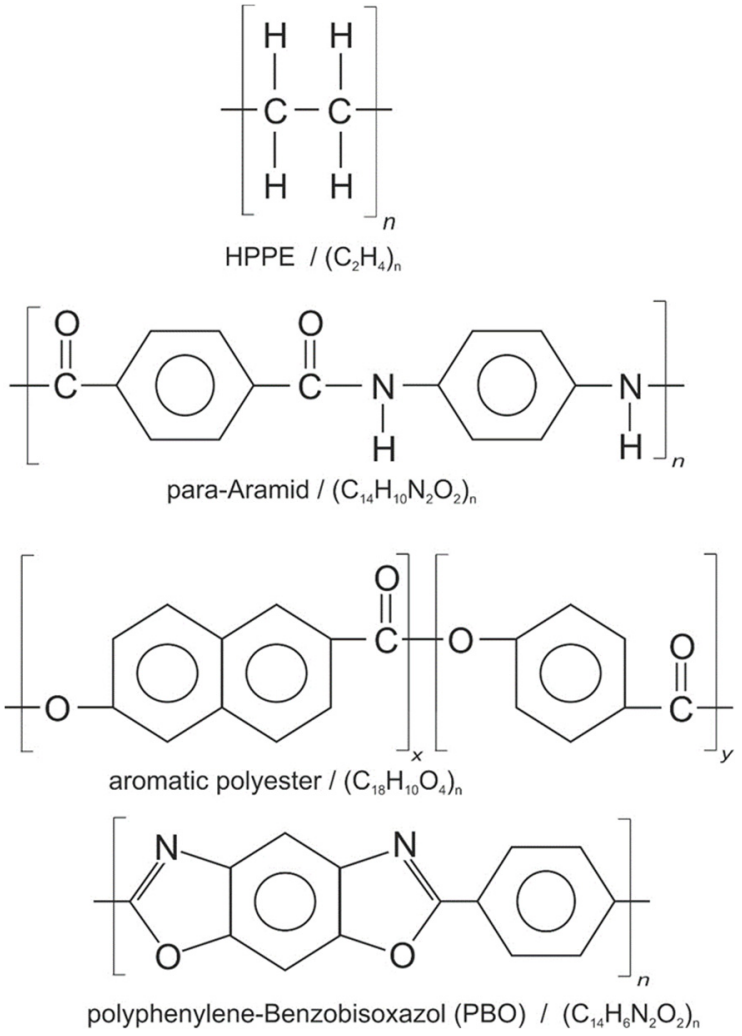


**Figure 5.** Chemical structures and sum formulas of high-performance fibers with high mechanical strength.

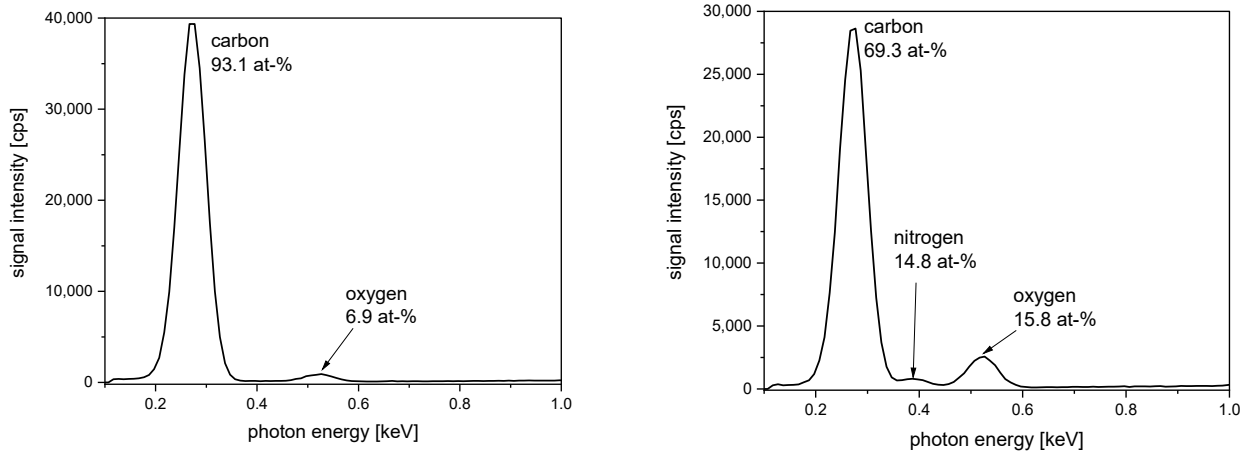


(**a**) (**b**)

**Figure 6.** EDS spectra taken from a high-strength rope—(**a**) HPPE fiber material (Dyneema) taken from the core of the rope; (**b**) PBO fiber material taken from the outer layer of the rope.

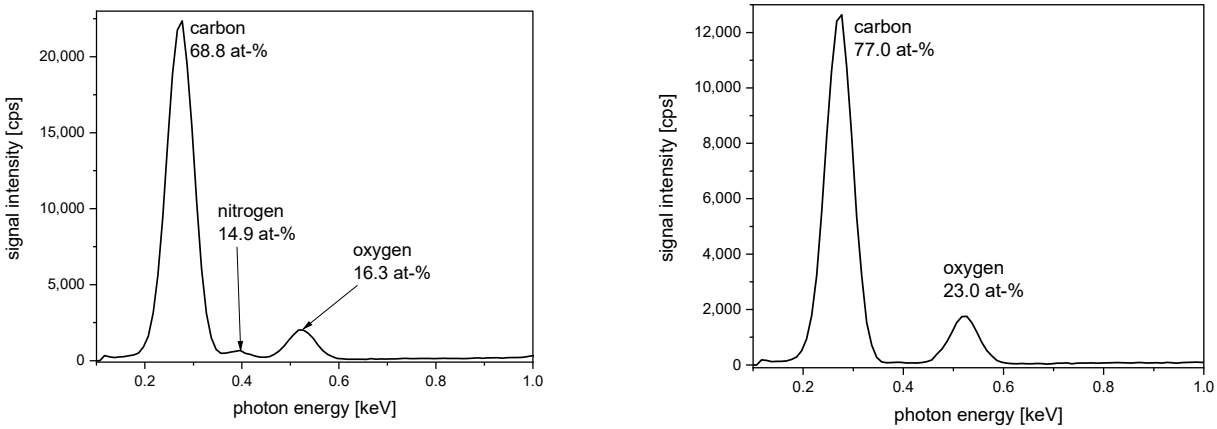


(**a**) (**b**)

**Figure 7.** EDS spectra taken from aromatic high-strength fibers—(**a**) aromatic polyamide (para-aramid)—Kevlar; (**b**) aromatic polyester—Vectran fiber.

## 4. Water- and Oil-Repellent Textiles

Water-repellent textiles are related to the presence of hydrophobic groups, either in the polymer structure or in the chemical structure of an applied finishing agent. In fact, there are different methods to realize a water-repellent textile as the treatment with polysiloxanes, paraffin waxes, or dendrimers [73–75]. In comparison, the realization of an oil-repellent textile material is only possible with components containing so-called fluorocarbon chemicals [73]. Due to environmental and health concerns, the use of fluoropolymers for soil-repellent textile finishing is legally restricted, and alternative materials are the focus of current research. One approach is to replace long-chain fluoropolymers with short-chain alternatives [76]. However, the potential bioaccumulation of such materials may also not be satisfactory. A second approach is to use completely fluorine-free textiles of which the surfaces are structured on a smaller length-scale [77]. However, it should be remarked that this second approach is reported in the scientific literature but did not find its way to industrial products until now. From a structural point of view, the simplest fluorocarbon fiber material is polytetrafluoroethylene PTFE, which is also supplied under the brand name Teflon. The chemical structure of PTFE is as simple as the structure of HPPE (compare Figures 5 and 8).

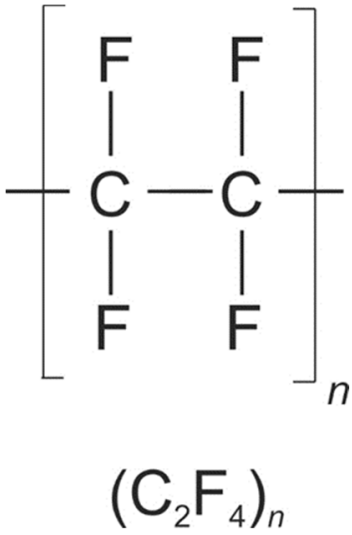


**Figure 8.** Chemical structure and sum formula of polytetrafluoroethylene (PTFE).

PTFE is built up only by the two chemical elements carbon and fluorine, which can both be detected in the related EDS spectrum (Figure 9). The amount of carbon and fluorine is determined as expected from the chemical sum formula of PTFE (compare Table 2 and Figure 8). The presented EDS spectrum is taken from a PTFE-based non-woven filter material. The related SEM image is also presented in Figure 9. Such filter materials are offered for the filtration of hot gases containing reactive chemicals. The determined amount of the determined elements is in the ratio which is expected from the sum formula of PTFE. The significantly better sensitivity of the EDS method for fluorine compared to carbon is especially remarkable. Cotton fabrics finished with fluoro-carbon containing dendrimer compounds are also investigated by using EDS. In addition, for these finished materials, it is possible to detect the fluorine component on the fabric surface [78].

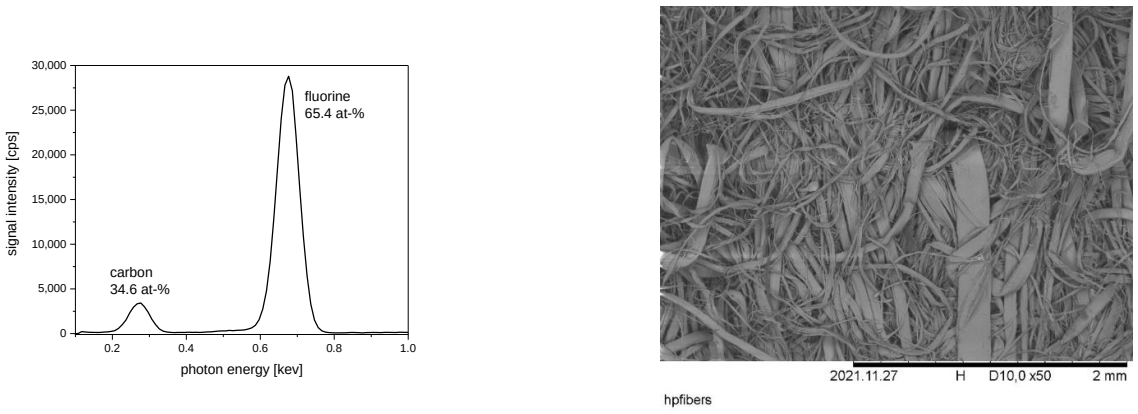


(**a**) (**b**)

**Figure 9.** Non-woven filter materials from PTFE fibers—(**a**) EDS spectrum of this PTFE material; (**b**) SEM image of this PTFE material.

For PTFE fiber materials, in addition to oleophobicity, the extraordinary chemical stability, high temperature stability ($T_{max}$ = 260 °C), and the strong fire resistance with LOI around 95% should be mentioned [11,47]. Out of all synthetic high-performance fibers, PTFE fibers can be named as the fibers with the highest chemical stability, which is probably the result of the high strength and stability of the C-F single bond. Nevertheless, two disadvantageous facts of PTFE fibers also have to be named. First, the high costs of PTFE in comparison to other conventional and high-performance fibers. Second, in the

case of the thermal decomposition of PTFE, volatile fluorine containing compounds, e.g., $COF_2$ can be formed [79]. Such compounds are quite toxic and can react with water under the formation of hydrogen fluoride gas HF.

**5. Fiber Materials with Extraordinary Chemical Stability**

The synthetic fiber material with the best chemical stability is clearly PTFE. However, other fibers are also named chemically stable. In fact, the term "chemically stable" is not exactly defined, so there is not an absolute criterium when a fiber is chemically stable or not. One reason for this is the broad range of different chemicals which could damage the fiber. Chemicals are often categorized into groups like acids, bases, oxidative agents, and organic solvents [1]. Other categories mentioned are hydrolysis stability, thermal-oxidative stability, seawater stability, or stability against chlorine $Cl_2$ [1,80]. In particular, the category "organic solvents" is confusing, because of the broad range of different organic solvents with completely different solving properties. Furthermore, the type of application of the chemicals to a fiber material can differ in a broad range. The main parameters are temperature during exposure, duration of exposure, and applied concentration. The exposition temperature can be set to room temperature up to the boiling point of a liquid solvent. A treatment at high temperature is demanding even with a shorter exposure duration. Another factor influencing the view of chemical stability is how the effect of chemical treatment on the fiber is determined. Often reported is the weight loss of the fiber material after chemical treatment. However, the weight loss indicates only if the fiber material is dissolved into the chemical. It does not indicate if the fiber properties are influenced by the chemical and if the fiber can still be used for demanded application. The weight loss after chemical treatment may be low, but the change in the mechanical stability of the fiber could be strong after the same treatment, so the fiber is too weak for dedicated use. For this, a determined fiber strength after chemical treatment is more reliable compared to a simple determination of the fiber weight.

With this background, it is clear that the decision is not easy, and fiber materials are presented in this section of "extraordinary chemical stability". Of course, PTFE fiber materials have to be mentioned. However, PTFE fibers are already discussed in the previous section due to their unique oleophobic properties. The decision is made to be presented here, especially the chemically stable fibers homo-polyacrylonitrile Homo-PAN and polyphenylene sulfide PPS (chemical structures shown in Figure 10). In contrast with conventional modacrylic fibers that are copolymers, homo-polyacrylonitrile is built up only by one type of repeating unit (Figure 10). Homo-PAN is a technical fiber which is not used in the clothing area. It exhibits an excellent stability under acidic and alkaline conditions, especially in contrast with other fibers containing ester, amide, or imide groups, which can be hydrolyzed under these conditions. Nevertheless, a strong alkaline treatment can lead to the reaction of the nitrile groups -CN on the fiber surface [81,82]. With this, the surface modification of PAN fibers for the improvement of dyeing properties is possible—while the main body of the fiber is not destroyed by the caustic treatment [81,82]. PAN-fibers can be damaged and solved by strong aprotic dipolar solvents, e.g., dimethylformamide DMF. On the other hand, this solubility in DMF offers the chance for the production of PAN-fibers by electrospinning, wet- or dry-spinning processes [83,84].

In contrast with PAN fibers, PPS fibers are even stable against solving with various types of organic solvents. Due to the extraordinary chemical stability, PPS fiber materials are often named as competing products for the replacement of PTFE fibers. This replacement is especially attractive, because of the moderate costs for PPS fibers compared to the high price of PTFE fibers. A shortcoming of PPS fiber materials is their sensitivity against oxidative agents. Even oxygen from air can damage PPS fibers during storage at high temperatures. Oxidative agents can oxidize the sulfur bridges of the PPS fibers in a first reactive step [85,86].

As examples of PAN materials, non-woven filter materials from PAN homopolymer fibers and PAN-copolymer are investigated by the EDS method (Figure 11). The EDS-

spectrum of the PAN homopolymer clearly exhibits signals according to the chemical elements carbon and nitrogen, as expected from the chemical structure of this polymer (compare also Table 2). However, small amounts oxygen and fluorine are detected on the surface of this non-woven material. The presence of fluorine can be explained by a fiber treatment using fluoro-carbon compounds to gain water- and oil-repellent properties. This is done to improve the cleaning procedures of the filter materials after a certain duration of usage. Furthermore, the determined oxygen can be part of a finishing agent applied to the PAN non-woven to improve its properties. The EDS spectrum of the PAN copolymer exhibits, additionally, the signals for carbon and nitrogen, and signals dedicated to oxygen and sulfur, which can be explained by the composition of the comonomer. PAN copolymers often contain methyl acrylate units or sulphonate groups [87,88].

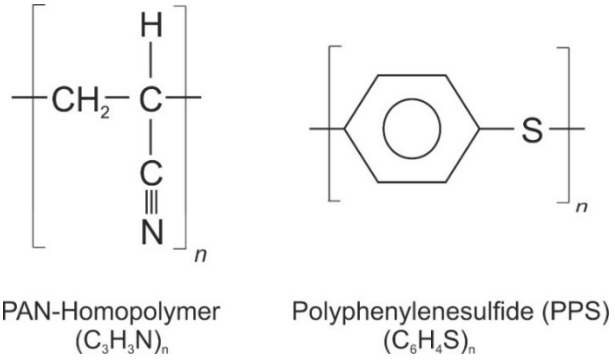


**Figure 10.** Chemical structures and sum formula of PAN-homopolymer and polyphenylene sulfide (PPS).

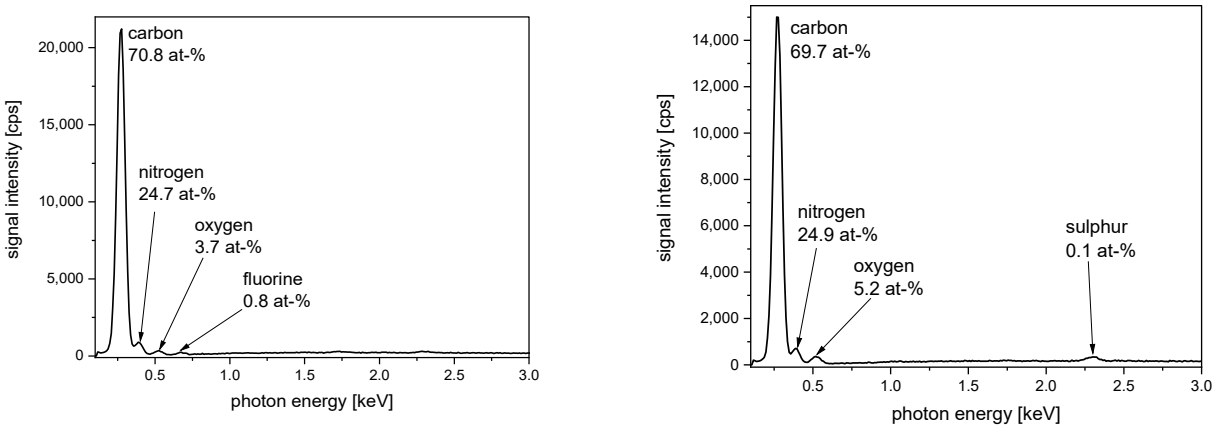


(**a**) (**b**)

**Figure 11.** EDS spectra of PAN samples taken from a non-woven filter material—(**a**) PAN homopolymer; (**b**) PAN copolymer.

For the presentation of SEM images and EDS spectra, different PPS fiber materials are investigated and presented. All PPS samples are taken from non-woven fiber felts offered as filtration materials. These filter materials are dedicated to the filtration of chemically aggressive hot gases. First, a PPS filter material is presented, which contains no further additives (Figure 12). The EDS spectrum of the PPS material clearly exhibits the composition of the elements carbon and sulfur in the expected ratio (compare also Table 2). Due to the stronger sensitivity of the EDS method for sulfur compared to carbon, the signal intensity for sulfur is nearly four times stronger, even if the sulfur content on the fiber is only 13 at-%. Additionally, to the main sulfur signal at 2.31 keV, a second signal occurs at 2.46 keV. Furthermore, a small signal at low photon energy at 0.15 keV is dedicated to the presence of sulfur. Additionally, to carbon and sulfur, a small signal occurs, which

can be assigned to oxygen. This occurrence of oxygen can be explained by the presence of finishing agents or by the part-oxidation of PPS at the sulfur bridge.

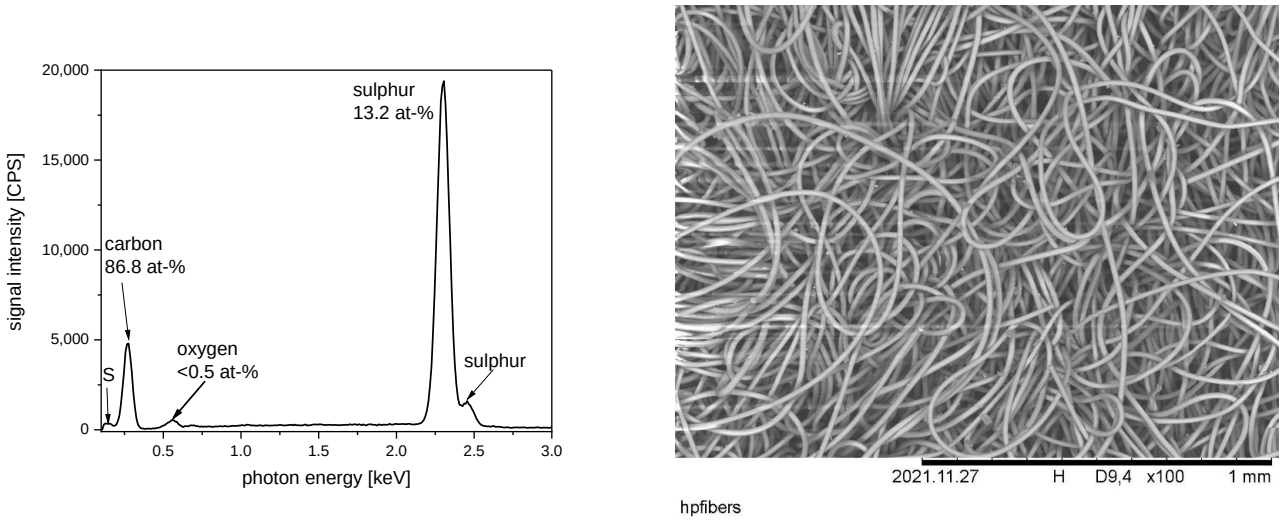


(**a**) (**b**)

**Figure 12.** PPS sample from a non-woven filter material—(**a**) EDS spectrum; (**b**) SEM image.

The second PPS fiber sample is modified by a fluoro carbon finish, probably applied to improve the cleaning properties of the non-woven filter material (Figure 13). The EDS spectrum taken from this sample clearly shows the presence of fluorine as a result of previous finishing and the elements carbon and sulfur related to the PPS fiber. Of course, the element carbon is also part of a fluoro carbon finishing agent. Furthermore, a weak signal dedicated to the presence of oxygen is detected. Furthermore, here, the presence of oxygen can be explained with its content in the finishing agent or by the part-oxidation of PPS at the sulfur bridge. The treatment of PPS microfiber membranes with PTFE ultrafine powders is reported to lead to materials with superhydrophobicity and superoleophobicity. These materials can be used for oil/water separation [89].

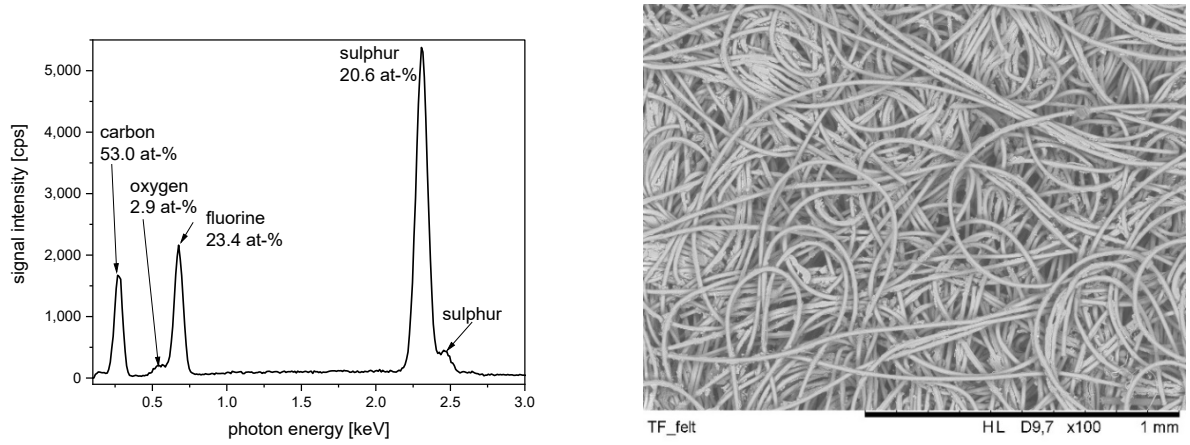


(**a**) (**b**)

**Figure 13.** PPS sample from a non-woven filter material with fluoro carbon finish—(**a**) EDS spectrum; (**b**) SEM image.

The third presented PPS containing sample is a non-woven filter material made by two different high-performance fibers (PPS and meta-aramid) (Figure 14). In the related SEM image, the two different types of fibers can already be identified. As a material contrast, the

PPS fibers appear brighter in the SEM image. The related EDS spectrum exhibits signals according to the four elements—carbon, oxygen, nitrogen, and sulfur. The difference in the element sensitivity of the EDS method for the different elements is impressively demonstrated by this EDS spectrum. This fiber sample contains nearly the same content of nitrogen compared to sulfur. However, the nitrogen-related EDS signal is nearly negligible and even weaker than the second sulfur signal, at 2.46 keV.

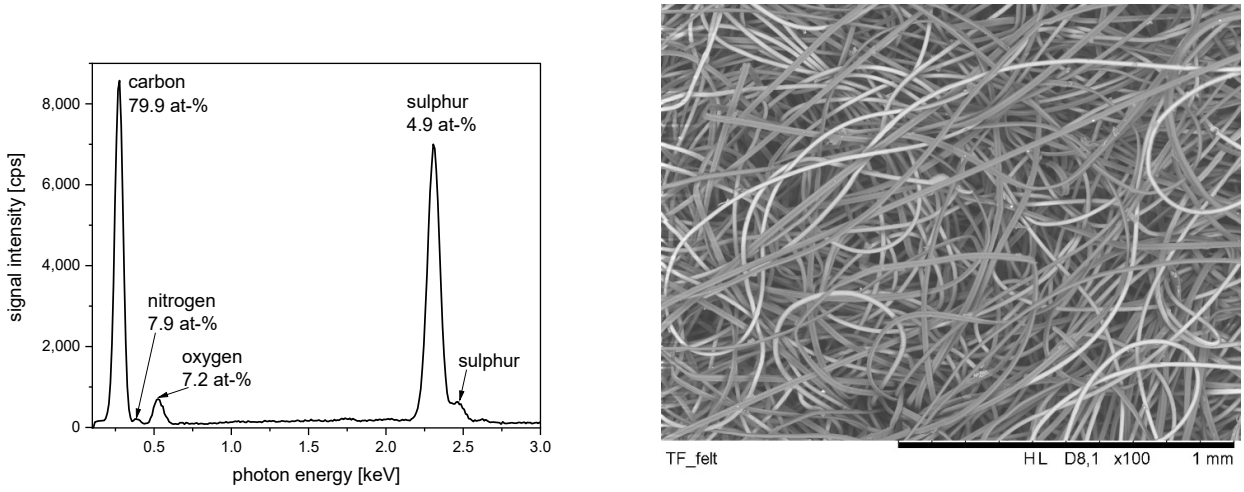


(**a**) (**b**)

**Figure 14.** Non-woven filter material made from PPS fibers and meta-aramid fibers—(**a**) EDS spectrum; (**b**) SEM image.

## 6. Fire-Retardant Textiles

Fire-retardant fiber materials are not ignited in contact with fire or are self-extinguishing after a flame contact is removed. Most often, the fire-retardant properties of textiles are ranked by the LOI value [90]. Nevertheless, other fiber properties also have to be considered, if the right fiber material is to be chosen for a certain application. For applications with possible contact with light or chemicals, the fiber should also exhibit a suitable light and chemical stability. Another important criterium is whether the fiber can melt or not. A fire-retardant textile with the ability to melt must be avoided for clothing applications in direct skin contact. Finally, an overview of a possible smoke formation (smoke density and toxicity) should also be carried out to choose the right fiber. Practical applications are found, for example, in flame-retardant home textiles or clothes for firefighters [91]. In these areas, usually, combinations of different flame-retardant textile materials are used. This combination can be done as blended yarn, mixed fabric, or multilayer material. The main aims of combing different materials are to realize flame-retardant properties, chemical stability, mechanical stability, and textile comfort together in one product [91].

Often, flame-retardant properties are explained by the fire cycle describing the exothermic reactions of the pyrolyzed textile material with oxygen from the air in a repeating cyclic process. If the fire must be stopped, this fire cycle has to be disrupted [92]. This disruption can be done by a different mechanism, e.g., cooling by endothermic reaction, the formation of non-burning gases diluting the oxygen content, char formation on the textile insulating it from the fire, or radical scavengers directly disrupting the radical chain reaction in the flame [92].

Flame-retardant fibers and finishing agents are usually categorized according to the chemical elements that they contain. The chemical elements related to different flame-retardant processes are halogens (fluorine, chlorine, and bromine), nitrogen, phosphorous, sulfur, and silicon. As a structural element from organic chemistry, aromatic ring systems also support the flame-retardant properties of fiber materials. However, the flame-retardant properties are not just related to the presence of specific chemical elements. Furthermore,

the formation of specific toxic components in burning gas is the result of different chemical elements present in the fiber. The formation of $NO_x$ and HCN in the burning gas is related to the presence of nitrogen. Sulfur-containing fiber materials often have $SO_2$ in burning gas, and halogen content is related to the acidic gases HCl, HF, and HBr.

Figure 15 summarizes the chemical structures of selected flame-retardant fibers. Figure 16 shows the chemical structure of a phenol-formaldehyde resin (novoloid) which is used for the production of flame-retardant Kynol fibers. The chlorine content of flame-retardant modacrylic fibers is obvious. For other flame-retardant fibers, the chemical structure clearly exhibits the aromatic structure, and with the exception of the Kynol resin fiber, also the content of nitrogen. For this reason, Kynol fibers are often promoted as flame-retardant fibers with less toxic smoke formation.

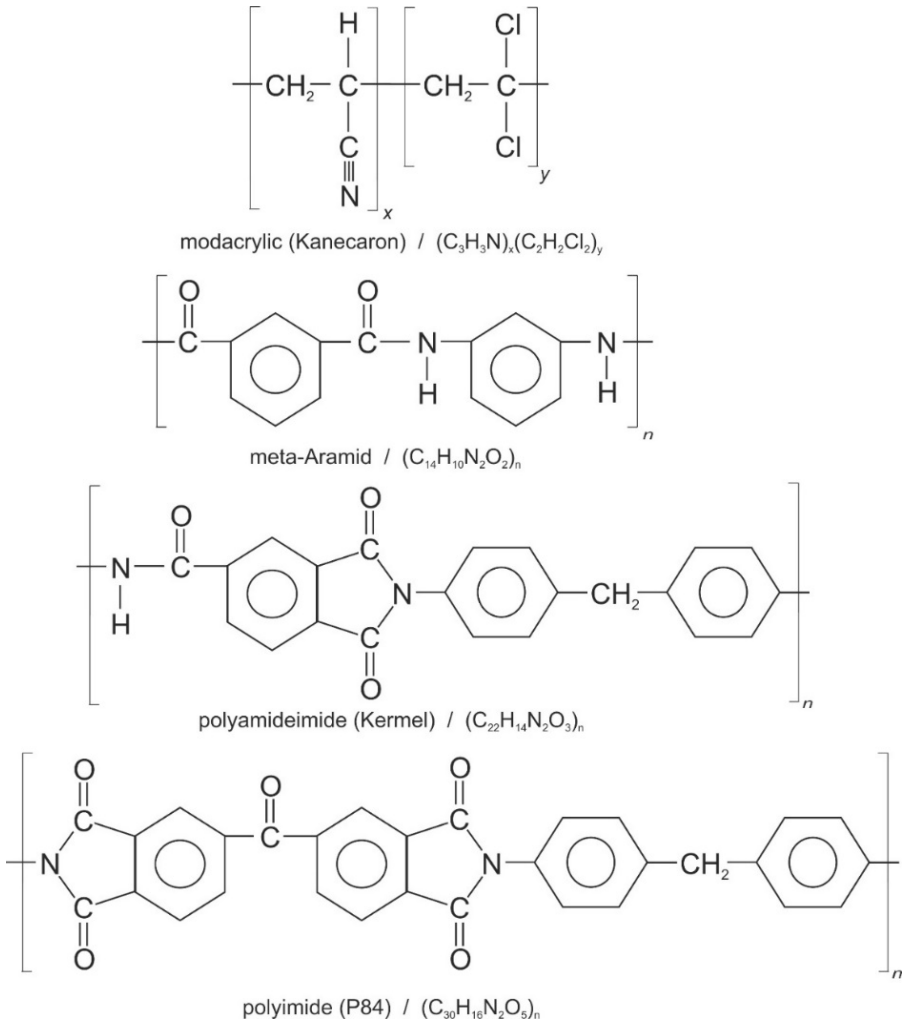


**Figure 15.** Chemical structures and sum formulas of high-performance fibers with fire-resistant properties.

Further, selected properties of those fibers are compared in Table 3. Especially mentioned here are the LOI values and the maximum temperature of usage $T_{max}$. Beside the here listed fire-retardant fibers, also other flame-retardant fibers should be mentioned, which are already presented and discussed in the previous sections of high-strength fibers and chemically stable fibers. Here especially PBO fibers with LOI of 56 to 68 and a $T_{max}$ between 310 °C to 350 °C, PPS fibers with LOI of 40 and reported $T_{max}$ in the range of 190 °C to 280 °C and PTFE fibers with LOI value > 90 have to be mentioned [11,47].

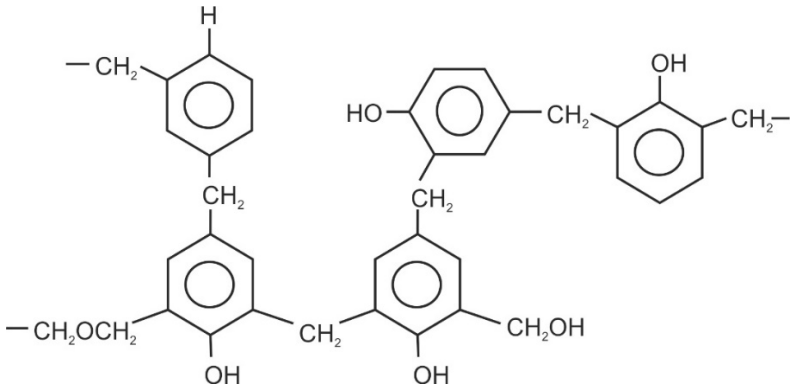


**Figure 16.** Chemical structure of novoloid resin which built up Kynol fibers.

**Table 3.** Comparison of properties of some flame-retardant fibers.

| Fiber | Density [g/cm$^3$] | LOI [%] | Maximum Temperature of Usage $T_{max}$ [°C] | Selected Properties | References |
|---|---|---|---|---|---|
| Chlorinated modacrylic, (Kanecaron) | — | 31 | | High chemical stability against acid and alkali | [48,93] |
| Meta-Aramid, (Nomex) | 1.38 | 30–32 | 200 | Good temperature stability | [11,47] |
| Polyamideimide, PAI, (Kermel) | 1.34 | 30–32 | 180/200 | Good temperature stability | [47,94] |
| Polyimide, PI (P84) | 1.41 | 36/38 | 180/260 | Good mechanical and thermal properties | [11,47,95] |
| Phenolic/formaldehyde resin, Novolac resin, (Kynol) | 1.27 | 30–34 | 150/200 | Resitant against heat and fire | [47,96] |
| FR viscose | — | 23–29 | | Humidity up-take, antistatic | [97,98] |

The EDS spectra of the flame-retardant materials meta-aramid and polyamideimide are compared in Figure 17. The meta-aramid sample is taken from a non-woven filter material made from Nomex. For recording the EDS-spectrum of polyamideimde here a polymer bullet is used as sample, instead of a fiber material. The bullet material is chosen, because polyamideimide was only available in fiber mixtures, made it quite difficult to separate a single fiber material and identify it clearly. Polyamideimide based fibers are supplied under the brand name Kermel. Similar to Dyneema fibers standing synonymous for HPPE fibers, Kermel fibers as brand represent often polyamideimide fibers [99]. Compared to other flame-retardant fibers, the LOI value of Kermel fibers is with around 32 only moderate. However, Kermel fibers are quite advantageous for application in flame-retardant clothes, because of non-melting, self-extinguishing and less smoke formation behavior.

The EDS-spectrum of meta-aramid exhibits signals related to the elements carbon, nitrogen and oxygen—as expected by its chemical composition. Meta-aramid and para-aramid show nearly similar EDS-spectra. Also, the EDS-spectrum of polyamideimide shows signals due to carbon, oxygen and nitrogen. However, the detected amount of nitrogen is smaller compared to the amount of oxygen, which is also expected from the chemical composition of the fiber material (compare Figure 15 and Table 2).

The EDS spectra of two different polyimide fiber materials are compared in Figure 18. The first polyimide material is a pure fiber material from the producer Evonik supplied under the brand name P84. As second polyimide material, a non-woven filter material is presented. The EDS spectrum of P84 exhibits clear signals for carbon and oxygen. Due to the small content of nitrogen, the nitrogen related signal is very weak but even also nitrogen can be detected (compare the chemical structure in Figure 15). It should be remarked that polyimide from the P84 fiber is not the only available polyimide. Also, other polyimide materials with other chemical structure are offered, e.g., Kapton [100]. For the polyimide filter material, additionally the element fluorine is clearly determined with a concentration of around 2 at-%. This detection of fluorine is probable related to a fluoro-carbon finishing of the non-woven to introduce soil repellent properties to this filter product. This finishing treatment is done to improve cleaning procedures of the filter materials.

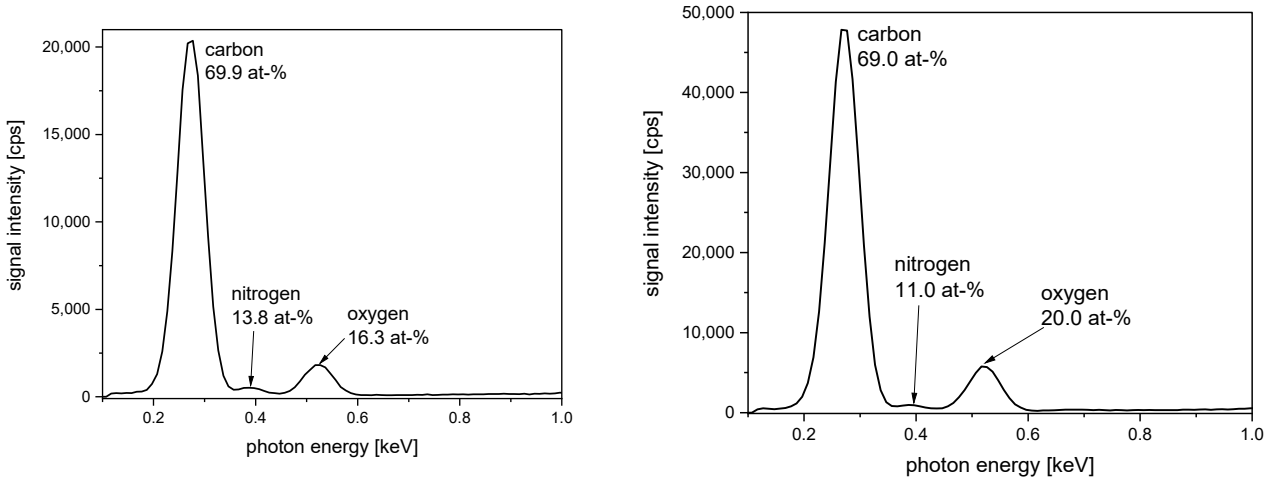


(**a**) (**b**)

**Figure 17.** EDS spectra of different flame-retardant fiber materials: (**a**) m-aramid (Nomex) taken from a non-woven filter material; (**b**) polyamideimide sample taken from a polymer bullet.

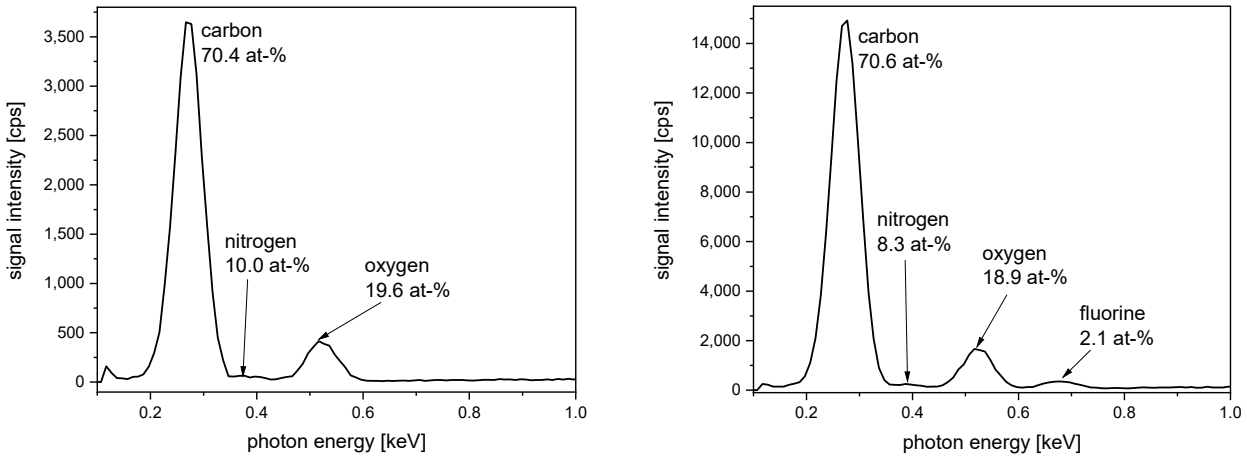


(**a**) (**b**)

**Figure 18.** EDS spectra of different flame-retardant polyimide PI fiber materials: (**a**) PI fiber material P84 from Evonik; (**b**) polyimide material taken from a non-woven filter material.

The EDS spectrum of a Kynol fiber material exhibits signals for the two elements carbon and oxygen (Figure 19). A high carbon content of more than 80 at-% is determined, which is related to the aromatic content of this resin fiber. It has been reported that, by laser treatment, the Kynol fiber can be partly carbonized. Related EDS-spectra show a higher carbon content with an increasing intensity of applied laser treatment [101].

Panox fibers—also called Preox fibers or preoxidized fibers—are partly pyrolyzed PAN fibers with flame-retardant properties [102]. This is remarkable, because the original PAN fibers exhibit tremendous burning behavior [103]. The flame-retardant concept of Panox fibers is different from other flame-retardant fibers. It could be stated that, via the pyrolysis process, the burning processes are performed and finished in a controlled manner. Afterwards, the remaining fiber—as result of pyrolysis—is no longer able to burn. Panox fibers are often also named as intermediate products for the production of carbon fibers from PAN precursor fibers. Meanwhile, Panox fibers are only partly carbonized by the pyrolysis of PAN. This pyrolysis process is done to complete carbonization, if carbon fibers are produced [102]. Due to the similarity of production processes, companies producing carbon fiber are often also suppliers of Panox fibers.

The EDS spectrum and SEM image of a Panox fiber are presented in Figure 20. Looking at the EDS spectrum, the increased content of oxygen is visible—compared to the EDS spectrum of the PAN homopolymer (see Figure 11 and compare to Figure 20). Given this, it is clear that the Panox fiber is an oxidized PAN fiber, so with this background, the name Panox fits very well.

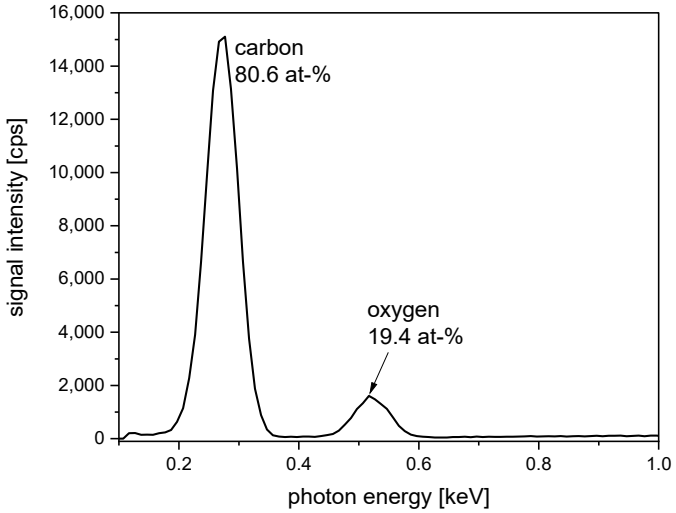


**Figure 19.** EDS spectrum of non-woven felt made from Kynol fibers.

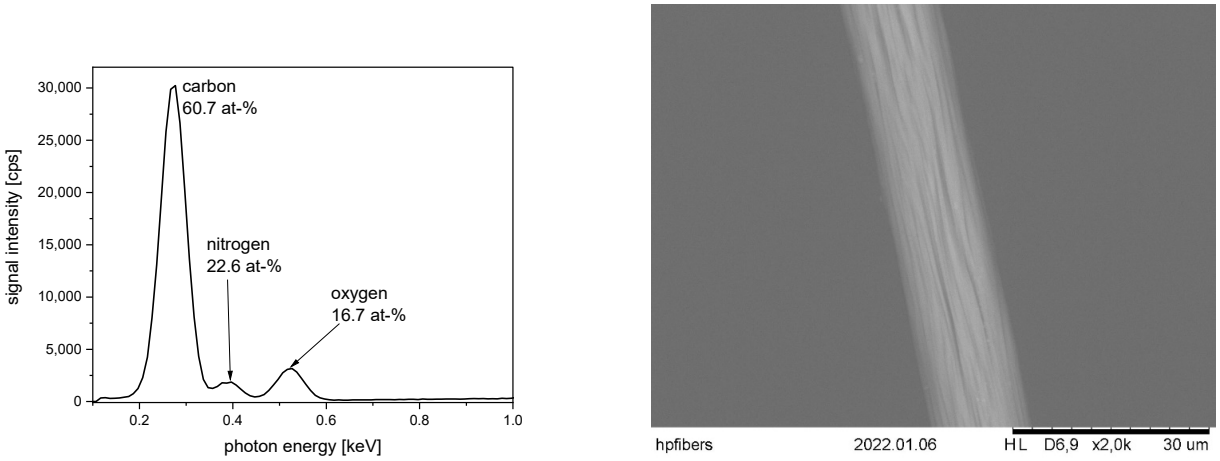


(**a**) (**b**)

**Figure 20.** Panox fiber—(**a**) EDS spectrum; (**b**) SEM image.

A flame-retardant fiber material with a high economic relevance—especially in the area of home textiles—is intrinsically flame-retardant polyester. Conventional PET fibers exhibit an LOI value of 21/22 and are therefore not as easy to ignite than, for example, cotton. In the case of flame-retardant polyester, this flame-retardant property is enhanced by the addition of phosphorous compounds to the fiber as part of a phosphorous-containing co-monomer [104]. In the case of the flame contact, the phosphorous-containing part is decomposed and leads to the formation of a char layer, which is isolating the fiber surface from further oxidation processes.

The related SEM image and EDS spectrum for such a functional flame-retardant polyester are presented in Figure 21. This product is distributed under the brand name Trevira CS. By the EDS, the chemical elements carbon and oxygen—related to the PET structure—are clearly determined. Furthermore, phosphorous can be detected even if the

concentration is, with 0.3 at-%, quite low. However, the sensitivity of the EDS method to detect phosphorous is significantly higher compared to the sensitivity for the lighter elements carbon or oxygen. On the SEM image, these functional PET fibers exhibit few white spots. These small and brighter areas are probably related to areas with higher concentrations of phosphorous on the fiber surface.

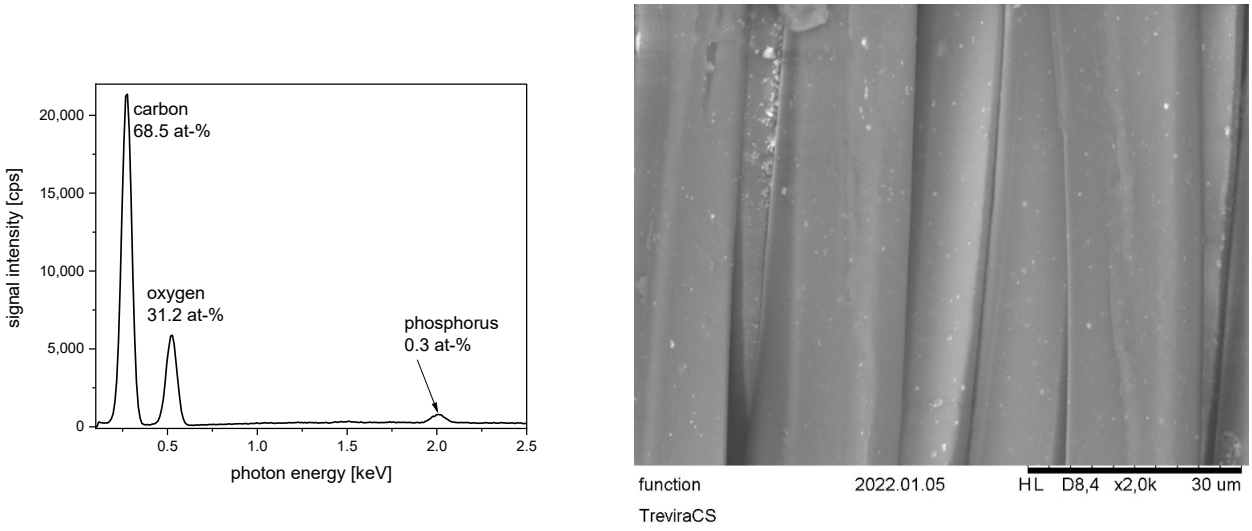


(**a**) (**b**)

**Figure 21.** Commercially available fabric made from functional polyester TreviraCS—(**a**) EDS spectrum; (**b**) SEM image.

While polyester fibers are modified with phosphorous compounds to reach flame-retardant properties, regenerated cellulose fibers can be modified with silicon compounds for the same reason [105,106]. One example of such a product is the fiber Danufil BF supplied by Kelheim Fibers. Compared to the analogous conventional cellulosic fiber from the same producer (type: Danufil), Danufil BF is modified by the addition of a silicon oxide-based component to the spinning mass. Due to the absence of other chemical elements, e.g., nitrogen or chlorine, such fibers are often promoted as flame-retardant fibers following a green concept [107]. The EDS spectra of Danufil and Danufil BF are compared with each other in Figure 22. The silicon content is clearly detected by this method. Additionally, a small amount of sodium is determined, which could be there as a residue from the fiber production process. The sodium could be, as counterion $Na^+$, part of the added silicon oxide compound.

Another example for a flame-retardant cellulose fiber is presented with the Arabon fibers in the Figures 23 and 24. Looking at the EDS spectrum of these fibers, a high number of different chemical elements are identified (Figure 23). It is clear that the silicon component is not the only flame-retardant additive. On the fiber surface, deposited particles are also detected by SEM (Figures 23 and 24). To analyze the composition of these particles and the fibers, EDS mapping is performed (Figure 24). This EDS mapping enables the detection of a specific chemical element depending on its position on the sample surface. However, such a mapping is mainly limited to elements that have a significant signal intensity in the EDS spectrum. In Figure 24, the SEM image is compared to the EDS mapping with the three chemical elements carbon, silicon, and phosphorous. It is clear that the elements carbon and silicon are detected at the same surface position related to the main body of the cellulosic fibers. Probably, here, similarly to Danufil BF, a silicon-containing fiber is present. In contrast, phosphorous is only detected in areas wherein the particles are placed on the fabric surface. For this, probable phosphorous-containing flame-retardant pigments are added to the flame-retardant cellulose—for the further improvement of flame-retardant properties.

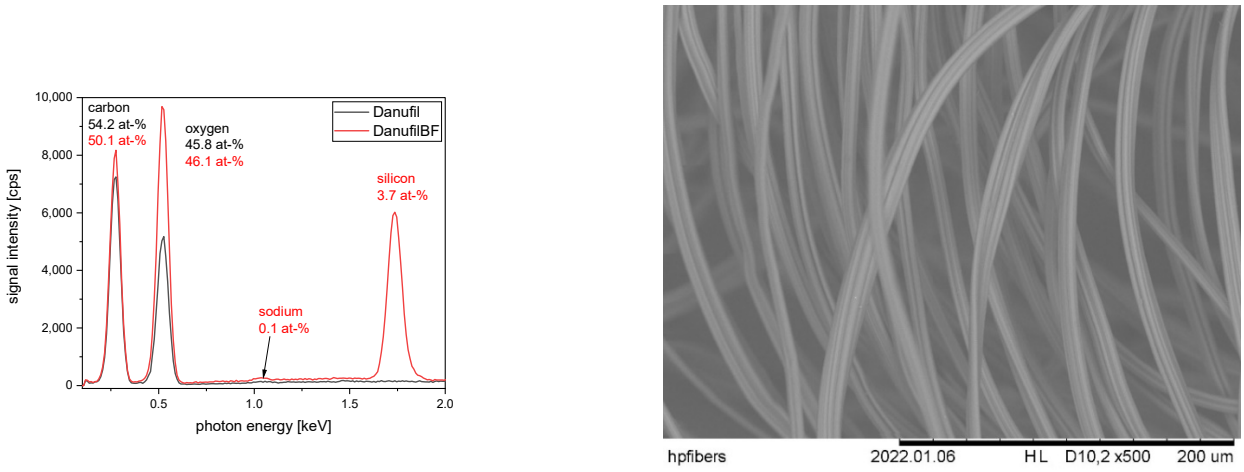


(**a**) (**b**)

**Figure 22.** Regenerated cellulose fiber types Danufil (conventional cellulosic fiber) and Danufil BF (flame-retardant cellulosic fiber with silica content)—(**a**) EDS spectra of Danufil and Danufil BF in comparison; (**b**) SEM image of Danufil BF.

Cotton as a natural fiber with an LOI value of 18 does not exhibit any flame-retardant property by itself. However, cotton is the most used natural fiber, and there is also a demand for flame-retardant cotton fabrics and clothes. For this reason, flame-retardant finishing agents are developed and applied on cotton, e.g., via the padding process [108,109]. The following two examples of cotton with flame-retardant finishes are presented and described with SEM and EDS.

As an example of a commercially available flame-retardant textile, a cotton fabric with flame-retardant finishing is examined by SEM and EDS (Figure 25). The SEM image clearly shows the structure of the cotton fibers. Additionally, small, deposited particles can be detected that are probably related to the applied flame-retardant finishing agents. The related EDS spectrum of this cotton sample supports the detection of five chemical elements (carbon, oxygen, phosphorous, silicon, and calcium). The highest ratio is clearly taken by carbon and oxygen, which are the elements building up the cotton fibers itself. Moreover, a flame-retardant finishing agent is supposed to contain carbon and oxygen in a certain amount. The determined phosphorous with a surface concentration of 1.7 at-% is clearly related to the application of a phosphorous-based flame-retardant agent. Often, such phosphorous-containing flame-retardant agents contain nitrogen as well [109–112]. However, due to the low sensitivity of the EDS method for nitrogen, this element cannot be detected here. Furthermore, small amounts of silicon and calcium are detected. These elements can be part of the flame-retardant agent but can also be residues from washing processes using silicate-containing washing agents.

For example, for a finishing agent applied in a padding process, the product Apyrol from CHT (Tübingen, Germany) is chosen and applied on cotton. The EDS spectrum and SEM image of a cotton fabric treated with the agent Apyrol are presented in Figure 26. In addition to the chemical elements carbon and oxygen, phosphorous, sulfur and a small content of calcium are determined by EDS. Carbon and oxygen are related to the composition of the cotton fiber itself. The presence of phosphorous and sulfur is probably attributed to the applied flame-retardant agent. The presence of calcium in very small amounts is explained as a residue from the finishing process, where water is used as the main solvent.

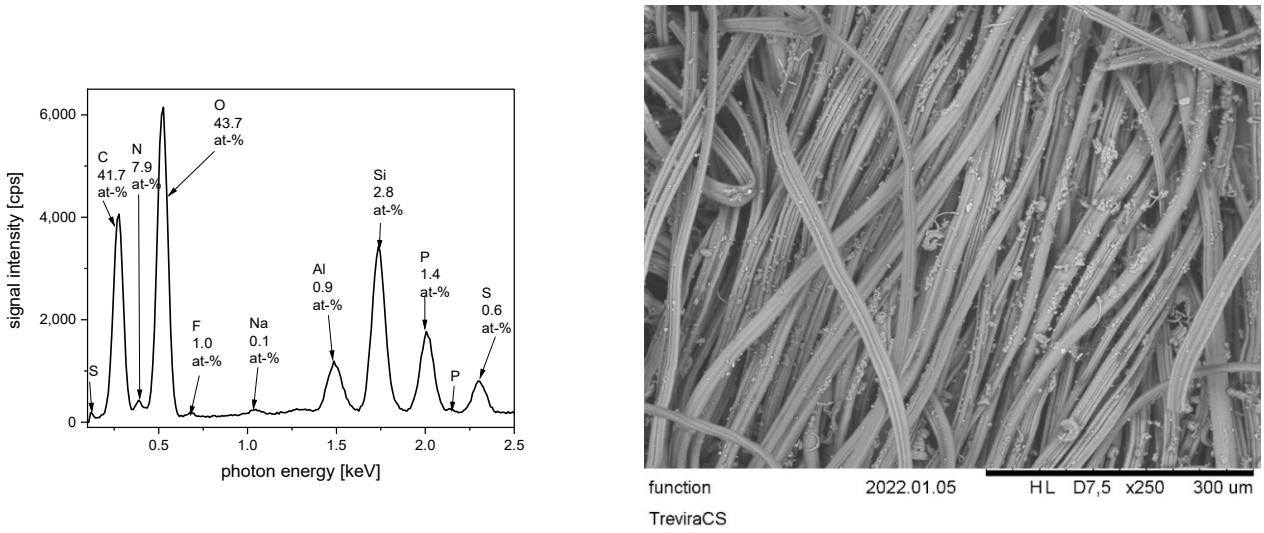


(**a**) (**b**)

**Figure 23.** Commercially available fabric made from functional cellulosic fibers Arabon—(**a**) EDS spectrum; (**b**) SEM image.

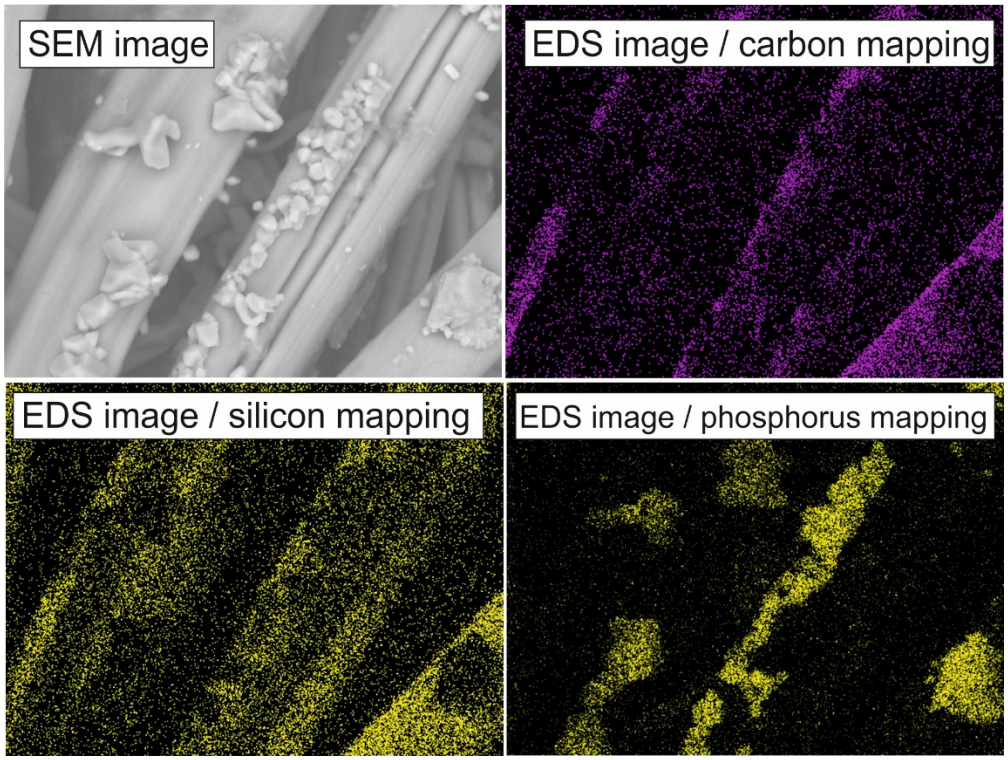


**Figure 24.** SEM image and related EDS images from Arabon. Compared are the mappings for the chemical elements silver and carbon.

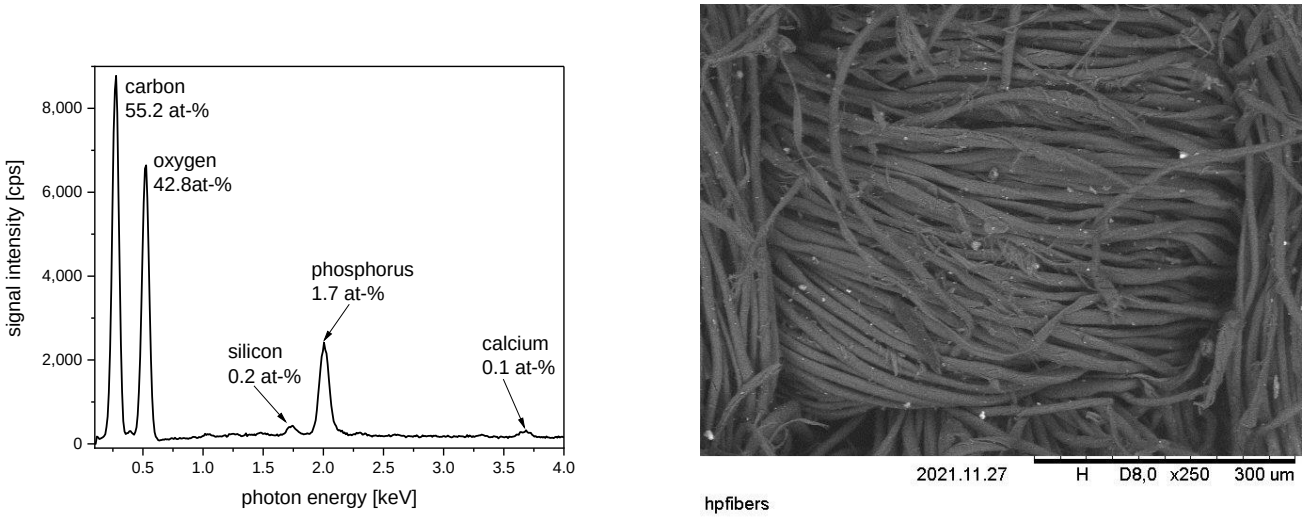


(**a**) (**b**)

**Figure 25.** Commercially available cotton fabric with flame-retardant finishing—(**a**) EDS spectrum; (**b**) SEM image.

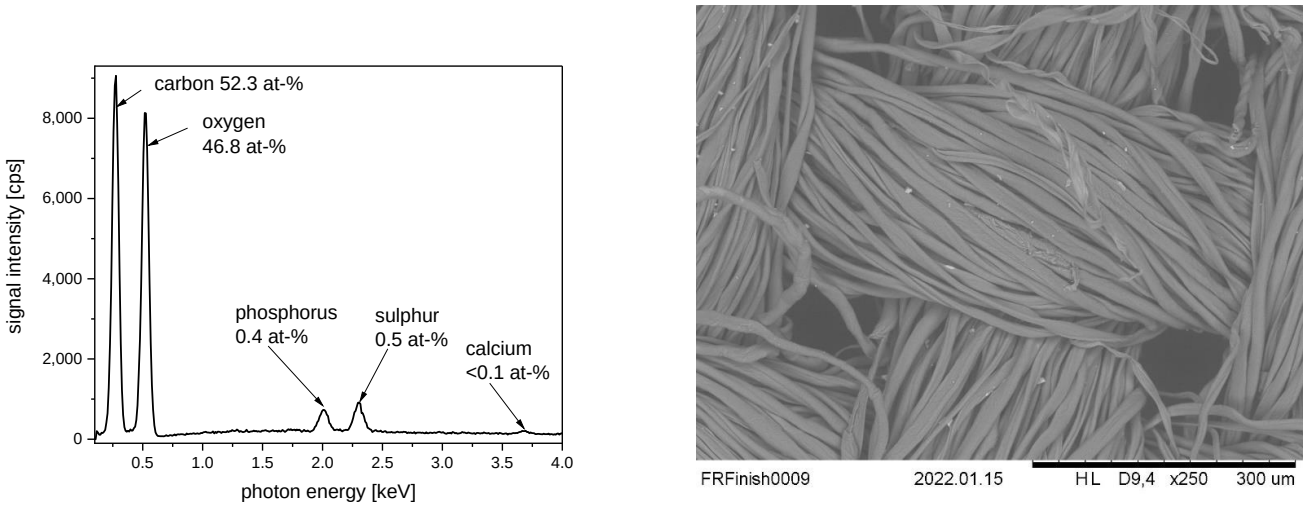


(**a**) (**b**)

**Figure 26.** Cotton fabric treated with commercially available flame-retardant finishing agent (Apyrol)—(**a**) EDS spectrum; (**b**) SEM image.

A flame-retardant textile belt supplied from Kübler Workwear is chosen as an example of a fire protective workwear offered for firefighters. According to the supplier information, this belt is made from different fibers—23% modacryl, 19% cotton, and 58% polyester. Due to the fact that conventional modacryl fibers are easy to ignite, it is obvious that the used modarylic fibers for this belt are chlorinated modacrylic fibers with fire-retardant properties similar to Kanecaron fibers [113]. The EDS spectrum and SEM image of the belt recorded in low magnification are presented in Figure 27. Additionally, when it comes to the chemical elements carbon and oxygen, chlorine is also determined by EDS with a content of 2.6 at-%. Even if the chlorine concentration is quite small, its EDS signal is even more significant compared to the EDS signal related to oxygen with a content of 25.7 at-%. The sensitivity of the EDS method for the detection of chlorine is significantly higher compared to the sensitivity of oxygen. The detection of chlorine is a clear hint of the presence of chlorinated modacrylic fibers, which can also be estimated by view of the related SEM image. On the

SEM image, it is visible that the fabric is made from mixed yarns built up by different fibers. Several fibers exhibit a brighter contrast, which is a hint of the presence of a heavier chemical element such as chlorine. By EDS, small amounts of three further chemical elements are also determined on the flame-retardant belt—silicon, sulfur, and antimony. In particular, the presence of antimony is remarkable, because antimony oxide $Sb_2O_5$ is known for its use as a synergistic flame-retardant agent improving the properties of chlorinated and brominated flame-retardant agents [112,114,115]. Probable components containing antimony trioxide are added to the fabric as finishing agents to improve the flame-retardant effect of the chlorinated modacrylic fibers. The presence of antimony on a textile material is, in any case, surprising, because antimony-containing substances are in discussion due to their possible hazardous effects [115].

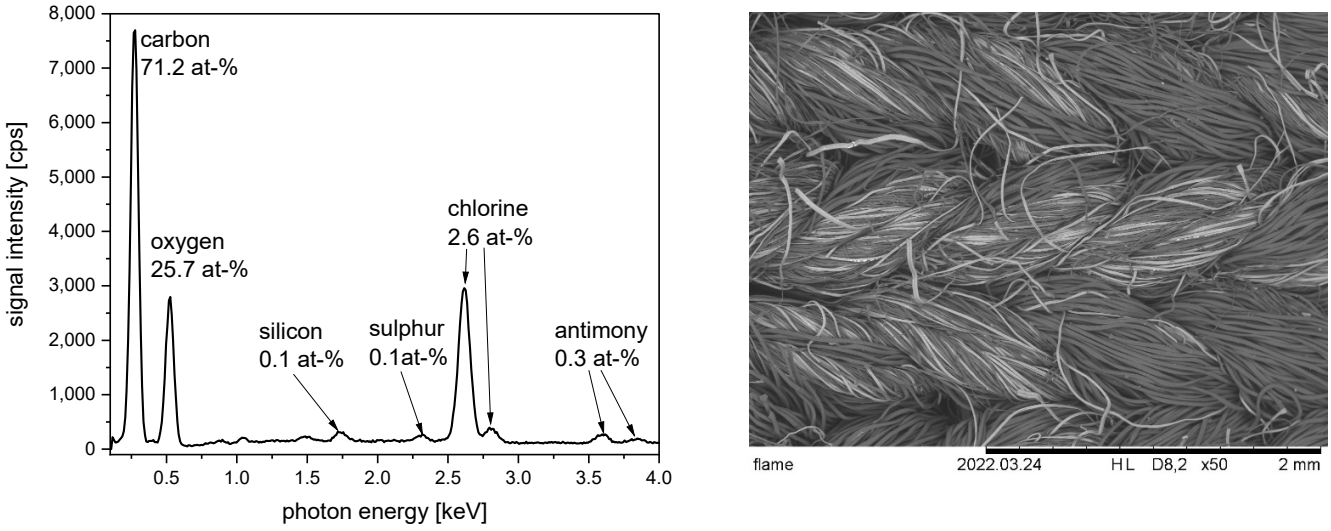


(**a**) (**b**)

**Figure 27.** Commercially available flame-retardant belt offered for firefighters—the fiber composition is 23% modacryl, 19% cotton, and 58% polyester (supplier Kübler workwear)—(**a**) EDS spectrum; (**b**) SEM image.

Figure 28 supports a more detailed view with an SEM image and EDS mappings recorded in higher magnifications. By EDS mapping, the chlorinated modacylic fibers can be clearly identified and distinguished from the oxygen-containing cotton and polyester fibers. Moreover, the deposition of antimony-containing areas is indicated.

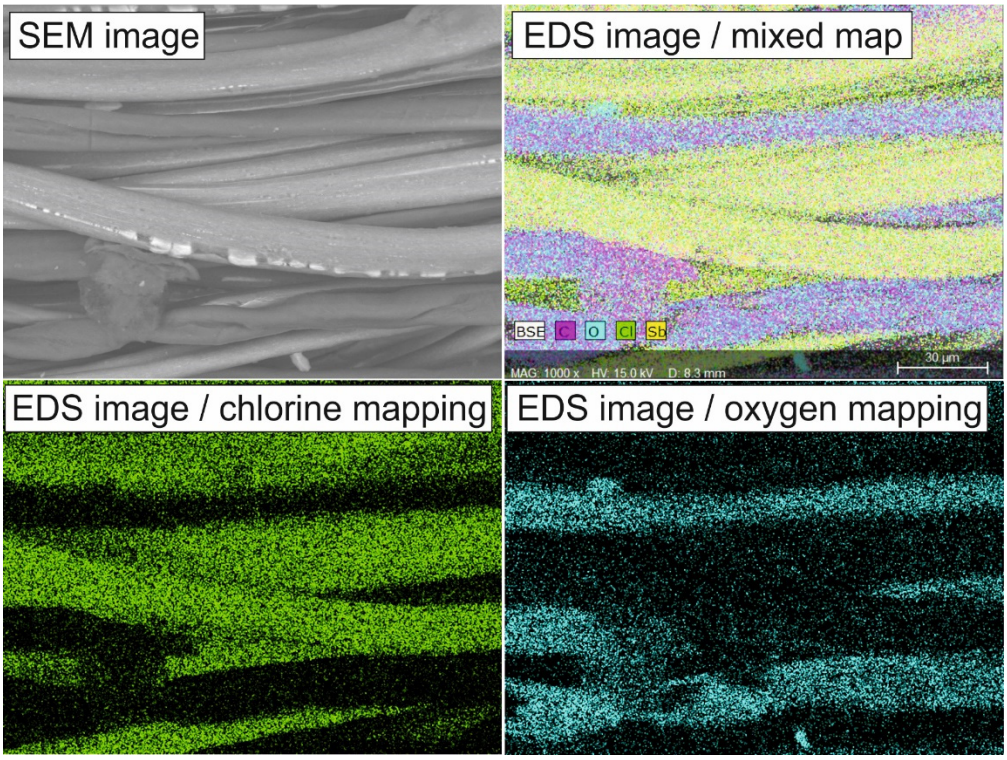


**Figure 28.** SEM image and related EDS images from a commercially available flame-retardant belt. The mappings for the chemical elements chlorine and oxygen are especially compared.

## 7. Inorganic Fiber Materials

Inorganic fibers are all fibers made from inorganic materials, in contrast to synthetic organic fibers made from organic polymers [116,117]. The definition of the terms "inorganic" and "organic" is based on chemistry nomenclature. "Organic" compounds are based on carbon–hydrogen compounds and "inorganic" compounds do not contain carbon–hydrogen bonds. According to this definition, elemental carbon (in types of graphite and diamond), carbon dioxide, and carbon disulfide are also inorganic compounds [118]. Following this scientific definition, carbon fibers are also counted as part of the group of inorganic fibers [116,117]. Other inorganic materials which often occur as fibers are based on glass, oxidic- and non-oxidic ceramics [116,119]. A special type of inorganic fibers are basalt fibers, which are prepared by spinning from a melt of natural volcanic rock [120–122]. One main feature of inorganic fibers compared to organic fibers is their high-temperature stability, even in the presence of oxygen. For inorganic fibers, maximum temperatures of usage—$T_{max}$—over 1000 °C are possible [116]. For this, they are often used in applications, where temperature resistance is demanded: these are heat-resistant, flame-resistant, but also cut-resistant clothes. Other applications are found in fiber-reinforced materials, where = extraordinary product design can also be realized [123].

### *7.1. Glass Fibers and Basalt Fibers*

Glass fibers are produced by spinning from molten glass and are usually amorphous [124,125]. The main components building up glass fibers are silica $SiO_2$ and alumina $Al_2O_3$. Furthermore, other components occur, such as $Na_2O$, CaO, or MgO [125,126]. Glass fibers with a special stability against alkaline treatment also contain zirconia in the form of $ZrO_2$ [127]. Ceramic fibers can also be made from silica and alumina—as so-called oxidic ceramics. Here, one main difference to glass fibers is the crystallinity of ceramic fibers. Other ceramic fibers based on silicon carbide SiC (distributed under the brand name Nicalon) are named non-oxidic ceramic, because of the lack of oxygen in the fiber [128,129].

As examples of glass fiber products, the EDS spectra of four different commercially available glass fiber fabrics are compared in Figure 29. These materials are supplied by the company Culimeta (Bersenbrück, Germany). The first product example is a conventional glass fiber fabric made from e-glass fibers. Oxygen with a content of nearly 60 at-% is the element determined with the highest concentration, due to the fact that glass is made from different metal oxides and silica. Other chemical elements with significant concentration in the e-glass fabric are silicon, calcium, and aluminum. Magnesium and potassium are determined only in small quantities. Surprisingly for an inorganic fiber, carbon is also observed in a significant amount on the fiber surface with around 15 at-%. It should be recalled that, via the EDS method, the surface of the fiber is investigated and the detected elements and concentrations are related to the chemical elements on the fiber surface. The inorganic fiber itself does not contain carbon, but quite often, the surface of glass fibers is treated with organic sizing agents [130,131]. These agents are applied to support yarn and fabric production processes. Furthermore, they influence the properties of the final glass fiber fabric. However, these organic agents are more sensitive to temperature influences, so by their use, the maximum temperature of use for the related glass fiber could be reduced drastically down to a temperature range from 150 °C to 300 °C. The second example is a caramelized glass fiber fabric. The term "caramelized" describes the light brown coloration as a result of thermal treatment at moderate temperatures [132,133]. By exposure to this temperature, the organic sizing agents are partly pyrolyzed, so a soft brown coloration occurs for the glass fiber fabric. Due to the part-carbonization of the sizing agent, the detected amount of carbon is also slightly increased to values around 18 at-%. However, no carbohydrates are in involved in this process, so the commonly used term is misleading regarding the involved chemistry. The third example is a silica fabric, for which EDS spectra are dominated by two main signals of oxygen and silicon, related to the component silica $SiO_2$. Furthermore, small amounts of sodium and aluminum are detected. Carbon is determined probable according to the presence of a sizing agent. The last example is a glass fiber fabric modified with vermiculite particles to improve temperature stability. An SEM image of this glass fiber fabric with vermiculite particles is presented above in Figure 4. The flat plate-like structure of the vermiculite particles is clearly visible. Vermiculites are naturally occurring clay minerals. They are built up by adjacent silicate layers [134,135]. In the interlayer between the silicate layer, water and metal ions can be incorporated. In natural vermiculite, often magnesium ions are present in this interlayer [136]. According to this background, the detection of magnesium by EDS in a concentration of 1.5 at-% can be explained (Figure 29).

An EDS spectrum taken from a basalt fiber sample is presented in Figure 30. This fiber sample is taken from a basalt roving (Kamenny Vek/Advanced Basalt Fiber). Additional to the mainly detected elements silicon, aluminum, and oxygen, iron and titanium are also visible in the spectrum. The presence of iron oxide is typical for basalt fibers and, due to the composition of the natural stone, used as material for basalt fiber production. This iron oxide is also responsible for the typical brown coloration of basalt fibers, making it easy to distinguish them visually from other glass and ceramic fibers [137,138]. Together with the also present titania as $TiO_2$, the iron oxide supports UV-protective properties to basalt fiber fabrics or coatings containing basalt fibers as additives [139]. Furthermore, the presence of iron oxide is often related to protection against heat radiation [140,141]. The chemical composition of basalt fibers varies in a broad range depending on the type and supplier of the basalt fiber [142]. The main reason for this broad variation is the use of natural stones as a source of fiber production. A comparative study of five different basalt fibers reports iron content in the range of 0.2 to 11.1 m% and titanium content in the range of 0.3 to 1.5 m% [142]. In comparison to these ranges, the actual EDS investigation of the basalt fiber leads to contents of iron and titanium which are in the former reported range, but with low values. In contrast, the determined amount of silicon is higher compared to earlier reported values.

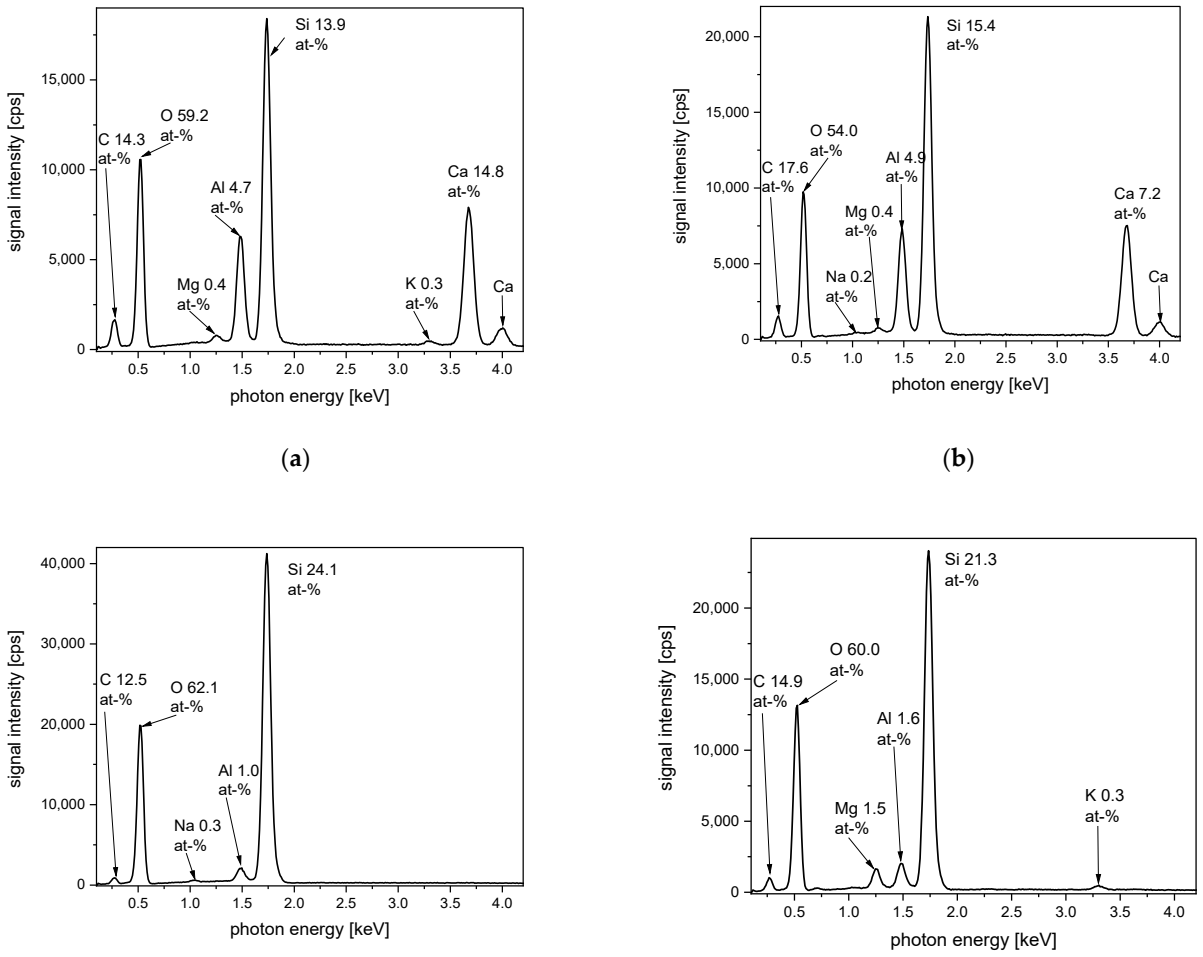


**Figure 29.** EDS spectra of different glass and silica fiber fabrics supplied by Culimeta: (**a**) e-glass fabric; (**b**) caramelized glass fabric; (**c**) silica fabric; (**d**) glass fabric modified with vermiculite particles.

Similar to the EDS spectra of glass fiber fabrics, the EDS spectrum of the basalt fibers also exhibits a signal for carbon. On this basalt fiber sample, carbon is recorded with around 37 at-%, which is a significant surface concentration. The presence of carbon on basalt fibers can be also be explained by the former application of sizing agents. An earlier investigation reports on the thermal and chemical removal of these carbon-containing compounds from the basalt fiber surface [143]. This former study also provides relevant information on the change in the mechanical properties of basalt fiber after thermal treatment. For basalt fibers, often $T_{max}$ values of around 700 °C are given, which are related to oxidative processes from FeO to $Fe_2O_3$. Nevertheless, even a thermal treatment in the range from 400 °C to 500 °C can significantly decrease the mechanical strength of basalt fibers [143].

### *7.2. Carbon Fibers*

Carbon fibers are mainly built up from the pure carbon of graphite specification [144]. Usually, they are produced by the pyrolysis of an organic precursor fiber under controlled conditions. Most often used are PAN fibers as precursors for carbon fibers [145–148]. However, other precursor fibers are also used, e.g., pitch-based fibers [149,150]. The main applications are found as fibers in fiber-reinforced materials. Carbon fibers are used for this purpose, because of their high strength [151,152]. However, their price is quite high compared to competing glass fibers or natural fibers, which are used in reinforcement materials as well [138].

For carbon fibers, two examples are given here, presented in Figures 31 and 32. Both samples are supplied by SGL Carbon AG (Wiesbaden, Germany). The first sample is taken from a roving and the other one from a carbon fiber fabric. The roving exhibits nearly a 98 at-% content of carbon, but oxygen also occurs with a concentration of around 2 at-% (Figure 31). This small content of oxygen can be explained by partial oxidation on the carbon fiber surface or by the application of organic sizing agents [153,154]. The electrochemical oxidation of carbon fibers is often used to improve the adhesion of carbon fibers to an epoxy-based matrix in a fiber-reinforced composite material [155].

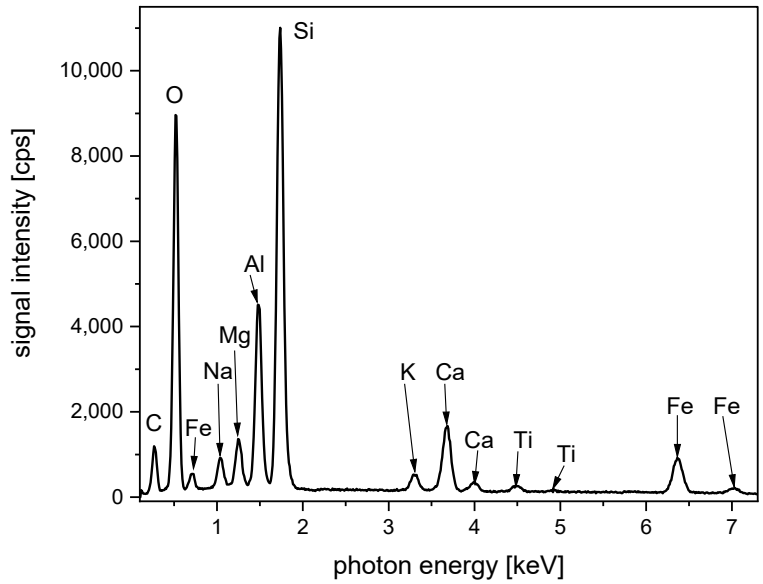


**Figure 30.** EDS spectrum taken from basalt fibers. The determined surface composition is in at-%: carbon 37.5; oxygen 36.9; silicon 13.3; aluminum 5.1; calcium 2.1; iron 1.6; magnesium 1.5; sodium 1.4; potassium 0.5; titanium 0.2.

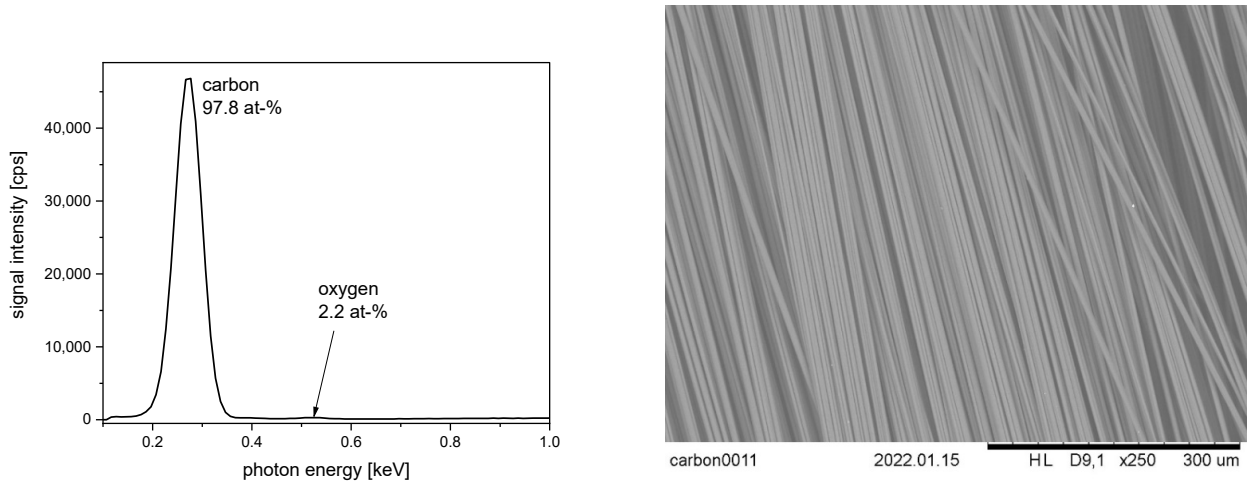


(**a**) (**b**)

**Figure 31.** Carbon fibers from roving (Sigrafil C)—(**a**) EDS spectrum; (**b**) SEM image.

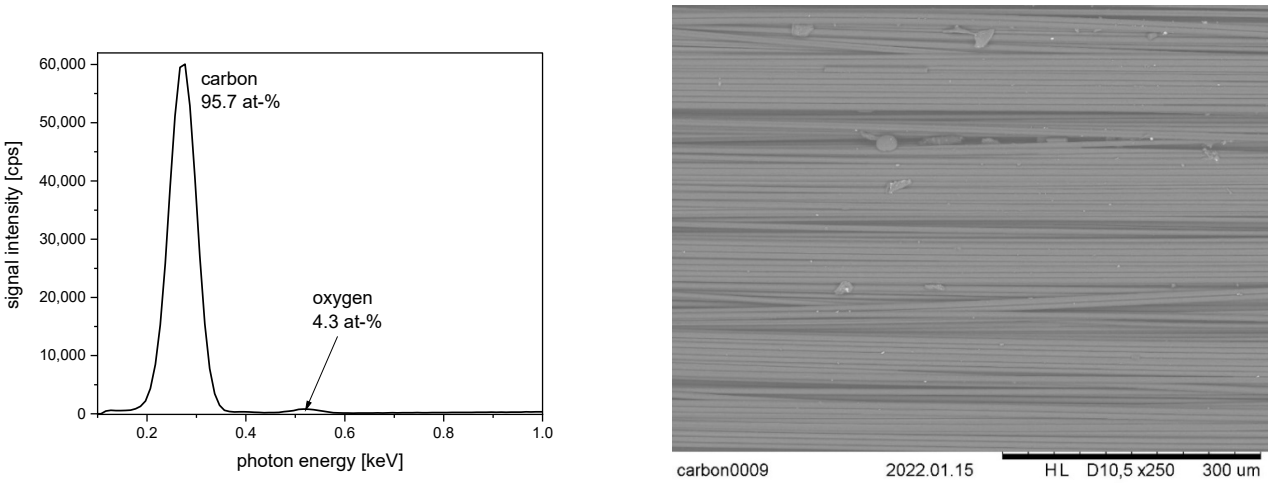


(**a**) (**b**)

**Figure 32.** Carbon fibers from fabric (Sigratex Fabric KDK)—(**a**) EDS spectrum; (**b**) SEM image.

The EDS spectrum taken from the carbon fiber fabric exhibits an increased amount of oxygen, with around 4 at-%. The related SEM image shows beside the carbon fibers also deposited agglomerates and particles which could also be related to the presence of sizing agents (Figure 32). These agglomerates are investigated in higher magnification by SEM and EDS mapping (Figure 33). By this, it is determined that, especially at surface areas with agglomerates, the oxygen content is high, so these agglomerates are probably related to the application of oxygen-containing sizing agents. Contamination by inorganic, oxidic particles can be excluded, due to the lack of other elements than carbon and oxygen in the spectrum.

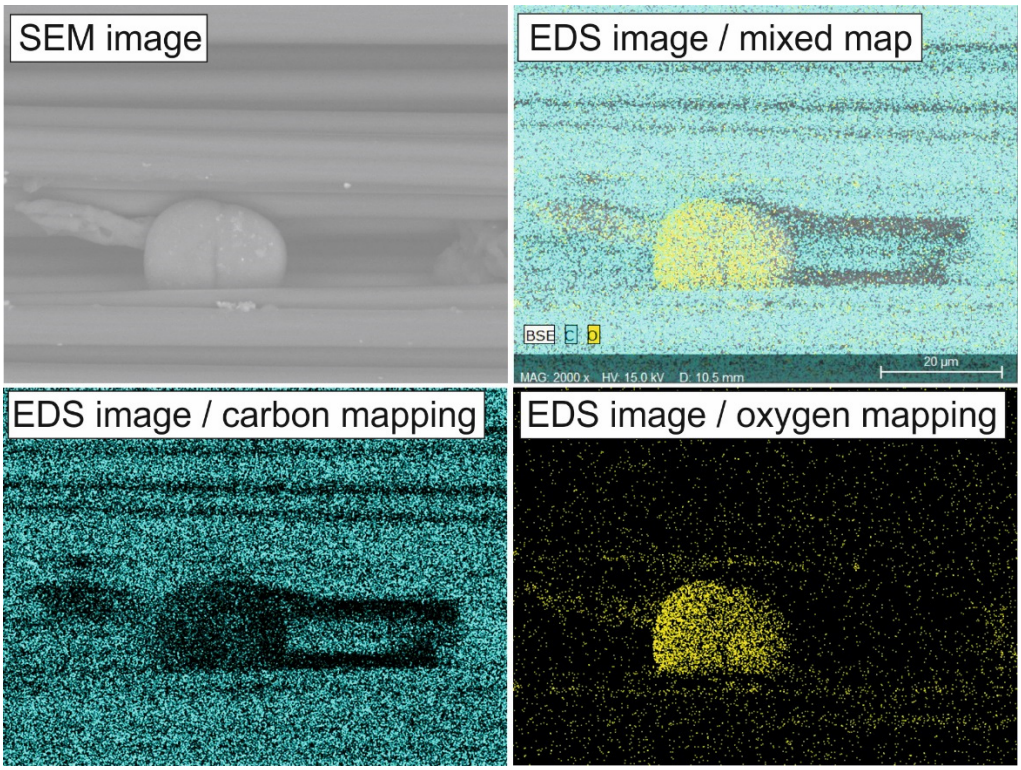


**Figure 33.** SEM image and related EDS images from fabric from carbon fibers (Sigratex Fabric KDK) recorded in higher magnification. The mappings for chemical elements carbon and oxygen are especially compared.

## 8. Metalized Textiles

This introduction should briefly address metalized fibers and textiles, which are probably the most fascinating materials combining the advantageous material properties of metals with textile properties and applications [156–158]. Either metal fibers introduced in conventional fabrics or fibers which are coated by metal layers can be used. Moreover, complete textile fabrics can be coated by metal layers [158,159]. From both types, several examples are presented here. Another method to realize metalized textiles is the application of coatings with embedded metal effect pigments [160]. Such metal effects containing coatings are not described, because for this topic, there is already a broad review published [161]. The metalization of textiles can also be achieved by physical vapor deposition ("sputtering"), usually of noble metals [158]. Such approaches are rather new and account for a niche of special applications. This can be catalytic functionalization, where noble metals are sputtered on top of a semiconductor nanoparticle finishing on textile fibers [162].

Applications of metalized textiles are found in areas where metal properties are especially demanded. Mostly, this is related to electric conductivity, antistatic properties, or the shielding of micro or radio waves [163–165]. In particular, the shielding of electrosmog is an important market segment [166]. An innovative field for metalized fibers is products like wearable E-textiles [167]. Another important application is antimicrobial textiles, mainly based on silver-coated fibers [168–172]. However, copper containing textile materials is also offered for antimicrobial purposes [173,174]. Membranes from metallized microfibers are also advantageous materials for the filtration of particles [175].

The first two examples are related to the applications for antimicrobial properties and electrosmog shielding (Figure 34). In both cases, a silver-coated polyamide fiber is introduced in a conventional fabric. The silver fiber exhibits a clear material contrast in the SEM-image. Because of the higher atomic weight of silver, silver-containing areas appear brighter compared to sample areas containing only light chemical elements, such as carbon, oxygen, and nitrogen.

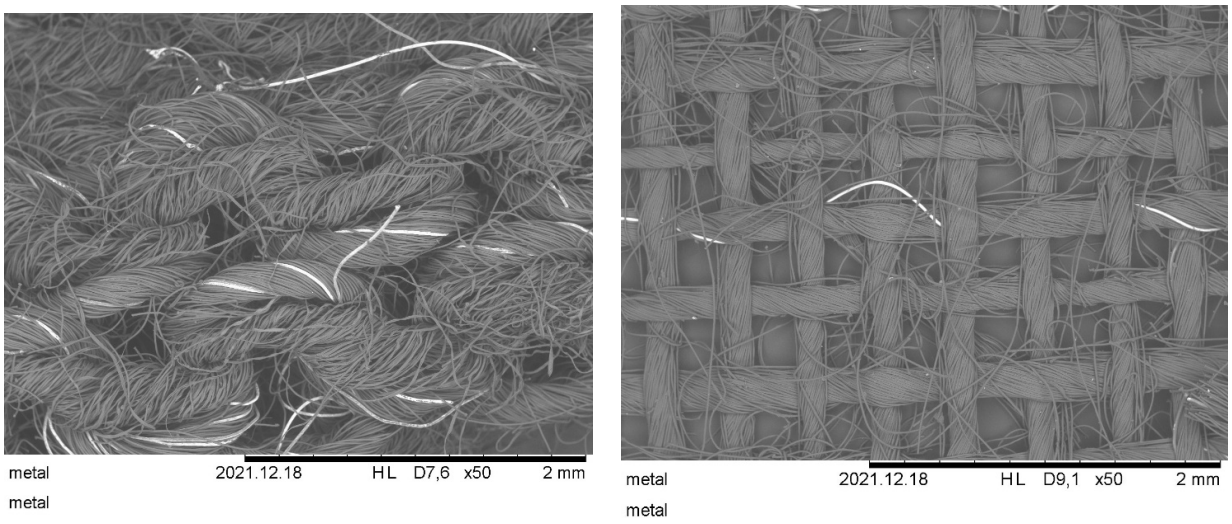


(**a**) (**b**)

**Figure 34.** SEM images of two commercial textile products containing silver fibers: (**a**) antimicrobial sock (Go Well MED X-Static); (**b**) woven fabric for electrosmog shielding (Evolution, YShield EMR-Protection).

To investigate such silver fiber products in more detail, SEM images and EDS mappings are recorded at higher magnification (Figure 35). The silver content can be clearly identified on the silver fiber. The according EDS-spectra of both textile samples are taken at a lower magnification of only 50x to obtain an average of the elemental content for a wider surface area (Figure 36). The surface concentration of silver is not high, but due to the good sensitivity of the EDS method for silver, this chemical element can be detected

clearly. Besides carbon and oxygen, the antimicrobial textile fabric contains only silver. The presence of silver is related to strong antimicrobial activity [176]. In comparison, the textile offered for shielding application also contains copper and phosphorous on the sample surface. The presence of copper is most likely due to its high electric conductivity, supporting the shielding of electrosmog. The presence of phosphorous can be related to corrosion protection to prevent the oxidation of the copper-containing coating into non-conductive copper oxide. Furthermore, a modification of the ductility of copper by the addition of phosphorous is reported [177,178].

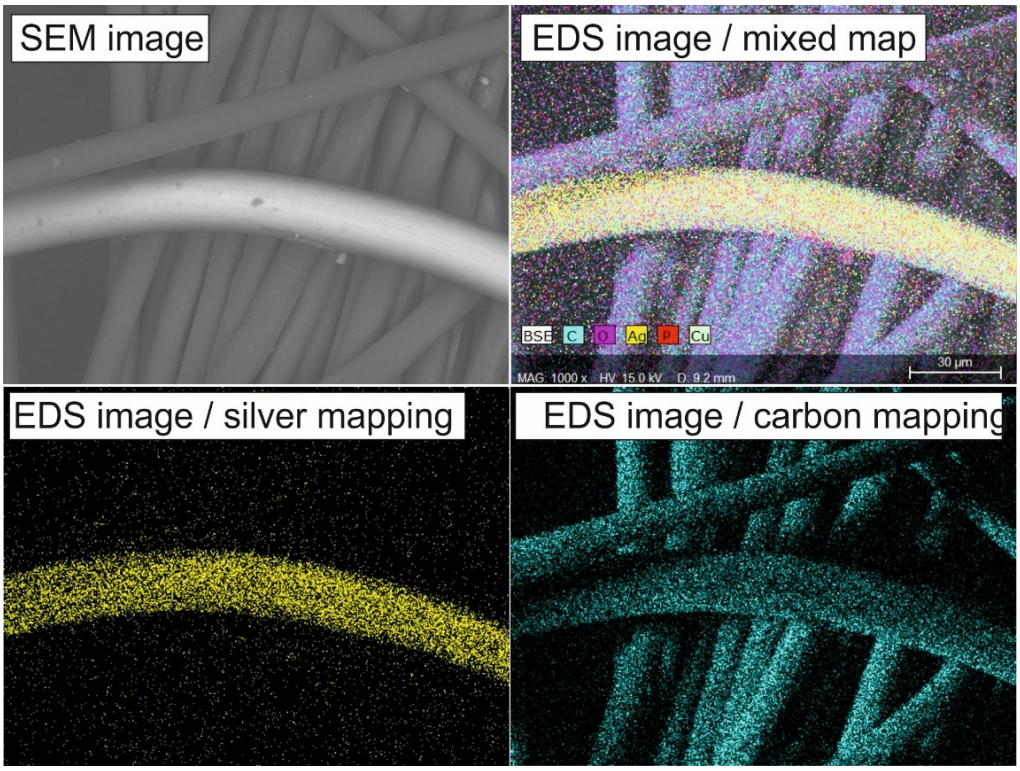


**Figure 35.** SEM image and related EDS images from a silver containing woven fabric (Evolution, YShield EMR-Protection). Compared are especially the mappings for the chemical elements silver and carbon.

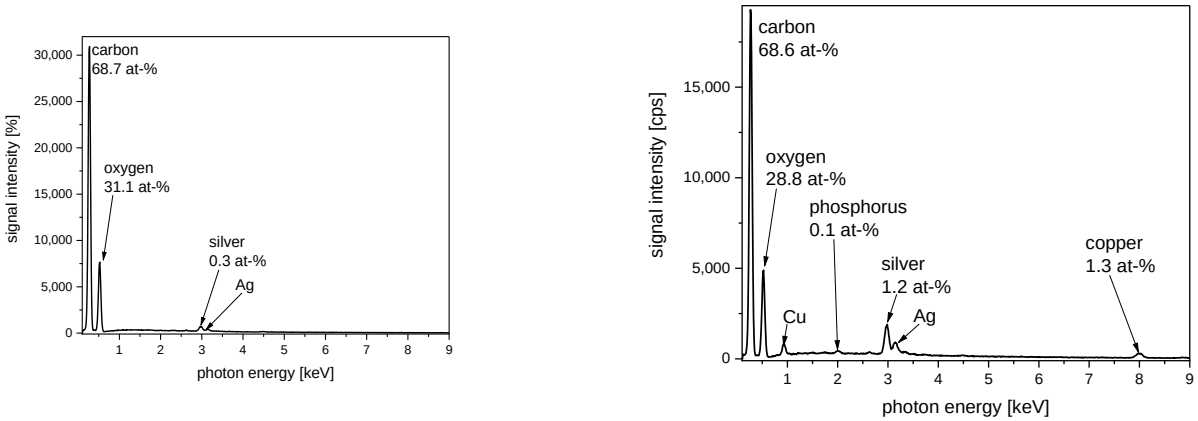


(**a**) (**b**)

**Figure 36.** EDS spectra of two commercial textile products containing silver fibers: (**a**) antimicrobial sock (Go Well MED X-Static); (**b**) woven fabric for electrosmog shielding (Evolution, YShield EMR-Protection).

The next product examples are both from the field of electrosmog shielding (Figures 37 and 38). At those samples, the complete fabrics are coated by metal layers of different compositions. With this complete coating, a strong shielding against microwaves up to 80 dB can be reached according to supplier information. As is visible in the SEM images, the metal coating covers the complete fabric evenly (Figure 37). By view of the EDS spectra, it is clear that the coatings are of different metal compositions (Figure 38). For sample (a), the coating is completely silver-based. Sample (b) contains a coating from copper and nickel. This coating can be described as an alloy in a certain way, similar to gold bronze materials.

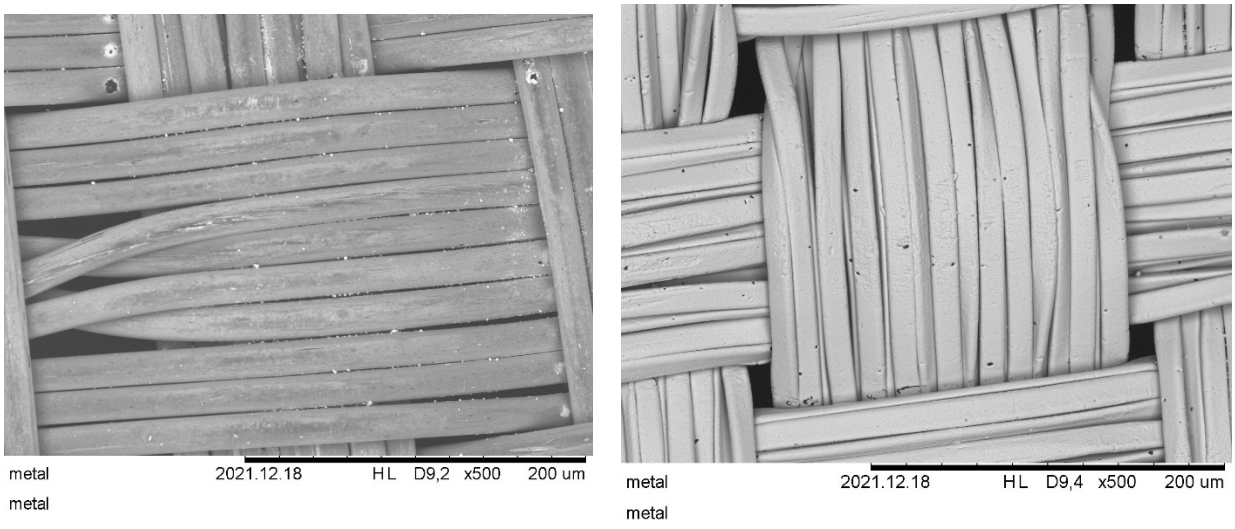


(**a**) (**b**)

**Figure 37.** SEM images of two commercial textile products offered for electrosmog shielding (YShield EMR-Protection): (**a**) fabric type silver silk with shielding rate of 60 dB; (**b**) fabric type HNG80 with a shielding rate 80 dB.

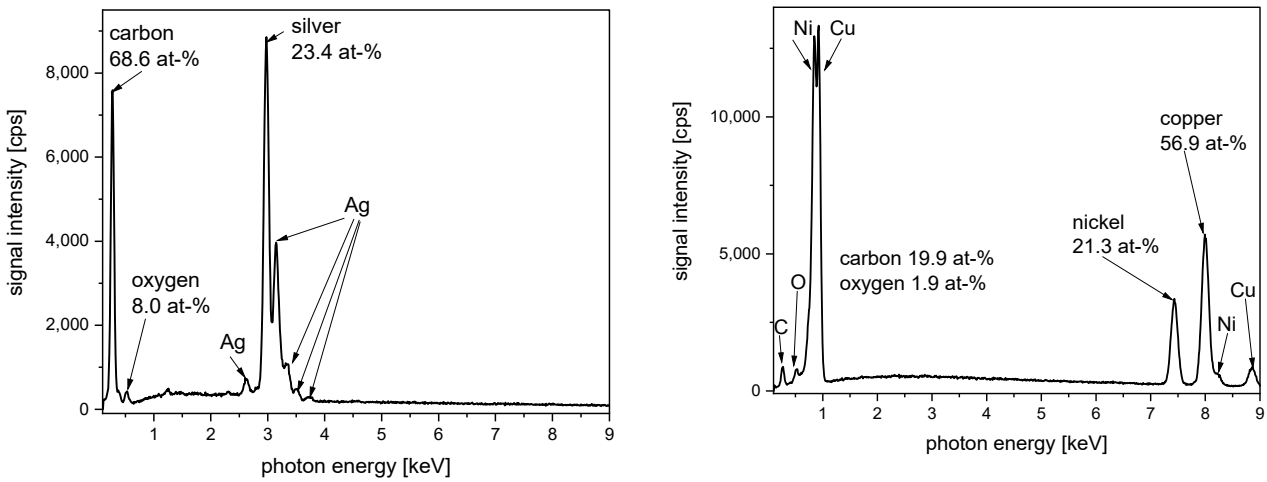


(**a**) (**b**)

**Figure 38.** EDS spectra of two commercial textile products offered for electrosmog shielding (YShield EMR-Protection): (**a**) fabric type silver silk with shielding rate of 60 dB; (**b**) fabric type HNG80 with a shielding rate 80 dB.

Figure 39 also presents a product example from electrosmog shielding. According to supplier information, this fabric is completely made up of metalized polyamide fibers. However, a polymer coating is also applied in addition to the metalization. This coating

also contains silicon-based components. The detected phosphorous can be related to the introduction of flame-retardant properties or as part of a corrosion protective component for the copper/nickel coating.

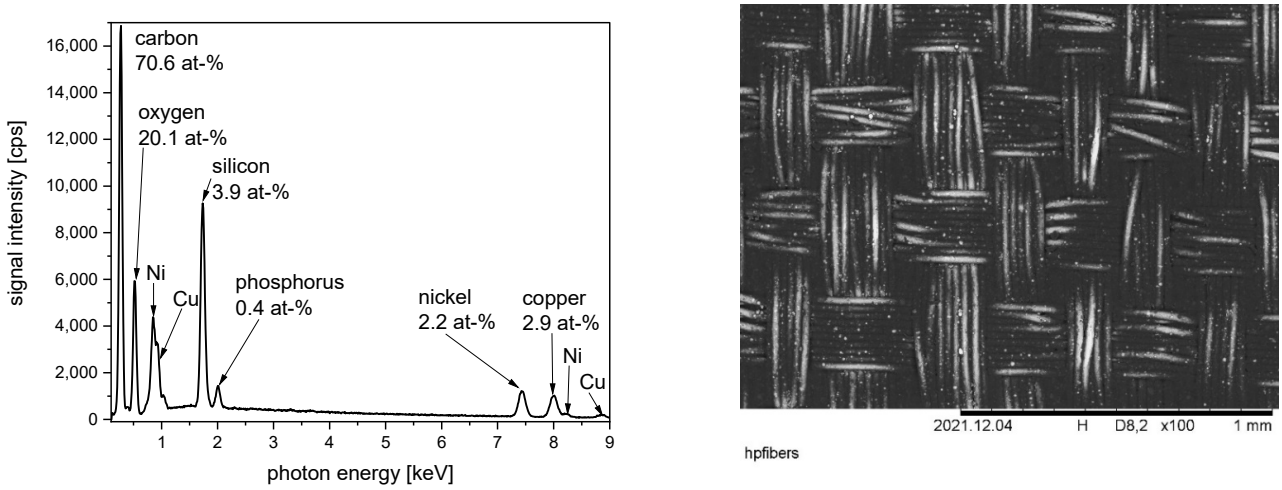


(**a**) (**b**)

**Figure 39.** Presentation of a commercially available metallized fabric supplied under the name SR-Shield (SR Webatex GmbH, Bayreuth, Germany) offered for the shielding of radio waves (electrosmog): (**a**) EDS spectrum of this fabric with detected chemical elements and their determined concentration; (**b**) SEM image.

Instead of using coated fibers or fabrics, complete metal fibers can also be introduced in textile fabrics [156,179]. For this type of product, an example is given here by a product using steel fibers for the realization of electrosmog shielding (Figures 40 and 41). The related EDS spectrum clearly exhibits signals for the three metals iron, chromium, and nickel (Figure 40). These metals are related to the composition of stainless steel. Furthermore, in the SEM image, these fibers are clearly visible, due to the materials contrast in the SEM-method for elements containing higher atomic weight.

To illustrate the distribution of chemical elements and the material contrast more in detail, SEM images are taken in higher magnification and are compared to EDS mappings (Figure 41). The difference between iron-containing steel fibers and carbon-containing cotton fibers is demonstrated.

The next product example for metallized textiles is given in Figure 42 with an aluminum-coated fabric. Such aluminum-coated fabrics are often used for heat management purposes, because of the strong reflectivity of aluminum for visible and infrared light. A window coverage made from such a fabric can avoid the unwished warming of a building by reflecting the heat radiation from the sun [180]. Besides aluminum, this product also contains phosphorous in small amounts. The phosphorous is probably added to prevent the unintended oxidation of aluminum on the metal surface, which would decrease the reflectivity drastically [181,182].

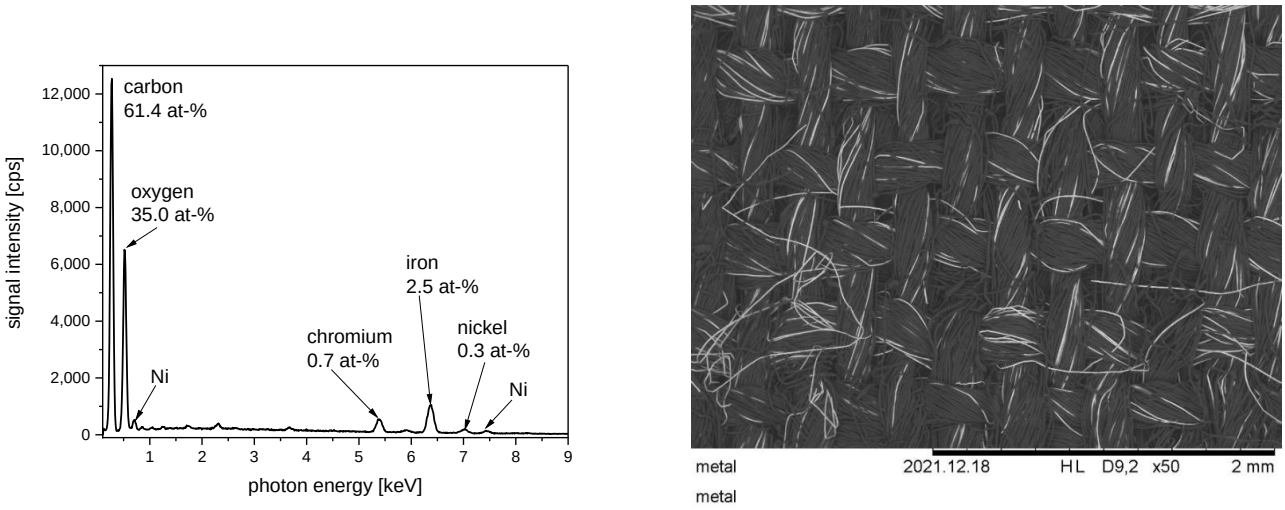


(**a**) (**b**)

**Figure 40.** Presentation of a commercially available fabric containing steel fibers offered for the shielding of radio waves (electrosmog) (product from YShield, type Steel-Twin): (**a**) EDS spectrum of this fabric with detected chemical elements and their determined concentration; (**b**) SEM image.

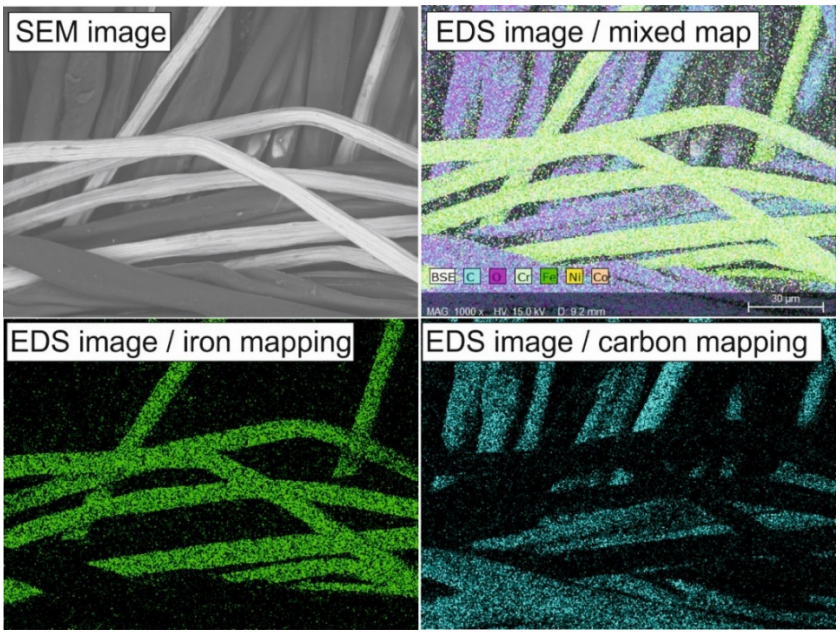


**Figure 41.** SEM image and related EDS images from fabric containing steel fibers (Steel Twin, YShield EMR-Protection). The mappings for the chemical elements iron and carbon are especially compared.

The last example in this review is a catalytic active textile material able to convert CO to $CO_2$ at room temperature. A polypropylene melt blown is covered with $TiO_2$ nanoparticles, and the composite material is subsequently coated with gold via a PVD process. The triple interface between the gas phase, $TiO_2$, and gold is the catalytic active site. In the SEM observation and EDS mapping (Figure 43), the distribution of titanium and gold is clearly visible and structural differences are evident. The titanium distribution is strongly correlated with the location of the particles visible in the SEM image, raising the suspicion that the particles are agglomerated. However, the local distribution of gold is much more even, which is expected due to the PVD process used to deposit the metal.

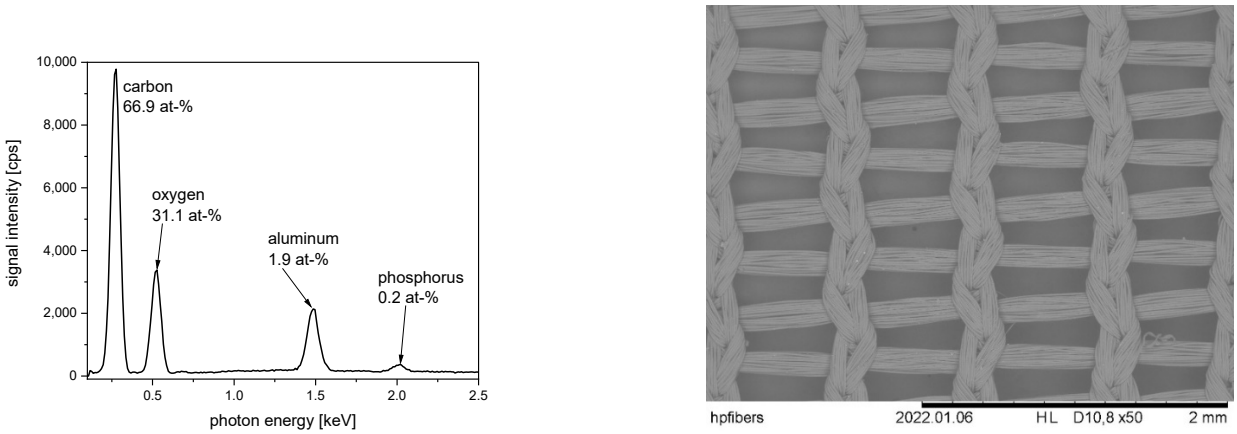


(**a**) (**b**)

**Figure 42.** Presentation of a commercially available fabric with aluminum plating (product from Creation Baumann AG, Langenthal, Switzerland): (**a**) EDS spectrum of this fabric with detected chemical elements and their determined concentration; (**b**) SEM image.

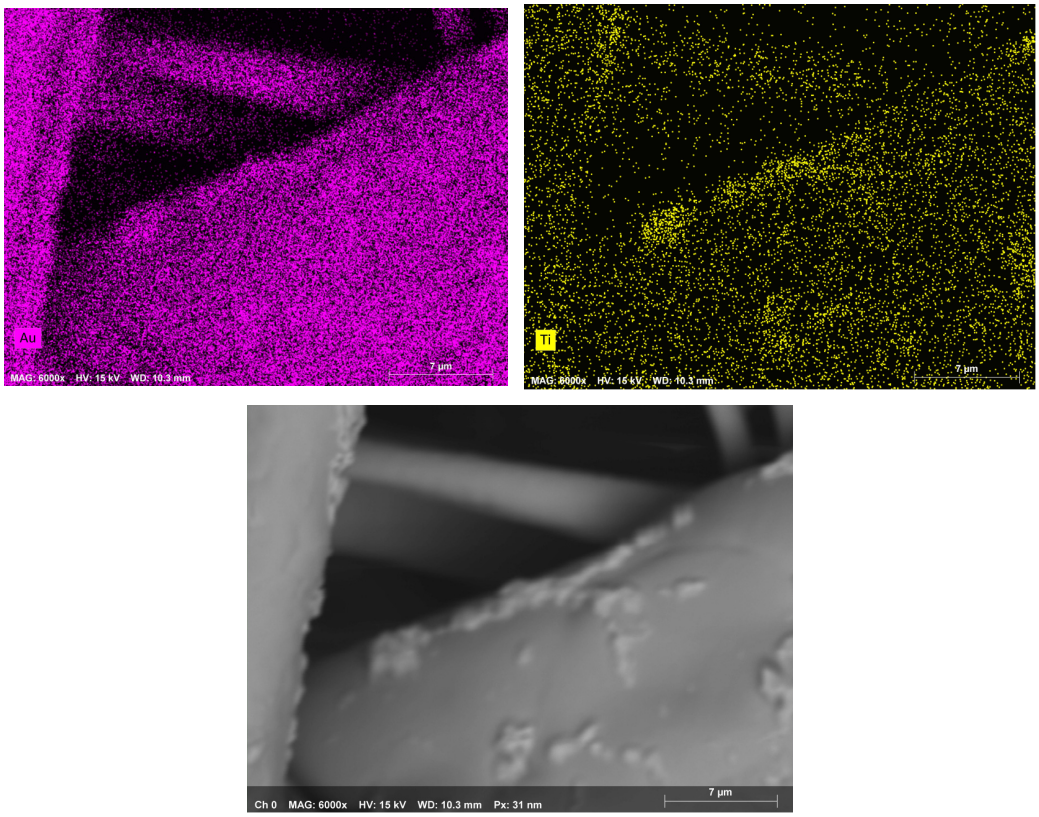


**Figure 43.** Presentation of a catalytic textile made from polypropylene melt blown material, equipped with a $TiO_2$ coating which was coated with gold by PVD. Gold mapping is shown in the top-left picture, titanium mapping on the right, and the lower image shows the corresponding SEM micrograph.

Although the resolution of the instrumentation is not sufficient to identify single $TiO_2$ nanoparticles or even the smaller gold depositions, valuable information about the sample composition can be derived from such analytics.

## 9. Summary and Conclusions

The concurrent evaluation of SEM micrographs and EDS measurements gives valuable information on textile materials and especially high-performance and functional fiber materials. These materials are in fact fascinating and exhibit outstanding properties in the areas of mechanical strength, flame-retardant properties, chemical stability, antimicrobial properties, and electric conductivity. In our modern world, the demand for high-performance and functional materials is high, and will probably increase in the future. Nevertheless, three issues have to be considered that could significantly influence the positive perspective of a certain high-performance material. First, the costs of high-performance and functional materials are significantly higher compared to conventional materials. Only if the benefit is absolutely clear will the consumer accept the costs and use the functional materials. Second, additional to the advantageous properties of high-performance materials, each of those materials also exhibits certain disadvantageous properties. These disadvantageous properties, like the low light stability of aramid fibers, limit the use of these fibers to certain areas. Third and most important, the use of specific fiber materials can be restricted by legal regulations, even if the material properties are excellent. There is probably a serious risk that several functional fiber materials will not be used in the future due to concern for health safety and environmental issues leading to drastic legal restrictions. The current review article reports additionally on selected material properties, and information on sample structure and chemical composition is reported. Although EDS can identify only chemical elements and not their connection among other forming molecules, the correlation of different EDS mappings can give helpful advice to estimate molecular compositions. For example, finding the same spatial distribution of silicon and oxygen but different from the distribution of other elements would place a high amount of suspicion on present $SiO_2$ or related silicates in the sample. For this, the presented paper is a useful tool for persons who are working in fiber analytics, especially in the field of high-performance and functional fiber materials. This conclusion statement is especially valid, because in recent years, there has been a strong development of SEM and EDS devices that can be easily operated. These devices allow even less skilled persons to access records of excellent SEM images and EDS spectra. However, the evaluation and interpretation of the recorded data are often still demanding. With this background, the presented and summarized data on high-performance and functional fiber materials are helpful for the analysis of unknown fiber materials.

**Author Contributions:** Both authors contribute measurements, data evaluation and writing of the article. All authors have read and agreed to the published version of the manuscript.

**Funding:** This research received no external funding.

**Institutional Review Board Statement:** Not applicable.

**Informed Consent Statement:** Not applicable.

**Data Availability Statement:** Not applicable.

**Acknowledgments:** The authors owe many thanks to Dipl.-Ing. Simone Wagner for her helpful advice and sample preparation done in the finishing laboratory (Hochschule Niederrhein, Faculty of Textile and Clothing Technology).

**Conflicts of Interest:** The authors declare no conflict of interest. All images or measurements presented in this review are originally performed. No funding was provided for this article to present any commercial products. All product and company names mentioned in this article may be trademarks of their respected owners, even without labeling.

## References

1. Hearle, J.W.S. *High-Performance Fibres*; Woodhead Publishing Limited: Cambridge, UK, 2001.
2. Paul, R. *High Performance Technical Textiles*; John Wiley & Sons: Hoboken, NJ, USA, 2019.

3. Sikkema, D.J.; Northolt, M.G.; Pourdeyhimi, B. Assessment of New High-Performance Fibers for Advanced Applications. *MRS Bull.* **2003**, *28*, 579–584. [CrossRef]
4. Afshari, M.; Sikkema, D.J.; Lee, K.; Bogle, M. High performance fibers based on rigid and flexible polymers. *Polym. Rev.* **2008**, *48*, 230–274. [CrossRef]
5. Avci, H.; Hassanin, A.; Hamouda, T.; Kilic, A. High performance fibers: A review on current state of art and future challenges. *J. Eng. Archit. Fac. Eskiseh. Osman. Univ.* **2019**, *27*, 130–155. [CrossRef]
6. Mahltig, B. High-Performance Fibres—A Review of Properties and IR-Spectra. *Tekstilec* **2021**, *64*, 96–118. [CrossRef]
7. Mahltig, B.; Textor, T. *Nanosols and Textiles*; World Scientific: Singapore, 2008.
8. Paul, R. *Functional Finishes for Textiles*; Woodhead Publishing: Cambridge, UK, 2005.
9. Mahltig, B.; Rabe, M.; Muth, M. Textiles, Dyeing, and Finishing. In *Kirk-Othmer Encyclopedia of Chemical Technology*; John Wiley & Sons, Inc.: Hoboken, NJ, USA, 2019; pp. 1–35. [CrossRef]
10. Mahltig, B.; Textor, T. Nanocoatings by sol-gel processes for functionalization of polymer surfaces and textiles. In *Handbook of Modern Coating Technologies*; Aliofkhazraei, M., Ali, N., Chipara, M., Laidani, N.B., de Hosson, J.T.M., Eds.; Elsevier: Amsterdam, The Netherlands, 2021; pp. 1–23.
11. Bourbigot, S.; Flambard, X. Heat resistance and flammability of high performance fibers: A review. *Fire Mater.* **2002**, *26*, 155–168. [CrossRef]
12. Mohd, Y. A Review on Flame Retardant Textile Finishing: Current and Future Trends. *Curr. Smart Mater.* **2018**, *3*, 99–108.
13. Engelhardt, A. Die Welt der Fasern. *Textilplus* **2018**, *7/8*, 10–13.
14. Hamburger Tauwerk Fabrik GmbH (Hamburg, Germany). Company Web Page. 2022. Available online: www.htf-hh.com/ (accessed on 31 January 2022).
15. Binamed Moll GmbH (Bayreuth, Germany). Company Web Page. 2022. Available online: www.binamed.de (accessed on 25 January 2022).
16. Colliex, C.; Kohl, H. *Elektronenmikroskopie*; Wissenschaftliche Verlagsgesellschaft: Stuttgart, Germany, 2007.
17. Gest, H. The discovery of microorganisms by Robert Hooke and Antoni van Leeuwenhoek, Fellows of The Royal Society. *Notes Rec. R. Soc. Lond.* **2004**, *58*, 187–201. [CrossRef]
18. Pawley, J. The Development of Field-Emission Scanning Electron Microscopy. *Scanning* **1997**, *19*, 324–336.
19. Brodusch, N.; Demers, H.; Gauvin, R. *Field Emission Scanning Electron Microscopy: New Perspectives for Materials Chazracterization*; Springer: Singapore, 2018.
20. Knoll, M.; Ruska, E. Das Elektronenmikroskop. *Z. Für Phys.* **1932**, *78*, 318–339. [CrossRef]
21. Chippindale, P. Replication of Textile Fibres in Electron Microscopy. *J. Text. Inst. Trans.* **1960**, *51*, T392–T397. [CrossRef]
22. Guthrie, J.C. Progress in the electron microscopy of textile fibres. *J. Text. Inst. Proc.* **1956**, *47*, P248–P268. [CrossRef]
23. Castaing, R.; Guinier, A. Sur l'exploration et l'analyse elementaire d'un echantillon par une sonde electronique. In Proceedings of the First International Congress of Electron Microscopy, Delft, The Netherlands, 4–8 July 1949; pp. 60–68.
24. Castaing, R.; Guinier, A. Point-by-point chemical analysis by X-ray spectroscopy. *Anal. Chem.* **1953**, *25*, 724–726. [CrossRef]
25. Colliex, C. The "father" of microanalysis: Raymond Castaing, creator of a generation of scientific instruments, still in worldwide operation. *Comptes Rendus Phys.* **2019**, *20*, 746–755. [CrossRef]
26. Duncumb, P. Precipitation studies with EMMA-a combined electron microscope and x-ray microanalyzer. *J. Electrochem. Soc.* **1964**, *111*, C203.
27. Duncumb, P. Microprobe design in the 1950s: Some examples in Europe. *Microsc. Microanal.* **2001**, *7*, 100–107. [CrossRef]
28. Weiying, T.; Collier, B.J. The Environmental Scanning Electron Microscope: A New Tool for Textile Studies. *Text. Chem. Colorist* **1994**, *26*, 29–31.
29. Danilatos, G.D. Introduction to the ESEM instrument. *Microsc. Res. Tech.* **1993**, *25*, 354–361. [CrossRef]
30. Jenkins, L.M.; Donald, A.M. Use of Environmental Scanning Electron Microscope for the Observation of the Swelling Behaviour of Cellulosic Fibres. *Scanning* **1997**, *19*, 92–97. [CrossRef]
31. Schellenberger, S.; Gillard, P.; Stare, A.; Hanning, A.; Levenstam, O.; Ross, S.; Cousins, I.T. Facing the rain after the phase out: Performance evaluation of alternative fluorinated and non-fluorinated durable water repellents for outdoor fabrics. *Chemosphere* **2018**, *193*, 675–684. [CrossRef]
32. Mahltig, B.; Bidu, J.; Grethe, T.; Pascuali, P.; Kyosev, Y. Rasterelektronenmikroskopie an textilen Oberflächen. *Textilplus* **2013**, *1*, 30–33.
33. Hitachi. Product Brochure TM3030. Available online: www.hitachi-hightech.com (accessed on 15 February 2022).
34. Wei, Q.F.; Wang, X.Q.; Mather, R.R.; Fotheringham, A.F. New Approaches to Characterisation of Textile Materials Using Environmental Scanning Electron Microscope. *Fibres Text. East. Eur.* **2004**, *12*, 79–83.
35. Muscariello, L.; Rosso, F.; Marino, G.; Giordano, A.; Barbarisi, M.; Cafiero, G.; Barbarisi, A. A critical overview of ESEM applications in the biological field. *J. Cell. Physiol.* **2005**, *205*, 328–334. [CrossRef] [PubMed]
36. Li, V.C. Large volume, high-performance applications of fibers in civil engineering. *J. Appl. Polym. Sci.* **2002**, *83*, 660–686. [CrossRef]
37. Grujicic, M.; Glomski, P.S.; He, T.; Arakere, G.; Bell, W.C.; Cheeseman, B.A. Material Modeling and Ballistic-Resistance Analysis of Armor-Grade Composites Reinforced with High-Performance Fibers. *J. Mater. Eng. Perform.* **2009**, *18*, 1169–1182. [CrossRef]
38. Park, J.H.; Rutledge, G.C. Ultrafine high performance polyethylene fibers. *J. Mater. Sci.* **2018**, *53*, 3049–3063. [CrossRef]

39. McQuerry, M. A Review of Ballistic, Slash, and Stab Protection for Integration in First Responder Personal Protective Clothing. *J. Text. Sci. Fash. Technol.* **2019**, *2*, 1–5. [CrossRef]
40. Zhai, Y.; Mao, L.; Shen, Y.; Yan, X. Research Progress of Cut-Resistant Textile Materials. *Front. Chem.* **2021**, *9*, 745467. [CrossRef]
41. Roy, R.; Majumdar, A.; Butola, B.S. Comparative Study of p-aramid Based Soft and Stiff Composite Panels for Protective Application. *Fibers Polym.* **2019**, *20*, 406–412. [CrossRef]
42. Khusiafan, F.J. Use of Kevlar49 in Aircraft Components. *Eng. Manag. Res.* **2018**, *7*, 14–19. [CrossRef]
43. Priyanka, P.; Dixit, A.; Mali, H.S. High strength Kevlar fiber reinforced advanced textile composites. *Iran. Polym. J.* **2019**, *28*, 621–638. [CrossRef]
44. Stockdale, T.A.; Cole, D.P.; Staniszewski, J.M.; Roenbeck, M.R.; Papkov, D.; Lustig, S.R.; Dzenis, Y.A.; Strawhecker, E. Hierarchical Mechanisms of Lateral Interactions in High-Performance Fibers. *ACS Appl. Mater. Interfaces* **2020**, *12*, 22256–22267. [CrossRef] [PubMed]
45. Tesoro, G.C.; Meiser, C.H. Some Effects of Chemical Composition on the Flammability Behavior of Textiles. *Text. Res. J.* **1970**, *40*, 430–436. [CrossRef]
46. Yang, C.Q.; He, Q.; Lyon, R.E.; Hu, Y. Investigation of the flammability of different textile fabrics using micro-scale combustion calorimetry. *Polym. Degrad. Stab.* **2010**, *95*, 108–115. [CrossRef]
47. BWF Protec. BWF Tec GmbH, Technical Data Sheet. 2021. Available online: https://bwf-group.com/en/protec/products/technical-needle-felts/ (accessed on 22 November 2021).
48. Loy, W. *Chemiefasern Für Technische Textilprodukte*; Deutscher Fachverlag: Frankfurt am Main, Germany, 2008.
49. Gul, R.; Islam, A.; Yasin, T.; Mir, S. Flame-retardant synergism of sepiolite and magnesium hydroxide in a linear low-density polyethylene composite. *J. Appl. Polym. Sci.* **2011**, *121*, 2772–2777. [CrossRef]
50. Bilisik, K. Experimental determination of yarn pull-out properties of para-aramid (Kevlar®) woven fabric. *J. Ind. Text.* **2011**, *41*, 201–221. [CrossRef]
51. Liu, X.; Yu, W.; Xu, P. Improving the Photo-stability of High Performance Aramid Fibers by Sol-gel treatment. *Fibers Polym.* **2008**, *9*, 455–460. [CrossRef]
52. Liu, X.; Yu, W. Degradation of PBO Fiber by Heat and Light. *RJTA* **2006**, *10*, 26–32. [CrossRef]
53. Kuraray. VectranTM, Product Brochure. 2021. Available online: https://www.kuraray.eu/products-solutions/product-ranges/vectran (accessed on 22 November 2021).
54. Chae, H.G.; Kumar, S. Rigid-rod polymeric fibers. *J. Appl. Polym. Sci.* **2006**, *100*, 791–802. [CrossRef]
55. Menczel, J.D.; Collins, G.L.; Saw, S.K. Thermal analysis of Vectran® fibers and films. *J. Therm. Anal.* **1997**, *49*, 201–208. [CrossRef]
56. Yao, K.D.; Han, W.; Han, D. Flame-retarding modification of nylon 6 textile. *J. Appl. Polym. Sci.* **1992**, *46*, 467–470. [CrossRef]
57. Kilinc, M.; Cakal, G.O.; Bayram, G.; Eroglu, I.; Özkar, S. Flame retardancy and mechanical properties of PET-based composites containing phosphorus and boron-based additives. *J. Appl. Polym. Sci.* **2015**, *132*, 42016. [CrossRef]
58. Mather, R.R.; Wardman, R.H. *The Chemistry of Textile Fibres*; RSC Publishing: Cambridge, UK, 2011.
59. Jakubke, H.-D.; Jeschkeit, H. *Concise Encyclopedia Chemistry*; Walter de Gruyter: Berlin, Germany, 1993.
60. Anton, C.; Mackley, M.R.; Solbai, S.B. Extrusion processing of ultra-high molecular weight polyethylene; a new method for the production of high performance structures. *Polym. Bull.* **1987**, *17*, 175–179. [CrossRef]
61. Deitzel, J.M.; McDaniel, P.; Gillespie, J.W. High performance polyethlyene fibers. In *Structure and Properties of High-Performance Fibers*; Bhat, G., Ed.; Woodhead Publishing: Cambridge, UK, 2017; pp. 167–185.
62. Kavesh, S.; Prevorsek, D.C. Ultra high strength, high modulus polyethylene spectra fibers and composites. *Int. J. Polym. Mater. Polym. Biomater.* **1995**, *30*, 15–56. [CrossRef]
63. Honeywell. Company Web Page. 2022. Available online: https://industrial.honeywell.com/us/en/products/high-strength-fibers (accessed on 25 January 2022).
64. Exxon Mobil. Product Data Sheets on Company Web Page. 2022. Available online: https://www.exxonmobilchemical.com/en/resources/product-data-sheets/polyethylene/exceed-xp-performance-pe-polymers (accessed on 25 January 2022).
65. Tongylzhong. Company Web Page. 2022. Available online: www.bjtyz.com/en/business/filamentary.html?gclid=CjwKCAiA3L6PBhBvEiwAINlJ9Pu_oKkuQ4KVR-w0x14WVyh-LfCvGGwL2I2fPFEk3G8-AIyTt4b3fxoCcOsQAvD_BwE (accessed on 25 January 2022).
66. Akonda, M.H.; Kandola, B.K.; Horrocks, A.R. Effect of alkali and ultraviolet aging on physical, thermal, and mechanical properties of fibers for potential use as reinforcing elements in glass/silicate composites. *Polym. Adv. Technol.* **2012**, *23*, 1454–1463. [CrossRef]
67. Liu, X.; Yu, W. Evaluating the thermal stability of high performance fibers by TGA. *J. Appl. Polym. Sci.* **2006**, *99*, 937–944. [CrossRef]
68. Song, B.; Meng, L.H.; Huang, Y.D. Influence of plasma treatment time on plasma induced vapor phase grafting modification of PBO fiber surface. *Appl. Surf. Sci.* **2012**, *258*, 5505–5510. [CrossRef]
69. Bartusch, M.; Hund, R.-D.; Hund, H.; Cherif, C. Surface Functionalisation of UHMW Polyethylene Textile with Atmospheric Pressure Plasma. *Fibers Polym.* **2014**, *15*, 736–743. [CrossRef]
70. FashionWorld Network. Web Page. 2022. Available online: https://www.fashionatingworld.com/new1-2/dyneema-fiber-is-stronger-than-steel (accessed on 16 February 2022).
71. Qin, Y.; Brydon, D.L.; Mather, R.R.; Wardman, R.H. Fibres from polypropylene and liquid crystal polymer blends: 3. A comparison of polyblend fibres containing Vectra A900, Vectra B950 and Rodrun LC3000. *Polymer* **1993**, *34*, 3597–3604. [CrossRef]

72. Biswas, M.A.K.; Shayed, M.A.; Hund, R.D.; Cherif, C. Surface modification of Twaron aramid fiber by the atmospheric air plasma technique. *Text. Res. J.* **2013**, *83*, 406–417. [CrossRef]
73. Mahltig, B. Hydrophobic and oleophobic finishes for textiles. In *Functional Finishes for Textiles*; Paul, R., Ed.; Woodhead Publishing: Cambridge, UK, 2015; pp. 387–428.
74. Türk, M.; Ehrmann, A.; Mahltig, B. Water-, oil-, and soil-repellent treatment of textiles, artificial leather, and leather. *J. Text. Inst.* **2015**, *106*, 611–620. [CrossRef]
75. Jung, H.; Kim, M.-K.; Jang, S. Liquid-repellent textile surfaces using zirconium (Zr)-based porous materials and a polyhedral oligomeric silsesquioxane coating. *J. Colloid Interf. Sci.* **2020**, *563*, 363–369. [CrossRef] [PubMed]
76. Gargoubi, S.; Baffoun, A.; Harzallah, O.A.; Hamdi, M.; Boudokhane, C. Water repellent treatment for cotton fabrics with long-chain fluoropolymer and its short-chain eco-friendly alternative. *J. Text. Inst.* **2020**, *111*, 835–845. [CrossRef]
77. Shabanian, S.; Khatir, B.; Nisar, A.; Golovin, K. Rational design of perfluorocarbon-free oleophobic textiles. *Nat. Sustain.* **2020**, *3*, 1059–1066. [CrossRef]
78. Mahltig, B.; Tatlises, B.; Fahmi, A. Dendrimers for the functionalisation of textiles. In *Dendrimers: Synthesis, Applications and Role in Nanotechnology*; Harris, H.B., Turner, B.L., Eds.; Nova Science Publishers Inc.: New York, NY, USA, 2013; pp. 229–248.
79. Paciorek, K.L.; Kratzer, R.H.; Kaufman, J. Oxidative thermal degradation of polytetrafluoroethylene. *J. Polym. Sci. Polym. Chem. Ed.* **1973**, *11*, 1465–1473. [CrossRef]
80. Zhang, M.; Niu, H.; Chang, J.; Ge, Q.; Cao, L.; Wu, D. High-performance fibers based on copolyimides containing benzimidazole and ether moieties: Molecular packing, morphology, hydrogen-bonding interactions and properties. *Polym. Eng. Sci.* **2015**, *55*, 2615–2625. [CrossRef]
81. Khan, M.U.; Mahltig, B. Modification of Polyacrylonitrile (PAN) fibers to improve affinity to anionic components. In *Polymer Research: Communicating Current Advances, Contributions, Applications and Educational Aspects*; Mendez-Vilas, A., Ed.; Formatex Research Center: Badajoz, Spain, 2018; pp. 19–26.
82. Gupta, M.L.; Gupta, B.; Oppermann, W.; Hardtmann, G. Surface modification of polyacrylonitrile staple fibers via alkaline hydrolysis for superabsorbent applications. *J. Appl. Polym. Sci.* **2004**, *91*, 3127–3133. [CrossRef]
83. Karbownik, I.; Rac-Rumijowska, O.; Fiedot-Tobola, M.; Rybicki, T.; Teterycz, H. The Preparation and Characterization of Polyacrylonitrile-Polyaniline (PAN/PANI) Fibers. *Materials* **2019**, *12*, 664. [CrossRef]
84. Wang, H.; Wang, P.; Zhang, H.; Hu, D. Preparation and characterization of triangular hollow porous polyacrylonitrile fiber made by coaxial wet spinning. *J. Appl. Polym. Sci.* **2021**, *138*, 50816. [CrossRef]
85. Tanthapanichakoon, W.; Furuuchi, M.; Nitta, K.-H.; Hata, M.; Endoh, S.; Otani, Y. Degradation of semi-crystalline PPS bag-filter materials by NO and $O_2$ at high temperature. *Polym. Degrad. Stab.* **2006**, *91*, 1637–1644. [CrossRef]
86. Lian, D.; Dai, J.; Zhang, R.; Niu, M.; Huang, Y. Enhancing the resistance against oxidation of polyphenylene sulphide fiber via incorporation of nano $TiO_2$-$SiO_2$ and its mechanistic analysis. *Polym. Degrad. Stab.* **2016**, *129*, 77–86. [CrossRef]
87. Xiao, H.; Zhao, T. One-Bath Union Dyeing of Wool/Acrylic Blend Fabric with Cationic Reactive Dyes Based on Azobenzene. *Fibers Polym.* **2019**, *19*, 331–339. [CrossRef]
88. Kalashnik, A.T.; Panishkina, O.N.; Serkov, A.T.; Budnitski, G.A. The structure of acrylic fibres. *Fibre Chem.* **2002**, *34*, 393–399. [CrossRef]
89. Huang, H.; Liu, M.; Li, Y.; Yu, Y.; Yin, X.; Wu, J.; Chen, S.; Xu, J.; Wang, L.; Wang, H. Polyphenylene sulfide microfiber membrane with superhydrophobicity and superoleophilicity for oil/water separation. *J. Mater. Sci.* **2018**, *53*, 13243–13252. [CrossRef]
90. Goodwin, P. Flammability Testing—A Burning Issue for Technical Textiles. *Technol. Text. Int.* **2006**, *15*, 11–14.
91. Mazari, A.; Mazari, F.B.; Naeem, J.; Havelka, A.; Marahatta, P. Impact of ultraviolet radiation on thermal protective performance and comfort properties of firefighter protective clothing. *Ind. Text.* **2022**, *73*, 54–61. [CrossRef]
92. Holder, K.M.; Smith, R.J.; Grunlan, J.C. A review of flame retardant nanocoatings prepared using layer-by-layer assembly of polyelectrolytes. *J. Mater. Sci.* **2017**, *52*, 12923–12959. [CrossRef]
93. Kaneka Corporation. Company Web Page. 2022. Available online: https://www.modacrylic.com/en/about/advantage05 (accessed on 16 February 2022).
94. Kakvan, A.; Najar, S.S.; Psikuta, A. Analysis of the Thermal Comfort Properties and Heat Protection Performance of Cotton/Nylon-Kermel Fabrics. *J. Text. Polym.* **2016**, *4*, 37–43.
95. Evonik. P84 Fibre Technical Brochure. 2021. Available online: https://www.p84.com/en/polyimide-fibres-chemistry (accessed on 22 November 2021).
96. Kynol. Product Brochure. 2021. Available online: http://www.kynol.de/products.html (accessed on 22 November 2021).
97. Kofler, P.; Herten, A.; Heinrich, D.; Bottoni, G.; Hasler, M.; Faulhaber, M.; Bechtold, T.; Nachbauer, W.; Burtscher, M. Viscose as an alternative to aramid in workwear: Influence of endurance performance, cooling and comfort. *Text. Res. J.* **2013**, *83*, 2085–2092. [CrossRef]
98. Heidari, S.; Paren, A. Surface Modification of Hybrid Fibres for Fire Protection. *Fire Mater.* **1993**, *17*, 65–69. [CrossRef]
99. Kermel. Company Webpage. 2022. Available online: http://www.kermel.com/en/ (accessed on 16 February 2022).
100. Ramgobin, A.; Fontaine, G.; Bourbigot, S. Investigation of the thermal stability and fire behavior of high performance polymer: A case study of polyimide. *Fire Saf. J.* **2021**, *120*, 103060. [CrossRef]
101. Borgstädt, T.; Mahltig, B. Laser treatment of high-performance Kynol fibers: An example as alternative tool for coloration and imaging on surfaces of high-performance fibers. *Tekst. Ind.* **2020**, *68*, 4–9. [CrossRef]

102. Pusch, J.; Wohlmann, B. Preox Fibers. In *Inorganic and Composite Fibers*; Mahltig, B., Kyosev, Y., Eds.; Woodhead Publishing: Cambridge, UK, 2018; pp. 53–60.
103. Khan, A.N.; Abir, N.; Rakib, M.A.N.; Bhuiyan, E.M.S.; Howlader, M.R. A Review Paper on Textile Fiber Identification. *IOSR J. Polym. Text. Eng.* **2017**, *4*, 14–20. [CrossRef]
104. Trevira. Company Web Page. 2022. Available online: https://www.trevira.de/trevira-cs/trevira-cs-wie-trevira-cs-funktioniert (accessed on 17 February 2022).
105. Mahltig, B. *Cellulosic-Based Composite Fibers*; Mahltig, B., Kyosev, Y., Eds.; Woodhead Publishing: Cambridge, UK, 2018; pp. 277–302.
106. Li, C.X.; Ji, Q.; Song, C.C.; Quan, F.Y. Flame Retardant Properties of Viscose Fibers Containing Talcum Powder. *Adv. Mater. Res.* **2014**, *884*, 208–211. [CrossRef]
107. Paul, B.; Mahmud-Ali, A.; Lenninger, M.; Eberle, S.; Bernt, I.; Mayer, D.; Bechthold, T. Silica incorporated cellulose fibres as green concept for textiles with reduced flammability. *Polym. Degrad. Stab.* **2022**, *195*, 109808. [CrossRef]
108. Xie, K.; Gao, A.; Zhang, Y. Flame retardant finishing of cotton fabric based on synergistic compounds containing boron and nitrogen. *Carbohydr. Polym.* **2013**, *98*, 706–710. [CrossRef]
109. Nabipour, H.; Wang, X.; Song, L.; Hu, Y. Hydrophobic and flame-retardant finishing of cotton fabrics for water–oil separation. *Cellulose* **2020**, *27*, 4145–4159. [CrossRef]
110. Kappes, R.S.; Urbainczyk, T.; Artz, U.; Textor, T.; Gutmann, J.S. Flame retardants based on amino silanes and phenylphosphonic acid. *Polym. Degrad. Stab.* **2016**, *129*, 168–179. [CrossRef]
111. Castellano, A.; Colleoni, C.; Iacono, G.; Mezzi, A.; Plutino, M.R.; Malucelli, G.; Rosace, G. Synthesis and characterization of a phosphorous/nitrogen based sol-gel coating as a novel halogen- and formaldehyde-free flame retardant finishing for cotton fabric. *Polym. Degrad. Stab.* **2019**, *162*, 148–159. [CrossRef]
112. Weil, E.D.; Levchik, S.V. Flame Retardants in Commercial Use or Development for Textiles. *J. Fire Sci.* **2008**, *26*, 243–281. [CrossRef]
113. Kemp, S.E.; Annaheim, S.; Rossi, R.M.; Camenzind, M.A. Test method for characterizing the thermal protective performance of fabrics exposed to flammable liquid fires. *Fire Mater.* **2017**, *41*, 750–767. [CrossRef]
114. Uddin, F. Recent Flame Retardant Consumption: Textiles. *Int. J. Sci. Eng. Res.* **2019**, *10*, 805–813.
115. Kim, H.; Kim, J.-S.; Jeong, W. Study on the Flame Retardancy and Hazard Evaluation of Poly(acrylonitrile-co-vinylidene chloride) Fibers by the Addition of Antimony-Based Flame Retardants. *Polymers* **2022**, *14*, 42. [CrossRef] [PubMed]
116. Cook, T.F. Inorganic Fibers—A Literature Review. *J. Am. Ceram. Soc.* **1991**, *74*, 2959–2978. [CrossRef]
117. Mahltig, B. Introduction to Inorganic Fibers. In *Inorganic and Composite Fibers*; Mahltig, B., Kyosev, Y., Eds.; Woodhead Publishing: Cambridge, UK, 2018; pp. 1–30.
118. Wiberg, N. *Lehrbuch der Anorganischen Chemie*; Walter de Gruyter: Berlin, Germany, 1995.
119. Schawaller, D.; Clauß, B.; Buchmeiser, M.R. Ceramic Filament Fibers—A Review. *Macromol. Mater. Eng.* **2012**, *297*, 502–522. [CrossRef]
120. Bauer, F.; Kempf, M.; Weiland, F.; Middendorf, P. Structure-property relationships of basalt fibers for high performance applications. *Compos. Part B Eng.* **2018**, *145*, 121–128. [CrossRef]
121. Kim, J.S.; Lim, J.H.; Huh, Y. Melt-spinning basalt fibers based on dielectric heating and steady-state process characteristics. *Fibers Polym.* **2013**, *14*, 1148–1156. [CrossRef]
122. Jamshaid, H.; Mishra, R. A green material from rock: Basalt fiber—A review. *J. Text. Inst.* **2016**, *107*, 923–937. [CrossRef]
123. Pala, I.E.; Kaya, C.P. Textile fibres in product design. *Ind. Text.* **2021**, *72*, 340–345. [CrossRef]
124. Martynova, E.; Cebulla, H. Glass Fibres. In *Inorganic and Composite Fibers*; Mahltig, B., Kyosev, Y., Eds.; Woodhead Publishing: Cambridge, UK, 2018; pp. 131–164.
125. Wallenberger, T.; Bingham, P.A. *Fiberglass and Glass Technology*; Springer: New York, NY, USA, 2010.
126. Teschner, R. *Glasfasern*; Springer: Berlin, Germany, 2019.
127. Lipatov, Y.V.; Gutnikov, S.I.; Manylov, M.S.; Lazoryak, B.I. Effect of $ZrO_2$ on the alkali resistance and mechanical properties of basalt fibers. *Inorg. Mater.* **2012**, *48*, 751–756. [CrossRef]
128. Flores, O.; Bordia, R.K.; Nestler, D.; Krenkel, W.; Motz, G. Ceramic Fibers Based on SiC and SiCN Systems: Current Research, Development, and Commercial Status. *Adv. Eng. Mater.* **2014**, *16*, 621–636. [CrossRef]
129. Mahltig, B.; Pastore, C. *Mineral and Ceramic Fibres*; Mahltig, B., Kyosev, Y., Eds.; Woodhead Publishing: Cambridge, UK, 2018; pp. 165–194.
130. Ivashchenko, E.A. Sizing and finishing agents for basalt and glass fibers. *Theor. Found. Chem. Eng.* **2009**, *43*, 511–516. [CrossRef]
131. Dibenedetto, A.T.; Lex, P.J. Evaluation of surface treatments for glass fibers in composite materials. *Polym. Eng. Sci.* **1989**, *29*, 543–555. [CrossRef]
132. Biefeld, L.P.; Philipps, T.E. Finishes for glass fabrics for reinforcing polyester plastics. *Ind. Eng. Chem.* **1953**, *45*, 1281–1286. [CrossRef]
133. Kiryukhin, D.P.; Krivonogova, E.A.; Kichigina, G.A.; Kushch, P.P.; Dorokhov, V.G.; Barelko, V.V. Preparation and properties of composites based on caramelized aluminoborosilicate fabric and tetrafluoroethylene telomers. *Russ. J. Appl. Chem.* **2016**, *89*, 758–765. [CrossRef]
134. Mathieson, A.M.; Walker, G.F. Crystal structure of magnesium-vermiculite. *Am. Mineral.* **1954**, *39*, 231–255.
135. Bassett, W.A. The Geology of Vermiculite Occurrences. *Clays Clay Miner.* **1961**, *10*, 61–69. [CrossRef]

136. Skipper, N.T.; Soper, A.K.; McConnell, J.D.C. The structure of interlayer water in vermiculite. *J. Chem. Phys.* **1991**, *94*, 5751–5760. [CrossRef]
137. Mahltig, B. *Basalt Fibers*; Mahltig, B., Kyosev, Y., Eds.; Woodhead Publishing: Cambridge, UK, 2018; pp. 195–214.
138. Pico, D.; Wilms, C.; Seide, D.; Gries, T. Natural volcanic rock fibers. *Chem. Fibers Int.* **2011**, *61*, 90–91.
139. Ruffen, C.; Mahltig, B. Basalt fibers as functional additives in coating of textiles. *J. Coat. Technol. Res.* **2021**, *18*, 271–281. [CrossRef]
140. Hao, L.; Yu, W. Evaluation of thermal protective performance of basalt fiber nonwoven fabrics. *J. Therm. Anal. Calorim.* **2010**, *100*, 551–555. [CrossRef]
141. Hao, L.; Yu, W. Comparison of thermal protective performance of aluminized fabrics of basalt fiber and glass fiber. *Fire Mater.* **2011**, *35*, 553–560. [CrossRef]
142. Deak, T.; Czigany, T. Chemical Composition and Mechanical Properties of Basalt and Glass Fibers: A Comparison. *Text. Res. J.* **2009**, *79*, 645–651. [CrossRef]
143. Overkamp, T.; Mahltig, B.; Kyosev, Y. Strength of basalt fibers influenced by thermal and chemical treatments. *J. Ind. Text.* **2018**, *47*, 815–833. [CrossRef]
144. Peebles, L.H. *Carbon Fibers*; CRC Press: Boca Raton, FL, USA, 1995.
145. Pusch, J.; Wohlmann, B. Carbon Fibers. In *Inorganic and Composite Fibers*; Mahltig, B., Kyosev, Y., Eds.; Woodhead Publishing: Cambridge, UK, 2018; pp. 31–52.
146. Wangxi, Z.; Jie, L.; Gang, W. Evolution of structure and properties of PAN precursors during their conversion to carbon fibers. *Carbon* **2003**, *41*, 2805–2812. [CrossRef]
147. Frank, E.; Hermanutz, F.; Buchmeiser, M.R. Carbon Fibers: Precursors, Manufacturing, and Properties. *Macromol. Mater. Eng.* **2012**, *297*, 493–501. [CrossRef]
148. Su, Y.-J.; Ko, T.-H.; Lin, J.-H. Preparation of ultra-thin PAN based activated carbon fibers with physical activation. *J. Appl. Polym. Sci.* **2008**, *108*, 3610–3617. [CrossRef]
149. Lee, Y.-S.; Basova, Y.V.; Edie, D.D.; Reid, L.K.; Newcombe, S.R.; Ryu, S.-K. Preparation and characterization of trilobal activated carbon fibers. *Carbon* **2003**, *41*, 2573–2584. [CrossRef]
150. Banerjee, C.; Chandaliya, V.K.; Dash, P.S. Recent advancement in coal tar pitch-based carbon fiber precursor development and fiber manufacturing process. *J. Anal. Appl. Pyrolysis* **2021**, *158*, 105272. [CrossRef]
151. Chand, S. Review Carbon fibers for composites. *J. Mater. Sci.* **2000**, *35*, 1303–1313. [CrossRef]
152. Lertwassana, W.; Parnklang, T.; Mora, P.; Jubsilp, C.; Rimdusit, S. High performance aramid pulp/carbon fiber-reinforced polybenzoxazine composites as friction materials. *Compos. Part B Eng.* **2019**, *177*, 107280. [CrossRef]
153. Aoki, R.; Yamaguchi, A.; Hashimoto, T.; Urushisaki, M.; Sakaguchi, T.; Kawabe, K.; Kondo, K.; Iyo, H. Preparation of carbon fibers coated with epoxy sizing agents containing degradable acetal linkages and synthesis of carbon fiber-reinforced plastics (CFRPs) for chemical recycling. *Polym. J.* **2019**, *51*, 909–920. [CrossRef]
154. Zhang, T.; Song, Y.; Zhao, Y.; Zhang, B. Effect of hybrid sizing with nano-$SiO_2$ on the interfacial adhesion of carbon fibers/nylon 6 composites. *Colloids Surf. A* **2018**, *553*, 125–133. [CrossRef]
155. Kim, D.-K.; An, K.-H.; Bang, Y.H.; Kwac, L.-K.; Oh, S.-Y.; Kim, B.-J. Effects of electrochemical oxidation of carbon fibers on interfacial shear strength using a micro-bond method. *Carbon Lett.* **2016**, *19*, 32–39. [CrossRef]
156. Küster, K.; Barburski, M.; Lomov, S.V.; Vanclooster, K. *Metal Fibers—Steel*; Mahltig, B., Kyosev, Y., Eds.; Woodhead Publishing: Cambridge, UK, 2018; pp. 219–242.
157. Zimmermann, Y.; Neudeck, A.; Möhring, U. *Metal-Coated Fibers*; Mahltig, B., Kyosev, Y., Eds.; Woodhead Publishing: Cambridge, UK, 2018; pp. 243–276.
158. Shahidi, S.; Moazzenchi, B.; Ghoranneviss, M. A review-application of physical vapor deposition (PVD) and related methods in the textile industry. *Eur. Phys. J. Appl. Phys.* **2015**, *71*, 31302. [CrossRef]
159. Mahltig, B.; Darko, D.; Günther, K.; Haase, H. Copper Containing Coatings for Metallized Textile Fabrics. *J. Fash. Technol. Text. Eng.* **2015**, *3/1*, 1–10.
160. Topp, K.; Haase, H.; Degen, C.; Illing, G.; Mahltig, B. Coatings with metallic effect pigments for antimicrobial and conductive coating of textiles with electromagnetic shielding properties. *J. Coat. Technol. Res.* **2014**, *11*, 943–957. [CrossRef]
161. Mahltig, B.; Zhang, J.; Wu, L.; Darko, D.; Wendt, M.; Lempa, E.; Rabe, M.; Haase, H. Effect pigments for textile coating—A review on the broad range of advantageous functionalization. *J. Coat. Technol. Res.* **2017**, *14*, 35–55. [CrossRef]
162. Grethe, T.; Lux, K.; Schwarz-Pfeiffer, A. Achieving Textile Based Supported Noble Metal Catalysts by Physical Vapor Deposition. In Proceedings of the Aachen-Dresden-Denkendorf International Textile Conference, Dresden, Germany, 28–29 November 2019.
163. Grethe, T.; Günther, K.; Weide, T.; Schwarz-Pfeiffer, A. Achieving Electrical Conductivity in Textiles: An Overview of Current Techniques. In *Textiles: Advances in Research and Applications (Chapter 6)*; Mahltig, B., Ed.; Nova Science Publishers: Hauppauge, NY, USA, 2017.
164. Roh, J.-S.; Chi, Y.-S.; Kang, T.J.; Nam, S.W. Electromagnetic Shielding Effectiveness of Multifunctional Metal Composite Fabrics. *Text. Res. J.* **2008**, *78*, 825–835. [CrossRef]
165. Kim, Y.I.; An, S.; Kim, M.-W.; Jo, H.-S.; Kim, T.-G.; Swihart, M.T.; Yarin, A.L.; Yoon, S.S. Highly transparent, conducting, body-attachable metallized fibers as a flexible and strechtable film. *J. Alloys Compd.* **2019**, *790*, 1127–1136. [CrossRef]
166. Poser, M. *Elektrosmog*; Crotona Verlag GmbH: Amerang, Germany, 2017.

167. Wu, Y.; Mechael, S.S.; Carmichael, T.B. Wearable E-Textiles Using a Textile-Centric Design Approach. *Acc. Chem. Res.* **2021**, *54*, 4051–4064. [CrossRef] [PubMed]
168. Protz, K. *Moderne Wundversorgung*; Elsevier GmbH: München, Germany, 2005.
169. Pollini, M.; Russo, M.; Licciulli, A.; Sannino, A.; Maffezzoli, A. Characterization of antibacterial silver coated yarns. *J. Mater. Sci. Mater. Med.* **2009**, *20*, 2361–2366. [CrossRef] [PubMed]
170. Elsner, P.; Piehler, E. Einfluss multipler Waschzyklen auf die antimikrobielle Aktivität eines silberbeschichteten Textils. *Dermatol. Beruf Und Umw.* **2020**, *68*, 179–182. [CrossRef]
171. Balagna, C.; Irfan, M.; Perero, S.; Miola, M.; Maina, G.; Santella, D.; Simone, A. Characterization of antibacterial silver nanocluster/silica composite coating on high performance Kevlar textile. *Surf. Coat. Technol.* **2017**, *321*, 438–447. [CrossRef]
172. Balagna, C.; Irfan, M.; Perero, S.; Miola, M.; Maina, G.; Crosera, M.; Santella, D.; Simone, A.; Ferraris, M. Antibacterial nanostructured composite coating on high performance Vectran fabric for aerospace structures. *Surf. Coat. Technol.* **2019**, *373*, 47–55. [CrossRef]
173. Irene, G.; Georgios, P.; Ioannis, C.; Anastasios, T.; Diamantis, P.; Marianthi, C.; Philippe, W.; Maria, S. Copper-coated textiles: Armor against MDR nosocomial pathogens. *Diagn. Microbiol. Infect. Dis.* **2016**, *85*, 205–209. [CrossRef]
174. Mahltig, B.; Fiedler, D.; Fischer, A.; Simon, P. Antimicrobial coatings on textiles–modification of sol–gel layers with organic and inorganic biocides. *J. Sol.-Gel Sci. Technol.* **2010**, *55*, 269–277. [CrossRef]
175. Kim, M.-W.; An, S.; Seok, H.; Yoon, S.S.; Yarin, A.L. Electrostatic Transparent Air Filter Membranes Composed of Metallized Microfibers for Particulate Removal. *ACS Appl. Mater. Interfaces* **2019**, *11*, 26323–26332. [CrossRef]
176. Mahltig, B.; Haase, H. Comparison of the effectiveness of different silver-containing textile products on bacteria and human cells. *J. Text. Inst.* **2012**, *103*, 1262–1266. [CrossRef]
177. Edwards, M.; Hidmi, L.; Gladwell, D. Phosphate inhibition of soluble copper corrosion by-product release. *Corros. Sci.* **2002**, *44*, 1057–1071. [CrossRef]
178. Sandstrom, R.; Wu, R. Influence of phosphorus on the creep ductility of copper. *J. Nucl. Mater.* **2013**, *441*, 364–371. [CrossRef]
179. Shyr, T.-W.; Shie, J.-W. Electromagnetic shielding mechanisms using soft magnetic stainless steel fiber enabled polyester textiles. *J. Magn. Magn. Mater.* **2012**, *324*, 4127–4132. [CrossRef]
180. Li, N.; Wang, J.; Liu, D.; Huang, X.; Xu, Z.; Zhang, C.; Zhang, Z.; Zhong, M. Selective spectral optical properties and structure of aluminum phosphate for daytime passive radiative cooling application. *Sol. Energy Mater. Sol. Cells* **2019**, *194*, 103–110. [CrossRef]
181. Supplit, R.; Schubert, U. Corrosion protection of aluminum pigments by sol-gel coatings. *Corros. Sci.* **2007**, *49*, 3325–3332. [CrossRef]
182. Verma, C.; Verma, D.K.; Ebenso, E.E.; Quraishi, M.A. Sulfur and phosphorus heteroatom-containing compounds as corrosion inhibitors: An overview. *Heteroat. Chem.* **2018**, *29*, e21437. [CrossRef]

*textiles*

MDPI

*Review*

# Geotextiles—A Versatile Tool for Environmental Sensitive Applications in Geotechnical Engineering

**Fulga Tanasă [1], Mărioara Nechifor [1], Mauruşa-Elena Ignat [2] and Carmen-Alice Teacă [2,*]**

[1] Polyaddition and Photochemistry Department, "Petru Poni" Institute of Macromolecular Chemistry, 41A Grigore Ghica-Vodă Alley, 700487 Iaşi, Romania; ftanasa@icmpp.ro (F.T.); nechifor@icmpp.ro (M.N.)
[2] Center for Advanced Research in Bionanoconjugates and Biopolymers, "Petru Poni" Institute of Macromolecular Chemistry, 41A Grigore Ghica-Vodă Alley, 700487 Iaşi, Romania; mignat@icmpp.ro
* Correspondence: cateaca@icmpp.ro

**Abstract:** Geotextiles, a group of high-performance materials, have grown during the last decades into needful auxiliaries when it comes to infrastructure, soil, construction, agriculture and environmental applications. Although geotextiles made of synthetic fibers (geosynthetics) are considered a modern achievement, the basic concept dates back to ancient times when textiles consisting of locally available natural fibers were employed to increase the stability of roads and soils. In recent decades, considering the growing interest in environmental protection and sustainable development based on using renewable resources and the recovery and recycling of waste of various origins, the use of natural fibers-based geotextiles is a viable alternative, despite their limited-life service owing to their biodegradability. In addition to this feature, their low cost, good mechanical properties and large-scale accessibility recommend them for geo-engineering applications, environmental sensitive applications in geotechnical engineering, such as land improvements and soil erosion control. This paper focuses on geotextiles as a versatile tool in environmental applications given their high theoretic and practical relevance as substantiated by recent literature reports. Natural and synthetic geotextiles are presented herein, as well as their features that recommend them for geo-engineering. Insights on the main types of applications of geotextiles are also included, along with a wide variety of materials employed to perform specific functions.

**Keywords:** geotextiles; natural fibers; synthetic fibers; geo-engineering; environmental applications

**Citation:** Tanasă, F.; Nechifor, M.; Ignat, M.-E.; Teacă, C.-A. Geotextiles—A Versatile Tool for Environmental Sensitive Applications in Geotechnical Engineering. *Textiles* **2022**, *2*, 189–208. https://doi.org/10.3390/textiles2020011

Academic Editor: Laurent Dufossé

Received: 8 March 2022
Accepted: 6 April 2022
Published: 8 April 2022



## 1. Introduction

### *1.1. General Considerations*

Geotextiles, a group of high-performance materials, have grown during the last decades into needful auxiliaries when it comes to infrastructure, soil, construction, agriculture and environmental applications. Although geotextiles made of synthetic fibers (geosynthetics) are considered a modern achievement, the basic concept dates back to ancient times when textiles consisting of locally available natural fibers were employed to increase the stability of roads and soils [1–3]. Nowadays, whether it is the stabilization of soil in arid regions [4] or the river banks and seafronts (in tidal areas or harbor infrastructure) [5,6], ground reinforcement for civil infrastructure [7–9] or filtration of water excess in farmlands and flood protection [10–12], hill slopes stabilization and drainage [13] or even the reinforcement of airstrips under the tarmac layer [14,15], geotextiles are successfully performing in civil engineering and agriculture and becoming an increasingly viable alternative in many other applications.

Geosynthetics [16], the geotextiles made of synthetic polymers (such as PP, PE, PET and PVC) manufactured as fibers, are used in notably large amounts as the polymer production is cost-effective and the corresponding fibers are easily obtained by melt spinning using already existing technology. Their remarkable mechanical properties (mainly tensile

strength), durability and hydrophobicity make them fit for geotechnical engineering applications, such as the improvement of the bearing capacity of the ground in preparation of construction sites [17]. On the other hand, some polymers require a supplemental employ of additives, prior to their spinning, in order to improve or customize some of their properties with respect to their further applications. Thus, the UV resistance of PE fibers is significantly increased by adding carbon black as a stabilizer to the pristine polymer [18], while composites based on epoxy resins or unsaturated polyesters have achieved improved thermal and mechanical characteristics upon incorporation of glass fibers or carbon fibers in their formulations [19]. The main drawback of the long-term use of geosynthetics is their degradation under environmental conditions (humidity, acid/base or salty atmosphere, pollutants, UV–vis irradiation, wind and particle abrasion, microorganisms attack, temperature variation and seasonal freeze–thaw cycles, etc.) [20–22]. Nevertheless, the lifetime of geosynthetics and their operating performance depend directly on the chemical and structural stability of the synthetic polymers in their composition [23]. The advanced geosynthetics are, thus, designed so as to have better stability during their service time. Even more, with the considerable help of intelligent geotextiles which have sensors and/or sensing-and-actuating devices incorporated in their structure, it was possible to first discern chemical and/or physical changes of materials and to identify precociously the imminent material failure, whether a brittle or ductile failure.

In recent decades, considering the growing interest in environmental protection and sustainable development based on using renewable resources and the recovery and recycling of waste of various origins, the use of natural fibers-based geotextiles is a viable alternative, despite their limited-life service owing to their biodegradability. In addition to this feature, their low cost, good mechanical properties and large-scale accessibility recommend them for geo-engineering applications, such as soil stabilization and reinforcement, and erosion control [13,24–26]. Moreover, natural fibers (such as sisal, kenaf, hemp, jute, ramie and coir, etc.) employed for geotextiles are locally available which counterbalances their properties' variation (sometimes within large limits). Therefore, complex approaches have been developed in order to improve their properties and include (but are not limited to) fiber surface modification by various treatments [27], use of special additives or degradable thermoplastic biopolymers [28], employment of hybrid yarns made of natural and synthetic fibers [29,30], etc. Recently, it was assessed that natural geotextiles are able to replace geosynthetics in almost 50% of their applications [26].

### *1.2. Types of Geotextiles*

Considering the structures obtained by manufacturing, geotextiles can be produced as various fabrics, as follows [1]:

1. **Woven**—these materials are obtained by classic weaving; their mesh opening (pore size and distribution) varies depending on the tightness of the weave; they provide high tensile strength and modulus but poor dimensional stability and resistance to abrasion;
2. **Nonwoven**—they are often referred to as mats, can be manufactured in a large variety of formulations and spatial layouts and provide high strain and permeability; their most relevant feature is their ability to resist damage by local lengthening, despite their low tensile strength;
3. **Knitted**—whether warp-knitted [31] or weft-knitted [32], these fabrics have tridimensional architectures with multiaxial, in-plane and out-of-plane reinforcements; they represent only 5% of the geotextiles currently used, but the demand for knitted geotextiles is rapidly increasing due to their particular mechanical properties [31].

Aside from these types of geotextiles, in practice there are other materials considered as geotextile-related products, such as geomesh, geonets, geocells, geogrids and geocomposites [3], which are used individually or in combination with others in order to enhance their action by working in synergy or to obtain a multitask layer.

General requirements that operative geotextiles need to meet in terms of properties are as follows [16]:

1. **Mechanical**—materials having specific mechanical properties, such as tensile strength and ultimate tensile strength, bursting strength, elasticity, abrasion resistance, bending strength and creep, are needed not only for infrastructure but for agriculture as well;
2. **Hydraulics**—properties such as water permeability and transverse water permeability are considered when geotextiles are used for drainage or to maintain soil humidity;
3. **Weathering**—this category of characteristics refers to the capability of geotextiles to withstand degradation under environmental conditions (humidity, UV–vis irradiation, biologic attack, temperature variation and seasonal freeze–thaw cycles, etc.). Due to the environmental impact of the degradation of geosynthetics, a wise selection of materials and scheduled maintenance (initial assessment of performance and service life, periodic inspections on site, replacement) are of high importance.

### *1.3. Geotextiles Main Functions*

Filtration is one of the most important functions of geotextiles. Materials used for geo-filtration must respond to two opposite demands: they must possess a satisfactory level of cross-plane permeability to allow fluids to pass through and provide suitable pore size and distribution fit to stop (or, at least, limit) the migration of the smallest soil particles through their pores. In the dynamic of these processes, a natural filter is formed by coarse particles blocked, and subsequently compacted, on the geotextile [33].

Closely related to filtration, drainage refers to the ability of geotextiles to allow fluids to flow through their structure and along it, as well. Properties such as soil retention, clogging and flow capacity must be considered when selecting a geotextile for drainage [34]. Furthermore, these functions can be successfully employed when it comes to soil decontamination of heavy metals such as lead [35] or even aluminium [36].

Separation—this function is mostly relevant when geotextiles are employed in reinforcing and the stabilization of aggregate layers (roads, buildings foundation) in order to prevent them sinking into more fluid (fine particles soil, labile layers of clay) base soils. Bursting strength refers to the property of a geotextile to withstand a force applied perpendicular to the plane, with a certain deformation, up to the bursting point when the applied force exceeds the material strength. In correlation with the grab strength and puncture resistance, it indicates if a selected geotextile is suitable for such an application [37].

Geotextiles are also used widely for soil reinforcement in different situations: slopes and river banks, roads and infrastructure [38], etc. For such applications, properties such as tensile strength, surface friction, compression strength, pull-out strength and creep are most relevant as they grant the selected materials a long-term service life.

Geotextiles with low permeability are often used as barriers, especially geosynthetics, because they prevent water (fluid) infiltration into the protected structure (waterproofing) [16,39]. At the same time, the performance of the state-of-the-art containment barrier technical designs depends on the geosynthetics stability, especially when it comes to modern landfills where the geosynthetics are employed to prevent the leachate contamination of the surrounding soil [40]. For such environmental sensitive applications, geotextiles with complex formulation have been employed (such as geosynthetic-clay liners), and the main requirements are the low hydraulic conductivity and high mechanical characteristics [41].

Geotextiles present a series of limitations due to service stress, weathering and degradation under environmental conditions, which limit their level of performance. Nevertheless, their lifespan and cost-effectiveness, associated with increasing environmental awareness, are the main driving forces to expand the range of applications and demand for geotextiles, as well as the impact on market growth. In this regard, the global geotextiles market size was estimated at USD 4.6 billion in 2019 (when the largest market share was in road construction) and the projection for the interval 2020–2027 indicates a compound annual growth rate (CAGR) of 11.9% [42]. As for the regional aspects, it is noteworthy that Asia Pacific will dominate the market in the period 2021–2028 due to fast urbanization, while

the EU strongly encourages "green" infrastructures in order to limit pollution and enhance environment protection [43].

This paper focuses on geotextiles as a versatile tool for environmental sensitive applications in geotechnical engineering given their high theoretic and practical relevance as substantiated by the most recent literature reports. Natural and synthetic geotextiles are presented herein, as well as their features that recommend them for geotechnical engineering. Insights on the main types of applications of geotextiles are also reviewed, along with a wide variety of materials employed to perform specific functions. Furthermore, some of the most recent advances in geotextiles, such as high-performance "green" (wholly or partially) geotextiles, intelligent geotextiles incorporating sensors and/or sensing-and-actuating devices, as well as other highly specialized geotextiles with complex formulations and multilevel architectures, such as composites containing high-performance fibers (carbon, glass or basalt fibers) or particulate fillers (clays, graphene oxide particles, carbon black), are included as well.

## 2. Fibers Selected for Geotextiles

### *2.1. Synthetic Fibers*

Geosynthetics are products made of synthetic or natural polymeric materials, or combinations of both, which are used in contact with soil or rock and/or other geotechnical materials. A general classification of geosynthetic materials based on their physical form mainly includes geomesh, geonets, geocells, geogrids, geopipes, geofoams that can be grouped as geotextiles, geosynthetic clay liners and plastic sheets that can be grouped as geomembranes and geocomposites which are a combination of the above-mentioned products as a single material. Technically, the term geosynthetics refers to synthetic polymer-based materials. Natural fibers, as well as synthetic fibers, are also important due to their cost-effectiveness, environmentally friendliness and improved strength, and therefore the natural geotextiles are incorporated in the general classification of geotextiles. Synthetic geotextiles are the most widely used geosynthetics due to the unique property and strength they exhibit. However, geotextiles made of synthetic polymer are less susceptible to biodegradation in comparison with the natural ones [44].

About 98% of geotextiles consist of non-degradable polymers belonging to four classes of polymers: polyolefins (low-density polyethylene LDPE, linear low-density polyethylene LLDPE, high-density polyethylene HDPE and polypropylene PP), polyester (polyethylene terephthalate PET), polyvinyl chloride (PVC) or polyamide (PA, nylon). Antioxidants, hindered amine light stabilizers, UV absorbers and stabilizers, long-term thermal stabilizers, processing modifiers, flame retardants, lubricants and antibacterial agents are usually added as additives to enhance the performance of geotextiles. Synthetic fibers are used in geotextiles manufacturing primarily because they are water resistant, or have low water absorption, and good resistance to biological and chemical degradation [44].

Geotextiles made of synthetic fibers need to have longevity and keep their characteristics when subjected to severe environmental conditions. Properties such as high thermal stability, resistance to UV radiation, oxidation and chemical degradation are of utmost importance and limited only by the chemical structure of the polymer. The rate of degradation is reduced by the addition of carbon black but not eliminated. Polypropylene is the most widely used fiber for geotextiles because of its low density, low cost, acceptable tensile properties and chemical inertness. However, polypropylene has a poor sensitivity to UV and a low thermal stability that results in poor creep characteristics. PET is inherently stable to ultraviolet light but susceptible to high pH environments. On the contrary, PP has excellent chemical and pH resistance but requires additives for UV stability [45].

The mechanical properties of the synthetic fibers depend on the molecular weight of the polymer but also on the conditions used in their production. These materials are produced in the form of continuous monofilament or multifilament yarns by the melt-spinning process. Generally, fiber fineness ranges from 2.2 to 60 dtex and the length ranges between 20 and 100 mm. Synthetic polymer yarns may also be produced by slitting

extruded plastic sheets or films into thin flat tapes or twisting fibrillated plastic ribbons into yarns.

The tensile characteristics of these fibers can be designed for the final application, but generally PET fibers have much higher strengths than PP fibers and much lower creep. In general, PET is more suitable for geotextiles for the reinforcement function and PP for less strength-critical applications. The deformation of amorphous regions in polymers also has a significant effect on the stress–strain behavior of geotextiles and in the prolonged loading. It is one of the reasons that polyolefins, such as polyethylene and polypropylene (70–80% crystallinity), have higher creep characteristics [46]. PET has excellent tensile properties, high thermal stability and high creep resistance. The main drawback of polyester fiber is the easy hydrolysis and degradation in the soil with a pH > 10. Chemicals in the groundwater can react with polymers. All polymers gain water with time if water is present. High pH water can be harsh on polyesters, while low pH water can be harsh on polyamides [47].

Although most geotextiles are polyolefin- and polyester-based, polyurethane, glass and carbon-based polymers could be used for special purposes and functions. Because the manufacture of geosynthetic products requires large quantities of polymer materials, their cost should be low. PP and PET are therefore the most used synthetic fibers.

The type of application demands geotextiles have certain qualities and properties. Thus, geosynthetics exposed for long intervals to harsh and complex environmental conditions (wind, temperature, moisture, friction, UV radiation and pH) must be made of high-performance polymers in order to avoid precocious material failure as a result of polymer degradation (chemical, biochemical and photochemical reactions cause the weight and structural integrity loss of polymers) [48]. Still, as soon as the geosynthetic fails to perform its function, replacement procedures are initiated in order to prevent any hazardous side effects.

Their enhanced properties, such as aperture size, moisture sorption depth, mesh thickness, tensile strength, corrosion resistance, water permeability, hydraulic roughness and ease of processing, allow geotextiles to be used in soil protection applications where they accomplish functions: as filters, separator soils and other fine materials, drainers to remove or gather rainwater in the soil, reinforcement to stabilize and strengthen and, lastly, for protection in landfills or waste dumping sites and vegetation (afforestation, greening). Due to their applications in environmental protection, earthwork constructions, roadway and railway construction, marine and coastal structures constructions, riverbank and channels construction, the mining industry and landscaping, geotextiles have become the fourth largest new building material following steel, wood and cement [3].

According to the manufacturing processes, geotextiles can be divided into three major forms, namely woven, nonwoven and knitted, and they have multiple applications in various technical fields, such as construction, hydraulic, structural, transportation and agricultural engineering. Woven synthetic geotextiles usually have higher strengths and a lower breaking extension than nonwoven geotextiles of the same areal weight and polymer type. In the domestic market, nonwoven geotextiles are primarily made with spunbonded, staple fiber needling and thermal bonding approaches. Spun-bonded geotextiles have good mechanical properties and filtration efficiency and a high production cost. Thermal bonded geotextiles have a higher tensile strength, tear strength, breaking elongation and vertical and horizontal ratio in comparison with needle-punched geotextiles that have the same specifications. Staple-fiber needle-punched geotextiles have a great thickness, a high density, a good permeability, a high pore fraction, a fluffy structure, a high deformation resistance and a low production cost, but their mechanical properties are not as good as those of common geotextiles [49,50].

### *2.2. Natural Fibers*

Natural fibers are largely available in the surrounding environment and present some advantageous properties (proper strength and thermal attributes, reduced density, high

level of mechanical resistance), making them suitable for ensuring an effective strategy which mainly envisages sustainable land management.

From natural fibers, those belonging to the plants' structural complex architecture are commonly used for natural geotextiles (known as limited life geotextiles—LLGs), given their abundance, easy processing for separation, reduced costs and excellent properties, mentioning only biodegradability which is essential for most short-term geotechnical applications from environmental considerations [51].

In Figure 1, a schematic presentation is given of some plant fibers investigated for employment in applications including geotextiles [52–55].

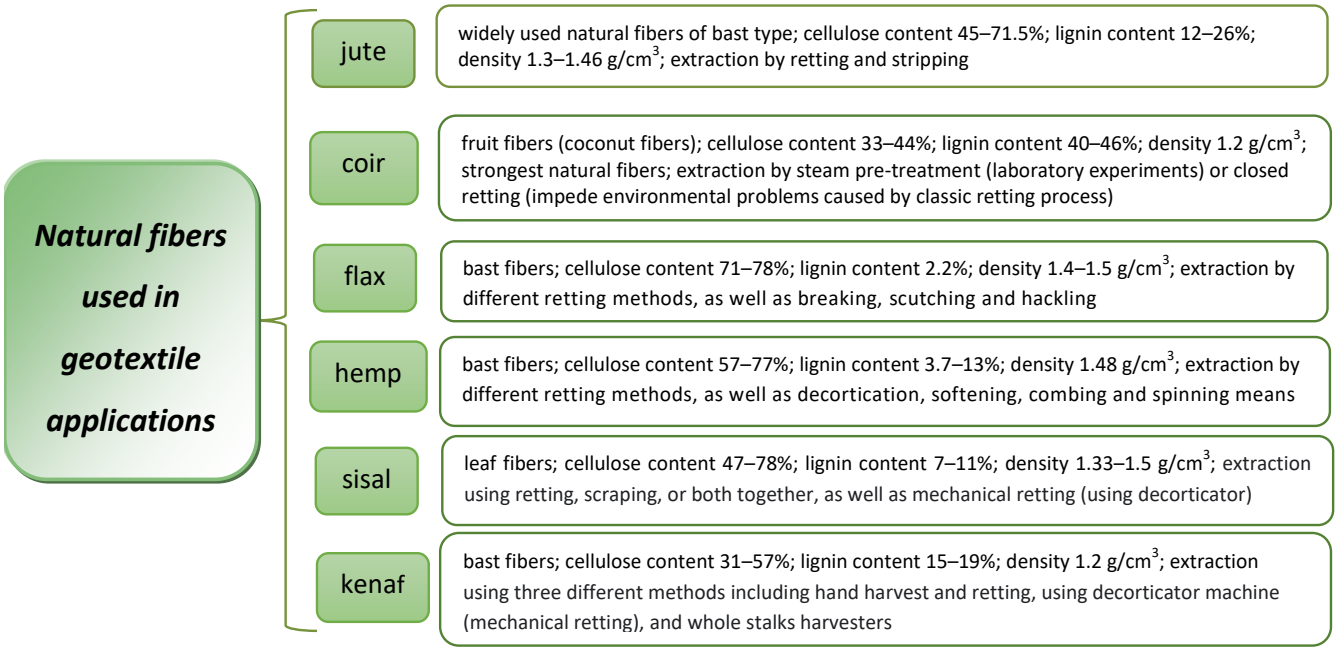


**Figure 1.** Most applicable natural fibers from plants for geotextile purposes.

The employment of the most suitable natural fibers in relation to their appropriate characteristics making them applicable for production of limited-life geotextiles has been comprehensively reviewed [26,51,52]. Most of the natural plant fibers present different strength and durability characteristics, for example, a high level of stiffness and outstanding thermal and soundproof properties [56].

Generally, natural fibers are suitable for the production of geotextiles when they have good mechanical performance and sometimes better hydraulic behavior depending on application and, as a pre-requisite, a better resistance to biodegradation processes. The final characteristics of the natural fibers are strongly related to their variable chemical structure, dimensions, the varying physical characteristics in close relation to their kind/species, place of growth, harvesting time, location in the originating plant, processing methodologies and so on [57].

The largely employed natural fibers for geotextiles are jute and coir in relation with their abundance, reduced density, excellent mechanical properties, recyclability and outstanding quality as reinforcement for specific applications. Jute contains a significant amount of lignin. Coir is suitable for ensuring the fixation of vegetation at a certain level as well as maintaining it through proper conservation tillage, usually being spinned and weaved into dense fabrics. These cover the soil in zones defenseless against the process of eroding and present good strength retention, a diminished degradation rate and good water absorption, meaning durability in field applications.

Coir-based geotextiles are fully biodegradable and present better resistance under sunlight exposure conditions. It was evidenced that the coir fibers can be effectively chemically modified by hydrophobization or acetylation [58] on a laboratory scale, with

benefits through prolonging two or three times the functional service period of the resulted coir products.

When comparing with the classical fibers employed for geotextiles production which are prepared from recycled synthetic polymers, namely polypropylene and polyester ones, jute has better mechanical properties (which make it suitable for reinforcement application) and it is more hygroscopic (which makes it suitable for drainage application) [59,60]. When biodegradable geotextiles are required, natural fibers such as coir and jute are used. As the vegetation is fixed and developed to a certain degree, the degradation process of the fibers generates by-products which are useful for plants' growth. When jute and coir fibers are employed in geotextile applications, these absorb water to a large extent. Thus, the water run-off process alleviates the soil motion which maintains a certain adequate level of humidity.

### *2.3. Other Fibers*

Along with the development of new technologies applied in geotechnical engineering, other high-performance synthetic fibers have been considered for geotextiles.

Carbon fibers are well represented in this category of applications due to their high strength, hydrophobic character and chemical and thermal stability [61]. In most geotechnical engineering applications, they are used in order to impart increased mechanical strength to materials. As felt [62], graphene oxide microparticles (0.5–5 μm) [63] and fibers [64], they can be found in various composites with geopolymers and are employed for filtration and building construction. Carbon fibers can be used as fabrics as well: sandwich structures made of electrospun polyimide nanofibers between two layers of carbon fabrics have been designed, produced and successfully used as filtration media able to retain PM 2.5 fine particles [65]. For reinforcing road structures, carbon fibers have been used in asphalt formulations, and the resulting geocomposites have improved resistance against crack growth, especially at low temperatures [66].

Glass fibers are also used in geotextiles as a nonwoven reinforcing material for soil stabilization, because the spatial orientation is random and the resulting structures are flexible, while imparting stability and strength to the engineered soils [67,68]. Another application of glass fibers refers to reinforced concrete formulations used in civil engineering [69,70], when materials with extended service life, fire resistance and improved thermal and mechanical characteristics were obtained.

Aramid fibers dominate the market of high-performance polymer materials. They have outstanding mechanical properties (e.g., high strength to weight ratio), impact resistance and chemical resistance and thermostability, along with low elongation. So, by consequence, the corresponding geotextiles showed excellent busting strength and satisfactory elastic properties. One major drawback of aramid fibers is their high production cost, and it limited the use of these fibers in geotextiles. In their stead, recycled Kevlar® fibers were employed for soil reinforcements in various geotextiles: as fiber in hybrid fibers [71,72], as a component in complex structures such as needle-punched nonwoven geotextiles, in combination with PET and PP fibers [73] or PET and nylon fibers [74], in epoxy- or PET-based composites as a reinforcing component [72,75] and in hybrid woven–nonwoven sandwich structures where nylon fabric was employed as an interlayer [76].

Other aramid fibers, such as Twaron® and Technora®, were also considered for geotextiles, as tridimensional nonwoven composites with epoxy resin as the polymer matrix [77]. A serious limitation of the service time of these geotextiles is the degradation of aramid fibers under alkaline and neutral conditions [78].

Basalt fibers, another group of high-performance fibers, are of natural origin (volcanic rock), and after industrial processing, they have properties close to glass fibers. They are used for soil reinforcement, not as typical geotextiles but as reinforcing fibers in mixtures with soil [79], or in other combinations intended for the reinforcement of roads and airstrips [80].

## 3. Applications of Geotextiles

### *3.1. Synthetic Geotextiles in Soil Erosion Control*

Erosion can cause severe deterioration in coastal areas, on slopes and riverbanks, especially where vegetation is weak or lacking. Preventing or limiting soil movement under the influence of erosive forces, such as moving water and wind, is the basic principle for controlling soil erosion. Tidal situations (i.e., coastal and river) occurring naturally or by the movement of water induced by maritime transport can be controlled by techniques that provide armored protection with geotextile support. Sludge retention and ground cover retention and revegetation on steep slopes involve techniques that use geotextiles. Erosion control uses synthetic materials for silt containment and soil retention as long-term solutions and synthetic and natural materials for revegetation on steep slopes [44].

The introduction of geotextiles in erosion and sediment control systems has offered significant advantages when used alone or combined with traditional natural materials (such as straw, rock, brush and soil) and unique and quantifiable functions in erosion and sediment control applications. Stabilization of the surface by restricting movement and preventing the dispersal of soil particles subject to erosion (rain or wind) takes place by placing geotextiles on the soil surface where they can also allow or promote vegetative growth. The control of soil erosion under the action of geotextiles involves the active control of soil dislocation, while the control or retention of sediments consists of retention and filtration of dislocated soil (called sediment), transported by runoff.

As a consequence, new geotextile materials have been developed, aiming at the revegetation of bare soil or as a support of vegetation in erodible soil, long-term non-biodegradable support and temporary biodegradable support for new seedlings.

Synthetic polymers such as PP, PET and PA are modified with additives to improve their resistance under UV irradiation and are used for a long-term permanency (keeping 75% of its original strength after 10 years of life) [3]. Geotextile erosion control products, such as erosion control nets (ECN), open-weave erosion control meshes (ECM), blankets (ECB) and turf reinforced mats (TRM), provide greater strength, enhanced performance and greater longevity than that of conventional natural mulches such as loose straw, brush, soil or compost [81]. These geotextile-enhanced systems reduce seed and soil loss owing to erosive forces and facilitate site revegetation. Erosion control nets (ECN) typically consist of polyolefin biaxially-oriented process mesh and are used to bring together loose fiber mulch. Having been flattened out over the seeded and mulched area, ECN are stapled or staked in place. Open-weave erosion control meshes (ECM) are woven of organic twine of jute or coir or polyolefin yarns. Usually, organic meshes have 0.6–1.2 cm thick and 2.5 cm or larger square uniform openings. Polyolefin meshes are considerably thinner with smaller openings. All meshes provide incomplete ground coverage, even though they are flexible and promote appropriate ground cover. At the same time, organic meshes absorb water and are beneficial for keeping soil moisture. Erosion control blankets (ECB) are organic fiber-filled blankets composed of straw, wood shavings or coconut fibers sewn to or between synthetic (or organic) nettings. The nets provide resistance to these materials to withstand the action of erosive forces. The durability of organic fibers decides the lifespan of these materials.

Fused or stitched polymer nettings (often filled with polymeric fibers), randomly settled monofilaments or yarns woven or tufted into an open and dimensionally stable mat, are the main components of turf-reinforced mats (TRM). An increased stiffness and strength are the result of the dimensional stability. Strong, durable and continuous soil-root-mat matrices are generated by these flexible, synthetic mats in combination with topsoil and seed or turf which can result in higher long-term erosion protection than grass alone.

Fabric-formed revetments (FFR) are low-cost, durable, synthetic fabrics used to produce three-dimensional mats for casting concrete slabs. They provide the durability of rigid linings such as cast-in-place concrete or asphaltic concrete and the flexibility and/or water permeability of protective rock systems such as riprap or gabions. Geocellular confinement systems, often called geocells (GCS), consist of strips of polymer sheets connected at stag-

gered points. When the strips are pulled apart, a large honey-comb mat is formed that can be filled with soil, rock or concrete.

Usually, geocell thickness varies between 5 and 30 cm. This erosion control product is efficient when the surface soil is retained on a slope. Geotextile filter systems are placed on the soil surface beneath a hard armor system when they perform the function of dynamic filtration. The geotextile provides support for the armor layer over the seepage-induced softened subgrade as the water surface rises, and when the water surface recedes, seepage from the subgrade cannot carry soil particles with it which could cause undermining of the armor layer [82].

### *3.2. Synthetic Geotextiles in Railway Infrastructure*

There are several factors such as the traffic, track structure, subgrade conditions, drainage conditions and maintenance requirements that impose the characteristics of geotextiles in a railroad track structure. In railway construction, geotextiles are used to increase track support for the laying of new lines and rail track rehabilitation and also to accomplish the separation, filtration and lateral drainage. Geotextiles have proved useful in the existing right-of-way where a large amount of track maintenance has been necessary due to poor drainage conditions, soft conditions and/or high-impact loadings. Usually, geotextiles are introduced between the subgrade and ballast layer or between the subgrade and subballast layer if one is present. Geotextiles are used in the "pumping track" and "ballast pocket areas" that are associated with fine-grained subgrade soil and difficult drainage conditions. The main foundation of a rail track is formed by subgrade soils, and layers of granular materials and subsequently the sleepers and rail lines are placed on them. The load-supporting intermediary between the railway lines and the subgrade is provided by the aggregate layers. When the wheels on each axle of a rolling stock traverse the line above a sleeper, the aggregate layers undergo a repeated cyclical stress. In time, a pocket of fouled and ineffective ballast is generated, and loss of track grade control takes place as ballast is forced deeper and deeper into the subgrade. Permanent track maintenance problems are attributed to these ballast pockets that collect water and decrease the strength of the roadbed around them. During the rehabilitation process, the geotextiles provide separation, filtration and drainage functions and can prevent the reoccurrence of a pumping track. Poor subgrade/drainage conditions, highway-railroad grade crossing, railroad crossings, turnouts and bridge approaches are locations of excessive track maintenance that require the installation of a geotextile in the railroad track. The installation of a geotextile in the track requires adequate drainage, otherwise water will be kept in the track structure and the insecurity of the track will be more damaged. Geotextiles are not used to decrease the ballast or subballast design thickness because they have no reinforcement effect on soft subgrades under the railroad track [83].

Woven geotextiles tend to clog with time and act almost as a plastic sheet preventing water from draining out of the subgrade. Consequently, they are not recommended for use in the track structure of railroads, and nonwoven geotextiles and needle-punched materials are used instead.

Geotextiles are used in embankments and to separate the ballast or subballast from the subgrade (or the ballast from the subballast) in a railroad track. A stable railroad track structure is based on adequate drainage and provisions for improving both internal and external track drainage. Drainage provisions involve deep side ditches to manage surface runoff and an adequate crown in both the subgrade and subballast layers to prevent water from ponding on the top of the subballast or subgrade. Water accumulation in the track can be avoided by the installation of perpendicular drains, and the removal of water from the track structure is supported by French drains. The creation of bath-tub or canal effects should be avoided during track rehabilitation by having the shoulders of the track below the level of the ballast/geotextile/subgrade interface. Before geotextiles should be placed in a railroad track structure, the existing drainage problems must be corrected [84].

### *3.3. Geosynthetics as Reinforcements*

The reinforcing function of geotextiles is one of the most used in geotechnical engineering. Tensile modulus, tensile strength and surface friction are the most important mechanical properties of a geotextile used for reinforcement.

The resistance of soils to tensile forces is much lower than to compressive forces. Soil stability through reinforcement can be achieved by inserting an appropriate geotextile into the soil and aligned with the direction of the tensile forces. The soil allows the transfer of these forces to the geotextile, using its axial strength.

Efficient reinforcement requires a high tensile strength and a high tensile modulus of the geotextile. The resistance of the geotextile to tensile loads generated in the soil occurs at sufficiently small strains to prevent excessive movement of the reinforced soil structure. The polymers used in these applications should have resistance to degradation by the soil and altering in these properties with time (i.e., creep behavior) must be insignificant [85,86].

Reinforcement exerted through a geotextile takes place when the stability of the weak subgrade or soil is complemented by the higher tensile strength of the fabric. The geotextiles embedded within the soil improve the cohesion between the grains and the resulting composite can sustain higher loads and tensile or shear forces. The forces applied on the soil structure through different loads are transferred into tensile stresses, which further influence other mechanical properties, such as puncture resistance [87].

An efficient reinforcement is provided by a geotextile with sufficient strength and embedment length to resist the tensile forces created. To prevent excessive movement of the reinforced structure, the strength must be developed at sufficiently small strains (i.e., high modulus). Woven geotextiles are used to reinforce embankments and retaining structures, because they provide high strength at small strains.

A compacted layer of aggregate has good compressive strength but very poor tensile resistance. As a consequence, a geotextile is necessary to reinforce the soil and confer resistance to a compacted soil from breaking up under tensile stresses [88]. Most reinforcements use fabrics obtained from PP or PET filaments. Very high strength applications, requiring strength of 400 kN/m, use *para*-aramid (e.g., Kevlar), glass or basalt filament. Applications where strength/cost ratio is a required factor use PET filaments. PP cannot always be used because it is susceptible to chemical attack in high pH environments. PP is more resistant to chemical degradation, but its long-term creep characteristics are much poorer than PET. Generally, PET is more suitable for geotextiles having a reinforcement function and PP for less strength-critical applications. The monofilament woven fabrics made of PET provide better permeability, because multifilament is used for higher strength reinforcement.

Slit film, flat-tape fabrics are usually PP materials, which are quite strong but have relatively poor permeability. On the other hand, fabrics from fibrillated tape yarns have better permeability and more uniform interstice openings than flat-tape products [85,89].

### *3.4. Geosynthetics for Filtration*

For a very long time, geotextiles have been widely applied for filtration purposes. One can mention here the drainage of pavements, dewatering of trenches, reinforcement of shorelines and slopes, inclusion in panels for drainage in their stage of prefabrication, as well as in systems for leachates' accumulation and caps for landfill function [90].

There are some filtration prerequisites to be fulfilled by geotextiles in order to function as an efficient filter [91]. Liquid is passing through the filter while the soil particles remain if they have a larger dimension than the pores of the geotextile filter from which those larger are in fact smaller, comparative with the size of soil particles.

The clogging of the geotextile filter may be prevented if a major part of the pores in the filter are large enough to allow the passing of the smaller soil particles. A proper flow through a geotextile filter is ensured by the presence of a significant number of large pores in its structure, the inter-relation between the flow dimension as volume passes through the filter and its effectiveness for filtration applications being well recognized. [92].

In the filtration application, the geotextile filter may function in three different manners, and these include close contact with soil particles, interaction with suspension of soil particles and cyclic loading when the migration of soil particles occurs. A geotextile filter should act as an effective barrier and/or as part of a self-filtration or vault network formation mechanism when combined with a natural filter. Thus, the migration of soil particles is ceased through the formation of a rough layer at the interface of the geotextile filter (self-filtration). The second mentioned mechanism (vault network formation) involves electrical and adsorption interactions usually present between soil particles as well as between lubricant and an antistatic agent at the interface of geotextile fibers/soil particles, when these particles appear as ordered vaults. A geotextile filter may present an impervious layer of particles formed through an interaction with a suspension of soil particles, impeding the flow in a given time period and consequently requiring its replacement. Easy soil particle migration at the geotextile filter interface is observed in the cyclic loading filtration mechanism when the hydraulic force pushes the smaller soil particles to migrate toward the filter [93].

Geotextile filters applied for filtration purposes should fulfill some important criteria, as follows:

(1) Blockage or retention criteria: The free flow of water through the pores of a geotextile filter is impeded to a certain extent or completely stopped when fine particles are present [91,94]. The retention ability of the filter is strongly related to its structure, as well as to both soil characteristics (type, uniformity, curvature, density) and flow regime [95,96]. For various fabrics, a simple relationship can be established considering the yarn diameter of the spinned geotextile and soil particle size [89].

(2) Blinding or permeability criteria: On the geotextile filter surface, overlays of fine particles are sometimes formed, usually when phenomena such as water flow ceasing and drying of the geotextile surface take place [97]. Generally, a certain relation between geotextiles' permeability and corresponding flow at the interface between soil particles and the filter can be established, meaning that based on this assumption, the geotextile filters have to be more pervious than the retained soil particles. An important issue related to these second above-mentioned criteria is the comparison between the permeability ability for both the geotextile filter and soil particles. Thus, a geotextile can be used as an effective filter through an appropriate design in order to allow an easy flow of liquids from one side of the material to the other side, impeding the soil particles passing from the upstream side.

A geosynthetic filter must fulfill a satisfactory level of permeability to allow the liquid flow and also have an average pore size and pore-size distribution sufficiently small to obstruct all particles migrating through its thickness, except the finest ones. These contradictory requirements are accomplished by textile structures, which are the only material form that can be readily manufactured.

Geo-filtration uses the basic mechanism of wet filtration, and a geotextile filter enables the finer particles to be either carried through the filter thickness by the fluid flow or lodged within it. Whether the fine particles leave the soil/filter interface, the coarse ones are blocked at the interface and form a compact porous layer that allows the appearance of small pores. An additional filter layer is formed by blocked coarser particles at the interface which becomes a new filtration zone for smaller particles. As the process goes on, the geotextile filter acts as a graduated soil filter and a catalyst to produce a natural filter within the soil. The dynamic equilibrium stage involves a gradation of permeability, when the geotextile filter is the most permeable, and the soil furthest from the filter has the lowest permeability. Thus, the fluid flow into the filter will ultimately be controlled by the parent soil. Therefore, the material cross-plane permeability and pore-size characteristics are the two properties that define the performance of geotextiles as filter media [98].

(3) Clogging criteria: This is a gradual clustering of soil particles within the geotextile pore openings as they are trying to pass through the pores [92]. It was suggested that the geotextile having more openings should be beneficial in comparison to the geotextile with fewer openings. As the liquid flows through the openings, some of them will be

blocked by soil particles, but the remaining openings are still available for keeping the satisfactory permeability characteristics [93]. The concept of positive wash through, as a lower limit for a filter criterion, is based on beneficial loose soil particles that provide a satisfactory permeability and resistance to clogging [94,99]. Preventing the clogging of a geotextile can be evaluated using a relationship between particle size to both the diametric and volumetric pore size distributions. When geotextiles are used for filtration, long-term clogging emerges as a serious issue [100].

A geotextile material designed to work as a filter must have an appropriate pore size and distribution and a corresponding degree of permeability in order to ensure the easy flow of liquid as required. Slit film geotextiles are not preferred because opening sizes are unpredictable [98,101].

A particular range of applications for synthetic-based geotextiles are summarized in Table 1.

**Table 1.** Applications of synthetic polymers in geotextiles.

| Polymer | Application | Ref. |
|---|---|---|
| PP | soil erosion control, prevent waterlogging and holding higher stable grounds | [102,103] |
| PP | carpet backing for unpaved road and inland reclamation drives at coastal lands | [104] |
| PP | as core material in geocomposite drains | [105] |
| PP | geotextile filters | [103] |
| PP | as a breakwater in marine engineering applications | [105] |
| PP | road construction and re-pavement | [106] |
| PP, PE | manufacturing artificial grass and geogrids, embankment support and soil reinforcement | [107] |
| PET | separation and filtration | [104] |
| PET | geogrids, embankment support and soil reinforcement | [105] |
| PET | as a puncture-resistant layer over geomembranes in civil applications | [108] |
| PET | for tidal barrage protective devices | [107] |

### *3.5. Applications of Geotextiles Made from Natural Fibers*

The main characteristics needed to decide if a given natural fiber could be appropriate for working in a specific geotextile application consist of its mechanical response, hydraulic properties and durability. These properties are intrinsic outcomes from specific fiber composition, structure, spatial architecture and size, but not all are translated without alterations into the end geotextile product. The variable extent of changes may be induced by choosing a particular fiber extraction technique, yarn and/or fabric structure.

Increased requests for biomass-derived fibers are largely driven by the strong environmental concerns regarding the extensive use and subsequent disposal of synthetic polymers [28]. The benefits of being non-toxic and biodegradable are furthermore accompanied by improvements in soil texture and fertility as a result of better blending and coalescence with soil particles, as well as increased organic content and humidity. It must be mentioned that moisture retention is possible due to the hydrophilic feature of natural

fibers, the usually good water absorption further contributing to a lower surface runoff during strong rainfalls which is a significant benefit. Unfortunately, these advantages come together with a limited durability and difficulties in the attempts to increase at will the available raw material volumes or to finely adjust the working properties. Fiber properties may also exhibit subtle variations between different batches of natural fibers, even for the same vegetal variety, due to the plants' growing environments such as soil type and treatment, inconstant climate, harvesting and conditioning circumstances.

The complex interplay between components and their structural arrangement is a determinant for the properties shown by natural fibers. Cotton, for instance, is lignin-free and may contain up to 96% cellulose [109]. It is highly hydrophilic, soft, but exhibits poor mechanical properties and rapidly degrades in soil, even in terms of weeks, strongly limiting its potential use as a geotextile. On the other hand, coir fibers, which have the highest lignin content (up to 46%), are less hydrophilic, rough and resist much better to microbial attacks and even to salty water [109]. Although, increased lignin content reduces the resistance to UV degradation [110]. Mechanical properties are mixed, a high elasticity being accompanied by low tensile strength and modulus. On the contrary, bast fibers have a low elongation at break comparable with leaf fibers. Foliage fibers are in turn weaker than most bast fibers, except jute [111]. Jute shows a rough texture that improves both the friction soil interface and water absorption. It was found that wet jute swells and could attain contents in moisture higher than 300% [2], which translates into an excellent flexibility over uneven surfaces and recommendations for use in applications such as hill slope protection, erosion control and road construction. In fact, both jute and coir are already used in such interventions, for example, under the form of open-weave woven fabrics, with the mention that coir exhibits a higher durability.

The process of fiber extraction could interfere with the specific mechanical properties. For example, a device-driven extraction of fibers from flax straw has almost halved the tensile strength as compared with classical manual extraction, together with a smaller decline in modulus [112].

After extraction, plant fibers are commonly processed by heavy duty mechanical equipment in nonwoven, woven and mixed fabrics [52]. Both techniques start with fiber opening and carding which homogenize, clean and segregate the raw material. In the case of nonwoven fabrics, the resulting web of longitudinally aligned fibers is made isotropic by cross-lapper and is finally needle punched to increase the cohesion, strength and density by inducing binding points on the randomly oriented fibers stuck by frictional forces. In the woven technique, carding results in a sliver (non-twisted rope strand). Furthermore, sliver fibers are parallelized by sequential drawing and spun into twisted yarns. An increased twist improves the yarn strength and water absorption but is detrimental to yarn tensile modulus. Two sets of threads, longitudinal and transverse, are finally interlaced in a weaving process to obtain the end structure of a woven fabric. Some relevant geotechnical applications of natural fibers are presented in Table 2.

**Table 2.** Examples of employment of natural fibers in geotechnical applications.

| Natural Fibers | Source/Types | Properties | Processing | Application | Ref. |
|---|---|---|---|---|---|
| Water hyacinth | *Eichhornia crassipes*/stem fibers | high water absorption, low strength, low cost, high availability | woven limited life geotextiles (LLGs) | soil erosion control | [113] |
| Reed | *Arundo donax/stem fibers* | high water absorption, low strength | woven limited life geotextiles | soil erosion control, improve soil quality | [114] |
| Roselle or Thai kenaf | *Hibiscus sabdariffa*/long bast fibers | low moisture absorption, high strength | woven limited life geotextiles | soil reinforcement | [51] |
| Sisal | *Agave sisalana Perr*/long leaves fibers | low moisture absorption, high strength | woven limited life geotextiles | soil reinforcement | [115] |
| Coir | *Cocos nucifera*/coconut shells | good hygroscopicity, with high moisture content per volume unit | coir matting | slope stabilization in highland regions, soil moisture retention | [13] |
| | *Cocos nucifera*/coconut husk | high compressibility, low shear strength, high swelling/shrinkage | coir netting | road construction and embankment, eco-friendly drainage/stabilization | [116] |
| Palm | *Borassus aethiopum*/leaves fibers | proper permeability for cohesive soils, highly effective in rainfall handling, increase saturation/infiltration and decrease runoff, high durability | Borassus palm mats | soil erosion control in temperate climates, soil stabilization and conservation in conditions of non-uniform torrential rains | [117] |
| | *Mauritia flexuosa*/leaves fibers | similar to *Borassus*, but slightly less durable and effective in rainfall handling | Buriti palm mats | soil erosion control, stabilization and conservation | [118] |
| Jute | *Corchorus capsularis*/bast fibers | size increase in pores under pressure allows fast dewatering rates, low tensile strengths limit their use to smaller tube diameter | woven/nonwoven jute geotextiles tubes | soil erosion control, filtration, drainage | [119] |
| Cotton | *Gossypium sp.*/seed fibers | high water repellency associated with dry patch formation underneath, increased water losses, low mechanical properties and durability | various limited-life cotton geotextiles | soil erosion control | [120] |
| Bamboo | *Bambuasa blumeana/grass* fibers | good tensile/breaking strengths, effective in rainfall handling of topsoil mass runoff | fiber ropes | surface erosion, slope stabilization | [121] |
| Kenaf | *Hibiscus sabdariffa var altissima*/bast fibers | high tensile strengths, high resistance at direct shear and pullout | hexagonal, plain and knot-plain woven yarns | soil reinforcement | [122] |
| Flax | *Linum usitatissimum*/bast fibers | high porosity, high hydraulic conductivity and sorption capacity of cationic metals | nonwoven geotextiles | design of wastewater, retention and runoff treatment systems | [123] |

## 4. Concluding Remarks and Future Trends

Geotextiles have proven to be classic, as well as high-performance, modern materials. They are successfully applied in geotechnical and civil engineering, in both developed and emerging countries, and the global demand is growing. On a historical scale, there is a certain cyclicity regarding the nature of the fibers used as geotextiles. In antiquity, natural fibers have been used for soil and road stabilization. Modern times have promoted synthetic fibers for geotextiles. Nowadays, the need to reduce the environmental impact of polymer waste has brought back to attention the natural fibers-based geotextiles.

Natural geotextiles respond to societal concerns about the environment by reducing the pollution. Used in short- and medium-term applications, natural geotextiles can replace geosynthetics up to a certain point and are recommended for controlling the soil erosion and in agriculture, for slopes and riverbank stabilization, and in other applications where revegetation is highly desirable. Aside from their properties and low production cost, the local availability of natural fibers is another advantage. Still, their limitation resides in their main feature—biodegradability—but their service life can be prolonged by different strategies, such as modification of natural fibers through various methods or the use of hybrid fibers.

Geosynthetics have superior properties, owing to the synthetic fibers they are made of, and a wider range of applications. Their performance can be further improved using additives during polymer processing or in post-processing stages, or by including the raw polymers in composite formulations along with other reinforcing components (clay micro- and nanoparticles, carbon nanotubes, graphene and graphene oxide particles, carbon fibers, basalt fibers).

The knowledge-based development of technical textiles opens new perspectives for geotextiles. For example, intelligent geotextiles used to stabilize railway infrastructure, dams, embankments or slopes incorporate sensors and are able to sense and monitor mechanical deformations, variation of temperature, humidity and pressure. Thus, they can be used for the early detection of structural failure and its location, which is a major advantage as it allows damage control and timely repairs. However, advances are constantly reported, which proves geotextiles remain an active field of research.

**Author Contributions:** Conceptualization, C.-A.T. and F.T.; methodology, C.-A.T. and F.T.; resources, F.T., M.N., M.-E.I., and C.-A.T.; writing—original draft preparation, F.T., M.N., M.-E.I., and C.-A.T.; writing—review and editing, F.T. and C.-A.T.; visualization, F.T. and C.-A.T.; supervision, F.T. and C.-A.T. All authors have read and agreed to the published version of the manuscript.

**Funding:** This research received no external funding.

**Institutional Review Board Statement:** Not applicable.

**Informed Consent Statement:** Not applicable.

**Conflicts of Interest:** The authors declare no conflict of interest.

## References

1. Haghi, A.K. *Experimental Analysis of Geotextiles and Geofibers Composites*; WSEAS Press: London, UK, 2019.
2. Ingold, T.S. *The Geotextiles and Geomembranes Manual*, 1st ed.; Elsevier: Oxford, UK, 2013; ISBN 9781483292625.
3. Lawrence, C.A. High performance textiles for geotechnical engineering: Geotextiles and related materials. In *High Performance Textiles and Their Applications*; Woodhead Publishing Limited: Sawston, UK, 2014; pp. 256–350. ISBN 9780857099075.
4. Shao, Q.; Gu, W.; Dai, Q.; Makoto, S.; Liu, Y. Effectiveness of geotextile mulches for slope restoration in semi-arid northern China. *CATENA* **2014**, *116*, 1–9. [CrossRef]
5. Hsieh, C.; Wang, J. The Degradation Behavior of Geotextiles in Ocean Environments. *Geosynth. Int.* **2006**, *13*, 543–552. [CrossRef]
6. Carneiro, J.R.; Almeida, P.J.; Lopes, M.D.L. Laboratory Evaluation of Interactions in the Degradation of a Polypropylene Geotextile in Marine Environments. *Adv. Mater. Sci. Eng.* **2018**, *2018*, 9182658. [CrossRef]
7. Shukla, S.K. Geosynthetics and Ground Engineering: Sustainability Considerations. *Int. J. Geosynth. Gr. Eng.* **2021**, *7*, 1–3. [CrossRef]

8. Puppala, A.J.; Banerjee, A.; Congress, S.S.C. Geosynthetics in geo-infrastructure applications. In *Durability of Composite Systems, Woodhead Publishing Series in Composites Science and Engineering*; Reifsnider, K.L., Ed.; Woodhead Publishing: Sawston, UK; Elsevier Ltd.: Amsterdam, The Netherlands, 2020; pp. 289–312. [CrossRef]
9. Vieira, C.S.; Ferreira, F.B.; Pereira, P.M.; de Lopes, M.L. Pullout behaviour of geosynthetics in a recycled construction and demolition material—Effects of cyclic loading. *Transp. Geotech.* **2020**, *23*, 100346. [CrossRef]
10. Adhikary, R. Geotextile and its Importance in Agriculture: A Review Study. *Int. J. Bioresour. Sci.* **2019**, *6*, 61–63. [CrossRef]
11. Heibaum, M. Geosynthetics for waterways and flood protection structures—Controlling the interaction of water and soil. *Geotext. Geomembr.* **2014**, *42*, 374–393. [CrossRef]
12. Ding, K.; Chang, X. Drainage and ecological service of irrigation schemes in China*. *Irrig. Drain.* **2020**, *69*, 97–107. [CrossRef]
13. Vishnudas, S.; Savenije, H.H.G.; Van der Zaag, P.; Anil, K.R. Coir geotextile for slope stabilization and cultivation—A case study in a highland region of Kerala, South India. *Phys. Chem. Earth* **2012**, *47*, 135–138. [CrossRef]
14. Bystrom, J.; Overmann, L.K.; Ericsson, L.O. Geosynthetic containment beneath Stockholm-Arlanda Airport. *Geotext. Geomembr.* **1996**, *14*, 201–205. [CrossRef]
15. Ma, D.X.; Yang, W.K.; Liu, Y.; Lai, Y.; Hou, S.; Ye, Q.; Xiang, H.L. Performance Study Research of New Maintenance Method in Airport Pavement Concrete of China. In *IOP Conference Series: Earth and Environmental Science*; IOP Publishing: Bristol, UK, 2020; Volume 568, p. 012006.
16. ISO 10318-1:2015(en). Geosynthetics—Part 1: Terms and Definitions. Available online: https://www.iso.org/obp/ui/#iso:std:iso:10318:-1:ed-1:v1:en (accessed on 31 March 2022).
17. Mehrpazhouh, A.; Moghadas Tafreshi, S.N.; Mirzababaei, M. Impact of repeated loading on mechanical response of a reinforced sand. *J. Rock Mech. Geotech. Eng.* **2019**, *11*, 804–814. [CrossRef]
18. Javadi, Y.; Hosseini, M.S.; Aghjeh, M.K.R. The effect of carbon black and HALS hybrid systems on the UV stability of high-density polyethylene (HDPE). *Iran. Polym. J.* **2014**, *23*, 793–799. [CrossRef]
19. Baillie, C. *Green Composite: Polymer Composites and the Environment*; CRC Press: Boca Raton, FL, USA, 2004; ISBN 9781845690397.
20. Miszkowska, A.; Lenart, S.; Koda, E. Changes of Permeability of Nonwoven Geotextiles due to Clogging and Cyclic Water Flow in Laboratory Conditions. *Water* **2017**, *9*, 660. [CrossRef]
21. Wiewel, B.V.; Lamoree, M. Geotextile composition, application and ecotoxicology—A review. *J. Hazard. Mater.* **2016**, *317*, 640–655. [CrossRef]
22. Koerner, G.R.; Hsuan, Y.G.; Koerner, R.M. The durability of geosynthetics. In *Geosynthetics in Civil Engineering*; Woodhead Publishing: Sawston, UK, 2007; pp. 36–65. ISBN 9781855736078.
23. Hsuan, Y.; Schroeder, H.; Rowe, K.; Müller, W.; Greenwood, J.; Cazzuffi, D.; Koerner, R. Long-Term Performance and Lifetime Prediction of Geosynthetics. In Proceedings of the Proceedings of the 4th European Conference on Geosynthetics (EuroGeo 2004), Scotland, UK, 1–3 March 2004; pp. 1–40.
24. English, B. Biobased, Biodegradable Geotextiles: Usda Forest Service Research Update. In Proceedings of the 2d Pacific Rim bio-based composites symposium, Vancouver, BC, Canada, 6–9 November 1994; University of British Columbia: Vancouver, BC, Canada, 1994; pp. 204–212.
25. Shirazi, M.G.; Rashid, A.S.B.A.; Bin Nazir, R.; Rashid, A.H.B.A.; Moayedi, H.; Horpibulsuk, S.; Samingthong, W. Sustainable Soil Bearing Capacity Improvement Using Natural Limited Life Geotextile Reinforcement—A Review. *Minerals* **2020**, *10*, 479. [CrossRef]
26. Wu, H.; Yao, C.; Li, C.; Miao, M.; Zhong, Y.; Lu, Y.; Liu, T. Review of application and innovation of geotextiles in geotechnical engineering. *Materials* **2020**, *13*, 1774. [CrossRef]
27. Jiniraj, R.B.; Jayasree, P.K.; Anusha, S.P. Effect of Surface Modification on the Performance of Natural Fibres—A Review. *Gr. Improv. Reinf. Soil Struct.* **2022**, *152*, 609–615. [CrossRef]
28. Prambauer, M.; Wendeler, C.; Weitzenböck, J.; Burgstaller, C. Biodegradable geotextiles—An overview of existing and potential materials. *Geotext. Geomembr.* **2019**, *47*, 48–59. [CrossRef]
29. Rawal, A.; Saraswat, H. Stabilisation of soil using hybrid needlepunched nonwoven geotextiles. *Geotext. Geomembr.* **2011**, *29*, 197–200. [CrossRef]
30. Basu, G.; Roy, A.N.; Mishra, L. Stabilization of earthen river embankment using jute-synthetic hybrid geotextiles—A case study. *Indian J. Geosynth. Gr. Improv.* **2020**, *9*, 39–45.
31. Bilisik, K.; Syduzzaman, M. Knitted geotextiles. In *Advanced Knitting Technology*; Maity, S., Rana, S., Pandit, P., Singha, K., Eds.; Woodhead Publishing: Sawston, UK; Elsevier Ltd.: Amsterdam, The Netherlands, 2022; pp. 345–394.
32. Anand, S. Designer natural fibre geotextiles—A new concept. *Indian J. Fibre Text. Res.* **2008**, *33*, 339–344.
33. Ding, Z.; Babar, A.A.; Wang, C.; Zhang, P.; Wang, X.; Yu, J.; Ding, B. Spunbonded needle-punched nonwoven geotextiles for filtration and drainage applications: Manufacturing and structural design. *Compos. Commun.* **2021**, *25*, 100481. [CrossRef]
34. Chattopadhyay, B.C.; Chakravarty, S. Application of jute geotextiles as facilitator in drainage. *Geotext. Geomembr.* **2009**, *27*, 156–161. [CrossRef]
35. Ge, S.; Zhang, X.; Wang, Y.; Zheng, L.; Xie, X. Electro-Osmosis Treatment of Lead-Contaminated Soil with Carbon Fiber-Based Geotextile Electrodes. *Int. J. Electrochem. Sci.* **2020**, *15*, 11454–11467. [CrossRef]
36. Jahan, I. Removal of Aluminium from Filter Backwash Water Using Adsorbents and a Geotextile. Doctoral Dissertation, Dalhousie University, Halifax, NS, Canada, 2016.

37. Koerner, G.R. Geotextiles used in separation. In *Geotextiles: From Design to Applications*; Koerner, R.M., Ed.; Woodhead Publishing: Sawston, UK, 2016; pp. 239–256. ISBN 9780081002346.
38. Broda, J.; Gawłowski, A.; Rom, M.; Laszczak, R.; Mitka, A.; Przybylo, S.; Grzybowska-Pietras, J. Innovative geotextiles for reinforcement of roadside ditch. *Tekstilec* **2016**, *59*, 115–120. [CrossRef]
39. Liu, J.; Li, X. Analytical solution for estimating groundwater inflow into lined tunnels considering waterproofing and drainage systems. *Bull. Eng. Geol. Environ.* **2021**, *80*, 6827–6839. [CrossRef]
40. Tano, F.; Olivier, F.; Touze-Foltz, N.; Dias, D. State-of-the-art of piggy-back landfills worldwide: Comparison of containment barrier technical designs and performance analysis in terms of geosynthetics stability. In Proceedings of the Geosynthetics, Portland, OR, USA, 15–18 February 2015; p. 11.
41. Shackelford, C.D.; Meier, A.; Sample-Lord, K. Limiting membrane and diffusion behavior of a geosynthetic clay liner. *Geotext. Geomembr.* **2016**, *44*, 707–718. [CrossRef]
42. Geotextiles Market Size & Share. Industry Report. 2020–2027. Available online: https://www.grandviewresearch.com/industry-analysis/geotextiles-industry (accessed on 7 March 2022).
43. Geotextiles Market Size. Share & Report. Industry Growth. 2028. Available online: https://www.fortunebusinessinsights.com/geotextiles-market-105063 (accessed on 7 March 2022).
44. Koerner, R.M. *Geotextiles: From Design to Applications*; Woodhead Publishing: Sawston, UK, 2016; ISBN 9780081002346.
45. Rawal, A.; Shah, T.H.; Anand, S.C. Geotextiles in civil engineering. In *Handbook of Technical Textiles: Technical Textile Applications*; Horrocks, A.R., Anand, S.C., Eds.; Woodhead Publishing: Amsterdam, The Netherlands, 2016; pp. 111–133. ISBN 9781782424659.
46. Kupolati, W.K.; Sadiku, E.R.; Ibrahim, I.D.; Adeboje, A.O.; Kambole, C.; Ojo, O.O.S.; Eze, A.A.; Paige-Green, P.; Ndambuki, J.M. The use of polyolefins in geotextiles and engineering applications. In *Polyolefin Fibres: Structure, Properties and Industrial Applications*; Elsevier Ltd.: Amsterdam, The Netherlands, 2017; pp. 497–516. ISBN 9780081012512.
47. Pelyk, L.V.; Vasylechko, V.O.; Kyrychenko, O.V. Influence of Biodestructors on the Wear Resistance of Polyester Geotextile Materials. *Colloids Interfaces* **2019**, *3*, 21. [CrossRef]
48. Koerner, R.M.; Hsuan, Y.G.; Koerner, G.R. Lifetime predictions of exposed geotextiles and geomembranes. *Geosynth. Int.* **2017**, *24*, 198–212. [CrossRef]
49. Rawal, A. Woven fabrics for geotextiles. In *Woven Textiles: Principles, Technologies and Applications*; Gandhi, K.L., Ed.; Woodhead Publishing Limited: Amsterdam, The Netherlands, 2012; pp. 367–386. ISBN 9781845699307.
50. Ajmeri, J.R.; Ajmeri, C.J. Developments in nonwoven as geotextiles. In *Advances in Technical Nonwovens*; Woodhead Publishing: Sawston, UK, 2016; pp. 339–363. [CrossRef]
51. Methacanon, P.; Weerawatsophon, U.; Sumransin, N.; Prahsarn, C.; Bergado, D.T. Properties and potential application of the selected natural fibers as limited life geotextiles. *Carbohydr. Polym.* **2010**, *82*, 1090–1096. [CrossRef]
52. Desai, A.N.; Kant, R. Geotextiles made from natural fibres. In *Geotextiles: From Design to Applications*; Koerner, R.M., Ed.; Woodhead Publishing: Sawston, UK, 2016; pp. 61–87. ISBN 9780081002346.
53. Koohestani, B.; Darban, A.K.; Mokhtari, P.; Yilmaz, E.; Darezereshki, E. Comparison of different natural fiber treatments: A literature review. *Int. J. Environ. Sci. Technol.* **2019**, *16*, 629–642. [CrossRef]
54. Lewin, M.; Sello, S.B. *Fibre Chemistry: Handbook of Fiber Science and Technology*; Lewin, M., Pearce, E.M., Eds.; Marcel Dekker Inc.: New York, NY, USA, 1983; Volume 4, ISBN 9780824773359.
55. Kirby, R.H. *Vegetable Fibres, Botany, Cultivation, and Utilization*; Leonard Hill Ltd.: London, UK, 1963.
56. Mwasha, A. Using environmentally friendly geotextiles for soil reinforcement: A parametric study. *Mater. Des.* **2009**, *30*, 1798–1803. [CrossRef]
57. Future Fibres: Publications. Available online: https://www.fao.org/economic/futurefibres/resources2/en/ (accessed on 8 March 2022).
58. Gosselink, R.J.A.; van der Putten, J.C.; van der Kolk, J.C.; van Dam, J.E.G.; de Klerk-Engels, B. Vegetable fibre based geotextiles with adjusted durability. In Proceedings of the IECA Annual Conference, Palm Springs, CA, USA, 21–25 February 2000.
59. Ghosh, S.K.; Bhattacharyya, R.; Mondal, M.M.; Choudhury, P.K.; Sanyal, T. Design and development of woven jute geotextiles for potential applications in the field of geotechnical constructions. *J. Text. Inst.* **2015**, *106*, 550–563. [CrossRef]
60. Ghosh, M.; Rao, G.V.; Chakrabarti, S.K.; Pal, S.; Sarma, U.S. Biodegradability study to develop longer life jute geotextiles for road applications. *Text. Res. J.* **2019**, *89*, 4162–4172. [CrossRef]
61. Ramzan, M.B.; Naeem, M.S.; ur Rehman, A.; Raza, A. Fibers for Geotextiles. In *Topics in Mining, Metallurgy and Materials Engineering*; Ahmad, S., Rasheed, A., Nawab, Y., Eds.; Springer: Cham, Switzerland, 2020; pp. 129–149.
62. Yan, S.; He, P.; Jia, D.; Yang, Z.; Duan, X.; Wang, S.; Zhou, Y. Effect of fiber content on the microstructure and mechanical properties of carbon fiber felt reinforced geopolymer composites. *Ceram. Int.* **2016**, *42*, 7837–7843. [CrossRef]
63. Saafi, M.; Tang, L.; Fung, J.; Rahman, M.; Liggat, J. Enhanced properties of graphene/fly ash geopolymeric composite cement. *Cem. Concr. Res.* **2015**, *67*, 292–299. [CrossRef]
64. Behera, P.; Baheti, V.; Militky, J.; Naeem, S. Microstructure and mechanical properties of carbon microfiber reinforced geopolymers at elevated temperatures. *Constr. Build. Mater.* **2018**, *160*, 733–743. [CrossRef]
65. Wang, Q.; Bai, Y.; Xie, J.; Jiang, Q.; Qiu, Y. Synthesis and filtration properties of polyimide nanofiber membrane/carbon woven fabric sandwiched hot gas filters for removal of PM 2.5 particles. *Powder Technol.* **2016**, *292*, 54–63. [CrossRef]

66. Golchin, B.; Safayi, R. Effect of Carbon Fibers on Fracture Toughness of Asphalt Mixtures Using Linear Elastic Fracture Mechanics. *J. Transp. Infrastruct. Eng.* **2018**, *4*, 77–92. [CrossRef]
67. Yetimoglu, T.; Inanir, M.; Inanir, O.E. A study on bearing capacity of randomly distributed fiber-reinforced sand fills overlying soft clay. *Geotext. Geomembr.* **2005**, *23*, 174–183. [CrossRef]
68. Baruah, H. Effect of glass fibers on red soiL. *Int. J. Technol. Eng. Sci.* **2015**, *3*, 217–223.
69. Zhang, P.; Han, S.; Ng, S.; Wang, X.H. Fiber-Reinforced Concrete with Application in Civil Engineering. *Adv. Civ. Eng.* **2018**, *2018*, 1698905. [CrossRef]
70. Qureshi, L.A.; Ahmad, J.; Salahuddin, H. Seismic vulnerability assessment of strengthened Glass Fiber Reinforced Concrete (GFRC). *KSCE J. Civ. Eng.* **2017**, *21*, 2235–2244. [CrossRef]
71. Hsing, W.H.; Lou, C.W.; Lin, C.W.; Chen, J.M.; Lin, J.H. Effects of the Content of High Strength Polyethylene Terephthalate Fiber and Kevlar Fiber on Properties of Geotextiles. *Appl. Mech. Mater.* **2013**, *365*, 1082–1085. [CrossRef]
72. Valen a, S.L.; Griza, S.; De Oliveira, V.G.; Sussuchi, E.M.; De Cunha, F.G.C. Evaluation of the mechanical behavior of epoxy composite reinforced with Kevlar plain fabric and glass/Kevlar hybrid fabric. *Compos. Eng.* **2015**, *70*, 1–8. [CrossRef]
73. Hsieh, J.-C.; Pan, Y.-J.; Tan, H.-J.; Hsing, W.-H.; Lou, C.-W.; Lin, J.-H. Property Evaluations of Geotextiles Containing High Modulus Fibers. *DEStech. Trans. Eng. Technol. Res.* 2017. [CrossRef]
74. Lin, C.W.; Hsing, W.H.; Lou, C.W.; Chen, J.M.; Lin, J.H. Manufacturing Technique and Property Evaluation of Eco-Friendly Kevlar/PET/Nylon Composite Geotextile. In *Applied Mechanics and Materials*; Trans Tech Publications Ltd.: Freienbach, Switzerland, 2013; Volume 365, pp. 1157–1160. [CrossRef]
75. Lin, J.H.; Hsieh, J.C.; Hsing, W.H.; Pan, Y.J.; Hsieh, C.T.; Tan, H.J.; Li, J.H.; Lou, C.W. Applications of geotextiles made of PET-filament-based nonwoven fabrics. *Fibers Polym.* **2016**, *17*, 1955–1962. [CrossRef]
76. Li, T.T.; Zhou, X.; Wang, Z.; Fan, Y.; Zhang, X.; Lou, C.W.; Lin, J.H. A study on design and properties of woven-nonwoven multi-layered hybrid geotextiles. *J. Ind. Text.* **2020**, 1528083720964703. [CrossRef]
77. Lewandowski, M.; Amiot, M.; Perwuelz, A. Development and characterization of 3D nonwoven composites. *Mater. Sci. Forum* **2012**, *714*, 131–137. [CrossRef]
78. Derombise, G.; Van Schoors, L.V.; Davies, P. Degradation of Technora aramid fibres in alkaline and neutral environments. *Polym. Degrad. Stab.* **2009**, *94*, 1615–1620. [CrossRef]
79. Gao, L.; Hu, G.; Xu, N.; Fu, J.; Xiang, C.; Yang, C. Experimental Study on Unconfined Compressive Strength of Basalt Fiber Reinforced Clay Soil. *Adv. Mater. Sci. Eng.* **2015**, *2015*, 561293. [CrossRef]
80. Krayushkina, K.; Bieliatynskyi, A. Perspectives of usage of seamless and fiber basalt filament for construction and rehabilitation of motor roads and airfields. In Proceedings of the 11th International Conference "Environmental Engineering", Vilnius, Lithuania, 21–22 May 2020; pp. 1–9.
81. Theisen, M.S. The role of geosynthetics in erosion and sediment control: An overview. *Geotext. Geomembr.* **1992**, *11*, 535–550. [CrossRef]
82. Carroll, R.G.; Rodencal, J.; Collin, J.G. Geosynthetics in erosion control—The principles. *Geotext. Geomembr.* **1992**, *11*, 523–534. [CrossRef]
83. Departments of the Army and the Air Force. Engineering Use of Geotextiles TM 5-818-8. 1995. Available online: https://citeseerx.ist.psu.edu/viewdoc/download?doi=10.1.1.433.4088&rep=rep1&type=pdf (accessed on 2 April 2022).
84. Raymond, G.P. Railway rehabilitation geotextiles. *Geotext. Geomembr.* **1999**, *17*, 213–230. [CrossRef]
85. Paulson, J.N. Geosynthetic Material and Physical Properties Relevant to Soil Reinforcement Applications. *Geotext. Geomembr.* **1987**, *6*, 211–223. [CrossRef]
86. Al-Barqawi, M.; Aqel, R.; Wayne, M.; Titi, H.; Elhajjar, R. Polymer Geogrids: A Review of Material, Design and Structure Relationships. *Materials* **2021**, *14*, 4745. [CrossRef]
87. Ghosh, T.K. Puncture resistance of pre-strained geotextiles and its relation to uniaxial tensile strain at failure. *Geotext. Geomembr.* **1998**, *16*, 293–302. [CrossRef]
88. Rawal, A.; Shah, T.; Anand, S. Geotextiles: Production, properties and performance. *Text. Prog.* **2010**, *42*, 181–226. [CrossRef]
89. van Harten, K. The relation between specifications of geotextiles and their essential properties. *Geotext. Geomembr.* **1986**, *3*, 53–76. [CrossRef]
90. Koerner, R.M.; Koerner, G.R. Lessons learned from geotextile filter failures under challenging field conditions. *Geotext. Geomembr.* **2015**, *43*, 272–281. [CrossRef]
91. Christopher, B.R.; Fischer, G.R. Geotextile filtration principles, practices and problems. *Geotext. Geomembr.* **1992**, *11*, 337–353. [CrossRef]
92. Palmeira, E.M.; Trejos Galvis, H.L. Opening sizes and filtration behaviour of nonwoven geotextiles under confined and partial clogging conditions. *Geosynth. Int.* **2017**, *24*, 125–138. [CrossRef]
93. Luettich, S.M.; Giroud, J.P.; Bachus, R.C. Geotextile filter design guide. *Geotext. Geomembr.* **1992**, *11*, 355–370. [CrossRef]

94. Watson, P.D.J.; John, N.W.M. Geotextile filter design and simulated bridge formation at the soil–geotextile interface. *Geotext. Geomembr.* **1999**, *17*, 265–280. [CrossRef]
95. Chen, R.H.; Ho, C.C.; Hsu, C.Y. The effect of fine soil content on the filtration characteristics of geotextile under cyclic flows. *Geosynth. Int.* **2008**, *15*, 95–106. [CrossRef]
96. Palmeira, E.M.; Gardoni, M.G. Drainage and filtration properties of non-woven geotextiles under confinement using different experimental techniques. *Geotext. Geomembr.* **2002**, *20*, 97–115. [CrossRef]
97. Zhang, Y.; Liu, W.; Shao, W.; Yang, Y. Experimental study on water permittivity of woven polypropylene geotextile under tension. *Geotext. Geomembr.* **2013**, *37*, 10–15. [CrossRef]
98. Wu, C.S.; Hong, Y.S.; Wang, R.H. The influence of uniaxial tensile strain on the pore size and filtration characteristics of geotextiles. *Geotext. Geomembr.* **2008**, *26*, 250–262. [CrossRef]
99. Palmeira, E.M.; Melo, D.L.A.; Moraes-Filho, I.P. Geotextile filtration opening size under tension and confinement. *Geotext. Geomembr.* **2019**, *47*, 566–576. [CrossRef]
100. Aydilek, A.H.; Edil, T.B. Long-term filtration performance of nonwoven geotextile-sludge systems. *Geosynth. Int.* **2003**, *10*, 110–123. [CrossRef]
101. Wu, C.S.; Hong, Y.S. The influence of tensile strain on the pore size and flow capability of needle-punched nonwoven geotextiles. *Geosynth. Int.* **2016**, *23*, 422–434. [CrossRef]
102. Dafalla, M.; Obaid, A. The Role of Polypropylene Fibers and Polypropylene Geotextile in Erosion Control. In Proceedings of the Second International Conference on Geotechnical and Earthquake Engineering, Lisboa, Portugal, 21–25 June 2013; pp. 669–676.
103. Patanaik, A.; Anandjiwala, R.D. Water flow through the polypropylene-based geotextiles. *J. Appl. Polym. Sci.* **2008**, *108*, 3876–3880. [CrossRef]
104. Rankilor, P.R. Textiles in civil engineering. Part 1—Geotextiles. In *Handbook of Technical Textiles*; Horrocks, A.R., Anand, S.C., Eds.; Woodhead Publishing: Cambridge, UK, 2000; pp. 358–371.
105. Koerner, R.M. Early background and history of geotextiles. In *Geotextiles: From Design to Applications*; Koerner, R.M., Ed.; Woodhead Publishing: Amsterdam, The Netherlands, 2016; pp. 3–15. ISBN 9780081002346.
106. Levy, T. The Use of Polypropylene Nonwoven Geotextiles Impregnated with Bituminous Binder in Road Pavements. *J. Coat. Fabr.* **1990**, *20*, 82–87. [CrossRef]
107. Agrawal, B.J. Geotextile: It's application to civil engineering–overview. In Proceedings of the National Conference on Recent Trends in Engineering & Technology, Gujarat, India, 13–14 May 2011; pp. 1–6.
108. Koerner, G.R.; Koerner, R.M. Puncture resistance of polyester (PET) and polypropylene (PP) needle-punched nonwoven geotextiles. *Geotext. Geomembr.* **2011**, *29*, 360–362. [CrossRef]
109. Daria, M.; Krzysztof, L.; Jakub, M. Characteristics of biodegradable textiles used in environmental engineering: A comprehensive review. *J. Clean. Prod.* **2020**, *268*, 122129. [CrossRef]
110. Lawrence, C.; Collier, B.J. Natural geotextiles. In *Biodegradable and Sustainable Fibres*; Blackburn, R.S., Ed.; Woodhead Publishing: Sawston, UK, 2005; pp. 343–366. ISBN 9781855739161.
111. Leão, A.L.; Cherian, B.M.; De Souza, S.F.; Kozłowski, R.M.; Thomas, S.; Kottaisamy, M. Natural fibres for geotextiles. In *Handbook of Natural Fibres*; Kozlowski, R., Ed.; Woodhead Publishing: Sawston, UK, 2012; pp. 280–311.
112. Le Guen, M.J.; Newman, R.H.; Fernyhough, A.; Hill, S.J.; Staiger, M.P. Correlations Between the Physiochemical Characteristics of Plant Fibres and Their Mechanical Properties. In *RILEM Bookseries*; Springer: Dordrecht, The Netherlands, 2016; Volume 12, pp. 35–47. ISBN 9789401775137.
113. Chow, M.F.; Hashrim, H.; Chong, S.T.; Ng, Y.J. Investigating the effectiveness of Water Hyacinth Fiber Mat for Soil Erosion Control. In *IOP Conference Series: Materials Science and Engineering*; IOP Publishing: Bristol, UK, 2019.
114. Visconti, D.; Fiorentino, N.; Cozzolino, E.; Di Mola, I.; Ottaiano, L.; Mori, M.; Cenvinzo, V.; Fagnano, M. Use of giant reed (Arundo donax L.) to control soil erosion and improve soil quality in a marginal degraded area. *Ital. J. Agron.* **2020**, *15*, 332–338. [CrossRef]
115. Sharma, A.K.; Prasannan, S.; Kolathayar, S. Comparative Study of Sisal and PVA Fiber for Soil Improvement. In *Eighth International Conference on Case Histories in Geotechnical Engineering, Geocongress*; American Society of Civil Engineers (ASCE): Philadelphia, PA, USA, 2019; pp. 298–304.
116. Meshram, K.; Mittal, S.K.; Jain, P.K.; Agarwal, P.K. Application of Coir Geotextile for Road Construction: Some Issues. *Orient. Int. J. Innov. Eng. Res.* **2013**, *1*, 25–29.
117. Davies, K.; Fullen, M.A.; Booth, C.A. A pilot project on the potential contribution of palm-mat geotextiles to soil conservation. *Earth Surf. Process. Landf.* **2006**, *31*, 561–569. [CrossRef]
118. Bhattacharyya, R.; Fullen, M.A.; Booth, C.A. Using palm-mat geotextiles on an arable soil for water erosion control in the UK. *Earth Surf. Process. Landf.* **2011**, *36*, 933–945. [CrossRef]
119. Kiffle, Z.B.; Steele, S.E.; Bhatia, S.K.; Smith, J.L. Use of Jute as a Sustainable Alternative for PP in Geotextile Tubes. In Proceedings of the Geotechnical Frontiers 2017, Orlando, Florida, 12–15 March 2017; pp. 369–378.
120. Giménez-Morera, A.; Ruiz Sinoga, J.D.; Cerdà, A. The impact of cotton geotextiles on soil and water losses from mediterranean rainfed agricultural land. *L. Degrad. Dev.* **2010**, *21*, 210–217. [CrossRef]

121. Valle, S.B.; Albay, R.D.; Montilla, A.M. Bambusa blumeana fiber as erosion control geotextile on steep slopes. In *IOP Conference Series: Materials Science and Engineering*; IOP Publishing: Bristol, UK, 2019; Volume 513. [CrossRef]
122. Artidteang, S.; Bergado, D.T.; Tanchaisawat, T.; Saowapakpiboon, J. Investigation of tensile and soil-geotextile interface strength of kenaf woven limited life geotextiles (llgs). *Lowl. Technol. Int.* **2012**, *14*, 1–8.
123. Abbar, B.; Alem, A.; Pantet, A.; Marcotte, S.; Ahfir, N.D.; Wang, H.; Ouahbi, T.; Duchemin, B.; Duriatti, D. Nonwoven flax fibres geotextiles effects on solute heavy metals transport in porous media. *Environ. Technol.* **2018**, *41*, 2061–2072. [CrossRef] [PubMed]

*textiles*

MDPI

*Review*

# Review of Fiber- or Yarn-Based Wearable Resistive Strain Sensors: Structural Design, Fabrication Technologies and Applications

**Fei Huang [1], Jiyong Hu [1,2,*] and Xiong Yan [1]**

[1] Shanghai Collaborative Innovation Center of High Performance Fibers and Composites, College of Textiles, Donghua University, Shanghai 201620, China; 1215016@mail.dhu.edu.cn (F.H.); yaxi@dhu.edu.cn (X.Y.)
[2] Key Laboratory of Textile Science & Technology, Ministry of Education, Donghua University, Shanghai 201620, China
* Correspondence: hujy@dhu.edu.cn

**Abstract:** Flexible textile strain sensors that can be directly integrated into clothing have attracted much attention due to their great potential in wearable human health monitoring systems and human–computer interactions. Fiber- or yarn-based strain sensors are promising candidate materials for flexible and wearable electronics due to their light weights, good stretchability, high intrinsic and structural flexibility, and flexible integrability. This article investigates representative conductive materials, traditional and novel preparation methods and the structural design of fiber- or yarn-based resistive strain sensors as well as the interconnection and encapsulation of sensing fibers or yarns. In addition, this review summarizes the effects of the conductive materials, preparation strategy and structures on the crucial sensing performance. Discussions will be presented regarding the applications of fiber- or yarn-based resistive strain sensors. Finally, this article summarizes the bottleneck of current fiber- or yarn-based resistive strain sensors in terms of conductive materials, fabrication techniques, integration and performance, as well as scientific understanding, and proposes future research directions.

**Keywords:** resistive strain sensor; fiber-based sensor; yarn-based sensor; interconnection

**Citation:** Huang, F.; Hu, J.; Yan, X. Review of Fiber- or Yarn-Based Wearable Resistive Strain Sensors: Structural Design, Fabrication Technologies and Applications. *Textiles* **2022**, 2, 81–111. https://doi.org/10.3390/textiles2010005

Academic Editor: Laurent Dufossé

Received: 29 December 2021
Accepted: 4 February 2022
Published: 8 February 2022



## 1. Introduction

As the demand for the real-time monitoring of human motion and physiological information has recently grown, miniature and intelligent wearable electronic devices have been rapidly developed. Nowadays, a variety of wearable electronic products, such as electronic skins, smart watches and sports wristbands, are becoming an indispensable part of our lives and changing our behavior patterns and lifestyles. Strain sensors are important components of wearable electronic devices, which register and transmit changes in human motion parameters and physical health indicators through electrical signal responses [1]. However, the rigidity of traditional semiconductor or metal sensors [2,3] limits effective interactions with the curved surface of the human body, resulting in the distortion or inaccuracy of the collected electrical signals. In addition, they are not deformable enough to meet the large strain requirements of the human body [4], as the tensile exerts stress and strain on the sensors in the various deformation modes (tensile, compression, bending, shear and torsion) [5]. Therefore, it is necessary to develop flexible and stretchable strain sensors.

According to the substrate structure, flexible sensors are divided into 1D fiber or yarn strain sensors [6–9], 2D film [10–12], fiber mat [13,14] or fabric [15–18] strain sensors, and 3D aerogel [19–21] or foam [22,23] strain sensors. Compared with 2D or 3D flexible strain sensors, fiber-based and yarn-based sensors are smaller in size and more flexible to better fit the soft and curved human body, and thus detect subtle movements more accurately.

Additionally, the multihierarchy nature of the fiber or yarn structure (fiber-yarn-fabric garment) shows outstanding softness and stretchability, enabling it to deform appropriately when subjected to additional stress or its own gravity. A large number of fibers can also disperse the stress to avoid excessive damage to the device structure. Moreover, they are easy to interconnect with the components of wearable electronics and hide in fabrics with different complex structures. Therefore, fiber or yarn sensors meet the requirements of excellent flexibility, air permeability and comfort for wearable electronic devices due to their advantages of softness, portability, ductility and easy implantation into complex structures. They are more suitable for the development of a new generation of flexible strain sensors. The characteristics of flexible strain sensors with different substrates are summarized in Table 1.

**Table 1.** Features of flexible strain sensors with different structures.

| Strain Sensors | Advantages | Disadvantages |
|---|---|---|
| Fibers or yarns | Good stretchability and flexibility, and easy to realize accurate detection of joint movement with a single direction. | Poor stability. |
| Fiber mats | Good stretchability and permeability. | Uneasy to integrate into clothing and realize the accurate detection of joint movement with single direction. |
| Fabrics | Easy to fabrication with various structures. | Poor stretchability, stability and durability. |
| Films | Good stretchability and easy-to-design patterns. | Poor permeability, difficult to integrate and unable to accurately detect joint movement with a single direction; poor comfort. |
| Aerogels or foams | Suitable for detect pressure. | Poor stretchability and hysteresis. |

According to the sensing mechanism, textile strain sensors are mainly categorized as resistive, capacitive [24–27], piezoelectric [28,29], inductive [30,31], triboelectric [32], or optical [33]. In terms of fiber- and yarn-based strain sensors, resistive and capacitive sensors are the most widely studied, as shown in Table 2. Resistive sensors realize strain detection by detecting changes in resistance. They have the advantages of a simple assembly process and easy signal identification, but their linearity is low. Capacitive sensors are composed of a dielectric layer and two electrode layers. The dielectric layer is sandwiched between the two electrode layers and deformed under the applied strain. This kind of strain sensor has a good linear response to strain, but it is easily affected by the environment, considering aspects such as temperature and humidity. This review mainly focuses on the research progress of resistive strain sensors.

There are two common methods for preparing 1D flexible resistive strain sensors. One is to prepare stretchable conductive composite fibers by a spinning method. The other is to coat conductive materials on the surface of a substrate to form stretchable conductive strain sensors by methods such as dip coating, in situ polymerization, layer-by-layer assembly and so on. The performances of strain sensors (in terms of mechanical properties, workable strain range, sensitivity, repeat stability, response time, linearity, etc.) are affected by the conductive materials and elastic matrix, conductive network and yarn structure. Although plenty of studies have been conducted and great progress has been made in the field of flexible strain sensors, most of the reported sensors are far from being implemented in practical applications due to technical obstacles and challenges. At present, there is still a lack of comprehensive reviews covering the selection of conductive materials, the preparation and structural design of fiber and yarn strain sensors, and

interconnection packaging and applications. In this review, the latest research progress and various modification strategies of fiber and yarn resistive strain sensors are first introduced, and the emphasis is placed on the influence of conductive materials on the electrical performance of the sensor, as well as the influence of different fabrication technologies and structural design on sensing performance. Moreover, the integration strategy and application prospects of existing fiber and yarn strain sensors are discussed. Finally, the limitations and prospects of fiber- and yarn-based strain sensors in terms of performances and scientific understanding are summarized and analyzed.

**Table 2.** Features of resistive and capacitive strain sensors.

| Strain Sensor | Principle | Gauge Factor | Benefits | Drawbacks |
|---|---|---|---|---|
| Resistive | Detection of resistance changes to achieve strain detection ($R = \rho l/A$). | $[(R - R_0)/R_0]/\varepsilon$ | Easy to identify signals, wide working strain range, good frequency response characteristics, and high sensitivity. | Poor linearity, poor long-term cycle stability, and high hysteresis. |
| Capacitive | Detection of capacitance changes to achieve strain detection ($C = \varepsilon_0\varepsilon_r A/d$). | $[(C - C_0)/C_0]/\varepsilon$ | Good linearity, long-term cycle stability, and low hysteresis. | Limited to working strain range, susceptible to the surrounding environment, and small sensitivity. |

## 2. Conductive Materials

In terms of the resistive flexible strain sensors, the conductivity of conductive materials and the structure of the conductive network not only determine their initial resistances, but also affect the range of resistance variation and the working strain. On the one hand, if the initial resistance of the strain sensor is too large, its resistance will easily increase beyond the range of the test instrument under large strain, which limits the application range of the strain sensor [34]. Additionally, it will cause an excessive static load and large power consumption. Therefore, the initial resistance range of the sensor should preferably not exceed megohms. On the other hand, if the initial resistance of the strain sensor is too small, it can easily be affected by other external resistances, such as interconnected contact resistance, which leads to a lower sensitivity and inaccurate measurement. Apart from the electrical resistance, the stability and the compatibility with the elastic matrix should also be considered when conductive materials are selected. At present, the common conductive materials include intrinsic conducting polymers, such as polypyrrole (PPy) [35], polyaniline (PANI), polythiophene (PTh) and PEDOT:PSS [36]; advanced carbon-based materials, such as carbon black (CB) [37], carbon nanotubes (CNTs) [38–40] and graphene (Gr) [4,41]; metal materials, such as gold (Au) [42], silver (Ag) [43–45], copper (Cu) [46,47] and liquid alloys [48]; and a new transition metal carbon/nitride 2D nano-layered material, MXene [16,49]. The characteristics of each conductive material are summarized in Table 3.

### *2.1. Conducting Polymer*

Conducting polymers have a conjugated long-chain structure and the delocalized $\pi$ electrons on the double bond migrate to the molecular chain to form a current, and thus the material exhibits conductivity. Due to the general solubility of their corresponding monomers, conducting polymers can be formed in situ in a soft polymer matrix and are flexible in processing and compatible with elastomeric polymers. However, their charge/discharge stability and ramp voltage are low, since the electron transfer of the con-

ducting polymers are controlled by the doping concentration (10–50%). The conductivity of conducting polymers is much lower than that of metal. Furthermore, conducting polymers are more brittle and rigid than linear aliphatic polymers, because their π-conjugated main chain structure is composed of olefin bonds or aromaticity [55]. Seyedin et al. reported PU/PEDOT: PSS elastomeric composite fibers by a wet-spinning method and their resistance shifted towards higher resistances with the increase in the stretching–releasing cycle period [56]. In actual applications, the stability of conducting polymers is not good enough, especially doping materials when considering air oxidation stability. Therefore, the combination of conducting polymers and carbon-based nanomaterials as conductive sensing materials is another used method [57]. For example, Li et al. proposed a wearable strain sensor by using thermoplastic polyurethane fibers as the core support, aligned and interconnected carbon nanotubes in the sub-outer layer as conductive filaments and the outer layer of PPy coating as the cladding layer [58]. It has a wide detectable range (from 0.1% to 50% tensile strain) and performs a multichannel detection of deformation capabilities (tension, bending and torsion). Wu et al. prepared a PEDOT: PSS/CNT/TPU composite fiber strain sensor by dip coating. In this layered microstructure, PEDOT: PSS is used as a sensing material to reduce the initial resistance and improve the sensitivity of the sensor, while the CNT aggregate acts as a conductive bridge to ensure conductivity at large strains, providing a larger sensing range for the sensor [59].

**Table 3.** Common conductive materials and their characteristics [4,50–54].

| Types | Conductive Materials | Conductivity (S/cm) | Characteristics |
|---|---|---|---|
| Conducting polymers | PPy | 2000 | Solution processability, low-temperature synthesis route. |
| | PANI | 112 | |
| | PTh | 560 | |
| | PEDOT: PSS | 4700 | |
| Carbon based | CB | 1000 | Light, good chemical and thermal stability, difficult to disperse. |
| | CNT | $3.8 \times 10^5$ | |
| | Gr | 7200 | |
| Metal | Au | $4.10 \times 10^7$ | Excellent electrical conductivity, brittle, heavy, poor interface compatibility. |
| | Ag | $6.31 \times 10^7$ | |
| | Cu | $5.96 \times 10^7$ | |
| | EGaIn | $4.8 \times 10^5$ | |
| Transition metal carbon/nitride material | MXene | 4600 | Hydrophilicity, good biocompatibility, but expensive, easy to oxidize. |

### *2.2. Carbon-Based Materials*

Carbon-based materials with excellent conductivity and multidimensional structures are suitable for manufacturing large-strain, high-sensitivity flexible strain sensors. Seyedin et al. used a variety of conductive fillers (such as spherical CB, rod-shaped SWCNTs and chemically converted Gr sheets) to prepare different conductive fibers by wet-spinning technology [60]. It was found that the electrical and mechanical properties of composite fibers depend on the length and the length-diameter ratio of fillers as well as the interaction between the fillers and the elastomer. Overall, CB has a lower cost and better dispersion than CNTs and graphene. Doping CB in CNTs and Gr can improve sensor performance while reducing manufacturing costs. For example, Zhang et al. prepared a simple and low-cost strain sensor by sequentially coating CNTs and CB on the PU yarn by a layer-by-layer assembly method [61]. Under small strain, the conductive network of the CB layer breaks, while the conductive network of the CNT layer does not break until a large enough strain is reached. The CB layer and CNT layer rupture successively with strain, so that the sensor exhibits super stretchability and a large linear range (15–150%).

Compared with CNTs with a high length-diameter ratio, 0D CB has a higher degree of freedom of deformation, so the point-to-point conductive network will be destroyed more obviously during the stretching process, giving the strain sensor better sensitivity [62–64].

CNTs tend to aggregate and entangle with each other when mixed with polymers due to the high length-diameter ratio and large specific surface area. Consequently, it is difficult for them to uniformly disperse in the polymer matrix, not allowing for the excellent conductivity they show in composite fibers. In addition to using dispersants, CNTs can also be modified with polar functional groups, such as carboxyl (-COOH) and hydroxyl (-OH), to improve the dispersibility and adhesion of CNTs in the matrix. However, the graphitized structure of CNTs will be destroyed, resulting in a decrease in electrical conductivity [65], and the same is true for reduced graphene oxide. Compared with CNT sensors, graphene-based strain sensors generally have a higher sensitivity and lower sensing strain due to their small size, sheet-like structure, which is easy to slide, and poor stretching ability. Therefore, appropriate materials should be selected according to the actual requirements in terms of prepared strain sensors. Additionally, the viscoelasticity of the stretchable substrate and the fracture of the carbon material will cause the hysteresis of the sensor under large strain [66], leading to a low sensitivity and poor repeatability and stability. In summary, it is still a challenge to manufacture flexible carbon-based strain sensors with good sensitivity and a broad strain range at low cost.

### *2.3. Metal-Based Materials*

For flexible strain sensors, low-dimensional metal nanostructures are very attractive due to their excellent electrical conductivity. In general, silver has better conductivity and stability than copper, and has a lower cost than other precious metals, such as gold. Copper nanowires (CuNWs) are considered as a promising alternative to silver nanowires (AgNWs) due to their comparable electrical and thermal conductivity, abundance and low cost. However, CuNWs have high inherent resistance and contact resistance due to their sensitivity to oxygen and moisture [47]. In addition, liquid metal has been used to prepare strain-sensing yarns. Zhu et al. reported super-stretched conductive fibers by injecting liquid alloy (EGaIn) into hollow SEBS fibers [48]. Due to the electrical continuity of the liquid metal, the fiber can maintain a certain degree of conductivity at a strain of more than 700%. Additionally, its resistance change mainly depends on the real-time geometrical size change when the fiber is stretched, showing less hysteresis and a higher durability. However, the limitation of this method is that the liquid core of the fiber will collapse under concentrated pressure or large strain, although the conductivity can be restored.

Metal nanomaterials can be assembled on the surface of fibers or yarns by methods such as in situ reduction, sputtering, electrochemical deposition and chemical deposition [67]. However, the bonding force between the conductive coating and the polymer fiber layer is usually poor, and the conductive coating easily peels off due to mechanical deformation, resulting in poor stability. Another method is to prepare stretchable conductive composite fibers by filling metal nanomaterials into a polymer matrix with elasticity through traditional spinning technology. However, the poor dispersibility of metal nanomaterials in the polymer matrix can easily lead to the clogging of the spinneret and poor performance of the composite fiber. To solve this issue, Lu et al. proposed using surface-modified AgNWs and elastic polyurethane (PU) to prepare stretchable conductive composite fibers, in which polyethylene glycol (PEG) derivatives were used to modify the surface of AgNWs [43]. The compatibility between the PU and AgNWs was remarkably improved, resulting in a high filling load and the effective dispersion of AgNWs in the PU. It was found that the electrical conductivity of the yarn without surface modification is 147 S/cm, while the electrical conductivity of the yarn with modified AgNWs was 331 S/cm. Although metal nanomaterials can realize the preparation of flexible electronics with good electrical conductivity, metal-based strain sensors are prone to failure due to the fragility and weak interfacial forces of metal. Therefore, it is worth make efforts to

enhance interfacial adhesion, such as the improvement of the interactions between metal nanoparticles and fiber functional groups.

### *2.4. MXene*

MXene has shown good potential in the field of wearable electronics due to its excellent properties, such as metal-like electrical conductivity, large specific surface area, excellent thermal conductivity, layered structure, etc. [68]. In addition, it has good dispersibility in aqueous solutions due to the large number of functional groups formed on the surface of MXene by hydrofluoric acid etching. Therefore, it is suitable for modifying textiles through solution processing methods. However, exposure to high humidity or air may cause the oxidation of MXene, thereby reducing its various properties, especially electrical properties [16,49]. For example, Gong et al. developed a spandex composite yarn sensor with a composite coating using MXene nanosheets as "bricks" and PDA/$Ni^{2+}$ as "mortars" through alternate dip-coating methods [69]. The yarn strain sensor has high sensitivity, a low detection limit (0.11%) and a wide sensing range (0.11–61.2%). However, due to the poor oxidation stability of MXene in water, the conductivity of the yarn gradually deteriorates at a temperature of 30–50 °C over a 20 h washing cycle.

## 3. Fabrication and Structure Design

Fiber- and yarn-based strain sensors are mainly manufactured by spinning and coating. For example, the conductive filler is mixed into the spinning solution to prepare conductive composite fibers. The structure of composite fibers prepared by spinning is round with uniformly distributed conductive materials, or coaxial, porous, hollow, and so on. In terms of coating conductive materials on fibers and yarns, the conductive coating can be designed as a microcrack, fold buckling, multilayer composite structure. Additionally, the geometry of the yarns was designed to control the sensing performance of strain sensors. These preparation strategies and structural design features will be discussed in the following sections. The performances of fiber and yarn strain sensors reported in the literature are summarized in Tables 4–6.

### *3.1. Conductive Composite Fibers*

#### 3.1.1. Uniform Mixing of Conductive Materials

Traditional spinning techniques, such as wet spinning, dry spinning and melt spinning, are the most common methods to prepare a 1D stretchable conductive composite materials; they mix the conductive filler and the elastic matrix directly and uniformly, and then extrude it through the spinneret hole to a coagulating bath to form the composite fiber. Li et al. uniformly mixed Gr into SBS and prepared SBS/Gr composite fiber flexible strain sensors by a simple wet-spinning method, and the Gr content had a significant impact on the morphology, mechanical properties and electromechanical properties of the composite fiber (Figure 1) [70]. The fiber with the 5 wt% graphene content has a wide working strain, which reaches 100%. However, its sensitivity increases with the increase in strain, and the sensitivity within 50% strain is changeable at different stretching speeds. He et al. proposed multiwalled carbon nanotube/thermoplastic polyurethane (MWCNT/TPU) fibers by wet spinning [71]. The gauge factors (GF) of the MWCNT/TPU fiber are about 550 and 2800 in the strain ranges of 1 to 4% and 5 to 100%, respectively. The strain of the MWCNT/TPU fibers decreases significantly under large hysteresis after multiple stretching–releasing cycles, indicating poor sensing repeat stability. At the same time, the influence of different weight ratios of MWCNTs to TPU on the mechanical and electrical properties of composite fibers has been studied. It was found that the concentration and arrangement of MWCNT would change the working strain range and GF of the sensor [72]. Wang et al. manufactured a fiber strain sensor with a wide response range (320%) and a fast response time (<200 ms) based on MWCNTs and TPU by a simple wet-spinning method [39]. However, the electrical response of the MWCNT/TPU strain sensor decreased slightly in the initial stage when multiple stretching–releasing cycles were carried out

at 100% strain, and it exhibited unstable sensitivity at the same time. To improve the conductivity and the stability of the conductive network, hybrid conductive fillers have been used to achieve a composite synergistic effect to prepare strain-sensing fibers. For instance, Zhang et al. demonstrated a highly conductive AgNW/MWCNT/TPU composite fiber by wet spinning, in which MWCNTs were regarded as the sensitive materials and silver nanowires were used to improve electrical conductivity [73]. When the contents of AgNWs reached the optimal amount (3%), the working strain range was 254%, and the conductivity was 0.0803 S/cm (Figure 2). Compared with single-filler composite fibers, the increase in AgNWs improves the conductivity and working strain range of the composite fiber, but its sensitivity decreases. In the case of a strain range of 50–150%, the relative resistance change of the sensor continues to decrease in stretching–releasing tests within 1000 s, showing poor stability.

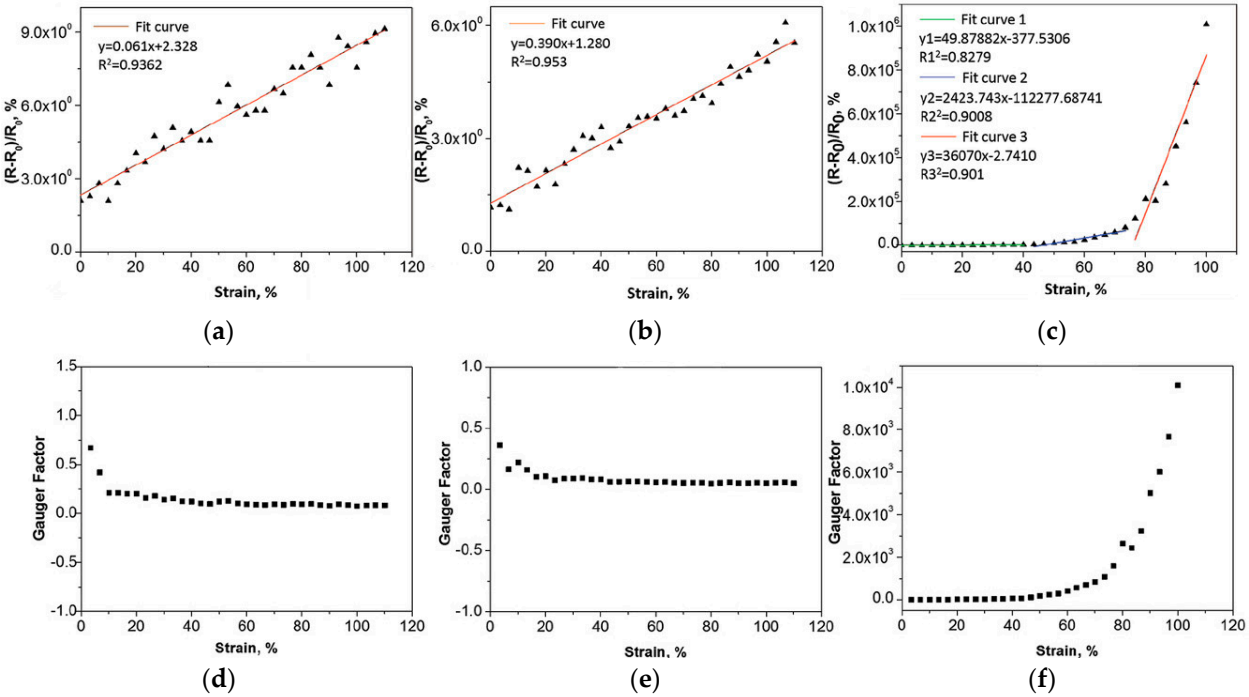


**Figure 1.** $\Delta R/R_0$–strain curve and GF–strain curve of SBS-xGr composite fiber with different graphene contents. (**a**,**d**) SBS-1Gr composite fiber; (**b**,**e**) SBS-3Gr composite fiber; (**c**,**f**) SBS-5Gr composite fiber [70].

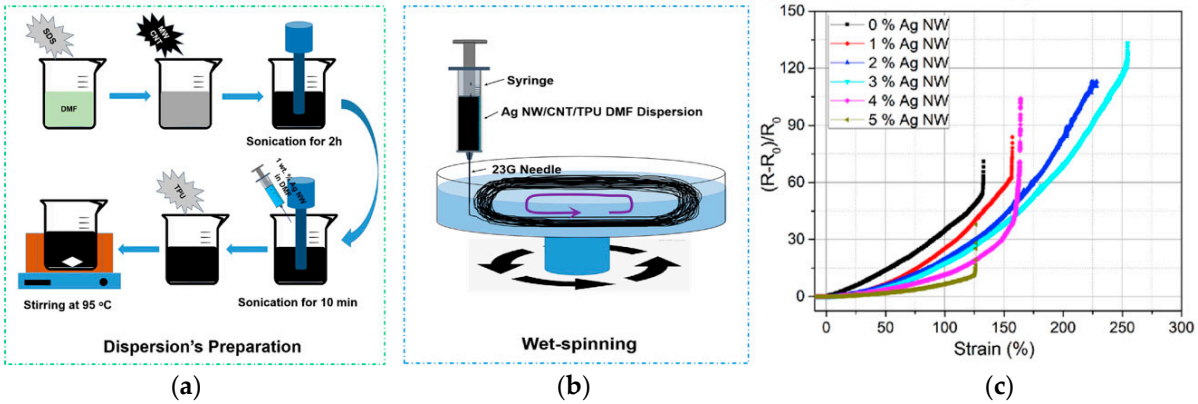


**Figure 2.** (**a**) Suspension preparation process; (**b**) AgNW/MWCNT/TPU spinning process; (**c**) the relative change resistance–strain curve of the fiber strain sensor with different AgNW contents [73].

3.1.2. Selective Localization of Conductive Materials

The conductive network was also designed by controlling the distribution of the fillers, such as selective positioning in multiple phases to form a co-continuous structure or a sea-island structure. In this case, the conductivity of the composite is improved by forming a double or triple permeation structure in the polymer matrix. The selective positioning of the fillers at the interface of the co-continuous polymer structure can further reduce the filler content, which is required to form the continuous conductive network. Zhou et al. used the coaxial wet-spinning method and post-treatment process to prepare the thermoplastic elastomer/single-walled carbon nanotube (TPE/SWCNT) ribbon coaxial fiber with good stretchability and high sensitivity (Figure 3a) [38]. The strain sensor composed of this fiber has a GF of 48 at 0–5% strain and a GF of 425 at 20–100% strain; a linear change cannot occur in in the full strain range. Tang et al. designed a stretchable core sheath fiber using a one-step coaxial wet-spinning assembly method, in which a high-stretch polymer elastomer Ecoflex wrapped CNT/Ecoflex composite material [74]. Similar to traditional cables, the outer insulating sheath effectively avoids short circuits and the falling off of conductive fillers. At the same time, it can have good conductivity under a low permeability threshold (0.74 vol%). Strain sensors made of this fiber achieve a high sensitivity of 1378 under 300% strain and show high durability under 100% strain, but they exhibit low sensitivity in a small strain range, non-linear resistance change and obvious overshoot behavior. Yue et al. demonstrated a highly stretchable TPU-CB@TPU fiber strain sensor with a porous core–sheath structure through the coaxial wet-spinning method (Figure 3b,c) [37]. Due to the countercurrent diffusion and coagulation of the solvent, this fiber has a porous structure with a wide strain range. The highest GF is 28,084 when the strain is 204%. However, its sensitivity is not large enough in a small strain range, and the resistance change gradually declines over multiple cycles of stretching. A coaxial fiber with an outer layer of MXene/PU composite and an inner layer of PU was prepared by Seyedin et al. [75]. Compared with the non-coaxial composite fiber, the coaxial fiber shows a larger strain range, a smaller data drift, and an improvement in the cyclic stability of the sensor response. Gao et al. fabricated a coaxial stretchable composite fiber with a double-layer hollow structure (Figure 3d), in which the conductive outer layer has a CNT/TPU composite as the sensitive area, and the insulating inner layer is made of pure TPU with a hollow core to serve as a flexible support [76]. The prepared composite fiber (TPU-8CNT@TPU) has an ultralow percolation threshold (0.17 wt%), good durability, and small compression deformation that can be detected. With an increase in the stretching speed, the relative resistance differently changes under the same strain. Additionally, there is an obvious shoulder phenomenon, which may disturb signal identification in an accurate strain monitoring. However, the reason for this shoulder phenomenon is still not clear. The mainstream is attributed to the competition between the destruction and reconstruction of CNT conductive networks in the fiber, which needs further verification.

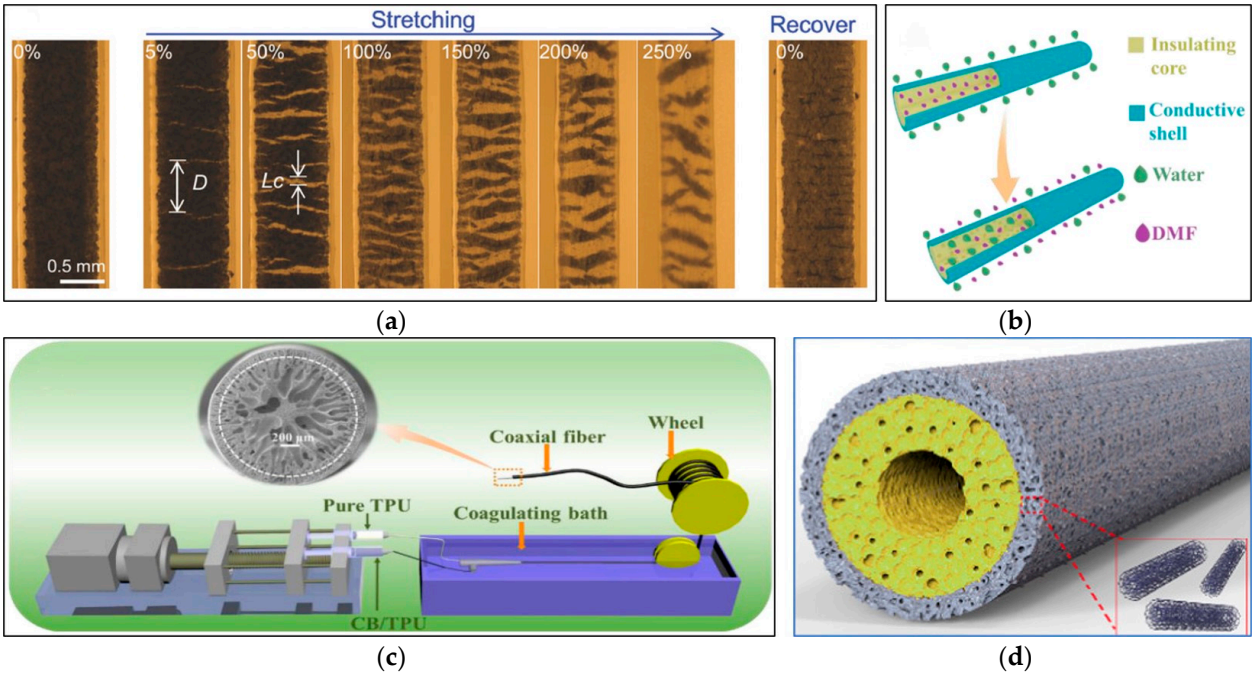


**Figure 3.** (**a**) The image of a typical coaxial fiber stretched from 0 to 250% strain and relaxed after unloading; D and Lc are the average crack spacing and the average crack opening displacement, respectively [38]. (**b**) Fiber cell structure evolution process (**c**) Schematic diagram of the TCTF preparation process [37]. (**d**) Schematic diagram of TPU-8CNT@TPU structure [76].

The characteristics of various fiber-based strain sensors prepared by spinning technology are summarized in Table 4. In general, the preparation of stretchable conductive composite fibers as strain sensors by mixing conductive materials and spinning is a process technology that can be produced on a large scale and is widely used in industry. However, the addition of conductive filler will enhance the rigidity of the elastic matrix, and shrink the tensile strain range of the fiber, which leads to the narrow working strain range of the fiber sensor. On the contrary, if the amount of conductive material is too low, the conductivity of the composite fiber will also limit its working strain range. Therefore, there is a paradox between the conductivity and the working strain range of the stretchable conductive fiber, which needs to be balanced. According to the percolation theory [60,77–81], the content of conductive materials in stretchable conductive composites has a percolation threshold. When the percolation threshold is exceeded, the polymer elastomer changes from an insulator to a conductor, and the conductivity increases with the increase in the content of conductive materials. When the content is near the percolation threshold, the sensitivity of the material is at its greatest [82]. Therefore, it is still a huge challenge to achieve a high strain range and high sensitivity at the same time for conductive composite fibers. In addition, there is a limit on the production costs of practical commercial applications with the increase in conductive fillers. To reduce the permeation threshold while achieving high conductivity, different strategies have been studied [50,83,84], such as functionalizing conductive fillers' surfaces, increasing the aspect ratio of fillers, controlling the arrangement of fillers, and using different mixture of fillers. However, such permeation-based composite strain sensors rarely exhibit good linearity. When the composite fiber is stretched, its resistance is mainly caused by changes in geometry and tunnel theory [37,39,85]. With an increase in tunneling distance and the destruction of the conductive path, the resistance of composites increases significantly during the tensile process. The maximum GF usually occurs when the conductive material content is close to the permeation threshold. Other shortcomings of strain sensors made of composite fibers include hysteresis, fatigue and so on, which are mostly due to the viscoelasticity and elastic recovery rate of composite fibers.

**Table 4.** Characteristics of conductive composite fiber-based strain sensors prepared by spinning technology.

| Structure | Substrate | Sensitive Materials | Breaking Stress and Strain | Conductivity | Strain Range | GF | Repeatability | Linearity | Response Time | Ref. |
|---|---|---|---|---|---|---|---|---|---|---|
| Monofilament | SBS | Gr | 10.16 MPa; 910.83% | N/A | 100% | 10,083.98 (73–100%) | 2500 (20%) | N/A | N/A | [70] |
| Monofilament | TPU | MWCNTs | 28 MPa; 320% | N/A | 100% | 2800 (5–100%) | N/A | N/A | N/A | [71] |
| Monofilament | SIBS | P3HT | 11.4 MPa; 975% | 0.38 S/cm | 770% | 20 (12.25%) | N/A | N/A | N/A | [86] |
| Monofilament | TPU | MWCNTs/ AgNWs | 32.49 MPa | 0.803 S/cm | 250% | 13 (50–150%) | N/A | N/A | N/A | [73] |
| Ribbon and coaxial | TPE | SWCNTs | N/A | N/A | 100% | 425 (100%) | 3250 (20–100%) | $R^2$ = 0.98 (20–100%) | N/A | [38] |
| Core–sheath | Ecoflex | CNTs | N/A | N/A | 330% | 1378 (330%) | >10,000 (100%) | N/A | >300 ms (100%) | [74] |
| Porous | TPU | CB | 2.15 MPa | N/A | 380% | 28,084 (204%) | 11,000 (60%) | N/A | 200 ms | [87] |
| Coaxial | PU | MXene | 20.3 GPa | N/A | 152% | 238 (50%) | 1000 (50%) | N/A | N/A | [75] |
| Hollow | TPU | CNTs | 2.92 MPa; 476% | N/A | >350% | 1344.1 (200%) | 10,000 (100%) | N/A | 167 ms | [76] |

### *3.2. Conductive Coated Fibers*

#### 3.2.1. Microcrack Structure

Coating conductive materials on stretchable fibers or yarns is another way to prepare one-dimensional strain sensors by dipping, spraying, and in situ chemical polymerization, etc. The dip-coating method is one of the easiest and most widely used methods among them, due to its simple, fast and cost-effective characteristics. For example, Lee et al. reported a conductive PU multifilament coated uniformly AgNPs by an in situ reduction method, with low initial resistance (0.16 Ω/cm) (Figure 4a,b) [45]. AgNPs are uniformly distributed inside the multifilament and form a dense shell on the outer layer. The GF of the strain sensor reaches about $9.3 \times 10^5$ (under 450% strain) when the strain sensor is first stretched, while the GF decreases to 659 (under 450% strain) after subsequent stretching. Although the strain sensor has high sensitivity and wide strain range, its sensitivity is unstable and its linearity is poor. Generally speaking, the microcrack structure constructed by the strain sensor in tension is an effective method to achieve a sensing response and high sensitivity of sensors. However, the microcrack structure is usually limited by strain range. Compared with monofilament, the increase in the number of multifilament structures greatly widens its working strain range according to the theory (Figure 4c,d) [45]. Eom et al. first polymerized conductive PEDOT on polyester (PS) fibers by in situ polymerization to prepare conductive coated fibers, and then embedded this conductive fiber into fabrics to manufacture textile-based strain/touch/pressure sensors and user interface (UI) equipment [36]. Due to the multifilament structure of its PEDOT/PS fiber, the resistance of the sensor tends to fall with the increase in strain, which is contrary to the common trend. During stretching, the overall conductivity of the PEDOT/PS multifilament increases, and the PEDOT/PS monofilament exhibits the opposite behavior. Liu et al. designed a monofilament strain sensor with a beaded structure using the Plateau–Rayleigh instability principle. The way to control the strain distribution along the fiber axis is by adjusting the size of the microbeads and the distance between the microbeads (Figure 5) [88]. This design effectively causes strain concentration and amplifies the local strain. Compared with a single uniform monofilament, the sensitivity of the sensor with a beaded structure is significantly improved. Overall, the sensitivity of the sensor with the crack effect usually increases significantly and then decreases, which is a characteristic of nonlinear sensing [45]. Due to the destruction and shedding of the conductive layer, the sensor also exhibits a certain amount of hysteresis and poor cycle stability.

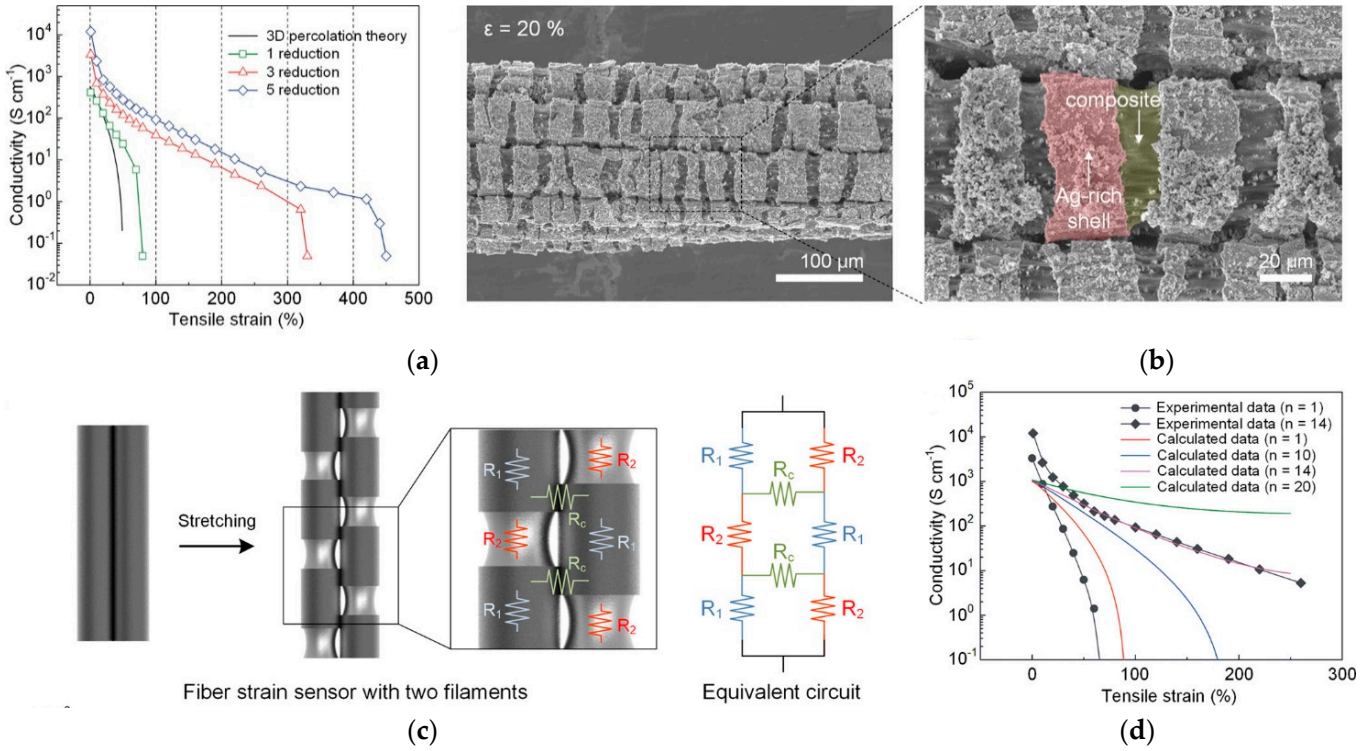


**Figure 4.** (**a**) The electrical conductivity of the sensor under different strains; (**b**) SEM images of the fiber strain sensor at $\varepsilon$ = 20%; (**c**) the resistance model of the double-filament strain sensor and the corresponding equivalent circuit; (**d**) the relationship between the electrical conductivity of the single-filament/multifilament fiber strain sensor and the tensile strain; *n* is the number of multiple filaments in the fiber strain sensor [45].

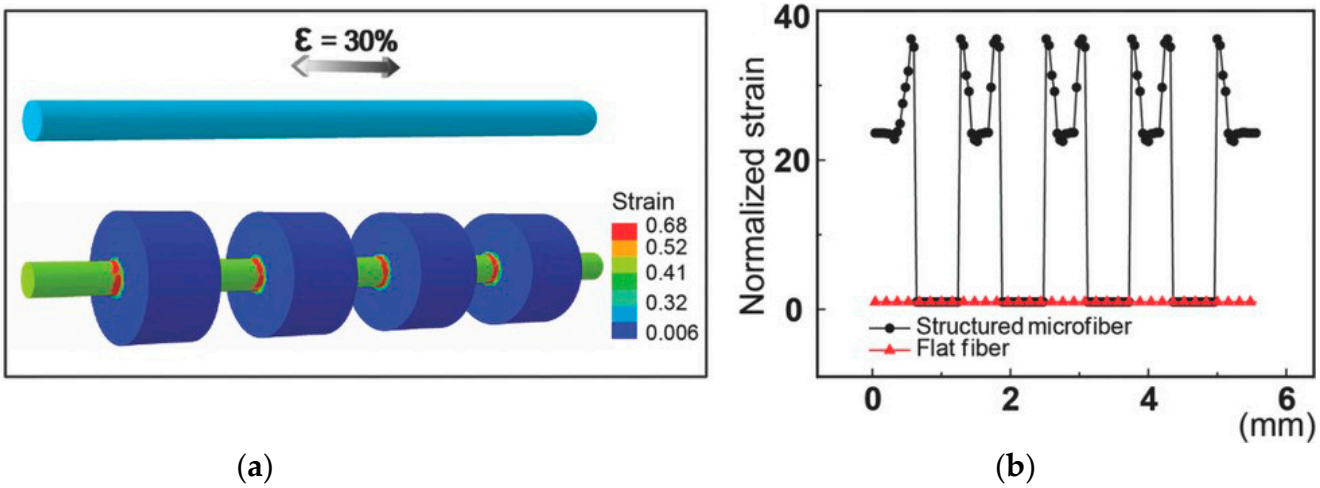


**Figure 5.** (**a**) Finite element simulation to study the strain adjustment effect of microstructured fibers compared with flat fibers; (**b**) the strain distribution of different structures along the fiber surface [88].

### 3.2.2. Wrinkle Structure

In order to improve the workable strain range, a conductive coating with a wrinkle structure was added to the fiber surface to design a flexible strain sensor. Wang et al. designed a highly stretchable NTSm@rubber@fiber strain sensor with a dual-sheath buckling structure by the pre-stretching method, in which NTS is the carbon nanotube sheets and m represents the number of NTS layers (Figure 6a) [89]. The elastic support fiber coaxially coated a curved rubber intermediate layer and a curved NTS conductive layer. At the same time, the GF of the sensor was controlled by changing the manufacturing

parameters to adjust the buckling structure, but its overall sensitivity values were very low, only 0.5 (0–200%) and 0.14 (200–600%). The design of a wrinkle structure makes the strain sensor bear high tensile deformation without destroying the conductivity of the material, thereby increasing its sensing range. However, it also causes a small resistance change in the stretched state, showing lower sensitivity. As shown in Figure 6b, CNT ink/PU yarns with a wrinkle-assisted crack microstructure were created by Sun et al. [90]. The yarn sensors have an ultralow detection limit and excellent repeat stability. As mentioned above, the complex and multistep manufacturing process poses challenges to realize a large-scale production of strain sensors.

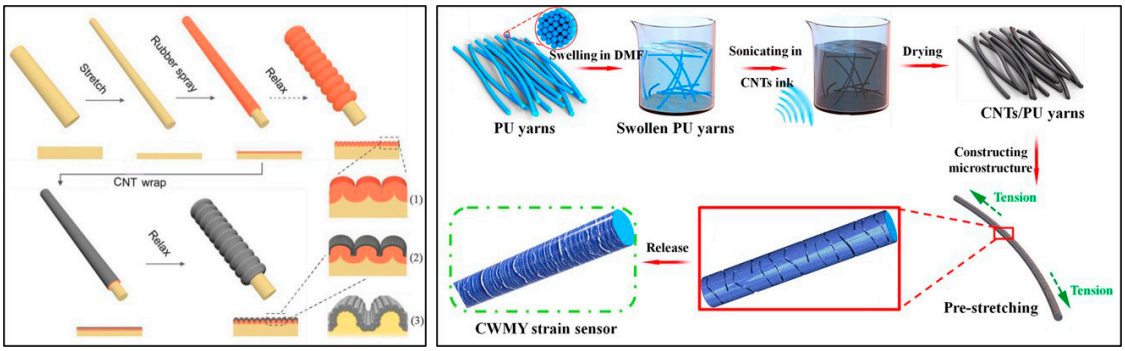


(**a**) (**b**)

**Figure 6.** (**a**) The manufacturing steps of NTS m @rubber@fiber, the longitudinal cross-sections of the fibers of different manufacturing steps are shown below the rubber fiber. Yellow, red and gray are used for SEBS core, SGE layer and NTS sheath, respectively [89]. (**b**) Schematic diagram of preparation of WCMYSS [90].

#### 3.2.3. Multilayer Structure

Building a multilayered structure at the fiber scale is another way to design flexible strain sensors. Cao et al. introduced a AgNW/PU fiber with a composite multilayer structure by using an adhesive layer with adjustable adhesion to adjust the interface adhesion and fiber microstructure (Figure 7a) [91]. The GF and stretchability of the strain sensor were adjusted by changing the interface layer combination (Figure 7b). However, its sensitivity was weak and the resistance response was nonlinear. After 100 and 1000 cycles of stretching at 10% strain, the drift rate values of the relative resistance of the sensor were 29.4 and 53.1%, respectively, showing poor repeatability. Liu et al. reported the silver plating polyurethane filaments (SPPF) with good electrical resistivity ($4.5 \pm 0.1\ \Omega$/cm) [92]. These AgNPs are bound to the surface of the filament by polydopamine, which remarkably improves the bonding between the conductive material and the fiber interface, but the nonlinear error and hysteresis of the SPPF strain sensor are up to 29.3 and 34.3%, respectively.

The layer-by-layer (LBL) assembly method has been used to develop strain sensors with multilayer structures. The LBL assembly method has been reported as an effective method for manufacturing carbon-based films. Instead of simple deposition, this process includes repeated immersion and evaporation, and various reactions such as electrostatic interactions, hydrogen bonding, or covalent bonding to enhance the adhesion of the interface [93]. Li et al. prepared a strain sensor using graphene/polyvinyl alcohol (Gr/PVA) composite material as the outer layer conductive sheath and polyurethane as the elastic core fiber [94]. When the Gr concentration is 1wt% and the number of coatings is nine, the composite coated fiber has the maximum GF (86.9) and a wide strain range (50%) and good linearity ($R^2$ = 0.97). However, the GF of the strain sensor only reaches more than 40 in the 50% strain extension–release cycles, and the repeatability is 1.81% and the hysteresis error is 9.08% over 100 cycles. A CPC@PU yarn strain sensor was prepared by Wu et al. (Figure 7c) [34], in which the ultrathin conductive CPC layer consists of positively charged chitosan (CS) and negatively charged carbon black (CB)/cellulose nanocrystal (CNC)/natural rubber (NR) nanohybrid. Although this fiber sensor based on CPC coat-

ing detects strains as low as 0.1% and shows a GF of approximately 38.9 at 1% strain, it is not reliable for detecting strains larger than 5%. Li et al. proposed a core–sheath structure strain sensor, which is composed of PU core yarn, a highly conductive multilayer sheath material, namely graphene nanosheets/thin gold film/graphene nanosheets (GNSs/Au/GNSs), and PDMS coating. This multilayer structure combination can simultaneously achieve high sensitivity, wide strain-sensing range and good waterproof performance. In 10,000 stretch–release cycles at 50% strain, its stability is excellent [42]. Although the LBL method improves the adhesion of the coating, it takes multiple cycles of treatment to achieve a high conductivity due to the introduction of the insulating polymer.

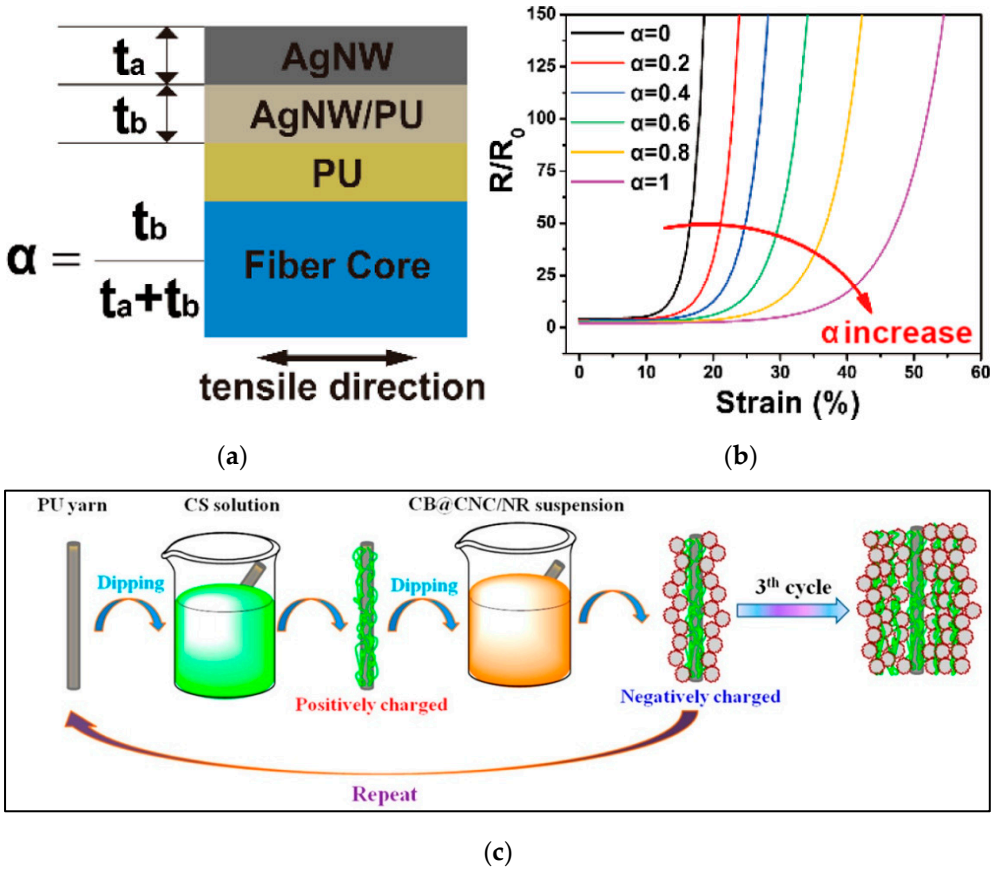


**Figure 7.** (**a**) Schematic diagram of the longitudinal section of Ag NW/PU fiber (**b**) Modeling of the resistance change and strain of Ag NW/PU fiber with different interface bonding strengths [91] (**c**) Schematic of the preparation of CPC@PU yarn by the LBL assembly process [34].

The characteristics of fiber strain sensors prepared by coating technology are summarized in Table 5. In general, the coating method is easy to implement and the 1D strain sensors produce via this method show good sensing performance. As the mechanical properties of conductive coatings and elastic substrates are inconsistent, conductive coatings propagate small and dense microcracks, which destroys conductive networks and causes the changes of resistance. However, the poor adhesion and the mechanical mismatch between the elastic substrate and the conductive coating often leads to degradation of the sensor response. Therefore, it is still a big challenge to achieve high linearity and cycle stability by a simple coating. Due to the irreversible fracture and shedding of the conductive layer, it is very necessary to explore the stress distribution and interface strength between the conductive coating and the substrate. Although the added adhesive (like the LBL method) has improved adhesion, the fatigue durability of the strain sensor is still a challenge. Additionally, there is a lack of systematic studies on how to control the crack propagation and stability, and on how it affects the sensing performance of strain sensors.

**Table 5.** Characteristics of fiber strain sensors prepared by coating technology.

| Method | Structure | Substrate | Adhesive | Sensitive Materials | Breaking Stress and Strain | Conductivity | Strain Range | GF | Repeatability | Linearity | Response Time | Ref. |
|---|---|---|---|---|---|---|---|---|---|---|---|---|
| In site reduction | Multifilament | PU | N/A | AgNPs | N/A | 0.16 Ω/cm | 200% | 659 (150–200%) | 10,000 (10%) | N/A | N/A | [45] |
| In situ polymerization | Multifilament | PS | N/A | PEDOT | 0.813 ± 0.057 GPa | 600 Ω/cm | 70% | 0.244 (70%) | 1000 (20%) | N/A | N/A | [36] |
| deposition | Beaded | PDMS | N/A | Au/CNTs | N/A | N/A | 125% | low | 5000 (30%) | $R^2$ = 0.96 | N/A | [88] |
| Spraying | Double sheath buckle | SBS | SGE | NTS | N/A | N/A | 600% | 0.14 (200–600%) | 5000 (100%) | N/A | 80 ms | [89] |
| Dip coating | Wrinkle assisted | PU | N/A | CNTs | N/A | N/A | 200% | 1344.1 (200%) | 10,000 (30%) | $R^2$ = 0.99 (0–50%) | <88 ms (1%) | [90] |
| Roller transfer | Core–sheath | PU | PU | AgNWs | 38.24 MPa; 980% | 240.36 S/cm | 60% | 5~9557 | 10,000 (10%) | N/A | 120 ms (0.5%) | [91] |
| In situ polymerization and reduction | Core–sheath | PF | PDA | AgNPs | 300 cN; 405.9% | 4.5 Ω/cm | N/A | N/A | N/A | nonlinear error < 29.3% | N/A | [92] |
| LBL | Core–sheath | PU | CS | CB/CNC/NR | N/A | 4.1 MΩ/cm | 1% | 38.9 (1%) | 10,000 (1%) | Good linearity | N/A | [34] |
| LBL and sputtering | Core–sheath | PU | PVA | GNSs/Au/GNSs | N/A | N/A | 75% | 661.59 (50%) | 10,000 (50%) | $R^2$ = 0.983 (0–50%) | N/A | [42] |

### *3.3. Conductive Composite Yarns*

#### 3.3.1. Wrapped Structure

The working strain range of the one-dimensional sensor may be limited if the resistance is changed only by the cracks on the surface of the fiber or yarn. To improve its working strain range and stability, the structural adjustment of the yarns has also been explored. Cai et al. prepared a cotton/CNT core-spun yarn sensor by coating CNTs and depositing PPy on the surface (Figure 8a,b) [95]. The yarn has a broad strain range, up to 350%, but its GF is small, only 5.11 and 3.41 at strains of 0–50% and 50–350%, respectively. Cheng et al. developed a simple and mass-produced graphene-based composite yarn with a compression spring structure by plasma treatment and dipping (Figure 8c,d) [96]. The minimum and maximum detection limits of this double-wrapped composite yarn are 0.2 and 100% strain, respectively. Additionally, the signal response speed is fast (<100 ms). After several stretching cycles under 30 and 50% strain, the performance is stable, but its sensitivity is very low. Zhu et al. introduced curcumin-assisted chemical deposition (ELD) to prepare a helical yarn with a metal coating, and established a model to analyze its sensing mechanism [46]. The relative resistance change of the yarn $\Delta\overline{R}$ can be expressed as a function related to the tensile strain $\varepsilon$, including $\theta(\varepsilon)$, $g(\varepsilon)$ and $R_{detach}(\varepsilon)$ ($\theta$ is the winding angle, g is the average gap of the separated winding, $R_{detach}$ is the resistance of an independent winding). As mentioned above, the yarn strain sensors based on geometric change sensing have excellent linearity, low hysteresis, high stability and a large sensing range, but their sensitivity is limited [15].

#### 3.3.2. Braided Structure

Another design is to use braided yarns to fabricate yarn-based strain sensors. Shi et al. reported a sensor (BWY-AgNWs) composed of stretchable yarns with a braided structure and silver nanowires by dip coating (Figure 9) [97]. The fiber sensor can not only detect various deformations such as stretching, torsion, and bending, but also has a high stable sensitivity (GF = 65) in a larger sensing range (strain can reach 100%). However, due to the insufficient recovery of the microstructure and the brittleness of the AgNWs film, the microcracks cannot be completely merged after release, resulting in the poor repeatability of the strain sensor during multiple cycles of stretching. Furthermore, the high hysteresis of the strain sensor makes its strain response slow, which limits its wearable application. Yang et al. proposed a PET/AgNW/PDMS yarn sensor with braid yarns as the substrate, AgNW as the active material and PDMS as the protective layer by dip coating [98]. The yarn sensor has high conductivity and a wide range of stretchable strain. However, the resistance change does not increase monotonously with the increase in strain, instead of a downward trend after 40% strain. In addition, the relative resistance changes in PET/AgNW/PDMS

yarns with an upward trend show relatively instability during multiple stretching and bending cycles. Pan et al. designed a yarn sensor with a core–sheath yarn structure, in which a braided composite yarn coated with CNTs is used as the core (BYs-CNT) and electrospun polyurethane nanofibers are used as the sheath [35]. This kind of combination of the yarn has extremely high sensing sensitivity (maximum GF up to 980) and long-term stability, but poor linearity. Additionally, the yarn preparation process is complicated and cannot be easily produced en masse. Similarly, the relative resistance change shows a downward trend after the strain exceeds 40%, due to the changes in the braid angle and contact area of braided yarns PET during the stretching process.

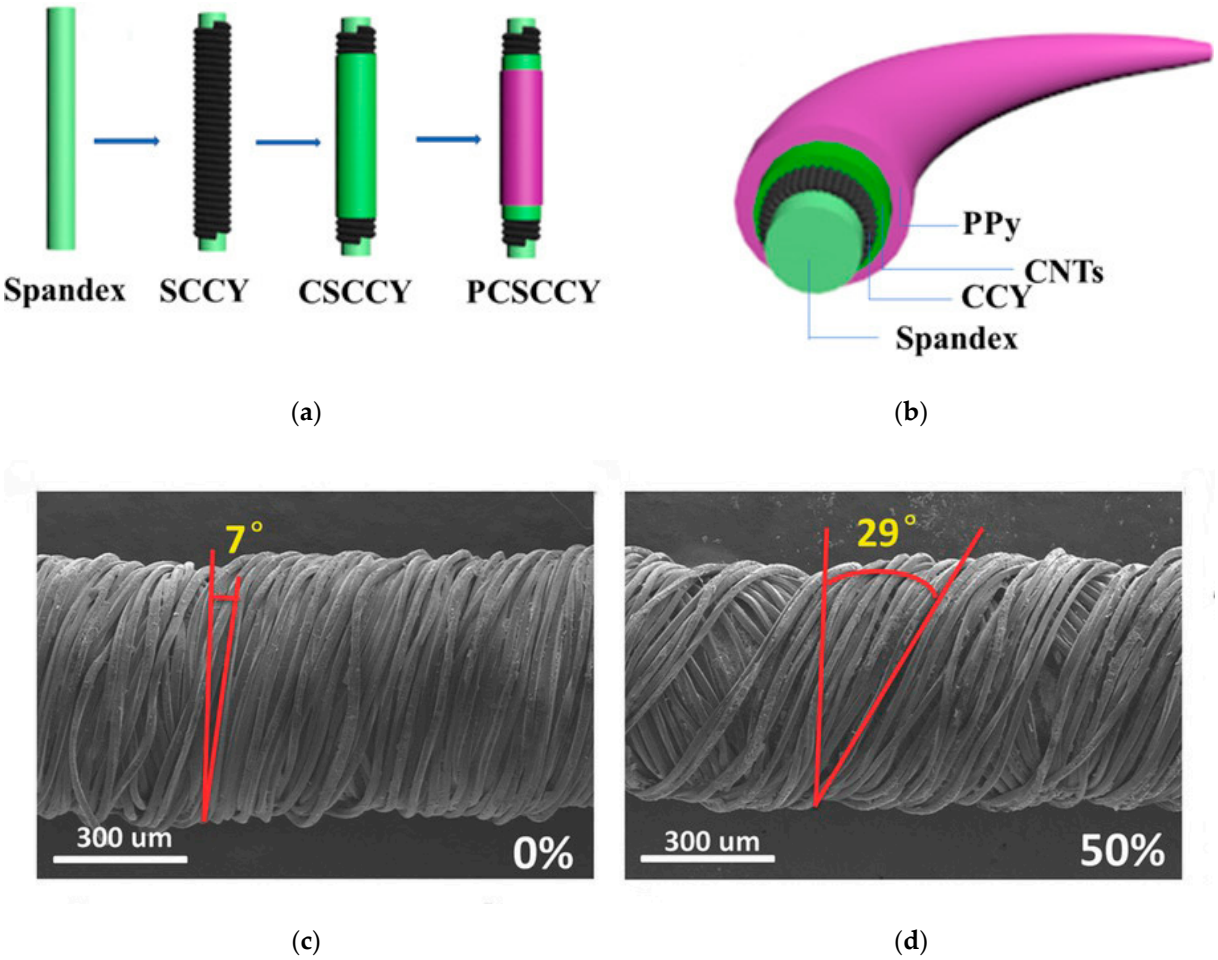


(**a**) (**b**)

(**c**) (**d**)

**Figure 8.** (**a**) Schematic diagram of rubber thread and different core-spun yarns (**b**) Cross-sectional structure of the PCSCCY yarn [95] (**c**) SEM image of PDCY-RGO under 0% strain, 7° (**d**) SEM image of PDCY-RGO under 50% strain, with the winding angle marked as 29° [96].

### 3.3.3. Helical and Winding Structure

In addition to fancy yarn, unconventional yarn sensors have been formed by twisting and winding conductive coated films, which remarkedly enhance the tensile strain range of one-dimensional sensors. Compared with the conventional planar wave structure, the coil structure has greater stretchability because the local stress is suppressed during the stretching process and the local maximum strain is reduced due to the non-planar motion of the coil [99]. Ultrahigh stretchable conductive helical yarn with CNT/PU nanocomposite fiber helical yarn was prepared by simple electrospinning, spraying and twisting processes (Figure 10a) [99]. With the help of the synergistic effect of the flexible polymer chain and the nanofiber spiral coil structure, the CNT/PU helical yarn will break the limitation of material stretchability due to its rigidity and excellent stretchability. Its recovery is within 900% strain, and the maximum of tensile elongation can reach 1700%, while its sensitivity

is very low. Xie et al. designed a SWCNT-RGO/TPU spiral layered composite yarn by spraying and winding technology (Figure 10b,c) [100]. Due to the special spiral layered structure of the composite yarn, the conductive layer is wrapped and protected by the elastic polymer layer, and there is no obvious interruption or crack on the surface of the yarn. Compared with the SWCNT-RGO/TPU thin-film sensor, the yarn sensor has a wider working strain range and has five linear regions. In the 50% tensile strain cycles, the relative resistance of the sensor continued to increase during the initial 100 cycles and then began to stabilize.

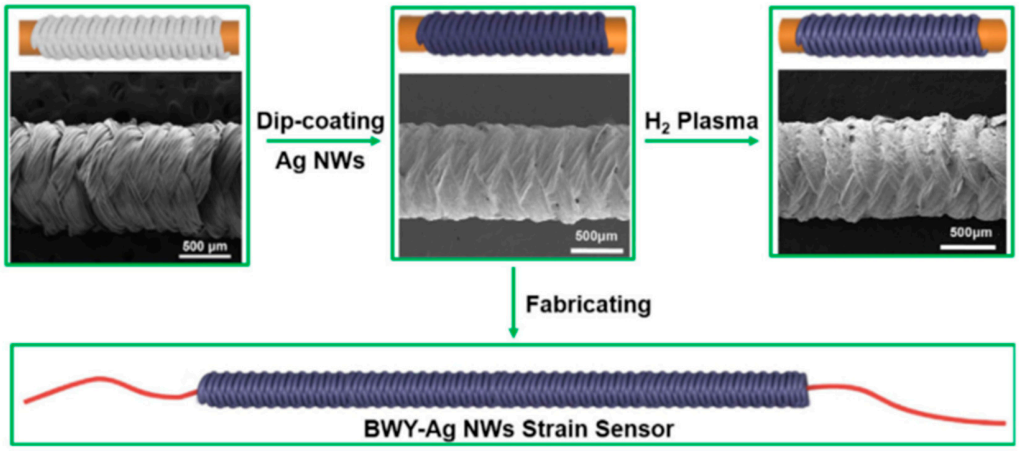


**Figure 9.** Schematic diagram of the manufacturing process of the BWY-Ag NW strain sensor [97].

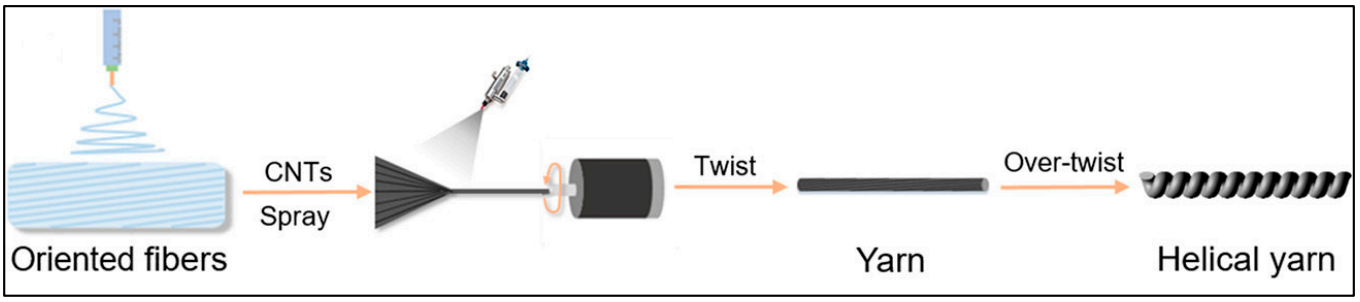


(**a**)

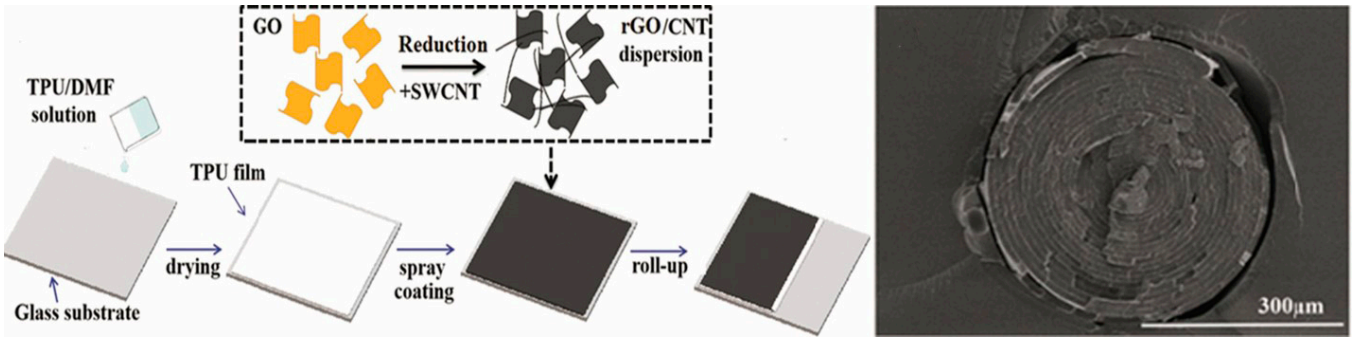


(**b**) (**c**)

**Figure 10.** (**a**) Schematic diagram of the preparation of helical CNT/PU yarn [99] (**b**) Schematic diagram of the preparation of SWCNT-RGO/TPU strain sensor (**c**) SEM image of spiral layered SWCNT-RGO/TPU yarn [100].

The performance of yarn-based strain sensors with different structures are summarized in Table 6. On the basis of the coating, improving the linearity and stability of the strain

sensor by changing the yarn structure is an excellent method because the resistance change mainly depends on the structure of the composite yarn. For example, in terms of wrapped yarn-based sensors, the decrease in the contact of the spiral winding leads to an increase in resistance, but this also reduces the sensitivity and working strain range to a certain extent. Therefore, it is necessary to discuss the influence of structural changes on the sensing performance so that the yarn strain sensor has balanced performance indicators.

**Table 6.** Characteristics of various yarn-based strain sensors.

| Method | Structure | Substrate | Sensitive Materials | Breaking Stress and Strain | Conductivity | Strain Range | GF | Repeatability | Linearity | Response Time | Ref. |
|---|---|---|---|---|---|---|---|---|---|---|---|
| Dip coating and in situ polymerization | Core-spun yarn | PU/cotton | CNT/PPy | >7 N; >300% | 310 Ω/cm | 350 | 5.11 (0–50%); 3.41 (50–100%) | N/A | Linearity at 0–50% and 50–350% strain, respectively | N/A | [95] |
| Dip coating | Wrapped yarn | PU/PE | Gr | 29.14 MPa; 676% | 0.012 S/m | 0.2–100% | 3.7 (50%) | 10,000 (30% and 50%) | N/A | <100 ms | [96] |
| ELD | Wrapped yarn | PU | Cu | N/A | 0.2 Ω/cm | 50% | N/A | 5000 (50%) | Good linearity | N/A | [46] |
| Dip coating | Braided yarn | PU/PET | AgNWs | N/A | 0.5 Ω/cm | 108.92% | 767.50 (97.28–108.92%) | 4000 (30%) | $R^2$ = 0.975 (97.28–108.92%) | <100 ms (0.5%) | [97] |
| Coating | Braided yarn | Rubber/PET | AgNWs | N/A | 3 Ω/cm | 100% | 11.4 (100%) | 1700 (30%) | N/A | N/A | [98] |
| Dip coating | Braided yarn | Rubber/PET | CNT | 44N; 350% | 0.12 kΩ/cm | 44% | 980 (29–44%) | 1000 (20%) | N/A | 200 ms | [35] |
| Spraying | Helical coil | PU | CNT | 50.2 MPa; 1700% | N/A | 900% | N/A | 100 (200%) | N/A | N/A | [99] |
| Spraying | Helical layer | TPU | SWCNT/RGO | 40.0 MPa; 1237% | 821.8 S/m | 620% | 2160.4 (550–620%) | 1000 (50%) | N/A | N/A | [100] |

## 4. Interconnection and Packaging

For wearable electronic applications, strain-sensing fibers or yarns need to be interconnected with other structural circuit elements or data acquisition circuits to fully integrate electronic devices. In wearable electronic devices, it is required that the sensing element must be firmly, elastically and electrically connected to the conductive wire or the data connector, and the interconnection point can still maintain high conductivity under considerable mechanical stress. In addition, the interconnection needs to robustly transmit the signal to the transmission board or processing electronics with minimal loss. At present, the common bonding methods in interconnection are mechanical bonding, physical bonding and chemical bonding [101,102]. However, the chemical bonding is not suitable for the interconnection of heterogeneous devices. Mechanical bonding refers to the use of friction to clamp or connect electronic components to wires, which is suitable for electronic connections of various conductive textiles. For fiber or yarn strain sensors, the mechanical bonding can be thread-to-thread knotting, or embroidery [103,104], stitching [72], or interlacing. Physical bonding includes soldering [105], adhesive bonding [96] and so on. The advantages and disadvantages of different interconnection methods are summarized in Table 7. Soldering is a process that the metal is melted with the high temperature to tightly coat and wrap electronic components to form a connection. However, few common fibers and yarns with conductive materials can withstand high temperature welding, and the narrow interface between the components is too small and difficult to handle. It is a method widely used in laboratories to connect strain-sensing yarns and functional components with conductive adhesives such as conductive glue and copper tape. For example, He et al. stitched MWCNT/TPU fibers onto an elastic bandage with cotton yarns to detect the wrist bending (Figure 11a) [72]. Both ends of the fibers were connected with conductive wires using silver paste and fixed by conductive tapes and medical tapes. Cheng et al. used conductive copper tape and silver paste to interconnect the two ends of graphene-based fibers as external electrodes with copper wires (diameter: 2 μm) (Figure 11b) [96]. Although this method is simple to operate, the electrical connection quality of the conductive adhesive is affected by humidity and temperature, and the copper tape is easily oxidized and has poor mechanical fatigue resistance, which may cause safety problems. Therefore, this type of interconnection often requires further suitable packaging protection.

**Table 7.** Features of various interconnection methods.

| Method | Merits | Demerits |
| --- | --- | --- |
| Soldering | Tight connection and high conductivity. | Brittle fracture, high welding temperature and limited welding interface. |
| Mechanical clamping | Flexible connection and wide range of application. | Easy to break under large deformation. |
| Conductive adhesive | Simple operation and less limitation to materials. | Easily affected by temperature and humidity. |

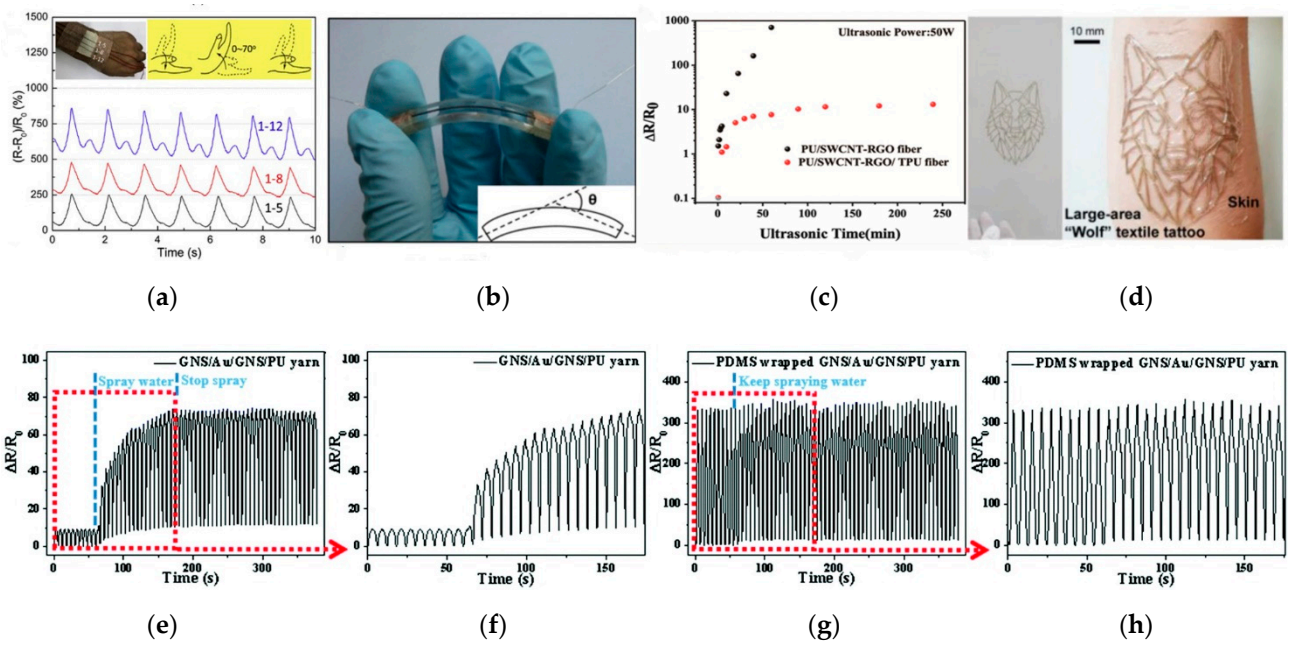


**Figure 11.** (**a**) MWCNT/TPU fiber sensors on an elastic bandage [72]. (**b**) The use of copper tape and silver paste to form the interconnections [96]. (**c**) $\Delta R/R_0$ of the sensor with 50 wt% RGO as a function of ultrasonic time [106]. (**d**) Photograph showing a large textile tattoo of a wolf on skin [107]. (**e**,**f**) Resistance–time relationships of the GNS/Au/GNS/PU yarn strain sensor (**g**,**h**) Resistance–time relationships of the PDMS-wrapped GNS/Au/GNS/PU yarn strain sensor with an applied strain of 50% under water spray [42].

Considering the stability and reliability of electrical interconnection and the durability of the strain sensor, the strain sensor is packaged for use. If strain sensors are integrated into clothing by textile technology, insulating coatings are considered to protect the sensors. For example, Li et al. used hydrophobic PDMS to pack the yarn-based strain sensor to achieve a good waterproof performance [42]. The relative resistance change values of the sensor without the hydrophobic packing increased significantly when the sensor was sprayed with water during the tensile cycle test (Figure 11e,f). On the contrary, the relative resistance change values changed slightly before and after water (Figure 11g,h). Xu et al. reported the encapsulated TPU/SWCNT-RGO/PU core–sheath fiber [106]. The ΔR/R0 of the encapsulated composite fiber firstly increased by 10 and then remained stable, showing great washability compared with the SWCNT-RGO/PU sensor (Figure 11c). Kwon et al. used self-healing polymers (T-SHPs) as self-adhesive and durable interconnection materials to encapsulate conductive sensing fibers. This method easily achieved the patterned design (Figure 11d), but also effectively improved the conductivity of the sensing fiber over the 1000 stretch cycles [107]. Additionally, it is easy and convenient to fabricate, but not safe and reliable, only being suitable for laboratory tests. In addition, the strain sensor can be directly integrated into fabrics by the hot-melting process. The hot-melting package is made of elastic thermoplastic materials, such as TPU hot-melting adhesives. The materials

are heated to the melting temperature and cooled after molding. For instance, Bahadir et al. reported a waterproof textile transmission line with GoreTex® waterproof welding tape by hot air sealing [108]. From the perspective of structural mechanics, electronic packaging can be seen as a composite structure made of different materials (substrate-conductive coating-encapsulation layer), and the physical parameters between the layers will affect the average strain transfer rate and sensing performance. In addition, when the device is subjected to thermo-mechanical loads, the interface between these materials is the most prone to failure. This is due to the inherent stress concentration generated by the interface bonds between different materials and the free surface of the two materials. Under repeated external mechanical action, cracks are not limited to the interface, but also propagate and expand parallelly to the interface [109]. Therefore, the system integration of interconnected wires and strain sensors under high-level strain loads is still a huge challenge. Poor interfaces will not only cause serious errors, but also lead to low reliability of the entire sensor system. The mechanical and sensing properties of conductive yarns before and after encapsulation will change to a certain degree. However, there is currently a lack of comprehensive research on the effect of packaging process on the sensing performance of stretchable conductive fibers or yarns.

## 5. Application

Fiber- and yarn-based strain sensors exhibiting outstanding sensing performances have broad application prospects. In the healthcare industry, wearable strain sensors are installed or worn on different parts of a patient's body, such as hands, fingers, waist and feet, to analyze posture and gait. The traditional sensor for human motion analysis is the accelerometer, but its rigid structure is not easy to integrate into clothing, and would be uncomfortable for wearers over long periods [110]. In addition, the performance of the accelerometer is easily interfered by the environmental magnetic field and temperature. Textile sensors are more comfortable and flexible in measuring human posture and movement with low cost. In particular, fiber or yarn strain sensors can be woven into fabrics that can be worn directly on various body parts, such as knees, elbows and fingers, without any support structure or frame. By contrast, the nanofiber mats and fabric sensors are usually integrated into clothing by adhesive binding and stitching. Fiber and yarn strain sensor devices can be used for a variety of applications without platform constraints and accurately monitor strain in a single direction. However, their electrical performances are still unsatisfactory for practical applications of consumer-level sensor systems. Additionally, it is essential to develop supporting circuit and algorithm to achieve wearable applications. For instance, the problem of resistance drift with time and repeated use can be solved in algorithms with periodic calibration. The performance of different strain sensors used to monitor human movement and human–computer interaction is compared in Table 8.

**Table 8.** Representative properties of different resistive strain sensors.

| Type | Fabrication Method | Substrate | Sensitive Materials | Strain Range | GF | Applications | Ref. |
|---|---|---|---|---|---|---|---|
| Nanofibrous membrane | Dipping | TPU | RGO | 79% | 11 | Human motions | [13] |
| Nanofibrous membrane | Dipping and in situ reduction | TPU | ACNTs/AgNPs | 20 to 70% | $1.04 \times 10^5$ | Human motions | [14] |
| Fabric | Dipping and screen printing | PET/SP | SWCNT/Ag pastes | 20% | 71.5 | Glove and speaking | [111] |
| Fabric | Screen printing and chemical vapor deposition | Nylon/Lycra | PPy | 50% | N/A | Trunk motion | [112] |
| Fabric | Dipping | PET/SP | SWCNT | 0–50% | 2.1–4.8 | Human Motion Recognition | [113] |
| Fiber | Melting extrusion | TPE | CB | 80% | N/A | Upper body postures recognition | [114] |
| Fiber | Spinning | TPE | SWCNT | 100% | 425 | Wrist motion | [38] |
| Fiber | Deposition | PDMS | Au or CNT | 125% | N/A | Knee joint motin | [88] |
| Thread | Coating | 64% Polyester, 36% Polyurethane | Carbon Resistive Ink | 10% | N/A | Head motion | [115] |
| Fiber | Spinning | TPU | AgNWs/MWCNT | 50–150% | 13 | Monitor the weight and shape of an object | [73] |
| Fiber | Coating and imprinting technique | PU | AgNPs/AgNWs/CB | 200% | 1041 | Data glove | [116] |
| Thread | Dripping | Nanofibers cladded core-spun thread | AgNWs/ | 10–50% | 0.688 | Data glove | [117] |

### *5.1. Human Motion Monitoring*

Generally, human motion detection can be classified into exercises with large strain (for example, limb bending or stretching) [118,119] and subtle movements with small strain (such as swallowing or emotional expression) [120]. According to clinical data, the flexion ranges of fingers or wrists, elbows and knees of people with every age group are different, ranging from 0 to 90°, 0 to 160°, and 0 to 130°, respectively [121,122]. Therefore, the large deformation experienced by the human skin ranges from 0 to 100% strain, and thus the corresponding flexible strain sensors require a wider workable strain range. For example, Li et al. used epoxy adhesive to connect two coaxial fibers to the wristband in a perpendicular manner [38]. The sensor monitors the bending and relaxation of the wrist to show a repeatable switching signal (Figure 12a,b). By stitching fibers into the sleeves of the jacket, the stretching, pressing, folding and twisting motions of the sleeves create different signals. Liu et al. reported an elastic garment with a stretchable fiber-based strain sensor can sensitively detect the bending motion of the knee (Figure 12c,d) [88]. Fiber sensors can be snugly integrated into textiles, so the wearer can move comfortably and freely with accurate sensor monitoring. Jiang et al. used two thread-based sensors to monitor the head motion, and characterized the electrical signals by using a machine learning algorithm to realize head motion classification [115]. The accuracy of a set of nine head directions is about 92%.

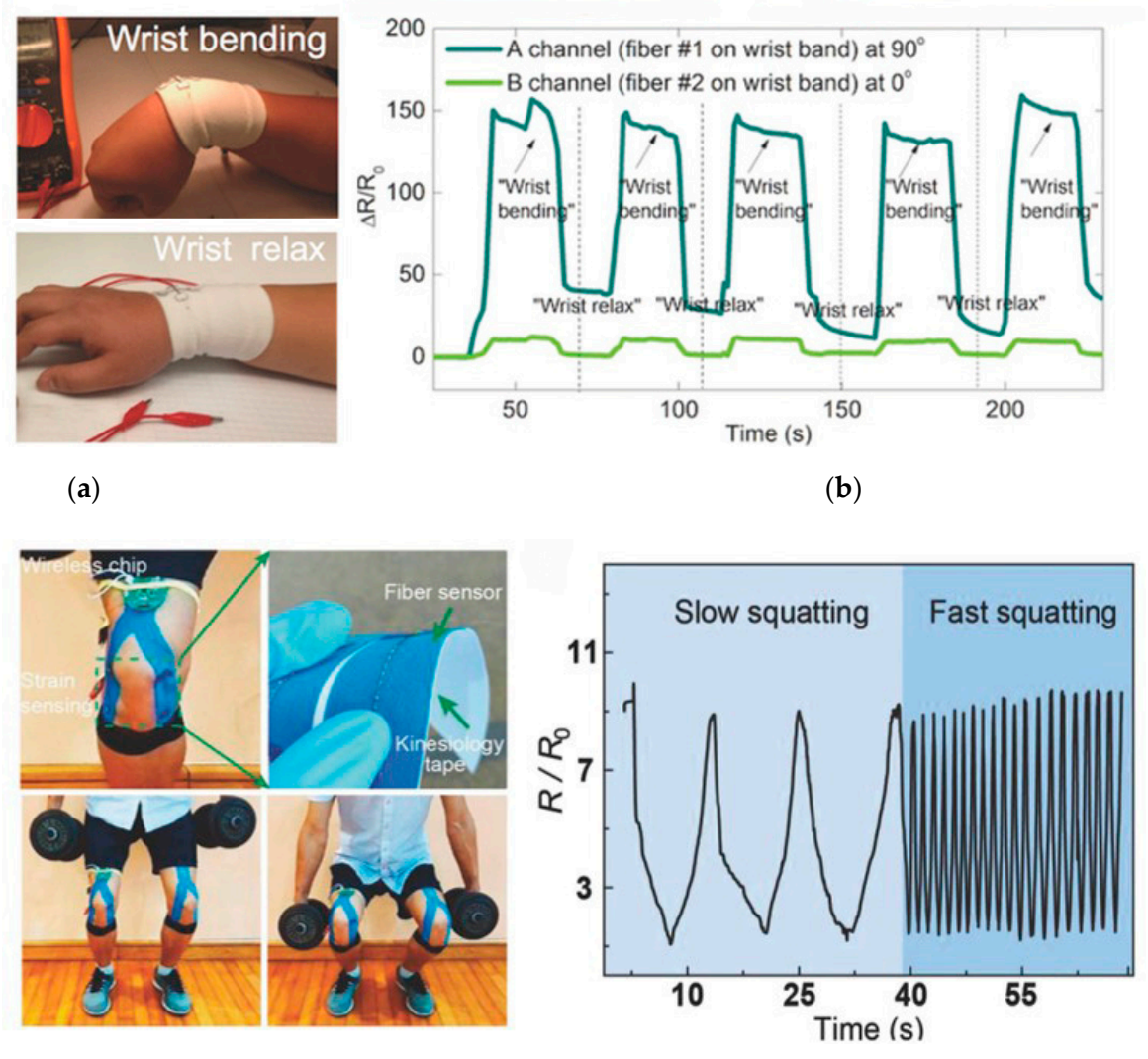


**Figure 12.** *Cont.*

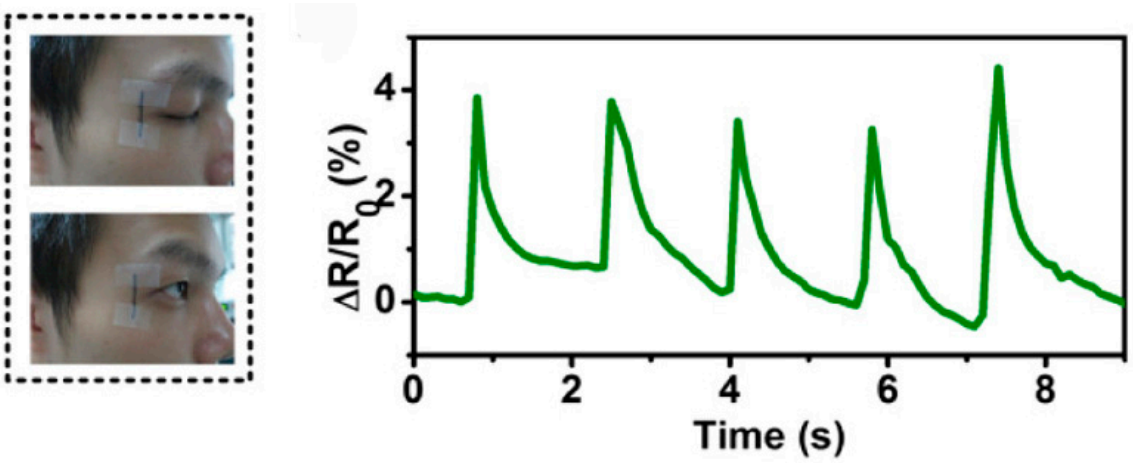


(**e**) (**f**)

**Figure 12.** (**a**) The movement of bending and relaxing the wrist (**b**) The relative resistance change when the wrist is bending and relaxing [38]. (**c**) The sensor was stuck on the joints of the lower limbs with tape to monitor the squatting posture (**d**) The typical raw data obtained by the fiber-based sensor when detecting the squat and the noise is caused by the natural vibration of the limbs [88]. (**e**) Optical images of open eyes (bottom) and closed eyes (top). (**f**) The relative resistance change of the sensor showing the movement of small muscles caused by blinking [74].

For small motion detection, the strain sensors necessarily have extremely high sensitivity. Otherwise, the electrical signals are not easily characterized to distinguish between the strains. For instance, a strain sensor is attached to the neck to detect the movement of the throat muscles. When people swallow something or say different words, different signals are recorded [95,106,123]. Strain sensors can detect complex epidermal/muscle movements by recording relative resistance changes, which have broad prospects in correcting standard pronunciation and expressing sounds of damaged vocal cords [124]. It is also possible to monitor facial expressions, such as crying, laughing, blinking and cheek bulging by installing flexible strain sensors on the cheeks, forehead or corners of the eyes (Figure 12e,f) [74]. Additionally, a high-performance strain sensor worn on the chest was used to track the breathing rate [96]. Flexible strain sensors were also implanted in the human bladder to monitor the size of the bladder to determine excretion [45,125].

In short, flexible fiber- and yarn-based strain sensors with excellent sensitivity have made significant progress in detecting human movement and activity information. They can be directly woven into clothes based on advanced textile machinery, which will facilitate low-cost and large-scale production. In addition, they can also be integrated with other one-dimensional flexible electronic devices, such as fiber-based batteries/supercapacitors, so as to realize miniaturized, portable wearable electronic products in the near future for potential medical care, rehabilitation and sports monitoring, etc.

### *5.2. Human–Computer Interaction*

A data glove is a multimode virtual reality hardware that perform actions such as grabbing, moving and rotating objects in a virtual scene through software programming [125]. The emergence of the data glove provides a new interactive means for virtual reality systems. The product has been able to detect the bending of the finger and use the strain sensor to accurately locate the movement state of the hand. This kind of data glove combined with finger curvature test is called "real glove", which can provide users with a very real and natural three-dimensional interactive means. In addition, the data glove can also be used as an auxiliary device for human or robot movement recognition and deaf–mute people. Fiber- or yarn-based strain sensors can not only detect various finger movements, but are also softs, light and knittable, and can be concealed in the glove without affecting

its appearance. Choi et al. designed a conductive fiber sensor with a layered microsized hair-like structure, which exhibits excellent ductility (<200%) and sensitivity to various stimuli (pressure, stretching, and bending) [116]. They knit this kind of conductive fiber sensor into the glove and made a smart glove to detect the movement of the finger joints, so that the virtual interface was controlled by detecting the movement of the hand (Figure 13a). Lee et al. implanted AgNP-loaded spandex multifilament as a strain sensor on the nodes of the five fingers of the glove, which was used as a true wearable sensor platform in the human–machine interface (Figure 13b,c) [45]. Due to the high sensitivity of the fiber strain sensor, smart gloves easily monitor the real-time movement of each finger. Through the signal processing of the drive circuit and the microcontroller, the response of the strain sensor integrated into the finger of the smart glove is used to control the bending motion of the corresponding finger of the hand-shaped robot. Chen et al. prepared a high-stretch conductive yarn composed of Poly(vinylidenefluoride-co-trifluoroethylene) (P(VDF-TrFE)) polymer nanofibers mat and AgNW coated on the surface of elastic woven yarn, and then integrated ten conductive yarns into a wearable data glove [117]. Human gestures were recognized by detecting the movement of human fingers (Figure 14).

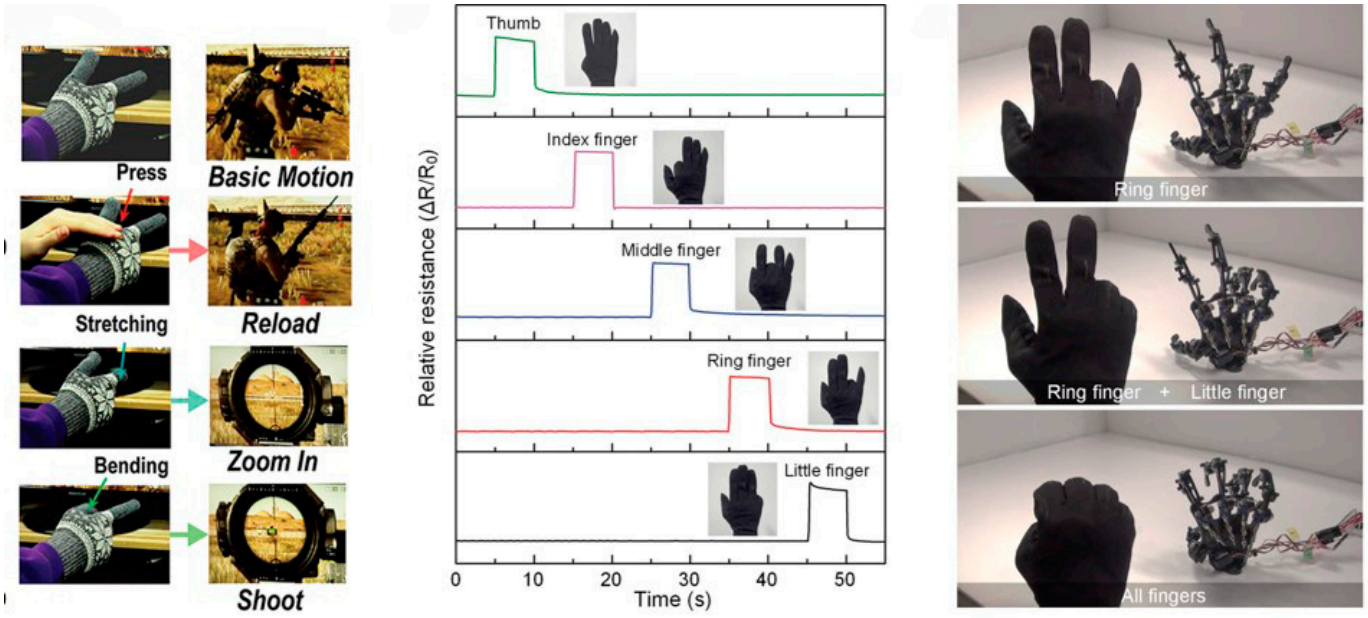


(**a**) (**b**) (**c**)

**Figure 13.** (**a**) Photos and virtual images of smart wearable gloves used for external stimulus control actions in the game interface [116]. (**b**) The resistance response of fiber strain sensor in the smart glove (**c**) Photograph of a remote hand robot controlled by the smart glove [45].

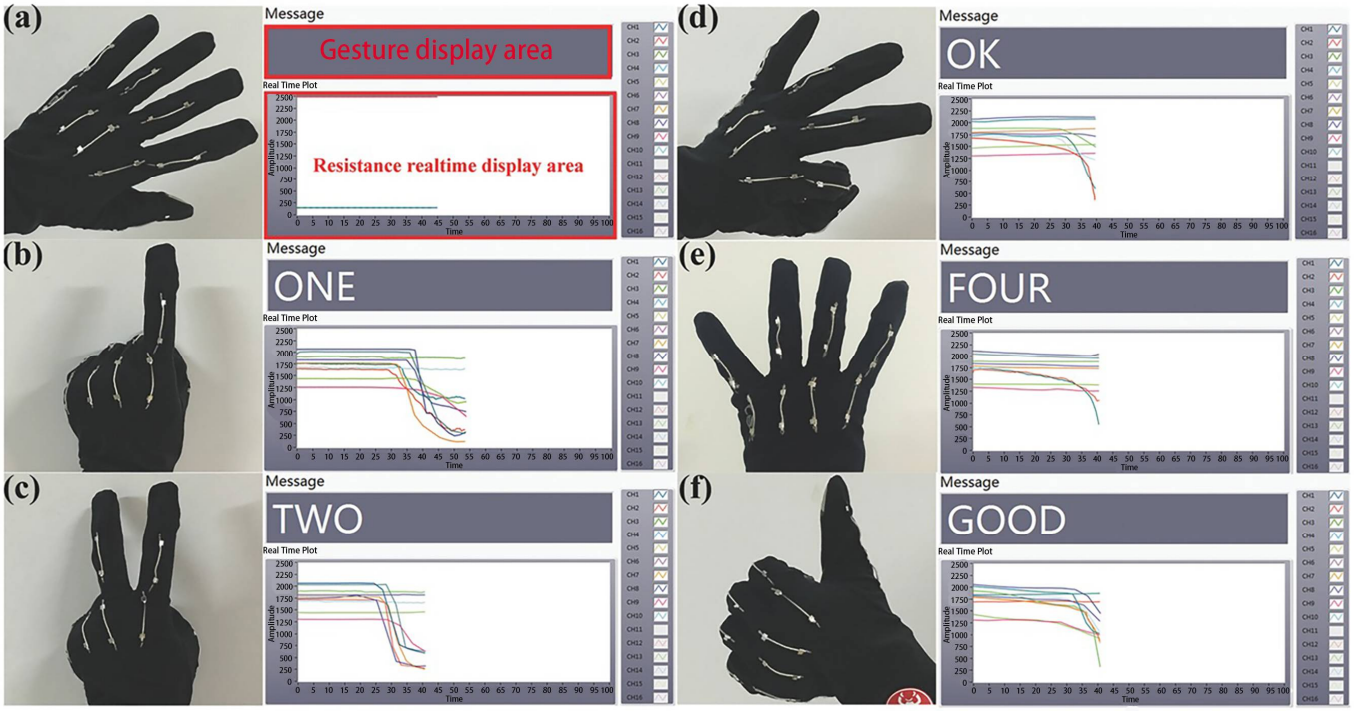


**Figure 14.** A data glove with ten fiber strain sensors fixed [117].

## 6. Conclusions and Outlook

In summary, this review summarized the recent developments in fiber- and yarn-based strain sensors, from commonly used conductive materials to common preparation methods (spinning and coating). The structural designs of strain sensors are introduced in detail, including internal structures (uniform, coaxial, porous, and hollow structures), surface microstructures (microcrack and wrinkled structures) and macrostructures (wrapped, braided, and winding structures). The internal structure design lowers the percolation threshold of materials, and the surface microstructure design improves the performance of the sensor. Each macrostructure has its own characteristics. In addition, the packaging and interconnection of strain sensors with other components are discussed. Finally, various potential practical applications of fiber- and yarn-based strain sensors are listed, such as health detection, biomedicine, data gloves, etc.

Although great progress has been made in the fabrication of strain sensors based on one-dimensional textile materials in recent years, there are still some problems that hinder their practical application. For example, strain sensors cannot have a high sensitivity, high stretchability, and high linearity at the same time. The crack mechanism or method of controlling conductive fillers near the percolation threshold can markedly improve the sensitivity of the materials, while they limit the working strain range of the sensor. The working strain range is not only related to the breaking strain of the elastic substrate, but also to the conductivity of the composite. The addition of conductive active materials by spinning or coating gives the textiles sufficient conductivity, but these treatments often reduce the breaking strain and elastic recovery rate of the composite. Furthermore, the hysteresis, repeatability, stability and durability of the sensor should be considered. At present, most of the current flexible strain sensors tend to use elastic polymers as the supporting substrate. However, the sensors inevitably present hysteresis, stress relaxation and creep phenomena due to the viscoelasticity of substrates. The interface between the conductive material and the supporting substrate will also affect the hysteresis and cycle stability of sensors. From a practical point of view, it is vital to study the interface between conductive materials and fiber ensembles.

The conductive sensing mechanisms of flexible fiber or yarn strain sensors are quite different from traditional semiconductor and metal sensors. For conductive compos-

ite fibers, the sensing mechanisms are mainly based on percolation theory [80,126] and tunnel theory [126,127]. Crack propagation is the main reason for the resistance variation of coating fiber sensors [118,128,129]. Geometric effects caused by changes in the structure or size of fibers or yarns will also affect the working effect of the sensor. The sensing mechanism is based on the contact resistances on different scales such as fibers and yarns [130]. These mechanisms allow us to understand the working mechanism of some flexible tensile strain sensors. However, for the "shoulder phenomenon" of existing strain sensors [64,81,131–133], there is still a lack of specific theoretical analyses to find the improvement methods for large hysteresis and unstable sensitivity. Therefore, it is meaningful to perfect the research on the controlling factors of the sensing performance of the fiber or yarn strain sensors. To fabricate the suitable working strain range and gauge factor of sensors, it is crucial to establish the relationship between yarn structure parameters and sensing performance.

At present, there are few reports of large-scale applications of flexible strain in the market, and the majority of reported fiber and yarn strain sensors are still in the laboratory study and development stage. It is also necessary to consider whether the sensor's performance and life will be interfered with by the external environment. For example, the washability of the wearable electronic textiles needs to be considered because they may be dirty during use. However, due to the lack of an insulating layer or protective layer, most current fiber or yarn strain sensors are not washable. The conductive coating on the yarn may crack or peel off during washing [134,135]. Moreover, there are few studies on the washability and instability mechanism of strain sensors at present. Another unsolved problem is the ability to reliably integrate these sensors with different components. The connection of strain sensors to other devices through soldering, mechanical clamping, or functional adhesives may cause safety issues. Therefore, it is worth studying the effect of packaging technology on the performance while meeting the security and stability requirements of the interconnection.

Finally, to achieve truly comfortable portable wearable applications, comprehensive advances in electronics, software, and textile manufacturing are required. For instance, these wearable power supplies and circuits should ideally be flexible and stretchable so as to withstand the large strains applied to the fabrics during their normal use. It is worth considering a method to highly integrate electronics with clothing comfortably and aesthetically. Artificial intelligence is a key step in realizing sensor applications. As well as applications in human movement monitoring and human–machine interactions, other applications are yet to be developed. In summary, although great progress has been made in fiber- and yarn-based strain sensors have achieved in terms of materials, preparation methods, and structural design, there are still many problems and challenges to be solved before their commercial use.

**Author Contributions:** The authors contributed to this paper as follows: material review, writing of the paper, methodology, draft preparation, revisions and final manuscript preparation, F.H.; supervisory, draft review and editing, J.H. and X.Y. All authors have read and agreed to the published version of the manuscript.

**Funding:** This research was funded by Shanghai Natural Science Foundation (20ZR1400500) and the Fundamental Research Funds for the Central Universities (2232021G-01).

**Institutional Review Board Statement:** Not applicable.

**Informed Consent Statement:** Not applicable.

**Data Availability Statement:** Not applicable.

**Acknowledgments:** Thank you to the supervisory team.

**Conflicts of Interest:** The authors declare no conflict of interest.

## References


1. Wu, Y.T.; Yan, T.; Pan, Z.J. Wearable carbon-based resistive sensors for strain detection: A review. *IEEE Sens. J.* **2020**, *21*, 4030–4041. [CrossRef]
2. Zheng, M.Y.; Li, W.Y.; Xu, M.J.; Xu, N.; Chen, P.; Han, M.; Xie, B. Strain sensors based on chromium nanoparticle arrays. *Nanoscale* **2014**, *6*, 3930–3933. [CrossRef]
3. Barlian, A.A.; Park, W.T.; Mallon, J.R.; Rastegar, A.J.; Pruitt, B.L. Review: Semiconductor piezoresistance for microsystems. *Proc IEEE Inst. Electr. Electron Eng.* **2009**, *97*, 513–552. [CrossRef]
4. Wang, T.; Ouyang, Z.; Wang, F.; Liu, Y. A review on graphene strain sensors based on fiber assemblies. *SN Appl. Sci.* **2020**, *2*, 862. [CrossRef]
5. Wang, B.; Facchetti, A. Mechanically flexible conductors for stretchable and wearable E-skin and E-textile devices. *Adv. Mater.* **2019**, *31*, 1901408. [CrossRef]
6. Lee, J.; Zambrano, B.L.; Woo, J.; Yoon, K.; Lee, T. Recent advances in 1D stretchable electrodes and devices for textile and wearable electronics: Materials, fabrications, and applications. *Adv. Mater.* **2020**, *32*, 1902532. [CrossRef] [PubMed]
7. Zhao, Y.N.; Huang, Y.; Hu, W.; Guo, X.H.; Wang, Y.; Liu, P.; Liu, C.X.; Zhang, Y.G. Highly sensitive flexible strain sensor based on threadlike spandex substrate coating with conductive nanocomposites for wearable electronic skin. *Smart Mater. Struct.* **2019**, *28*, 035004. [CrossRef]
8. Quan, Y.N.; Hu, J.Y.; Yang, X.D.; Lu, Z. Preparation and characterization of resistive strain sensor based on braided skin-core rope. *J. Donghua Univ.* **2019**, *36*, 458–465.
9. Dong, X.L.; Wang, T.T.; Hu, J.Y.; Dong, H.Q.; Lu, Z.; Yang, X.D. Effect of dip coating process on the performance of graphene/spandex yarn strain sensor. *J. Donghua Univ.* **2019**, *36*, 451–457.
10. Wang, X.; Sparkman, J.; Gou, J.H. Strain sensing of printed carbon nanotube sensors on polyurethane substrate with spray deposition modeling. *Compos. Commun.* **2017**, *3*, 1–6. [CrossRef]
11. Yu, Y.; Luo, Y.F.; Guo, A.; Yan, L.J.; Wu, Y.; Jiang, K.L.; Li, Q.Q.; Fan, S.S.; Wang, J.P. Flexible and transparent strain sensors based on super-aligned carbon nanotube films. *Nanoscale* **2017**, *9*, 6716–6723. [CrossRef] [PubMed]
12. Amjadi, M.; Turan, M.; Clementson, C.P.; Sitti, M. Parallel microcracks-based ultrasensitive and highly stretchable strain sensors. *ACS Appl. Mater. Interfaces* **2016**, *8*, 5618–5626. [CrossRef] [PubMed]
13. Wang, Y.L.; Hao, J.; Huang, Z.Q.; Zheng, G.Q.; Dai, K.; Liu, C.T.; Shen, C.Y. Flexible electrically resistive-type strain sensors based on reduced graphene oxide-decorated electrospun polymer fibrous mats for human motion monitoring. *Carbon* **2018**, *126*, 360–371. [CrossRef]
14. Lin, L.; Wang, L.; Li, B.; Luo, J.; Huang, X.; Gao, Q.; Xue, H.; Gao, J. Dual conductive network enabled superhydrophobic and high performance strain sensors with outstanding electro-thermal performance and extremely high gauge factors. *Chem. Eng. J.* **2020**, *385*, 123391. [CrossRef]
15. Seyedin, S.; Zhang, P.; Naebe, M.; Qin, S.; Chen, J.; Wang, X.A.; Razal, J.M. Textile strain sensors: A review of the fabrication technologies, performance evaluation and applications. *Mater. Horiz.* **2019**, *6*, 219–249. [CrossRef]
16. Luo, J.C.; Gao, S.J.; Luo, H.; Wang, L.; Huang, X.W.; Guo, Z.; Lai, X.J.; Lin, L.W.; Li, R.K.Y.; Gao, J.F. Superhydrophobic and breathable smart MXene-based textile for multifunctional wearable sensing electronics. *Chem. Eng. J.* **2021**, *406*, 126898. [CrossRef]
17. Hu, J.; Zhou, S.; Shi, J.; Zhang, H.; Zhu, F.; Yang, X. Determinants of electrical resistance change of in situ PPy-polymerized stretch plain woven fabric under uniaxial tensile strain. *J. Text. Inst.* **2017**, *108*, 1545–1551. [CrossRef]
18. Jiyong, H.; Xiaofeng, Z.; Guohao, L.; Xudong, Y.; Xin, D. Electrical properties of PPy-coated conductive fabrics for human joint motion monitoring. *Nephron Clin. Pract.* **2016**, *16*, 7–12. [CrossRef]
19. Wang, L.; Zhang, M.; Yang, B.; Tan, J.; Ding, X. Highly compressible, thermally stable, light-weight, and robust aramid nanofibers/$Ti_3AlC_2$ MXene composite aerogel for sensitive pressure sensor. *ACS Nano* **2020**, *14*, 10633–10647. [CrossRef]
20. Bi, L.; Yang, Z.; Chen, L.; Wu, Z.; Ye, C. Compressible AgNWs/Ti3C2Tx MXene aerogel-based highly sensitive piezoresistive pressure sensor as versatile electronic skins. *J. Mater. Chem. A* **2020**, *8*, 20030–20036. [CrossRef]
21. Cao, X.; Zhang, J.; Chen, S.; Varley, R.J.; Pan, K. 1D/2D nanomaterials synergistic, compressible, and response rapidly 3D graphene aerogel for piezoresistive sensor. *Adv. Funct. Mater.* **2020**, *30*, 2003618. [CrossRef]
22. Wei, X.D.; Cao, X.H.; Wang, Y.L.; Zheng, G.Q.; Dai, K.; Liu, C.T.; Shen, C.Y. Conductive herringbone structure carbon nanotube/thermoplastic polyurethane porous foam tuned by epoxy for high performance flexible piezoresistive sensor. *Compos. Sci. Technol.* **2017**, *149*, 166–177. [CrossRef]
23. Li, Q.; Li, J.; Tran, D.Q.; Luo, C.Q.; Gao, Y.; Yu, C.J.; Xuan, F.Z. Engineering of carbon nanotube/polydimethylsiloxane nanocomposites with enhanced sensitivity for wearable motion sensors. *J. Mater. Chem. C* **2017**, *5*, 11092–11099. [CrossRef]
24. Geng, W.H.Y.; Cuthbert, T.J.; Menon, C. Conductive thermoplastic elastomer composite capacitive strain sensors and their application in a wearable device for quantitative joint angle prediction. *ACS Appl. Polym.* **2021**, *3*, 122–129. [CrossRef]
25. Choi, C.; Lee, J.M.; Kim, S.H.; Kim, S.J.; Di, J.T.; Baughman, R.H. Twistable and stretchable sandwich structured fiber for wearable sensors and supercapacitors. *Nano Lett.* **2016**, *16*, 7677–7684. [CrossRef] [PubMed]
26. Atalay, A.; Sanchez, V.; Atalay, O.; Vogt, D.M.; Haufe, F.; Wood, R.J.; Walsh, C.J. Batch fabrication of customizable silicone-textile composite capacitive strain sensors for human motion tracking. *Adv. Mater. Technol.* **2017**, *2*, 1700136. [CrossRef]
27. Cooper, C.B.; Arutselvan, K.; Liu, Y.; Armstrong, D.; Lin, Y.L.; Khan, M.R.; Genzer, J.; Dickey, M.D. Stretchable capacitive sensors of torsion, strain, and touch using double helix liquid metal fibers. *Adv. Funct. Mater.* **2017**, *27*, 1605630. [CrossRef]

28. Chen, H. Application of precipitate free zone growth kinetics to the beta-phase depletion behavior in a CoNiCrAlY coating alloy: An analytical approach. *Metall. Mater Trans. A* **2018**, *49A*, 2551–2560. [CrossRef]
29. Persano, L.; Dagdeviren, C.; Su, Y.W.; Zhang, Y.H.; Girardo, S.; Pisignano, D.; Huang, Y.G.; Rogers, J.A. High performance piezoelectric devices based on aligned arrays of nanofibers of poly(vinylidenefluoride-co-trifluoroethylene). *Nat. Commun.* **2013**, *4*, 1633. [CrossRef]
30. Wu, R.; Ma, L.; Liu, S.; Patil, A.B.; Hou, C.; Zhang, Y.; Zhang, W.; Yu, R.; Yu, W.; Guo, W.; et al. Fibrous inductance strain sensors for passive inductance textile sensing. *Mater. Today Phys.* **2020**, *15*, 100243. [CrossRef]
31. Xing, Z.G.; Lin, J.; McCoul, D.; Zhang, D.P.; Zhao, J.W. Inductive strain sensor with high repeatability and ultra-low hysteresis based on mechanical spring. *IEEE Sens. J.* **2020**, *20*, 14670–14675. [CrossRef]
32. Chen, J.; Zhu, G.; Yang, W.Q.; Jing, Q.S.; Bai, P.; Yang, Y.; Hou, T.C.; Wang, Z.L. Harmonic-resonator-based triboelectric nanogenerator as a sustainable power source and a self-powered active vibration sensor. *Adv. Mater.* **2013**, *25*, 6094–6099. [CrossRef]
33. Hsieh, H.H.; Hsu, F.C.; Chen, Y.F. Energetically autonomous, wearable, and multifunctional sensor. *ACS Sens.* **2018**, *3*, 113–120. [CrossRef] [PubMed]
34. Wu, X.; Han, Y.; Zhang, X.; Lu, C. Highly sensitive, stretchable, and wash-durable strain sensor based on ultrathin conductive layer@polyurethane yarn for tiny motion monitoring. *ACS Appl. Mater. Interfaces* **2016**, *8*, 9936–9945. [CrossRef] [PubMed]
35. Pan, J.J.; Hao, B.W.; Song, W.F.; Chen, S.X.; Li, D.Q.; Luo, L.; Xia, Z.G.; Cheng, D.S.; Xu, A.C.; Cai, G.M.; et al. Highly sensitive and durable wearable strain sensors from a core-sheath nanocomposite yarn. *Compos. B Eng.* **2020**, *183*, 107683. [CrossRef]
36. Eom, J.; Jaisutti, R.; Lee, H.; Lee, W.; Heo, J.S.; Lee, J.Y.; Park, S.K.; Kim, Y.H. Highly sensitive textile strain sensors and wireless user-interface devices using all-polymeric conducting fibers. *ACS Appl. Mater. Interfaces* **2017**, *9*, 10190–10197. [CrossRef]
37. Yue, X.; Jia, Y.; Wang, X.; Zhou, K.; Zhai, W.; Zheng, G.; Dai, K.; Mi, L.; Liu, C.; Shen, C. Highly stretchable and durable fiber-shaped strain sensor with porous core-sheath structure for human motion monitoring. *Compos. Sci. Technol.* **2020**, *189*, 108038. [CrossRef]
38. Zhou, J.; Xu, X.Z.; Xin, Y.Y.; Lubineau, G. Coaxial thermoplastic elastomer-wrapped carbon nanotube fibers for deformable and wearable strain sensors. *Adv. Funct. Mater.* **2018**, *28*, 1705591. [CrossRef]
39. Wang, X.; Sun, H.; Yue, X.; Yu, Y.; Zheng, G.; Dai, K.; Liu, C.; Shen, C. A highly stretchable carbon nanotubes/thermoplastic polyurethane fiber-shaped strain sensor with porous structure for human motion monitoring. *Compos. Sci. Technol.* **2018**, *168*, 126–132. [CrossRef]
40. Li, Y.H.; Zhou, B.; Zheng, G.Q.; Liu, X.H.; Li, T.X.; Yan, C.; Cheng, C.B.; Dai, K.; Liu, C.T.; Shen, C.Y.; et al. Continuously prepared highly conductive and stretchable SWNT/MWNT synergistically composited electrospun thermoplastic polyurethane yarns for wearable sensing. *J. Mater. Chem. C* **2018**, *6*, 2258–2269. [CrossRef]
41. Zhang, M.; Wang, C.; Wang, Q.; Jian, M.; Zhang, Y. Sheath-core graphite/silk fiber made by dry-meyer-rod-coating for wearable strain sensors. *ACS Appl. Mater. Interfaces* **2016**, *8*, 20894–20899. [CrossRef]
42. Li, X.T.; Koh, K.H.; Farhan, M.; Lai, K.W.C. An ultraflexible polyurethane yarn-based wearable strain sensor with a polydimethylsiloxane infiltrated multilayer sheath for smart textiles. *Nanoscale* **2020**, *12*, 4110–4118. [CrossRef] [PubMed]
43. Lu, Y.; Jiang, J.W.; Yoon, S.; Kim, K.S.; Kim, J.H.; Park, S.; Kim, S.H.; Piao, L.H. High-performance stretchable conductive composite fibers from surface-modified silver nanowires and thermoplastic polyurethane by wet spinning. *ACS Appl. Mater. Interfaces* **2018**, *10*, 2093–2104. [CrossRef] [PubMed]
44. Ma, R.; Kang, B.; Cho, S.; Choi, M.; Baik, S. Extraordinarily high conductivity of stretchable fibers of polyurethane and silver nanoflowers. *ACS Nano* **2015**, *9*, 10876–10886. [CrossRef] [PubMed]
45. Lee, J.; Shin, S.; Lee, S.; Song, J.; Kang, S.; Han, H.; Kim, S.; Kim, S.; Seo, J.; Kim, D.; et al. Highly sensitive multifilament fiber strain sensors with ultrabroad sensing range for textile electronics. *ACS Nano* **2018**, *12*, 4259–4268. [CrossRef] [PubMed]
46. Zhu, C.; Li, R.; Chen, X.; Chalmers, E.; Liu, X.; Wang, Y.; Xu, B.B.; Liu, X. Ultraelastic yarns from curcumin-assisted ELD toward wearable human-machine interface textiles. *Adv. Sci.* **2020**, *7*, 2002009. [CrossRef] [PubMed]
47. Zhao, S.F.; Han, F.; Li, J.H.; Meng, X.Y.; Huang, W.P.; Cao, D.X.; Zhang, G.P.; Sun, R.; Wong, C.P. Advancements in copper nanowires: Synthesis, purification, assemblies, surface modification, and applications. *Small* **2018**, *14*, 1800047. [CrossRef]
48. Zhu, S.; So, J.H.; Mays, R.; Desai, S.; Barnes, W.R.; Pourdeyhimi, B.; Dickey, M.D. Ultrastretchable fibers with metallic conductivity using a liquid metal alloy core. *Adv. Funct. Mater.* **2013**, *23*, 2308–2314. [CrossRef]
49. Ahmed, A.; Hossain, M.M.; Adak, B.; Mukhopadhyay, S. Recent advances in 2D MXene integrated smart-textile interfaces for multifunctional applications. *Chem. Mat.* **2020**, *32*, 10296–10320. [CrossRef]
50. Huang, Y.; Ellingford, C.; Bowen, C.; McNally, T.; Wu, D.; Wan, C. Tailoring the electrical and thermal conductivity of multi-component and multi-phase polymer composites. *Int. Mater. Rev.* **2019**, *65*, 129–163. [CrossRef]
51. Tseghai, G.B.; Mengistie, D.A.; Malengier, B.; Fante, K.A.; Van Langenhove, L. PEDOT:PSS-based conductive textiles and their applications. *Sensors* **2020**, *20*, 1881. [CrossRef]
52. Qi, G.J.; Huang, L.Y.; Wang, H.L. Highly conductive free standing polypyrrole films prepared by freezing interfacial polymerization. *Chem. Commun.* **2012**, *48*, 8246–8248. [CrossRef] [PubMed]
53. Worfolk, B.J.; Andrews, S.C.; Park, S.; Reinspach, J.; Liu, N.; Toney, M.F.; Mannsfeld, S.C.B.; Bao, Z.N. Ultrahigh electrical conductivity in solution-sheared polymeric transparent films. *Proc. Natl. Acad. Sci. USA* **2015**, *112*, 14138–14143. [CrossRef] [PubMed]

54. Li, X.K.; Li, M.J.; Zong, L.; Wu, X.C.; You, J.; Du, P.K.; Li, C.X. Liquid metal droplets wrapped with polysaccharide microgel as biocompatible aqueous ink for flexible conductive devices. *Adv. Funct. Mater.* **2018**, *28*, 1804197. [CrossRef]
55. Pan, Z.Y.; Ma, J.Z.; Zhang, W.B.; Wei, L.F. Flexible conductive polymer composites in strain sensors. *Prog. Chem.* **2020**, *32*, 1592–1607.
56. Seyedin, M.Z.; Razal, J.M.; Innis, P.C.; Wallace, G.G. Strain-responsive polyurethane/PEDOT:PSS elastomeric composite fibers with high electrical conductivity. *Adv. Funct. Mater.* **2014**, *24*, 2957–2966. [CrossRef]
57. Meer, S.; Kausar, A.; Iqbal, T. Trends in conducting polymer and hybrids of conducting polymer/carbon nanotube: A review. *Polym. Plast. Technol. Eng.* **2016**, *55*, 1416–1440. [CrossRef]
58. Li, L.; Shi, P.; Hua, L.; An, J.; Gong, Y.; Chen, R.; Yu, C.; Hua, W.; Xiu, F.; Zhou, J.; et al. Design of a wearable and shape-memory fibriform sensor for the detection of multimodal deformation. *Nanoscale* **2017**, *10*, 118–123. [CrossRef]
59. Wu, H.; Liu, Q.; Chen, H.; Shi, G.; Li, C. Fibrous strain sensor with ultra-sensitivity, wide sensing range, and large linearity for full-range detection of human motion. *Nanoscale* **2018**, *10*, 17512–17519. [CrossRef]
60. Seyedin, S.; Razal, J.M.; Innis, P.C.; Wallace, G.G. A facile approach to spinning multifunctional conductive elastomer fibres with nanocarbon fillers. *Smart Mater. Struct.* **2016**, *25*, 035015. [CrossRef]
61. Zhang, R.; Pan, P.; Dai, Q.; Yang, X.; Yang, Z.; Wei, J.; Liu, J.; Yuan, Q. Sensitive and wearable carbon nanotubes/carbon black strain sensors with wide linear ranges for human motion monitoring. *J. Mater. Sci. Mater. Electron.* **2018**, *29*, 5589–5596. [CrossRef]
62. Zhang, W.Y.; Liu, Q.; Chen, P. Flexible strain sensor based on carbon black/silver nanoparticles composite for human motion detection. *Materials* **2018**, *11*, 1836. [CrossRef]
63. Zheng, Y.; Li, Y.; Dai, K.; Liu, M.; Zhou, K.; Zheng, G.; Liu, C.; Shen, C. Conductive thermoplastic polyurethane composites with tunable piezoresistivity by modulating the filler dimensionality for flexible strain sensors. *Compos. Part A Appl. Sci. Manuf.* **2017**, *101*, 41–49. [CrossRef]
64. Zheng, Y.J.; Li, Y.L.; Li, Z.Y.; Wang, Y.L.; Dai, K.; Zheng, G.Q.; Liu, C.T.; Shen, C.Y. The effect of filler dimensionality on the electromechanical performance of polydimethylsiloxane based conductive nanocomposites for flexible strain sensors. *Compos. Sci. Technol.* **2017**, *139*, 64–73. [CrossRef]
65. Heo, J.S.; Hossain, M.F.; Kim, I. Challenges in design and fabrication of flexible/stretchable carbon- and textile-based wearable sensors for health monitoring: A critical review. *Sensors* **2020**, *20*, 3927. [CrossRef] [PubMed]
66. Yan, T.; Wang, Z.; Pan, Z.-J. Flexible strain sensors fabricated using carbon-based nanomaterials: A review. *Curr. Opin. Solid State Mater. Sci.* **2018**, *22*, 213–228. [CrossRef]
67. Ojstrsek, A.; Plohl, O.; Gorgieva, S.; Kurecic, M.; Jancic, U.; Hribernik, S.; Fakin, D. Metallisation of textiles and protection of conductive layers: An overview of application techniques. *Sensors* **2021**, *21*, 3508. [CrossRef]
68. Qin, R.; Shan, G.; Hu, M.; Huang, W. Two-dimensional transition metal carbides and/or nitrides (MXenes) and their applications in sensors. *Mater. Today Phys.* **2021**, *21*, 100527. [CrossRef]
69. Gong, M.; Yue, L.C.; Kong, J.Y.; Lin, X.; Zhang, L.; Wang, J.P.; Wang, D.R. Knittable and sewable spandex yarn with nacre-mimetic composite coating for wearable health monitoring and thermo- and antibacterial therapies. *ACS Appl. Mater. Interfaces* **2021**, *13*, 9053–9063. [CrossRef]
70. Li, W.Y.; Zhou, Y.F.; Wang, Y.H.; Li, Y.; Jiang, L.; Ma, J.W.; Chen, S.J. Highly stretchable and sensitive SBS/graphene composite fiber for strain sensors. *Macromol. Mater. Eng.* **2020**, *305*, 1900736. [CrossRef]
71. He, Z.; Zhou, G.; Byun, J.H.; Lee, S.K.; Um, M.K.; Park, B.; Kim, T.; Lee, S.B.; Chou, T.W. Highly stretchable multi-walled carbon nanotube/thermoplastic polyurethane composite fibers for ultrasensitive, wearable strain sensors. *Nanoscale* **2019**, *11*, 5884–5890. [CrossRef] [PubMed]
72. He, Z.; Byun, J.H.; Zhou, G.; Park, B.J.; Kim, T.H.; Lee, S.B.; Yi, J.W.; Um, M.K.; Chou, T.W. Effect of MWCNT content on the mechanical and strain-sensing performance of thermoplastic polyurethane composite fibers. *Carbon* **2019**, *146*, 701–708. [CrossRef]
73. Zhang, S.; He, Z.; Zhou, G.; Jung, B.-M.; Kim, T.-H.; Park, B.-J.; Byun, J.-H.; Chou, T.-W. High conductive free-written thermoplastic polyurethane composite fibers utilized as weight-strain sensors. *Compos. Sci. Technol.* **2020**, *189*, 108011. [CrossRef]
74. Tang, Z.; Jia, S.; Wang, F.; Bian, C.; Chen, Y.; Wang, Y.; Li, B. Highly stretchable core-sheath fibers via wet-spinning for wearable strain sensors. *ACS Appl. Mater. Interfaces* **2018**, *10*, 6624–6635. [CrossRef] [PubMed]
75. Seyedin, S.; Uzun, S.; Levitt, A.; Anasori, B.; Dion, G.; Gogotsi, Y.; Razal, J.M. MXene composite and coaxial fibers with high stretchability and conductivity for wearable strain sensing textiles. *Adv. Funct. Mater.* **2020**, *30*, 1910504. [CrossRef]
76. Gao, J.C.; Wang, X.Z.; Zhai, W.; Liu, H.; Zheng, G.Q.; Dai, K.; Mi, L.W.; Liu, C.T.; Shen, C.Y. Ultrastretchable multilayered fiber with a hollow-monolith structure for high-performance strain sensor. *ACS Appl. Mater. Interfaces* **2018**, *10*, 34592–34603. [CrossRef]
77. Marsden, A.J.; Papageorgiou, D.G.; Valles, C.; Liscio, A.; Palermo, V.; Bissett, M.A.; Young, R.J.; Kinloch, I.A. Electrical percolation in graphene-polymer composites. *2D Mater.* **2018**, *5*, 032003. [CrossRef]
78. Zhang, H.B.; Zheng, W.G.; Yan, Q.; Yang, Y.; Wang, J.W.; Lu, Z.H.; Ji, G.Y.; Yu, Z.Z. Electrically conductive polyethylene terephthalate/graphene nanocomposites prepared by melt compounding. *Polymer* **2010**, *51*, 1191–1196. [CrossRef]
79. Babinec, S.J.; Mussell, R.D.; Lundgard, R.L.; Cieslinski, R. Electroactive thermoplastics. *Adv. Mater.* **2000**, *12*, 1823–1834. [CrossRef]
80. Janssen, H.K.; Tauber, U.C. The field theory approach to percolation processes. *Ann. Phys.* **2005**, *315*, 147–192. [CrossRef]
81. Liu, H.; Li, Y.L.; Dai, K.; Zheng, G.Q.; Liu, C.T.; Shen, C.Y.; Yan, X.R.; Guo, J.; Guo, Z.H. Electrically conductive thermoplastic elastomer nanocomposites at ultralow graphene loading levels for strain sensor applications. *J. Mater. Chem. C* **2016**, *4*, 157–166. [CrossRef]

82. Balberg, I. Tunneling and nonuniversal conductivity in composite-materials. *Phys. Rev. Lett.* **1987**, *59*, 1305–1308. [CrossRef]
83. Pang, H.; Xu, L.; Yan, D.X.; Li, Z.M. Conductive polymer composites with segregated structures. *Prog. Polym. Sci.* **2014**, *39*, 1908–1933. [CrossRef]
84. Xu, Y.T.; Wang, Y.; Zhou, C.G.; Sun, W.J.; Dai, K.; Tang, J.H.; Lei, J.; Yan, D.X.; Li, Z.M. An electrically conductive polymer composite with a co-continuous segregated structure for enhanced mechanical performance. *J. Mater. Chem. C* **2020**, *8*, 11546–11554. [CrossRef]
85. Zhang, X.W.; Pan, Y.; Zheng, Q.; Yi, X.S. Time dependence of piezoresistance for the conductor-filled polymer composites. *J. Polym. Sci. B Polym. Phys.* **2000**, *38*, 2739–2749. [CrossRef]
86. Granero, A.J.; Wagner, P.; Wagner, K.; Razal, J.M.; Wallace, G.G.; in het Panhuis, M. Highly stretchable conducting SIBS-P3HT fibers. *Adv. Funct. Mater.* **2011**, *21*, 955–962. [CrossRef]
87. Ren, M.N.; Zhou, Y.J.; Wang, Y.; Zheng, G.Q.; Dai, K.; Liu, C.T.; Shen, C.Y. Highly stretchable and durable strain sensor based on carbon nanotubes decorated thermoplastic polyurethane fibrous network with aligned wavelike structure. *Chem. Eng. J.* **2019**, *360*, 762–777. [CrossRef]
88. Liu, Z.; Qi, D.; Hu, G.; Wang, H.; Jiang, Y.; Chen, G.; Luo, Y.; Loh, X.J.; Liedberg, B.; Chen, X. Surface strain redistribution on structured microfibers to enhance sensitivity of fiber-shaped stretchable strain sensors. *Adv. Mater.* **2018**, *30*, 1704229. [CrossRef] [PubMed]
89. Wang, R.; Jiang, N.; Su, J.; Yin, Q.; Zhang, Y.; Liu, Z.; Lin, H.; Moura, F.A.; Yuan, N.; Roth, S.; et al. A bi-sheath fiber sensor for giant tensile and torsional displacements. *Adv. Funct. Mater.* **2017**, *27*, 1702134. [CrossRef]
90. Sun, H.; Dai, K.; Zhai, W.; Zhou, Y.; Li, J.; Zheng, G.; Li, B.; Liu, C.; Shen, C. A highly sensitive and stretchable yarn strain sensor for human motion tracking utilizing a wrinkle-assisted crack structure. *ACS Appl. Mater. Interfaces* **2019**, *11*, 36052–36062. [CrossRef]
91. Cao, Z.R.; Wang, R.R.; He, T.Y.; Xu, F.F.; Sun, J. Interface-controlled conductive fibers for wearable strain sensors and stretchable conducting Wires. *ACS Appl. Mater. Interfaces* **2018**, *10*, 14087–14096. [CrossRef]
92. Liu, H.; Zhu, L.L.; He, Y.; Cheng, B.W. A novel method for fabricating elastic conductive polyurethane filaments by in-situ reduction of polydopamine and electroless silver plating. *Mater. Design* **2017**, *113*, 254–263. [CrossRef]
93. Fu, L.; Yu, A.M. Carbon nanotubes based thin films: Fabrication, characterization and applications. *Rev. Adv. Mater. Sci.* **2014**, *36*, 40–61.
94. Li, X.; Hua, T.; Xu, B. Electromechanical properties of a yarn strain sensor with graphene-sheath/polyurethane-core. *Carbon* **2017**, *118*, 686–698. [CrossRef]
95. Cai, G.; Hao, B.; Luo, L.; Deng, Z.; Zhang, R.; Ran, J.; Tang, X.; Cheng, D.; Bi, S.; Wang, X.; et al. Highly stretchable sheath-core yarns for multifunctional wearable electronics. *ACS Appl. Mater. Interfaces* **2020**, *12*, 29717–29727. [CrossRef]
96. Cheng, Y.; Wang, R.; Sun, J.; Gao, L. A stretchable and highly sensitive graphene-based fiber for sensing tensile strain, bending, and torsion. *Adv. Mater.* **2015**, *27*, 7365–7371. [CrossRef]
97. Shi, B.; Wang, T.; Shi, L.; Li, J.; Wang, R.; Sun, J. Highly stretchable and strain sensitive fibers based on braid-like structure and sliver nanowires. *Appl. Mater. Today* **2020**, *19*, 100610. [CrossRef]
98. Yang, Z.; Wang, W.; Bi, L.; Chen, L.; Wang, G.; Chen, G.; Ye, C.; Pan, J. Wearable electronics for heating and sensing based on a multifunctional PET/silver nanowire/PDMS yarn. *Nanoscale* **2020**, *12*, 16562–16569. [CrossRef]
99. Gao, Y.; Guo, F.Y.; Cao, P.; Liu, J.C.; Li, D.M.; Wu, J.; Wang, N.; Su, Y.W.; Zhao, Y. Winding-locked carbon nanotubes/polymer nanofibers helical yarn for ultrastretchable conductor and strain sensor. *ACS Nano* **2020**, *14*, 3442–3450. [CrossRef]
100. Xie, X.X.; Huang, H.; Zhu, J.; Yu, J.R.; Wang, Y.; Hu, Z.M. A spirally layered carbon nanotube-graphene/polyurethane composite yarn for highly sensitive and stretchable strain sensor. *Compos. Part A Appl. Sci. Manuf.* **2020**, *135*, 105932. [CrossRef]
101. de Mulatier, S.; Nasreldin, M.; Delattre, R.; Ramuz, M.; Djenizian, T. Electronic circuits integration in textiles for data processing in wearable technologies. *Adv. Mater. Technol.* **2018**, *3*, 1700320. [CrossRef]
102. Simegnaw, A.A.; Malengier, B.; Rotich, G.; Tadesse, M.G.; Van Langenhove, L. Review on the integration of microelectronics for E-textile. *Materials* **2021**, *14*, 5113. [CrossRef]
103. Linz, T.; Kallmayer, C.; Aschenbrenner, R.; Reichl, H. Embroidering electrical interconnects with conductive yarn for the integration of flexible electronic modules into fabric. In Proceedings of the Ninth IEEE International Symposium on Wearable Computers, Osaka, Japan, 18–21 October 2005; pp. 86–89.
104. Trindade, I.G.; da Silva, J.M.; Miguel, R.; Pereira, M.; Lucas, J.; Oliveira, L.; Valentim, B.; Barreto, J.; Silva, M.S. Design and evaluation of novel textile wearable systems for the surveillance of vital signals. *Sensors* **2016**, *16*, 1573. [CrossRef] [PubMed]
105. Fang, Z.Q.; Mao, X.; Yang, J.L.; Yang, F.H. A wafer-level Sn-rich Au-Sn intermediate bonding technique with high strength. *J Micromech. Microeng.* **2013**, *23*, 095008. [CrossRef]
106. Xu, Y.M.; Xie, X.X.; Huang, H.; Wang, Y.; Yu, J.R.; Hu, Z.M. Encapsulated core-sheath carbon nanotube-graphene/polyurethane composite fiber for highly stable, stretchable, and sensitive strain sensor. *J. Mater. Sci.* **2021**, *56*, 2296–2310. [CrossRef]
107. Kwon, C.; Seong, D.; Ha, J.; Chun, D.; Bae, J.H.; Yoon, K.; Lee, M.; Woo, J.; Won, C.; Lee, S.; et al. Self-bondable and stretchable conductive composite fibers with spatially controlled percolated Ag nanoparticle networks: Novel integration strategy for wearable eectronics. *Adv. Funct. Mater.* **2020**, *30*, 2005447. [CrossRef]
108. Bahadir, S.K.; Kalaoglu, F.; Jevsnik, S. The use of hot air welding technologies for manufacturing E-textile trasmission lines. *Fibers Polym.* **2015**, *16*, 1384–1394. [CrossRef]

109. Nied, H.F. Mechanics of interface fracture with applications in electronic packaging. *IEEE Trans. Device Mater. Reliab.* **2003**, *3*, 129–143. [CrossRef]
110. Yang, C.-C.; Hsu, Y.-L. A review of accelerometry-based wearable motion detectors for physical activity monitoring. *Sensors* **2010**, *10*, 7772–7788. [CrossRef]
111. Vu, C.C.; Kim, J. Highly sensitive E-textile strain sensors enhanced by geometrical treatment for human monitoring. *Sensors* **2020**, *20*, 2383. [CrossRef]
112. Mokhlespour Esfahani, M.I.; Zobeiri, O.; Moshiri, B.; Narimani, R.; Mehravar, M.; Rashedi, E.; Parnianpour, M. Trunk motion system (TMS) using printed body worn sensor (BWS) via data fusion approach. *Sensors* **2017**, *17*, 112. [CrossRef]
113. Vu, C.; Kim, J. Human motion recognition using E-textile sensor and adaptive neuro-fuzzy inference system. *Fiber Polym.* **2018**, *19*, 2657–2666. [CrossRef]
114. Mattmann, C.; Clemens, F.; Tröster, G. Sensor for measuring strain in textile. *Sensors* **2008**, *8*, 3719–3732. [CrossRef]
115. Jiang, Y.W.; Sadeqi, A.; Miller, E.L.; Sonkusale, S. Head motion classification using thread-based sensor and machine learning algorithm. *Sci. Rep.* **2021**, *11*, 2646. [CrossRef]
116. Choi, S.; Yoon, K.; Lee, S.; Lee, H.J.; Lee, J.; Kim, D.; Kim, M.S.; Lee, T.; Pang, C. Conductive hierarchical hairy fibers for highly sensitive, stretchable, and water-resistant multimodal gesture-distinguishable sensor, VR applications. *Adv. Funct. Mater.* **2019**, *29*, 1905808. [CrossRef]
117. Chen, S.; Lou, Z.; Chen, D.; Jiang, K.; Shen, G.Z. Polymer-enhanced highly stretchable conductive fiber strain sensor used for electronic data gloves. *Adv. Mater. Technol.* **2016**, *1*, 1600136. [CrossRef]
118. Pu, J.H.; Zhao, X.; Zha, X.J.; Li, W.D.; Ke, K.; Bao, R.Y.; Liu, Z.Y.; Yang, M.B.; Yang, W. A strain localization directed crack control strategy for designing MXene-based customizable sensitivity and sensing range strain sensors for full-range human motion monitoring. *Nano Energy* **2020**, *74*, 104814. [CrossRef]
119. Huang, Y.; Hao, C.; Liu, J.; Guo, X.; Zhang, Y.; Liu, P.; Liu, C.; Zhang, Y.; Yang, X. Highly stretchable, rapid-response strain sensor based on SWCNTs/CB nanocomposites coated on rubber/latex polymer for human motion tracking. *Sens. Rev.* **2019**, *39*, 233–245. [CrossRef]
120. Yang, Z.; Wang, D.Y.; Pang, Y.; Li, Y.X.; Wang, Q.; Zhang, T.Y.; Wang, J.B.; Liu, X.; Yang, Y.Y.; Jian, J.M.; et al. Simultaneously detecting subtle and intensive human motions based on a silver nanoparticles bridged graphene strain sensor. *ACS Appl. Mater. Interfaces* **2018**, *10*, 3948–3954. [CrossRef]
121. Reissner, L.; Fischer, G.; List, R.; Taylor, W.R.; Giovanoli, P.; Calcagni, M. Minimal detectable difference of the finger and wrist range of motion: Comparison of goniometry and 3D motion analysis. *J. Orthop. Surg. Res.* **2019**, *14*, 173. [CrossRef] [PubMed]
122. Lee, K.S.; Jung, M.C. Flexion and extension angles of resting fingers and wrist. *Int. J. Occup. Saf. Ergo* **2014**, *20*, 91–101. [CrossRef] [PubMed]
123. Li, W.Y.; Zhou, Y.F.; Wang, Y.H.; Jiang, L.; Ma, J.W.; Chen, S.J.; Zhou, F.L. Core-sheath fiber-based wearable strain sensor with high stretchability and sensitivity for detecting human motion. *Adv. Electron. Mater.* **2021**, *7*, 2000865. [CrossRef]
124. Lee, S.; Shin, S.; Lee, S.; Seo, J.; Lee, J.; Son, S.; Cho, H.J.; Algadi, H.; Al-Sayari, S.; Kim, D.E.; et al. Ag nanowire reinforced highly stretchable conductive fibers for wearable electronics. *Adv. Funct. Mater.* **2015**, *25*, 3114–3121. [CrossRef]
125. Zhang, Y.J.; Li, X.Y.; Kim, J.; Tong, Y.X.; Thompson, E.G.; Jiang, S.; Feng, Z.; Yu, L.; Wang, J.H.; Ha, D.S.; et al. Thermally drawn stretchable electrical and optical fiber sensors for multimodal extreme deformation sensing. *Adv. Opt. Mater.* **2021**, *9*, 2001815. [CrossRef]
126. Lin, Y.; Liu, S.Q.; Chen, S.; Wei, Y.; Dong, X.C.; Liu, L. A highly stretchable and sensitive strain sensor based on graphene-elastomer composites with a novel double-interconnected network. *J. Mater. Chem. C* **2016**, *4*, 6345–6352. [CrossRef]
127. Hu, N.; Karube, Y.; Yan, C.; Masuda, Z.; Fukunaga, H. Tunneling effect in a polymer/carbon nanotube nanocomposite strain sensor. *Acta Mater.* **2008**, *56*, 2929–2936. [CrossRef]
128. Kim, T.; Kim, D.; Joo, Y.; Park, J.; Yoon, J.; Hong, Y. Crack propagation design in transparent polymeric conductive films via carbon nanotube fiber-reinforcement and its application for highly sensitive and mechanically durable strain sensors. *Smart Mater. Struct.* **2019**, *28*, 025008. [CrossRef]
129. Zhang, B.; Lei, J.; Qi, D.; Liu, Z.; Wang, Y.; Xiao, G.; Wu, J.; Zhang, W.; Huo, F.; Chen, X. Stretchable conductive fibers based on a cracking control strategy for wearable electronics. *Adv. Funct. Mater.* **2018**, *28*, 1801683. [CrossRef]
130. Zhang, H. Flexible textile-based strain sensor induced by contacts. *Meas. Sci. Technol.* **2015**, *26*, 105102. [CrossRef]
131. Zhang, R.; Deng, H.; Valenca, R.; Jin, J.H.; Fu, Q.; Bilotti, E.; Peijs, T. Carbon nanotube polymer coatings for textile yarns with good strain sensing capability. *Sens. Actuator A Phys.* **2012**, *179*, 83–91. [CrossRef]
132. Zhang, R.; Deng, H.; Valenca, R.; Jin, J.H.; Fu, Q.; Bilotti, E.; Peijs, T. Strain sensing behaviour of elastomeric composite films containing carbon nanotubes under cyclic loading. *Compos. Sci. Technol.* **2013**, *74*, 1–5. [CrossRef]
133. Yang, H.; Yao, X.; Yuan, L.; Gong, L.; Liu, Y. Strain-sensitive electrical conductivity of carbon nanotube-graphene-filled rubber composites under cyclic loading. *Nanoscale* **2019**, *11*, 578–586. [CrossRef] [PubMed]

134. Rotzler, S.; Krshiwoblozki, M.V.; Schneider-Ramelow, M. Washability of E-textiles: Current testing practices and the need for standardization. *Text. Res. J.* **2021**, *91*, 2401–2417. [CrossRef]
135. Yang, Z.H.; Zhai, Z.R.; Song, Z.M.; Wu, Y.Z.; Liang, J.H.; Shan, Y.F.; Zheng, J.R.; Liang, H.C.; Jiang, H.Q. Conductive and elastic 3D helical fibers for use in washable and wearable electronics. *Adv. Mater.* **2020**, *32*, 78. [CrossRef] [PubMed]

*textiles*

MDPI

*Review*

# Wearable Actuators: An Overview

**Yu Chen [1], Yiduo Yang [1], Mengjiao Li [2], Erdong Chen [2], Weilei Mu [2], Rosie Fisher [1] and Rong Yin [1,*]**

[1] Textile Engineering, Chemistry and Science, Wilson College of Textiles, North Carolina State University, Raleigh, NC 27695, USA; ychen242@ncsu.edu (Y.C.); yyang72@ncsu.edu (Y.Y.); arfishe3@ncsu.edu (R.F.)
[2] College of Engineering, Ocean University of China, Qingdao 266100, China; limengjiao567@163.com (M.L.); cchenerdong@163.com (E.C.); muweilei@ouc.edu.cn (W.M.)
* Correspondence: ryin@ncsu.edu

**Abstract:** The booming wearable market and recent advances in material science has led to the rapid development of the various wearable sensors, actuators, and devices that can be worn, embedded in fabric, accessorized, or tattooed directly onto the skin. Wearable actuators, a subcategory of wearable technology, have attracted enormous interest from researchers in various disciplines and many wearable actuators and devices have been developed in the past few decades to assist and improve people's everyday lives. In this paper, we review the actuation mechanisms, structures, applications, and limitations of recently developed wearable actuators including pneumatic and hydraulic actuators, shape memory alloys and polymers, thermal and hygroscopic materials, dielectric elastomers, ionic and conducting polymers, piezoelectric actuators, electromagnetic actuators, liquid crystal elastomers, etc. Examples of recent applications such as wearable soft robots, haptic devices, and personal thermal regulation textiles are highlighted. Finally, we point out the current bottleneck and suggest the prospective future research directions for wearable actuators.

**Keywords:** smart textiles; wearable; fiber actuators; soft exoskeleton; haptic action

**Citation:** Chen, Y.; Yang, Y.; Li, M.; Chen, E.; Mu, W.; Fisher, R.; Yin, R. Wearable Actuators: An Overview. *Textiles* **2021**, *1*, 283–321. https://doi.org/10.3390/textiles1020015

Academic Editor: Ivo Grabchev

Received: 1 June 2021
Accepted: 20 August 2021
Published: 24 August 2021



## 1. Introduction

The global wearable market showed a dramatic swell in the past decade with a market size valued at USD 28 billion in 2020 and is expected to expand continually in the next decade. Wearable technology, an emerging trend, integrates sensors, actuators, and electronics that can be worn, embedded in fabric or accessories, or tattooed directly onto the skin to assist daily activities and address changing lifestyles. Wearable actuators, a subcategory of wearable technology, require a compatible modulus to the human body, a huge scope of motion with high precision and velocity, great strain energy density to generate a high force level, a low fatigue rate for a long lifetime, and good reliability.

Conventional actuators including rotary or linear electrical motors, pneumatic and hydraulic actuators [1] provide high power, fast response time, and have been applied in industries for centuries; they are, however, stiff, heavy, noisy, and nonbiological, which limit their applications in wearables. People expect the wearable actuators to be lightweight, inconspicuous, lifelike, and versatile when on the human body, while still achieving their purpose outstandingly. These requirements impelled the development of soft actuation technologies and have attracted enormous interest from researchers in various disciplines [2]. Unlike those traditional actuators, these actuators are small and light, and are not limited to the electrical–mechanical force conversion method. These soft actuators can respond to multiple stimuli such as heat, light, electricity and moisture, exerting force or producing shape changes [2].

Applications of wearable actuators mainly include wearable robotics, haptic devices, and smart textiles. Wearable robotics have been proven valuable in rehabilitation, body assistance, and/or virtual reality [3]. These applications cover systems of various sizes, from millimeter-scale biorobots to large deployable structures. Haptic devices allow the intent

recognition and information transmission through the interface link between the device and the skin. They contain flexible tactile actuators that can transfer the signal through vibration or morphological change [4]. Smart textiles are textiles that can interact with the environment or respond to stimuli [5,6]. Examples of smart textile applications include electrocardiography-T-shirts/wristbands, electroencephalography caps and photovoltaic curtains [1].

There are several review articles introducing the material and working principles of various soft actuators, but few of them are focused on the scope of wearable actuators [2,5,7,8]. In this paper, we review the actuation mechanisms, structures, applications, and limitations of recently developed wearable actuators including pneumatic and hydraulic actuators, shape memory alloys and polymers, thermal and hygroscopic materials, dielectric elastomers, ionic and conducting polymers, piezoelectric actuators, electromagnetic actuators, liquid crystal elastomers, etc. Examples of the recent applications such as wearable soft robots, haptic devices, and personal thermal regulation textiles are highlighted. Finally, we point out the current bottleneck and suggest the prospective future research directions for wearable actuators.

## 2. Wearable Actuators: Materials, Structures, Applications, Merits and Limitations

### *2.1. Pneumatic and Hydraulic Actuator*

Artificial muscles are born out of human needs for biological muscles, with a wide range of applications in soft robots, wearable devices, and medicine [9,10]. They are typically demonstrated to be alternatives to rigid electrostatic and electromagnetic actuators, since they possess unique advantages such as being silent, soft, and compliant. Among different forms of artificial muscles, fluid-driven actuators are commonly used due to their simplicity, large driving stress and deformation, good energy efficiency, and processability [11]. By far, pneumatic and hydraulic actuators are one of the most applied actuators in the industry. According to previous research, fluid-driven actuators can be simply divided into three major types of devices: elastic fluidic actuator, piston–cylinder fluidic actuators, and drag-based fluidic actuators [12]. Note that in this review we mainly focus on elastic fluidic actuators, specifically McKibben actuators, since they are by far the most common in wearable actuators [12]. Pneumatic and hydraulic actuators will be introduced together since they share similar structures and mechanisms. Compared to pneumatic, hydraulic actuator systems are more complicated and normally require the installation of a pump, valves, hoses, and an electric motor [13]. Nevertheless, hydraulic motors typically possess the better power to weight ratio [14].

#### 2.1.1. Structure

McKibben actuators are typical pneumatic artificial muscles (PAMs). These actuators generally consist of an expandable chamber, normally a balloon, with other structures. By the pressurization of fluid in the chamber, these actuators can transform the expansion to a contraction force. Pneumatic and hydraulic actuators can generate linear, torsional, and bending actuation through the control of internal structures, which are normally inspired by bio-architectures. For example, inspired by muscular hydrostat, Schaffner et al. demonstrated complex motion modes on soft actuators by printing stiff silicone stripes on top of a soft silicone cylinder [15] (Figure 1a). With the arrangement of stiff fiber, this actuator can achieve bending, elongation, and other movements. Similarly, Kim et al. reported a lamina composed of not stretchable fiber, super-elastic matrix, and an adhesive backing [16]. This lamina is also named Stretchable Adhesive Uni-Directional prepreg (STAUD-prepreg) (Figure 1b). By adhering multiple prepreg on a stack, this soft actuator demonstrates complex motion. It is worth noting that with the rearrangement of prepregs, this actuator is reprogrammable, which makes it different than other predefined fluid-driven actuators. Based on vacuum-actuated muscle-inspired pneumatic structures (VAMPs), Li et al. proposed fluid-driven origami-inspired artificial muscles (FOAMs) composed of a folding skeleton, flexible fluid-tight skin, and fluid medium (Figure 1c) [17].

Through programing the geometry of the skeleton, various motions and contractions can be achieved. Experiments reveal that these muscles can contract over 90% of their initial lengths, generate stresses of ~600 kPa, and produce peak power densities over 2 kW/kg.

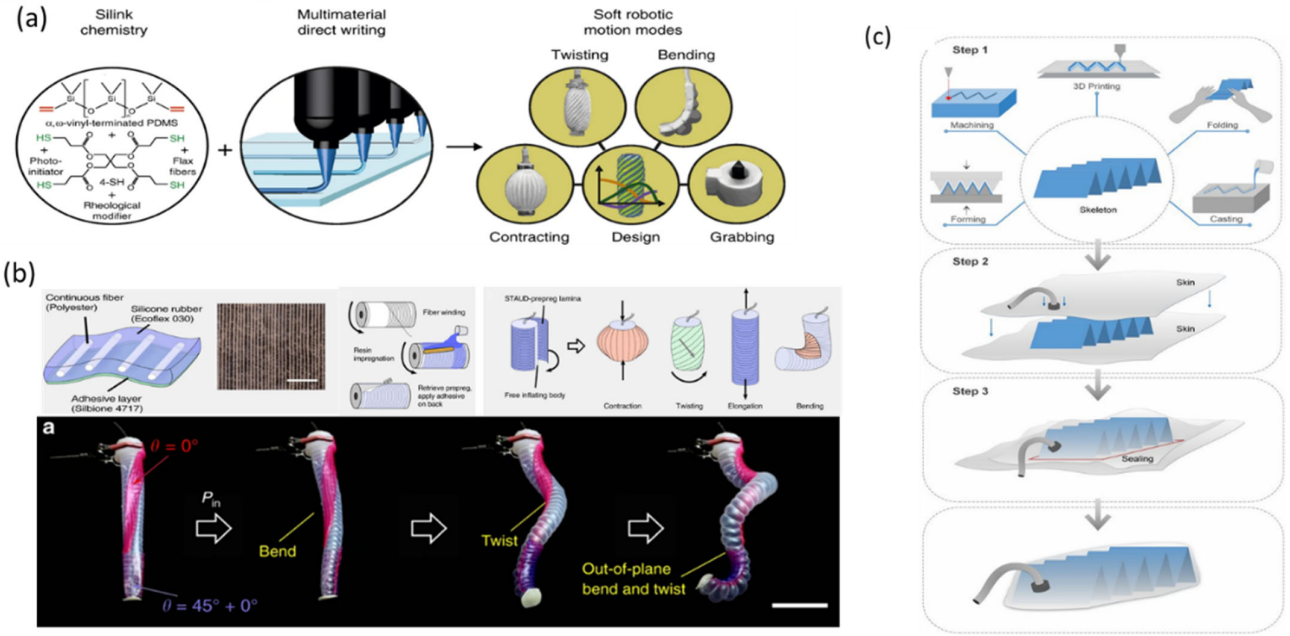


**Figure 1.** Schematic diagram of structures of pneumatic and hydraulic actuators. (**a**) Silicone-based 3D-printing pneumatic actuators [15] copyright 2018, the authors, published by Springer Nature. (**b**) Stretchable Adhesive Uni-Directional prepreg (STAUD-prepreg) [16] copyright 2019, the authors, published by Springer Nature. (**c**) Fluid-driven origami-inspired artificial muscles (FOAMs) [17] copyright 2017, the author(s), published by PNAS.

#### 2.1.2. Applications

A typical application of pneumatic and hydraulic actuators is Robotic orthoses, also called exoskeletons. These devices are usually used to assist human movement, or for rehabilitation of upper or lower limbs [18]. The electric, hydraulic, and pneumatic actuators are the most popular in current orthoses. Here, we briefly introduce some recent research of pneumatic/hydraulic actuators on exoskeleton devices. These devices use simple but well-designed materials with novel actuation mechanisms to achieve lightness and high efficiency.

An inflatable wrinkle pneumatic actuator with fast inflation and deflation responses was proposed [19]. A theoretical model was built to improve the design of the torque required to fit the joints that need to be assisted. A pneumatic circuit was designed to instantly generate negative pressure at the exit of the actuator, thereby shortening the exhaust time. This wrinkle actuator was applied on a wearable knee suit to exhibit rapid inflation and deflation times (0.40 s and 0.16 s) (Figure 2a). A textile based pneumatic actuator was designed to assist the movement of the upper arm through shoulder abduction and horizontal flexion/extension [20]. By coordinated movement of Abduction Actuators (ABA) with the Horizontal Extension/Flexion Actuator (HEFA), the device can provide comprehensive support for movement in different directions of the shoulder. With only 0.48 kg for the whole actuator systems, this device can generate 8 Nm under 70 kpa.

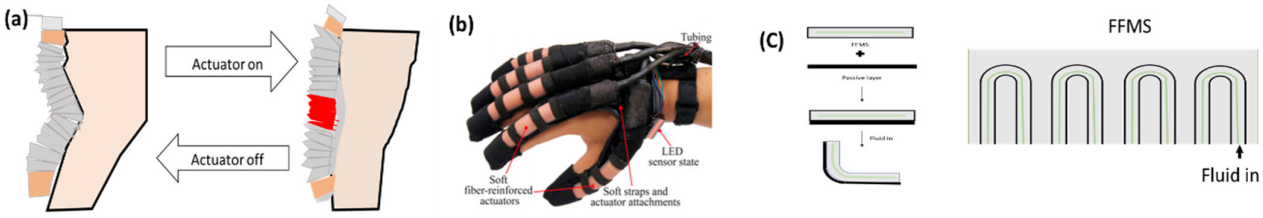


**Figure 2.** Applications of pneumatic/hydraulic actuators as wearable devices. (**a**) Pneumatic based wearable knee suit [19]. (**b**) A hydraulic soft glove for combined assistance and at-home rehabilitation [21]. Copyright 2015, Elsevier. (**c**) Fluidic Fabric Muscle Sheets (FFMS) [22].

A soft robotic glove based on a fluid-driven actuator demonstrated assistance in the grasping movement of the hand [21]. Different actuation modes for the thumb and the rest of the fingers were applied to achieve a typical grasping movement (Figure 2b). Inspired by sheet-like biological muscles, the Zhu group presented a new family of soft actuators, named Fluidic Fabric Muscle Sheets (FFMS) [22]. The elastic tubes were stitched into fabric to achieve actuation by the movement of fluid in and out. By the design of the fluid route, these actuators exhibit multiple deformation. Through the application of textile technology, this type of actuator can be made into a micro execution unit, or can be developed as a large, meter-level actuator. Data shows that this type of actuator can withstand a force of more than 150 n, which is more than 115 times its weight, and up to 100% engineering strain (Figure 2c).

#### 2.1.3. Merit and Limitations

A major problem with pneumatic/hydraulic actuators is poor portability [23]. These actuators usually require a large fluid tank and assorted control units. In addition, the seal of the actuator is also a challenge [24]. Although they are made of soft materials, these actuators still contain some hard parts, which limit their applications. At the same time, their advantages are obvious. The actuation mechanism determines that these actuators are not limited by material. Through the integration of the control system and structure, pneumatic/hydraulic actuators can achieve very complex movements [25]. Fluid pressure can generate a greater driving force than other soft materials, which promise their applications for exoskeletons. Due to the maturity of the process technique, these actuators have been made into commercial products for daily use [26].

### *2.2. Shape Memory Effect*

Shape memory effect (SME) is a phenomenon in which a material recovers to its original size and shape when heated above a certain characteristic transformation temperature [27]. The two most prevalent shape-memory materials are shape memory alloys (SMAs) and shape memory polymers (SMPs).

#### 2.2.1. SMAs

SMAs are characterized by solid state displacive transformations between austenite and martensite phases in response to a stimulus such as heat. This provides the materials with the capability for sustaining and recovering from strains up to 10% which imbues them with unique actuator and potential sensor capabilities in smart material systems [28]. As shown in Figure 3, upon heating, phase transformation from martensite to austenite starts at temperature $A_s$ and stops at temperature $A_f$, whilst the reverse phase transformation starts at temperature $M_s$ and stops at temperature $M_f$ during cooling (Figure 3a). There are three major shape memory characteristics for SMAs, namely one-way memory effect, two-way memory effect, and pseudoelasticity [29]. In one-way SMAs, the material is deformed at a low temperature, and the shape can be restored after heating, in which the SME only exists in the heating process. In two-way SMAs, the material has SME during both heating and cooling by training. In pseudoelasticity, the phase transition of the material comes from an external mechanical stress instead of thermal excitation. The SME

was first observed in gold-cadmium alloy by Arne Ölander in 1932 [30]. So far, more than 50 alloy metals with shape memory effect have been found. Among them, Nickel-titanium (NiTi) has become the most popular and studied SMA due to its outstanding mechanical and thermomechanical properties, such as biocompatibility, high corrosion, and high work capacity [31,32]. SMA wires can achieve a high stress of about 700 Mpa and strain of 10% in length. Higher strains can be obtained with special geometries such as helix or zigzag but with lower stresses. Due to their excellent properties, SMAs are widely used in aerospace, mechatronics, biomedicine, bridge construction, automobiles, and daily life [33].

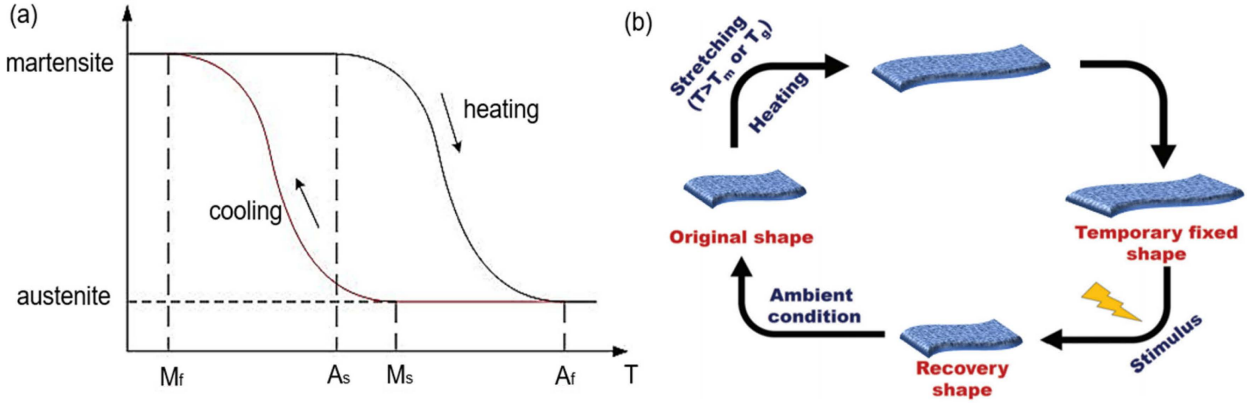


**Figure 3.** Shape memory principles of SMAs (**a**) and SMPs (**b**).

2.2.2. SMPs

SMPs are polymeric smart materials that have the ability to return from a deformed state (temporary shape) to their original (permanent) shape in response to an external trigger, such as temperature, an electric or magnetic field, light, or solution [34–36]. As demonstrated for a heat triggered SMP in Figure 1b, the original shape of an SMP is determined after manufacturing by conventional methods such as extrusion, spinning, pressing, etc. The SMP is changed into a temporary shape by processing through heating, deformation, and cooling. The material maintains this temporary shape until it is activated by a predetermined external stimulus. This cycle of programming and recovering can be repeated multiple times. The mechanism behind this phenomenon depends on their molecular network structure, which contains at least two separate phases, namely a fixing phase and a reversible phase [37]. The fixing phase, showing the highest thermal transition, is the temperature that must be exceeded to establish the physical crosslinks responsible for the permanent shape. The fixing phase can be the cross-linked structure, the partial crystalline structure or the glassy state of the polymer, while the reversible phase can be a partial crystalline phase with reversible change of crystallization and melting, or a phase structure with reversible transition between a glass state and rubber state. SMPs can be a single component polymer or a copolymer, a mixture of two components with different softening temperatures but good compatibility. SMPs also cover a wide property-range from stable to biodegradable, from soft to hard, and from elastic to rigid, depending on the structural units that constitute the SMP [38].

2.2.3. Applications

SMAs, especially SMA wires, have been widely employed in various soft exoskeletons to replace conventional rigid motors or pneumatic/hydraulic actuators for rehabilitation and assisting patients' daily life including hand [39], elbow [40], wrist [41], ankle [42], etc. For instance, a lower limb-worn, soft wearable robot using an SMA wire has been designed to assist ankle plantar flexion, which can generate a stroke of 3 cm and an ankle moment of 100 N cm in each ankle during walking (Figure 4a) [42]. A soft muscle glove containing SMA wires has been developed to replicate the functionalities of a human hand. The glove can achieve a functional range of motion of the human hand and can perform a wide range

of grasp types [43]. A suit-type wearable robot (STWR) containing SMA fabric muscle has been developed to assist the muscular strength of wearers [44]. The STWR can lift barbells weighing 4 kg to a certain target position and demonstrated a fast response time of less than 1 s (Figure 4b). A medical rehabilitation exoskeleton using SMA wires as the actuator for the elbow has been proposed for proper patient elbow joint articulation. The proposed exoskeleton is lightweight and has low noise, which improves the medical rehabilitation process and their ability to perform daily activities (Figure 4c) [45].

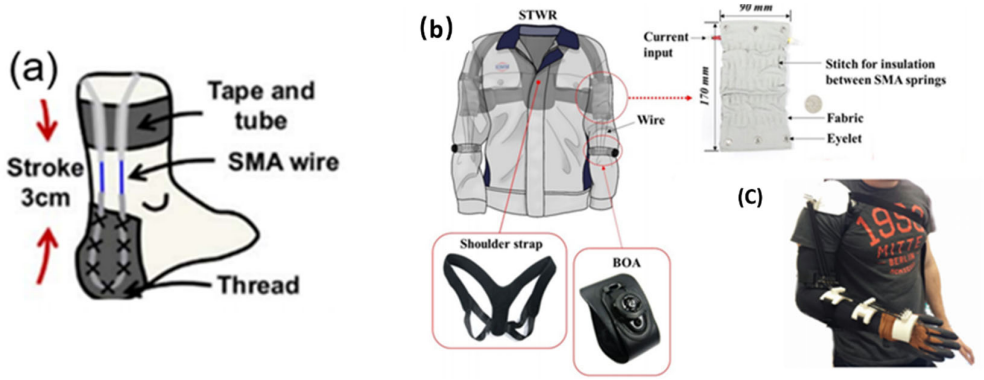


**Figure 4.** Soft wearable robots using SMA wires. (**a**) A soft wearable robot using a SMA wire to assist ankle plantar flexion [42]. Copyright 2020, IOP Publishing Ltd. (**b**) An STWR to assist the muscular strength of wearers [44]. Copyright, 2019, Springer Nature. (**c**) A medical rehabilitation exoskeleton for proper patient elbow joint articulation [45] Copyright 2017, Dorin Copaci et al.

SMPs have plentiful applications in textiles, such as wrinkle-free fabrics, self-cleaning fabrics, breathable garments, and self-adaptable textiles [6]. Lamination, coating, knitting, and weaving are methods that integrate SMPs into textiles [5]. Thermal responsive SMPs can be applied onto textile fabrics via finishing process. Wrinkle-free, crease retention, or anti-shrinkage textiles can be fabricated by treating SMPs on fabrics. The cotton fabric treated with SMPU showed a good wrinkle-free effect and can return to its original flat shape quickly upon blowing steam over it [46]. Taking the advantages of the change of water vapor permeability of SMPs with temperature makes them capable of regulating the human body temperature [47]. As the body temperature is above the glass transition temperature of SMPs, the molecular free volume of the SMPs significantly increases, which aids the transfer of vapor and heat through perspiration, and vice versa.

#### 2.2.4. Merits and Demerits

SMAs have outstanding mechanical and thermomechanical properties, such as biocompatibility, high corrosion, and high work capacity. These allow them to have several commercialized applications in medical tools. However, SMAs exhibit large thermal hysteresis, which makes it hard to control the actuation process. Moreover, the low durability and high material cost ($200–300/kg) hinder their applications in wearable robots. In contrast to SMAs, SMPs possess many advantages such as light weight, flexibility, high elastic deformation (up to 800%), high shape recovery (>90%), and low recovery temperature, etc. SMPs can be integrated into textiles by various textile processes. Although many textile prototypes and commercial trials have been demonstrated, many issues remain to be resolved. Several difficulties lie in meeting the stringent textile requirements, such as color, dimensional stability, comfort and tactile properties, washability, strength, flexibility, stretchability, as well as compatibility with many other chemical, mechanical, and thermal processing standards, and low-cost production [37].

### *2.3. Thermal and Hygroscopic Expansion*

#### 2.3.1. Mechanism

Thermal or hygroscopic expansion is the tendency of matter to change its volume in response to a change in temperature or moisture content. The macroscopic effect of hygroscopic expansion is similar to that of thermal expansion, but the microscopic causes are very different. Thermal expansion is a result of molecules' vibration and movement when heated, while hygroscopic expansion is caused by hygroscopy, the phenomenon of attracting and holding water molecules via either absorption or adsorption from the ambient environment. The coefficient of thermal expansion ($\alpha$T) is defined to quantify the magnitude of the volume change in relation to temperature change, which is given by

$$\alpha_T = \frac{1}{V}\left(\frac{\partial V}{\partial T}\right)_p \quad (1)$$

where $V$ is the volumetric expansion, $T$ is the temperature, and $p$ is the pressure held constant during the expansion. In the case of hygroscopic expansion, the temperature ($T$) in Equation (1) is replaced by the relative humidity ($\varphi$).

High thermal expansion materials include low-density polyethylene (500 ppm/K) [48], polydimethylsiloxane (~300 ppm/K) [49], biaxial oriented polypropylene (~120 ppm/K) [50], etc., while textile cellulose and protein fibers have a high expansion in diameter when wet, such as cotton (7–20%), jute (20–21%), wool (14–17%), and silk (16–19%) [51]. These materials' expansion behavior has been utilized to fabricate various tensile, bending, and torsional actuators for wearable applications, as shown in Figure 5.

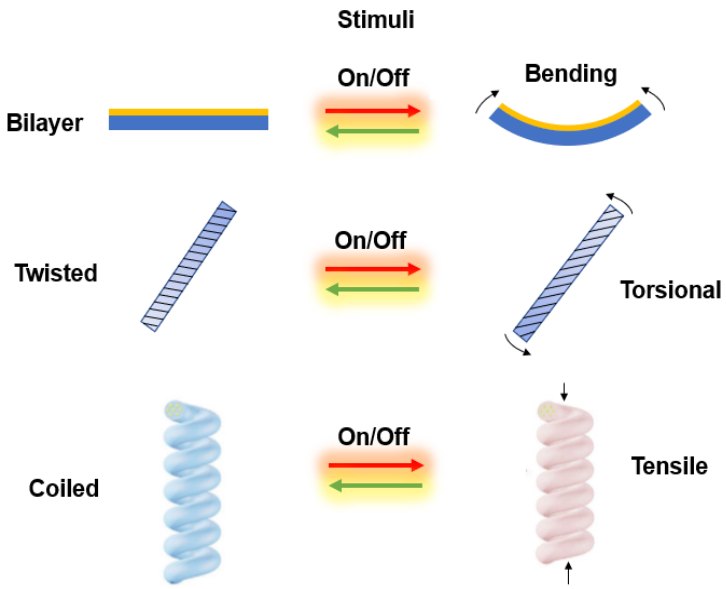


**Figure 5.** A schematic diagram of heat or moisture induced actuators.

#### 2.3.2. Structure

Bimorph structure is a widely adopted strategy to generate bending motion via asymmetric deformation of the two layers, an active layer that contracts or expands by an external stimulation and a passive layer that remains intact. The interfacial stress generated between the two layers due to the volume mismatch leads to bending deformations. There are many examples of bending actuators in the film form, such as LDPE/PVC film [48], poly(vinyl alcohol-co-ethylene) (EVOH)/cellulose film [52]. Alternatively, asymmetric exposure of water vapors or heat to the thin film of moisture or heat responsive materials can also achieve the bending motions, but the bending performance is thickness sensitive. Examples includes microfibrillated cellulose film [53] and nylon beam coated with thermally conductive graphene flakes [54]. Some bimorph fibers have also been developed.

Cyclic olefin copolymer elastomer/HDPE fiber was developed by using a fiber-drawing technique, and can lift more than 650 times its own weight at a low temperature [55]. A moisture trigged acetate-based conjugate fiber (Ventcool$^{TM}$) was created by the Kaiteki company to automatically adjust ventilation of clothing [56].

Torsional fiber actuators are realized by twisting moisture and heat responsive fibers to form a yarn like structure with free-standing torque balanced status. The yarn torque or torsional movement is generated by anisotropic swelling of fibers in the radial direction when exposed to a stimulus. When the stimulus is off, the deswelling of fibers causes the actuator to rotate in the opposite direction and finally returns to the balanced status. Accompanying the torsional movement, the twisted yarn or fiber actuators also show a tensile expansion and contraction behavior due to the twist contraction effect. For example, degummed silk fibers were twisted and folded into torsional silk muscles that provided a reversible torsional stroke of 547° mm$^{-1}$, a maximum rotary speed of 975 rpm, and a peak torque of 0.063 Nm/kg [57]. Twisted graphene oxide (GO) fiber demonstrated remarkable performance as a reversible rotary motor with a torsional stroke 588° mm$^{-1}$, a rotary speed of up to 5190 rpm, a tensile expansion of 4.7%, and a peak power output of 71.9 W/kg. The moisture-triggered electric generator based on GO fibers produced an open-circuit voltage of up to 1 mV, and a short-circuit current of up to 40 μA [58]. Hydrophobic carbon nanotube (CNT) twisted yarns offered a maximal torsional moment of 0.4 Nm/kg, close to the commercial electric motor (the Aerotech model 1410-01motor) in response to water and moisture after oxygen plasma treatment [59]. Other fiber materials include bamboo [60], cotton [61], lotus [62], chitosan [63], etc. The performance of several fiber-based torsional actuators is summarized in Table 1.

**Table 1.** Performance of fiber-based torsional actuators.

| Material | Stimulus | Amplitude of Stimulus | Stroke (° mm$^{-1}$) | Rotary Speed (rpm) | Peak Torque (Nm/kg) | Reference |
|---|---|---|---|---|---|---|
| GO | moisture | 85% RH | 588 | 5190 | 0.082 | [64] |
| CNT | moisture | water droplet | 62.16 | - | 0.4 | [59] |
| Bamboo | moisture | wet | 64.4 | - | - | [60] |
| Cotton | moisture | wet | 42.55 | 720 | - | [61] |
| Chitosan | moisture | wet | 1155 | - | - | [63] |
| Silk | moisture | 60% RH | 547 | 975 | 0.063 | [57] |
| Lotus | moisture | 60% RH | 200 | 200 | 0.488 | [62] |

Fiber-based tensile actuators are achieved by twisting and coiling the fibers to form a spring-like structure. The actuating principle lies in anisotropic swelling of the fibers in the radial direction, causing the yarn to untwist and in turn the coil to change its writhe, which pulls the adjacent coils close to each other, shortening the coil. When used as a tensile actuator, the cylindrical yarn coil should be torsionally tethered such that the two ends can slide but not be allowed to rotate, which prevents the yarn from untwisting. This concept was first proposed by Harins et al. [65] in 2014, in which low-cost high-strength nylon fibers, used as fishing line or sewing thread, have demonstrated a high stroke of 34% for a temperature variation of ~220 °C. Likely, composite yarns made of polyimide and PDMS have achieved a tensile actuation of 20.7% and a competitive specific work of 158.9 J/kg, four times that of natural muscle [64]. Surfactant-treated wool yarn coils generated a contraction stroke up to 38% and a maximum work capacity of 194 J/kg [66]. Viscose fiber artificial muscles demonstrated a 35% contraction and a maximum work capacity of 90.4 J/kg [67]. Degummed silk fibers were twisted and wrapped around a mandrel to form tensile actuators that provided a maximum 70% contraction and peak work capacity up to 73 J/kg [57]. Other fiber materials include carbon fiber (CF)/PDMS [68], lotus [62], bamboo [60], etc. The performance of several fiber-based tensile actuators is summarized in Table 2.

**Table 2.** Performance of fiber-based tensile actuators.

| Material | Stimulus | Amplitude of Stimulus | Strain (%) | Stress (Mpa) | Work Density (J/kg) | Reference |
|---|---|---|---|---|---|---|
| Nylon 6,6 | heat | 240 °C | 34 | 22 | 2480 | [65] |
| Polyethylene | heat | 130 °C | 16 | 16 | 2630 | [65] |
| PI/PDMS | heat | 210 °C | 20.7 | 1.2 | 158.9 | [64] |
| CF/PDMS | heat | 200 °C | 25 | 60 | 758 | [68] |
| Bamboo | moisture | 90% RH | 50 | 0.75 | 1.08 | [60] |
| Wool | moisture | wet | 38 | 2.6 | 194 | [66] |
| Viscose | moisture | wet | 35 | 0.28 | 90.4 | [67] |
| Silk | moisture | 60% RH | 70 | 3.2 | 73 | [57] |
| Lotus | moisture | 70% RH | 38 | 13 | 450 | [62] |

#### 2.3.3. Applications

There are many applications of moisture or heat responsive materials for smart textiles, which dynamically change the structure or pore size of clothing for enhanced personal thermal management [69]. For instance, two kinds of moisture responsive bendable smart clothing were designed based on the successful application of the Nafion film from DuPont that can reversibly adapt their thermal insulation functionality [70]. The first design is pre-cut flaps, which open to produce pores in Nafion sheets when humidity increases, allowing air flow and reducing both the humidity level and the apparent temperature (Figure 6a). The second design is thickness adjustable clothes by inserting the bent Nafion films between two fabrics. When the humidity increases, the films become thinner, thus reducing the gap between the two fabrics to reduce the thermal insulation (Figure 6b). Knitted fabrics made of CNTs coated triacetate-cellulose bimorph fibers effectively shifted the infrared radiation (IR) by more than 35% as the relative humidity of the underlying skin changed [71]. When hot and wet, the multiple metafibers move close to each other, leading to resonant electromagnetic coupling that modulates the IR emissivity to spectrally overlap with that of the human body and enhance radiative cooling effect. A woven textile from silk fiber muscles demonstrated excellent comfort and drapability. The sleeves, made by weaving coiled silk muscle fibers in the warp direction and untwisted fibers in the weft direction, shrink in the warp direction when humidity increases, and then expand when humidity decreases [57]. This moisture-responsive textile, which can change macroshape or microstructure, is promising to be very effective for moisture and thermal management to increase comfort between skin and fabric (Figure 6c). In addition to hygroscopic polymer materials, living cells have been engineered to design biohybrid wearables [72]. A bilayer-structured biohybrid film was proposed by depositing genetically tractable microbes on a humidity-inert material to form a heterogeneous multilayered structure, which can reversibly change shape within a few seconds in response to environmental humidity gradients (Figure 6d).

#### 2.3.4. Merits and Limitations

There are some advantages and limitations for the thermal or hygroscopic driven actuators. Commercially available fibers such as nylon, PE, and bamboo are inexpensive and they can be easily converted into torsional and tensile actuators. In terms of the structure, although several film-based actuators have been demonstrated, they are difficult to be developed into a textile structure for wearables. Fiber-based actuators are more promising and have demonstrated their capabilities to be used for personal thermal regulation. Moreover, thermal responsive actuators usually need a high temperature for desired stress and strain, causing possible discomfort and injuries for humans, and thus hinders their applications in smart textiles. In addition, the energy efficiency of heat driven actuators is very low (<1%), and the cycling rate is low due to the poor heat diffusion and dissipation, especially during the cooling process, so they take a longer time for heating

and cooling [2]. For moisture responsive actuators, their durability and performance need to be further explored.

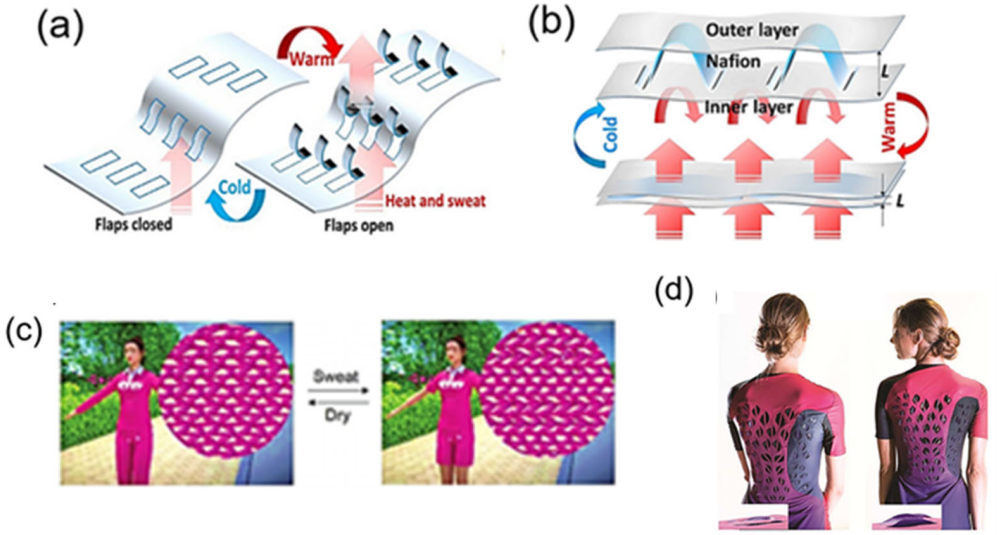


**Figure 6.** Moisture and heat responsive smart textiles. (**a**) Nafion sheet schematics with openable flaps mimicking thermo-adaptive functionality of human skin [70]. Copyright 2017, Springer Nature. (**b**) The schematic of the thickness reversible structure using nafion as a thermally adaptive interlayer [70]. Copyright 2017, Springer Nature. (**c**) Schematic diagram of moisture sensitive clothing changing sleeve and pant length before and after exercise [57] Copyright 2017, Wiley-VCH. (**d**) Running suit prototype with ventilation flaps based on the moisture sensitive biohybrid two-layer film [72]. Copyright 2017, the authors, published by AAAS.

### *2.4. Dielectric Elastomer Actuators*

#### 2.4.1. Mechanism

Dielectric elastomer actuators (DEAs) are electronic electroactive polymers that enable electromechanical transduction at effective electrical fields, transferring electrical energy into mechanical work [7,73]. The working principle of a DEA is based on the basic configuration that two compliant electrodes are coated on each side of a thin polymer film to form a deformable capacitor (Figure 7). According to the elastic electrostatic model first established by Pelrine et al. [74,75], due to the inherent volume incompressibility, when an electrical field is applied perpendicularly to the plane of the two electrodes, two mechanisms are generally induced: the attractive electrostatic forces among opposite charges on each electrode cause the polymer film to compress in thickness and the repulsive electrostatic forces among like charges over the same electrode render further expansion in area, reducing the electrical energy [7,74]. For an ideal elastic model, electrostatic energy is equally converted to mechanical energy through lateral and transverse displacement [74]. The capacitance ($C$) of the dielectric film is

$$C = \varepsilon_0 \varepsilon A / z \tag{2}$$

and thus the stored electrostatic energy ($U$) is given by:

$$U = 0.5 \frac{Q^2}{C} = 0.5 \frac{Q^2 z}{\varepsilon_0 \varepsilon A} \tag{3}$$

where $Q$ is the fixed charge on the electrodes, $A$ is the area of the electrode, $z$ is the thickness of the DE film, $\varepsilon_0$ is the free-space permittivity, and $\varepsilon$ is the relative permittivity (dielectric constant) of the DE material.

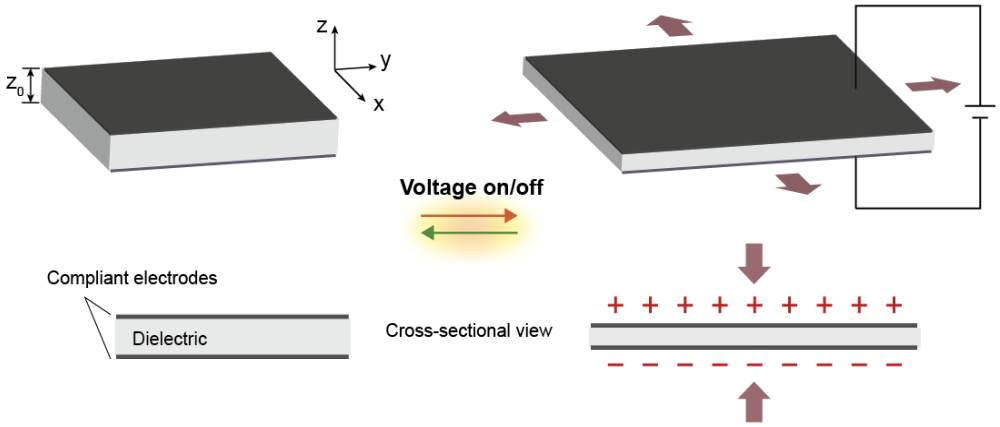


**Figure 7.** Schematic diagram of the operational principle of a DEA.

The electrostriction effect of a DEA upon the application of a proper electric field is believed to be caused by the formation of the effective compressive pressure $P$, also known as the Maxwell stress, which is defined as the electrostatic energy change per unit thickness displacement per unit area [74]:

$$p = \varepsilon_0 \varepsilon E^2 = \varepsilon_0 \varepsilon \left(\frac{V}{z}\right)^2 \tag{4}$$

Given that $Az$ = *constant*, the effective stress ($p$) can be obtained:

$$p = \varepsilon_0 \varepsilon E^2 = \varepsilon_0 \varepsilon \left(\frac{V}{z}\right)^2 \tag{5}$$

where $E$ is the applied electric field, and $V$ is the applied voltage.

For low strains (<10%), the actuated strain in the thickness direction ($s_z$) can be defined as below according to the Hooke's Law in compression [3,5]:

$$s_z = -\frac{p}{Y} = -\frac{\varepsilon_0 \varepsilon \left(\frac{V}{z}\right)^2}{Y} \tag{6}$$

where $Y$ is the elastic modulus of the dielectric elastomer.

The above equations are built on the assumption of linearly elastic behavior of the DEA under relatively small strains. However, polymers are generally nonlinear materials and more complex constitutive relationship need to be taken into account. For example, the elastic modulus essentially depends on the strain (i.e., $Y = Y(s)$) for nonlinear materials. In addition, as large in-plane extension is exhibited, the actual thickness under actuation can be described in relation to the original value ($z_0$) as:

$$z = z_0(1 + s_z) \tag{7}$$

and the constancy of volume can be expressed as

$$(1 + s_x)(1 + s_y)(1 + s_z) = 1 \tag{8}$$

If the in-plane deformation is symmetric, i.e., $s_x = s_y = s_{xy}$, more accurate thickness strain can be expressed by [76]:

$$s_z = (1 + s_k)^{-2} - 1 \tag{9}$$

As described in Equations (5) and (6), the dielectric constant ($\varepsilon$), elastic modulus ($Y$), electric field ($E$)/applied voltage ($V$) and film thickness ($z$) proportional to the Maxwell stress and thickness strain are key parameters to consider in assessing the actuation perfor-

mance of DEAs. Normally high voltage (>1 kV) or electric fields (~100 MV/m) are needed for better actuation output and allow for higher energy efficiency as they lead to smaller current, yet they are often considered disadvantageous for practical applications [73,76]. Hence, key pathways of countering the common limitation of high driving voltage and improving the electrical stimulated actuation performance of a DEA membrane consist in: (1) decreasing film thickness, (2) increasing DE dielectric constant, and (3) reducing DE intrinsic stiffness and viscoelastic loss. Common approaches of enhancing electromechanical responses include physically pre-straining (pre-stretching), chemically modifying the elastomer to tune its modulus/stiffness and electromechanical properties through composites, polymer blends and copolymers, and employ highly compliant electrodes that have high conductivity, little/no stiffening effect upon large strains and the ability of self-clearing such as carbon particle-based electrodes [77].

Since the early investigation of DEAs, acrylic and silicone elastomers have stood out and been widely studied due to their superior overall actuation performance compared to other commonly reported materials such as polyurethane, polyisoprene and fluoroelastomers [75,76]. General comparison between the properties of the two main elastomeric matrices: acrylics (mixtures of aliphatic acrylate) and silicones (polysiloxanes, e.g., most commonly used polydimethylsiloxane (PDMS)), is summarized in Table 3.

**Table 3.** Comparison between acrylic and silicone elastomers [77–79].

| Material | Viscoelasticity | Dielectric Constant (at 1 Hz) | Actuated Strain (Prestrained) | Adhesion Property | Thermal Stability | Moisture Property |
|---|---|---|---|---|---|---|
| Acrylics | High, resulting in long-term relaxation and slower response | High (4.5–4.8) | High (~380%, area) | Good | Low (−10~80 °C) | Sensitive to humidity |
| Silicones | Low, due to flexible backbone (-Si-O-) | Low (2.5–3) | Modest (~120%, linear) | Poor (low surface energy) | High (−65~240 °C) | Low rate of moistureabsorption |

#### 2.4.2. Structure

Configurational designs of DEAs differ with applications and generally manipulate the basic operational mechanism to transduce electrical power into mechanical work to achieve amplified performance of in-/out-of-plane deformation such as contraction, expansion and bending. Common structures derived from the fundamental membrane prototype include multi-stack [80], interdigitated [81], and twisted [82] contractile devices; rolled [83], cone-shaped [84], and diaphragm [4]. DEAs exhibit linear or areal expansion. Multi-stack architecture is an effective approach to augmenting the effect of the Maxwell stress and generating amplified contractile actuation and load-bearing capacity (Figure 8a). Twisted actuators are developed from spiral cylindrical stacked DEAs to enhance their operational stability and ensure inherent flexibility, the actuated strain of which depends on the helix angle (Figure 8b) [82]. In contrast, cone-shaped (Figure 9a) and rolled (Figure 9b) DEAs utilize areal expansion to produce axial extension and amplified forces. Tunable two-cone actuators with proper voltage excitation modes enable the control of multi-directional and rotational actuation [85]. Zhao et al. [83] developed rolled multilayer DEAs that are able to produce a force of 1 N and strain of 10% at small driving voltages lower than 1 kV. The out of plane protrusion of diaphragm DEAs is triggered by two working modes: one is based on a physical support or boundary constraint and the other requires an external pressure for amplified actuation [86], which has found its applications in optical lenses [87], haptic interfaces [4] and braille displays [88], etc. Additionally, bendable DEAs with functional elements such as laminated passive layers in the form of unimorphs or bimorphs are also commonly investigated (Figure 10a) [89,90]. Bending motion has also been realized by multi-degree-of-freedom spring roll configuration with patterned electrodes that are circumferentially aligned (Figure 10b) [91]. The actuation performance of several DEAs with common structures is shown in Table 4.

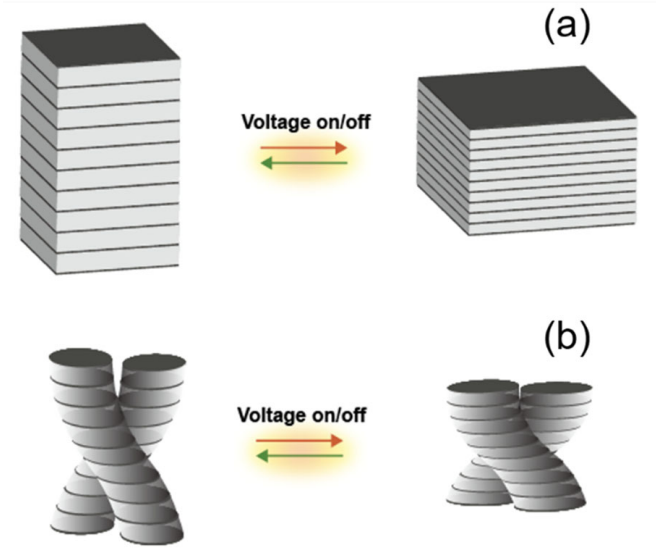


**Figure 8.** Schematics of contractile DEAs: (**a**) multi-stack structure; (**b**) twisted structure.

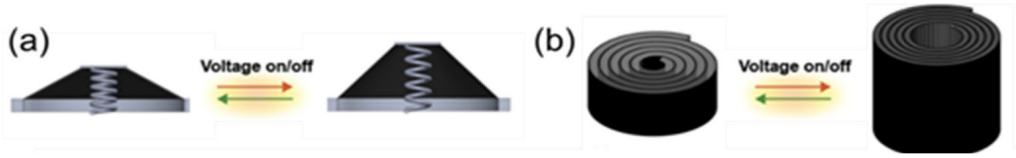


**Figure 9.** Schematics of expansion DEAs. (**a**) Cone-shape structure [78]. (**b**) Rolled structure [78] Reproduced under the terms and conditions of the Creative Commons Attribution (CC BY) license (http://creativecommons.org/licenses/by/4.0/). Copyright 2020, The authors. Licensee MDPI, Basel.

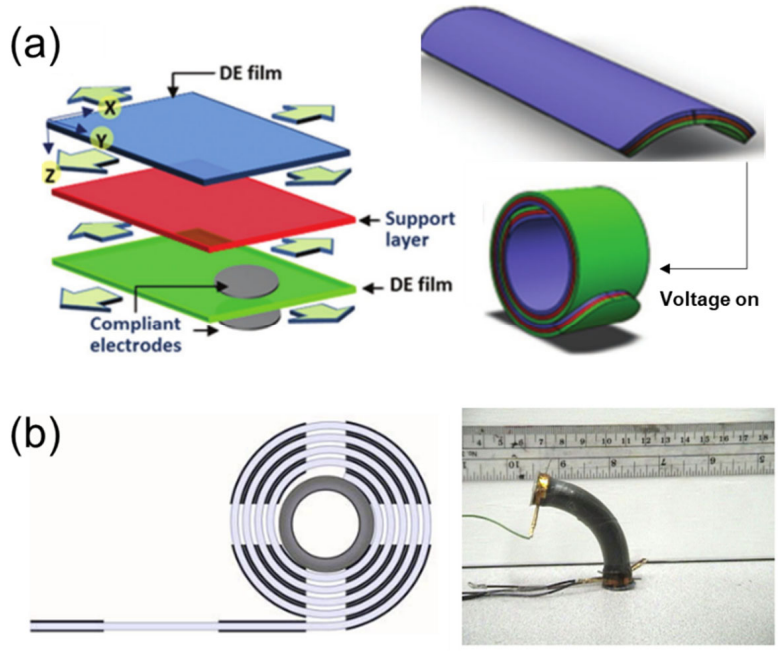


**Figure 10.** Schematics of bending DEAs: (**a**) multilayer bistable structure with bending features [90]. Copyright 2018, Wiley-VCH; (**b**) 2-degree-of-freedom spring roll structure and a prototype [91]. Copyright 2004, IOP Publishing.

**Table 4.** Performance of dielectric elastomer actuators with common structures.

| Structure | Multi-Stack | Twisted | Rolled | Cone | Buckling Diaphragm | Bending Unimorph |
|---|---|---|---|---|---|---|
| DE material | Acrylic (VHB 4910, IPN post-processed) | Silicone (Wacker Elas tosil P7670) | Silicone (Sylgard 184 and Ecoflex 0030) | Silicone (Wacker Elas Tosil) | PDMS | Formulated acrylic (oligomer: CN9014) |
| Electrode material | Silicone/ carbon-black mixture | Carbon black, graphite and ethanol | Single-walled carbon nanotubes (SWCNTs) | Carbon black | Silver nanowires (AgNWs) | SWCNTs |
| Prestrain | 200% areal | None | None | 10% areal | None | None |
| Voltage (kV) | 4.2 | 6.5 | 1 | 4.5 | 4 | 4 |
| Specific power (W/kg) | - | 13.7 | 55 | - | - | $19.5 \pm 1.01$ |
| Energy density (J/kg) | 12.9 | - | 0.275 | - | - | $1.95 \pm 0.10$ |
| Strain/displacement (without load) | 30% | 5.2% | 10% | 2.3% | 650 μm | 16 mm |
| Blocking/output force (mN) | - | - | 1000 | 185 | 255 | $12.5 \pm 0.9$ |
| Reference | [80] | [92] | [83] | [84] | [4] | [89] |

PDMS-based DEAs with a pyramidal microstructure allowed for the tunability of modulus and dielectric properties and achieved enhanced actuation performance (pressure up to 25 kPa and vibrotactile cycles up to 250,000) [93]. A novel design of a dielectric liquid actuator utilized hydraulic-coupled electrostatic effect to amplify electrical simulated actuation and enable peak performance surpassing that of natural muscle (specific power of 614 W/kg and load capacity of 700 g for a 2-unit planar hydraulically amplified self-healing electrostatic (HASEL) actuator) [94]. Inspired by the HASEL actuators, a recent effort incorporated the mechanism into origami and created programmable shape-altering interfaces with three dimensional folding features [94].

DEAs with bistable structures have also been developed for the purpose of shape transformation between two equilibrium states. Shao et al. [90] developed disk and tape-spring bistable actuators with a support layer sandwiched by two DE layers based on the bioinspired snap-through mechanism. A pair of electrodes on each DE layer and the control of a dual power supply enable the disk DEAs to shift the curvature bidirectionally, while with two electrodes on one DE layer, the tape-spring DEAs, snap upon electrical stimulation mimicking a chameleon's tongue [90]. Another established bistable mechanism lies within the bistable electroactive polymers (BSEPs). The actuated shape can be maintained by decreasing the temperature below the glass transition temperature of the DE after electrical excitation, saving the need for a constant power supply and thus energy consumption and increasing stiffness for adaptive applications, the rubbery-to-rigid transition of which is recoverable and repeatable [95].

#### 2.4.3. Applications

The properties of DEAs fit into a wide realm of applications owing to their versatility and outstanding actuation performance. For wearable assistance in particular, research has mainly explored communication and rehabilitation. As haptic feedback is an important part of electronic textiles and wearable technologies, integrating DE tactile actuators into wearable systems through haptic sensation has been a rising field of interest attributed to material softness, small size, ease of fabrication, and adaptability compared to traditional rigid motors with fixed frequencies [96]. A crucial factor for effective sensing of haptic cues is skin perceptibility, which means the output force and resonance frequency should reach perceivable levels and depends on both human and device factors, such as placement on bodies and material stiffness [96,97]. For example, typically fingertips are ideal positions on tactile devices due to their higher sensitivity than other parts such as arms, and are usually susceptible to a force threshold around 30 mN depending on the fingers [98]. Hence, one of the main goals in the current development of DEA haptic wearable interfaces is to generate large force and displacement outputs at such a small (millimeter) scale [96,99]. Meanwhile,

as human contact is involved, the design of wearable haptic interfaces using DEAs needs to account for various aspects such as compactness, weight, comfort, safety, etc.

Most current designs of wearable haptics have leveraged the out-of-plane deformation of diaphragm/membrane [96,100] and linear displacement of rolled multilayer [101] configurations, as well as the hydraulic amplification with liquid coupling effect [99]. Multilayered PDMS membranes coated by AgNWs electrodes with a perforated polymeric frame support were able to generate an output force up to 255 mN and a protrusive displacement of 650 μm [14]. More recently, hydraulically amplified taxel (HAXEL) actuators designed with four quadrants consisting of P(VDF-TrFE-CTFE) liquid dielectric and segmented aluminum electrodes were able to simulate directional motions and produce forces over 300 mN and a vertical displacement of 500 μm (Figure 11) [99]. Prototype demonstrations have integrated the haptic functions into wearables such as armbands [4,99,101], rubber gloves [4] and fingertip devices (Figure 12) [96,100] for potential applications of human-machine interaction and virtual/augmented reality. Untethered wearable tactile actuators were realized by on-board battery integration into compact feel-through low-voltage (<500 V) DEAs (FT-DEAs) with a thickness of only 18 μm and a wide vibrotactile frequency range of 1–500 Hz, and the fingertip prototype with incorporated photodetector was demonstrated to be applicable in assisting text-reading for people with vision impairment (Figure 12) [96].

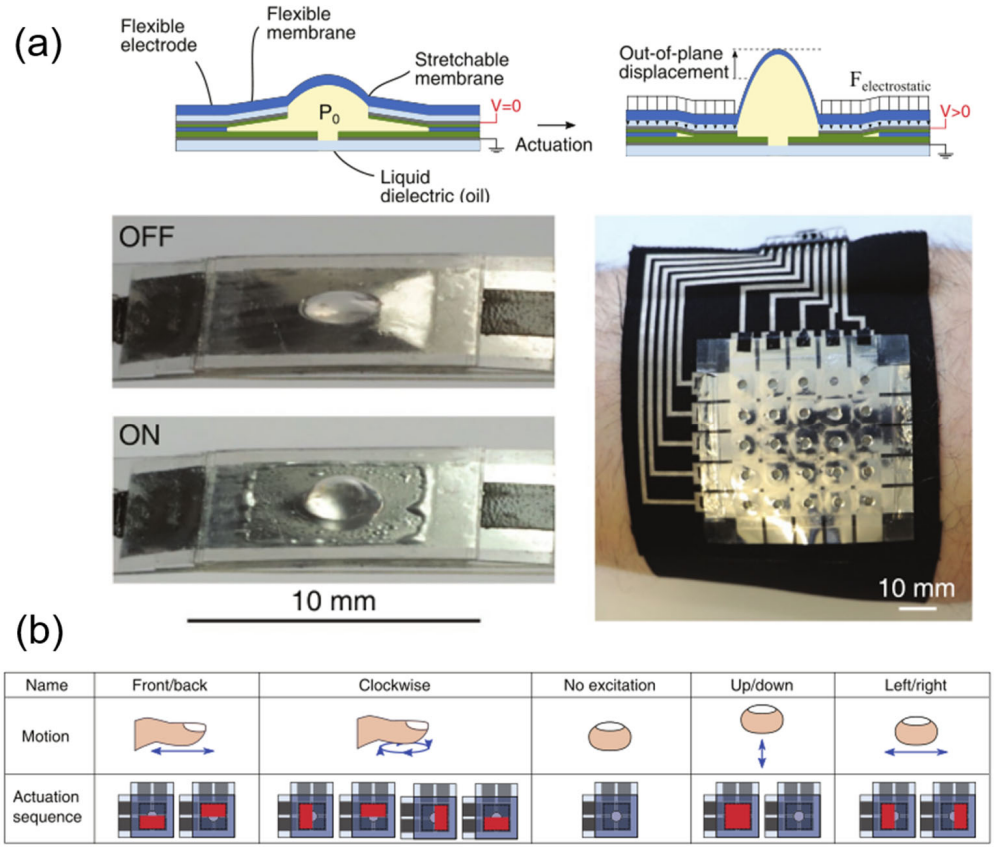


**Figure 11.** Schematics and prototypes of wearable HAXEL actuators. (**a**) Schematic diagrams of a HAXEL actuator and an armband prototype of 5x5 array HAXELs [99]. Copyright 2020, Wiley-VCH. (**b**) Haptic testing modes with various directional motions based on a four-quadrant HAXEL [99]. Copyright 2020, Wiley-VCH.

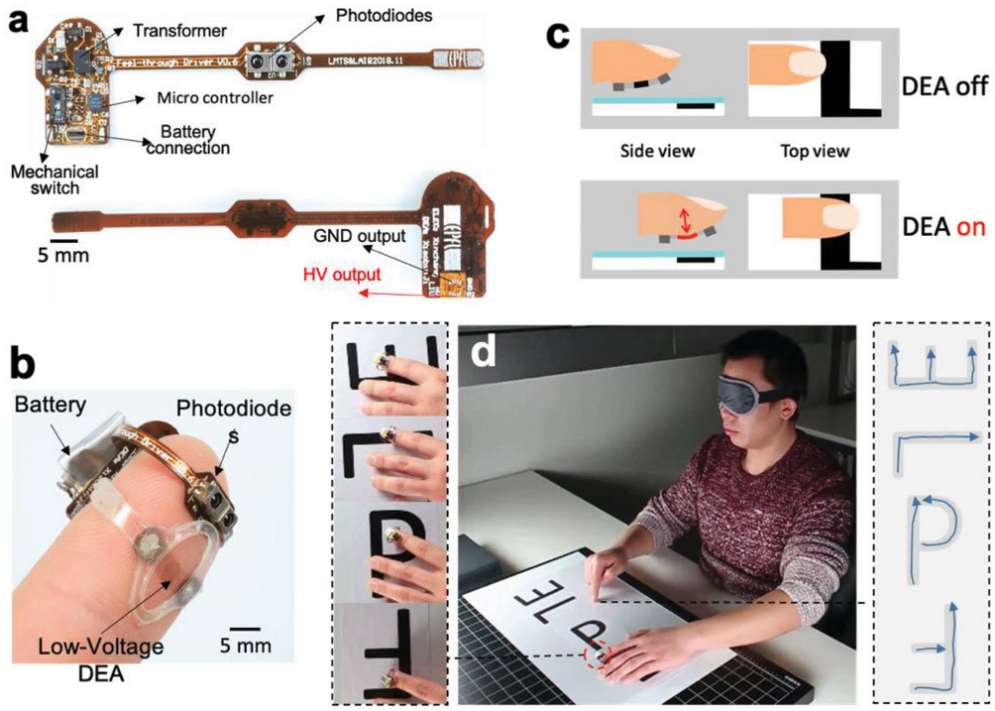


**Figure 12.** Schematics and prototypes of wearable fingertip tactile DEAs. (**a**) The wireless driver circuit. (**b**) Untethered "feel-through" haptic device on a fingertip. (**c**) Operating principle of Untethered FT-DEA. (**d**) The blindfolded user correctly identifies randomly rotated and placed letters E, P, F, and L [96]. Copyright 2020, Wiley-VCH.

Apart from the aforementioned properties, the muscle-like and variable-stiffness behavior of DEAs without bulkiness and noise makes it favorable for wearable rehabilitation devices. Examples include active hand splints for hand/finger rehabilitation (Figure 13a) [102], ankle-foot orthosis (AFO) remedying foot drop (ankle dorsiflexion inability) (Figure 13b) [103] and compression bandages targeting the disorder of venous systems (Figure 13c) [104]. Compared to conventional passive ones with elastic bands, dynamic hand splints with folded contractile silicone DEAs enable flexible modulation of mechanical compliance and finger exercise by varying the driving voltage [102]. AFO designed with DEAs allows for lighter weight and less energy consumption with a charge recovery power system, and at the same time does not hinder plantarflexion function [104].

#### 2.4.4. Merits and Limitations

As an outstanding smart material, DEAs hold promising potentials in wearable actuator technologies attributed to their intrinsic softness, light-weight and compactness, straightforward mechanism and fabrication, and high electromechanical performances. Compared to other existing actuator technologies such as shape memory alloys and electromagnetic and piezoelectric polymers, the distinctive actuation mechanism of DEAs has been reported to be capable of producing prominent resulting strain (>100%) and stress (~7 MPa), fast response speed (μs), high energy density (~3.4 $MJ/m^3$) and high efficiency [75,78]. In addition, the self-sensing characteristic of DEAs, i.e., the phenomenon that electrical properties such as capacitance alter under deformation, makes it possible to monitor the actuation response and develop closed-loop systems for smart human assist. Meanwhile, various challenges to some extent prevent their widespread applications in real-life scenarios. First and foremost, high driving voltage often requires an external power supply, constraining the integration of DEAs into electronic textile systems and bringing about safety concerns. Furthermore, biocompatibility, the need for additional rigid frames supporting pre-stretched films, and unstable electrical and mechanical properties are also

crucial obstacles to overcome towards improving wearability, efficiency and sustainability of DEAs.

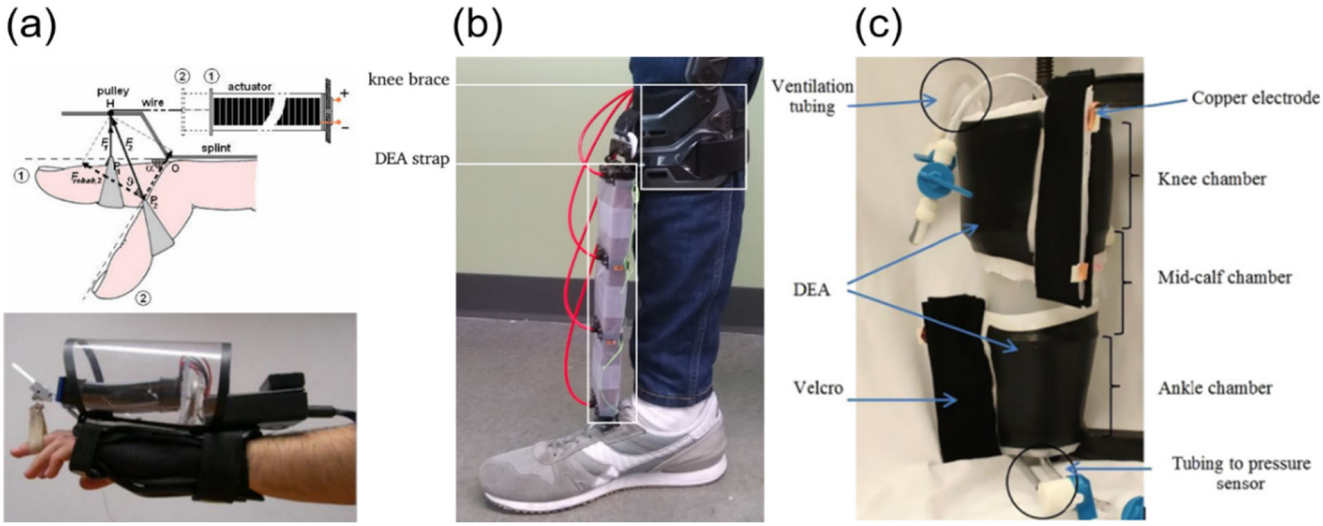


**Figure 13.** Schematics and prototypes of wearable DEAs for rehabilitation. (**a**) A schematic diagram and prototype of a DEA-based hand splint protected by a plastic guard [102]. Copyright 2008, SPIE. (**b**) A DEA AFO prototype consisting of a DEA strap and a knee brace [103]. Copyright 2014, IOP Publishing. (**c**) An active compression bandage prototype for the ankle, mid-calf and knee region [104]. Copyright 2021, Elsevier.

### *2.5. Ionic-Polymer/Metal Composites and Conducing Polymers*

Ionic-Polymer/Metal Composites (IPMCs), as a category of Electroactive polymers (EAPs), have been proposed as the active material in a wide-range of applications, including biomimetic sensors and mechanical actuators [105]. Kuhn [106] and Katchalsky [107] are generally considered to be the first reporters of deformable polyelectrolytes ion solution such as polyacrylic acid (PAA) and polyvinyl chloride (PVA) systems. After that, numerous researchers have demonstrated that IPMCs can show a large deformation when placed in a time-varying electric field due to their inherent properties [108]. IPMCs can be seen as an electrolyte sandwiched by two layers of ionically conducting membranes with two electrodes. Typically, the ionically conducting membranes are made of Nafion and Flemion due to their fast response time and good durability [92]. Gold and platinum were generally used as electrodes for IPMCs. Recently, CNTs appeared as an attractive alternative material for metal electrodes due to their extraordinary electrical and mechanical properties (Figure 14a). However, compared to metal electrodes, CNTs have some limitations such as poor dispersibility and special requirements for electrolytes [109].

#### 2.5.1. Mechanism

The mechanism for IPMCs varies slightly depending on the different electrodes, electrolyte and conductive membranes. Briefly, under the applied electric field, cations (or anions) in IPMCs electrolyte move to the cathode (anode) [8]. This transportation of ions generates the volumetric difference, which leads to a pressure gradient in the ionic polymer followed by a swelling of one side and shrinkage of another side of the membrane [110]. In traditional IPMCs, water was commonly used as solvent. However, water has several major problems: poor electrochemical stability in high-voltage and gradual leakage and a high vapor pressure inside a membrane due to evaporation [111]. Therefore, some researchers use other solvents such as organic solvents instead of water. Ionic liquids are considered to be a good alternative for water due to their negligible vapor pressure and high conductivity. In water driven IPMCs, the cations gather under the applied electric field squeezing out the water molecules, which create strain pressure on the ionic polymer (Figure 14b) [108]. In ionic liquid driven IPMCs, the deformation is caused by the different transfer rates of

cations and anions. The anions moves slower to the anode due to electrostatic repulsion from the polymer matrix (Figure 14c) [110].

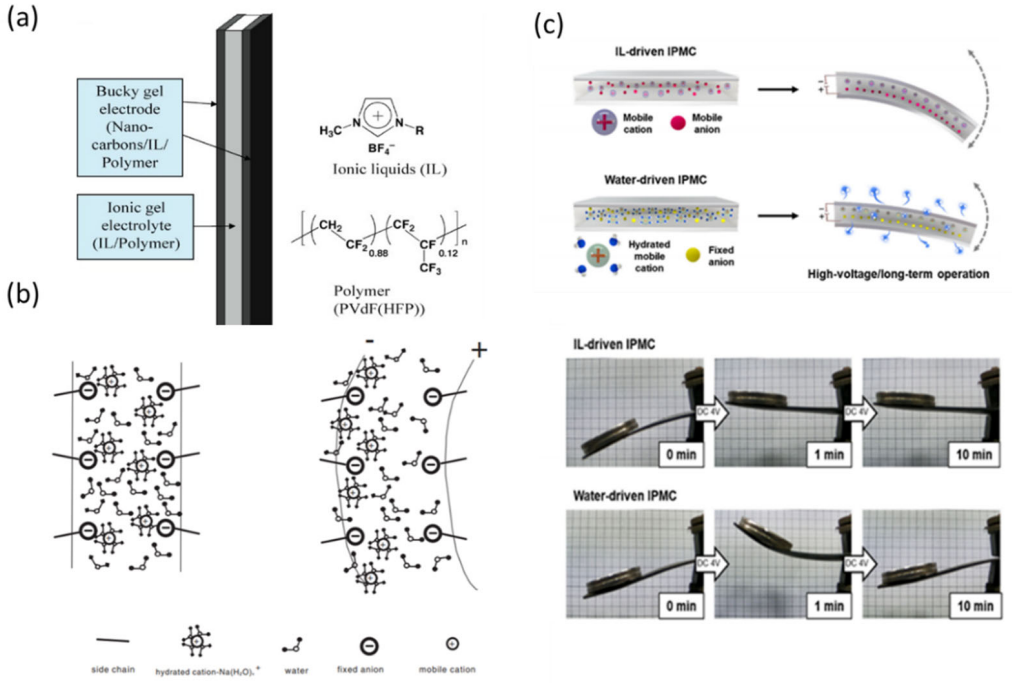


**Figure 14.** Schematic diagram of some IPMCs. (**a**) Structure of bucky-gel actuator (CNT as electrodes) [109]. Copyright 2013, Wiley-VCH. (**b**) A typical IPMCs and its actuation mechanism [108]. Copyright 2001, IOP Publishing. (**c**) Schematic illustrations of the actuation mechanism and performance differences of IPMCs driven by an IL or by water [110]. Copyright 2021, Elsevier.

Conducting polymers (CPs) are another category of EAPs which have similar mechanisms to IPMCs. CPs are typically composed of the constituent monomers of pyrrole, aniline, and thiophene and its derivatives (Figure 15) [8]. These polymers can be electrochemically oxidized and reduced repeatedly. During the redox reaction, ions can move in or out from the CPs depending on the ion (called a dopant) and the reaction [112]. Typically, there are two different reactions. When CPs contain mobile anions ($e^-$), the anions will leave the polymer during reaction and the anions ($A^-$) in electrolyte will enter CP [8].

$$(M)_n - me^- + mA^- \rightarrow (M)_n^{m+}\left(A^-\right)_m \tag{10}$$

($M$) is the monomer, $m$ is the number of electrons transferred, and $A^-$ is the anion responsible for maintaining the electroneutrality.

On the contrary, if CPs contain immobile anions ($A^-$), they will require cations for the charge neutrality inside the polymer matrix. The cations $M^+$ will move in and out of the CP during redox reaction [8].

$$(M)_n + me^- + mA^- \rightarrow (M)_n^{m+}\left(A^+\right)_m \tag{11}$$

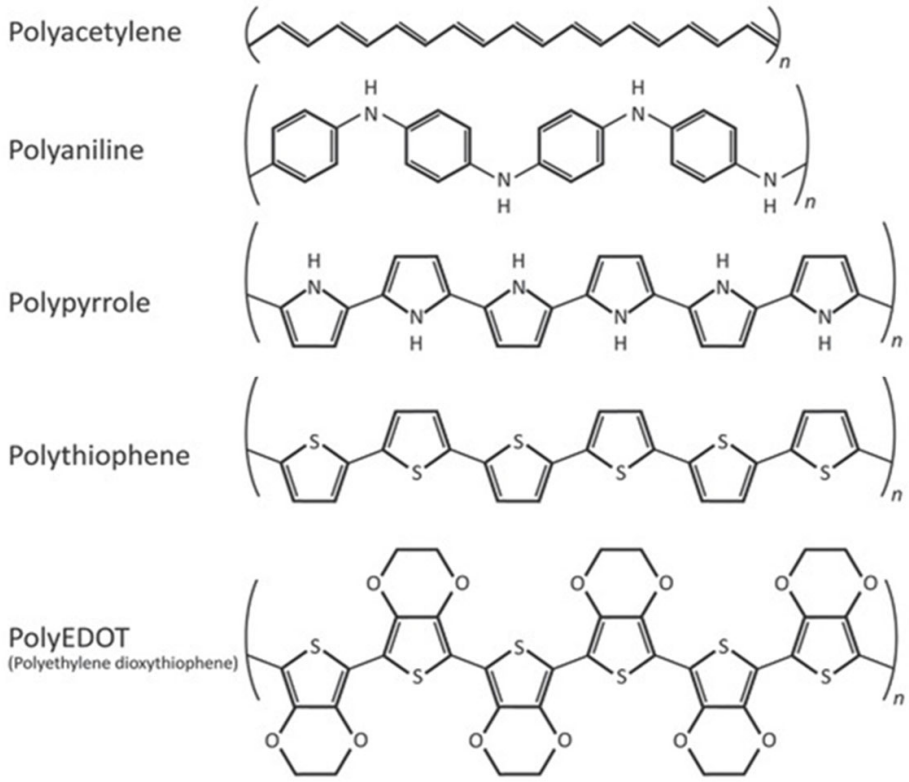


**Figure 15.** Chemical structure of some common CPs [8]. Copyright 2013, Wiley-VCH.

2.5.2. Applications

IPMCs and CPs, have been widely applied in textiles, sensors, and soft exoskeletons (Figure 16a). The electrochemical conductive polymer is combined with textile weaving technology to provide an electrochemical artificial muscle. Jager et al. reported a wearable, soft, and strain adjustable rayon fabric, which was achieved by continuously coating cellulose fibers with a PEDOT layer as a conductive electrode and a PPY layer for actuation [11]. By weaving and knitting, this actuator has an increasing output force with the increase of the number of actuator yarns. Similarly, a PEDOT:PSS coated SWCNT wired ZIF-8 structure has been reported (Figure 16b) [113]. Hydrophilization treatments enable the formation of electrode ink on the surface of the fabric and highly increase the ionic conductivity. The textile-structure actuator demonstrated large strain (0.28%) and a high blocking force (0.62 mN at 0.1 Hz). Li group demonstrated a plasticized polyvinyl chloride (PVC) gel-based exoskeleton for hip joint support. Electroresponsive hydrogels have demonstrated that they can be deformed under an electric field, similar to the mechanism of IPMCs [114]. This device can provide up to 94 N and 10% biological torque at hip joints during walking (Figure 16c). In addition to being able to undergo shape changing under an electric field, some IPMCs can generate voltage under deformation, which makes them a potential sensor (Figure 16d). An IPMCs based heart rate monitoring sensor was first explored by Chattaraj et al. [115]. The mechanical impact induced by pulsating blood flow generates a potential difference on the metal plate electrode. Data retrieved from this device exhibited error percentages of 4–15% when evaluated against standard plethysmographic measures.

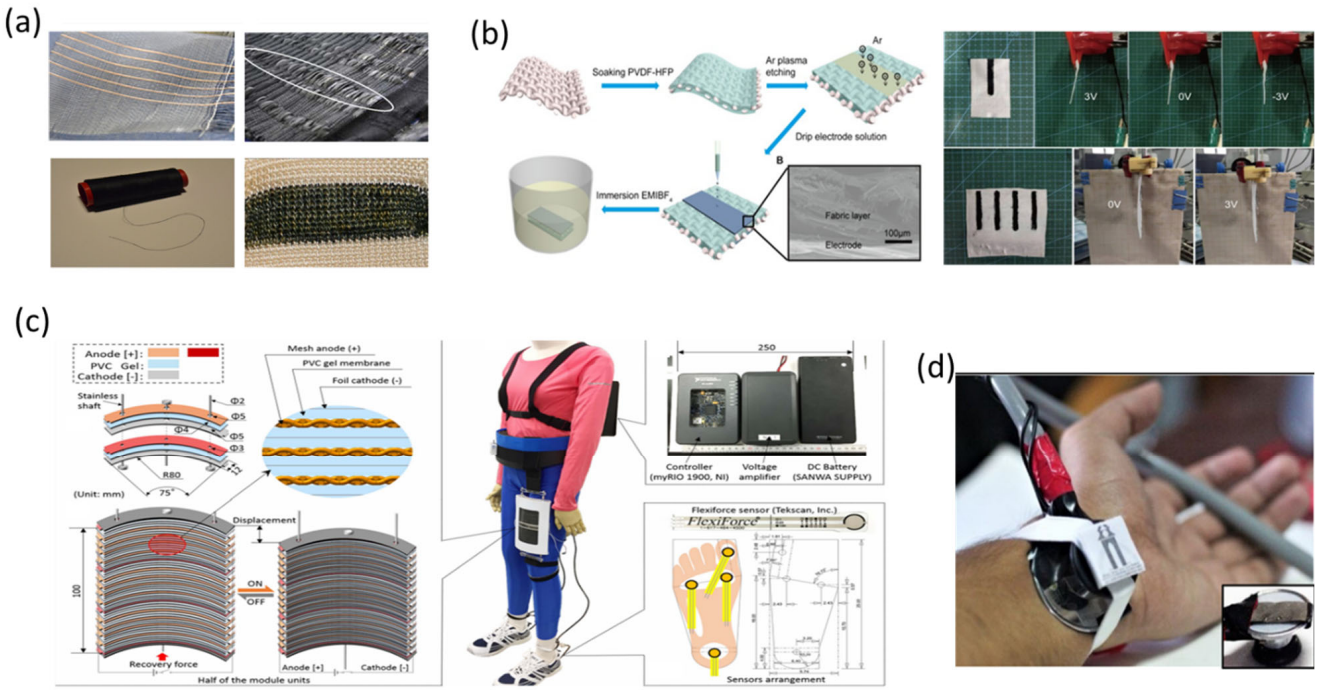


**Figure 16.** (**a**) Processing and integration of electroactive textiles [11]. Copyright 2017, the authors, published by AAAS, (**b**) textile actuator based on PEDOT:PSS/MOF-derivative electrode ink [113]. Copyright 2020, Wu, Yang, Li, Li and Chen. (**c**) PVC gel soft actuator-based assist wear [114]. Copyright 2017, IOP Publishing. (**d**) IPMCs based heart rate monitoring sensor [115]. Copyright 2018, Elsevier.

#### 2.5.3. Merits and Limitations

IPMCs are considered to be promising actuators for practical application and have been investigated since 1965 [116]. They can deform by themselves through charge transfer. IPMCs based actuators have fast response times and good repeatability. At the same time, this type of material can be designed at a millimeter-sized scale and can work in synergy with other structures such as textile structures. Large deformation under low voltage, extremely short reaction time and high stability allow them to have unique advantages. However, the main problem of IPMCs is the poor durability due to the loss of traditional electrodes in air or liquid. There are many methods for preparing IPMCs using non-metal electrodes. The effect of these new type of electrodes needs further research. In addition, when water is used as the electrolyte solvent, problems such as ionization and leakage may occur. Although IPMCs with ionic liquid as electrolyte have good stability, their response time and actuation force are decreased. As the research progresses, the performance of IPMCS is still improving. Complicated preparation processes and expensive costs are the main limitations of IPMCs. The electrolyte and polymer matrix may have certain limitations as well.

In wearable applications, CPs are more advantageous than traditional IPMCs because they eliminate the limitations of electrodes. CPs can be considered a storage element of a capacitor that can change shape during charging and discharging [8]. Therefore, reducing their thickness can improve the response time, but it will reduce the driving force [117]. Due to the existence of the degradation potential, the ion concentration of CPs is limited [118]. The single actuation mode and low accuracy are also limiting factors in the application of such materials in wearable drives.

### *2.6. Piezoelectric Actuators*

#### 2.6.1. Mechanism

Piezoelectric effect is a phenomenon in which mechanical energy and electric energy are exchanged in dielectric materials. There are two kinds of piezoelectric effect, namely positive piezoelectric effect and inverse piezoelectric effect. Positive piezoelectricity is the electric charge that accumulates in certain solid materials in response to applied mechanical stress (Figure 17a). Inverse piezoelectric effect refers to when an electric field is applied in the polarization direction of piezoelectric sensing elements; this will produce mechanical deformation or mechanical stress in a certain direction. When the applied electric field is removed, this deformation or stress will disappear (Figure 17b). The stress deformation can be divided into five basic forms: thickness deformation, length deformation, volume deformation, thickness shear deformation, and plane shear deformation.

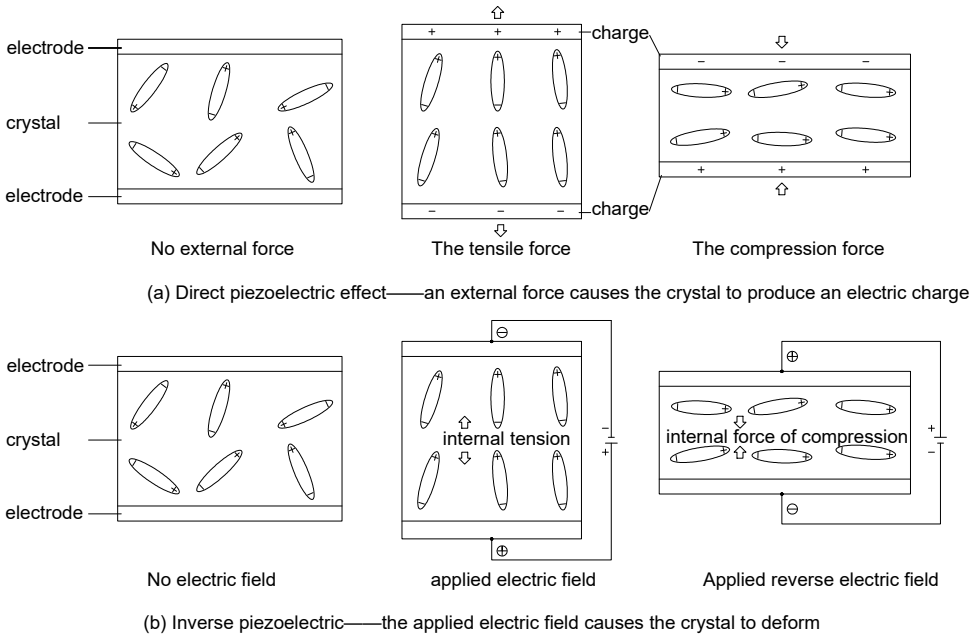


**Figure 17.** Schematic diagram of piezoelectric effect. (**a**) Direct piezoelectric effect. (**b**) Inverse piezoelectric.

For piezoelectric actuators, the inverse piezoelectric effect is the basic working principle, and the governing equation can be expressed as follows:

$$S_j = d_{ij} E_i \tag{12}$$

where $S$ is the strain, $E$ is the electric field intensity, $i$ and $j$ are the electric field and strain direction respectively, $d_{ij}$ is its piezoelectric strain constant. The basic deformation mode and its main parameters are shown in Table 5 [119].

**Table 5.** The basic deformation mode and its main parameters.

| Strain Mode of Actuators | | Piezoelectric Constant | Strain or Displacement * |
|---|---|---|---|
| Stretch-extending | Longitudinal | $d_{33}$ | $S_3 = d_{33} E_3$<br>$\triangle L_3 = d_{33} V_3$ |
| | Transverse | $d_{31}$ | $S_1 = d_{i31} E_3$<br>$\triangle L_1 = d_{31} V_3 L_1 / L_3$ |
| Bending | | $d_{31}$ | $Y = 3\left(\frac{L}{T}\right)^2 d_{31} V_3$ |

* L: Length of piezo-wafer, T: Width of piezo-wafer.

Piezoelectric materials include inorganic piezoelectric materials and organic piezoelectric materials [120]. Inorganic piezoelectric materials are divided into piezoelectric crystals and piezoelectric ceramics. Organic piezoelectric materials, also known as piezoelectric polymers, are being increasingly pursued for wearable applications because of their soft nature. Current piezoelectric actuators are based on organic piezoelectric materials, such as polyvinylidene fluoride (PVDF); it is necessary to mention that the PVDF piezoelectric film is softer compared to piezoelectric ceramics, light weight, has a large piezoelectric constant, high application sensitivity, good matching state, a compliance coefficient that is 30 times of PZT, and can be used in tactile measurement, mechanical measurement, energy collection, medical monitoring and so on. It is worth noting that the PVDF piezoelectric film requires polarization and stretching to improve the piezoelectric properties. Different tensile rate and other factors will affect its piezoelectric properties, but change in the preparation process can improve piezoelectric properties without additional polarization, such as electrostatic electricity. In the electrospinning process, the viscous solution is stretched and solidified into nanofibers in a strong electric field so that the molecular dipole of the polymer is oriented in the nanofiber length direction, and the transformation of $\alpha$ is converted into $\beta$ phase completion. However, PVDF-TRFE does not require additional polarization and stretching. The parameters of some piezoelectric materials are shown in Table 6.

**Table 6.** Piezoelectric properties of some piezoelectric materials at room temperature.

| Property | PVDF | PVDF-TRFE | PZT [8] |
|---|---|---|---|
| Piezoelectric coefficient($d_{31}$) (Pc $N^{-1}$) | 30 | 25 | 350 |
| Piezoelectric coefficient($d_{33}$) (Pc $N^{-1}$) | 20 | −25 | 750 |
| Modulus (Mpa) | 2500 | 2300 | 76,500 |
| Efficiency (%) | 75 [121] | - | 90 |
| Stress (Mpa) | 30–50 | 60 | 110 |
| Strain (%) | 30–400 | - | 0.2 |

2.6.2. Structure

The unimorph, single crystal structure is the basic structure for piezoelectric actuators. The deformation of the piezoelectric actuator depends on the basic principle of the piezoelectric inverse effect. The piezoelectric film layer is bent or elongated in alternating current; meanwhile, the passive layer is not shortened, and the stress between the two layers causes bending deformation of the piezoelectric actuator due to subsequent bending or volume mismatch. For example, Akther et al. [122] used piezoelectric single crystal actuators to amplify the haptic feedback of the vibration signal, so that humans can clearly perceive the vibration (Figure 18a,b). Wu et al. [123] combined PVDF with PET and adopted a piezoelectric single crystal structure to create a soft robot. The soft robot was bent and a leg structure was added to increase the walking speed. The soft robot has reached the rapid movement of 20 body length/s at the resonant frequency, and it can still move even if crushed one million times, demonstrating strong robustness. Maccabi et al. [124] designed three piezoelectric spiral arms using a curved piezoelectric single crystal structure which generated torsional deformation through alternating current to achieve parallel plane piston movement (Figure 18c).

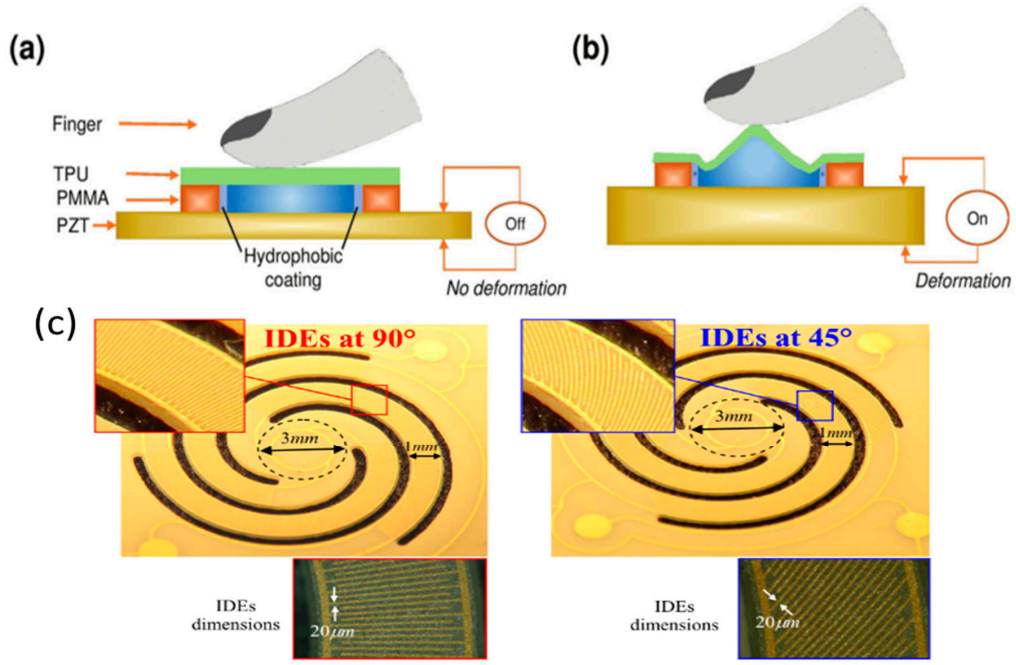


**Figure 18.** (**a**) Schematic side view of a piezoelectric actuator, which includes PZT at the bottom, glycerin/water solution in the middle, thermoplastic polyurethane (TPU) at the top and polymethyl methacrylate (PMMA) at both sides [122]. (**b**) Power on [122]. Copyright 2019, The Royal Society of Chemistry. (**c**) In the picture of the actuator, the angles between the interdigitated electrodes (IDEs) and the spiral arm are 90° and 45° respectively, and the spiral arm is made of PZT [124]. Copyright 2016, Elsevier.

The piezoelectric bimorph three-layer structure, has piezoelectric materials on the top and bottom layers. This structure has different mechanisms compared to the unimorph structure. The two piezoelectric film layers are bent in alternating current. One of the piezoelectric sheets is elongated, and the other is shortened, and their bending strain is enlarged. The advantage of this structure is that it doubles the displacement of the soft robot and achieves more excellent moving characteristics. Piezoelectric ceramics are widely used in this structure. For example, Xu et al. [125] developed a piezoelectric actuator that can rotate rapidly. When using a piezoelectric bimorph structure, driven by piezoelectric vibration, the maximum rotation speed is as high as 118.3 r/min. Kwon et al. [126] developed a mobile phone vibration driver by using bimorph piezoelectric ceramics. This structure can also be applied in other materials; for example, Park et al. [127] used the upper and lower layers of PVDF piezoelectric film and magnetic tape as the main body and the PVDF piezoelectric film and magnetic tape as the legs to make the soft robot. Under the 160 Hz resonance frequency, the robot applied ±65 V AC voltage and achieved a good mobility performance of 35.3 mm/s.

In addition, according to the direction of vibration, the piezoelectric actuator can be divided into a longitudinal structure [128], a longitudinal bending structure [129], a longitudinal torsion [130], and a curved bending structure [128]. The length affects the modal frequency of the longitudinal structure, and length and cross-sectional dimensions structure affect the modal frequency of the bending and torsional structure [131].

### 2.6.3. Applications

Piezoelectric sensors have many applications in the medical field to detect human health, and much wearable research has also demonstrated great potential for them in biomechanical energy collection. Moreover, piezoelectric actuators can be applied in various fields, such as miniature pumps and piezoelectric motors, etc. This section mainly introduces the application of piezoelectric drivers in wearable applications. Wearable

devices based on piezoelectric actuators are light in weight, especially organic piezoelectric materials, which can be made very thin and move unconstrained. Theoretically, there are many applications for piezoelectric actuators in wearable applications. First, piezoelectric actuators can be directly applied to the skin to recognize fonts or objects and their colors through vibrational tactile feedback. For example, Sauvet et al. [132] study a wearable actuator that can make the skin feel. Through experiments they verified that people can correctly perceive the location and strong level of vibration when piezoelectric actuators achieve vibration response with the index finger and palm soft contact. This further improves the user interaction with the product, while providing inspiration for identifying fonts, color and so on (Figure 19a). Additionally, Zhu et al. [133] developed a tactile feedback smart glove. Its accuracy of the target recognition can reach 96%, in which the piezoelectric unit is applied to PZT, the main function is to use the reverse piezoelectric effect to vibrate and stimulate the touch. They can achieve a different interaction result by adjusting power at a resonant frequency (Figure 19b). Piezoelectric actuators also have applications in medicine. For example, in the study of Dagdeviren et al. [134], PZT piezoelectric plates, where the actuator is the larger part and the sensor is the smaller part, were installed on the human skin surface. The combination of the driver and the sensor was used to accurately measure the elastic modulus of the skin and predict the pathophysiological conditions.

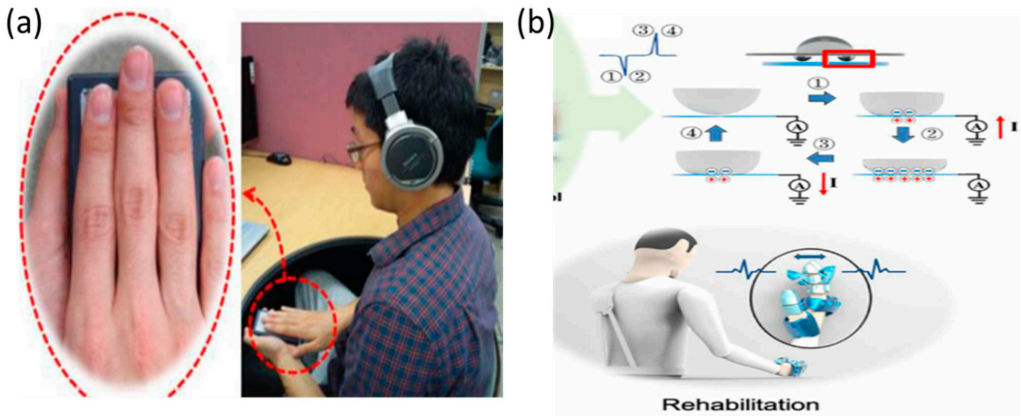


**Figure 19.** (**a**) The experimenter touched the piezoelectric actuator and felt the vibration [132]. Copyright 2017, Elsevier. (**b**) Wearable gloves vibrate to irritate finger skin [133]. Copyright 2020, the authors, published by AAAS.

#### 2.6.4. Merits and Limitations

Advantages of the piezoelectric actuator include a simple manufacturing method, and for organic piezoelectric polymer with the flexible combination of organic ground substance, advantages include good flexibility, light quality, good sensitivity, small size, and low power consumption. Additionally, compared with the traditional rigid or general shape memory alloy's heat, humidity, pH value, and chemical stimulation, the piezoelectric actuator has the advantage for quick response. Theoretically, this kind of soft robot has infinite degrees of freedom. It can be in smooth contact with the skin, integrate sensors and actuators, and can make small self-driven devices by using piezoelectric power generation. Its limitations are mainly manifested in the small amplitude of motion in the wearable, the required voltage is large, and the combination of textile problems.

### *2.7. Electromagnetic Actuators*

#### 2.7.1. Mechanism

Recently, electromagnetic actuators have been widely used in robots and wearable tactile feedback devices. Electromagnetic actuators are mainly composed of energized coils and magnetic materials, and the interaction force generated between them is used as the power source. The basic mechanism of action is mainly divided into two situations.

The first situation is that it is affected by magnetic force or magnetic moment, causing deformation/displacement of the magnetic object, which is expressed as follows [135]:

$$f_m = \int_{Vm} (M \cdot \Delta) dV_m \tag{13}$$

$$\tau_m = \int_{Vm} (M \times B) dV_m \tag{14}$$

where $f_m$ is the magnetic force experienced by a magnetic field, $\tau_m$ is the magnetic moment experienced by an external magnetic field, $M$ is the magnetization of the external magnetic field, $\Delta$ is the gradient of the gradient magnetic field, $V$ is the volume of the magnetic shield, and B is the magnetic flux density of the external magnetic field.

The second is that the electrified conductor is deformed by Lorentz force in the external magnetic field, which is expressed as follows [136]:

$$F = I \int dl \times B \tag{15}$$

where $F$ is the Lorentz force, $I$ is the current through the wire, $l$ is the length of wire, and $B$ is the magnetic flux density of the external magnetic field.

At present, the driving magnetic field of many electromagnetic actuators is generated by the energized coil, and the magnetic flux density generated by them conforms to the Biot–Saffar law, which is expressed as follows [137]:

$$\vec{B} = \int_L \frac{\mu_0 I}{4\pi} \frac{dl \times \vec{e_r}}{r^2} \tag{16}$$

where $I$ is the current through the wire and does not change with time, $dl$ is an infinitesimal segment of the wire, $e_r$ is the unit vector of the current element pointing to the field point to be solved, $\mu_0$ is the permeability of vacuum.

#### 2.7.2. Structure

Electromagnetic actuators used in wearable tactile devices are usually composed of coils, magnets, vibration generating parts, and flexible materials. The changing magnetic field generated by the coils drives the magnets to move. The movement of the magnets and the vibration generating parts will cause the surface of the human skin to be generated. The tactile and vibration generating part is usually a rigid shell, and the flexible material is usually wrapped around the outside of the device to fit the skin. For instance, the wearable electromagnetic actuator researched by Pece et al. uses [138] this type of structure. The common magnetic materials that have been reported in the literatures and include nickel-plated neodymium and NdFeB magnet and the Flexible materials include PMMA, parylene, polyimide and PDMS elastomer [139].

The electromagnetic actuator can not only move in a straight line, but also complete the bending effect. It can be used as a soft gripper. For instance, Do et al. [140] demonstrated a flexible electromagnetic actuator. The magnet is mounted on the flexible beam and driven by the magnetic field generated by soft 3D coil to achieve bending deformation (Figure 20a).

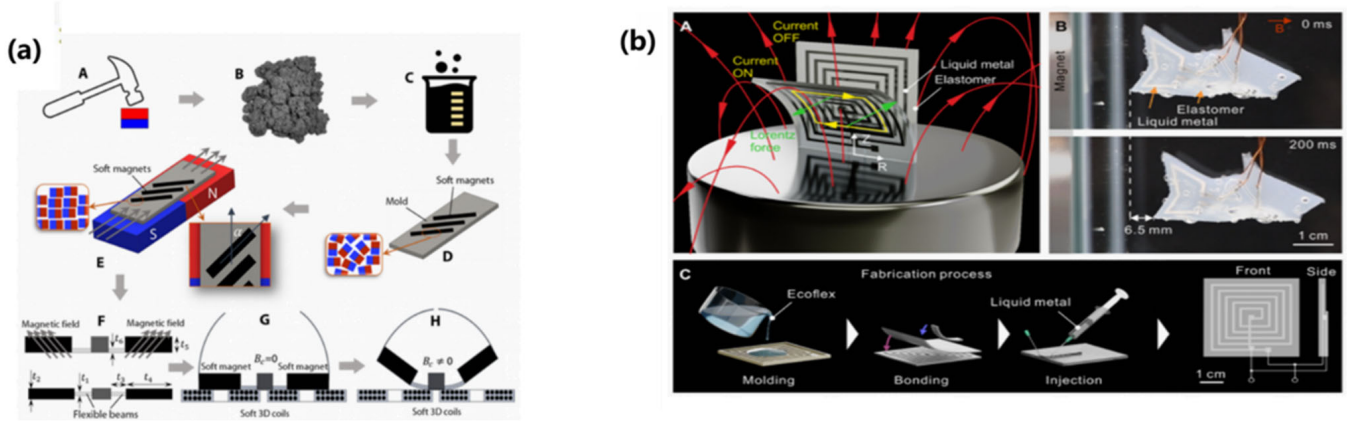


**Figure 20.** Structure of electromagnetic actuators. (**a**) Electromagnetic actuator with bending motion [140]. Copyright 2018, Wiley-VCH. (**b**) Electromagnetic actuator composed of liquid metal coil (69%gallium, 22%Indium, 9%tin) and silicon elastomer [136]. Copyright 2020, the authors, published by AAAS.

Recently, many scholars have studied a new structure of electromagnetic actuator that uses liquid metal instead of traditional copper as the coil for the electromagnetic actuator and is integrated into flexible materials. When the flexible coil is energized, it is driven by Lorentz force. This kind of structure has more degrees of freedom than traditional structures. For instance, Mao et al. [136] embedded liquid metals (69% gallium, 22% indium, 9% tin) into silicon elastomers to replace traditional metal coils as an actuator. The soft actuator is placed on the flat magnet, and the Lorentz force generated by different types of voltage signals makes the actuator move in different ways. They use actuators as fins, agitators, etc. to demonstrate their greater deformability (Figure 20b). Likewise, liquid metal coils made of Ga-In alloys are also used in soft electromagnetic actuators. The actuator that was composed of a liquid metal coil, and PDMS could reach a maximum displacement amplitude of 21.5 mm [141].

#### 2.7.3. Applications

Among wearable devices, electromagnetic actuators are an area that has not yet been completely developed. Due to their advantages of low driving voltage and large deformation, it is one of the important directions for the future development of wearable tactile devices. Ozioko et al. demonstrated [142] a dual-function wearable tactile device that can collect tactile information and provide tactile vibration feedback. The tactile feedback component was realized by an electromagnetic actuator composed of flexible coils and permanent magnets assembled in PDMS. The tactile collection component was realized by the tablet capacitor; these components were integrated. The information was transmitted between deaf-blind and sighted and hearing individuals via a mobile app through different touch and vibration modes, similar to Morse code (Figure 21a). In their later work, they made gloves for communication between the blind [143]. In each pair of gloves, six tactile devices were placed on the index finger, middle finger and ring finger of each glove, representing six points in Braille. The tactile feedback information generated by tactile device and the collected touch information were processed by the microcontroller integrated on the glove and transmitted wirelessly through the Bluetooth module (Figure 21b).

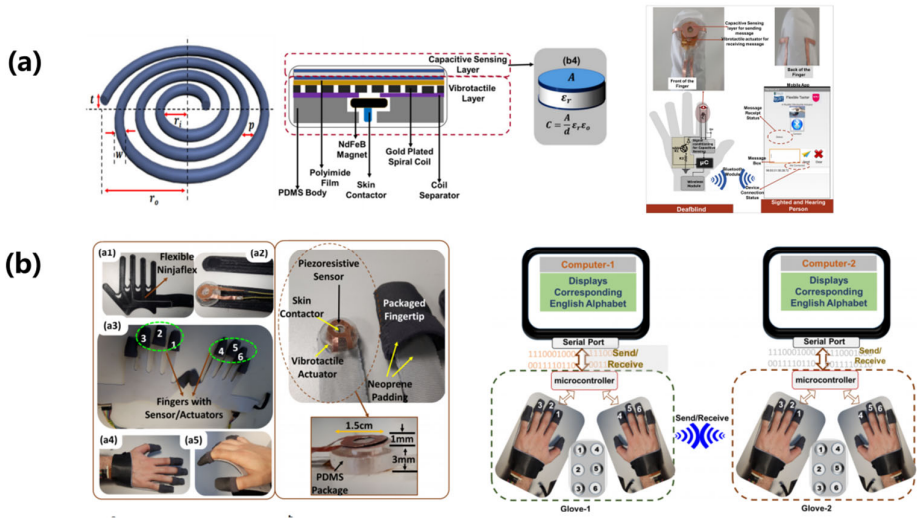


**Figure 21.** Application of electromagnetic actuators in wearable devices. (**a**) Working principle of dual-function wearable tactile device [142] copyright 2020 by the authors. Licensee MDPI, Basel, Switzerland. (**b**) Structure and application of tactile feedback glove [143]. Reproduced under the terms of the CC-BY Creative Commons Attribution 4.0 International License (https://creativecommons.org/licenses/by/4.0/), Copyright 2020, published by IEEE.

Likewise, Rogers et al. integrated 32 electromagnetic actuators with a wireless power supply as wearable devices for tactile feedback. The primary coil obtained power from the outside to supply power to the coil, so as to drive the magnet to vibrate. The force acting on the skin of the actuator with the input power of 1.75 mW was 135 mN, and the NFC antenna received control information from the outside. Each actuator can be controlled individually. This device can be applied in games, helping the disabled, and in other fields [133,144].

#### 2.7.4. Merits and Limitations

Generally speaking, the electromagnetic actuator has the advantages of low driving voltage (typically from 0 to 30 V) [140], fast response speed (millisecond) [144] and large displacement, but it is difficult to be completely flexible. Furthermore, most electromagnetic actuators must be driven by wires or in an external driving magnetic field, which cannot achieve remote wireless control.

### *2.8. Liquid Crystal Elastomer*

#### 2.8.1. Mechanism

Liquid crystal polymers are materials that exhibit liquid crystallinity and can be divided into liquid crystal elastomers (LCEs) and liquid crystal polymer networks (LCNs) [145]. Compared to LCNs, LCEs consist of loosely crosslinked liquid-crystal side-chain and/or main-chain mesogenic units with a low crosslink density, which cause greater deformability and flexibility [146]. LCEs can undergo reversible transitions between polydomain, monodomain, and isotropic phases (Figure 22). These different phases depend on the orientation of mesogens, which normally refers to the aromatic groups [147]. Phase transition from polydomain to monodomain can be achieved through mechanical deformation while the phase transition from monodomain or polydomain to isotropic can be achieved through heating up the temperature above isotropic clearing temperature ($T_i$) [148]. They have large (~40%) and reversible actuation, high processability, and programmability, making LCEs a desired material for soft actuators.

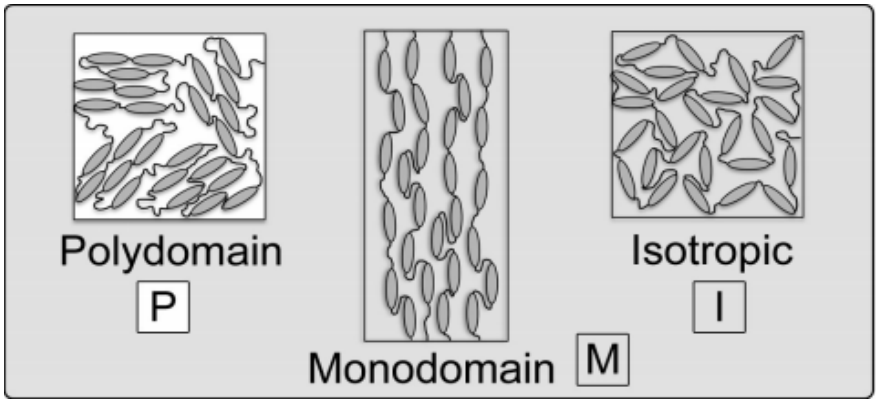


**Figure 22.** Schematic of different phases of LCE.

2.8.2. Structure

LCEs based on a two-stage thiol–acrylate Michael addition and photopolymerization (TAMAP) reaction were reported by Yakacki et al. [149]. Two step reactions allow for pre-stretch before full crosslinking of polymer networks, which enable up to 100% strain for actuation. Cai et al. reported an LCE artificial muscle film using the two step reaction. By embedding heating wires, this artificial film can lift a load of 3.92 N (the stress was 0.312 MPa) by 38% of its initial length under electrical control [148]. An electrically actuated soft artificial muscle made by flexible electrothermal film and liquid crystal elastomer was reported by Liu et al. [150]. The LCE was assembled with MWCNT/AgNW composite to achieve fast responsive uniform temperature deformation and constant resistance. At 6.5 V, a saturation temperature of 189 °C can be reached with a heating rate of 21 °C/s, leading to a work density of 9.97 kJ/m3 and an actuating stress of 0.46 MPa.

Beside direct heating and electrical heating, photothermal actuation is another common method to trigger the deformation of LCE. To achieve photothermal control, conventional energy converters such as gold nanoparticles, carbon nanotubes and liquid metals have been reported to apply in the LCE matrix. An AuNR/LCE film reported by Yang et al. obtained a 100° bending angle under laser (800 nm, ≈1.0 W/cm$^2$) (Figure 23a) [151]. Yang et al. demonstrated a heat/UV/near-infrared (NIR) triple-stimuli-responsive LCE material using a two-step cross-linking process coupled with a uniaxial stretching technique [152]. Carbon nanotubes (CNTs) enable the conversion of near-infrared light to thermal energy while the azobenzene group A44 V6 can trigger the deformation under UV light (Figure 23b). Ware et al. exhibited a 4D-printed LM-LCEs which can absorb NIR (730 nm) (Figure 23c) [153]. By the dispersion of Eutectic gallium−indium (EGaIn) in LCE, the composite is 4D-printable to different patterns, achieving up to 150° bending angle under 800 mw/cm$^2$ NIR light within 40 s.

Photoisomerization is another mechanism for photoexcited actuators. Polymers with azobenzene, diarylethene and spiropyrans functional group can undergo cis–trans photoisomerization transitions triggered by radiation with high energy photons [154]. This microscopic chemical structure change can cause macroscopic deformation to a certain extent. This method normally accompanies other polymer networks to induce photoexcited actuation and improve deformability. Priimagi et al. designed a self-regulating iris based on light-actuated liquid crystal elastomer (Figure 23d) [155]. It can automatically adjust the shape by reacting to the power density of the incident light. When the light intensity increases, the device will close, and when the minimum pupil size is reached, the light transmittance is reduced to one seventh.

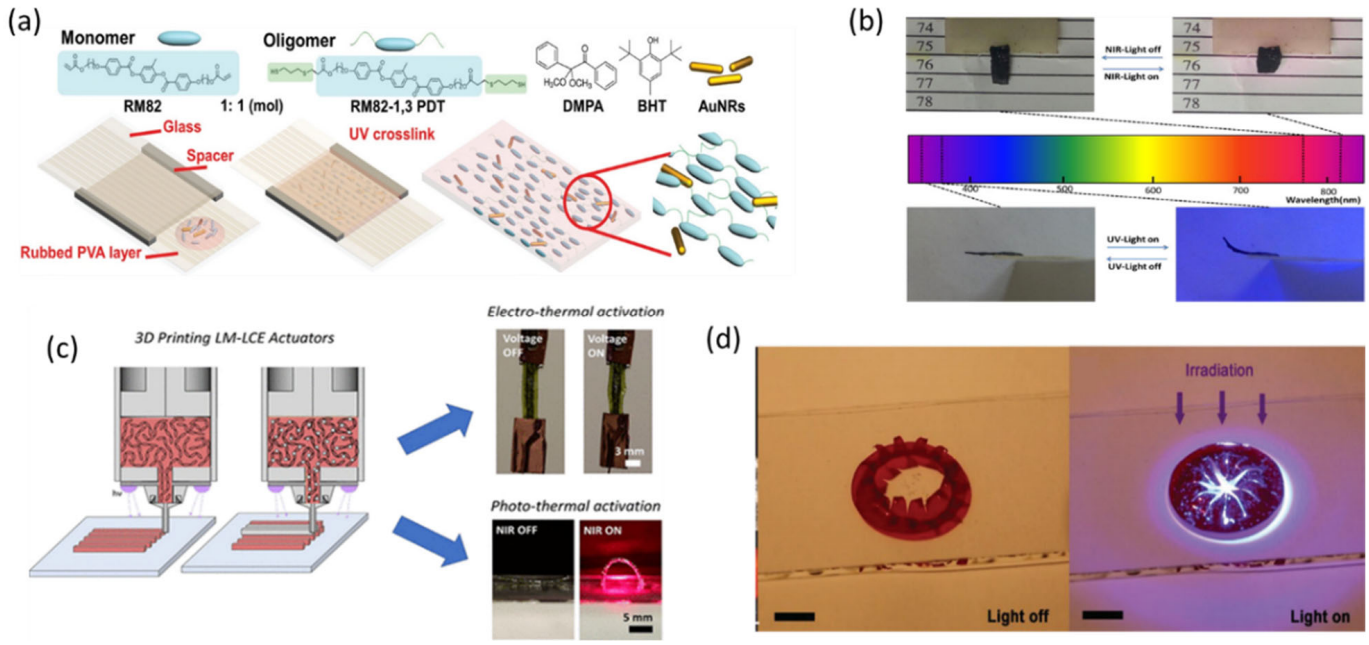


**Figure 23.** Modification of LCEs for multi-actuation modes. (**a**) Illustration of the fabrication process of AuNR/LCE films [151]. Copyright 2018, Wiley-VCH. (**b**) NIR/UV actuated CNT/Azobenzene/LCEs [152]. Copyright 2016, American Chemical Society. (**c**) 4D-Printable Liquid Metal–Liquid Crystal Elastomer Composites [153]. Copyright 2016, American Chemical Society. (**d**) Light-actuated LCE [155]. Copyright 2017, Wiley-VCH.

#### 2.8.3. Applications

The main applications of LCE in wearable actuators are artificial muscles, smart textiles and exoskeletons. Qi et al. demonstrate a loom woven smart textile using LCE fibers [156]. LCE undergoes shrinkage during heating process, which creates pores in the textile. This shrinkage starts at 40 °C and reaches the maximum at 80 °C. After cooling, the LCE fiber expands and the textile returns to its original shape (Figure 24a). These results indicate that LCE can use loom weaving to create a stimulus responsive, two-way shape memory textile. Inspired by vascular artificial muscle, Cai et al. designed a vascular LCE-based artificial muscle (VLAM) which showed a potential application for LCE to be used as exoskeletons (Figure 24b) [157]. With the injection of hot and cold water in its internal fluidic channel, VLAM achieved fast thermal actuation and recovery, and can be applied in a wide range of external temperatures. In Figure 24b, VLAM demonstrated different actuation modes of motion of a skeleton model.

#### 2.8.4. Merits and Limitations

LCE has outstanding advantages such as large deformation, softness, multi-function, multiple response modes, durability, etc. However, the limitation of LCE as a wearable actuator material lies in its inherent properties. Phase changing from isotropic to smectic can only be induced by heating, which restricts its application. Although a variety of actuation modes have been achieved through the modification of LCE, they are realized through the form of energy conversion. In addition, the excessively high driving temperature of LCE (>100 °C) hinders its application on the human body. Some research has shown that the LCE molecular structure can be modified to reduce its driving temperature [158,159]. However, it will weaken the performance. Aside from these, slow response speed is a major problem. However, its excellent deformability, structure stability and processability endow its significant advantages as actuator. The application of LCE as a wearable actuator still needs further research.

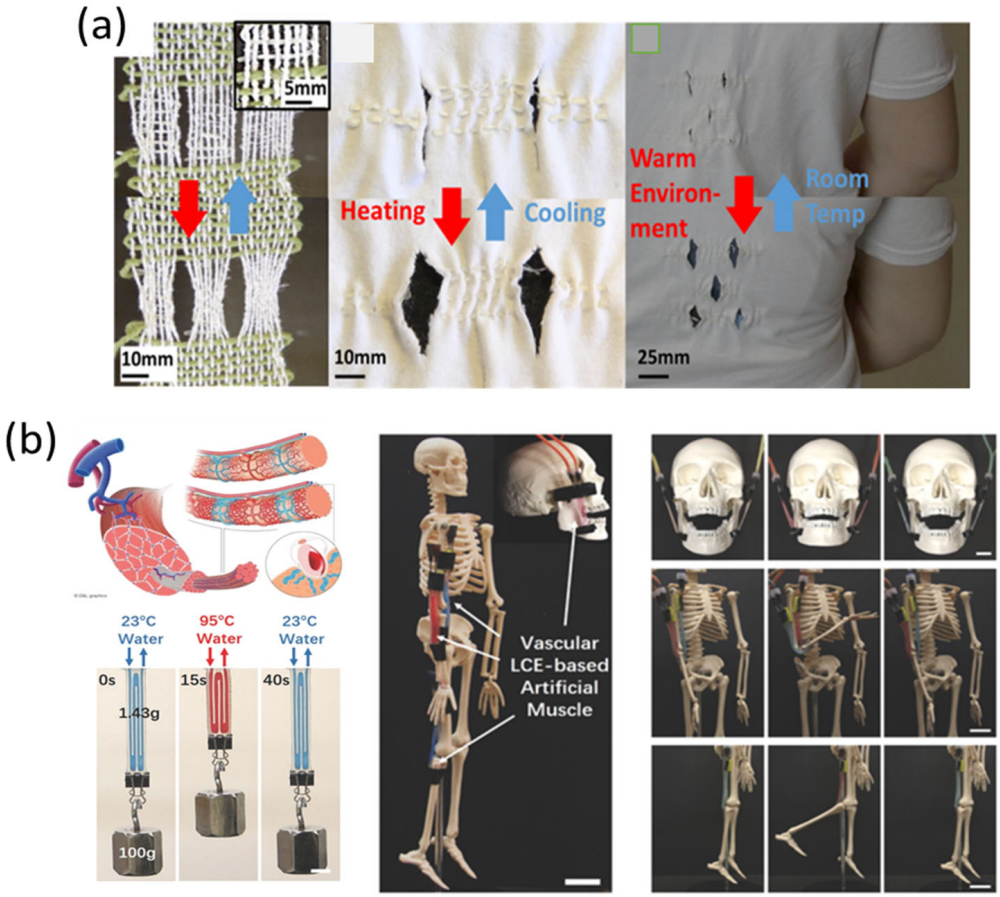


**Figure 24.** Wearable LCE actuators. (**a**) LCE based thermal management textile [156]. Copyright 2019, American Chemical Society. (**b**) A vascular LCE-based artificial muscle (VLAM) [157]. Copyright 2018, Wiley-VCH.

### *2.9. Other Actuators*

#### 2.9.1. Electric Motor

Besides pneumatic and hydraulic actuators, electric-driven actuators are also widely applied in exoskeletons. Compared to pneumatic or hydraulic actuators, electric actuator systems inevitably come with many problems, such as: friction, stiffness, electrical disturbance and complex systems [13]. Nevertheless, electric actuators are still the most common actuators in the industry due to their irreplaceable processability and designability. Gassert et al. present a wearable glove system for grasping assistance [160]. Due to a compliant finger mechanism and versatile thumb mechanism, this system can provide assistance for the most commonly used grabbing exercises. An exoskeleton that can assist walking and running separately was first reported by Kim et al. [161]. Through the electrical motors connected to the cable, this device applies tension between the waist belt and the thigh wrap, creating an external extension moment around the hip joint. Based on the estimation of potential energy fluctuation of the wearer's center of mass, this device can switch the actuation modes between running or walking.

#### 2.9.2. Carbon Nanotubes

Carbon nanotubes (CNTs) have attracted great interest in recent research due to their distinguished mechanical, electrical and chemical properties [162]. With the advancement of process methods, carbon nanotube-based sensors, electrodes, actuators and energy storage materials have been widely used in smart systems. In particular, CNTs-based yarns with twist, or introducing a yarn structure in CNTs, can further enhance its flexibility, allowing it to be used in actuators such as artificial muscles [163]. By far, researchers

find that CNTs can be actuated by electrical, chemical, thermal, or photonic power [164]. Among them, electrochemical actuation of CNTs received special attention [165]. Compared to electrothermally driven CNT yarns, electrochemical driven CNT yarns provide higher efficiencies and larger torsional or tensile actuation with lower voltage requirements [166]. Similar to CPs, the mechanism of electrochemical actuation is the strain and volume change on the graphene layers induced by electrochemical double-layer charge injection (Figure 25a) [162]. Foroughi et al. have first demonstrated a torsional and rotational CNT yarn which can provide a reversible 15,000° rotation and 590 revolutions per minute. [167]. This kind of CNT yarn, which was twist-spun from forests of multi-walled carbon nanotubes (MWCNTs), can undergo partial untwisting in the electrolyte applied with an electric field to achieve actuation. Kim et al. have designed a hierarchically twisted electrochemical driven CNT yarn with a maximum tensile stroke of 15.1% and work capacity of 3.78 kJ/kg. [168]. This twisted and coil structure achieves the transformation of electrochemical driven CNT yarn from rotation actuation to stretching actuation (Figure 25b).

CNTs yarn can be considered as CPs and applied into textile structures. For example, they can be fabricated with other yarns or applied in smart textile systems. However, due to their poor stretchability, high cost and low energy conversion efficiency, CNTs based wearable actuators need further research. For more detail about CNTs actuators, we refer to a review by Jang et al. [163].

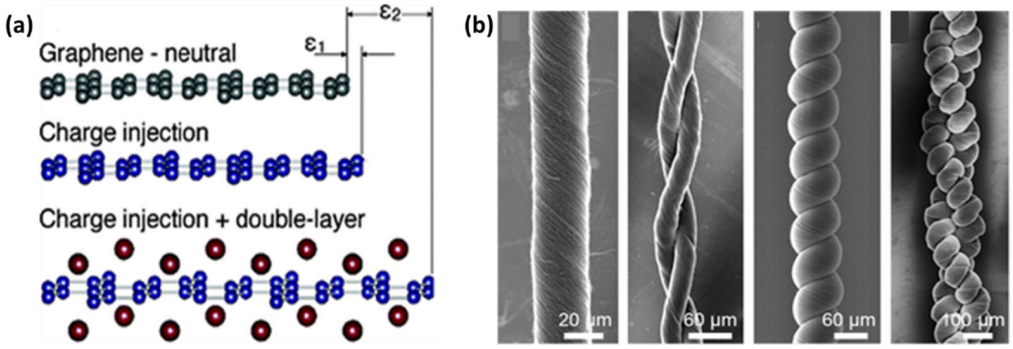


**Figure 25.** (**a**) Schematic of the mechanism for electrochemical actuation of CNT [162]. Copyright 2015, Elsevier. (**b**) MWNT yarn structures for torsional and tensile actuation [166]. Copyright 2014, American Chemical Society.

### 2.9.3. Hydrogels

Stimuli-responsive gels refer to a category of hydrogels that can respond to external stimuli. These stimuli include temperature, electric field, light and PH change. The mechanism of actuation of hydrogels is similar to the material mentioned in Section 2. These materials are widely used in biomedical applications and wearable actuators. The exoskeleton made by PVC gel in Section 2 is one example of hydrogels as wearable devices. The chemical stability and durability are the limitation for them to be applied in wearable actuators. For more information we refer to a review by Mirvakili et al. [8].

### 2.9.4. Organic Molecule-Driven Polymeric Actuators

Organic molecule-driven polymeric actuators can be defined as actuators that can have mechanical motions induced by organic solvents. This driving principle is usually the volume change or molecular structure change caused by the absorption and release of the organic solution. For example, LCEs can generate inhomogeneous swelling when absorbing polar organic solvents. Such materials can also be twisted into artificial muscles. However, the actuation mechanism and complex synthesis process are the major problems. For detailed information, we refer to a review of Lin et al. [169].

## 3. Outlook

Recent applications of wearable actuators are mainly concentrated in three categories: wearable robots, haptic devices, and personal thermal regulation textiles. Current orthosis robots are dominated by electric motors [18], which are high-output, stable, multifunctional, but also bulky, stiff, and inconvenient. In the future, these rigid electric motors will be gradually replaced by high-performance soft and smart materials, although they have a long way to go. For pneumatic and hydraulic actuators, research on the structure and functional design enables this type of actuator to achieve complex motions with simple strategies. Further, the efficiency of these actuators has been improved through the integration of motors, pumps and valves [170]. Recently, the combination of pneumatic and hydraulic actuators and textiles allows us to see new possibilities [22] which make the pneumatic/hydraulic wearable robots not limited to medical treatment and rehabilitation. With the emerging material science and technology, new smart materials enable the possibility of wearable robots, getting rid of bulky, rigid, and heavy equipment. Thermally driven materials such as shape memory alloys have problems such as high thermal hysteresis, high temperature, and high cost [29]. The actuation force of IPMCs, CNTs and CPs is too small, and it is difficult to make large-scale devices [18]. Among these new materials, DEAs are the most promising, due to fast response speed, high electromechanical performances, and high efficiency [18]. The research direction of reducing the operating voltage, improving the stability, and structure design of DEAs will be the mainstream. Wearable orthosis robots require high output force and precise control, especially for lower limb rehabilitation, which needs to be addressed in the future. Moreover, ideal combination of textile structure and smart materials for wearable robots is still a major challenge and we look forward to seeing more wearable assistive robots based on textile structures in the future.

Virtual and augmented reality (VR/AR) technology is a system that generates perceptual information through a computer and interacts with the real or virtual world. As the VR/AR technology evolves, the market demands matching or even better performance equipment. Haptic technology is an indispensable part of the VR/AR system. Wearable haptic devices mainly include three different methods: skin-attachable haptic interfaces, wearable haptic interfaces, and touch-based haptic interfaces [171]. Traditional haptic feedback is usually achieved by using the vibration motor such as the eccentric rotating mass (ERM) and linear resonant actuator (LRA) [171]. These actuators have the problems of poor portability and low resolution. Fine tactile feedback can be achieved through fine texture and tiny shapes, which makes soft actuators a potential alternative [171]. Soft actuators such as dielectric, electromagnetic, and piezoelectric actuators have been widely applied in this field. Future research is likely to take the advantage of soft materials to achieve multi-point stimulations and multi-shape generation [171]. Moreover, reducing the driving voltage and increasing the reliability of materials are also main research directions. Integration of haptic actuators and textiles into smart textiles to replace traditional tactile feedback devices is another potential for breakthrough of haptic technologies.

Thermal regulation textiles, as the first generation of smart textile, have been used in commerce and the market for decades [1]. These textiles are typically made of materials (nylon, wool, silk etc.) that can undergo expansion by moisture or heat. Through structural design such as twisting or chemical modification, these materials can passively respond to environmental stimuli. Future research may lie on the improvement of material performance and the design of the active regulation system.

Due to the advantages of programmability and comfort, textiles are very likely to be the main implementation method for wearable actuators. The new soft material has good compatibility with the textile structure. CNTs, shape memory alloys, and LCEs can be directly used as yarns for textile design. As an indispensable element of human life, textiles can also serve as a carrier of actuators. How to achieve actuation without affecting the original function of the textile is a problem that needs to be overcome.

## 4. Conclusions

In this review, we summarized the materials and structures that can be applied to wearable actuators including pneumatic and hydraulic actuators, shape memory alloys and polymers, thermal and hygroscopic materials, dielectric elastomers, ionic and conducting polymers, piezoelectric actuators, electromagnetic actuators, liquid crystal elastomers, etc. We have cited examples of wearable applications recently reported. These actuator applications are mainly concentrated in orthosis robots, haptic actuators, and smart textiles. There is no doubt that the application prospects of smart wearable actuators are wide, and the research of new soft actuator materials and structures is still in progress. The prospective future research directions for wearable actuators include: (1) smart materials with high performance, precise control, durable, and low cost; (2) integration of smart materials into textile structures to achieve required functions; (3) exploration of more applications for wearable actuators. We expect to see the application of wearable actuators that are comparable to biological structures in all aspects in the future.

**Author Contributions:** Writing—original draft preparation, visualization, analysis, Y.C.; writing—original draft preparation, visualization, analysis, Y.Y.; writing—original draft preparation, visualization, analysis, M.L.; writing—original draft preparation, visualization, analysis, E.C.; writing—original draft preparation, visualization, analysis, Y.Y.; review and editing, W.M.; review and editing, R.F.; conceptualization, supervision, writing—original draft preparation, review and editing, R.Y. All authors have read and agreed to the published version of the manuscript.

**Funding:** This work was supported by the start-up at North Carolina State University.

**Institutional Review Board Statement:** Not applicable.

**Informed Consent Statement:** Not applicable.

**Data Availability Statement:** The data presented in this study are available within the manuscript.

**Conflicts of Interest:** The authors declare no conflict of interest.

## References

1. Persson, N.K.; Martinez, J.G.; Zhong, Y.; Maziz, A.; Jager, E.W.H. Actuating Textiles: Next Generation of Smart Textiles. *Adv. Mater. Technol.* **2018**, *3*, 1700397. [CrossRef]
2. Xiong, J.; Chen, J.; Lee, P.S. Functional Fibers and Fabrics for Soft Robotics, Wearables, and Human-Robot Interface. *Adv. Mater.* **2021**, *33*, 2002640. [CrossRef]
3. Fritz, H.; Patzer, D.; Galen, S.S. Robotic exoskeletons for reengaging in everyday activities: Promises, pitfalls, and opportunities. *Disabil. Rehabil.* **2019**, *41*, 560–563. [CrossRef]
4. Mun, S.; Yun, S.; Nam, S.; Park, S.K.; Park, S.; Park, B.J.; Lim, J.M.; Kyung, K.U. Electro-Active Polymer Based Soft Tactile Interface for Wearable Devices. *IEEE Trans. Haptics* **2018**, *11*, 15–21. [CrossRef]
5. Hu, J.; Meng, H.; Li, G.; Ibekwe, S.I. A review of stimuli-responsive polymers for smart textile applications. *Smart Mater. Struct.* **2012**, *21*, 053001. [CrossRef]
6. Suman, T. Shape Memory Polymers for Smart Textile Applications. In *Textiles for Advanced Applications*; Kumar, B., Thakur, S., Eds.; IntechOpen: London, UK, 2017. [CrossRef]
7. O'Halloran, A.; O'Malley, F.; McHugh, P. A review on dielectric elastomer actuators, technology, applications, and challenges. *J. Appl. Phys.* **2008**, *104*, 9. [CrossRef]
8. Mirvakili, S.M.; Hunter, I.W. Artificial Muscles: Mechanisms, Applications, and Challenges. *Adv. Mater.* **2018**, *30*, 1704407. [CrossRef] [PubMed]
9. Madden, J.D.W.; Vandesteeg, N.A.; Anquetil, P.A.; Madden, P.G.A.; Takshi, A.; Pytel, R.Z.; Lafontaine, S.R.; Wieringa, P.A.; Hunter, I.W. Artificial muscle technology: Physical principles and naval prospects. *IEEE J. Ocean. Eng.* **2004**, *29*, 706–728. [CrossRef]
10. Rus, D.; Tolley, M.T. Design, fabrication and control of soft robots. *Nature* **2015**, *521*, 467–475. [CrossRef]
11. Maziz, A.; Concas, A.; Khaldi, A.; Stalhand, J.; Persson, N.K.; Jager, E.W.H. Knitting and weaving artificial muscles. *Sci. Adv.* **2017**, *3*, e1600327. [CrossRef]
12. De Volder, M.; Reynaerts, D. Pneumatic and hydraulic microactuators: A review. *J. Micromech. Microeng.* **2010**, *20*, 043001. [CrossRef]
13. Otten, A.; Voort, C.; Stienen, A.; Aarts, R.; van Asseldonk, E.; van der Kooij, H. LIMPACT: A Hydraulically Powered Self-Aligning Upper Limb Exoskeleton. *IEEE ASME Trans. Mechatron.* **2015**, *20*, 2285–2298. [CrossRef]
14. Huber, J.E.; Fleck, N.A.; Ashby, M.F. The selection of mechanical actuators based on performance indices. *Proc. R. Soc. London Ser. A Math. Phys. Eng. Sci.* **1997**, *453*, 2185–2205. [CrossRef]

15. Schaffner, M.; Faber, J.A.; Pianegonda, L.; Ruhs, P.A.; Coulter, F.; Studart, A.R. 3D printing of robotic soft actuators with programmable bioinspired architectures. *Nat. Commun.* **2018**, *9*, 878. [CrossRef]
16. Kim, S.Y.; Baines, R.; Booth, J.; Vasios, N.; Bertoldi, K.; Kramer-Bottiglio, R. Reconfigurable soft body trajectories using unidirectionally stretchable composite laminae. *Nat. Commun.* **2019**, *10*, 1–8. [CrossRef]
17. Li, S.; Vogt, D.M.; Rus, D.; Wood, R.J. Fluid-driven origami-inspired artificial muscles. *Proc. Natl. Acad. Sci. USA* **2017**, *114*, 13132–13137. [CrossRef]
18. Veale, A.J.; Xie, S.Q. Towards compliant and wearable robotic orthoses: A review of current and emerging actuator technologies. *Med. Eng. Phys.* **2016**, *38*, 317–325. [CrossRef] [PubMed]
19. Park, J.; Choi, J.; Kim, S.J.; Seo, K.-H.; Kim, J. Design of an Inflatable Wrinkle Actuator With Fast Inflation/Deflation Responses for Wearable Suits. *IEEE Robot. Autom. Lett.* **2020**, *5*, 3799–3805. [CrossRef]
20. Neill, C.T.O.; Phipps, N.S.; Cappello, L.; Paganoni, S.; Walsh, C.J. A soft wearable robot for the shoulder: Design, characterization, and preliminary testing. In Proceedings of the 2017 International Conference on Rehabilitation Robotics (ICORR), London, UK, 17–20 July 2017; pp. 1672–1678.
21. Polygerinos, P.; Wang, Z.; Galloway, K.C.; Wood, R.J.; Walsh, C.J. Soft robotic glove for combined assistance and at-home rehabilitation. *Robot. Auton. Syst.* **2015**, *73*, 135–143. [CrossRef]
22. Zhu, M.; Do, T.N.; Hawkes, E.; Visell, Y. Fluidic Fabric Muscle Sheets for Wearable and Soft Robotics. *Soft Robot.* **2020**, *7*, 179–197. [CrossRef] [PubMed]
23. Shepherd, R.F.; Stokes, A.A.; Freake, J.; Barber, J.; Snyder, P.W.; Mazzeo, A.D.; Cademartiri, L.; Morin, S.A.; Whitesides, G.M. Using Explosions to Power a Soft Robot. *Angew. Chem. Int. Ed.* **2013**, *52*, 2892–2896. [CrossRef] [PubMed]
24. Unger, M.A. Monolithic Microfabricated Valves and Pumps by Multilayer Soft Lithography. *Science* **2000**, *288*, 113–116. [CrossRef]
25. Dzahir, M.; Yamamoto, S.-I. Recent Trends in Lower-Limb Robotic Rehabilitation Orthosis: Control Scheme and Strategy for Pneumatic Muscle Actuated Gait Trainers. *Robotics* **2014**, *3*, 120–148. [CrossRef]
26. Walker, J.; Zidek, T.; Harbel, C.; Yoon, S.; Strickland, F.S.; Kumar, S.; Shin, M. Soft Robotics: A Review of Recent Developments of Pneumatic Soft Actuators. *Actuators* **2020**, *9*, 3. [CrossRef]
27. Bose, S.; Bandyopadhyay, A. Chapter 1—Introduction to Biomaterials. In *Characterization of Biomaterials*; Bandyopadhyay, A., Bose, S., Eds.; Academic Press: Oxford, UK, 2013. [CrossRef]
28. Sedmák, P.; Pilch, J.; Heller, L.; Kopeček, J.; Wright, J.; Sedlák, P.; Frost, M.; Šittner, P. Grain-resolved analysis of localized deformation in nickel-titanium wire under tensile load. *Science* **2016**, *353*, 559–562. [CrossRef]
29. Stachiv, I.; Alarcon, E.; Lamac, M. Shape Memory Alloys and Polymers for MEMS/NEMS Applications: Review on Recent Findings and Challenges in Design, Preparation, and Characterization. *Metals* **2021**, *11*, 415. [CrossRef]
30. Ölander, A. An electrochemical investigation of solid cadmium-gold alloys. *J. Am. Chem. Soc.* **1932**, *54*, 3819–3833. [CrossRef]
31. Huang, W. On the selection of shape memory alloys for actuators. *Mater. Design* **2002**, *23*, 11–19. [CrossRef]
32. Šittner, P.; Heller, L.; Pilch, J.; Curfs, C.; Alonso, T.; Favier, D. Young's modulus of austenite and martensite phases in superelastic NiTi wires. *J. Mater. Eng. Perform.* **2014**, *23*, 2303–2314. [CrossRef]
33. Zareie, S.; Issa, A.S.; Seethaler, R.J.; Zabihollah, A. Recent advances in the applications of shape memory alloys in civil infrastructures: A review. *Structures* **2020**, *27*, 1535–1550. [CrossRef]
34. Osada, Y.; Matsuda, A. Shape-Memory in Hydrogels. *Nature* **1995**, *376*, 219. [CrossRef]
35. Lendlein, A.; Jiang, H.Y.; Junger, O.; Langer, R. Light-induced shape-memory polymers. *Nature* **2005**, *434*, 879–882. [CrossRef] [PubMed]
36. Takeuchi, I.; Asaka, K.; Kiyohara, K.; Sugino, T.; Terasawa, N.; Mukai, K.; Fukushima, T.; Aida, T. Electromechanical behavior of fully plastic actuators based on bucky gel containing various internal ionic liquids. *Electrochim. Acta* **2009**, *54*, 1762–1768. [CrossRef]
37. Hu, J.; Zhu, Y.; Huang, H.; Lu, J. Recent advances in shape–memory polymers: Structure, mechanism, functionality, modeling and applications. *Prog. Polym. Sci.* **2012**, *37*, 1720–1763. [CrossRef]
38. Xia, Y.; He, Y.; Zhang, F.; Liu, Y.; Leng, J. A review of shape memory polymers and composites: Mechanisms, materials, and applications. *Adv. Mater.* **2021**, *33*, 2000713. [CrossRef]
39. Hadi, A.; Alipour, K.; Kazeminasab, S.; Elahinia, M. ASR glove: A wearable glove for hand assistance and rehabilitation using shape memory alloys. *J. Intel. Mat. Syst. Str.* **2018**, *29*, 1575–1585. [CrossRef]
40. Copaci, D.; Martín, F.; Moreno, L.; Blanco, D. SMA based elbow exoskeleton for rehabilitation therapy and patient evaluation. *IEEE Access* **2019**, *7*, 31473–31484. [CrossRef]
41. Serrano, D.; Copaci, D.S.; Moreno, L.; Blanco, D. SMA based wrist exoskeleton for rehabilitation therapy. In Proceedings of the 2018 IEEE/RSJ International Conference on Intelligent Robots and Systems (IROS), Madrid, Spain, 1–5 October 2018; pp. 2318–2323.
42. Kim, C.; Kim, G.; Lee, Y.; Lee, G.; Han, S.; Kang, D.; Koo, S.H.; Koh, J.-S. Shape memory alloy actuator-embedded smart clothes for ankle assistance. *Smart Mater. Struct.* **2020**, *29*, 055003. [CrossRef]
43. Yao, Z.; Linnenberg, C.; Argubi-Wollesen, A.; Weidner, R.; Wulfsberg, J.P. Biomimetic design of an ultra-compact and light-weight soft muscle glove. *Prod. Eng.* **2017**, *11*, 731–743. [CrossRef]
44. Park, S.J.; Park, C.H. Suit-type wearable robot powered by shape-memory-alloy-based fabric muscle. *Sci. Rep.* **2019**, *9*, 1–8.

45. Copaci, D.; Cano, E.; Moreno, L.; Blanco, D. New design of a soft robotics wearable elbow exoskeleton based on shape memory alloy wire actuators. *Appl. Bionics Biomech.* **2017**, *2017*, 1605101. [CrossRef]
46. Li, Y.; Chung, S.; Chan, L.; Hu, J. Characterisation of shape memory fabrics. *Text. Asia* **2004**, *35*, 32–37.
47. Principles of SMP's Environmental Temperature Adaption Feature. Available online: https://www.mcf.co.jp/en/service/diaseries/diaplex.html (accessed on 17 May 2021).
48. Kim, H.; Lee, H.; Ha, I.; Jung, J.; Won, P.; Cho, H.; Yeo, J.; Hong, S.; Han, S.; Kwon, J. Biomimetic color changing anisotropic soft actuators with integrated metal nanowire percolation network transparent heaters for soft robotics. *Adv. Funct. Mater.* **2018**, *28*, 1801847. [CrossRef]
49. Yao, S.; Cui, J.; Cui, Z.; Zhu, Y. Soft electrothermal actuators using silver nanowire heaters. *Nanoscale* **2017**, *9*, 3797–3805. [CrossRef] [PubMed]
50. Yin, R.; Yang, B.; Ding, X.; Liu, S.; Zeng, W.; Li, J.; Yang, S.; Tao, X. Wireless Multistimulus-Responsive Fabric-Based Actuators for Soft Robotic, Human–Machine Interactive, and Wearable Applications. *Adv. Mater. Technol.* **2020**, *5*, 2000341. [CrossRef]
51. Yu, W.; Chu, C. *Textile Physics*; Donghua University Press: Shanghai, China, 2002; pp. 2–25.
52. Zhu, Q.; Jin, Y.; Wang, W.; Sun, G.; Wang, D. Bioinspired Smart Moisture Actuators Based on Nanoscale Cellulose Materials and Porous, Hydrophilic EVOH Nanofibrous Membranes. *ACS Appl. Mater. Inter.* **2018**, *11*, 1440–1448. [CrossRef] [PubMed]
53. Wang, M.; Tian, X.; Ras, R.H.; Ikkala, O. Sensitive Humidity-Driven Reversible and Bidirectional Bending of Nanocellulose Thin Films as Bio-Inspired Actuation. *Adv. Mater. Interfaces* **2015**, *2*, 1500080. [CrossRef]
54. Mirvakili, S.M.; Hunter, I.W. Multidirectional artificial muscles from nylon. *Adv. Mater.* **2017**, *29*, 1604734. [CrossRef]
55. Kanik, M.; Orguc, S.; Varnavides, G.; Kim, J.; Benavides, T.; Gonzalez, D.; Akintilo, T.; Tasan, C.C.; Chandrakasan, A.P.; Fink, Y. Strain-programmable fiber-based artificial muscle. *Science* **2019**, *365*, 145–150. [PubMed]
56. Acetate-Based Conjugate Fiber Ventcool™. Available online: https://www.m-chemical.co.jp/en/products/departments/mcc/fibersmat/product/1201225_7496.html (accessed on 17 May 2021).
57. Jia, T.J.; Wang, Y.; Dou, Y.Y.; Li, Y.W.; de Andrade, M.J.; Wang, R.; Fang, S.L.; Li, J.J.; Yu, Z.; Qiao, R.; et al. Moisture Sensitive Smart Yarns and Textiles from Self-Balanced Silk Fiber Muscles. *Adv. Funct. Mater.* **2019**, *29*, 1808241. [CrossRef]
58. Cheng, H.; Hu, Y.; Zhao, F.; Dong, Z.; Wang, Y.; Chen, N.; Zhang, Z.; Qu, L. Moisture-activated torsional graphene-fiber motor. *Adv. Mater.* **2014**, *26*, 2909–2913. [CrossRef]
59. He, S.; Chen, P.; Qiu, L.; Wang, B.; Sun, X.; Xu, Y.; Peng, H. A mechanically actuating carbon-nanotube fiber in response to water and moisture. *Angew. Chem. Int. Ed.* **2015**, *54*, 14880–14884. [CrossRef] [PubMed]
60. Hu, X.; Leng, X.; Jia, T.; Liu, Z. Twisted and coiled bamboo artificial muscles for moisture responsive torsional and tensile actuation. *Chin. Phys. B* **2020**, *29*, 118103. [CrossRef]
61. Li, Y.; Leng, X.; Sun, J.; Zhou, X.; Wu, W.; Chen, H.; Liu, Z. Moisture-sensitive torsional cotton artificial muscle and textile. *Chin. Phys. B* **2020**, *29*, 048103. [CrossRef]
62. Wang, Y.; Wang, Z.; Lu, Z.; Jung de Andrade, M.N.; Fang, S.; Zhang, Z.; Wu, J.; Baughman, R.H. Humidity-and Water-Responsive Torsional and Contractile Lotus Fiber Yarn Artificial Muscles. *ACS Appl. Mater. Inter.* **2021**, *13*, 6642–6649. [CrossRef]
63. Mirabedini, A.; Aziz, S.; Spinks, G.M.; Foroughi, J. Wet-spun biofiber for torsional artificial muscles. *Soft Robot.* **2017**, *4*, 421–430. [CrossRef] [PubMed]
64. Zhang, Z.; Zhu, B.; Peng, Z.; Yin, R.; Baughman, R.H.; Tao, X. Programmable and thermally hardening composite yarn actuators with a wide range of operating temperature. *Adv. Mater. Technol.* **2020**, *5*, 2000329. [CrossRef]
65. Haines, C.S.; Lima, M.D.; Li, N.; Spinks, G.M.; Foroughi, J.; Madden, J.D.W.; Kim, S.H.; Fang, S.L.; de Andrade, M.J.; Goktepe, F.; et al. Artificial Muscles from Fishing Line and Sewing Thread. *Science* **2014**, *343*, 868–872. [CrossRef] [PubMed]
66. Yang, X.H.; Wang, W.H.; Miao, M.H. Moisture-Responsive Natural Fiber Coil-Structured Artificial Muscles. *ACS Appl. Mater. Inter.* **2018**, *10*, 32256–32264. [CrossRef] [PubMed]
67. Li, Y.; Miao, M. Water-responsive artificial muscles from commercial viscose fibers without chemical treatment. *Mater. Res. Lett.* **2020**, *8*, 232–238. [CrossRef]
68. Lamuta, C.; Messelot, S.; Tawfick, S. Theory of the tensile actuation of fiber reinforced coiled muscles. *Smart Mater. Struct.* **2018**, *27*, 055018. [CrossRef]
69. Peng, Y.; Cui, Y. Advanced textiles for personal thermal management and energy. *Joule* **2020**, *4*, 724–742. [CrossRef]
70. Zhong, Y.; Zhang, F.; Wang, M.; Gardner, C.J.; Kim, G.; Liu, Y.; Leng, J.; Jin, S.; Chen, R. Reversible humidity sensitive clothing for personal thermoregulation. *Sci. Rep.* **2017**, *7*, 1–8. [CrossRef]
71. Zhang, X.A.; Yu, S.; Xu, B.; Li, M.; Peng, Z.; Wang, Y.; Deng, S.; Wu, X.; Wu, Z.; Ouyang, M. Dynamic gating of infrared radiation in a textile. *Science* **2019**, *363*, 619–623. [CrossRef] [PubMed]
72. Wang, W.; Yao, L.; Cheng, C.-Y.; Zhang, T.; Atsumi, H.; Wang, L.; Wang, G.; Anilionyte, O.; Steiner, H.; Ou, J. Harnessing the hygroscopic and biofluorescent behaviors of genetically tractable microbial cells to design biohybrid wearables. *Sci. Adv.* **2017**, *3*, e1601984. [CrossRef]
73. Qiu, Y.; Zhang, E.; Plamthottam, R.; Pei, Q. Dielectric Elastomer Artificial Muscle: Materials Innovations and Device Explorations. *Acc. Chem. Res.* **2019**, *52*, 316–325. [CrossRef]
74. Pelrine, R.E.; Kornbluh, R.D.; Joseph, J.P. Electrostriction of polymer dielectrics with compliant electrodes as a means of actuation. *Sens. Actuators A Phys.* **1998**, *64*, 77–85. [CrossRef]

75. Pelrine, R.; Kornbluh, R.; Pei, Q.; Joseph, J. High-Speed Electrically Actuated Elastomers with Strain Greater Than 100%. *Science* **2000**, *287*, 836. [CrossRef]
76. Shankar, R.; Ghosh, T.K.; Spontak, R.J. Dielectric elastomers as next-generation polymeric actuators. *Soft Matter* **2007**, *3*, 1116–1129. [CrossRef] [PubMed]
77. Romasanta, L.J.; Lopez-Manchado, M.A.; Verdejo, R. Increasing the performance of dielectric elastomer actuators: A review from the materials perspective. *Prog. Polym. Sci.* **2015**, *51*, 188–211. [CrossRef]
78. Youn, J.-H.; Jeong, S.M.; Hwang, G.; Kim, H.; Hyeon, K.; Park, J.; Kyung, K.-U. Dielectric Elastomer Actuator for Soft Robotics Applications and Challenges. *Appl. Sci.* **2020**, *10*, 640. [CrossRef]
79. Brochu, P.; Pei, Q. Advances in Dielectric Elastomers for Actuators and Artificial Muscles. *Macromol. Rapid Commun.* **2010**, *31*, 10–36. [CrossRef]
80. Kovacs, G.; Düring, L.; Michel, S.; Terrasi, G. Stacked dielectric elastomer actuator for tensile force transmission. *Sens. Actuators A: Phys.* **2009**, *155*, 299–307. [CrossRef]
81. Chortos, A.; Hajiesmaili, E.; Morales, J.; Clarke, D.R.; Lewis, J.A. 3D Printing of Interdigitated Dielectric Elastomer Actuators. *Adv. Funct. Mater.* **2020**, *30*, 1907375. [CrossRef]
82. Jung, H.S.; Yang, S.Y.; Cho, K.H.; Song, M.G.; Nguyen, C.T.; Phung, H.; Kim, U.; Moon, H.; Koo, J.C.; Nam, J.-D.; et al. Design and fabrication of twisted monolithic dielectric elastomer actuator. *Int. J. Control Autom. Syst.* **2017**, *15*, 25–35. [CrossRef]
83. Zhao, H.; Hussain, A.M.; Duduta, M.; Vogt, D.M.; Wood, R.J.; Clarke, D.R. Compact Dielectric Elastomer Linear Actuators. *Adv. Funct. Mater.* **2018**, *28*, 1804328. [CrossRef]
84. Phung, H.; Nguyen, C.T.; Jung, H.; Nguyen, T.D.; Choi, H.R. Bidirectional tactile display driven by electrostatic dielectric elastomer actuator. *Smart Mater. Struct.* **2020**, *29*, 035007. [CrossRef]
85. Nalbach, S.; Banda, R.M.; Croce, S.; Rizzello, G.; Naso, D.; Seelecke, S. Modeling and Design Optimization of a Rotational Soft Robotic System Driven by Double Cone Dielectric Elastomer Actuators. *Front. Robot. AI* **2020**, *6*, 150. [CrossRef]
86. Rosset, S.; Niklaus, M.; Dubois, P.; Shea, H.R. Large-Stroke Dielectric Elastomer Actuators With Ion-Implanted Electrodes. *J. Microelectromechanical Syst.* **2009**, *18*, 1300–1308. [CrossRef]
87. Liang, D.; Lin, Z.-F.; Huang, C.-C.; Shih, W.-P. Tunable lens driven by dielectric elastomer actuator with ionic electrodes. *Micro Nano Lett.* **2014**, *9*, 869–873. [CrossRef]
88. Qu, X.; Ma, X.; Shi, B.; Li, H.; Zheng, L.; Wang, C.; Liu, Z.; Fan, Y.; Chen, X.; Li, Z.; et al. Refreshable Braille Display System Based on Triboelectric Nanogenerator and Dielectric Elastomer. *Adv. Funct. Mater.* **2021**, *31*, 2006612. [CrossRef]
89. Duduta, M.; Wood, R.J.; Clarke, D.R. Multilayer Dielectric Elastomers for Fast, Programmable Actuation without Prestretch. *Adv. Mater.* **2016**, *28*, 8058–8063. [CrossRef]
90. Shao, H.; Wei, S.; Jiang, X.; Holmes, D.P.; Ghosh, T.K. Bioinspired Electrically Activated Soft Bistable Actuators. *Adv. Funct. Mater.* **2018**, *28*, 1802999. [CrossRef]
91. Pei, Q.; Rosenthal, M.; Stanford, S.; Prahlad, H.; Pelrine, R. Multiple-degrees-of-freedom electroelastomer roll actuators. *Smart Mater. Struct.* **2004**, *13*, N86–N92. [CrossRef]
92. Yan, Y.; Santaniello, T.; Bettini, L.G.; Minnai, C.; Bellacicca, A.; Porotti, R.; Denti, I.; Faraone, G.; Merlini, M.; Lenardi, C.; et al. Electroactive Ionic Soft Actuators with Monolithically Integrated Gold Nanocomposite Electrodes. *Adv. Mater.* **2017**, *29*, 1606109. [CrossRef] [PubMed]
93. Pyo, D.; Ryu, S.; Kyung, K.-U.; Yun, S.; Kwon, D.-S. High-pressure endurable flexible tactile actuator based on microstructured dielectric elastomer. *Appl. Phys. Lett.* **2018**, *112*, 061902. [CrossRef]
94. Acome, E.; Keplinger, C.; Gross, M.D.; Bruns, C.; Leithinger, D. Soft Electrohydraulic Actuators for Origami Inspired Shape-Changing Interfaces. In Proceedings of the CHI '21 Extended Abstracts, Yokohama, Japan, 8–13 May 2021.
95. Ren, Z.; Hu, W.; Liu, C.; Li, S.; Niu, X.; Pei, Q. Phase-Changing Bistable Electroactive Polymer Exhibiting Sharp Rigid-to-Rubbery Transition. *Macromolecules* **2016**, *49*, 134–140. [CrossRef]
96. Ji, X.; Liu, X.; Cacucciolo, V.; Civet, Y.; El Haitami, A.; Cantin, S.; Perriard, Y.; Shea, H. Untethered Feel-Through Haptics Using 18-μm Thick Dielectric Elastomer Actuators. *Adv. Funct. Mater.* **2020**, 2006639. [CrossRef]
97. Lee, H.S.; Phung, H.; Lee, D.-H.; Kim, U.K.; Nguyen, C.T.; Moon, H.; Koo, J.C.; Nam, J.-D.; Choi, H.R. Design analysis and fabrication of arrayed tactile display based on dielectric elastomer actuator. *Sens. Actuators A Phys.* **2014**, *205*, 191–198. [CrossRef]
98. King, H.H.; Donlin, R.; Hannaford, B. Perceptual thresholds for single vs. Multi-Finger Haptic interaction. In Proceedings of the 2010 IEEE Haptics Symposium, Waltham, MA, USA, 25–26 March 2010; pp. 95–99.
99. Leroy, E.; Hinchet, R.; Shea, H. Multimode Hydraulically Amplified Electrostatic Actuators for Wearable Haptics. *Adv. Mater.* **2020**, *32*, 2002564. [CrossRef]
100. Koo, I.M.; Jung, K.; Koo, J.C.; Nam, J.; Lee, Y.K.; Choi, H.R. Development of Soft-Actuator-Based Wearable Tactile Display. *IEEE Trans. Robot.* **2008**, *24*, 549–558. [CrossRef]
101. Zhao, H.; Hussain, A.M.; Israr, A.; Vogt, D.M.; Duduta, M.; Clarke, D.R.; Wood, R.J. A Wearable Soft Haptic Communicator Based on Dielectric Elastomer Actuators. *Soft Robot.* **2020**, *7*, 451–461. [CrossRef]
102. Carpi, F.; Mannini, A.; de Rossi, D. Elastomeric contractile actuators for hand rehabilitation splints. In Proceedings of the SPIE Smart Structures and Materials + Nondestructive Evaluation and Health Monitoring, San Diego, CA, USA, 29 April 2008.
103. Pourazadi, S.; Ahmadi, S.; Menon, C. Towards the development of active compression bandages using dielectric elastomer actuators. *Smart Mater. Struct.* **2014**, *23*, 065007. [CrossRef]

104. Allen, D.P.; Little, R.; Laube, J.; Warren, J.; Voit, W.; Gregg, R.D. Towards an ankle-foot orthosis powered by a dielectric elastomer actuator. *Mechatronics* **2021**, *76*, 102551. [CrossRef]
105. Kim, K.J.; Shahinpoor, M. Ionic polymer metal composites: II. Manufacturing techniques. *Smart Mater. Struct.* **2003**, *12*, 65–79. [CrossRef]
106. Kuhn, H.; Möbius, D. Systems of Monomolecular Layers—Assembling and Physico-Chemical Behavior. *Angew. Chem. Int. Ed. Engl.* **1971**, *10*, 620–637. [CrossRef]
107. Katchalsky, A. Rapid swelling and deswelling of reversible gels of polymeric acids by ionization. *Experientia* **1949**, *5*, 319–320. [CrossRef]
108. Shahinpoor, M.; Kim, K.J. Ionic polymer-metal composites: I. Fundamentals. *Smart Mater. Struct.* **2001**, *10*, 819–833. [CrossRef]
109. Asaka, K.; Mukai, K.; Sugino, T.; Kiyohara, K. Ionic electroactive polymer actuators based on nano-carbon electrodes. *Polym. Int.* **2013**, *62*, 1263–1270. [CrossRef]
110. Wang, H.S.; Cho, J.; Park, H.W.; Jho, J.Y.; Park, J.H. Ionic polymer–metal composite actuators driven by methylammonium formate for high-voltage and long-term operation. *J. Ind. Eng. Chem.* **2021**, *96*, 194–201. [CrossRef]
111. Bar-Cohen, Y. *Electroactive Polymer (EAP) Actuators as Artificial Muscles: Reality, Potential, and Challenges*; SPIE: Bellingham, WA USA, 2004.
112. Zou, M.; Li, S.; Hu, X.; Leng, X.; Wang, R.; Zhou, X.; Liu, Z. Progresses in Tensile, Torsional, and Multifunctional Soft Actuators. *Adv. Funct. Mater.* **2021**, 2007437. [CrossRef]
113. Wu, Y.; Yang, Y.; Li, C.; Li, Y.; Chen, W. Flexible and Electroactive Textile Actuator Enabled by PEDOT:PSS/MOF-Derivative Electrode Ink. *Front. Bioeng. Biotechnol.* **2020**, *8*, 212. [CrossRef] [PubMed]
114. Li, Y.; Hashimoto, M. PVC gel soft actuator-based wearable assist wear for hip joint support during walking. *Smart Mater. Struct.* **2017**, *26*, 125003. [CrossRef]
115. Chattaraj, R.; Bhaumik, S.; Khan, S.; Chatterjee, D. Soft wearable ionic polymer sensors for palpatory pulse-rate extraction. *Sens. Actuators A Phys.* **2018**, *270*, 65–71. [CrossRef]
116. Hamlen, R.P.; Kent, C.E.; Shafer, S.N. Electrolytically Activated Contractile Polymer. *Nature* **1965**, *206*, 1149–1150. [CrossRef]
117. Lu, W.; Fadeev, A.G.; Qi, B.; Smela, E.; Mattes, B.R.; Ding, J.; Spinks, G.M.; Mazurkiewicz, J.; Zhou, D.; Wallace, G.G.; et al. Use of Ionic Liquids for $\pi$-Conjugated Polymer Electrochemical Devices. *Science* **2002**, *297*, 983. [CrossRef]
118. Lewis, T.W.; Spinks, G.M.; Wallace, G.G.; Mazzoldi, A.; De Rossi, D. Investigation of the applied potential limits for polypyrrole when employed as the active components of a two-electrode device. *Synth. Met.* **2001**, *122*, 379–385. [CrossRef]
119. Chen, D.; Guorong, L.; Yin, Q. Piezoelectric Constants Measured from Converse Piezoelectric Effect and Piezoelectric Ceramic Actuators. *J. Inorg. Mater.* **1997**, *12*, 861–866.
120. Brook, R.J. Advanced Ceramic Materials: An Overview. In *Concise Encyclopedia of Advanced Ceramic Materials*; Brook, R.J., Ed.; Pergamon: Oxford, UK, 1991; pp. 1–8.
121. Sun, Q.; Wang, J.; Zhang, L.; Mao, P.; Liu, S.; He, L.; Kang, F.; Xue, R. Achieving high energy density and discharge efficiency in multi-layered PVDF–PMMA nanocomposites composed of 0D $BaTiO_3$ and 1D $NaNbO_3$@$SiO_2$. *J. Mater. Chem. C* **2020**, *8*, 7211–7220. [CrossRef]
122. Akther, A.; Castro, J.O.; Mousavi Shaegh, S.A.; Rezk, A.R.; Yeo, L.Y. Miniaturised acoustofluidic tactile haptic actuator. *Soft Matter* **2019**, *15*, 4146–4152. [CrossRef] [PubMed]
123. Wu, Y.; Yim, J.K.; Liang, J.; Shao, Z.; Qi, M.; Zhong, J.; Luo, Z.; Yan, X.; Zhang, M.; Wang, X.; et al. Insect-scale fast moving and ultrarobust soft robot. *Sci. Robot.* **2019**, *4*, eaax1594. [CrossRef]
124. Maccabi, N.; Grinberg, I.; Kassie, A.; Shmulevich, S.; Elata, D. Bulk PZT Actuator for Parallel out-of-plane motion: The Superiority of Torsion Deformation over Bending Deformation. *Procedia Eng.* **2016**, *168*, 1513–1516. [CrossRef]
125. Xu, C.; Reng, Y.; Liu, S.; Zhu, J.; Liu, Y.; Wu, H. A fast rotating soft actuator based on piezoelectric vibration. *Chin. Sci. Bull.* **2020**, *65*, 109–116. [CrossRef]
126. Kwon, O.D.; Yoo, J.S.; Yun, Y.J.; Lee, J.S.; Kang, S.H.; Lim, K.J. A research on the piezoelectric vibration actuator for mobile phone. In Proceedings of the 2005 International Symposium on Electrical Insulating Materials, 2005. (ISEIM 2005), Kitakyushu, Japan, 5–9 June 2005; Volume 673, pp. 676–678.
127. Park, T.; Cha, Y. Soft mobile robot inspired by animal-like running motion. *Sci. Rep.* **2019**, *9*, 14700. [CrossRef]
128. Jeong, S.-S.; Cheon, S.-K.; Kim, M.-H.; Song, J.-S.; Park, T.-G. Motional characteristics of ultrasonic motor using $\Lambda$ (lambda)-shaped stator. *Ceram. Int.* **2013**, *39*, S715–S719. [CrossRef]
129. Li, X.; Yao, Z.; Wu, R. Modeling and analysis of stick-slip motion in a linear piezoelectric ultrasonic motor considering ultrasonic oscillation effect. *Int. J. Mech. Sci.* **2016**, *107*, 215–224. [CrossRef]
130. Qiu, W.; Mizuno, Y.; Koyama, D.; Nakamura, K. Efficiency improvement of hybrid transducer-type ultrasonic motor using lubricant. *IEEE Trans. Ultrason. Ferroelectr. Freq. Control* **2013**, *60*, 786–794. [CrossRef] [PubMed]
131. Tian, X.; Liu, Y.; Deng, J.; Wang, L.; Chen, W. A review on piezoelectric ultrasonic motors for the past decade: Classification, operating principle, performance, and future work perspectives. *Sens. Actuators A Phys.* **2020**, *306*, 111971. [CrossRef]
132. Sauvet, B.; Laliberté, T.; Gosselin, C. Design, analysis and experimental validation of an ungrounded haptic interface using a piezoelectric actuator. *Mechatronics* **2017**, *45*, 100–109. [CrossRef]
133. Zhu, M.; Sun, Z.; Zhang, Z.; Shi, Q.; He, T.; Liu, H.; Chen, T.; Lee, C. Haptic-feedback smart glove as a creative human-machine interface (HMI) for virtual/augmented reality applications. *Sci. Adv.* **2020**, *6*, eaaz8693. [CrossRef]

134. Dagdeviren, C.; Shi, Y.; Joe, P.; Ghaffari, R.; Balooch, G.; Usgaonkar, K.; Gur, O.; Tran, P.L.; Crosby, J.R.; Meyer, M.; et al. Conformal piezoelectric systems for clinical and experimental characterization of soft tissue biomechanics. *Nat. Mater.* **2015**, *14*, 728–736. [CrossRef]
135. Ba, J. Research on Magnetically Controlled Miniature Soft Crawling Robot Based on Magneto-elastic Composite Material. Ph.D. Thesis, Tianjin University of Technology, Tianjin, China, 2020.
136. Mao, G.; Drack, M.; Karami-Mosammam, M.; Wirthl, D.; Stockinger, T.; Schwödiauer, R.; Kaltenbrunner, M. Soft electromagnetic actuators. *Sci. Adv.* **2020**, *6*, eabc0251. [CrossRef]
137. Ebrahimi, N.; Schimpf, P.; Jafari, A. Design optimization of a solenoid-based electromagnetic soft actuator with permanent magnet core. *Sens. Actuators A Phys.* **2018**, *284*, 276–285. [CrossRef]
138. Pece, F.; Zarate, J.J.; Vechev, V.; Besse, N.; Gudozhnik, O.; Shea, H.; Hilliges, O. MagTics: Flexible and Thin Form Factor Magnetic Actuators for Dynamic and Wearable Haptic Feedback. In Proceedings of the 30th Annual ACM Symposium on User Interface Software and Technology, Québec City, QC, Canada, 20 October 2017; pp. 143–154.
139. Yunas, J.; Mulyanti, B.; Hamidah, I.; Mohd Said, M.; Pawinanto, R.E.; Wan Ali, W.A.; Subandi, A.; Hamzah, A.A.; Latif, R.; Yeop Majlis, B. Polymer-Based MEMS Electromagnetic Actuator for Biomedical Application: A Review. *Polymers* **2020**, *12*, 1184. [CrossRef]
140. Do, T.N.; Phan, H.; Nguyen, T.-Q.; Visell, Y. Miniature Soft Electromagnetic Actuators for Robotic Applications. *Adv. Funct. Mater.* **2018**, *28*, 1800244. [CrossRef]
141. Guo, R.; Sheng, L.; Gong, H.; Liu, J. Liquid metal spiral coil enabled soft electromagnetic actuator. *Sci. China Technol. Sci.* **2018**, *61*, 516–521. [CrossRef]
142. Ozioko, O.; Navaraj, W.; Hersh, M.; Dahiya, R. Tacsac: A Wearable Haptic Device with Capacitive Touch-Sensing Capability for Tactile Display. *Sensors* **2020**, *20*, 4780. [CrossRef]
143. Ozioko, O.; Karipoth, P.; Hersh, M.; Dahiya, R. Wearable Assistive Tactile Communication Interface Based on Integrated Touch Sensors and Actuators. *IEEE Trans. Neural Syst. Rehabil. Eng.* **2020**, *28*, 1344–1352. [CrossRef] [PubMed]
144. Yu, X.; Xie, Z.; Yu, Y.; Lee, J.; Vazquez-Guardado, A.; Luan, H.; Ruban, J.; Ning, X.; Akhtar, A.; Li, D.; et al. Skin-integrated wireless haptic interfaces for virtual and augmented reality. *Nature* **2019**, *575*, 473–479. [CrossRef]
145. White, T.J.; Broer, D.J. Programmable and adaptive mechanics with liquid crystal polymer networks and elastomers. *Nat. Mater.* **2015**, *14*, 1087–1098. [CrossRef] [PubMed]
146. Kularatne, R.S.; Kim, H.; Boothby, J.M.; Ware, T.H. Liquid Crystal Elastomer Actuators: Synthesis, Alignment, and Applications. *J. Polym. Sci. Pol. Phys.* **2017**, *55*, 395–411. [CrossRef]
147. Ohm, C.; Brehmer, M.; Zentel, R. Liquid Crystalline Elastomers as Actuators and Sensors. *Adv. Mater.* **2010**, *22*, 3366–3387. [CrossRef]
148. He, Q.; Wang, Z.; Wang, Y.; Minori, A.; Tolley, M.T.; Cai, S. Electrically controlled liquid crystal elastomer-based soft tubular actuator with multimodal actuation. *Sci. Adv.* **2019**, *5*, 10. [CrossRef] [PubMed]
149. Yakacki, C.M.; Saed, M.; Nair, D.P.; Gong, T.; Reed, S.M.; Bowman, C.N. Tailorable and programmable liquid-crystalline elastomers using a two-stage thiol-acrylate reaction. *Rsc. Adv.* **2015**, *5*, 18997–19001. [CrossRef]
150. Liu, H.R.; Tian, H.M.; Shao, J.Y.; Wang, Z.J.; Li, X.M.; Wang, C.H.; Chen, X.L. An Electrically Actuated Soft Artificial Muscle Based on a High-Performance Flexible Electrothermal Film and Liquid-Crystal Elastomer. *Acs. Appl. Mater. Inter.* **2020**, *12*, 56338–56349. [CrossRef]
151. Wang, Y.C.; Dang, A.L.; Zhang, Z.F.; Yin, R.; Gao, Y.C.; Feng, L.; Yang, S. Repeatable and Reprogrammable Shape Morphing from Photoresponsive Gold Nanorod/Liquid Crystal Elastomers. *Adv. Mater.* **2020**, *32*, 2004270. [CrossRef] [PubMed]
152. Wang, M.; Sayed, S.M.; Guo, L.X.; Lin, B.P.; Zhang, X.Q.; Sun, Y.; Yang, H. Multi-Stimuli Responsive Carbon Nanotube Incorporated Polysiloxane Azobenzene Liquid Crystalline Elastomer Composites. *Macromolecules* **2016**, *49*, 663–671. [CrossRef]
153. Ambulo, C.P.; Ford, M.J.; Searles, K.; Majidi, C.; Ware, T.H. 4D-Printable Liquid Metal-Liquid Crystal Elastomer Composites. *Acs. Appl. Mater. Inter.* **2021**, *13*, 12805–12813. [CrossRef]
154. Lu, X.L.; Guo, S.W.; Tong, X.; Xia, H.S.; Zhao, Y. Tunable Photocontrolled Motions Using Stored Strain Energy in Malleable Azobenzene Liquid Crystalline Polymer Actuators. *Adv. Mater.* **2017**, *29*, 1606467. [CrossRef]
155. Zeng, H.; Wani, O.M.; Wasylczyk, P.; Kaczmarek, R.; Priimagi, A. Self-Regulating Iris Based on Light-Actuated Liquid Crystal Elastomer. *Adv. Mater.* **2017**, *29*, 1701814. [CrossRef] [PubMed]
156. Roach, D.J.; Yuan, C.; Kuang, X.; Li, V.C.F.; Blake, P.; Romero, M.L.; Hammel, I.; Yu, K.; Qi, H.J. Long Liquid Crystal Elastomer Fibers with Large Reversible Actuation Strains for Smart Textiles and Artificial Muscles. *Acs. Appl. Mater. Inter.* **2019**, *11*, 19514–19521. [CrossRef]
157. He, Q.G.; Wang, Z.J.; Song, Z.Q.; Cai, S.Q. Bioinspired Design of Vascular Artificial Muscle. *Adv. Mater. Technol.* **2019**, *4*, 1800244. [CrossRef]
158. Yoon, H.H.; Kim, D.Y.; Jeong, K.U.; Ahn, S.K. Surface Aligned Main-Chain Liquid Crystalline Elastomers: Tailored Properties by the Choice of Amine Chain Extenders. *Macromolecules* **2018**, *51*, 1141–1149. [CrossRef]
159. Saed, M.O.; Ambulo, C.P.; Kim, H.; De, R.; Raval, V.; Searles, K.; Siddiqui, D.A.; Cue, J.M.O.; Stefan, M.C.; Shankar, M.R.; et al. Molecularly-Engineered, 4D-Printed Liquid Crystal Elastomer Actuators. *Adv. Funct. Mater.* **2019**, *29*, 1806412. [CrossRef]
160. Butzer, T.; Lambercy, O.; Arata, J.; Gassert, R. Fully Wearable Actuated Soft Exoskeleton for Grasping Assistance in Everyday Activities. *Soft Robot.* **2021**, *8*, 128–143. [CrossRef]

161. Kim, J.; Lee, G.; Heimgartner, R.; Arumukhom Revi, D.; Karavas, N.; Nathanson, D.; Galiana, I.; Eckert-Erdheim, A.; Murphy, P.; Perry, D.; et al. Reducing the metabolic rate of walking and running with a versatile, portable exosuit. *Science* **2019**, *365*, 668–672. [CrossRef]
162. Zang, X.; Zhou, Q.; Chang, J.; Liu, Y.; Lin, L. Graphene and carbon nanotube (CNT) in MEMS/NEMS applications. *Microelectron. Eng.* **2015**, *132*, 192–206. [CrossRef]
163. Jang, Y.; Kim, S.M.; Spinks, G.M.; Kim, S.J. Carbon Nanotube Yarn for Fiber-Shaped Electrical Sensors, Actuators, and Energy Storage for Smart Systems. *Adv. Mater.* **2020**, *32*, e1902670. [CrossRef]
164. Haines, C.S.; Li, N.; Spinks, G.M.; Aliev, A.E.; Di, J.; Baughman, R.H. New twist on artificial muscles. *Proc. Natl. Acad. Sci. USA* **2016**, *113*, 11709–11716. [CrossRef] [PubMed]
165. Rogers, G.W.; Liu, J.Z. Graphene actuators: Quantum-mechanical and electrostatic double-layer effects. *J. Am. Chem. Soc.* **2011**, *133*, 10858–10863. [CrossRef] [PubMed]
166. Lee, J.A.; Kim, Y.T.; Spinks, G.M.; Suh, D.; Lepro, X.; Lima, M.D.; Baughman, R.H.; Kim, S.J. All-solid-state carbon nanotube torsional and tensile artificial muscles. *Nano Lett.* **2014**, *14*, 2664–2669. [CrossRef]
167. Foroughi, J.; Spinks, G.M.; Wallace, G.G.; Oh, J.; Kozlov, M.E.; Fang, S.; Mirfakhrai, T.; Madden, J.D.; Shin, M.K.; Kim, S.J.; et al. Torsional carbon nanotube artificial muscles. *Science* **2011**, *334*, 494–497. [CrossRef] [PubMed]
168. Kim, K.J.; Hyeon, J.S.; Kim, H.; Mun, T.J.; Haines, C.S.; Li, N.; Baughman, R.H.; Kim, S.J. Enhancing the Work Capacity of Electrochemical Artificial Muscles by Coiling Plies of Twist-Released Carbon Nanotube Yarns. *ACS Appl. Mater. Interfaces* **2019**, *11*, 13533–13537. [CrossRef]
169. Lin, H.; Zhang, S.; Xiao, Y.; Zhang, C.; Zhu, J.; Dunlop, J.W.C.; Yuan, J. Organic Molecule-Driven Polymeric Actuators. *Macromol. Rapid Commun.* **2019**, *40*, e1800896. [CrossRef] [PubMed]
170. Scheidl, R.; Winkler, B.; Kogler, H.; Ladner, P.; Haas, R.; Lukachev, E. Digital Fluid Technologies for the Steel Industry. *BHM Berg Hüttenmännische Mon.* **2016**, *161*, 504–509. [CrossRef]
171. Yang, T.-H.; Kim, J.R.; Jin, H.; Gil, H.; Koo, J.-H.; Kim, H.J. Recent Advances and Opportunities of Active Materials for Haptic Technologies in Virtual and Augmented Reality. *Adv. Funct. Mater.* **2021**, 2008831. [CrossRef]

*textiles*

MDPI

*Perspective*

# Bacterial Secondary Metabolites as Biopigments for Textile Dyeing

**Ana Kramar [1,*] and Mirjana M. Kostic [2,*]**

[1] Department of Materials Science and Engineering and Chemical Engineering, Instituto Tecnológico de Química y Materiales "Álvaro Alonso Barba", Universidad Carlos III de Madrid, Avda. Universidad 30, 28911 Leganés, Spain
[2] Department of Textile Engineering, Faculty of Technology and Metallurgy, University of Belgrade, Karnegijeva 4, 11000 Belgrade, Serbia
* Correspondence: akramar@ing.uc3m.es (A.K.); kostic@tmf.bg.ac.rs (M.M.K.)

**Abstract:** In the past two decades, a growing body of research regarding the utilization of natural bacterial pigments or dyes for textile dyeing has emerged. Bacterial pigments are bacterial secondary metabolites that usually have bright colors and some special properties (e.g., antimicrobial, antioxidative, UV protective etc.). In addition to their high production yield, these special properties led scientists to research and develop methods for utilizing bacterial pigments in textile dyeing. This study presents the current state this field of research, with a focus on the dyeing potential of bacterial pigments for different types of textile material. The potential future directions of research in this area are also highlighted. In addition to the durable dyeing of textiles, bacterial pigments with special properties, such as antimicrobial activity, can add multifunctionality to dyed materials, thus increasing the value of the final product. This emerging field of research will also have a great impact on sustainability and the environment, contributing to the decreased usage of synthetic dyes in the textile industry.

**Keywords:** microbial pigments; bacterial pigments; textile; fibers; dyeing

**Citation:** Kramar, A.; Kostic, M.M. Bacterial Secondary Metabolites as Biopigments for Textile Dyeing. *Textiles* **2022**, 2, 252–264. https://doi.org/10.3390/textiles2020013

Academic Editor: Laurent Dufossé

Received: 1 March 2022
Accepted: 15 April 2022
Published: 19 April 2022



## 1. Introduction

The coloration of textile materials has been performed since ancient times [1,2]. The textile dyeing industry has long been environmentally challenging in several respects. First, there is very high water consumption during all stages of dyeing, which consequently generates a significant amount of contaminated water waste. Second, the use of very harsh chemicals is also a significant threat to the environment, especially given that residue from these chemicals can come into contact with consumers during their use of textile products. Third, the energy consumption during dyeing through the heating and drying stages is also very high. Finally, the dyes that are currently used are mostly of synthetic origin. One of the ways to reduce these issues is to use natural dyes. Natural dyes were in use before synthetic ones [1,3]; however, their extraction and use are technologically time-consuming and very expensive. In the past decade, research has focused on emerging, novel and exciting sources of natural dyes: bacteria [3–5]. Bacterial, or, as they are sometimes called, microbial dyes are byproducts of bacteria that represent a relatively novel and scarcely investigated source of natural dyes, with tremendous potential for dyeing various textile materials in very intense, durable and esthetically beautiful colors, which are nontoxic and safe for human skin, thus producing environmentally sustainable textile products.

Research into the possibility of using bacterial pigments as natural sources of dyes for the textile industry has grown. For this study, the Scopus and ScienceDirect databases were used with several research keywords, including "bacterial pigments dyes microbial textile fibers fabrics dyeing." After refining the search results by excluding all articles related to processes involving the decolorization of textile dyes from wastewater using bacteria or

the dyeing of textiles using plant extracts, there was only a small number of publications in the field relevant to the dyeing of textiles with bacterial pigments, and a slight increase in publication numbers occurring with time (Figure 1).

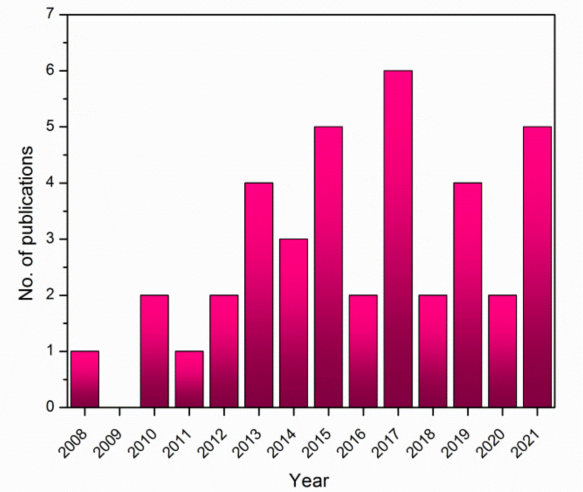


**Figure 1.** Number of publications per year (for years between 2008 and 2021) regarding textile dyeing using bacterial pigments, according to Scopus database.

In the search for representative articles, the term "microbial pigments" was used, even though microbial pigments cover pigments and dyes derived from both bacteria and fungi [5]. Fungal pigments are also important sources of natural dyes and have potential for the dyeing of textiles [6], but the use of fungal pigments as dye sources is beyond the scope of this study.

One of the first suggestions in the literature, which is not presented in Figure 1, is the possibility of using color pigment, published in 2000 by Shirata et al. [7]. This publication was followed by a study by Alihosseini et al. [8] in 2008; therefore, there was a gap of several years before the interest in bacterial pigments as textile dyes was revived. Together, the authors of these two studies can be considered pioneers in this field, since they produced the first results about the possibility of using a naturally occurring pigment derived from bacteria to dye various fabrics. The following years marked the growth of research groups studying this field, while in 2017, there was even a first mention of the use of biopigment for ink formulation in printing [9].

Their high production yield, non-toxicity and good safety profile make bacterial pigments or dyes novel, sustainable and promising alternatives to synthetic dyes. In this article, important studies regarding the utilization of bacterial pigments on different textile materials and fibers are presented, with a focus on the necessary step of the preparation of pigment solutions, the use of mordants, and other pre- or post-textile treatments to improve dye fixation on specific fibers and increase the exhaustion of the dyebath, as well as the possibility of imparting additional properties to colored materials, in order to obtain high-added-value textile products.

## 2. Bacterial Dyes

Bacterial metabolites/secondary metabolites are by-products of bacterial growth [5]. Usually, these byproducts are bacterial responses to external stimuli [10]. Besides color, these metabolites can possess important additional properties, such as potent antimicrobial activity against different pathogens, anticancer activity, antioxidative activity, UV properties, etc. [3,11–13]. These properties suggest that these pigments could be used as functional dyes for different textile materials, since they offer a range of potential applications in addition to their esthetic, qualities (Figure 2). Bacterial pigments, or biopigments, are terms that are used to describe these types of colorant or dyestuff, but from a textile-science point of view, these bacterial metabolites behave more as dyes than as pigments. Even though

they are not soluble in water, they can be considered dyes rather than pigments because it has been shown that they are chemically bound to textile materials, forming bonds with functional groups on fibers and, therefore, behaving as dyes. However, in current research, the term pigment is frequently used, since these bacterial products are usually insoluble in water, they are in powder form after isolation and drying and, in some cases, they are used as suspensions and not solutions.

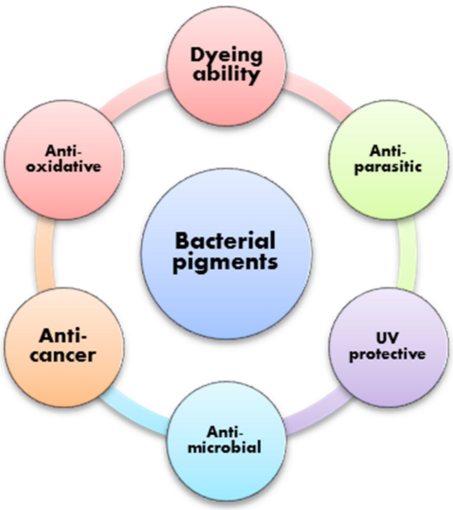


**Figure 2.** Some of the properties of bacterial pigments that have potential to be transferred to textile materials during dyeing.

If dyes can offer additional properties to textile materials, by binding to textiles in a way that it does not disturb their antimicrobial or anticancer function, for example, then certain functions can be transferred to textile materials after dyeing. The vast range of special properties of bacterial pigments presented in Figure 2 opens up the possibility that dyed textiles possess the same properties. This is one of the most important aspects that should be explored in the future, i.e., whether certain properties of bacterial pigments are retained on textile materials after dyeing.

Several bacterial strains are able to produce pigments or dyes capable of imparting color to textile materials [11]. These bacteria are isolated from various sources, such as soil, water, plants, insects, etc. [11,12]. Among many, the most important are *Serratia, Streptomyces* and *Pseudomonas* [4,13]. The range of colors that these bacteria produce is wide, including pink, red-orange, yellow, blue, green, etc. [14,15]. However, it is important to note that the color of the extracted pigment does not always match the resulting color of the dyed fiber/fabric. As discussed later in this article, the resulting color depends on the nature of the substrate, meaning that various shades can be obtained by the same pigment on different fabrics; the shade also depends on the dyeing conditions (the temperature, pH, and use of mordants).

Pigment production using certain bacteria can be altered by using different conditions during growth. For example, Alihoseini et al. investigated the possibility of mutating *Vibrio gazogenes* to selectively develop the best pigment-producing strain capable of imparting, in addition to color, durable antimicrobial activity against *E. coli* and *S. aureus* to textile materials [16]. On the other hand, Kanelli et al. optimized the culture conditions of *Janthinobacterium lividum* for pigment (violacein) production and the simultaneous dyeing of fabrics, which resulted in dyed fabrics with significant antifungal activity against several *Candida* pathogens, *C. albicans*, *C. parapsilosis* and *C. krusei*, as well as antibacterial properties against *Escherichia coli*, *Staphylococcus aureus* and the methicillin-resistant *S. aureus*, MRSA [17].

## 3. Dyeing of Textile Materials with Biopigments

### *3.1. Type of Bacteria Used for Textile Dyeing and Resulting Color*

Bacterial pigments have a wide range of colors that can be utilized in textile dyeing, as mentioned above. However, not all pigments can impart color to different textile materials. This is mostly related to the structures of the pigments and how they bond to fibers during dyeing. In Table 1, an overview of various pigments and their current use in the dyeing of different textile materials is given. As can be seen from the table, the most commonly used bacterial extracts frequently have prodigiosin, violacein, and melanin as major components. Their molecular structure is given in Figure 3.

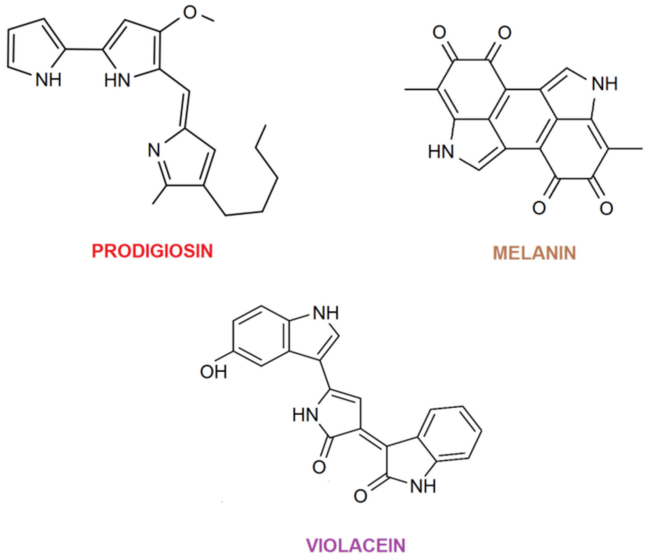


**Figure 3.** Molecular structure of prodigiosin, melanin and violacein.

By observing their molecular structure, it can be concluded that these compounds have the ability to produce ionic interactions with textile fibers, depending on the pH of the used dyebath, which is also proven to be important during dyeing [18]. Prodigiosin is mostly known as an antibacterial, antioxidative pigment, even exhibiting UV-protective properties [5,13,19]. Violacein is known as an antifungal, antibacterial, antiparasitic and antitumoral pigment, while melanin has anticancer properties [5,17].

**Table 1.** Overview of different pigment-producing bacteria, use of pigments for different textile materials, colors of the pigments and resulting colors of textiles, as well as auxiliaries in the dyeing process.

| Pigment/Active Substance | Textile Material | Color of Pigment/Color of Dyed Material | Use of Mordants | Reference |
|---|---|---|---|---|
| *Chromobacterium violaceum UTM5/violacein* | cotton, silk, rayon, polyester | violet/dark blue | alum, $Fe_2(SO_4)_3$, $CuSO_4$, $Ca(OH)_2$ | [20] |
| *Janthinobacterium lividu*/violacein | polyamide 6.6 | deep purple/purple | / | [17] |
| *Serratia marcescens SB08/prodigiosin* | cotton, silk | dark red/pink | $Na_2SO_4$ | [21,22] |
| *Serratia marcescens /prodigiosin* | cotton, nylon, polyester, muslin, rubber | red/pink | / | [10] |
| *Serratia rubidaea*/prodigiosin | cotton, wool, polyester | dark pink/pink | $FeSO_4$, $CuSO_4$, $NaHCO_3$, lemon | [23,24] |
| *Serratia sakuensis*/prodigiosin | cotton, silk, wool | red/red-pink | $Na_2SO_4 \cdot 10H_2O$ | [25] |
| *Rhodonellum psychrophylium* GL8/prodigiosin | cotton, silk, rayon | dark red/red | NaCl | [26] |
| *Serathia plymuthica*/prodigiosin | bacterial cellulose, polyvinyl alchohol chitosan nanofibers | red/pink | / | [27] |
| *Streptomyces virginiae*/melanin | wool (dyeing and printing) | yellow, light brown, dark brown | / | [28] |
| *Pseudomonas aureginosa*/pyocyanin | polyester | blue-green/yellow | / | [29] |

**Table 1.** *Cont.*

| Pigment/Active Substance | Textile Material | Color of Pigment/Color of Dyed Material | Use of Mordants | Reference |
|---|---|---|---|---|
| *Serratia* sp. *KH-1*/prodigiosin | cotton and wool | red/pink | tannic acid, FeSO4, CuSO4, NaCl, ammonium alum ($(NH_4)Al(SO_4)_2$) | [30] |
| *Pseudomonas* sp. *HOB1*/indigo | cotton | blue/blue | aluminum, NaOH | [31] |
| *Streptomyces* sp. NP2 and NP4/prodigiosin | multifiber fabric | dark red/red-pink | / | [18] |
| *Streptomyces* sp. NP4/prodigiosin | viscose | dark red/red-blue | / | [32] |

According to Table 1, it is obvious that there is a limitation on the possible colors that can be imparted to textile materials. Currently successful dyeing procedures make it possible to obtain materials in pink, red, violet, blue and brown color. Furthermore, the authors of some studies have used mordants to improve dyeing ability, while in other studies, it was possible to dye textiles without mordants. This is further explored in next section.

### *3.2. Dyeing Procedure Using Biopigments*

Bacterial pigments or dyes are usually prepared for dyeing as a solution of extract in a liquid [4]. The extract is cultured and purified and can be utilized further for dyeing through the dissolution/suspension of the pigmented extract to a suitable solvent. Other dyeing parameters include pH, temperature and the use of auxiliaries; the conditions are chosen according to the pigment and fabric/fiber type.

The usual procedure for the dyeing of textiles with bacterial pigments follows the scheme given in Figure 4.

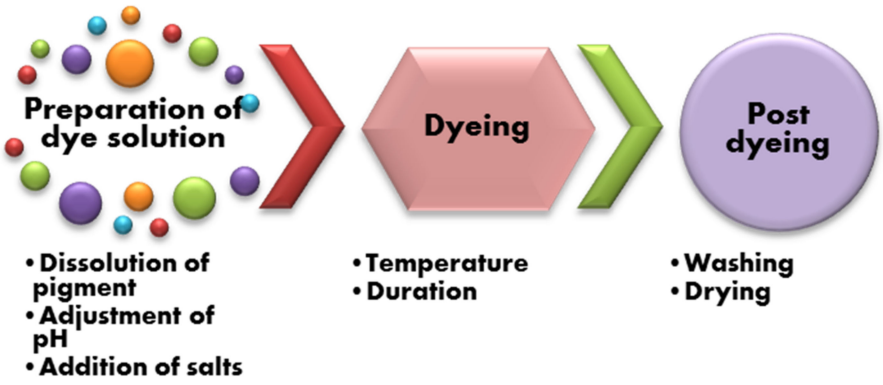


**Figure 4.** Scheme of phases for preparation and dyeing of textile material using microbial pigment.

The first step, the preparation of the solution, is important to ensure the proper dissolution of the pigment. Dissolution depends on the nature of the pigment; bacterial pigments are usually soluble in ethanol [24,33,34], methanol [8,18,35,36] or acetone [32]. Kramar et al. [32] used a pigment that was previously presented as soluble in a methanol/water system [18], but their new work showed that the same pigment can be dissolved in an acetone/water (1:99) system, thus obtaining a highly ecofriendly dyebath with a high exhaustion rate [32]. In this case, the bacterial extract was dissolved in acetone, rendering a highly concentrated solution that was later diluted with water to produce a dyebath with a desirable concentration.

In fact, the preparation of dyebaths using acetone, ethanol or water is considered highly ecofriendly and can lead to the production of sustainable dyebaths. In the future, researchers should aim to investigate the possible recycling and reuse of the excess dye from dyebaths or the decolorization of unused dye from liquid waste, thus closing the loop of the dyeing procedure with bacterial colorants.

### *3.3. The pH and Temperature Used for Dyeing Textiles with Biopigments*

In textile dyeing, the pH should always be optimized and chosen according to the type of textile material used. For cellulose and other plant-based materials, a higher pH is desirable, while for protein-based fibers (wool, silk) acidic dyebaths are acceptable.

In a study by Gong et al. [37], the authors used a suspension of prodigiosin nanomicelle for dyeing and obtaining antimicrobial cotton at a very low pH of 3. In this study, particularly interesting was the step involving the extraction of the nanomicelles that were used for the dyeing. Surfactant Tween 80 was added to the culture media and the pigment from the bacteria cells of *Serratia marcescens* migrated from the bacteria cells to the surfactant micelle under continuous oscillation. Upon preparation for dyeing, the pH of the suspension was adjusted to pH 1–5 and under acidic conditions and a higher dyeing temperature (90 °C), the nanomicelle of the surfactant-containing pigment broke down, releasing prodigiosin into the solution and penetrating the cotton fiber. The highest color intensity was obtained when the dyebath had a pH of 3. However, dyebaths with low pH are not desirable if used with cellulose-based materials, since this can lead to the degradation of cellulose under acidic conditions.

In addition to assessing the pH of the dyebath according to fiber type, it is important to determine whether a chosen bacterial extract is sensitive to pH.

Prodigiosin is known to possess pH sensitivity [18,22,25]. For example, an increase in the pH of the ethanol solution of prodigiosin obtained from *Serratia marscences* changed the color of the solution from pink, in a pH range of 2–8, to yellow, for a pH of 10–12 [22]. Pigment from *Serratia sakuensis* exhibits pH sensitivity, producing different-colored solutions at pH 4 (pink), pH 5 (red), pH 7 (orange) and pH 9 (yellow) [25].

Another study, using prodigiosin from the strains *Streptomyces* sp. NP2 and NP4, showed that an extracted pigment and its solution in water–methanol exhibited a brownish-to-red color at low pH values of 3.5 and 4.5 and gray-to-blue at a pH of 8 [18]. Additionally, the strongest color was obtained in polyamide and triacetate fabrics (Figure 5), and a fair color intensity was achieved on polyester PES and polyacrylonitrile PAN. Dyeing in solutions of different pH induced different shades and colors in the multifiber fabric, as seen in Figure 5.

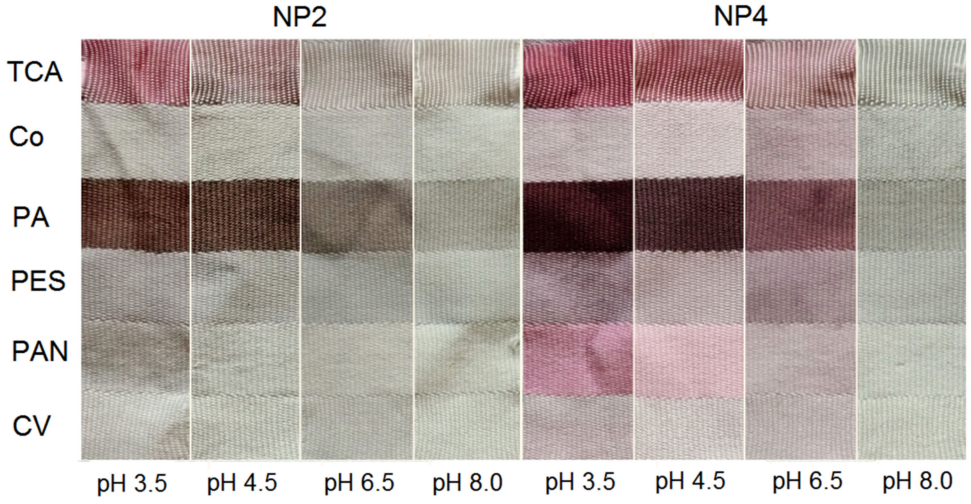


**Figure 5.** Multifiber fabric (TCA-cellulose triacetate, co-cotton, PA-polyamide, PES-polyester, PAN-polyacrylonitrile, CV-viscose) dyed with prodigiosin isolated from *Streptomyces* sp. strains NP2 and NP4 in dyebaths with different pH (reprinted with permission from reference [18]. Copyright 2014 Springer).

The temperature of the dyebath significantly affects the dyeing performance of bacterial dyes, i.e., dyeing rate and color depth. Furthermore, the extent of the dyeing differs according to the duration of the immersion in the dye bath. For example, Shirata et al. [7] used the methanol solution of a pigment isolated from *Janthinobacterium lividum* to dye silk

fabric and achieve color variation in the dyed silk fabric by changing the dipping time and temperature of the dye bath. To achieve the color depth obtained after 15 min of dyeing at 20 °C, the immersion time at 40 °C was decreased down to 5 min, at 60 °C to 1 min and at 70 °C to only 30 s. The immersion times required for the color depth obtained after 6 h at 20 °C were one day at 10 °C and three days at 0 °C.

The influences of various dyeing conditions, including the pigment concentration (2–14% owl), pH (4–9), retention time (20–120 min) and temperature (20–90 °C), on the dyeing of pure silk, China silk and cotton yarns with pigment from *Serratia marcescens* SB08 was studied by Venil et al. [21]. The optimized conditions for effective dyeing, namely a pigment concentration of 5% owl, a pH of 6, a retention time of 100 min and temperatures of 70 °C for pure silk and 60 °C for China silk and cotton, resulted in maximum pigment exhaustions of 96.0%, 90.0% and 81.6% for pure silk, China silk and cotton, respectively.

In addition to the color depth and dye exhaustion, the dyeing parameters, such as the pH values and temperatures, can affect the results of dyeing, which cannot be easily predicted. For example, the pigment isolated from *Pseudomonas Aeruginosa* was blue under alkali pH, but the color of dyed polyester was yellow [29], which was explained by the pyrolisis of the pigment pyocynanin when the dyeing was performed at 130 °C, since PES dyeing requires high temperatures. This also shows that it is important to determine the sensitivity of pigments that are intended to be used for dyeing at both different pH values and different temperatures.

### *3.4. Mordants Used for Dyeing Textile with Biopigments*

Mordants are salts that are frequently used as additives in dyebaths to improve the fixation of natural dyes to fibers [1,38]. Mordants form complexes with dyes and are additionally able to attach to the surfaces of fibers, thus increasing the exhaustion of dyebaths and improving the washing fastness of dyed fabrics. Frequently used conventional mordants are aluminum, iron and copper salts, among others [38]. Furthermore, mordants influence the resulting shade on the material; this was demonstrated in [24], where the uses of various mordants were tested during dyeing with prodigiosin pigment extracted from marine *Serratia rubidaea* RAM_Alex bacteria. The fabrics exhibited different shades and hues, as shown in Figure 6. The lowest color depth in all the samples was obtained using $CuSO_4$ salt, while for other types of mordants, the color intensity was satisfying; the color hue strongly depended on the type of mordant.

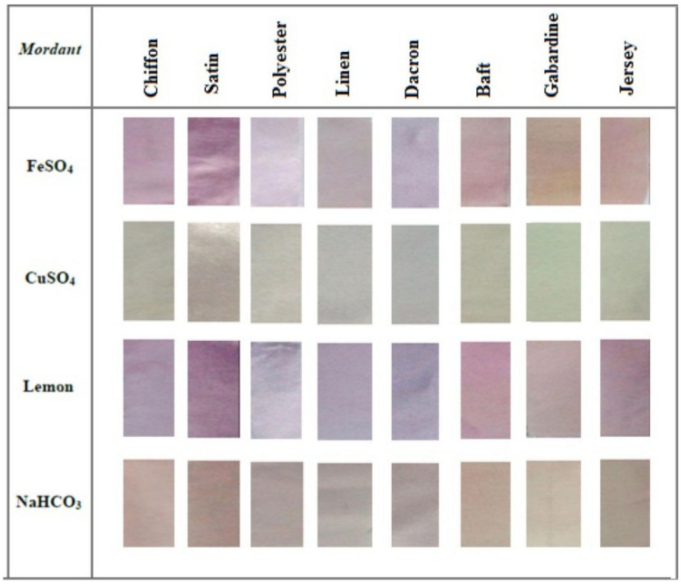


**Figure 6.** Different color hues obtained after applying different mordants (Reprinted with permission from reference [24]. Copyright 2021 Elsevier).

Kim and Choi [34] studied the addition of Al, Fe, Cu and Ti mordants for the dyeing of silk using prodiginin extracted from *Zooshikella rubidus*. They concluded that Al and Ti mordants have a significant positive impact on dye uptake during dyeing with this pigment. The washing fastness, rubbing, perspiration and dry-cleaning of the dyed fabrics were good, except the light fastness, which was poor even with the use of mordants.

Another pigment from actinobacteria [39] can be used, for example, as a textile colorant and lip-balm colorant. When used with wool and cotton, dyeing with the addition of 5% $FeSO_4$ and $CuSO_4$ salt improved washing fastness. Additionally, the pigment exhibited antioxidant and hemolytic activity; however, the authors studied these properties only on pigment and not on samples dyed with this pigment.

From these results, it can be concluded that the type of mordant used in dyeing is dependent on the bacteria strain rather than the major component of the pigment, since for the same type (e.g., prodigiosin), different mordants were proven to be effective for the resulting colors.

As shown in Table 1, there are various successful investigations of dyeing without using any kind of mordant. For example, prodigiosin pigment can be used without purification and without the addition of mordant when isolated from *Vibrio* sp. [8] or *Streptomyces* sp. [18].

Prodigiosin from *Vibrio* sp. has the ability to impart colors to a wide range of fabrics without mordant (Figure 7), providing the highest color intensity on modacrylic, polyamide PA 6.6, silk and wool.

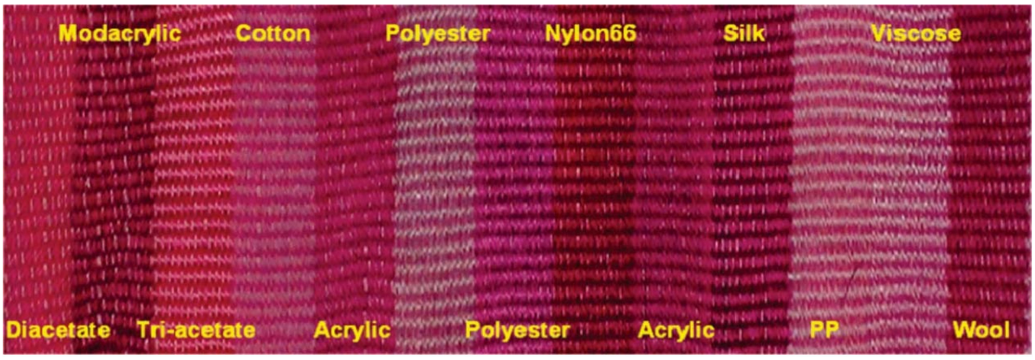


**Figure 7.** Multifiber fabrics dyed with prodigiosin isolated from *Vibrio* sp. KSJ45 (reprinted with permission from reference [8]. Copyright 2008 Wiley).

## 4. Other Properties of Biopigments for Obtaining Functional Textile Materials

Since bacterial dyes show various additional properties, including antimicrobial, anticancer and antioxidative activity, among others, in the future, researchers should aim to study whether these properties could be imparted to textiles to obtain materials for special applications. Among many, the most important properties are antimicrobial, antioxidative and antitumoral activity [5]. In several studies, it has been shown that some of those properties can be transferred to dyed textile materials.

Venil et al. [21] used pigment from *Serracia marscensc* SB08 to dye silk and cotton. Additionally, these fabrics and yarns exhibited a good level of antibacterial activity and zone of inhibition against pathogenic bacteria, namely *B. subtillis*, *E. coli* and *P. aeruginosa*.

Ren et al. [22] studied the utilization of prodigiosin from *Serratia marscences* to dye silk. In addition to its good coloration, the dyed fabric showed an excellent bacteriostatic rate against *S. aureus*, while a cytotoxicity test indicated that the dyed fabric was not cytotoxic.

A very interesting study explored the addition of prodigiosin isolated from *Serratia plymuthica* to composite nanofibers prepared from PVA/chitosan/bacterial cellulose [27] to obtain antimicrobial food packaging films. Prior to the addition of prodigiosin, the bacterial cellulose was TEMPO-oxidized. Furthermore, the authors investigated different routes to the production of an antibacterial layer by adding prodigiosin in PVA/CH solution prior to electrospinning and adding the whole layer to the bacterial cellulose (Figure 8).

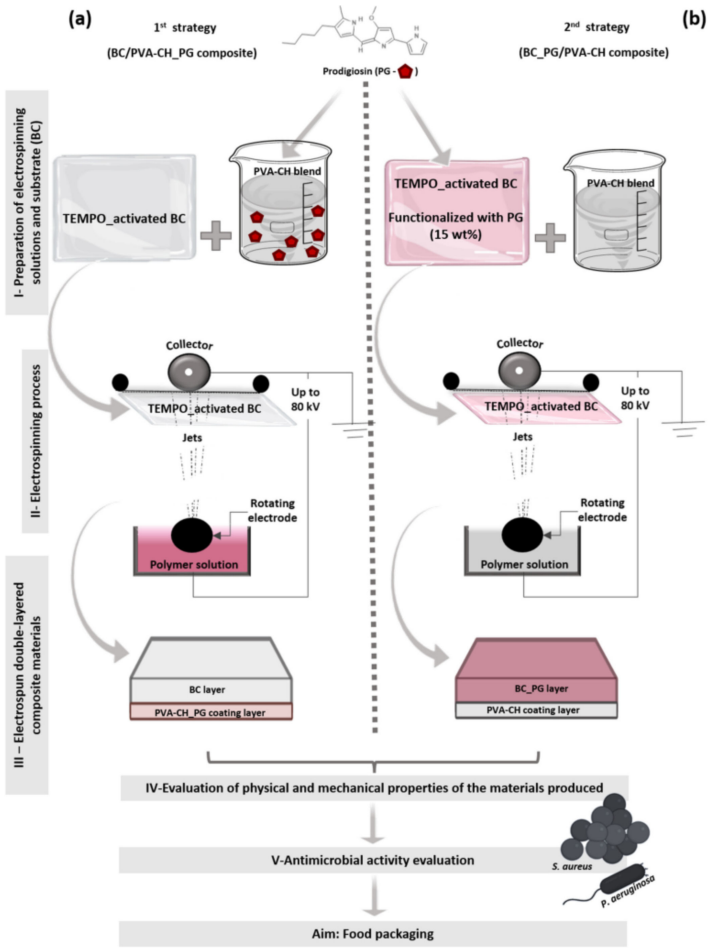


**Figure 8.** Schematic representation of the production strategies used in composite preparation: (**a**) BC/PVA-CH_PG composite, with TEMPO-activated BC, used as a substrate for PVA-CH_PG nanofiber deposition; (**b**) BC_PG/PVA-CH composite, with PVA-CH nanofiber deposition in TEMPO-activated BC, previously functionalized with PG (reprinted with permission from reference [27]. Copyright 2022 MDPI).

Gao et al. [34] studied the synergistic effect of the bacterial pigment, violacein, and silver nanoparticles for imparting antimicrobial activity to silk. Finishing the silk with only violacein produced a good antimicrobial effect on *S. aureus* (81.25% reduction); however, the synergistic effect of the pigment and AgNP provided excellent antimicrobial activity against all the tested pathogens, *S. aureus, E. coli* and *C. albicans*, producing a reduction of over 99.9% (Figure 9).

Similarly, pigment violacein produced by *Janthinobacterium lividum*, when combined with silver and titanium dioxide nanoparticles, was shown to impart excellent antimicrobial properties [40]. The authors coated a viscose fabric, after pigment dyeing, with silver and titanium dioxide nanoparticles and concluded that the violacein created a hybrid with the nanoparticles, causing greater antimicrobial activity against *E. coli* than only dyed fabric.

The antimicrobial activity imparted by bacterial pigments can be also influenced by the type of knitted textile that is used for dyeing, as shown in [24]. *Serratia rubidaea* RAM_Alex produces a prodigiosin-type pigment [24]. This pigment can dye a wide range of different fabrics and it was interesting to study the influence of the type of fabric on coloration (Figure 10). Cotton fabrics (baft, gabardine and jersey), linen and synthetic fabrics (chiffon, satin, Dacron and polyester) were used. The authors did not give the detailed fiber composition of the synthetic fabrics used in this work. The antimicrobial

activity against *S. aureus* and *E. coli* was exceptionally high for all the fabrics, except for gabardine. This type of fabric also exhibited low color intensity, which may have been related to the fact that this type of fabric is very tight and densely woven.

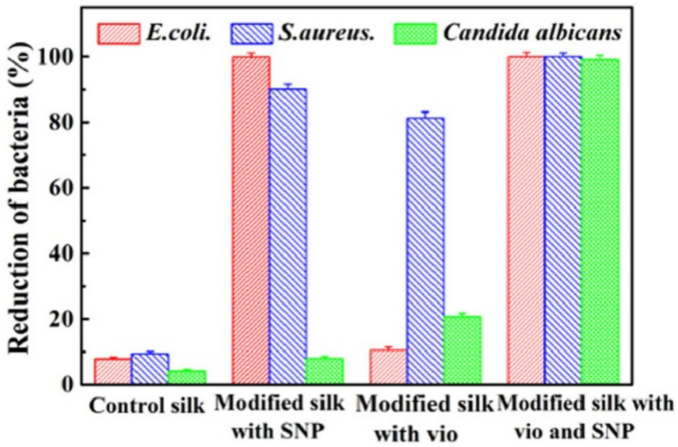


**Figure 9.** Differences in antimicrobial activity against *S. aureus*, *E. coli* and *C. albicans* of silk modified with only silver nanoparticles (SNP), only violacein pigment (vio) and with combined treatment (reprinted with permission from reference [34]. Copyright 2019. Elsevier).

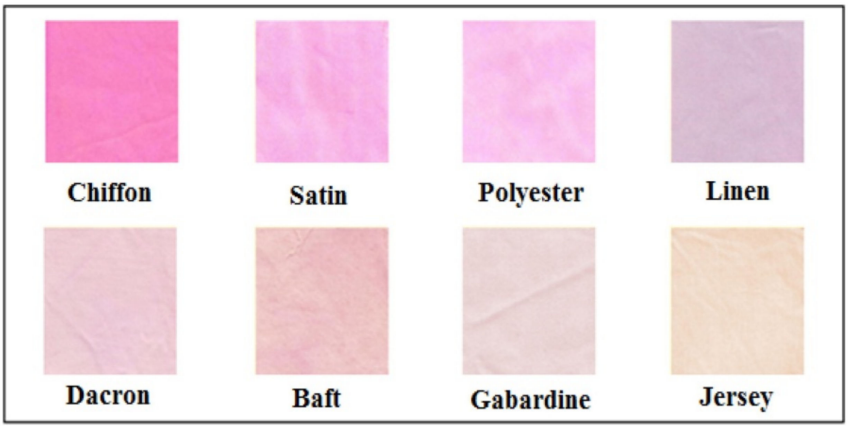


**Figure 10.** Fabrics of different weaving patterns dyed with *Serratia rubidaea* RAM_Alex prodigiosin (Reprinted with permission from reference [24]. Copyright 2021 Elsevier).

Kramar et al. successfully developed a pH-sensitive viscose fabric using prodigiosin pigment isolated from *Streptomyces* sp. NP4 [32]. The fabric was functionalized prior to dyeing following an oxidation procedure and the deposition of chitosan to make it susceptible to dyeing with this pigment. As can be seen (Figure 11, left), the bacterial isolate possessed pH sensitivity, which was preserved and imparted to the dyed viscose cellulose fabric after dyeing (Figure 11, right). The functionalized and dyed fabric showed pH responsiveness in a wide range of pH, from 4 to 10 (Figure 11); the fabrics showed no cytotoxicity and the authors proposed that the material can be used as a burn-dressing indicator, since severe burns cause an increases in the pH of wounds, while healing lowers the pH.

This represents a novel approach to obtaining color-changing textiles dyed with prodigiosin, a color changing-pigment. Future research could also focus on this aspect of investigating the pH sensitivity of natural bacterial dyes and the possibility of obtaining pH-sensitive textile materials, thereby obtaining high-value products.

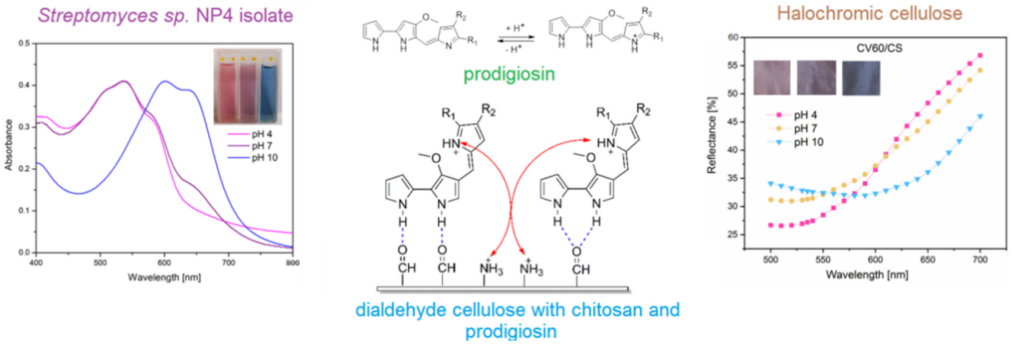


**Figure 11.** Schematic representation of interaction between oxidized viscose (dialdehyde cellulose) and deposited chitosan and color-changing prodigiosin isolate to obtain pH-sensitive color-changing fabric (reprinted with permission from reference [32] Copyright 2021 Springer).

## 5. Conclusions

The new and emerging field of the application of bacterial dyes in the textile industry has received a significant amount of research interest in recent years. Bacterial pigments or dyes are natural, sustainable and environmentally friendly alternatives to the synthetic dyes that have been used in the textile industry for decades. Further research is encouraged, especially towards exploring new pigments and investigating their potential use as textile colorants. No less important is the fact that besides color, these dyes possess additional functionalities, such as antimicrobial, antioxidative and anticancer properties, among many others, which could be used to prepare special textile materials with ecofriendly, sustainable and nontoxic compounds. There are already several successful procedures for obtaining durable colors on textile materials and, additionally, imparting antimicrobial or color-changing properties. There are, however, almost endless possibilities and combinations of different bacterial pigments to investigate with different types of fibers; moreover, it is possible to investigate their combinations with other antimicrobial compounds, such as metallic nanoparticles, which can be used to produce materials with exceptionally high antibacterial activity.

Currently, for successful textile dyeing, most biopigments contain prodigiosin, melanin, and violacein. As was shown, different strains of bacteria produce the same compound, such as, for example, prodigiosin, but these bacterial metabolites have different abilities to dye certain types of textile fiber. This leads to the conclusion that there is a need for future research regarding dye–fiber interactions in the coloration of textiles using bacterial dyes, in order to elucidate the exact mechanism behind the successful dyeing of textiles and, moreover, to establish exact and predictive protocols for the possible future use of these dyes on an industrial scale. The current limitations of these studies lie in the fact that the majority of the presented research is focused more on the isolation and general application of bacterial dyes for textile dyeing, rather than on in-depth studies of dye–fiber interactions. Moreover, there is still a need to expand research in two directions: the first should focus on exploring more metabolites with dyeing potential and widening the range of colors that can be extracted from bacteria in order to compete with synthetic dyes and consumer demands. Current research covers only limited shades of pink, red, violet and blue. Another direction that should be strengthened the repeatability and durability of achieved colors on materials, the impact of dyes on the physicomechanical properties of textiles and their influence on consumers in terms of potential cytotoxicity and safety of use.

Nevertheless, research regarding bacterial pigments and dyes can bring sustainability to the textile industry and improve its environmental impact and safety.

**Author Contributions:** Conceptualization A.K. and M.M.K.; writing—original draft preparation, A.K.; writing—review and editing M.M.K.; supervision M.M.K. All authors have read and agreed to the published version of the manuscript.

**Funding:** This work was supported by the Ministry of Education, Science and Technological Development of the Republic of Serbia (contract no. 451-03-68/2022-14/200135).

**Institutional Review Board Statement:** Not applicable.

**Informed Consent Statement:** Not applicable.

**Data Availability Statement:** Not applicable. All data are available in the review and references herein.

**Acknowledgments:** We thank Jasmina Nikodinović-Runić and Tatjana Ilić-Tomić from the Institute of Molecular Genetics and Genetic Engineering, University of Belgrade for introducing us to the world of bacterial pigments and our fruitful collaboration over many years.

**Conflicts of Interest:** The authors declare no conflict of interest.

## Abbreviations

| | |
|---|---|
| AgNP | silver nanoparticles |
| BC | bacterial cellulose |
| CH | chitosan |
| PA 6.6 | polyamide 6.6 |
| PAN | polyacrylonitrile |
| PES | polyester |
| PVA | poly (vinyl alcohol) |
| TEMPO | (2,2,6,6-Tetramethylpiperidin-1-yl) oxyl |
| UV | ultraviolet |

## References

1. Bechtold, T.; Turcanu, A.; Ganglberger, E.; Geissler, S. Natural dyes in modern textile dyehouses-How to combine experiences of two centuries to meet the demands of the future? *J. Clean. Prod.* **2003**, *11*, 499–509. [CrossRef]
2. Hill, D.J. Is there a future for natural dyes? *Rev. Prog. Color. Relat. Top.* **1997**, *27*, 18–25. [CrossRef]
3. Venil, C.K.; Zakaria, Z.A.; Ahmad, W.A. Bacterial pigments and their applications. *Process Biochem.* **2013**, *48*, 1065–1079. [CrossRef]
4. Aman Mohammadi, M.; Ahangari, H.; Mousazadeh, S.; Hosseini, S.M.; Dufossé, L. Microbial pigments as an alternative to synthetic dyes and food additives: A brief review of recent studies. *Bioprocess Biosyst. Eng.* **2022**, *45*, 1–12. [CrossRef]
5. Narsing Rao, M.P.; Xiao, M.; Li, W.J. Fungal and bacterial pigments: Secondary metabolites with wide applications. *Front. Microbiol.* **2017**, *8*, 1–13. [CrossRef]
6. Vicente, A.; Hernández, F.G.; Thibaut, R.; Müller, A. Fungal dyes for textile applications: Testing of industrial conditions for wool fabrics dyeing. *J. Text. Inst.* **2019**, *110*, 61–66.
7. Shirata, A.; Tsukamoto, T.; Yasui, H.; Hata, T.; Hayasaka, S.; Kojima, A.; Kato, H. Isolation of bacteria producing bluish-purple pigment and use for dyeing. *Jpn. Agric. Res. Q.* **2000**, *34*, 131–140.
8. Alihosseini, F.; Ju, K.S.; Lango, J.; Hammock, B.D.; Sun, G. Antibacterial colorants: Characterization of prodiginines and their applications on textile materials. *Biotechnol. Prog.* **2008**, *24*, 742–747. [CrossRef]
9. Venil, C.K.; Wahidin, M.A.B.; Aruldass, C.A.; Ahmad, W.A. Production of bacterial pigments in low cost medium and formulation of biodegradable ink. *Indian J. Exp. Biol.* **2017**, *55*, 441–447.
10. El-Bialy, H.A.; Abou El-Nour, S.A. Physical and chemical stress on Serratia marcescens and studies on prodigiosin pigment production. *Ann. Microbiol.* **2015**, *65*, 59–68. [CrossRef]
11. Mazotto, A.M.; De Ramos Silva, J.; De Brito, L.A.A.; Rocha, N.U.; De Souza Soares, A. How can microbiology help to improve sustainability in the fashion industry? *Environ. Technol. Innov.* **2021**, *23*, 101760. [CrossRef]
12. Mumtaz, R.; Bashir, S.; Numan, M.; Shinwari, Z.K.; Ali, M. Pigments from Soil Bacteria and Their Therapeutic Properties: A Mini Review. *Curr. Microbiol.* **2019**, *76*, 783–790. [CrossRef]
13. Stankovic, N.; Senerovic, L.; Ilic-Tomic, T.; Vasiljevic, B.; Nikodinovic-Runic, J. Properties and applications of undecylprodigiosin and other bacterial prodigiosins. *Appl. Microbiol. Biotechnol.* **2014**, *98*, 3841–3858. [CrossRef]
14. Malik, K.; Tokkas, J.; Goyal, S. Microbial Pigments: A review. *Int. J. Microb. Resour. Technol.* **2012**, *1*, 361–365.
15. Usman, H.M.; Abdulkadir, N.; Gani, M.; Maiturare, H.M. Bacterial Pigments and its Significance. *MOJ Bioequivalence Bioavailab.* **2017**, *4*, 285–288. [CrossRef]
16. Alihosseini, F.; Lango, J.; Ju, K.S.; Hammock, B.D.; Sun, G. Mutation of bacterium Vibrio gazogenes for selective preparation of colorants. *Biotechnol. Prog.* **2010**, *26*, 352–360. [CrossRef]
17. Kanelli, M.; Mandic, M.; Kalakona, M.; Vasilakos, S.; Kekos, D.; Nikodinovic-Runic, J.; Topakas, E. Microbial production of violacein and process optimization for dyeing polyamide fabrics with acquired antimicrobial properties. *Front. Microbiol.* **2018**, *9*, 1–13. [CrossRef]

18. Kramar, A.; Ilic-Tomic, T.; Petkovic, M.; Radulović, N.; Kostic, M.; Jocic, D.; Nikodinovic-Runic, J. Crude bacterial extracts of two new Streptomyces sp. isolates as bio-colorants for textile dyeing. *World J. Microbiol. Biotechnol.* **2014**, *30*, 2231–2240. [CrossRef]
19. Stankovic, N.; Radulovic, V.; Petkovic, M.; Vuckovic, I.; Jadranin, M.; Vasiljevic, B.; Nikodinovic-Runic, J. Streptomyces sp. JS520 produces exceptionally high quantities of undecylprodigiosin with antibacterial, antioxidative, and UV-protective properties. *Appl. Microbiol. Biotechnol.* **2012**, *96*, 1217–1231. [CrossRef]
20. Venil, C.K.; Yusof, N.Z.; Aruldass, C.A.; Ahmad, W.A. Application of violet pigment from Chromobacterium violaceum UTM5 in textile dyeing. *Biologia* **2016**, *71*, 121–127. [CrossRef]
21. Venil, C.K.; Dufossé, L.; Velmurugan, P.; Malathi, M.; Lakshmanaperumalsamy, P. Extraction and Application of Pigment from Serratia marcescens SB08, an Insect Enteric Gut Bacterium, for Textile Dyeing. *Textiles* **2021**, *1*, 3. [CrossRef]
22. Ren, Y.; Gong, J.; Fu, R.; Zhang, J.; Fang, K.; Liu, X. Antibacterial dyeing of silk with prodigiosins suspention produced by liquid fermentation. *J. Clean. Prod.* **2018**, *201*, 648–656. [CrossRef]
23. Siva, R.; Subha, K.; Bhakta, D.; Ghosh, A.R.; Babu, S. Characterization and enhanced production of prodigiosin from the spoiled coconut. *Appl. Biochem. Biotechnol.* **2012**, *166*, 187–196. [CrossRef]
24. Metwally, R.A.; El Sikaily, A.; El-Sersy, N.A.; Ghozlan, H.A.; Sabry, S.A. Antimicrobial activity of textile fabrics dyed with prodigiosin pigment extracted from marine Serratia rubidaea RAM_Alex bacteria. *Egypt. J. Aquat. Res.* **2021**, *47*, 301–305. [CrossRef]
25. Vaidyanathan, J.; Bhathena-Langdana, Z.; Adivarekar, R.V.; Nerurkar, M. Production, partial characterization, and use of a red biochrome produced by Serratia sakuensis subsp. nov strain KRED for dyeing natural fibers. *Appl. Biochem. Biotechnol.* **2012**, *166*, 321–335. [CrossRef]
26. Bisht, G.; Srivastava, S.; Kulshreshtha, R.; Sourirajan, A.; Baumler, D.J.; Dev, K. Applications of red pigments from psychrophilic Rhodonellum psychrophilum GL8 in health, food and antimicrobial finishes on textiles. *Process Biochem.* **2020**, *94*, 15–29. [CrossRef]
27. Amorim, L.F.A.; Mouro, C.; Riool, M.; Gouveia, I.C. Antimicrobial Food Packaging Based on Prodigiosin-Incorporated Double-Layered Bacterial Cellulose and Chitosan Composites. *Polymers* **2022**, *14*, 315. [CrossRef]
28. Amal, A.M.; Abeer, K.A.; Samia, H.M.; Nadia, A.E.-N.H.; Ahmed, K.A.; El-Hennawi, H.M. Selection of pigment (melanin) production in Streptomyces and their application in printing and dyeing of wool fabrics. *Res. J. Chem. Sci.* **2011**, *1*, 22–28.
29. Govindaraj, C.; Ugamoorthi, R.; Ramarethinam, S. Isolation of pseudomonas aeruginosa for bacterial pigment production and its application on synthetic knitted fabric. *Indian J. Fibre Text. Res.* **2021**, *46*, 168–173.
30. Chauhan, K.; Dalsaniya, P.; Pathak, H. Optimization of prodigiosin-type biochrome production and effect of mordants on textile dyeing to improve dye fastness. *Fibers Polym.* **2015**, *16*, 802–808. [CrossRef]
31. Pathak, H.; Madamwar, D. Biosynthesis of indigo dye by newly isolated naphthalene-degrading strain pseudomonas sp. HOB1 and its application in dyeing cotton fabric. *Appl. Biochem. Biotechnol.* **2010**, *160*, 1616–1626. [CrossRef] [PubMed]
32. Kramar, A.D.; Ilic-Tomic, T.R.; Lađarević, J.M.; Nikodinovic-Runic, J.B.; Kostic, M.M. Halochromic cellulose textile obtained via dyeing with biocolorant isolated from Streptomyces sp. strain NP4. *Cellulose* **2021**, *28*, 8771–8784. [CrossRef]
33. Kim, Y.; Choi, J. Dyeing properties of microbial prodiginine from Zooshikella rubidus for silk fabrics. *Fibers Polym.* **2015**, *16*, 1981–1987. [CrossRef]
34. Gao, A.; Chen, H.; Hou, A.; Xie, K. Efficient antimicrobial silk composites using synergistic effects of violacein and silver nanoparticles. *Mater. Sci. Eng. C* **2019**, *103*, 109821. [CrossRef]
35. Mohammed, S.J.; Luti, K.J.K. A kinetic model for prodigiosin production by Serratia marcescens as a bio-colorant in bioreactor. *AIP Conf. Proc.* **2020**, *2213*, 020027. [CrossRef]
36. Chauhan, R.; Choudhuri, A.; Abraham, J. Evaluation of antimicrobial, cytotoxicity, and dyeing properties of prodigiosin produced by Serratia marcescens strain JAR8. *Asian J. Pharm. Clin. Res.* **2017**, *10*, 279–283. [CrossRef]
37. Gong, J.; Ren, Y.; Fu, R.; Li, Z.; Zhang, J. pH-mediated antibacterial dyeing of cotton with prodigiosins nanomicelles produced by microbial fermentation. *Polymers* **2017**, *9*, 468. [CrossRef]
38. Shahid, M.; Shahid-Ul-Islam; Mohammad, F. Recent advancements in natural dye applications: A review. *J. Clean. Prod.* **2013**, *53*, 310–331. [CrossRef]
39. Chakraborty, I.; Redkar, P.; Munjal, M.; Sathish Kumar, S.R.; Bhaskara Rao, K.V. Isolation and characterization of pigment producing marine actinobacteria from mangrove soil and applications of bio-pigments. *Der Pharm. Lett.* **2015**, *7*, 93–100.
40. Khaksar, F.; Rigi, G.; Mirdamadian, S.H. Creation of a violacein pigment hybrid with silver and titanium dioxide nanoparticles to produce multifunctional textiles with antimicrobial properties. *Nanomed. Res. J.* **2021**, *6*, 60–72. [CrossRef]

*textiles*

MDPI

*Article*

# Loop Order Analysis of Weft-Knitted Textiles

**Levi Kapllani [1,2], Chelsea Amanatides [2], Genevieve Dion [2,3] and David E. Breen [1,2,*]**

[1] Computer Science Department, Drexel University, Philadelphia, PA 19104, USA; lk489@drexel.edu
[2] Center for Functional Fabrics, Drexel University, Philadelphia, PA 19104, USA; cek56@drexel.edu (C.A.); gd63@drexel.edu (G.D.)
[3] Design Department, Drexel University, Philadelphia, PA 19104, USA
* Correspondence: david@cs.drexel.edu

**Abstract:** In this paper, we describe algorithms that perform loop order analysis of weft-knitted textiles, which build upon the foundational TopoKnit topological data structure and associated query functions. During knitting, loops of yarn may be overlayed on top of each other and then stitched together with another piece of yarn. Loop order analysis aims to determine the front-to-back ordering of these overlapping loops, given a stitch pattern that defines the knitted fabric. Loop order information is crucial for the simulation of electrical current, water, force, and heat flow within functional fabrics. The new algorithms are based on the assumption that stitch instructions are executed row-by-row and for each row the instructions can be executed in any temporal order. To make our algorithms knitting-machine-independent, loop order analysis utilizes precedence rules that capture the order that stitch commands are executed when a row of yarn loops are being knitted by a two-bed flat weft knitting machine. Basing the algorithms on precedence rules allows them to be modified to adapt to the analysis of fabrics manufactured on a variety of knitting machines that may execute stitch commands in different temporal orders. Additionally, we have developed visualization methods for displaying the loop order information within the context of a TopoKnit yarn topology graph.

**Keywords:** knitted textiles; topological modeling; contact neighborhood; loop order analysis; precedence rule; visualization

**Citation:** Kapllani, L.; Amanatides, C.; Dion, G.; Breen, D.E. Loop Order Analysis of Weft-Knitted Textiles. *Textiles* **2022**, *2*, 275–295. https://doi.org/10.3390/textiles2020015

Academic Editors: Philippe Boisse and Laurent Dufossé

Received: 13 April 2022
Accepted: 11 May 2022
Published: 18 May 2022



## 1. Introduction

Throughout history, knitting as a manufacturing technique has been mostly used for clothing. However, knitted textiles offer great promise in other applications due to their mechanical and physical properties. While knitted textiles have become increasingly important to many industries (e.g., medical, military, etc.) in the last decades, the lack of computer modeling and simulation tools have limited the ability of knitted textiles to be widely deployed. There is a need to robustly design and model knitted textiles in a manner similar to those used for vehicles, buildings, and bridges. The TopoKnit system [1,2] provides significant progress toward this goal by implementing a foundational topological representation of knitted fabrics that supports modeling, simulation, and analysis.

The work presented here builds upon the yarn-based topological structures available in TopoKnit by expanding its query and analysis capabilities, thus capturing additional topological relationships present in knitted fabrics manufactured on a two-bed flat weft knitting machine. Specifically, we present algorithms that implement loop order analysis of weft-knitted textiles. This analysis aims to determine the front-to-back ordering of overlapping yarn loops, given a stitch pattern that defines a knitted fabric.

Expanding our understanding of the topology of weft-knitted textiles, not only advances the correctness and robustness of their associated geometric models, but also contributes to the development and application of knitted structures. Loop order information is crucial for the simulation of electrical current, water, force, and heat flow, as well as

for determining fabric properties such as density and porosity [3–6]. Additionally, a loop order analysis capability contributes to the development of inverse design, the process of determining the stitch instructions that would produce a fabric with desired properties.

Since knitted textiles are composed of consecutive connected rows of intertwined yarn loops, we assume and observe that knitting machines execute stitch instructions row-by-row. However, the order in which these stitch instructions are executed within a row can be arbitrary, i.e., there is no inherent order in which stitch instructions must be carried out. Thus, the algorithms described in this paper are based on the assumption that stitch instructions in each row of a stitch pattern can be executed in any temporal order, depending on the type of the knitting machine performing the instructions. To keep our algorithms machine-independent, the loop order analysis utilizes precedence rules that capture the order that stitch commands are executed when a row of yarn loops are being knitted by a two-bed flat weft knitting machine. The loop order algorithm first determines which loops are brought to a specific location. Then, by analyzing the stitch instructions used to manipulate the loops and by applying the proper precedence rule, the front-to-back ordering is determined. Additionally, we have developed visualization methods for displaying the order information within the context of a TopoKnit yarn topology graph. The precedence rules presented in this paper were derived by analyzing knitting simulations in the Shima Seiki SDS-One APEX3 KnitPaint system (Wakayama, Japan). Since the precedence rules are a variable in the algorithms, they can take different values when modeling/analyzing the fabrics produced by different two-bed flat weft knitting machines. This keeps our approach knitting-machine-independent.

The remainder of the paper is structured as the following. In Section 2, we present related work and its relationship to the presented work. In Section 3, we provide a description of the weft-knitting process and the stitch commands utilized during machine knitting. In Section 4, we give a summary of the TopoKnit system. In Section 5, we detail our algorithms for performing yarn order analysis. In Section 6, we describe the algorithms developed to visualize yarn order information with the context of TopoKnit's topology graph. In Section 7, we detail the tests that were performed to validate our yarn order analysis and include some of the test results. Finally, in Section 8, we summarize our research and present directions for future work.

## 2. Related Work

Meissner and Eberhardt developed KnitSim, a pioneering system in modeling and visualizing knitted fabrics [7,8]. This system takes Stoll knitting machine commands as input and outputs an explicit topological representation of the knitted textiles generated from the input commands. A 2D geometric layout of the knitted fabric is generated through a relaxation process making assumptions about the length of yarns between crossings. While this work was promising for its time, it does have some limitations. The approach required a full simulation of the knitting process and imposes constraints that limit the complexity of the modeled knitted structures. The lack of available technical detail hinders the evaluation of the generality and robustness of their approach.

Another similar approach that approximates the 2D layout of knitted textiles is presented by Counts [9]. The developed algorithms employ simulation of the knitting process to generate a graph-based topological representation of the resulting fabric and are able to extract knitting machine instructions from the graph representation. Similar to the Meissner et al. work, Counts' work requires a full knitting simulation to generate the graph. The choice to use loops as the fundamental primitive, as well as the small set of supported machine instructions, limits the yarn topology that can be represented.

There has been abundant work on the 3D geometric modeling of yarns in knitted textiles. In efforts to create more realistic models, Kyosev et al. [10] propose a model that considers yarn cross section properties by including the compression of the yarns in the loop. Sherburn, Lin, et al. [11,12] developed a multiscale modeling approach aiming to predict the mechanical properties of knitted textiles. To further explore the unique

mechanical properties of knitted textiles, Wadekar et al. [13] developed a yarn-level model for weft-knitted fabrics that can be used in finite element analysis simulations. In recent work, Knittel et al. [14] and Wadekar et al. [15,16] explore helicoid scaffolds as a framework for modeling and analyzing the structure and properties of knitted fabrics.

Kaldor et al.'s cutting-edge work [17,18] simulated entire knitted swatches and garments by modeling the geometry and physics of individual yarns in these items. Inspired by this work, Yuksel et al. [19] and Wu et al. [20] introduce a modeling technique that builds yarn-level geometric models of knitted clothing from polygonal models that represent the surface of the knitted cloth. Part of this work was adapted by Leaf et al. [21] to create an interactive design tool for simulating yarn-level patterns for knit and woven textiles.

Cirio et al. [22] define a topological representation of knitted textiles created by a set of limited stitch commands, some of which are not manufacturable on knitting machines. They introduce a compact and simplified representation of yarn geometry and mechanics, capturing essential yarn deformation in their virtual knitted textiles. Their simulation was integrated into a hybrid yarn-triangle model by Casafranca et al. [23]. In related work, Kapllani et al. [1] developed a topological model, TopoKnit, a process-oriented representation that defines a foundational data structure for representing the topology of weft-knitted textiles at the yarn scale. This representation allows for additional topological and manufacturability and stability analysis [2].

McCann et al. [24], Narayanan et al. [25,26] and Lin et al. [27] created algorithms for determining knitting machine commands given polygonal models. These algorithms facilitate interactive design and manufacturing of 3D knitted objects. Popescu et al. [28] described an approach for automatically generating a knitting pattern given a 3D model, without being constrained to developable surfaces. Motivated by Narayanan et al. [25], Kaspar et al. [29] introduced an interactive system which allows users of different skill levels to create and customize machine-knitted textiles. Nader et al. [30] introduced KnitKit, a flexible and customizable system aiming to simplify the knitting of 3D objects by isolating the high-level design from the low-level machine-specific knitting instruction generation.

Our work extends a previously developed topological model (Kapllani et al. [1,2]) to provide additional topological information about a knitted fabric based on the manipulations of its yarn loops. Specifically, in this paper, we present analysis algorithms that define and visualize the order of overlapping loops in a knitted fabric. While Cirio et al. [22], Meissner and Eberhardt [7], and Counts [9] presented work that represents yarn topology in knits, none of them performed any kind of loop ordering determination. Our work produces unique modeling information (loop order) that does not require a full simulation of the knitting process.

## 3. Fabrication of Weft-Knitted Textiles

A fundamental unit of knitted textiles is the yarn loop. A loop is created when a yarn is drawn through a previously existing loop, as seen in Figure 1. When this process is repeated across a row, and then subsequently again in other rows, the fabric is formed. The actions that create a loop or modify an existing loop are specified by stitch instructions. The two simplest/most common stitch instructions are the Knit and the Purl stitches. As viewed from the front side of the knitting machine, when a yarn is drawn through the loop(s) held on a needle from back to front to form a new loop, a Knit stitch is created, as shown in Figure 2b. When the direction that the yarn is drawn is front to back, a Purl stitch is created, as shown in Figure 3b. A Purl stitch is simply the back side of a Knit stitch. Additionally, a number of other stitch instructions can be executed, which may be combined to produce a vast variety of knitted textiles. These stitches include:

### *3.1. Front and Back Transfer Stitches*

A Transfer stitch is produced when a Knit or Purl stitch is created and then its head loop is transferred, via a sequence of needle bed transfers and rackings, to another needle location. Whether the stitch created is a Knit or Purl determines the type of Transfer stitch.

A Front Transfer stitch transfers the head of a Knit stitch and a Back Transfer stitch transfers the head of a Purl stitch (see Figures 4b and 5b respectively).

The Transfer stitches presented in Figures 4b and 5b transfer the loop one needle to the left; however, depending on the type of Transfer stitch, there can be up to three loop movements to the left or right. When a new yarn comes to the needle holding the transferred loop, both overlapping loops will be knit together. The transferred loops are highlighted in magenta in Figures 4b and 5b.

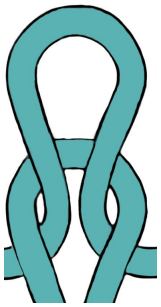

**Figure 1.** A single stitch, with its "legs" holding the "head" (upper loop) of the stitch below.

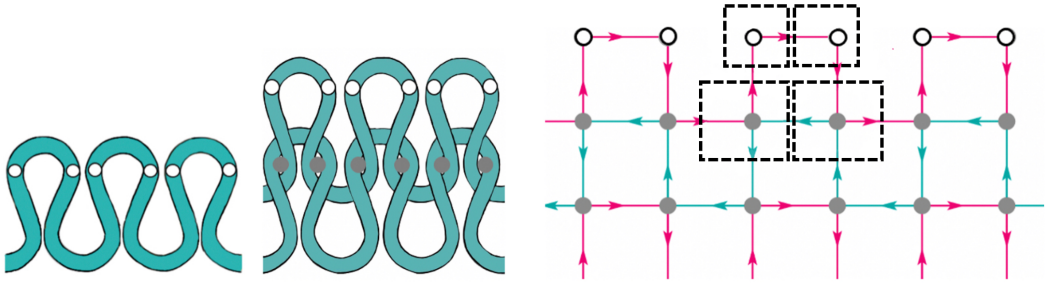

(**a**) (**b**) (**c**)

**Figure 2.** A Knit stitch is created by pulling a loop of yarn through a loop held from the previous row from back to front. (**a**) Row of loops. (**b**) Knit stitches produced from another row of stitches. (**c**) Topological representation. A single stitch is represented by the potential CNs (white disks) of its upper loop and the actualized CNs (gray disks) where its legs intertwine with the previous loop.

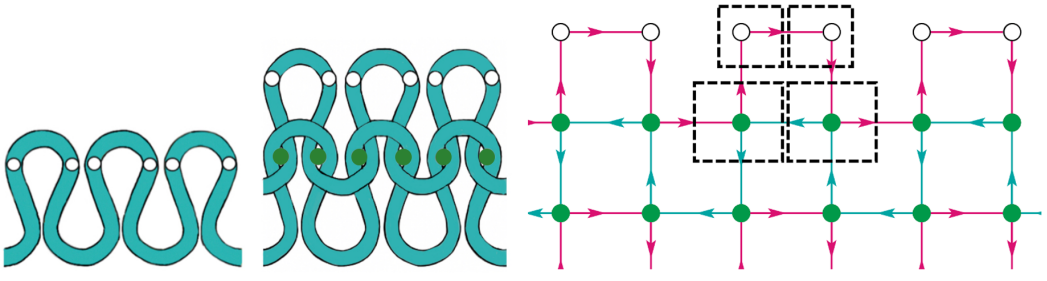

(**a**) (**b**) (**c**)

**Figure 3.** A Purl stitch is created by pulling a loop of yarn through a loop held from the previous row from front to back. (**a**) Row of loops. (**b**) Purl stitches produced from another row of stitches. (**c**) Topological representation. Note that an ACN produced by a Purl stitch is colored green, as compared to the gray disks of Knit-stitch-produced ACNs.

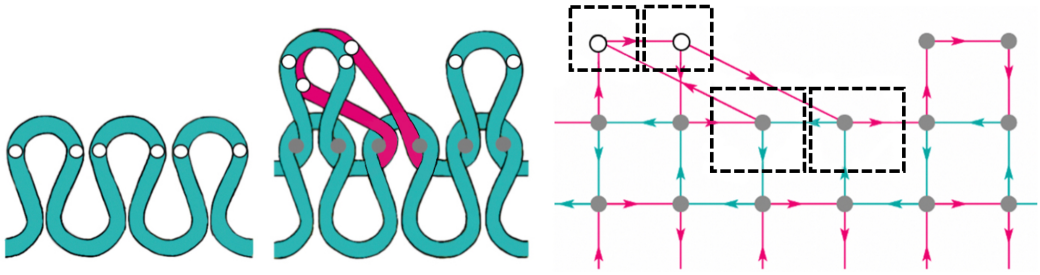

(**a**) (**b**) (**c**)

**Figure 4.** A Front Transfer stitch is created when the loop of a Knit stitch is transferred up to three needle positions away to the left or right. (**a**) Row of loops. (**b**) Two Knit stitches and a Front Transfer stitch produced from another row of stitches. (**c**) Topological representation.

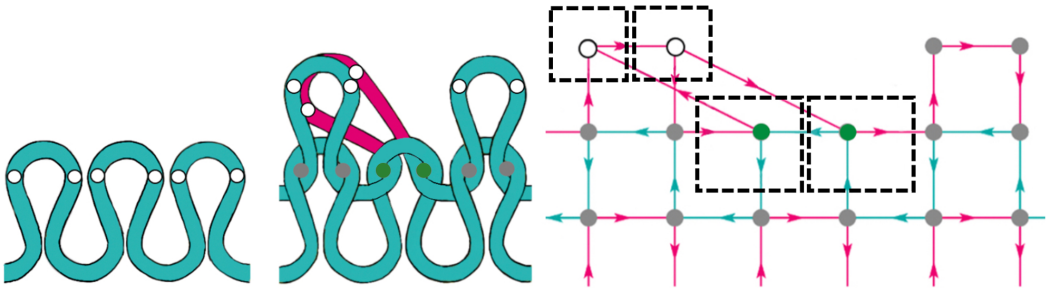

(**a**) (**b**) (**c**)

**Figure 5.** A Back Transfer stitch is created when the loop of a Purl stitch is transferred up to three needle positions away to the left or right. (**a**) Row of loops. (**b**) Two Knit stitches and a Back Transfer stitch produced from another row of stitches. (**c**) Topological representation.

### *3.2. Front and Back Tuck Stitches*

A Tuck stitch is created when a yarn is tucked onto the needle and pulled up, instead of being pulled through the held loop. The tucked loop is held on the needle together with the loop from the previous row, as shown in Figures 6b and 7b. Executing a Back or Front Tuck stitch will determine if the tucked loop is positioned in front of or in back of the held loop, respectively. The needle holds both loops, which will be knitted together when a stitch instruction is executed above it on the next row. The tucked loops are highlighted in magenta in Figures 6b and 7b.

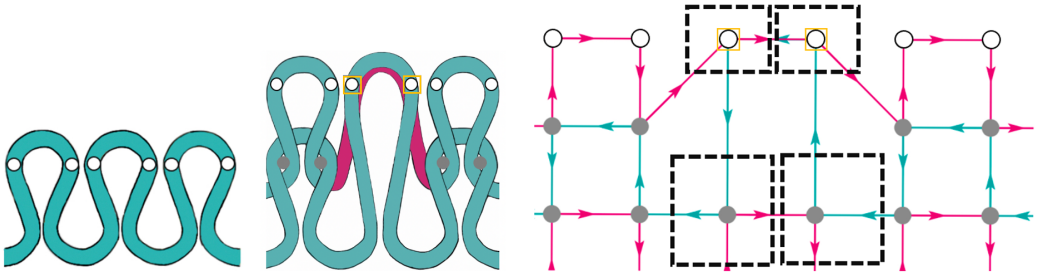

(**a**) (**b**) (**c**)

**Figure 6.** A Front Tuck stitch is created by tucking a yarn onto a loop held by a needle on the front bed from the previous row, instead of creating a new stitch. (**a**) Row of loops. (**b**) Two Knit stitches and a Front Tuck stitch produced from another row of stitches. (**c**) Topological representation.

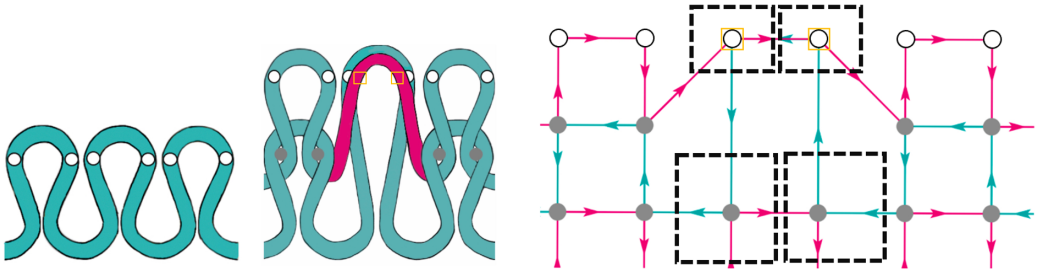

(**a**) (**b**) (**c**)

**Figure 7.** A Back Tuck stitch is created by tucking a yarn onto a loop held by a needle on the back bed from the previous row, instead of creating a new stitch. (**a**) Row of loops. (**b**) Two Knit stitches and a Back Tuck stitch produced from another row of stitches. (**c**) Topological representation.

### *3.3. Front and Back Miss Stitches*

Similarly to the Tuck stitch, during the execution of a Miss stitch, the needle holds the loop from the previous row, but the new yarn is not hooked by the needle. Instead, the yarn passes by, creating a horizontal segment of yarn across the front or the back of the held loop. Executing a Back or Front Miss stitch will determine whether the yarn passes in front of or in back of the held loop, respectively. The resulting horizontal yarns are highlighted in magenta in Figures 8b and 9b.

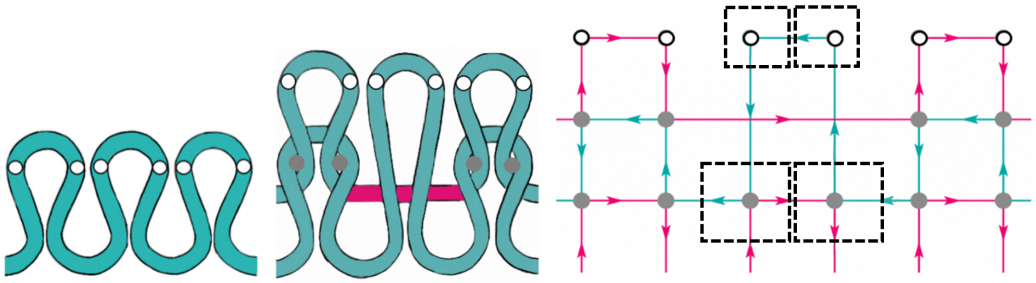

(**a**) (**b**) (**c**)

**Figure 8.** A Front Miss stitch is created when a needle on the front bed holds a loop from a previous row as the yarn passes by, without knitting a new stitch, creating the magenta horizontal yarn. (**a**) Row of loops. (**b**) Two Knit stitches and a Front Miss stitch produced from another row of stitches. (**c**) Topological representation.

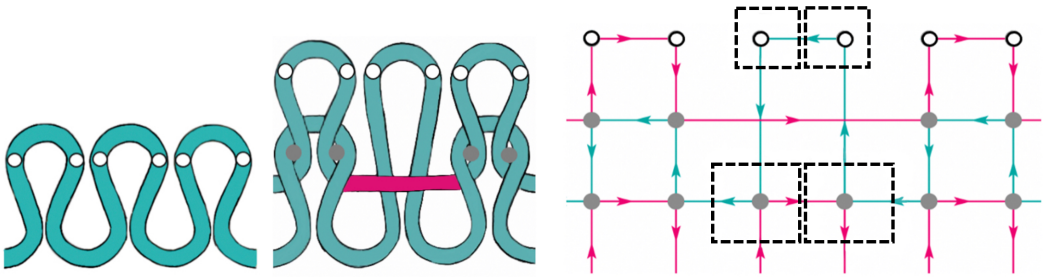

(**a**) (**b**) (**c**)

**Figure 9.** A Back Miss stitch is created when a needle on the back bed holds a loop from a previous row as the yarn passes by, without knitting a new stitch, creating the magenta horizontal yarn. (**a**) Row of loops. (**b**) Two Knit stitches and a Back Miss stitch produced from another row of stitches. (**c**) Topological representation.

### *3.4. Empty Stitch*

An Empty stitch specifies that no machine operation will be executed for a specific needle. In our work, we assume that Empty stitches cannot be completely surrounded

by non-Empty stitches, i.e., Empty stitches only occur outside the borders of the fabric. Therefore, no yarn passes by nor is looped on the needle at that stitch location.

These nine stitches (Knit, Purl, Front and Back Transfer, Front and Back Tuck, Front and Back Miss, and Empty) are the fundamental stitches needed to create most knitted textiles and can be combined to generate complicated knitted patterns. TopoKnit supports all of these stitches, thus allowing for a broad representation of intricate knitted fabrics.

## 4. TopoKnit

TopoKnit is a topological model of knitted textiles defined within a process-oriented space that represents aspects of the fabric itself, as well as the processes that manipulate the fabric during knitting (Kapllani et al. [1]). The primary primitives of this modeling space are yarn intertwinings and the yarns that connect them. The complexity of a yarn intertwining is encapsulated in a primitive called the Contact Neighborhood (CN). There are three types of CNs: the potential CN (PCN), the actualized CN (ACN), and the unanchored CN (UACN). When a loop is formed, two PCNs are created. When the yarn comes back to the location of these PCNs and is pulled through the existing loop to form a new loop (creating two intertwinings), the PCNs are actualized to ACNs. An ACN is defined by a contact point and four directed incident edges. See the gray (ACNs) and white (PCNs) disks in Figure 2c, which are defined by a Knit stitch. Depending on the loop manipulations during the knitting process, PCNs can be actualized at their creation location or at another location in the fabric grid. An example of the latter would be the PCNs created by Transfer stitches, as seen in Figures 4 and 5. The third CN type, a UACN, is created when the yarn is grabbed by the needle, but the loop's legs are not intertwined with (i.e., anchored by) another loop from directly below. The squares in Figure 10c represent UACNs. These CNs are connected horizontally with their neighbors along the magenta edge flowing from left to right and therefore are unanchored.

TopoKnit defines a data structure which stores information about these CNs, as well as their mappings, i.e., movements within the fabric grid. For each CN $(i, j)$, four parameters are stored in the data structure. They are: stitch type (ST), actualization value (AV), movement vector (MV), and yarn path index (YPI). The first parameter is the only location-based parameter and it specifies the type of stitch executed at location $(i, j)$ when a CN (created at or transferred to $(i, j)$) is actualized at the location. The actualization value and movement vector make up the mapping information for each CN. The actualization value shows if a CN has been created at a location $(i, j)$ and if so defines its state. The four actualization parameter values are: PCN, ACN, UACN and E. 'E' implies that no CN was instantiated at the associated location, i.e., the CN is Empty. The movement vector $[\Delta i, \Delta j]$ specifies if the CN is being moved vertically or horizontally and by how many units. The YPI parameter stores information about the CN's location in the yarn path list as a set of indices into the list. The yarn path list consists of a set of locations the yarn passes through in the fabric grid. Having this information stored in the data structure allows for constant-time information access during the analysis stage.

Given a stitch pattern composed of the stitch instructions supported by TopoKnit, populating the data structure is the first step toward the analysis stage. See Figure 10d. The analysis stage consists of algorithms developed to evaluate the data structure and support topological query functions. TopoKnit's main evaluation routine produces the path of the yarn through the fabric and stores it as a sequential list of grid locations in the fabric. The yarn path may be used to visualize the topology graph of the resulting knitted fabric, as seen in Figure 10c, which is produced from the stitch pattern in (a). Examples of supported topological queries include determining the final location of a CN in the fabric grid, identifying which CNs will ultimately be situated at a particular fabric grid location, returning a list of neighboring CNs, as well as providing a list of topological structures we call open loops. Our current work adds loop order determination to this list. In addition to yarn-level topological analysis, TopoKnit supports manufacturability and structural stability analysis (Kapllani et al. [2]).

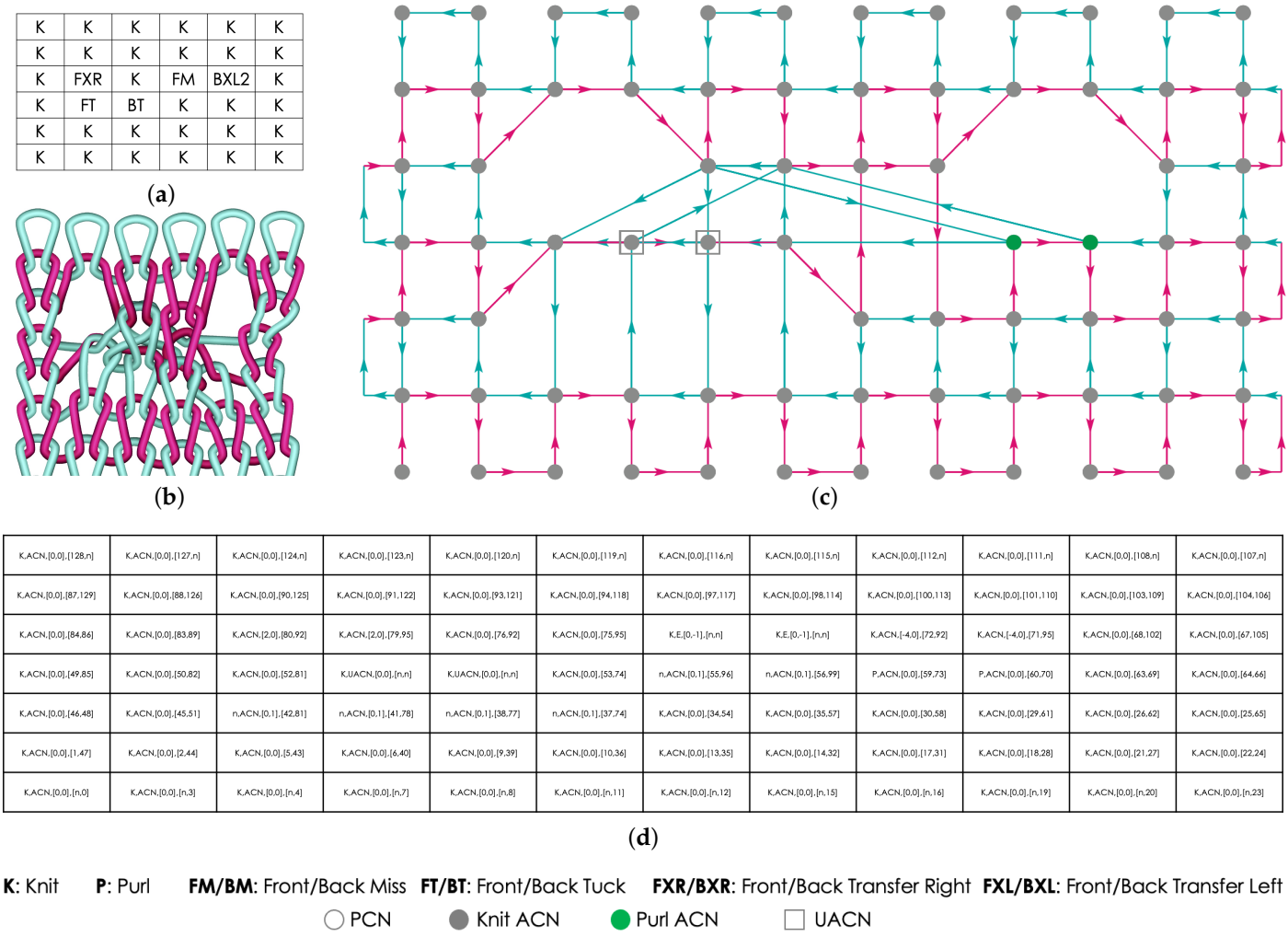


**Figure 10.** Stitch pattern with a combination of Knit, Front Transfer, Back Transfer, Front Miss, Front Tuck, and Back Tuck stitches. (**a**) Stitch instructions. (**b**) Simulation of stitch pattern. (**c**) Topology graph. (**d**) Corresponding data structure after evaluation.

## 5. Loop Order Analysis

A new topological query has been added to the TopoKnit system, specifically the front-to-back order of yarn loops. Due to the manipulations of the yarn during the knitting process, multiple overlapping loops may end up at the same location in the fabric. The final spatial order of these loops (front-to-back) is determined by the temporal order that the loops were manipulated and placed during knitting. The loop order query makes use of this fact, along with the information stored in the TopoKnit data structure to define the spatial order of loops at a location $(i, j)$ in the fabric grid. It is important to note that since we are trying to define the order of loops, our analysis only involves stitch instructions that create new loops, such as Knit (K), Purl (P), Front (FX) and Back (BX) Transfer, and Front (FT) and Back (BT) Tuck Stitch and excludes the Miss (M) stitch.

Both hand and machine knitting are row-by-row processes. Therefore, the loop order analysis algorithms assume that the stitch commands are processed row-by-row. The execution order for stitches within a row depends on the type of knitting machine performing them. To represent and isolate this machine dependency in our algorithms, precedence rules are introduced as input to the loop order algorithm. The precedence rules consist of a sequence of stitch instructions starting with the stitch instruction that is executed first in a row of instructions and ends with the stitch instruction that is executed last. The precedence rules can be easily changed when analyzing the fabric manufactured by a specific knitting machine.

The first step of the loop order query determines which loops are brought to the queried location in the fabric grid. The loops that end up at the location in the fabric may have originated from multiple lower rows in the fabric. When analyzing these loops, they are processed row-by-row, with lowest originating row being processed first. A precedence rule is then applied to determine the order of stitch command execution, and therefore the ordering of the associated yarn loops, for that row. The stacked loops from one row are then recursively concatenated with loops that are ordered from successive rows.

### *5.1. Precedence Rules*

For each type of knitting machine, precedence rules specify the temporal order that stitch instructions in a single row of a stitch pattern are executed by the machine. The examples presented in this paper use precedence rules that were inferred by analyzing simulations of different stitch patterns in the Shima Seiki SDS-One APEX3 KnitPaint system. Over one hundred patterns were simulated and examined to determine the order that Shima Seiki knitting machines execute Knit, Purl, Front and Back Transfer, and Front and Back Tuck stitches in a row of stitches. The order that these stitches are executed depend on what types of stitches exist in a row. Knit, Purl, and Transfer (K-P-X) stitches are executed as a block. If the row contains a Back Tuck (BT), the K-P-X block is executed first, then followed by the execution of the BT stitch. This is seen at location (4,3) and (5,3) in Figures 11 and 12. If the row contains a Front Tuck (FT), the FT stitch is executed first and the K-P-X block of stitches is then executed.

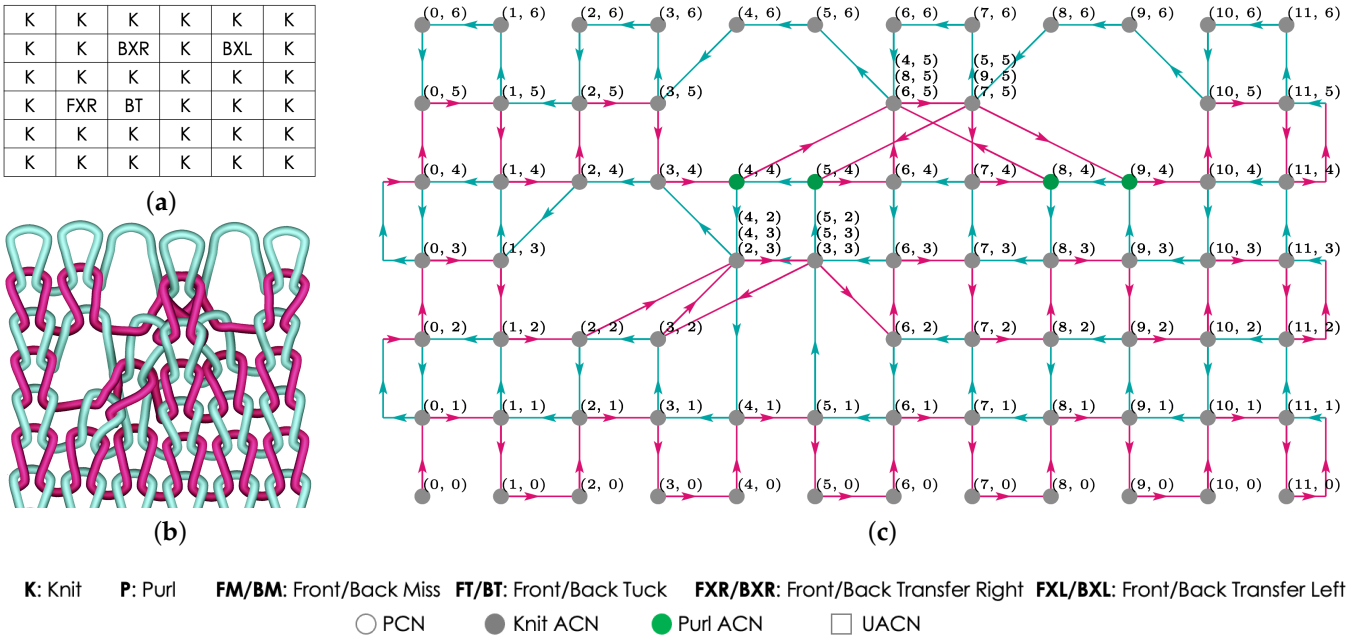


**Figure 11.** Stitch pattern with a combination of Knit, Front and Back Transfer, and Back Tuck stitches: (**a**) Stitch instructions. (**b**) Simulated knitted pattern. (**c**) Topology graph displaying CN (loop) order.

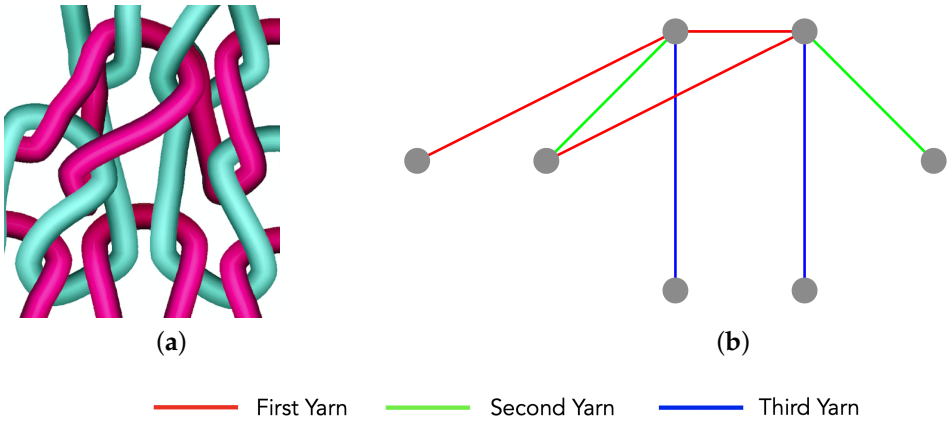


**Figure 12.** Yarn order zoom-in at location (4, 3) in the yarn topology graph of Figure 11: (**a**) Simulated knitted pattern. (**b**) Corresponding zoom-in topology graph.

Therefore, there are two precedence rules for the K-P-X block of stitches, depending if the block contains Front Transfer (FX*) or Back Transfer (BX*) stitches. Knit stitches are always executed first and Purl stitches are executed last in the block. What determines the precedence of the block is the presence of Front Transfer stitches, with or without the inclusion of Back Transfer stitches. The first rule accounts for the existence of Front Transfer stitches in the row being processed, whereas the second accounts for all Transfer stitches in the row being Back Transfer stitches. Within these rules, the direction of the transfer, the number of needle positions shifted (shift units) and the stitch type (FX or BX) determine the execution order of the stitches. In the first rule, the smaller the shift unit, the higher the precedence of the Transfer stitch instruction, i.e., the sooner the stitch is executed (See locations $(4, 2)$ and $(5, 2)$ in Figures 13 and 14). For stitches with equal shift units, the left movement direction precedes the right one (See locations $(6, 5)$ and $(7, 5)$ in Figures 11 and 15), and for stitches with equal shift units and direction, Front Transfer stitches precede Back Transfer stitches. Given this information, the first precedence rule, from highest to lowest precedence, for K-P-X blocks is

$$(K, FXL, BXL, FXR, BXR, FXL2, BXL2, FXR2, BXR2, FXL3, BXL3, FXR3, BXR3, P).$$

Similar to the first rule, the second precedence rule uses shift units and movement direction to define the execution order of blocks containing only Knit, Purl, and Back Transfer stitches. However, contrary to the first rule, the higher the shift unit is, the higher the execution precedence of the stitch instruction is in the second rule. For stitches with equal shift units, the left movement direction precedes the right one. Given this information, the second rule for K-P-X blocks with only Back Transfers is

$$(K, BXL3, BXR3, BXL2, BXR2, BXL, BXR, P).$$

These precedence rules are codified in Algorithm 1.

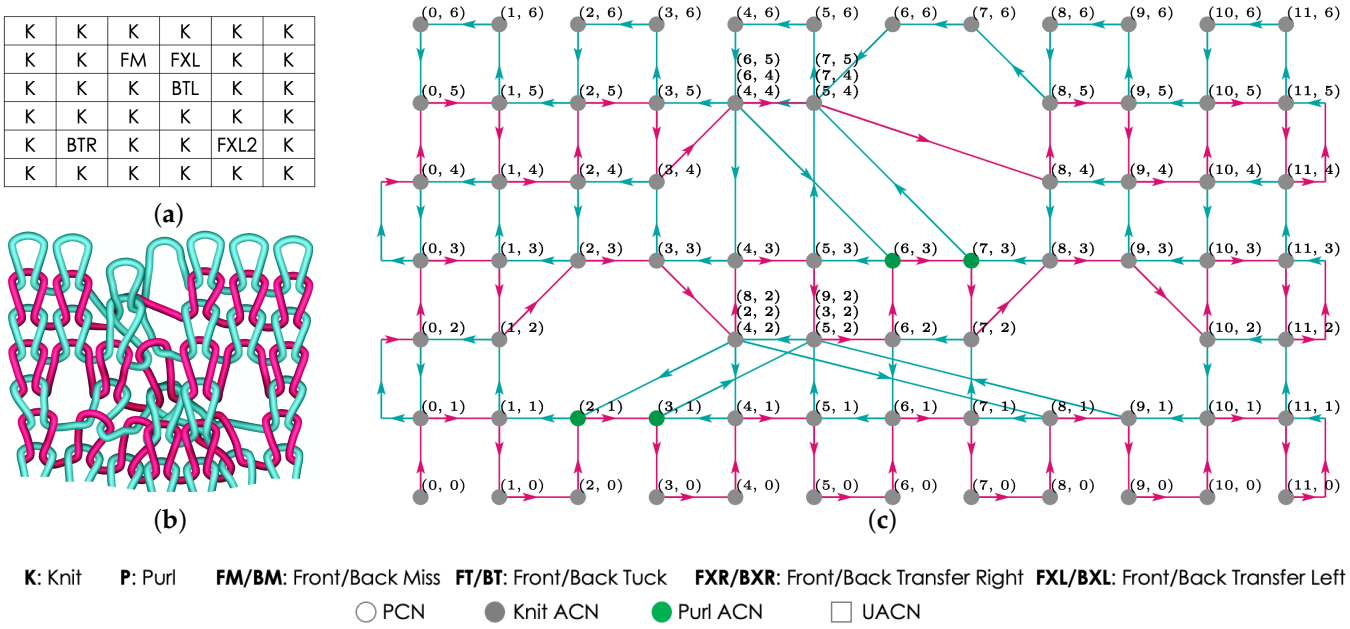


**Figure 13.** Stitch pattern with a combination of Knit and Front and Back Transfer stitches: (**a**) Stitch instructions. (**b**) Simulated knitted pattern. (**c**) Topology graph displaying CN (loop) order.

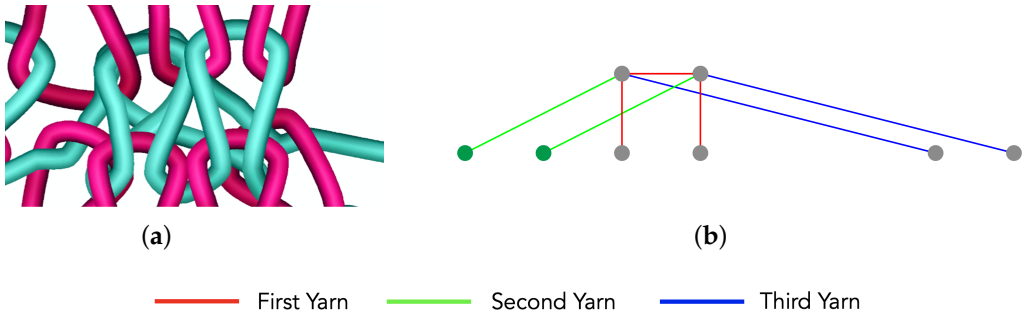


**Figure 14.** Yarn order zoom-in at location (4, 2) in the yarn topology graph of Figure 13: (**a**) Simulated knitted pattern. (**b**) Corresponding zoom-in topology graph.

**Algorithm 1** *DETERMINE_RULE*(*rowj*, *pattern*)
Returns the precedence rule for row *j* in pattern

```
rule = {}
currentRow = pattern[*,rowj]
if FX* in currentRow then
    rule = (K,FXL1,BXL1,FXR1,BXR1,FXL2,BXL2,FXR2,BXR2,FXL3,BXL3,FXR3,BXR3,P)
else if BX* in currentRow then
    rule = (K,BXL3,BXR3,BXL2,BXR2,BXL1,BXR1,P)
else
    rule = (K,P)
if FT in currentRow then
    rule = FT + rule                          ▷ Front Tuck has highest precedence
else if BT in currentRow then
    rule = rule + BT                          ▷ Back Tuck has the lowest precedence
return rule
```

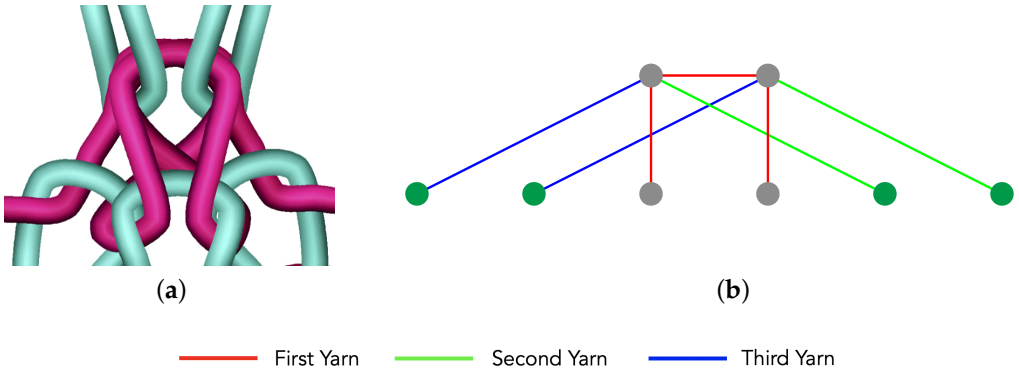


**Figure 15.** Yarn order zoom-in at location (6, 5) in the yarn topology graph of Figure 11: (**a**) Simulated knitted pattern. (**b**) Corresponding zoom-in topology graph.

### *5.2. Contact Neighborhood Order*

As noted in Section 3, a loop in TopoKnit is defined by a list of edges that adhere to certain constraints. An edge defines a yarn connection between two CNs. Thus, the order of loops at a location $(i, j)$ mirrors the order of head CNs of the loops present at that location. Therefore, our algorithm (Algorithm 2) for determining loop order finds the order of CNs at a given location in the fabric grid. The algorithm begins by finding all of the CNs that end up at the location (if any) (Line 2, Algorithm 2). This is accomplished with the CNS_AT algorithm, which is a slight modification of the ACNS_AT algorithm (Algorithm 5 in [1]). Specifically, the CNS_AT algorithm returns all CNs at a location by omitting the condition that the CN's actualization value be "ACN".

**Algorithm 2** $YARN\_ORDER(i, j, pattern, DS)$
Return the list of CNs at location $(i, j)$ ordered by their spacial position (front-to-back).

```
1: orderedCNs = []
2: CNList = CNS_AT(i, j, DS)                          ▷ CNs at location (i, j)
3: if CNList == [] then                               ▷ No CNs at this location
4:     PRINT("There are no CNs at this location")
5:     return orderedCNs
6: CNStitchPairs = CN_STITCH_PAIRS(CNList, pattern)   ▷ Define the stitches that create each CN at location (i,j)
7: sortedCNStitchPairs = SORT_BY_J(CNStitchPairs)     ▷ Sort pairs by the row the CNs were defined at
8: return YARN_ORDER_RECURSIVE(sortedCNStitchPairs, pattern, orderedCNs)
```

Each CN is created when a loop is formed by the execution of a stitch instruction. Since the order of CNs depends on the stitches that create them, each CN is paired with the corresponding stitch that formed it. For instance, CNs $(4, 3)$ and $(5, 3)$ in Figure 11c were formed by the Back Tuck (BT) stitch in the pattern shown in Figure 11a. The pairings between the CNs and the stitch are specified with the helper function CN_STITCH_PAIRS (See Algorithm 3). When a stitch instruction at coordinate m, n) in the stitch pattern is executed, four CN cells are populated in the TopoKnit data structure. Two correspond to two leg CNs ((2m, n), (2m + 1, n)) and two correspond to two head CNs ((2m, n + 1), (2m + 1, n + 1)). See Figure 16. Since only head CNs can be moved in the fabric grid by a stitch, they are considered when determining corresponding stitch instructions. Therefore a head CN located at $(i, j)$ in the CN grid can be associated with a stitch command located at $(i/2, j - 1)$, if $i$ is even, and at $((i - 1)/2, j - 1)$, if $i$ is odd. Note that $CNStitchPairs$ is a dictionary where the CN (i,j) IDs are the keys and the corresponding stitch codes are the values.

**Algorithm 3** *CN_STITCH_PAIRS*(*CNList*, *pattern*)
Return a dictionary of CN-Stitch pairs given a list of CNs

```
1: CNStitchPairs = {}
2: for (CNi,CNj) in CNList do
3:     n = CNj - 1                          ▷ Determine n coordinate of the corresponding stitch in the pattern matrix
4:     if CNi % 2 == 0 then                 ▷ Determine m coordinate of the corresponding stitch in the pattern matrix
5:         m = CNi / 2
6:     else
7:         m = (CNi - 1) / 2
8:     correspondingStitch = pattern[m][n]  ▷ Access corresponding stitch at (m,n) in pattern matrix
9:     CNStitchPairs[(CNi,CNj)] = correspondingStitch   ▷ Assign CN-stitch pair for the current CN
   return CNStitchPairs
```

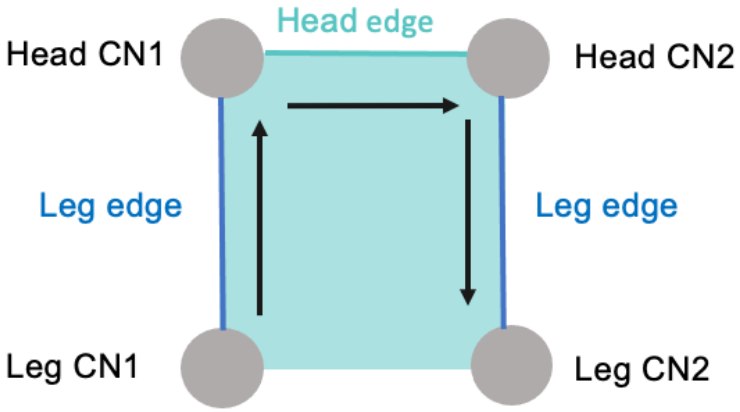


**Figure 16.** Single open loop consisting of four contact neighborhoods. Leg edges highlighted in blue and head edges are highlighted in teal.

CNs whose final location is $(i, j)$ may be created by stitch instructions within a small neighborhood of the location, possibly from a different row. Since knitting is a sequential process, stitch instructions in lower rows are processed before the ones in higher rows. Therefore, the entries in *CNStitchPairs* are sorted by their row number, with the algorithm SORT_BY_J (not included here). Stitch pairs from lower rows come before stitches from higher rows and are stored in *sortedCNStitchPairs*.

Once the CN-Stitch pairs have been created and sorted by their row $j$ (Lines 6 and 7), Algorithm 2 determines the CN order at location $(i, j)$ by calling the function YARN_ORDER_RECURSIVE (Algorithm 4), which recursively processes CN-Stitch pairs at location $(i, j)$ row-by-row, starting with the lowest row. For each row of stitch instructions, which is stored in *currentRow*, *DETERMINE_RULE* returns the appropriate precedence rule for the current row (Line 4, Algorithm 4), as described in Section 5.1. The function ORDER_ROW_CNS (Algorithm 5) is called to order the CNs in *currentRow* using the precedence rule in *rule* (Line 13 and 15, Algorithm 4). ORDER_ROW_CNS sorts the CNs based on the index of its corresponding stitch in the precedence rule.

**Algorithm 4** $YARN\_ORDER\_RECURSIVE(sortedCNStitchPairs, pattern, orderedCNs)$
Recursive function used to define the order of CNs at location $(i, j)$

```
1:  if len(sortedCNStitchPairs) != 0 then                          ▷ Process until no CNs are left
2:      currentRow = {}                                            ▷ Stores the CN-Stitch pairs for the current row
3:      smallestJ = sortedCNStitchPairs[0].CNj                     ▷ Row being processed
4:      rule = DETERMINE_RULE(smallestJ)                           ▷ Precedence rule for the row being processed
5:      for CN(i,j),stitch in sortedCNStitchPairs do
6:          if j == smallestJ then                                 ▷ CN defined in the row being processed
7:              currentRow[CN(i,j)] = stitch
8:          else
9:              break
10:     for CN(i,j) in currentRow.keys() do                        ▷ Delete CN-Stitch pairs about to be processed
11:         delete sortedCNStitchPairs[CN(i,j)]
12:     if rule[-1] == BT then                                     ▷ Row contains a BT
13:         orderedCNs = ORDER_ROW_CNS(currentRow, rule) + orderedCNs
14:     else                                                       ▷ Row does not contain a BT
15:         orderedCNs = orderedCNs + ORDER_ROW_CNS (currentRow, rule)
16:     return YARN_ORDER_RECURSIVE(sortedCNStitchPairs,pattern, orderedCNs)   ▷ Process the CNs in next row
17: return orderedCNs
```

**Algorithm 5** $ORDER\_ROW\_CNS(currentRow, rule)$
Return ordered CNs in currentRow given a precedence rule

```
1: stitchIndexCNPairs = []
2: orderedCNs = []
3: for CN(i,j),stitch in currentRow.items() do                 ▷ Create pairs of stitch index and CNs for current row
4:     stitchIndexCNPairs.append((rule.index(stitch),CN(i,j)))
5: sortedStitchIndexCNPairs = sorted(stitchIndexCNPairs)]      ▷ Order by the index of stitches in the precedence rule
6: for index, CN(i,j) in sortedStitchIndexCNPairs do           ▷ Extract ordered CNs
7:     orderedCNs.append(CN(i,j))
8: return orderedCNs
```

Tuck stitches (Front (FT) and Back (BT)) not only have a precedence relative to the other stitches in their row, but they also affect the precedence of the stitch block that has been ordered in the previous row. As seen in Lines 9 and 10 in Algorithm 1, Front Tuck (FT) has the highest precedence of all the supported stitches, while Back Tuck (BT) has the lowest, seen in Lines 11 and 12. Conversely, when concatenating a new line of stitches (those returned by ORDER_ROW_CNS) containing a Back Tuck (BT) with a previous line (*orderedCNs*), as seen in Lines 12 and 13 of Algorithm 4, the block containing the BT has higher precedence than the stitch block from a lower row. The ordered *currentRow* is placed before the stitch block from the previous row (*orderedCNs*). If no BT is present in the current row, the previous stitch block (*orderedCNs*) is placed in front of the current row (Line 15, Algorithm 4).

### 6. Yarn Order Visualization

The algorithms presented in Section 5 describe how the ordering of stacked CNs, and, therefore, yarn loops, is determined for a knitted fabric. This ordering information, provided by the execution of the YARN_ORDER function, has been incorporated into TopoKnit's yarn topology graph visualization algorithm (Algorithm 7 (DRAW_TOPOLOGY_GRAPH) in Kapllani et al. [1]) in the form of textual data. Examples of these visualizations are provided in the yarn topology graphs in Figures 11c, 13c and 17c. In each $(i, j)$ location in the graphs where at least one CN is present, labels corresponding to the CN order are

added. In locations where there are more than one CN, the displayed bottom-to-top order of the CNs corresponds to the order of yarns from front to back.

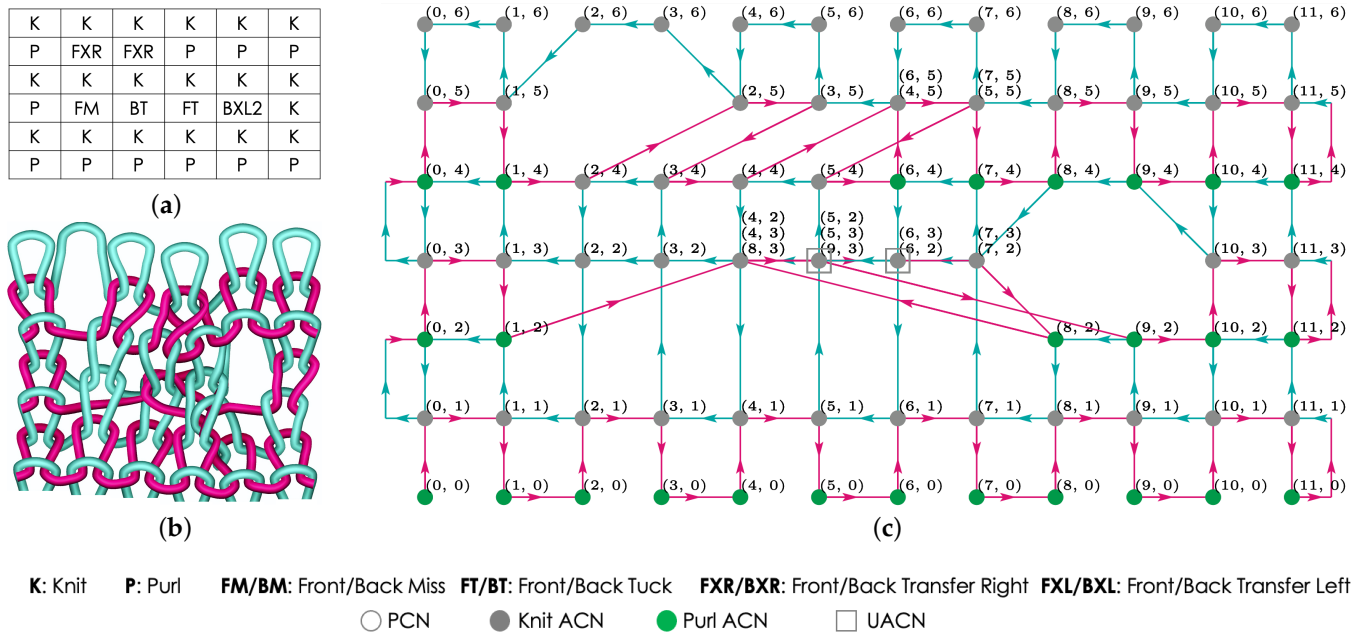


**Figure 17.** Stitch pattern with a combination of Knit, Purl, Front and Back Transfer, Front Miss, and Front and Back Tuck stitches: (**a**) Stitch instructions. (**b**) Simulated knitted pattern. (**c**) Topology graph displaying CN (loop) order.

*Zoom-in Visualizations*

Using textual data to convey loop ordering may not be ideal for all scenarios or users. Therefore, Algorithm 6 was developed to display a zoom-in view of the stacked loops that go through location $(i, j)$, using color instead of textual data to present ordering information. The zoom-in graphs presented in this paper use three colors, where the red loop represents the front loop, the green loop represents the middle loop, and the blue loop represents the back loop. We chose three colors based on the assumption that three is the maximum number of loops a needle can hold without breaking, as described in [2]. Algorithm 6 can be easily modified for a different assumption, i.e., the needle can hold more than three loops, by adding colors to the *yarnColors* variable accordingly. An example of a zoom-in graph is given in Figure 15b. This figure displays loop ordering at locations $(6, 5)$ and $(7, 5)$ for the yarn topology graph presented in Figure 11c.

To create a zoom-in graph, the list of ordered CNs at location $(i, j)$ is generated and a yarn color is assigned to each depending on its order position. The zoom-in graph draws the corresponding loop for each CN in their specified order. To ensure that intersections between pairs of yarns are correctly ordered visually, the list of CNs is reversed. Thus, the loops are drawn in a back-to-front order. See Lines 1–7 in Algorithm 6.

**Algorithm 6** *YARN_ORDER_ZOOM_IN*$(i, j, pattern, DS)$
Generate a zoom-in topology graph showing the order of loops at location $(i, j)$.

```
yarnColors = [red, green, blue]                                   ▷ Front-to-back yarn colors
orderedCNs = YARN_ORDER(i, j, pattern, DS)
if len(orderedCNs) == 0 then return
colorOrderedCNs = []
for index, CN in enumerate(orderedCNs) do          ▷ Assign a color to each CN depending on its order
    colorOrderedCNs.append([CN, yarnColors[index]])
colorOrderedCNs.reverse()                                ▷ Reverse to draw loops from back to front
yarnPathList = FOLLOW_THE_YARN(DS)
loops, edgeLoopPair, indexLoopPair = DEFINE_OPEN_LOOPS(yarnPathList)
while There are CNs in colorOrderedCNs to process do
    (CNi, CNj), currentColor = colorOrderedCNs.pop(0)                          ▷ CN being processed
    currIndex = DS[CNi][CNj].YPI[0]          ▷ CN's index in the yarn path when visited as a head CN
    if currIndex == "null" then                                  ▷ CN is not visited on the yarn path
        headEdge = FIND_HEAD_EDGE(i,j,DS)                ▷ Get edge that goes through this location
        colorOrderedCNs.insert(0, [headEdge[0], currentColor])                  ▷ Add edge's first head CN
    else                                                                        ▷ CN is visited as head
        I, J = yarnPathList[currIndex].FL
        prevIndex = currIndex - 1                                  ▷ Yarn path index for previous CN
        nextIndex = currIndex + 1                                      ▷ Yarn path index for next CN
        prevI, prevJ = yarnPathList[prevIndex].FL                   ▷ Final location for previous CN
        nextI, nextJ = yarnPathList[nextIndex].FL                       ▷ Final location for next CN
        CNiOddity = CNi % 2 != 0
        currentStitchRow = yarnPathList[currIndex].CR
        rowOddity = currentStitchRow % 2 != 0
        if CNiOddity != rowOddity then                  ▷ Previous CN is the first head of the loop
            headCNs = [[yarnPathList[prevIndex].CNL[0], yarnPathList[prevIndex].FL],[(CNi,CNj), (I,J)]]
                                    ▷ List of the two head CNs, initial location and final location for each head
            loopIndex = edgeLoopPair[((I,J),(nextI,nextJ))]                 ▷ Find loop index using leg edge
        else                                          ▷ Next CN is the second head of the loop
            headCNs = [[(CNi,CNj), (I,J),[yarnPathList[nextIndex].CNL[0], yarnPathList[nextIndex].FL]
                                    ▷ List of the two head CNs, initial location and final location for each head
            loopIndex = edgeLoopPair[((prevI,prevJ),(I,J))]                 ▷ Find loop index using leg edge
        loop = indexLoopPair[loopIndex[0]]          ▷ Get list of CNs and loop locations given loop index
        for index, (CNi, CNj), (CNi_FL,CNj_FL) in enumerate(loop) do          ▷ Draw each loop edge/connection
            if index < len(loop) - 1 then
                DRAW_CONN(CNi_FL,CNj_FL,loop[index+1][0],loop[index+1][1],currentColor)
            stitchType = DS[CNi][CNj][0]                  ▷ Get stitch type for CN from data structure
            if stitchType == "K" then                                                      ▷ Knit stitch
                CNColor = gray
            else                                                                           ▷ Purl stitch
                CNColor = green
            DRAW_CN(CNi_FL,CNj_FL,CNColor)
        sortedHeadCNs = sorted(headCNs)                  ▷ Order head CNs by their i coordinate
        head1I, head2I = sortedHeadCNs[0][0][0], sortedHeadCNs[1][0][0]          ▷ Get heads i coordinates
        for btwI in range(head1I+1, head2I) do                ▷ Draw UACNs on the head edge/connection
            if DS[btwI][head1J].AV == "UACN" then
                DRAW_SQUARE_STROKE(btwI, head1J, gray)
```

To identify and draw the loops, Algorithm 6 makes use of algorithms from the previous Kapllani et al. work, specifically Algorithm 1 (FOLLOW_THE_YARN) [1] and a modified version of Algorithm 12 (DEFINE_OPEN_LOOPS) [2]. The FOLLOW_THE_YARN algorithm returns a yarn path, which is an ordered list of locations that the yarn passes through

as it flows through the fabric grid. Each node of the yarn path has three elements: the list of CNs (CNL) that are engaged in the yarn intertwining at the associated final location $(i, j)$ (FL), and the current stitch row (CR). The modified DEFINE_OPEN_LOOPS algorithm returns a set of open loops that are extracted from the yarn path (Lines 8 and 9). An open loop is a portion of the yarn path that begins and ends on the same fabric row. See Figure 11 in Kapllani et al. [2] for an example. The algorithm returns three variables: *loops*, *edgeLoopPair*, and *indexLoopPair*. The variable *loops* is a list of lists where each inner list contains the CNs and their final locations that make up a loop. Each open loop consists of four or more CNs, two of which are head CNs. The CNs define one head edge (a connection between two head CNs) and two or more leg edges (a connection between two leg CNs or a leg CN and a head CN). See Figure 16. The *edgeLoopPair*, and *indexLoopPair* variables are both dictionaries storing edge-loop index and loop index-loop pairs, respectively.

The algorithm goes through the CNs that end up at location $(i, j)$ (Line 10) and draws the corresponding loop with the CNs that make up each loop. It is possible for YARN_ORDER_ZOOM_IN to be called at a location with no ACNs (yarn intertwinings) but with just an unanchored CN (UACN). Here, the index into the yarn path (YPI), which only stores actualized CNs (ACNs), is "null" (Line 13). In this case, the head edge through location $(i, j)$ is retrieved from the data structure, with the function FIND_HEAD_EDGE (Line 14) and one of its head CNs is placed in the list *colorOrderedCNs* (Line 15), which guarantees that the loop through the UACN is drawn. An example of this situation is the green loop in Figure 18, with the UACNs displayed with gray squares, which is a zoom-in of CNs $(5, 3)$ and $(6, 3)$ in Figure 17.

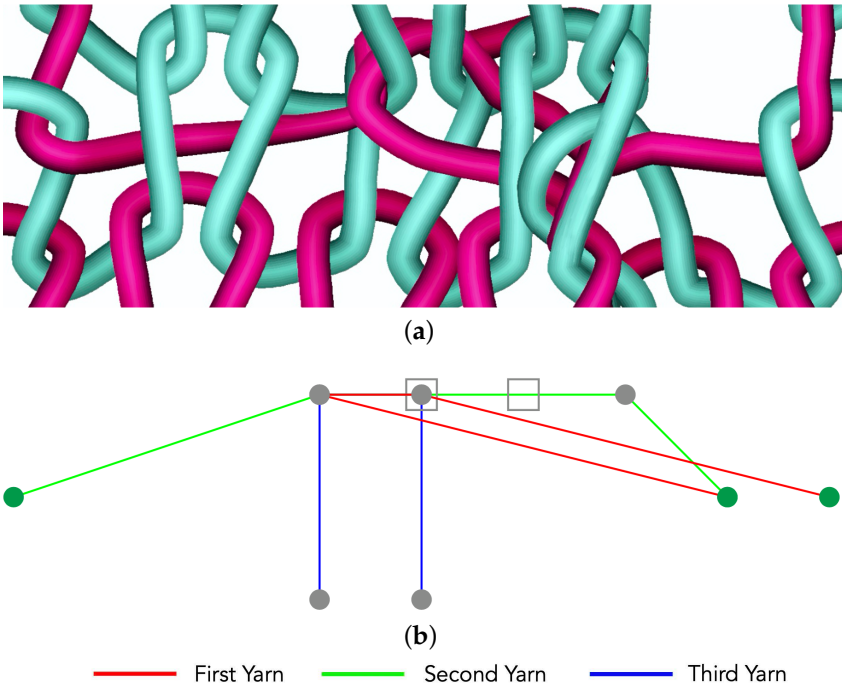


**Figure 18.** Yarn order zoom-in at location (5, 3) in the yarn topology graph of Figure 17: (**a**) Simulated knitted pattern. (**b**) Corresponding zoom-in topology graph.

The CNs that make up a loop are extracted in Lines 17 through 32. Note that the CNs that end up at location $(i, j)$ are head CNs, and using the index of the current CN in the yarn path (YPI), we can retrieve the previous and next CNs in the path, one of which is a head CN and the other a leg CN. Knowing the parity of the $i$ component of the CN and its current row, we can determine which is the head CN and which is the leg CN. See Lines for 22–32. Since head CNs can move/shift vertically and horizontally, different loops can have overlapping head edges. The connection between the processed CN and its adjacent leg CN is used as the identifying edge to determine the loop. Thus to uniquely identify a loop,

a leg edge is used to determine the index in the *edgeLoopPair* dictionary. See Lines 28 and 32. The loop index can then be used to extract the list of CNs that make up the loop in the *indexLoopPair* dictionary (Line 33).

Once the CNs of the current loop have been identified, Algorithm 6 draws the loop's edges. Specifically, lines 35–36 are responsible for drawing the connections between CNs of the loop (loop edges) and lines 37–47 are responsible for drawing the CN icons of the loop. In Lines 37 through 41, the color of the ACN icon is determined, with Knit stitches colored gray and Purl stitches colored green. The commands in Lines 43 through 47 iterate through the locations along the head edge and draw a gray square at locations containing a UACN.

## 7. Testing and Results

The correctness of the algorithms presented in this paper was evaluated by comparing our results to the graphical outputs from the Shima Seiki SDS-One APEX3 KnitPaint and KnitDesign systems. The input precedence rules were extracted by observing the simulation of 200 $6 \times 6$ stitch patterns within the Shima software. Thus, we would expect the loop stacking order defined by the algorithms to match the Shima simulations. Specifically, we analyzed 100 random $6 \times 6$ stitch patterns, 50 of which were a combination of Knit, Purl, and Front and Back Transfer stitches and 50 which added Front and Back Tuck stitches to the original combination. For each group of 50, half of the patterns produced fabric locations with a maximum of two overlapping yarn loops and half had a maximum of three overlapping loops at a specific location $(i, j)$. The ordering of CNs produced by our algorithms at each location for all of the tested patterns matched the order of loops in the Shima simulation outputs. Some of these test examples are described below.

Figures 11c, 13c and 17c show topology graphs corresponding to the stitch patterns in Figures 11a, 13a and 17a, respectively. In Figure 11c, three CNs end up at location $(6, 5)$, where CN $(6, 5)$ is in front, followed by CN $(8, 5)$ in the middle, and CN $(4, 5)$ is at the back. Looking at the fabric, we would see the loop created by the Knit stitch first, followed by the loop created by the Back Transfer Left (BXL) stitch, followed by the loop created by the Back Transfer Right (BXR) stitch, which is what is seen in the simulation created by Shima Seiki SDS-OneAPEX3 KnitDesign software in Figures 11b and 15a. Similarly, two CNs end up at location $(6, 4)$ in Figure 17c, where CN $(4, 5)$ is in front, followed by CN $(6, 4)$. The simulation in Figure 17b also confirms this ordering with the loop created by the Front Transfer Right (FTX) first, followed by the Purl stitch. Note that the labeled CNs can have ACN or UACN actualization values. For instance, three CNs end up at location $(5, 3)$ in Figures 17c and 18a, one UACN (5, 3) (visualized with a gray square), and two ACNs ($(5, 2)$ and $(9, 3)$). Figure 13c also contains two regions with three overlapping loops, which can be seen at locations $(4, 2)$ and $(4, 5)$, which are confirmed by the corresponding Shima output. See Figures 14 and 19.

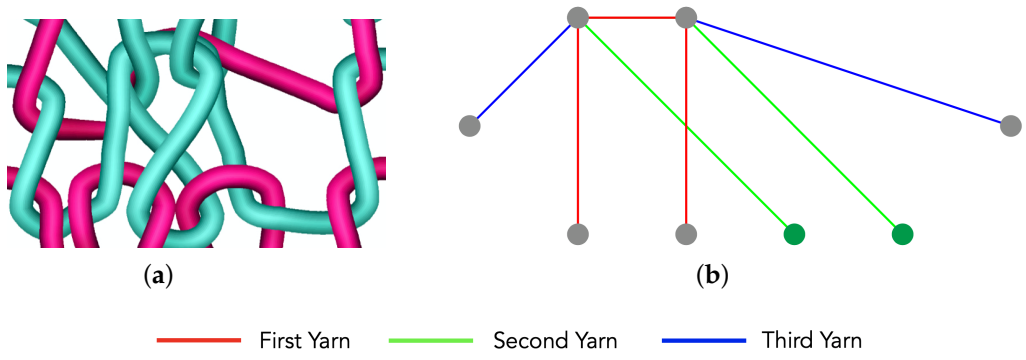


**Figure 19.** Yarn order zoom-in at location (4, 5) in the yarn topology graph of Figure 13: (**a**) Simulated knitted pattern. (**b**) Corresponding zoom-in topology graph.

Once the correctness of the loop stacking order was verified, we tested Algorithm 6 by randomly choosing two locations for each pattern and generating their zoom-in topology graph. The generated zoom-in graphs were visually compared to their associated ordered topology graph that included textual order data. In all cases, they produced consistent, correct outputs. Examples of some of the examined visualizations are the following. A zoom-in topology graph of location $(6, 5)$ in Figure 11c is shown in Figure 15b. A zoom-in graph for location $(4, 3)$ is presented in Figure 12b. A zoom-in topology graph of location $(4, 2)$ in Figure 13c is shown in Figure 14b and the zoom-in at location $(4, 5)$ is presented in Figure 19b. Finally, a zoom-in topology graph of location $(5, 3)$ in Figure 17c is shown in Figure 18b. The confirming Shima output is included with all of these cases.

## 8. Conclusions

In this paper, we described algorithms that perform loop order analysis of weft-knitted textiles, which build upon the foundational TopoKnit topological data structure and associated query functions. During knitting, loops of yarn may be overlayed on top of each other and then stitched together with another piece of yarn. Loop order analysis aims to determine the front-to-back ordering of these overlapping loops, given a stitch pattern that defines the knitted fabric. The new algorithms are based on the assumption that stitch instructions are executed row-by-row and for each row the instructions can be executed in any temporal order. To make our algorithms knitting-machine-independent, loop order analysis utilizes precedence rules that capture the order that stitch commands are executed when a row of yarn loops are being knitted by a two-bed flat weft knitting machine. Basing the algorithms on precedence rules allows them to adapt to the analysis of fabrics manufactured on a variety of knitting machines that may execute stitch commands in different temporal orders.

Additionally, we have developed visualization methods for displaying the computed loop order information. Specifically, the order of stacked loops may be displayed with textual information that is added to the TopoKnit yarn topology graph. Additionally, a zoom-in visualization algorithm has been developed that graphically displays yarn order at a specific location in a knitted fabric. We have evaluated the robustness of our algorithms and their implementation by conducting tests with 100 randomly generated stitch patterns and comparing our loop ordering results with the simulation outputs from the Shima Seiki SDS-One APEX3 KnitDesign system.

In future work, we plan to utilize these loop order capabilities as part of a system that converts a yarn topology graph into a knot diagram. This transformation will enable additional analysis of a knitted fabric's topology, structure and properties. We also intend to incorporate loop order analysis into future simulations to determine electrical properties that are embedded into a knitted fabric structure.

**Author Contributions:** Conceptualization, L.K., C.A., G.D. and D.E.B.; methodology, L.K. and D.E.B.; software, L.K.; validation, L.K., C.A., G.D. and D.E.B.; resources, C.A. and G.D.; writing—original draft preparation, L.K. and D.E.B.; writing—review and editing, L.K., C.A., G.D., and D.E.B.; visualization, L.K.; supervision, D.E.B. and G.D.; project administration, G.D.; funding acquisition, G.D. and D.E.B. All authors have read and agreed to the published version of the manuscript.

**Funding:** This material is based on research sponsored by the US Army Manufacturing Technology Program (US Army DEVCOM) under Agreement number W15QKN-16-3-0001. The U.S. Government is authorized to reproduce and distribute reprints for Governmental purposes. Additional financial support was provided by National Science Foundation grants CMMI-1344205 and CMMI-1537720.

**Institutional Review Board Statement:** Not applicable.

**Informed Consent Statement:** Not applicable.

**Data Availability Statement:** Not applicable.

**Conflicts of Interest:** The authors declare no conflict of interest. The funders had no role in the design of the study; in the collection, analyses, or interpretation of data; in the writing of the manuscript, or in the decision to publish the results.

## References


1. Kapllani, L.; Amanatides, C.; Dion, G.; Shapiro, V.; Breen, D.E. TopoKnit: A Process-Oriented Representation for Modeling the Topology of Yarns in Weft-Knitted Textiles. *Graph. Model.* **2021**, *118*, 101114. [CrossRef]
2. Kapllani, L.; Amanatides, C.; Dion, G.; Shapiro, V.; Breen, D.E. Topological, Manufacturability and Stability Analysis of Weft-Knitted Textiles. *Comput. Aided Des.* **2022**, *under review*. Available online: https://papers.ssrn.com/sol3/papers.cfm?abstract_id=3976858 (accessed on 15 May 2022). [CrossRef]
3. Vallett, R.; Knittel, C.; Christe, D.; Castaneda, N.; Kara, C.; Mazur, K.; Liu, D.; Kontsos, A.; Kim, Y.; Dion, G. Digital fabrication of textiles: An analysis of electrical networks in 3D knitted functional fabrics. In Proceedings of the Micro-and Nanotechnology Sensors, Systems, and Applications IX, Anaheim, CA, USA, 18 May 2017; Volume 10194, p. 1019406.
4. Hong, C.J.; Kim, B.J. Model-Based Simulation Analysis of Wicking Behavior in Hygroscopic Cotton Fabric. *J. Fash. Bus.* **2016**, *20*, No. 6, 66–78. [CrossRef]
5. Zheng, Z.; Zhang, N.; Zhao, X. Simulation of heat transfer through woven fabrics based on the fabric geometry model. *Therm. Sci.* **2018**, *22*, No. 6B, 2815–2825. [CrossRef]
6. Shen, H.; Xie, K.; Shi, H.; Yan, X.; Tu, L.; Xu, Y.; Wang, J. Analysis of heat transfer characteristics in textiles and factors affecting thermal properties by modeling. *Text. Res. J.* **2019**, *89*, No. 20–21. 4681–4690. [CrossRef]
7. Meissner, M.; Eberhardt, B. The Art of Knitted Fabrics, Realistic & Physically Based Modeling Of Knitted Fabrics. *Comput. Graph. Forum* **1998**, *17*, No. 3, 355–362.
8. Eberhardt, B.; Meissner, M.; Strasser, W. Knit Fabrics. In *Cloth Modeling and Animation*; House, D., Breen, D., Eds.; AK Peters/CRC Press: New York, NY, USA, 2000; Chapter 5, pp. 123–144.
9. Counts, J. Knitting with Directed Graphs. Master's Thesis, Massachusetts Institute of Technology, Cambridge, MA, USA, 2018.
10. Kyosev, Y.; Angelova, Y.; Kovar, R. 3D Modeling of Plain Weft Knitted Structures of Compressible Yarn. *Res. J. Text. Appar.* **2005**, *9*, No. 1, 88–97. [CrossRef]
11. Sherburn, M. Geometric and Mechanical Modelling of Textiles. Ph.D. Thesis, University of Nottingham, Nottingham, UK, 2007.
12. Lin, H.; Zeng, X.; Sherburn, M.; Long, A.C.; Clifford, M.J. Automated geometric modelling of textile structures. *Text. Res. J.* **2012**, *82*, No. 16, 1689–1702. [CrossRef]
13. Wadekar, P.; Perumal, V.; Dion, G.; Kontsos, A.; Breen, D. An optimized yarn-level geometric model for Finite Element Analysis of weft-knitted fabrics. *Comput. Aided Geom. Des.* **2020**, *80*, 101883. [CrossRef]
14. Knittel, C.E.; Tanis, M.; Stoltzfus, A.L.; Castle, T.; Kamien, R.D.; Dion, G. Modelling textile structures using bicontinuous surfaces. *J. Math. Arts* **2020**, *14*, No. 4, 331–344. [CrossRef]
15. Wadekar, P.; Goel, P.; Amanatides, C.; Dion, G.; Kamien, R.D.; Breen, D.E. Geometric modeling of knitted fabrics using helicoid scaffolds. *J. Eng. Fibers Fabr.* **2020**, *15*, 1558925020913871. [CrossRef]
16. Wadekar, P.; Amanatides, C.; Kapllani, L.; Dion, G.; Kamien, R.; Breen, D.E. Geometric modeling of complex knitting stitches using a bicontinuous surface and its offsets. *Comput. Aided Geom. Des.* **2021**, *89*, 102024. [CrossRef]
17. Kaldor, J.M.; James, D.L.; Marschner, S. Simulating Knitted Cloth at the Yarn Level. In Proceedings of the ACM SIGGRAPH Conference, Los Angeles, CA, USA, 11–15 August 2008; Article No. 65, pp. 1–9.
18. Kaldor, J.M.; James, D.L.; Marschner, S. Efficient Yarn-based Cloth with Adaptive Contact Linearization. *ACM Trans. Graph.* **2010**, *29*, No. 4, Article No. 105, 1–10. [CrossRef]
19. Yuksel, C.; Kaldor, J.M.; James, D.L.; Marschner, S. Stitch Meshes for Modeling Knitted Clothing with Yarn-level Detail. *ACM Trans. Graph.* **2012**, *31*, No. 4, Article No. 37, 1–12. [CrossRef]
20. Wu, K.; Gao, X.; Ferguson, Z.; Panozzo, D.; Yuksel, C. Stitch Meshing. *ACM Trans. Graph.* **2018**, *37*, No. 4, Article No. 130, 1–14. [CrossRef]
21. Leaf, J.; Wu, R.; Schweickart, E.; James, D.L.; Marschner, S. Interactive Design of Periodic Yarn-level Cloth Patterns. *ACM Trans. Graph.* **2018**, *37*, No. 6, Article No. 202, 1–15. [CrossRef]
22. Cirio, G.; Lopez-Moreno, J.; Otaduy, M.A. Yarn-level Cloth Simulation with Sliding Persistent Contacts. *IEEE Trans. Vis. Comput. Graph.* **2017**, *23*, No. 2, 1152–1162. [CrossRef] [PubMed]
23. Casafranca, J.; Cirio, G.; Rodríguez, A.; Miguel, E.; Otaduy, M.A. Mixing Yarns and Triangles in Cloth Simulation. *Comput. Graph. Forum* **2020**, *39*, No. 2, 101–110. [CrossRef]
24. McCann, J.; Albaugh, L.; Narayanan, V.; Grow, A.; Matusik, W.; Mankoff, J.; Hodgins, J. A Compiler for 3D Machine Knitting. *ACM Trans. Graph.* **2016**, v, No. 4, Article No. 49, 1–11. [CrossRef]
25. Narayanan, V.; Albaugh, L.; Hodgins, J.; Coros, S.; McCann, J. Automatic Machine Knitting of 3D Meshes. *ACM Trans. Graph.* **2018**, *37*, No. 3, Article No. 35, 1–15. [CrossRef]
26. Narayanan, V.; Wu, K.; Yuksel, C.; McCann, J. Visual Knitting Machine Programming. *ACM Trans. Graph.* **2019**, *38*, No. 4, Article No. 63, 1–13. [CrossRef]
27. Lin, J.; Narayanan, V.; McCann, J. Efficient Transfer Planning for Flat Knitting. In Proceedings of the 2nd ACM Symposium on Computational Fabrication, Cambridge, MA, USA, 17–19 June 2018; Article No. 1, pp. 1–7.

28. Popescu, M.; Rippmann, M.; Van Mele, T.; Block, P. Automated generation of knit patterns for non-developable surfaces. In *Humanizing Digital Reality*; Springer: Singapore, 2017; pp. 271–284.
29. Kaspar, A.; Makatura, L.; Matusik, W. Knitting Skeletons: A Computer-Aided Design Tool for Shaping and Patterning of Knitted Garments. In Proceedings of the ACM Symposium on User Interface Software and Technology, New Orleans, LA, USA, 20–23 October 2019; pp. 53–65.
30. Nader, G.; Quek, Y.H.; Chia, P.Z.; Weeger, O.; Yeung, S.K. KnitKit: A flexible system for machine knitting of customizable textiles. *ACM Trans. Graph.* **2021**, *40*, No. 4, Article No. 64, 1–16. [CrossRef]

textiles

*Article*

# New Geometrical Modelling for 2D Fabric and 2.5D Interlock Composites

**Mohamad Abbas Kaddaha [1,2], Rafic Younes [1,*] and Pascal Lafon [2]**

[1] Faculty of Engineering, Lebanese University, Beirut 1002, Lebanon; mohamad.kaddaha@utt.fr
[2] Laboratory of Mechanical & Material Engineering, University of Technology of Troyes, 10420 Troyes, France; pascal.lafon@utt.fr
* Correspondence: ryounes@ul.edu.lb

**Abstract:** A new geometrical modeling tool has been developed to predict the elastic stiffness properties of 2D orthogonal and 2.5D woven interlock composites. The model estimates the change in performance due to changes in the ordering weaving parameters of the 2.5D weave architecture. Analysis results were validated compared to other models developed in published articles and the literature. Numerical analysis was performed to evaluate the accuracy of the results from the proposed models. These results demonstrate the effectiveness of the models presented by comparisons with experimental results, showing that the model could replicate the mechanical behaviors of 2D fabric and 2.5D interlock composite laminates for predicting 2D textile structures and 2.5D interlock composites with different types, shapes, and conditions. The model presented in this paper is able to replicate the behavior of woven composites of fiber reinforced with various types.

**Keywords:** 2D fabric; 2.5D; interlock composite; compliance matrix; homogenization

**Citation:** Kaddaha, M.A.; Younes, R.; Lafon, P. New Geometrical Modelling for 2D Fabric and 2.5D Interlock Composites. *Textiles* **2022**, 2, 142–161. https://doi.org/10.3390/textiles2010008

Academic Editor: Laurent Dufossé

Received: 13 January 2022
Accepted: 24 February 2022
Published: 7 March 2022



## 1. Introduction

Woven compounds are being increasingly considered for lots of applications because they provide ease in making complex geometries, but the mechanical properties of the different weave material supports are less visible than non-woven (angle-ply) laminates [1]. Note that there is no mathematical modelling of structural fiber-reinforced composite structures, though one measurement was obtained here using estimates in which woven fibers were formed from two orthotropic unidirectional fiber results in a curved twist using a weave. Recently, there has been in increased focus on exploring integrated and complete mechanical properties and methods of textile composites tested for uniaxial or biaxial tension, pressure, flexibility, and short-beam cutting [2–5]. Various analytical techniques have been developed to predict the elastic properties of representative volume elements (RVEs) of textile composites that include 2D and 3D weave composite. Woven composites can provide a potential solution to the basic limitations of traditional laminated composites: delamination and production that requires more workers. The addition of binder yarns provides through-thickness reinforcement, leading to highly advanced interlaminar materials and fabric binding to allow near-net-shape preforms to be woven and handled [6].

However, apart from these benefits, the use of 2.5D woven compounds is very limited in niche applications. One of the main reasons for this is the lack of predictive numerical tools, which limit their use in the early stages of design. Another method of production is to cut a simple three-dimensional weave, consisting of two two-dimensional (2D) fabrics connected by twisted loops of yarn, to form a 'hairy' fabric. These 2.5D fabrics are then coated with epoxy resin in a standard way, laminated, and treated with autoclave [7]. Woven Composites (2.5D-WC) not only have a higher delamination resistance compared to 2D laminated composites, but also have a simpler structure than 3D textile composites.

Recently, most parts in the aero-engine sector, namely fan/compressor blades and casing, were made using 2.5D-WC [8].

### *1.1. Objective*

The purpose of this paper is to introduce new content and a new, simple geometrical model for analyzing the mechanical properties of woven composites, i.e., 2D and 2.5D. In addition, the model will estimate the change in performance due to changing the weaving parameters that dictates the 2.5D weave architecture about the elastic properties; this is discussed in detail. Finally, important conclusions are reached.

An effective recursive algorithm, a matrix solidification method, is designed for multilayer media that is usually anisotropic. This algorithm has the efficiency and calculation of the standard transmission matrix method and is unconditional in terms of a high frequency calculation system and layer thickness. In this algorithm, the stiffness (compliance) matrix is calculated.

This algorithm allows researchers and end users to calculate the durability and compliance matrix of any woven compound material, of any type, shape, or thickness, while saving time and cost in finding the right solution.

This paper introduces a geometric modeling tool to predict the expandable stiffness features of 2.5D woven orthogonal interlock composites. The model is able to reproduce the behavior of woven composites formed by different fiber-reinforced types.

### *1.2. State of the Art*

Various analytical techniques have been developed to predict the expansive properties of volume representation (RVEs) of textile composites that include 2D and 2.5D weave composites. Bogdanovich and Pastore [9], Whitcomb et al. [10], and Potluri and Thammandra [11] have conducted a complete review of the topic. Based on stiffness averaging and rigidity ratio, Ishikawa and Chou [12–14] managed a two-orthogonal set of fabric compositions such as laminate with two laminae placed at 0/90 position. They proposed different models for predictable expansion, such as (1) a mosaic model (where fiber continuity and retraction was left), (2) a crimp model (where fiber continuity and undulation geometry were defined using the functions of -trigonometric), and (3) bridge coupling model (rigid or compliant dimensions in two orthogonal directions and suitable for satin weave combinations). Naik et al. [15,16] analyzed fiber retreat to the two orthogonal directions and used detailed trigonometric functions to extend the crimson models of Ishikawa and Chou (i.e., parallel two-dimensional series models and series-parallel models) to test expandable structures different combinations of PWF. Saka and Harding [17] and Carey et al. [18] developed rectilinear and sinusoidal crimp models to predict expansion structures using the classic laminate plate theory applied in the context of an expandable base and using the same power system. Tong et al. [19] take fiber as a curved rod based on stretch elastic or shear base in a woven composite structure and present a curved bark model to investigate the impact of fiber flexibility on the strength of woven composite material based on the concept of classical laminate plate theory. Kollegal and Sridharan [20] employed hierarchic works to determine the original curved profile of the strings and plate displays and introduced the micro-plate model for PWF analysis.

A significant amount of research was performed using the principles of differential stress [11,21] or FE (FEA) analysis [22–24] to analyze the expandable tracts of woven compounds and a detailed stress field across the RVE from the limited equipment. Regarding basic properties, in order to produce FE models, precise vertical segments or continuous mathematical functions are used to demonstrate in detail the ideal PWF geometry and to represent the thread path and cross section shape.

Mesoscopic simulations of transverse compaction have attracted recent interest. Geometric modeling methods have been developed using fabric matching software such as TexGen [25,26] or WiseTex [27,28], which have been used in various articles [29–33]. Multi-chain digital element-based methods have also been used [34–38]. Green et al. [39,40]

proposed a numerical procedure for creating mesostructural geometric models in simulated fabrics by combining appropriate TexGen models with multi-chain digital materials. Nguyen et al. [41] followed the method developed by Hivet and Boisse [42] to produce mesostructural geometric models of 2D woven fabrics to mimic the opposite combination. Numerical simulations of hypo elastic material based on fiber rotation were well matched to experiments. Alternatively, based on the discrete homogenization method, Goda et al. [43] and Rahali et al. [44] can reproduce the functional properties of 2.5D machines and 3D interlock textiles. Zhang et al. [45] developed a model based on the optical aspect ratio to predict mechanical responses and failure location under uniaxial and biaxial loading.

However, these methods are based on appropriate geometrical models, therefore cannot explain mesostructural changes in fiber structure, i.e., a detailed study of how fibers degenerate under bonding. Consideration and simplicity are often needed in numerical matching, which reduces calculation costs, facilitates the modeling process, and provides computer estimations. However, this simplification may prevent the investigation of other events occurring in real systems, especially in the case of mesoscopic and microscopic disorders.

Specific studies of mesoscopic transformation of fibrous reinforcement can also be performed with minimally invasive imaging such as X-ray micro-computed tomography (Micro-CT). With this process, it is possible to measure, model, and analyze the geometric structure of fiber cables. Desplentere et al. [46] and Schell et al. [47,48] were among the first to demonstrate the power of Micro-CT to show the geometric features of 3D fabrics on a mesoscopic scale. In Pazmino et al.'s study [49], the geometric features are directly measured by the fiber pulse from small tomographic images to read a single layer of 3D non-crimp woven fabric. Naouar et al.'s [50,51] mesostructural geometry models successfully reconstructed 2D woven fabric and 3D orthogonal fabric from small tomographic images. Wang et al. [52] studied longitudinal compression and the Poisson number of fiber cables followed a similar pattern. Badel et al. [53] performed both numerical simulations and tomographic analyzes of 2D woven fabrics under biaxial tension and in-plane shear deformation.

Combined with digital volume integration, Mendoza et al. [54] developed a mathematical model for the distortion of woven compounds, which was recently used to measure the flexibility caused by the production process [55]. However, no research studies to date have reported on the analysis of variables based on meso-structural models of fiberglass fabrics separated by these simplified methods at different levels of assembly.

Methodology:

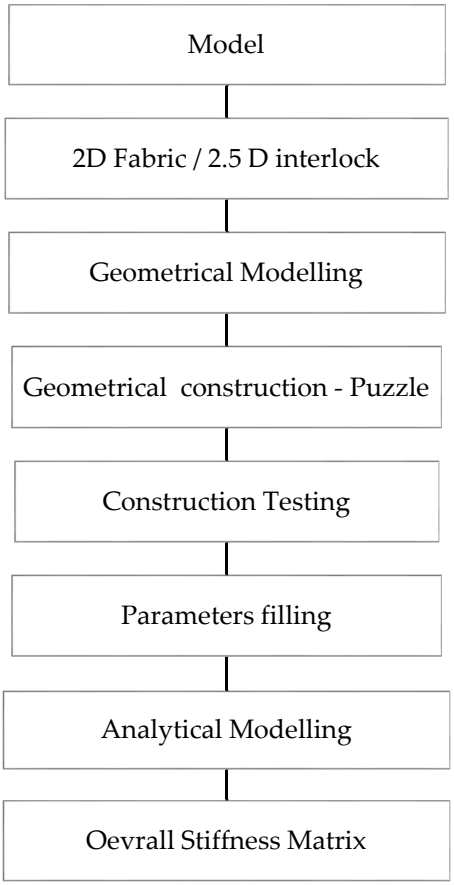


## 2. Geometrical Modelling

### *2.1. 2D Fabric*

The user—whether a student or a fellow researcher—can themselves design a fabric composite. To construct the whole structure of composite as he or she likes from the beginning and to make the whole process "user friendly", the process took the shape of building a puzzle by a simple "click and drop" game as shown in the figure below (Figure 1).

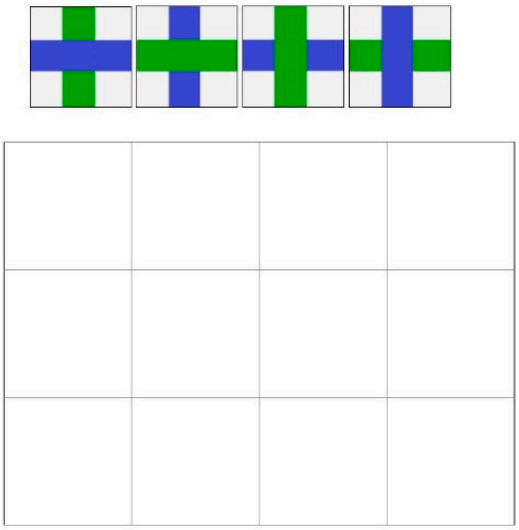

**Figure 1.** Puzzle structure for 2D fabric.

As 2D woven fabrics are made by interlacing yarns in a weaving loom, yarns are divided into two components: one called the warp, running along the length of the loom, and the other is the weft, running in the cross direction. The woven structure is characterized by orthogonal linking of two sets of threads, called warp and weft yarn. The warp threads are aligned with the direction of the fabric leaving the weaving equipment, which is also called the warp direction. As shown in Figure 2, 2D woven fabric has two yarn sets as warp (0°) and filling (90°) and interlaced to each other to form the surface.

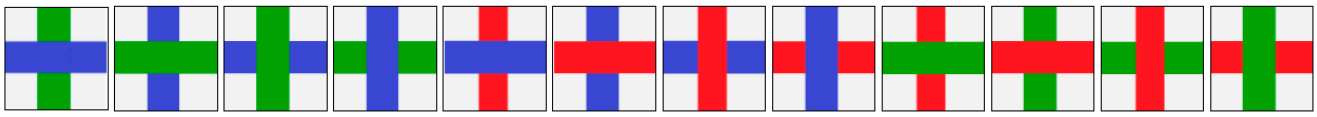

**Figure 2.** 2D fabric components.

To start from the beginning, the user is free to choose the settings of the puzzle in each dimension, i.e., number of columns and rows, and the number of fibers, as shown in Figure 3.

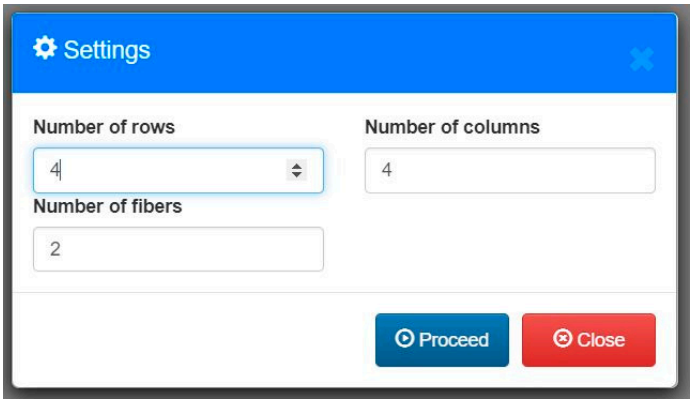


**Figure 3.** Puzzle settings for 2D fabric.

The next step is to construct the geometry as desired and shown in the following examples in Figures 4–7.

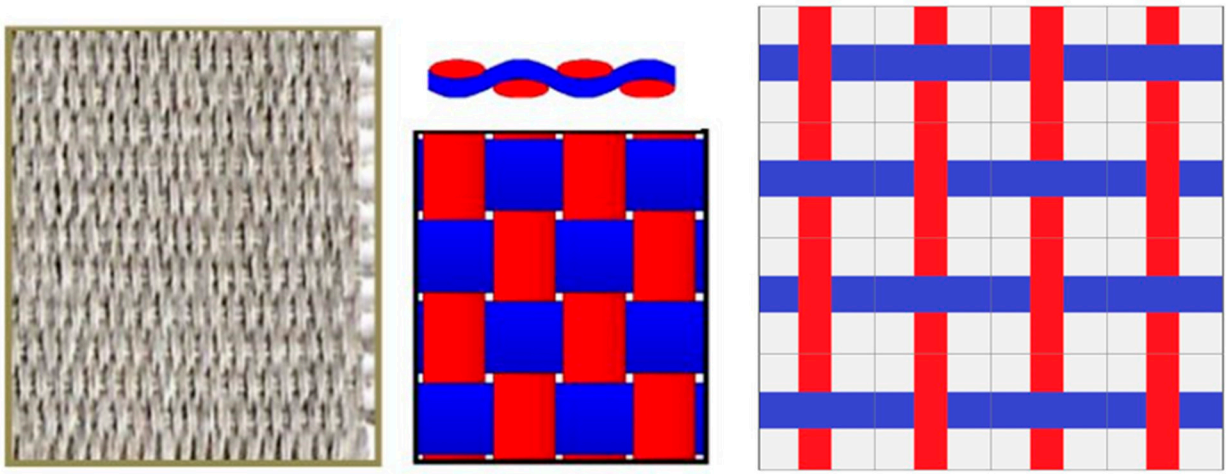

**Figure 4.** Plain weave fabric.

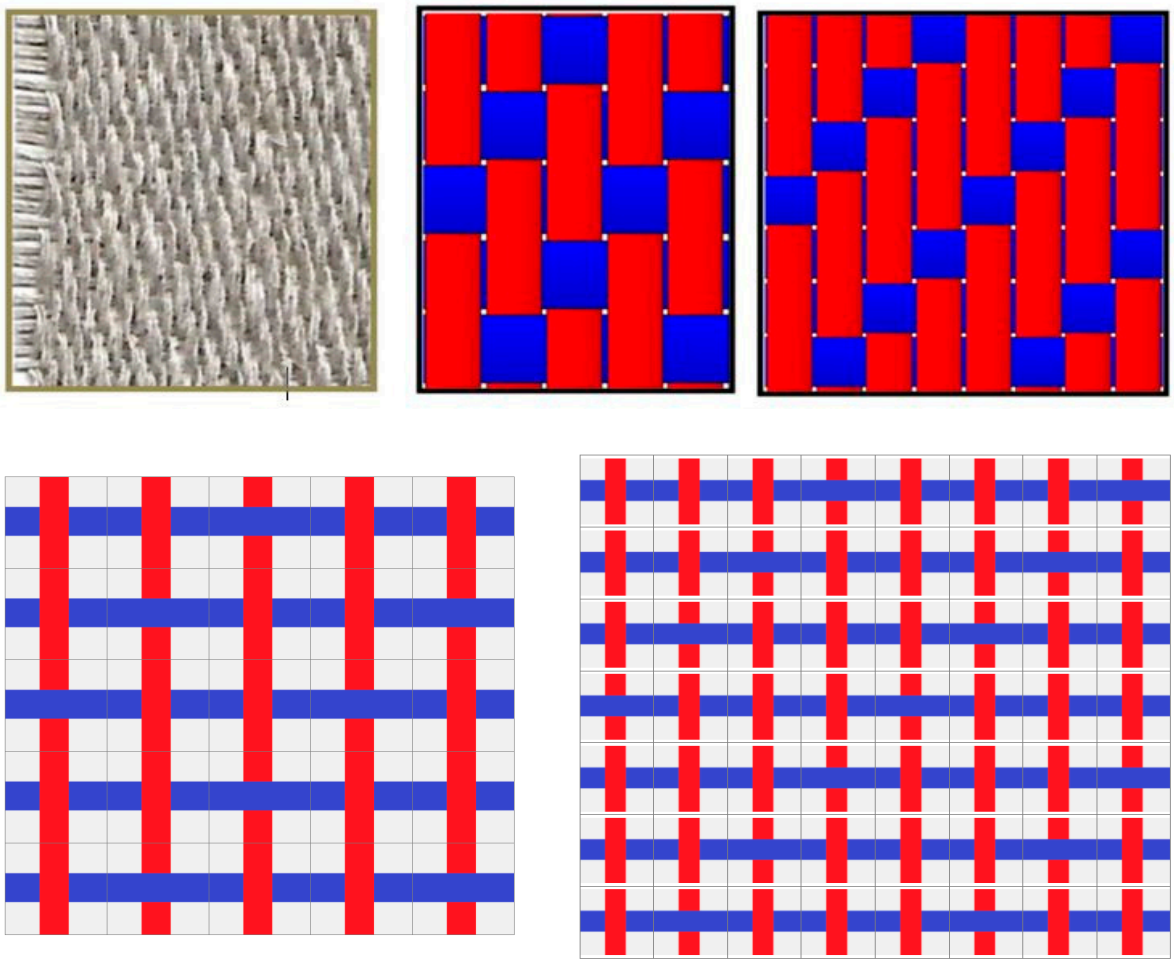

**Figure 5.** Twill weave fabric.

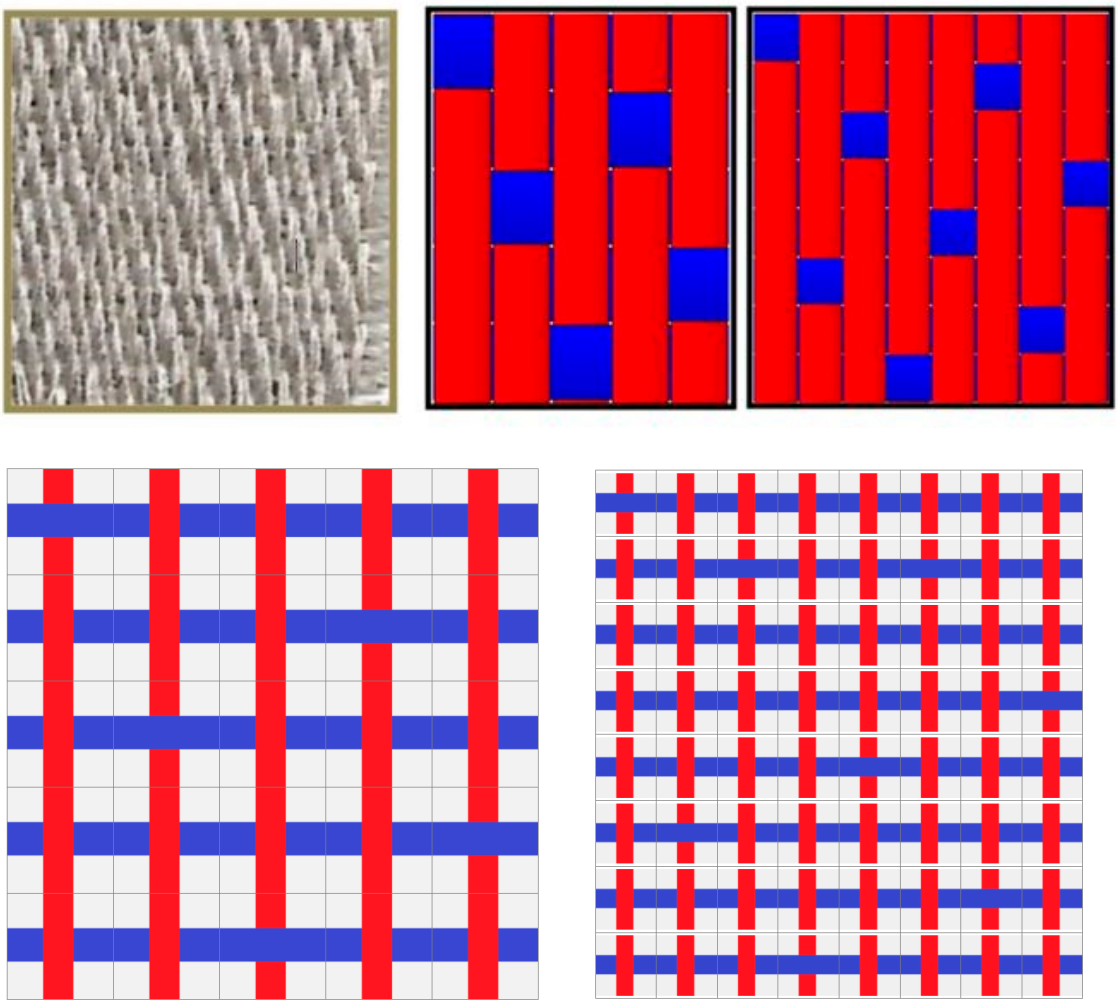

**Figure 6.** Sateen/Satin weave fabric.

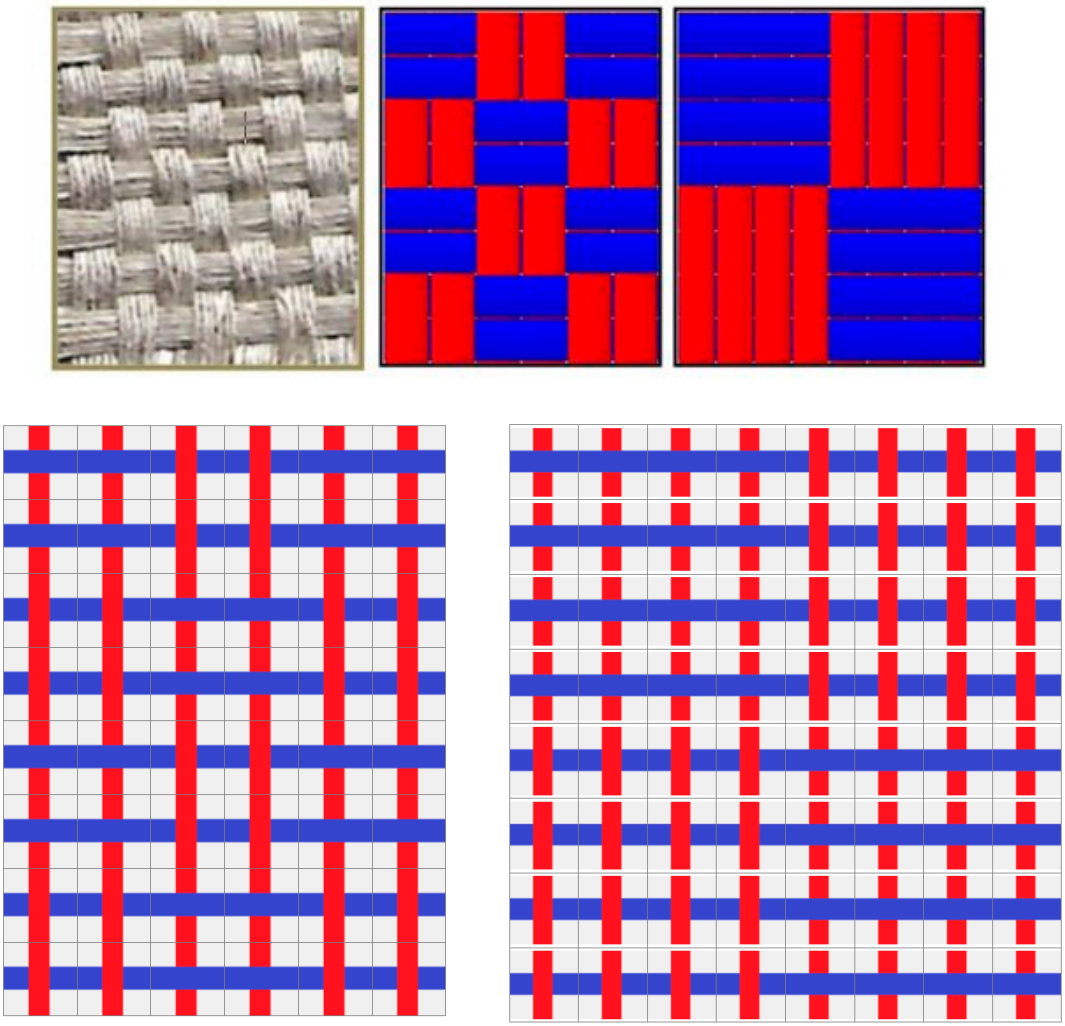

**Figure 7.** Basket weave fabric.

#### 2.1.1. Plain Weave Fabric [1/1]

Plain weave is a very common and very strong basic weave where each warp fiber passes alternately below and above each weft. The fabric is symmetrical and has good stability and logical porosity. However, they are the most difficult to weave, and the high quality of fiber crimp offers lower mechanical features compared to other weaving styles.

#### 2.1.2. Twill [2/1, 3/1]

Twill is a type of textile weave with a pattern of corresponding diagonal ribs. It can be seen by observing the presence of diagonal lines that are pronounced along the width of the fabric. It has a higher resistance to cracking than plain weave because it has fewer wires that connect to each area, hence the greater the internal flow rate. In addition, two strings will carry the load when the fabric is torn.

#### 2.1.3. Sateen/Satin [5-end, 8-end]

Sateen is a fabric that usually has a shiny surface and a hidden back, one of the three basic types of fabric weaving, seamless weaving, and twill. Four or more full-length or single-stranded strands floating over a straight rope, and four straight strands floating on a single weft thread indicate satin weaving. Floating strings are missed interfaces, where the warp thread lies on the weft in a satin with a straight face and where the weft thread lies on straight strands on satin with a weft face.

2.1.4. Basket Weave [2/2, 4/4]

Basket weave is known also as Hopsack and Matt Weave. Hopsack weave, a variant of plain weave, uses two or more warp and/or two or more weft fibers joined as a single thread. This weave is obtained by doubling or repeating the combined points of a plain weave in both the direction of the wrap and weft. These fabrics are made of two or more strings placed in the same shed. The stitching pattern is similar to a plain weave, but two or more strands follow the same parallel pattern. Fabrics designed by Matt are flexible and cannot wrinkle as there are a few cutters that are a square inch. Fabrics look flatter than conventional weaving fabrics. However, longer floats are more flexible. Matt fabric has great anti-tear properties. Matt's design tends to offer more smooth fabrics. For a repetitive Matt weave size, the warp numbers and weft threads are equal.

2.1.5. 2D Fabric Hybrid Composites

Hybrid yarns are where two or more fibers are brought together to combine the performance and aesthetic of both, as shown in Figure 8. Although environmental concerns are encouraging many manufacturers to focus on the use of a single fiber, there are still and will remain reasons for bringing fibers with different qualities together, particularly for performance and health and safety applications.

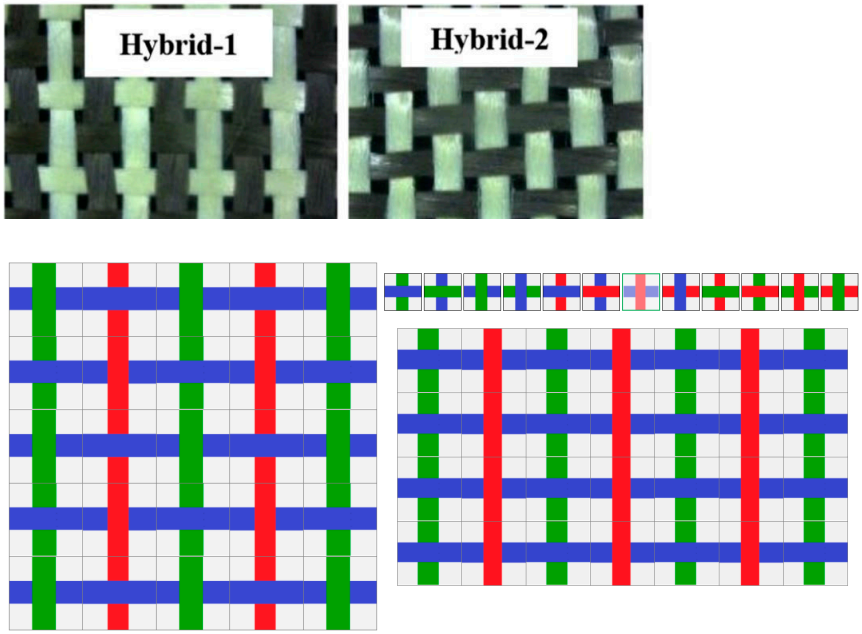


**Figure 8.** Hybrid composites.

*2.2. Interlock Composite 2.5D*

The 2.5D, or so-called 3D, interlock composite is a special fabric combination in which mechanical properties are closely related to its structure. The geometry of the interlock is complex and the number of possible structures is infinite. Fabric architecture depends on the extraction, crimp, and size of the fiber fibers. It is made up of a system of two woven and interconnected yarns, straight yarns, and weft (or filling) yarns. Interlacing caused by bending is called "tow crimp".

The shapes in the "puzzle" represent the filler element and the bounder (interlock fiber) of the structure, as shown in the figure below (Figure 9), in 2D view.

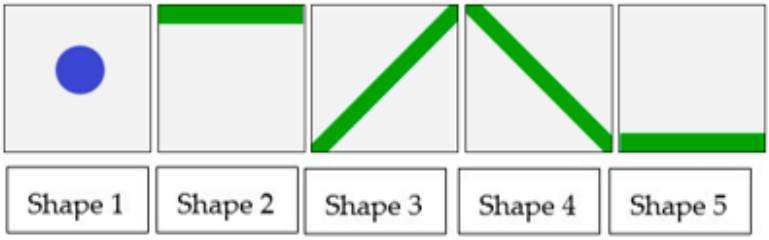


**Figure 9.** Shapes of the puzzle: Shape 1: the filler element; Shape 2: upper change in direction (horizontal); Shape 3: the reflected interlock; Shape 4: the incident interlock; Shape 5: lower change in direction (horizontal).

2.5D angle closing fabrics can be divided into two types: thick fabrics and fabrics from layer to layer. This type of combination is characterized by its intricate structure. The cell unit consists of a warp weaver and weft fibers attached to 90° plane (xy) (Figures 10 and 11). A 2.5D angle woven joint includes warp that binds to warp straight cords by attaching warp threads. Warp wires can be tied to different depths where different layout arrangements could be used to produce a wide range of these types of compounds. Tight fabric is a multi-layered fabric where warp weavers move from one piece of fabric to another, holding all the layers together. The layer-to-layer fabric as shown in Figure 10 is a multi-layer fabric that the warp weavers move from one layer to the nearest layer and back. A collection of warp woven together holds all the layers of fabric. In addition, complex geometry as shown in Figure 11, fractional volume fraction, cable volume, and inclination angle of warp strands are not able to allow the structural properties of specific applications. In other words, designers can replicate the efficient performance of fabrics for the necessary mechanical properties.

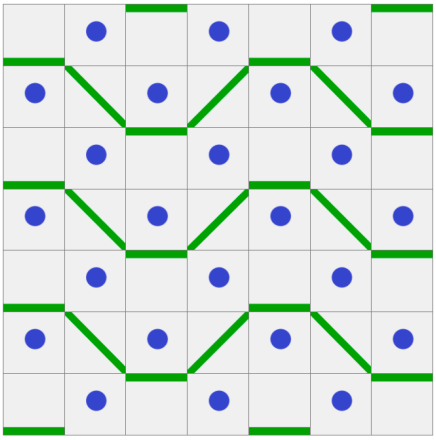

**Figure 10.** Layer to layer angle interlock.

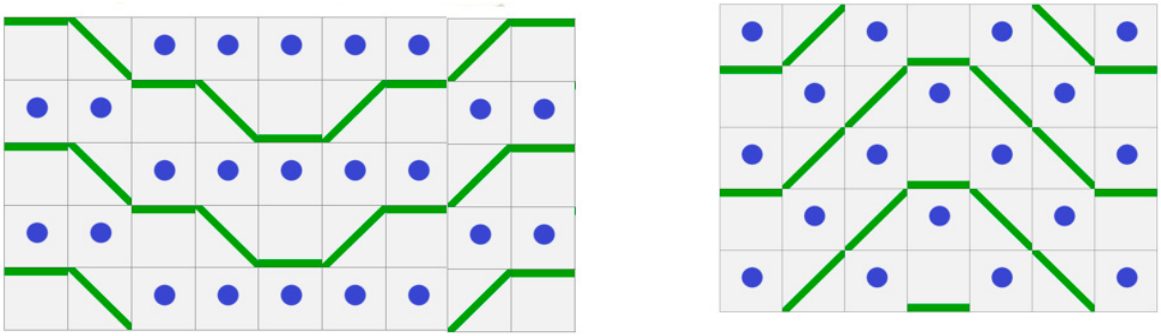

**Figure 11.** Through the thickness angle interlock.

1 Layer to Layer Angle Interlock
2 Through the Thickness Angle Interlock

*2.3. Construction Testing*

Tests should be performed as shown in Figures 10 and 11 to validate the shape suggested by the user. These tests are:

- Follow up test.
- Pattern test.
- Symmetry test (not obligatory).

These tests obtained by logical geometrical construction of the 2.5D interlock structure are as constrains that define whether the design (structure) from the user is valid–applicable—as shown in Figure 10.

As named, the function of the tests are to check if there is a continuity of structure and if there is a possibility to add a shape in the puzzle as shown in Figure 12. For example, Shape 3 cannot be similar to Shape 2′s incident and reflected interlock at the same time. The puzzle should be symmetrical if the user is constructing a symmetrical shape. If not, the test to check symmetry can be deactivated. Shapes 2, 3, and 4 cannot be repeated vertically. Shapes 2 and 4 cannot be repeated horizontally. Shapes 2 and 4 should be separated only by Shape 3. Shape 3 cannot follow Shape 1 or 2. At least one instance of Shape 1 should separate Shapes 2 and 4 horizontally. In addition, there are other structural and geometrical conditions and boundaries related to the shape.

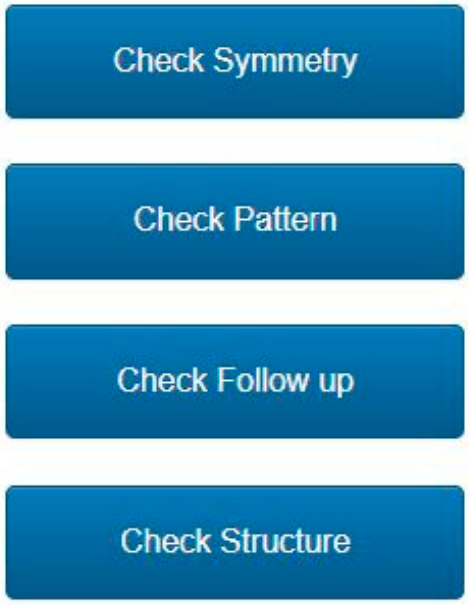


**Figure 12.** Validation tests.

Note that all these conditions/boundaries are tested automatically by the JavaScript code created by the author.

Moreover, if there is any structural mistake made by the designer (user) the code will identify the mistake with the relation of the mentioned tests. In addition, the code will specify exactly the place of the error with the messages: “Pattern problem at column 2—Follow up problem at (2,2)—Invalid structure” for the designer have to reshape its structure to continue and the sentences “No pattern problem—No follow up problem—Valid structure”, as shown in Figure 13

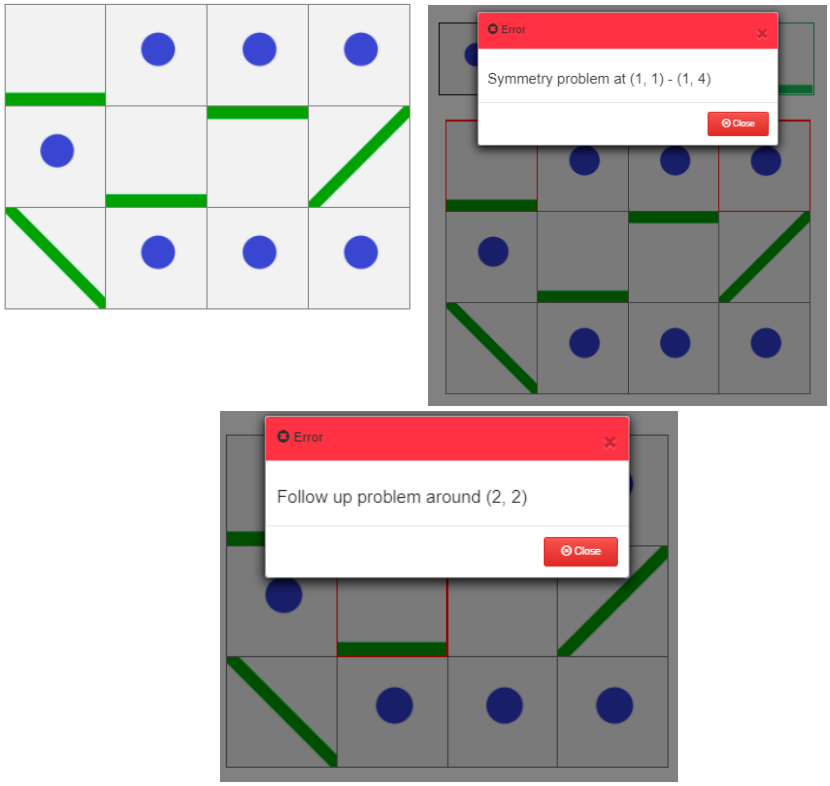


**Figure 13.** Validation tests.

### *2.4. Analytical Modelling*

First, the user should fill fibers and matrix parameters such as Young's and shear modulus ($E_i$,$G_i$) and fiber volume fraction (Vf) as shown in Figure 14 as a user interface to the analytical modelling.

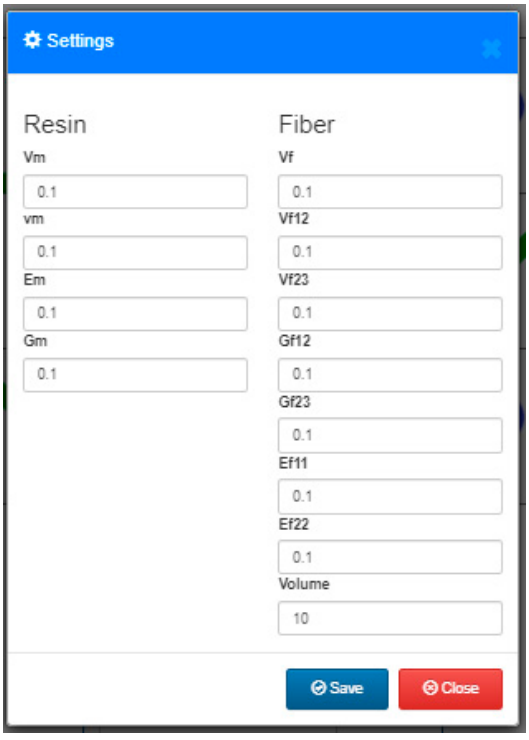


**Figure 14.** Fiber and matrix parameters.

Then, to calculate the characteristics of the key elements and the contribution rate, they make a macroscopic layer and subsequently the whole unit cell. The current approach creates expressions at the micro level with the aim of calculating more representative volume fractions of a group of elements to the layer to improve the elastic stiffness speculation compared to existing analytical modeling methods that use the 2.5D woven composite as a composite component containing layers of unidirectional elements (which are fibrous tows encased in resin). The new modelling approach creates expressions that discretize the unit cell into elements

To calculate the macroscopic stiffness of the whole unit cell, it must be broken down or discretized to the microscale. The microscale looks at the individual elements that make a cell and then the layers that make up the macroscopic unit cell. Therefore, the unit cell undergoes the first level discretization into layers, then the second level discretization into the individual elements that make up the layer. An element can be an individual, filler, binder, or matrix region within a layer. Having determined the stiffness of each element, the stiffness of whole row can be found. Once the stiffness of all rows is known, the model formulates and calculates the stiffness of the whole unit cell and finally outputs the elastic constants. The prediction of the unit cell or macroscopic stiffness begins with the calculation at the micro scale (the constituent elements within a cell).

The algorithm applied is as follows:

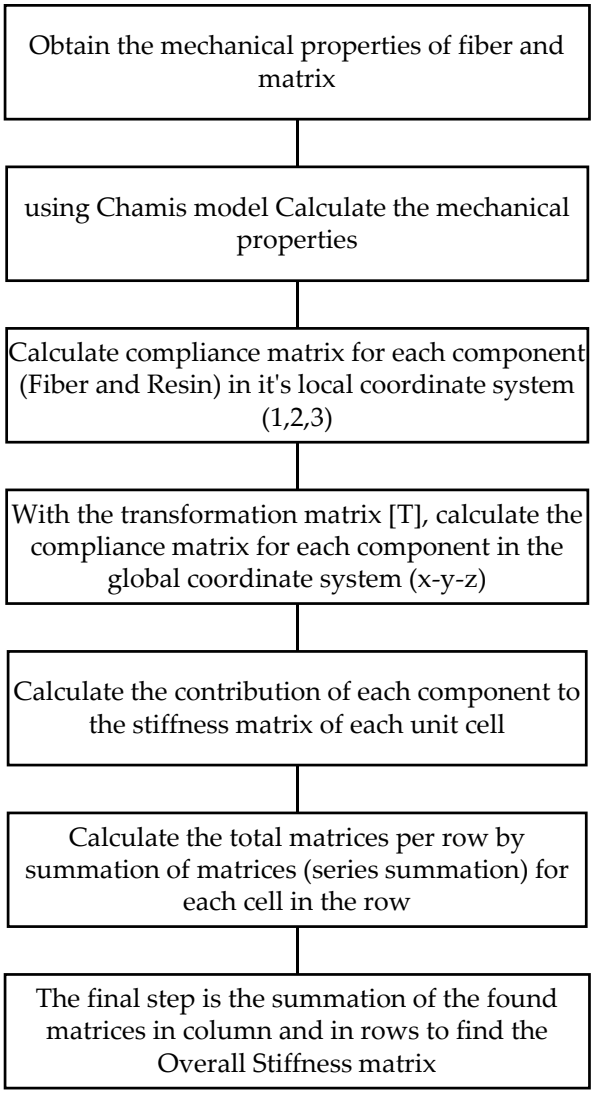

The fiber matrix (S) strength can be easily calculated. In the pocket of a pure resin matrix, it is generally regarded as isotropic substances. When the elastic modulus and Poisson's ratio of resin matrix are given, it is easy to determine its basic relationship. It is easy to obtain their compliance matrix in the local material coordinate systems (1- 2- 3) to (x- y- z) by inverting their stiffness matrix (Sij) as shown in Equations (1) and (2).

$$\left[S^f\right] = \begin{bmatrix} \frac{1}{E^f{}_1} & -\frac{\nu^f{}_{12}}{E^f{}_1} & -\frac{\nu^f{}_{13}}{E^f{}_1} & 0 & 0 & 0 \\ -\frac{\nu^f{}_{21}}{E^f{}_2} & \frac{1}{E^f{}_2} & -\frac{\nu^f{}_{23}}{E^f{}_2} & 0 & 0 & 0 \\ -\frac{\nu^f{}_{31}}{E^f{}_3} & -\frac{\nu^f{}_{32}}{E^f{}_3} & \frac{1}{E^f{}_3} & 0 & 0 & 0 \\ 0 & 0 & 0 & \frac{1}{G^f{}_{23}} & 0 & 0 \\ 0 & 0 & 0 & 0 & \frac{1}{G^f{}_{31}} & 0 \\ 0 & 0 & 0 & 0 & 0 & \frac{1}{G^f{}_{12}} \end{bmatrix} \quad (1)$$

$$[S^m] = \begin{bmatrix} \frac{1}{E^m} & -\frac{\nu^m}{E^m} & -\frac{\nu^m}{E^m} & 0 & 0 & 0 \\ -\frac{\nu^m}{E^m} & \frac{1}{E^m} & -\frac{\nu^m}{E^m} & 0 & 0 & 0 \\ -\frac{\nu^m}{E^m} & -\frac{\nu^m}{E^m} & \frac{1}{E^m} & 0 & 0 & 0 \\ 0 & 0 & 0 & \frac{1}{G^m} & 0 & 0 \\ 0 & 0 & 0 & 0 & \frac{1}{G^m} & 0 \\ 0 & 0 & 0 & 0 & 0 & \frac{1}{G^m} \end{bmatrix} \quad (2)$$

Each type of cell unit consists of two types of elements, namely fiber and a pure resin matrix. First, the lamina compliance matrix was calculated. Like most micro-mechanical models, the fibers and the resin matrix assume transversely isotropic, and both of them assume to be linearly elastic in the model. In order to achieve the elastic properties of the composites, the Chamis-proposed fiber-matrix ROM was selected to compute the engineering elastic constants. The Chamis micro-mechanical is a widely used and reliable model, providing an equation of all five independent structures that stretch like this [56]:

$$E_{11} = V^f E^f{}_{11} + V^m E^m \quad (3)$$

$$E_{22} = E_{33} = E^m/(1 - \sqrt{V^f}\,(1 - E^m/(E^f{}_{22}))) \quad (4)$$

$$G_{23} = G^m/(1 - \sqrt{V^f}\,(1 - G^m/(G^f{}_{23}))) \quad (5)$$

$$G_{12} = G_{13} = G^m/(1 - \sqrt{V^f}\,(1 - G^m/(G^f{}_{22}))) \quad (6)$$

$$\nu_{23} = V^f \nu^f{}_{23} + V^m\,(2\nu^m - \nu_{12}\,(E_{22}/E_{11})) \quad (7)$$

$$\nu_{12} = \nu_{13} = \nu^m + \nu^f\,(\nu^f{}_{12} - \nu^m) \quad (8)$$

where $V^f$ is the fiber volume fraction, $E^f{}_{11}$ is the Young's elastic modulus of the fiber in principle axis 1, $E^f{}_{22}$ is the Young's elastic modulus of the fiber in principle axis 2, $G^f{}_{12}$ is the longitudinal shear modulus of the fiber, $G^f{}_{23}$ is the transverse shear modulus of the fiber, $\nu^f{}_{12}$ is the primary Poisson's ratio of the fiber, and $E^m$, $\nu^m$, and $G^m$ represent the Young's elastic modulus, Poisson's ratio, and shear modulus of the matrix, respectively.

The compliance matrix of the fiber can be easily calculated. For the pure resin matrix pocket, it is generally regarded as isotropic material. When the elastic modulus and Poisson's ratio of resin matrix are given, it is easy to determine its basic relationship.

After that, we can obtain the stiffness in the global coordinate system by transforming the stresses and strains with the generalized transformation matrix as the next form:

$$[C^b] = [T]_k{}^T [C]_k [T]_k \quad (9)$$

where k is the number of unit cells in the Puzzle structure and the angle defined as the cosines of the angle between the axes of the local and global coordinate systems before and after rotation:

$$[T] = \begin{bmatrix} c^2 & s^2 & 2sc_1^2 & 0 & 0 & 0 \\ s^2 & c^2 & -2sc & 0 & 0 & 0 \\ -sc & sc & c^2 - s^2 & 0 & 0 & 0 \\ 0 & 0 & 0 & c^2 - s^2 & 0 & 0 \\ 0 & 0 & 0 & 0 & c^2 - s^2 & 0 \\ 0 & 0 & 0 & 0 & 0 & c^2 - s^2 \end{bmatrix} \quad (10)$$

$$c = \text{Cos}\,(\theta) \quad (11)$$

$$s = \text{Sin}\,(\theta) \quad (12)$$

where θ is the angle of weaving for the yarns.

A unidirectional cell falls under the orthotropic material category. As the cell is thin and does not carry any out-of-plane loads, one can assume plane stress conditions for the cell.

Therefore, assuming σ3 = 0, τ23 = 0, and τ31 = 0, calculation of element contribution is required so that the stiffness of the whole cell can be calculated as well as the overall unit cell stiffness. In our case, the contribution is related to the percentage in volume of the bounder (interlock fiber) with reference to the matrix volume (for example 30% bounder, 70% resin).

$$Mij = (p)\, C^{bK}ij + (1 - p)\, C^{K}mij \quad (13)$$

where [$C^b$] and [Cm] are the bounder and resin stiffness matrix in the global coordinate system, respectively, p is the percentage in volume of the bounder and resin in the composite structure, and k is the number of element in the whole structure.

Calculating the total matrix/row by summation of matrices (series summation) as shown in Equation (14):

$$Mt = \frac{\sum_{i=1}^{m} M_i}{m} \quad (14)$$

where *n* is the number of rows in the puzzle and [$M_i$] are the inverse of matrices found in Equation (14).

The final step is the summation of the found matrices in column and in rows as shown in Equation (15):

$$[S] = \frac{\sum_{i=1}^{n} Mt\text{-}_i^1}{n} \quad (15)$$

where *m* is the number of columns in the puzzle and [$Mt\text{-}^1{}_i$] are the matrices found in Equation (15).

## 3. Materials

### *3.1. 2D Fabric*

To ensure the effectiveness of this model based on this work. In comparison between current results modeling, experimental data, and previously developed multi-scale modelling, four different examples are generated. As studies, different mechanical features are considered and results are released. Examples were chosen from the specimens studied by J.J. Xiong and his co-workers [57] to calculate the engineering elastic constants of 2D Fabric Woven composites.

The composites studied in this section are the following:

E-glass/epoxy—I;
E-glass/epoxy—II;
T300/epoxy;
EW220/5284.

The fabric specifications and mechanical properties of the above four kinds of textile composites are listed in Table 1

**Table 1.** Fabric specifications and properties of 2D orthogonal fiber and resin.

| Geometry Parameters | E-Glass/Epoxy—I | E-Glass/Epoxy—II | T300/Epoxy | EW220/5284 |
|---|---|---|---|---|
| $V^f$ | 0.42 | 0.25 | 0.44 | 0.55 |
| $E_1$ (GPa) | 51.5 | 51.1 | 148.8 | 65.1 |
| $E_2$ (GPa) | 17.5 | 16 | 12.2 | 22.9 |
| $G_{12}$ (GPa) | 5.8 | 5.77 | 4.81 | 8.4 |
| $\nu_{12}$ | 0.31 | 0.31 | 0.29 | 0.24 |
| $E^m$ (GPa) | 3.5 | 3.5 | 3.5 | 3.2 |
| $G^m$ (GPa) | 1.3 | 1.3 | 1.3 | 1.1 |
| $\nu^m$ (GPa) | 0.35 | 0.35 | 0.35 | 0.42 |

### *3.2. 2.5D Interlock*

The composites are made from carbon fibers T300J and resin matrix RTM6 (Table 2). Two examples were chosen from the specimens studied by Hallal and his co-workers on 3SHM (3 stages homogenization method) [58]. The architecture of these composites involves only warp weaver yarns and weft straight yarns, as shown in Figures 10 and 11. The REV of the composite-H2 is composed of 6 warp yarns and 12 weft yarns, while the REV of the composite 71 is composed of 3 warp yarns and 24 weft yarns. The REV of composite 69 contains 6 warp yarns and 6 weft yarns. Warp yarns have a mean inclination angle equal to 29° for the linear longitudinal part of weft yarns. The warp yarns have a linear plus undulated longitudinal parts and a flattened elliptical cross-section. They are interlocked with weft yarns in two steps. Undulated parts have a mean inclination angle equal to 24° for H2 and 12° for 71. The weft yarns have a linear longitudinal part while its cross-section is a flattened ellipse. In addition, the fiber volume fractions in both warp and weft yarns is taken equal to 0.6. Table 2 shows the mechanical properties of carbon fibers and matrix. Carbon fibers assumed transversely isotropic material, which gives the following assumption:

**Table 2.** Mechanical properties of carbon fibers and matrix [58].

| Carbon Fibers | $Ef_{11}$ (GPa) | $Ef_{22}$ (GPa) | $Gf_{12}$ (GPa) | $vf_{12}$ | $vf_{23}$ |
|---|---|---|---|---|---|
| T300-J | 230 | 15 | 50 | 0.278 | 0.3 |
| Resin RTM6 | $E^m$ (GPa) | — | — | vm | — |
| — | 2.89 | — | — | 0.35 | — |

## 4. Results and Discussion

With the purpose of validating the developed modeling technique, the results were compared with experimental data published in the open literature. A comparison between the results of the present modeling, experimental data, and previously developed multi-scale modeling was conducted. As case studies, different mechanical properties were considered, and the results are shown in Tables 3–5, each of which shows a clear comparison between the experimental results and the presented model.

**Table 3.** Comparison between experiments and predictions for tension moduli (GPa).

| | $E_1$ (GPa) [57] | $E_1$ (GPa)—Author | Percentage of Error (%) |
|---|---|---|---|
| E-glass/epoxy—I | 14.5 | 14.38 | 0.82 |
| E-glass/epoxy—II | 60.3 | 60.57 | 0.44 |
| T300/epoxy | 58.91 | 59.39 | 0.814 |
| EW220/5284 | 19.3 | 19.67 | 1.91 |

**Table 4.** Analytical results of the iso-strain model compared to numerical results for the composites H2 [58].

| Effective Elastic Properties | $E_x$ (GPa) | $E_y$ (GPa) | $G_{xy}$ (GPa) |
|---|---|---|---|
| Results by 3SHM | 25.93 | 54.82 | 3.22 |
| Results by Author | 28.8 | 55.3 | 2.86 |
| Percentage of error (%) | 10 | 1 | 1.125 |

**Table 5.** Analytical results of the iso-strain model compared to numerical results for the composites 71 [58].

| Effective Elastic Properties | $E_x$ (GPa) | $E_y$ (GPa) | $G_{xy}$ (GPa) |
|---|---|---|---|
| Results by 3SHM | 40.7 | 31.21 | 3.14 |
| Results by Author | 40.95 | 32.5 | 3.102 |
| Percentage of error (%) | 0.614 | 4.13 | 1.21 |

For example, Table 3 shows the comparison of longitudinal and Young's moduli between four different materials and fibers studied by J.J. Xiong [57]. On the other hand, Tables 4–6 show a clear comparison for the section of 2.5D interlock composite with its different types.

**Table 6.** Analytical results of the iso-strain model compared to numerical results for the composites 69 [58].

| Effective Elastic Properties | $E_x$ (GPa) | $E_y$ (GPa) | $G_{xy}$ (GPa) |
|---|---|---|---|
| Results by 3SHM | 28.98 | 37.23 | 3.41 |
| Results by Author | 28.69 | 39.12 | 3.365 |
| Percentage of error (%) | 1 | 5.07 | 1.31 |

### *4.1. 2D Fabric*

As shown in Table 3, the comparison was focused on tension moduli from the specimens studied by J.J. Xiong and his co-workers [57]. The method present accurate and precise values with the percentages of error varied from 0.44% for longitudinal Young's modulus Ex, in E-glass/epoxy—II experiment up 1.91% for EW220/5284.

### *4.2. 5D Interlock*

The following table presents the results found by a previous analytical model from the reference validation mentioned earlier

The comparison was made to the engineering properties found using the code. A few notes should be taken into consideration: The model does not have curvature shape between Shapes 2, 3, and 4. The structure is in the coordinate system (x, y) by the reference. The dimensions of fiber are considered to be a tube shaped form and not elliptical. By comparing the result, we see that there is a validation to the code and the new model with a marginal error due to the curvature shape missing and the real/theoretical shape relation between the numerical, analytical, and geometrical model. It was observed from Table 4 that the Young's modulus in direction 2 is the most accurate parameter, up to 1% in comparison 3SHM found in Hallal [58], and that the maximum average error is shown for the Young's modulus in direction 1 with 10% of error. From Table 4, the percentage of error of transverse Young's modulus is much higher than for the longitudinal Young's modulus, with a value of 4.13% as the percentage of error of longitudinal Young's modulus was 0.614%. In addition, the percentages of error for shear modulus in Tables 4 and 5 were 1.12% and 1.21%, respectively. Finally, from Table 6, the percentage of error of transverse Young's modulus was also much higher than for the longitudinal Young's modulus, with a value of 5.07% and the percentage of error of longitudinal Young's modulus was 1%. The percentage of error for shear modulus in Table 6 was 1.31%.

In addition to the high accuracy level of the current modelling technique, the very short runtime required of the modelling renders the developed multi-scale modelling as a cost-effective computational tool for estimating the Young's moduli of laminate composites. The results showed that the present model could be used to effectively evaluate the elastic properties for laminate composites.

## 5. Conclusions

A geometrical-modelling tool has been presented to predict the elastic stiffness characteristics of 2D fabric and 2.5D woven interlock composites with the ability to assess change in performance as a consequence of altering weaving parameters. The models presented in this paper are able to reproduce the behavior of woven composites formed by different fiber-reinforced types. This approach has been validated against experimental data produced independently of this work for orthogonal interlock weaves and compared to existing modelling approaches. The present model performs better in all predictions compared to the existing modelling efforts. Good agreement was observed among numerical results, with small differences in the longitudinal strains, as shown in the results section that the shear modulus was the most accurate parameter up to 1% in the 2.5D interlock section, while the error in 2D fabric section was lower with values such as 0.44% in tension moduli. As for the longitudinal Young's modulus, the maximum average error is shown with 10% but with an average percentage of error of transversal strains of 4%. This may be due to a lack of precision in the mechanical properties of the components, i.e., the fibers, which are used as input data. The percentage is related to the lack of an accurate and precise database structure of the used material, but it shows a great ability to use the algorithm.

The suggested hypotheses are the simplest that can be applied for determining the engineering data with all required information, and specifications from the user are presented in a "user friendly" form that can make studying and searching a new level of excitement and interactivity. As shown in the methodology section, applying the algorithm is easy and simple. All this research can be accessed easily with all its codes and models, along with its regulations and explanations needed. Working on these codes will eliminate the hard work caused by the computational efforts using software such as Abaqus or Ansys, etc.

At any given time, the user can calculate required forces to have a known deformation or to predict the deformation for a known force; in addition, they would have easy access to all engineering properties such as stiffness or compliance matrices. A future scope is now set in each section to have more research and data analysis by using these codes and models without any super computers and losing time, money, and effort. Any researcher can now find the optimum set of materials for all levels of woven composites materials (2D Plain weave, Twill, Satin, or Basket), along with altering materials for 2.5D interlock composites such as layer to layer or through the thickness angle interlock. The model works best on other types of combinations, and further analysis and evaluation of the models is required. The introduced framework may apply to other fiber conditions as part of a fiber volume, but these conditions will require further development.

**Author Contributions:** R.Y.: Methodology and Supervision, P.L.: Data and spelling, M.A.K.: Writing, calculating, programming and analyzing. All authors have read and agreed to the published version of the manuscript.

**Funding:** This research received no external funding.

**Institutional Review Board Statement:** Not applicable.

**Informed Consent Statement:** Not applicable.

**Data Availability Statement:** Not applicable.

**Conflicts of Interest:** The authors declare no conflict of interest.

## References


1. Ghlaim, D.K. Woven factor for the mechancial properties of woven composite materials. *J. Eng.* **2010**, *16*, 4.
2. Ishikawa, T.; Matsushima, M.; Hayashi, Y.; Chou, T.W. Experimental confirmation of the theory of elastic moduli of fabric composites. *J. Compos. Mater.* **1985**, *19*, 443–458. [CrossRef]
3. Tan, P.; Tong, L.Y.; Steven, G.P.; Ishikawa, T. Behavior of 3D orthogonal woven CFRP composites. Part I. Experi-mental investi-gation. *Composites A* **2000**, *31*, 259–271. [CrossRef]
4. Botelho, E.C.; Figiel, L.; Rezende, M.C.; Lauke, B. Mechanical behavior of carbon fiber reinforced polyamide compo-sites. *Com-pos. Sci. Technol.* **2003**, *63*, 1843–1855. [CrossRef]
5. Wang, Y.J.; Zhao, D.M. Effect of Fabric Structures on the Mechanical Properties of 3-D Textile Composites. *J. Ind. Text.* **2006**, *35*, 239–256. [CrossRef]
6. Greena, S.D.; Matveevb, M.Y. Mechanical modelling of 3D woven composites considering realistic unit cell ge-ometry. *Compos. Struct.* **2014**, *118*, 284–293. [CrossRef]
7. Wvan, A.; Vuure, J.; Ivens, A.; Verpoest, I. Mechanical properties of composite panels based on woven sand-wich-fabric preforms. *Compos. Part A Appl. Sci. Manuf.* **2000**, *31*, 671–680.
8. Song, J.; Wen, D.W. Fatigue life prediction model of 2.5D woven composites at various temperatures. *Chin. J. Aeronaut.* **2018**, *31*, 310–329. [CrossRef]
9. Bogdanovich, A.E.; Pastore, C.M. *Mechanics of Textile and Laminated Composites*, 1st ed.; Chapman & Hall: London, UK, 1996.
10. Whitcomb, J.; Noh, J.; Chapman, C. Evaluation of Various Approximate Analyses for Plain Weave Composites. *J. Compos. Mater.* **1999**, *33*, 1958–1980. [CrossRef]
11. Potluri, P.; Thammandra, V.S. Influence of uniaxial and biaxial tension on meso-scale geometry and strain fields in a woven composite. *Compos. Struct.* **2007**, *77*, 405–418. [CrossRef]
12. Ishikawa, T.; Chou, T.-W. Elastic Behavior of Woven Hybrid Composites. *J. Compos. Mater.* **1982**, *16*, 2–19. [CrossRef]
13. Ishikawa, T.; Chou, T.W. Stiffness and strength behavior of woven fabric composite. *J. Mater. Sci.* **1982**, *17*, 3211–3220. [CrossRef]
14. Ishikawa, T.; Chou, T.W. One-dimensional micro-mechanical analysis of woven fabric composites. *AIAA J.* **1983**, *21*, 1714–1721. [CrossRef]
15. Naik, N.K.; Shembekar, P.S. Elastic Behavior of Woven Fabric Composites: I—Lamina Analysis. *J. Compos. Mater.* **1992**, *26*, 2196–2225. [CrossRef]
16. Naik, N.K.; Tiwari, S.I.; Kumar, R.S. An analytical model for compressive strength of plain weave fabric composites. *Compos. Sci. Technol.* **2003**, *63*, 609–625. [CrossRef]
17. Saka, K.; Harding, J. A simple laminate theory approach to the prediction of the tensile impact strength of woven hybrid composites. *Composites* **1990**, *21*, 439–447. [CrossRef]
18. Carey, J.; Munro, M.; Fahim, A. Longitudinal Elastic Modulus Prediction of a 2-D Braided Fiber Composite. *J. Reinf. Plast. Compos.* **2003**, *22*, 813–831. [CrossRef]
19. Tong, L.Y.; Tan, P.; Steven, G.P. Effect of yarn waviness on strength of 3D orthogonal woven CFRP composite ma-terials. *J. Reinf. Plast. Compos.* **2002**, *21*, 153–173. [CrossRef]
20. Kollegal, M.G.; Sridharan, S. A Simplified Model for Plain Woven Fabrics. *J. Compos. Mater.* **2000**, *34*, 1756–1786. [CrossRef]
21. Sheng, S.Z.; Hoa, V.S. Three-dimensional micro-mechanical modeling of woven fabric composites. *J. Compos. Mater.* **2003**, *37*, 763–789.
22. Zhang, Y.C.; Harding, J. A numerical micromechanics analysis of the mechanical properties of a plain weave composite. *Comput. Struct.* **1990**, *36*, 839–844. [CrossRef]
23. Thom, H. Finite Element Modeling of Plain Weave Composites. *J. Compos. Mater.* **1999**, *33*, 1491–1510. [CrossRef]
24. *ASTM D3039M-2000 (R06)*; Standard Test Method for Tensile Properties of Polymer Matrix Composite Materials. American Society for Testing and Materials: West Conshohocken, PA, USA, 2000.
25. *ASTM D695-02a*; Standard Test Method for Compressive Properties of Rigid Plastics. ASTM: WEST Conshohocken, PA, USA, 2003. [CrossRef]
26. Sherburn, M. *Geometric and Mechanical Modelling of Textiles*; University of Nottingham: London, UK, 2007.
27. Long, A.C.; Brown, L.P. Modelling the geometry of textile reinforcements for composites: TexGen. In *Composite Reinforcements for Optimum Performance*; Woodhead Publishing: Sawston, UK, 2011; pp. 239–264.
28. Verpoest, I.; Lomov, S.V. Virtual textile composites software WiseTex: Integration with micro-mechanical, permeability and structural analysis. *Compos. Sci. Technol.* **2005**, *65*, 2563–2574. [CrossRef]
29. Lomov, S.V.; Ivanov, D.S.; Verpoest, I.; Zako, M.; Kurashiki, T.; Nakai, H.; Hirosawa, S. Meso-FE modelling of textile composites: Road map, data flow and algorithms. *Compos. Sci. Technol.* **2007**, *67*, 1870–1891. [CrossRef]
30. Cao, Y.; Cai, Y.; Zhao, Z.; Liu, P.; Han, L.; Zhang, C. Predicting the tensile and compressive failure behavior of angleply spread tow woven composites. *Compos. Struct.* **2019**, *234*, 111701. [CrossRef]
31. Zhang, C.; Binienda, W.K. A meso-scale finite element model for simulating free-edge effect in carbon/epoxy textile composite. *Mech. Mater.* **2014**, *76*, 1–19. [CrossRef]
32. Zeng, X.S.; Long, A.C.; Gommer, F.; Endruweit, A.; Clifford, M. Modelling compaction effect on permeability of 3D carbon reinforcements. In Proceedings of the 18th International Conference on Composites Materials, Jeju Island, Korea, 21–26 August 2011.

33. Yousaf, Z.; Potluri, P.; Withers, P.J. Influence of Tow Architecture on Compaction and Nesting in Textile Preforms. *Appl. Compos. Mater.* **2017**, *24*, 337–350. [CrossRef]
34. Zeng, Q.; Sun, L.; Ge, J.; Wu, W.; Liang, J.; Fang, D. Damage characterization and numerical simulation of shear experiment of plain woven glass-fiber reinforced composites based on 3D geometric reconstruction. *Compos. Struct.* **2019**, *233*, 111746. [CrossRef]
35. Wang, Y.; Sun, X. Digital-element simulation of textile processes. *Compos. Sci. Technol.* **2001**, *61*, 311–319. [CrossRef]
36. Zhou, G.; Sun, X.; Wang, Y. Multi-chain digital element analysis in textile mechanics. *Compos. Sci. Technol.* **2004**, *64*, 239–244. [CrossRef]
37. Durville, D. Simulation of the mechanical behaviour of woven fabrics at the scale of fibers. *Int. J. Mater. Form.* **2010**, *3*, 1241–1251. [CrossRef]
38. Durville, D.; Baydoun, I.; Moustacas, H.; Périé, G.; Wielhorski, Y. Determining the initial configuration and characterizing the mechanical properties of 3D angle-interlock fabrics using finite element simulation. *Int. J. Solids Struct.* **2018**, *154*, 97–103. [CrossRef]
39. Mahadik, Y.; Hallett, S.R. Finite element modelling of tow geometry in 3D woven fabrics. *Compos. A Appl. Sci. Manuf.* **2010**, *41*, 1192–1200. [CrossRef]
40. Green, S.D.; Long, A.C.; El Said, B.S.F.F.; Hallett, S.R. Numerical modelling of 3D woven preform deformations. *Compos. Struct.* **2014**, *108*, 747–756. [CrossRef]
41. Nguyen, Q.T.; Vidal-Sallé, E.; Boisse, P.; Park, C.H.; Saouab, A.; Bréard, J.; Hivet, G. Mesoscopic scale analyses of textile composite reinforcement compaction. *Compos. Part B Eng.* **2013**, *44*, 231–241. [CrossRef]
42. Hivet, G.; Boisse, P. Consistent 3D geometrical model of fabric elementary cell. Application to a meshing preprocessor for 3D finite element analysis. *Finite Elements Anal. Des.* **2005**, *42*, 25–49. [CrossRef]
43. Goda, I.; Assidi, M.; Ganghoffer, J.-F. Equivalent mechanical properties of textile monolayers from discrete asymptotic homogenization. *J. Mech. Phys. Solids* **2013**, *61*, 2537–2565. [CrossRef]
44. Rahali, Y.; Assidi, M.; Goda, I.; Zghal, A.; Ganghoffer, J.F. Computation of the effective mechanical properties including nonclassical moduli of 2.5D and 3D interlocks by micromechanical approaches. *Compos. Part B Eng.* **2016**, *98*, 194–212. [CrossRef]
45. Zhang, D.; Sun, Y.; Wang, X.; Chen, L. Meso-scale finite element analyses of three-dimensional five-directional braided composites subjected to uniaxial and biaxial loading. *J. Reinf. Plast. Compos.* **2015**, *34*, 1989–2005. [CrossRef]
46. Desplentere, F.; Lomov, S.V.; Woerdeman, D.L.; Verpoest, I.; Wevers, M.; Bogdanovich, A. Micro-CT characterization of variability in 3D textile architecture. *Compos. Sci. Technol.* **2005**, *65*, 1920–1930. [CrossRef]
47. Schell, J.S.U.; Renggli, M.; van Lenthe, G.H.; Müller, R.; Ermanni, P. Micro-computed tomography determination of glass fibre re-inforced polymer meso-structure. *Compos. Sci. Technol.* **2006**, *66*, 2016–2022. [CrossRef]
48. Schell, J.S.U.; Deleglise, M.; Binetruy, C.; Krawczak, P.; Ermanni, P. Numerical prediction and experimental characterisation of meso-scale-voids in liquid composite moulding. *Compos. Part A Appl. Sci. Manuf.* **2007**, *38*, 2460–2470. [CrossRef]
49. Pazmino, J.; Carvelli, V.; Lomov, S.V. Micro-CT analysis of the internal deformed geometry of a non-crimp 3D or-thogonal weave E-glass composite reinforcement. *Compos. B Eng.* **2014**, *65*, 147–157. [CrossRef]
50. Naouar, N.; Vidal-Sallé, E.; Schneider, J.; Maire, E.; Boisse, P. Meso-scale FE analyses of textile composite reinforcement deformation based on X-ray computed tomography. *Compos. Struct.* **2014**, *116*, 165–176. [CrossRef]
51. Naouar, N.; Vidal-Salle, E.; Schneider, J.; Maire, E.; Boisse, P. 3D composite reinforcement meso F.E. analyses based on X-ray computed tomography. *Compos. Struct.* **2015**, *132*, 1094–1104. [CrossRef]
52. Wang, D.; Naouar, N.; Vidal-Salle, E.; Boisse, P. Longitudinal compression and Poisson ratio of fiber yarns in meso-scale finite element modeling of composite reinforcements. *Compos. Part B Eng.* **2018**, *141*, 9–19. [CrossRef]
53. Badel, P.; Vidal-Sallé, E.; Maire, E.; Boisse, P. Simulation and tomography analysis of textile composite reinforcement deformation at the mesoscopic scale. *Compos. Sci. Technol.* **2008**, *68*, 2433–2440. [CrossRef]
54. Mendoza, A.; Schneider, J.; Parra, E.; Obert, E.; Roux, S. Differentiating 3D textile composites: A novel field of application for Digital Volume Correlation. *Compos. Struct.* **2019**, *208*, 735–743. [CrossRef]
55. Mendoza, A.; Schneider, J.; Parra, E.; Roux, S. Measuring yarn deformations induced by the manufacturing process of woven composites. *Compos. Part A Appl. Sci. Manuf.* **2019**, *120*, 127–139. [CrossRef]
56. Parvanesh, V.; Shariati, M.; Nezakati, A. Statistical analysis of the parameters influencing the mechanical properties of layered MWCNTs/PVA nano composites. *Int. J. Nano Dimens.* **2015**, *6*, 509–516.
57. Xiong, J.J.; Shenoi, R.A.; Cheng, X. A modified micromechanical curved beam analytical model to predict the tension modulus of 2D plain weave fabric composites. *Compos. Part B* **2009**, *40*, 776–783. [CrossRef]
58. Hallal, A.; Younes, R.; Fardoun, F.; Nehme, S. Improved analytical model to predict the effective elastic properties of 2.5D interlock woven fabrics composite. *Compos. Struct.* **2012**, *94*, 3009–3028. [CrossRef]

textiles

*Article*

# Meso-Macro Simulations of the Forming of 3D Non-Crimp Woven Fabrics

**Jie Wang [1,*], Peng Wang [2], Nahiene Hamila [3] and Philippe Boisse [1]**

[1] Université de Lyon, LaMCoS CNRS, INSA-Lyon, F-69621 Lyon, France; philippe.boisse@insa-lyon.fr
[2] Université de Haute Alsace, ENSISA, LPMT, F-68000 Mulhouse, France; peng.wang@uha.fr
[3] Ecole Nationale d'Ingénieurs de Brest, IRDL CNRS, F-29200 Brest, France; nahiene.hamila@enib.fr
* Correspondence: jie.wang@outlook.fr

**Abstract:** The RTM (Resin Transfer Molding) manufacturing process is largely used for the fabrication of textile composites. During the forming phase, the deformations of composite reinforcements at the mesoscopic scale, such as the positions, orientations, and changes in the sections of deformed yarns, are essential to calculate the permeability of the reinforcement in the injection phase and evaluate the mechanical behaviors of the final products. However, the mesoscopic models of the forming simulation lead to a high computational cost due to the numerous yarns and their complex contacts, especially for thick reinforcements. In this paper, a macro-meso method for predicting the mesoscopic deformations of composite reinforcements with a reasonable calculation time is presented in this paper. The proposed multi-scale method allows for the linkage of the macroscopic simulation of reinforcements with the mesoscopic modelling of an RVE (Representative Volume Element) through a macro-meso embedded approach. Based on macroscopic simulations using a 3D hyperelastic constitutive law, an embedded mesoscopic geometry is first deduced. The macro-meso embedded solution can lead to excessive extensions of yarns. To overcome this inconvenience, a local mesoscopic simulation based on the macro-meso embedded analysis is carried out on a single RVE. Finally, the multi-scale forming simulations are investigated in comparison with the experimental results, illustrating the efficiency of the proposed method.

**Keywords:** forming simulation; multi-scale analyses; RVE; hyperelasticity; thick reinforcements

**Citation:** Wang, J.; Wang, P.; Hamila, N.; Boisse, P. Meso-Macro Simulations of the Forming of 3D Non-Crimp Woven Fabrics. *Textiles* **2022**, *2*, 112–123. https://doi.org/10.3390/textiles2010006

Academic Editors: Jiri Militky, Raul Fangueiro and Rajesh Mishra

Received: 15 December 2021
Accepted: 2 February 2022
Published: 11 February 2022



## 1. Introduction

Composite materials with excellent performance are becoming more attractive in the field of high technology. The RTM manufacturing process of textile composites is widely used, which includes two main stages: the forming stage and the injection stage. The forming phase is important because it strongly influences the mechanical behavior of the final composite parts. In order to better predict the geometrical and mechanical characteristics of textile composites, different types of simulations can be distinguished at three different scales: macroscopic (the fabric), mesoscopic (the yarns), and microscopic (the fibers).

To simulate the forming process of textile composites, approaches are generally carried out at the macroscopic scale [1–4], in which the reinforcement is considered as a continuous medium. At this scale, it is possible to predict the appearance of wrinkles, which is the major defect that appears during this phase [5,6]. However, some important phenomena may appear on a smaller scale during the forming process of reinforcements [7–11]. Mesoscopic models, which consider reinforcements as a set of yarns in contact with their neighbors, are able to predict possible defects, such as the rupture, the gaping, and the local buckling of yarns. In addition, the information about deformations and orientations of yarns allows for the determination of the mechanical behavior of the final parts and the calculation of the permeability tensor of the deformed reinforcement, which can be used to simulate the

resin flow in the injection stage [12–14]. Nevertheless, it is difficult to simulate the shaping of woven reinforcements at this mesoscopic scale taking into account the large number of yarns and their complex interactions, especially for 3D fabrics. In these models, one of the most critical problems is the computing time.

In this context, the objective of this paper is to develop an efficient multi-scale method that allows one to obtain the deformations and orientations of yarns for a whole composite structure during the shaping process of woven reinforcements, with a reasonable computation time. The multi-scale methods that have been developed in the literature consist of creating a passage of information between the macro and meso scales [15–20]. This passage makes it possible to transform the deformed information between the macroscopic and mesoscopic scales. In other words, the deformations and the orientations of yarns, as well as the variations of the transverse sections of yarns for the entire composite part, can be calculated from macroscopic forming simulations of woven reinforcements. This proposed method is divided into three main parts: (1) the macroscopic simulation of the woven reinforcements, (2) macro-meso embedded analysis, and (3) the mesoscopic results enriched by a local mesoscopic simulation of RVE. The objective is to present the method in a simple way, postponing the presentation of the laws of macroscopic and mesoscopic behavior to the appendix. The analysis of the number of RVEs in the mesoscopic analysis is presented as well as a comparison of the method with the experiment. The material studied here is an orthogonal 3D glass woven reinforcement (see Figure 1) [21].

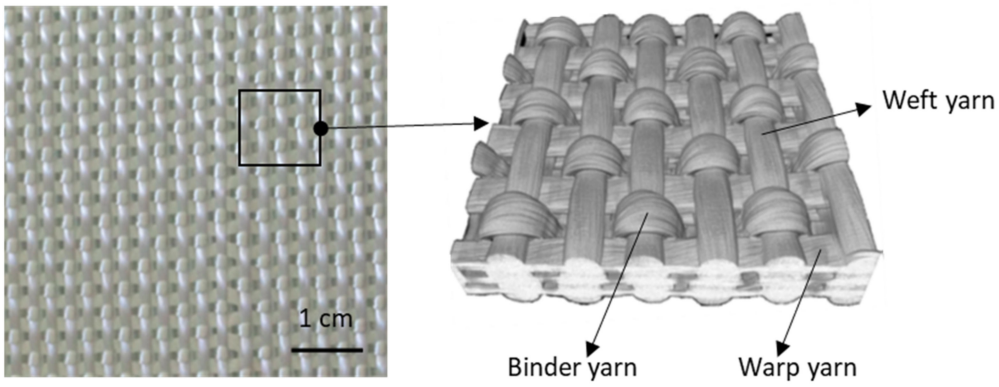


**Figure 1.** Structure of the 3D non-crimp orthogonal woven fabric by X-ray tomography and its mesh.

## 2. Macroscopic Analysis of Woven Reinforcements

This part consisted of implementing the numerical simulations of the woven reinforcements at the macroscopic scale using the PlasFib software [22], which calculation codes based on the finite element method (FEM), developed by the LaMCoS laboratory. This finite element code uses a temporal scheme in an explicit dynamic. In macroscopic approaches, woven reinforcements are considered as a continuous medium with a continuous constitutive law. In order to describe the mechanical characteristics of thick textile reinforcements during draping, a 3D hyperelastic constitutive law is applied in the macroscopic simulations [23–25]. In this hyperelastic constitutive law, six independent deformation modes of the reinforcement are considered: elongation in the warp and weft direction, transverse compaction, in-plane shear, and transverse shear in the warp and weft direction. The stress–strain relationship is determined through the derivative of the strain energy density $w$, which is the sum of the strain energy of every deformation mode (Equation (1)). Then, the second Piola–Kirchhoff stress tensor $\underline{\underline{S}}$ can be calculated by the differentiation $\partial w_k / \partial I_k$ and the right Cauchy–Green tensor $\underline{\underline{C}}$ (Equation (2)). $I_k$, namely $I_{elong1}$, $I_{elong2}$, $I_{comp}$, $I_{sh}$, $I_{shT1}$, and $I_{shT2}$, is the physical invariant associated with each deformation mode. In addition, the contribution of curvature in the hexahedral finite elements is taken into account by adding a local flexural stiffness [25].

$$w = w_{elong1}\left(I_{elong1}\right) + w_{elong2}\left(I_{elong2}\right) + w_{comp}\left(I_{comp}\right) + w_{sh}(I_{sh}) + w_{shT1}(I_{shT1}) + w_{shT2}(I_{shT2}) \quad (1)$$

$$\underline{\underline{S}} = 2\frac{\partial w}{\partial \underline{\underline{C}}} = 2\frac{\partial w_k}{\partial I_k}\frac{\partial I_k}{\partial \underline{\underline{C}}} \quad (2)$$

The characterization of the material parameters was carried out by different classical tests: tensile test, transverse compaction, in-plane shear, transverse shear, and bending test, by means of the inverse method with the Levenberg–Marquardt algorithm. The details of these tests have been described in [17], and the identified material parameters are given in Appendix A.

Once all the material parameters in the hyperelastic constitutive law were identified, the forming simulation of reinforcements was carried out in the PlasFib software. Macroscopic simulations were realized in two cases: three-point bending and hemispherical forming (Figures 2 and 3). Finally, in comparison with the corresponding experiments, the results obtained by the simulation were in good agreement. This was the case for the deformed mid-surface of the bending specimen in Figure 2b and for the shear angles after forming the hemisphere in Figure 3.

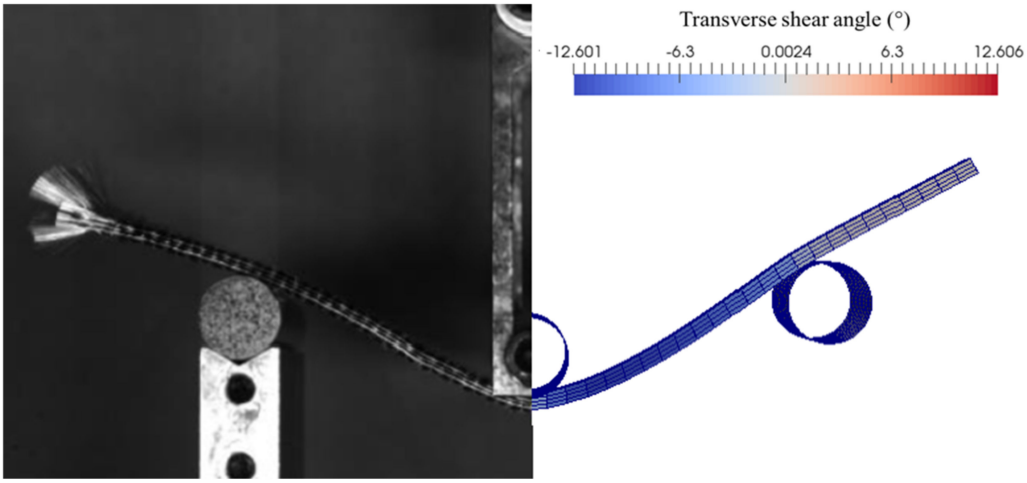


(**a**)

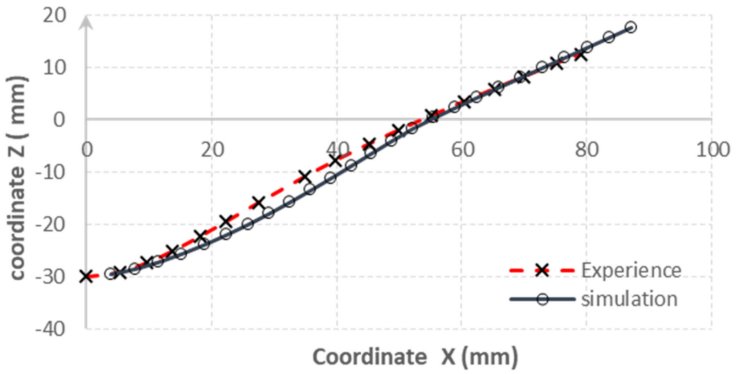


(**b**)

**Figure 2.** Comparisons between the numerical and experimental results for three-point bending (**a**) deformed geometry and (**b**) the deformation of the middle line of the reinforcement.

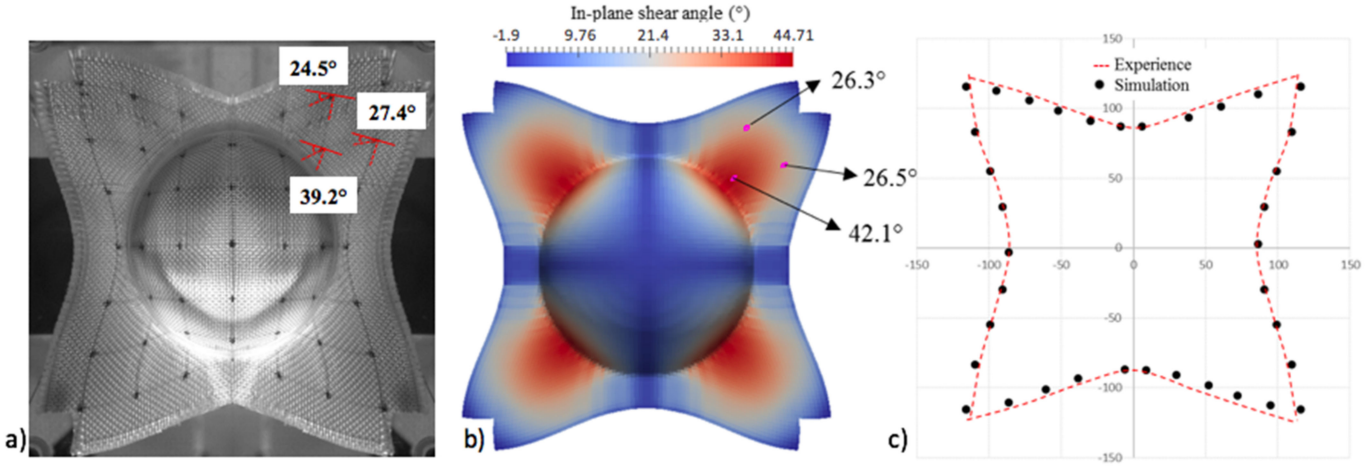


**Figure 3.** Comparisons between the experimental and numerical results for hemispherical forming. (**a**,**b**) In-plane shear angle in the same position. (**c**) Deformed geometry.

## 3. Mesoscopic Analysis by Macro-Meso Embedded Approach

Some mesoscopic models of the entire reinforcement have been used in different studies [8,16,26] to obtain the mesoscopic deformed information of woven composites; however, the size of the numerical model is large and the computational time is long. Therefore, the objective of the developed macro-meso embedded approach is to estimate the deformation of yarns for the entire reinforcement during the forming process with a reasonable computational time.

In this macro-meso embedded approach, the numerical results obtained by the macroscopic simulations of reinforcement are the basis. If the macroscopic results are relevant, they should be able to provide some basic and useful information at the mesoscopic scale. In short, the embedded mesoscopic geometry is determined from the result of the macroscopic simulation.

The macro-meso embedded approach allows one to link macroscopic simulations of thick reinforcements and mesoscopic modeling of RVEs (representative volume elements). For periodic textile reinforcements, the geometrical modeling of the RVE is first reconstructed according to X-ray tomography images based on the real geometry of the reinforcement [27]. The modeling of the entire reinforcement at the mesoscopic scale can then be generated in the initial configuration by the repetitions and translations of the RVE. Then, each mesoscopic node of the yarns in the woven reinforcement can be located or integrated into a macroscopic element (Figure 4). During deformation, the integrated mesoscopic element deforms together with the macroscopic element where this mesoscopic element is located, and its mesoscopic nodes have constant natural coordinates in the reference and real macroscopic element.

During deformation, the natural coordinates of a mesoscopic node in the corresponding macroscopic element remain identical. In other words, the material position of an embedded mesoscopic node remains constant in the macroscopic element. Therefore, the deformation obtained by the macroscopic simulations can provide a first geometry of reinforcements at the mesoscopic scale in the deformed configuration. As shown in Figures 5 and 6, the mesoscopic deformed geometries of the reinforcement can be obtained by the macro-meso embedded approach.

The mesoscopic results based on macroscopic simulations allow for the determination of the deformations and the deformed orientations of the yarns, and the voids in the elementary cell. The calculation time is very fast, from a few minutes to one hour depending on the reinforcement size.

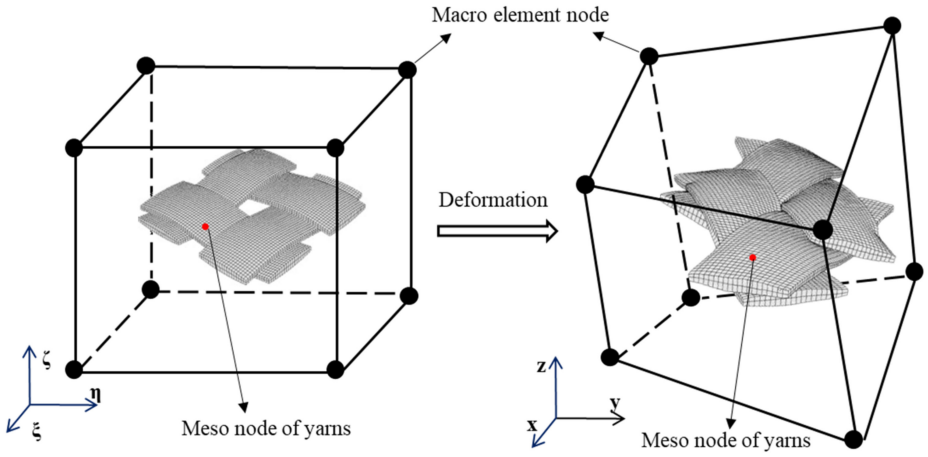


**Figure 4.** Meso node of yarns embedded in a macro element. Reference and real frames.

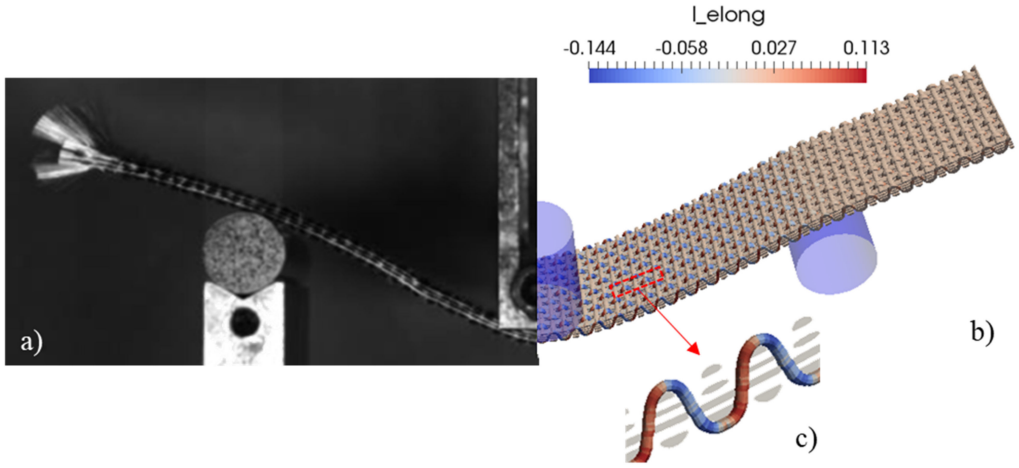


**Figure 5.** Three-point bending. (**a**) Deformed geometry in experimental result. (**b**) Elongation of yarns in mesoscopic analysis. (**c**) Elongation of an extracted yarn.

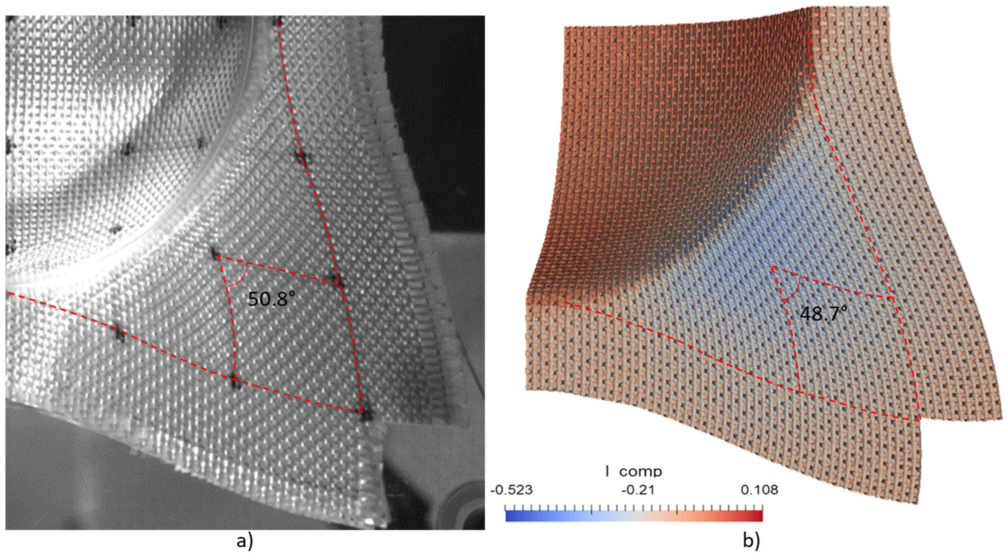


**Figure 6.** Hemispherical stamping. (**a**) Deformed geometry in experimental result. (**b**) Compaction of yarns in mesoscopic analysis.

## 4. Mesoscopic Analysis Enriched by Local Mesoscopic Simulation

### *4.1. Local Mesoscopic Simulation*

As shown in Section 3, the mesoscopic analyses of the woven reinforcement obtained by the macro-meso embedded approach are efficient in providing a mesoscopic scale solution during shaping. However, this approach is based on the assumptions of continuous medium and the finite element method. The mesoscopic deformed configuration is directly obtained from the macroscopic analysis, without solving a mechanical problem. From the point of view of the constitutive law, the local equilibrium of the stresses is not attained, for example in the red zones in Figure 5. That is to say, local slippages between the yarns is not been taken into account, which can, in some cases, lead to an excessive elongation of yarns. For example, as shown in Figure 5, the local elongation in the yarns obtained by the macro-meso embedded approach can reach 11%, which is much higher than the reality. In order to overcome this difficulty, a local mesoscopic simulation based on macroscopic simulations and macro-meso embedded mesoscopic analysis is proposed.

The local mesoscopic simulation is performed locally, usually on one or more representative volume elements (RVEs) based on the results of the macro-meso embedded approach. The deformed configuration obtained by the embedded mesoscopic simulation constitutes the initial state of the local mesoscopic simulation. A relatively simple transverse isotropic hyperelastic behavior law (neo-Hookean) was used to describe the mechanical behavior of the yarns [28,29]. The material parameters used are given in Appendix B. Consequently, stress equilibrium was achieved within the yarns and the local mesoscopic simulation eliminated the phenomena of the excessive elongation of yarns. The results obtained by the local mesoscopic simulation are compared with the results obtained by the macro-meso embedded approach in Figures 7 and 8. In both cases, the spurious elongations obtained in the yarns by the embedded calculation were reduced to small values after the mesoscopic calculation on a RVE both in the bending case (Figure 7) and in the hemispherical forming case (Figure 8). In addition, the calculation time of each step in this multi-scale method is shown in Table 1.

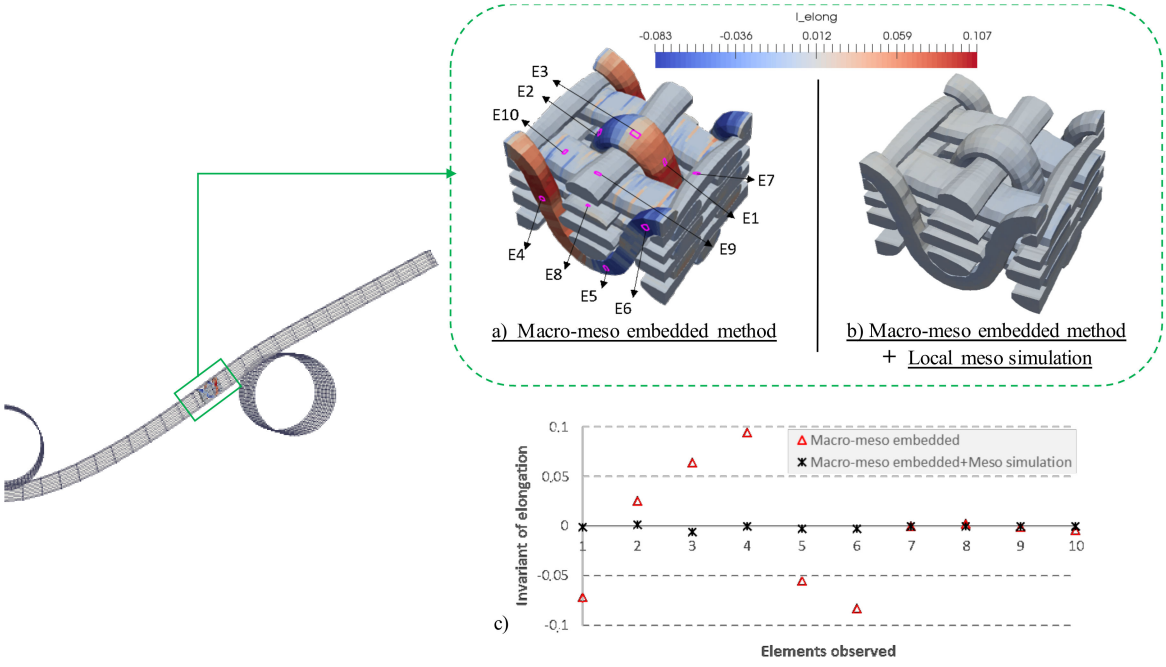


**Figure 7.** Influence of the enriched local mesoscopic simulation on the elongation of yarns in three-point bending. (**a**) Macro-meso embedded analysis. (**b**) Macro-meso embedded method with local mesoscopic simulation analysis. (**c**) Change in elongation for the same elements.

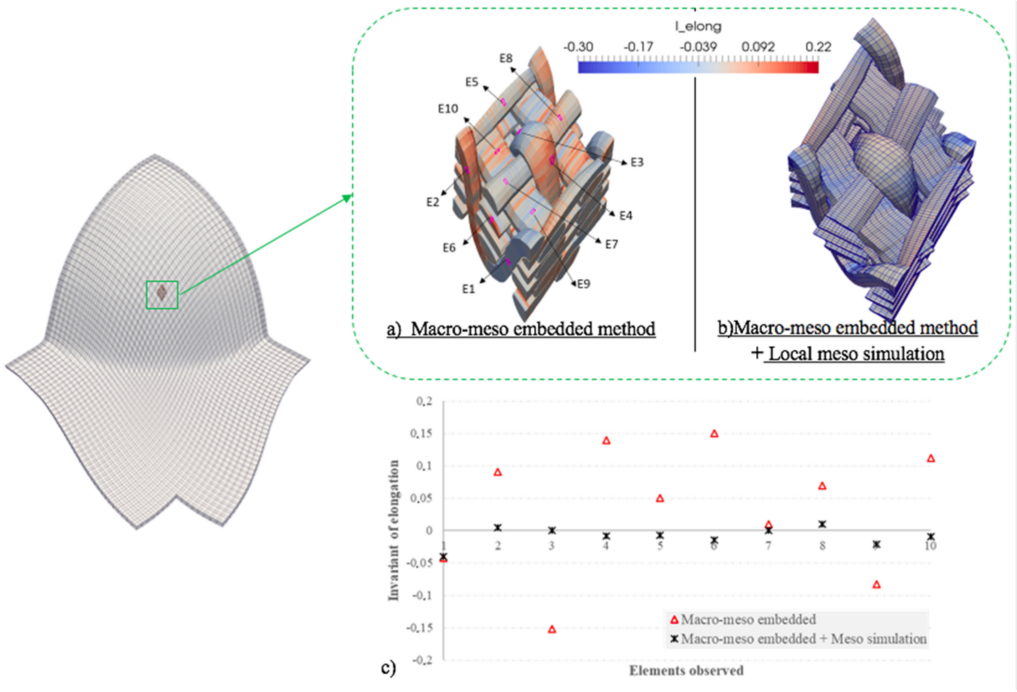


**Figure 8.** Influence of the enriched local mesoscopic simulation on the elongation of yarns in hemispherical forming. (**a**) Macro-meso embedded analysis. (**b**) Macro-meso embedded method with local mesoscopic simulation analysis. (**c**) Change in elongation for the same elements.

### *4.2. Comparison with Experimental Results*

Finally, the mesoscopic numerical results are compared with the experimental results and the numerical results with three RVEs for three-point bending. The deformations of the longitudinal and transverse sections of the yarns were observed and analyzed by a microscope.

In comparison with the experimental results (Figure 9b), it can be seen that the numerical result (Figure 9a) based on the multi-scale method was in good agreement with the experimental result relating to the deformed geometry and the outlines of the yarns.

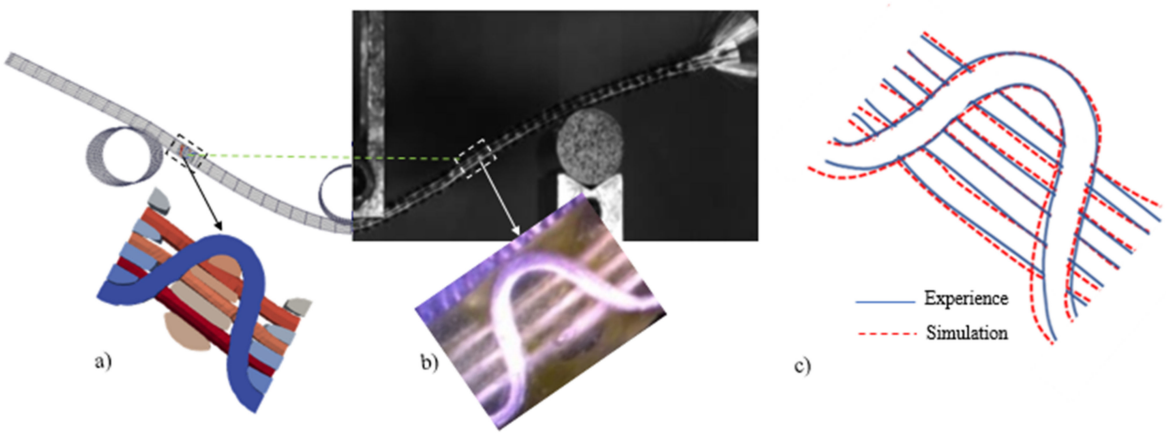


**Figure 9.** Deformed geometry of RVE in the same position obtained by: (**a**) simulation, (**b**) experiment, and (**c**) comparison of the outlines of binder yarns and warp yarns.

### *4.3. Influence of the Number of RVEs*

The local mesoscopic simulation was performed on a single RVE, and the boundary conditions from the macro-meso embedded approach were applied on the RVE edges. The

influence of the number of RVEs was not taken into account. Therefore, to analyze the edge effects on the mesoscopic results, another simulation was carried out on three successive RVEs for three-point bending, in which the middle RVE had the same location as the single RVE. The results shown in in Figures 10 and 11 indicate that the number of RVEs had only a very weak influence on the mesoscopic results.

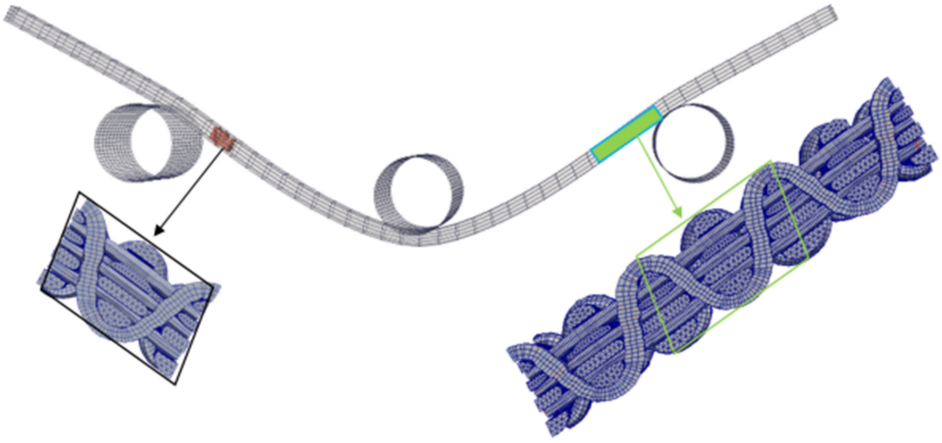

**Figure 10.** Influence of the number of RVEs on the meso results.

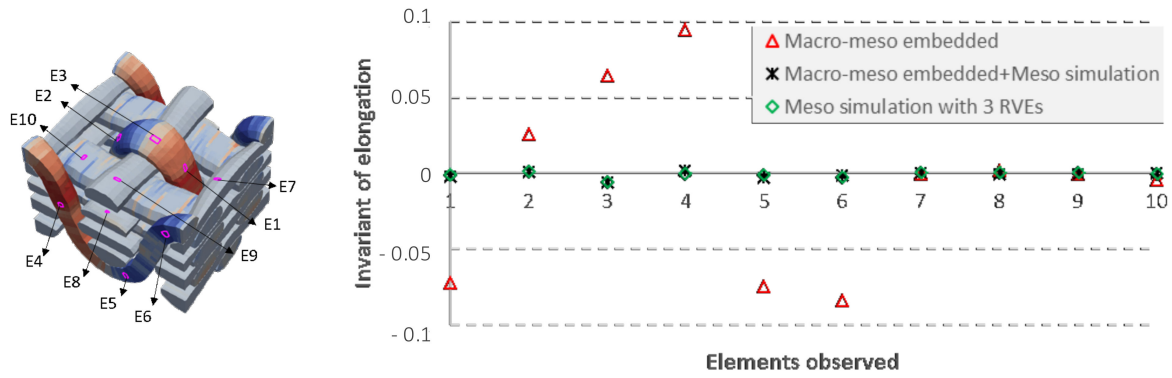


(**a**)

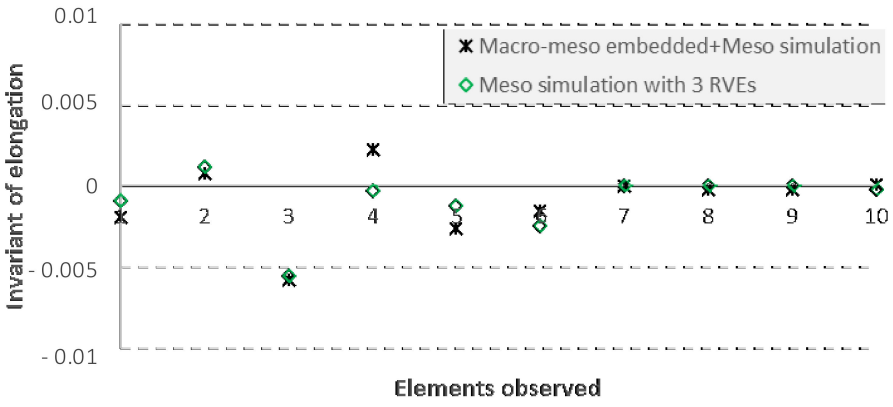


(**b**)

**Figure 11.** Comparisons of yarn elongation for ten elements in the same positions between the meso results of one RVE and threes RVEs: (**a**) with the result of Macro-Meso embedded approach, (**b**) without the result of Macro-Meso embedded approach.

**Table 1.** Calculation time of three-point bending and hemispherical forming.

| | **Size of Model RVE: 4.78 × 4.64 × 3.25 mm³** | **Number of Elements (RVE: 39,888 Elements)** | **Calculation Time** | | |
|---|---|---|---|---|---|
| | | | **Macro Simulation** | **Macro-Meso Embedded Analysis** | **Meso Local Simulation** |
| Three-point bending | 41 RVEs | 1.6 millions | 6 h | 15 min | 30 min |
| Hemispherical forming | 625 RVEs | 25 millions | 1 day | 1 h | 2 h |

## 5. Conclusions

The deformation information of woven reinforcements on the mesoscopic scale is essential to evaluate the mechanical properties of the final composite part, as well as to simulate resin flow during the next injection step. In this paper, the developed macro-meso embedded approach allows one to obtain the deformed configuration at the mesoscopic scale of woven reinforcements during the forming process. However, it has drawbacks, especially the excessive elongation of the yarns. To overcome this problem, a local mesoscopic simulation that takes into account the local slippage of yarns can be carried out by defining specific boundary conditions. This step requires a reasonable computational cost. The results of one RVE were satisfactory in comparison with the experimental results and the numerical results with three RVEs. Furthermore, the comparison with the full meso simulation at a large scale was interesting. Another perspective to validate the quality of the multi-scale approach consists in using the Hill–Mandell macro-homogeneity condition to ensure that the same amount of energy is dissipated in the RVE and the corresponding part of material in the macro-model.

**Author Contributions:** J.W.: investigation, methodology, software, validation, visualization, and writing—original draft. P.W.: investigation. N.H.: software and supervision. P.B.: conceptualization, methodology, supervision. All authors have read and agreed to the published version of the manuscript.

**Funding:** This research received no external funding.

**Institutional Review Board Statement:** Not applicable.

**Informed Consent Statement:** Not applicable.

**Data Availability Statement:** Not applicable.

**Conflicts of Interest:** The authors declare no conflict of interest.

## Appendix A

The 3D hyperelastic anisotropic constitutive law is applied in the macroscopic simulations. The second Piola–Kirchhoff stress tensor $\underline{\underline{S}}$ can be calculated by the differentiation $\partial w_k / \partial I_k$ and the right Cauchy–Green tensor $\underline{\underline{C}}$ (see Equation (2) in Section 2). For each deformation mode, the physical invariant $I_k$ described in Section 2 is defined by the classical invariants (Equation (A1)), and the strain energy density $w_k$ can be expressed in polynomial form (Equation (A2)). In order to take into consideration the curvature of the fibers, an independent bending stiffness of fibers $\chi$ is added to calculate the bending moment $M_{bend}$ by Equation A3. The material parameters $ki$, $D_0$, and $D_1$ are characterized by the corresponding mechanical tests (Table A1).

$$\begin{aligned} I_{elong\alpha} &= \ln(\sqrt{I_{4\alpha}}) \ (\alpha = 1, 2) & I_{comp} &= \tfrac{1}{2} \ln\left( \frac{I_3}{I_{41} I_{42} (1 - I_{cp}^2)} \right) \\ I_{cp} &= \frac{I_{412}}{\sqrt{I_{41} I_{42}}} = \sin(\gamma_{12}) & I_{ct\alpha} &= \frac{I_{4i3}}{\sqrt{I_{4\alpha} I_{43}}} = \sin(\gamma_{\alpha 3}) \end{aligned} \tag{A1}$$

$$w = \begin{cases} \sum_{i=1}^{6} k_i I^i & \text{if } I > 0 \\ \sum_{i=1}^{6} k_{i+6} I^i & \text{if } I \leq 0 \end{cases} \tag{A2}$$

$$M_{bend} = \begin{cases} (D_0 - D_1|\chi|)\chi & \text{if } \chi < \frac{D_0}{2D_1} \\ \frac{D_0}{2}\chi & \text{if not} \end{cases} \tag{A3}$$

**Table A1.** Material parameters identified in the macroscopic simulations ($k_i$ in MPa; $D_0$ in Nmm; $D_1$ in Nmm$^2$).

| | | | | | | |
|---|---|---|---|---|---|---|
| $w_{elong1/2}$ | $k_1$<br>8.692 | $k_2$<br>4816 | $k_3$<br>$-1.002 \times 10^6$ | $k_4$<br>$8.275 \times 10^7$ | $k_5$<br>$-2.419 \times 10^9$ | $k_6$<br>$2.442 \times 10^{10}$ |
| | $k_7$<br>8.692 | $k_8$<br>$-505.6$ | $k_9$<br>$1.073 \times 10^5$ | $k_{10}$<br>$-2.687 \times 10^6$ | $k_{11}$<br>0 | $k_{12}$<br>0 |
| $w_{comp}$ | $k_1/k_7$<br>$9.69 \times 10^{-2}$ | $k_2/k_8$<br>0.7009 | $k_3/k_9$<br>$6.426 \times 10^{-2}$ | $k_4/k_{10}$<br>$-1.339$ | $k_5/k_{11}$<br>0.8777 | $k_6/k_{12}$<br>$2.855 \times 10^{-2}$ |
| $w_{sh}$ | $k_1/k_7$<br>0.3441 | $k_2/k_8$<br>$-2.019$ | $k_3/k_9$<br>7.416 | $k_4/k_{10}$<br>$-14.01$ | $k_5/k_{11}$<br>14.01 | $k_6/k_{12}$<br>$-5.444$ |
| $w_{shT1}$ | $k_1/k_7$<br>$3.721 \times 10^{-2}$ | $k_2/k_8$<br>$3.844 \times 10^{-2}$ | $k_3/k_9$<br>$-0.521$ | $k_4/k_{10}$<br>1.877 | $k_5/k_{11}$<br>$-2.78$ | $k_6/k_{12}$<br>1.572 |
| $w_{shT2}$ | $k_1/k_7$<br>347.3 | $k_2/k_8$<br>$-5.674 \times 10^{-2}$ | $k_3/k_9$<br>$-1.46 \times 10^{-2}$ | $k_4/k_{10}$<br>0.5835 | $k_5/k_{11}$<br>$-1.201$ | $k_6/k_{12}$<br>0.8084 |
| | | $D_0$ (warp)<br>3.6 | $D_1$ (warp)<br>117.9 | $D_0$ (weft)<br>3.748 | $D_1$ (weft)<br>123.6 | |

## Appendix B

In the hyperelastic transverse isotropic (Neo-Hookean) constitutive law, the potential is considered to consist of two potentials [28]: the isotropic potential $w_{iso}$, concerning the longitudinal behavior of a yarn, and the potential $w_{trans}$, concerning the mechanical behavior in the transverse plane of a yarn (Equation (A4)).

$$\begin{cases} w = w_{iso}(I_1, I_2, I_3) + w_{trans}(I_1, I_2, I_3, I_4, I_5) \\ w_{iso} = \frac{1}{2}\mu(I_1 - 3) - \mu \ln(J) + \frac{1}{2}\lambda(J-1)^2 \\ w_{trans} = [\alpha + \beta \ln(J) + \gamma(I_4 - 1)](I_4 - 1) - \frac{1}{2}\alpha(I_5 - 1) \end{cases} \tag{A4}$$

For simplification, the parameters λ, μ, α, β and γ are defined by four material parameters in Equation (A5): transverse modulus of elasticity E, longitudinal modulus of elasticity $E_A$, Poisson's ratio ν, and longitudinal shear modulus $G_A$, respectively. The material parameters used in the mesoscopic simulation are given in Table A2 (details in [29]).

$$\begin{gathered} \lambda = \frac{E(\nu + n\nu^2)}{m(1+\nu)} \\ \mu = \frac{E}{2(1+\nu)} \\ \alpha = \mu - G_A \\ \beta = \frac{E\nu^2(1-n)}{4m(1+\nu)} \\ \gamma = \frac{E_A(1-\nu)}{8m} - \frac{\lambda+2\mu}{8} + \frac{\alpha}{2} - \beta \\ m = 1 - \nu - 2n\nu^2 \\ n = E_A/E \end{gathered} \tag{A5}$$

**Table A2.** Material parameters identified in the mesoscopic simulations (in MPa).

| E | $E_A$_Elongation | $E_A$_Compression | $\nu$ | $G_A$ |
|---|---|---|---|---|
| 3200 | 45,516 | 100 | 0 | 1600 |

## References


1. Ten Thije, R.H.W.; Akkerman, R.; Huétink, J. Large deformation simulation of anisotropic material using an updated Lagrangian finite element method. *Comput. Methods Appl. Mech. Eng.* **2007**, *196*, 3141–3150. [CrossRef]
2. Boisse, P. Finite element analysis of composite forming. In *Composites Forming Technologies*; Woodhead Publishing: Cambridge, UK, 2007; pp. 46–79.
3. Gereke, T.; Döbrich, O.; Hübner, M.; Cherif, C. Experimental and computational composite textile reinforcement forming: A review. *Compos. A Appl. Sci. Manuf.* **2013**, *46*, 1–10. [CrossRef]
4. Bussetta, P.; Correia, N. Numerical forming of continuous fibre reinforced composite material: A review. *Compos. A Appl. Sci Manuf.* **2018**, *113*, 12–31. [CrossRef]
5. Boisse, P.; Hamila, N.; Vidal-Sallé, E.; Dumont, F. Simulation of wrinkling during textile composite reinforcement forming. Influence of tensile, in-plane shear and bending stiffnesses. *Compos. Sci. Technol.* **2011**, *71*, 683–692. [CrossRef]
6. Dangora, L.M.; Mitchell, C.J.; Sherwood, J.A. Predictive model for the detection of out- of-plane defects formed during textile-composite manufacture. *Compos. A Appl. Sci. Manuf.* **2015**, *78*, 102–112. [CrossRef]
7. Chen, X.; Zhu, F.; Wells, G. An analytical model for ballistic impact on textile based body armour. *Compos. Part B Eng.* **2013**, *45*, 1508–1514. [CrossRef]
8. Gatouillat, S.; Bareggi, A.; Vidal-Sallé, E.; Boisse, P. Meso modelling for composite preform shaping–simulation of the loss of cohesion of the woven fibre network. *Compos. A Appl. Sci. Manuf.* **2013**, *54*, 135–144. [CrossRef]
9. Allaoui, S.; Hivet, G.; Soulat, D.; Wendling, A.; Ouagne, P.; Chatel, S. Experimental preforming of highly double curved shapes with a case corner using an interlock reinforcement. *Int. J. Mater. Form.* **2014**, *7*, 155–165. [CrossRef]
10. Schirmaier, F.J.; Dörr, D.; Henning, F.; Kärger, L. A macroscopic approach to simulate the forming behaviour of stitched unidirectional non-crimp fabrics (UD-NCF). *Compos. A Appl. Sci. Manuf.* **2017**, *102*, 322–335. [CrossRef]
11. Schirmaier, F.J.; Weidenmann, K.A.; Kärger, L.; Henning, F. Characterisation of the draping behaviour of unidirectional non-crimp fabrics (UD-NCF). *Compos. A Appl. Sci. Manuf.* **2016**, *80*, 28–38. [CrossRef]
12. Bréard, J.; Henzel, Y.; Trochu, F.; Gauvin, R. Analysis of dynamic flows through porous media. Part I: Comparison between saturated and unsaturated flows in fibrous reinforcements. *Polym. Compos.* **2003**, *24*, 391–408. [CrossRef]
13. Loix, F.; Badel, P.; Orgéas, L.; Geindreau, C.; Boisse, P. Woven fabric permeability: From textile deformation to fluid flow mesoscale simulations. *Compos. Sci. Technol.* **2008**, *68*, 1624–1630. [CrossRef]
14. Tran, T.; Comas-Cardona, S.; Abriak, N.E.; Binetruy, C. Unified microporomechanical approach for mechanical behavior and permeability of misaligned unidirectional fiber reinforcement. *Compos. Sci. Technol.* **2010**, *70*, 1410–1418. [CrossRef]
15. Llorca, J.; Gonzalez, C.; Molina-Aldaregui, J.M.; Segurado, J.; Seltzer, R.; Sket, F. Multiscale modelling of composite materials: A road map towards virtual testing. *Adv. Mater.* **2011**, *23*, 5130–5147. [CrossRef]
16. Iwata, A.; Inoue, T.; Naouar, N.; Boisse, P.; Lomov, S.V. Coupled meso-macro simulation of woven fabric local deformation during draping. *Compos. A Appl. Sci. Manuf.* **2019**, *118*, 267–280. [CrossRef]
17. Wang, J.; Wang, P.; Hamila, N.; Boisse, P. Mesoscopic analyses of the draping of 3D woven composite reinforcements based on macroscopic simulations. *Compos. Struct.* **2020**, *250*, 112602. [CrossRef]
18. Whitcomb, J.; Srirengan, K.; Chapman, C. Evaluation of homogenization for global/local stress analysis of textile composites. *Compos. Struct.* **1995**, *31*, 137–149. [CrossRef]
19. Carvelli, V.; Poggi, C. A homogenization procedure for the numerical analysis of woven fabric composites. *Compos. A Appl. Sci Manuf.* **2001**, *32*, 1425–1432. [CrossRef]
20. Lomov, S.V.; Ivanov, D.S.; Verpoest, I.; Zako, M.; Kurashiki, T.; Nakai, H.; Hirosawa, S. Meso-FE modelling of textile composites: Road map, data flow and algorithms. *Compos. Sci. Technol.* **2007**, *67*, 1870–1891. [CrossRef]
21. Chen, X. (Ed.) *Advances in 3D Textiles*; Elsevier: Amsterdam, The Netherlands, 2015.
22. Software PLASFIB. *Inter Deposit Certification*; Agence Pour la Protection des Programmes: Paris, France, 2015.
23. Boisse, P.; Aimène, Y.; Dogui, A.; Dridi, S.; Gatouillat, S.; Hamila, N.; Vidal-Sallé, E. Hypoelastic, hyperelastic, discrete and semi-discrete approaches for textile composite reinforcement forming. *Int. J. Mater. Form.* **2010**, *3*, 1229–1240. [CrossRef]
24. Charmetant, A.; Orliac, J.G.; Vidal-Sallé, E.; Boisse, P. Hyperelastic model for large deformation analyses of 3D interlock composite preforms. *Compos. Sci. Technol.* **2012**, *72*, 1352–1360. [CrossRef]
25. Mathieu, S.; Hamila, N.; Bouillon, F.; Boisse, P. Enhanced modeling of 3D composite preform deformations taking into account local fiber bending stiffness. *Compos. Sci. Technol.* **2015**, *117*, 322–333. [CrossRef]
26. Creech, G.; Pickett, A.K. Meso-modelling of non-crimp fabric composites for coupled drape and failure analysis. *J. Mater. Sci.* **2006**, *41*, 6725–6736. [CrossRef]
27. Naouar, N.; Vidal-Salle, E.; Schneider, J.; Maire, E.; Boisse, P. 3D composite reinforcement meso FE analyses based on X-ray computed tomography. *Compos. Struct.* **2015**, *132*, 1094–1104. [CrossRef]

28. Bonet, J.; Burton, A.J. A simple orthotropic, transversely isotropic hyperelastic constitutive equation for large strain computations. *Comput. Methods Appl. Mech. Eng.* **1998**, *162*, 151–164. [CrossRef]
29. Florimond, C. Contribution à la Modélisation Mécanique du Comportement de Mèches de Renforts Tissés à L'Aide d'un Schéma Éléments Finis Implicite. Ph.D. Thesis, INSA Lyon, Lyon, France, 2015.

*textiles*

MDPI

*Review*

# Continuous Yarn Electrospinning

**Shakir Zainuddin [1] and Thomas Scheibel [1,2,3,4,5,*]**

[1] Department of Biomaterials, University of Bayreuth, 95447 Bayreuth, Germany; shakir.zainuddin@bm.uni-bayreuth.de
[2] Bayreuth Center for Colloids and Interfaces (BZKG), University of Bayreuth, 95447 Bayreuth, Germany
[3] Bayreuth Center for Molecular Biosciences (BZMB), University of Bayreuth, 95447 Bayreuth, Germany
[4] Bayreuth Center for Material Science (BayMAT), University of Bayreuth, 95447 Bayreuth, Germany
[5] Bavarian Polymer Institute (BPI), University of Bayreuth, 95447 Bayreuth, Germany
* Correspondence: thomas.scheibel@bm.uni-bayreuth.de

**Abstract:** Nanofiber-based nonwoven mats produced in electrospinning setups are usually very fragile, which often limits their applicability. Yarns have the potential to enable the incorporation of nanofibers into other materials using well-established techniques such as sewing, knitting, weaving and embroidering, thus broadening the application of nanofibers. Here, we review the development of continuous yarn electrospinning processes. Amongst several possible approaches, funnel-based collector systems have been widely adopted. Here, we summarize recent developments in the field and highlight studies providing visions on how to expand that field of research in future studies of continuous yarn electrospinning.

**Keywords:** nanofibers; PAN; cellulose acetate; biopolymers; spider silk; silk fibroin

**Citation:** Zainuddin, S.; Scheibel, T. Continuous Yarn Electrospinning. *Textiles* **2022**, *2*, 124–141. https://doi.org/10.3390/textiles2010007

Academic Editors: Issei Otsuka and Philippe Boisse

Received: 22 December 2021
Accepted: 19 February 2022
Published: 23 February 2022



## 1. Introduction

Electrospinning is an electrostatic-based technique used to produce ultrafine fibers from the micrometer down to the nanometer scale [1]. It is a simple yet highly customizable process which can be used in conjunction with many systems such as polymer melts [2], polymer solutions [1], sol-gels [3], and even ceramics [4]. Due to the process versatility, electrospun fibers and mats have found potential applications in various fields such as air filtration [5], tissue engineering and drug delivery [6,7], gas sensing [8], material reinforcement [9], and catalysis [10].

Generally speaking, the direct products of the electrospinning process are either one-dimensional as in the case of bundles and yarns, or two-dimensional as in the case of nonwoven mats. Within these two forms, the fiber orientation can be random, aligned, or a mixture of both. Between the two forms, nonwoven mats are arguably the far easier form to produce due to the bending instability that almost inevitably occurs during the extension of the electrostatically generated jets (Figure 1), which results in the random deposition of solidified fibers on a surface. Thus, the manufacture of electrospun mats does not require an elaborate setup.

Electrospun yarns on the other hand are more difficult to produce. Once the jet has been generated from the liquid reservoir—typically the tip of a needle—the challenge is to ensure the alignment of up to thousands of tiny, solidified fibers into a bundle before the fibers touch and adhere to a surface, then twisting the bundle into a yarn in a controlled manner. For the past two decades, various groups have come up with different techniques for producing electrospun yarns of different composition and qualities. We will see that one particular method and its variants have been used repeatedly by different groups. However, as these works were dictated by their own specific research interests and applications, the experiments were not conducted in such a way that the results are easily comparable.

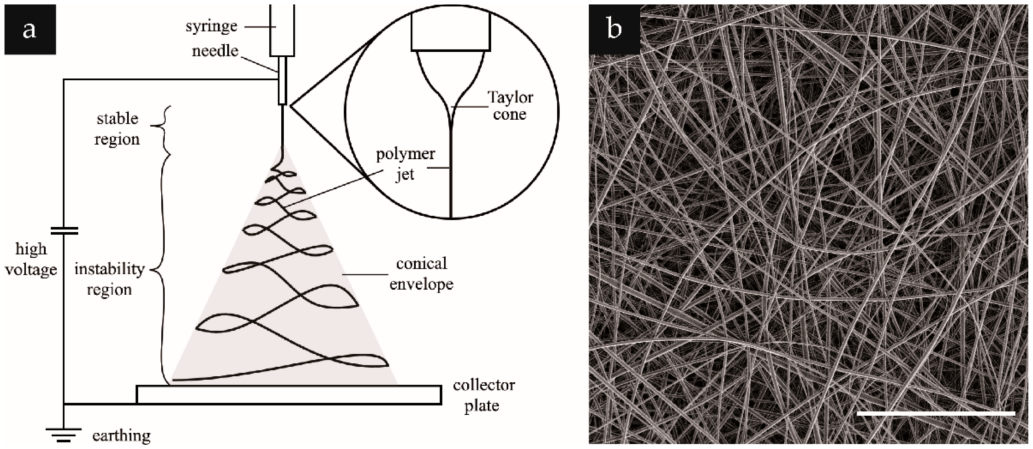


**Figure 1.** (**a**) Scheme of basic electrospinning setup with three major components: a needle contacted by an electrode, a high voltage source, and a grounded collector plate. Applying a sufficiently high voltage at the needle, after a droplet of polymer solution or melt has formed at its tip, results in a jetting thereof. The path of the jet is straight near the needle; however, it quickly turns chaotic due to bending instabilities but is nevertheless confined within a conical envelope visible using long exposure photography [11]. During the flight, jets are stretched, yielding thin diameters, facilitating the evaporation of the solvent and accelerating the formation of fibers. The fibers accumulate on the collector in a random orientation, resulting in a nonwoven mat. Figure self-drawn. (**b**) SEM of a typical cellulose acetate nonwoven mesh resulting from such a basic electrospinning setup. Scale bar = 20 μm.

There had so far been several reviews on the topic of yarn electrospinning [12–15], though none of them specifically discussed the problem of direct comparison between the various methods. If yarn electrospinning is to be a method that is widely adopted, researchers should be able to decide which methods are the most suitable for their own application based on certain parameters such as production speed, fiber fineness, yarn fineness, and fiber mechanical properties. Additionally, one widely available polymer that is easily electrospun should also be used as a standard polymer whose characterization allows the comparison between various yarn electrospinning setups.

## 2. Continuous Yarn Electrospinning

The phenomenon known today as electrospinning has been known as early as the 19th century. One account was given in 1887 by CV Boys, in which he described the behavior of organic melts on an insulated dish subjected to high voltage. Upon reaching the edge of the dish, the droplets of the melt could be observed flying away from the dish, leaving a trail of fibers in their path. He further observed a rosy shade on a piece of paper when sealing wax was used, attributing it to "innumerable fibres separately almost invisible", possibly the first account of an electrospun nonwoven mesh [16].

The first patent concerning fiber electrospinning, according to Tucker et al. [17], was published in 1900 by Cooley [18]. Arguably, this was also the first patent on the continuous electrospinning of fiber bundles, the schematics of which is seen in Figure 2. The patent describes the delivery of the spinning solution by means of a glass capillary (B) into the electric field generated by two electrodes (e and e') charged to a high voltage by using e.g., a Wimshurst machine (D), a common high voltage generator at that time. Interestingly, the electrode does not need to directly contact the spinning solution. Instead, the solution gets charged in mid-air upon entering the electric field and dispersed into smaller streams that, upon evaporation of the solvent, solidify into fibers, which are attracted to the opposite electrode. By intercepting the fibers using a glass rod (not shown in the schematics) and bringing them onto a reel (F), the fibers can be continuously collected. The electrospinning takes place in an enclosure (G) which can be evacuated using a pump

(K). The evacuated atmosphere can then be treated to recycle the evaporated solvent. Apart from the modernization of most of the components used by Cooley, the general principle and arrangement of the electrospinning setup have remained unchanged since then.

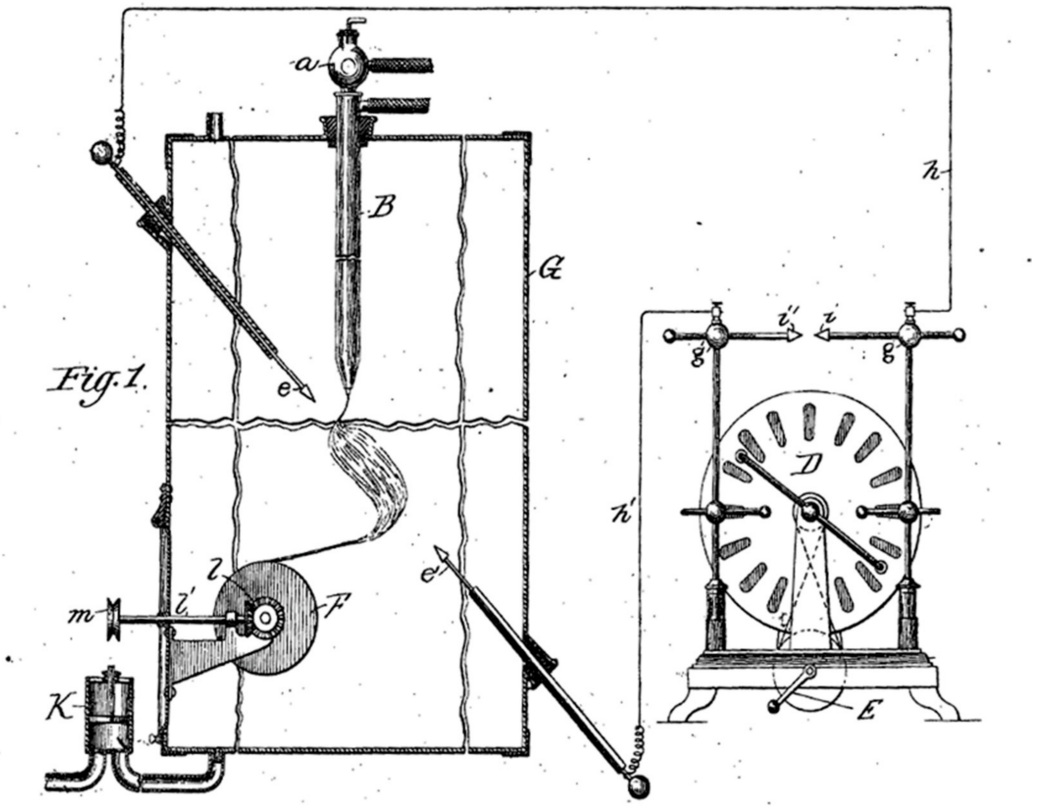


**Figure 2.** The schematic drawing of Cooley's electrospinning device. Enclosed in the electrospinning chamber (**G**), the capillary (**B**) delivers the polymer solution into the electric field between two opposite electrodes (e and e'), thereby generating a stream of jets which solidifies into fibers. The fibers, on their flight towards the electrode e', are intercepted by a glass rod (not shown in the diagram) and thus are bundled together and brought to a reel (**F**) which winds the bundle. The pump K evacuates the spinning chamber for a possible solvent recovery. D is a Wimshurst machine (or any suitable machine) for generating high voltage. Reprinted with permission from Ref. [18]. Copyright 1900 United Kingdom Patent.

In 1934, a particularly prolific inventor named Anton Formhals published his first patent [19] on electrospinning. During the following decade, he published at least another 21 patents [17] on the subject. His inventions consisted of various improvements on the electrospinning method, especially those concerning the upscaling of the method, including the use of multiple spinnerets and conveyor belts to collect and transport the fibers.

It was not until the early 1990s that "electrospinning" as a term was popularized by several research groups such as that of Reneker [1]. The introduction of a single word to denote the phenomenon of fiber formation through electrostatic jetting of fluids facilitated the discussion of the subject. Combined with the advent of nanotechnology, the interest in nanoscale materials, including electrospun fibers, increased rapidly. Since then, the number of publications has grown exponentially. Over the past two decades, many researchers have used different techniques to produce nanofiber mats and yarns.

Many research groups cited the difficulty in handling nanofibers as a motivation for developing systems to produce electrospun bundles and yarns [20,21], which, due to the distribution of load among the constituent fibers, increases the robustness of the fibers. Initial efforts towards realizing such setups tended to be systems enabling fiber bundle production. This was achieved through various means. Water-based collectors (Figure 3a),

such as used by Smit et al. [22] and Teo et al. [23], rely on water's fluidity to help realign the fibers. As the collector surface is not stiff, the fibers can be pulled on one end without the fibers experiencing too much tension that would break them due to their adhesion to the collector surface, as is the case with a solid collector. As the fibers are pulled out of water, surface tension pulls them together into a bundle. Other works, such as those from Pan et al. [24] (Figure 3b), rely on opposite charges to align the fibers. One or several pairs of nozzles charged with opposite voltages are pointed towards each other, such that the jets that emanate from the nozzles are attracted to each other. This partially cancels out the whipping motion caused by the bending instabilities and aligns and bundles the fibers together. The bundles can then be easily captured using an insulated rod and brought to a motorized winder for automatic collection.

True yarns, however, contain twists, which require an extra step or element to be incorporated into the electrospinning system. This can be done in several ways. One approach is to rotate the winder itself, meaning that, in addition to the winding action of the winder, the winder is placed on a rotating platform, through which the twist in the yarn is achieved as seen in the work of Maleki et al. [25] (Figure 3c).

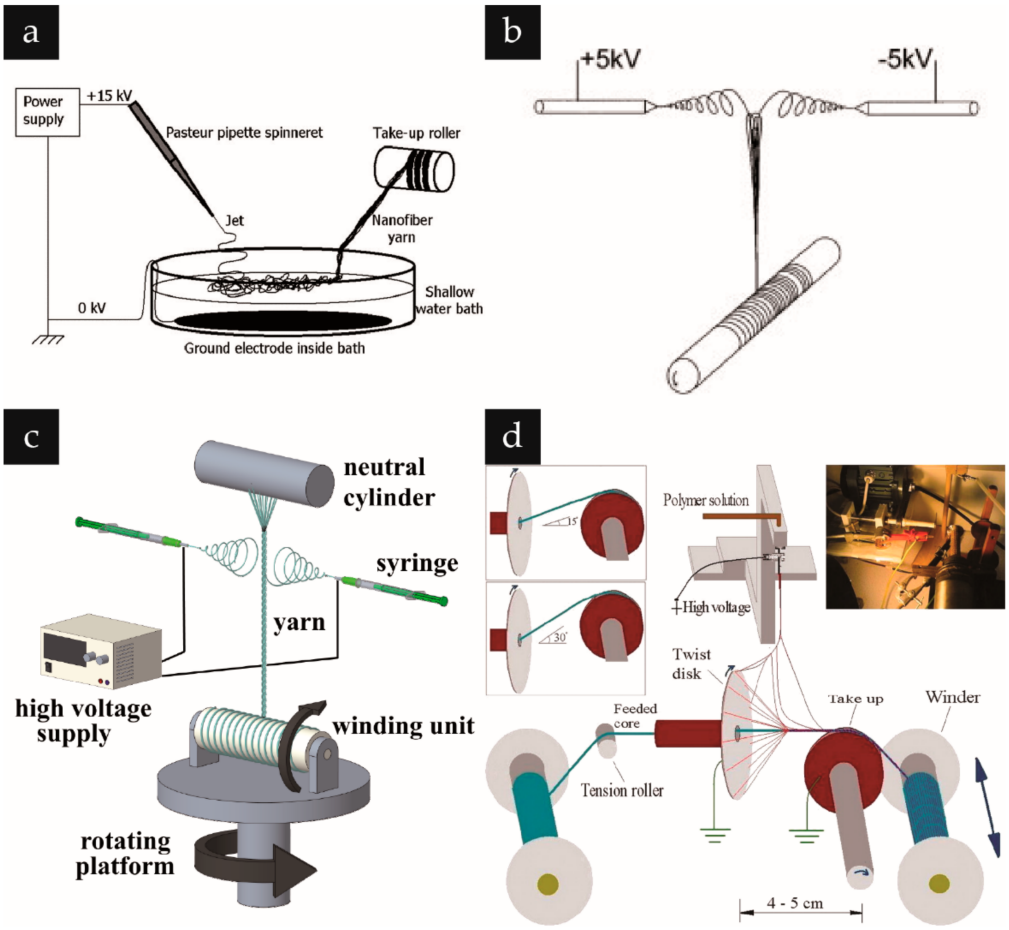


**Figure 3.** Various methods used to produce electrospun bundles and yarns since the 2000s. (**a**) Water-based collector as used by Smit et al. [22] and Teo et al. [23]. Reprinted with permission from Ref. [22]. Copyright 2005 Elsevier. (**b**) Opposite charged nozzles as used by Pan et al. Reprinted with permission from Ref. [24]. Copyright 2006 Elsevier. (**c**) Winder on a rotating platform as used by Maleki et al. [25]. Image self-drawn. (**d**) Spinning disc combined with a core thread as used by Bazbouz et al. Reprinted with permission from Ref. [26]. Copyright 2011 Wiley.

Another approach, taken by Bazbouz et al. [26], used a rotating disk onto which the fibers are jetted. A hole in the middle of the disk permits the passage of a core thread,

which is unwound on one side of the disk and wound on the other side of the disk. By the spinning of the disk, the electrospun fibers are continuously twisted around this core thread, and the winding of the core thread ensures constant material removal. This results in the continuous production of a core fiber sheathed in electrospun fibers (Figure 3d).

A particularly popular approach involves a rotating funnel to twist fiber bundles into yarns and a winder to collect the yarns. In one of the simpler versions of this method (Figure 4a), a single nozzle is used to convey the spinning solution. This nozzle is connected to a high voltage supply and is pointed at an angle towards a rotating circular or annular geometry, which in turn is pointed towards a winder. When the spinning solution is pumped through the nozzle and high voltage is applied, fibers land across the opening of the funnel, eventually forming a nonwoven mat covering the funnel opening. By bringing the tip of an insulated rod close to the nonwoven mat, some of the freshly formed fibers will land both on the tip and the mat, forming a connection. With sufficient material bridging between the tip and the mat, the mat can now be deformed into a nonwoven cone by pulling the rod away. The rotation of the funnel twists the cone into a yarn, which steadily extends in length from the tip of the cone as the rod is pulled further from the funnel. If the yarn is now brought towards a mandrel on a motorized winder, material will be continuously removed from the cone, while the nozzle continuously deposits fibers onto the cone. With the correct configuration, a mass transfer equilibrium takes place, the cone retains its shape, and the process can be run continuously. This approach has proven quite successful in continuously producing yarns, such that many groups have adopted or modified it for their own works, as will be discussed in the following.

## 3. Variations of the Rotating Funnel Collector System for Yarn Electrospinning

Figure 4 shows the schematic drawing of the setup used in selected works, which is based on the general principle of using a rotating funnel for the simultaneous deposition and twisting the electrospun fibers into a yarn and a motorized winder that collects the yarn. In its simplest form, the setup involves only four major components: A single nozzle for material extrusion and jetting, a high voltage source, a grounded rotating funnel collector, and a motorized winder, as used by Afifi et al. [27] in an early work from 2010 (Figure 4a).

A subsequent, two-nozzle variation is especially widespread and has been adopted in various works [28–33]. The first nozzle is arranged opposite to the second, with both nozzles most commonly being charged with opposite voltages (Figure 4b), although some authors, e.g., Jin et al. [29] and Tong et. al. [32], used the same charge for both nozzles. Electrospinning using a pair of nozzles with opposite charges is termed "conjugate electrospinning" [34]. This setup comes with several advantages. Using two nozzles is a straightforward way to double the material throughput, which increases yarn production speed. Because the two electrostatically generated jets neutralize each other's charges, earthing the funnel is not necessary. Positioning the nozzles opposite to each other ensures an even material distribution on the funnel and the subsequently formed nonwoven cone, which is important in ensuring that the cone retains its shape by evenly replenishing material at the same time as material is being continuously removed by the winding unit. To further increase throughput, multiple pairs of nozzles can be arranged around the funnel, as was demonstrated in the 2013 work of He et al. [35], in which two pairs of nozzles were used and a subsequent work in 2014 by He et al. [36], where four pairs of nozzles were used.

The geometry of the rotating object, which imparts the twist in the yarn, does not strictly have to be a funnel. Wu et al. [30], for example, used a setup almost identical to the one used by Li et al., exchanging the funnel with a spinning metal disc (Figure 4c). Shuakat and Lin [37] went further and showed that, in essence, the geometry only needs to be circular. Instead of a funnel, they used a ring and under it they positioned a contacted rotating disc. The lower part of the disc was partially immersed in the polymer solution bath and, as the disc turned, the solution was continuously transferred to the upper part of the disc, where multiple Taylor cones formed and supplied the ring with freshly formed

fibers, which were then twisted into a yarn by the rotation of the ring and subsequently rolled by the winding unit above. This setup greatly increased the throughput of the yarn electrospinning process.

Another interesting variation of the funnel-based setup is seen in the work of Yang et al. [38], who used a single nozzle as Afifi et al. [27], but introduced a variation in the winder. The motorized winder was mounted on a slider, which oscillated the winder uniaxially. This distributed the yarn over the length of the winder mandrel. The winder was placed close to the rotating funnel, such that the jets landed both on the funnel and on the mandrel. This resulted in yarns interlaced with randomly ordered nonwoven mats (Figure 4d).

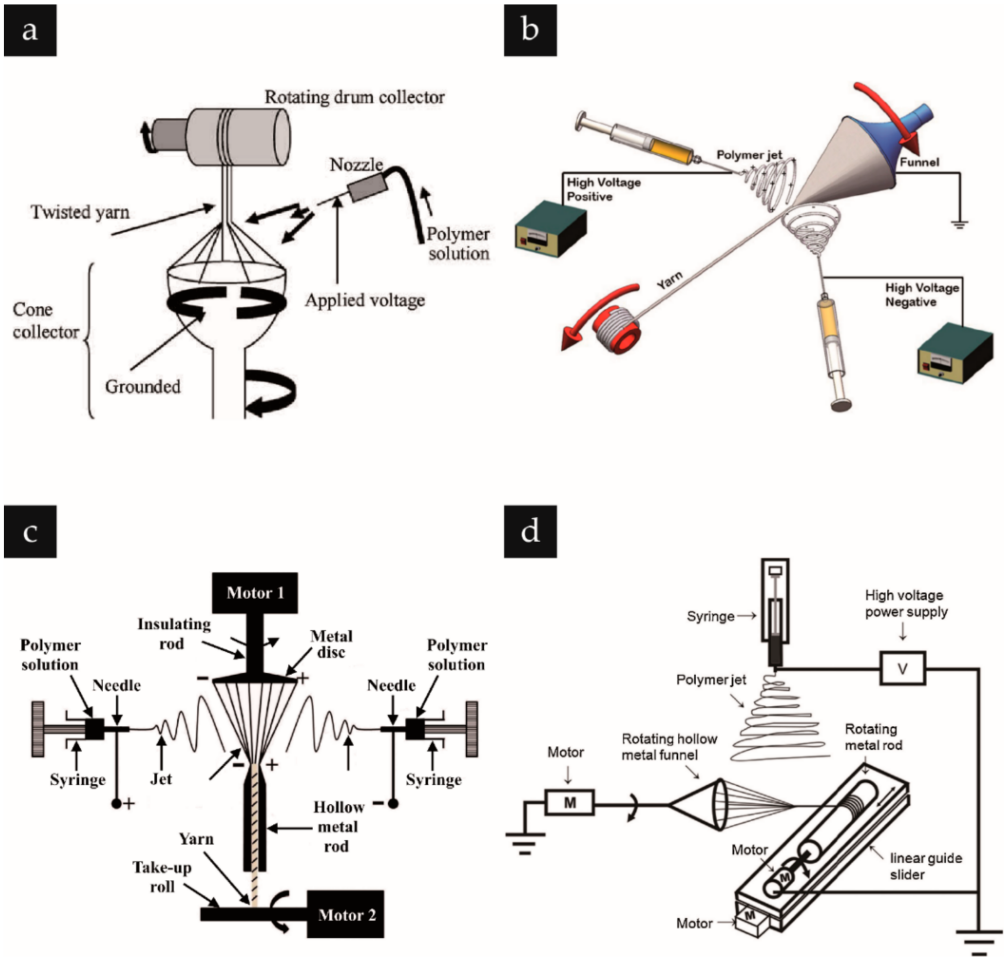


**Figure 4.** Variations of yarn electrospinning setups using a funnel. (**a**) The simplest variation of such setup is the one used by Afifi et al. Reprinted with permission from Ref. [27]. Copyright 2010 Wiley. (**b**) Li et al. used two nozzles, doubling the throughput and stabilizing the nonwoven cone forming on the rotating funnel. The oppositely charged nozzles made earthing the funnel no longer necessary. Reprinted with permission from Ref. [28]. Copyright 2020 American Chemical Society. (**c**) Wu et al. used a disc instead of the funnel in combination with a guiding metal rod. Reprinted with permission from Ref. [30]. Copyright 2013 Elsevier. (**d**) Yang et al. used a winder placed on a slider to distribute the yarn along the winder mandrel to produce a combination of yarns and randomly oriented fiber mat. Reprinted with permission from Ref. [38]. Copyright 2014 Elsevier.

These strategies all resulted in the formation of yarns, whose qualities differ in terms of alignment, yarn hairiness, and uniformity of diameter. In contrast to the previous works reported in the 19th century and the early half of the 20th century, these recent works included SEM images of the resulting yarns to demonstrate the quality of their process.

As examples, we included in Figure 5 the SEM images corresponding to the experimental setups shown in Figure 4.

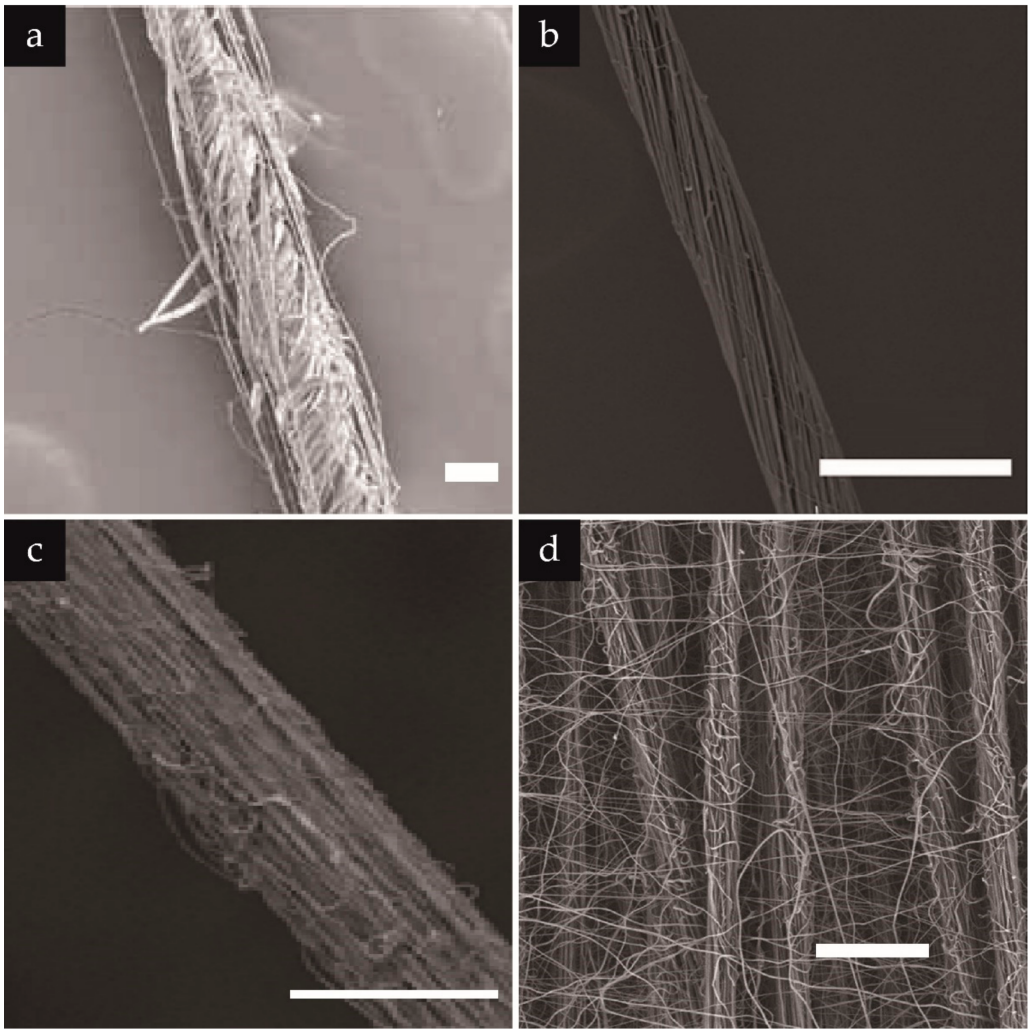


**Figure 5.** SEM images of electrospun yarns from the works of (**a**) Afifi et al. showing fibers lacking uniformity in alignment. Several fibers were aligned parallel to the yarn axis. Reprinted with permission from Ref. [27]. Copyright 2010 Wiley. (**b**) Li et al. produced yarns with highly aligned fibers. Reprinted with permission from Ref. [28]. Copyright 2020 American Chemical Society. (**c**) Wu et al. spun yarns with no apparent twist. Reprinted with permission from Ref. [30]. Copyright 2013 Elsevier. (**d**) Yang et al. produced a mixture of yarns and randomly aligned fiber mats. Reprinted with permission from Ref. [38]. Copyright 2014 Elsevier. Scale bars = 100 μm.

Figure 5a shows the result of the work of Afifi et al. [27]. Here, the twist can be seen in the fibers in the core of the yarn, but some fibers on the outside laid straight along the yarn length. The yarn diameter therefore was ill-defined along the yarn length. Many individual fibers could be seen protruding out of the yarn. In contrast, Li et al. [28] produced yarns with highly aligned fibers and apparent twist. The yarn depicted in the SEM image also had a uniform diameter, and fibers could be seen protruding out of the yarn (Figure 5b). Only some occasional fibers could be seen winding around the yarn in a disordered manner. Wu et al. [30] produced a yarn of intermediate quality. The yarn diameter appeared uniform along the yarn length. However, the twist was not apparent, and individual fibers were loosely packed in the main yarn body. Yang et al. [38] had a slightly different goal, thus the perfect containment of individual fibers within a single yarn was not as important. Instead, the construct was a mixture of yarns with randomly arranged fibers laid on top of them

(Figure 5d). Overall, funnel-based yarn electrospinning proved successful in continuously producing yarns.

## 4. Electrospun Biogenic Polymer Yarns

Biogenic polymers are polymers produced or derived from compounds of living organisms. Apart from the independence from traditional sources of polymers, i.e., petroleum, biogenic polymers present an interesting class of materials because of their properties, such as biodegradability in most cases, making them attractive in terms of environmental sustainability [39]. Many biogenic polymers are also biocompatible and thus suitable for medical applications [40]. Polypeptide or polysaccharide-based polymers occur either naturally such as cellulose, alginate, and collagen or are produced recombinantly such as recombinant collagen [41], elastin-like polymers [42], and spider silk proteins [43].

Biogenic fibers are widely used in many applications, cellulose and wool, for example, in human clothing for millennia. Regeneration of biogenic polymers liberates them from being constrained to the form imparted to them by biological systems. Thus, we can have biogenic polymers such as spider silk, which naturally occurs for the most part as fibers, in forms never occurring in nature such as films, hydrogels, and foams [44]. In this context, the production of electrospun biogenic polymer nanofibers has been investigated. [45–49] However, despite their wealth of potential in future applications, as well as their demonstrated electrospinnability, there seems to be a lack of data in continuous electrospinning of yarns based on biogenic polymers. Most work in literature so far focused on synthetic polymers. We, therefore, utilized continuous yarn electrospinning on biogenic polymers and characterized the properties of the resulting yarns.

Here, we electrospun yarns made of cellulose acetate and the recombinant spider silk protein eADF4(C16) by using a conjugate electrospinning setup adapted from the one used by Li et al. [28]. Minor adjustments of the setup included the vertical arrangement of the funnel and the placement of the winding unit above the funnel (Figure 6a). Each needle (of size 21 G) was clamped to an electrode wire with crocodile clamps. The needles were pointed towards the funnel at an angle of about 30° from the horizontal plane, and were positioned, each on one side of the funnel, between 3 and 5 cm horizontally and between 2 and 4 cm vertically away from the middle of the funnel. The funnel (5 cm in diameter in the opening, 3 cm in diameter in the lower part, and 5 cm high) was connected by a polymer shaft to a motor, which rotated at 200 rpm. The voltage used was between +4 and +7 kV on one needle and between $-4$ and $-7$ kV on the other. The flow rate used for feeding the solution into each needle was 10.5 μL/min. At the start of the process, the motor connected to the funnel as well as the syringe pump were turned on. As soon as a droplet formed at each needle, the high voltage was turned on. Fiber bundles formed at the space above the funnel, part of which were also adhering to the funnel. These were fished up using a polymer rod and were led onto the motorized winding unit placed vertically above the funnel. The motorized winding unit was then turned on and set to rotate at 6 rpm (roll diameter = 10 mm). For morphological characterization, the collected yarns were then sputter coated with platinum (1.2 nm thick) and analyzed using SEM at magnifications of 250×–15,000× at a voltage of 2 kV and working distance of about 8 mm. For tensile testing, the yarns were twisted manually to improve the adhesion between the individual fibers. The yarns were then fixed onto frames with a gauge length of 10 mm and pulled at a rate of 1 mm $min^{-1}$, measuring the load and displacement as a function of time. These were then plotted onto a stress–strain diagram, with the stress being calculated by dividing the load by the diameter of the yarn, determined using light microscope images.

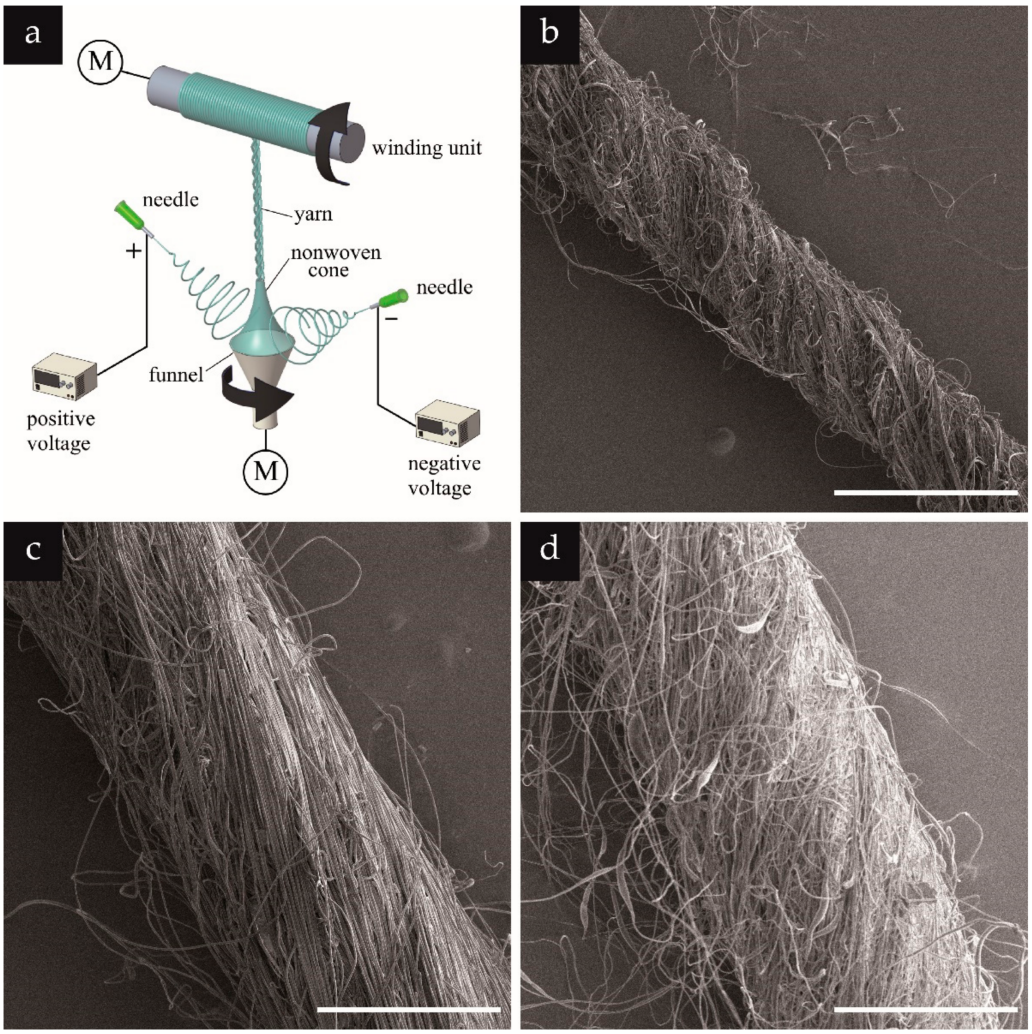


**Figure 6.** (**a**) Electrospinning setup based on Li et al.'s work with a slightly different arrangement: the funnel was vertical and the winding unit was positioned above the funnel. Two needles charged with opposite voltages were used, generating fibers that were twisted using the motorized rotating funnel, from which a yarn was drawn and collected using a motorized winding, allowing continuous electrospinning of biopolymer yarns. (**b**–**d**) SEM images of yarns with apparent twists electrospun out of recombinant spider silk eADF4(C16) (**b**), PAN (**c**), and cellulose acetate (**d**) solutions, respectively. Scale bars = 100 μm.

Concerning morphology, the yarns showed remarkably uniform diameters along their lengths even with manual twisting. The yarns tended to be hairy with individual fibers easily disentangled from the main yarn body when in contact with adhesive surfaces, which can be either an advantage or a disadvantage depending on the application. For example, in composites, a hairy yarn embedded in a matrix may prove advantageous due to the increased surface interaction between reinforcement and matrix, compared to smooth yarns [20]. Examples of an eADF4(C16), cellulose acetate, and PAN (as a control) yarn are shown in Figure 6b–d.

Concerning physical properties, the yarns were able to be handled by hand, and it did not require excessive care to prevent the yarns from rupturing. It was possible, for example, to tie a knot using the yarns. Some inconvenience did arise in handling the yarns as they were very light, and the weight of a stretch of yarn was not enough to cause them to dangle vertically due to gravity as a typical thread would; instead, an unfixed end would float about in the air. The yarns also tended to be highly attracted to surfaces, such that it was very difficult to place short lengths of yarn in a Petri dish and let them go, as

they would continue to be attracted to the objects used to handle them (such as a pair of tweezers). Typical stress–strain curves of the yarns are shown in Figure 7a–c. Yarns of each polymer showed their own distinct behavior. The PAN yarns showed a steep elastic region, followed by an extended plastic region and a sudden drop in stress when the fibers in the yarn appeared to break unison. The eADF4(C16) yarns showed a brittle behavior with a very short plastic deformation regime. Upon rupture, the stress dropped abruptly, although not until zero, but until a low value. Possibly, several surviving fibers that still held together the two ends of the partially-torn yarn accounted for the residual tensile stress, which eventually diminished completely as they either slipped or tore. The cellulose acetate yarns showed most clearly the gradual disentanglement of the individual fibers in the yarn through the very gradual fall in tension after a maximum had been reached. The tensile strength and elongation at break of the yarns are summarized in Table 1.

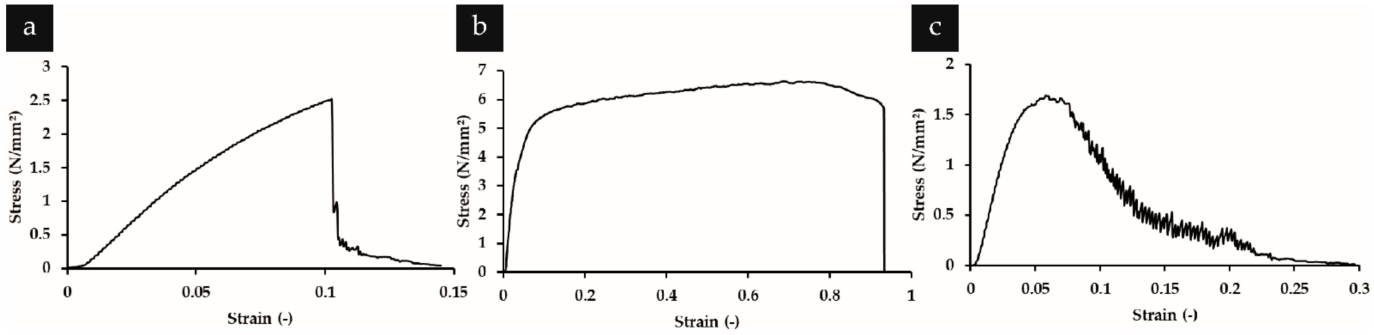


**Figure 7.** Typical stress–strain curve of (**a**) eADF4(C16), (**b**) PAN, and (**c**) cellulose acetate yarns.

## 5. Production Speed and Nanofiber Yarn Properties

Production speed is one of the most important factors dictating whether a process can be feasibly implemented at an industrial scale. The throughput limitation is a long-known issue that hinders the implementation of electrospinning for most applications at large scale. In a basic electrospinning setup, the polymer solution or melt is fed through a nozzle. The flow of material is limited by the Taylor cone, whose diameter is much smaller than that of the droplet that forms at the nozzle tip. While this tiny diameter enables the formation of tiny fibers, which sets electrospinning apart from other conventional fiber processing methods, it also turns out to be the limiting factor which makes electrospinning a very low throughput process. Therefore, we have seen various strategies [50] developed to overcome this problem, ranging from the use of multiple needles [51] to abandoning needles altogether and using solution-wetted objects of various geometries [52] to increase the number of Taylor cones forming at the same time.

Here, production speed is the rate of yarn collection, which, in the case of funnel-based continuous yarn electrospinning, is determined by the linear speed of the yarn winder. Earlier works, such as those from Afifi et al. [27] and Dabirian et al. [53], are characterized by low production speeds, using a single needle and achieving production speeds in the cm $min^{-1}$ range. Many later works using a two-needle approach achieved higher production speeds in the m $min^{-1}$ range such as those from Ali et al. [31], Li et al. [28], and Wu et al. [30]. While increasing the number of needles enables a higher flow rate at the needles, this does not guarantee a higher yarn production speed, which is determined directly by the winder speed. On the other hand, increasing the winder speed increases the risk of tearing the nonwoven cone, which would halt the production, as connection between yarn and funnel would need to be re-established manually. It appears that optimization plays a large role in dictating the production speed, which explains the large variation in the collection speed between works using the two-needle setup.

Nevertheless, literature shows a progression of increasing production speed by increasing the throughput in a series of works from He et al., who started with two pairs of needles [35], followed by another work using four pairs of needles, then yet another

using two pairs of larger nozzles with an inner diameter of 16 mm [54], which extruded polymer solution and air bubbles coaxially, such that multiple Taylor cones could form on the bubble surface. Thus, the production speed progressed from 2 to 4 to 5 m $min^{-1}$. The move away from a needle-based electrospinning can also be observed in the work of Shuakat and Lin [37], where they used a combination of a needle and a disc, achieving a production speed of 4 m $min^{-1}$, the second highest among the works that we surveyed. Curiously, the highest production speed of 5 m $min^{-1}$ found in literature was achieved both by Ali et al. using a needle-based approach, and by He et al. using a needleless approach. However, based on the large diameter distribution of the generated fibers from the work of Ali et al. [31], it can be concluded that a needleless approach is more suitable in achieving a narrower fiber diameter distribution, which lies well below 1 μm.

In addition to the production speed, dimensions of fibers as well as the tensile properties vary greatly between various groups working with the same technique on the same material. Taking PAN as an example, and comparing values reported in MPa, tensile strength values of 8.60 ± 3.03 MPa were achieved in our experiments. In contrast, the highest reported values, which ranged between 100–180 MPa, came from the study of Yan et al., who used a single needle with a collection speed of 8.6 cm $min^{-1}$, which is among the lowest collection speeds reported. The compiled data reveal a high variability in yarn properties even between works that utilized similar techniques, highlighting the importance of optimizing a setup to achieve the best results.

Until quite recently, most yarns have been made out of microfibers. While these have been useful for many different applications, it has been quite unknown how yarns of certain materials would behave, if their constituent fibers are made of nano- instead of microfibers. Recent works are beginning to probe the properties and behavior of nanofiber yarns in traditional textile scenarios such as wicking property [29] and behavior in a weave [28,55].

**Table 1.** List of materials electrospun into yarns, along with fiber and yarn fineness, yarn tensile properties, nozzle type and production speed of continuous yarn electrospinning. Our data and data from the four exemplary works discussed in the previous sections are listed above the double lines, while additional data from the literature are listed below. TS: tensile strength, ε: elongation at break, N/A: not available, PAN: polyacrylonitrile, P(AN-co-MA): poly(acrylonitrile-co-methylacrylate), PCL: polycaprolactone, PLA: polylactic acid, PLLA: poly l-lactic acid, PSA: polysulfone amide, PVDF-HFP: poly(vinylidene fluoride-hexafluoropropylene), P(VDF-TrFE): poly(vinylidene fluoride-co-trifluoroethylene). * Calculated from given RPM and estimated winding unit diameter. ** Not mentioned explicitly, estimated from a graph. ***: Assumed from needle color. Ø: diameter, $Ø_i$: inner diameter.

| Material | Fiber Fineness | Yarn Fineness | Yarn Tensile Properties | Nozzle Type | Production Speed | Reference |
|---|---|---|---|---|---|---|
| eADF4(C16) | 503 ± 276 nm | 226 ± 65 µm | TS:1.57 ± 0.57 MPa<br>ε: 8.1 ± 3.4 % | two needles (21G) | 18.8 cm $min^{-1}$ | This work |
| cellulose acetate | 849 ± 453 nm | 249 ± 105 µm | TS: 3.97 ± 3.81 MPa<br>ε: 6.1 ± 1.4 % | | | |
| PAN | 1000 ± 243 nm | 210 ± 53 µm | TS: 8.60 ± 3.03 MPa<br>ε: 81.6 ± 46.7 % | | | |
| PLA | 6.0 ± 1.9 µm | 164 µm (average) | TS: 0.017 g $denier^{-1}$<br>ε: 110% | single needle (24G) | 6.3 cm $min^{-1}$ | Afifi et al. (2010) [27] |
| PLLA | 558 ± 158 nm | 69 ± 19 µm | TS: 23 MPa<br>ε: 27.7% | two needles (Ø 0.8 mm) | 1 m $min^{-1}$ | Li et al. (2020) [28] |
| PAN | 475–625 nm | 52–105 µm | TS: 7.6–9.1 cN $dtex^{-1}$<br>ε: 33.32–65.21% | two needles | 2 m $min^{-1}$ | Wu et al. (2013) [30] |
| Silk fibroin/ PLA/PCL | 868.94 ± 227.63 nm | 30.56 ± 6.32 µm | TS: 24.25±0.76 MPa<br>ε: 40.82±1.4% | single needle | 62.82 cm $min^{-1}$ | Yang et al. (2014) [38] |
| PAN | 411.77 nm (average) | 160.43–170.14 µm | TS: 58.08 MPa<br>ε: 62.14% | single needle | 23 cm $min^{-1}$ | Dabirian et al. (2007) [53] |
| PAN | 474 nm (average) | N/A | TS: 54.57 MPa<br>ε: 60.81 % | two needles, (Ø 0.7 mm) | 9.65 cm $min^{-1}$ | Dabirian & Hosseini (2009) [56] |
| PAN | 473 nm (average) | 340.65 µm (average) | TS: 1.3 MPa<br>ε: 54.21% | two needles (Ø 0.7 mm) | 9.65 cm $min^{-1}$ | Dabirian et al. (2011) [57] |
| PAN | N/A | N/A | TS: 100–180 MPa<br>ε: 32.5–40% | single needle | 8.6 cm $min^{-1}$ * | Yan et al. (2011) [58] |

**Table 1.** *Cont.*

| Material | Fiber Fineness | Yarn Fineness | Yarn Tensile Properties | Nozzle Type | Production Speed | Reference |
|---|---|---|---|---|---|---|
| PAN | 480–1500 nm | 30–450 µm | TS: 60.4 MPa<br>ε: 250% | two needles (21G) *** | 5 m $min^{-1}$ | Ali et al. (2012) [31] |
| PAN | 400–650 nm ** | 50–200 µm | TS: 55.7 MPa<br>ε: 41.31% | four needles | 40 cm $min^{-1}$ | He et al. (2013) [35] |
| PAN | 425–700 nm | 82.5–105 µm | TS: 50.71 MPa<br>ε: 43.56% | eight needles ($Ø_i$ 0.5 mm) | 2 m $min^{-1}$ | He et al. (2014) [36] |
| PAN | 186–398 nm | 200–386 µm | TS: 0.592 cN $dtex^{-1}$<br>ε: 65.7% | four bubble nozzles ($Ø_i$ 16 mm) | 5 m $min^{-1}$ | He et al. (2014) [54] |
| PAN | N/A | N/A | N/A | two needles | N/A | Ravandi et al. (2015) [55] |
| PAN | 450–600 nm ** | 45–190 µm ** | TS: 13.33 cN $dtex^{-1}$<br>ε: 54.9% | two needles | 2 m $min^{-1}$ | Wu et al. (2016) [59] |
| PAN | 1200–1650 nm | N/A | TS: 3.80–4.25 MPa<br>ε: 7.83–17.71% | two needles (21G) | N/A | Levitt et al. (2017) [60] |
| P(VDF-TrFE) | 790–970 nm | | TS: 2.81–10.16 MPa<br>ε: 129.65–190.43% | | | |
| PCL | 810–1320 nm | | TS: 1.56–2.03 MPa<br>ε: 212.74–306.50% | | | |
| PVDF-HFP | 541 nm–1.6 µm | 52–206 µm | TS: 128.9 MPa<br>ε: 222.1% | single needle and disc (Ø 50–80 mm, thickness 1–6 mm) | 4 m $min^{-1}$ | Shuakat & Lin (2015) [37] |
| PSA | 355–559 nm | 90–212 µm | TS: 30 cN $dtex^{-1}$ **<br>ε: 2.18 mm ** | two needles ($Ø_i$ 0.5 mm) | N/A | Jin et al. (2019) [29] |
| P(AN-co-MA) | 1170 ± 120 nm | 130 ± 12 µm | TS:72 ± 3 MPa<br>ε: N/A | two needles | 82 cm $min^{-1}$ | Liao at al. (2019) [61] |

## 6. Standardized Reporting

The four referenced works on continuous yarn electrospinning using the funnel-based setup are exemplary works, and schematics or actual photograph of the experimental setup and SEM images of the yarns produced provide insights into the technologies. Along with the tensile properties of the nanofiber yarns and the production speed of the process, this set of information gave a first impression on the quality of the process. In addition to the data from these four works as well as novel data obtained by us, several other works on continuous yarn electrospinning are listed in Table 1. All of the works contain the schematics of the electrospinning setup and SEM pictures of the produced yarns, while some even provide photographs of the electrospinning process in action. However, some of the references provide more information regarding the process and yarn properties compared to others. This is understandable, as not every experiment was conducted under the same circumstances and with the same aim. Certain works are by definition process optimization work and, therefore, focus extensively on optimizing the process, with some of them using various polymers to demonstrate the versatility of their process. Other works are probably much more focused on the application of the yarns in subsequent experiments, thus acquiring the yarns is the goal. Therefore, the setup could be provisional, and the detailed description and characterization of the process parameters are of secondary importance. Nevertheless, we would encourage future researchers to survey previous works and include a similar set of data in their work to facilitate comparison, especially if this does not detract from achieving their own research goals.

We also observed discrepancies in the units used for one of the most important parameters, namely tensile strength. Elongation at break can be given either in percentage of the original length or as absolute elongation, which can be easily converted into percentage given the gauge length. Tensile strength, however, is reported in MPa, cN dtex$^{-1}$, or g denier$^{-1}$. While cN dtex$^{-1}$ and g denier$^{-1}$ can be converted into each other, MPa cannot be converted directly to cN dtex$^{-1}$ or g denier$^{-1}$ and vice versa because MPa is a unit of stress and is calculated using the yarn's cross-sectional area, while cNdtex$^{-1}$ and g denier$^{-1}$ are a unit of force and are calculated using the yarn's linear density. This discrepancy renders direct comparison difficult. cN dtex$^{-1}$ and g denier$^{-1}$ are units commonly used in the textile industry and have the advantage of not having to consider the possibly large variations in yarn diameter along the length of the yarn [62]. Due to the limited lengths of yarns produced in this current work, which did not permit the reliable determination of the yarn linear densities, we reported the tensile properties of our yarns in MPa. However, we would recommend that future works report the tensile properties in cN dtex$^{-1}$ and g denier$^{-1}$, so that the literature on electrospun nanofiber yarns can gain more relevance in the textile industry.

Schematics of the experimental setup, along with a detailed explanation thereof, SEM images of fibers, fiber fineness in diameter, yarn fineness in diameter, yarn linear density, and process speed, would be an appropriate basis for a uniform yarn characterization.

Detailed schematics of the experimental setup and its explanation will help others to reproduce the experimental setup, as is the case with this current work, whose setup was adopted from the one used by Li et al. [28] with slight modification. A morphological analysis, especially using SEM, gives an overall information on fiber appearance and smoothness. Certain processes, such as the water-based bundling as used by Smit et al. [22] and Teo et al. [23] result in bundles with fiber loops that may be undesirable. Smoothness may play an important role in certain applications. Smoother fibers contain less surface area and, conversely, rougher fibers contain more surface area. This plays a significant role in certain applications such as drug release [63] and in tissue engineering, where the cells' attachment and adhesion depends on surface roughness [64]. Fiber fineness and diameter helps to decide whether the fibers are suitable for certain applications. For example, in tissue engineering, cell adherence and proliferation vary significantly with fiber diameter [65]. Yarn linear density may be a consideration for researchers looking to use as little material as possible but at the same time creating longest possible yarns.

Information of process speed is especially important in deciding whether it is possible to use a certain process in large-scale production.

Additionally, a commercially available polymer should always accompany the development of a new yarn electrospinning process so that the characteristics of the yarns can be used to compare the processes directly. Out of 18 works surveyed regarding continuous yarn electrospinning, 13 used PAN (if we also include the work of Liao et al. [61], which used a PAN copolymer). From the 13 works that used PAN, only Ravandi et al. [55] cited briefly the relevance of choosing PAN for continuous yarn electrospinning, stating its potential as precursor for high performance carbon fibers. This echoes the opinion of Fennessey and Farris in their 2004 work [20], which discussed in the introduction of their paper the relevance of their choice of PAN for electrospinning aligned nanofibers. In the cases where there was no mention of the motivation for choosing PAN, it seems reasonable to assume that the ease of electrospinning of PAN makes it a convenient choice to demonstrate the capability of a novel electrospinning method. PAN is a widely available polymer with various applications in textiles, water purification, air filtration, and forming precursors of carbon fibers [66], and, especially in the context of electrospinning, its behavior has been extensively characterized [67,68]. It is readily electrospun in a concentration range of 10–15 wt% and voltage range of 10–13 kV, producing smooth fibers without beads and a diameter within the range of 165–400 nm [67]. This makes it highly suitable to serve as a standard polymer.

If this set of abovementioned information is provided, while using PAN as a standard polymer, comparing the potential of various yarn electrospinning processes can be greatly facilitated. This helps future researchers or process planners in deciding whether a certain experimental setup would suit their purpose, or even be worth further optimization. This would assist in the development of continuous yarn electrospinning and hopefully accelerate the integration of nanofiber yarns into established textile processing.

## 7. Conclusions

Continuous yarn electrospinning is still in its infancy, with most work being proof of concept and process optimization studies using model polymers such as PAN. As processes, such as the funnel-based continuous yarn electrospinning, become more understood and reliable, research will shift towards the use of the processes in conjunction with novel materials with exciting potential applications. The field of medicine and tissue engineering appears to be especially promising. The works of Li et al. [28] and Wu et al. [69] demonstrated the robustness of nanofiber yarns enabling the processing of said yarns into woven material suited for cell scaffolds. Richard et al. [70] used sutures made of electrospun PLLA yarns loaded with drugs, which showed sustained drug release and superior wound healing compared to controls. Work such as that from Dai et al. [71] managed to overcome limitations of inherent material properties such as brittleness of ceramics by bringing the material into a form usually unattainable without the help of yarn electrospinning. Others such as Sheng et al. [72] have recognized the potential of conjugate electrospinning combined with the funnel-based collection in creating multifunctional materials. These works, coming from just the past two years, are only beginning to scratch the surface of what may be possible with continuous yarn electrospinning.

In this review, yarn electrospinning is shown to trace its history back to the 1900s. Apart from modernization of the components involved in the setup, its main principles are still applied to this day. Following the advent of nanotechnology in the 1990s and early 2000s, interest in electrospinning has seen a resurgence, particularly because of its ability to produce nanoscale fibers. In trying to find applications for variously produced nanofibers, the common problem of handling weak nonwoven meshes kept emerging, leading researchers to find techniques to produce electrospun yarns. Among various methods to continuously produce electrospun yarns, the funnel-winding unit variant proved highly successful, spawning multiple variants of its own. Several of these have been discussed in this review, along with the properties of the resulting yarns. The methods

delivered yarns of different qualities and at different rates, the comparison of which is enabled by the inclusion of information such as tensile properties and production speed in the publications. It was also observed that a shift towards needleless electrospinning seemed to result in higher throughput, indicating that future works aiming at increasing throughput should focus thereon. We would like to recommend that future publications include data on yarn morphology (SEM images), tensile properties in units corresponding to textile industry conventions, and production speed, as well as using the standard polymer PAN to allow direct comparison between different processes. This would hopefully facilitate the development of yarn electrospinning so that electrospun yarns can be used in combination with conventional textile processing techniques in the future.

**Author Contributions:** Conceptualization, T.S.; funding acquisition, T.S.; investigation, S.Z.; methodology, S.Z.; project administration, T.S.; resources, T.S.; software, S.Z.; supervision, T.S.; validation, T.S.; visualization, S.Z.; writing—original draft, S.Z.; writing—review and editing, T.S. All authors have read and agreed to the published version of the manuscript.

**Funding:** The authors would like to thank Technology Alliance of Upper Franconia (TAO) and the Bavarian Polymer Institute (BPI) for financial support.

**Data Availability Statement:** The data that support the findings of this study are available from the corresponding author upon reasonable request.

**Conflicts of Interest:** The authors declare no conflict of interest. The funders had no role in the design of the study; in the collection, analyses, or interpretation of data; in the writing of the manuscript, or in the decision to publish the results.

## References

1. Doshi, J.; Reneker, D.H. Electrospinning process and applications of electrospun fibers. *J. Electrost.* **1995**, *35*, 151–160. [CrossRef]
2. Lyons, J.; Li, C.; Ko, F. Melt-electrospinning part I: Processing parameters and geometric properties. *Polymer* **2004**, *45*, 7597–7603. [CrossRef]
3. Choi, S.-S.; Lee, S.G.; Im, S.S.; Kim, S.H.; Joo, Y.L. Silica nanofibers from electrospinning/sol-gel process. *J. Mater. Sci. Lett.* **2003**, *22*, 891–893. [CrossRef]
4. Praeger, M.; Saleh, E.; Vaughan, A.; Stewart, W.; Loh, W. Fabrication of nanoscale glass fibers by electrospinning. *Appl. Phys. Lett.* **2012**, *100*, 063114. [CrossRef]
5. Lang, G.; Jokisch, S.; Scheibel, T. Air filter devices including nonwoven meshes of electrospun recombinant spider silk proteins. *J. Vis. Exp. JoVE* **2013**, *75*, e50492. [CrossRef]
6. Ashammakhi, N.; Ndreu, A.; Piras, A.M.; Nikkola, L.; Sindelar, T.; Ylikauppila, H.; Harlin, A.; Gomes, M.E.; Neves, N.; Chiellini, E. Biodegradable nanomats produced by electrospinning: Expanding multifunctionality and potential for tissue engineering. *J. Nanosci. Nanotechnol.* **2007**, *7*, 862–882. [CrossRef]
7. Sill, T.J.; Von Recum, H.A. Electrospinning: Applications in drug delivery and tissue engineering. *Biomaterials* **2008**, *29*, 1989–2006. [CrossRef]
8. Ding, B.; Yamazaki, M.; Shiratori, S. Electrospun fibrous polyacrylic acid membrane-based gas sensors. *Sens. Actuators B Chem.* **2005**, *106*, 477–483. [CrossRef]
9. Chen, S.; Han, D.; Hou, H. High strength electrospun fibers. *Polym. Adv. Technol.* **2011**, *22*, 295–303.
10. Pontelli, G.C.; Reolon, R.P.; Alves, A.K.; Berutti, F.A.; Bergmann, C.P. Application of cerium oxide electrospun fibers in the catalytic combustion of methane. *Appl. Catal. A Gen.* **2011**, *405*, 79–83. [CrossRef]
11. Hohman, M.M.; Shin, M.; Rutledge, G.; Brenner, M.P. Electrospinning and electrically forced jets. I. Stability theory. *Phys. Fluids* **2001**, *13*, 2201–2220. [CrossRef]
12. Göktepe, F.; Buzol Mülayim, B. Long path towards to success in electrospun nanofiber yarn production since 1930′s: A critical review. *Autex Res. J.* **2018**, *18*, 87–109. [CrossRef]
13. O'Connor, R.A.; McGuinness, G.B. Electrospun nanofibre bundles and yarns for tissue engineering applications: A review. *Proc. Inst. Mech. Eng. Part H J. Eng. Med.* **2016**, *230*, 987–998. [CrossRef] [PubMed]
14. Wei, L.; Qin, X. Nanofiber bundles and nanofiber yarn device and their mechanical properties: A review. *Text. Res. J.* **2016**, *86*, 1885–1898. [CrossRef]
15. Shuakat, M.N.; Lin, T. Recent developments in electrospinning of nanofiber yarns. *J. Nanosci. Nanotechnol.* **2014**, *14*, 1389–1408. [CrossRef]
16. Boys, C.V. LVII. On the production, properties, and some suggested uses of the finest threads. *Lond. Edinb. Dublin Philos. Mag. J. Sci.* **1887**, *23*, 489–499. [CrossRef]

17. Tucker, N.; Stanger, J.J.; Staiger, M.P.; Razzaq, H.; Hofman, K. The history of the science and technology of electrospinning from 1600 to 1995. *J. Eng. Fibers Fabr.* **2012**, *7*, 63–73. [CrossRef]
18. Cooley, J.F. Improved Methods of and Apparatus for Electrically Separating the Relatively Volatile Liquid Component from the Component of Relatively Fixed Substances of Composite Fluids. United Kingdom Patent 6385, 19 May 1900.
19. Formhals, A. Process and apparatus for preparing artificial threads. U.S. Patent 1,975,504, 2 October 1934.
20. Fennessey, S.F.; Farris, R.J. Fabrication of aligned and molecularly oriented electrospun polyacrylonitrile nanofibers and the mechanical behavior of their twisted yarns. *Polymer* **2004**, *45*, 4217–4225. [CrossRef]
21. Yousefzadeh, M.; Latifi, M.; Teo, W.E.; Amani-Tehran, M.; Ramakrishna, S. Producing continuous twisted yarn from well-aligned nanofibers by water vortex. *Polym. Eng. Sci.* **2011**, *51*, 323–329. [CrossRef]
22. Smit, E.; Bűttner, U.; Sanderson, R.D. Continuous yarns from electrospun fibers. *Polymer* **2005**, *46*, 2419–2423. [CrossRef]
23. Teo, W.-E.; Gopal, R.; Ramaseshan, R.; Fujihara, K.; Ramakrishna, S. A dynamic liquid support system for continuous electrospun yarn fabrication. *Polymer* **2007**, *48*, 3400–3405. [CrossRef]
24. Pan, H.; Li, L.; Hu, L.; Cui, X. Continuous aligned polymer fibers produced by a modified electrospinning method. *Polymer* **2006**, *47*, 4901–4904. [CrossRef]
25. Maleki, H.; Gharehaghaji, A.; Moroni, L.; Dijkstra, P.J. Influence of the solvent type on the morphology and mechanical properties of electrospun PLLA yarns. *Biofabrication* **2013**, *5*, 035014. [CrossRef] [PubMed]
26. Bazbouz, M.B.; Stylios, G.K. A new mechanism for the electrospinning of nanoyarns. *J. Appl. Polym. Sci.* **2012**, *124*, 195–201. [CrossRef]
27. Afifi, A.M.; Nakano, S.; Yamane, H.; Kimura, Y. Electrospinning of continuous aligning yarns with a 'funnel'target. *Macromol. Mater. Eng.* **2010**, *295*, 660–665. [CrossRef]
28. Li, D.; Tao, L.; Shen, Y.; Sun, B.; Xie, X.; Ke, Q.; Mo, X.; Deng, B. Fabrication of Multilayered Nanofiber Scaffolds with a Highly Aligned Nanofiber Yarn for Anisotropic Tissue Regeneration. *ACS Omega* **2020**, *5*, 24340–24350. [CrossRef]
29. Jin, S.; Xin, B.; Zheng, Y. Preparation and characterization of polysulfone amide nanoyarns by the dynamic rotating electrospinning method. *Text. Res. J.* **2019**, *89*, 52–62. [CrossRef]
30. Wu, S.-H.; Qin, X.-H. Uniaxially aligned polyacrylonitrile nanofiber yarns prepared by a novel modified electrospinning method. *Mater. Lett.* **2013**, *106*, 204–207. [CrossRef]
31. Ali, U.; Zhou, Y.; Wang, X.; Lin, T. Direct electrospinning of highly twisted, continuous nanofiber yarns. *J. Text. Inst.* **2012**, *103*, 80–88. [CrossRef]
32. Tong, X.; Bin-Jie, X. Preparation and Characterization of Polyester Staple Yarns Nanowrapped with Polysulfone Amide Fibers. *Ind. Eng. Chem. Res.* **2015**, *54*, 12303–12312. [CrossRef]
33. Gu, Z.Q.; Yin, H.Y.; Wang, J.; Ma, L.L.; Morsi, Y.; Mo, X.M. Fabrication and characterization of TGF-beta 1-loaded electrospun poly (lactic-co-glycolic acid) core-sheath sutures. *Colloid Surf. B-Biointerfaces* **2018**, *161*, 331–338. [CrossRef] [PubMed]
34. Smit, E.; Büttner, U.; Sanderson, R. Continuous yarns from electrospun nanofibers. In *Nanofibers and nanotechnology in textiles*; Elsevier: Amsterdam, The Netherlands, 2007; pp. 45–70.
35. He, J.; Zhou, Y.; Qi, K.; Wang, L.; Li, P.; Cui, S. Continuous twisted nanofiber yarns fabricated by double conjugate electrospinning. *Fibers Polym.* **2013**, *14*, 1857–1863. [CrossRef]
36. He, J.; Qi, K.; Zhou, Y.; Cui, S. Multiple conjugate electrospinning method for the preparation of continuous polyacrylonitrile nanofiber yarn. *J. Appl. Polym. Sci.* **2014**, *131*, 1288–1294. [CrossRef]
37. Shuakat, M.N.; Lin, T. Highly-twisted, continuous nanofibre yarns prepared by a hybrid needle-needleless electrospinning technique. *RSC Adv.* **2015**, *5*, 33930–33937. [CrossRef]
38. Yang, C.; Deng, G.; Chen, W.; Ye, X.; Mo, X. A novel electrospun-aligned nanoyarn-reinforced nanofibrous scaffold for tendon tissue engineering. *Colloids Surf. B Biointerfaces* **2014**, *122*, 270–276. [CrossRef]
39. Kolybaba, M.; Tabil, L.; Panigrahi, S.; Crerar, W.; Powell, T.; Wang, B. Biodegradable polymers: Past, present, and future. In Proceedings of the ASABE/CSBE North Central Intersectional Meeting, Fargo, ND, USA, 3–4 October 2003; pp. 1–15.
40. Velema, J.; Kaplan, D. Biopolymer-based biomaterials as scaffolds for tissue engineering. *Tissue Eng. I* **2006**, *102*, 187–238.
41. Olsen, D.; Yang, C.; Bodo, M.; Chang, R.; Leigh, S.; Baez, J.; Carmichael, D.; Perälä, M.; Hämäläinen, E.-R.; Jarvinen, M. Recombinant collagen and gelatin for drug delivery. *Adv. Drug Deliv. Rev.* **2003**, *55*, 1547–1567. [CrossRef]
42. Sallach, R.E.; Conticello, V.P.; Chaikof, E.L. Expression of a recombinant elastin-like protein in pichia pastoris. *Biotechnol. Prog.* **2009**, *25*, 1810–1818.
43. Huemmerich, D.; Helsen, C.W.; Quedzuweit, S.; Oschmann, J.; Rudolph, R.; Scheibel, T. Primary structure elements of spider dragline silks and their contribution to protein solubility. *Biochemistry* **2004**, *43*, 13604–13612. [CrossRef]
44. Hardy, J.G.; Römer, L.M.; Scheibel, T.R. Polymeric materials based on silk proteins. *Polymer* **2008**, *49*, 4309–4327. [CrossRef]
45. Kulpinski, P. Cellulose nanofibers prepared by the N-methylmorpholine-N-oxide method. *J. Appl. Polym. Sci.* **2005**, *98*, 1855–1859. [CrossRef]
46. Ohkawa, K.; Cha, D.; Kim, H.; Nishida, A.; Yamamoto, H. Electrospinning of chitosan. *Macromol. Rapid Commun.* **2004**, *25*, 1600–1605. [CrossRef]
47. DeSimone, E.; Aigner, T.B.; Humenik, M.; Lang, G.; Scheibel, T. Aqueous electrospinning of recombinant spider silk proteins. *Mater. Sci. Eng. C* **2020**, *106*, 110145. [CrossRef] [PubMed]

48. Huang, L.; Nagapudi, K.; Apkarian, P.R.; Chaikof, E.L. Engineered collagen–PEO nanofibers and fabrics. *J. Biomater. Sci. Polym. Ed.* **2001**, *12*, 979–993. [CrossRef]
49. Vega-Lugo, A.-C.; Lim, L.-T. Electrospinning of soy protein isolate nanofibers. *J. Biobased Mater. Bioenergy* **2008**, *2*, 223–230. [CrossRef]
50. SalehHudin, H.S.; Mohamad, E.N.; Mahadi, W.N.L.; Muhammad Afifi, A. Multiple-jet electrospinning methods for nanofiber processing: A review. *Mater. Manuf. Processes* **2018**, *33*, 479–498. [CrossRef]
51. Varesano, A.; Rombaldoni, F.; Mazzuchetti, G.; Tonin, C.; Comotto, R. Multi-jet nozzle electrospinning on textile substrates: Observations on process and nanofibre mat deposition. *Polym. Int.* **2010**, *59*, 1606–1615. [CrossRef]
52. Niu, H.; Wang, X.; Lin, T. Needleless electrospinning: Influences of fibre generator geometry. *J. Text. Inst.* **2012**, *103*, 787–794. [CrossRef]
53. Dabirian, F.; Hosseini, Y.; Ravandi, S.H. Manipulation of the electric field of electrospinning system to produce polyacrylonitrile nanofiber yarn. *J. Text. Inst.* **2007**, *98*, 237–241. [CrossRef]
54. He, J.X.; Qi, K.; Zhou, Y.M.; Cui, S.Z. Fabrication of continuous nanofiber yarn using novel multi-nozzle bubble electrospinning. *Polym. Int.* **2014**, *63*, 1288–1294. [CrossRef]
55. Ravandi, S.H.; Tork, R.B.; Dabirian, F.; Gharehaghaji, A.; Sajjadi, A. Characteristics of yarn and fabric made out of nanofibers. *Mater. Sci. Appl.* **2015**, *6*, 103. [CrossRef]
56. Dabirian, F.; Hosseini, S. Novel method for nanofibre yarn production using two differently charged nozzles. *Fibres Text. East. Eur.* **2009**, *17*, 45–47.
57. Dabirian, F.; Ravandi, S.H.; Sanatgar, R.H.; Hinestroza, J. Manufacturing of twisted continuous PAN nanofiber yarn by electrospinning process. *Fibers Polym.* **2011**, *12*, 610–615. [CrossRef]
58. Yan, H.; Liu, L.; Zhang, Z. Continually fabricating staple yarns with aligned electrospun polyacrylonitrile nanofibers. *Mater. Lett.* **2011**, *65*, 2419–2421. [CrossRef]
59. Wu, S.; Zhang, Y.; Liu, P.; Qin, X. Polyacrylonitrile nanofiber yarns and fabrics produced using a novel electrospinning method combined with traditional textile techniques. *Text. Res. J.* **2016**, *86*, 1716–1727. [CrossRef]
60. Levitt, A.S.; Knittel, C.E.; Vallett, R.; Koerner, M.; Dion, G.; Schauer, C.L. Investigation of nanoyarn preparation by modified electrospinning setup. *J. Appl. Polym. Sci.* **2017**, *134*, 44813. [CrossRef]
61. Liao, X.; Dulle, M.; e Silva, J.M.d.S.; Wehrspohn, R.B.; Agarwal, S.; Förster, S.; Hou, H.; Smith, P.; Greiner, A. High strength in combination with high toughness in robust and sustainable polymeric materials. *Science* **2019**, *366*, 1376–1379. [CrossRef]
62. Schultze-Gebhardt, K.H. Karl-Heinz. 1. Survey. In *Fibers*; Wiley-VCH, Ed.; Wiley-VCH Verlag GmbH & Co. KGaA: Weinheim, Germany, 2008; Volume 1, p. 5.
63. Lian, H.; Meng, Z.X. Melt electrospinning vs. solution electrospinning: A comparative study of drug-loaded poly (epsilon-caprolactone) fibres. *Mater. Sci. Eng. C-Mater. Biol. Appl.* **2017**, *74*, 117–123. [CrossRef]
64. Metwally, S.; Ferraris, S.; Spriano, S.; Krysiak, Z.J.; Kaniuk, Ł.; Marzec, M.M.; Kim, S.K.; Szewczyk, P.K.; Gruszczyński, A.; Wytrwal-Sarna, M.; et al. Surface potential and roughness controlled cell adhesion and collagen formation in electrospun PCL fibers for bone regeneration. *Mater. Des.* **2020**, *194*, 108915. [CrossRef]
65. Chen, M.; Patra, P.K.; Warner, S.B.; Bhowmick, S. Role of fiber diameter in adhesion and proliferation of NIH 3T3 fibroblast on electrospun polycaprolactone scaffolds. *Tissue Eng.* **2007**, *13*, 579–587. [CrossRef]
66. Khayyam, H.; Jazar, R.N.; Nunna, S.; Golkarnarenji, G.; Badii, K.; Fakhrhoseini, S.M.; Kumar, S.; Naebe, M. PAN precursor fabrication, applications and thermal stabilization process in carbon fiber production: Experimental and mathematical modelling. *Prog. Mater. Sci.* **2020**, *107*, 100575. [CrossRef]
67. Jalili, R.; Morshed, M.; Ravandi, S.A.H. Fundamental parameters affecting electrospinning of PAN nanofibers as uniaxially aligned fibers. *J. Appl. Polym. Sci.* **2006**, *101*, 4350–4357. [CrossRef]
68. Gomes, D.S.; da Silva, A.N.; Morimoto, N.I.; Mendes, L.T.; Furlan, R.; Ramos, I. Characterization of an electrospinning process using different PAN/DMF concentrations. *Polímeros* **2007**, *17*, 206–211. [CrossRef]
69. Wu, S.; Liu, J.; Cai, J.; Zhao, J.; Duan, B.; Chen, S. Combining electrospinning with hot drawing process to fabricate high performance poly (L-lactic acid) nanofiber yarns for advanced nanostructured bio-textiles. *Biofabrication* **2021**, *13*, 045018. [CrossRef] [PubMed]
70. Richard, A.S.; Verma, R.S. Bioactive nano yarns as surgical sutures for wound healing. *Mater. Sci. Eng. C* **2021**, *128*, 112334. [CrossRef] [PubMed]
71. Dai, Z.; Yan, F.; Qin, M.; Yan, X. Fabrication of flexible SiO2 nanofibrous yarn via a conjugate electrospinning process. *e-Polymers* **2020**, *20*, 600–605. [CrossRef]
72. Sheng, Y.; Tian, J.; Xie, Y.; Yang, X.; Qi, H.; Ma, Q.; Yu, W.; Dong, X.; Yu, H.; Liu, G. Neoteric conjugative electrospinning towards alloplastic nanofiber yarns affording enhanced upconversion luminescence and tailored magnetism. *ChemNanoMat* **2020**, *6*, 298–307. [CrossRef]

*textiles*

MDPI

*Review*

# A Review on Tough Soft Composites at Different Length Scales

**Wei Cui [1,2,*] and Ruijie Zhu [3]**

[1] State Key Laboratory of Polymer Materials Engineering, College of Polymer Science and Engineering, Sichuan University, Chengdu 610065, China
[2] Faculty of Advanced Life Science, Hokkaido University, Sapporo 001-0021, Japan
[3] Graduate School of Chemical Sciences and Engineering, Hokkaido University, Sapporo 060-8628, Japan; ruijie.zhu.b5@elms.hokudai.ac.jp
* Correspondence: cuiwei1991@126.com or cuiwei@sci.hokudai.ac.jp

**Abstract:** Soft composites are widely employed in industrial and biomedical fields, which often serve as load-bearing structural materials by virtue of a special combination of high strength, high toughness, and low flexural stiffness. Understanding the toughening mechanism of such composites is crucial for designing the next-generation soft materials. In this review, we give an overview of recent progress in soft composites, focusing on the design strategy, mechanical properties, toughening mechanisms, and relevant applications. Fundamental design strategies for soft composites that dissipate energy at different length scales are firstly described. By subsequently elucidating the synergistic effects of combining soft and hard phases, we show how a resulting composite can achieve unprecedented mechanical performance by optimizing the energy dissipation. Relevant toughening models are discussed to interpret the superior strength and fracture toughness of such soft composites. We also highlight relevant applications of these soft composites by taking advantage of their special mechanical responses.

**Keywords:** soft composite; mechanical property; toughness; toughening mechanism; fabrication; application

**Citation:** Cui, W.; Zhu, R. A Review on Tough Soft Composites at Different Length Scales. *Textiles* **2021**, *1*, 513–533. https://doi.org/10.3390/textiles1030027

Academic Editor: Laurent Dufossé

Received: 26 October 2021
Accepted: 16 November 2021
Published: 17 November 2021



## 1. Introduction

Composite materials are widely applied in industrial and biomedical fields as structural materials due to their superior comprehensive properties, such as high strength, high stiffness, low weight, corrosion resistance, etc. [1–4]. Conventional hard composites are generally composed of rigid matrices (resins, metals, ceramics, etc.) and rigid fibers or fabrics, showing isotropically high stiffness [5–7]. Soft composite, in contrast, is a sort of composite material with low flextural stiffness [8–12]. Commonly, both hard and soft composites show very high fracture stress and Young's modulus in tension, which can reach values on the order of $10^0$ and $10^1$ GPa, respectively. The biggest difference between hard and soft composites is their mechanical performance upon bending. The bending stiffness of soft composites ($10^0$ MPa) is usually several orders of magnitude lower than that of hard composites ($10^1$ GPa) [5,12]. Because of a unique combination of high stiffness in tension and low hardness upon bending, soft composites are uniquely applicable to numerous applications such as soft robotics, sensors, actuators, etc. [9,11,12].

Although a variety of soft composites have been developed for specific applications, a timeless topic is how to toughen them, as mechanical properties always determine the reliability and lifespan of relevant products. The toughening of materials has a long history and the main concept is widely accepted for either soft or hard materials, i.e., simultaneously enhancing the size of energy dissipation zone and energy dissipation density [13–16]. In other words, a material with high toughness should, on one hand, dissipate energy at a large length scale, and on the other hand, dissipate as much as energy per unit volume [16–18]. For instance, glass is a strong, stiff, but extremely brittle material.

This is because the glass plate can only dissipate energy at the atom scale, although it has a high energy dissipation density (Figure 1a) [19]. In contrast, rubber is not as strong as glass, whereas it possesses a much higher fracture toughness due to a significantly increased energy dissipation zone at the polymer chain scale (Figure 1b) [15,20]. Double network materials can show even superior fracture toughness to rubbers because their energy dissipation density is further increased due to the introduction of extra network chains (Figure 1c) [21–23]. That is, tough soft composites always possess high fracture toughness over $10^0$ kJ $m^{-2}$ and are highly resistant to crack growth even when they are notched.

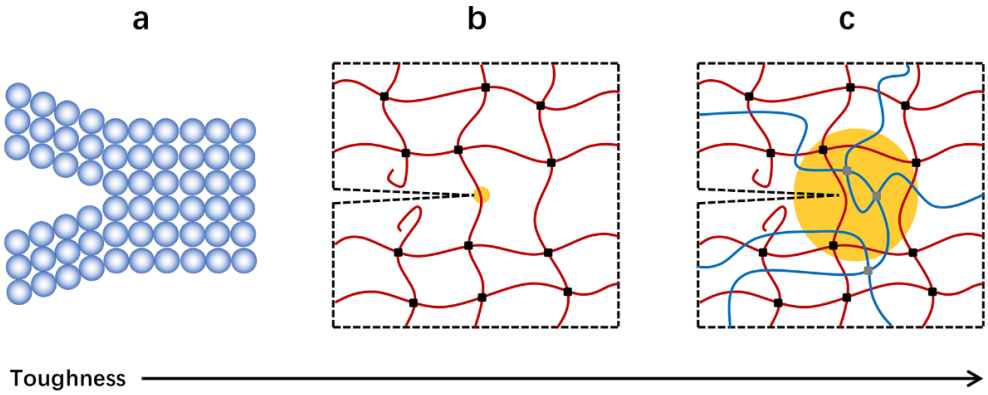


**Figure 1.** Different energy dissipation mechanisms give distinct toughness. (**a**) Breaking a layer of bonds. (**b**) Snapping a layer of chains. (**c**) Dissipating energy in the bulk.

Many biological tissues are essentially tough soft composites by exploiting the above concept [24–27]. These natural materials, generally consisting of stiff fibrous skeletons and soft extracellular matrices, are anisotropic, strong, and tough via the synergy of a large energy dissipation zone and high energy dissipation density. For example, heart valves possess fracture toughness around 1200 J $m^{-2}$ while showing high resilience [28]. Tendon is a strong connective tissue that connects muscle to bone and muscle to muscle, which can sustain over 1 million cycles of loading per year and show fracture toughness as high as 20–30 kJ $m^{-2}$ [28]. The efficient stress transfer between the stiff and soft phases enables these tissues to dissipate energy at a large length scale, and the energy-dissipative components both contribute to a high energy dissipation density.

Until now, immense efforts using synthetic approaches have been taken in an endeavor to fabricate tough soft composites. Generally, soft composites can be classified by their energy dissipation mechanisms at different length scales (Figure 2). At the molecular level, double network (DN) material is a typical soft composite, which dissipates energy by breaking polymer chains [29,30]. At the nanometer scale, phase-separated material is an example, dissipating energy via the rupture of nanophases [31–33]. At the micron scale, common soft composites are micro-fiber-reinforced polymers. The energy dissipation relies on the stress transfer between the stiff fibrils and soft matrices [34–37]. At the millimeter scale, macroscopic fiber fabrics are combined with soft polymer matrices, generating soft composites that dissipate energy by breaking both fibers and matrices [18,38–40].

Reviews on traditional hard composites are well documented and have provided widespread instruction for the development of next-generation industrial and biomedical products [41–43]. However, important reviews focusing on soft composites are still rare. Therefore, we are stimulated to propose this review. Herein, we give a summary of recently developed tough soft composites with energy dissipation mechanisms at a variety of length scales. In Section 2, we describe the common design strategies of tough soft composites and relevant structure characteristics. In Section 3, we show how these soft composites can achieve superior mechanical properties via a delicate combination of stiff and soft phases. In Section 4, we explain the toughening mechanism of different soft composites that dissipate energy from micro- to macro-scales. In Section 5, some intriguing applications

enabled by the soft composite design are demonstrated. Finally, we provide a summary and outlook on the future directions of soft composites.

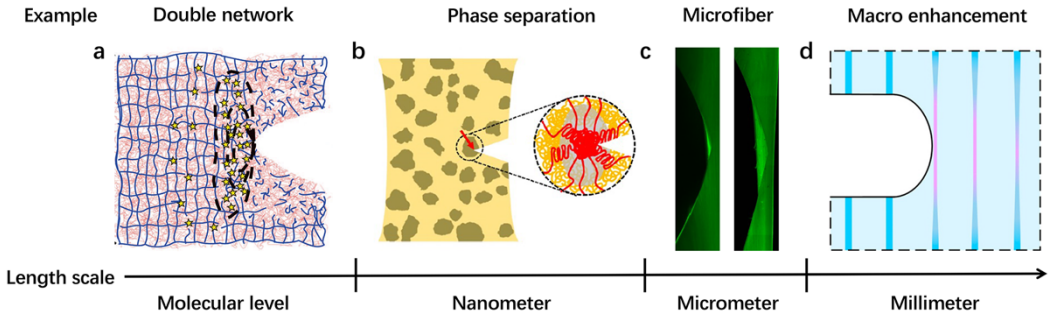


**Figure 2.** Energy dissipation mechanisms at different length scales of soft composites. (**a**) Double network materials with sacrificial bonds at the molecular scale. Reproduced with permission from reference [29] Copyright 2014 The American Association for the Advancement of Science. (**b**) Phase-separated materials with hard phases at the nanoscale. Reproduced with permission from reference [31] Copyright 2021 American Chemical Society. (**c**) Micro-fiber-reinforced soft composites dissipate energy at the micrometer scale. Reproduced with permission from reference [37] Copyright 2019 National Academy of Sciences. (**d**) Soft composites with macroscopic reinforcing phases dissipate energy at the millimeter scale. Reproduced with permission from reference [38] Copyright 2019 National Academy of Sciences.

## 2. Fabrication

### *2.1. Double Network*

The double network (DN) method is one of the most pioneering strategies to toughen soft materials, especially for hydrogels and elastomers. The general concept of the DN strategy is to combine two interpenetrating polymer networks with contrasting structures (Figure 3a) [44]. The first network is usually densely cross-linked, which is rigid and brittle. The second network is a sparsely cross-linked neutral polymer with a much higher concentration, which is soft and stretchable [45]. A DN gel or elastomer can be deemed as a molecular-level soft composite with high heterogeneity, although it behaves like a homogenous material.

The key factors to construct an efficient DN network instead of a simple interpenetrating network are, on one hand, to highly pre-stretch the first network, resulting in taut molecular chains with high stiffness, on the other hand, to swell the first network as much as possible in the second monomer solution with a low concentration of the cross-linking agent, enabling the high concentration ratio of the second network to the first network. In classical hydrogel systems, such a contrasting DN structure is realized by utilizing polyelectrolytes as the first network, which dramatically swell in the second neutral monomer solution due to high osmotic pressure. This effect leads to highly extended first network chains and a high concentration ratio between two networks (Figure 3b) [46]. Because both networks are chemically cross-linked, the classical DN hydrogels cannot self-recover after damage. Physical DN hydrogels are then developed to enable recoverable energy dissipation mechanisms. A typical example is the $Ca^{2+}$-alginate/polyacrylamide system, which exploits the unzipping of ionic crosslinks between $Ca^{2+}$ and alginate to dissipate energy and the re-zipping of the ionic bonds to heal the damage [23]. Another example is the physical DN gels based on an amphiphilic triblock copolymer that contains strong hydrophobic domains and sacrificial hydrogen bonds [47]. The reversible physical interactions of the first network enable the resulting DN gels to partially restore the mechanical properties after damage. The fabrication of physical DN gels is different from that of chemical ones. Only a one-pot method is required when preparing physical DN gels because the first network is usually a pre-polymer, which can dissolve in the second monomer solution by either stirring or heating (Figure 3c) [46]. As long as the concentration ratio between the first and second networks is carefully controlled, physical hydrogels with DN features can also be successfully fabricated. The DN method was firstly employed in the hydrogel systems and later proven to be applicable in elastomer systems [29,48–50].

The preparation of typical DN elastomers is slightly different from that of DN hydrogels since neutral monomers are commonly utilized to construct the first network. A multi-step swelling method was introduced to sufficiently pre-stretch the first network and form a high concentration contrast between the soft and the rigid networks. A drawback of this multi-step method is that it consumes significant time and energy. To overcome this dilemma, Matsuda et al. employed polyelectrolytes as the first network and dissolved them in organic solvents that have a similar dielectric constant to the monomer, giving rise to the formation of highly extended first network chains and enabling the dramatic swelling of the first network in second neutral monomer solutions (Figure 3d) [51]. In this way, a DN elastomer can be manufactured using the traditional method for DN hydrogels.

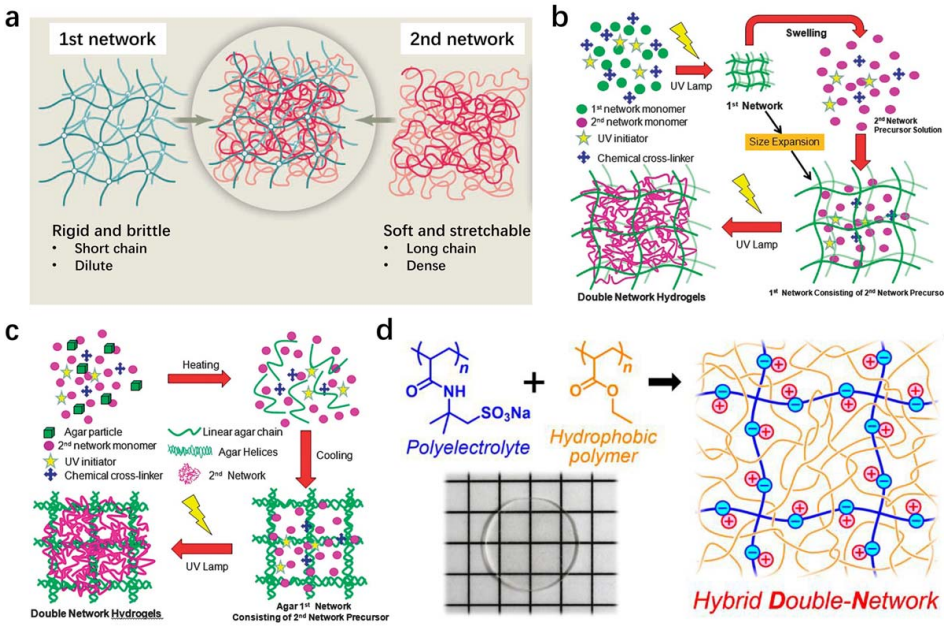


**Figure 3.** Fabrication of double network hydrogels and elastomers. (**a**) The composition of conventional chemical double network hydrogels. Reproduced with permission from reference [44] Copyright 2014 The American Association for the Advancement of Science. (**b**) Fabrication of conventional chemical double network hydrogels. Reproduced with permission from reference [46] Copyright 2015 Royal Society of Chemistry. (**c**) Fabrication of physical double network hydrogels. Reproduced with permission from reference [46] Copyright 2015 Royal Society of Chemistry. (**d**) Fabrication of double network elastomers. Reproduced with permission from reference [51] Copyright 2019 American Chemical Society.

### *2.2. Phase Separation*

Phase separation results in hydrogels or elastomers that possess dilute and dense polymer phases [52–54]. The dilute phase is soft, consisting of polymers with low volume fractions. On the contrary, the dense phase is relatively hard, which is composed of polymers with high volume fractions. The energy dissipation of phase-separated materials depends on the rupture of massive dense polymer phases at the nanometer scale. Therefore, phase-separated materials can be simply considered nano-scale soft composites.

There are a variety of methods to fabricate hydrogels or elastomers with phase-separated structures. One simple way is to utilize mixed-solvent-induced phase separation. Equilibrating a neutral hydrogel in a mixture of both good and poor solvents induces phase separation, resulting in an inhomogeneous network structure with bicontinuous domains (Figure 4a) [55]. Because of the low polymer-solvent affinity between the network chains and the poor solvent, a portion of polymer chains aggregate into local dense phases, which possess a considerably high polymer volume fraction to induce inter-/intra- polymer interactions. In contrast, other polymer chains in low volume fractions form the dilute polymer phases, which have relatively low modulus. Another example is the polyampholyte (PA)

hydrogel system (Figure 4b) [52,56]. Unlike the solvent-initiated phase separation, the PA gels show a bicontinuous network structure due to the distribution of ionic bonds. The different density of ionic bonds leads to the local aggregation of polymer backbones via hydrophobic association, giving rise to a network structure with soft and hard phases. The phase separation method is also applicable in elastomer systems by using an ionic polymer as the first network and a nonpolar polymer as the second network (Figure 4c) [31]. Firstly, the polyelectrolyte network is polymerized and then soaked into the second monomer solution using a cosolvent of a high dielectric constant. Due to the high osmotic pressure, the first network is highly pre-stretched and brittle. Afterward, the second network is polymerized and formed within the first network, producing DN materials with a highly contrasting architecture. A DN elastomer is formed by finally removing the cosolvent.

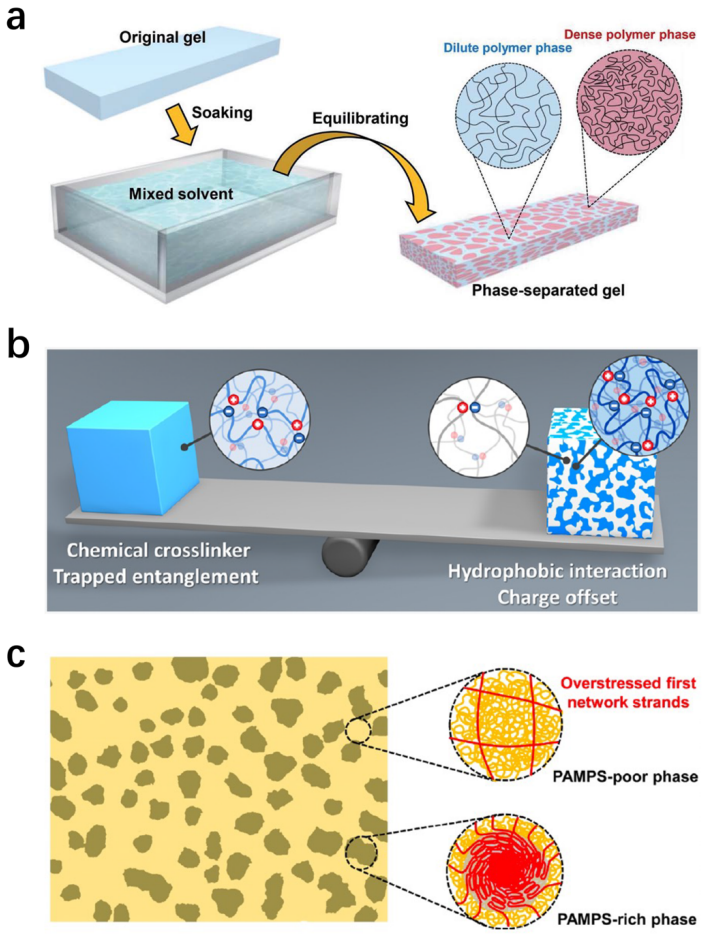


**Figure 4.** Fabrication of phase-separated hydrogels and elastomers. (**a**) Fabrication via mixed-solvent-induced phase separation. Reproduced with permission from reference [55] Copyright 2021 Royal Society of Chemistry. (**b**) The bicontinuous phase-separated structure of polyampholyte hydrogels. Reproduced with permission from reference [52] Copyright 2020 American Chemical Society. (**c**) Elastomers fabricated via nanophase separation. Reproduced with permission from reference [31] Copyright 2021 American Chemical Society.

### *2.3. Microscopic Reinforcement*

Introducing microfibers into a soft matrix is a well-established way to develop soft composites [57–60]. Usually, the added microfibers have a relatively low volume fraction, which, however, can lead to obvious mechanical enhancement of the soft composites. Interfacial interactions between the fibers and the matrix are crucial for efficient stress transmission and resulting energy dissipation. In this part, we give several common ways to fabricate tough soft composites by introducing micro-fibers as the enhancement phases.

The most common way to fabricate micro-fiber-reinforced soft composites is direct blending. A great number of examples can be listed because this method is simple and efficient. For the hydrogel system, it is worth noting that the micro-fiber should interact strongly with the hydrophilic polymer matrix to prevent interfacial delamination upon load. For instance, aramid micro-fibers can form massive hydrogen bonding with polyvinyl alcohol chains, the mixture of which gives rise to a strong and tough composite hydrogel (Figure 5a) [61]. The efficient stress transfer between the stiff fibers and the soft matrices enables the gel to show self-organization behaviors, resembling biological tissues. Apart from common fillers, 3D printed fibers can also be used to fabricate strong soft composites. By employing a 3D rapid prototyping technique, crossed log-piles of elastic fibers are fabricated (Figure 5b) [62]. Epoxy-based hydrogels are combined with the fibers to form an interpreting structure. Adjusting the construct geometry, corresponding mechanical properties of the soft composite such as strength, modulus, and toughness can be facilely regulated. The above methods mainly involve the introduction of external fiber fillers, which must carefully consider the interfacial interactions between the fillers and the matrices. An emerging method that can ignore the interface problem is to form microfibers in situ in soft composites [63]. This strategy is originally inspired by biological fibrous tissues. In bio-tissues, microfibers impregnate thoroughly with soft extracellular matrices, without the concern of interfacial problems. The key to the formation of microfibers is the utilization of rigid polymers with a large persistence length. By orienting and drying such polymers, strong microfibers can be formed, which are capable of maintaining the fibrous structure after reswelling. On the contrary, an oriented soft polymer with a small persistence length tends to restore the isotropic network structure after reswelling. Based on the contrasting reswelling behaviors, soft hydrogel composites can be fabricated by orienting and reswelling two interpreting networks with different persistence lengths (Figure 5c) [64].

### *2.4. Macroscopic Reinforcement*

Soft composites with satisfactory mechanical properties can also be produced by using macroscopic reinforcement, which includes, but is not limited to, fiber fabrics, metal meshes, plastic grids, etc. The preparation method of soft composites with macroscopic enhancement is similar to that of micro-filler-reinforced soft materials and the interface is still a key point that should be taken into account. Here, we give some examples for developing soft composites with macroscopic reinforcing phases.

A very familiar system with macroscopic phases is the fabric-reinforced soft composite. Unlike soft composites enhanced by microfibers, fabric-reinforced soft composites are usually fabricated by combining soft matrices with woven fiber fabrics (Figure 6a) [18]. In this case, the fiber volume fraction is relatively high, and the mechanical properties are mainly dominated by the fabric phases. Moreover, the mechanical and structural anisotropy of the soft composites can be regulated by exploiting a variety of weave patterns of the fabrics, which are different from the random distribution of fillers in micro-fiber-reinforced soft composites. Besides common fabrics, some novel rigid phases are also applicable to develop soft composites. Hydrogel composites with a series of desired properties, such as excellent mechanical performance, shape memory, and thermal healing, are created by integrating a low-melting-point alloy into a hydrogel system (Figure 6b) [65]. The alloy is able to transform from a load-bearing solid state to a free-deformable liquid state upon temperature increase, enabling the release of stress concentration between the soft and rigid phases. The resulting hydrogel composites can be uniquely applied in controlled electrochemical reactions and channel-structure templating by virtue of the special metal-hydrogel combination. The 3D printed rigid plastic grids are also proven efficient to construct tough soft composites. By simply combining silicon rubber and such rigid grids, macroscopic double network composites are fabricated (Figure 6c) [66]. The topological interlocking enables significant force transmission between the soft and rigid phases, preventing delamination. The optimal mechanical properties appear when

the grid/matrix strength ratio is approaching one. Interestingly, soft composites with macroscopic reinforcement can also be fabricated from the same type of elastomers with different rigidity. By tuning the cross-linking density, a hard elastomer and a soft elastomer can be prepared, which shows contrasting Young's modulus. The hard elastomer acts as the macroscopic reinforcing phase while the soft elastomer is the matrix (Figure 6d) [67,68]. Such a soft/hard combination allows the composite elastomers to show excellent fatigue resistance by virtue of the efficient stress de-concentration.

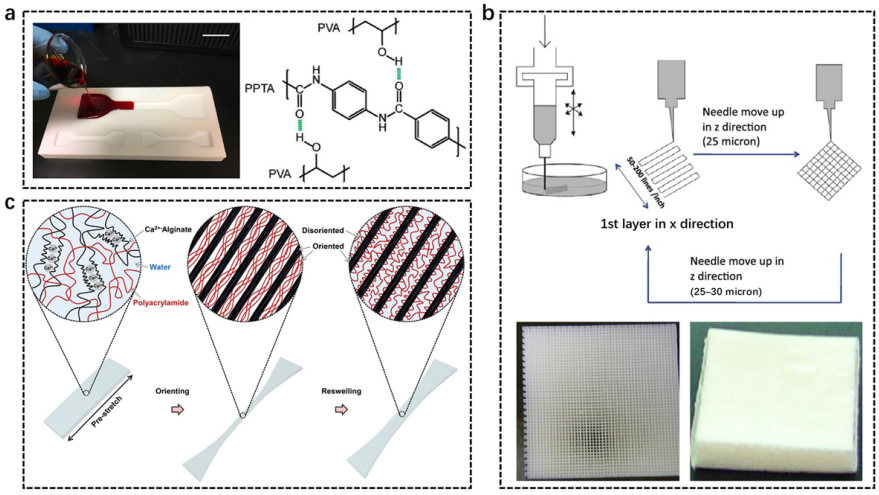


**Figure 5.** Fabrication of micro-fiber-reinforced soft composites. (**a**) Micro aramid fiber-reinforced hydrogels. Reproduced with permission from reference [61] Copyright 2017 Wiley. (**b**) Hydrogel composites reinforced by 3D printed skeletons. Reproduced with permission from reference [62] Copyright 2012 Elsevier. (**c**) Hydrogel composites fabricated via reswelling disparity of two oriented polymers with contrasting persistence lengths. Reproduced with permission from reference [64] Copyright 2021 Royal Society of Chemistry.

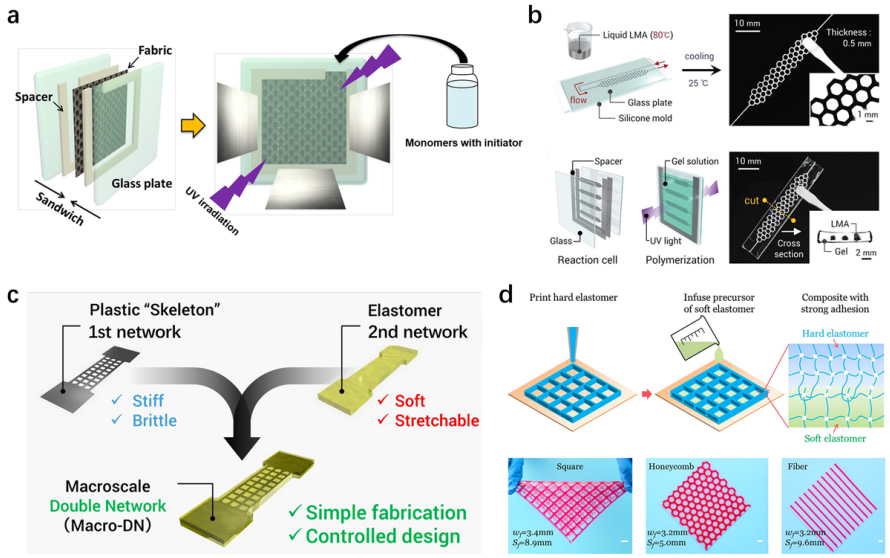


**Figure 6.** Fabrication of soft composites with macroscopic reinforcing phases. (**a**) Fabrication of traditional woven fabric-reinforced soft composites. Reproduced with permission from reference [18] Copyright 2020 Wiley. (**b**) Soft composites made up of low-melting-point alloy reinforced hydrogels. Reproduced with permission from reference [65] Copyright 2018 Wiley. (**c**) Elastomer composites with 3D printed plastic skeletons as the reinforcing phases. Reproduced with permission from reference [66] Copyright 2019 American Chemical Society. (**d**) Combining two elastomers with different stiffness into a tough soft composite. Reproduced with permission from reference [67] Copyright 2020 Elsevier.

## 3. Mechanical Property

Depending on the size scale and volume fraction of the reinforcing phase, soft composites can show very different mechanical properties. In this section, we summarize the mechanical performance of typical soft composites at different length scales.

### *3.1. Tensile Performance*

Double network (DN) hydrogel is a typical molecular-scale soft composite, consisting of a stiff but brittle first network and a soft, stretchable second network. The mechanical performance of DN hydrogels usually far exceeds its components via the synergy of significantly enlarged process zone and energy dissipation density. One of the important features of DN gels is the rate-independent hysteresis, i.e., dramatic energy dissipation during the first loading-unloading cycle, which is entirely different from traditional elastic gels or elastomers such as polyacrylamide hydrogel and natural rubber. Interestingly, during the second loading cycle, it is impossible to observe the large hysteresis again, indicating the fracture of covalent bonds in the first network. This is also well-known as the sacrificial bond effect. Another interesting characteristic during the tension of DN gels is the yielding and necking phenomenon (Figure 7a) [21]. Narrow zones appear in the sample during loading and grow up with further stretching, which again is attributed to the fracture of the fragile first network. After the neck propagation, the DN gel becomes rather soft, showing a greatly reduced stiffness compared with the original sample. Large elongation can be sustained by the second network before the entire sample is failed. By introducing physical interactions into the DN systems, self-recover in DN hydrogels can be realized. Either via ionic cross-linking or hydrophobic association, corresponding DN hydrogels can recover the initial shape after a certain amount of resting time (Figure 7b) [69]. Compared with traditional gels and biological tissues, DN hydrogels exhibit superior comprehensive properties while they still contain more than 90 wt% of water, which are ideal candidates for biomedical applications.

Nanometer-level soft composites formed by phase separation have a distinct tensile behavior in contrast to non-phase-separated ones. For instance, homogenous network structure is usually observed in non-phase-separated hydrogels, which can be soft, stretchable, but relatively weak. Phase separation leads to the formation of polymer dense phases in the hydrogels and the reduction of overall water content. These effects allow the formation of strong inter-/intra- polymer interactions and contribute to a significantly improved tensile performance (Figure 7c) [70,71]. The elongation firstly leads to the rupture of the hard phases in the gels, which play a similar sacrificial role to the first networks in DN hydrogels. Afterward, the soft phases sustain the load until the entire sample fails. Notably, owing to the dynamic nature of physical interactions in phase-separated hydrogels, damage in structures can usually be recovered. That is, the gels are able to show a large hysteresis due to massive viscous dissipation, yet they can finally restore the initial hysteresis loop after a certain amount of resting time. Moreover, the phase-separated gels are often viscoelastic and show a rate-dependent tensile behavior (Figure 7d) [32]. These special features enable phase-separated gels to be applied in many fields that require self-healing ability, viscoelasticity, etc.

Soft composites with hard phases at the micron-scale also have their unique tensile behaviors. These composites can behave very similarly to biological tissues such as ligaments, skin, and blood vessels. J-shaped non-linear stress-strain curves during elongation of biological tissues can be commonly observed, mainly attributed to wavy and crimped collagen fibers within the tissue that progressively uncoil and eventually straighten. These tissues are fairly soft at low strains, whereas they become extremely stiff at high strains. Soft composites containing wavy and crimped micro-fibers are also able to show such J-shaped stress-strain curves, demonstrating three load-bearing regions during elongation (Figure 7e) [72]. When the strain is quite low, the tensile performance is dominated by the matrix, and the wavy fibers do not contribute significantly to the energy dissipation. As the strain increases, the fibers gradually uncoil and start to sustain load, resulting in a

gradually increasing stiffness and strength of the composites. Finally, when the strain is high enough, the fibers become extremely taut. In this case, rapid strain hardening occurs, and the tensile performance at this stage mainly stems from fibers.

Macroscopic soft composites dissipate energy similarly to the strain-hardening stage of the micro-level soft composites since the macroscopic reinforcing phases are usually extremely stiff compared with the matrix phases. Glass fiber fabric-reinforced polyampholyte hydrogels exhibit high fracture stress but low fracture strain, similar to the tensile performance of neat glass fiber fabric (Figure 7f) [39]. Notably, by utilizing macroscopic reinforcing phases that have relatively low fracture force compared with the soft matrix phases, the energy dissipation of the resulting soft composites can be optimized by a multi-step fracture process, which is superior to either the soft or hard phase (Figure 7g) [65]. The tensile fracture stresses of soft composites that dissipate energy at different length scales are summarized in Table 1.

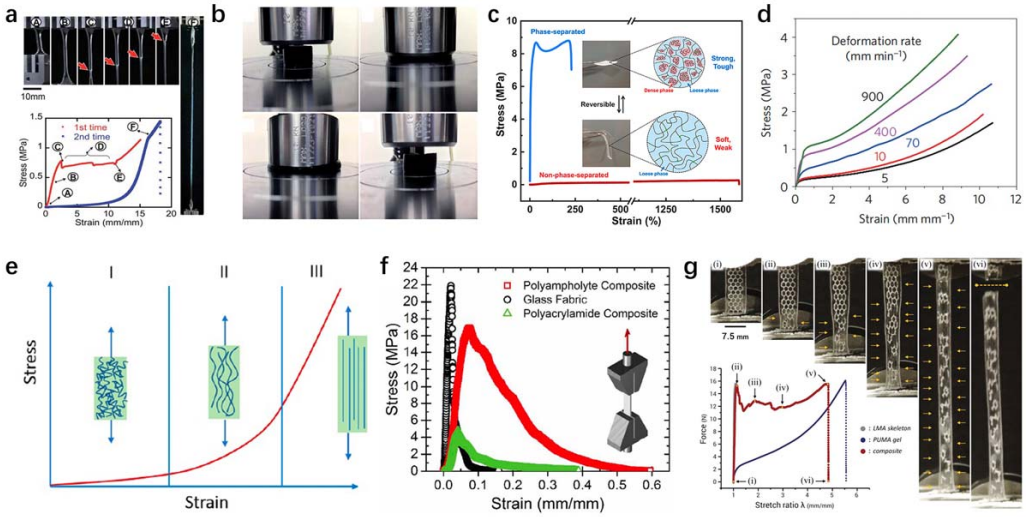


**Figure 7.** Tensile properties of soft composites at different length scales. (**a**) Typical tensile behaviors and properties of double network hydrogels. Reproduced with permission from reference [21] Copyright 2010 Royal Society of Chemistry. (**b**) The superior compressive performance of tough hydrogels. Reproduced with permission from reference [69] Copyright 2015 Royal Society of Chemistry. (**c**) Phase-separation results in dramatic mechanical enhancement of hydrogels. Reproduced with permission from reference [70] Copyright 2020 Elsevier. (**d**) Rate-dependent tensile properties of phase-separated hydrogels. Reproduced with permission from reference [32] Copyright 2013 Springer Nature. (**e**) The J-shaped stress-strain curve of micro-fiber-based soft composites. Reproduced with permission from reference [72] Copyright 2020 American Chemical Society. (**f**) Tensile performance of fabric-reinforced soft composites. Reproduced with permission from reference [39] Copyright 2015 Royal Society of Chemistry. (**g**) Multi-step fracture process of low-melting-point alloy reinforced soft composites. Reproduced with permission from reference [65] Copyright 2018 Wiley.

### *3.2. Fracture Toughness*

The toughness of a material is usually characterized by fracture energy, i.e., the energy to create unit surface area for crack growth [73–76]. Soft composites at different length scales are all able to show excellent fracture toughness above $10^3$ J m$^{-2}$ [77]. For the individual network of DN hydrogels, either the stiff first one or the soft second one can hardly achieve fracture toughness on the $10^1$ J m$^{-2}$ [78–80]. The combination of two weak networks, in contrast, generates an extremely tough material by virtue of the sacrificial bond effect. Meanwhile, the fracture toughness of molecular-scale double network hydrogels can be adjusted by simply tuning the network concentration (Figure 8a) [23], allowing a wide window of mechanical tunability for practical applications. Phase-separated materials commonly show fracture toughness similar to that of DN materials. The way of energy dissipation is also close. Polymer dense phases in phase-separated elastomers, i.e.,

the hard phases, fracture preferentially upon crack growth, serving the role of sacrificial bonds (Figure 8b) [31]. Because the polymer density in the hard phases is considerably high, the energy to propagate the crack growth is greatly increased compared with non-phase-separated homogenous structures. In other words, the energy dissipation density of the bulk materials is enhanced, leading to a rise of fracture toughness even when the energy dissipation zone remains constant. For the micro-level soft composites consisting of microscopic fibers, the fracture toughness can be one or two orders of magnitude higher than molecular or nanoscale soft composites. The reason stems from efficient stress transfer between the stiff fillers and the soft matrices, which enables the bulk materials to dissipate energy in a broad area with a high energy dissipation density. Such composites are usually highly notch-insensitive and achieve fracture energy of around $10^1$ to $10^2$ J m$^{-2}$ (Figure 8c) [34]. By introducing macroscopic reinforcing phases into soft composites, the fracture energy can be improved to an even higher level. Because the stiff phases, such as woven fabrics can possess an extremely high Young's modulus of tens of GPa, the force transfer between the hard and soft phases is further optimized. The resultant soft composites are capable of achieving unprecedented fracture toughness, rivaling best-in-class tough materials in industrial and biomedical fields (Figure 8d) [77]. The fracture energies of soft composites that dissipate energy at different length scales are summarized in Table 1.

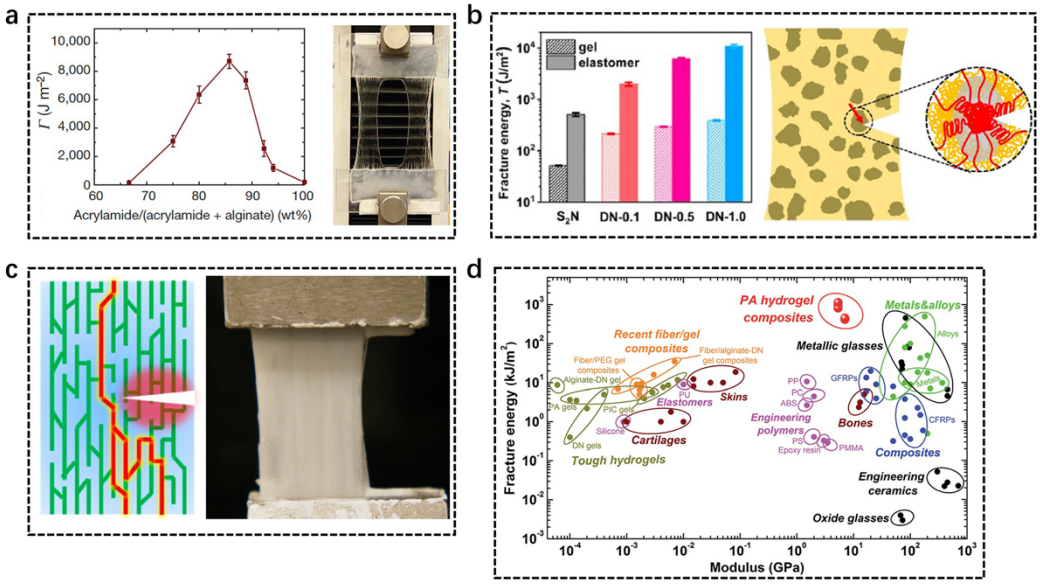


**Figure 8.** Fracture toughness of soft composites at different length scales. (**a**) Superior crack resistance of physical double network hydrogels. Reproduced with permission from reference [23] Copyright 2012 Springer Nature. (**b**) Nanophase-separated elastomers prevent crack growth via nanophase pinning. Reproduced with permission from reference [31] Copyright 2021 American Chemical Society. (**c**) Crack deflection in micro-fiber-based soft composites. Reproduced with permission from reference [34] Copyright 2021 Springer Nature. (**d**) Extremely high fracture energy of fabric-reinforced soft composites compared with common tough materials. Reproduced with permission from reference [77] Copyright 2019 Royal Society of Chemistry.

### *3.3. Fatigue Resistance*

Fatigue resistance of a material is usually represented by the fatigue threshold under repeated loading-unloading cycles (Figure 9a). By tuning the input energy to a notched material, the critical energy release rate at which the notch starts to propagate can be determined by extrapolation, which is defined as the fatigue threshold, i.e., the reflect of fatigue resistance.

Molecular-level soft composites, such as DN hydrogels, have relatively limited fatigue resistance, the fatigue threshold of which is on the order of $10^1$ J m$^{-2}$. Once DN hydrogels

are notched, the crack will propagate continuously as the gels are repetitively loaded and unloaded (Figure 9b) [81]. The irreversible fracture of covalent bonds in the first network is the main reason for the low fatigue resistance of DN hydrogels, which can be improved by utilizing physical cross-links to construct a recoverable first network [82–85]. Phase-separated gels show a desirable fatigue resistance due to the existence of the bicontinuous network structure. Very different fatigue behavior can be observed when the input energy is above or below the critical point to fracture the hard phases (Figure 9c) [86]. Below the critical energy, the hard phases are able to pin the crack growth and delay the fatigue fracture, resulting in a crack blunting ahead of the crack tip. Above the critical energy, the hard phases rupture and give rise to a fast crack propagation during the loading-unloading process. Micro-fiber-reinforced soft composites are extremely fatigue resistant. As shown in Figure 9d, the crack does not propagate after loading-unloading process for $N = 5000$ cycles [34]. The fatigue threshold ($\Gamma_0$) of these composites can be several orders of magnitude higher than molecular and nanoscale soft composites, mainly attributed to the efficient stress transmission and highly energy dissipative components.

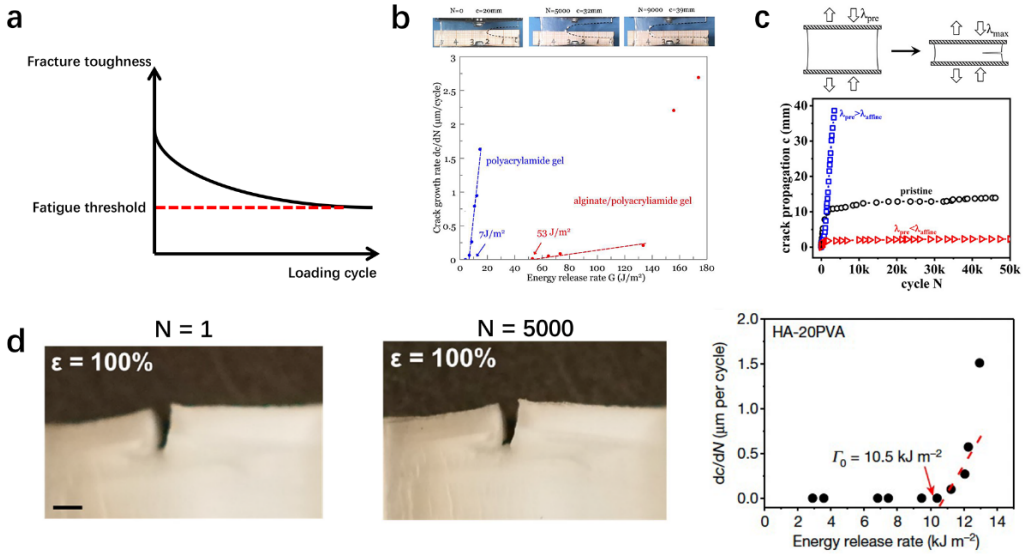


**Figure 9.** Fatigue resistance of soft composites at different length scales. (**a**) Common materials show gradually decreased fracture toughness upon continuous loading-unloading cycles, which can be utilized to determine the fatigue threshold of a material. (**b**) Limited fatigue resistance of double network hydrogels. Reproduced with permission from reference [81] Copyright 2018 Elsevier. (**c**) Phase-separated hydrogels show excellent fatigue resistance via a multiscale energy dissipation mechanism. Reproduced with permission from reference [86] Copyright 2020 National Academy of Sciences. (**d**) Extremely high fatigue resistance of micro-fiber-based soft composites. Reproduced with permission from reference [34] Copyright 2021 Springer Nature.

Soft composites with macroscopic fiber reinforcing phases are usually not fatigue-resistant since the mechanical properties are dominated by the rigid phases, which break at relatively low fracture strain despite having high energy dissipation density. However, by utilizing macroscopic phases that have relatively low Young's modulus, fatigue-resistant soft composites can also be obtained. An example is a soft composite made up of two elastomer phases that have a high and low cross-linking density, respectively. Compared with a neat elastomer composed of merely a soft phase, the soft composites with a modulus contrast show superior fatigue resistance (Figure 10a) [38]. The velocity of crack growth of the soft composites is greatly reduced by crack deflection, which is attributed to the existence of stiff phases that can stop the crack propagation (Figure 10b). Even after a loading-unloading cycle of over $10^4$ times, the composites still maintain a high energy release rate. The fatigue threshold ($\Gamma_0$) is estimated to be around 500 J m$^{-2}$ (Figure 10c) [67]. Through such a soft/hard design, a combination of high fatigue resistance and fracture

toughness is realized, exceeding a great many of traditional elastomers (Figure 10d). It is worth noting that the interface between the soft and hard phases is extremely important for achieving high fatigue resistance, which is usually realized via topological entanglement of two polymer phases (Figure 10e). The fatigue thresholds of soft composites that dissipate energy at different length scales are summarized in Table 1.

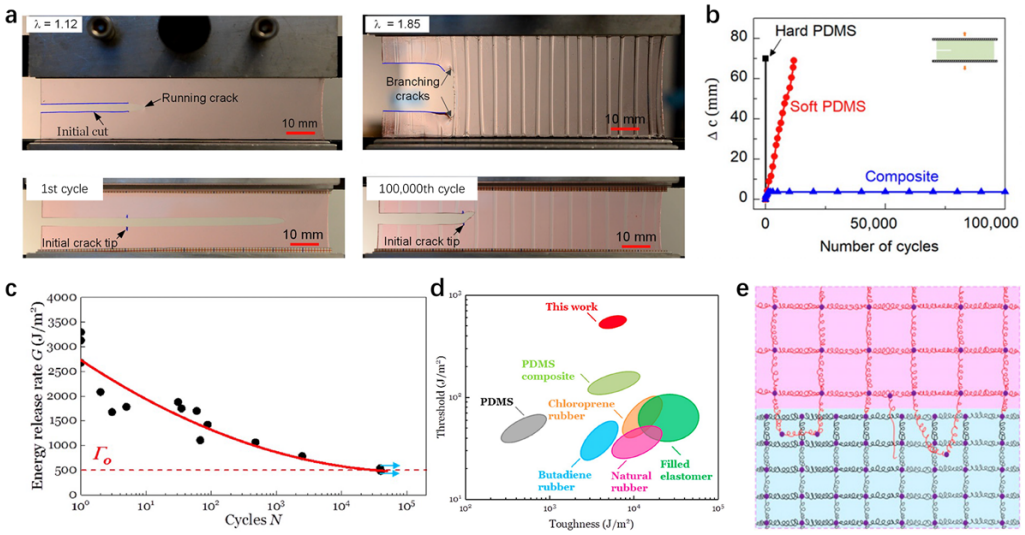


**Figure 10.** Fatigue resistance of macroscopic soft composites consisting of two elastomers with different stiffness. (**a**) Distinct crack growth behavior in a neat elastomer and composite elastomer. Reproduced with permission from reference [38] Copyright 2019 National Academy of Sciences. (**b**) Superior fatigue resistance of the composite elastomer to its individual components. Reproduced with permission from reference [38] Copyright 2019 National Academy of Sciences. (**c**) The critical energy release rate of the composite elastomer. Reproduced with permission from reference [67] Copyright 2020 Elsevier. (**d**) Fatigue threshold versus fracture toughness of the composite elastomer compared with other elastomers. Reproduced with permission from reference [38] Copyright 2019 National Academy of Sciences. (**e**) The topological adhesion between the soft and hard components. Reproduced with permission from reference [38] Copyright 2019 National Academy of Sciences.

## 4. Toughening Mechanisms

Soft composites composed of different reinforcing phases have distinguished toughening mechanisms. In this section, we explain how soft composites from molecular- to macro-scales can achieve remarkable toughness that far exceeds what can be expected from a simple mixture of individual components.

### *4.1. Molecular Cluster*

DN hydrogel as a molecular-scale soft composite attains high fracture toughness depending on the preferential fracture of the sacrificial first network. Because the first network is highly pre-stretched and brittle, it is prone to fracture ahead of the second network rupture. A damage zone is formed once a crack tends to propagate in a DN hydrogel (Figure 11a) [87], inside which the sacrificial network breaks into molecular clusters and connects the second network as cross-linking points (Figure 11b) [21,88,89]. To further grow the crack, additional energy has to be input to fracture the second network. Thus, the double network hydrogels are endowed with high fracture toughness. The size scale of the damage zone determines the energy dissipation area of the DN gel, which is found to be hundreds of microns (Figure 11c) [90,91]. Physical DN gels dissipate energy in a similar way to conventional DN gels. The sacrificial networks are usually physically cross-linked by ionic bonds, hydrogen bonding, hydrophobic association, etc. The stress transmission between the first and second networks enables a relatively large energy dissipation zone, giving rise to a high fracture toughness (Figure 11d) [23]. Because the

non-covalent bonds are self-healable, physical DN gels can partially or entirely restore the initial toughness after a certain amount of healing time.

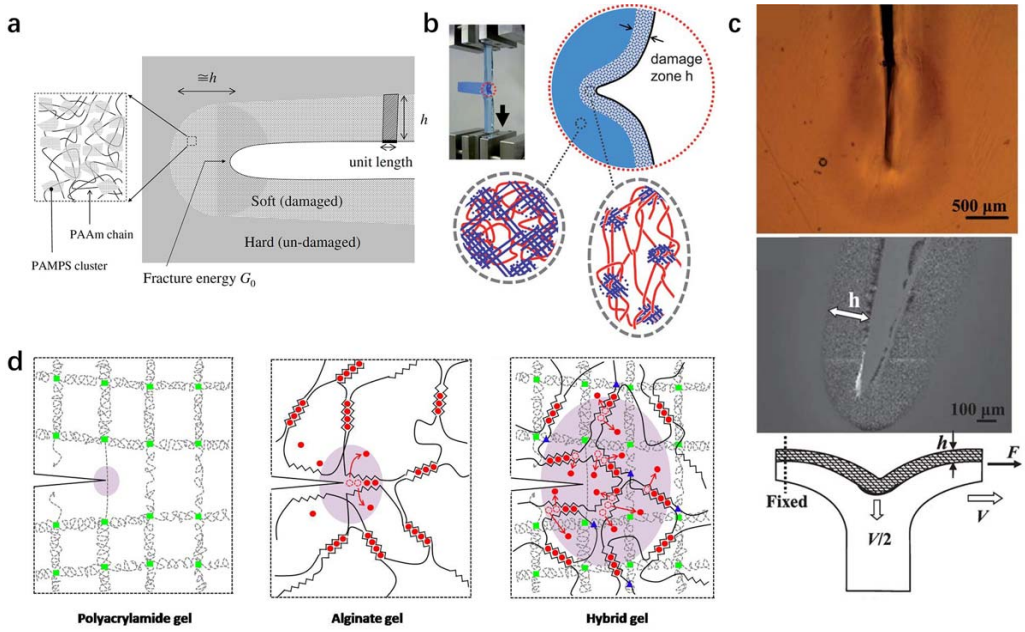


**Figure 11.** Energy dissipation mechanism of double network hydrogel. (**a**) A damage zone is formed when a crack tends to propagate in a double network hydrogel. Reproduced with permission from reference [87] Copyright 2007 IOP Publishing. (**b**) Inside the damage zone, the first network breaks into molecular clusters, which work as cross-linking points to connect the second network. Reproduced with permission from reference [21] Copyright 2010 Royal Society of Chemistry. (**c**) Direct observation of the damage zone in the double network hydrogels. Reproduced with permission from reference [90] Copyright 2009 American Chemical Society. (**d**) Double network structure gives rise to a significantly increased process zone for energy dissipation. Reproduced with permission from reference [23] Copyright 2012 Springer Nature.

### *4.2. Nanophse Pinning*

Soft composites with nanophase separation commonly have a multiscale toughening mechanism. The deformation of the bicontinuous network is affine to the macroscopic deformation of the bulk material. Taking polyampholyte hydrogel as an example, the fracture process can be divided into three regimes (Figure 12a) [33]. At the initial state, the bicontinuous soft and hard networks, represented by red and green areas, are isotropic, which have a length scale of hundreds of nanometers. Because of the ionic association, all polymer chains are in globule conformation. Once the bulk material starts to sustain load, the ionic association breaks, leading to the unfolding of the aggregated polymer chains. This effect allows the hydrogel network to sustain a considerably large yet reversible affine deformation. As the deformation increases, some hard phases reach the strength limit and begin to rupture. Subsequently, the load will be transferred to neighboring hard phases via soft phases. Since the soft phases are still intact and can sustain much larger deformation, the bulk gel softens yet are able to revert to the initial state when unloaded. After the fracture of most of the hard phases, the soft phases have to rupture, resulting in global failure of the bulk hydrogel. The above multiscale fracture process leads to a great amount of energy dissipation, enabling the polyampholyte hydrogel to exhibit high toughness.

Another example is the nanophase-separated elastomer, which shows a similar energy dissipation mechanism to the polyampholyte hydrogel although it does not show a bicontinuous network structure (Figure 12b) [31]. The nanophases form via the dipole-dipole interaction induced collapse of hard phases (gray island). This kind of phase-separated structure, on one side, results in overstressing of the hard phases, which show a significant increase in stiffness, on the other side, gives rise to structural changes even at small defor-

mations to dissipate massive energy. When the deformation is below the yielding point, the collapsed hard phases are partially unfolded by the rupture of the non-covalent dipole-dipole interaction, dissipating energy. At moderate deformation, more and more hard phases start to unfold, along with the rupture of some soft phases. When the deformation is sufficiently large, both phases rupture globally, leading to the failure of the bulk sample.

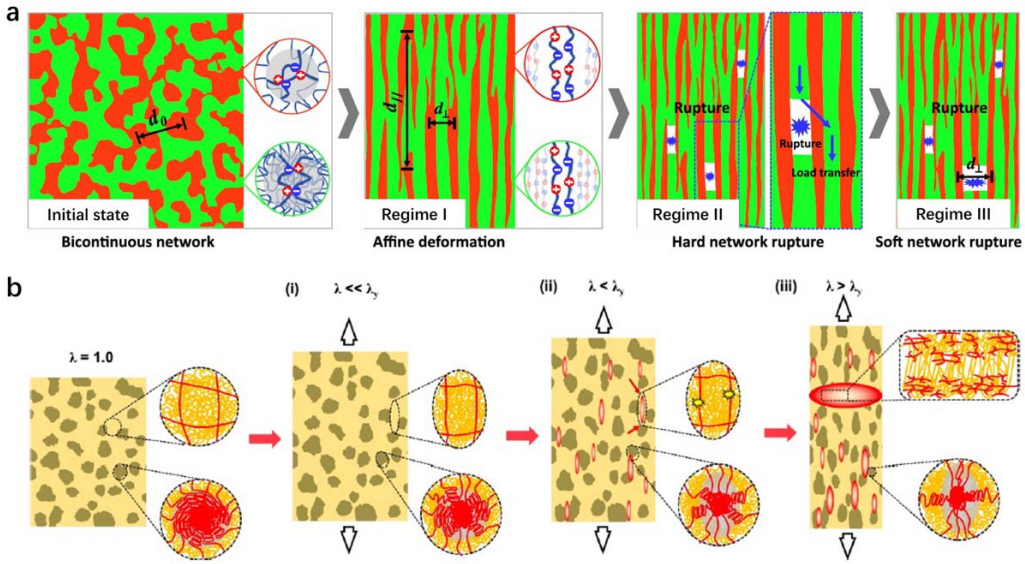


**Figure 12.** Energy dissipation mechanisms of different phase-separated soft composites. (**a**) Polyampholyte hydrogels obtain high toughness via a multiscale energy dissipation mechanism. Reproduced with permission from reference [33] Copyright 2018 American Physical Society. (**b**) Nanophases acting as sacrificial bonds in nanophase-separated elastomers at different strains. (i) The strain is small and far below the yielding point; (ii) The strain is moderate but still below the yielding point. (iii) The strain is large and above the yielding point. Reproduced with permission from reference [31] Copyright 2021 American Chemical Society.

### *4.3. Microfiber Enhancement*

The energy dissipation mechanisms of micro-fiber-reinforced soft composites need to be classified into two types. One is for the short micro-fiber-reinforced soft composites. In this case, the fracture process of the soft composites is dominated by the matrix, while the fiber phases enhance the overall performance. As a crack is initiated, its propagation must fracture a broad area of the matrix due to the efficient force transmission between the fiber and matrix phases. That is, the energy dissipation zone is relatively large compared with that of the neat matrix, which leads to high fracture toughness. Strong interfacial interactions between the fiber and matrix are important for force transmission (Figure 13a) [61]. The other type is for long micro-fiber-reinforced soft composites, inside which the fibers are continuous and exist throughout the entire sample. Such soft composites show an anisotropic fracture behavior. When the crack is made perpendicular to the fiber direction, the soft composites demonstrate superior fracture toughness due to the high difficulty of growing crack through the stiff and strong fiber phases. In contrast, if the crack is made along the fiber direction, the soft composites show a much-decreased fracture toughness because the crack can grow by fracturing the soft matrix along fibers (Figure 13b) [37].

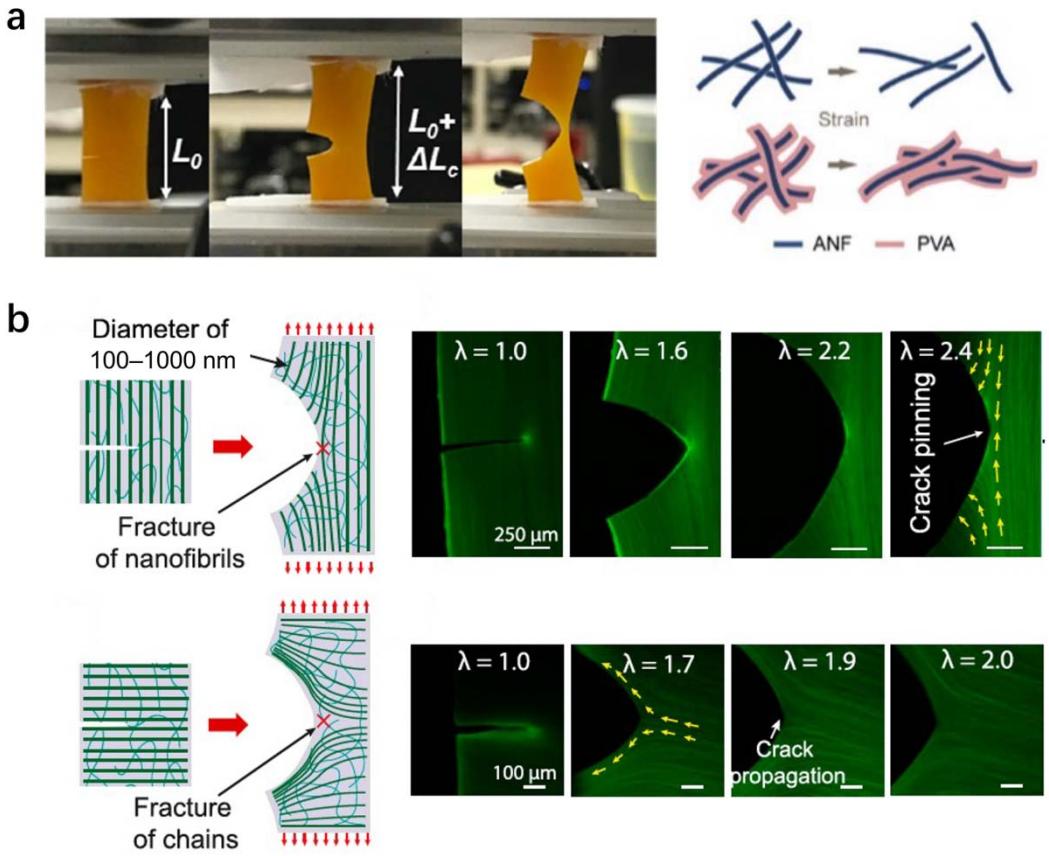


**Figure 13.** Energy dissipation mechanisms of micro-fiber-based soft composites with discontinuous or continuous microfibers. (**a**) Micro aramid fiber-reinforced hydrogels dissipate energy via stress transmission between the soft and stiff phases. Reproduced with permission from reference [61] Copyright 2018 Wiley. (**b**) Polyvinyl alcohol fiber-based hydrogels show anisotropic fracture toughness. The fracture toughness along the fiber direction is orders of magnitude higher than that perpendicular to the fiber direction. Reproduced from reference [37] Copyright 2019 National Academy of Sciences.

### *4.4. Macroscale Bulk Dissipation*

Macroscopic fabric-reinforced soft composites can dissipate energy in a macro length scale, and the fracture toughness is size-dependent. Taking the fiber-reinforced viscoelastic polymer as an example, the change of sample width leads to three regions with different fracture behaviors (Figure 14a) [92]. When the sample width is below a first characteristic with, $w_1$, the soft composite fails via fiber pullout-induced matrix rupture (region I). In this case, the fiber itself does not fracture to dissipate energy. However, the fiber bundle geometry significantly influences the load transfer between the stiff and soft phases, affecting the fracture toughness of the resulting soft composites. Under such conditions, the fracture energy of the soft composites is determined by the work to pull out transverse fiber bundles in a unit area, which is related to the matrix toughness ($T_m$), fiber bundle geometry ($K$), center-to-center distance between adjacent fiber bundles ($w_{cc}$), and composite width ($w$) (Figure 14b). Another special region appears when the sample size is above the other characteristic width, $l_T$, which is dominated by fiber fracture. In this region III, the fracture energy of the soft composites is decided by two factors: load transfer length ($l_T$) and energy dissipation density ($W_{eff}$) (Figure 14c) [18,93]. The load transfer length is found to be proportional to the fiber/matrix modulus ratio, while the energy dissipation density stems from the work of extension of two-component phases. By optimizing the above two factors, the fracture toughness of soft composites can achieve $10^3$ J m$^{-2}$, even exceeding metals. When the sample width is larger than $w_1$ but smaller than $l_T$, the fracture behavior of the soft composite is concurrent fiber fracture and pullout. The fracture mechanism in this region II is a mixed-mode of region I and region III.

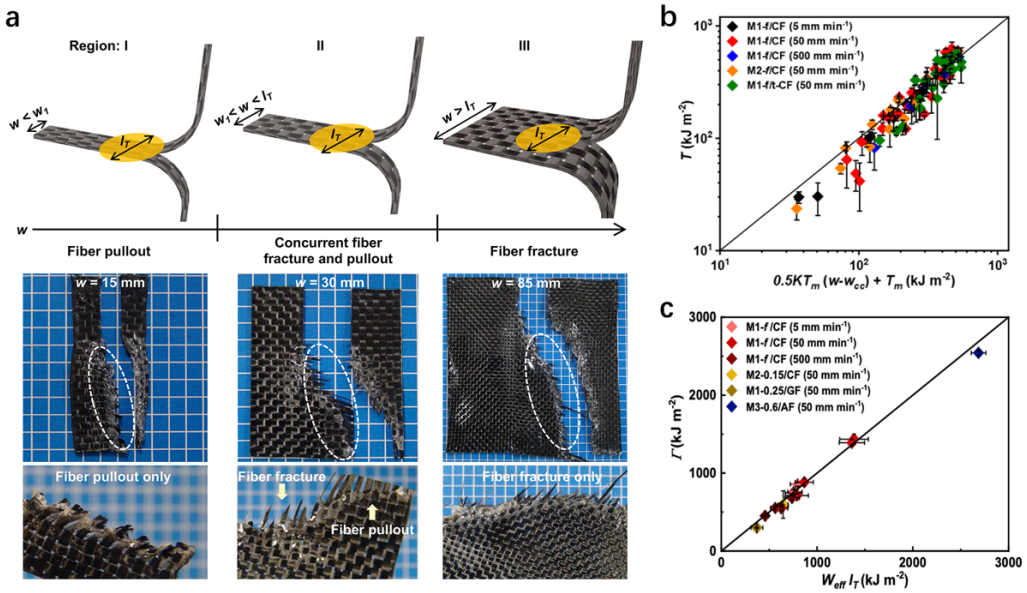


**Figure 14.** Energy dissipation mechanisms of macroscopic woven fabric-reinforced soft composites. (**a**) Size-dependent fracture behavior of the soft composites. Reproduced with permission from reference [92] Copyright 2021 Elsevier. (**b**) Fracture toughness of the soft composites in the fiber-pullout region is related to fiber bundle geometry ($K$), center-to-center distance between adjacent fiber bundles ($w_{cc}$), matrix toughness ($T_m$), and composite width. Reproduced with permission from reference [92] Copyright 2021 Elsevier. (**c**) The fracture toughness of the soft composites in the fiber-fracture region is related to load transfer length ($l_T$) and energy dissipation density ($W_{eff}$). Reproduced with permission from reference [18] Copyright 2020 Wiley.

## 5. Applications

Soft composites, due to their unique mechanical and physical properties, have found great potential for numerous applications in biomedical and industrial fields. For example, DN hydrogels, due to their biocompatibility, can be utilized in cartilage regeneration (Figure 15a) [94]. By plugging in a DN gel into the vacant space in the damaged cartilage, induction of cartilage regeneration can be realized. After four weeks of repairing, the defect treated with the DN gel is almost filled with regenerated white tissue, whereas the defects without any treatment are still insufficiently repaired. These results open the opportunity of applying DN gel as a tissue-repairing agent in biomedical applications. Interestingly, some other types of DN gels can also be employed in industrial fields such as pressure sensors. A photonic DN hydrogel consisting of self-assembled bilayer structures shows fast-response time, full-color tunable range, and fast color-switching via small compressive stress (Figure 15b) [95–99]. Phase-separation soft gels are found to be tough adhesives. Because of the greatly increased polymer chain density at the surface as well as the enhanced energy dissipation capability, a phase-separated hydrogel can show superior adhesion properties to a variety of solid surfaces. Soft-rigid hybrid devices such as hybrid conductors are enabled by the tough bonding between the phase-separated gels and hard substrates (Figure 15c) [55]. Soft composites with micro-fiber reinforcing phases are applicable in other fields. Taking wood hydrogels with continuous cellulose fibers, the anisotropic, low-tortuosity, and negatively charged structures facilitate ion transport, enabling the gels to show high ionic conductivity even at low ion concentrations (Figure 15d) [100–102]. Moreover, by utilizing thermal-responsive fibers as the main components, the soft composites are able to behave like human muscles under temperature change (Figure 15e) [103]. Soft composites with macroscopic reinforcing phases are mainly employed as load-bearing structural materials. However, functionalities can be realized by special designs of the composite structure. By using two soft matrices with different solvent responses and bonding them using a fabric phase, a soft composite actuator can be fabricated, which

shows different bending behaviors under solvent change (Figure 15f) [12]. Relevant applications of soft composites that dissipate energy at different length scales are summarized in Table 1.

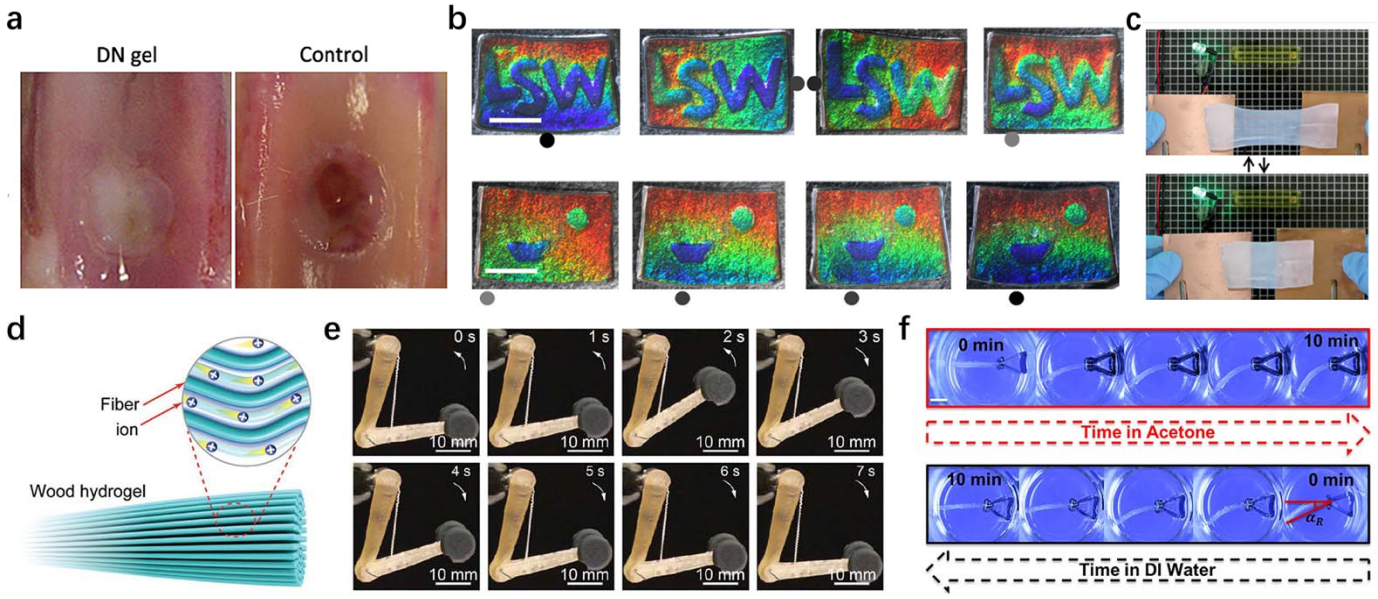


**Figure 15.** Various applications of soft composites at different length scales. (**a**) Double network hydrogels as cartilage repairing agents. Reproduced with permission from reference [94] Copyright 2010 Elsevier. (**b**) Photonic double network hydrogels as pressure sensors. Reproduced with permission from reference [95] Copyright 2014 Springer Nature. (**c**) Phase-separated hydrogels as tough adhesives. Reproduced with permission from reference [55] Copyright 2021 Royal Society of Chemistry. (**d**) Micro-fiber-based hydrogels used for ion transport. Reproduced with permission from reference [100] Copyright 2018 Wiley. (**e**) Artificial muscle based on thermal micro-fiber-based soft composites. Reproduced with permission from reference [103] Copyright 2019 The American Association for the Advancement of Science. (**f**) Solvent-responsive actuators based on woven fabric-reinforced soft composites. Reproduced with permission from reference [12] Copyright 2019 Elsevier.

**Table 1.** Summarized mechanical properties and applications of soft composites that dissipate energy at different length scales.

| Soft Composite | Length Scale for Energy Dissipation | Fracture Stress (MPa) | Fracture Toughness (kJ $m^{-2}$) | Fatigue Threshold (kJ $m^{-2}$) | Application | Reference |
|---|---|---|---|---|---|---|
| DN materials | Molecular level | $10^{-1}$–$10^{0}$ | $10^{-1}$–$10^{0}$ | $10^{-2}$ | Tissue engineering, sensors | [21,23,29,44,46,51,81,94,95] |
| Phase-separated materials | Nanometer | $10^{-1}$–$10^{0}$ | $10^{0}$–$10^{1}$ | $10^{-1}$ | Adhesives | [31–33,52,55,70,86] |
| Microfiber-reinforced gels | Micrometer | $10^{0}$–$10^{1}$ | $10^{0}$–$10^{2}$ | $10^{0}$–$10^{1}$ | Conductor, artificial muscles | [34,37,61,62,64,72,100,103] |
| Macrophase-reinforced composites | Millimeter | $10^{0}$–$10^{2}$ | $10^{0}$–$10^{3}$ | $10^{-1}$ | Actuators | [12,18,38,39,65–67,77,92] |

## 6. Conclusions

Soft composite is not a strange word in many fields. This special type of composite has been widely applied in biomedical engineering and industry. Either on the micro- or the macro-scale, the soft composites always show superior comprehensive properties to their individual components, or understanding the underlying toughening mechanisms of such materials will greatly benefit the development of next-generation soft materials. In this

review, we have given an overview of the fabrication, mechanical properties, toughening mechanisms, and relevant applications of common soft composites. The energy dissipation mechanisms at different length scales give these composites distinguishing properties and behaviors. By a suitable structural and mechanical design, soft composites are able to dissipate massive energy from the molecular to the macroscopic scale. Based on their different physical and structural properties, soft composites are applicable to a wide range of practical applications, including, but not limited to, tissue engineering, sensors, adhesives, conductors, artificial muscles, and actuators.

**Author Contributions:** Conceptualization, W.C.; methodology, W.C. and R.Z.; software, W.C.; validation, W.C. and R.Z.; formal analysis, W.C.; investigation, W.C.; resources, W.C.; data curation, W.C.; writing—original draft preparation, W.C.; writing—review and editing, W.C. and R.Z.; visualization, W.C.; supervision, W.C.; project administration, W.C.; funding acquisition, W.C. All authors have read and agreed to the published version of the manuscript.

**Funding:** This work was supported by start-up funding at Sichuan University.

**Institutional Review Board Statement:** Not applicable.

**Informed Consent Statement:** Not applicable.

**Data Availability Statement:** No new data were created or analyzed in this study. Data sharing is not applicable to this article.

**Conflicts of Interest:** The authors declare no conflict of interest.

## References

1. Coleman, J.N.; Khan, U.; Blau, W.J.; Gun'ko, Y.K. Small but strong: A review of the mechanical properties of carbon nanotube–polymer composites. *Carbon* **2006**, *44*, 1624–1652. [CrossRef]
2. Akil, H.; Omar, M.; Mazuki, A.M.; Safiee, S.; Ishak, Z.M.; Bakar, A.A. Kenaf fiber reinforced composites: A review. *Mater. Des.* **2011**, *32*, 4107–4121. [CrossRef]
3. Miracle, D. Metal matrix composites–from science to technological significance. *Compos. Sci. Technol.* **2005**, *65*, 2526–2540. [CrossRef]
4. Summerscales, J.; Virk, A.; Hall, W. A review of bast fibres and their composites: Part 3–Modelling. *Compos. Part A Appl. Sci. Manuf.* **2013**, *44*, 132–139. [CrossRef]
5. Ku, H.; Wang, H.; Pattarachaiyakoop, N.; Trada, M. A review on the tensile properties of natural fiber reinforced polymer composites. *Compos. Part B Eng.* **2011**, *42*, 856–873. [CrossRef]
6. Thomas, W. High Strength Glass Fibre-Resin Composites. *Nature* **1973**, *242*, 455–456. [CrossRef]
7. McLoughlin, J. New high temperature carbon fibre composite. *Nature* **1970**, *227*, 701. [CrossRef] [PubMed]
8. Whitesides, G.M. Soft robotics. *Angew. Chem. Int. Ed.* **2018**, *57*, 4258–4273. [CrossRef] [PubMed]
9. Liu, J.A.-C.; Gillen, J.H.; Mishra, S.R.; Evans, B.A.; Tracy, J.B. Photothermally and magnetically controlled reconfiguration of polymer composites for soft robotics. *Sci. Adv.* **2019**, *5*, eaaw2897. [CrossRef]
10. Horne, J.; McLoughlin, L.; Bury, E.; Koh, A.S.; Wujcik, E.K. Interfacial phenomena of advanced composite materials toward wearable platforms for biological and environmental monitoring sensors, armor, and soft robotics. *Adv. Mater. Interfaces* **2020**, *7*, 1901851. [CrossRef]
11. Kim, S.Y.; Choo, Y.; Bilodeau, R.A.; Yuen, M.C.; Kaufman, G.; Shah, D.S.; Osuji, C.O.; Kramer-Bottiglio, R. Sustainable manufacturing of sensors onto soft systems using self-coagulating conductive Pickering emulsions. *Sci. Robot.* **2020**, *5*, eaay3604. [CrossRef] [PubMed]
12. Hubbard, A.M.; Cui, W.; Huang, Y.; Takahashi, R.; Dickey, M.D.; Genzer, J.; King, D.R.; Gong, J.P. Hydrogel/elastomer laminates bonded via fabric interphases for stimuli-responsive actuators. *Matter* **2019**, *1*, 674–689. [CrossRef]
13. Cox, H. The elasticity and strength of paper and other fibrous materials. *Br. J. Appl. Phys.* **1952**, *3*, 72. [CrossRef]
14. Lake, G.; Thomas, A. The strength of highly elastic materials. *Proc. Math. Phys. Eng. Sci.* **1967**, *300*, 108–119.
15. Thomas, A.; Whittle, J. Tensile rupture of rubber. *Rubber Chem. Technol.* **1970**, *43*, 222–228. [CrossRef]
16. Hui, C.-Y.; Liu, Z.; Phoenix, S.L.; King, D.R.; Cui, W.; Huang, Y.; Gong, J.P. Mechanical behavior of unidirectional fiber reinforced soft composites. *Extrem. Mech. Lett.* **2020**, *35*, 100642. [CrossRef]
17. Volokh, K.; Trapper, P. Fracture toughness from the standpoint of softening hyperelasticity. *J. Mech. Phys. Solids* **2008**, *56*, 2459–2472. [CrossRef]
18. Cui, W.; King, D.R.; Huang, Y.; Chen, L.; Sun, T.L.; Guo, Y.; Saruwatari, Y.; Hui, C.Y.; Kurokawa, T.; Gong, J.P. Fiber-reinforced viscoelastomers show extraordinary crack resistance that exceeds metals. *Adv. Mater.* **2020**, *32*, 1907180. [CrossRef]
19. Sih, G.; Liebowitz, H. On the Griffith energy criterion for brittle fracture. *Int. J. Solids Struct.* **1967**, *3*, 1–22. [CrossRef]

20. Greensmith, H. Rupture of rubber. XI. Tensile rupture and crack growth in a noncrystallizing rubber. *J. Appl. Polym. Sci.* **1964**, *8*, 1113–1128. [CrossRef]
21. Gong, J.P. Why are double network hydrogels so tough? *Soft Matter* **2010**, *6*, 2583–2590. [CrossRef]
22. Gong, J.P.; Katsuyama, Y.; Kurokawa, T.; Osada, Y. Double-network hydrogels with extremely high mechanical strength. *Adv. Mater.* **2003**, *15*, 1155–1158. [CrossRef]
23. Sun, J.-Y.; Zhao, X.; Illeperuma, W.R.; Chaudhuri, O.; Oh, K.H.; Mooney, D.J.; Vlassak, J.J.; Suo, Z. Highly stretchable and tough hydrogels. *Nature* **2012**, *489*, 133–136. [CrossRef] [PubMed]
24. Davey, C.L.; Gilbert, K. Tensile strength and the tenderness of beef sternomandibularis muscle. *Meat Sci.* **1977**, *1*, 49–61. [CrossRef]
25. Kuthe, C.D.; Uddanwadiker, R.; Ramteke, A. Experimental evaluation of fiber orientation based material properties of skeletal muscle in tension. *Mol. Cell. Biomech.* **2014**, *11*, 113.
26. Bennett1, M.; Ker1, R.; Imery, N.J.; Alexander1, R.M. Mechanical properties of various mammalian tendons. *J. Zool.* **1986**, *209*, 537–548. [CrossRef]
27. Yang, W.; Sherman, V.R.; Gludovatz, B.; Schaible, E.; Stewart, P.; Ritchie, R.O.; Meyers, M.A. On the tear resistance of skin. *Nat. Commun.* **2015**, *6*, 1–10. [CrossRef] [PubMed]
28. Zhao, X.; Chen, X.; Yuk, H.; Lin, S.; Liu, X.; Parada, G. Soft Materials by Design: Unconventional Polymer Networks Give Extreme Properties. *Chem. Rev.* **2021**, *121*, 4309–4372. [CrossRef]
29. Ducrot, E.; Chen, Y.; Bulters, M.; Sijbesma, R.P.; Creton, C. Toughening elastomers with sacrificial bonds and watching them break. *Science* **2014**, *344*, 186–189. [CrossRef]
30. Brown, H.R. A model of the fracture of double network gels. *Macromolecules* **2007**, *40*, 3815–3818. [CrossRef]
31. Zheng, Y.; Kiyama, R.; Matsuda, T.; Cui, K.; Li, X.; Cui, W.; Guo, Y.; Nakajima, T.; Kurokawa, T.; Gong, J.P. Nanophase Separation in Immiscible Double Network Elastomers Induces Synergetic Strengthening, Toughening, and Fatigue Resistance. *Chem. Mater.* **2021**, *33*, 3321–3334. [CrossRef]
32. Sun, T.L.; Kurokawa, T.; Kuroda, S.; Ihsan, A.B.; Akasaki, T.; Sato, K.; Haque, M.A.; Nakajima, T.; Gong, J.P. Physical hydrogels composed of polyampholytes demonstrate high toughness and viscoelasticity. *Nat. Mater.* **2013**, *12*, 932–937. [CrossRef]
33. Cui, K.; Sun, T.L.; Liang, X.; Nakajima, K.; Ye, Y.N.; Chen, L.; Kurokawa, T.; Gong, J.P. Multiscale energy dissipation mechanism in tough and self-healing hydrogels. *Phys. Rev. Lett.* **2018**, *121*, 185501. [CrossRef]
34. Hua, M.; Wu, S.; Ma, Y.; Zhao, Y.; Chen, Z.; Frenkel, I.; Strzalka, J.; Zhou, H.; Zhu, X.; He, X. Strong tough hydrogels via the synergy of freeze-casting and salting out. *Nature* **2021**, *590*, 594–599. [CrossRef] [PubMed]
35. Guo, Y.Z.; Nakajima, T.; Mredha, M.T.I.; Guo, H.L.; Cui, K.; Zheng, Y.; Cui, W.; Kurokawa, T.; Gong, J.P. Facile preparation of cellulose hydrogel with Achilles tendon-like super strength through aligning hierarchical fibrous structure. *Chem. Eng. J.* **2022**, *428*, 132040. [CrossRef]
36. Liu, R.; Xu, X.; Zhuang, X.; Cheng, B. Solution blowing of chitosan/PVA hydrogel nanofiber mats. *Carbohydr. Polym.* **2014**, *101*, 1116–1121. [CrossRef]
37. Lin, S.; Liu, J.; Liu, X.; Zhao, X. Muscle-like fatigue-resistant hydrogels by mechanical training. *Proc. Natl. Acad. Sci. USA* **2019**, *116*, 10244–10249. [CrossRef]
38. Wang, Z.; Xiang, C.; Yao, X.; Le Floch, P.; Mendez, J.; Suo, Z. Stretchable materials of high toughness and low hysteresis. *Proc. Natl. Acad. Sci. USA* **2019**, *116*, 5967–5972. [CrossRef] [PubMed]
39. King, D.R.; Sun, T.L.; Huang, Y.; Kurokawa, T.; Nonoyama, T.; Crosby, A.J.; Gong, J.P. Extremely tough composites from fabric reinforced polyampholyte hydrogels. *Mater. Horiz.* **2015**, *2*, 584–591. [CrossRef]
40. Huang, Y.; King, D.R.; Sun, T.L.; Nonoyama, T.; Kurokawa, T.; Nakajima, T.; Gong, J.P. Energy-dissipative matrices enable synergistic toughening in fiber reinforced soft composites. *Adv. Funct. Mater.* **2017**, *27*, 1605350. [CrossRef]
41. Cantwell, W.J.; Morton, J. The impact resistance of composite materials—a review. *Composites* **1991**, *22*, 347–362. [CrossRef]
42. De Zanet, A.; Casalegno, V.; Salvo, M. Laser surface texturing of ceramics and ceramic composite materials–A review. *Ceram. Int.* **2021**, *47*, 7307–7320. [CrossRef]
43. Yu, X.; Manthiram, A. A review of composite polymer-ceramic electrolytes for lithium batteries. *Energy Stor. Mater.* **2021**, *34*, 282–300. [CrossRef]
44. Gong, J.P. Materials both tough and soft. *Science* **2014**, *344*, 161–162. [CrossRef]
45. Chen, Q.; Chen, H.; Zhu, L.; Zheng, J. Engineering of tough double network hydrogels. *Macromol. Chem. Phys.* **2016**, *217*, 1022–1036. [CrossRef]
46. Chen, Q.; Chen, H.; Zhu, L.; Zheng, J. Fundamentals of double network hydrogels. *J. Mater. Chem. B* **2015**, *3*, 3654–3676. [CrossRef]
47. Zhang, H.J.; Sun, T.L.; Zhang, A.K.; Ikura, Y.; Nakajima, T.; Nonoyama, T.; Kurokawa, T.; Ito, O.; Ishitobi, H.; Gong, J.P. Tough physical double-network hydrogels based on amphiphilic triblock copolymers. *Adv. Mater.* **2016**, *28*, 4884–4890. [CrossRef] [PubMed]
48. Murai, J.; Nakajima, T.; Matsuda, T.; Tsunoda, K.; Nonoyama, T.; Kurokawa, T.; Gong, J.P. Tough double network elastomers reinforced by the amorphous cellulose network. *Polymer* **2019**, *178*, 121686. [CrossRef]
49. Nakajima, T.; Ozaki, Y.; Namba, R.; Ota, K.; Maida, Y.; Matsuda, T.; Kurokawa, T.; Gong, J.P. Tough double-network gels and elastomers from the nonprestretched first network. *ACS Macro Lett.* **2019**, *8*, 1407–1412. [CrossRef]
50. Wang, W.; Zhang, Z.; Davris, T.; Liu, J.; Gao, Y.; Zhang, L.; Lyulin, A.V. Simulational insights into the mechanical response of prestretched double network filled elastomers. *Soft Matter* **2017**, *13*, 8597–8608. [CrossRef]

51. Matsuda, T.; Nakajima, T.; Gong, J.P. Fabrication of tough and stretchable hybrid double-network elastomers using ionic dissociation of polyelectrolyte in nonaqueous media. *Chem. Mater.* **2019**, *31*, 3766–3776. [CrossRef]
52. Cui, K.; Ye, Y.N.; Sun, T.L.; Yu, C.; Li, X.; Kurokawa, T.; Gong, J.P. Phase separation behavior in tough and self-healing polyampholyte hydrogels. *Macromolecules* **2020**, *53*, 5116–5126. [CrossRef]
53. Durmaz, S.; Okay, O. Phase separation during the formation of poly (acrylamide) hydrogels. *Polymer* **2000**, *41*, 5729–5735. [CrossRef]
54. Broguiere, N.; Husch, A.; Palazzolo, G.; Bradke, F.; Madduri, S.; Zenobi-Wong, M. Macroporous hydrogels derived from aqueous dynamic phase separation. *Biomaterials* **2019**, *200*, 56–65. [CrossRef]
55. Cui, W.; Zhu, R.; Zheng, Y.; Mu, Q.; Pi, M.; Chen, Q.; Ran, R. Transforming non-adhesive hydrogels to reversible tough adhesives via mixed-solvent-induced phase separation. *J. Mater. Chem. A* **2021**, *9*, 9706–9718. [CrossRef]
56. Ihsan, A.B.; Sun, T.L.; Kuroda, S.; Haque, M.A.; Kurokawa, T.; Nakajima, T.; Gong, J.P. A phase diagram of neutral polyampholyte–from solution to tough hydrogel. *J. Mater. Chem. B* **2013**, *1*, 4555–4562. [CrossRef] [PubMed]
57. Yodmuang, S.; McNamara, S.L.; Nover, A.B.; Mandal, B.B.; Agarwal, M.; Kelly, T.-A.N.; Chao, P.-h.G.; Hung, C.; Kaplan, D.L.; Vunjak-Novakovic, G. Silk microfiber-reinforced silk hydrogel composites for functional cartilage tissue repair. *Acta Biomater.* **2015**, *11*, 27–36. [CrossRef]
58. Caves, J.M.; Cui, W.; Wen, J.; Kumar, V.A.; Haller, C.A.; Chaikof, E.L. Elastin-like protein matrix reinforced with collagen microfibers for soft tissue repair. *Biomaterials* **2011**, *32*, 5371–5379. [CrossRef] [PubMed]
59. Surajarusarn, B.; Hajjar-Garreau, S.; Schrodj, G.; Mougin, K.; Amornsakchai, T. Comparative study of pineapple leaf microfiber and aramid fiber reinforced natural rubbers using dynamic mechanical analysis. *Polym. Test.* **2020**, *82*, 106289. [CrossRef]
60. Caves, J.M.; Kumar, V.A.; Martinez, A.W.; Kim, J.; Ripberger, C.M.; Haller, C.A.; Chaikof, E.L. The use of microfiber composites of elastin-like protein matrix reinforced with synthetic collagen in the design of vascular grafts. *Biomaterials* **2010**, *31*, 7175–7182. [CrossRef]
61. Xu, L.; Zhao, X.; Xu, C.; Kotov, N.A. Water-rich biomimetic composites with abiotic self-organizing nanofiber network. *Adv. Mater.* **2018**, *30*, 1703343. [CrossRef] [PubMed]
62. Agrawal, A.; Rahbar, N.; Calvert, P.D. Strong fiber-reinforced hydrogel. *Acta Biomater.* **2013**, *9*, 5313–5318. [CrossRef]
63. Mredha, M.T.I.; Guo, Y.Z.; Nonoyama, T.; Nakajima, T.; Kurokawa, T.; Gong, J.P. A facile method to fabricate anisotropic hydrogels with perfectly aligned hierarchical fibrous structures. *Adv. Mater.* **2018**, *30*, 1704937. [CrossRef]
64. Cui, W.; Pi, M.; Zhu, R.; Xiong, Z.; Ran, R. Strong anisotropic hydrogels with ion transport capability via reswelling contrast of two oriented polymer networks. *J. Mater. Chem. A* **2021**, *9*, 20362–20370. [CrossRef]
65. Takahashi, R.; Sun, T.L.; Saruwatari, Y.; Kurokawa, T.; King, D.R.; Gong, J.P. Creating Stiff, Tough, and Functional Hydrogel Composites with Low-Melting-Point Alloys. *Adv. Mater.* **2018**, *30*, 1706885. [CrossRef] [PubMed]
66. King, D.R.; Okumura, T.; Takahashi, R.; Kurokawa, T.; Gong, J.P. Macroscale double networks: Design criteria for optimizing strength and toughness. *ACS Appl. Mater. Interfaces* **2019**, *11*, 35343–35353. [CrossRef]
67. Li, C.; Yang, H.; Suo, Z.; Tang, J. Fatigue-resistant elastomers. *J. Mech. Phys. Solids* **2020**, *134*, 103751. [CrossRef]
68. Zhang, G.; Yin, T.; Nian, G.; Suo, Z. Fatigue-resistant polyurethane elastomer composites. *Extrem. Mech. Lett.* **2021**, *48*, 101434. [CrossRef]
69. Cui, W.; Ji, J.; Cai, Y.; Li, H.; Ran, R. Robust, anti-fatigue, and self-healing graphene oxide/hydrophobically associated composite hydrogels and their use as recyclable adsorbents for dye waste water treatment. *J. Mater. Chem. A* **2015**, *3*, 17445–17458. [CrossRef]
70. Cui, W.; Cai, Y.; Zheng, Y.; Ran, R. Mechanical enhancement of hydrophobically associating hydrogels by solvent-regulated phase separation. *Polymer* **2020**, *210*, 123042. [CrossRef]
71. Sato, K.; Nakajima, T.; Hisamatsu, T.; Nonoyama, T.; Kurokawa, T.; Gong, J.P. Phase-separation-induced anomalous stiffening, toughening, and self-healing of polyacrylamide gels. *Adv. Mater.* **2015**, *27*, 6990–6998. [CrossRef]
72. Zhalmuratova, D.; Chung, H.-J. Reinforced gels and elastomers for biomedical and soft robotics applications. *ACS Appl. Polym. Mater.* **2020**, *2*, 1073–1091. [CrossRef]
73. Long, R.; Hui, C.-Y. Fracture toughness of hydrogels: Measurement and interpretation. *Soft Matter* **2016**, *12*, 8069–8086. [CrossRef] [PubMed]
74. Long, R.; Hui, C.-Y.; Gong, J.P.; Bouchbinder, E. The fracture of highly deformable soft materials: A tale of two length scales. *Annu. Rev. Condens. Matter Phys.* **2021**, *12*, 71–94. [CrossRef]
75. Creton, C.; Ciccotti, M. Fracture and adhesion of soft materials: A review. *Rep. Prog. Phys.* **2016**, *79*, 046601. [CrossRef]
76. Zhang, T.; Lin, S.; Yuk, H.; Zhao, X. Predicting fracture energies and crack-tip fields of soft tough materials. *Extrem. Mech. Lett.* **2015**, *4*, 1–8. [CrossRef]
77. Huang, Y.; King, D.R.; Cui, W.; Sun, T.L.; Guo, H.; Kurokawa, T.; Brown, H.R.; Hui, C.-Y.; Gong, J.P. Superior fracture resistance of fiber reinforced polyampholyte hydrogels achieved by extraordinarily large energy-dissipative process zones. *J. Mater. Chem. A* **2019**, *7*, 13431–13440. [CrossRef]
78. Li, Z.; Liu, Z.; Ng, T.Y.; Sharma, P. The effect of water content on the elastic modulus and fracture energy of hydrogel. *Extrem. Mech. Lett.* **2020**, *35*, 100617. [CrossRef]
79. Yang, C.; Yin, T.; Suo, Z. Polyacrylamide hydrogels. I. Network imperfection. *J. Mech. Phys. Solids* **2019**, *131*, 43–55. [CrossRef]
80. Liu, J.; Yang, C.; Yin, T.; Wang, Z.; Qu, S.; Suo, Z. Polyacrylamide hydrogels. II. Elastic dissipater. *J. Mech. Phys. Solids* **2019**, *133*, 103737. [CrossRef]

81. Zhang, W.; Liu, X.; Wang, J.; Tang, J.; Hu, J.; Lu, T.; Suo, Z. Fatigue of double-network hydrogels. *Eng. Fract. Mech.* **2018**, *187*, 74–93. [CrossRef]
82. Hou, J.; Ren, X.; Guan, S.; Duan, L.; Gao, G.H.; Kuai, Y.; Zhang, H. Rapidly recoverable, anti-fatigue, super-tough double-network hydrogels reinforced by macromolecular microspheres. *Soft Matter* **2017**, *13*, 1357–1363. [CrossRef]
83. Chen, Q.; Yan, X.; Zhu, L.; Chen, H.; Jiang, B.; Wei, D.; Huang, L.; Yang, J.; Liu, B.; Zheng, J. Improvement of mechanical strength and fatigue resistance of double network hydrogels by ionic coordination interactions. *Chem. Mater.* **2016**, *28*, 5710–5720. [CrossRef]
84. Chen, Q.; Zhu, L.; Chen, H.; Yan, H.; Huang, L.; Yang, J.; Zheng, J. A novel design strategy for fully physically linked double network hydrogels with tough, fatigue resistant, and self-healing properties. *Adv. Funct. Mater.* **2015**, *25*, 1598–1607. [CrossRef]
85. Chen, Q.; Zhu, L.; Zhao, C.; Wang, Q.; Zheng, J. A robust, one-pot synthesis of highly mechanical and recoverable double network hydrogels using thermoreversible sol-gel polysaccharide. *Adv. Mater.* **2013**, *25*, 4171–4176. [CrossRef]
86. Li, X.; Cui, K.; Sun, T.L.; Meng, L.; Yu, C.; Li, L.; Creton, C.; Kurokawa, T.; Gong, J.P. Mesoscale bicontinuous networks in self-healing hydrogels delay fatigue fracture. *Proc. Natl. Acad. Sci. USA* **2020**, *117*, 7606–7612. [CrossRef] [PubMed]
87. Tanaka, Y. A local damage model for anomalous high toughness of double-network gels. *Europhys. Lett.* **2007**, *78*, 56005. [CrossRef]
88. Tominaga, T.; Tirumala, V.R.; Lee, S.; Lin, E.K.; Gong, J.P.; Wu, W.-l. Thermodynamic interactions in double-network hydrogels. *J. Phys. Chem. B* **2008**, *112*, 3903–3909. [CrossRef] [PubMed]
89. Tominaga, T.; Tirumala, V.R.; Lin, E.K.; Gong, J.P.; Furukawa, H.; Osada, Y.; Wu, W.-l. The molecular origin of enhanced toughness in double-network hydrogels: A neutron scattering study. *Polymer* **2007**, *48*, 7449–7454. [CrossRef]
90. Yu, Q.M.; Tanaka, Y.; Furukawa, H.; Kurokawa, T.; Gong, J.P. Direct observation of damage zone around crack tips in double-network gels. *Macromolecules* **2009**, *42*, 3852–3855. [CrossRef]
91. Liang, S.; Wu, Z.L.; Hu, J.; Kurokawa, T.; Yu, Q.M.; Gong, J.P. Direct observation on the surface fracture of ultrathin film double-network hydrogels. *Macromolecules* **2011**, *44*, 3016–3020. [CrossRef]
92. Cui, W.; Huang, Y.; Chen, L.; Zheng, Y.; Saruwatari, Y.; Hui, C.-Y.; Kurokawa, T.; King, D.R.; Gong, J.P. Tiny yet tough: Maximizing the toughness of fiber-reinforced soft composites in the absence of a fiber-fracture mechanism. *Matter* **2021**, *4*, 3646–3661. [CrossRef]
93. Hui, C.-Y.; Liu, Z.; Phoenix, S.L. Size effect on elastic stress concentrations in unidirectional fiber reinforced soft composites. *Extrem. Mech. Lett.* **2019**, *33*, 100573. [CrossRef]
94. Haque, M.A.; Kurokawa, T.; Gong, J.P. Super tough double network hydrogels and their application as biomaterials. *Polymer* **2012**, *53*, 1805–1822. [CrossRef]
95. Yue, Y.; Kurokawa, T.; Haque, M.A.; Nakajima, T.; Nonoyama, T.; Li, X.; Kajiwara, I.; Gong, J.P. Mechano-actuated ultrafast full-colour switching in layered photonic hydrogels. *Nat. Commun.* **2014**, *5*, 1–8. [CrossRef]
96. Yue, Y.F.; Haque, M.A.; Kurokawa, T.; Nakajima, T.; Gong, J.P. Lamellar Hydrogels with High Toughness and Ternary Tunable Photonic Stop-Band. *Adv. Mater.* **2013**, *25*, 3106–3110. [CrossRef] [PubMed]
97. Ye, Y.N.; Haque, M.A.; Inoue, A.; Katsuyama, Y.; Kurokawa, T.; Gong, J.P. Flower-like Photonic Hydrogel with Superstructure Induced via Modulated Shear Field. *ACS Macro Lett.* **2021**, *10*, 708–713. [CrossRef]
98. Haque, M.A.; Kurokawa, T.; Kamita, G.; Yue, Y.; Gong, J.P. Rapid and reversible tuning of structural color of a hydrogel over the entire visible spectrum by mechanical stimulation. *Chem. Mater.* **2011**, *23*, 5200–5207. [CrossRef]
99. Haque, M.A.; Kurokawa, T.; Gong, J.P. Anisotropic hydrogel based on bilayers: Color, strength, toughness, and fatigue resistance. *Soft Matter* **2012**, *8*, 8008–8016. [CrossRef]
100. Kong, W.; Wang, C.; Jia, C.; Kuang, Y.; Pastel, G.; Chen, C.; Chen, G.; He, S.; Huang, H.; Zhang, J. Muscle-Inspired Highly Anisotropic, Strong, Ion-Conductive Hydrogels. *Adv. Mater.* **2018**, *30*, 1801934. [CrossRef]
101. Zhou, Y.; Wan, C.; Yang, Y.; Yang, H.; Wang, S.; Dai, Z.; Ji, K.; Jiang, H.; Chen, X.; Long, Y. Highly stretchable, elastic, and ionic conductive hydrogel for artificial soft electronics. *Adv. Funct. Mater.* **2019**, *29*, 1806220. [CrossRef]
102. Park, H.; Lee, K.; Kim, Y.; Ambade, S.; Noh, S.; Eom, W.; Hwang, J.; Lee, W.; Huang, J.; Han, T. Dynamic assembly of liquid crystalline graphene oxide gel fibers for ion transport. *Sci. Adv.* **2018**, *4*, eaau2104. [CrossRef] [PubMed]
103. Kanik, M.; Orguc, S.; Varnavides, G.; Kim, J.; Benavides, T.; Gonzalez, D.; Akintilo, T.; Tasan, C.C.; Chandrakasan, A.P.; Fink, Y. Strain-programmable fiber-based artificial muscle. *Science* **2019**, *365*, 145–150. [CrossRef] [PubMed]

*textiles*

MDPI

*Review*

# Textile Branch and Main Breakthroughs of the Czech Republic in the Field of Textile Machinery: An Illustrated Review

**Jiří Militký [1,*], Dana Křemenáková [1], Miroslav Václavík [2], Václav Klička [3] and Stanislav Dídek [4,†]**

[1] Department of Material Engineering, Faculty of Textile Engineering, Technical University of Liberec, 461 17 Liberec, Czech Republic; dana.kremenakova@tul.cz
[2] Research Institute of Textile Machinery, 460 01 Liberec, Czech Republic; miroslav.vaclavik@vuts.cz
[3] Science & Management Consulting, 562 01 Ústí nad Orlicí, Czech Republic; vk@wo.cz
[4] Research Institute of Cotton Industry, 562 23 Ústí nad Orlicí, Czech Republic; didekS@seznam.cz
* Correspondence: jiri.militky@tul.cz
† Retired.

**Abstract:** The main aim of this review is to discuss and explain breakthrough solutions and main improvements in the construction of textile machinery originating in Czech Republic and their influence on processing and quality of textile products. Open-end spinning, jet weft insertion and jet looms, perpendicularly layered nonwovens and needleless electrospinning machines for manufacturing nanofibrous assemblies and corresponding technologies developed in Czech Republic are briefly discussed and pictorially illustrated. This review is also focused on specifying the different factors responsible for the development of technology and products in textile branches. The human and civilization factors influencing textile production and general requirement for advanced textile products are critically discussed. The unique position of the textile industry in society is demonstrated. The future basic needs that influence textile branch development are discussed.

**Keywords:** textile development; human and civilization factors; clothing and technical textiles; open end spinning; jet looms; perpendicularly layered nonwovens; needleless electrospinning

**Citation:** Militký, J.; Křemenáková, D.; Václavík, M.; Klička, V.; Dídek, S. Textile Branch and Main Breakthroughs of the Czech Republic in the Field of Textile Machinery: An Illustrated Review. *Textiles* **2021**, *1*, 466–482. https://doi.org/10.3390/textiles1030024

Academic Editor: Laurent Dufossé

Received: 14 September 2021
Accepted: 7 October 2021
Published: 19 October 2021



## 1. Introduction

The production of textiles and the construction of clothing are two of the oldest industries, with a traditionally high degree of automation and the use of new energy sources, new types of materials and new production facilities. It is interesting that the basic principles of yarn preparation by twisting and the production of fabrics by intertwining warp and weft threads do not actually differ in principle from the original manual procedures known for thousands of years. Textile machines enabled the realization of the first continuous technologies, and they used punched cards before the development of computer technology; very quickly, the elements of cognitive robots were applied to them when handling materials. Their speeds (with open end spinning up to 200,000 rpm) are extremely high and require the use of special solutions. On the other hand, textiles are directly connected with the three basic human needs, i.e., "food, housing and clothing." Textile products that satisfy the need for clothing must, therefore, have both a functional (utility) and aesthetic aspect. The aesthetic aspect is related to the shape of the textile on the wearer and its changes when worn (characterized by drape) [1].

The need for textiles is generally related to the size of the human population (clothing textiles) and its maturity (technical textile structures). The question now turns to what locations and individuals can ensure this need. The current trend is to realize the production of textiles as close as possible to the sources of raw materials. Competition on world markets and a surplus of mass-produced products from Asian countries are causing a shift in production in Europe and USA towards customer-oriented textile products with new effects, quality and comfort [1].

The aim of this contribution is to show the unique position of the textile industry in society, the basic reasons of its development and the requirements for basic types of textile products. The main breakthroughs in textile machinery developed in Czech Republic are briefly discussed.

## 2. Development of Textile Branch

The textile branch includes mainly the processing of textile fibers, the production of yarns and various fabrics (fabrics, knitwear and nonwovens) and their use for clothing purposes and technical applications. This branch belonged, belongs and will probably continue to belong to fields using new technical solutions very quickly [1].

The textile and clothing industries are an important part of the global manufacturing industry. Globally, the textile and clothing industries are in the third place (ahead of only informatics and tourism) according to the importance expressed by the financial amount of the annual profit. In EU countries, employment in the textile and clothing sector numbered around 6.2 million people (approximately 9.3% of all jobs in the manufacturing industry). The number of companies is around 250,000, and the total turnover represents about 4% of the total added value in the manufacturing industries of EU countries. Half of it is made up of the textile industry. About 68% of textile and clothing employees are women. All this indicates that it is a field that has a relatively large number of employees. With the growth of competition on the world market, the structure of textile fabrics produced in developed countries is shifting significantly from standard and mass-produced to special and customer-oriented structure [2]. This results in a reduction in the number of employees while maintaining or increasing sales turnover.

The human population is in daily contact with clothing textiles, using home textiles and textiles for industrial applications (transport, composite structures, filtration and wastewater treatment, electronics, etc.). Thus, the main advantages of textiles as unique products are known, including the following: extremely low density due to high overall porosity (over 70%), unique drape, flexibility and easy formability, resistance to environmental influences (UV, humidity and temperature), abrasion, long-term heat and chemical resistance, low degradation under storage conditions and slow aging under conditions of use. The advantages are also the simple joining and cutting techniques enabling the preparation of "tailor-made" shapes; simple surface modification allowing changes in a number of properties related to interface behavior; layering and combining into structures with controlled geometry; and properties anisotropy, as well as easy maintenance, cleaning and easy reparation.

The developments of textiles and clothing are closely related to both human factors and the influence of civilization. Influences related to human factors can be divided into the following groups [3]:

- Earth's population growth: The planet's population is expected to increase to 8.9 billion by 2050. With an expected consumption of 20 kg of textiles per person per year, this amounts to a total of 178 billion tons of textiles per year in 2050 [1,2];
- Prolongation of life expectancy: Based on a stochastic model, the expected life expectancy in 2050 was found in the range of 80–83 years (USA) and 83–91 years (Japan) [4]. This is also related to an increase in the relative share of seniors in society. The category of seniors will have other requirements for a number of textiles related mainly to ensuring their safety with limited mobility (e.g., improved visibility of objects, identifiable edges, etc.);
- Growth in the share of free time: Free time that can also be spent on activities requiring special textiles (FITNESS and WELNESS);
- A lifestyle that significantly changes the size range of clothing textiles and also affects the way they are purchased;
- Civilizational influences that usually have a negative effect on health and require the provision of special barrier functions (against microorganisms, allergies, environmental pollution, etc.);

- Protection and prevention of health (fitness sports and rehabilitation), which again require special textiles both in clothing and in some products (especially composites).

Closely related to the human factor are changes in the availability and acquisition of information, the virtualization of virtually everything (including the supply of textiles) and the globalization of society. Civilization factors are directly related to the development of the level of human society and the corresponding consumption. They can be divided into the following groups [3]:

- Energy: This is about methods to reduce the consumption of different types of energy in the production and maintenance of textiles, as well as the search for new energy sources using renewable raw materials and environmentally friendly technologies;
- Raw materials for textile production: Methods are being sought to replace raw materials from non-renewable sources with raw materials from renewable sources. A separate problem is the effective use of textile waste for recycling or extraction of raw materials;
- Transport: As fossil fuel stocks decrease, transport costs from producer to customer increase, which is likely to result in a revival of local production of standard quality textiles in the future;
- Housing: With the increasing level of living comfort, the volume of textiles used in living rooms is not only growing but also textiles used as a part of buildings and architectural solutions of their surroundings;
- Environmental quality: Textiles as materials with a number of advantages serve to improve environmental conditions both directly (filters, protective layers, etc.) and indirectly (geo-textiles, agrotextiles, artificial turf, etc.).

In addition to the objective factors of textile development, subjective factors have of course also appeared. Subjective factors of textile development are related to two basic approaches. This typically includes, especially for Asian countries, the desire for a new (non-traditional) textiles. Examples are textiles with new functions, intelligent structures and special fibers enabling, for example, the conversion of solar (light) energy into electricity. In many western countries, there is a tendency to believe in traditional (i.e., old) techniques and products. An example is the popularity of materials made of viscose, where the raw material is bamboo. These fibers are available under the misleading name "bamboo fibers" and are attributed to therapeutic and health-promoting effects. Subjective factors often cause manufacturers to return to old techniques and processes (e.g., dyeing with natural dyes and the use of milk casein fibers), which they sometimes combine with modern techniques to ensure practical applicability.

In the future, the predominant long-term trend can be expected to be the integration of development results in materials, chemistry, physics and engineering for the production of new textile structures for clothing textiles capable of adapting to changes in environmental conditions and special technical textiles with unique properties required for their applications. In the case of textiles for clothing purposes, the aspects of fashion, style and comfort have traditionally prevailed. From the consumer's point of view, it will be necessary to ensure that these textiles will have the following abilities:

- Optimal humidity control;
- Heat flow control;
- Air breathability control;
- Improved thermal insulation properties;
- Water vapor permeability (diameter 0.4 μm), but not liquid water (diameter 100 μm) permeability;
- Protection against dangerous influences from the environment (microorganisms and ultraviolet UV radiation);
- Ecological production and disposal of used textiles (biodegradability);
- Self-cleaning effects and dust repellency;
- Improved wear resistance (abrasion);

- Support of health care (vital functions and healing processes);
- Support of cosmetic functions (regenerative processes on the skin);
- Easy maintenance including cleaning and ironing;
- Improved hand, aesthetic sensations and appearance even after several cycles of use and maintenance;
- Controlled active identifiability of textiles in conditions of low visibility.

There are already partial solutions enabling the implementation of some of these requirements. In the future, the prevailing multifunctional effects and solutions will ensure durability throughout the planned life cycle of textiles. The use of clothing textiles as information systems for monitoring the condition of the wearer can also be expected.

In the field of technical textiles, the situation is usually simpler, as the requirements for their properties can often be precisely specified according to the intended purpose of use [5]. The general requirements for technical textiles for industrial use and composites include the following.

- High strength and modulus (tension, bending and torsion);
- Low deformability to break;
- Low creep;
- Resistance to environmental influences (UV radiation, humidity and rot);
- Mechanical shock absorption;
- Resistance to cyclic stress;
- Slow aging under conditions of use;
- Low thermal expansion.

For protective clothing and barrier textiles, sufficient comfort is also a necessary, which often requires a special solution. Textiles are increasingly being used as special flexible construction materials and composite structures. For these purposes and for special applications (light conducting systems, electrically conductive systems, etc.), polymers, metals and ceramic materials are used. A separate problem here is the possibility of creating fibrous structures by textile techniques. Many special materials can be converted into the form of thin wires, but for weaving purposes with respect to knitting, these structures often do not have the required flexibility expressed in bending stiffness, which is directly proportional to the modulus of elasticity of the fibers in tension and the square of their diameter.

In some cases (see Figure 1), textile structures are combined with active materials (side emitting optical polymer fibers SEPOF) for the construction of new structures such as a linear composite for linear economic lighting (international patent WO 2014/071898A1 of research team from the Technical University of Liberec) [6].


**Figure 1.** Structure of SEPOF and line lighting system.

Applications of this portable illumination system range from protective materials, textile, clothing with light effect, artistic design, lighting in remote areas and visualization of silhouettes, etc. (see Figure 2) [6–8].

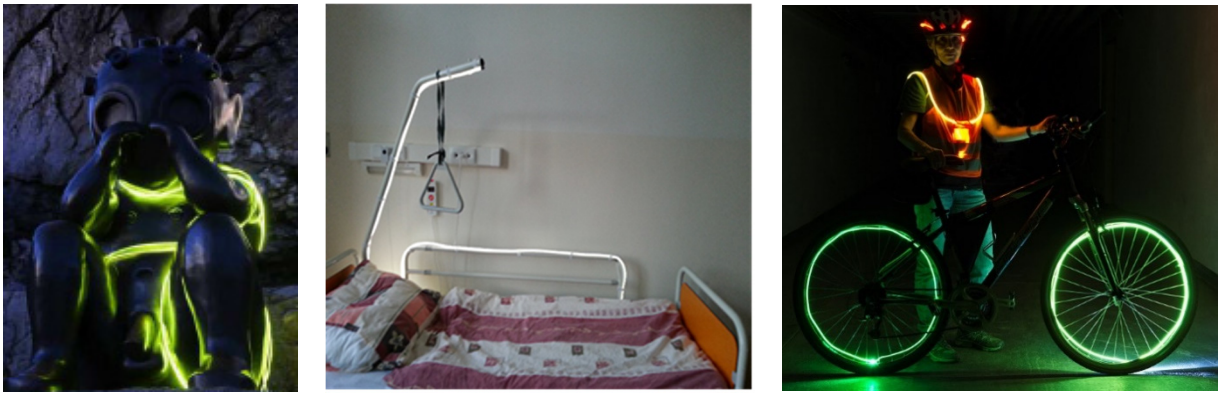

(**a**) (**b**) (**c**)

**Figure 2.** (**a**) Sculpture with illumination, (**b**) lighting of the hospital bed and (**c**) safety aids.

The advantage of active line lighting systems is energy savings, easy installation and the possibility of adaptive exposure along any path, even where there is no electrical network available.

## 3. Production of Yarns and Fabrics

For the production of yarns and various kind of fabrics (fabrics, knitwear and nonwovens), the starting element is fibers, and they are typically thin (thickness about 5–20 μm) long (length about 2–10 cm) formations. Final lengths are typical for natural fibers. For man-made fibers (chemical and synthetic), shortening of the originally endless fibers (filaments) is performed by cutting and tearing. This seemingly illogical step (division into short lengths and subsequent joining into a continuous yarn) is necessary to obtain a number of useful properties of textiles (sorption, thermal insulation, hand, drape, etc.).

The weight of a typical cotton fiber with a length of 2.5 cm and a fineness of 1.5 dtex is only 3.8 micrograms. In one square meter (the area of human skin is about 1.5 $m^2$) of finer cotton fabric with a basis weight of 150 $g/m^2$, there are 39.5 million fibers. During the preparation for spinning and during the production of the yarn, this amount of fibers is handled (loosening, cleaning, mixing, carding, drawing and twisting). Similarly, in weaving, a relatively large length of yarn must be intertwined. It is, therefore, clear that machinery must be relatively sophisticated and, above all, capable of producing large quantities of textiles in a period of short time [9].

### *3.1. Spinning*

Ring spinning, based on the same principle as hand spinning on a spinning wheel, still remains the dominant method of yarn production worldwide [10]. The fibers are mechanically transformed (loosening, cleaning, mixing, carding, stretching and combing) into a linear structure—sliver. It is processed by drafting, twisted in the system ring—runner—spindle into the form of yarn, which is wound on a bobbin. The ring spinning yarn has a structure characterized in particular by the presence of protruding fibers (hairiness) (see Figure 3).

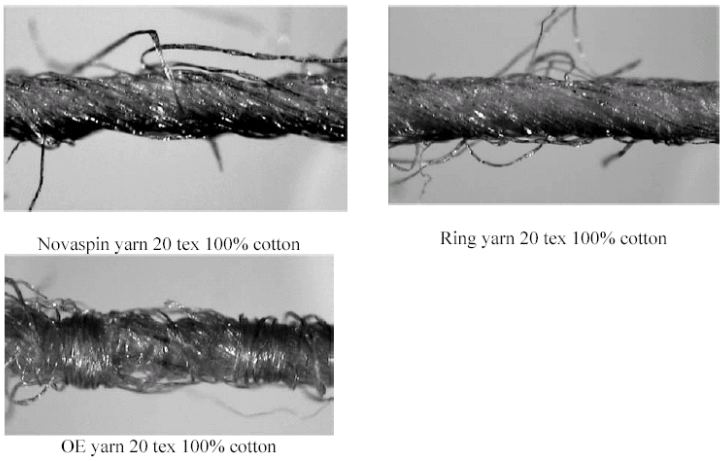


**Figure 3.** Structure of Novaspin, ring and open-end yarns.

The ring yarn is relatively strong, and the corresponding products have a good hand and absorbency. Today, the so-called compact ring spinning is often used for spinning cotton yarns, where, with the use of a suction zone located behind the drawing device, their hairiness is reduced and their strength is increased [11]. The revolutionary principle of so-called rotor spinning (open-ended spinning) was the result of many years of research and development by teams of Czech researchers from the Research Institute of Textile Machinery (VÚTS) and, subsequently, from the Cotton Research Institute (VÚB) Ústí nad Orlicí [12]. The idea of open-ended spinning was created in VÚTS, the first patents were filed and the yarn in the rotor was spun for the first time (Figure 4).

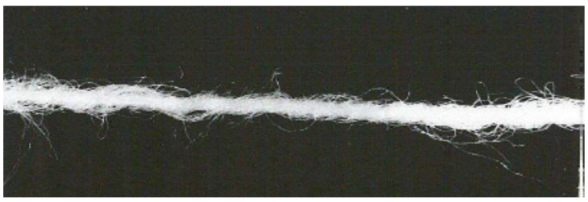

**Figure 4.** The world's first yarn spun in a rotor.

The VUB team patented and developed the first prototype of the BD 200 rotor spinning device and enabled its industrial application (Figure 5) [12].

(**a**) (**b**)

**Figure 5.** (**a**) The first open-end spinning machine BD 200 and (**b**) section by a rotor spinning unit.

The core of the rotor spinning system is the rotor (see Figure 5b). In the rotor, the fibers slide along its wall into the collecting groove where a fiber ribbon is formed. After introducing the free end of the yarn into the rotor, yarn is formed. It is, thus, a discontinuous

system of disintegration into fibers, their transport and re-association with twisting [13,14]. The rotor spinning yarn has a structure with typical wraps, is stiffer and the yarn strength is usually 20 to 30% lower compared to ring spinning yarns [15] (see Figure 3). During fiber separation and their deformation in the rotor, the fiber breaks appear [16,17]. The mechanics of the functioning of rotor machine and the influence of some of the process parameters were comprehensively investigated [18]. Rotor technology is used mainly for manufacturing coarser yarns [10]. The main challenge was to use rotor spinning for the creation of cotton yarns and for the prediction of their properties. The influence of cotton fiber properties on selected properties of open-end yarn was investigated comprehensively in work [19]. The basic construction parameters of yarns were yarn count and yarn twist characterized by the Phrix twist coefficient. From these parameters, the structural characteristics such as packing density, orientation and mean surface helix angle were predicted. Total numbers of 180 cotton rotor yarns were prepared from seventeen kinds of cottons in five levels of yarn count and two levels of Phrix twist coefficient. For the prediction of yarn strength and mass unevenness based on fiber quality and yarn structural parameters, the dimension reduction approach combined with linear regression was used. It was found that yarn strength is critically dependent on fiber strength as was in accordance with the majority of models presented in work [20]. The simple models for yarn strength prediction based on the reduction in fiber strength by the multiplicative factors from orientation, Poisson ratio and volume fraction (see [21,22]) combined with linear regression was used as well. The influence of process parameters was "hidden" in yarn fineness, and process parameters were not as important as fiber strength. Yarn unevenness (mass variation between portions of yarn with lengths 0.8 mm) was critically dependent on yarn packing density, fiber helix angle in yarn, number of fibers in yarn and fiber length parameters (upper half mean length). The complex criterion of cotton fibers quality correlated significantly with yarn unevenness. Coarser yarns with lower packing density were more uneven. These results were not generalized due to practical range of technological parameters of yarn creation (yarn count and yarn twist), but they were in accordance with the conclusions obtained from experiments with other types of cotton yarns [23].

The Czech machine for industrial rotor spinning was firstly presented at the exhibition of the International Association of Textile Machinery (ITMA) in 1967 in Basel, Switzerland. The first generation of this breakthrough technology (well-known Czech BD 200 machines, see Figure 5a) proved that spinning has reached the threshold of a new era.

The rotor speed of 35,000 rpm was quite astonishing compared to the spindle speed of ring spinning of 10,000 to 12,000 rpm, and the size of a 1 kg yarn bobbin was significantly larger than the 120 g bobbin of a ring spinning machine. In 1991, the world's first automated open-end spinning mill was exhibited at the ITMA Hannover trade fair, which was developed in cooperation with VÚTS Liberec and the manufacturer of rotor machines BDA10N, Elitex s. P. Ústí nad Orlicí (Figure 6).

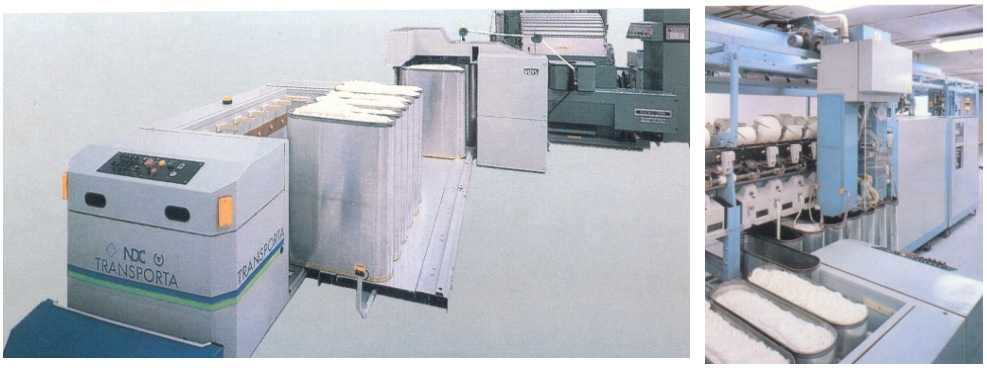


(**a**) (**b**)

**Figure 6.** The world's first automated open-end spinning mill: (**a**) general view, (**b**) detail.

At present time, the production of yarn on a ring spinning machine is about 20 m of yarn per minute and the range of processed fineness is 5–300 tex. On a rotor spinning machine, the yarn production is about 350 m of yarn per minute, and the range of fineness processed is 10–500 tex. There are also other principles of spinning (friction, Vortex, etc.), where the production of yarn is even higher, but their application (depending on the qualitative characteristics of the yarn) is so far only limited [24]. The principles of rotor and ring spinning will probably be maintained as the most applied in the future [25].

Czech researchers from VUB led by Stanislav Dídek also succeeded in developing a NOVASPIN spinning system, with ring-quality yarn and with a significantly higher spinning speed (see Figure 7). As in the case of ring spinning, the sliver is drafted and twisted in a system of a rotating surface at the edge of which a rotating loop of the formed yarn is subsequently wound on a bobbin. This principle removed the speed limiting element of the ring spin machines, the runner, which heats up at higher speeds until it breaks. The NOVASPIN system is patented, and it works as a prototype, but its practical application is still unclear even though several thousand kilograms of yarns of various fineness were produced, and these yarns were subsequently processed into fabrics of very good properties. A comparison of the production speeds of the mentioned yarn production technologies (rotor, ring and NOVASPIN) according to the spun yarn fineness is shown in Figure 7.

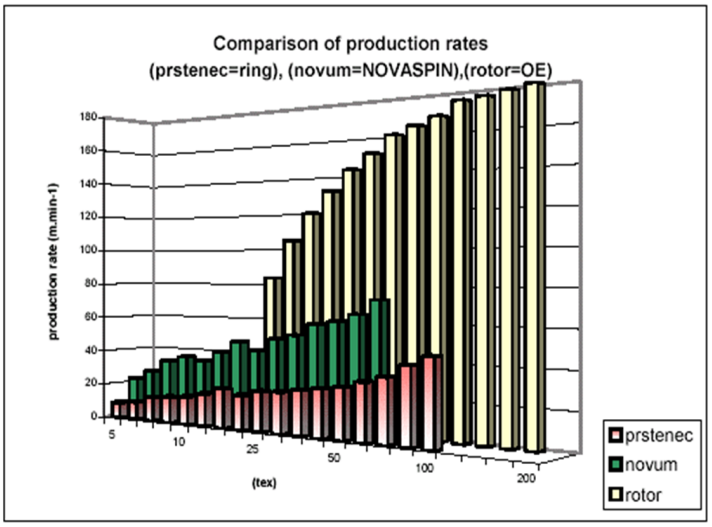


**Figure 7.** Production speed of rotor (yellow), ring (red) and NOVASPIN (green) technologies.

### *3.2. Weaving*

Weaving is a technology for the production of flat textiles (fabrics), where two systems of threads, i.e., war and weft, are interlaced. The warp threads are placed longitudinally in the fabric, while the weft threds are inserted in the transverse direction, and the warp threads are inserted across the binding points [26]. Independently of the weft insertion principle, the produced fabric structure depends on the construction parameters that are set for warp and weft [9].

In conventional shuttle looms, the weft threads are inserted with a shuttle (typical weight 300 g) carrying a spool of weft thread inside. The shuttle is given high acceleration at the beginning and is stopped abruptly at the end (after the weft is inserted). This is followed by mechanical beating of the weft to the front of the fabric and contacting the warp at the contact points of the fabric by means of an impact mechanism weighing several hundred kilograms. The weaving sequence is, thus, discontinuous, and the weft insertion takes place regularly from left to right and back during each weaving cycle. The weft is uninterrupted after inserting so that solid edges are formed. The speed of weft insertion in modern shuttle looms is around 650 m/min, and the noise level is around 92–107 dB. Shuttle looms also tend to vibrate. The main disadvantage of shuttle looms is

the limited speed of the loom, higher energy consumption and frequent replacement of spare parts [27,28].

The shuttle less looms are characterized by the insertion of only the necessary part of the weft thread so that false edges are formed. There are three basic and very sophisticated weft insertion systems: shuttle (weft insertion speed is around 1500 m/min), rapier (weft insertion speed is around 1000 m/min) and jet (weft insertion speed for air nozzle condition is around 3500 m/min and for a water jet around 2600 m/min). The weft is inserted from only one side of the loom and cut on each side of the fabric [26]. The most productive shuttle looms use the water jet weft insertion [29].

Air and water jets used for weft insertion were patented and realized by the Czech inventor Vladimír Svatý who worked at VÚTS Liberec. The first 45 cm wide air jet (see Figure 8) was demonstrated in December 1952.

**Figure 8.** The first air jet loom in the world.

These inventions have caused tremendous changes in weaving technology. It is estimated that the number of air looms reached 100,000 machines during the 1960s–1970s, and the number of water looms was 25,000. Currently, the number of more sophisticated jet looms based on the same principle of weft insertion (air and water jet) is around 40,000 machines per year.

Air jet looms have the highest weft insertion performance and are most productive for the production of light to medium weight fabrics. At present, there are looms for high-weight fabrics (jeans) and technical fabrics, e.g., made of glass threads. Fabric widths generally range from 190 to 600 cm.

It is not necessary to have heavy impact mechanisms for the creation of fabrics (increasing the weight of the loom and noise), but sufficient rigidity is sufficient (ability to transfer mechanical work into the fabric without its own deformation).

Using new composite materials, a team of researchers from VÚTS led by Josef Dvořák patented and created a lightweight composite impact mechanism, which is used in the construction of the CAMEL loom (Figure 9) for the production of leno fabric. This construction, which also brings significant energy savings, may become another unconventional solution in the field of textile engineering in the future. Leno fabrics comprise a warp and weft thread system that is just the same as normal plain fabrics. The warp system is split into straight and looping warp threads. Straight warp threads are always under the weft threads and represent the lower shed during weaving. Looping warp threads are always above the filling threads and represent the upper shed during weaving [27,29]. The number of crossing threads within a binding point is higher, and the wrapping angle of thread crossings is larger (see Figure 9).

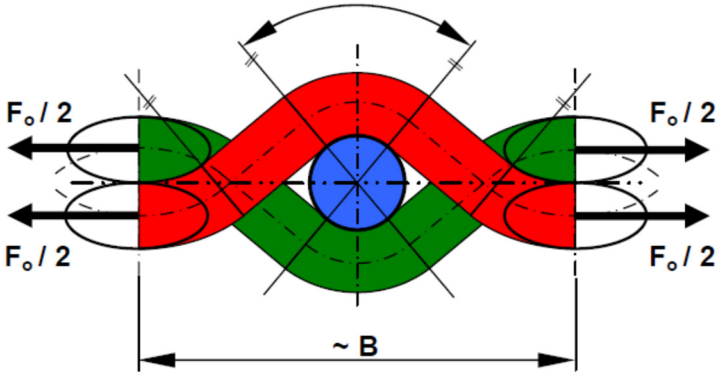


**Figure 9.** Structure of leno weave binding point.

The binding point for plain weave is planar, but it is spatially arranged for leno. Leno fabric cohesion is attained by positioning looping warp threads once on the left and once on the right of straight warp threads of a leno group. This leno interlaces supports leno fabrics with non-slip, latticed cloth designs with open fabric construction in warp and weft directions. The slip force in the fabric element $F_P$ is generally defined as the force in the thread that results in disrupting the balance in the binding point [27]. For the plain weave, $F_P$ is dependent on the thread axial force $F_0$, friction coefficient $f$ and wrap angle $\alpha_P$, according to the following relation [27].

$$F_P = F_0 e^{f\alpha_P} \tag{1}$$

The slip force of leno fabric $F_L$ (in the warp direction) is defined as follows [27]:

$$F_L = F_0 e^{f(\alpha_L + \beta_L)} \tag{2}$$

where $\alpha_L$ is the wrap angle of weft-warp, and $\beta_L$ is wrap angle warp-warp. For the Pierce model and symmetric angles, $\alpha_L = \beta_L$ is valid.

$$F_L = F_0 e^{2f\alpha_L} \tag{3}$$

The slip force in leno weave is, therefore, higher than the slip force in plain weave ($\alpha_L > \alpha_P$). The ratio between slip forces is dependent on the fabric set and fineness [27]. This is the main motivation to use leno fabrics for technical textile and composites.

The loom CAMEL ADAPTIVE for leno weaving (Figure 10b) developed by a team of researchers from VÚTS led by Petr Karel is currently the most productive loom in the world (speed 700 rpm).

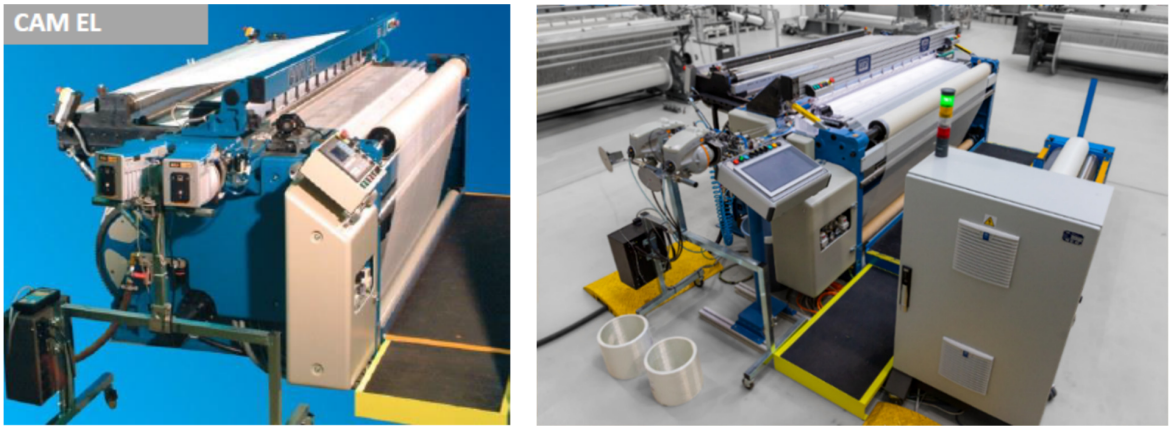


(**a**) (**b**)

**Figure 10.** (**a**) Air Jet loom CAMEL and (**b**) Air jet loom CAMEL ADAPTIVE.

The last breakthrough solution in the field of jet weaving is the DIFA weaving loom for the production of 3D layered fabrics composed of two woven layers (distance between layers 12–50 cm) connected by binding threads. This loom (Figure 11) is the result of a joint project of VÚTS (machine development) and TTRI-Taiwan Textile Research Institute (3D fabric creation patent).

**Figure 11.** Air jet loom DIFA.

It can be expected that the application of textiles from the DIFA machine will be relatively wide for industrial and construction purposes (see Figure 12).


**Figure 12.** 3D woven structures from the DIFA loom and their applications.

A very ambitious research and development of a multi-shed weaving loom by a team from VUB led by Stanislav Nosek was successfully completed up to the prototype and industrial equipment phase (Kontis C4-330), but practical expansion was not successful [16].

### *3.3. Special Nonwovens and Nanofibrous Structures*

In the field of nonwovens production, the breakthrough results were mainly vertically laid nonwovens produced by STRUTO and ROTIS technologies [30–32]. Both technologies' main advantage is the ability to tune their thickness, which is beneficial for higher thermal insulation and sound absorption [33,34]. Nonwoven fabric thickness $H$ (m) is generally functionally dependent on planar mass $W$ (kg m$^{-2}$) and total volume porosity $P$ (-):

$$H = \frac{W}{\rho_F (1 - P)} \tag{4}$$

where $r_F$ is fiber radius. Therefore, increased planar mass for thicker layers is observed.

STRUTO technology uses the creation of vertically laid nonwovens with a lever system to create transversely laid layers and is strengthened by thermal bonding (Figure 13).

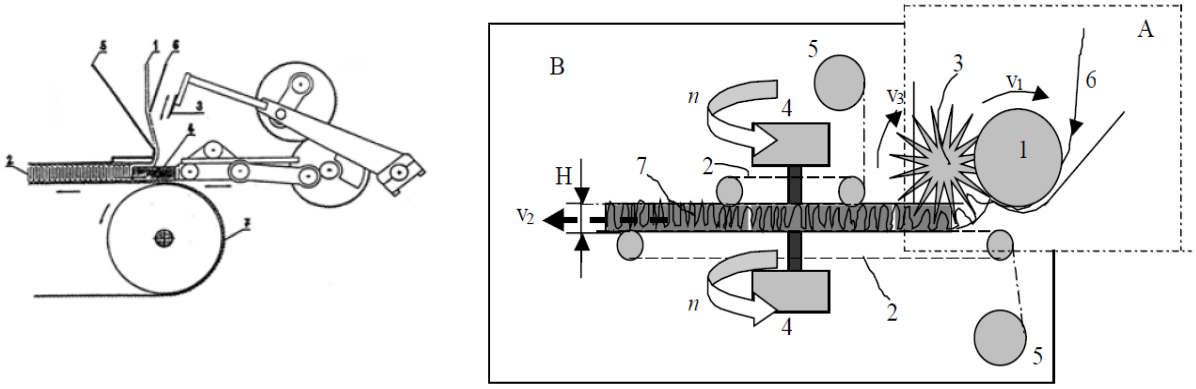


(**a**) (**b**)

**Figure 13.** Principles of vertically laid nonwovens technology (**a**) STRUTO and (**b**) ROTIS.

ROTIS technology uses vertically laid nonwoven with a toothed roller to create transversely laid layers, and the reinforcement takes place by means of mechanical reinforcement with the use of so-called "quasi" yarns based on mechanical entanglement of protruding surface fibers (see Figure 14) [31,32].

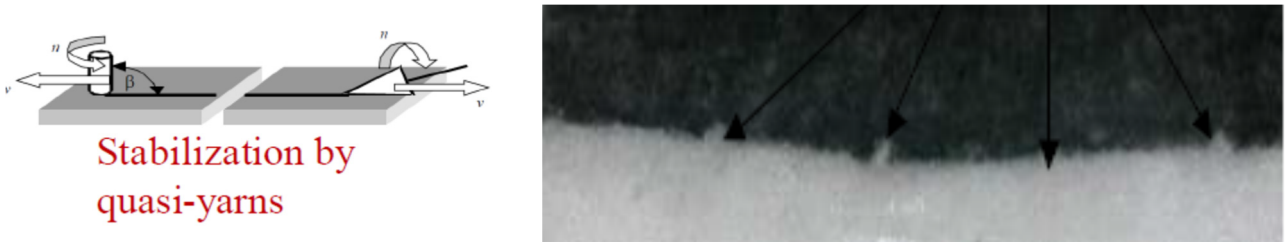


(**a**) (**b**)

**Figure 14.** Surface quasi yarns on surface of ROTIS structures (**a**) principle of forming and (**b**) appearance.

There are advantages of ROTIS technology important for the preparation of special products [30]:

- ROTIS technology is versatile and allow combining mechanical fixation by quasi-yarns with needling and thermal bonding by low melted fibers portion or adhesive bonding by special binders.
- It is possible to prepare products with variable density and thickness according to the aims of application.
- It is possible to prepare multilayer structures from different kind of sheets and laminated products (application of surface fixation by quasi-yarns).

- Non-conventional products are expected to bring more convenient pressure distribution.
- The technology of nonwoven structures fixation by quasi-yarns is expected to bring material savings for technical applications and energy savings.

Both of these technologies were patented by teams of specialists from the Faculty of Textiles of the Technical University of Liberec (TUL). STRUTO technology is used industrially by several foreign companies, and the pilot version of ROTIS is used in TUL laboratories. The differences in the structure of the two types of nonwovens are evident from Figure 15.

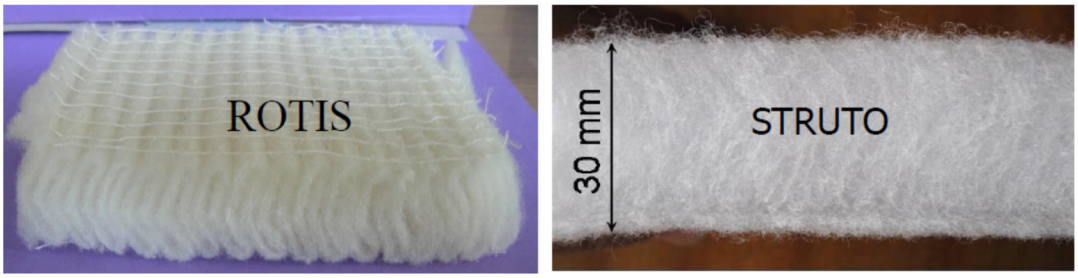


(**a**) (**b**)

**Figure 15.** Typical structures of (**a**) ROTIS (with surface grid fixed "quasi" yarns) and (**b**) STRUTO.

Creation of quasi-yarn enables the production of produce ROTIS with thickness up to 200 mm.

In the field of nanofibrous layers preparation, many of technologies based mainly on the principle of needle electrospinning were published [35–37]. TUL researchers are the authors of a number of patents relating to the production of nanofiber webs based on needleless electrospinning [36]. The original international patent of Jirsák et al. from 2004 was used for the production of Nanospider equipment by company Elmarco (Figure 16).

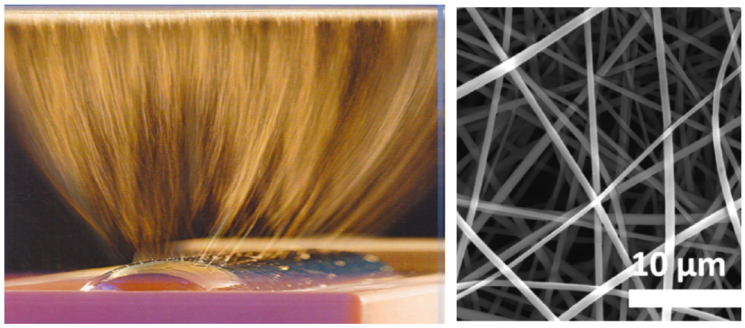


(**a**) (**b**)

**Figure 16.** NANOSPIDER principle (**a**) picture, (**b**) structure of nanofibrous assembly.

The original patented principle of production of nanofibrous assembly is currently further modified (especially on TUL); the modifications are protected by a number of other patents and laboratory, pilot plant and operational equipment are implemented (Figure 17).

Significant progress and practical application can also be expected in the field of nanofibrous assembly production, and further development of the corresponding machinery can also be expected.

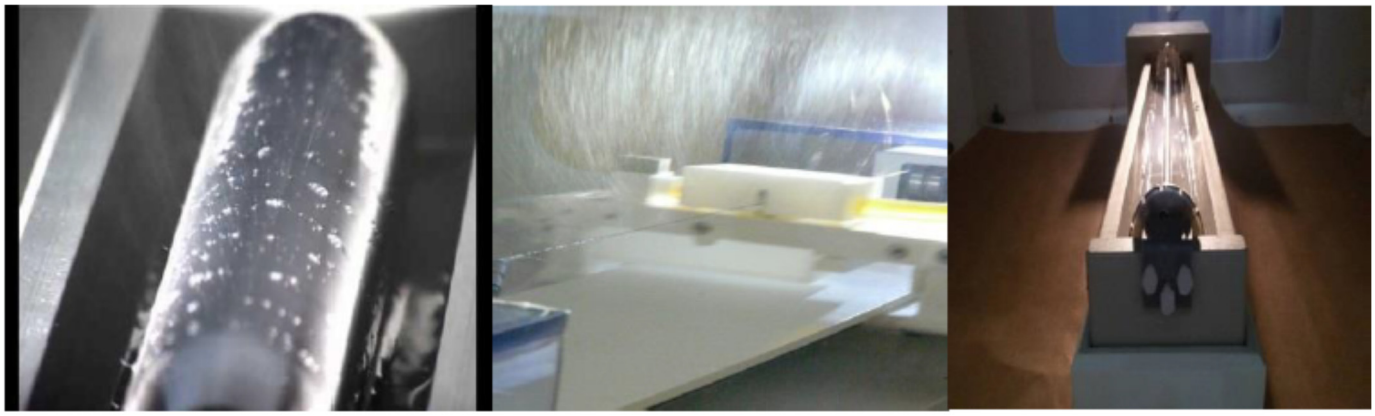

(**a**) (**b**) (**c**)

**Figure 17.** Modification of the NANOSPIDER system with (**a**) rotating cylindrical electrode with a pit on the surface, (**b**) wire electrode and (**c**) rotating wire electrode.

## 4. Future of the Textile Industry

The textile industry of the future will be focused on the following areas:

- Implementation of ecological production (not worsening the environment and not endangering life on earth);
- Reducing the share of waste from production (waste-free technologies, regeneration, recuperation and reuse);
- Reducing energy consumption (alternative reaction media, process optimization and alternative energy sources);
- Use of renewable resources (biotechnology and green chemistry);
- Elimination or replacement of toxic compounds (new solvents and replacement of heavy metals);
- Disposal of waste and used products (biodegradation, reuse of raw materials and special disposal).

In general, it is economical to use fewer machines with higher production speeds while maintaining product quality. That is why technologies with higher production speeds are developed and will be used. The two basic principles, i.e., rotor and ring spinning machines, will most probably be important for the production of yarns in the future [24]. Other principles will be used for special needs. This is the case of the most intensive yarn production system, Bobtex, using adhesive bonding (production speed around 700 m/min). The production speed of Bobtex is followed by the Dreft friction spinning system and the Vortex jet spinning system [10].

In weaving mills, the most productive system of weft insertion is the air jet (weft insertion speed over 3000 m/min) [26]. In the field of textile engineering, in addition to increasing the speed of production, efforts will continue to reduce the weight of machines, apply mechatronic principles, control the functions of machines with a computer and ensure flexible production. However, all of this will concern the textile industry in the longer term because it will be an investment-intensive modification of machinery where the return will be relatively slow. This is already evident today where a number of successful companies do not have top machinery and are still able to produce high-quality fabrics.

The development of most textile technologies will be increasingly influenced by ecological factors in the coming years. Human activities were in balance with the sustainable biocapacity of the globe in 1985. At present, the globe would require a 1.3 times larger surface area to ensure sustainable biocapacity. This imbalance is continuously growing [3]. It can, therefore, be expected that environmentally friendly "green" technologies using renewable resources will be preferred in the production of raw materials and materials for

textile applications. There will be increasing pressure on recycling or reuse of textile waste both from the production end and application end.

Textile technologies still have the potential to reduce energy consumption by up to 25% [3]. Thus, the search for new technologies with lower energy consumption (bio processes, catalytic processes and use of alternative energy sources), reduction in machine weight, reduction in reaction volumes, application of regulation and optimal control, effective insulation of machines and thermal energy transfer systems can be expected. The persisting basic and simple method for heat transfer by conduction using air and water is already supplemented by IR heating (many polymer fibers have absorption bands in the near IR region) and microwave heating (based on rapid changes in polarity-rotation of polar molecules). Microwave heating requires 10 to 100 times less energy than conventional heating. In IR heating, the surfaces of the materials are heated first and the edges and inner parts of the materials are heated first in microwave heating. By combining both types of heating, increasingly even heating of the entire volume can be obtained. Another possibility of intensive (local) heating of surfaces and thin subsurface layers is the use of plasma [38] or laser for local intensive heating until local surface destruction [39].

A separate problem of textiles fabrication and textiles maintenance is the enormous water consumption and production of polluted water [40–43]. What is alarming is that around 20% of water pollution in the world result from textiles wet processing [43]. Prospective possibilities for the replacement of water and volatile organic solvents in textile technologies are as follows [3]:

- Solvent-free techniques (complications of exothermic reactions and inhomogeneous environment mixing problem);
- Liquids in super critical state ($CO_2$);
- Ionic liquids;
- Lactate esters.

There is no universal solution yet, but water consumption will probably need to be severely reduced in the future [1]. During the solution of water consumption problems, the concept of "virtual water" should necessarily be focused on. Virtual water is defined as water that is only required for processing a fabric [43].

## 5. Conclusions

This incomplete overview, focused mainly on not only patented but also industrially long-term applied excellent and groundbreaking solutions, still demonstrates the very good potential of Czech scientists and researchers in the field of textile engineering development. In parallel with the development of new machines and textiles (especially yarns), mathematical descriptions of the principles of creating corresponding fiber products were solved and was reflected in the generalization of the achieved results and optimization of machinery. The modeling of the structures and properties of new textiles was mainly theoretically dealt with by TUL scientists. Their results in the field of models of structure and properties of linear and planar textile structures were culminated in the original monographs, prepared in both Czech and English [25,29,44,45]. The theoretical level and complexity of these monographs is still considered exceptional in the world. It is unique to TUL in that students of the Faculty of Textiles learn methods and models of textile structures based on the results achieved by their teachers [45]. It was, therefore, possible to organically combine the machine part, production technology and modeling of product structures in the above-described breakthrough technologies. All this combine to form good assumptions that the next generations of Czech researchers and scientists will implement new and certainly groundbreaking technologies in the field of textile engineering.

**Author Contributions:** Conceptualization, J.M. and M.V.; methodology, D.K.; software, S.D.; validation, S.D., V.K. and M.V.; formal analysis, J.M.; investigation, J.M.; resources, D.K.; data curation, D.K.; writing—original draft preparation, J.M.; writing—review and editing, J.M.; visualization V.K.;

supervision, J.M.; project administration, D.K.; funding acquisition, J.M. All authors have read and agreed to the published version of the manuscript.

**Funding:** This research received no external funding.

**Institutional Review Board Statement:** Not applicable.

**Informed Consent Statement:** Not applicable.

**Data Availability Statement:** The data presented in this study are available within the manuscript.

**Acknowledgments:** This study was supported by the project "Modular platform for autonomous chassis of specified electric vehicles for freight and equipment transportation", Reg. No. CZ.02.1.01/0.0/0.0/16_025/0007293 and the project of Ministry of Education, Youth, and Sports of the Czech Republic and the European Union-European Structural and Investment Funds in the Frames of Operational Programme Research, Development and Education-project Hybrid Materials for Hierarchical Structures (HyHi, Reg. No. CZ.02.1.01/0.0/0.0/16_019/0000843).

**Conflicts of Interest:** The authors declare no conflict of interest.

## References

1. Aneja, A.P.; Caldwell, E.W.; Hietpas, P.B. Textile Business Strategies in the New Millennium. In Proceedings of the Textile Institute's 80th World Congress, Manchester, UK, 16–19 April 2000.
2. Rept Euratex. European Technology Platform for the Future of Textiles and Clothing—A Vision for 2020. December 2004. Available online: https://www.certh.gr/dat/141D2148/file.pdf (accessed on 6 October 2021).
3. Militký, J. *Trends in the Development of the Textile and Clothing Industry, Implementation Action Plan of Czech Technology Platform (ČTPT)*; TUL: Liberec, Czech Republic, 2011. (In Czech)
4. Tuljapurkar, S.; Li, N.; Boe, C. A universal pattern of mortality decline in the G7 countries. *Nature* **2000**, *405*, 789–792. [CrossRef] [PubMed]
5. Militký, J.; Křemenaková, D. Some Ways of Technical Textiles Development. *IVUZ Technol. Text. Prom.* **2009**, *317*, 112–121.
6. Křemenáková, D.; Militký, J.; Mishra, R. Fibers for optical textiles. In *Handbook of Fibrous Materials 2*; Hu, J., Kumar, B., Lu, J., Eds.; Wiley VCH: Weinheim, Germany, 2020; Chapter 23.
7. Křemenáková, D.; Militký, J.; Šašková, J.; Ledrová, Z.; Vydra, J.; Bubelová, B.; Baxa, M. Testing of Emergency Line Light System in Radiation Therapy Rooms. In Proceedings of the 18th World Textile Conference, Istambul, Turkey, 20–22 June 2018.
8. Kremenakova, D.; Militky, J.; Meryova, B.; Ledl, V. Characterization of Side Emitting Polymeric Optical Fibers. *J. Fiber Bioeng. Inform.* **2012**, *5*, 423–431.
9. Křemenáková, D.; Militký, J.; Ibrahim, S. Cotton yarn and fabric production: Future trends. In *Cotton: Technology for the 21st Century*; Wakelyn, P.J., Chaudhry, M.R., Eds.; International Cotton Advisory Committee: Washington, DC, USA, 2010; Chapter 12.
10. Lawrence, C.A. *Fundamentals of Spun Yarn Technology*; CRC Press: Boca Raton, FL, USA, 2003.
11. Kašpárek, J.V. Future prospects of rotor spinning. *Indian J. Fibre Text. Res.* **1992**, *17*, 238–245.
12. Rohlena, V. *Open End Spinning*; North-Holland Biomedical Press: Amsterdam, The Netherlands, 1975.
13. Lawrence, C.A. (Ed.) *Advances in Yarn Spinning Technology*; Woodhead Publishing: Philadelphia, PA, USA, 2010.
14. Cormack, D.; Grosberg, P.; Ho, K.H. The yarn twist inside the rotor in open-end spinning. *J. Text. Inst.* **1979**, *70*, 380–384. [CrossRef]
15. Militký, J.; Křemenáková, D.; Ibrahim, S. Influence of fiber characteristics and yarn structure on OE yarn unevenness. In Proceedings of the 86-th World Textile Conference, Hong Kong, China, 18–21 November 2007.
16. Basal, G.; Oxenham, W. Vortex spun yarn vs. air jet spun yarn. *AUTEX Res. J.* **2003**, *3*, 96–101.
17. Basal, G.; Oxenham, W. Comparison of Properties and Structures of Compact and Conventional Spun Yarns. *Text. Res. J.* **2006**, *76*, 567–575. [CrossRef]
18. Elhawary, I.A. *Mechanics of Rotor Spinning Machines*; CRC Press: Boca Raton, FL, USA, 2017.
19. Militký, J.; Křemenáková, D.; Krupincová, G.; Ibrahim, S. Prediction of the selected properties of cotton type rotor yarns. In Proceedings of the Beltwide Cotton Conferences, New Orleans, LA, USA, 5–7 January 2010.
20. Ghosh, A.; Ishtiaque, S.; Rengasamy, S.; Mal, P.; Patnaik, A. Predictive models for strength of spun yarns: An overview. *AUTEX Res. J.* **2005**, *5*, 20–29.
21. Pan, N.; Hua, T.; Qiu, Y. Relationship between Fibre and Yarn Strength. *Text. Res. J.* **2001**, *71*, 960–964. [CrossRef]
22. Pan, N. Prediction of statistical strength of twisted structure. *J. Mater. Sci.* **1993**, *28*, 6107–6114. [CrossRef]
23. Soliman, A.S. Factors Affecting Rotor Spinning of Fine Cotton Yarns. Ph.D. Thesis, Texas Tech University, Lubbock, TX, USA, August 1985.
24. Oxenham, W. Current and Future trends in yarn production. *JTATM* **2002**, *2*, 1–20.
25. Neckář, B.; Das, D. *Theory of Structure and Mechanics of Yarns*; Woodhead Publishing: New Delhi, India, 2018.
26. Gandhi, K. (Ed.) *Woven Textiles*; Elsevier: Oxford, UK, 2020.
27. Dvořák, J.; Karel, P. Webmaschine mit litzenlosen System. *Meliand Text.* **2007**, *3*, 118–119.

28. Seyam, A.M. Weaving technology, advances and challenges. *J. Text. Appar.* **2003**, *3*, 1–10.
29. Nosek, S. *The Structure and Geometry of the Woven Fabrics, Mineo*; TU Liberec Press: Liberec, Czech Republic, 1996. (In Czech)
30. Hanuš, J.; Militký, J.; Aneja, A.P. Local Compression of Corrugated Nonwoven Structures. In Proceedings of the Ninth International Conference on Composites Engineering, San Diego, CA, USA, 1–6 July 2002.
31. Hanuš, J.; Militký, J. Reinforcement of 3D Cotton Nonwovens by Quasi-Yans. In Proceedings of the Beltwide Cotton Conferences, Cotton Utilization, San Antonio, TX, USA, 5–9 January 2004.
32. Hanuš, J.; Militký, J. Quasi-Yarn Applications in Nonwowen Production. In Proceedings of the HPTEX, Coimbatore, India, 7–9 July 2004.
33. Jirsak, O.; Wadsworth, L. *Nonwoven Textiles*; Academic Press: Durham, NC, USA, 1998.
34. Yang, T.; Saati, F.; Horoshenkov, K.V.; Xiong, X.; Yang, K.; Mishra, R.; Militký, J. Study on the Sound Absorption Behavior of Multi-Component Polyester Nonwovens: Experimental and Numerical Methods. *Text. Res. J.* **2019**, *89*, 3342–3361. [CrossRef]
35. Ramakrishna, S.; Fujihara, K.; Teo, W.E.; Yong, T.; Ma, Z.; Ramaseshan, R. Electrospun nanofibers: Solving global issues. *Mater. Today* **2006**, *9*, 40–50. [CrossRef]
36. Ramakrishna, S. *An Introduction to Electrospinning and Nanofibers*; World Scientific Publishing Company: Singapore, 2005.
37. Mishra, R.; Militký, J. *Nanotechnology in Textiles—Theory and Application*; Elsevier Woodhead Publishing: Sawston, UK, 2019.
38. Poll, H.V.; Schladitz, V.; Schrenter, S. Penetration of plasma effects into textile structures. *Surf. Coat. Technol.* **2001**, *142*, 489–493. [CrossRef]
39. Knittel, D.; Scholmeyer, E. Surface Structuring of Synthetic Fibres by UV Laser Irradiation, Part I: Phenomenological Report. *Polym. Int.* **1997**, *43*, 231–239. [CrossRef]
40. Muthu, S.S. (Ed.) *Environmental Footprints of Recycled Polyester*; Springer Nature: Singapore, 2020.
41. Muthu, S. (Ed.) *Water in Textiles and Fashion*; Woodhead Publishing: Duxford, UK, 2019.
42. Chavan, R.B. Thirsty Textile and Fashion Industry PART I: Water Distribution on Earth and Virtual Water. *Trends Text. Fash. Des.* **2018**, *2*, 249–270.
43. Schwarzenbach, R.P.; Egli, T.; Hofstetter, T.B.; Von Gunten, U.; Wehrli, B. Global Water Pollution and Human Health. *Annu. Rev. Environ. Resour.* **2010**, *35*, 109–136. [CrossRef]
44. Neckář, B. *Yarns: Creation, Structure, Properties*; SNTL: Prague, Czech Republic, 1990. (In Czech)
45. Militký, J.; Periyasamy, A.P.; Venkataraman, M. *Textiles and Their Use in Microbial Protection*; CRC Press: Boca Raton, FL, USA, 2021.

textiles

*Review*

# Recent Efforts in Modeling and Simulation of Textiles

**Julia Orlik [1,*], Maxime Krier [1], David Neusius [1], Kathrin Pietsch [2], Olena Sivak [1] and Konrad Steiner [1]**

[1] Fraunhofer Institute for Industrial Mathematics, Fraunhofer-Platz 1, 67663 Kaiserslautern, Germany; maxime.krier@itwm.fraunhofer.de (M.K.); david.neusius@itwm.fraunhofer.de (D.N.); olena.sivak@itwm.fraunhofer.de (O.S.); konrad.steiner@itwm.fraunhofer.de (K.S.)
[2] Textilinstitut ITM, University of Dresden, 01069 Dresden, Germany; kathrin.pietsch@tu-dresden.de
* Correspondence: julia.orlik@itwm.fraunhofer.de; Tel.: +49-631-31600-4330; Fax: +49-631-31600-5004

**Abstract:** In many textiles and fiber structures, the behavior of the material is determined by the structural arrangements of the fibers, their thickness and cross-section, as well as their material properties. Textiles are thin plates made of thin long yarns in frictional contact with each other that are connected via a rule defined by a looping diagram. The yarns themselves are stretchable or non-stretchable. All these structural parameters of a textile define its macroscopic behavior. Its folding is determined by all these parameters and the kind of the boundary fixation or loading direction. The next influencing characteristic is the value of the loading. The same textile can behave similar to a shell and work just for bending, or behave as a membrane with large tension deformations under different magnitudes of the loading forces. In our research, bounds on the loading and frictional parameters for both types of behavior are found. Additionally, algorithms for the computation of effective textile properties based on the structural information are proposed. Further focus of our research is the nature of folding, induced by pre-strain in yarns and some in-plane restriction of the textile movements, or by the local knitting or weaving pattern and the yarn's cross-sections. Further investigations concern different applications with spacer fabrics. Structural parameters influencing the macroscopic fabric behavior are investigated and a way for optimization is proposed. An overview of our published mathematical and numerical papers with developed algorithms is given and our numerical tools based on these theoretical results are demonstrated.

**Keywords:** textile modeling; homogenization; beam-based model; buckling; folding; spacer fabrics

**Citation:** Orlik, J.; Krier, M.; Neusius, D.; Pietsch, K.; Sivak, O.; Steiner, K. Recent Efforts in Modeling and Simulation of Textiles. *Textiles* **2021**, *1*, 322–336. http://doi.org/10.3390/textiles1020016

Academic Editors: Noureddine Abidi and Stepan Lomov

Received: 31 May 2021
Accepted: 23 August 2021
Published: 26 August 2021



## 1. Introduction

A textile is a flexible material made by creating an interlocking network of yarns. Yarns are produced by several spinning technologies from length-limited or endless fibers (from either natural or synthetic sources) into long and twisted lengths. Through a defined interlocking of one or several yarn systems, a 2D or 3D textile is formed by means of textile technologies, e.g., weaving, weft knitting, warp knitting or braiding. A technical textile is a textile product manufactured for non-aesthetic purposes, where function is the primary criterion. For an extensive introduction to technical textiles, see, e.g., [1,2]. Technical textiles include textiles for automotive applications, medical textiles (e.g., implants and bandages), geotextiles (reinforcement of embankments), agrotextiles (textiles for crop protection), protective clothing with thermophysiological effect (e.g., heat and radiation protection for fire fighter clothing), functional and sports clothing as well as light-weight constructions.

The functional and especially the mechanical behavior of a textile can be modeled as thin plates or shells. In particular, the effective bending and tensile behavior as well as the folding or wrinkling of a textile can be described by the mechanical theory of plates and shells [3,4]. The underlying textile structure, i.e., the woven or knitted fabric made of threads, determines the mechanical behavior and can be analyzed rigorously with the help of asymptotic analysis and homogenization theory [5–7].

In general, the functional behavior of the textile is determined by the functional behavior of the different yarns and the structure of the interlocking network. The yarns

can be characterized by their thickness, cross-section and tensile properties. Often, the textile structure is periodic in the plane and specified by the textile manufacturing process. The arrangement of the yarns and the friction between the yarns in contact determine the resulting material behavior [8,9], where simulation validates industrial experiments.

In this paper, an application of the mathematical framework of homogenization and asymptotic analysis is presented, which enables to quantify the mechanical behavior of textiles as well determining the sensitive and influencing parameters. These quantifications are critical for the computation of buckling pre-strain in yarns and of folding shear angles in non-stretchable textiles.

Currently, the state of the art for the prediction of the textile folding under compression or shear is mostly by trial and error through expensive experiments. Some recent modelling works use ANSYS, LS-DYNA and ESI-Software for simulations [10,11]. Although those commercial tools include many possibilities to simulate shells and their buckling, the main modelling issue of textiles, especially in the non-crimp regime, is the contact between yarns. The contact changes the macroscopic behavior of the pre-forming textiles (see, e.g., advanced modelling papers [12–15] and the contact issues between yarns in [16]). Yarn contacts cause higher gradients and rotations along one or multiple directions to join the constitutive equations [6,7,11–14], which is, according to the authors, beyond the state of the art in the commercial software tools.

In several papers of the Boisse group, different types of loading and problems with textiles were considered [15–18]. In our work, sharp bounds for the change of the limiting textile plate-like behavior are provided, e.g., at changing magnitude of the loading or strength of the contact (if the yarns are almost glued or can slide almost without friction).

The aim of our research is to give ranges of applicability of each homogenized model [5–7,19] and to extend the available computational tools by correct simulation of different single- and multi-layer textiles and different applications with them [8,9].

The derived mathematical framework is exemplified by our recent numerical simulations for multiple different textiles. Additionally, our currently developed simulation tool, TexMath (Version 0.4.0) [20], is presented, which allows us to systematically optimize textiles with respect to their desired functional behavior [21–23].

## 2. Simulation of Textiles with Stretchable Yarns

If the yarns are stretchable, stretching is coupled with the bending of the textile shell due to the strong frictional contact or adhesion. The coupling results in folding under tension. This effect is known as von Karman regime of shells, and it is derived from the yarn properties by asymptotic analysis [7]. This paper and a complementary structure optimization of the folding or buckling under tension [23] fully describe the folding mechanisms of textile strips under tension driven by the stretchable yarns integrated in a textile pattern.

A computational algorithm for textiles made of stretchable yarns with frictional contact and sliding at their crossing areas, with redistribution of the meshes due to the relaxation of the pre-stress in nodes caused by the sliding, is presented in [8,9]. The general model is applicable to woven fabrics made of stretchable yarns as well as knitted fabrics, as presented in Figure 1.

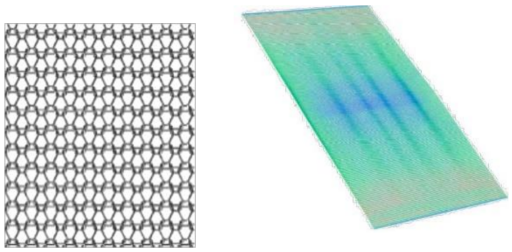

(**a**) (**b**)

**Figure 1.** (**a**) Knitted textile made of stretchable yarns; (**b**) folding simulation under tension.

In Figure 2 below, the algorithm is applied to a weft knitted textile sheet to simulate the loading-unloading under unit-axial tension. The simulation results are compared with experimental measurements. The simulation is performed with varying friction coefficient $\mu$.

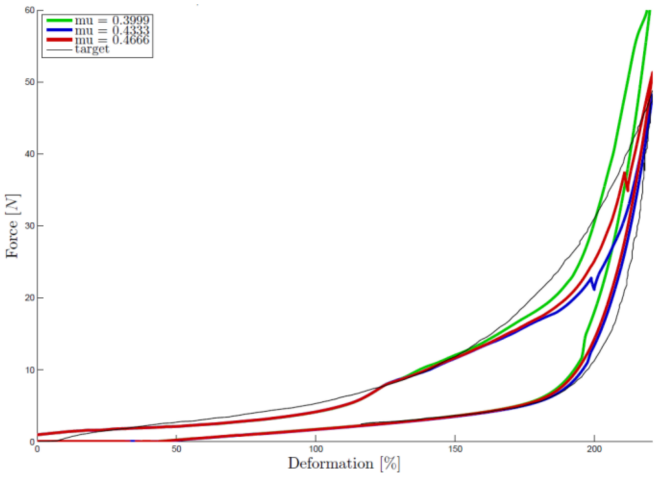


**Figure 2.** Comparison of simulation results (colored plots) and experimental data (black plot) for loading-unloading of weft knitted textile sheet. Varying friction coefficient $\mu$.

In [21], structure (pattern) optimization with state constraints (a desired stress or pressure profile in the fabric) for knitted fabrics is presented. In the paper, meshes in the knitting pattern are parametrized in a very simple way, corresponding to the knitting machine control parameters such as the stich-height, distance between needles and pre-stress in the yarns during the production in the machine. This allows to simulate the production, to relax to the table-measure with relaxation of the pre-stresses in the yarns between nodes and to find the residual pre-stress in nodes. Afterwards, the knitted fabric can be virtually put on a given body in an appropriate format (e.g., common for CAD-software).

## 3. Control Parameters for Textile Folding

Textile behavior under mechanical loading is influenced by multiple different aspects. The most important aspects considered in our research are: (i) elastic energy of yarns: linear (as in Section 4)–nonlinear (as in Section 2); (ii) order of the possible sliding in terms of the geometric parameters, the distance between yarns and their thickness, compared to the order of elastic strains-energy ("weak" or "strong" contact, [5,6]); (iii) influence of the boundary fixation (see Figure 3).

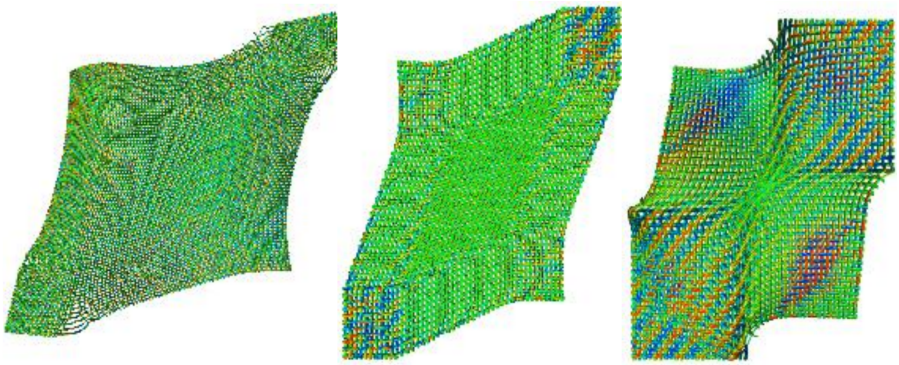

**Figure 3.** Qualitative simulation of a shear test with increasing measure of the clamped boundary (studied in [6]).

(iv) issue, if the radius of yarns is one order of magnitude smaller compared to the distance between them; (v) tension in yarns during the production (see Figure 4), which defines whether, after the relaxation, yarn's mean axis stays straight or oscillates, how big this crimp is, whether the averaged aces of the oscillating weft or warp belong to the mean plane of the effective plate, or if it is situated above or below this plane.

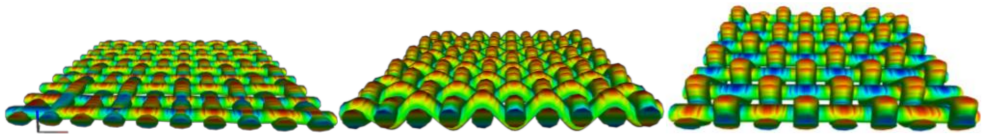

**Figure 4.** The left figure demonstrates yarns, as they are produced in the machine under high tension. The second and third figure show how the production tension influences the relaxed state of the fabric with the same yarns and weaving kind.

(vi) pre-stress in yarns, induced by thermo- (see Figure 5), electric- or moisture extension-swelling under some in-plane restrictions of the complete fabric.

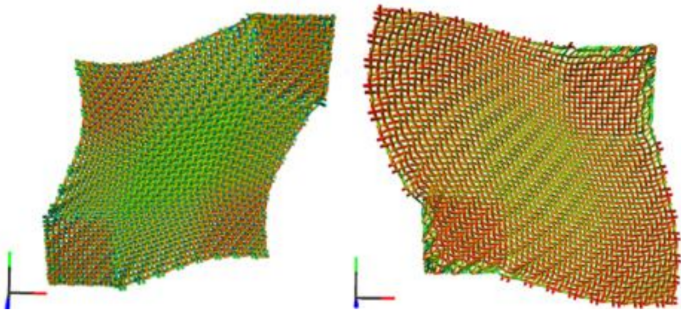

**Figure 5.** Simulation under the same boundary conditions and applied tension: without thermal expansion in yarns and with an expansion.

All the mentioned aspects play a crucial role in our numerical simulations and are considered in our modular software, TexMath (Version 0.4.0), which is further described in Section 6.

## 4. Asymptotic Modeling of Woven Textiles with Not Very Stretchable Yarns and High Friction or Weak Contact

In this section, the results obtained in [5,6] are emphasized and explained. These papers are dedicated for the modeling and asymptotic investigation of a linear elasticity problem on woven textile structures. The textiles are made of long and thin fibers, forming a periodic squared domain.

The domain is clamped only partially (see Figure 6c), and an in-plane sliding between the fibers is bounded by a contact function, which is related to the friction between yarns. It is expressed in the powers of the distance between two weft or two warp yarns. Both partial clamp and loose contact result in a domain split with different behaviors in each of the four parts schematically shown in Figure 6c.

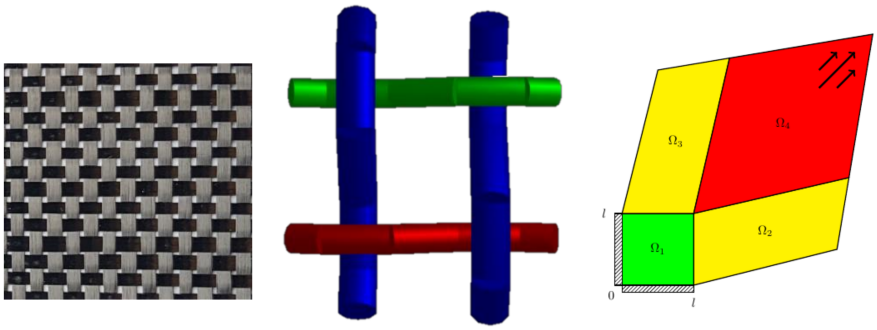


(**a**) (**b**) (**c**)

**Figure 6.** (**a**) Simple weave pattern; (**b**) periodicity cell parametrized by the distance between yarns, their thickness and contact between yarns; (**c**) schematic structure domain with fixation on a part of the lateral boundary.

In [5–7], two small parameters were introduced, which denote the radius of yarns and the distance between them. Homogenization and dimension reduction is used to derive the macroscopic behavior in each textile part. In the papers, the limit in the contact elasticity problem on the yarn's structure (a fabric) with respect to both small geometric parameters is investigated. In the limit, different limiting plate-behaviors for different scaling regimes are obtained, i.e., if sliding or elastic deformation dominates. The applied forces are chosen in a way to stay in the elastic regime without large stretching in the yarns.

Practically, this means that one needs to measure the applied forces and tractions and estimate them in terms of powers of the radius or distance between yarns, in order to apply the correct simulation model.

The main results of these papers are illustrated in Figure 7; Figure 8. In the case that sliding dominates the elastic energy of the yarns, the macroscopic effective solution results in two macroscopic plates. The plates are spanned on only weft or only warp yarns with high gradients just along the yarns in each plate. Both are coupled by the macroscopic contact condition including the in-plane rotations. Paper [6] provides the critical shear angles for woven textiles, computed only from the weaving pattern and fiber cross-sections.

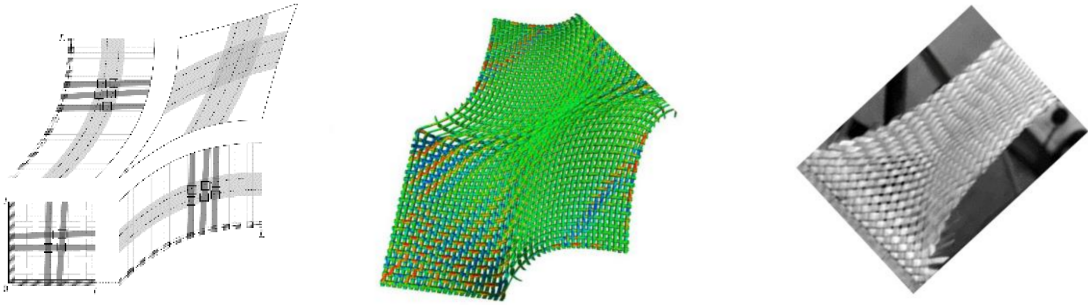

(**a**) (**b**) (**c**)

**Figure 7.** (**a**) Schematic deformation of yarns with a weak contact (small friction) obtained by asymptotic analysis in [5,6]; (**b**) its numerical implementation; (**c**) experiment showing a shear angle.

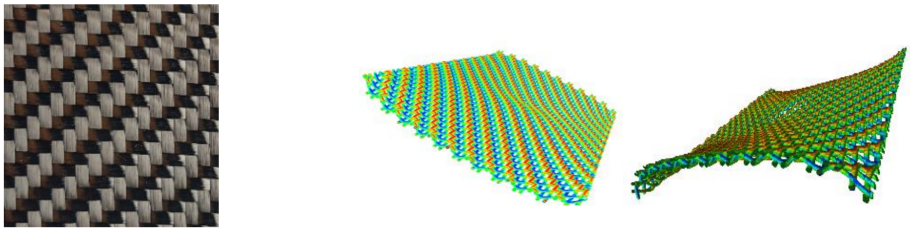

(**a**) (**b**)

**Figure 8.** (**a**) Double twill woven fabric; (**b**) folding simulation of the fabric under tension caused by the diagonal pattern and strong contact between yarns.

Table 1 shows the experimental validation of the theoretical prediction in [6]. The computational errors are 1–2%, which corresponds to an angle difference of 3°.

**Table 1.** Calculated critical shear angles $\gamma_{cr}$ and comparison to the measurement.

| Material | Type | Weave | $\gamma_{cr}$(°) | Computational Error (°) |
|---|---|---|---|---|
| Glass | Fabric | Twill | 49 | 0.01 |
| Glass | Fabric | Canvas | 34 | 0.23 |
| Carbon | Fabric | Cr. twill | 47 | 3.02 |
| Carbon | Fabric | Canvas | 26 | 2.82 |

The experimental validation was performed by RWTH Aachen Institute of Textile Technology. The sensitivity study of the shear angles to the textile design can be found in [24]. Further technical details for Table 1 on rowing cross-sections, distances between rowing axes and rowing stiffness are listed in [24].

In paper [7], a homogenization algorithm is proposed, which computes the effective pre-strain in textiles from known pre-strain in the single yarns. Furthermore, simple formulas are presented, which allow to compute the effective pre-strain that is critical for buckling of a fabric under tension: the buckling across the tension direction or under compression (buckling in the compressed direction). The effective pre-strain (that is) critical for buckling is computed from the fabric's effective bending and tension properties, as well as its length and width.

## 5. Simulation of Spacer Fabrics with a Significant Dimension Reduction

Due to their 3D structure, spacer fabrics possess outstanding properties, such as compressive elasticity and permeability, resulting in enhanced functionality of the products manufactured from them. Especially warp knitted spacer fabrics are already established as foam alternatives, upholstery pads and pressure-elastic components with rear-ventilation effect, as well as filter materials and reinforcing materials for composites. In [25], a simulation of the compressional elastic, relaxation and permeability properties of spacer fabrics was proposed. The detailed structural modeling helps to better understand the energy-driven processes in warp knitted spacer fabrics and the basic underlying mechanisms. Such simulations can be used for function-adapted product developments and replace the previous extremely time-consuming and costly experimental technology.

One focus of our current research is to find an optimum for local reinforcement of warp knitted spacer fabrics using seams. The local reinforcement should provide desired compression stiffness and a desired curvature of the fabric between two seams. The aim here is to develop a method to variably design the distance between the knitted surfaces in the seam area and to achieve a defined curvature by finding the optimal seam characteristics (height, width and so on) and distance between the seams.

Unlike previous sections, where an overview about particular algorithms and results from other papers was given and illustrated by some qualitative examples, a particular example is considered in this section. A warp knitted spacer fabric with closed structure

and thickness of 20 mm is investigated. Seams of types of double quilt stiches with varying stitch parameters were inserted using an "M-Type" Delta machine (Dürkopp-Adler AG, Bielefeld, Germany). The tension in the sewing yarn as well as the stitch length are known and can be varied.

Using the TexMath module MeshUp (Figure 9), the spacer fabric was digitalized in the computer in the stage as it comes from the machine. Afterwards, it was virtually extended in the plane and then compressed. All the performed deformations were carried out within the TexMath module FiberFEM for mechanical simulation of textiles. At the end of the mentioned steps, the yarns are already pre-strained. This is the preparation step for the insertion of stitches in the 3D structures.

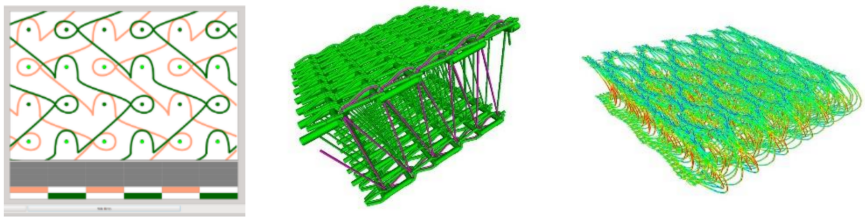

(**a**) (**b**) (**c**)

**Figure 9.** (**a**) Generation of each layer and connector by the TexMath module MeshUp; (**b**) visualization of the mesh with individual threads; (**c**) simulation of the outer-plane compression of the spacer fabric by the module FiberFEM.

Figure 10 shows the process of the seam insertion under given machine parameters, reasoning the seam-yarn pre-stress. Using the known pre-strain in the seam, it was placed in the digitalized fabric; see Figure 11a. The compression is simulated as the next step by FiberFEM. To simulate further compression under large tension in the seam, the commercial tool, ABAQUS, was used; see Figure 11c.

**Figure 10.** Warp knitted fabric with seams of different 3D sewing parameters of quilt stitches (TU-Dresden).

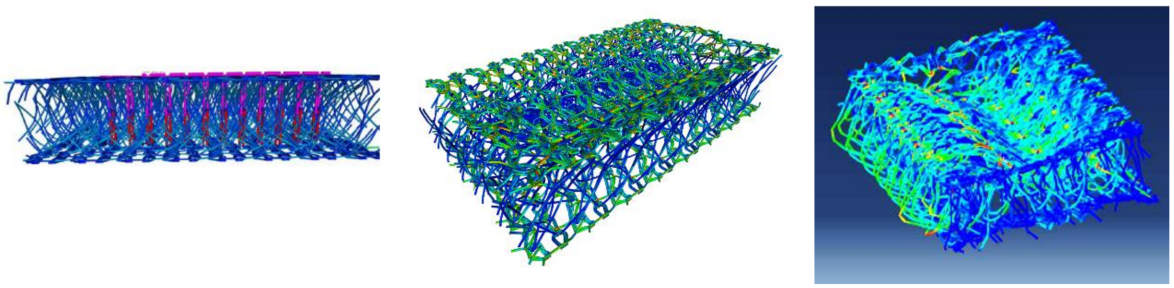

(**a**) (**b**) (**c**)

**Figure 11.** (**a**) "3D sewing" and spacer fabric with a seam. A seam-yarn is integrated into the spacer structure of the fabric under pre-strain; (**b**) TexMath simulation of the compression of the spacer fabric under this pre-strain; (**c**) ABAQUS simulation for large deformations.

In another focus of our current research, horizontal non-viscous fluid flow through a spacer fabric is considered, see Figure 12. The spacer fabric is insulated at the top and bottom. Periodicity of the fabric allows to reduce the problem to one periodicity cell for simulation. The deflection of the monofilaments connecting the knitted layers caused by fluid-solid interaction is of special interest.

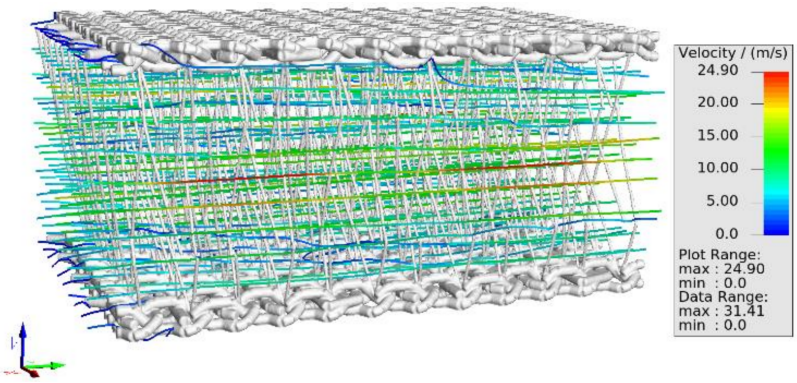


**Figure 12.** Flow stream lines of horizontal non-viscous fluid flow through a spacer fabric.

In [25], the stationary Stokes flow through spacer fabrics in the compressed and non-compressed state of the fabric was already simulated; see Figure 13. The simulations were performed in the Software GeoDict (www.geodict.com). However, the fluid–solid interaction was not considered there. The spacer fabric was assumed to be rigid, and the flow through the uncompressed fabric was simulated first (the first row in Figure 13). Afterwards, the fabric was compressed with TexMath, and the Stokes flow in the compressed structure was simulated, again, assuming it to be rigid for this simulation.

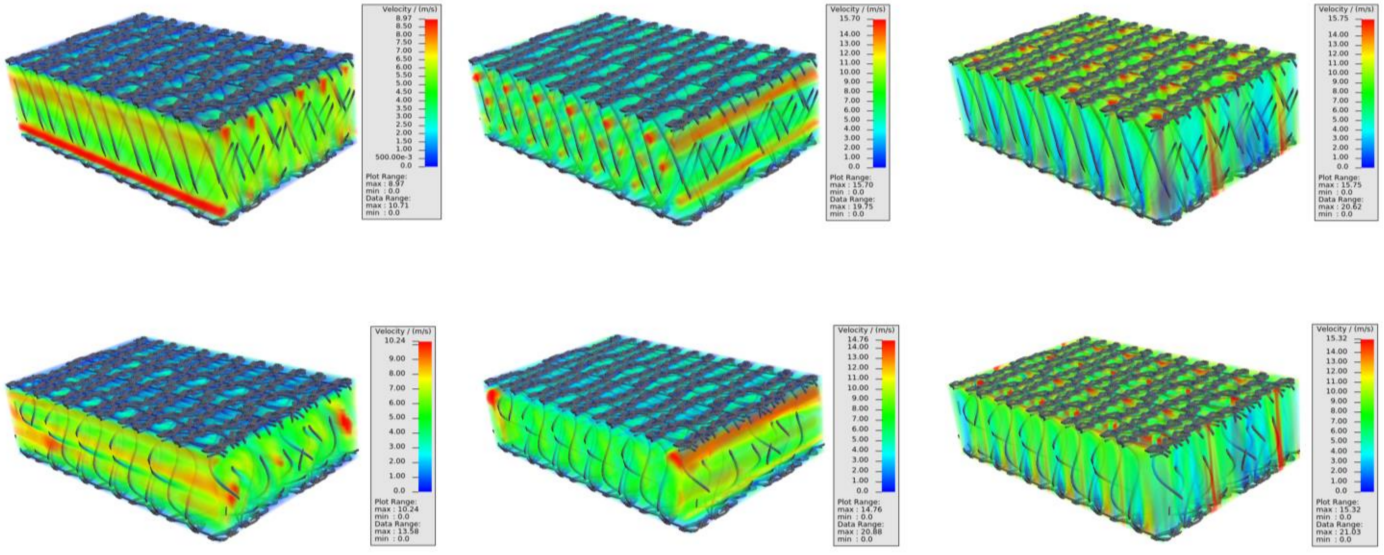

**Figure 13.** Stationary Stokes flow in a spacer fabric before and after an outer-plane compression, similar to [25]. The flow direction is horizontal in the first two figures and vertical in the third figure in each row, respectively.

In Figure 14, the experimental validation from [25] is recalled.

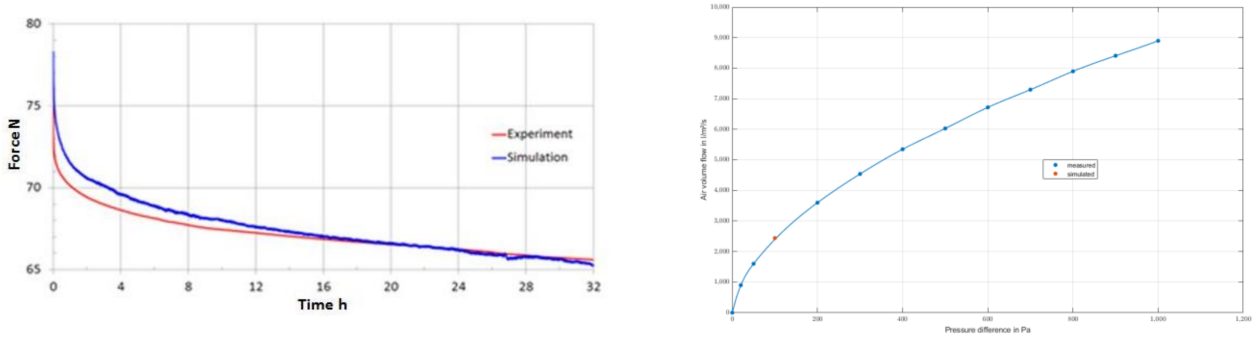


(**a**) (**b**)

**Figure 14.** (**a**) Compression of spacer fabric with relaxation over 32 h, comparison of experiment and the simulation; (**b**) air volume flow per area as a function of pressure difference through a spacer fabric. Measured values and simulation for pressure difference 100 Pa.

Examining the pressure distribution in the fluid computed within the assumption of rigid beams in one time-step by GeoDict, one can observe that it jumps over vertical lattices as shown in Figure 15 below.

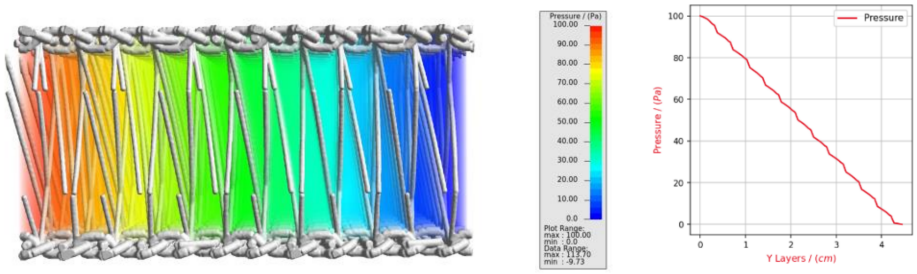


(**a**) (**b**)

**Figure 15.** (**a**) GeoDict simulation of the horizontal flow in the spacer fabric. Pressure profile in the fluid with jumps on the vertical monofilament lattices; (**b**) snapshot taken in the middle point of the cross-section.

Our first algorithmic idea for the computation of the monofilament deflection is to restrict the pressure jump in the fluid to the 1-dimensional center axes of the monofilaments for each time step. The reduction approach is sketched in Figure 16. The result is a force $F$ that acts on the monofilament axes and that can be expressed in a few nodal points along the axes.

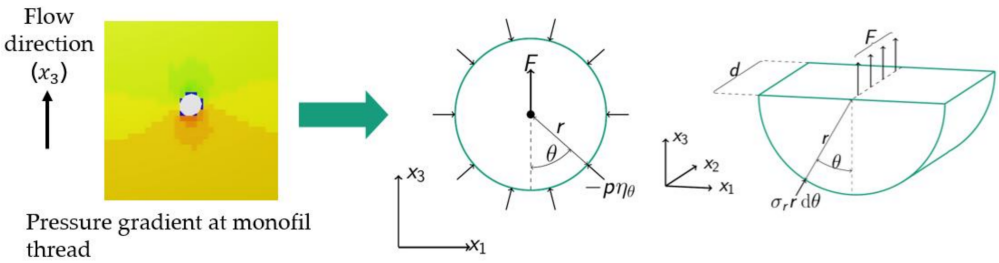


**Figure 16.** Restriction of applied pressure to beam axes.

The computed force is then used as an artificial right-hand side in the linear elasticity problem for the monofilament deflection. This problem can be solved efficiently with the TexMath module FiberFEM. The simulation results for a spacer fabric with varying yarn radii are presented in Figure 17.

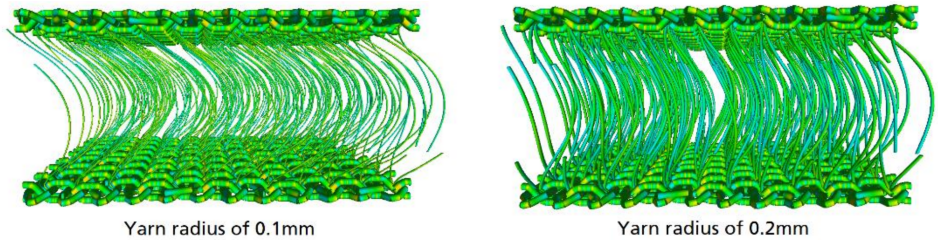


**Figure 17.** Simulation of the fluid-solid interaction with the same in- and out-flow conditions, same initial conditions but different yarn thicknesses. Fixated bottom and top. The yarn deflection and axial stresses in yarns are visualized.

Although, some time ago, such an iterative coupling of separate fluid and solid evolutions was considered state of the art in the solution accuracy and resolving of single fibers, it was time costly and not very precise in the sense of the statement of a coupled fluid–solid interaction problem.

Therefore, the coupled fluid–solid problems are solved simultaneously in a second approach. An asymptotic dimension reduction in thin beams and the coupling of 3D and 1D problems are employed. The idea is to reduce the problem to finding the displacement field, velocity field and fluid pressure only in some nodes/points along the monofilament axes. Afterwards, the solution fields are extended inside the monofilament and inside the fluid domain, to be able to reconstruct the solution in each point of the coupled, geometrically multi-scale domain.

As stated, the correct modeling is a main and delicate question. Exactly as in the previous sections, the relation between the textile thickness and applied forces will determine if the textile will behave as a stretchable membrane or as a bending-resistant plate or shell. In fact, here, in the fluid–solid interaction, the relation between the yarn's stiffness and the fluid viscosity plays a crucial role. If their relation is proportional to the yarn's thickness, the frictional forces at the monofilaments will rise their tension, and they all together will work like an extensional membrane. However, if the monofilaments are much stiffer than the fluid, as in the case of the spacer fabric infiltrated by water (this corresponds to the cubic yarn-thickness in their relation), the forest of monofilaments will bend and the curvature of the monofilaments will be proportional to the pressure jump in a non-local (such as memory or relaxation) setting [19].

The problem described in [19] is initially formulated with 3D fields, i.e., velocity and displacements, which can be restricted to the 2D mean surface of the monofilament axes. Our numerical approach uses a finite element method that further reduces the problem to a few nodes along the axes. The arising test functions are illustrated in Figure 18. In between two adjacent monofilament forests, linear interpolation is applied.

After solving the finite element formulation, the global nodal solution is extended to the 3D beam domain by an interpolation technique described in [6]. The extension is then used to reconstruct the fluid velocity and pressure in the whole fluid domain. The numerical implementation is currently in progress and will be the subject of future publications.

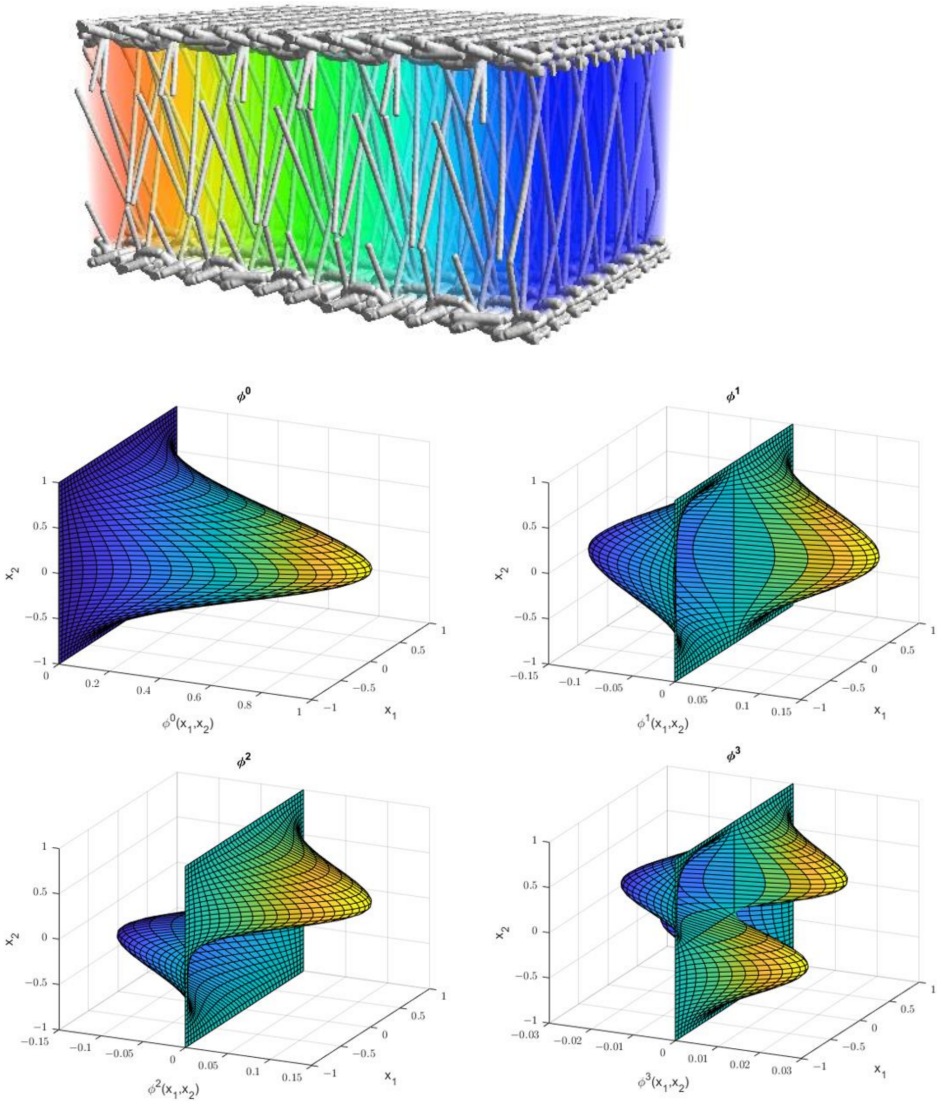


**Figure 18.** Test functions on the mean surface of monofilament forests for the finite element method.

## 6. Textile Simulation and Optimization within the TexMath Software Tool

Our software tool, TexMath [20], is a modular program for simulating mechanical material properties and optimizing textile products as well as multi-scale problems for textile applications. One area of application for the TexMath software is the optimization of compression textiles for the medical sector or for sports. For optimal effectiveness, the fit of the material is particularly important.

As a practical example, the optimal design of a knitted bandage with predefined compression properties was considered. The textile has to develop a given pressure profile on the body. In [21], an efficient two-scale optimization algorithm, based on modern numerical methods and newest developments in homogenization approaches, is proposed. This multiscale optimization method is implemented and combined in TexMath. The design process is illustrated in Figure 19. As a first step, the knitting process is simulated with TexMath. The resulting virtual bandage is then loaded in another simulation and put on a virtual arm or leg. The calculated pressure profile makes it possible to evaluate the compression properties of the bandage in advance and also to directly control the knitting machine according to the optimal design.

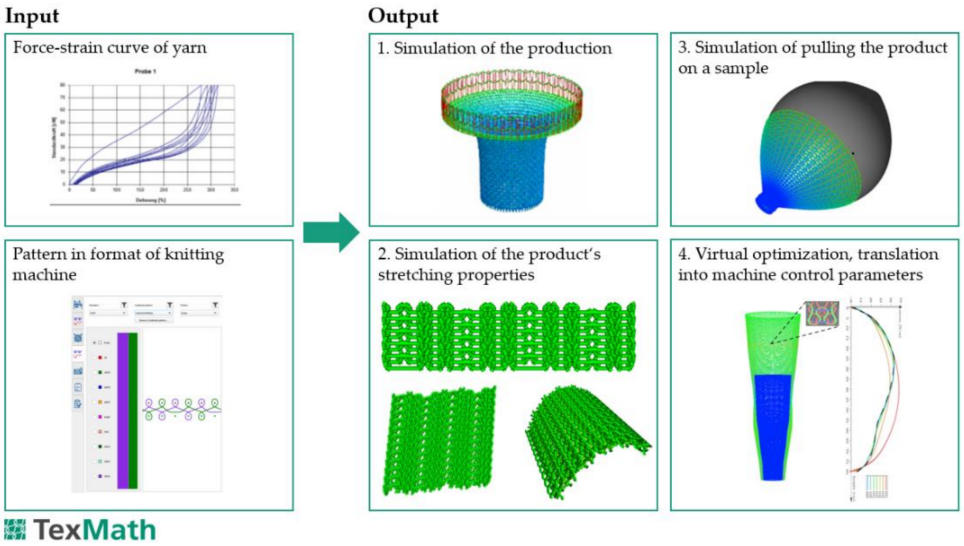


**Figure 19.** Design optimization loop from the knitting machine to the knitting fabrics with desired properties.

In a second example, the process of putting on a medical mask produced from knitted fabric is simulated. The simulation results are presented in Figure 20.

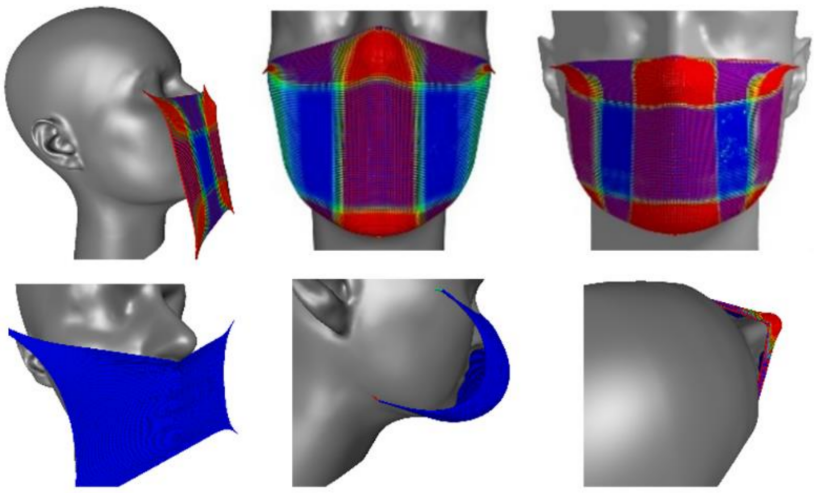

**Figure 20.** Simulation of putting on a mask with the yarn resolution. Colors provide information about tension. The influence of face shape and knitting tension on the mask fitting form is demonstrated. ©Fraunhofer ITWM.

The second row of figures, in Figure 20, demonstrates an advantage of the simulation with the full yarn resolution: it allows to control the fabric behavior by changing the production pre-strain in the yarns. The left mask is produced with a high pre-stress and it slides at the unsupported boundary and high-curvature regions of the body. Its macroscopic behavior corresponds to an elastic membrane, working only on tension. One sees small folding under the nose, which is of the same nature as in Figure 1. The second mask in the second row of Figure 20 is produced with fewer pre-stress, hence being denser. Macroscopically, it behaves similar to a shell that works rather on bending than on tension. Its behavior corresponds to Figure 8.

TexMath can also be used to design and simulate spacer textiles, as seen in the previous section. The goal is to optimize them in advance in terms of structure and infiltration properties.

A demo version of the software program will soon be available. The newly developed input interface is particularly user-friendly. The textile class (i.e., knitted, warp-knitted,

woven and spacer fabrics) can be easily set. The new graphic interface allows simple and fast configuration, see Figure 21.

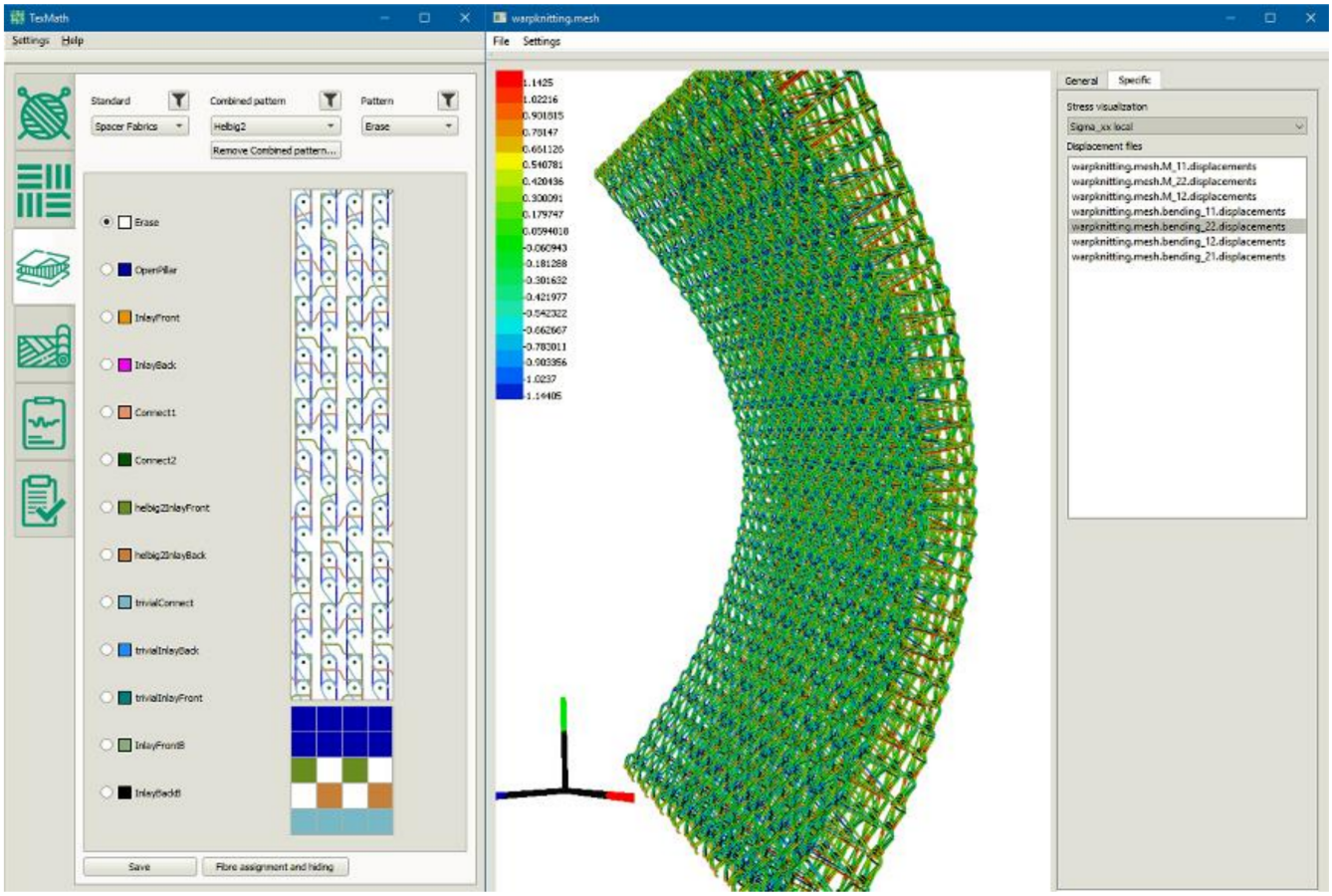


**Figure 21.** Structure generation and bending simulation of a spacer fabric. ©Fraunhofer ITWM.

The experimental validation of simulations by the TexMath software can be found in [9] for weft knitted, in [25] for spacer fabrics and in reports of a joint AIF-project "OptiDrape" with the Textile institute ITA in Aachen for woven simple and twill patterns with different shifts and pre-forming textiles; see [24].

## 7. Conclusions

In this paper, an overview of our recent publications concerning different aspects of the simulation of textiles was provided. Modeling approaches and results in the mathematical analysis for textiles with stretchable yarns, as well as for textiles with not very stretchable yarns and high friction or weak contact were presented. Moreover, our latest research in the simulation of spacer fabrics, which will be the topic of future publications, were shown. Additionally, examples for the numerical simulation and design optimization process within our software tool, TexMath, were provided. As only a survey and interpretation of some mathematical investigations was given, we refer the interested reader to our presented papers for detailed results and further information.

**Author Contributions:** Conceptualization, J.O.; methodology, J.O.; software, D.N. and O.S.; validation, K.P. and K.S.; formal analysis, J.O. and M.K.; investigation, O.S., D.N., M.K. and K.P.; resources, K.P.; data curation, J.O. and K.S.; writing—original draft preparation, J.O. and K.S.; writing—review and editing, M.K., K.P. and K.S.; visualization, M.K., D.N. and O.S.; supervision, J.O. and K.S.; project administration, J.O. and K.S.; funding acquisition, J.O. and K.S.; All authors have read and agreed to the published version of the manuscript.

**Funding:** The research is funded by DFG, German Research Foundation, project numbers ROE 1303/20-1, PI 1251/1-3, OR 190/6-1, OR 190/6-3.

**Institutional Review Board Statement:** Not applicable.

**Informed Consent Statement:** Not applicable.

**Data Availability Statement:** Not applicable.

**Acknowledgments:** We thank the colleagues from RWTH Aachen Institute of Textile Technology and the support of the AIF-project OPTI-DRAPE, as well as the German national foundation supporting our project about the simulation of spacer fabrics.

**Conflicts of Interest:** The authors declare no conflict of interest.

## References

1. Byrne, C. Technical textiles market–an overview. In *Handbook of Technical Textiles*, 1st ed.; Horrocks, A.R., Anand, S.C., Eds.; Woodhead Publishing: Sawston, UK, 2000; pp. 1–23. [CrossRef]
2. Milwich, M.; Speck, T.; Speck, O.; Stegmaier, T.; Planck, H. Biomimetics and technical textiles: solving engineering problems with the help of nature's wisdom. *Am. J. Bot.* **2006**, *93*, 1455–1465. [CrossRef] [PubMed]
3. Ciarlet, P.G. Finite Element Methods for the Plate Problem. In *The Finite Element Method for Elliptic Problems*, 2nd ed.; SIAM: Philadelphia, PA, USA, 2002; pp. 333–380. [CrossRef]
4. Ciarlet, P.G. Finite Element Methods for Shells. In *The Finite Element Method for Elliptic Problems*, 2nd ed.; SIAM: Philadelphia, PA, USA, 2002; pp. 425–468. [CrossRef]
5. Griso, G.; Orlik, J.; Wackerle, S. Asymptotic behavior for textiles. *SIAM J. Math. Anal.* **2020**, *52*, 1639–1689. [CrossRef]
6. Falconi, R.; Griso, G.; Orlik, J.; Wackerle, S. Homogenization for textile with loose contact. *SIAM J. Math. Anal.*. under review.
7. Griso, G.; Orlik, J.; Wackerle, S. Asymptotic behavior for textiles in von-Karman regime. *J. Math. Pures Appl.* **2020**, *144*, 164–193. [CrossRef]
8. Shiryaev, V.; Neusius, D.; Orlik, J. Extension of One-Dimensional Models for Hyperelastic String Structures under Coulomb Friction with Adhesion. *Lubricants* **2018**, *6*, 33. [CrossRef]
9. Shiryaev, V.; Orlik, J. A one-dimensional computational model for hyperelastic string structures with Coulomb friction. *Math. Methods Appl. Sci.* **2017**, *40*, 741–756. [CrossRef]
10. Nezami, F.N.; Gereke, T.; Cherif, C. Analyses of interaction mechanisms during forming of multilayer carbon woven fabrics for composite applications. *Compos. Part A Appl. Sci. Manuf.* **2016**, *84*, 406–416. [CrossRef]
11. Bardl, G.; Nocke, A.; Hübner, M.; Gereke, T.; Pooch, M.; Schulze, M.; Heuer, H.; Schiller, M.; Kupke, R.; Klein, M.; et al. Analysis of the 3D draping behavior of carbon fiber non-crimp fabrics with eddy current technique. *Compos. Part B Eng.* **2018**, *132*, 49–60. [CrossRef]
12. Barbagallo, G.; Madeo, A.; Azehaf, I. Bias extension test on an unbalanced woven composite reinforcement: experiments and modeling via a second gradient continuum approach. *J. Compos. Mater.* **2017**, *51*, 2–153. [CrossRef]
13. Madeo, A.; Barbagallo, G.; D'Agostino, M.V.; Boisse, P. Continuum and discrete models for unbalanced woven fabrics. *Int. J. Solids Struct.* **2016**, *94–95*, 263–284. [CrossRef]
14. Boisse, P.; Hamila, N.; Madeo, A. The difficulties in modeling the mechanical behavior of textile composite reinforcements with standard continuum mechanics of Cauchy. Some possible remedies. *Int. J. Solids Struct.* **2018**, *154*, 55–65. [CrossRef]
15. Galkin, S.; Kunze, E.; Kärger, L.; Böhm, R.; Gude, M. Experimental and Numerical Determination of the Local Fiber Volume Content of Unidirectional Non-Crimp Fabrics with Forming Effects. *J. Compos. Sci.* **2019**, *3*, 19. [CrossRef]
16. Durville, D. Modeling Frictional Contact Interactions in Fiber Assemblies. In Proceedings of the 3rd International Conference on Computational Contact Mechanics (ICCCM 2013), Lecce, Italy, 10–12 July 2013.
17. Boisse, P.; Borr, M.; Buet, K.; Cherouat, A. Finite element simulations of textile composite forming including the biaxial fabric behavior. *Compos. Part B Eng.* **1997**, *28*, 453–464. [CrossRef]
18. Boisse, P.; Hamila, N.; Vidal-Sallé, E.; Dumont, F. Simulation of wrinkling during textile composite reinforcement forming. Influence of tensile, in-plane shear and bending stiffnesses. *Compos. Sci. Technol.* **2011**, *71*, 683–692. [CrossRef]
19. Orlik, J.; Panassenko, G.; Stavr, R. Asymptotic analysis of a viscous fluid layer separated by a thin rigid stratified elastic plate. *J. Appl. Anal.* **2021**, *100*, 589–629. [CrossRef]
20. TexMath Software Tool for the Simulation of Knitted, Woven and Warp Knitted Fabrics. Available online: https://www.itwm.fraunhofer.de/en/departments/sms/products-services/texmath.html (accessed on 25 May 2021).
21. Orlik, J.; Panassenko, G.; Shiryaev, V. Optimization of textile-like materials via homogenization and dimension reduction. *SIAM Multiscale Model. Simul.* **2016**, *14*, 637–667. [CrossRef]
22. Hauck, M.; Klar, A.; Orlik, J. Design optimization in periodic structural plates under the constraint of anisotropy. *ZAMM* **2017**, *97*, 1220–1235. [CrossRef]
23. Wackerle, S.; Pinnau, R.; Orlik, J. Optimization of Buckling for Textiles. In *Progress in Industrial Mathematics at ECMI 2018*, 1st ed.; Farago, I., Izsak, F., Simon, P., Eds.; Springer: Cham, Switzerland, 2019. [CrossRef]

24. Wackerle, S.; Orlik, J.; Hauck, M.; Lykhachova, O.; Steiner, K. The Way to Design a Textile with Required Critical Folding Deformation. *Procedia Manuf.* **2020**, *47*, 174–181. [CrossRef]
25. Orlik, J.; Pietsch, K.; Fassbänder, A.; Sivak, O.; Steiner, K. Simulation and Experimental Validation of Spacer Fabrics Based on their Structure and Yarn's Properties. *Appl. Compos. Mater.* **2018**, *25*, 709–724. [CrossRef]

textiles

MDPI

*Article*

# A Comparison of Two Different Light Booths for Measuring Color Difference of Metameric Pairs

**Azmary Akter Mukthy *, Michal Vik and Martina Viková**

Department of Materials Engineering, Faculty of Textile Engineering, Technical University of Liberec, Studentská 1402/2, 461 17 Liberec, Czech Republic; michal.vik@tul.cz (M.V.); martina.vikova@tul.cz (M.V.)
* Correspondence: azmary.akter.mukthy@tul.cz

**Abstract:** A standardized source of light is essential for visual color assessments, which is why lighting booths were developed. For the best results in visual assessment, it is important to consider the right choice of light source, the right viewing conditions, and the variability of the viewer. To date, many light booth technologies have been introduced to meet user demands. Since most of the light sources on the market are characterized by the designer or manufacturer, the resulting variations from booth-to-booth remain. In this study, we compared the performance of two standard light booths to assess the color difference of eleven metameric pairs. In this study, we checked an earlier technology-based light booth that is still used in the textile industry and contains illuminant A (Tungsten lamp) with CCT 2700 K, TL84 (tri-band fluorescent tube) with CCT 4000 K, and simulator D65 (CCT 6500 K) with a different light booth whose original light sources have been replaced by currently available LED retro kits from equivalent CCTs. As an inexperienced customer or industrial user, our question was, how important is this replacement? The results revealed that two different standard lighting technologies with similar CCTs cannot reproduce the same estimates because the light sources produced different SPDs. It is illustrating that caution is necessary when comparing results obtained from two different light booths containing light sources with similar CCTs but different SPDs. This comparative study suggested that the variability of the light sources' SPDs or the observer or the sample should be modeled considering light booth's technology to estimate its contribution to the overall variability. The close relationship between perceived and CAM02-UCS suggests that if both booths are used after the light sources have been calibrated, a formula based on color appearance models must be used to predict color appearance. To obtain better agreement between perceived and calculated color difference, one must need to avoid light booths with nominally white light sources.

**Keywords:** light booth; metameric pairs; visual assessment; gray scale; standard deviation; CAM02-UCS; color difference formula

**Citation:** Mukthy, A.A.; Vik, M.; Viková, M. A Comparison of Two Different Light Booths for Measuring Color Difference of Metameric Pairs. *Textiles* **2021**, *1*, 558–570. https://doi.org/10.3390/textiles1030030

Academic Editor: Rajesh Mishra

Received: 7 November 2021
Accepted: 30 November 2021
Published: 2 December 2021



## 1. Introduction

The visual appearance of color is a sensory attribute and is the result of a complex interaction of the object, the incident light, and human perception [1–4]. Judgment of visual appearance of color is often influenced by environmental elements, surface conditions, and optical illusions. Therefore, the visual assessment of colors is particularly complex and depends on many factors, such as observer sensitivity, age and color memory, viewing angle, light source, surface condition, object's background, area of the colored surface, and so on. To overcome these complexities in color evaluation, the implementation of color control technologies such as spectrophotometers, software, and other tools such as light booths are being developed [5]. ASTM D1729 [6] specifies the viewing geometry, quantity, and spectral properties of the lighting as well as environmental conditions for critical visual color measurements. Both the viewing environment and the lighting are critical factors for a consistent color appearance and effective color communication.

To optimally meet the application and operational requirements, there are many lighting booths on the market that are equipped with many standard light sources (the

illuminant) as defined by the Commission Internationale de l'Eclairage (CIE) [7,8]. The use of high-performance light booths enables reliable color assessment and helps identify color inconsistencies, metameric effects, and the influence of brighteners. However, the performance of different light and lighting booths with the same specification can vary greatly [9]. CIE guidelines describe several parameters including lighting and sample presentation methods [10] for visual color assessment. Different sample presentation methods may introduce variations in the measurement [1], but if the same sample presentation methods are used, variations may be attributed to the light booth conditions such as the actual color temperature of the light, light intensity, lamp operation time, etc. A studied revealed that the luminance level in several light booths varied from 100 to >1000 $cd/m^2$ [11]. There are studies that show how correlated color temperature and illuminance affect color perception [12–15] and users' feeling [16–19].

In practice, calibrated light booths are recommended for assessing objects' color differences [20]. Lighting booths that use older filtered technology are more expensive to maintain. Light booths that use newer fluorescent technology require much less maintenance and are more affordable; nevertheless, at present, fluorescent lamps are gradually being replaced by LED technology, so it is important to compare both technologies. To ensure correct color quality and compliance with user specifications, they only need to be recalibrated and replaced with new light. The regular and appropriate use of a light booth improves the workflow, shortens the cycle time, and shows a positive return on investment. The LED retro kits available today allow the replacement of previously used fluorescent tubes, but the important question arises as to how these fit together with the earlier usability of such a light booth.

In this study, we used two standard light booths to compare their performance in assessing the color differences of twelve metameric samples under different light sources equipped with them. We have also studied the variability within and among observer responses under two booths. Several predictive models have been developed to correlate visual assessment with measured values. The perceived values set the benchmark for the instrumental measurement comparisons [21–23]. Some models for calculating color difference are CIELAB, CIEDE2000 [24], OSA-UCS [25], ULAB [26], CAM02-UCS [27], and CAM16-UCS [28].

The purposes of the present study were (i) to assess and compare the visual color difference of the eleven metameric samples for two light booths, (ii) to analyze the correlation between the visual and calculated color difference under tested light sources, and (iii) to evaluate the performance of color difference formulas for experimental conditions. With this study, advantage may be taken of the special merits of a particular light booth such as affordability and easy maintenance while still enabling the comparison of results obtained for a more comprehensive but expensive light booth.

## 2. Materials and Methods

### *2.1. Samples*

The visual experiment used eleven metameric pairs of samples to examine different metamerism indices under different light sources. Figure 1 depicts the distribution of eleven metameric pairs in the a*b* and L*a* plane of the CIELAB color space under Illuminant D65/2°.

As we can see from both figures, sample pairs 1 to 7 have almost a constant lightness value (64.5 approximately). Sample pairs 8, 9, and 11 have similar chroma and hue, whereas sample pairs 3 and 10 have high chroma value with nearly similar lightness. The mean color difference of the 11 metamers calculated under standard D65/2° was 3.8 ΔE*ab units.

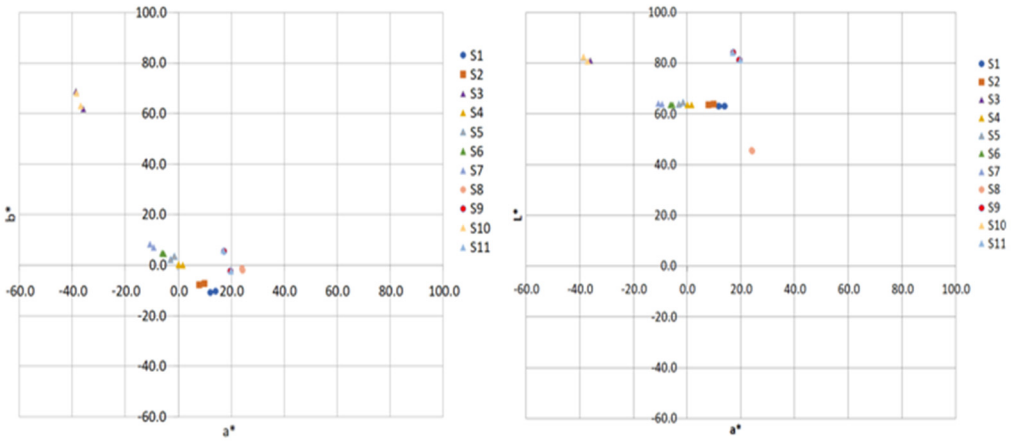


**Figure 1.** Distribution of 11 sample pairs on the a*b* plane (**left**) and L*a* (**right**) plane under standard D65/2°.

### *2.2. Light Sources*

The visual experiment used eleven metameric pairs of samples to examine different metamerism indices under different light sources. Two standard lighting booths were used for this experiment. Light booth I is based on an old ICS-Texicon Multilight lighting cabinet, where the original light sources were replaced by corresponding LED retro kits with similar correlated color temperature (CCT). Light booth II was Gretag Macbeth (now X-Rite) Judge-II. For the visual assessment, we selected BLED65, BLED40, and BLED27, which represent the light sources with nominal CCT 6500 K, 4000 K, and 2700 K, respectively, for light booth I; and Daylight (Simulator D65), TL84 (Tri-band fluorescent tube), and A (Tungsten lamp), which represent the light sources with a nominal CCT of 6500 K, 4000 K, and 2700 K respectively for light booth II. Throughout this article, the name of the light sources indicates their respected nominal CCT. The spectral power distribution and the colorimetric values of the different configurations was measured with a Photo Research PR-740 spectroradiometer over a plaque containing pressed Barium Sulfate white standard produced by Merck placed in the center of the bottom surface of each lighting booth. The spectral power distribution and position of the light sources in the xy chromaticity diagram are shown in Figures 2 and 3, respectively.

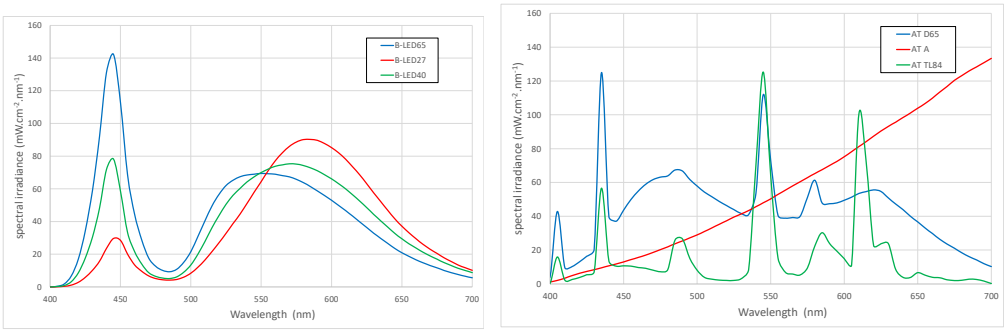


**Figure 2.** SPDs of test light sources in the two test booths. **Left**: light booth I and **right**: light booth II. In the figure: BLED65, BLED40, and BLED27 representing the light sources with nominal CCT 6500 K, 4000 K, and 2700 K respectively for light booth I; and Daylight (Simulator D65), TL84 (Tri-band fluorescent tube), and A (Tungsten lamp) representing the light sources with nominal CCT values of 6500 K, 4000 K, and 2700 K respectively for light booth II.

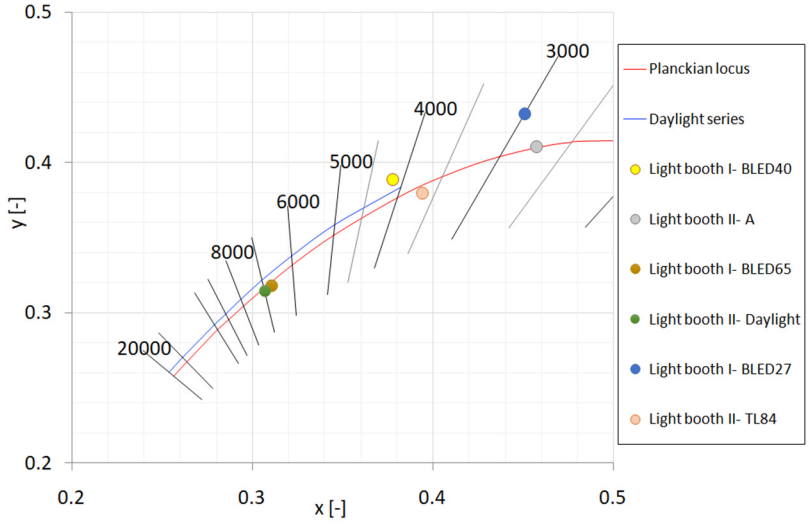


**Figure 3.** Different positions of the test light sources in the xy chromaticity diagram. In the figure, BLED65, BLED40, and BLED27 represent the light sources with nominal CCT 6500 K, 4000 K, and 2700 K respectively for light booth I; and Daylight (Simulator D65), TL84 (Tri-band fluorescent tube), and A (Tungsten lamp) represent the light sources with nominal CCT 6500 K, 4000 K, and 2700 K respectively for light booth II.

Table 1 summarizes measurements of chromaticity, correlated color temperature (CCT), and luminance level. From Table 1 and Figure 3, the light sources of viewing booth II are located on or close to the Planckian locus, whereas for booth I, BLED40 and BLED27 are situated even outside the daylight series. From Table 1 and Figure 3, the light sources of viewing booth II are on or near Planckian locus, while BLED40 and BLED27 of booth I are even outside the daylight series. Figure 2 is showing that both viewing booths have a relatively different spectral quality of the light sources.

**Table 1.** The parameters of the light sources. In the table, BLED65, BLED40, and BLED27 represent the light sources with nominal CCT 6500 K, 4000 K, and 2700 K, respectively for light booth I; and Daylight (Simulator D65), TL84 (Tri-band fluorescent tube) and A (Tungsten lamp) represent the light sources with nominal CCT 6500 K, 4000 K, and 2700 K respectively for light booth II.

| **Measured Values** | **Light Booth I** | | | **Light Booth II** | | |
|---|---|---|---|---|---|---|
| | **Light Source** | | | **Light Source** | | |
| | **BLED65** | **BLED40** | **BLED27** | **Daylight** | **TL84** | **A** |
| x | 0.311 | 0.378 | 0.451 | 0.307 | 0.395 | 0.458 |
| y | 0.318 | 0.388 | 0.432 | 0.314 | 0.380 | 0.410 |
| CCT (K) | 6477 | 3826 | 2733 | 6866 | 3492 | 2667 |
| Luminance ($cd/m^2$) | 257.5 | 167.4 | 243.4 | 111.8 | 75.5 | 160.0 |

### *2.3. Observers*

A psychophysical experiment was conducted under two standard lighting booths to obtain visual data from 10 observers for eleven metameric sample pairs. All observers had normal color vision tested by the Ishihara color vision test. A total of 11 people (6 men and 5 women) took part in the pretest, including one man with color vision deficiency. The ages of the participants ranged from 20 to 57 with the average of 31 years old and SD 13.01. Data from the observers with defective color vision were discarded. All eleven metameric pairs were presented to all observers in five consecutive sessions under testing lighting conditions. The observers were asked to adapt to the mid-gray interior of the booth for

2 min after each new lighting condition. After adaptation, they were provided with the gray scale and sample pairs.

Due to the determination method used in the experiment; the participants were required to evaluate and compare the sample pair with gray scale. Each participant was asked to determine a closest gray-scale value according to his/her own perception. The distance between observers and sample was 50 cm. The illumination: viewing geometry was always approximately 0°:45°. The visual experiment was conducted in a completely darkened room. Figure 4 is demonstrating the position of a sample pair along with gray scale during visual assessment.

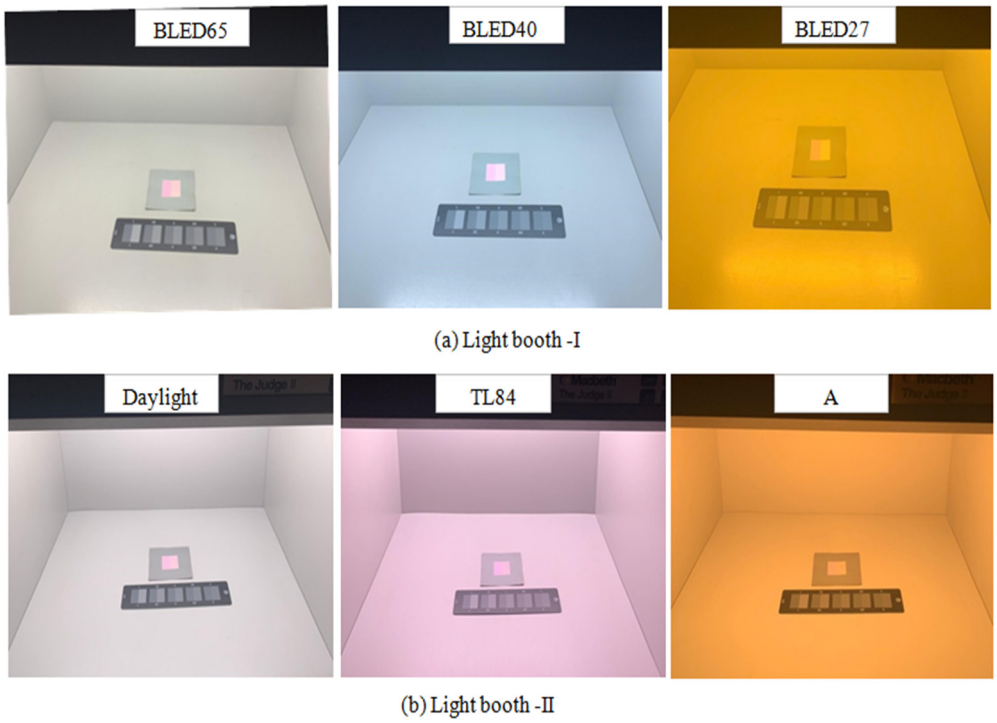


**Figure 4.** Viewing condition for color difference experiment under two lighting booths.

### *2.4. Data Analysis*

#### 2.4.1. Standard Deviation (SD) and Standard Error of the Mean (SEM)

Standard deviation (SD) measures the deviation of the individual estimate from the mean value, while standard error of the mean (SEM) gives the accuracy of a sample's mean by measuring the sample-to-sample variability of the sample means. The SEM describes how precise the mean of the sample is as an estimate of the true mean of the population. Standard deviation (SD) and standard error of the mean (SEM) are calculated by using Equations (1) and (2):

$$\text{Standard Deviation (SD)} = \sqrt{\frac{\sum_{i=1}^{n}(x_\iota - \overline{x})^2}{n-1}} \quad (1)$$

$$\text{Standard Error of Mean (SEM)} = \frac{SD}{\sqrt{n}} \quad (2)$$

where $\overline{x}$ = the sample's mean and n= the sample size.

#### 2.4.2. Visual Color Difference with Gray Scale

The gray scale is used to visually assess and compare the change in color difference appearance, as described in ISO 105-A02 [29]. It consists of a 9-grade point from 1 to 5 within a half-step rating of 5, 4–5, 4, 3–4, 3, 2–3, 2, 1–2, and 1, with 1 indicating extreme

color differences and 5 meaning that there is no color difference in a pair. After visual assessments, the gray scale number (GS) for each pair was transformed to the corresponding visual color difference (ΔV) in CIELAB unit by Equation (3):

$$\Delta V = 26.36e^{-GS/1.659} - 0.9532 \quad (3)$$

This exponential Equation (3) is used to predict the CIELAB color difference from the gray-scale rating, as shown in Figure 5.

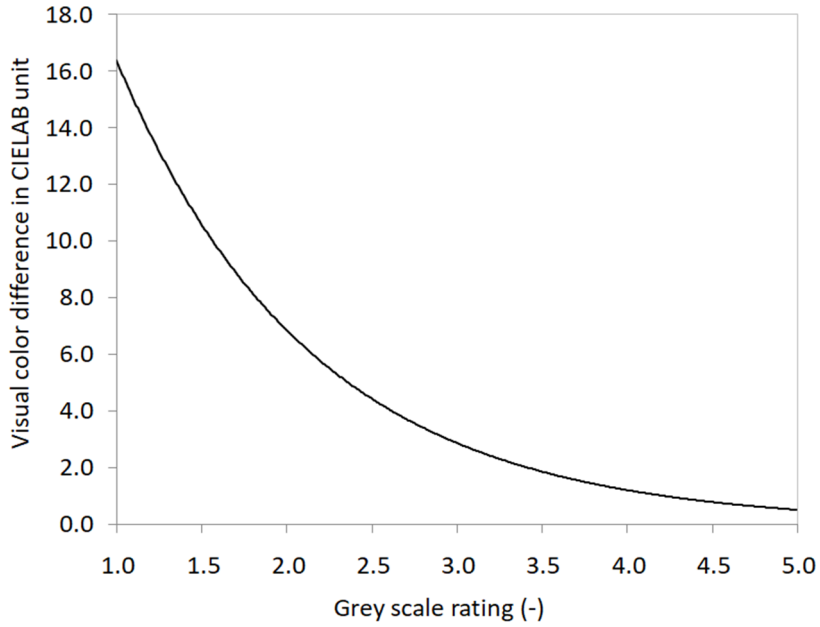


**Figure 5.** Visual color difference in CIELAB unit as a function of gray-scale rating.

2.4.3. STRESS and Performance Factor (PF/3)

The repeatability and reproducibility of measurements in a psychophysical experiment depends on the ability of a single observer's or a group of observers' ability to produce the same measurements consistently under the same experimental setup. A higher variability of the measurement indicates a lower reliability of the estimate. In order to determine inter-variability (the deviation between the estimate of each individual from the mean) and intra-variability (the deviation between the results of an individual on repeated attempts in an experiment), a metric index, which is called the "standardized residual sum of squares" (STRESS), is used by many researchers in the color science field [30–33]. The percentage STRESS values are always between 0 and 100. STRESS values close to zero indicate a better match between two data sets. In color difference studies, a STRESS value above 35 is typically an indicator of poor performance of the color difference formula [34]. In addition to the STRESS index, the performance factor (PF) modified by Guan and Luo [35] is also used to compare the best fitted model with different experimental data sets.

The STRESS value and performance factor can be calculated by using Equation (4):

$$\text{STRESS} = 100\left(\sqrt{\frac{\sum(\Delta E_i - F_i\Delta V_i)^2}{(F_1{}^2\Delta V_1{}^2)}}\right) \text{ and } F_1 = \frac{\sum \Delta E_i{}^2}{\sum \Delta E_i \Delta V_i} \quad (4)$$

where $\Delta E_i$ and $\Delta V_i$ are the computed and the perceived color difference for the i =1, n sample pair respectively and $F_1$ is an adjusting factor between $\Delta E_i$ and $\Delta V_i$.

Meanwhile, the performance factor is as follows:

$$PF/3 = (100/3) * (\text{Gamma} - 1 + V_{ab} + CV/100) \quad (5)$$

PF/3 is obtained as an average of three terms including the Gamma factor and two coefficients of variation $V_{ab}$ and CV.

## 3. Results and Discussion

### *3.1. Visual Assessment Variability within Samples under Two Lighting Booths*

The effects of the light booth's design in term of light source on the L*a*b* values and inter-observer variability are shown in Figures 6 and 7, respectively. Table 2 shows that the light booth technology has a clear impact on the resulting L*a*b* values.

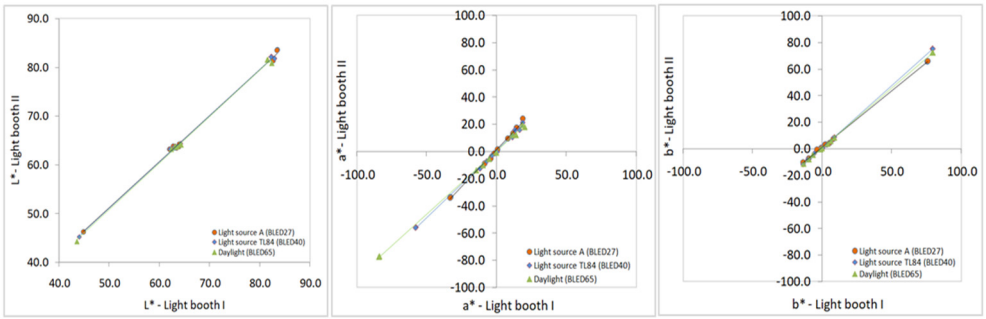


**Figure 6.** CIE L*a*b* values for different light sources of the two booths. In the figure, BLED65, BLED40, and BLED27 represent the light sources with nominal CCT 6500 K, 4000 K, and 2700 K respectively for light booth I; and Daylight (Simulator D65), TL84 (Tri-band fluorescent tube), and A (Tungsten lamp) represent the light sources with nominal CCT 6500 K, 4000 K, and 2700 K, respectively for light booth II.

There were significant differences between the two booths for all mean CIELAB values for the test metameric pairs, as shown in Table 2. All observed correlations, which are shown in Figure 6, agree with the hypothesis that both light booths gave the same values up to a linear transformation.

The results from Figure 7a show that the inter-variability among observers for samples 9 and 11 is large, while it is low for samples 3,4,5,6, and 7 under all experimental conditions. Almost the same average variability was found for samples 8 and 10 under CCT 4000 K and CCT 2700 K, but the highest was found for CCT 6500 K for both booths. Samples 1 and 2 showed the highest variability with changes of light sources for two booths. Among all light sources, all samples under CCT 2700 K showed a high degree of variability.

Figure 7a,b show the visual color difference among samples with standard deviation bars and standard error of the mean (SEM) bars of two light booths. In the figure, the vertical lines denote standard deviation and standard error of the mean (SEM). It also shows that the visual evaluation of the tested sample pairs was consistent.

Figure 7a shows that light booth I had a comparatively smaller influence on the visual assessment than light booth II, as expected, and the results from the standard error of the mean (SEM) of Figure 7b justified the results from Figure 7a. Analysis of the results shows that the observer and sample's variability should be modeled considering light booth's technology to estimate its contribution to the overall variability.

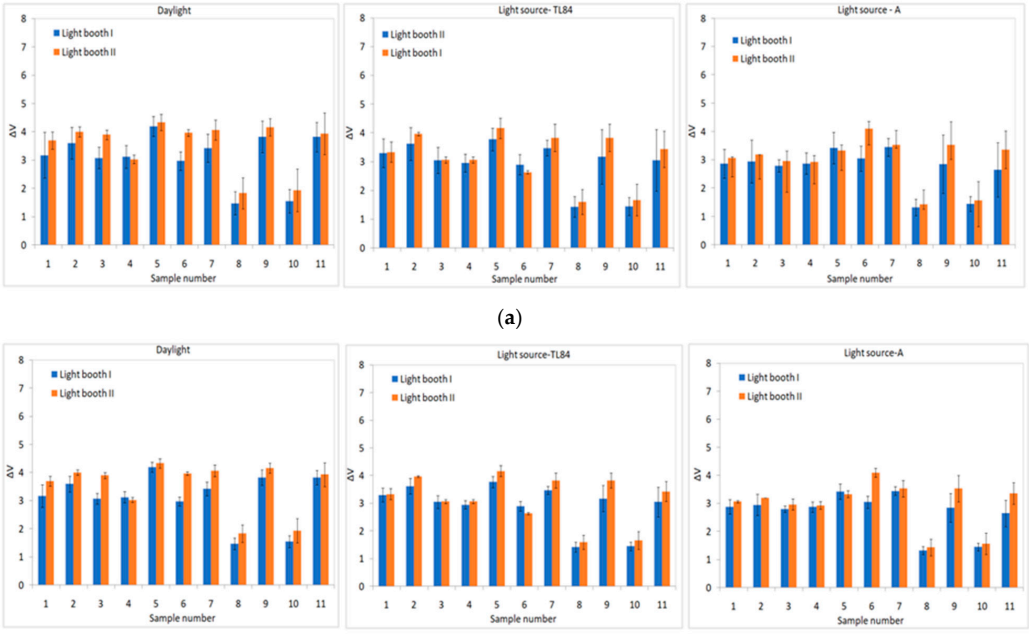


**Figure 7.** Average inter-observer variability of all metameric pairs under each light source with (**a**) standard deviation (SD) bars; (**b**) standard error of the mean (SEM). In the figure, BLED65, BLED40, and BLED27 represent the light sources with nominal CCT 6500 K, 4000 K, and 2700 K, respectively for light booth I; and Daylight (Simulator D65), TL84 (Tri-band fluorescent tube), and A (Tungsten lamp) represent the light sources with nominal CCT 6500 K, 4000 K, and 2700 K respectively, for light booth II.

**Table 2.** Mean CIE L*a*b* values for different light sources of the two booths. In the table, BLED65, BLED40, and BLED27 represents the light sources with nominal CCT 6500 K, 4000 K, and 2700 K respectively for light booth I; and Daylight (Simulator D65), TL84 (Tri-band fluorescent tube), and A (Tungsten lamp) represent the light sources with nominal CCT 6500 K, 4000 K, and 2700 K, respectively for light booth II.

| **Light Booth I** | | | | | | | | | |
|---|---|---|---|---|---|---|---|---|---|
| | BLED65 | | | BLED40 | | | BLED27 | | |
| Sample | L * | a * | b * | L * | a * | b * | L * | a * | b * |
| 1 | 62.34 | 20.30 | −13.49 | 62.06 | 16.38 | −13.92 | 61.97 | 11.81 | −13.68 |
| 2 | 63.14 | 13.89 | −9.54 | 62.90 | 11.16 | −9.91 | 62.78 | 8.09 | −9.91 |
| 3 | 82.43 | −84.05 | 79.23 | 82.97 | −57.60 | 79.24 | 82.66 | −33.08 | 75.62 |
| 4 | 63.33 | −0.27 | −0.24 | 63.21 | 0.06 | −0.42 | 63.03 | 0.65 | −0.95 |
| 5 | 64.02 | −5.41 | 3.76 | 64.00 | −3.56 | 3.69 | 63.94 | −1.60 | 3.34 |
| 6 | 63.55 | -9.83 | 6.22 | 63.47 | −7.23 | 6.03 | 63.27 | −4.33 | 5.32 |
| 7 | 64.32 | −14.68 | 8.87 | 64.24 | −11.94 | 8.64 | 63.86 | −8.77 | 8.02 |
| 8 | 43.54 | 18.17 | −6.60 | 44.02 | 18.71 | −5.73 | 44.89 | 18.67 | −3.83 |
| 9 | 81.55 | 11.47 | −1.30 | 82.28 | 13.19 | 0.03 | 83.50 | 14.34 | 1.96 |
| 10 | 82.45 | −84.44 | 79.48 | 82.99 | −57.96 | 79.47 | 82.66 | −33.41 | 75.84 |
| 11 | 81.50 | 11.36 | −1.21 | 82.22 | 13.13 | 0.13 | 83.45 | 14.32 | 2.05 |

**Table 2.** *Cont.*

| | Light Booth II | | | | | | | | |
|---|---|---|---|---|---|---|---|---|---|
| | Daylight | | | Light Source TL84 | | | Light Source A | | |
| Sample | L * | a * | b * | L * | a * | b * | L * | a * | b * |
| 1 | 63.23 | 18.15 | −11.26 | 63.20 | 15.77 | −11.66 | 63.26 | 13.43 | −10.26 |
| 2 | 63.84 | 12.23 | −7.81 | 63.77 | 10.60 | −8.18 | 63.81 | 9.44 | −7.25 |
| 3 | 80.84 | −77.04 | 72.30 | 81.79 | −55.69 | 75.10 | 81.46 | −33.38 | 65.76 |
| 4 | 63.64 | −0.70 | 0.48 | 63.84 | −0.29 | 0.82 | 63.55 | 1.49 | 0.19 |
| 5 | 64.22 | −5.57 | 3.70 | 63.92 | −3.12 | 3.22 | 64.24 | −1.28 | 3.15 |
| 6 | 63.72 | −10.00 | 5.95 | 63.44 | −7.13 | 5.55 | 63.50 | −4.91 | 4.71 |
| 7 | 64.10 | −13.78 | 8.28 | 64.40 | −12.77 | 8.63 | 63.77 | −8.92 | 7.36 |
| 8 | 44.28 | 19.56 | −4.80 | 45.24 | 21.13 | −3.44 | 46.29 | 24.29 | −0.53 |
| 9 | 81.59 | 12.34 | −0.63 | 82.21 | 15.80 | 0.37 | 83.58 | 17.47 | 3.22 |
| 10 | 80.85 | −77.45 | 72.55 | 81.78 | −56.07 | 75.31 | 81.44 | −33.80 | 65.98 |
| 11 | 81.54 | 12.23 | −0.54 | 82.16 | 15.73 | 0.47 | 83.53 | 17.46 | 3.28 |

### *3.2. Comparison of Visual and Measured Color Difference of Two Light Booths*

The effects of light sources on the visual and measured color differences for two different standard lighting booths are shown in Figures 8 and 9. Figure 8 shows the correlation of the visual color difference between two booths under experimental lighting conditions. As shown in Figure 8, the strongest correlation was found for CCT 4000 K and a relatively poor correlation was found for CCT 2700 K. The reason could be the relatively distant position of light BLED27 of light booth I from the daylight series. As expected, observers had performed better under daylight. The measurements showed significant differences related to light booth conditions, while Figure 9 shows how visual performance correlates with the measured color differences between pairs of samples.

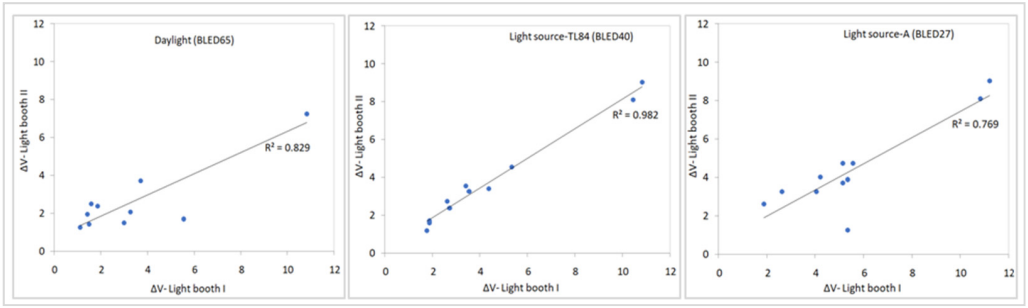


**Figure 8.** Visual color difference under different light sources between two booths. In the figure, BLED65, BLED40, and BLED27 represent the light sources with nominal CCT 6500 K, 4000 K, and 2700 K respectively for light booth I; and Daylight (Simulator D65), TL84 (Tri-band fluorescent tube), and A (Tungsten lamp) represent the light sources with nominal CCT 6500 K, 4000 K, and 2700 K respectively for light booth II.

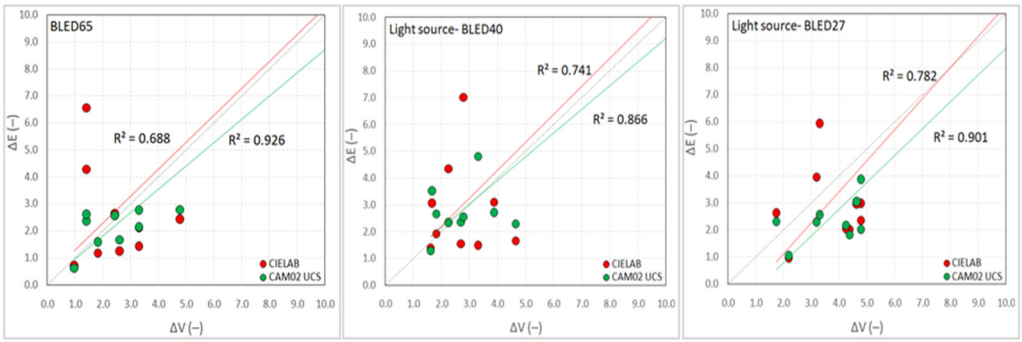


(**a**)

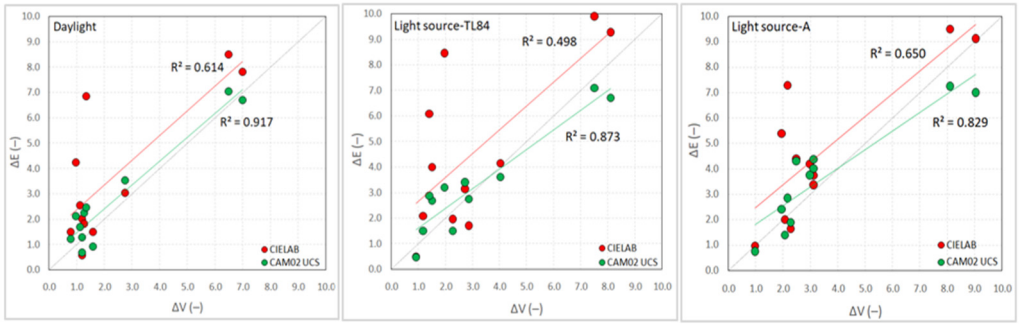


(**b**)

**Figure 9.** Correlation between visual and formula-based color difference of different light sources. In the figure, BLED65, BLED40, and BLED27 represent the light sources with nominal CCT 6500 K, 4000 K, and 2700 K, respectively for light booth I; and Daylight (Simulator D65), TL84 (Tri-band fluorescent tube), and A (Tungsten lamp) represent the light sources with nominal CCT 6500 K, 4000 K, and 2700 K respectively for light booth II. (**a**) Light booth I, (**b**) Light booth II.

The spectra and the CCT values (from Figures 2 and 3; and Table 1) show differences between the two booths. For all lighting settings, the formula based on CAM02-UCS showed better agreement than CIELAB. Both CIELAB and CAM02-UCS performed better under light booth I than light booth II as expected. Considering our results, it can be said that the variability between the visual and measured color difference is influenced by booth conditions.

### *3.3. Performance of Color Difference Formula*

The reliability of the color difference assessment was evaluated by inter-observer variability in terms of STRESS value, performance factor (PF/3), and correlation coefficient (COQ), as shown in Figure 10 and Table 3. According to our results, all three metrics such as STRESS, PF/3, and COQ showed better results for the CAM02-UCS model than the CIELAB among all light sources. The reason for this could be that the appearance-based models predict well the role of illuminations in perceived color differences [20].

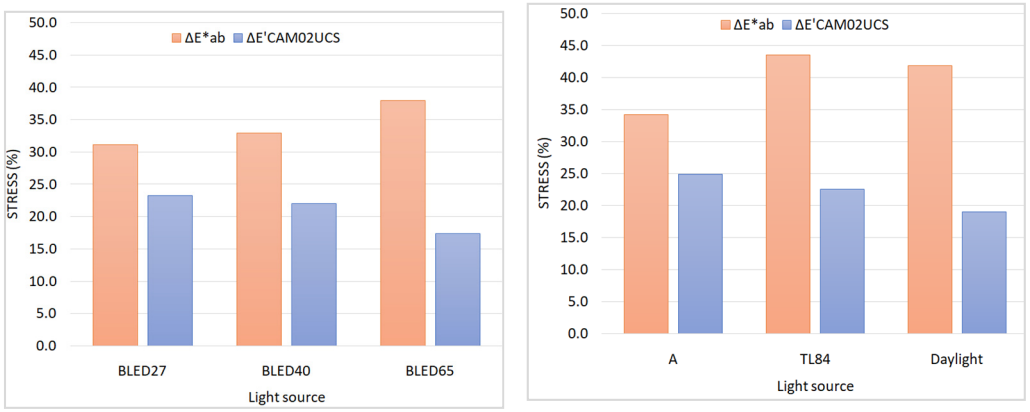


**Figure 10.** Performance of color difference formula in term of STRESS. **Left**: light booth I, **right**: light booth II. In the figure, BLED65, BLED40, and BLED27 represent the light sources with nominal CCT 6500 K, 4000 K, and 2700 K respectively for light booth I; and Daylight (Simulator D65), TL84 (Tri-band fluorescent tube), and A (Tungsten lamp) represent the light sources with nominal CCT 6500 K, 4000 K, and 2700 K respectively for light booth II.

**Table 3.** Performance of color difference formulas in term of STRESS, COQ, and PF/3. In the table, BLED65, BLED40, and BLED27 represent the light sources with nominal CCT 6500 K, 4000 K, and 2700 K respectively for light booth I; and Daylight (Simulator D65), TL84 (Tri-band fluorescent tube), and A (Tungsten lamp) represent the light sources with nominal CCT 6500 K, 4000 K, and 2700 K respectively for light booth II.

| **Light Booth I** | | | | | | |
|---|---|---|---|---|---|---|
| | ΔE*ab | | | ΔE′CAM02-UCS | | |
| Light source | STRESS | COQ | PF/3 | STRESS | COQ | PF/3 |
| BLED27 | 31.2 | 0.88 | 52.22 | 23.3 | 0.95 | 35.76 |
| BLED40 | 33.0 | 0.86 | 60.68 | 22.1 | 0.93 | 37.01 |
| BLED65 | 38.0 | 0.83 | 78.67 | 17.4 | 0.96 | 34.41 |
| **Light Booth II** | | | | | | |
| | ΔE*ab | | | ΔE′CAM02-UCS | | |
| | STRESS | COQ | PF/3 | STRESS | COQ | PF/3 |
| A | 34.2 | 0.81 | 47.09 | 24.9 | 0.91 | 30.73 |
| TL84 | 43.6 | 0.71 | 73.27 | 22.6 | 0.93 | 38.74 |
| Daylight | 41.9 | 0.78 | 69.64 | 19.02 | 0.958 | 38.28 |

As can be seen from Table 1, and Figures 2 and 3 in Section 2.2, the fluctuations between the SPDs and luminances of all three light sources between two booths were significant compared to CCTs. This may be the reason why the observers under light booth II had more difficulties with the visual assessment than under light booth I. Moreover, it can be seen from Table 3 that both formulas gave a comparatively better correlation coefficient but failed to show acceptable performance of fit to the current data set.

The average STRESS values for light booth I were lower than in light booth II, as can be seen from Figure 10. Our results imply that two different standard lighting technologies with the same light sources cannot reproduce the same estimates. The close relationship between perceived and CAM02-UCS suggests that if both booths are used after the light sources have been calibrated, a formula based on color appearance models must be used to predict color appearance. To obtain better agreement between perceived and calculated color difference, one must need to avoid light booths with nominally white light sources.

## 4. Conclusions

Visual assessments under two light booths differed because of the variation among the light sources' spectral and colorimetric characteristics. We compared an earlier technology-based light booth, which is still used in the textile industry, and which contains illuminant A (Tungsten lamp) with CCT 2700 K, TL84 (tri-band fluorescent tube) with CCT 4000 K, and simulator D65 (CCT 6500 K), with a different light booth, whose original light sources have been replaced by currently available LED retro kits from equivalent CCTs. As an inexperienced customer or industrial user, our question was, how important is this replacement? The results indicated that two different standard lighting technologies with the similar CCTs cannot reproduce the same estimates because the light sources produced different SPDs. It is illustrating that caution is necessary when comparing results obtained from two different light booths. The variability of the light sources' SPDs or the observer or the sample should be modeled considering the light booth's technology to estimate its contribution to the overall variability. The close relationship between perceived and CAM02-UCS suggests that if both booths are used after the light sources have been calibrated, a formula based on color appearance models must be used to predict color appearance. To obtain better agreement between perceived and calculated color difference, one must need to avoid light booths with nominally white light sources.

**Author Contributions:** Conceptualization, M.V. (Michal Vik); Data curation, A.A.M.; Formal analysis, A.A.M.; Investigation, A.A.M.; Methodology, A.A.M. and M.V. (Martina Viková); Software, M.V. (Martina Viková); Supervision, M.V. (Michal Vik) and M.V. (Martina Viková); Visualization, A.A.M.; Writing—original draft, A.A.M.; Writing—review and editing, A.A.M. and M.V. (Martina Viková). All authors have read and agreed to the published version of the manuscript.

**Funding:** This research was funded by the Technical University of Liberec as part of the Student Grant Competition under the project number SGS-2020-6038, as provided by the Ministry of Education, Youth and Sports of the Czech Republic in the year 2020.

**Institutional Review Board Statement:** Not applicable.

**Informed Consent Statement:** Not applicable.

**Data Availability Statement:** The data presented in this study are available on request from the corresponding author.

**Conflicts of Interest:** No potential conflict of interest was reported by the authors.

## References

1. Hunter, R.S.; Harold, R.W. *The Measurement of Appearance*, 2nd ed.; Wiley-Inter Science: New York, NY, USA, 1987.
2. Billmeyer, F.; Hammond, H. Color and Light. In *ASTM Manual 17*; ASTM: West Conshohocken, PA, USA, 1996.
3. Billmeyer, F.; Saltzman, M. *Principles of Color Technology*, 3rd ed.; John Wiley & Sons: Hoboken, NJ, USA, 2000.
4. HunterLab: The Worldstrue Measure of Color. Available online: https://www.hunterlab.com/media/documents/basics-of-color-theory.pdf (accessed on 21 November 2021).
5. Datacolor. How Medication, Lighting and More Impact Color Perception. Available online: https://www.datacolor.com/factors-that-impact-color-perception/ (accessed on 21 November 2021).
6. ASTM, D1729-96 (2009). *Standard Practice for Visual Appraisal of Colors and Color Differences of Diffusely-Illuminated Opaque Materials*; ASTM International: West Conshohocken, PA, USA, 2014; Available online: www.astm.org (accessed on 17 October 2021).
7. CIE15.4:2018. *Colorimetry*; Commission Internationale de I'Eclairage: Vienna, Austria, 2018.
8. CIE51.2:1995. *A Method for Assessing the Quality of Daylight Simulators for Colorimetry*; Commission Internationale de I'Eclairage: Vienna, Austria, 1999.
9. Luo, M.R.; Lv, X. LED simulators for the reproduction of the new CIE standard LED sources. In Proceedings of the 29th Quadrennial Session of the CIE, Washington, DC, USA, 14–22 June 2019.
10. CIE101-1993. *Parametric Effects in Color-Difference Evaluation*; Commission Internationale de I'Eclairage Central Bureau: Vienna, Austria, 1993.
11. Hinks, D.; Shamey, R. Review of retail store lighting: Implications for colour control of products. *Color Technol.* **2011**, *127*, 121–128. [CrossRef]
12. Liuo, J.J. A Novel color recognition model for improvement on color differences in products via grey relational grade. *Axioms* **2021**, *10*, 266. [CrossRef]

13. Xu, C.; Wu, C.F.; Xu, D.D.; Lai, Y.S. Have the Display Illumination Design Misled Customers on Color Perception? A Study on Differences of Color Caused by LED Lighting on Leather Products. In Proceedings of the AHFE 2020 Virtual Conferences on Design for Inclusion, Affective and Pleasurable Design, Interdisciplinary Practice in Industrial Design, Kansei Engineering, and Human Factors for Apparel and Textile Engineering, Chicago, IL, USA, 16–20 July 2020; Di Bucchianico, G., Shin, C., Shim, S., Fukuda, S., Montagna, G., Carvalho, C., Eds.; Springer Cham: Berlin/Heidelberg, Germany, 2020; Volume 1202, pp. 346–354.
14. Dou, X.; Wu, C.F.; Lin, K.C.; Liou, J.J. What color does the consumer see? Perceived color differences in plastic products in an LED-Lit environment. *Sustainability* **2019**, *11*, 5985. [CrossRef]
15. Chao, W.C.; Hong, L.Y.; Hsieh, M.C.; Yang, C.C.; Su, L.C. Effect of correlated colour temperature and illuminance levels on user's visual perception under LED lighting in Taiwan. *Ergonomics* **2020**, *63*, 175–190. [CrossRef]
16. Tantanatewin, W.; Inkarojrit, V. Effects of color and lighting on retail impression and identity. *J. Environ. Psychol.* **2016**, *46*, 197–205. [CrossRef]
17. Lo, V.W.L.; Steemers, K.A. Measuring light in field experiments using dummies and objects: A Study of concert lighting. *Light. Res. Technol.* **2018**, *50*, 827–841. [CrossRef]
18. Ru, T.; deKort, Y.A.; Smolders, K.C.H.J.; Chen, Q.; Zhou, G. Non-image forming effects of illuminance and correlated colortemperature of office light on alertness, mood, and performance across cognitive domains. *Build. Environ.* **2019**, *149*, 253–263. [CrossRef]
19. Dikel, E.E.; Burns, G.J.; Veitch, J.A.; Mancini, S.; Newsham, G.R. Preferred chromaticity of color- tunable LED lighting. *Leukos* **2014**, *10*, 101–115. [CrossRef]
20. Kulappurath, S.K.; Shamey, R. The effect of luminance on the perception of small color differences. *Color. Res. Appl.* **2021**, *46*, 929–942. [CrossRef]
21. Setser, C.S. Color: Reflections and transmissions. *J. Food Qual.* **1984**, *6*, 183–197. Available online: https://onlinelibrary.wiley.com/doi/epdf/10.1111/j.1745-4557.1984.tb00824.x (accessed on 21 November 2021). [CrossRef]
22. Strange, E.D.; Benedict, R.C.; Gugger, R.E.; Metzger, V.G.; Swift, C.E. Simplified methodology for Measuring Meat color. *J. Food Sci.* **1974**, *39*, 988–992. [CrossRef]
23. Hunt, M.C.; Kropf, D.H. Fresh and cured meat color analysis. In Proceedings of the Muscle foods Symposium-Institute of Food Technologists' Annual Meeting, Chicago, IL, USA, 8–12 June 1985.
24. Luo, M.R.; Cui, G.; Rigg, B. The development of the CIE 2000 colour difference formula: CIEDE2000. *Color. Res. Appl.* **2001**, *26*, 340–350. [CrossRef]
25. Claudio, O.M.M.; Huertas, R. Euclidean color difference formula for small medium color differences in log compressed OSA-UCS space. *J. Opt. Soc. Am. A* **2009**, *26*, 121–134. [CrossRef]
26. Kim, D.H. The ULAB colour space. *Color. Res. Appl.* **2013**, *40*, 17–30. [CrossRef]
27. Luo, M.R.; Cui, G.; Li, C. Uniform colour spaces based on CIECAM02 colour appearance model. *Color. Res. Appl.* **2006**, *31*, 320–330. [CrossRef]
28. Li, C.; Li, Z.; Wang, Z.; Xu, Y.; Luo, M.R.; Cui, G.; Melgosa, M.; Brill, M.H.; Pointer, M. Comprehensive color solutions: CAM16, CAT16, and CAM16-UCS. *Color. Res. Appl.* **2017**, *42*, 703–718. [CrossRef]
29. ISO 105: 1996. *Textiles—Tests for Colour Fastness—Part A02: Grey Scale for Assessing Change in Colour*; International Organization for Standardization: Geneva, Switzerland, 1996.
30. García, P.A.; Huertas, R.; Melgosa, M.; Cui, G. Measurement of the relationship between perceived and computed color differences. *J. Opt. Soc. Am. A* **2007**, *24*, 1823–1829. [CrossRef] [PubMed]
31. Shamey, R.; Cárdenas, L.M.; Hinks, D.; Woodard, R. Comparison of naïve and expert subjects in the assessment of small color differences. *J. Opt. Soc. Am. A* **2010**, *27*, 1482. [CrossRef] [PubMed]
32. Barcenas, P.; Elortondo, F.P.; Albisu, M. Projective mapping in sensory analysis of ewes milk cheeses: A study on consumers and trained panel performance. *Food Res. Int.* **2004**, *37*, 723–729. [CrossRef]
33. García, P.A.; Gómez-Robledo, L.; Melgosa, M.; Shamey, R.; Luo, M.R.; Hinks, D.; Cui, G. Notes on the application of the standardized residual sum of squares index for the assessment of intra-and inter–observer variability in color–difference experiments. *J. Opt. Soc. Am. A* **2011**, *28*, 949. [CrossRef]
34. Wei, M.; Ma, S.; Wang, Y.; Luo, M.R. Evaluation of whiteness formulas for FWA and non-FWA whites. *J. Opt. Soc. Am. A* **2017**, *34*, 640–647. [CrossRef] [PubMed]
35. Guan, S.S.; Luo, M.R. Investigation of parametric effects using small colour differences. *Color. Res. Appl.* **1999**, *24*, 331–343. [CrossRef]

*textiles*

MDPI

*Article*

# Effect of Textile Characteristics on the AR-Glass Fabric Efficiency

**Marco Carlo Rampini [1,*], Giulio Zani [1], Louis Schouler [2], Matteo Colombo [1] and Marco di Prisco [1]**

[1] Department of Civil and Environmental Engineering, Politecnico di Milano, 20133 Milan, Italy; giulio.zani@polimi.it (G.Z.); matteo.colombo@polimi.it (M.C.); marco.diprisco@polimi.it (M.d.P.)
[2] Gavazzi Tessuti Tecnici S.p.a., 23801 Calolziocorte, Italy; lschouler@gavazzispa.it
* Correspondence: marcocarlo.rampini@polimi.it

**Abstract:** Alkali-resistant (AR) glass textiles are used as the main reinforcement in several composite applications due to their good performance-to-cost ratio. A huge variety of textiles are already present in the market; they differ on various parameters, such as, for example, the filaments' diameters, the geometry, the type of weaving, or the nature of the impregnation coating. To orient manufacturers towards the production of efficient textiles, the most important aspect is the balance between cost and performance. In this paper, a series of different fabrics designed for textile-reinforced cementitious composites were considered. Performance was assessed by means of uniaxial tensile tests and the results are presented in terms of load vs. displacement. Then, the selected AR-glass textiles were compared in terms of fabric efficiency, targeting the effect of each parameter on the textile capacity. The research here presented is part of a comprehensive campaign aimed at the optimization of glass-fabric-reinforced cementitious composites for structural retrofitting. To better discuss the different solutions tested, at the end, only considering a small number of the investigated textiles, an efficiency evaluation was carried out at the cementitious composite level.

**Keywords:** alkali-resistant glass textile; weaving; epoxy coating; filament diameters; roving fineness; fabric efficiency; textile-reinforced concrete; TRC; fabric-reinforced cementitious matrix; FRCM

**Citation:** Rampini, M.C.; Zani, G.; Schouler, L.; Colombo, M.; di Prisco, M. Effect of Textile Characteristics on the AR-Glass Fabric Efficiency. *Textiles* **2021**, *1*, 387–404. https://doi.org/10.3390/textiles1020020

Academic Editor: Fernando G. Branco

Received: 31 July 2021
Accepted: 7 September 2021
Published: 14 September 2021



## 1. Introduction

The use of textile-reinforced composites has steadily been growing in various sectors during recent years. In the construction field, alkali-resistant (AR) glass fabrics are mainly used due to their cost-to-performance ratio [1].

Typical cementitious-based composites embedding textiles of different nature (e.g., glass, carbon, basalt, PBO, etc.) are textile-reinforced concrete (TRC) [2,3], generally employed in new buildings, and fabric-reinforced cementitious matrix (FRCM) [4,5], conceived for the strengthening and retrofitting of existing structures. In TRCs and FRCMs the tensile capacity is ascribed to the reinforcing fabrics and a proper uniaxial response should result in a trilinear behavior in which the initial elastic branch is followed by the multi-cracking of the fine-grained inorganic matrix and, finally, by a marked strain-hardening phase mainly governed by the textiles.

For both manufacturers and designers, the most important aspects in devising and employing efficient composites for construction are, respectively, the reduction of the manufacturing cost and the selection, among many textiles available in the market, of those characterized by the highest performance-to-cost ratios. The weaving, the geometry, and the coating process influence the mechanical performance of the woven textiles [6,7], their suitability for the various applications, the sustainability of the different solutions, and the manufacturing costs. Moreover, the chemical nature of the coating [8–12] and the weaving characteristics [13–15] significantly affect the behavior of cementitious-based composites.

In this paper, several alternative textiles are characterized in tension and compared in terms of efficiency and costs, on the basis of the main textile characteristics. The here pre-

sented investigation represents the preliminary part of an extensive experimental campaign devoted to the optimization of AR-glass textile-based cementitious composites, namely fabric-reinforced cementitious matrix (FRCM), used in the strengthening and retrofitting of existing reinforced concrete structures, in particular those exposed to seismic actions.

## 2. Textiles Description: Production Method and Geometrical Properties

In this section, the description of the twenty different investigated AR-glass textiles is reported, together with the explanation of the procedures for their production and impregnation. To identify the effects of the different textile characteristics on their mechanical responses, the main differences between the various fabrics are highlighted. A summary of the main geometrical properties of the fabrics investigated in this study is reported in Tables 1 and 2.

The AR-glass textiles are ordered at increasing equivalent thickness in the warp direction and they mainly differ in terms of roving fineness, weaving pattern, grid spacing, and nature of the coating used for the impregnation.

With the aim to compare the manufacturing costs of the different AR-glass textiles (considering material, weaving, and impregnation), the ratio between the cost of each fabric and that of one of the cheapest textiles, i.e., the raw fabric cost of F1-(S1), was computed and is reported in Table 1 as normalized cost, $C_N$.

**Table 1.** AR-glass fabric properties and costs (part 1, equivalent thickness in the warp direction lower than 0.05 mm/m).

| Fabric | | Roving Fineness | Filament Diameter | Wire Spacing | Equivalent Thickness | Coating | | Normalized Cost, $C_N$ | |
|---|---|---|---|---|---|---|---|---|---|
| | | | | | | Nature | Percentage | Raw Fabric | Coated Fabric |
| ID. | dir. | [Tex] | [μm] | [mm] | [mm/m] | | [%] | [-] | [-] |
| F1-(S1) | warp | 1200 | 19 | 25 | 0.035 | SBR 1 | 18.8 | 1 | 1.2 |
| | weft | 2 × 1200 | 19 | 25 | 0.035 | | | | |
| F1-(E2) | warp | 1200 | 19 | 25 | 0.035 | Epoxy 2 | 18.75 | 1 | 2.3 * |
| | weft | 2 × 1200 | 19 | 25 | 0.035 | | | | |
| F2-(S1) | warp | 640 | 14 | 25 | 0.038 | SBR 1 | 17.1 | 1 | 1.3 |
| | weft | 2 × 1200 | 19 | 25 | 0.035 | | | | |
| F2-(E1) | warp | 640 | 14 | 25 | 0.038 | Epoxy 1 | 17.1 | 1 | 2.2 |
| | weft | 2 × 1200 | 19 | 25 | 0.035 | | | | |
| F3-(S1) | warp | 2400 | 27 | 38 | 0.046 | SBR 1 | 18.75 | 1.3 | 2.2 |
| | weft | 2 × 2400 | 27 | 38 | 0.046 | | | | |
| F4-(S1) | warp | 1200 | 19 | 38 | 0.046 | SBR 1 | 19 | 1.3 | 2.2 |
| | weft | 2 × 2400 | 27 | 38 | 0.046 | | | | |
| F4-(S2) | warp | 1200 | 19 | 38 | 0.046 | SBR 2 | 19 | 1.3 | 2.2 |
| | weft | 2 × 2400 | 27 | 38 | 0.046 | | | | |
| F4-(E2) | warp | 1200 | 19 | 38 | 0.046 | Epoxy 2 | 15 | 1.3 | 2.3 * |
| | weft | 2 × 2400 | 27 | 38 | 0.046 | | | | |
| F5-(S1) | warp | 1200 | 19 | 18 | 0.049 | SBR 1 | 14.2 | 1.5 | 2.3 |
| | weft | 2400 | 27 | 18 | 0.05 | | | | |
| F6-(S2) | warp | 1200 | 19 | 18 | 0.049 | SBR 2 | 11.5 | 1.5 | 2.3 |
| | weft | 2400 | 27 | 18 | 0.05 | | | | |

* evaluated in proportion to the epoxy 1 coating cost and in proportion to the coating percentage.

### *2.1. Roving, Weaving, and Pattern Descriptions*

The investigated textiles are based on the weavings of AR-glass rovings produced with filaments of different diameters. The roving is a flat yarn, without any torsion, composed of continuous AR-glass filaments. The diameter of each filament corresponds to the fineness of the single yarns, computed in Tex. The Tex is a direct measurement of the linear density, corresponding to the weight in grams per 1000 m of a yarn (glass yarn density is considered equal to 2680 kg/m$^3$). The employed AR-glass rovings are the following:

1. Roving 320 Tex, composed of 800 filaments of 14 μm diameter;
2. Roving 640 Tex, composed of 1600 filaments of 14 μm diameter;
3. Roving 1200 Tex, composed of 1600 filaments of 19 μm diameter;
4. Roving 2400 Tex, composed of 1600 filaments of 27 μm diameter.

**Table 2.** AR-glass fabric properties and costs (part 2, equivalent thickness in the warp direction higher than 0.05 mm/m).

| Fabric | | Roving Fineness | Filament Diameter | Wire Spacing | Equivalent Thickness | Coating | | Normalized Cost, $C_N$ | |
|---|---|---|---|---|---|---|---|---|---|
| | | | | | | Nature | Percentage | Raw Fabric | Coated Fabric |
| ID. | dir. | [Tex] | [μm] | [mm] | [mm/m] | | [%] | [-] | [-] |
| F7-(S1) | warp | 1200 | 19 | 33 | 0.053 | SBR 1 | 13.5 | 1.5 | 2.4 |
| | weft | 2 × 2400 | 27 | 33 | 0.053 | | | | |
| F7-(E1) | warp | 1200 | 19 | 33 | 0.053 | Epoxy 1 | 17.9 | 1.5 | 2.7 |
| | weft | 2 × 2400 | 27 | 33 | 0.053 | | | | |
| F8-(S2) | warp | 2400 | 27 | 38 | 0.093 | SBR 2 | 13.5 | 2.6 | 3.3 |
| | weft | 4 × 2400 | 27 | 38 | 0.093 | | | | |
| F8-(E2) | warp | 2400 | 27 | 38 | 0.093 | Epoxy 2 | 13.8 | 2.6 | 4.8 * |
| | weft | 4 × 2400 | 27 | 38 | 0.093 | | | | |
| F8-(E1) | warp | 2400 | 27 | 38 | 0.093 | Epoxy 1 | 17 | 2.6 | 5.3 |
| | weft | 4 × 2400 | 27 | 38 | 0.093 | | | | |
| F9-(S1) | warp | 2400 | 27 | 38 | 0.093 | SBR 1 | 10.2 | 2.5 | 3.2 |
| | weft | 4 × 2400 | 27 | 42 | 0.085 | | | | |
| F10-(E1) | warp | 2400 | 27 | 33 | 0.106 | Epoxy 1 | 11.7 | 2.9 | 4.6 |
| | weft | 4 × 2400 | 27 | 33 | 0.106 | | | | |
| F11-(S2) | warp | 2400 | 27 | 10 | 0.179 | SBR 2 | 12.9 | 3.3 | 4.3 |
| | weft | 2 × 1200 | 19 | 14 | 0.062 | | | | |
| F11-(E1) | warp | 2400 | 27 | 10 | 0.179 | Epoxy 1 | 12.9 | 3.3 | 5.9 |
| | weft | 2 × 1200 | 19 | 14 | 0.062 | | | | |
| F12-(S1) | warp | 1200 | 19 | 5 | 0.179 | SBR 1 | 16 | 3.1 | 3.7 |
| | weft | 2400 | 27 | 12 | 0.071 | | | | |

* evaluated in proportion to the epoxy 1 coating cost and in proportion to the coating percentage.

In the weaving process, the AR-glass spools forming the warp direction, according to the mesh construction, are placed on the creel and pulled in parallel to the weaving loom, where the weft rovings are inserted in the perpendicular direction, Figure 1a,b. The pattern of the mesh is built by the loom during the weaving process. Fabrics realized by two different patterns were taken into account in this study: plain and leno weave ones. In the case of the leno weave pattern, two warp yarns are twisted around the weft yarns, in order to guarantee a strong shear resistance of the mesh junctions. Leno weave produces an open fabric, with almost no yarn slip and higher flexibility to the warp direction, while the weft yarns remain completely flat. To increase the junction stiffness and the textile grammage, it is possible to produce textile meshes with double or triple leno patterns.

Plain weave is a textile pattern in which each warp roving crosses the perpendicular direction, passing alternatively over and under subsequent weft rovings during the entire weaving process. The rigidity and the tensile responses of the plain weave mesh are substantially the same in the two main directions, because both the warp and the weft rovings remain flat.

The different patterns of the textiles investigated in this study were: (i) the plain one for fabrics F1, F3, and F5; (ii) the leno one for the F11 and F12 meshes; and (iii) the double leno one for the F2, F4, F6, F7, F8, and F9 textiles (see Figure 2). The effect of the pattern on the mechanical response of the textiles is not herein discussed, due to numerically insufficient data.

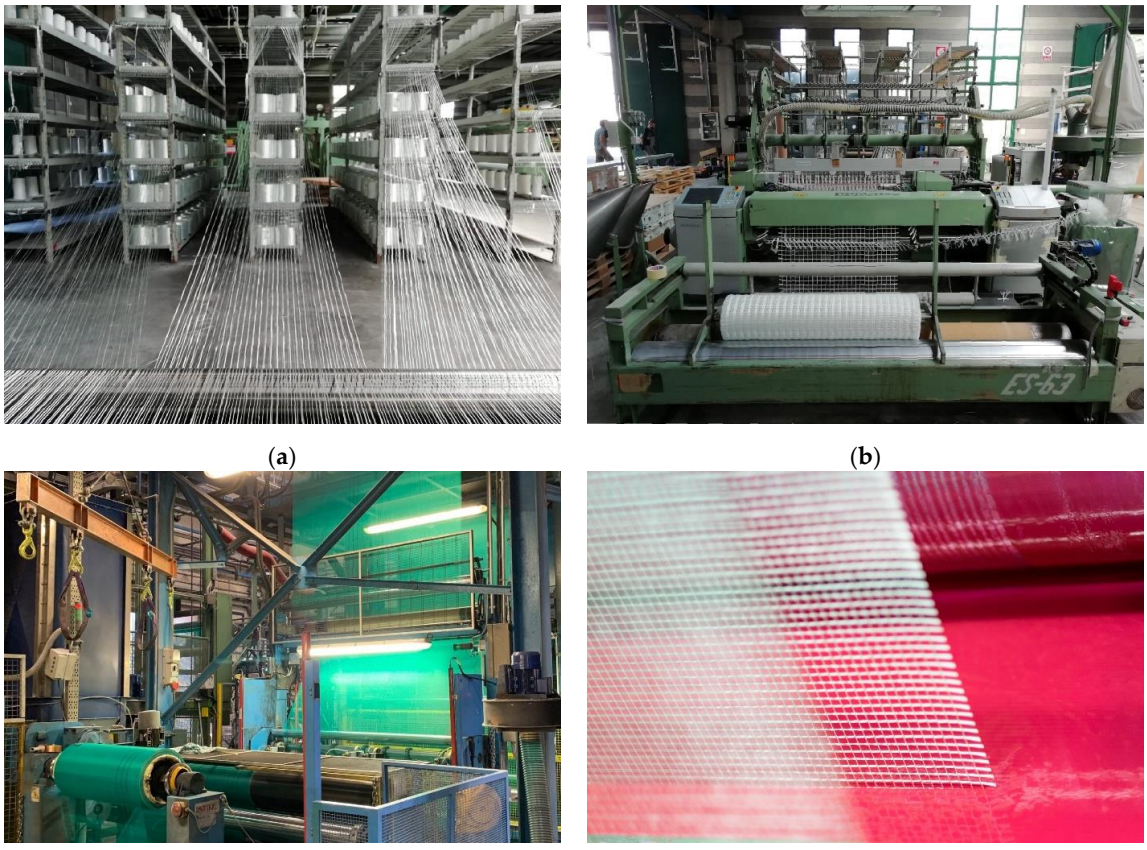


**Figure 1.** Textile manufacturing phases: AR-glass spools on the creel (**a**), weaving loom machine (**b**), impregnation machine (**c**), and detail of the dip-coating process within the impregnation tank (**d**).

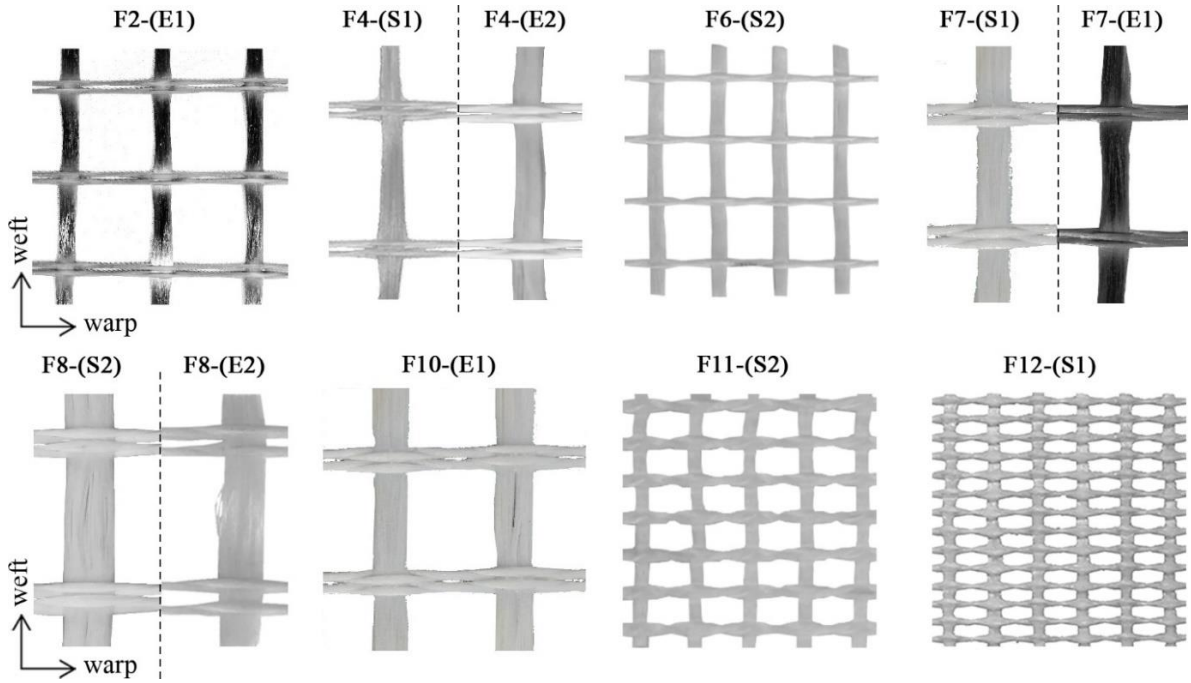


**Figure 2.** Overview of the some of the investigated AR-glass textiles (70 × 70 $mm^2$ in size).

*2.2. Impregnation Phase and Coatings Description*

Following the weaving of the raw mesh, fabrics are impregnated through a dip-coating process (Figure 1c,d), by means of wet liquids obtained with various chemical formulations; such compounds provide the impregnated textiles with stability, durability, higher stiffness under tensile actions, and an increase of mechanical performance with respect to the uncoated fabrics.

The most common chemical formulations for the impregnation of the textiles, in the case of building applications, are: (i) the butadiene-styrene rubber copolymer latex (SBR) and (ii) the epoxy (E) resin system. Both were considered in the process of impregnation of the textiles investigated in this study.

The SBR coating is an aqueous, anionic dispersion of a carboxylate self-crossing butadiene styrene copolymer, in which the dry content of polymers is equal to around 50% of the weight and the viscosity corresponds to approximately 250 mPa·s. After drying and curing at temperatures above 140 °C, the polymer forms a tack-free, flexible, and tough film (glass transition of 0 °C) with an excellent water and alkali resistance (needed in case of cementitious-based composites). The crosslinking reticulation is guaranteed by the reaction with the heat reactive monomer, as the *N*-methylacrylamide groups are grafted on the co-polymer chain. The condensation of two methylol groups forms a methylene bridge between the two amide functions, releasing water and formaldehyde. Carboxylic acids, mostly used as functional co-monomers, provide a good adhesion with the sizing of the AR-glass yarns.

In this study, two alternative SBR latex formulations were used: (i) without any addition of additives, called SBR 1 (S1), and (ii) with the addition of a thermoset stiff additive in a fraction of 10% by weight, named SBR 2 (S2). This was done in order to evaluate the effect of the film rigidity on the mechanical responses of both the plain mesh and of the cementitious-based composite.

The epoxy resin system is a bi-component thermoset formulation consisting of an epoxy resin, based on bisphenol A, and a polyamine hardener, which should be introduced according to a stochiometric ratio in order to ensure the complete reticulation of the system after curing. The latter takes place at 250 °C and the system becomes highly reticulated and forms a very stiff resin film.

As for the SBR, two different epoxy systems are used: (i) epoxy 1 (E1), a medium-viscosity (around 300 mPa·s) solvent-free epoxy system that provides high adhesion with the glass fibers, and ii) epoxy 2 (E2), a very low-viscosity (less than 100 mPa·s) and low-surface-tension solvent-based system that allows users to "open" the glass fibers, improving the resin impregnation of the roving filaments (a study on the effect of the epoxy viscosity on the textile-reinforced mortar composites performance is reported in [16]).

Due to the chemical formulation and to the differences in the curing process (i.e., temperature and process velocity), the costs of the two alternative coating solutions, SBR and epoxy, are substantially different. The SBR solution is generally cheaper than the epoxy one and a small variation is already present between the SBR 1 and SBR 2 coatings due to the addition of a thermoset stiff additive.

As declared by the manufacturer, the epoxy coating has a glass transition temperature, Tg, of around 60 °C, higher than the one of the SBR coatings. The study of its effect on the textile's efficiency was not investigated in the present study.

With the exclusion of the epoxy 2 system, all the coatings were made by the manufacturing company that weaves the AR-glass meshes. In order to ensure a fair comparison, the cost of the impregnation of epoxy 2 textiles was taken as equal to the one of the epoxy 1 system, proportionally to the applied coating percentage. This preliminary hypothesis, which was aimed at excluding the seller markup on epoxy 2 coating, can be considered acceptable, considering the balance between the lower cost of the resin and the higher cost of the impregnation process with respect to the epoxy 1 solution. In fact, the production process of solvent-free epoxy resin requires much more steps, compared to the manufactur-

ing of the epoxy solvent-based system, which, on the contrary, implies a higher cost of the raw material (i.e., the resin).

### 3. Mechanical Characterization of the AR-Glass Textiles

The selected AR-glass fabrics were tested under uniaxial tensile action, according to the strip method [17], in both the warp and the weft directions. The fabric samples ($70 \times 400$ mm$^2$ in size) were clamped to an electromechanical jack and tested in displacement control at a stroke rate of 100 mm/min. To prevent stress localization and slip within the clamps, epoxy resin tabs were created at the specimen ends. Three or five nominally identical specimens were tested for each fabric type; it is worth noting that some results were removed from the comparison due to their premature failure, not complying with the [17] prescriptions (i.e., yarn misalignment and failure in the clamping zones). The nominal free lengths of the different samples were chosen equal to 300 mm; the effect of the effective free length of the tested samples on the global response is not discussed in this paper. The average peak loads, $P_{max}$, are reported in Tables 3 and 4 and the standard deviations (std) were computed for all the cases in which at least three samples exhibited a satisfactorily failure. Starting from the average loads over 70 mm width, the corresponding maximum value over 1 m was computed ($P_{max}$ divided by the number of yarns in 70 mm and multiplied by the number of yarns in 1 m). Then, the efficiency of the fabric was evaluated, as proposed by Rampini et al. [18], as:

$$EF_f = \frac{P_{f,max,avg}}{A_f \cdot \sigma_{fu}}, \tag{1}$$

where $\sigma_{fu}$ is the glass filament strength, assumed equal to 2000 MPa accordingly to the manufacturer data. This efficiency parameter provides important information about the rate of utilization of the glass material, identifying the quantity of AR-glass filaments that effectively contributed to the mechanical performance of the fabric under tension. The computed parameters for both the warp and the weft fabric directions are reported in Tables 3 and 4.

In order to introduce cost-efficiency considerations, the normalized costs, $C_N$, evaluated as explained before, were divided by the maximum load, referring to a 1 m width mesh. This parameter, reported in Table 3 only for the warp direction, represents the normalized cost needed to obtain 1 kN of tensile load. Please note that, to evaluate the $C_N$ value referring only to the warp yarns, the total fabric costs of all the textiles were multiplied by the relative grammage ratio in the warp direction.

In Figure 3, some examples of the tensile response curves in terms of load vs. displacements are reported. It is possible to appreciate the similar slope of the different curves when geometrically identical fabrics (i.e., F4-F6-F7 in Figure 3c,d) are considered and the general increase of the maximum capacity with increasing grammage content.

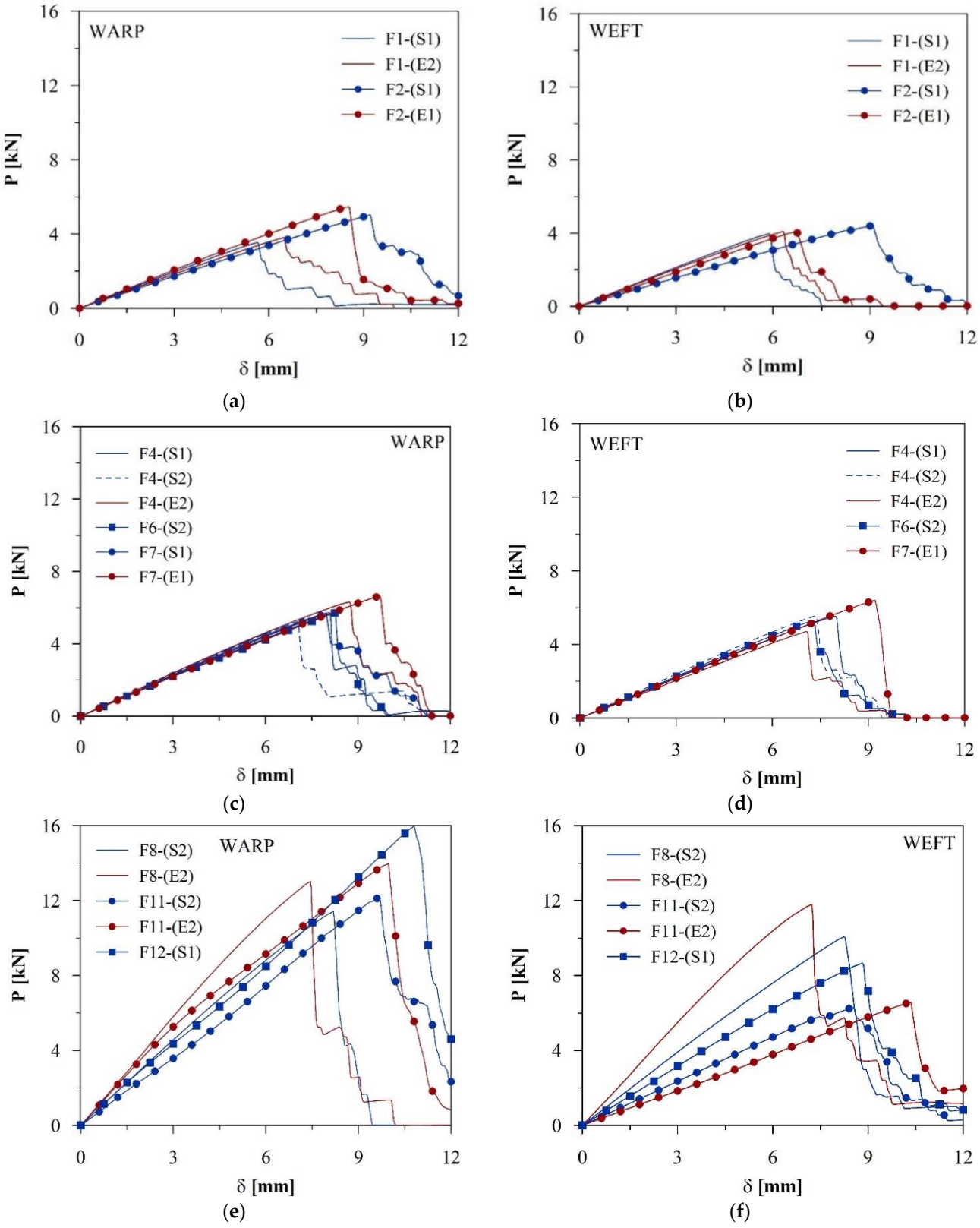


**Figure 3.** Examples of average load vs. displacement response curves for the investigated textiles in the warp and in the weft direction: low (**a**,**b**), medium (**c**,**d**), and high warp grammage textiles (**e**,**f**).

**Table 3.** Tensile test results in the warp direction and normalized cost per kN of the AR-glass textiles.

| Fabric | Nr. Sample | $P_{max}$ over 70 mm | | $A_f$ over 70 mm | $P_{max}$ over 1 m | $EF_f$ | Normalized Cost $C_N$ per kN | |
|---|---|---|---|---|---|---|---|---|
| | | | | | | | (Raw Fabric) | (Coated Fabric) |
| ID. | [-] | [kN] | | [mm$^2$] | [kN] | [-] | [1/kN] | [1/kN] |
| F1-(S1) | 5 | avg. | 3.57 | 2.687 | 47.62 | 0.66 | 0.010 | 0.013 |
| | | (std) | (0.21) | | | | | |
| F1-(E2) | 5 | avg. | 3.90 | 2.687 | 52.02 | 0.73 | 0.010 | 0.022 |
| | | (std) | (0.33) | | | | | |
| F2-(S1) | 5 | avg. | 5.17 | 2.866 | 68.93 | 0.90 | 0.008 | 0.010 |
| | | (std) | (0.52) | | | | | |
| F2-(E1) | 4 * | avg. | 5.47 | 2.866 | 72.98 | 0.95 | 0.007 | 0.016 |
| | | (std) | (0.11) | | | | | |
| F3-(S1) | 5 | avg. | 5.19 | 3.582 | 67.44 | 0.72 | 0.010 | 0.016 |
| | | (std) | (0.23) | | | | | |
| F4-(S1) | 5 | avg. | 5.77 | 3.582 | 74.99 | 0.81 | 0.009 | 0.015 |
| | | (std) | (0.28) | | | | | |
| F4-(S2) | 4 * | avg. | 5.25 | 3.582 | 68.25 | 0.73 | 0.010 | 0.016 |
| | | (std) | (0.99) | | | | | |
| F4-(E2) | 5 | avg. | 6.41 | 3.582 | 83.34 | 0.89 | 0.008 | 0.014 |
| | | (std) | (0.29) | | | | | |
| F5-(S1) | 5 | avg. | 5.06 | 3.518 | 70.89 | 0.72 | 0.010 | 0.016 |
| | | (std) | (0.17) | | | | | |
| F6-(S2) | 5 | avg. | 5.72 | 3.518 | 80.13 | 0.81 | 0.009 | 0.014 |
| | | (std) | (0.27) | | | | | |
| F7-(S1) | 5 | avg. | 5.67 | 3.582 | 85.04 | 0.79 | 0.009 | 0.014 |
| | | (std) | (0.68) | | | | | |
| F7-(E1) | 3 | avg. | 6.65 | 3.582 | 99.68 | 0.93 | 0.008 | 0.014 |
| | | (std) | (0.13) | | | | | |
| F8-(S2) | 4 * | avg. | 11.44 | 7.164 | 148.72 | 0.80 | 0.009 | 0.011 |
| | | (std) | (0.63) | | | | | |
| F8-(E2) | 4 * | avg. | 12.50 | 7.164 | 162.46 | 0.87 | 0.008 | 0.015 |
| | | (std) | (0.67) | | | | | |
| F8-(E1) | 3 | avg. | 13.16 | 7.164 | 171.04 | 0.92 | 0.008 | 0.015 |
| | | (std) | (0.25) | | | | | |
| F9-(S1) | 5 | avg. | 10.54 | 7.164 | 137.08 | 0.74 | 0.010 | 0.012 |
| | | (std) | (0.76) | | | | | |
| F10-(E1) | 2 * | avg. | 12.83 | 7.164 | 192.47 | 0.90 | 0.008 | 0.012 |
| | | (std) | - | | | | | |
| F11-(S2) | 4 * | avg. | 12.20 | 12.537 | 174.29 | 0.49 | 0.014 | 0.018 |
| | | (std) | (0.20) | | | | | |
| F11-(E1) | 5 | avg. | 13.99 | 12.537 | 199.80 | 0.56 | 0.012 | 0.022 |
| | | (std) | (0.36) | | | | | |
| F12-(S1) | 5 | avg. | 15.98 | 12.537 | 228.25 | 0.64 | 0.010 | 0.012 |
| | | (std) | (0.15) | | | | | |

* one sample removed from the comparison.

**Table 4.** Tensile test results in the weft direction of the AR-glass textiles.

| Fabric | Nr. Sample | $P_{max}$ over 70 mm | | $A_f$ over 70 mm | $P_{max}$ over 1 m | $EF_f$ |
|---|---|---|---|---|---|---|
| **ID.** | **[-]** | | **[kN]** | **[mm$^2$]** | **[kN]** | **[-]** |
| F1-(S1) | 5 | avg. | 4.01 | 2.687 | 53.47 | 0.75 |
| | | (std) | (0.22) | | | |
| F1-(E2) | 4 * | avg. | 4.15 | 2.687 | 55.32 | 0.77 |
| | | (std) | (0.13) | | | |
| F2-(S1) | 5 | avg. | 4.43 | 2.687 | 59.08 | 0.82 |
| | | (std) | (0.33) | | | |
| F2-(E1) | 4 * | avg. | 4.12 | 2.687 | 54.94 | 0.77 |
| | | (std) | (0.43) | | | |
| F3-(S1) | 5 | avg. | 5.37 | 3.582 | 69.81 | 0.75 |
| | | (std) | (0.21) | | | |
| F4-(S1) | 5 | avg. | 5.58 | 3.582 | 72.60 | 0.78 |
| | | (std) | (0.30) | | | |
| F4-(S2) | 5 | avg. | 5.58 | 3.582 | 72.51 | 0.78 |
| | | (std) | (0.11) | | | |
| F4-(E2) | 5 | avg. | 4.81 | 3.582 | 62.54 | 0.67 |
| | | (std) | (0.33) | | | |
| F5-(S1) | 5 | avg. | 4.97 | 3.518 | 69.64 | 0.71 |
| | | (std) | (0.32) | | | |
| F6-(S2) | 5 | avg. | 5.36 | 3.582 | 74.98 | 0.75 |
| | | (std) | (0.27) | | | |
| F7-(S1) | not tested | | | | | |
| F7-(E1) | 3 | avg. | 6.41 | 3.582 | 96.13 | 0.89 |
| | | (std) | (0.06) | | | |
| F8-(S2) | 4 | avg. | 11.44 | 7.164 | 131.17 | 0.70 |
| | | (std) | (0.63) | | | |
| F8-(E2) | 4 * | avg. | 12.41 | 7.164 | 161.33 | 0.87 |
| | | (std) | (0.74) | | | |
| F8-(E1) | not tested | | | | | |
| F9-(S1) | 5 | avg. | 10.54 | 7.164 | 126.52 | 0.74 |
| | | (std) | (0.76) | | | |
| F10-(E1) | not tested | | | | | |
| F11-(S2) | 5 | avg. | 6.34 | 4.478 | 88.76 | 0.71 |
| | | (std) | (0.41) | | | |
| F11-(E1) | 4 * | avg. | 6.66 | 4.478 | 93.27 | 0.74 |
| | | (std) | (0.53) | | | |
| F12-(S1) | 5 | avg. | 8.69 | 5.373 | 115.93 | 0.81 |
| | | (std) | (0.71) | | | |

* one sample removed from the comparison.

## 4. Discussion of the Results: Performance and Cost Considerations

In this section, the effect of the main fabric characteristics on the mechanical performance of the different textiles is discussed, starting from the experimental results reported in Figure 3 and in Tables 3 and 4. Moreover, both the performance efficiency and the manufacturing costs of the various textiles are accounted for in the comparison.

### *4.1. Considerations on the Fabric Efficiency*

As visible from Figures 4a and 5a, the increase of AR-glass quantity (reported in terms of the equivalent thickness on a 1 m width strip) generally corresponds to higher average maximum capacities. This observed trend can be considered linear up to medium

grammage textiles (equivalent thickness up to about 0.1 mm/m), while, for high grammage textiles (i.e., F11 and F12 fabrics in the warp direction) the load increment is limited. It is also interesting to observe the crucial effect of the coating nature and process on the fabric efficiency; in fact, as clearly visible in Figure 4b for the warp direction, the epoxy-based coating entails a higher rate of utilization of the AR-glass strength with respect to SBR-coated fabrics. This is probably related to the already mentioned better impregnation of the filaments offered by the epoxy resin (better penetration due to lower resin viscosity and glass fibers opening in case of solvent treatment), which limits the telescopic failure [19], increasing the overall capacity.

In the weft direction, as shown in Figures 4b and 5b, due to the flat shape of the weft yarn, which generally favors the resin penetration, the effect of the different coating nature appears negligible.

The limited load increase in case of high grammage textiles is probably related to both the crimp effect on the warp strand and the to the higher filament diameters. Moreover, in those cases, the yarn impregnation results are more complicated, limiting the beneficial effect of the use of an epoxy coating.

From the results reported in Figure 6, it is possible to observe the effect of the filament diameter on the fabric efficiency. Higher diameters imply lower flexibility of the AR-glass yarns and, consequently, the development of damage to the yarns at different stages of the weaving process due to abrasion and breakage when sliding against the loom machinery [20,21]. Moreover, increasing filament diameter causes a higher amount of surface defects, reducing the wire tensile strength [22]. In case of the F11 textiles, the limited fabric efficiency is related to both the filament diameters and the above-mentioned high grammage.

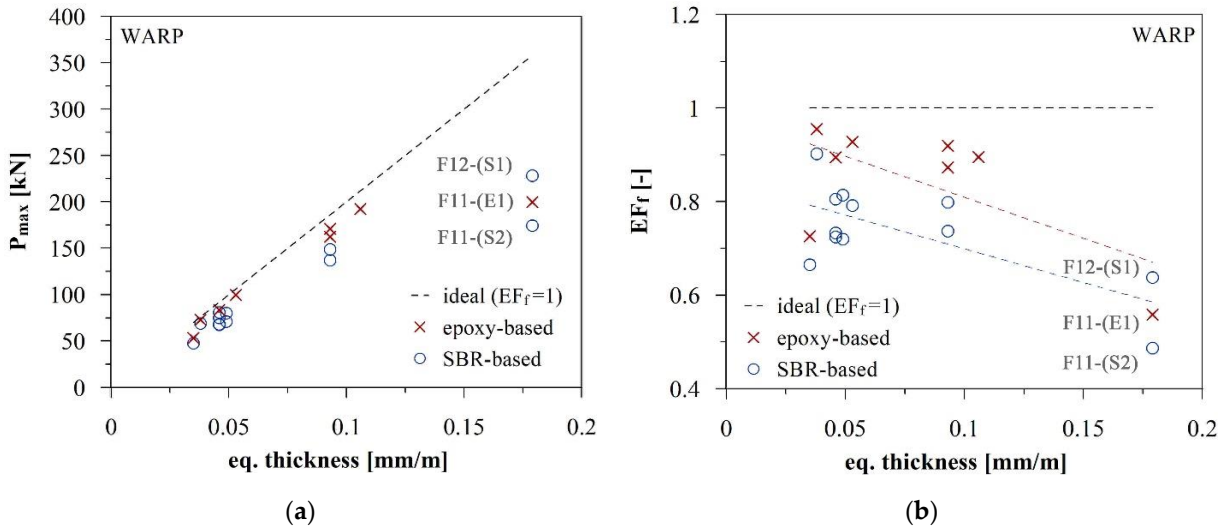


**Figure 4.** Average maximum load (**a**) and fabric efficiency (**b**) vs. equivalent thickness of the investigated textiles in the warp direction.

As previously observed, the coating process based on epoxy resin improves the mechanical performance with respect to the SBR case in the presence of higher filament diameters. In particular, considering geometrically identical meshes and comparing the fabric efficiency achieved with different coatings (normalized fabric efficiency in Figure 7 is the ratio between the fabric efficiency of each textile and the one of the mesh impregnated with SBR 1 coating), it is possible to appreciate that the effect of the better impregnation offered by the epoxy resin is more influenced by the increasing of the filament diameters than by the equivalent thickness. The beneficial effect of the epoxy coating is more significant in the cases with higher filament diameters, which suffer the most from the poor impregnation offered by the SBR coatings.

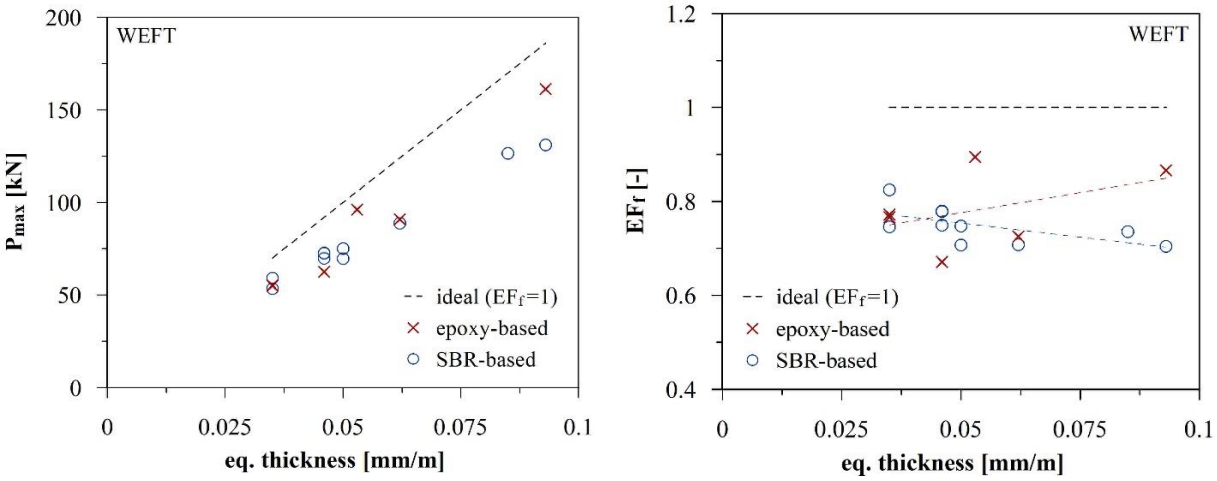


(**a**) (**b**)

**Figure 5.** Average maximum load (**a**) and fabric efficiency (**b**) vs. equivalent thickness of the investigated textiles in the weft direction.

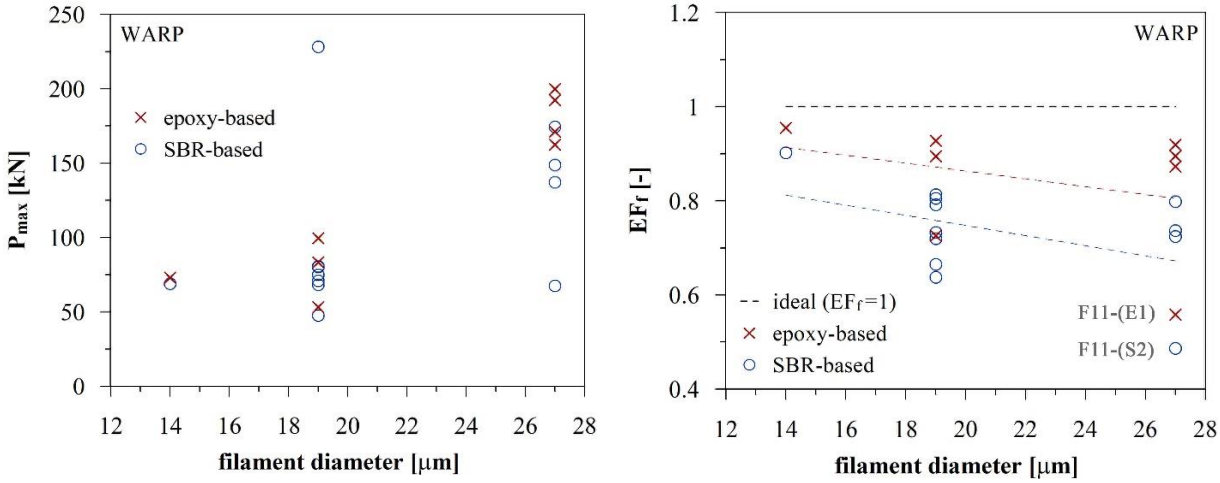


(**a**) (**b**)

**Figure 6.** Average maximum load (**a**) and fabric efficiency (**b**) vs. filament diameters of the investigated textiles in the warp direction.

Please note that, in case of fabric F4-(S2) impregnated with the stiffer solution of the SBR coating (SBR 2), the lower tensile capacity is related to an overestimation of the maximum load due to the significant dispersion of the test results (a standard deviation of 0.99 kN and an average maximum load of 5.25 kN were recorded). The effect of the stiffer SBR coating, with respect to the base version, becomes visible in the cementitious composite application, as discussed in the following section.

### *4.2. Cost–Performance Considerations*

The previous observations on the main features influencing the fabric efficiency of the textile can be a starting point to orient practitioners and manufacturers, respectively, to the design and to the production of more efficient textiles. In parallel to the efficiency considerations, the manufacturing cost of the AR-glass textiles must be taken into account in order not to waste raw glass and to make the process of production more sustainable from an economic standpoint. Due to this reason, the ratio between the normalized cost, $C_N$, which comprises both the raw material and impregnation costs, and the maximum tensile

capacity experimentally obtained, $P_{max}$, were computed for each investigated textile. From the comparison of these parameters, which substantially represent the required cost to improve of 1 kN the fabric capacity, it is possible to highlight the balance between cost and mechanical performance, targeting optimized solutions. The following observations refer only to the warp direction, which, as mentioned, is the most influenced by the textile characteristics.

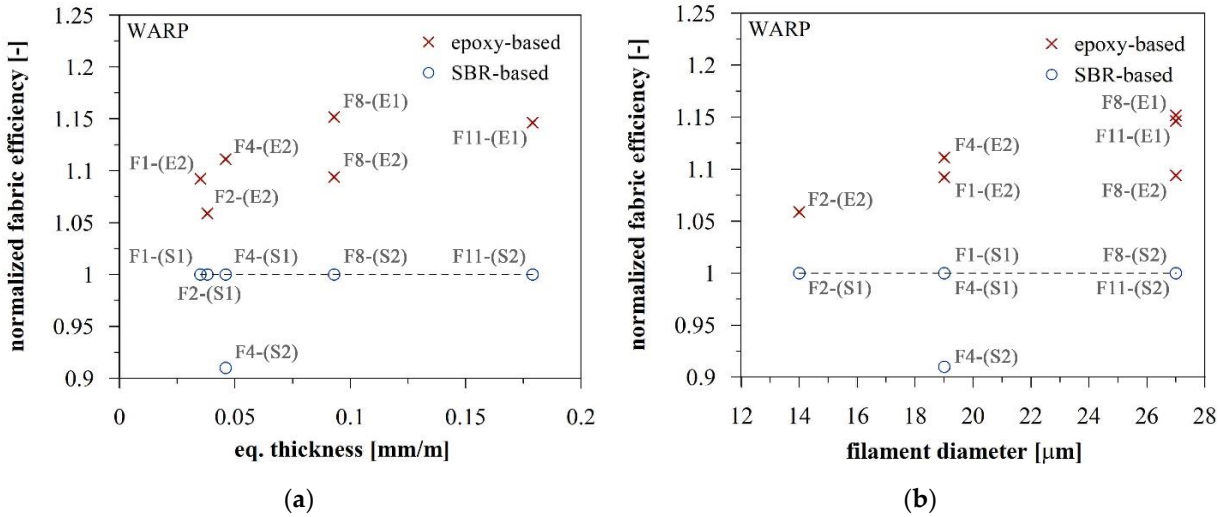


**Figure 7.** Normalized fabric efficiency vs. equivalent diameter (**a**) and filament diameters (**b**) in the warp direction.

Although the effect of the coating in the yarn impregnation—especially in case of epoxy resins—is evident, the correlation between the coating percentage and the increasing of the mechanical capacity needs more investigation. In some cases, such as, for example, observed by visual inspection of the fabric F9-(S2), the increasing coating percentage does not correspond to a deep impregnation of the filaments and a significant amount of coating remains on the external surface of the fabrics. Moreover, in parallel to the coating percentage, other parameters influence the impregnation quality, such as, for example, the process velocity and the temperature and time of curing. Due to this reason, in addition to the normalized cost per unit load, $C_N/P_{max}$, for the coated textiles, the same parameters were evaluated neglecting the impregnation cost (both resin and dip-coating processes).

From the results reported in Figures 8a and 9a, it is possible to observe that the variation of the defined cost/performance parameter on coated fabrics is not particularly influenced by either the equivalent thickness or the filament diameters. This means that increasing manufacturing costs correspond higher fabric capacities (see the $C_N/P_{max}$ vs. $EF_f$ data in Figure 10a). On the contrary, considering only the cost of the uncoated fabrics, as shown in Figures 8b, 9b and 10b, the effect of the geometrical characteristics and of the coating nature are obviously more evident, confirming the observations related to the fabric efficiency trends highlighted in the previous section.

Note that, in real applications, the input data are the required tensile capacities of the textile. In Figure 11a, entering in the graph abscissa with the target load value, it is possible to identify the textile solution, which allows for a reduction in the manufacturing costs (both raw material and impregnation). In addition to this, observing the fabric efficiency reported in Figure 11b, it is worth noting that, once the input load is fixed, the cheapest textile may not correspond to the one with the highest rate of utilization of the AR-glass. This is an important aspect that may orient the decision-making process of the textiles, ensuring the best balance between cheapness, performance, and sustainability, minimizing the waste of raw material.

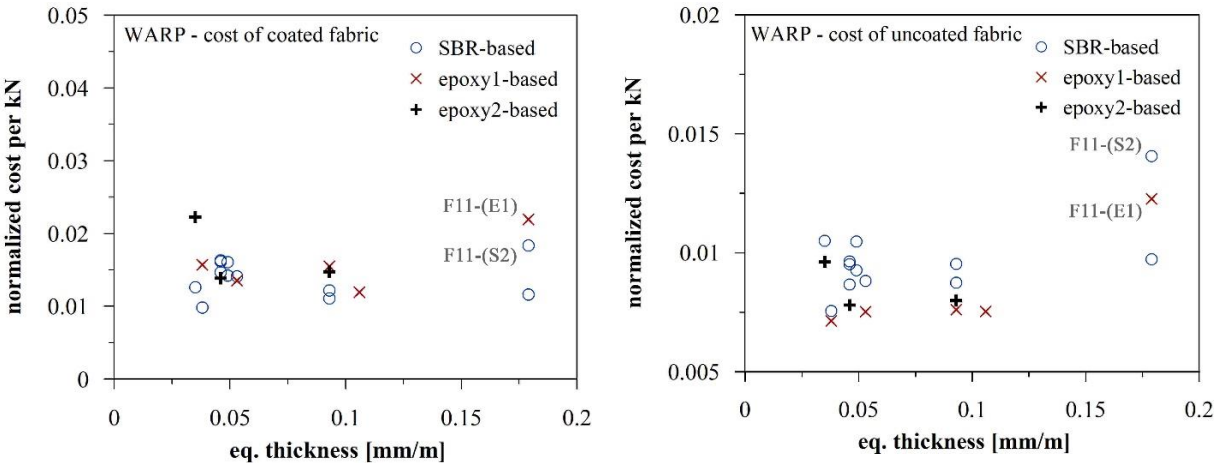


(**a**) (**b**)

**Figure 8.** Normalized cost per kN vs. equivalent thickness: cost of the coated (**a**) and of the uncoated fabrics (**b**).

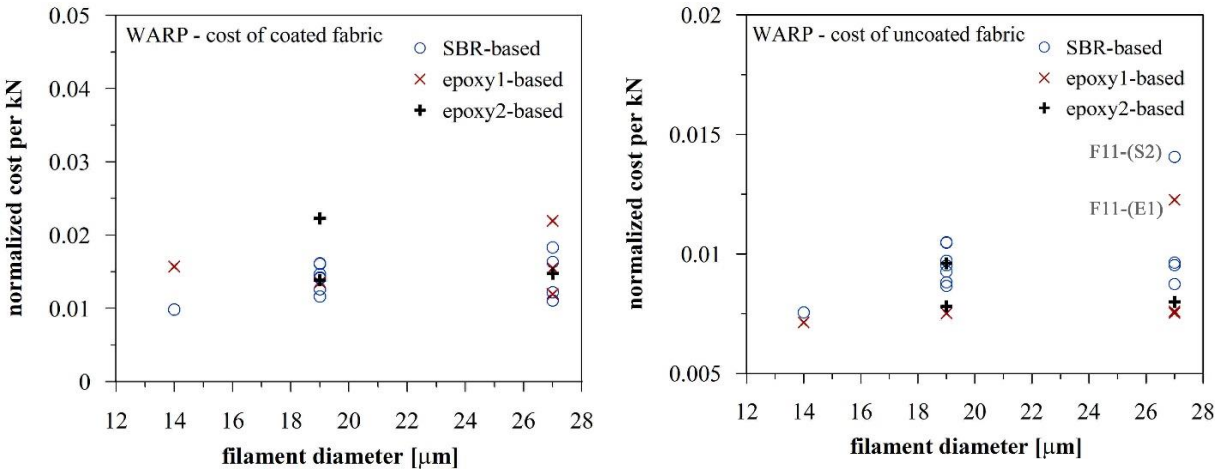


(**a**) (**b**)

**Figure 9.** Normalized cost per kN vs. filament diameters: cost of the coated (**a**) and of the uncoated fabrics (**b**).

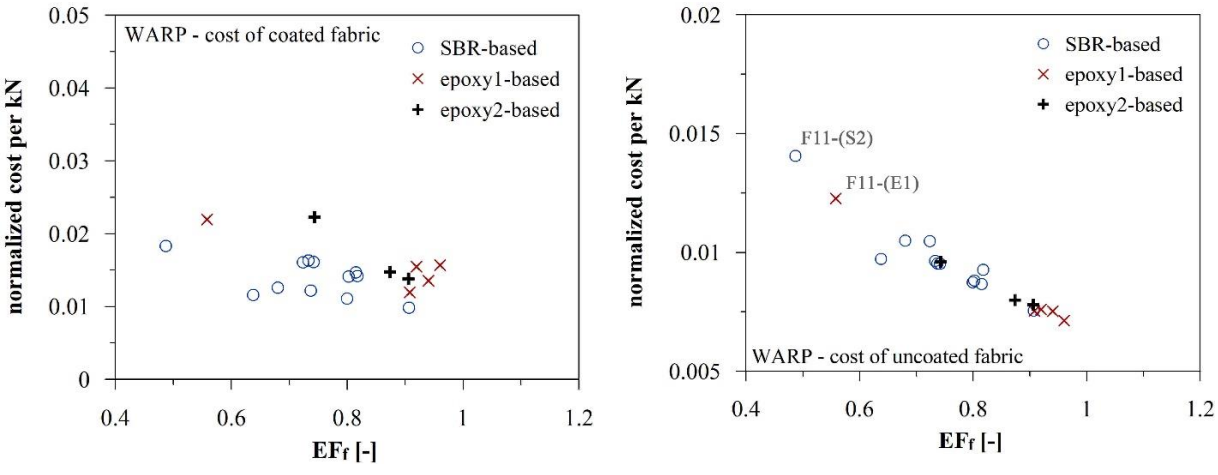


(**a**) (**b**)

**Figure 10.** Normalized cost per kN vs. fabric efficiency, $EF_f$: cost of the coated (**a**) and of the uncoated fabrics (**b**).

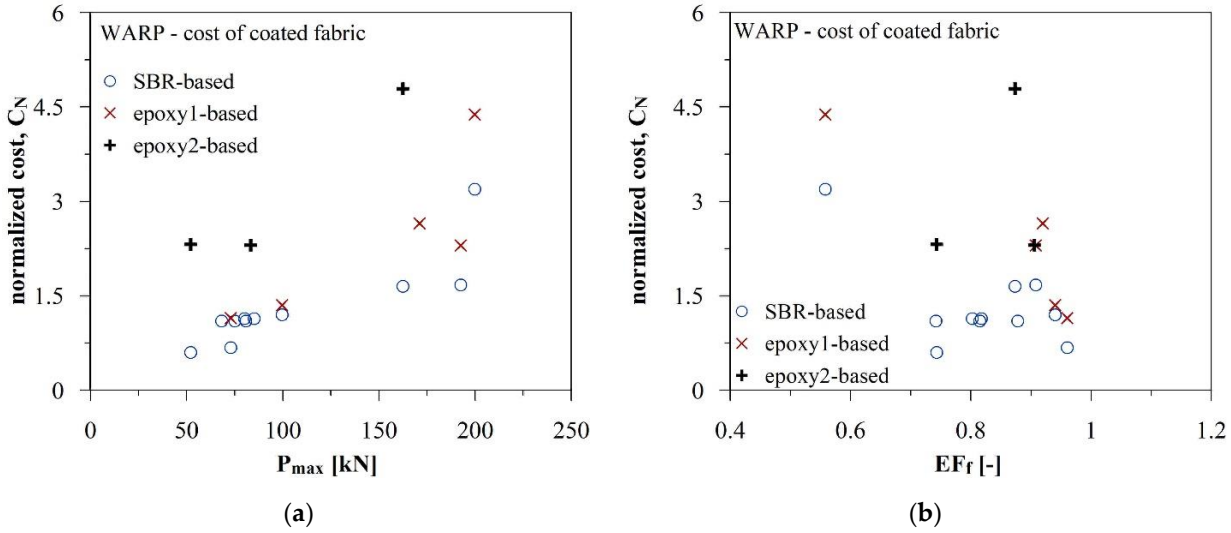


(**a**) (**b**)

**Figure 11.** Normalized cost, $C_N$, vs. average maximum tensile load (**a**) and fabric efficiency (**b**) in the warp direction.

## 5. Cementitious-Based Composites: Preliminary Performance and Cost Considerations

From an economical point of view, the choice of the textile to be used in different applications cannot be related only to the cost to the previously computed fabric performance ratios ($C_N/P_{max}$). In fact, for any kind of application, the requests in terms of mesh geometry (grid spacing, thickness, or raw material grammage) are different and they might mutually affect the interaction of the fabric with the surrounding matrix. The latter plays the most important role in the overall composite behavior. For example, in the case of cementitious-based composites (textile-reinforced concrete, TRC, or fabric-reinforced cementitious matrix, FRCM) the fabric-to-mortar bond is generally improved by more rigid warp-to-weft junctions and by stiffer coatings.

In this section, some of the previously investigated fabrics were used as reinforcements in cement-based TRC composites and performance and cost considerations have been similarly drawn. Three different fabrics (F1, F4, F8) coated with both SBR and epoxy resins were considered. In particular, only the epoxy 2 system was taken into account, with the aim of quantifying the beneficial effect of the coating on the overall response in case of the most expensive textiles. The chosen matrix was a fine-grained self-compacting high-performance concrete (HPC), characterized by an average flexural tensile strength of around 14 MPa and an average cubic compressive strength of around 90 MPa.

Three nominally identical samples ($70 \times 400 \times 6$ mm$^3$ in size and free length between the clamps, $L_0$, of about 300 mm) for each TRC composite system were cast and tested under tensile action, after at least 28 days of natural curing. Please note that, in case of composites made with fabric F8, the sample nominal thickness was increased to 9 mm, to account for the higher grammage of the fabric. For the sake of brevity, the details of the mortar mix design, its mechanical characterization, as well as the casting and testing procedures are here omitted and reported in [18].

From the average curves of the uniaxial tensile tests depicted in terms of load vs. displacement curves in Figure 12, the beneficial effect of the epoxy coating on the overall composite response appears clearly visible. In fact, the reached maximum loads in case of epoxy-impregnated textiles are higher than the SBR ones for all the tested TRC composites. Moreover, in the composites reinforced with SBR-impregnated low-grammage textiles, F1-(S1) and F4-(S1)/(S2), a slip of the fabric within the mortar occurred, preventing the development of the typical tri-linear response of TRC/FRCM composites and of a dense multi-cracking. The reason of that may be found in the lower impregnation, which implies that a certain amount of coating remains on the surface, degrading the bond with the

cementitious mortar, and in the limited stiffness of the warp-to-weft nodes in the case of SBR coatings. Similar observations were already shown by several authors in [18,23].

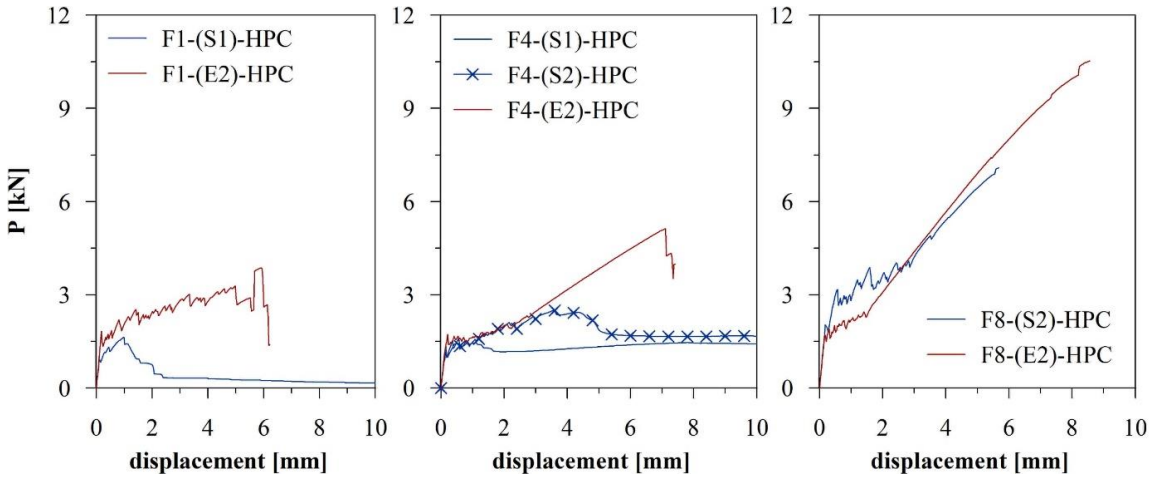


**Figure 12.** Average tensile response in terms of load vs. displacement curves for the F1/F4/F8-based TRC composites in the warp direction.

In Table 5, in addition to the geometrical and mechanical parameters, the efficiency of the composite system, $EF_{TRC,f}$, computed with respect to the maximum tensile strength of the AR-glass filaments (2000 MPa), is reported. This parameter, originally proposed in [18], was evaluated as follows:

$$EF_{TRC,f} = \frac{P_{max}}{A_f \cdot \sigma_{fu}} = \frac{\sigma_{TRC,f,max}}{2000\ \text{MPa}} \quad (2)$$

where the $A_f$ is the glass section over a width of 70 mm.

As in the case of the tensile tests on the plain textile samples, the increasing of the equivalent fabric thickness is accompanied by an increase of the experimentally evaluated maximum tensile capacity. Please note that the trend is close to linear, as was the one reported in Figure 4a for the low and medium-grammage textiles in the warp direction. However, the main difference between the results at the fabric and at the composite levels appears visible by computing the system efficiency. In fact, on the contrary to what was observed for the plain textiles and depicted in Figure 4b, by augmenting the fabric grammage it is possible to obtain at least a constant value of the utilization rate (or even an increasing evolution of the $EF_{TRC,f}$ in case of SBR-coated mesh) with respect to the ultimate tensile strength of the glass filaments (Figure 13b). Even in case of poor impregnation, the stiffness of the grid nodes grows if more AR-glass yarns are introduced in the fabric weaving.

As for the plain textiles, the normalized cost per unit load was computed for the TRC composites and is reported in Table 5. In Figure 14, those values are expressed as a function of the equivalent thickness of the fabrics and of the maximum load recorded during the tensile test on the composites. The cost over performance ratio is generally lower in the case of epoxy-impregnated textiles. Only with regard to the F8-based composites does the difference obtained between the two types of impregnations seem negligible.

As determined for the plain textiles, the choice of the optimum composite solution should start from the required tensile capacity. In this way, for example, it is possible to highlight the effect of the epoxy impregnation, which leads to cheaper and more sustainable solutions with fixed required mechanical performance (See Figures 13a and 14a). For example, assuming a target capacity of around 5 kN over a 70 mm wide strip, the F4-(E2)-HPC system would be less expensive than the F8-based one and require half of the glass quantity (equivalent thickness in the warp direction of 0.046 mm/m instead of 0.093 mm/m). Moreover, it is important to notice that, to reach certain load values, the adoption of an epoxy impregnation appears imperative.

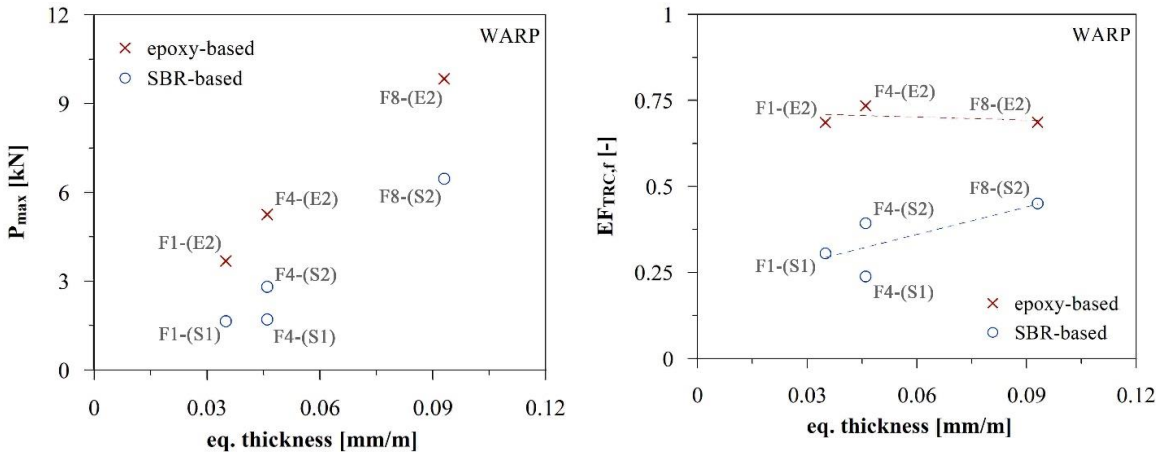


(**a**) (**b**)

**Figure 13.** Average maximum load (**a**) and fabric efficiency (**b**) vs. equivalent thickness of the investigated textiles in the case of TRC composites reinforced with the fabrics in the warp direction.

**Table 5.** Tensile test results for TRC samples: geometry, mechanical parameters, and normalized costs per unit load.

| | | $t$ | $b$ | $L_0$ | $P_{max}$ | $A_f$ | $\sigma_{TRC,f,max}$ | $EF_{TRC,f}$ | Normalized Cost per kN |
|---|---|---|---|---|---|---|---|---|---|
| | | [mm] | [mm] | [m] | [kN] | [mm$^2$] | [MPa] | [-] | [1/kN] |
| F1-(S1)-HPC | avg. | 5.72 | 69.97 | 295.67 | 1.64 | 2.69 | 611.94 | 0.31 | 0.36 |
| | (std) | (0.12) | (0.50) | (1.53) | (0.14) | | (50.63) | | |
| F1-(E2)-HPC | avg. | 5.97 | 70.35 | 294.67 | 3.69 | 2.69 | 1371.67 | 0.69 | 0.31 |
| | (std) | (0.21) | (0.36) | (0.58) | (0.41) | | (151.89) | | |
| F4-(S1)-HPC | avg. | 5.68 | 69.90 | 298.00 | 1.71 | 3.58 | 477.96 | 0.24 | 0.64 |
| | (std) | (0.42) | (0.48) | (1.00) | (0.40) | | (112.25) | | |
| F4-(S2)-HPC | avg. | 5.97 | 70.43 | 295.33 | 2.82 | 3.58 | 785.95 | 0.39 | 0.39 |
| | (std) | (0.39) | (0.96) | (1.53) | (0.32) | | (90.60) | | |
| F4-(E2)-HPC | avg. | 5.89 | 70.04 | 295.67 | 5.26 | 3.58 | 1468.86 | 0.73 | 0.22 |
| | (std) | (0.23) | (0.26) | (1.53) | (0.15) | | (42.76) | | |
| F8-(S2)-HPC | avg. | 8.77 | 70.58 | 294.00 | 6.46 | 7.16 | 902.36 | 0.45 | 0.26 |
| | (std) | (0.12) | (0.89) | (1.00) | (0.82) | | (114.31) | | |
| F8-(E2)-HPC | avg. | 8.89 | 70.66 | 293.33 | 9.84 | 7.16 | 1373.14 | 0.69 | 0.24 |
| | (std) | (0.29) | (0.57) | (0.58) | (0.68) | | (94.33) | | |

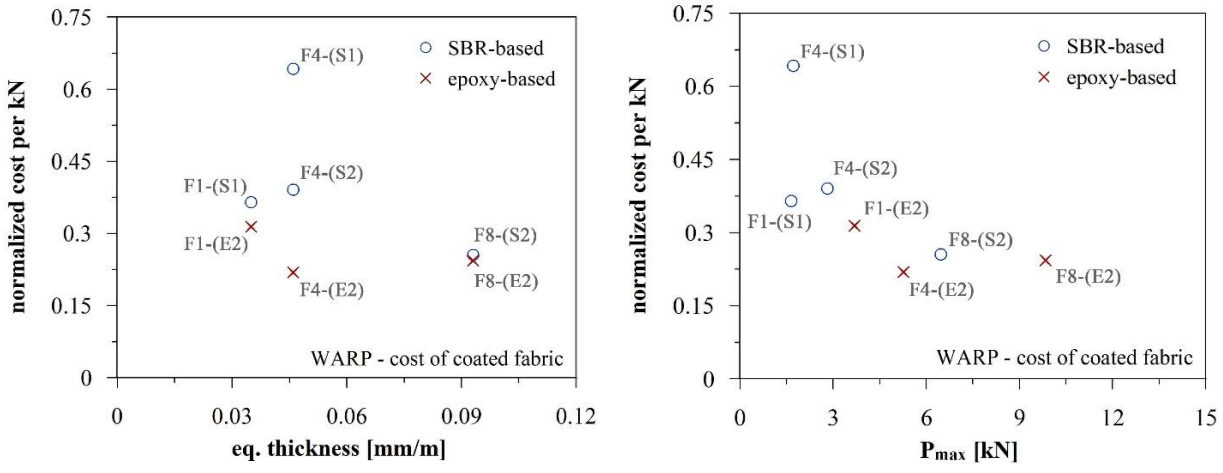


(**a**) (**b**)

**Figure 14.** Normalized cost per kN vs. equivalent thickness (**a**) and maximum tensile capacity (**b**) for the TRC composites reinforced in the warp direction.

Note that an important aspect that deserves further investigation is the possibility of using a combination of different fabrics within the same TRC composite. Further developments of this research could address the possible variation of the system efficiency, in the case of a single fabric with a defined sectional area or, as an alternative, multiple fabrics ensuring the same total amount of reinforcement. In those cases, the cost increase can be considered linear with the number of fabric layers (cost of the single fabric times the number of layers, neglecting the labor cost, which may increase with multiple fabric layers), but the performance efficiency may vary, affecting the identification of the optimum solution.

## 6. Conclusions

The behavior of the AR-glass based textiles under tension is significantly influenced by the mesh characteristics, such as the equivalent thickness, the filament diameter, and the nature of the impregnation coating. The fabric efficiency generally increases with the reduction of both the glass grammage and the roving fineness (i.e., filament diameters). Epoxy-impregnated textiles generally imply an increase of the manufacturing costs, but the better penetration within the filaments with respect to SBR-based solutions improves the fabric efficiency, making them excellent from a cost–performance point of view.

Similar observations regarding the efficiency increase due to the coating nature may be drawn at the TRC composite level. In the case of reinforcement with low-grammage textiles, the stiffer and low-viscosity epoxy coating is required to develop the typical trilinear composite response and ensure the multi-crack of the cement-based sample. This aspect plays a key role, especially when fabric-reinforced cement-based composites (e.g., FRCM) are used in retrofitting/strengthening applications. Note that the above-mentioned observation shall be confirmed in the case of lime-based mortar composites (typically used in masonry applications), since the efficiency may be limited by the poor characteristics of the inorganic matrix. Moreover, cost–performance considerations are needed in order to limit the waste of raw glass material, orienting towards more sustainable and efficient fabric-reinforced composites.

Some open problems deserve further investigation, including the effects of the different weave patterns (plain or leno) and the relationship between the performance increase and the coating percentage at the textile levels, as well as the use of multiple fabric layers or different mortars at the composite scale.

**Author Contributions:** Conceptualization, M.C.R., G.Z., L.S., M.C. and M.d.P.; methodology, M.C.R., G.Z., L.S. and M.C.; investigation, M.C.R., G.Z. and L.S.; data curation, M.C.R., G.Z. and L.S.; writing—original draft preparation, M.C.R. and L.S.; writing—review and editing, M.C.R., G.Z., L.S., M.C. and M.d.P.; visualization, M.C.R.; supervision, G.Z., M.C. and M.d.P.; funding acquisition, L.S. and M.d.P. All authors have read and agreed to the published version of the manuscript.

**Funding:** This research was funded by the ReLUIS interuniversity consortium (ReLUIS WP 14 2019–2021) and by Gavazzi Tessuti Tecnici Spa in the field of a private research project.

**Institutional Review Board Statement:** Not applicable.

**Informed Consent Statement:** Not applicable.

**Data Availability Statement:** The data presented in this study are available within the manuscript.

**Acknowledgments:** The authors would like to acknowledge Gavazzi Tessuti Tecnici Spa. This company, founded in 1881 and located near Lecco in the north of Italy, is a leading manufacturer of technical textiles, especially for building applications, and it has been working with Politecnico di Milano since 2008 in the framework of the development and manufacturing of AR-glass reinforcements.

**Conflicts of Interest:** The authors Marco Carlo Rampini, Giulio Zani, Matteo Colombo, and Marco di Prisco declare no conflict of interest. The author Louis Schouler, representing one of the funders of this study, declares his role in the design of the study, in the collection and interpretation of data, in the writing of the manuscript, and in the decision to publish the results.

## References


1. Hagnell, M.; Åkermo, M. The economic and mechanical potential of closed loop material usage and recycling of fibre-reinforced composite materials. *J. Clean. Prod.* **2019**, *223*, 957–968. [CrossRef]
2. Brameshuber, W. Textile reinforced concrete-state-of-the-art report of RILEM TC 201-TRC. In Proceedings of the Reunion Internationale des Laboratoires et Experts des Materiaux, Systemes de Construction et Ouvrages (RILEM), Aachen, Germany, 6 September 2006.
3. Peled, A.; Bentur, A.; Mobasher, B. *Textile Reinforced Concrete*, 1st ed.; CRC Press: Boca Raton, FL, USA, 2017.
4. De Felice, G.; De Santis, S.; Garmendia, L.; Ghiassi, B.; Larrinaga, P.; Lourenço, P.B.; Papanicolaou, C.G.; Paolacci, F.; Oliveira, D.V. Mortar-based systems for externally bonded strengthening of masonry. *Mater. Struct.* **2014**, *47*, 2021–2037. [CrossRef]
5. Ascione, L.; De Felice, G.; De Santis, S. A qualification method for externally bonded Fibre Reinforced Cementitious Matrix (FRCM) strengthening systems. *Compos. Part B Eng.* **2015**, *78*, 497–506. [CrossRef]
6. Saiman, M.P.; Wahab, M.S.; Wahit, M.U. The effect of fabric weave on the tensile strength of woven kenaf reinforced unsaturated polyester composite. In Proceedings of the International Colloquium in Textile Engineering, Fashion, Apparel and Design, Singapore, 9 October 2014; pp. 25–29.
7. Kim, S.J.; Kim, H.A. Effect of fabric structural parameters and weaving conditions to warp tension of aramid fabrics for protective garments. *Text. Res. J.* **2017**, *88*, 987–1001. [CrossRef]
8. Hegger, J.; Voss, S. Investigations on the bearing behaviour and application potential of textile reinforced concrete. *Eng. Struct.* **2008**, *30*, 2050–2056. [CrossRef]
9. Scheffler, C.; Gao, S.; Plonka, R.; Mäder, E.; Hempel, S.; Butler, M.; Mechtcherine, V. Interphase modification of alkali-resistant glass fibres and carbon fibres for textile reinforced concrete II: Water adsorption and composite interphases. *Compos. Sci. Technol.* **2009**, *69*, 905–912. [CrossRef]
10. D'Antino, T.; Papanicolaou, C. Mechanical characterization of textile reinforced inorganic-matrix composites. *Compos. Part B Eng.* **2017**, *127*, 78–91. [CrossRef]
11. Messori, M.; Nobili, A.; Signorini, C.; Sola, A. Mechanical performance of epoxy coated AR-glass fabric Textile Reinforced Mortar: Influence of coating thickness and formulation. *Compos. Part B Eng.* **2018**, *149*, 135–143. [CrossRef]
12. Bompadre, F.; Donnini, J. Surface modification of glass textile for the reinforcement of a cement-based composite: A review. *Appl. Sci.* **2021**, *11*, 2028. [CrossRef]
13. Peled, A.; Bentur, A. Geometrical characteristics and efficiency of textile fabrics for reinforcing cement composites. *Cem. Concr. Res.* **2000**, *30*, 781–790. [CrossRef]
14. Peled, A.; Bentur, A. Fabric structure and its reinforcing efficiency in textile reinforced cement composites. *Compos. Part A Appl. Sci. Manuf.* **2003**, *34*, 107–118. [CrossRef]
15. Donnini, J.; Corinaldesi, V.; Nanni, A. Mechanical properties of FRCM using carbon fabrics with different coating treatments. *Compos. Part B Eng.* **2016**, *88*, 220–228. [CrossRef]
16. Signorini, C.; Nobili, A.; Sola, A.; Messori, M. Designing epoxy viscosity for optimal mechanical performance of coated Glass Textile Reinforced Mortar (GTRM) composites. *Constr. Build. Mater.* **2019**, *233*, 117325. [CrossRef]
17. The British Standards Institution. *Implementation of ISO 4606:1995 Textile Glass—Woven Fabric—Determination of Tensile Breaking Force and Elongation at Break by the Strip Method*; ISO: Geneva, Switzerland, 1995; Volume 1995, pp. 1–16.
18. Rampini, M.C.; Zani, G.; Colombo, M.; Di Prisco, M. Mechanical behaviour of TRC composites: Experimental and analytical approaches. *Appl. Sci.* **2019**, *9*, 1492. [CrossRef]
19. Cohen, Z.; Peled, A. Controlled telescopic reinforcement system of fabric—Cement composites—Durability concerns. *Cem. Concr. Res.* **2010**, *40*, 1495–1506. [CrossRef]
20. Lee, B.; Leong, K.H.; Herszberg, I. Effect of weaving on the tensile properties of carbon fibre tows and woven composites. *J. Reinf. Plast. Compos.* **2001**, *20*, 652–670. [CrossRef]
21. Lee, L.; Rudov-Clark, S.; Mouritz, A.; Bannister, M.; Herszberg, I. Effect of weaving damage on the tensile properties of three-dimensional woven composites. *Compos. Struct.* **2002**, *57*, 405–413. [CrossRef]
22. Scheffler, C.; Gao, S.; Plonka, R.; Mäder, E.; Hempel, S.; Butler, M.; Mechtcherine, V. Interphase modification of alkali-resistant glass fibres and carbon fibres for textile reinforced concrete I: Fibre properties and durability. *Compos. Sci. Technol.* **2009**, *69*, 531–538. [CrossRef]
23. Raupach, M.; Orlowsky, J.; Büttner, T.; Dilthey, U.; Schleser, M.; Hegger, J. Epoxy-impregnated textiles in concrete-load bearing capacity and durability. In Proceedings of the 1st International RILEM Conference, Aachen, Germany, 6–7 September 2006; pp. 77–88.

textiles

MDPI

*Review*

# Dielectric Properties of Textile Materials: Analytical Approximations and Experimental Measurements—A Review

**Yusuke Yamada**

Yamada Shoten, Osaka 556-0001, Japan; ymukai@ncsu.edu

**Abstract:** Deciphering how the dielectric properties of textile materials are orchestrated by their internal components has far-reaching implications. For the development of textile-based electronics, which have gained ever-increasing attention for their uniquely combined features of electronics and traditional fabrics, both performance and form factor are critically dependent on the dielectric properties. The knowledge of the dielectric properties of textile materials is thus crucial in successful design and operation of textile-based electronics. While the dielectric properties of textile materials could be estimated to some extent from the compositional profiles, recent studies have identified various additional factors that have also substantial influence. From the viewpoint of materials characterization, such dependence of the dielectric properties of textile materials have given rise to a new possibility—information on various internal components could be, upon successful correlation, extracted by measuring the dielectric properties. In view of these considerable implications, this invited review paper summarizes various fundamental theories and principles related to the dielectric properties of textile materials. In order to provide an imperative basis for uncovering various factors that intricately influence the dielectric properties of textile materials, the foundations of the dielectrics and polarization mechanisms are first recapitulated, followed by an overview on the concept of homogenization and the dielectric mixture theory. The principal advantages, challenges and opportunities in the analytical approximations of the dielectric properties of textile materials are then discussed based on the findings from the recent literature, and finally a variety of characterization methods suitable for measuring the dielectric properties of textile materials are described. It is among the objectives of this paper to build a practical signpost for scientists and engineers in this rapidly evolving, cross-disciplinary field.

**Keywords:** textile materials; complex relative permittivity; effective medium approximation; dielectric mixture theory; electromagnetics; dielectric characterization

**Citation:** Yamada, Y. Dielectric Properties of Textile Materials: Analytical Approximations and Experimental Measurements—A Review. *Textiles* **2022**, *2*, 50–80. https://doi.org/10.3390/textiles2010004

Academic Editor: Laurent Dufossé

Received: 6 December 2021
Accepted: 10 January 2022
Published: 14 January 2022



## 1. Introduction

The dielectric properties, which are measures of the internal responses of electrically insulating materials under alternating electric fields, offer a broad range of knowledge. On the atomic and molecular levels, the dielectric properties are well-correlated to the chemical composition including the moisture content and presence of impurities [1–3]. From the structural and geometrical points of view, the dielectric properties contain information on the shape, size, arrangement, and orientation of various internal components [4–8]. It is due to these reasons that the dielectric properties of fibers and yarns have been considered as one of the fundamental parameters for processing and quality control in the textile industry. For example, fibers and yarns produced by spinning machinery have often uneven thickness and/or foreign matters that cause breakage during the further processing (e.g., weaving, knitting, sewing and embroidering) or affects the aesthetic appearance and/or durability of end products, but such defects can be timely detected through continuous monitoring of the dielectric properties [9–14].

In recent years, the dielectric properties of textile materials have been featured for the development of textile-based electronics such as antennas and transmission lines for

wireless communication [15–23], rectennas for energy harvesting [24–26], and capacitive sensors for pressure, strain and moisture sensing [27–30] and health monitoring [31], as well as for the development of microwave-absorbing fabrics for various electromagnetic interference (EMI) shielding applications [32,33]. Offering both electronic functionalities and traditional fabric-like comfort, the textile-based approach has a great potential to overcome the technical challenges associated with the conventional, non-flexible electronics [34–37]. One crucial parameter in the design process of textile-based electronics is the dielectric permittivity. It has been documented that the performance and form factor of many electronic devices are critically dependent on the dielectric properties of electrically insulating materials. For instance, Ng et al. reported that fabrics with higher dielectric constants such as cotton and linen could enhance the overall performance of textile capacitive biosensors, while those with lower dielectric constants such as Nylon and polyester may lower the signal-to-noise ratio [31]. For textile patch antennas, it has been reported that fabrics with higher dielectric constants could reduce the antenna size, but higher gains and broader bandwidths are attainable with those with lower dielectric constants [5,7,15,38]. For these reasons, the dielectric properties of textile materials have gained tremendous interest with the recent advancements in the textile-based electronics.

Although the dielectric properties of textile materials are determined to some extent by the constituent polymers and moisture and impurity profiles, crystallinities and chain orientations [1], recent studies [4–7,39,40] have identified additional parameters that have also substantial effects, such as the yarn structure, fabric construction, fiber (solid) volume fraction and fiber (yarn) orientation. Consequently, the dielectric properties of textile materials summarized from literature (Table A1) should be used as a reference only, and myriad aspects must be carefully taken into account to successfully design textile materials that possess the dielectric properties required for specific applications.

From another viewpoint, the dependence of the dielectric properties of textile materials on the various factors have given rise to a new possibility in materials characterization. For instance, since the dielectric properties contain information on the compositional, structural and geometrical aspects, these properties of textile materials could be estimated, upon successful correlation, through the measurement of the dielectric properties [5–7,40–42].

In this context, this paper reviews the key factors that affect the dielectric properties of textile materials from the recent literature. Fundamental theories pertaining to the dielectrics and polarization mechanisms are first described to provide profound insights into underlying science, followed by an overview on the concept of homogenization and the dielectric mixture theory. Advantages and challenges of the analytical approximations of the dielectric properties are then discussed, and finally, the methods for measuring the dielectric properties of textile materials are reviewed. It is among the objectives of this paper to build a useful signpost for scientists and engineers on this highly cross-disciplinary field of research.

## 2. General Theory of Dielectrics

### *2.1. Dielectrics and Polarization Mechanisms*

Dielectrics can be defined as electrical insulators that are polarizable by an external electric field. Unlike conductors, dielectrics do not support flow of electrons through its body but respond internally to an applied electric field with a phenomenon called polarization. This internal response leads to the storage and loss of the electrical energy, enabling a wide range of applications in the electronics industry.

Dielectrics are generally classified into non-polar and polar dielectrics. Non-polar dielectrics are dielectrics that do not possess a permanent dipole moment; they become polarized in an electric field by relative displacement of electrons with respect to the nuclei [43,44]. This phenomenon is called electronic polarization (Figure 1), and the resonant process is typically observed at optical frequencies. Polar dielectrics are substances made up of molecules that possess inherent dipole moment. Accordingly, this class of dielectrics undergoes not only the electronic polarization, but also an atomic (or ionic) polarization,

which is a change in the relative positions of atoms (or ions) in the manner depicted in Figure 1 [43,44]. Additionally, polar dielectrics may exhibit an orientation (or dipolar) polarization, where spatial reorientation of the permanent dipoles is induced by the electric field (Figure 1) [43,44].

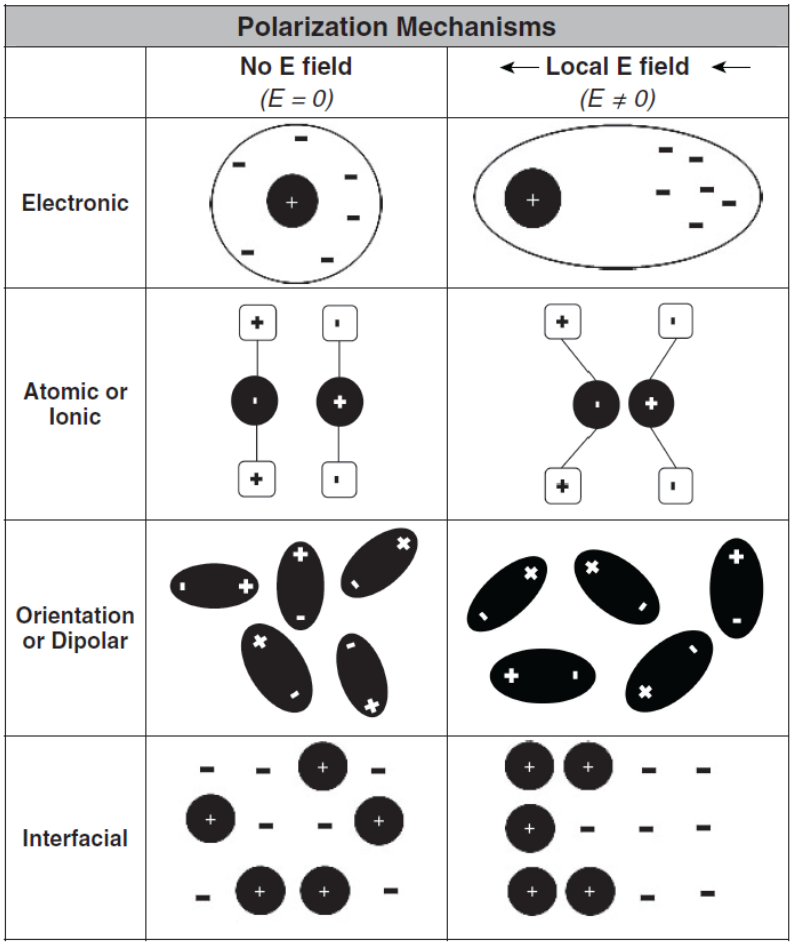


**Figure 1.** Polarization mechanisms. Reprinted with permission from Ref. [44] (p. 36). Copyright 2007 John Wiley & Sons.

In addition to the electronic, atomic and dipolar polarizations, there is another class of polarization termed interfacial (or space charge) polarization (Figure 1), which can be found in dielectrics having structural interfaces [43,44]. In the interfacial polarization, free charges accumulate at interfaces between two materials or between two regions of different electrical conductivities, and this separation of charges results in a local dipole moment [45]. Although the interfacial polarization could potentially exist in any materials having physical interfaces, this type of polarization usually appears only in the lower frequency regime because of the limited mobility of charges [45,46].

### *2.2. Permittivity*

When an electric field is applied, a dielectric material responds by polarization; inside the dielectric medium, another electric field is generated in the opposite direction to the applied electric field as illustrated in Figure 2. As such, the electric field inside the dielectric material is reduced by this opposing electric field.

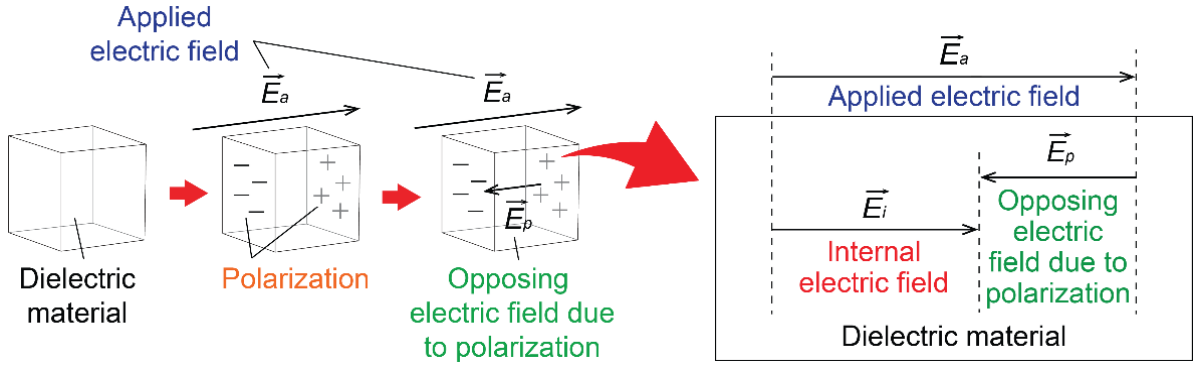


**Figure 2.** Relationship between the applied (external) and internal electric fields.

The strength of the internal electric field can be addressed by using the relative permittivity ($\varepsilon_r$)—a parameter by which the internal electric field is related to the applied electric field. The relationship is given by:

$$\vec{E}_i = \frac{1}{\varepsilon_r}\vec{E}_a \tag{1}$$

Accordingly, the strength of the opposing electric field can be written as:

$$\vec{E}_p = \vec{E}_i - \vec{E}_a = \frac{(1-\varepsilon_r)}{\varepsilon_r}\vec{E}_a \tag{2}$$

It can be seen from the energy conservation point of view that the strength of this opposing electric field is the energy stored by the dielectric material. Upon removal from the external electric field, the polarized medium will undergo a depolarization process, where the relative positions of atoms and molecules return to the original, low energy state by releasing the stored energy.

During these storing and releasing processes, there are losses associated with the physical movements of atoms and molecules. As such, the relative permittivity of the physical dielectric materials is more formally written in the complex form ($\varepsilon_r^*$) as [45]:

$$\varepsilon_r^* = \varepsilon_r' - j\varepsilon_r'' \tag{3}$$

where $\varepsilon_r'$ and $\varepsilon_r''$ are the real and imaginary parts of the relative permittivity, respectively. The real part of the relative permittivity is also referred to as the dielectric constant and is a measure of the ability of a material to store the electric energy by polarization. The imaginary part of the relative permittivity is also known as the relative dielectric loss factor and quantifies the losses associated with the polarization. The tangent of the angle between the storage and loss components ($\tan\delta$) is termed loss tangent and is expressed as [47]:

$$\tan\delta = \frac{\varepsilon_r''}{\varepsilon_r'} \tag{4}$$

The loss tangent is a convenient index to assess the performance of dielectric materials-low-loss dielectrics with a large storage capacity exhibit a small loss tangent ($\tan\delta \ll 1$) while a large loss tangent ($\tan\delta \gg 1$) is due for lossy dielectrics that have a limited energy-storing capability [47].

*2.3. Dispersion*

The physical mechanisms responsible for causing polarizations depend on the time variation of the electric field. In other words, the permittivity needs to be treated as a function of frequency of an alternating electric field. This frequency dependence of the permittivity is called dispersion and a representative curve is illustrated in Figure 3.

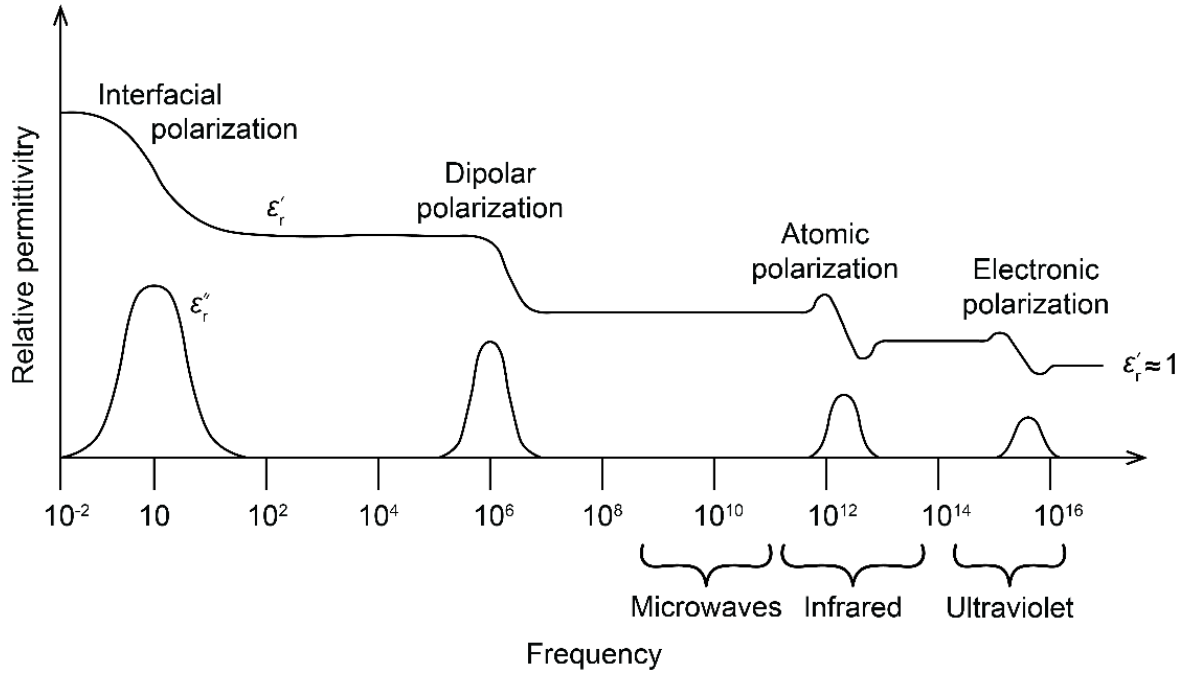


**Figure 3.** Frequency dependence of the complex relative permittivity: interfacial and dipolar polarizations exhibiting relaxation processes whereas ionic and electronic polarizations exhibiting resonant processes. Redrawn from [45] (p. 608).

As the dispersion curve of $\varepsilon_r'$ shows, the relaxation process of the interfacial polarization is typically in the low frequency regime ($10^{-2}$–$10^2$ Hz), whereas that of the dipolar polarization could be in the radio ($10^5$–$10^7$ Hz) frequency domain. These relaxations occur because of the limited mobility of space charges and permanent dipoles—as the frequency increases, these physical components will be too sluggish to respond [45]. For electronic and atomic polarizations, resonant processes are observed in the infrared and visible-ultraviolet regimes. The loss ($\varepsilon_r''$) peaks are associated with these relaxation and resonant processes.

With an aim to elucidate the dispersion characteristics, various models have been developed. For electronic and atomic polarizations, the Lorentz model [48] has been used extensively in literature. In this model, each atom is regarded to consist of a positive stationary charge surrounded by a mobile electron cloud, where the electron cloud experiences damping and tensional forces by an alternating electric field in an analogy to a mechanical spring [47]. The equation of motion is given by [47]:

$$qE_0 e^{j\omega t} = m\frac{d^2 l}{dt^2} + a\frac{dl}{dt} + sl \quad (5)$$

where $q$ is the dipole charge; $m$ is the mass of the electron cloud; $l$ is the displaced distance; $t$ is the time; $a$ is the friction (damping) coefficient; and $s$ is the tension (spring) coefficient.

From this equation, the real and imaginary parts of the relative permittivity can be derived as a function of frequency, and the results are given by [47]:

$$\varepsilon'_{\mathrm{r}} = 1 + \frac{\frac{nq^2}{\varepsilon_0 m}\left(\omega_0^2 - \omega^2\right)}{\left(\omega_0^2 - \omega^2\right) + \left(\omega\frac{a}{m}\right)^2} \tag{6}$$

$$\varepsilon''_{\mathrm{r}} = \frac{nq^2}{\varepsilon_0 m}\frac{\omega\frac{a}{m}}{\left(\omega_0^2 - \omega^2\right) + \left(\omega\frac{a}{m}\right)^2} \tag{7}$$

where $n$ is the number of dipoles per unit volume and $\omega_0$ is the resonant angular frequency of the dielectric material.

Although the Lorentz model is widely used for its simplicity and explicitness, one critical limitation is that the model does not take the absorption into account [49]. Accordingly, the single Lorentzian oscillator is not suitable for examining absorbing materials such as amorphous solids and semiconductors, and more than one oscillator needs to be incorporated to analyze such dielectrics [49].

For dipolar polarizations, the Debye model [50] is often used to obtain the frequency dependence of the complex permittivity. In this model, molecules are assumed to be spherical in shape, and the real and imaginary parts of the relative permittivity are given, respectively, by [50]:

$$\varepsilon'_{\mathrm{r}} = \varepsilon'_{\mathrm{r},\infty} + \frac{\varepsilon'_{\mathrm{r,s}} - \varepsilon'_{\mathrm{r},\infty}}{1 + (\omega\tau)^2} \tag{8}$$

$$\varepsilon''_{\mathrm{r}} = \frac{\omega\tau\left(\varepsilon'_{\mathrm{r,s}} - \varepsilon'_{\mathrm{r},\infty}\right)}{1 + (\omega\tau)^2} \tag{9}$$

where $\varepsilon'_{\mathrm{r,s}}$ and $\varepsilon'_{\mathrm{r},\infty}$ are the dielectric constants at a static frequency (i.e., the frequency just before the dipolar relaxation occurs) and at a much higher frequency (but not high enough to involve any resonant processes of electronic and atomic polarizations), respectively; and $\tau$ is the relaxation time. $\varepsilon'_{\mathrm{r}}$ exhibits a peak when $\omega = 1/\tau$, and this peak is called the Debye loss peak. Many gaseous and some liquid materials with dipolar molecules are reported to follow the Debye relaxation model [45]. For most solids, however, this peak could become much broader because the loss cannot be expressed in terms of just a single well-defined relaxation time $\tau$; the relaxation in the solid is usually represented by a distribution of relaxation times [45]. In addition, Equations (8) and (9) assume that the dipoles do not influence each other either through their electric fields or through their interactions with the lattice; however, in solid dielectrics, dipoles can also couple, convoluting the relaxation process and limiting the accuracy of the Debye relaxation model [45].

Interfacial polarizations, on the other hand, are the results of the charges accumulated at the boundaries of different conductivities; accordingly, the shapes and geometries of the boundaries have substantial impact on the polarizability as well as the dispersion profile. In view of this, several dispersion theories were developed for different types of boundaries. One consequential premise is the Maxwell–Wagner theory, where spherical regions are considered to be sparsely dispersed in the medium of different conductivity [51]. According to this theory, the frequency-dependent complex relative permittivity is given by [51]:

$$\varepsilon^*_{\mathrm{r}} = \varepsilon'_{\mathrm{r,h}} + \frac{\varepsilon'_{\mathrm{r,l}} - \varepsilon'_{\mathrm{r,h}}}{1 + j\omega\tau} + \frac{g}{j\omega}\kappa_{\mathrm{l}} \tag{10}$$

$$\varepsilon'_{\mathrm{r,h}} = \varepsilon'_{\mathrm{r,e}}\frac{2\varepsilon'_{\mathrm{r,e}} + \varepsilon'_{\mathrm{r,i}} - 2\varphi_{\mathrm{s}}\left(\varepsilon'_{\mathrm{r,e}} - \varepsilon'_{\mathrm{r,i}}\right)}{2\varepsilon'_{\mathrm{r,e}} + \varepsilon'_{\mathrm{r,i}} + \varphi_{\mathrm{s}}\left(\varepsilon'_{\mathrm{r,e}} - \varepsilon'_{\mathrm{r,i}}\right)} \tag{11}$$

$$\varepsilon'_{\mathrm{r,l}} = \varepsilon'_{\mathrm{r,e}}\frac{\kappa_{\mathrm{l}}}{\kappa_{\mathrm{e}}} + \frac{9\varphi_{\mathrm{s}}\kappa_{\mathrm{e}}\left(\varepsilon'_{\mathrm{r,i}}\kappa_{\mathrm{e}} - \varepsilon'_{\mathrm{r,e}}\kappa_{\mathrm{i}}\right)}{\left[2\kappa_{\mathrm{e}} + \kappa_{\mathrm{i}} + \varphi_{\mathrm{s}}(\kappa_{\mathrm{e}} - \kappa_i)\right]^2} \tag{12}$$

$$\tau = \frac{2\varepsilon'_{\mathrm{r,e}} + \varepsilon'_{\mathrm{r,i}} + \varphi_{\mathrm{s}}\left(\varepsilon'_{\mathrm{r,e}} - \varepsilon'_{\mathrm{r,i}}\right)}{2\kappa_{\mathrm{e}} + \kappa_{\mathrm{i}} + \varphi_{\mathrm{s}}(\kappa_{\mathrm{e}} - \kappa_{\mathrm{i}})} \cdot \frac{1}{g} \tag{13}$$

$$\kappa_{\mathrm{l}} = \kappa_{\mathrm{e}} \frac{2\kappa_{\mathrm{e}} + \kappa_{\mathrm{i}} - 2\varphi_{\mathrm{s}}(\kappa_{\mathrm{e}} - \kappa_{\mathrm{i}})}{2\kappa_{\mathrm{e}} + \kappa_{\mathrm{i}} + \varphi_{\mathrm{s}}(\kappa_{\mathrm{e}} - \kappa_{\mathrm{i}})} \tag{14}$$

where $\varepsilon'_{\mathrm{r,i}}$ and $\varepsilon'_{\mathrm{r,e}}$ are the real part of the relative permittivity of the inclusions and the environment, respectively; $\kappa_{\mathrm{i}}$ and $\kappa_{\mathrm{e}}$ are the electrical conductivities of the inclusions and the environment, respectively; $\varphi_s$ is the volume fraction of the inclusion; $\omega$ is the angular frequency; and $g$ is the numerical factor ($112.94 \times 10^{11}$).

For mixtures with ellipsoidal inclusions, the Maxwell–Wagner–Sillars model is often employed. This model is an extension of the Maxwell–Wagner model by Sillars [52] and incorporates an additional parameter that accounts for the eccentricity of the ellipsoids. Further details on the Maxwell–Wagner–Sillars model are available in [52].

While some of the most representative dispersion relationships have been discussed in this subsection, there are several notations. Firstly, for many dielectric materials, there could be more than just a single type of atoms and/or molecules. Secondly, microstructural configurations (e.g., crystalline and amorphous regions in polymers) make the atoms and molecules behave differently under the electric field [53,54]. As such, many dielectrics do not exhibit a simple, well-defined resonance or a relaxation process [45]. Analysis on the dispersion characteristic is usually of high complexity and requires technical proficiency because of these factors [41,46,55].

### *2.4. Anisotropy*

The simple relationship between the applied electric field ($\vec{E}_{\mathrm{a}}$) and the internal electric field ($\vec{E}_{\mathrm{i}}$) given in Equation (1) is only valid when the polarization of a dielectric medium does not vary by the direction of the applied electric field. In both natural and artificial materials, however, there could exist microstructures that break the directional symmetry [8]. Such substances are called anisotropic materials; in an anisotropic medium, the internal electric field is oriented at an angle different from the applied electric field. On this account, Equation (1) becomes a second-rank tensor division for anisotropic materials as given by:

$$\vec{E}_{\mathrm{i}} = \frac{1}{\bar{\bar{\varepsilon}}_{\mathrm{r}}} \vec{E}_{\mathrm{a}} \tag{15}$$

where $\bar{\bar{\varepsilon}}_{\mathrm{r}}$ is a second-rank, relative permittivity tensor. In the Cartesian coordinate, $\bar{\bar{\varepsilon}}_{\mathrm{r}}$ is expressed as a nine-entry matrix [47]:

$$\bar{\bar{\varepsilon}}_{\mathrm{r}} = \begin{bmatrix} \varepsilon_{\mathrm{r},xx} & \varepsilon_{\mathrm{r},xy} & \varepsilon_{\mathrm{r},xz} \\ \varepsilon_{\mathrm{r},yx} & \varepsilon_{\mathrm{r},yy} & \varepsilon_{\mathrm{r},yz} \\ \varepsilon_{\mathrm{r},zx} & \varepsilon_{\mathrm{r},zy} & \varepsilon_{\mathrm{r},zz} \end{bmatrix} \tag{16}$$

where each entry ($\varepsilon_{\mathrm{r},xx}$, $\varepsilon_{\mathrm{r},xy}$, $\cdots$ $\varepsilon_{\mathrm{r},zz}$) represents an independent material parameter and may be a complex number. By using Equations (15) and (16), this can be rewritten as:

$$\begin{bmatrix} E_{\mathrm{a},x} \\ E_{\mathrm{a},y} \\ E_{\mathrm{a},z} \end{bmatrix} = \begin{bmatrix} \varepsilon_{\mathrm{r},xx} & \varepsilon_{\mathrm{r},xy} & \varepsilon_{\mathrm{r},xz} \\ \varepsilon_{\mathrm{r},yx} & \varepsilon_{\mathrm{r},yy} & \varepsilon_{\mathrm{r},yz} \\ \varepsilon_{\mathrm{r},zx} & \varepsilon_{\mathrm{r},zy} & \varepsilon_{\mathrm{r},zz} \end{bmatrix} \begin{bmatrix} E_{\mathrm{i},x} \\ E_{\mathrm{i},y} \\ E_{\mathrm{i},z} \end{bmatrix} \tag{17}$$

where $E_{\mathrm{a},x}$, $E_{\mathrm{a},y}$ and $E_{\mathrm{a},z}$ are $\hat{x}$, $\hat{y}$ and $\hat{z}$ components of the applied electric field, respectively; and $E_{\mathrm{i},x}$, $E_{\mathrm{i},y}$ and $E_{\mathrm{i},z}$ are $\hat{x}$, $\hat{y}$ and $\hat{z}$ components of the internal electric field, respectively. Equation (17) is the most generic form to express the permittivity of an anisotropic dielectric material.

In many practical cases, however, each entry is not necessarily unique. For example, a rectangular lattice that forms a basic structure in crystals may be expressed only in the three principal directions because of its biaxiality [8]. For uniaxial media, the permittivity component along the axis of crystal is different from the transversal permittivity, and thus it could have only one unique diagonal term in the permittivity matrix [8]. In addition to these symmetrical scenarios, for certain applications such as planar capacitors, transmission lines and antennas, the electric field is often limited to one principal direction [38,56,57]. If this is the case, then the permittivity may be considered only in such direction.

### *2.5. Inhomogenity and Homogenization*

Inhomogeneity is another leading parameter in the science of dielectrics. When the permittivity is consistent regardless of the position within a material, the material is called homogeneous. On the other hand, if the permittivity varies as a function of position, this type of materials is called electrically non-homogeneous (heterogeneous) [8]. Often fiber-forming polymers are non-homogenous on the microstructural level since they could have both amorphous and crystalline regions that are characterized by different electrical polarizability [43]. In addition, mixtures of two or more components could be also non-homogeneous. For instance, a fabric may be considered as a non-homogeneous mixture of fiber and air [58]. Furthermore, materials having defects (e.g., voids) or impurities may also exhibit inhomogeneous behaviors on microscopic scale. Therefore, in many physical dielectrics, some degree of inhomogeneity potentially exists, and the permittivity may be more formally addressed as a function of position.

On one side, however, even such materials could be considered homogenous from the macroscopic point of view [8]. For example, when an observer is close enough to a woven fabric, the individual warp and weft yarns and their interlacing structure would be visible; however, when the fabric is placed far enough from the observer's eyes, the detail structure of the fabric would no longer be recognizable, leaving an impression of just a uniform, homogenized sheet. Although the distance between the observer and the object was the parameter to describe the homogenization in this example, it is the wavelength (λ) of electromagnetic waves that critically distinguishes homogenized and non-homogenized substances in dielectric analysis [8]. In practice, the medium may be regarded homogenized when structural inhomogeneity is much smaller than ~0.1λ; the positional terms can then be dropped and a single, macroscopic permittivity value could be used [59–61]. This approach of describing microscopically heterogeneous dielectrics with a macroscopic, homogenized permittivity is called effective medium approximation [62,63] (Figure 4) and is the fundamental process in the dielectric mixture theory [64].

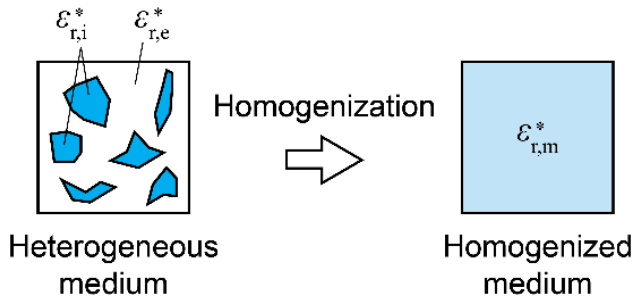


**Figure 4.** Conceptual illustration of homogenization of an electrically heterogeneous medium.

### *2.6. Dielectric Mixture Theory*

The dielectric mixture theory is a statement of a relationship between the homogenized (macroscopic) dielectric properties of a heterogeneous medium and the local (microscopic) dielectric properties of its constituent materials (i.e., inclusions and environments) [64]. This relationship is expressed as a function of volume fractions of the components as an averaging factor. Since the geometry plays a pivotal role in the resulting dielectric properties of a heterogeneous medium, each dielectric mixture theory was developed for a specific geometry [8].

One of the most fundamental mixing theories is the Maxwell Garnett theory [65,66], which explicates the macroscopic complex relative permittivity ($\varepsilon^*_{r,m}$) of a heterogeneous system of isotropic, spherical inclusions of complex relative permittivity $\varepsilon^*_{r,i}$ randomly positioned in the environment of complex permittivity $\varepsilon^*_{r,e}$ (Figure 5a). According to the theory, the macroscopic, complex relative permittivity is given by [65,66]:

$$\varepsilon^*_{r,m} = \varepsilon^*_{r,e} + 3\varphi_s\varepsilon^*_{r,e}\frac{\varepsilon^*_{r,i} - \varepsilon^*_{r,e}}{\varepsilon^*_{r,i} + 2\varepsilon^*_{r,e} - \varphi_s\left(\varepsilon^*_{r,i} - \varepsilon^*_{r,e}\right)} \tag{18}$$

where $\varphi_s$ is the volume fraction of the spherical inclusions.

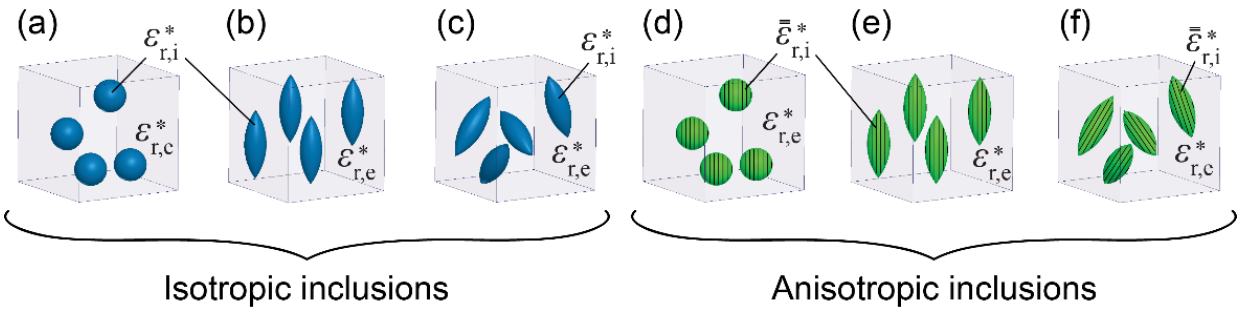


**Figure 5.** Examples of randomly positioned inclusions of various shapes in the environment ($\varepsilon^*_{r,e}$): (**a**) isotropic spheres, (**b**) aligned isotropic ellipsoids, (**c**) randomly oriented isotropic ellipsoids, (**d**) aligned anisotropic spheres, (**e**) aligned anisotropic ellipsoids and (**f**) randomly oriented anisotropic ellipsoids. Adapted from [41] (p. 40). Copyright 2019 YUSUKE MUKAI.

For many dielectrics, the spherical requirement for the inclusions needs to be relaxed—however, numerical effort is required for other shapes, and ellipsoids are among a few of the exceptions for which general analytical solutions can be obtained by extending the Maxwell Garnett theory [8]. For locally isotropic ellipsoids of permittivity $\varepsilon^*_{r,i}$ randomly positioned in the environment $\varepsilon^*_{r,e}$ (Figure 5b), its homogenized permittivity becomes a tensor if the ellipsoids are aligned. The x-component ($\varepsilon^*_{r,m,x}$) of this permittivity tensor is given by [8]:

$$\varepsilon^*_{r,m,x} = \varepsilon^*_{r,e} + \varphi_l\varepsilon^*_{r,e}\frac{\varepsilon^*_{r,i} - \varepsilon^*_{r,e}}{\varepsilon^*_{r,i} + (1-\varphi_l)N_x\left(\varepsilon^*_{r,i} - \varepsilon^*_{r,e}\right)} \tag{19}$$

where $\varphi_l$ is the volume fraction of the ellipsoidal inclusions; and $N_x$ is the depolarization factor in the direction of x-axis. Similarly, y- and z-components are given, respectively, by:

$$\varepsilon^*_{r,m,y} = \varepsilon^*_{r,e} + \varphi_l\varepsilon^*_{r,e}\frac{\varepsilon^*_{r,i} - \varepsilon^*_{r,e}}{\varepsilon^*_{r,i} + (1-\varphi_l)N_y\left(\varepsilon^*_{r,i} - \varepsilon^*_{r,e}\right)} \tag{20}$$

$$\varepsilon^*_{\mathrm{r,m,z}} = \varepsilon^*_{\mathrm{r,e}} + \varphi_{\mathrm{l}}\varepsilon^*_{\mathrm{r,e}}\frac{\varepsilon^*_{\mathrm{r,i}} - \varepsilon^*_{\mathrm{r,e}}}{\varepsilon^*_{\mathrm{r,i}} + (1-\varphi_{\mathrm{l}})N_{\mathrm{z}}\left(\varepsilon^*_{\mathrm{r,i}} - \varepsilon^*_{\mathrm{r,e}}\right)} \tag{21}$$

where $N_{\mathrm{y}}$ and $N_{\mathrm{z}}$ are depolarization factors in the corresponding axes and satisfy [8]:

$$N_{\mathrm{x}} + N_{\mathrm{y}} + N_{\mathrm{z}} = 1 \tag{22}$$

Many natural and engineered materials possess this type of anisotropic structure, where the constituent materials themselves are isotropic in microscopic scale but the geometrical arrangement creates anisotropy [8].

For randomly oriented isotropic ellipsoids (Figure 5c), the macroscopic permittivity becomes a scalar as the directional terms are canceled. The expression is thus given by [8]:

$$\varepsilon^*_{\mathrm{r,m}} = \varepsilon^*_{\mathrm{r,e}} + \varepsilon^*_{\mathrm{r,e}}\frac{\frac{\varphi_{\mathrm{l}}}{3}\sum\limits_{i=\mathrm{x,y,z}}\frac{\varepsilon^*_{\mathrm{r,i}} - \varepsilon^*_{\mathrm{r,e}}}{\varepsilon^*_{\mathrm{r,e}} + N_i\left(\varepsilon^*_{\mathrm{r,i}} - \varepsilon^*_{\mathrm{r,e}}\right)}}{1 - \frac{\varphi_{\mathrm{l}}}{3}\sum\limits_{i=\mathrm{x,y,z}}\frac{N_i\left(\varepsilon^*_{\mathrm{r,i}} - \varepsilon^*_{\mathrm{r,e}}\right)}{\varepsilon^*_{\mathrm{r,e}} + N_i\left(\varepsilon^*_{\mathrm{r,i}} - \varepsilon^*_{\mathrm{r,e}}\right)}} \tag{23}$$

So far, only isotropic inclusions are discussed. However, inclusions such as cotton fibers have anisotropic local permittivities due to the oriented polymer chains [67,68]. If this is the case, then the permittivity of inclusions needs to be treated as a second-rank tensor as discussed in this section. For inclusions of randomly positioned anisotropic spheres aligned in the environment (Figure 5d), the macroscopic permittivity tensor ($\overline{\overline{\varepsilon}}^*_{\mathrm{r,m}}$) is given by [8]:

$$\overline{\overline{\varepsilon}}^*_{\mathrm{r,m}} = \varepsilon^*_{\mathrm{r,e}} I + 3\varepsilon^*_{\mathrm{r,e}}\varphi_{\mathrm{s}}\frac{\overline{\overline{\varepsilon}}^*_{\mathrm{r,i}} - \varepsilon^*_{\mathrm{r,e}}\overline{\overline{I}}}{\left[\overline{\overline{\varepsilon}}^*_{\mathrm{r,i}} + 2\varepsilon^*_{\mathrm{r,e}} - \varphi_{\mathrm{s}}\left(\overline{\overline{\varepsilon}}^*_{\mathrm{r,i}} - \varepsilon^*_{\mathrm{r,e}}\overline{\overline{I}}\right)\right]} \tag{24}$$

where $I$ is the unit dyadic. Similarly, for inclusions of randomly positioned, but aligned anisotropic ellipsoids (Figure 5e), the macroscopic permittivity tensor is given by [8]:

$$\overline{\overline{\varepsilon}}^*_{\mathrm{r,m}} = \varepsilon^*_{\mathrm{r,e}}\overline{\overline{I}} + \varphi_l\varepsilon^*_{\mathrm{r,e}}\frac{\overline{\overline{\varepsilon}}^*_{\mathrm{r,i}} - \varepsilon^*_{\mathrm{r,e}}\overline{\overline{I}}}{\varepsilon^*_{\mathrm{r,e}}\overline{\overline{I}} + (1-\varphi_l)\overline{\overline{L}}\cdot\left(\overline{\overline{\varepsilon}}^*_{\mathrm{r,i}} - \varepsilon^*_{\mathrm{r,e}}\overline{\overline{I}}\right)} \tag{25}$$

where $\overline{\overline{L}}$ is the depolarization dyadic. Although not elaborated in detail in this paper, the macroscopic permittivity of inclusions of randomly positioned and randomly aligned anisotropic ellipsoids (Figure 5f) becomes a scalar, on a similar rationale to that of randomly positioned and randomly oriented isotropic ellipsoidal inclusions.

While the Maxwell Garnett theory and its extensions have been employed as powerful analytical tools for various dielectric mixtures, there are several limitations. For instance, the Maxwell Garnett theory assumes the inclusions to be small so that the interaction between the inclusions become negligible [69]. As such, the application of the Maxwell Garnett theory is practically limited to dilute systems [69].

The Bruggeman theory, on the other hand, is symmetric with respect to all medium components and can be applied to composites with arbitrary volume fractions without causing obvious geometrical contradictions [70]. For spherical inclusions of volume fraction $f_{\mathrm{s}}$, the macroscopic permittivity ($\varepsilon^*_{\mathrm{r,m}}$) is related to its constituent permittivities by [8]:

$$(1-\varphi_s)\frac{\varepsilon^*_{r,e}-\varepsilon^*_{r,m}}{\varepsilon^*_{r,e}+2\varepsilon^*_{r,m}}+\varphi_s\frac{\varepsilon^*_{r,i}-\varepsilon^*_{r,m}}{\varepsilon^*_{r,i}+2\varepsilon^*_{r,m}}=0 \tag{26}$$

where $\varepsilon^*_{r,i}$ and $\varepsilon^*_{r,e}$ are the complex relative permittivities of the inclusions and environment, respectively. For randomly oriented ellipsoidal inclusions, the macroscopic permittivity ($\varepsilon^*_{r,m}$) is given by [8]:

$$\varepsilon^*_{r,m}=\varepsilon^*_{r,e}+\frac{\varphi_l}{3}\left(\varepsilon^*_{r,i}-\varepsilon^*_{r,e}\right)\sum_{i=x,y,z}\frac{\varepsilon^*_{r,m}}{\varepsilon^*_{r,m}+N_i\left(\varepsilon^*_{r,i}-\varepsilon^*_{r,m}\right)} \tag{27}$$

Another crucial theory in dielectric homogenization is the coherent potential theory. In this theory, the Green's function enumerates the field of a given polarization density of the effective medium, leading to the relationship between the macroscopic and constituent permittivities. For the spherical inclusions, the coherent potential formula is given by [8]:

$$\varepsilon^*_{r,m}=\varepsilon^*_{r,e}+\varphi_s\left(\varepsilon^*_{r,i}-\varepsilon^*_{r,e}\right)\frac{3\varepsilon^*_{r,m}}{3\varepsilon^*_{r,m}+(1-\varphi_s)\left(\varepsilon^*_{r,i}-\varepsilon^*_{r,e}\right)} \tag{28}$$

For randomly oriented ellipsoids of volume fraction $f_e$, the coherent potential formula is given by [8]:

$$\varepsilon^*_{r,m}=\varepsilon^*_{r,e}+\frac{\varphi_e}{3}\left(\varepsilon^*_{r,i}-\varepsilon^*_{r,e}\right)\sum_{i=x,y,z}\frac{(1+N_i)\varepsilon^*_{r,m}-N_i\varepsilon^*_{r,e}}{\varepsilon^*_{r,m}+N_i\left(\varepsilon^*_{r,i}-\varepsilon^*_{r,e}\right)} \tag{29}$$

For dilute mixtures, all of the Maxwell Garnett, Bruggeman and coherent potential theories predict the same result. For spherical inclusions, those expressions are reduced to [8]:

$$\varepsilon^*_{r,m}\simeq\varepsilon^*_{r,e}+3\varphi_s\varepsilon^*_{r,e}\frac{\varepsilon^*_{r,i}-\varepsilon^*_{r,e}}{\varepsilon^*_{r,i}+2\varepsilon^*_{r,e}} \tag{30}$$

In this subsection, the effects of the geometrical shapes, volume fractions and permittivities of various internal components on the homogenized dielectric properties were discussed based on the fundamental theories of dielectric mixtures. There is, however, an additional factor that could also hold an important role in the mixture analysis—interfacial polarization. Since mixtures involve at least two electrically non-identical components, the interfacial polarization could take place at the internal boundaries [6,41], but such a phenomenon is not considered in these theories. Yet, owing to its simplicity, explicitness and versatility the dielectric mixture theory has found a variety of uses, such as in analysis of chemical composition, structure and internal geometry and in designing composites with dielectric properties desirable for intended applications [41,42].

## 3. Dielectric Properties of Fabrics—The Air-Fiber System

In one view, textile materials are mixtures of fibers (or yarns) and air. Thus, by putting into the framework of the dielectric mixture theory, the dielectric properties of textile materials can be expressed as functions of the volume fraction and dielectric properties of the constituent fibers (or yarns). One of the early insights into this approach was presented by Bal and Kothari [39], who aimed to elucidate the dielectric properties of high-density polyethylene woven fabrics. In their work, measured dielectric constants of the woven fabrics were compared with those calculated by the dielectric mixing formulas. Although some of the mixing rules (e.g., the Maxwell Garnett formula) assume specific geometries and hence were not supposed to perfectly apply to woven fabrics, it was reported that any of the tested formulas predicted somewhat similar and acceptable results, most likely due to the fact that the volume fractions of the fabric samples were on the significantly lower side [39]. Later studies have demonstrated that the permittivity of textile materials could

be dependent, not only on the volume fraction of fibers, but also on the fabric construction (e.g., woven versus knit) and fiber (yarn) orientation in a strict sense [5–7,40,41].

A model that represents a plain-woven fabric was proposed by Bal and Kothari [58] and is given in Figure 6. Based on the fundamental fabric geometry developed by Peirce [71], the repeating unit of the interlaced structure was considered to be the region encompassed by the rectangle in the schematic illustration. From this model, the capacitance ($C$) of a plain-woven fabric was formulated as [58]:

$$C = \frac{\varepsilon_0}{h} \times (A \times \eta_1 \times \eta_2) \times \left[ \begin{array}{l} \int_{-d_2}^{+d_2} \int_{-d_1}^{+d_1} \frac{dxdy}{\left\{1-\left(1-\frac{1}{\varepsilon'_{r,i}}\right)\times\frac{2\times u_1(0,y)}{d_1}\times\sqrt{\left(\frac{d_1}{2}\right)^2-x^2}+\frac{2\times u_2(0,y)}{d_2}\times\sqrt{\left(\frac{d_2}{2}\right)^2-y^2}\right\}} \cdots \\ + \int_{-\frac{d_1}{2}}^{+\frac{d_1}{2}} \int_{\frac{d_2}{2}}^{(P_2-\frac{d_2}{2})} \frac{dxdy}{\left\{1-\left(1-\frac{1}{\varepsilon'_{r,i}}\right)\times\frac{2\times\sec\theta_1\times\sqrt{\left(\frac{d_1}{2}\right)^2-x^2}}{h}\right\}} \cdots \\ + \int_{\frac{d_1}{2}}^{(P_1-\frac{d_1}{2})+\frac{d_2}{2}} \int_{-\frac{d_2}{2}}^{\frac{d_2}{2}} \frac{dxdy}{\left\{1-\left(1-\frac{1}{\varepsilon'_{r,i}}\right)\times\frac{2\times\sec\theta_2\times\sqrt{\left(\frac{d_2}{2}\right)^2-y^2}}{h}\right\}} \cdots \\ +(P_1-d_1)\times(P_2-d_2) \end{array} \right] \quad (31)$$

where $\eta_1$ and $\eta_2$ are the thread counts of warp and weft yarns, respectively; $P_1$ and $P_2$ are the spacings of the warp and weft yarns, respectively; $u_1$ and $u_2$ are the lengths of warp and weft yarns along the z-axis, respectively; $d_1$ and $d_2$ are the diameters of warp and weft yarns, respectively; $\theta_1$ and $\theta_2$ are the weaving angles of warp and weft yarns, respectively; $h$ is the fabric thickness; $A$ is the area of fabric; $\varepsilon'_{r,i}$ is the dielectric constant of the fiber; and $\varepsilon_0$ is the absolute permittivity of free space. Because the capacitance is related to the dielectric constant by [57]:

$$\varepsilon'_{r,i} = \frac{L}{\varepsilon_0 A} C \quad (32)$$

the homogenized dielectric constant of a plain-woven fabric can be obtained by solving Equations (31) and (32). Based on comparisons to experimental data, the authors reported that this model predicted the dielectric constants of high-density polyethylene woven fabrics with reasonable accuracy [58].

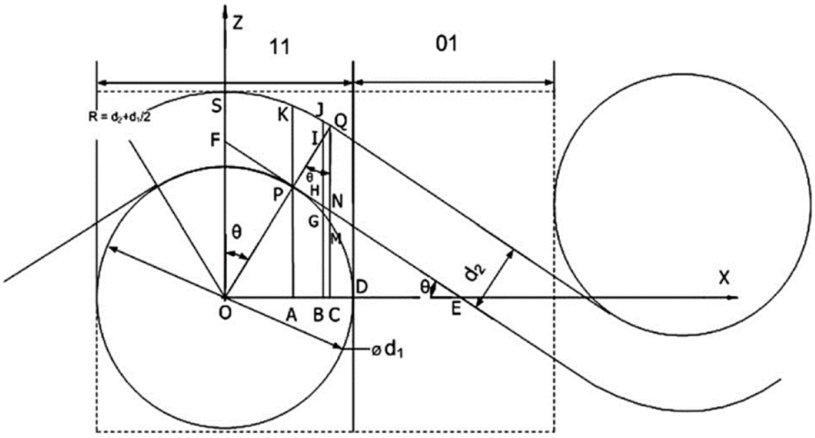


**Figure 6.** A cross section of a two-phase, plain-woven fabric consisting of fibers (yarns) and air. Reprinted with permission from Ref. [58] (p. 754). Copyright 1974 ELSEVIER BV.

Although not discussed in [57], this mathematical procedure of estimating the homogenized dielectric properties from fabric geometries and the permittivity of fibers (or yarns) may also be applied for staple or multifilament yarns if the macroscopic dielectric properties of such yarns are known. Moreover, it may be extended to cover broader types of fabric geometries such as various patterns of woven and knit fabrics by further elaborating the formulation.

## 4. Dielectric Properties of Fabrics—The Air-Fiber-Moisture System

The two-phase (air-fiber) models reviewed in Section 3 are applicable only for textile materials that are unaffected by moisture. Many natural (e.g., cotton, silk and wool) and artificial (e.g., polyamides) fibers, however, are hygroscopic and hence their dielectric properties can be radically altered by moisture [4,6,7,16,41,72,73]. The moisture absorbed by hygroscopic fibers is known to exist in two primary forms—free water and bound water [74,75]. Free water is water that has the thermodynamic state identical to the liquid (or bulk) water [76]. Bound water, on the other hand, takes the form chemically attached to a functional group of polymer chains, and thus the mobility of bound water is largely impeded [76]. Consequently, the electric polarizabilities of free and bound water are substantially different; the relaxation frequency of free water is observed in the gigahertz range [77,78], whereas bound water exhibits relaxation at much lower, megahertz frequencies because of the limited mobility [79,80]. Furthermore, absorbed water could drastically enhance the interfacial polarization by creating various types of boundaries with air and fiber [6,41].

Although the consideration of moisture is imperative in decent dielectric analysis of hygroscopic textile materials, the quantification and modeling of free and bound water is challenging. This is because the amounts, shapes and locations of free and bound water are intricately influenced by a number of factors including but not limited to temperature, relative humidity and microstructural profiles (e.g., crystallinity and porosity) [41,67,76,81–83]. Accordingly, most mixing models and theories available in literature are concerned with the moisture content without further distinction of its free and bound states.

In a recent work, the relationship between the dielectric properties and the geometrical parameters were investigate for cotton fabrics at various relative humidity conditions [7]. Based on the out-of-plane dielectric characterization of woven and knitted fabric samples made of a five-ply cotton yarn, it was observed that the dielectric constant increases with the solid volume fraction (Figure 7a) [7]. It was also shown that the dielectric constant increases as the relative humidity increases (Figure 7a) [7], as reported in previous works [16,73]. Surprisingly, however, when the dielectric constants of the woven and knitted fabric samples of the same solid volume fractions were compared, the dielectric constants of woven samples were consistently higher than those of knitted samples (Figure 7b,c) [7]. This observation was substantiated by the evidence that the yarns (and hence fibers) in the woven samples were oriented more in the fabric thickness (out-of-plane) direction than in the case of knitted samples (Figure 8)—according to the extended Maxwell Garnett theory [8], the orientation of high aspect ratio materials affects the permittivity of the mixture and the permittivity in the fabric thickness direction will be higher if the fibers (yarns) are aligned more in this direction [7].

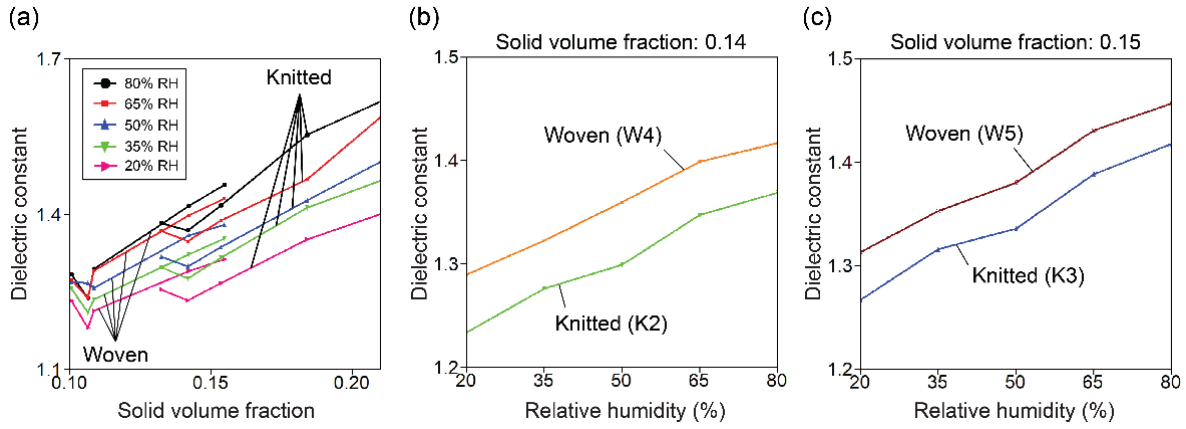


**Figure 7.** (**a**) Dielectric constants of woven and knitted cotton fabrics plotted as a function of the solid volume fraction; and comparison of the dielectric constants of woven and knitted cotton fabrics at various relative humidifies under the same solid volume fractions: (**b**) 0.14 and (**c**) 0.15. Adapted from [7] (pp. 8–9). Copyright 2020 YUSUKE MUKAI & MINYOUNG SUH.

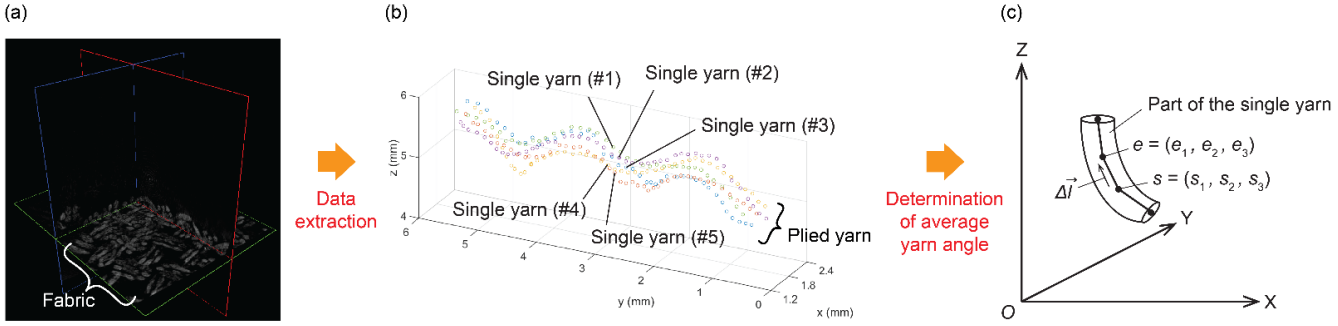


**Figure 8.** 3D visualization of the cotton fabric geometry for determination of the average yarn orientation: (**a**) micro-computed tomography (micro-CT) image, (**b**) five-ply cotton yarn plotted in the Cartesian coordinate system, and (**c**) yarn discretization for calculation of the local orientation. Adapted from [7] (pp. 10–11). Copyright 2019 YUSUKE MUKAI.

A theoretical model that predicts the dielectric properties of textile materials from the moisture content was proposed by Mukherjee in 2018 [84]. According to this model, the real ($\varepsilon'_{r,m}$) and imaginary ($\varepsilon''_{r,m}$) components of the relative permittivity are expressed as a function of moisture by:

$$\varepsilon'_{r,m}(\omega, T, M) = \varepsilon'_{r,ie} + \frac{1}{u\left(1 + \frac{\omega^2 v^2}{u^2}\right)} \tag{33}$$

$$\varepsilon''_{r,m}(\omega, T, M) = \varepsilon''_{r,ie} + \frac{\omega v}{u^2\left(1 + \frac{\omega^2 v^2}{u^2}\right)} \tag{34}$$

$$u = z - \frac{\gamma^2 P_0^2}{A_1^2 + \frac{\omega_2}{\Gamma_1^2}} \tag{35}$$

$$v = \frac{1}{\Gamma_2} + \frac{\gamma^2 P_0^2}{\Gamma_1\left(A_1^2 + \frac{\omega_2}{\Gamma_1^2}\right)} \tag{36}$$

$$z = \frac{1}{2\chi_0} - \frac{1}{2}\gamma\psi_0 \tag{37}$$

$$A_1 = a(T - x - T^*) - B\psi_0 + \frac{3}{2}C\psi_0^2 \quad (38)$$

where $\chi_0$ is the susceptibility; $\psi_0$ is the equilibrium order parameter; $P_0$ is the equilibrium polarization density; $\varepsilon'_{r,ie}$ is the real part of the relative permittivity due to ionic and electronic polarizations; $\varepsilon''_{r,ie}$ is the imaginary part of the relative permittivity due to ionic and electronic polarizations; $x$ is the moisture content; $T$ and $T^*$ are the temperature and supercooled temperature; $\Gamma_1$ and $\Gamma_2$ are the kinetic coefficients; and $a$, $B$, $C$ and $\gamma$ are the Landau coefficients. The accuracy of this model was rigorously evaluated in a later work—the results obtained from this model were well comparable to the experimental data reported in the literature [85].

## 5. Measurement Methods

For the last couple of decades, methods for measuring the dielectric properties of textile materials have gained increasing interest. One critical facet has been its application in material characterization. Since the dielectric properties contain a wide range of information, such as the compositional, structural and geometrical properties, dielectric characterization could estimate these properties of textile materials [5–7,40–42], for instance for quality control of fabrics in a similar way to the capacitance-based fiber and yarn testing widely adopted in the textile industry [9–14]. Another unmissable application has been for development of textile-based wearable electronics. The performance and the form factor of electronic devices such as capacitors, transmission lines and antennas are well-documented to be impacted by the dielectric properties [38,47,57], and accordingly, the knowledge on the dielectric properties of textile materials is essential to design optimal textile-based electronics [7,15,41].

Dielectric characterization methods can be classified into the following two groups: resonant and non-resonant methods (Figure 9) [86,87]. In the resonant methods (Figure 9a), dielectric properties are determined through the measurement of resonant frequency and quality factor of resonant circuit embedded or covered with a dielectric material, whose dielectric properties are of interest [88]. Although resonant methods generally offer a higher level of accuracy and hence could be more suitable for low loss materials than the non-resonant methods, resonant methods can determine the dielectric properties only at a single or discrete set of frequencies [86,87]. Moreover, due to the physical size requirement of resonant structures, characterization is typically limited to certain microwave frequencies. Furthermore, since the resonant (and hence, the characterization) frequency is perturbed by the dielectric properties of the material under test, dielectric properties are often analyzed at a frequency that is slightly different from the target frequency [7,89].

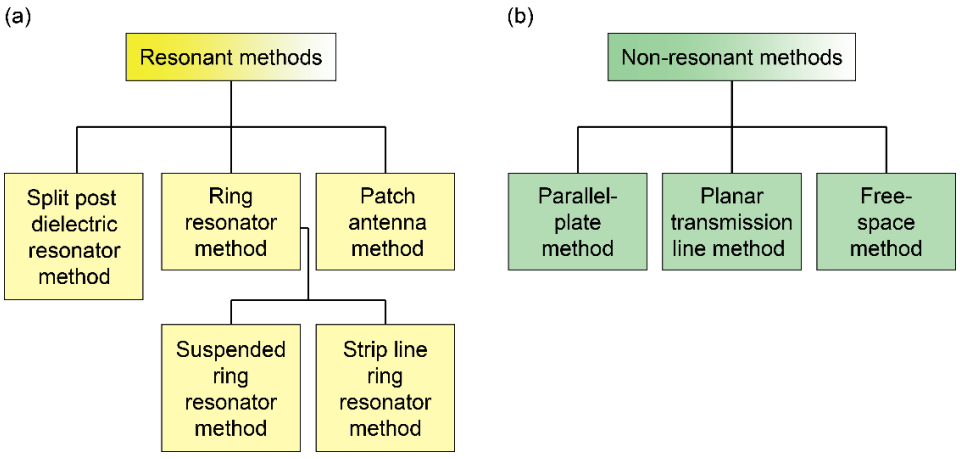


**Figure 9.** (**a**) Resonant and (**b**) non-resonant methods commonly used for dielectric characterization of textile materials.

Non-resonant methods (Figure 9b), on the other hand, could measure the dielectric properties in a broad range of frequency. The underlying principle in non-resonant methods is that electrical properties of a non-resonant circuit embedded or covered with a dielectric material are mathematically related to the dielectric properties. Although the measurement accuracy is generally limited in comparison with that of resonant methods, non-resonant methods offer information on the frequency-dependent dielectric properties. The following subsections review some of the most versatile dielectric characterization methods for textile materials from recent literature.

### *5.1. Resonant Methods*

#### 5.1.1. Split Post Dielectric Resonator Method

The split post dielectric resonator method employs a hollow enclosure (Figure 10) whose resonant frequencies and quality factors are pre-determined by its shape and dimensions, but which can be altered by placing a dielectric material inside it. The resonant frequencies and quality factors of the split post dielectric resonator are measured with and without a testing material (Figure 10) by using a vector network analyzer. The real part of the complex relative permittivity ($\varepsilon'_{r,m}$) can then be calculated from the shift in the resonant frequency by using the formula [90]:

$$\varepsilon'_{r,m} = 1 + \frac{f_{wo} - f_w}{h f_{wo} K_\varepsilon\left(\varepsilon'_{r,m}, h\right)} \tag{39}$$

where $f_w$ and $f_{wo}$ are the resonant frequencies with and without sample, respectively; $h$ is the sample thickness; and $K_\varepsilon$ is a function of $\varepsilon'_{r,m}$ and $h$, and can be computed by an iterative method [90]. The loss tangent ($\tan\delta$) can be obtained from the measured quality factors by using the expression [90]:

$$\tan\delta = \frac{\left[Q_w^{-1} - Q_d^{-1} - \left(Q_c K_1\left(\varepsilon'_{r,m}, h\right)\right)^{-1}\right]}{h\varepsilon'_{r,m} K_2\left(\varepsilon'_{r,m}, h\right)} \tag{40}$$

where $Q_w$ is a quality factor of the sample-filled resonator; $Q_d$ is the quality factor that accounts for the dielectric loss of the sample-filled resonator; $Q_c$ is the quality factor that accounts for the conductor-related losses of the empty resonator; and $K_1$ and $K_2$ are functions of $\varepsilon'_{r,m}$ and $h$ and can be determined by an iterative method. Therefore, the imaginary part of the relative permittivity can be obtained by using Equations (4) and (40).

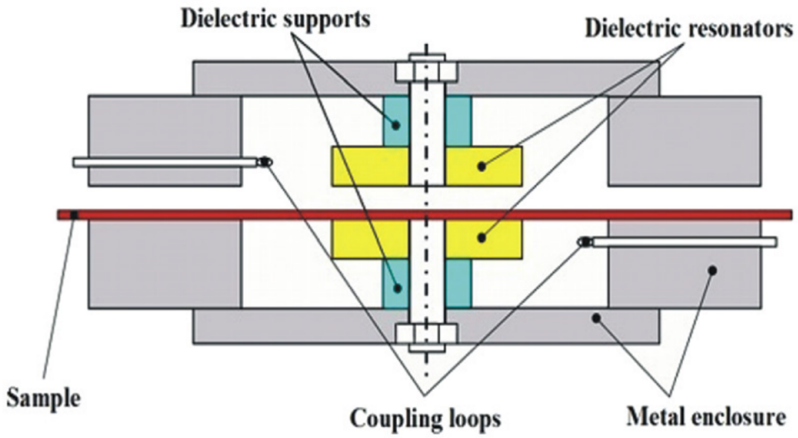


**Figure 10.** Schematic illustration of a split post dielectric resonator for dielectric characterization. Reprinted with permission from Ref. [91] (p. 102904). Copyright 2013 AMERICAN INSTITUTE OF PHYSICS.

One considerable feature of the split post dielectric resonator method is that predefined, standard fixtures are commercially available on the market, and the complex relative permittivity of thin, planar materials, including fabrics, can be rapidly determined with excellent accuracy [92]. However, the characterization frequencies are typically limited to 1.1 to 20 GHz because of the physical size constraints of the fixture and testing material [92]. In addition, high permittivity samples need to be sufficiently thin to avoid undesirable resonances particularly at higher frequencies [93].

5.1.2. Ring Resonator Method

A ring resonator, as drawn in Figure 11, is a type of resonant structure whose resonant frequencies and quality factor in given dimensions are predominantly determined by the complex relative permittivity of the substrate [94]. Hence, in this method, the material under test is embedded as the substrate, and its complex relative permittivity is determined through the measurement of the resonant frequency and quality factor by using a vector network analyzer [94]. The real part of the relative permittivity ($\varepsilon'_{r,m}$) can be calculated from the resonant frequency of the ring resonator by using the expression [95]:

$$\varepsilon'_{r,m} = \frac{2\varepsilon_{eff} + \left(1 + \frac{12h}{w_{eff}}\right)^{-\frac{1}{2}} - 1}{\left(1 + \frac{12h}{w_{eff}}\right)^{-\frac{1}{2}} + 1} \tag{41}$$

where $f_r$ is the resonant frequency of the ring resonator; $r$ is the radius of the ring; $h$ is the thickness of the material under test; $w_{eff}$ and $\varepsilon_{eff}$ are the effective width and permittivity that account for the thickness of the strip ($t$), respectively. The effective width and permittivity are given respectively by [95]:

$$w_{eff} = w + \frac{1.25t}{\pi}\left(1 + \ln\left(\frac{2h}{t}\right)\right) \tag{42}$$

$$\varepsilon_{eff} = \left(\frac{nc}{2\pi r f_r}\right)^2 \tag{43}$$

The loss tangent ($\tan\delta$) of the test sample can be obtained by [95]:

$$\tan\delta = \frac{\lambda_0 \alpha_d \sqrt{\varepsilon_{eff}}(\varepsilon_{r,m} - 1)}{8.686\pi\varepsilon_r(\varepsilon_{eff} - 1)} \tag{44}$$

where $\lambda_0$ is the wavelength of the free-space radiation from the ring at the resonant frequency; and $\alpha_d$ is the attenuation due to the dielectric loss. $\alpha_d$ can be obtained by subtracting the attenuation due to the conductor ($\alpha_c$) and radiation ($\alpha_r$) losses from the total attenuation ($\alpha_{total}$) as [95]:

$$\alpha_d = \alpha_{total} - \alpha_c - \alpha_r \tag{45}$$

where $\alpha_{total}$ is related to the quality factor of the ring resonator at the resonant frequency ($Q_0$) by [95]:

$$\alpha_{total} = \frac{\pi\sqrt{\varepsilon_{eff}}}{Q_0\lambda_0} \tag{46}$$

$\alpha_c$ can be determined by using the expression [95]:

$$\alpha_c = \frac{\frac{\sqrt{\pi\mu_0 f_r}}{\sigma} \times \left[1 + \frac{2}{\pi}\tan^{-1}\left(\frac{1.4\Delta^2}{\varsigma^2}\right)\right]}{hZ_0} \times \frac{8.686}{\left[\frac{w_{eff}}{h} + \frac{2}{\pi}\ln\left\{2\pi e\left(\frac{w_{eff}}{2h} + 0.94\right)\right\}\right]^2} \times \left(\frac{w_{eff}}{2h} + \frac{\frac{w_{eff}}{2h}}{\frac{w_{eff}}{2h} + 0.94}\right) \times \left[1 + \frac{h}{w_{eff}} + \frac{h}{\pi w_{eff}}\left\{\ln\left(\frac{2h}{t} + 1\right) - \frac{1 - \frac{t}{h}}{1 + \frac{t}{2h}}\right\}\right] \tag{47}$$

where $\sigma$ is the static conductivity of the ring; $\Delta$ is the surface roughness; and $\varsigma$ is the skin depth. Since the radiation from the ring structure is typically negligibly small, the $\alpha_r$ term can be dropped. Accordingly, the loss tangent of the testing material can be obtained by

using Equations (44)–(47), and finally the imaginary part of the relative permittivity can be obtained by using Equation (4).

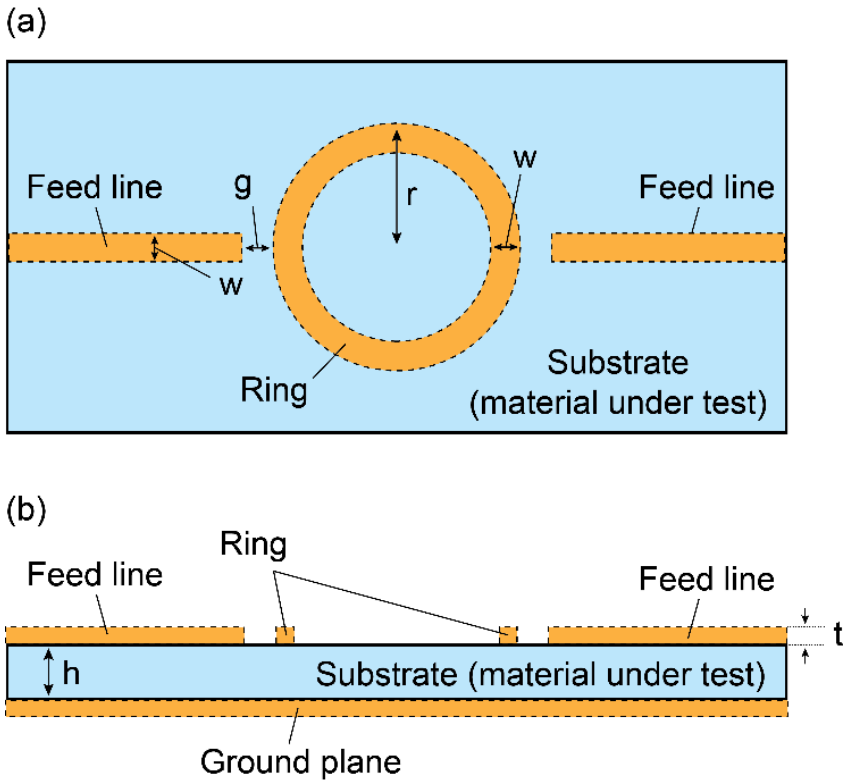


**Figure 11.** Schematic illustration of a ring resonator embedded with a material under test for dielectric characterization in (**a**) top and (**b**) cross-sectional views. Redrawn from [94] (p. 15).

Although the ring resonator method could offer a good estimation of the complex relative permittivity in the microwave frequency domain, a preparatory phase is required to embed a testing material into the ring resonator geometry, but such process could be laborious and for certain samples even impracticable [94]. In order to ease the challenges in the sample preparation, multilayer methods such as the suspended ring resonator method and the strip line ring resonator method were proposed.

In the suspended ring resonator method, the ring resonator geometry is divided, for instance, into three sections, as follows: the lower layer, the sample, and the upper layer [94,96] (Figure 12). The lower layer consists of a ground plane and two feed lines mounted onto a dielectric medium of known complex permittivity, and the upper layer consist of the same dielectric material but this time with a ring. These lower and upper layers can be fabricated based on the conventional, printed circuit board technology. The sample is then placed in-between, and its complex relative permittivity can be determined through the measurements of the resonant frequency and quality factor in a similar manner to the original, ring resonator method. The specific formulas for the suspended ring resonator method are available in [94,96].

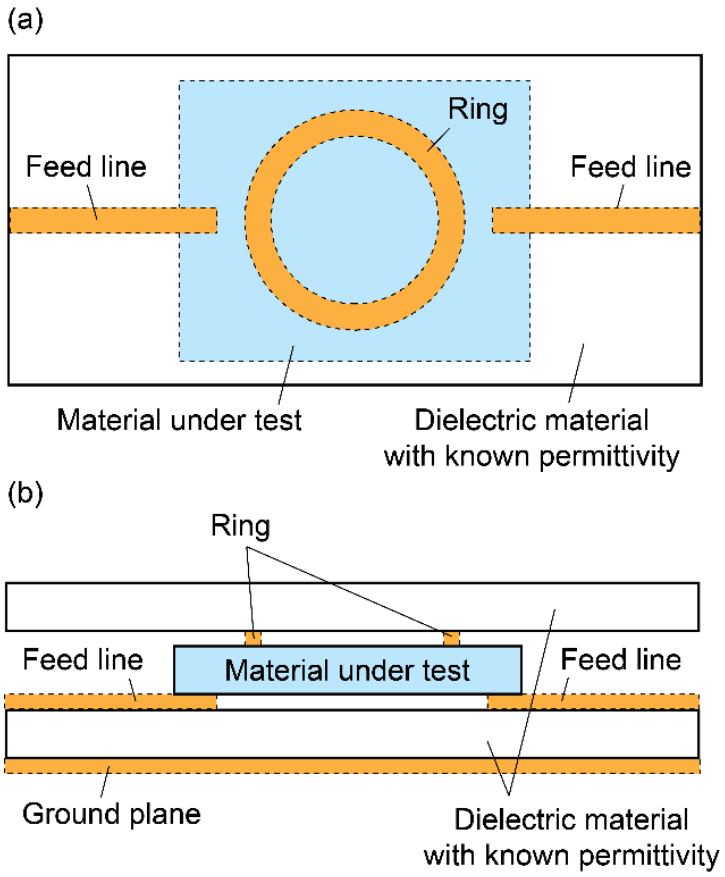


**Figure 12.** Schematic illustration of a suspended ring resonator for dielectric characterization: (**a**) top and (**b**) cross-sectional views. Redrawn from [94] (p. 21).

The strip line ring resonator method [97], on the other hand, employs a pre-established ring resonator, onto which the testing material is placed with a metal cover (Figure 13). The complex relative permittivity of the sample is then determined through the resonant frequency and quality factor measurements by using the formulas given in [97]. For both types of the multilayer ring resonator methods, ring resonator fixtures can be reused many times. Hence, these methods can be timesaving and cost-efficient alternatives to the original ring resonator method.

#### 5.1.3. Patch Antenna Method

The patch antenna method is another resonant technique suitable for thin, planar samples including fabrics. The leading principle in this method is that a patch antenna, which consists of a conductive thin patch mounted on a grounded dielectric material, has a resonant frequency that is dependent on the dielectric constant of the substrate and antenna dimensions [38,47]; accordingly, the dielectric constant of the dielectric material can be estimated from the antenna dimensions and the measurement of the resonant frequency [5,7,41,89,98].

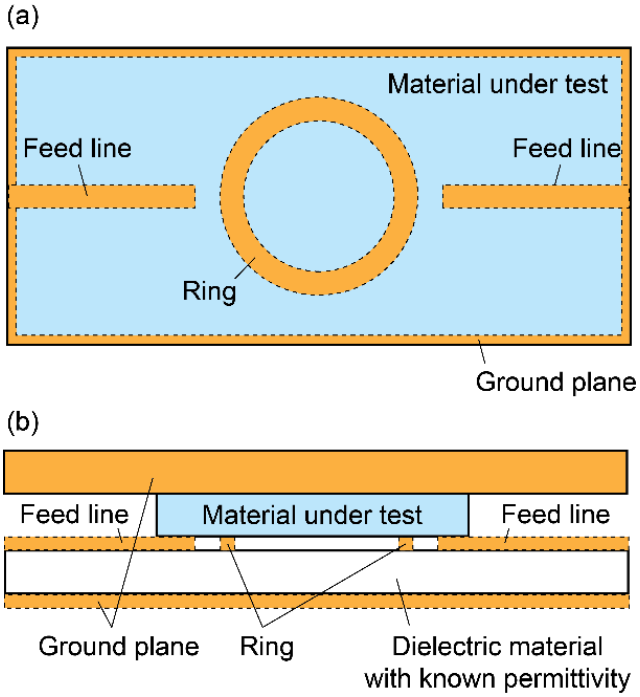


**Figure 13.** Schematic illustration of a strip line ring resonator for dielectric characterization: (**a**) top and (**b**) cross-sectional views. Redrawn from [97] (p. 2).

While various types of patch antennas could be designed for dielectric characterization, those in simple geometrical shapes such as rectangles are most commonly chosen for straightforward calculation. For a rectangular patch antenna depicted in Figure 14, the dielectric constant ($\varepsilon'_{\mathrm{r,m}}$) of the test sample can be extracted from the analytical formula [41,89]:

$$\varepsilon'_{\mathrm{r,eff}} = \left(\frac{\varepsilon'_{\mathrm{r,m}}+1}{2}\right) + \left(\frac{\varepsilon'_{\mathrm{r,m}}-1}{2}\right)\left(1+\frac{12h}{W_{\mathrm{p}}}\right)^{-\frac{1}{2}} \tag{48}$$

where $h$ is the thickness of the test sample; $W_{\mathrm{p}}$ is the width of the patch; and $\varepsilon'_{r,eff}$ is the effective dielectric constant and can be calculated using the expression [41,89]:

$$L_{\mathrm{p}} = \left(\frac{c}{2f_{\mathrm{r}}\sqrt{\varepsilon'_{\mathrm{r,eff}}}}\right) - 0.824h\left(\frac{\varepsilon'_{\mathrm{r,eff}}+0.3}{\varepsilon'_{\mathrm{r,eff}}-0.258}\right)\left(\frac{\frac{W_{\mathrm{p}}}{h}+0.264}{\frac{W_{\mathrm{p}}}{h}+0.8}\right) \tag{49}$$

where $L_{\mathrm{p}}$ is the length of the patch and $f_{\mathrm{r}}$ is the resonant frequency of the patch antenna.

It should be noted that while the patch antenna method could offer excellent accuracy in determining the real part of the relative permittivity [5,7,41,89,98], the imaginary part may not be acquired by this method. This is because typical patch antennas have non-negligible radiation and surface-wave losses, which are challenging to experimentally quantify. Therefore, the patch antenna method is primarily used for dielectric materials whose loss behavior is not of major concern [89] or in combination with another characterization method [41].

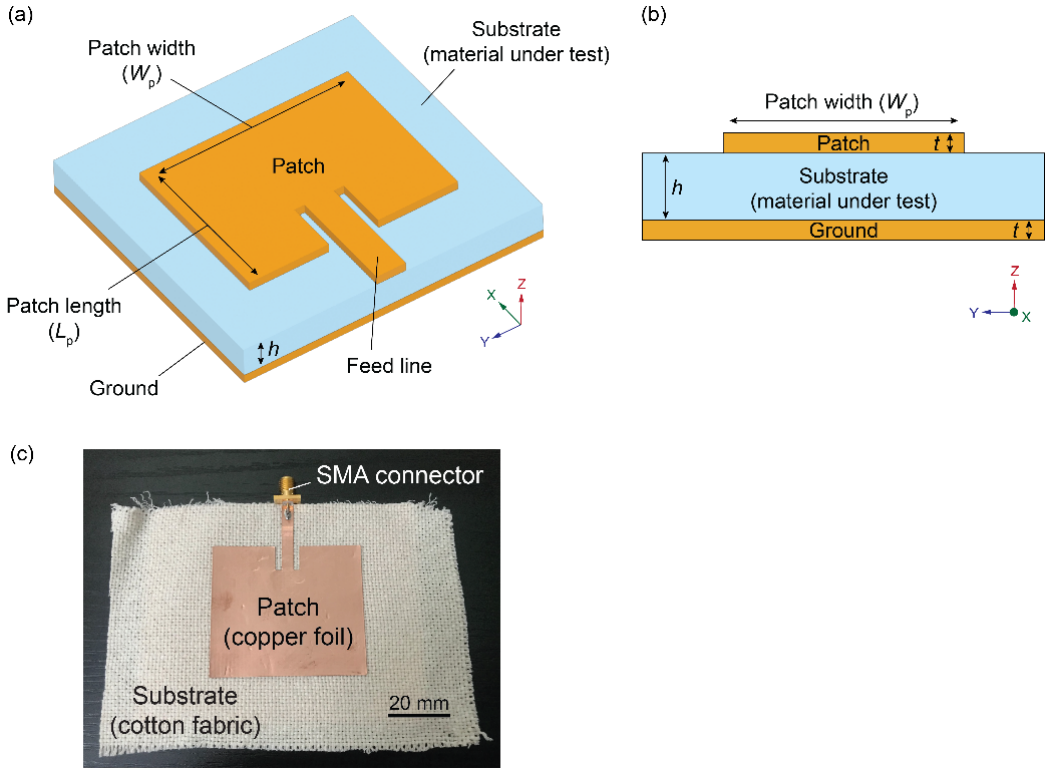


**Figure 14.** Schematic illustration of a rectangular patch antenna in (**a**) perspective and (**b**) cross-sectional views. Redrawn and simplified from [41] (p. 110); and (**c**) patch antenna sample with an embedded cotton fabric for dielectric characterization. Reprinted with permission from [7] (p. 5). Copyright 2020 YUSUKE MUKAI & MINYOUNG SUH.

### *5.2. Non-Resonant Methods*

#### 5.2.1. Parallel-Plate Method

The parallel-plate method is one of the most common characterization methods in the low frequency regime typically below 1 GHz [86]. In this method, a sample is placed between a pair of electrodes and capacitance and dissipation factor ($D$) are measured by an LCR meter (Figure 15). The real part of the relative permittivity ($\varepsilon'_{r,m}$) is then calculated using the formula [57]:

$$\varepsilon'_{r,m} = \frac{dC}{\varepsilon_0 A} \tag{50}$$

where $A$ is the area of the electrode, and $d$ is the distance between the electrodes. For test samples whose static conductivities are negligibly small, the dissipation factor is equal to the loss tangent. Therefore, the imaginary part of the relative permittivity ($\varepsilon''_{r,m}$) can be calculated as [57]:

$$\varepsilon''_{r,m} = \tan\delta \cdot \varepsilon'_{r,m} \simeq D\varepsilon'_{r,m} \tag{51}$$

One critical advantage of the parallel-plate method is its simplicity in sample preparation and measurement setup [86]—samples in a wide range of thickness can be non-destructively measured with adjustable electrodes commercially available on the market. There is, however, one major notation in this method. It has been reported that charges accumulated at the sample-electrode interface during measurement could cause a large polarization (called electrode polarization) that mask the true response of the test sample [46]. This unwanted parasitic effect could be especially pronounced at lower frequencies for materials with high moisture contents including cotton fabrics [6,40,41], and can result in an extremely large, apparent complex permittivity [46]. Although several workarounds

have been proposed to alleviate the effect of the electrode polarization [100–103], complete removal or compensation is almost unattainable.

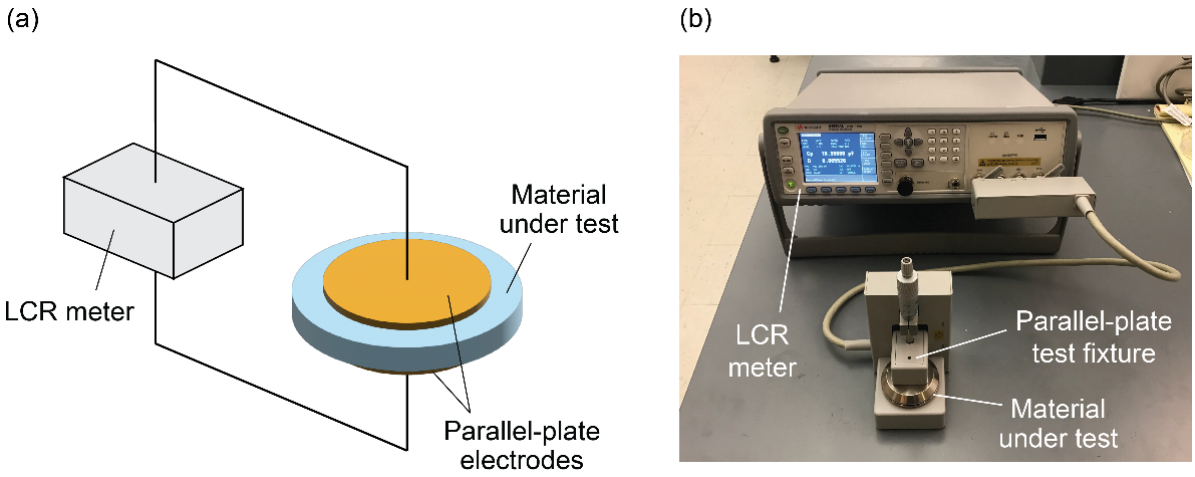


**Figure 15.** (**a**) Schematic illustration of a sample-filled parallel-plate capacitor connected to an LCR meter. Redrawn from [99] (p. 109); and (**b**) commercially available setup. Adapted from [41] (p. 76). Copyright 2019 YUSUKE MUKAI.

5.2.2. Planar Transmission Line Method

The planar transmission line method is a high-frequency technique that measures the complex permittivity of a thin test sample embedded in or placed in the vicinity of a planar transmission line. This method is based on the transmission line theory—the reflection and transmission characteristics of a planar transmission line is dependent on the dielectric properties of the embedded or the covered material [41,88,104]. Accordingly, the complex permittivity of the test material can be determined through the measurement of the reflection and transmission coefficients or the scattering parameters [41,88,104].

Planar transmission lines can be produced in various geometries; however, those in simple forms such as microstrip lines (Figure 16) are usually preferable for ease of fabrication and calculation. For the microstrip line geometry, the real part of the relative permittivity ($\varepsilon'_{r,m}$) is given by [41,56,105]:

$$\varepsilon'_{r,m} \simeq \frac{2\varepsilon'_{r,eff} - 1 + \frac{1}{\sqrt{1+\frac{12h}{W}}}}{1 + \frac{1}{\sqrt{1+\frac{12h}{W}}}} \quad (52)$$

where $W$ is the width of the trace; $h$ is the thickness of the sample; and $\varepsilon'_{r,eff}$ is the effective dielectric constant given by [41,47]:

$$\varepsilon'_{r,eff} = \left(\frac{c\beta}{2\pi f}\right) \quad (53)$$

where $\beta$ is the phase constant. The phase constant can be calculated from the scattering parameters, which are measurable by a vector network analyzer with an appropriate calibration technique—the full details of the processes are described in [41].

The loss tangent can be calculated by the formula [41,105]:

$$\tan\delta \simeq \frac{c\alpha}{\pi f\sqrt{\varepsilon'_{r,eff}}} \quad (54)$$

where $\alpha$ is the attenuation constant and can be calculated from the measured scattering parameters as described in [41]. The imaginary part of the relative permittivity can then be obtained from Equations (4) and (54).

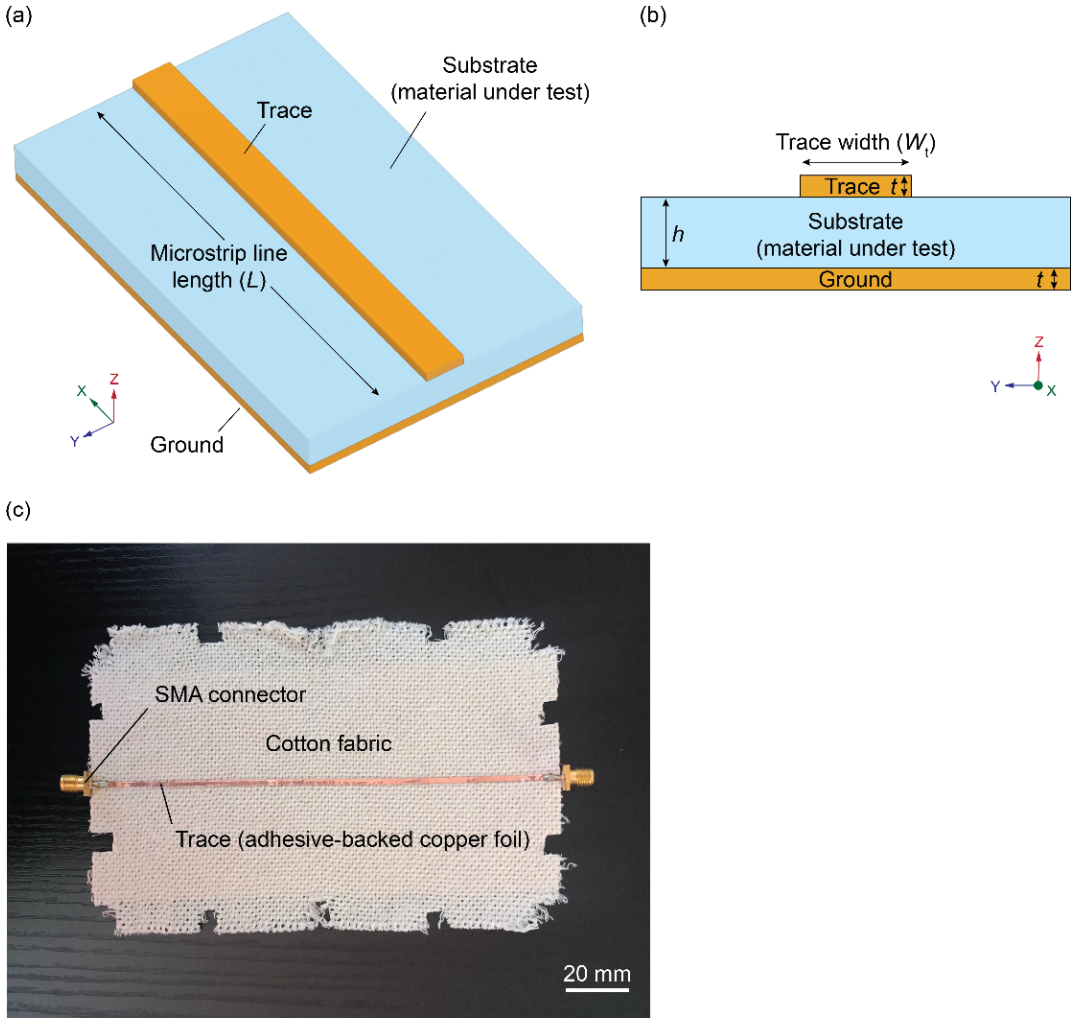


**Figure 16.** (**a**) Schematic illustration of a microstrip line in (**a**) perspective and (**b**) cross-sectional views. Redrawn and simplified from [41] (p. 99); and (**c**) microstrip line sample fabricated for dielectric characterization of a cotton fabric. Reprinted from [41] (p. 101). Copyright 2019 YUSUKE MUKAI.

Although there are several drawbacks, such as the necessity of calibration to remove the effect of feeding systems (e.g., connectors) and limited accuracy in characterization, one of the main features of the planar transmission line method is its simplicity in fabrication—for instance, planar transmission lines can be easily fabricated for a test sample by mounting thin conductive sheets such as a copper foil tape [41]. In addition, the frequency dependence of the complex permittivity can be acquired by this method since planar transmission lines support broadband microwave frequencies [106].

#### 5.2.3. Free-Space Method

Another non-resonant method suitable for textile materials is the free space method, where a test specimen is placed between a pair of horn antennas connected to a vector

network analyzer (Figure 17). Under this configuration, the complex relative permittivity ($\varepsilon^*_{r,m}$) of the testing material is expressed as [107]:

$$\varepsilon^*_{r,m} = \frac{\lambda_0^2}{\mu^*_r}\left[\frac{1}{\lambda_c^2} - \left\{\frac{1}{2\pi h}\ln(T)\right\}^2\right] \quad (55)$$

where $\lambda_c$ and $\lambda_0$ are the cutoff and free-space wavelengths, respectively; $h$ is the sample thickness; $\mu^*_r$ is the complex relative permeability of the sample; and $T$ is the transmission coefficient. Since $T$ can be obtained from scattering parameter measurements with an appropriate calibration technique [107], the complex relative permittivity can be determined from Equation (55).

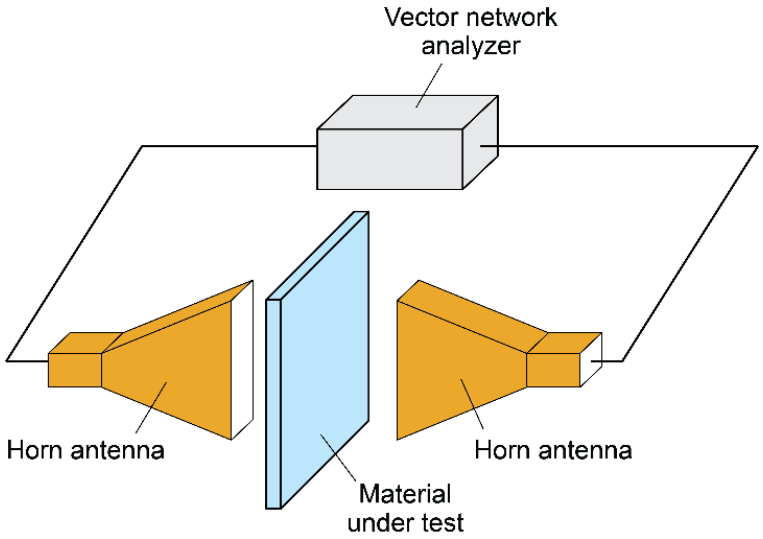


**Figure 17.** Schematic illustration of a free-space measurement setup with a pair of horn antennas. Redrawn from [108] (p. 102).

The major advantage of the free-space method is that the dielectric properties of sheet samples including textile materials can be non-destructively evaluated in the broad microwave frequencies simply by placing them between the horn antennas [107]. On the other hand, a calibration process is necessary to eliminate the effect of the feeding systems (e.g., connectors and antennas) in a similar rationale to the planar transmission method. In addition, a large sample surface is required to minimize the diffraction effects at the edges of the sample [109].

## 6. Conclusions

This paper reviewed various indispensable theories and principles related to the dielectric properties of textile materials. In order to provide a profound basis for unraveling the various intricate factors that affect the dielectric properties of textile materials, foundations on the dielectrics and polarization mechanisms were first recapitulated, followed by an overview on the concept of homogenization and some of the most prominent mixing rules. The key advantages, challenges and opportunities in the analytical approximations of the dielectric properties of textile materials were then discussed based on the findings and implications from the recent literature, and finally the variety of characterization methods were described for determination of the dielectric properties of textile materials.

**Funding:** This research received no external funding.

**Conflicts of Interest:** The author declares that there is no conflict of interest.

## Appendix A

**Table A1.** Dielectric properties of some pure fabrics reported in literature.

| Fabric Specification | | | Measurement Conditions | | | | Dielectric Properties | | | Ref. |
|---|---|---|---|---|---|---|---|---|---|---|
| Composition | Construction | Solid Volume Fraction | Frequency (Hz) | Temperature (°C) | Relative Humidity (%) | Moisture Content (wt%) | Real Part | Imaginary Part | Loss Tangent | |
| Cotton | Plain weave | 0.134 * | $1 \times 10^6$ | 21 | 40 | – | 5.59 | 0.352 ‡ | 0.063 | [73] |
| | | | | | 60 | | 6.12 | 0.514 ‡ | 0.084 | |
| | | | | | 80 | | 7.08 | 0.722 ‡ | 0.102 | |
| Cotton | Twill weave | 0.293 * | $2.45 \times 10^9$ | – | – | – | 1.71 | 0.034 ‡ | 0.020 | [16] |
| Cotton | Plain weave | 0.10 | ~$2.45 \times 10^9$ | 21 ± 0.2 | 80 ± 2.5 | 8.42 | 1.28 | – | – | [7] |
| | Plain weave | 0.11 | | | | | 1.24 | – | – | |
| | Plain weave | 0.11 | | | | | 1.29 | – | – | |
| | Plain weave | 0.14 | | | | | 1.42 | – | – | |
| | Plain weave | 0.15 | | | | | 1.46 | – | – | |
| Cotton | Plain weave | 0.10 | ~$2.45 \times 10^9$ | 21 ± 2 | 65 ± 5 | 7.57 | 1.27 | – | – | [7] |
| | Plain weave | 0.11 | | | | | 1.24 | – | – | |
| | Plain weave | 0.11 | | | | | 1.29 | – | – | |
| | Plain weave | 0.14 | | | | | 1.40 | – | – | |
| | Plain weave | 0.15 | | | | | 1.43 | – | – | |
| Cotton | Plain weave | 0.10 | ~$2.45 \times 10^9$ | 21 ± 0.2 | 50 ± 2.5 | 6.43 | 1.27 | – | – | [7] |
| | Plain weave | 0.11 | | | | | 1.27 | – | – | |
| | Plain weave | 0.11 | | | | | 1.26 | – | – | |
| | Plain weave | 0.14 | | | | | 1.36 | – | – | |
| | Plain weave | 0.15 | | | | | 1.38 | – | – | |
| Cotton | Plain weave | 0.10 | ~$2.45 \times 10^9$ | 21 ± 0.2 | 35 ± 2.5 | 5.27 | 1.26 | – | – | [7] |
| | Plain weave | 0.11 | | | | | 1.21 | – | – | |
| | Plain weave | 0.11 | | | | | 1.24 | – | – | |
| | Plain weave | 0.14 | | | | | 1.32 | – | – | |
| | Plain weave | 0.15 | | | | | 1.35 | – | – | |
| Cotton | Plain weave | 0.10 | ~$2.45 \times 10^9$ | 21 ± 0.2 | 20 ± 2.5 | 3.77 | 1.23 | – | – | [7] |
| | Plain weave | 0.11 | | | | | 1.18 | – | – | |
| | Plain weave | 0.11 | | | | | 1.21 | – | – | |
| | Plain weave | 0.14 | | | | | 1.29 | – | – | |
| | Plain weave | 0.15 | | | | | 1.31 | – | – | |
| Cotton | Plain knit (single jersey) | 0.10 | ~$2.45 \times 10^{11}$ | 21 ± 0.2 | 80 ± 2.5 | 8.42 | 1.38 | – | – | [7] |
| | Plain knit (single jersey) | 0.11 | | | | | 1.37 | – | – | |
| | Plain knit (single jersey) | 0.11 | | | | | 1.42 | – | – | |
| | Plain knit (single jersey) | 0.14 | | | | | 1.55 | – | – | |
| | Plain knit (single jersey) | 0.15 | | | | | 1.62 | – | – | |
| Cotton | Plain knit (single jersey) | 0.10 | ~$2.45 \times 10^9$ | 21 ± 2 | 65 ± 5 | 7.57 | 1.37 | – | – | [7] |
| | Plain knit (single jersey) | 0.11 | | | | | 1.35 | – | – | |
| | Plain knit (single jersey) | 0.11 | | | | | 1.39 | – | – | |
| | Plain knit (single jersey) | 0.14 | | | | | 1.47 | – | – | |
| | Plain knit (single jersey) | 0.15 | | | | | 1.59 | – | – | |

**Table A1.** *Cont.*

| Fabric Specification | | | Measurement Conditions | | | | Dielectric Properties | | | Ref. |
|---|---|---|---|---|---|---|---|---|---|---|
| **Composition** | **Construction** | **Solid Volume Fraction** | **Frequency (Hz)** | **Temperature (°C)** | **Relative Humidity (%)** | **Moisture Content (wt%)** | **Real Part** | **Imaginary Part** | **Loss Tangent** | |
| Cotton | Plain knit (single jersey) | 0.10 | ~$2.45 \times 10^9$ | $21 \pm 0.2$ | $50 \pm 2.5$ | 6.43 | 1.32 | – | – | [7] |
| | Plain knit (single jersey) | 0.11 | | | | | 1.30 | – | – | |
| | Plain knit (single jersey) | 0.11 | | | | | 1.34 | – | – | |
| | Plain knit (single jersey) | 0.14 | | | | | 1.43 | – | – | |
| | Plain knit (single jersey) | 0.15 | | | | | 1.50 | – | – | |
| Cotton | Plain knit (single jersey) | 0.10 | ~$2.45 \times 10^9$ | $21 \pm 0.2$ | $35 \pm 2.5$ | 5.27 | 1.30 | – | – | [7] |
| | Plain knit (single jersey) | 0.11 | | | | | 1.28 | – | – | |
| | Plain knit (single jersey) | 0.11 | | | | | 1.32 | – | – | |
| | Plain knit (single jersey) | 0.14 | | | | | 1.41 | – | – | |
| | Plain knit (single jersey) | 0.15 | | | | | 1.47 | – | – | |
| Cotton | Plain knit (single jersey) | 0.10 | ~$2.45 \times 10^9$ | $21 \pm 0.2$ | $20 \pm 2.5$ | 3.77 | 1.25 | – | – | [7] |
| | Plain knit (single jersey) | 0.11 | | | | | 1.23 | – | – | |
| | Plain knit (single jersey) | 0.11 | | | | | 1.27 | – | – | |
| | Plain knit (single jersey) | 0.14 | | | | | 1.35 | – | – | |
| | Plain knit (single jersey) | 0.15 | | | | | 1.40 | – | – | |
| Flax | Plain weave | 0.235 * | $1 \times 10^6$ | 21 | 40 | – | 4.22 | 0.156 ‡ | 0.037 | [73] |
| | | | | | 60 | | 4.43 | 0.177 ‡ | 0.040 | |
| | | | | | 80 | | 6.20 | 0.360 ‡ | 0.058 | |
| Jute | Plain weave | 0.223 * | $1 \times 10^6$ | 21 | 40 | – | 2.99 | 0.093 ‡ | 0.031 | [73] |
| | | | | | 60 | | 3.90 | 0.137 ‡ | 0.035 | |
| | | | | | 80 | | 4.95 | 0.233 ‡ | 0.047 | |
| Hemp | Plain weave | 0.249 * | $1 \times 10^6$ | 21 | 40 | – | 4.08 | 0.114 ‡ | 0.028 | [73] |
| | | | | | 60 | | 4.50 | 0.162 ‡ | 0.036 | |
| | | | | | 80 | | 4.77 | 0.248 ‡ | 0.052 | |
| Wool | Plain weave | 0.303 * | $1 \times 10^6$ | 21 | 40 | – | 4.11 | 0.115 ‡ | 0.028 | [73] |
| | | | | | 60 | | 4.65 | 0.214 ‡ | 0.046 | |
| | | | | | 80 | | 5.70 | 0.296 ‡ | 0.052 | |
| Polyester | $2 \times 2$ rib knit | – | $1.13 \times 10^3$ | $20 \pm 1$ | $65 \pm 2$ | – | 4.06 | 1.67 | 0.46 | [110] |
| Polyester | Plain weave | 0.387 * | $1 \times 10^6$ | 21 | 40 | – | 3.20 | 0.058 ‡ | 0.018 | [73] |
| | | | | | 60 | | 3.39 | 0.088 ‡ | 0.026 | |
| | | | | | 80 | | 3.66 | 0.117 ‡ | 0.032 | |
| Polyester | 3D spacer knit | 0.0706 * | $2.25 \times 10^9$ | – | – | – | 1.10 | 0.006 ‡ | 0.005 | [83] |
| Polyester | 3D spacer knit | 0.0821 * | $2.25 \times 10^9$ | – | – | – | 1.10 | 0.007 ‡ | 0.006 | |
| Polyester | 3D spacer knit | 0.0745 * | $2.25 \times 10^9$ | – | – | – | 1.12 | 0.019 ‡ | 0.017 | |
| Polyester | 3D spacer knit | 0.0982 * | $2.25 \times 10^9$ | – | – | – | 1.13 | 0.020 ‡ | 0.018 | |
| Polyester | 3D spacer knit | 0.0627 * | $2.25 \times 10^9$ | – | – | – | 1.11 | 0.004 ‡ | 0.004 | |

**Table A1.** *Cont.*

| Fabric Specification | | | Measurement Conditions | | | | Dielectric Properties | | | Ref. |
|---|---|---|---|---|---|---|---|---|---|---|
| Composition | Construction | Solid Volume Fraction | Frequency (Hz) | Temperature (°C) | Relative Humidity (%) | Moisture Content (wt%) | Real Part | Imaginary Part | Loss Tangent | |
| Polyester | Plain weave | 0.43 † | $2.26 \times 10^9$ | – | – | – | 1.55 | 0.013 ‡ | 0.009 | [111] |
| Polyester | Felt | – | $2.45 \times 10^9$ | – | – | – | 1.2 | 0.028 ‡ | 0.023 | [24] |
| Polyester | Woven | – | | – | – | – | 1.5 | 0.042 ‡ | 0.028 | |
| Polyester | – | – | $2.45 \times 10^9$ | – | – | – | 1.44 | – | – | [89] |
| Polyester | Fleece | 0.103 * | $2.45 \times 10^9$ | – | – | 0.40 § | 1.15 | 0.000 ‡ | 0.000 | [16] |
| High density polyethylene | Plain weave | 0.1326 | $1 \times 10^3$ | – | – | – | 1.12 | – | – | [39] |
| | Plain weave | 0.1633 | $1 \times 10^3$ | – | – | – | 1.14 | – | – | |
| | Plain weave | 0.1190 | $1 \times 10^3$ | – | – | – | 1.10 | – | – | |
| | Plain weave | 0.2560 | $1 \times 10^3$ | – | – | – | 1.23 | – | – | |

* Calculated by the formula: $\varphi = G/h\rho$, where $\varphi$ is the solid volume fraction; $G$ is the fabric weight; $h$ is the fabric thickness; and $\rho$ is the fiber density [6]. The commonly accepted values of 1.52 g/cm$^3$ [112], 1.45 g/cm$^3$ [113,114], 1.5 g/cm$^3$ [115], 1.45 g/cm$^3$ [116], 1.31 g/cm$^3$ [117] and 1.39 g/cm$^3$ [118,119] were used for the densities of cotton, flax, jute, hemp, wool and polyester fibers, respectively. † Calculated by the formula: $\varphi = 1 - p/100$, where $p$ is the porosity (%) [120]. ‡ Calculated by Equation (4). § Calculated by $M = 100R/(100 + R)$, where $M$ and $R$ are the moisture content (%) and the moisture regain (%), respectively [121].

## References


1. Bal, K.; Kothari, V.K. Measurement of Dielectric properties of textile materials and their applications. *Indian J. Fibre Text. Res.* **2009**, *34*, 191–199.
2. Ivanovska, A.; Cerovic, D.; Maletic, S.; Jankovic Castvan, I.; Asanovic, K.; Kostic, M. Influence of the alkali treatment on the sorption and dielectric properties of woven jute fabric. *Cellulose* **2019**, *26*, 5133–5146. [CrossRef]
3. Ivanovska, A.; Cerovic, D.; Tadic, N.; Jankovic Castvan, I.; Asanovic, K.; Kostic, M. Sorption and dielectric properties of jute woven fabrics: Effect of chemical composition. *Ind. Crops Prod.* **2019**, *140*, 111632. [CrossRef]
4. Cerovic, D.D.; Petronijevic, I.; Dojcilovic, J.R. Influence of temperature and fiber structure on the dielectric properties of polypropylene fibrous structures. *Polym. Adv. Technol.* **2014**, *25*, 338–342. [CrossRef]
5. Mukai, Y.; Suh, M. Structure-Microwave Dielectric Property Relationship in Cotton Fabrics. In Proceedings of the Techtextil North America, Raleigh, NC, USA, 26–28 February 2019.
6. Mukai, Y.; Dickey, E.C.; Suh, M. Low Frequency Dielectric Properties Related to Structure of Cotton Fabrics. *IEEE Trans. Dielectr. Electr. Insul.* **2020**, *27*, 291–298. [CrossRef]
7. Mukai, Y.; Suh, M. Relationships between Structure and Microwave Dielectric Properties in Cotton Fabrics. *Mater. Res. Express* **2020**, *7*, 015105. [CrossRef]
8. Sihvola, A.H. *Electromagnetic Mixing Formulas and Applications*; IEE Electromagnetic Waves Series 47; Institution of Electrical Engineers: London, UK, 1999; ISBN 978-0-85296-772-0.
9. Gandhi, K.L. Yarn Preparation for Weaving: Winding. In *Woven Textiles*; Elsevier: Amsterdam, The Netherlands, 2020; pp. 35–79. ISBN 978-0-08-102497-3.
10. Carvalho, V.; Cardoso, P.; Belsley, M.; Vasconcelos, R.M.; Soares, F.O. Development of a Yarn Evenness Measurement and Hairiness Analysis System. In Proceedings of the IECON 2006-32nd Annual Conference on IEEE Industrial Electronics, Paris, France, 7–10 November 2006; pp. 3621–3626.
11. Ghosh, A.; Mal, P. Testing of Fibres, Yarns and Fabrics and Their Recent Developments. In *Fibres to Smart Textiles*; Patnaik, A., Patnaik, S., Eds.; CRC Press: Boca Raton, FL, USA, 2019; pp. 221–256. ISBN 978-0-429-44651-1.
12. Thilagavathi, G.; Karthik, T. *Process Control and Yarn Quality in Spinning*; Woodhead Publishing India in Textiles; CRC Press: Boca Raton, FL, USA, 2016; ISBN 978-93-80308-18-0.
13. Ott, P.; Schmid, P. Verfahren und Vorrichtung zur Erkennung von Fremdstoffen in Einem Bewegten, Festen, Länglichen Prüfgut. European Patent EP2108949A1, 7 June 2006.
14. *ASTM D1425*; Standard Test Method for Evenness of Textile Strands Using Capacitance Testing Equipment. ASTM International: West Conshohocken, PA, USA, 2014.
15. Salvado, R.; Loss, C.; Gonçalves, R.; Pinho, P. Textile Materials for the Design of Wearable Antennas: A Survey. *Sensors* **2012**, *12*, 15841–15857. [CrossRef]
16. Hertleer, C.; Laere, A.V.; Rogier, H.; Langenhove, L.V. Influence of Relative Humidity on Textile Antenna Performance. *Text. Res. J.* **2010**, *80*, 177–183. [CrossRef]
17. Xu, F.; Zhu, H.; Ma, Y.; Qiu, Y. Electromagnetic performance of a three-dimensional woven fabric antenna conformal with cylindrical surfaces. *Text. Res. J.* **2017**, *87*, 147–154. [CrossRef]

18. Mukai, Y.; Bharambe, V.T.; Adams, J.J.; Suh, M. Effect of bending and padding on the electromagnetic performance of a laser-cut fabric patch antenna. *Text. Res. J.* **2019**, *89*, 2789–2801. [CrossRef]
19. Mukai, Y.; Suh, M. Development of a Conformal Woven Fabric Antenna for Wearable Breast Hyperthermia. *Fash. Text.* **2021**, *8*, 1–12. [CrossRef]
20. Locher, I.; Klemm, M.; Kirstein, T.; Trster, G. Design and Characterization of Purely Textile Patch Antennas. *IEEE Trans. Adv. Packag.* **2006**, *29*, 777–788. [CrossRef]
21. Mukai, Y.; Suh, M. Development of a Conformal Textile Antenna for Thermotherapy. In Proceedings of the Fiber Society's Fall 2018 Technical Meeting and Conference, Davis, CA, USA, 29–31 October 2018.
22. Mukai, Y.; Suh, M. Conformal Cotton Antenna for Wearable Thermotherapy. In Proceedings of the Fiber Society's Spring 2019 Conference, Hong Kong, China, 21–23 May 2019.
23. Jia, X.; Tennant, A.; Langley, R.J.; Hurley, W.; Dias, T. Moisture effects on a knitted waveguide. In Proceedings of the 2016 Loughborough Antennas & Propagation Conference (LAPC), Loughborough, UK, 14–15 November 2016; pp. 1–3.
24. Adami, S.-E.; Proynov, P.; Hilton, G.S.; Yang, G.; Zhang, C.; Zhu, D.; Li, Y.; Beeby, S.P.; Craddock, I.J.; Stark, B.H. A Flexible 2.45-GHz Power Harvesting Wristband With Net System Output From −24.3 dBm of RF Power. *IEEE Trans. Microw. Theory Tech.* **2018**, *66*, 380–395. [CrossRef]
25. Chi, Y.-J.; Lin, C.-H.; Chiu, C.-W. Design and modeling of a wearable textile rectenna array implemented on Cordura fabric for batteryless applications. *J. Electromagn. Waves Appl.* **2020**, *34*, 1782–1796. [CrossRef]
26. Wagih, M.; Hilton, G.S.; Weddell, A.S.; Beeby, S. Broadband Millimeter-Wave Textile-Based Flexible Rectenna for Wearable Energy Harvesting. *IEEE Trans. Microw. Theory Tech.* **2020**, *68*, 4960–4972. [CrossRef]
27. Zhang, R.Q.; Li, J.Q.; Li, D.J.; Xu, J.J. Study of the Structural Design and Capacitance Characteristics of Fabric Sensor. Available online: http://www.scientific.net/AMR.194-196.1489 (accessed on 6 June 2018).
28. Seyedin, S.; Zhang, P.; Naebe, M.; Qin, S.; Chen, J.; Wang, X.; Razal, J.M. Textile strain sensors: A review of the fabrication technologies, performance evaluation and applications. *Mater. Horiz.* **2019**, *6*, 219–249. [CrossRef]
29. Bansal, N.; Ehrmann, A.; Geilhaupt, M. Textile Capacitors as Pressure Sensors. In Proceedings of the Aachen-Dresden International Textile Conference, Dresden, Germany, 27–28 November 2014.
30. Ma, L.; Wu, R.; Patil, A.; Zhu, S.; Meng, Z.; Meng, H.; Hou, C.; Zhang, Y.; Liu, Q.; Yu, R.; et al. Full-Textile Wireless Flexible Humidity Sensor for Human Physiological Monitoring. *Adv. Funct. Mater.* **2019**, *29*, 1904549. [CrossRef]
31. Ng, C.; Reaz, M. Characterization of Textile-Insulated Capacitive Biosensors. *Sensors* **2017**, *17*, 574. [CrossRef] [PubMed]
32. Liu, Y.; Yu, Y.; Zhao, X. The influence of the ratio of graphite to silver-coated copper powders on the electromagnetic and mechanical properties of single-layer coated composites. *J. Text. Inst.* **2021**, *112*, 1709–1716. [CrossRef]
33. Liu, Y.; Yu, Y.; Zhao, X. The influence of wave-absorbing functional particles on the electromagnetic properties and the mechanical properties of coated fabrics. *J. Text. Inst.* **2021**, 1–21. [CrossRef]
34. Yamada, Y. Textile-Integrated Polymer Optical Fibers for Healthcare and Medical Applications. *Biomed. Phys. Eng. Express* **2020**. [CrossRef]
35. Yamada, Y.; Suh, M. Textile Materials for Mobile Health: Opportunities and challenges. In Proceedings of the WTiN Innovate Textile & Apparel Virtual Trade Show, Online, 15–30 October 2020.
36. Wang, L.; Fu, X.; He, J.; Shi, X.; Chen, T.; Chen, P.; Wang, B.; Peng, H. Application Challenges in Fiber and Textile Electronics. *Adv. Mater.* **2020**, *32*, 1901971. [CrossRef] [PubMed]
37. Hasan, M.M.; Hossain, M.M. Nanomaterials-patterned flexible electrodes for wearable health monitoring: A review. *J. Mater. Sci.* **2021**, *56*, 14900–14942. [CrossRef] [PubMed]
38. Balanis, C.A. *Antenna Theory: Analysis and Design*, 4th ed.; Wiley: Hoboken, NJ, USA, 2016.
39. Bal, K.; Kothari, V.K. Permittivity of woven fabrics: A comparison of dielectric formulas for air-fiber mixture. *IEEE Trans. Dielectr. Electr. Insul.* **2010**, *17*, 881–889. [CrossRef]
40. Mukai, Y.; Suh, M. Effect of Fabric Construction, Thread Count and Solid Volume Fraction on the Dielectric Properties of Cotton Fabrics. In Proceedings of the Fiber Society's Fall 2018 Technical Meeting and Conference, Davis, CA, USA, 29–31 October 2018.
41. Mukai, Y. Dielectric Properties of Cotton Fabrics and Their Applications. Doctoral Dissertation, North Carolina State University, Raleigh, NC, USA, 2019.
42. Giordano, S. Effective medium theory for dispersions of dielectric ellipsoids. *J. Electrost.* **2003**, *58*, 59–76. [CrossRef]
43. Bunget, I.; Popescu, M. *Physics of Solid Dielectrics*; Materials Science Monographs 19; Elsevier: Amsterdam, The Netherlands, 1984; ISBN 978-0-444-99632-9.
44. Gupta, M.; Wong, W.L. *Microwaves and Metals*; John Wiley & Sons: Singapore; Hoboken, NJ, USA, 2007; ISBN 978-0-470-82272-2.
45. Kasap, S.O. *Principles of Electronic Materials and Devices*, 3rd ed.; McGraw-Hill: Boston, MA, USA, 2006; ISBN 978-0-07-295791-4.
46. Kremer, F.; Schönhals, A. *Broadband Dielectric Spectroscopy*; Springer: Berlin/Heidelberg, Germany, 2003; ISBN 978-3-540-43407-8.
47. Balanis, C.A. *Advanced Engineering Electromagnetics*, 2nd ed.; Wiley: Hoboken, NJ, USA, 2012; ISBN 978-0-470-58948-9.
48. Oughstun, K.; Cartwright, N. On the Lorentz-Lorenz formula and the Lorentz model of dielectric dispersion. *Opt. Express* **2003**, *11*, 1541. [CrossRef]
49. Patel, D.; Shah, D.; Hilfiker, J.; Linford, M. Characterization of Thin Films and Materials: A Tutorial on Spectroscopic Ellipsometry (SE) 5. *Vac. Technol. Coat.* **2019**, *20*, 34–37.

50. Onimisi, M.Y.; Ikyumbur, J.T. Comparative Analysis of Dielectric Constant and Loss Factor of Pure Butan-1-ol and Ethanol. *Am. J. Condens. Matter Phys.* **2015**, *5*, 69–75.
51. Hanai, T. Dielectric Theory on the Interfacial Polarization for Two-Phase Mixtures. *Bull. Inst. Chem. Res. Kyoto Univ.* **1962**, *39*, 341–367.
52. Sillars, R.W. The properties of a dielectric containing semiconducting particles of various shapes. *Inst. Electr. Eng-Proc. Wirel. Sect. Inst.* **1937**, *12*, 139–155. [CrossRef]
53. Arous, M.; Amor, I.B.; Kallel, A.; Fakhfakh, Z.; Perrier, G. Crystallinity and dielectric relaxations in semi-crystalline poly(ether ether ketone). *J. Phys. Chem. Solids* **2007**, *68*, 1405–1414. [CrossRef]
54. Hikosaka, S.; Ishikawa, H.; Ohki, Y. Effects of crystallinity on dielectric properties of poly(L-lactide). *Electron. Commun. Jpn.* **2011**, *94*, 1–8. [CrossRef]
55. Pelster, R. Dielectric relaxation spectroscopy in polymers: Broadband ac-spectroscopy and its compatibility with TSDC. In Proceedings of the 10th International Symposium on Electrets (ISE 10), Proceedings (Cat. No.99 CH36256), Athens, Greece, 22–24 September 1999; pp. 437–444.
56. Bahl, I.J.; Trivedi, D.K. A designer's guide to microstrip line. *Microwaves* **1977**, 174–182.
57. Natarajan, R. *Power System Capacitors*; Power Engineering 26; CRC Press: Boca Raton, FL, USA, 2005; ISBN 978-1-57444-710-1.
58. Bal, K.; Kothari, V.K. Study of dielectric behaviour of woven fabric based on two phase models. *J. Electrost.* **2009**, *67*, 751–758. [CrossRef]
59. Driscoll, T.; Basov, D.N.; Padilla, W.J.; Mock, J.J.; Smith, D.R. Electromagnetic characterization of planar metamaterials by oblique angle spectroscopic measurements. *Phys. Rev. B* **2007**, *75*, 115114. [CrossRef]
60. Khoshman, J.M.; Kordesch, M.E. Vacuum Ultra-Violet Spectroscopic Ellipsometry Study of Sputtered BeZnO Thin Films. *Optik* **2011**, *122*, 2050–2054. [CrossRef]
61. Jean-Mistral, C.; Sylvestre, A.; Basrour, S.; Chaillout, J.-J. Dielectric properties of polyacrylate thick films used in sensors and actuators. *Smart Mater. Struct.* **2010**, *19*, 075019. [CrossRef]
62. Li, S.; Chen, R.; Anwar, S.; Lu, W.; Lai, Y.; Chen, H.; Hou, B.; Ren, F.; Gu, B. Applying effective medium theory in characterizing dielectric constant of solids. In Proceedings of the 2012 International Workshop on Metamaterials (Meta), Nanjing, China, 8–10 October 2012; pp. 1–3.
63. Zhuromskyy, O. Applicability of Effective Medium Approximations to Modelling of Mesocrystal Optical Properties. *Crystals* **2016**, *7*, 1. [CrossRef]
64. Tinga, W.R.; Voss, W.A.G.; Blossey, D.F. Generalized approach to multiphase dielectric mixture theory. *J. Appl. Phys.* **1973**, *44*, 3897–3902. [CrossRef]
65. Garnett, J.C.M.; Larmor, J. XII. Colours in metal glasses and in metallic films. *Philos. Trans. R. Soc. Lond. Ser. Contain. Pap. Math. Phys. Character* **1904**, *203*, 385–420. [CrossRef]
66. Sihvola, A. Homogenization principles and effect of mixing on dielectric behavior. *Photonics Nanostruct.-Fundam. Appl.* **2013**, *11*, 364–373. [CrossRef]
67. Morton, W.E.; Hearle, J.W.S. *Physical Properties of Textile Fibres*; Woodhead Publishing: Sawston, UK, 2008; ISBN 978-1-84569-220-9.
68. Balls, W.L. Dielectric Properties of Raw Cotton. *Nature* **1946**, *158*, 9–11. [CrossRef]
69. Humlicek, J. Data Analysis for Nanomaterials: Effective Medium Approximation, Its Limits and Implementations. In *Ellipsometry at the Nanoscale*; Losurdo, M., Hingerl, K., Eds.; Springer: Berlin/Heidelberg, Germany, 2013; pp. 145–178. ISBN 978-3-642-33955-4.
70. Markel, V.A. Introduction to the Maxwell Garnett approximation: Tutorial. *J. Opt. Soc. Am. A* **2016**, *33*, 1244. [CrossRef]
71. Peirce, F.T. 5—The Geometry of Cloth Structure. *J. Text. Inst. Trans.* **1937**, *28*, T45–T96. [CrossRef]
72. Bal, K.; Kothari, V.K. Dielectric behaviour of polyamide monofilament fibers containing moisture as measured in woven form. *Fibers Polym.* **2014**, *15*, 1745–1751. [CrossRef]
73. Cerovic, D.D.; Dojcilovic, J.R.; Asanovic, K.A.; Mihajlidi, T.A. Dielectric investigation of some woven fabrics. *J. Appl. Phys.* **2009**, *106*, 084101. [CrossRef]
74. Igarashi, T.; Hoshi, M.; Nakamura, K.; Kaharu, T.; Murata, K. Direct Observation of Bound Water on Cotton Surfaces by Atomic Force Microscopy and Atomic Force Microscopy–Infrared Spectroscopy. *J. Phys. Chem. C* **2020**, *124*, 4196–4201. [CrossRef]
75. Sakabe, H.; Ito, H.; Miyamoto, T.; Inagaki, H. States of Water Sorbed on Wool as Studied by Differential Scanning Calorimetry. *Text. Res. J.* **1987**, *57*, 66–72. [CrossRef]
76. Skaar, C. *Wood-Water Relations*; Springer Series in Wood Science; Springer: Berlin/Heidelberg, Germany, 1988; ISBN 978-3-642-73685-8.
77. Buchner, R.; Barthel, J.; Stauber, J. The dielectric relaxation of water between 0 °C and 35 °C. *Chem. Phys. Lett.* **1999**, *306*, 57–63. [CrossRef]
78. Hippel, A.R. von The dielectric relaxation spectra of water, ice, and aqueous solutions, and their interpretation. I. Critical survey of the status-quo for water. *IEEE Trans. Electr. Insul.* **1988**, *23*, 801–816. [CrossRef]
79. Sugimoto, H.; Takazawa, R.; Norimoto, M. Dielectric relaxation due to heterogeneous structure in moist wood. *J. Wood Sci.* **2005**, *51*, 549–553. [CrossRef]
80. Kuttich, B.; Grefe, A.-K.; Kröling, H.; Schabel, S.; Stühn, B. Molecular mobility in cellulose and paper. *RSC Adv.* **2016**, *6*, 32389–32399. [CrossRef]

81. Cerovic, D.D.; Asanovic, K.A.; Maletic, S.B.; Dojcilovic, J.R. Comparative study of the electrical and structural properties of woven fabrics. *Compos. Part B Eng.* **2013**, *49*, 65–70. [CrossRef]
82. Gezici-Koç, Ö.; Erich, S.J.F.; Huinink, H.P.; van der Ven, L.G.J.; Adan, O.C.G. Bound and free water distribution in wood during water uptake and drying as measured by 1D magnetic resonance imaging. *Cellulose* **2017**, *24*, 535–553. [CrossRef]
83. Loss, C.; Gonçalves, R.; Pinho, P.; Salvado, R. Influence of some structural parameters on the dielectric behavior of materials for textile antennas. *Text. Res. J.* **2018**. [CrossRef]
84. Mukherjee, P.K. Dielectric properties in textile materials: A theoretical study. *J. Text. Inst.* **2018**, *110*, 1–4. [CrossRef]
85. Mukherjee, P.K.; Das, S. Improved analysis of the dielectric properties of textile materials. *J. Text. Inst.* **2021**, *112*, 1890–1895. [CrossRef]
86. Jilani, M.T.; Rehman, M.Z.; Khan, A.M.; Khan, M.T.; Ali, S.M. A Brief Review of Measuring Techniques for Characterization of Dielectric Materials. *Int. J. Inf. Technol. Electr. Eng.* **2012**, *1*, 5.
87. Chen, L.F.; Ong, C.K.; Neo, C.P.; Varadan, V.V.; Varadan, V.K. *Microwave Electronics: Measurement and Materials Characterization*; Wiley: Chichester, UK, 2004.
88. Baker-Jarvis, J. *Dielectric and Conductor-Loss Characterization and Measurements on Electronic Packaging Materials*; NIST Technical Note 1520; U.S. Department of Commerce, National Institute of Standards and Technology: Boulder, CO, USA, 2001.
89. Sankaralingam, S.; Gupta, B. Determination of Dielectric Constant of Fabric Materials and Their Use as Substrates for Design and Development of Antennas for Wearable Applications. *IEEE Trans. Instrum. Meas.* **2010**, *59*, 3122–3130. [CrossRef]
90. Mazierska, J.; Krupka, J.; Jacob, M.V.; Ledenyov, D. Complex permittivity measurements at variable temperatures of low loss dielectric substrates employing split post and single post dielectric resonators. In Proceedings of the 2004 IEEE MTT-S International Microwave Symposium Digest (IEEE Cat. No.04CH37535), Fort Worth, TX, USA, 6–11 June 2004; pp. 1825–1828.
91. Kowerdziej, R.; Krupka, J.; Nowinowski-Kruszelnicki, E.; Olifierczuk, M.; Parka, J. Microwave complex permittivity of voltage-tunable nematic liquid crystals measured in high resistivity silicon transducers. *Appl. Phys. Lett.* **2013**, *102*, 102904. [CrossRef]
92. Krupka, J.; Nguyen, D.; Mazierska, J. Microwave and RF methods of contactless mapping of the sheet resistance and the complex permittivity of conductive materials and semiconductors. *Meas. Sci. Technol.* **2011**, *22*, 085703. [CrossRef]
93. Krupka, J. Microwave Measurements of Electromagnetic Properties of Materials. *Materials* **2021**, *14*, 5097. [CrossRef]
94. Waldron, I. Ring Resonator Method for Dielectric Permittivity Measurement of Foams. Master's Thesis, Worcester Polytechnic Institute, Worcester, MA, USA, 2006.
95. Yang, L.; Rida, A.; Vyas, R.; Tentzeris, M.M. RFID Tag and RF Structures on a Paper Substrate Using Inkjet-Printing Technology. *IEEE Trans. Microw. Theory Tech.* **2007**, *55*, 2894–2901. [CrossRef]
96. Waldron, I.; Makarov, S.N. Measurement of dielectric permittivity and loss tangent for bulk foam samples with suspended ring resonator method. In Proceedings of the 2006 IEEE Antennas and Propagation Society International Symposium, Albuquerque, NM, USA, 9–14 July 2006; pp. 3175–3178.
97. Tu, H.; Zhang, Y.; Hong, H.; Hu, J.; Ding, X. A strip line ring resonator for dielectric properties measurement of thin fabric. *J. Text. Inst.* **2021**, *112*, 1772–1778. [CrossRef]
98. Shimin, D. A New Method for Measuring Dielectric Constant Using the Resonant Frequency of a Patch Antenna. *IEEE Trans. Microw. Theory Tech.* **1986**, *34*, 923–931. [CrossRef]
99. Rabih, A.A.S.; Begam, K.M.; Ibrahim, T.; Burhanudin, Z.A. Dielectric Properties of Properly Slaughtered and Non-properly Slaugheterd Chicken. *J. Med. Res. Dev.* **2014**, *3*, 15.
100. Pizzitutti, F.; Bruni, F. Electrode and interfacial polarization in broadband dielectric spectroscopy measurements. *Rev. Sci. Instrum.* **2001**, *72*, 2502–2504. [CrossRef]
101. Chassagne, C.; Dubois, E.; Jiménez, M.L.; van der Ploeg, J.P.M.; van Turnhout, J. Compensating for Electrode Polarization in Dielectric Spectroscopy Studies of Colloidal Suspensions: Theoretical Assessment of Existing Methods. *Front. Chem.* **2016**, *4*. [CrossRef]
102. Ishai, P.B.; Talary, M.S.; Caduff, A.; Levy, E.; Feldman, Y. Electrode polarization in dielectric measurements: A review. *Meas. Sci. Technol.* **2013**, *24*, 102001. [CrossRef]
103. Klein, R.J.; Zhang, S.; Dou, S.; Jones, B.H.; Colby, R.H.; Runt, J. Modeling electrode polarization in dielectric spectroscopy: Ion mobility and mobile ion concentration of single-ion polymer electrolytes. *J. Chem. Phys.* **2006**, *124*, 144903. [CrossRef] [PubMed]
104. Gupta, K.C.; Ramadoss, R.; Zhang, H. RF and microwave network characterization-a concept-map-based tutorial. *IEEE Trans. Microw. Theory Tech.* **2003**, *51*, 1326–1329. [CrossRef]
105. Ravelo, B.; Thakur, A.; Saini, A.; Thakur, P. Microstrip Dielectric Substrate Material Characterization with Temperature Effect. *Appl. Comput. Electromagn. Soc.* **2015**, *30*, 1322–1328.
106. Maloratsky, L.G. Reviewing The Basics Of Microstrip Lines A. *Microw. RF* **2000**, *39*, 79–88.
107. Rocha, L.S.; Junqueira, C.C.; Gambin, E.; Nata Vicente, A.; Culhaoglu, A.E.; Kemptner, E. A free space measurement approach for dielectric material characterization. In Proceedings of the 2013 SBMO/IEEE MTT-S International Microwave & Optoelectronics Conference (IMOC), Rio de Janeiro, Brazil, 4–7 August 2013; pp. 1–5.
108. Fwen, W.; Ping, S.; Abd Malek, M.F.; Hasss, N. Alternatives for PCB Laminates: Dielectric Properties' Measurements at Microwave Frequencies. In *Dielectric Material*; Silaghi, M.A., Ed.; InTech: Rijeka, Croatia, 2012; ISBN 978-953-51-0764-4.
109. Pometcu, L.; Sharaiha, A.; Benzerga, R.; Tamas, R.D.; Pouliguen, P. Method for material characterization in a non-anechoic environment. *Appl. Phys. Lett.* **2016**, *108*, 161604. [CrossRef]

110. Liu, Y.; Zhao, X. Influence of the Yarn Fineness and Stitch Length of Polyester Knitted Fabric on the Dielectric Constant. *Fibres Text. East. Eur.* **2019**, *27*, 63–66. [CrossRef]
111. Mukai, Y.; Bharambe, V.T.; Adams, J.J.; Suh, M. Effect of Bending and Padding on the Electromagnetic Performance of a Laser-Cut Woven Fabric Patch Antenna. In Proceedings of the Textiles Research Open House, Raleigh, NC, USA, 16 April 2018.
112. Shao, X.; Qiu, Y.; Wang, Y. Theoretical modeling of the tensile behavior of low-twist staple yarns: Part II–theoretical and experimental results. *J. Text. Inst.* **2005**, *96*, 69–76. [CrossRef]
113. Van de Velde, K.; Kiekens, P. Development of a Flax/Polypropylene Composite with Optimal Mechanical Characteristics by Fiber and Matrix Modification. *J. Thermoplast. Compos. Mater.* **2002**, *15*, 281–300. [CrossRef]
114. Van de Velde, K.; Kiekens, P. Influence of Fibre and Matrix Modifications on Mechanical and Physical Properties of Flax Fibre Reinforced Poly(propylene). *Macromol. Mater. Eng.* **2001**, *286*, 237–242. [CrossRef]
115. Dalbehera, S.; Acharya, S.K. Study on mechanical properties of natural fiber reinforced woven jute-glass hybrid epoxy composites. *Adv. Polym. Sci. Technol.* **2014**, *4*, 1–6.
116. Wang, L.; Kumar, R.; Zhang, L. Investigation into hemp fiber- and whisker-reinforced soy protein composites. *Front. Chem. China* **2009**, *4*, 313–320. [CrossRef]
117. Li, Y.V. Proteins and Protein-Based Fibers. In *ACS Symposium Series*; Yang, Y., Xu, H., Yu, X., Eds.; American Chemical Society: Washington, DC, USA, 2014; Volume 1175, pp. 21–36. ISBN 978-0-8412-2990-7.
118. Xiang, P.; Kuznetsov, A.V.; Seyam, A.-F.M. Simulation of Fiber Entanglement by Modeling Vorticity in Water Flow Field. *Text. Res. J.* **2007**, *77*, 312–329. [CrossRef]
119. Shaikh, T.N.; Bhattacharya, S.S. Deriving an empirical formula to determine the optimum level of false-twist in mechanically-crimped textured polyester yarn. *Text. Res. J.* **2011**, *81*, 1995–2005. [CrossRef]
120. Mao, N.; Russell, S.J. Fibre to Fabric: Nonwoven Fabrics-ScienceDirect. In *Textiles and Fashion*; Woodhead Publishing Limited: Sawston, UK, 2015; pp. 307–335. ISBN 978-0-85709-561-9.
121. *ASTM D2495-17*; Standard Test Method for Moisture in Cotton by Oven-Drying. ASTM International: West Conshohocken, PA, USA, 2012.

*textiles*

MDPI

*Article*

# Development of a Consumer-Based Quality Scale for Artisan Textiles: A Study with Scarves/Shawls

**Denis Richard Seninde, Edgar Chambers IV *, Delores H. Chambers and Edgar Chambers V**

Center for Sensory Analysis and Consumer Behavior, Kansas State University, Manhattan, KS 66506, USA; seninde@ksu.edu (D.R.S.); delores@ksu.edu (D.H.C.); echambersv@gmail.com (E.C.V.)
* Correspondence: eciv@ksu.edu

**Abstract:** Modern textile consumers are increasingly becoming more watchful of the quality of the textiles that they purchase. This has increased the need for textile producers, especially artisan textile makers (e.g., knitters, tailors, dressmakers, seamstresses, and quilters), to improve the quality of their textile products. Information on several analytical tools that are commonly used for assessing the quality of textiles is abundant, but consumer-based tools for evaluating the quality of textiles remain limited. A consumer-based artisan textile-quality scale was developed using data collected from two focus groups (Phase 1) and a consumer quantitative study, $n$ = 196 (Phase 2). Ten scarves and shawls were evaluated in the quantitative study and analysis of variance (ANOVA) was used to determine the differences between the mean textile ratings for all the statements. Coefficient alpha (final raw alpha = 0.87) was also used to assess if the statements were consistent in the way they measured the quality of the textiles. Pearson correlation tests were used to validate the six-statement quality scale that included statements such as overall attention to detail, the fabric is durable, and stitching is even and consistent. Artisan textile makers in the USA can use this scale to better meet the functional needs of their customers. Additionally, the process that was employed in the development of the six-statement quality scale can be used by researchers in other countries to understand better the key quality characteristics of artisan as well other textile products.

**Keywords:** textiles; quality; artisan; fabrics; women in textiles

**Citation:** Seninde, D.R.; Chambers IV, E.; Chambers, D.H.; Chambers V, E. Development of a Consumer-Based Quality Scale for Artisan Textiles: A Study with Scarves/Shawls. *Textiles* **2021**, *1*, 483–503. https://doi.org/10.3390/textiles1030025

Academic Editor: Rajesh Mishra

Received: 6 August 2021
Accepted: 22 October 2021
Published: 27 October 2021



## 1. Introduction

History shows that men and women have always been involved in the production of textiles for various uses. However, the role of women often has been greater than men in different cultures or countries such as the USA [1,2], Nigeria [3], Britain [4], Guatemala [5–7], China [8,9], and India [10,11]. For example, in the Owe region in Nigeria (Africa), while the men prepared the soil for planting (clearing and tilling), the women planted and removed weeds from the cotton fields. Both men and women took part in the harvesting process, but the women processed the cotton to the point it was ready for weaving. Men and women shared roles during cloth weaving with the men using the horizontal loom while the women used the vertical loom [3]. The cotton textile products that the families produced in the Owe region were primarily used as needed by the households, though later (during colonial rule), men engaged more in the selling of cotton and textiles as their production capacities increased.

Based on Marketline [12], the revenues for global textiles (e.g., fabrics and yarns) grew between the years 2014 to 2018, with this industry (textile mills) attaining a total of USD 676.3 billion in 2018. The textile mills industry in the United States of America accounted for USD 81.5 billion of the total global revenues the same year, which placed the USA in third position after China and India [12]. Consumer preferences for textiles are mainly based on the functional and emotional properties of the textile products [6,13–16]. Additionally, current trends in the textile industry show more segmentation among consumers based on

population demographics and psychographics. For example, 27% of children and teens (particularly females) in the USA spend a significantly larger portion of their allowance on clothing as compared to other expenses, mainly because it is fashionable (it is what is offered and worn by most peers at the time) and not because it is unique [17].

Artisan textiles are gaining in value, in part because of the support for fair-trade and sustainable markets. However, those textile products still make up a small part of the market and some reports suggest that artisans themselves are becoming more scared because of economic, social, cultural, or environmental sustainability issues [18]. These result in a lack of market access or marketability of some artisan products. One potential reason for this is that artisans often do not have knowledge of the product preferences of their target consumers. Thus, it is necessary to help artisans understand the needs and wants of their consumers [19].

Sender [20] reported that the COVID-19 outbreak has been characterized by a significant reduction in production and marketing (closure of warehouses and stores) by large fashion retailers as they veered towards more sustainable strategies amidst the nation-wide lockdowns. Conversely, local and smaller fashion businesses adapted to the crisis and have thrived as shown by the fact that 26% of consumers were purchasing their textiles more from local businesses since the start of the pandemic [20]. Sales by smaller local textile businesses are likely to increase in the long run as textile consumers, particularly those interested in artisan products, may want to source locally in support of their communities and those retailers that are more environmentally friendly [16,20].

Koca and Koc [21] emphasized the impact of demographic aspects such as gender on the way consumers purchased textiles, with men's liking persuaded by brand name, while women were influenced by fashion. DeSalva [22] reported that women in the USA are motivated to purchase textiles because they need the items as replacements for those that are worn out and also in preparation for the upcoming season(s). Additionally, one study in Bangladesh found that young men and women were driven to purchase casual clothes by different fashion attributes [23]. Men have been reported to go textile shopping mainly because they are hunting for a particular item that they need in addition to other non-textile products that they may need [24,25]. DeSalva [25] reported that >80% of men (aged 18+) in the USA shopped for clothes at any retailer available whether online or face-to-face, indicating that men had limited loyalty to retailers.

Another major reason for purchase of textiles or clothing, particularly among women, is for pleasure ("to indulge oneself"), not because they "needed" them [24]. In addition, 40% of women in the USA purchased clothing four or fewer times in the year 2018. This indicated a need for textile producers and retailers to better appeal to the functional and emotional needs of their textile consumers if they were to drive up sales by increasing potential consumers' willingness to purchase. Mintel's online survey with women aged 18 + found that 66% of women in the USA preferred casual clothing (e.g., jeans and active wear) and 37% of them would be willing to purchase textiles if they were given the try-before-you-buy option [22].

Literature on instrumental approaches to determine textile quality is abundant [26–32]. There also is consumer-based research on people's perceptions of the quality of textiles, but this type of research is quite limited [33]. Benkirane et al. [34] developed a multi-attribute ranking method based on an overall quality score to rank and determine perceived quality. Li et al. [14] noted that consumers identified brand and fashion as the least important characteristics of tight-fit garments, while comfort and garment fit were pinpointed as the most important characteristics. These results in part supported earlier work by Kwok et al. [35], who had identified comfort and fabric quality as the most important quality characteristics when choosing children's denim garments. Hatch et al. [36] also stated that consumers focused on intrinsic properties (e.g., functional and compositional characteristics) but not external aspects such as price when evaluating the quality of textiles. Furthermore, Earl et al. [37] stated that textile colorfastness, durability, the status of seams,

and fabric construction were among other aspects that needed to be controlled if textiles were to meet the requirements of consumers.

Several consumer textile-quality values have been based on online surveys that used ideal (non-physical) textiles or pictures of textiles to collect consumer perceptions [16,34,38,39]. This method assumes that respondents used past textile experiences and only the sense of sight to evaluate the quality of the samples. Furthermore, in some cases, the reliability of the quality terms was not assessed, which made them unfit for practical application by process owners in the industry. Hatch [36] and Li [14] noted a growing demand by modern consumers for higher-quality textiles that satisfied functional and psychological needs and an opportunity to give textile manufacturers a competitive edge in their markets. To improve the quality of textiles, the makers and retailers need more understanding of what matters most to their consumers when it comes to textile quality.

The objectives of this study were to (1) identify statements used by consumers to describe "quality" differences (using sight, smell, touch, and hearing) in women's scarves/shawls, (2) to determine which of those statements actually differentiated among artisan textile scarves, (3) and determine reliability of that group of statements to better understand quality characteristics that artisans must consider when making and selling textile products to US consumers.

## 2. Materials and Methods

### *2.1. Phase 1 Study: Focus Groups (FGs)*

Focus groups were conducted by two professionally trained (Riva Institute, MD, USA) focus-group moderators at Kansas State University with experience in conducting focus groups for idea and terminology generation.

(a) Artisan textile samples

A set of 20 scarves and shawls, which varied in origin, price, design, and sensory properties, was used for the study. For example, some fabrics had fringes or tassels, while others did not. The scarves and shawls were selected from a large collection of artisan textiles that encompass a range of techniques (e.g., weaving techniques, embroidery styles, printing and dyeing methods, and sewing and hemming/finishing). Ten scarves representing a range of characteristics were evaluated in the first focus group and a different set of ten scarves with a range of characteristics was evaluated in the second focus group.

(b) Participant recruitment and statement generation

Characteristics that describe the quality of artisan textiles were generated using two 90 min focus groups of consumers ($n$ = 8, $n$ = 7) with considerable textile experience. The consumers (all female) were recruited from local sewing/quilting guilds in the Manhattan, KS (USA) area. The women were highly skilled in designing, making, and sewing home decor products and clothing, had experience working with artisan textiles, purchased textiles regularly, and most of the consumers had experience printing/dyeing or weaving textiles. A lump-sum donation was made to the organizations as payment for the time of its members. The women were 25–75 years of age, and most were in households with middle- to upper-middle-class incomes in the USA.

(c) Generating of statements related to the quality of artisan textiles

The first FG opened with a discussion of the perceptions, opinions, beliefs, and attitudes (POBAs) the women had on the quality of fabrics and textiles. The discussion segued into the differences between artisan and commercial textiles as regards quality and what matters most when it comes to the quality of a scarf or shawl. The participants then engaged in an "activity" (first activity) during which each participant was provided a scarf or shawl and asked to rate the textile based on a five-point scale from High quality (score = 1 or 2) to Low quality (score = 4 or 5). On the same individual grading form, participants were asked to list four quality characteristics that explained the grade they had awarded to each of the textiles. Each participant was allowed up to 2 min to assess

each scarf before passing it on to the person seated to their right side. The activity was conducted until each of the eight women had seen all the scarves. The moderator then used two columns on an easel to collect the two groups of quality characteristics as the participants briefly explained their reasons for classifying some textiles as high quality and others as low quality.

A second activity similar to the preceding activity was conducted with 10 additional scarves or shawls. The participants were given 1–2 min to individually evaluate each scarf/shawl, and listed quality characteristics of the textiles from the previous list as well as additional statements that they believed needed to be added to the list. Separating the two activities allowed the participants to attain a clearer understanding of the objectives in the first activity, to better separate "quality" from "liking" in their use of statements, and helped them exhibit more confidence, which allowed them to identify more quality descriptions.

The latter part of the FG concentrated on participants identifying ten statements that described high-quality scarves (scarves that received scores of 1 or 2) and ten statements that described the low-quality scarves (scarves that received scores of 4 or 5) based on how important the statements were to quality of the scarves or shawls.

FG 2 proceeded much like FG 1 with several minor modifications. (A) The authors scheduled a week between FG 1 and FG 2, which allowed the authors to review the findings of the first group and make any necessary changes for the second focus group. For instance, during the first focus-group discussion, the authors noticed that the participants sometimes mixed-up high quality and low quality with "like" and "dislike", i.e., a consumer might say 'I don't think this scarf is good because I don't like the color'. In such cases, discussion determined whether the consumer simply did not like the color/pattern/texture, etc., (affective characteristics), or if, for example, the color was actually low quality (i.e., faded, splotchy, poorly applied, etc.), which would make them descriptive quality characteristics. Thus, for the second focus group, the moderator started by explaining to the participants that the discussion would be focused on quality and not about whether they liked or did not like the textiles. (B) Some statements that were generated by FG 1 but were somewhat ambiguous or poorly defined/described in the first focus group were revisited during the FG 2 discussion. For example, terms such as "snuggle-feel", "design consistency", "deformities", "harsh hand-feel", and "sturdy weave" were specifically discussed by participants in FG 2 to determine if they could better describe the specific characteristics. (C) Several of the scarves/shawls used in FG 1 were replaced in FG 2 to provide additional potential to determine quality traits. Focus groups have been used before in other studies to gather textile-product-specific terminology from consumers [40].

(d) Selection of statements

FG 1 and FG 2 together produced a total of 86 quality terms. As expected, some of the statements that were generated by FG1 were also identified by FG 2. Furthermore, FG 2 participants refined some statements which were identified in FG 1 but were ambiguous.

### *2.2. Phase 2 Study: Quantitative Consumer Study*

(a) Artisan textile samples

Ten scarves and shawls from the initial set of 20 used in the two FG discussions were used for the quantitative consumer study. The authors chose a wide range of scarves/shawls representing higher and lower quality based on feedback in the FG. The textiles included in Phase 2 included samples that had various structural differences, design differences, edge finishes, fiber contents, and other variations (Table 1).

**Table 1.** Description and images of the ten scarves and shawls that were used as samples during the quantitative consumer study.

| Sample Label | Image | Sample Description |
|---|---|---|
| Sample 1 |  | Made in Turkey<br>Silk<br>Block Print<br>Hand-rolled Edge |
| Sample 2 |  | Made in India<br>Cotton<br>Block Print and Batik<br>Knotted Fringed Hems |
| Sample 3 |  | Made in India<br>Silk<br>Bandhani (tie-dye)<br>Machine-stitched Hems |
| Sample 4 |  | Made in India<br>Cotton and Wool<br>Handwoven<br>Hand-finished Hems |

**Table 1.** *Cont.*

| Sample Label | Image | Sample Description |
| --- | --- | --- |
| Sample 5 |  | Made in Laos<br>Silk<br>Handwoven<br>Braided Fringe Hems |
| Sample 6 |  | Made in India<br>Wool<br>Handwoven and Hand Embroidered<br>Twisted Fringe Hems |
| Sample 7 |  | Made in India<br>Silk<br>Bandhani (tie-dye)<br>Machine-rolled Hem |
| Sample 8 |  | Made in India<br>Cotton and Polyester<br>Hand Embroidered<br>Bound Hem |
| Sample 9 |  | Made in India<br>Silk<br>Batik (one color)<br>Knotted Fringe Hems |

**Table 1.** *Cont.*

| Sample Label | Image | Sample Description |
|---|---|---|
| Sample 10 |  | Made in India<br>Cotton<br>Batik (two color)<br>Unhemmed |

(b) Consumers

Women between the ages of 18 and 75 years (includes Generation Z through Baby Boomers) were included. Consumers selected had to have usually purchased their own clothes, had no fabric-related restrictions or allergies, and were available and interested in participating in the study. A total of 196 consumers evaluated the artisan textiles at the Center for Sensory Analysis and Consumer Behavior in Manhattan, KS (USA).

(c) Questionnaire development

The study questionnaire included an informed consent statement, demographic (5) questions, a five-point scale question (with anchor points of "very poor" and "excellent") that assessed how participants rated the quality of a scarf or shawl, and a five-point purchase-interest question [30]. The five questions on consumer demographics included questions on age, gender, level of education, and nine-point Likert scales on level of interest in artisan textiles and willingness to purchase natural or organic and environmentally friendly products. A five-point intensity scale that ranged from "does not apply at all" to "applies completely" assessed the degree of applicability for each of the quality statements selected for the quantitative phase for each scarf/shawl.

(d) Consumer testing

Consumer testing occurred throughout several sessions at a central location in Manhattan, KS (USA). Up to ten consumers participated in each session. Each participant was given a translucent plastic bin containing a single textile labeled with a three-digit code. Consumers had 3 min to evaluate each sample. After each sample evaluation, research assistants gathered the samples, refolded, and distributed samples again. The testing design was randomized and balanced in a Williams square design such that each participant assessed all 10 samples.

(e) Textile-Quality Index

A TQI was calculated by adding up the individual scores for each of the six (or eight) key statements that were indicated based on the statistical analysis (Cronbach's alpha). In the case of the six-statement index, the TQI could range from 6 to 30, with 6 indicating extremely poor quality and 30 indicating the highest quality.

(f) Statistical analysis

Percentage counts were computed for demographic questions on age and education. Analysis of variance (ANOVA) was conducted for data collected by each of the different intensity scales. It is worth noting that the data were, in general, normally distributed, and parametric analysis could be used.

Computations of unstandardized coefficient alpha (Cronbach's alpha) were used to assess the internal consistency of the quality statements. Internal validation of the

shortlisted statements that were identified by Cronbach's alpha for the consumer-based quality scale was conducted using Pearson correlation coefficients. A set of two correlation tests comprised one based on the participants as a whole sample and another where correlations were determined for each participant. These correlation tests assessed the association between a quality score and a Textile-Quality Index (TQI) score. The TQI scores were generated by summing up the individual scores received for each of the quality statements that were recommended by coefficient alpha. Based on the findings from coefficient alpha computations, it would be assumed that the recommended quality statements were found to perform consistently within as a group versus as individual quality parameters. This, then, would imply that by measuring the correlation between the quality score and the TQI, the authors could determine whether the recommended set of statements was indeed assessing, and could be relied on to measure, the quality of artisan clothing by consumer researchers. Indices similar in performance to the TQI have been previously used to internally validate consumer-based scales [41,42]. A Pearson correlation coefficient (R) value of R = 0.55 was used a reference. This meant that for the 196 participants, any $R \geq 0.55$ was considered to indicate between a moderate positive and strong positive relationship between that particular participant's quality score and the TQI. Put simply, when that person's score for the TQI increases, their score for quality would also increase. The same can be said for when the overall correlation tests where participants were treated as a whole.

All analyses were run using XLSTAT (version 2020.1, AddinSoft, New York, NY, USA).

## 3. Results

### *3.1. Phase 1—Qualitative Studies (Focus Groups)*

The FGs participants gave 46 high-quality statements (Table 2) and 40 low-quality statements (Table 3). In refining statements from FG1, the FG 2 participants modified some statements. For example, FG 2 replaced "harsh hand-feel" with "rough feel", which the FG 2 participants found to be a more appropriate consumer descriptor for the quality of the scarves and shawls.

**Table 2.** List of 46 high-quality terms/statements for textiles that were generated from the focus groups.

| High-Quality Statements for Textiles Generated during the Focus Groups |
|---|
| Evenness of stitching |
| Overall attention to detail in workmanship |
| Smaller size (narrow and shorter) for silky fabric and larger (blanket) size for a thicker fabric |
| Reversibility of fabric (front and back match/similar) |
| Nicely finished edge of the fabric |
| Lastingness/durability of the fabric |
| Finished look |
| Evenness and similar style of stitching all the way round |
| Evenly dyed |
| No raveling |
| High colorfastness |
| Proper/well-matched prints |
| Ease of use (not having to apply extras such as starch after many washings) |
| Not itchy |
| Finished edges |
| Tear-resistant design (e.g., tassels should be formed together properly not just bunched, especially when using thinner threads, not doing too much embroidery to the point the base fabric cannot handle it) |
| Weave needs to be consistent |
| Natural fabrics: they breathe, they drape nicely, (silk, rayon, cotton) |
| Soft, and flows and drapes nicely |
| No fraying on edges and unraveling |
| Light and lace-like embroidery |

**Table 2.** *Cont.*

| High-Quality Statements for Textiles Generated during the Focus Groups |
|---|
| Uniform and consistent embroidery on each side of the fabric |
| The weave of the fabric: smooth with no bumps, silky to touch |
| No aroma/smell |
| Evenness of pattern placement |
| Evenness of edges |
| Color blendedness/balance |
| Intricate work on fringes—not going to come out—lay nicely |
| Uniformity of all edges |
| Evenness of twisting of yarn on the entire fabric |
| Curving of the corners of the hem |
| Evenness of the hem |
| Light-weight thread used for the hem |
| The thread does not pull the fabric too much |
| Hand-stitched roll of hem |
| Finer twist yarn with linen or silk |
| High-density weave |
| The organic and more "natural" fabric |
| Fuzzy—very soft, good hand-feel |
| Does not wrinkle unless it is meant to |
| Finer thread |
| Higher thread count per inch |
| Woven threads are invisible (Satin weave) |
| Fine edge finish of tassels |
| Appropriate tassel placement on fabric |
| Handmade (it is unique) |

The 86 generated statements were reviewed by the authors, and statements that were not directly related to quality, and statements that were ambiguous and/or confusing, were removed, which brought the total list of statements down to 52 statements (Table 4). Some statements were reworded to shorter phrases or words that would be suitable for quantitative consumer testing (but only if the core meaning was maintained).

Items that were considered the same, similar, or opposite to a selected statement and were eliminated.

**Table 3.** A list of 40 low-quality statements for textiles that were generated from the focus groups.

| Low-Quality Statements for Textiles Generated during the Focus-Group Discussions |
|---|
| Synthetic fabrics (e.g., polyester, spandex) |
| Unraveling and fraying of fabric edges |
| The coarseness of weave of the fabric |
| Rough hand-feel |
| Aroma (e.g., dye-like aroma, formaldehyde residue) |
| Springiness of fabric |
| Overdyed/much-too-high dye intensity |
| Scratchy |
| Small/invisible finish of the edge |
| Dye residue in hand |
| Non-finished/incomplete edges |
| Low embroidery-fabric fitting (embroidery does not match the kind of fabric it is placed on) |
| Out of balance of color |
| Too-tight stitching |
| Selvaged edge (curtain-like impression) |
| Waxy hand-feel |
| Non-uniform edges of the fabric |
| An unevenness of twisting of yarn on the entire fabric |

**Table 3.** *Cont.*

| Low-Quality Statements for Textiles Generated during the Focus-Group Discussions |
|---|
| Zigzag hemstitching which makes it roll |
| Heavy-weight thread used for the hem (thread sits on top of the fabric) |
| Coarser yarns (lesser twist) |
| Low colorfastness |
| Plastic-like hand-feel |
| Embellishment too strong for fabric |
| Stretchy-like edges which are wonky |
| Wavy-like and forms wrinkles that are not supposed to be there |
| Lower thread count per inch (fewer threads used for warp and weft) |
| Woven threads are visible |
| Machine stitched |
| Tacky tape on the edge |
| Uneven and unfinished look (Note: younger consumers may consider this high quality as a more organic look) |
| Fabric residue and dirty-like after-feel |
| Crunchy sound/noise |
| Stiff fabric and fabric that pokes out |
| High shrink ability |
| Pilling or formation of small balls of fluff from looser threads on the fabric surface |
| Many ravelings—threads from a woven or knitted fabric that have frayed or started to unravel |
| Low colorfast (ability to keep the same color without fading or running even if washed, placed in harsh light, exposed to perspiration, or treated with certain chemicals) |
| Vibrancy (muddy coloring is a sign of poor quality, not drab or muted but muddy coloring) |
| Too big (should not be a shawl when wanting a scarf) |

Items that were eliminated after consideration as vague, covered by another or combination of statements, or not really relevant to these garments.

Following another review, the authors further removed statements that had similar meaning or interpretation or were opposites (Table 4, items in parentheses), or items that were covered by other combinations of statements or were deemed less relevant for these garments (Table 4). For instance: "Finished edges" was removed because it was an opposite with "Unfinished edges", and "Even stitches" was removed because it had a similar meaning to "Stitching is even and consistent" which was kept. "Scratchy" was removed because it overlapped meaning (similar or opposite) with "smooth", "rough", and "coarse". Finally, terms such as "springy" were eliminated because they were not deemed particularly relevant to the sample of shawls/scarves in the study. The list of 52 statements was reduced to 30 statements (Table 4, *statements), which were included in the quantitative consumer study. The statements represented both positive and negative characteristics.

The final set of 30 statements was checked against the focus-group statements by the authors. They were chosen based on frequency of use, ability to be understood by most or all focus-group participants, and to ensure that they captured the breadth and essence of the statements determined by focus groups.

**Table 4.** Shortlist of 52 initial quality statements and 30 final (*) statements for textiles following first and final review by authors.

| **Overall Attention to Detail *** |
|---|
| Front and back are similar * |
| Fabric is durable * |
| Fringe or tassels look like they will last * |
| Unfinished edges * (Finished edges) |
| Stitching is even and consistent * (Even stitches) |
| Hems are even * |
| Consistent weave * (Evenness of weave of the fabric) |
| Ravels/frays at edges * |
| Evenly dyed * |
| Looks like it would be colorfast * |
| Patterns do not match properly when printed or dyed * (Pattern or print is consistent) |
| Smooth * (Bumpy) |
| Scratchy |
| Rough * |
| Coarse * |
| Soft * |
| Holes/loose threads/raveling in interior * |
| Embroidery too loose or too tight * (Embroidery is smooth and tight) |
| Silky |
| Has an aroma/smell * |
| Fringe or tassels are neat/tidy * |
| Corners are straight or curve correctly * |
| Edges are wavy or crooked * (Fabric edges are consistent) (Even edges) |
| Hand-stitched |
| Handmade (looks to be unique) * |
| Fuzzy |
| No wrinkles except as part of the design * |
| -Embroidery causes the fabric to gather/bunch |
| Waxy/sticky feel * (Sticky feel) |
| Makes a sound * |
| Dye spots * |
| Feels like a natural fabric* (Feels like a synthetic fabric) |
| Drapes well * (Stiff) |
| Springy |
| Fine weave* (Heavy weave) (High-density weave) (Tight Weave) (Fine threads/yearns used for weaving) |
| Thread for hems is thin and does not show |

* Items included in the final questionnaire.

### *3.2. Phase 2—Quantitative Study*

Except for Generation Z participants, many of whom were still in college, approximately 80% of the other consumers had completed college, whereas the remaining had completed high-school education. Although this is not representative of the U.S. population, this more highly educated demographic may be more representative of women who have interest in artisan products and may have, on average, more money to spend on clothing [43]. Data are conflicting on the age groups that are most interested in purchasing artisan products. Some authors [42] have suggested that younger consumers are most interested, while others [43] have found that the older the consumer, the more likely they are to purchase artisan textiles. On, average, consumers in this study held average interest in searching out and purchasing organic and natural products, and on average held moderate to higher interest in purchasing artisan clothing (Table 5).

**Table 5.** LS means for consumers' interest in artisan products and willingness to purchase environmentally friendly products ($n$ = 196; $\alpha$ = 0.05).

| What Year Were You Born? | Rate Your Interest in Clothing Products That Are Partly or Entirely Artisan-Made (i.e., Made or Partly Made by People Skilled in Designing and Making Clothing)? [1] | Please Indicate Your Agreement with the Following Statement. "I Mostly Try to Buy Organic/Natural and Environmentally Friendly Products" [2] |
|---|---|---|
| 1944–1979 | 7.1 [a] | 5.7 [a] |
| 1995–2001 | 7.2 [a] | 5.1 [a] |
| 1980–1994 | 6.9 [a] | 5.7 [a] |
| $p$-value | 0.46 | 0.17 |

[a] Row means within an attribute with a common superscript did not differ ($p > 0.05$). [1] Nine-point scale; 1 = Extremely Disinterested, 5 = Have no opinion, 9 = Extremely Interested. [2] Nine-point scale; 1 = Strongly Disagree, 5 = Undecided, 9 = Strongly Agree.

#### 3.2.1. Discrimination among Textile Samples

Mean scores showed that how consumers rated the 30 quality statements, or how they scored the textiles based on quality, or purchase interest, significantly differed among the samples (Table 6). For example, whereas Sample 1 was rated as a very-good-quality scarf and participants indicated that they would probably purchase the scarf if the price was reasonable, Sample 10 was rated as a poor-quality scarf which they would probably not purchase even if the price was reasonable. Furthermore, based on the 30 quality statements that were investigated, Sample 1 attained significantly higher ratings than Sample 10 for positive statements such as Overall attention to detail, Stitching is even and consistent, Hems are even, Consistent weave, Evenly dyed, Looks like it would be colorfast, Smooth, Soft, Corners are straight or curve correctly, Drapes appropriately, and Fine weave. On the other hand, Sample 10 received higher ratings for negative statements such as Unfinished edges, Ravels or frays at edges, Coarse, has an Aroma or smell, Edges are wavy or crooked, and Waxy or sticky feel.

**Table 6.** LS means for consumers' ratings for quality, purchase interest, and the 30 quality statements for textiles ($\alpha$ = 0.05).

| | Sample | | | | | | | | | | |
|---|---|---|---|---|---|---|---|---|---|---|---|
| | **1** | **2** | **3** | **4** | **5** | **6** | **7** | **8** | **9** | **10** | ***p*-Value** |
| Quality [1] | 4.5 [a] | 3.5 [e] | 3.7 [d] | 4.1 [c] | 4.1 [bc] | 4.3 [b] | 3.4 [e] | 3.0 [f] | 2.8 [g] | 2.4 [h] | <0.0001 |
| Purchase interest [2.] | 3.9 [a] | 2.9 [d] | 3.2 [c] | 3.4 [bc] | 3.2 [c] | 3.5 [b] | 2.7 [d] | 2.1 [e] | 2.1 [e] | 1.8 [f] | <0.0001 |
| Overall attention to detail [3] | 4.4 [a] | 3.2 [c] | 3.3 [c] | 4.2 [b] | 4.4 [a] | 4.2 [ab] | 3.4 [c] | 3.2 [c] | 2.7 [d] | 2.3 [e] | <0.0001 |
| Front and back are similar [3] | 3.5 [e] | 4.1 [cd] | 4.1 [c] | 3.8 [d] | 4.4 [b] | 3.4 [e] | 4.7 [a] | 1.9 [f] | 3.5 [e] | 4.0 [cd] | <0.0001 |
| Fabric is durable [3] | 3.7 [bc] | 3.6 [c] | 2.9 [d] | 4.1 [a] | 3.8 [b] | 3.9 [b] | 2.6 [e] | 2.1 [f] | 2.3 [f] | 2.3 [f] | <0.0001 |
| Fringe or tassels look like they will last [3] | 2.1 [d] | 3.3 [c] | 1.9 [de] | 3.9 [b] | 4.2 [a] | 3.9 [b] | 2.0 [d] | 1.7 [e] | 1.4 [f] | 1.4 [f] | <0.0001 |
| Unfinished edges [3] | 1.1 [h] | 2.4 [c] | 1.4 [g] | 1.7 [ef] | 1.9 [de] | 1.7 [ef] | 1.5 [fg] | 2.1 [d] | 3.6 [b] | 4.5 [a] | <0.0001 |
| Stitching is even and consistent [3] | 4.2 [a] | 3.1 [d] | 3.6 [c] | 4.0 [b] | 4.2 [ab] | 4.0 [ab] | 3.6 [c] | 2.6 [e] | 2.8 [e] | 2.2 [f] | <0.0001 |
| Hems are even [3] | 4.3 [a] | 3.1 [c] | 3.6 [b] | 3.6 [b] | 4.1 [a] | 3.8 [b] | 3.7 [b] | 2.8 [d] | 2.5 [e] | 1.7 [f] | <0.0001 |
| Consistent weave [3] | 4.1 [a] | 3.5 [d] | 3.7 [cd] | 3.9 [bc] | 4.2 [a] | 4.0 [ab] | 3.6 [d] | 3.0 [ef] | 3.2 [e] | 2.9 [f] | <0.0001 |
| Ravels/frays at edges [3] | 1.2 [g] | 2.2 [d] | 1.6 [f] | 2.0 [d] | 1.6 [ef] | 1.8 [e] | 1.7 [ef] | 2.8 [c] | 4.1 [b] | 4.4 [a] | <0.0001 |
| Evenly dyed [3] | 4.30 [a] | 2.8 [e] | 2.9 [e] | 4.0 [bc] | 4.0 [bc] | 3.9 [bc] | 4.1 [ab] | 3.8 [c] | 3.3 [d] | 2.8 [e] | <0.0001 |
| Looks like it would be colorfast [3] | 3.3 [a] | 2.8 [b] | 2.9 [b] | 3.3 [a] | 3.4 [a] | 3.2 [a] | 2.9 [b] | 2.7 [bc] | 2.6 [c] | 2.6 [c] | <0.0001 |
| Patterns do not match properly when printed or dyed [3] | 1.3 [gh] | 2.3 [a] | 1.9 [bc] | 1.3 [fgh] | 1.2 [h] | 1.6 [de] | 1.4 [efg] | 1.5 [ef] | 1.8 [cd] | 2.0 [b] | <0.0001 |
| Smooth [3] | 4.8 [a] | 3.3 [c] | 4.6 [b] | 2.4 [fg] | 3.1 [d] | 2.8 [e] | 2.4 [fg] | 2.2 [g] | 2.5 [f] | 2.4 [fg] | <0.0001 |
| Rough [3] | 1.1 [f] | 2.2 [e] | 1.2 [f] | 3.0 [ab] | 2.8 [b] | 2.3 [de] | 2.5 [cd] | 2.6 [c] | 3.1 [a] | 3.0 [ab] | <0.0001 |
| Coarse [3] | 1.2 [d] | 2.3 [c] | 1.2 [d] | 3.0 [a] | 3.0 [a] | 2.3 [bc] | 2.4 [bc] | 2.5 [b] | 3.2 [a] | 3.0 [a] | <0.0001 |
| Soft [3] | 4.7 [a] | 2.8 [d] | 4.5 [b] | 2.2 [ef] | 2.2 [e] | 3.0 [c] | 2.7 [d] | 2.7 [d] | 2.0 [f] | 2.1 [ef] | <0.0001 |

**Table 6.** *Cont.*

| | Sample | | | | | | | | | | |
|---|---|---|---|---|---|---|---|---|---|---|---|
| Holes/loose threads/raveling in interior [3] | 1.3 $^{f}$ | 1.7 $^{de}$ | 2.0 $^{c}$ | 1.5 $^{e}$ | 1.5 $^{e}$ | 1.6 $^{e}$ | 1.8 $^{cd}$ | 3.9 $^{a}$ | 2.9 $^{b}$ | 2.8 $^{b}$ | <0.0001 |
| Embroidery too loose or too tight [3] | 1.2 $^{d}$ | 1.4 $^{c}$ | 1.4 $^{c}$ | 1.6 $^{c}$ | 1.5 $^{c}$ | 1.6 $^{c}$ | 1.5 $^{c}$ | 3.2 $^{a}$ | 2.1 $^{b}$ | 2.0 $^{b}$ | <0.0001 |
| Has an aroma/smell [3] | 1.5 $^{f}$ | 1.9 $^{cd}$ | 1.6 $^{ef}$ | 1.8 $^{cde}$ | 1.7 $^{def}$ | 2.1 $^{a}$ | 1.9 $^{bc}$ | 2.1 $^{ab}$ | 2.1 $^{ab}$ | 2.3 $^{a}$ | <0.0001 |
| Fringe or tassels are neat/tidy [3] | 2.2 $^{d}$ | 3.6 $^{c}$ | 2.0 $^{d}$ | 4.0 $^{b}$ | 4.5 $^{a}$ | 4.1 $^{b}$ | 2.1 $^{d}$ | 1.7 $^{e}$ | 1.6 $^{ef}$ | 1.3 $^{f}$ | <0.0001 |
| Corners are straight or curve correctly [3] | 4.3 $^{a}$ | 3.6 $^{c}$ | 3.9 $^{b}$ | 3.9 $^{b}$ | 4.1 $^{ab}$ | 4.0 $^{b}$ | 3.6 $^{c}$ | 2.9 $^{d}$ | 2.7 $^{d}$ | 1.8 $^{e}$ | <0.0001 |
| Edges are wavy or crooked [3] | 1.7 $^{f}$ | 2.6 $^{d}$ | 2.1 $^{e}$ | 2.2 $^{e}$ | 2.0 $^{e}$ | 1.6 $^{f}$ | 3.1 $^{c}$ | 3.5 $^{b}$ | 3.0 $^{c}$ | 3.9 $^{a}$ | <0.0001 |
| Handmade [3] | 2.4 $^{d}$ | 3.2 $^{b}$ | 2.9 $^{c}$ | 3.8 $^{a}$ | 2.6 $^{d}$ | 3.1 $^{bc}$ | 2.6 $^{d}$ | 3.2 $^{b}$ | 3.1 $^{bc}$ | 3.0 $^{bc}$ | <0.0001 |
| No wrinkles except as part of design [3] | 3.1 $^{d}$ | 3.7 $^{bc}$ | 3.5 $^{c}$ | 3.5 $^{c}$ | 4.2 $^{a}$ | 4.1 $^{a}$ | 3.9 $^{ab}$ | 3.0 $^{d}$ | 2.7 $^{e}$ | 3.0 $^{de}$ | <0.0001 |
| Waxy or sticky feel [3] | 1.2 $^{b}$ | 1.4 $^{b}$ | 1.3 $^{b}$ | 1.2 $^{b}$ | 1.7 $^{a}$ | 1.3 $^{b}$ | 1.7 $^{a}$ | 1.3 $^{b}$ | 1.7 $^{a}$ | 1.8 $^{a}$ | <0.0001 |
| Makes a sound [3] | 1.5 $^{d}$ | 1.8 $^{c}$ | 1.5 $^{d}$ | 1.9 $^{c}$ | 2.8 $^{a}$ | 1.5 $^{d}$ | 2.4 $^{b}$ | 1.5 $^{d}$ | 2.2 $^{b}$ | 2.0 $^{c}$ | <0.0001 |
| Dye spots [3] | 1.2 $^{f}$ | 3.5 $^{a}$ | 3.1 $^{b}$ | 1.2 $^{f}$ | 1.2 $^{f}$ | 1.6 $^{e}$ | 1.6 $^{e}$ | 1.2 $^{f}$ | 2.3 $^{d}$ | 2.9 $^{c}$ | <0.0001 |
| Feels like natural fabric [3] | 3.3 $^{cd}$ | 3.5 $^{bc}$ | 3.1 $^{de}$ | 3.9 $^{a}$ | 2.7 $^{f}$ | 3.7 $^{ab}$ | 2.4 $^{g}$ | 2.5 $^{fg}$ | 2.9 $^{e}$ | 3.0 $^{e}$ | <0.0001 |
| Drapes appropriately [3] | 4.4 $^{a}$ | 3.8 $^{c}$ | 4.2 $^{b}$ | 3.6 $^{d}$ | 3.6 $^{d}$ | 4.1 $^{b}$ | 3.7 $^{cd}$ | 3.6 $^{d}$ | 3.3 $^{e}$ | 3.1 $^{e}$ | <0.0001 |
| Fine weave [3] | 4.0 $^{a}$ | 3.4 $^{b}$ | 3.5 $^{b}$ | 3.5 $^{b}$ | 4.0 $^{a}$ | 3.5 $^{b}$ | 3.4 $^{b}$ | 3.0 $^{c}$ | 3.0 $^{c}$ | 2.9 $^{c}$ | <0.0001 |

$^{a,b,c,d,e,f,g,h}$ Row means within an attribute/column with no common superscripts differ ($p \leq 0.05$). [1] Five-point scale; 1 = Very Poor quality, 3 = Fair quality, 5 = Excellent quality. [2] Five-point scale; 1 = Definitely would not purchase, 3 = Possibly would purchase, 5 = Definitely would purchase. [3] Seven–point scale; 1 = Strongly Disagree, 4 = Neither Agree/Disagree, 7 = Strongly Agree.

#### 3.2.2. Internal Consistency of Quality Statements

Computation of coefficient alpha for all 30 statements had a raw alpha of 0.53 and further analysis of the data showed that 13 statements showed inconsistency/unreliability among consumers for measurement of quality. Those statements were: Unfinished edges, Ravels or frays at edges, Patterns do not match when printed or dyed, Rough, Coarse, Soft, Holes loose threads raveling in the interior, Embroidery too loose or too tight, Has an aroma/smell, Edges are wavy or crooked, Waxy or sticky feel, Makes a sound, and Dye spots. That suggests that some consumers (a) were more sensitive to certain characteristics (e.g., smell), (b) varied considerably in how important certain characteristics were (e.g., unfinished edges or raveling), or (c) may not have noticed some characteristics based on their handling of the scarves/shawls (e.g., holes or dye spots). That finding suggests that additional analysis with fewer statements would be beneficial. Such analysis is performed in development of questionnaires for measuring such things as science literacy [44].

After removing the 13 inconsistent statements, the remaining 17 statements showed a Cronbach's alpha of coefficient of 0.86, a reasonably high reliability, but further analysis showed that eight additional statements were potentially inconsistent. Those eight statements were: Front and back are similar, Evenly dyed, Looks like it would be colorfast, Smooth, Handmade, No wrinkles except as part of the design, Feels like natural fabric, and Drapes appropriately. Those statements were ones that may differ based on their perception of "Quality" in artisan textiles. For example, in the focus groups conducted for this study, some consumers expected small variations in artisan products such as uneven dyeing or wrinkles, while others thought of those as "flaws". Some consumers noted that it was difficult to determine if a fabric felt like natural fabric, and, in fact, stated that natural fabrics vary so much (cotton is different from wool is different from silk) that such terminology could not be assessed by feeling the fabric.

Thus, a third analysis was conducted with only the nine remaining statements and the Cronbach's alpha coefficient increased slightly to 0.87, a relatively high number, suggesting that the statements were addressing the quality issue. One additional statement, "fine weave", was noted as being inconsistent in this third round so an analysis was conducted after removing that statement. Those results showed an alpha coefficient of 0.87, consistent with the higher number of statements and no statements that were found to be inconsistent in judging quality among the consumers. Alpha remained 0.87 (Table 7).

**Table 7.** Reliability of quality statements remaining in the scale (overall coefficient $\alpha = 0.87$).

| Quality Statement | Coefficient Raw Alpha |
|---|---|
| Overall attention to detail | 0.85 |
| Fabric is durable | 0.86 |
| Fringe or tassels look like they will last | 0.86 |
| Stitching is even and consistent | 0.85 |
| Hems are even | 0.86 |
| Consistent weave | 0.86 |
| Fringe or tassels are neat or tidy | 0.85 |
| Corners are straight or curve correctly | 0.86 |

The eight statements that constituted the textile-quality scale included the statements Overall attention to detail, Fabric is durable, Fringe or tassels look like they will last, Stitching is even and consistent, Hems are even, Consistent weave, Fringe or tassels are neat or tidy, and Corners are straight or curve correctly. This approach of assessing the reliability of the textile-quality scale using coefficient alpha has been used previously by multiple authors [45–47].

#### 3.2.3. Textile-Quality Scale (TQI)

Table 8 shows data for the TQI with eight and six statements. It is clear from the data that the TQI differentiated quite well among the various textiles. The TQ with eight statements was slightly more differentiating among these samples but shows the problem of using the eight statements when some of them do not apply. Sample 1, which did not have fringe or tassels, is the highest-scoring product for the TQI based on six statements, but compares less well to other products when using the TQI with eight statements. Low scores for the statement related to fringe, which obviously did not apply to five of the samples, resulted in a reordering of the samples based on TQI for eight and six statements. However, regardless of which index was used, both differentiated low-quality textiles, those with poor attention to detail, poor-quality seams, poor stitching, inconsistent weave, etc.

**Table 8.** The least-squares means for textile-quality indices (TQI) for the 10 textile samples ($\alpha = 0.05$).

| | TQI8 [1] | TQI6 [2] |
|---|---|---|
| Sample 1 | 29.3 $^{c}$ | 25.0 $^{a}$ |
| Sample 2 | 27.1 $^{d}$ | 20.2 $^{d}$ |
| Sample 3 | 24.8 $^{e}$ | 20.9 $^{d}$ |
| Sample 4 | 31.5 $^{b}$ | 23.7 $^{c}$ |
| Sample 5 | 33.5 $^{a}$ | 24.8 $^{ab}$ |
| Sample 6 | 32.0 $^{b}$ | 24.0 $^{bc}$ |
| Sample 7 | 24.5 $^{e}$ | 20.4 $^{d}$ |
| Sample 8 | 20.2 $^{f}$ | 16.7 $^{e}$ |
| Sample 9 | 19.2 $^{f}$ | 16.9 $^{e}$ |
| Sample 10 | 15.8 $^{g}$ | 13.1 $^{f}$ |

TQI8 [1] = Textile-quality index generated by summing the scores for all the eight terms that were identified by Cronbach's alpha (range 8–40). TQI6 [2] = Textile-quality index generated by summing the scores for six terms (i.e., eight terms minus "fringe or tassels look like they will last" and "fringe or tassels are neat or tidy" quality terms) that were identified by Cronbach's alpha (range 6–30). $^{a,b,c,d,e,f,g}$ Means within a column with one or more matching letters are not significantly ($p \leq 0.05$) different.

#### 3.2.4. Internal Validation of the Textile-Quality Scale

The Pearson correlation coefficient (all participants as a whole sample) for the score for Overall Quality and the TQI based on eight statements was 0.69, a good correlation. Note that all correlations reported were significant, but the size of the correlation is most important. When the Overall Quality scores and TQI were correlated for each individual participant, only 16%, or 31/196 consumers, had R values < 0.55, suggesting that the TQI for each individual consumer was reasonably representative of their overall quality score.

However, half of the ten samples tested in this study did not have any fringes or tassels. Thus, a TQI based on all eight statements included contributions for the "fringe or tassels look like they will last" and "fringe or tassels are neat or tidy" quality statements. This definitely affected scores for products without a fringe or tassels because consumers give a score for the statement that is not meaningful to the product, which can create confusion for the consumers and potential error in the TQI. Using only six quality statements (removing those related to fringe/tassels) to calculate the TQI provided a correlation for the overall data of 0.71, a slight increase from the eight-statement TQI. Of particular note, however, is that only 10%, or 20 of the 196 consumer participants, had R values <0.55 for their individual TQIs. This suggests an overall improvement, and improvement when considering the percentage of consumers for whom the TQI gave a reasonable representation of the Overall Quality score.

The TQI is not needed when consumers can measure quality directly, but that frequently is not the case for artisans, producers, or sellers who must decide whether their textiles are of high quality using more specific criteria. The use of a TQI composed of various statements of the properties of the textiles allows individuals to learn what consumers believe in terms of textile product quality.

## 4. Discussion

Durability, and factors that can affect durability such as attention to detail, were found to be important in this study of artisan textiles. Consumers continue to check for comfort and durability when buying clothing [14]. Yotsutsuji [48] reported that key quality aspects of textile-consumer complaints in Japan were centered on the durability of textiles. This stems from the inherent features of the raw fiber (e.g., silk, wool, cotton, synthetic fibers) to be resistant to wear and tear, resistant to structural changes (e.g., shrinkage, and skewing of textile), and appearance changes (e.g., aging, discoloration, fuzzing). For example, silk (e.g., Sample 1) a natural fiber, has been characterized by a higher percentage increase in length before breaking (breaking extension) as compared to other fibers such as cotton (another natural fiber, e.g., in Sample 10) and polyester (synthetic fiber) [49]. However, the type of processing received by the textile can influence the quality of the resulting textile or clothing [50]. Mechanical processing of the finished textile by the artisan, such as weaving (e.g., consistent weave), sewing (e.g., seams are even and consistent), and edge treatments (e.g., corners are straight or curve correctly) clearly indicated quality to the consumers in this study.

The softness of fibers remains a complex subject today in the clothing textile industry. For instance, while textile makers and sellers may attribute higher quality to higher intensities of fabric softness, the reverse is true for consumers, who may not be drawn to lavish softness [14]. Thus, it is no wonder that for the current study, softness was found to be an unreliable value for quality assessment of artisan textiles such as shawls and scarves. For example, Sample 5 was perceived as high in quality but low in softness, probably because of the stiffness of the weave structure. Furthermore, softness is a difficult attribute to describe because it often is a "lack of" a physical characteristic that provides a soft sensory property. That is, softness often, but not always, results from a lack of stiffness, a lack of roughness, a lack of compression resistance, rather than the presence of a certain attribute.

A study by Ezazshahabi et al. [28] indicated that textiles that had consistent weaves and whose stitching was even and consistent were smoother and thus of higher quality (e.g., Sample 1 in this current study) as compared to textiles with inconsistent weaves and uneven stitching which had a rougher hand-feel (e.g., Samples 9 and 10 in the current study).

Today, evenness of yarns remains a key basis for determining textile quality as consumers continue to find textiles whose stitching is even and consistent more appealing [51]. Although unevenness of yarns to a considerable extent is expected when working with natural fibers such as cotton, Barbu et al. [26] noted that the degree of unevenness can be significantly increased depending on processing. The structural aspects of the textile

clearly influence the quality of the clothing as much as the fiber. That is evident in the current study where Samples 1, 4, 5, and 6 all scored highly for durability and quality even though they were made with different yarns (silk, wool, cotton) and weave structures. In contrast samples 8, 9, and 10 also were cotton, silk, or a cotton and polyester blend, but appeared less durable to consumers and had other issues associated with lower-quality textiles. Sukran [52] found that the type of stitching that is applied to a fabric (e.g., seams or hems) has a significant contribution to the fabric's level of bending rigidity. The level of bending rigidity of the textiles in turn affects their appearance, wrinkle resistance, crease resistance, and draping ability [53]. This lower level of bending rigidity due to type of stitching was illustrated by higher consumer ratings for related statements such as Hems are even, Drapes appropriately, No wrinkles except as part of the design, and Corners are straight or curve correctly for Samples such as 1 and 5 in the current study.

Yarns that are even and which are made from fine fibers produce textiles that are soft and drape appropriately (e.g., yarns used to make Sample 1). Additionally, such artisan textiles usually have even and consistent stitching and are likely to have a consistent weave [54]. The level of importance that textile consumers accord quality statements can vary depending on the function and intended purpose of the particular textile clothing. For instance, in hospitals, the key quality characteristics for knitted surgical gowns and face masks could be their durability and breathability, while for airbags used in cars, the key quality statements could include elongation of yarns used to weave the fabric [29]. Ziegenfus [29] noted also that artisan textiles that can endure abrasion without pilling are considered to be durable and are perceived to have higher quality compared to textiles that form lint balls and lose fibers easily due to wear.

Garside [55] identified hydrolysis, light damage, and oxidation as the main sources of fiber and fabric degradation in textiles. Benkirane et al. [34] stated that durability does not just cover the physical endurance of abrasion and colorfastness, but rather also the emotional durability that a consumer associates with the textile. When purchasing textile clothing, consumers usually think about what the color of the textile would be when washed, dry cleaned, ironed, or when exposed to water or light, as all these are known to affect the color of textile [48]. This would thus partly explain the significantly higher respondent rating for quality and purchase interest for Sample 1 which was associated with being durable and more likely to be colorfast as compared to other scarves or shawls such as Sample 10 and Sample 9.

However, Saville [54] stated that the degree of colorfastness of textile clothing is influenced by various aspects including factors related to the process of dyeing such as the type of dye that was used, the specific color that was used and the color strength (percentage of shade) that was applied to the textile. One study that examined the colorfastness of natural dyes made from eastern red cedar sawdust, Kansas black walnut, and Osage orange on wool yarns that were mordanted with potassium aluminum sulfate, and non-mordanted wool yarns showed that pre-mordanted (with potassium aluminum sulfate) wool yarns had higher absorptions for the Kansas black walnut and eastern red cedar sawdust dyes. This indicated that an increase in depth of shade for the yellow color consequently increased colorfastness to light for pre-mordanted wool yarns as compared to wool yarns that were not mordanted [30]. In the same study, colorfastness to laundering increased only for the Osage orange wool yarns that were pre-mordanted. Their findings highlighted the fact that the loss of color of textiles can be ascribed to several aspects (e.g., water, light, rubbing, domestic laundering, and hot pressing). For the current study, it is thus likely that when consumers were asked to rate the samples based on the degree of colorfastness, they might have interpreted the question differently based on their past personal experiences with colorfastness [34]. The ambiguous nature of the colorfastness question had a significant effect on the internal consistency (reliability) of the textile-quality scale, which explains why the statement was dropped.

It would be expected that textiles whose fringes or tassels are neat or tidy and those that look like they will last (Sample 5) would be perceived by consumers to be of higher

quality as compared to similar textiles (Sample 9) whose fringes or tassels are neither neat nor tidy and do not look like they will last. However, at the time of this writing, available literature on the quality of textiles based on fringes or tassels is limited. The findings of one study [32] indicated that dyes and materials could impact the quality of tassels of a textile. For example, a combination of ultra-performance liquid chromatography and time-of-flight spectrometry revealed that tassels (all made from silk fabric) that were directly dyed (no mordant added) with cork tree were more resistant to fading or bleeding due to light as compared to similar, yellow-colored tassels that were directly dyed with cheaper-cost turmeric and had a lesser degree of lightfastness.

Liu et al. [56,57] reported that textiles that were scent infused (with lavender) could be more appealing to potential consumers. Although not related to consumer liking, the current findings show that consumer textile scores for quality could be influenced by the smell or aroma the textile possesses. In many cases for the textiles used in this study, any odor present was quite low and was not noticeable to some focus-group participants. This made the textile smell statement inconsistent in assessing the quality of the scarves and is the reason the statement was dropped during Cronbach's alpha computations.

Respondents rated the quality of scarves and shawls that produced a more pronounced sound when rubbed between fingers as lower in quality than ones that made little or no sound. That could be because consumers believe textiles that produce more-intense sounds wear out easily as compared to those that produce no sounds [58].

Yashi [59] stated that, beyond the primary quality values of textiles (e.g., colorfastness, and durability), secondary quality aspects such as aesthetics and characteristics we measured such as Overall attention to detail and Corners are straight or curve correctly, have a significant contribution to consumers' acceptance and willingness to purchase textiles. This would explain why the quality of samples such as Sample 1 and Sample 5 was rated higher as compared to that of samples such as Sample 9 and Sample 10, which scored significantly lower on Overall attention to detail and Corners are straight or curve correctly. According to Webster [13] and Engel [6], the growing fashion trend that favors fast delivery and quantity over quality where certain aspects of the textile production process such as fabric material sourcing, custom dye applications, and quality control (attention to detail) could explain the poor quality of artisan textiles. Based on this, it is likely that the production of samples such as Sample 9 and Sample 10, which were dyed using a batik technique, was done hurriedly, by lesser skilled artisans, and at a lower cost as compared to other scarves or shawls in this study.

Clearly, it is evident that the eight statements identified by Cronbach's alpha were consistent in measuring the quality of artisan textiles. However, in practice, use of the eight-statement quality scale could be limited to assessment of quality of textiles that have fringes or tassels. Conversely, the six-statement quality scale can be used more universally by producers of artisan textiles (whether they have fringes or tassels or not) to develop products in similar categories that have a higher success rate in the US market. It is important to note that the process of development of the six-statement quality scale can be adopted and used to develop related quality scales for other types of textiles and clothing and in different countries and regions.

Alternatively, the implications of this six-statement quality scale could be compared with those of previously developed consumer-based scales for assessing textile products. Unfortunately, at the time of this writing, comparable literature on similar quality scales was non-existent. For example, Renata [60] stated that characteristics such as durability, comfort [61], and function mattered most to consumers when they were asked about quality of clothing and house textiles. However, because no inquiry/analysis was performed into how those characteristics (as a group) assessed quality of textiles, those results cannot be comparable to the current findings.

## 5. Limitations

As each scarf/shawl was a single artisan piece, the reuse of pieces throughout the testing may have changed some aspects of the garment. For example, one sample received a small tear that had to be gently repaired in one of the last sessions. However, in most cases the original and ending quality of the textile appeared to be similar. For future consumer studies on textiles, researchers could ensure that two or three identical versions of each textile sample are available so that in case one is damaged during evaluation, it can be swapped out with another. However, artisan products often are unique production items that are not reproduced as with industrial production, which could make sampling difficult if multiple identical items are needed.

In addition, this study was limited to scarves and shawls, which do not represent the range of artisan or larger-scale production textiles that are available. However, the statements found in this study could apply to many other types of products and statements that were specific to a more limited scope of products (i.e., those with fringes) were removed from the final quality index without losing any benefit of the scale. Additionally, certain statements could be added to the index when needed for certain types of products. Furthermore, it would be quite informative to compare the current results with those collected similarly for other textile products. However, at the time of this writing, prior literature on processes used to study quality of artisan textile products from the consumer's point of view was lacking. Therefore, this provided a limited degree for comparison of the current results with related earlier studies. This highlights the need for more research on what quality parameters consumers use when choosing different textile products.

Another limitation of this study was the fact that these data were collected from textile consumers in the Midwest region of the USA. Obviously, this sample of study participants may not be representative of the entire country. However, we believe this study, and in particular the process discussed here, could be a source of insight for future related investigations in other locations.

## 6. Conclusions

A list of statements that consumer textile experts found to be important in artisan textiles (in this case scarves/shawls) was determined with 30 of those statements being used to help develop a six-statement textile-quality scale. Those 30 statements, with a focus on the six-statement TQI scale established in this study, can serve as critical guidelines for artisans or process owners in the US textile industry. These specific textile construction and finishing issues should be a focus when training artisans or quality-control technicians of finished artisan textiles. In addition, these statements can be used to explain the importance of every step in the process for people who are responsible for spinning fibers; weaving, knitting, or bonding yarns and threads into textiles; dyeing; sewing; and finishing textiles and fabrics.

Ensuring that textiles, especially artisan textiles, meet all the specifications of the quality scale would improve the product(s) positioning among the targeted textile consumers (higher market success). That can boost textile makers' revenues, especially those of artisans who depend on producing a smaller number of goods and must show consistently high quality. Finally, the process of development of this six-statement quality scale can be applied to other goods in other countries and regions to establish custom quality scales for different types of textiles and clothing.

**Author Contributions:** Conceptualization, D.H.C., E.C.IV; methodology, D.R.S., E.C.V.; software, D.R.S., E.C.IV; validation, D.R.S.; formal analysis, D.R.S.; investigation, D.R.S., E.C.IV, D.H.C., E.C.V.; resources, D.H.C.; data curation, D.R.S., E.C.IV, E.C.V.; writing—original draft preparation, D.R.S.; writing—review and editing, E.C.IV, D.H.C.; visualization, D.R.S.; supervision, E.C.IV, D.H.C.; project administration, E.C.IV; funding acquisition, D.H.C., E.C.IV. All authors have read and agreed to the published version of the manuscript.

**Funding:** This research was supported, in part, by the National Institute of Food and Agriculture, US Department of Agriculture, Hatch, under accession number 1016242.

**Institutional Review Board Statement:** The study was conducted according to the guidelines of the Declaration of Helsinki, and approved by the Institutional Review Board (or Ethics Committee) of Kansas State University with protocol #5930.2.

**Informed Consent Statement:** A notice of informed consent was provided to all participants involved in the study.

**Data Availability Statement:** The data presented in this study are available within the manuscript.

**Acknowledgments:** The authors appreciate the various textile experts and consumers who took time to participate in the various aspects of the study, especially members of the Prairie Star Quilt Guild, Manhattan, KS (USA) who helped make this project a success.

**Conflicts of Interest:** The authors declare no conflict of interest.

## References

1. van Voss, L.H.; Hiemstra-Kuperus, E.; van Nederveen Meerkerk, E. *The Ashgate Companion to the History of Textile Workers, 1650–2000*; Routledge: London, UK, 2010.
2. Jenkins, C. Southern Women Mill Workers: How Poor Southern Women's Lives Were Changed by Employment in the Textile Industry. Ph.D. Thesis, Southern New Hampshire University, Spartanburg, SC, USA, 2020.
3. Oshewolo, R.M. Reconsidering the Owe Woven Cloth of Nigeria from a Gendered Perspective. *J. Pan Afr. Stud.* **2018**, *12*, 110–121.
4. Gowrley, F. The Sister Arts: Textile Crafts between Paint, Print and Practice. *J. Eighteenth-Century Stud.* **2020**, *43*, 139–159. [CrossRef]
5. Vandewiele, C. "Picb'il": Digital Repatriation and Textile Production as Cultural Revival in the Alta Verapaz of Guatemala. Ph.D. Thesis, University of Cambridge, Cambridge, UK, 2019.
6. Engel-Enright, C. Consumer Product Preferences of Cultural Textile Products: Co-Design with Textile Artisans from Guatemala and Peru. Ph.D. Thesis, Colorado State University, Fort Collins, Co, USA, 2016.
7. Ashby, K.A. The Impact of the Changing Weaving Industry on the Culture and Socioeconomic Development of Maya Women in Guatemala. Ph.D. Thesis, Florida International University, Miami, FL, USA, 1994.
8. Cantin, É. Modes of Production, Rules for Reproduction and Gender: The Fabrication of China's Textile Manufacturing Workforce since the Late Empire. *Third World Q.* **2009**, *30*, 453–468. [CrossRef]
9. Xiaohui, L. Gender Equality in China's Overseas Investment: Case Studies on Chinese Textile and Apparel Enterprises in Vietnam, Myanmar, and Bangladesh. *Front. Law China* **2019**, *2019*, 478–499. [CrossRef]
10. Wendt, I.C. Four Centuries of Decline? Understanding the Changing Structure of the South Indian Textile Industry. In *How India Clothed World*; Brill: Leiden, The Netherlands, 2013; Volume 4, pp. 193–215.
11. Svedevall, I. CSR as a Tool to Prevent Gender-Based Discrimination. A Case Study of the Textile Export Industry in India. Master Thesis, UiT The Arctic University of Norway, Tromsø, Norway, 2015.
12. Marketline Global Textile Mills. Available online: https://store.marketline.com/report/ohmf8140--global-textile-mills-5/#tab-table-of-contents (accessed on 5 August 2020).
13. Webster, K. Fusion of Artisan and Virtual: Fashion's New World Opportunities. In *Fashion and Textiles: Breakthroughs in Research and Practice*; IGI Global: Hershey, PA, USA, 2017; pp. 299–325.
14. Li, Y.I.; Wong, A.S.W. Introduction to clothing biosensory engineering. In *Clothing Biosensory Engineering*; Woodhead Publishing: Sawston, UK, 2006; pp. 1–8.
15. Kamalha, E.; Zeng, Y.; Mwasiagi, J.I.; Kyatuheire, S. The Comfort Dimension. *J. Sens. Stud.* **2013**, *28*, 423–444. [CrossRef]
16. Brewster, K.M. A Quantitative Analysis of the Effect of Textile Mill Water Quality Labels on Consumer Purchase Intention for Apparel. Ph.D. Thesis, University of Missouri, Columbia, MO, USA, 2015.
17. Simmons Research Spring 2018 NCS Youth Study. Available online: https://www.mrisimmons.com/2018/10/23/fashionable_kids_clothes/ (accessed on 5 August 2020).
18. Mazzarella, F.; Escobar-Tello, C.; Mitchell, V. Moving Textile Artisans' Communities towards a Sustainable Future—A Theoretical Framework. In Proceedings of the Design Research Society's 50th Anniversary Conference, Future-Focused Thinking (DRS2016), Brighton, UK, 27–30 June 2016. [CrossRef]
19. Littrell, M.A.; Miller, N.J. Marketing Across Cultures. *J. Glob. Mark.* **2001**, *15*, 67–86. [CrossRef]
20. Sender, T. Independent Fashion Retailers Show Flexibility in Adapting to Covid-19 Crisis—29th April 2020. Available online: https://reports.mintel.com/display/1017058/?fromSearch=%3FcontentType%3DInsight%26filters.category%3D124 (accessed on 7 August 2020).
21. Chea, P. Gender Differences in the Fashion Consumption and Store Characteristics in Swedish Clothing Stores. Master's Thesis, University of Borås, Borås, Sweeden, 2011.

22. DeSalva, A. Men's Clothing—US—April. 2018. Available online: https://reports.mintel.com/display/860349/?fromSearch=%3Ffreetext%3Dmen%2520clothing (accessed on 7 August 2020).
23. Koca, E.; Koc, F. A Study of Clothing Purchasing Behavior by Gender with Respect to Fashion and Brand Awareness. *Eur. Sci. J.* **2016**, *12*, 234–248. [CrossRef]
24. DeSalva, A. Women's Clothing—US—August 2019. Available online: https://reports.mintel.com/display/919888/ (accessed on 5 August 2020).
25. Chowdhury, T.A.; Akter, T. Fashion Attributes Preferred by Young Bangladeshi Consumers While Buying Casual Clothes. *J. Fash. Mark. Manag. Int. J.* **2018**, *22*, 540–556. [CrossRef]
26. Barbu, I.; Szabo, M.; Fogorasi, M.S. The High Quality Yarns—the First Condition for Quality Textiles. In *IOP Conference Series: Materials Science and Engineering*; IOP Publishing: Bristol, UK, 2018; Volume 400, p. 62004. [CrossRef]
27. Cheng, S.Y.; Yuen, C.W.M.; Kan, C.W.; Cheuk, K.K.L.; Tang, J.C.O. Systematic Characterization of Cosmetic Textiles. *Text. Res. J.* **2010**, *80*, 524–536. [CrossRef]
28. Ezazshahabi, N.; Tehran, M.; Latifi, M.; Madanipour, K. Surface Roughness Assessment of Woven Fabrics Using Fringe Projection Moiré Techniques. *Fibres Text. East. Eur.* **2015**, *23*, 76–84. [CrossRef]
29. Ziegenfus, T. Maintaining Specialty Textiles Quality. *Text. World* **2005**, *4*, 32.
30. Doty, K.; Haar, S.; Kim, J. Black Walnut, Osage Orange and Eastern Redcedar Sawmill Waste as Natural Dyes: Effect of Aluminum Mordant on Color Parameters. *Fash. Text.* **2016**, *3*, 22. [CrossRef]
31. Paul, R. Functional finishes for textiles: An overview. In *Functional Finishes for Textiles: Improving Comfort, Performance and Protection*; Woodland Publishing: Sawston, UK, 2014; pp. 1–14.
32. Zhang, Y.; Wei, L.; Cui, Z.; Zhang, T.; Lei, Y.; Gu, A.; Chen, Y.; Zhang, L.Y.; Du, Z.X. Characterizations of Palace Lantern Tassels Preserved in The Palace Museum, Beijing, by UPLC-ESI-Q-TOF. *Archaeometry* **2020**, *62*, 660–676. [CrossRef]
33. Salerno-Kochan, R.; Turek, P. Consumer Perception vs Sensory Assessment of the Quality of Clothes of Selected Brands Available on the Polish Market. *J. Fash. Mark. Manag. Int. J.* **2021**, *25*, 682–696. [CrossRef]
34. Benkirane, R.; Thomassey, S.; Koehl, L.; Perwuelz, A. A Consumer-Based Textile Quality Scoring Model Using Multi-Criteria Decision Making. *J. Eng. Fibers Fabr.* **2019**, *14*, 155892501985477. [CrossRef]
35. Kwok, Y.L.; Li, Y.; Wong, B.S.H.; Wu, W.S.S. Perceptual Requirements of Hong Kong Consumers on Children's Denim Wear. *J. Text. Inst.* **1998**, *89*, 96–110. [CrossRef]
36. Hatch, K.L.; Roberts, J.A. Use of Intrinsic and Extrinsic Cues to Assess Textile Product Quality. *J. Consum. Stud. Home Econ.* **1985**, *9*, 341–357. [CrossRef]
37. Earl, S.; Best-Gordon, H.W.; Thomas, H.A. The Control of Textile Quality in Relation to Consumer Requirements. *J. Text. Inst. Proc.* **1957**, *48*, P648–P673. [CrossRef]
38. Valentini, A.C. Consumer Perception on Inkjet Printed Textiles. Ph.D. Thesis, Rochester Institute of Technology, Henrietta, NY, USA, 2012.
39. Adebisi, S.A. Strategic Marketing of Made-in-Nigeria Goods and Consumer's Acceptance in Nigeria. An Empirical Analysis of Textile Products. *Manag. J.* **2011**, *13*, 107–122.
40. Saricam, C.; Aksoy, A.; Kalaoglu, F. Determination of the Priorities of Customer Requirements and Quality in Apparel Retail Industry. *Int. J. Bus. Soc. Sci.* **2012**, *3*, 242–250.
41. Pliner, P.; Hobden, K. Development of a Scale to Measure the Trait of Food Neophobia in Humans. *Appetite* **1992**, *19*, 105–120. [CrossRef]
42. Lusk, J.L.; Briggeman, B.C. Food Values. *Am. J. Agric. Econ.* **2009**, *91*, 184–196. [CrossRef]
43. Troshina, Z. Consumer Value Perception of Artisan Craft Work. Available online: https://www.linkedin.com/pulse/consumer-value-perception-artisan-craft-work-zhanna-troshina-1f/?articleId=6598908810163695618 (accessed on 4 August 2021).
44. Adadan, E.; Savasci, F. An Analysis of 16–17-Year-Old Students' Understanding of Solution Chemistry Concepts Using a Two-Tier Diagnostic Instrumentle. *Int. J. Sci. Educ.* **2011**, *34*, 513–544. [CrossRef]
45. Almehrizi, R.S. Coefficient Alpha and Reliability of Scale Scores. *Appl. Psychol. Meas.* **2013**, *37*, 438–459. [CrossRef]
46. Serbetar, I.; Sedlar, I. Assessing Reliability of a Multi-Dimensional Scale by Coefficient Alpha. *Rev. Za Elem. Izobr.* **2016**, *9*, 189–195.
47. Bi, J. *Sensory Discrimination Tests and Measurements: Sensometrics in Sensory Evaluation*, 2nd ed.; John Wiley & Sons Inc.: Newark, NJ, USA, 2015; ISBN 9781118994856.
48. Yotsutsuji, S. Report of the Practical Lecture on Apparel: Introduction to "Quality Complaints of Textiles"—To Prevent Quality Complaints in Advance. *J. Jpn. Res. Assoc. Text. End-Uses* **2015**, *56*, 56.
49. Luxford, N. 11—Silk Durability and Degradation. In *Understanding and Improving The Durability of Textiles*; Woodland Publishing: Sawston, UK, 2012; pp. 205–232.
50. Delhom, C.D.; Indest, M.O.; Wanjura, J.D.; Armijo, C.B.; Boman, R.K.; Faulkner, W.B.; Holt, G.A.; Pelletier, M.G. Effects of Harvesting and Ginning Practices on Southern High Plains Cotton: Textile Quality. *Text. Res. J.* **2019**, *89*, 4938–4958. [CrossRef]
51. USTER STATISTICS. The Common Language of Textile Quality. *Pak. Text.* **2017**, *66*, 36–38.
52. Sukran, K. Comparison of Sewn Fabric Bonding Rigidities Obtained by Heart Loop Method: Effects of Different Stitch Types and Seam Directions. *Ind. Text.* **2020**, *71*, 105–111. [CrossRef]
53. Ghosh, T.K. Characterization of Fabric Bending Behavior: A Review of Measurement Principles. *Indian J. Fibre Text. Res.* **2003**, *28*, 471–476.

54. Saville, B.P. *Physical Testing of Textiles*; Manchester, E., Ed.; Woodhead Publishing: Cambridge, UK; Boca Raton, FL, USA, 1999.
55. Garside, P. 10—Durability of Historic Textiles. In *Understanding And Improving The Durability Of Textiles*; Woodland Publishing: Sawston, UK, 2012; pp. 184–204.
56. Liu, Y.; Tovia, F.; Balasubramian, K.; Pierce, J.D.; Dugan, J. Scent Infused Textiles to Enhance Consumer Experiences. *J. Ind. Text.* **2008**, *37*, 263–274. [CrossRef]
57. Liu, Y.; Tovia, F.; Pierce, J.D. Consumer Acceptability of Scent-Infused Knitting Scarves Using Functional Melt-Spun PP/PLA Bicomponent Fibers. *Text. Res. J.* **2009**, *79*, 566–573. [CrossRef]
58. Leclinche, F.; Adolphe, D.C.; Drean, E.; Schacher, L.; Zimpfer, V. Modeling of Wear Sound Production Based on Mechanical and Friction Properties of Woven Fabric. *Text. Res. J.* **2018**, *89*, 2511–2521. [CrossRef]
59. Yashi, S.K. Consideration of the Quality of Textiles. *J. Jpn. Res. Assoc. Text. End-Uses* **2017**, *58*, 4–5.
60. Salerno-Kochan, R. Consumer Approach to the Quality and Safety of Textile Products. Part I. Quality of textile products from the Point of View of Consumers. *Fibers Text. East. Eur.* **2008**, *16*, 8–12.
61. ASTM F1154-18. *Standard Practices for Evaluating the Comfort, Fit, Function, and Durability of Protective Ensembles, Ensemble Elements, and Other Components*; ASTM International: West Conshohocken, PA, USA, 2018.

*textiles*

MDPI

*Article*

# Organic Cotton Clothing Purchase Behavior: A Comparative Study of Consumers in the United States and Bangladesh

**Md Nakib Ul Hasan *, Chuanlan Liu and Bulbul Ahmed**

Textiles, Apparel Design and Merchandising, Louisiana State University, Baton Rouge, LA 70803, USA; clliu@lsu.edu (C.L.); bahmed1@lsu.edu (B.A.)
* Correspondence: mhasa27@lsu.edu

**Abstract:** The purpose of this research was to evaluate the differences and similarities of organic cotton clothing (OCC) purchase behaviors of the consumers who lie at the top and the bottom of the apparel supply chain. The influences of consumers' sustainability knowledge and social norms on consumers' attitudes and purchase intentions were examined to understand within the framework of the Theory of Reasoned Action (TRA). Sample data were collected from the United States and Bangladesh and, finally, 136 useable responses were used for the data analysis. Among the useable responses, 85 samples were from the US (containing 91.76% female participants and 4.71% male participants) and 51 responses were from the Bangladesh sample (containing 7.84% female participants and 88.24% male participants). A structural equation model was conducted to test the proposed hypotheses. Findings showed that for US consumers, sustainability knowledge was a powerful predictor of positive attitudes towards OCC, while for Bangladeshi consumers, it was not. In the context of social norms, Bangladeshi consumers demonstrated a strong positive attitudes formation whereas American consumers were found to display less strong relationships. OCC marketers and retailers should concentrate on educating consumers about the real benefits of organic cotton consumption by disseminating proper information about organic cotton fiber and its processing.

**Keywords:** organic cotton; clothing; consumer behavior; Theory of Reasoned Action

**Citation:** Hasan, M.N.U.; Liu, C.; Ahmed, B. Organic Cotton Clothing Purchase Behavior: A Comparative Study of Consumers in the United States and Bangladesh. *Textiles* **2021**, *1*, 376–386. https://doi.org/10.3390/textiles1020019

Academic Editors: Noureddine Abidi and Laurent Dufossé

Received: 2 July 2021
Accepted: 6 September 2021
Published: 13 September 2021



## 1. Introduction

Textiles and clothing industries are developing rapidly to meet the growing demand for short-lived fast fashion. Agriculture-based natural fiber production or laboratory-based synthetic fiber production and final garment manufacturing are damaging the ecosystem by polluting the environment. Cotton, for instance, needs a large quantity of water and pesticides to grow. In terms of pesticide consumption compared to other crops, cotton ranks third in the USA [1] and fourth throughout the world [2]. Furthermore, an estimated 8000 chemicals including dyes, and auxiliaries are required in the manufacturing processes of cotton clothing [3]. Traditional cotton fiber production processes damage the soil, water, and air, thus polluting the environment [4]. Moreover, exposure to various chemicals, pesticides, and insecticides used in these processes can cause serious health complications for farmers, manufacturers, animals, plants, and even consumers [5]. Organic cotton fiber production, in contrast, is based on the use of organic seeds, and chemical-pesticide free farming methods [6]. According to The Soil Association, the production and processing of organic cotton reduces the carbon footprint and protects the environment by maintaining the quality of soil and water [7]. Increased awareness of an environment-friendly lifestyle through sustainable consumption (organic food, organic cotton, reusing, repurposing) is becoming popular presently. A study of 30,000 consumer found that two-third of the participants indicated their interest in consumer environmentally sustainable products despite higher prices [8]. The global market of sustainable apparel is expected to reach USD 95 billion by 2025 from USD 74.65 billion in 2020 [9].

Recent studies on consumer behavior have suggested that growing awareness of environmental pollution encourages consumers to purchase sustainable clothing. According to fashion revolution research on 5000 European Union consumers almost all of them (90%) believed that brands should consider tackling climate change and environmental protection [10]. Environmental sustainability is largely dependent on the use of sustainable materials such as organic cotton, cutting down the usage of resources i.e., land, water, and oil usage, ensuring reuse, recycling, and upcycling of materials. Besides this, the textile industry should focus on, protection of human health, workplace safety, and protection of the environment [11]. Interestingly, as a result of growing consumer concern, the demand for organic cotton cultivation has been increasing significantly. According to an organic cotton market report from the Textile Exchange, organic cotton production in 2018/19 increased by 31% compared to the previous year [12]. Statistically, 418,935 hectares of land were used to produce 239,787 metric tons of organic cotton in 19 countries worldwide. Moreover, 55,833 hectares of conventional cotton growing lands have been converted to accommodate organic cotton production [13]. According to the industry survey of Organic Trade Associations, in the US, organic fiber sales increased by 15% reaching USD 1.8 billion in 2018 compared to the sales of 2017 [14]. Many renowned and emerging brands and retailers have been offering products made of organic cotton such as Conscious by H&M, Boden, Patagonia, Pact, Eileen Fisher, and Able.

The study of sustainable consumer behavior is a growing domain of research all over the world. There are some important reasons behind the emergence of this research. Considering Bangladesh, the second-largest exporter of worldwide apparel, the country is having environmental and social problems. First, the country has been going through significant socio-economic development from rapid industrialization particularly in the textile and apparel sectors. The textile and apparel industry sector is one of the major environmental polluters [15]. In a collaborative approach, Bangladeshi factories, and brands are working to reduce water consumption and initiate cleaner production with the help of the International Finance Corporation. According to the IFC, more than 700 dyeing, finishing, and washing industries have discharged 200,000 L of wastewater during the processing of only one ton of fabric [16]. Besides environmental pollution, the country has gone through some textile industrial disasters due to unauthorized and unregulated industry standards. In 2013, the collapse of the Rana Plaza, the worst industrial disaster, caused the death of more than 1100 workers and over 2500 workers injured as a result of not following proper building safety recommendations [17]. In the aftermath of Rana Plaza collapse, an agreement called the Accord on Fire and Building Safety in Bangladesh was created to improve the working condition for 2.5 million workers in more than 1600 factories [18]. Moreover, brands are pushing manufacturers to comply with regulations of favorable working conditions, ethical practices, fair trade, and corporate social responsibility to produce sustainable apparel. According to the U.S. Green Building Council (USGBC), Bangladesh has the highest number (67, including 13 factories with the highest LEED Platinum rating) of Leadership in Energy and Environmental Design (LEED) certified textile and apparel factories in the world, followed by Indonesia with 40 factories [19]. Bangladesh has reported a 29% increase in the use of organic raw materials from 2017 to 2018 which is the highest global growth rate [20]. According to the Global Organic Textile Standard (GOTS), Bangladesh is second in the world in providing GOTS-certified facilities [21]. Many of the research studies have been focused on the evaluation of sustainable consumption of organic cotton mostly in Western countries while little attention has been focused on countries such as Bangladesh which is at the bottom of the supply chain. There is a significant gap in the literature studying Bangladeshi consumer's organic cotton clothing (OCC) purchase behavior. To date, no known research has been found studying people's buying behavior in this country. Therefore, the research aims to compare the sustainable organic cotton consumption of US and Bangladeshi consumers.

The research objectives were as follows:

1. To understand how consumers' knowledge of environmental sustainability influences attitudes towards OCC purchase behavior and the difference between the US and Bangladeshi consumers.
2. To understand how social norms influence consumers' attitudes towards OCC purchase behavior and the difference between the US and Bangladeshi consumers.

## 2. Organic Cotton Clothing (OCC)

Merriam-Webster defines organic as, "of, relating to, yielding, or involving the use of food produced with the use of feed or fertilizer of plant or animal origin without employment of chemically formulated fertilizers, growth stimulants, antibiotics, or pesticides" [22]. The basic differences between organic and conventional cotton production are based on the way of farming and agricultural management. Organic cotton fibers, on one hand, are grown from unmodified raw plants without harming humans and the environment i.e., preserving soil fertility and protecting biodiversity [23]. Conventional cotton is grown from genetically modified plants with the use of chemical fertilizers, herbicides, pesticides, and defoliants [24]. Due to the use of toxic pesticides and synthetic fertilizers, conventional cotton production is harmful to both humans and the environment [5]. Organic farming involves a rotational system of agriculture that replenishes and maintains soil fertility [25]. The absence of chemicals and pesticides ensures biodiversity [26]. Organic cotton farming provides the following benefits reducing the potential of global warming by 46%, acidification by 70%, soil erosion by 26%, blue water consumption by 91%, and primary energy demand by 62% [27]. Overall, according to The Soil Association, "Switching to organic cotton production could reduce the global warming impact of cotton production overall by 46% compared to non-organic cotton" [7]. OCC production ensures the use of organic cotton, natural dyes-chemicals, and eco-friendly technologies [28]. Throughout its lifecycle, OCC reduces its carbon footprint and hence contributes to environmental sustainability [29].

## 3. Literature Review

Organic food, organic clothing, recycling, upcycling, and an eco-friendly lifestyle are novel concepts throughout the world particularly in the developed and emerging countries. Developed countries have already been pioneering the fair trade movement, and environmental sustainability [30]. Therefore, consumption of eco-friendly products and their impacts on sustainable business, along with consumer behavior has always been an interesting topic of research while very little focus has been given to studying consumer behavior of the less developed countries [31].

Han [32] explored the US and South Korean consumers' green apparel purchase behavior. The research used the Theory of Planned Behavior to test various constructs influencing consumer purchase behavior. Injunctive norms were found to have a significant influence on attitude formation while perceived behavioral control and descriptive norms were found to be the most important forecasters of purchase intentions for both countries. However, there was a notable difference in attitudes as a strong predictor of purchase intention which was significant in US consumers but not significant for South Korean consumers. Social pressure, on the other hand, had a considerable impact on South Korean consumption behavior but was not dominant for US consumers. The differences and similarities of the consumers purchase behaviors are presumably because of the diverse socio-cultural perspectives of both countries [32].

Su, Watchravesringkan [33] investigated the factors influencing US and Chinese Millennials perception and behavioral intentions towards eco-friendly clothing and apparel. Sustainability knowledge and value were the influencing factor of consumers' attitudes and finally attitudes to the willingness to buy green apparel. The research showed that sustainability knowledge of apparel and personal value had a considerable impact on the formation of attitudes towards sustainable apparel consumption and which lead to a strong willingness to buy. Interestingly, US millennials were found to be more knowledgeable

about environmental sustainability and socially responsible consumer behavior whereas their Chinese counterpart had insufficient knowledge of the issues of sustainability and the apparel industry. The research emphasized the importance of incorporating sustainability knowledge in the educational system so more young consumers aware of environmental sustainability.

Khare and Varshneya [31] studied the OCC consumption by Indian youth considering past eco-friendly behavior, peer influence, and knowledge of organic clothing as the key influencers. Research findings show that past environment-friendly behavior plays a significant role during green apparel purchase whereas consumers' knowledge of green apparel and peer influence were not influential in organic clothing purchase behavior. Past environmental value and buying an organic product that represents consumers self-concept [34] were more likely to influence future purchase of similar organic products [31].

## 4. Theoretical Framework

Theory of Reasoned Action (TRA) can be used to explain the reason for certain human behaviors. TRA uses two determinants of intention such as attitudes and subjective norms to understand psychological or cognitive processes of consumer behavior [35]. Consumer's belief affects the attitudes which influences the intention to engage in behavior and eventually impacts actual behavior. An individual develops a positive attitude for the behavior if they believe that performing the behavior will result in a desirable outcome, or vice versa. More favorable attitudes will always result in a strong behavioral intention towards performing the behavior [35,36].

Consumer's belief in environmental awareness and the ethical importance of sustainability forms attitudes towards OCC purchase. Previous studies have evaluated the influence of environmental awareness of the purchase of ethically made products [37,38]. Social norms, awareness of environmental sustainability, and environmental degradation are stated to be intensifying moral obligations to protect the environment [39]. Research studies dedicated to finding the predictors of environmental-friendly products have exhibited the influence of pro-environmental norms, social values, and self-monitoring behavior [40,41]. Environmental awareness and the ethical importance of conserving the environment can comprehensively constitute knowledge of sustainability. Limited knowledge of sustainability is found to be the most difficult obstruction in the development of a sustainable society [42]. Consumer's pro-environmental behavior is formed when a consumer has proper knowledge of environmental sustainability. Consumers knowing environmental sustainability can lead to positive attitudes and a behavioral intention to an eco-friendly product purchase [43–45]. Research has demonstrated that environmentally friendly clothing purchases are positively influenced by a consumer's knowledge of environmental sustainability [31,33]. Thus, we formulate the following Hypothesis H1:

**H1.** *Environmental sustainability knowledge positively influences consumer's attitudes towards OCC purchase.*

Another attribute of the TRA is that subjective norms [36] form attitudes towards and eventually an intention towards a certain behavior. Subjective norms in the form of descriptive and social norms involves real activities and social pressure [46]. Many of the previous studies have found a positive influence of subjective norms during purchasing of green food [46], organic and sustainable food [47], organic skin/hair care products [48], and ethically product fashion products [38,49]. An individual may be influenced by those who are important to the person e.g., family members, friends, colleagues, or influencers [50]. Social norms influence a consumer's engagement with behavior that leads to actual behavior. Social norms are a very important factor that could be affecting a consumer's behavioral intention for organic cotton consumption. Social identification which is exhibited by environment-friendliness, organic, ethical, and socially responsible has been found to influence consumers buying behavior of OCC [51]. Since organic cotton is human and

environment-friendly consumers are expected to form positive attitudes and intentions towards OCC. Thus, we formulate the Hypothesis H2–H4:

**H2.** *Social norms positively influence consumer's attitudes toward OCC.*

**H3.** *Social norms positively influence consumer's behavioral intentions toward OCC purchases.*

**H4.** *Attitudes positively influences consumer's behavioral intentions toward OCC purchases.*

Environmental sustainability is predominantly based on the role of government regulation. Eco-friendly practices are being applied by agencies across a wide spectrum of regulations by implementing processes, procedures, and policies. Common people are divided in their attitudes in terms of environmental issues. Study findings show that sustainable consumption as well as establishment of a sustainable environment are governed by government rules and legislations [52]. To develop sustainable consumption it is important to enhance awareness of the mass populace about ecological biodiversity which can be done by implementing favorable government policy and regulations [52,53].

An individual's training from the surrounding social environment where he/she grew up is defined as culture. Based on the context of culture, consumer behavior changes and it is evident that the consumption patterns also change [54]. The United States has an individualistic culture where people are more interested in individual benefits and preferences, personal success, and independence [32,55] whereas Asian countries such as Bangladesh have a more collective culture, where people focus on in-group/ aggregate benefits, social harmony, and integrity of family [32,56]. The cultural dimension is related to sustainability by the way a culture maintains a link with the past dealing with environmental challenges [57]. Sustainable consumption is connected to the common traditional practice of a society which brings individual consumers feeling about what their actions may contribute to present and future outcomes [58]. In a developing country such as Bangladesh, it is a moral obligation for citizens to not waste food, or clothing. Religion also teaches the importance of morality, be friendly to the environment, and to practice living a frugal life. Citizens of a developed nation such as the USA can live a lavish life with more independence and freedom which may include wasting money, food, clothing, etc. Previous studies have demonstrated that consumer's country of residence and their behavior on sustainability is mediated by sustainability attitudes [58,59]. Hence, presumably, there is an influence of social-cultural perspectives on consumer sustainability knowledge and social norms considering the diverse cross-cultural position of Bangladesh and the USA. Thus, we formulate the following Hypothesis H5:

**H5.** *The salience of the relationship between TRA constructs will be different across consumers from the US and Bangladesh.*

## 5. Methodology

All constructs driven from the theoretical framework were administered in a survey to test the formulated hypotheses. Most of the items were adopted from the previous literature on OCC purchase behaviors. The items and the sources of the items are described in Appendix A (Table A1).

## 6. Questionnaire Design

The research questionnaire was adopted from previous research [32,51]. The questionnaire written in English, contained three sections. The first section provided a general description of the research, the aim of the research, questions on whether the participants have used organic cotton or not, and a short description of organic cotton. In the subsequent section, the participants were requested to indicate their perception, attitudes, and intentions towards the use of OCC. Questions that symbolize the constructs of the conceptual model were measured using a 5-point Likert scale with "1 = strongly disagree, to 5 = strongly agree [60]". The final section consisted of demographic information, gender,

age, level of education, and income level. Participants were advised of their rights to withdraw from the study at any time without any negative consequences.

## 7. Sample

To conduct the research, sample groups from a metropolitan city area of the USA and Bangladesh were selected. Participants of age 18 or over were recruited for the online survey. Convenience sampling was used for data collection. The questionnaire was uploaded in Qualtrics.com, an online data collection website, and then distributed among participants through email by sending the survey link starting from November 2020. Social media platforms such as Facebook, Twitter, and Instagram were also used to invite participants to participate in the survey. Out of 145 responses, a total of 136 (response rate of 93.80%) useable responses were collected and used in the main analysis. Among the useable responses, 85 were from the US sample (91.76% were female; 4.71% were male) and 51 responses from the Bangladesh sample (7.84% were female; 88.24% were male) were analyzed to evaluate the consumer behavioral intention to use OCC (see Table 1). Demographically, a significant proportion (92.94% US and 49.02% Bangladesh) of the participants were in between age 18 to 25 years. A majority (69.41%) of US participants were college students while 54.90% of Bangladeshi participants were college graduates. In terms of household income, 86.27% of Bangladeshi participants earned less than USD 25,000 while 25.88% of American participants were in this income group.

**Table 1.** Demographic information.

| | | **USA ($n_1$ = 85)** | **Bangladesh ($n_2$ = 51)** |
|---|---|---|---|
| Variable | Description | Percentage | Percentage |
| Gender | Female | 91.76% | 7.84% |
| | Male | 4.71% | 88.24% |
| | Other | 3.53% | 3.92% |
| Age | 18 to 25 years | 92.94% | 49.02% |
| | 26 to 35 years | 3.53% | 47.06% |
| | 36 to 45 years | 3.53% | 3.92% |
| Education | Did not graduate high school | - | 1.96% |
| | High school graduate | 17.65% | - |
| | Some college/Associate degree | 69.41% | 13.73% |
| | College graduate | 9.41% | 54.90% |
| | Masters/MBA | 1.18% | 21.57% |
| | PhD or higher | 2.35% | 7.84% |

## 8. Results Analysis

Exploratory factor analysis (EFA) with principal component analysis was first conducted to purify and confirm the scale dimensionality, using a varimax rotation. The factor loading of each item for EFA in both the US and Bangladesh dataset were from 0.501 to 0.836. Then, confirmatory factor analysis (CFA) was conducted to test the measurement model. The result of the measurement model exhibited an acceptable model fit ($\chi^2_{(df = 129)} = 212.295$, $p = 0.000$, $\chi^2/df = 1.646$; RMSEA = 0.088; CFI = 0.915; TLI = 0.9177) [61] in terms of US data. The measurement model for the Bangladesh data exhibited an acceptable model fit ($\chi^2_{(df = 129)} = 297.777$, $p = 0.000$, $\chi^2/df = 2.308$; root mean square error of approximation (RMSEA) = 0.162; comparative fit index (CFI) = 0.664; Tucker-Lewis index (TLI) = 0.602) [61]. For both the US and Bangladesh data, the convergent validity and discriminant validity were assessed to represent the construct validity. All CFA loadings were higher than 0.5, which provided evidence for convergent validity; and the average variance extracted (AVE) for each construct was greater than 0.5 [62], suggesting that each construct is well represented by its own indicators. Finally, the structural equation model (SEM) was then conducted to evaluate the proposed hypotheses

based on the literature review [61]. The statistical results revealed an acceptable model fit ($\chi^2_{(df = 131)}$ = 365.908, $p < 0.000$, $\chi^2/df$ = 2.79; RMSEA = 0.189; CFI = 0.532; TLI = 0.454) for the Bangladesh dataset and an acceptable model fit ($\chi^2_{(df = 131)}$ = 285.75, $p < 0.000$, $\chi^2/df$ = 2.181; RMSEA = 0.119; CFI = 0.842; TLI = 0.815) for the US dataset. The summary of the SEM has shown in Figure 1 and Table 2.

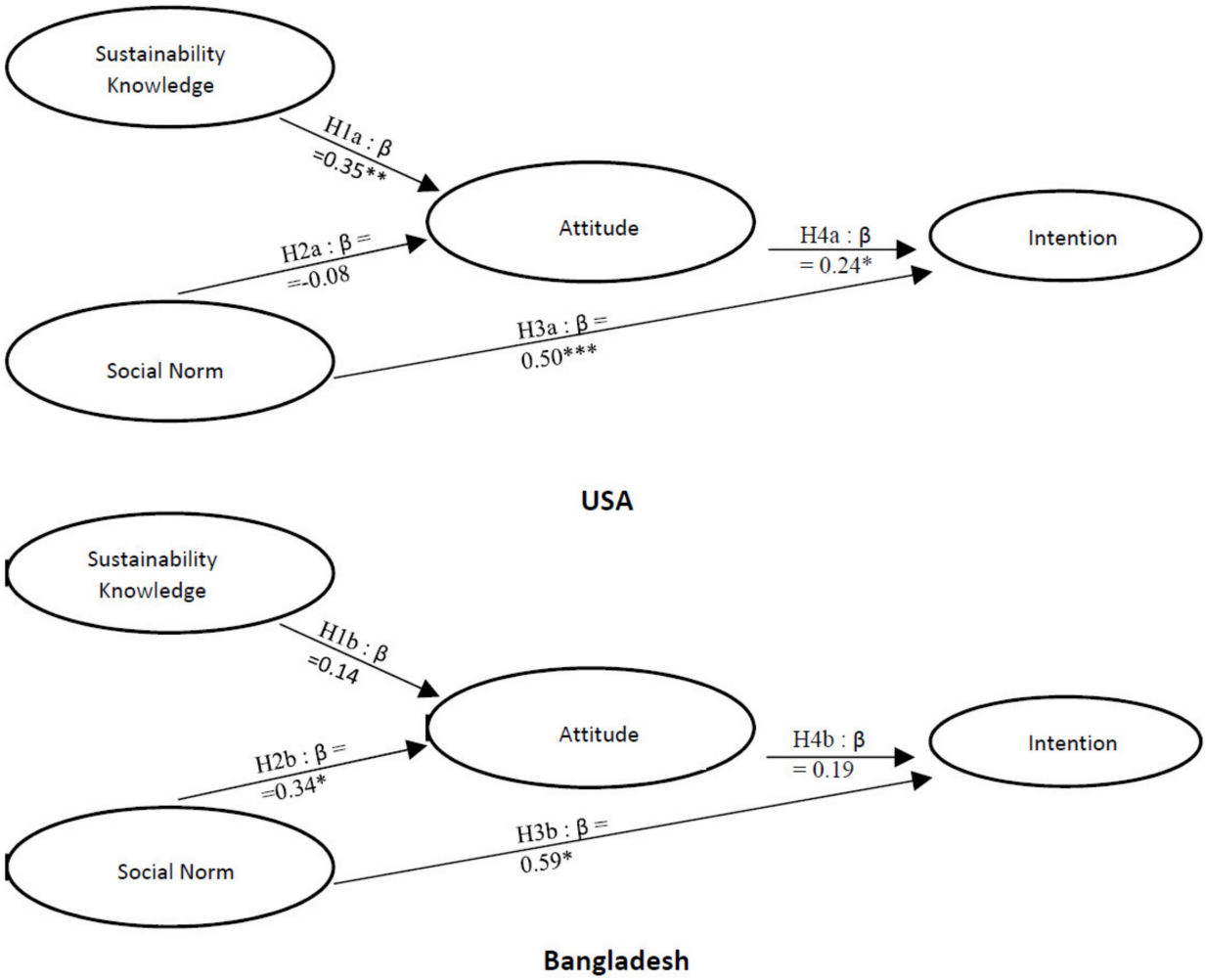


**Figure 1.** Comparison of standardized estimates from SEM analysis. Significance * $p < 0.05$, ** $p < 0.01$, *** $p < 0.001$. Here a represents the USA dataset and b represents the Bangladeshi dataset.

**Table 2.** Path analysis result (USA vs Bangladesh).

| | **USA** | | **Bangladesh** | |
|---|---|---|---|---|
| | **β** | ***p*-Value** | **β** | ***p*-Value** |
| H1: Sustainability Knowledge → Attitudes | 0.35 ** | 0.004 | 0.14 | 0.274 |
| H2: Social Norms → Attitudes | −0.08 | 0.451 | 0.34 * | 0.010 |
| H3: Social Norms → Intention | 0.50 *** | .0001 | 0.59 * | 0.003 |
| H4: Attitudes → Intention | 0.24 * | 0.033 | 0.19 | 0.349 |

Note: * *p*-value < 0.05, ** *p*-value < 0.01, *** *p*-value < 0.001.

## 9. Discussion

The primary focus of this study was to examine the similarities and differences of people from different socio-cultural backgrounds in terms of OCC purchase intentions. A theoretical model based on the Theory of Reasoned Action was constructed to test the formulated hypotheses. This study is the first-ever to study consumer behavioral intention to purchase OCC from the US and Bangladeshi consumers' perspectives.

There are many similarities and differences between the people of the two target groups. First, sustainability knowledge was a strong predictor of consumers' positive attitudes towards OCC in the US data while sustainability knowledge of the Bangladeshi consumers was not found to be a strong predictor of attitudes. This finding is consistent with a previous comparative study in the US and Chinese consumers' purchase behavior of green apparel [33]. This is believed to be due to the existence of consumers' distinct hedonic and utilitarian shopping behaviors based on socio-cultural differences [63,64]. Similarly, Attitudes were found to be an important predictor of US consumers' purchase intention of OCC whereas in terms of Bangladeshi consumers' this relation was not significant. A notable difference between US and Bangladesh consumers was that social pressure influences consumers' positive attitudes formation. Social norms were not found to be a strong predictor in US consumers' positive attitudes formation towards OCC whereas social norms were a very strong predictor for Bangladeshi consumers' positive attitudes formation. This major difference in the consumers' purchase decision is primarily because of the cultural differences influencing consumer behavior and the finding is consistent with a previous study on the US and South Korean consumers [32]. This is presumed to be because Bangladeshi consumers are from a collective culture where they are mostly influenced by other people who are important to them [65,66]. Interestingly, the social norms were a strong predictor of consumer's behavioral intentions to purchase OCC from consumers of both countries. When consumers perceive it is significant to the people purchasing OCC, they are more likely to form a positive intention to purchase. To form a positive attitudes and purchase intention for American consumers, marketers should focus on educating consumers by providing more information about the positive impact of OCC and resulting environmental sustainability. On the other hand, marketers need to put more emphasis on forming positive social viewpoints by endorsing social influencers to market leaders which are assumed to encourage Bangladeshi consumers to form a positive attitudes and purchase intention.

## 10. Limitations and Future Research

This research has been conducted in metropolitan areas in the United States and Bangladesh. Hence, participants of this study may not represent the view of the whole population and the results cannot be generalized. Future research may examine the association between attitudes and purchase intention of consumers from both urban and rural contexts with diverse demographic profiles such as age, education level, and income representing the population properly. Additionally, the research was conducted on small sample groups with unequal gender distribution which is a potential limitation. The research was conducted by describing the differences between organic and conventional cotton fibers. However, analysis of experienced consumers' behavioral intention may provide more valuable insights on OCC usage. Therefore, future research can be conducted on consumers who have used OCC in their daily lives.

**Author Contributions:** Conceptualization, writing—original draft preparation, data analysis, M.N.U.H.; supervision, review and editing, C.L.; writing—original draft preparation, data collection, B.A. All authors have read and agreed to the published version of the manuscript.

**Funding:** This research received no external funding.

**Institutional Review Board Statement:** Not applicable.

**Informed Consent Statement:** Informed consent was obtained from all subjects involved in the study.

**Data Availability Statement:** The data presented in this study are available within the manuscript. Additional data is available upon request from the corresponding author.

**Conflicts of Interest:** The authors declare no conflict of interest.

## Appendix A

**Table A1.** Research item and sources.

| Construct | Items | Source |
|---|---|---|
| Sustainability knowledge | Growing organic cotton does not need hazardous chemical and pesticides.<br>Organic cotton clothing good for human health and environment.<br>I am concerned about the impact of clothing production on the environment.<br>The use of larger quantities of natural fibers will significantly decrease energy consumption.<br>Organic cotton clothing ensure fair trade, and sustainable environmental development. | [51] |
| Social Norms | People who influence my decisions would approve of me buying organic cotton clothing.<br>People who are important in my life would approve of me buying organic cotton clothing.<br>Close friends and family think it is a good idea for me to purchase organic cotton clothing. | [32] |
| Attitudes | For me buying organic cotton clothing would be:<br>Bad/Good<br>Negative/Positive<br>Not favorable/Favorable<br>Unpleasant/Pleasant<br>Undesirable/Desirable<br>A bad idea/A good idea | [32] |
| Purchase Intentions | I would like to purchase organic cotton clothing in the future.<br>If I see organic cotton clothing, I intend to purchase or consider purchasing it.<br>If I see a retail store selling organic cotton clothing, I intend to visit the store to purchase a product. | [32] |

## References

1. U.S. Department of Agriculture. 2019 Agricultural Chemical Use Survey: Cotton. NASS Highlights. No. 2020-3. 2020. Available online: https://www.nass.usda.gov/Surveys/Guide_to_NASS_Surveys/Chemical_Use/2019_Field_Crops/chem-highlights-cotton-2019.pdf (accessed on 28 April 2021).
2. Ferrigno, S.; Guadagnini, R.; Tyrell, K. *Is Cotton Conquering its Chemical Addiction? A Review of Pesticide Use in Global Cotton Production*; Pesticide Action Network UK: Brighton, UK, 2017.
3. Rajan, K.; Sundramurthy, V.P.; Merine, M.K. A Harmless Approach on Textile Effluent Detoxification: Bioremediation and Recent Strategies. In *Strategies and Tools for Pollutant Mitigation*; Aravind, J., Kamaraj, M., Prashanthi Devi, M., Rajakumar, S., Eds.; Springer Nature Switzerland AG: Gewerbestrasse, Switzerland, 2021.
4. Eyupoglu, S. Organic Cotton and Environmental Impacts. In *Organic Cotton*; Springer: Singapore, 2019; pp. 157–176.
5. Kooistra, K.; Termorshuizen, A.J.; Pyburn, R. *The Sustainability of Cotton: Consequences for Man and Environment*; Science Shop Wageningen UR: Wageningen, The Netherlands, 2006.
6. Kumar, P.S.; Yaashikaa, P. Organic Cotton and Its Environmental Impacts. In *Organic Cotton*; Springer: Berlin/Heidelberg, Germany, 2019; pp. 127–139.
7. The Soil Association. Cool Cotton—Cotton and Climate Change. 2015. Available online: https://www.soilassociation.org/media/6491/cool-cotton-organic-cotton-and-climate-change-2015.pdf (accessed on 28 April 2021).
8. Green Generation: Millennials Say Sustainability Is a Shopping Priority. 2015. Available online: https://www.nielsen.com/us/en/insights/article/2015/green-generation-millennials-say-sustainability-is-a-shopping-priority/ (accessed on 15 February 2021).
9. Khare, A.; Kautish, P. Cosmopolitanism, self-identity, online communities and green apparel perception. *Mark. Intell. Plan.* **2021**, *39*, 91–108. [CrossRef]
10. Fashion Revolution. Consumer Survey Report. 2018. Available online: https://www.fashionrevolution.org/resources/consumer-survey/201118_resultsonly_fashrev_consumersurvey_2018/ (accessed on 16 December 2020).
11. Speranskaya, O.; Buonsante, V.A.; Adan, H.; Gorial, M. The Sustainability of Fashion: What Role can Consumers Play? Hej-support. 2020. Available online: https://hej-support.org/the-sustainability-of-fashion-what-role-can-consumers-play/ (accessed on 24 April 2021).
12. Textile Exchange. 2020 Organic Cotton Market Report (OCMR) Released. 2020. Available online: https://textileexchange.org/2020-organic-cotton-market-report-ocmr-released-2/ (accessed on 10 June 2021).
13. Cengiarslan, F. Global Organic Cotton Production Increased by 31%. Textilegence. 2020. Available online: https://www.textilegence.com/en/global-organic-cotton-production-increased/ (accessed on 15 January 2021).

14. Organic Trade Association. Get the Facts about Organic Cotton. 2019. Available online: https://ota.com/advocacy/fiber-and-textiles/get-facts-about-organic-cotton#:~{}:text=HOW%20MUCH%20ORGANIC%20COTTON%20IS,metric%20tons%20(831%2C193%20bales) (accessed on 14 June 2021).
15. Sakamoto, M.; Ahmed, T.; Begum, S.; Huq, H. Water pollution and the textile industry in Bangladesh: Flawed corporate practices or restrictive opportunities? *Sustainability* **2019**, *11*, 1951. [CrossRef]
16. Mehta, A. Apparel brands join forces to clean up their act in Bangladesh. Reuters. 2018. Available online: https://www.reutersevents.com/sustainability/apparel-brands-join-forces-clean-their-act-bangladesh (accessed on 16 December 2020).
17. Star Business Report. 'Justice still Eludes Rana Plaza Victims: CPD'. The Daily Star. 2016. Available online: http://www.thedailystar.net/business/justice-still-eludes-rana-plaza-victims-cpd-1213720 (accessed on 24 April 2021).
18. International Labor Rights Forum. 5 Years after Rana Plaza, What has Changed? 2018. Available online: https://laborrights.org/releases/5-years-after-rana-plaza-what-has-changed (accessed on 13 August 2021).
19. Brooker. The Country with the Most Certified Sustainable Garment Factories is . . . . 2019. Available online: https://www.techstyler.fashion/post/the-country-with-the-most-certified-sustainable-garment-factories-is (accessed on 15 January 2021).
20. Mirdha, R.U. Organic Push Earns Global Praise. The Daily Star. Available online: https://www.thedailystar.net/business/organic-textile-manufacturing-earns-global-praise-1718191 (accessed on 21 March 2019).
21. Textile Today. BD Sees Highest Growth in using Organic Raw Materials. Textile Today. 2019. Available online: https://www.textiletoday.com.bd/bd-sees-highest-growth-in-using-organic-raw-materials-in-world/ (accessed on 24 April 2021).
22. Merriam-Webster. Organic. Merriam-Webster.com Dictionary. Available online: https://www.merriam-webster.com/dictionary/organic (accessed on 15 August 2021).
23. EJF. *The Deadly Chemicals in Cotton*; Environmental Justice Foundation in Collaboration with Pesticide Action Network UK: London, UK, 2007; ISBN 1-904523-10-2.
24. Zulfiqar, F.; Thapa, G.B. Is 'Better cotton' better than conventional cotton in terms of input use efficiency and financial performance? *Land Use Policy* **2016**, *52*, 136–143. [CrossRef]
25. Reganold, J.P.; Glover, J.D.; Andrews, P.K.; Hinman, H.R. Sustainability of three apple production systems. *Nature* **2001**, *410*, 926–930. [CrossRef] [PubMed]
26. Angelova, R.A. Organic Cotton: Technological and Environmental Aspects. In Proceedings of the XXIII Int. Scientific Conference FPEPM, Sozopol, Bulgaria, 17–20 September 2018.
27. Textile Exchange. Life Cycle Assessment (LCA) of Organic Cotton, PE International. 2014. Available online: http://farmhub.textileexchange.org/upload/library/Farm%20reports/LCA_of_Organic_Cotton%20FiberSummary_of%20Findings.pdf (accessed on 25 April 2021).
28. Chang, H.J.; Watchravesringkan, K.T. Who are sustainably minded apparel shoppers? An investigation to the influencing factors of sustainable apparel consumption. *Int. J. Retail. Distrib. Manag.* **2018**, *46*, 148–162. [CrossRef]
29. Fu, W.; Kim, Y.K. Eco-fashion consumption: Cognitive-experiential self-theory. *Fam. Consum. Sci. Res. J.* **2019**, *47*, 220–236. [CrossRef]
30. Koszewska, M. A typology of Polish consumers and their behaviours in the market for sustainable textiles and clothing. *Int. J. Consum. Stud.* **2013**, *37*, 507–521. [CrossRef]
31. Khare, A.; Varshneya, G. Antecedents to organic cotton clothing purchase behaviour: Study on Indian youth. *J. Fash. Mark. Manag. Int. J.* **2017**, *21*, 51–69. [CrossRef]
32. Han, T.-I. Determinants of organic cotton apparel purchase: A comparison of young consumers in the USA and South Korea. *Sustainability* **2018**, *10*, 2025. [CrossRef]
33. Su, J.; Watchravesringkan, K.T.; Zhou, J.; Gil, M. Sustainable clothing: Perspectives from US and Chinese young Millennials. *Int. J. Retail. Distrib. Manag.* **2019**, *47*, 1141–1162. [CrossRef]
34. Young, C.; Jirousek, C.; Ashdown, S. Undesigned: A study in sustainable design of apparel using post-consumer recycled clothing. *Cloth. Text. Res. J.* **2004**, *22*, 61–68. [CrossRef]
35. Azjen, I. Understanding Attitudes and Predicting Social Behavior. In *Englewood Cliffs*; Prentice-Hall: Hoboken, NJ, USA, 1980.
36. Ajzen, I. Attitudes, Traits, and Actions: Dispositional Prediction of Behavior in Personality and Social Psychology. In *Advances in Experimental Social Psychology*; Elsevier: Amsterdam, The Netherlands, 1987; Volume 20, pp. 1–63.
37. Zareie, B.; Navimipour, N.J. The impact of electronic environmental knowledge on the environmental behaviors of people. *Comput. Hum. Behav.* **2016**, *59*, 1–8. [CrossRef]
38. Weiner, H.E. Wearing your Ethics: Investigating Consumer Purchase Intention of Ethically Produced Fashion Products. 2017. Available online: https://scholarcommons.sc.edu/etd/4351 (accessed on 28 April 2021).
39. Harland, P.; Staats, H.; Wilke, H.A. Situational and personality factors as direct or personal norm mediated predictors of pro-environmental behavior: Questions derived from norm-activation theory. *Basic Appl. Soc. Psychol.* **2007**, *29*, 323–334. [CrossRef]
40. Lee, K. Gender differences in Hong Kong adolescent consumers' green purchasing behavior. *J. Consum. Mark.* **2009**, *26*, 87–96. [CrossRef]
41. Lee, K. Opportunities for green marketing: Young consumers. *Mark. Intell. Plan.* **2008**, *26*, 573–586. [CrossRef]
42. Geng, D.; Liu, J.; Zhu, Q. Motivating sustainable consumption among Chinese adolescents: An empirical examination. *J. Clean. Prod.* **2017**, *141*, 315–322. [CrossRef]

43. Paul, J.; Modi, A.; Patel, J. Predicting green product consumption using theory of planned behavior and reasoned action. *J. Retail. Consum. Serv.* **2016**, *29*, 123–134. [CrossRef]
44. McNeill, L.; Moore, R. Sustainable fashion consumption and the fast fashion conundrum: Fashionable consumers and attitudes to sustainability in clothing choice. *Int. J. Consum. Stud.* **2015**, *39*, 212–222. [CrossRef]
45. Harris, F.; Roby, H.; Dibb, S. Sustainable clothing: Challenges, barriers and interventions for encouraging more sustainable consumer behaviour. *Int. J. Consum. Stud.* **2016**, *40*, 309–318. [CrossRef]
46. Ham, M.; Jeger, M.; Ivković, A.F. The role of subjective norms in forming the intention to purchase green food. *Econ. Res. Ekon. Istraživanja* **2015**, *28*, 738–748. [CrossRef]
47. Vermeir, I.; Verbeke, W. Sustainable food consumption among young adults in Belgium: Theory of planned behaviour and the role of confidence and values. *Ecol. Econ.* **2008**, *64*, 542–553. [CrossRef]
48. Kim, H.Y.; Chung, J.E. Consumer purchase intention for organic personal care products. *J. Consum. Mark.* **2011**, *28*, 40–47.
49. Yan, R.-N.; Hyllegard, K.H.; Blaesi, L.F. Marketing eco-fashion: The influence of brand name and message explicitness. *J. Mark. Commun.* **2012**, *18*, 151–168. [CrossRef]
50. Ahn, J.-M.; Koo, D.-M.; Chang, H.-S. Different impacts of normative influences on pro-environmental purchasing behavior explained by differences in individual characteristics. *J. Glob. Sch. Mark. Sci.* **2012**, *22*, 163–182. [CrossRef]
51. Hustvedt, G.; Dickson Marsha, A. Consumer likelihood of purchasing organic cotton apparel: Influence of attitudes and self-identity. *J. Fash. Mark. Manag. Int. J.* **2009**, *13*, 49–65. [CrossRef]
52. Yahya, W.K.; Hashim, N.H. The Role of Public Awareness and Government Regulations in Stimulating Sustainable Consumption of Malaysian Consumers. In Proceedings of the 2011 International Conference on Business, Engineering and Industrial Applications, Kuala Lumpur, Malaysia, 5–7 June 2011.
53. Chen, T.B.; Chai, L.T. Attitudes towards the environment and green products: Consumers' perspective. *Manag. Sci. Eng.* **2010**, *4*, 27–39.
54. Markus, H.R.; Kitayama, S. Culture and the self: Implications for cognition, emotion, and motivation. *Psychol. Rev.* **1991**, *98*, 224–253. [CrossRef]
55. Han, S.P.; Shavitt, S. Persuasion and culture: Advertising appeals in individualistic and collectivistic societies. *J. Exp. Soc. Psychol.* **1994**, *30*, 326–350. [CrossRef]
56. Kabir, T.; Sarker, B.C. Effect of cultural dimensions on customers' susceptibility to interpersonal influence in the context of Bangladesh. *Prime Univ. J.* **2015**, *9*, 77–108.
57. Hofstede, G.; Hofstede, G.J.; Minkov, M. *Cultures and Organizations—Software of the Mind: Intercultural Cooperation and Its Importance for Survival*; McGraw-Hill: New York, NY, USA, 2010.
58. Minton, E.A.; Kahle, L.R.; Kim, C.-H. Religion and motives for sustainable behaviors: A cross-cultural comparison and contrast. *J. Bus. Res.* **2015**, *68*, 1937–1944. [CrossRef]
59. Thøgersen, J. Country differences in sustainable consumption: The case of organic food. *J. Macromarketing* **2010**, *30*, 171–185. [CrossRef]
60. Premkumar, G.; Ramamurthy, K. The role of interorganizational and organizational factors on the decision mode for adoption of interorganizational systems. *Decis. Sci.* **1995**, *26*, 303–336. [CrossRef]
61. Kline, R.B. *Principles and Practice of Structural Equation Modeling*, 3rd ed.; The Guilford Press: New York, NY, USA, 2010.
62. Anderson, J.C.; Gerbing, D.W. Structural equation modeling in practice: A review and recommended two-step approach. *Psychol. Bull.* **1988**, *103*, 411–423. [CrossRef]
63. Babin, B.J.; Darden, W.R.; Griffin, M. Work and/or fun: Measuring hedonic and utilitarian shopping value. *J. Consum. Res.* **1994**, *20*, 644–656. [CrossRef]
64. Khare, A. Influence of hedonic and utilitarian values in determining attitudes towards malls: A case of Indian small city consumers. *J. Retail. Leis. Prop.* **2011**, *9*, 429–442. [CrossRef]
65. Hofstede, G. Values and Culture. In *Culture's Consequences: International Differences in Work-Related Values*; Sage Publications: Beverly Hills, CA, USA, 1980.
66. Kitayama, S.; Markus, H.R.; Lieberman, C. The Collective Construction of Self Esteem. In *Everyday Conceptions of Emotion*; Springer: Berlin/Heidelberg, Germany, 1995; pp. 523–550.

*textiles*

MDPI

*Review*

# A Review on Textile Recycling Practices and Challenges

**Jeanger P. Juanga-Labayen [1], Ildefonso V. Labayen [2] and Qiuyan Yuan [3,*]**

[1] College of Industrial Technology, Carlos Hilado Memorial State College, Talisay City 6115, Negros Occidental, Philippines; jeanger.labayen@chmsc.edu.ph
[2] Manufacturing Engineering Technology, Technological University of the Philippines Visayas, Talisay City 6115, Negros Occidental, Philippines; ildefonso_labayen@tup.edu.ph
[3] Environmental Engineering, Civil Engineering Department, University of Manitoba, Winnipeg, MB R3T 5V6, Canada
* Correspondence: qiuyan.yuan@umanitoba.ca

**Abstract:** The expansion of clothing and textile industry and the fast fashion trend among consumers have caused a rapid global increase in textile waste in the municipal solid waste (MSW) stream. Worldwide, 75% of textile waste is landfilled, while 25% is recycled or reused. Landfilling of textile waste is a prevalent option that is deemed unsustainable. Promoting an enhanced diversion of textile waste from landfills demands optimized reuse and recycling technologies. Reuse is the more preferred option compared with recycling. Various textile reuse and recycling technologies are available and progressively innovated to favor blended fabrics. This paper aims to establish reuse and recycling technologies (anaerobic digestion, fermentation, composting, fiber regeneration, and thermal recovery) to manage textile waste. Improved collection systems, automation of sorting, and discovering new technologies for textile recycling remains a challenge. Applying extended producer responsibility (EPR) policy and a circular economy system implies a holistic consensus among major stakeholders.

**Keywords:** textile waste; reuse and recycling; municipal solid waste; composting; sustainability

**Citation:** Juanga-Labayen, J.P.; Labayen, I.V.; Yuan, Q. A Review on Textile Recycling Practices and Challenges. *Textiles* **2022**, *2*, 174–188. https://doi.org/10.3390/textiles2010010

Academic Editor: Philippe Boisse

Received: 6 February 2022
Accepted: 9 March 2022
Published: 16 March 2022

**Publisher's Note:** MDPI stays neutral with regard to jurisdictional claims in published maps and institutional affiliations.



## 1. Introduction

Population growth, improvement of living standards, an increasing assortment of textile materials, and the decreasing life cycle time of textile products contributed to global fiber consumption that generates a significant amount of post-industrial and post-consumer fiber waste [1,2]. Globalization has made the apparel industry produce more clothing at lower costs, and many consumers have adapted a 'fast fashion' trend that considers clothing to be a disposable product [3]. Fast fashion characterized by mass production, variety, agility, and affordability has brought about a surge of apparel consumption [4].

The rising cost associated with textile manufacturing in terms of energy, raw materials, and waste management is putting pressure on businesses across the globe. The textile industry accounts for about 10% of total carbon emissions [5] and has been identified as the fifth largest contributor of carbon emissions [6,7]. In this regard, it is crucial to understand that 20th-century approaches in meeting 21st-century demands are not affordable for sustainable development [8]. It is essential to consider the efficient use and management of natural resources by reducing the raw material consumption through reuse and recycling of textile products regarded as waste, which would offer a sustainable approach for textile waste management. To improve the current behavior of clothing consumption and waste generation, an environmentally and financially sound long-term national program should be established [9].

Globally, approximately 75% of textile waste is disposed of in landfills, 25% is reused or recycled, and less than 1% of all textile is recycled back into clothing [10,11]. In this respect, advancing reuse and recycling technologies for textile waste in diverting waste

from landfill is crucial. More importantly, closed-loop recycling of fabric is highly promoted. There have been several reinforced global actions integrating many expert stakeholders addressing both economic and environmental challenges that the clothing industry faces; among them are the Textile Exchange, Council for Textile Recycling, Sustainable Apparel Coalition, and the Boston Consulting Group, among others. For instance, Textile Exchange commits to reducing $CO_2$ emissions by 30% from textile fibers and material production by 2030 and fosters the role of the circular economy as a powerful instrument for mitigating impacts and contributing to the urgent need for climate action [11]. Hence, textile reuse and recycling are vital in promoting this innovative act. This paper determines the existing textile waste reuse and recycling technologies and the status of textile waste generation and management in some leading economies.

## 2. Textile Production

Clothing and textiles contributed 6% to the world exports of manufactured goods in 2017 (Figure 1); China and the European Union (EU) are the two leading regions for clothing and textile exports [12]. The worldwide volume production of textile fibers in 1975 was about 23.9 million metric tons (MMT), in 2017 it reached 98.5 MMT [13], and it increased further to about 111 MMT in 2019 [11]. For many years, cotton fiber demand dominated polyester; however, in 2002, polyester demand surpassed cotton fiber and has continued to grow at a faster rate than cotton fiber [14]. Polyester and cotton are the most common fibers used worldwide [14,15]. Moreover, the global fiber consumption in 2017 consists of 60% synthetic fibers or polyester/cotton blend (polycotton) and 40% cellulosic, which is the typical example of most textiles [16]. Nevertheless, the global fiber market in 2019 was dominated by polyester and cotton (Figure 2). From these figures, it is apparent that textile waste management is a critical issue that presents enormous challenges for the textile industry, policymakers, and consumers.

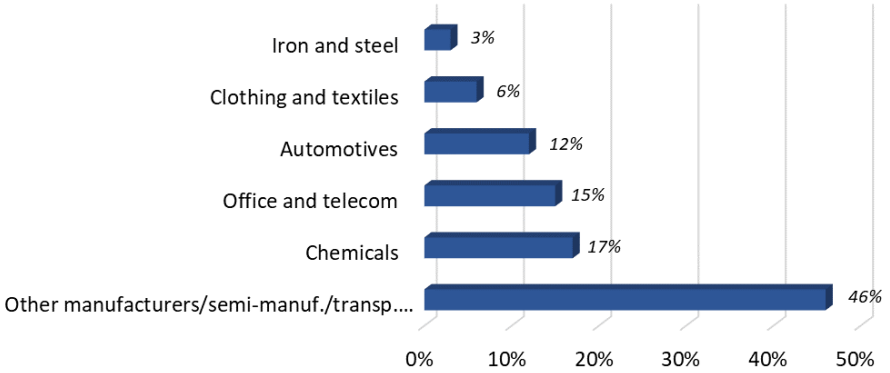


**Figure 1.** Percentage share of world exports of manufactured goods in 2017 [12].

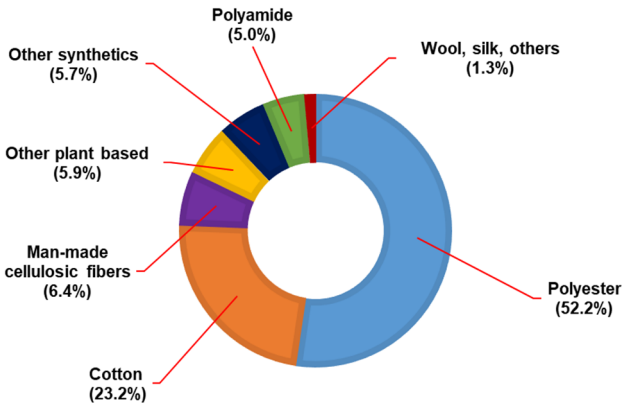


**Figure 2.** Global fiber production share in 2019 [11].

## 3. Textile Waste Generation and Management in Leading Economies

Textile waste is considered as discarded or unwanted material from the production and use of fiber, textile, and clothing, which can be categorized into three types, pre-consumer, post-consumer, and industrial textile waste [8,17]. The pre-consumer textile waste is viewed as 'clean waste', as a by-product during the manufacturing process of fibrous materials. The post-consumer textile waste consists of discarded garments or household textiles (sheets, towels, and pillowcases) that are worn-out, damaged, and outgrown of no value to consumers after their service life [18]. Industrial textile waste is deemed as 'dirty waste' generated from commercial and industrial textile applications. The expansion of the clothing and textile industry and the consumer's fast fashion trend have caused a rapid global increase in textile wastes. The increased consumption of fashion textiles generates a growing amount of waste. As fashion textiles, are almost 100% recyclable, nothing in the textile and apparel industry should be wasted in an ideal scenario. Furthermore, more than 60% of all recovered clothes could be reused, 35% could be converted into wipers and fiber recycling, and only 5% would need to be discarded [19]. However, in the real world, a significant portion of textile waste is disposed of in landfills. As a result, it is critical to comprehend the challenges that leading economies face when it comes to textile production and waste management. In terms of textile exports, the leading economies considered in this study are China, The European Union, The United States, and Canada.

China has the largest economy in clothing and textiles exports globally, yet the industry faces unprecedented crises [20,21]. The country's dominance as a textile provider across the globe is challenged by the loss of competitive advantages in terms of low labor costs as wages are rising. China attempts to maintain its dynamic advantage in labor-intensive textile products by encouraging the relocation of Chinese textile production bases to poorer Chinese provinces and neighboring least developed countries (LDCs). Simultaneously, China's global competitiveness was upgraded through technological advancement, implementing sound policies to develop capital-intensive textile goods, launching niche products and international brands [21,22]. The Chinese textile industry sector has experienced consistent economic growth over the last decade and is primarily focused on the production of apparel made of synthetic fabrics. Furthermore, China produces approximately 31% of the global ratio of synthetic fibers required by the modern textile industry [23] and produces nearly 65% of the world's clothing [24]. When China started imposing strict environmental standards on textile production, China's cloth products became more competitive in the United States (US) market [25].

Furthermore, many people in China have easy access to low-cost fashion clothing with a short service life. Roughly 45% of the textile produced in China is wasted. Approximately 26 million tons (MT) of garments are left untreated and dumped annually, while only 3.5 MT of the collected textile waste was recycled and reused in 2017 [24]. China's textile waste generation is estimated to range from 20 to 26 MT per year, with a low utilization rate [26]. The Chinese government is encouraging businesses to recycle their own brand clothing through mechanical and chemical recycling. China recognized the two-fold benefits of donating textile waste as it gives clothes a second life while generating revenue for charity. However, in the absence of effective recycling practices, used clothing is sent to waste-to-energy (WTE) incinerators [24]. In 2013, China's State Council mandated that textile manufacturers create a circular value chain to promote environmental sustainability in the disposal of post-consumer textiles [26].

The EU textile industry generates approximately 16 MT of waste annually. European consumers discard 5.8 MT of textiles per year, where only 26% is recycled, while a significant fraction of this waste is disposed of into landfills or incinerated [4,27]. The disposal cost of textile waste into landfills is about €60/ton in some countries in Europe, including France [28]. The European Waste Framework Directive (2008/98/EC) established the fundamental waste management principle and requires the EU member states to adopt a waste management hierarchy (prevention, reuse, recycling, and disposal) in waste management plans and waste prevention programs [29]. Furthermore, the European

Council (EC) promoted sustainability by substituting the Waste Framework Directive with a Circular Economy Package, which set a target for the municipal solid waste (MSW) recovery to 70% and limits the fraction to be landfilled to 10% by 2030 [30]. The extended producer responsibility (EPR) policy was essential in achieving such targets. The EPR holds the producers responsible for collecting, processing, and treatment, including recycling and disposal of products at the post-consumer stage of a product's life cycle [31]. The EPR policy has led to an average annual increase of 13% in post-consumer textile collection [4]. Furthermore, the EPR policy encourages waste prevention at source, promotes green product design, and encourages public recycling [31]. The financial responsibility of the producer, as well as separate collection and recycling agencies, are critical to the success of EPR-based environmental policies [32].

Furthermore, the EU establishes new waste management rules, with a focus on closed-loop recycling from production to waste management, with the goal of making economies more sustainable and environmentally friendly [33]. The closed-loop system reduces waste by a repeated process of recycling and reusing materials until they become biodegradable waste. The system can address the fashion industry's intensive use of finite land, water, and energy resources in a sustainable manner [34]. The EU member states' reuse and recycling targets for municipal waste have been set at 55% by 2025, 60% by 2030, and 65% by 2035. By January 2025, a separate collection of textiles and hazardous waste from households will be implemented [33]. Across the European countries, only 18% of clothing is reused and recycled, while 30% is incinerated and a significant fraction of 70% goes to landfills [16]. In France, 40% of the post-consumer textiles collected are exported to African countries for reuse. As of 2017, France is the only European country that globally introduced EPR for textiles, household linen, and shoes [4]. European companies are innovative in formulating sustainability targets where the raw materials, design and development, manufacturing, and end-of-use are the priority on the agenda [34].

In the US, the majority of textile waste in the MSW stream is discarded apparel. However, other sources were identified such as furniture, carpets, tires, footwear, as well as other non-durable goods such as towels, sheets, and pillowcases [35,36]. Textile waste generation and the fraction of textile waste in MSW is increasing with time. In 2010, an estimated 13.2 MT of textile waste were generated, which is equivalent to 5.3% of total MSW stream. While in 2015 and 2017, the generated textile waste increased to 16.1 MT and 16.9 MT, accounting to 6.1% and 6.3% of the total MSW generation, respectively (Figure 3). Approximately 85% of all textiles in the US end up in landfills, and only 15% is donated or recycled [37]. The United States Environmental Protection Agency (USEPA) estimated that textile waste occupies nearly 5% of landfill space [37]. Among the leading economies in the textile industry, the US has the highest share of landfilling textile waste, amounting to 29.3 kg/ca in 2016 (Figure 4), and the estimated cost of textile waste sent to landfills is $45/ton [38]. Since landfilling keeps the largest share in textile waste management in the US, promoting recycling technologies to many textile industries is crucial. Composting is not a common method of managing textile waste. Nevertheless, incineration and recycling are gaining popularity in textile waste management (Figure 5).

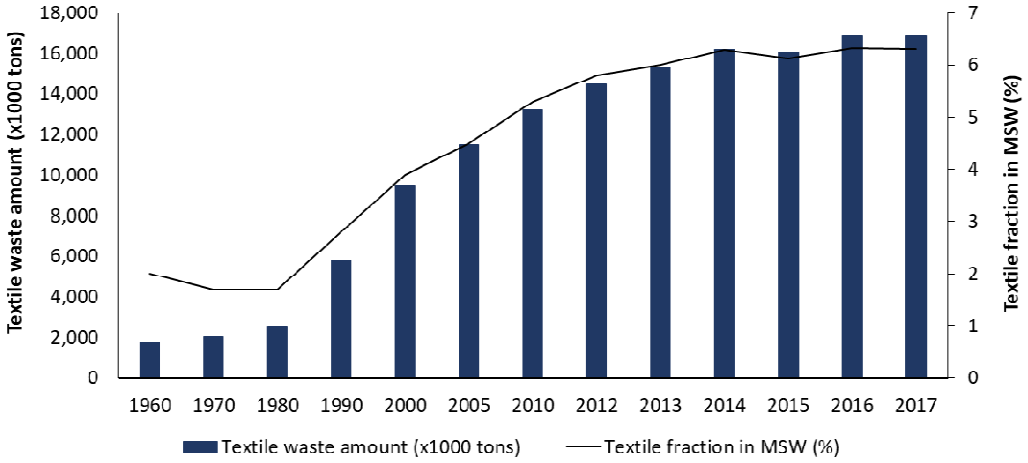


**Figure 3.** Textile waste generation in the US [39].

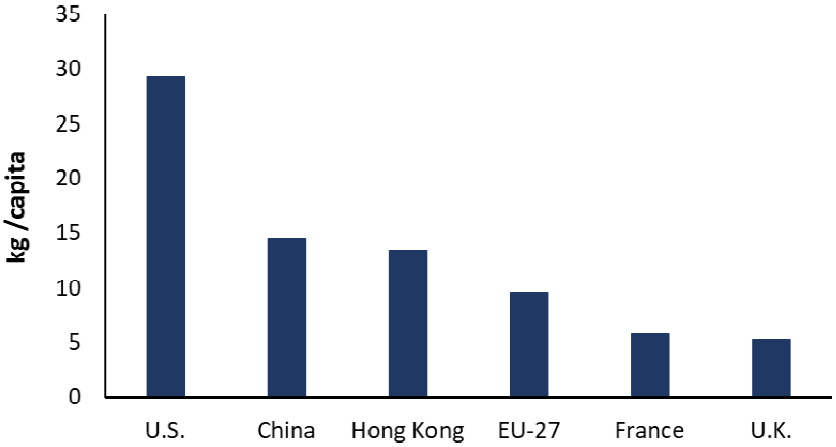


**Figure 4.** Annual generation of landfilled textiles (in kg/ca) in 2016 [4].

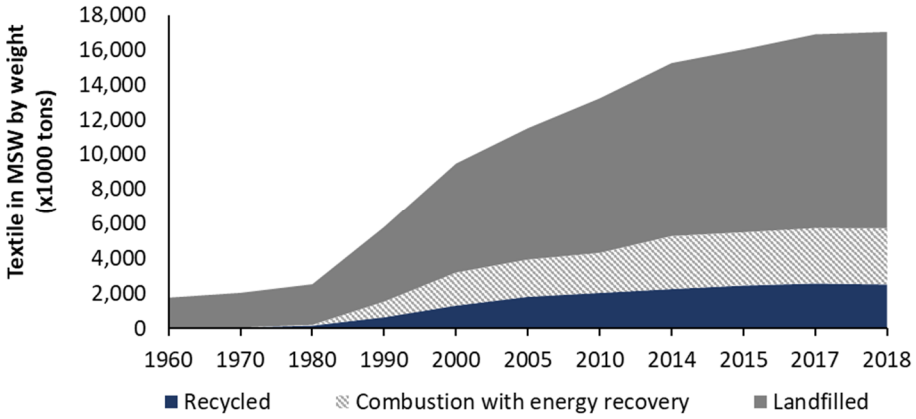


**Figure 5.** Textile waste management in the US [40].

In Canada, an estimated 500,000 tons of apparel waste is disposed of annually [41]. The average Canadian discards between 30 [42] and 55 [43] pounds of textiles annually [44]; almost 95% of those clothes could be reused or recycled [45]. Globally, textile waste has increased dramatically due to the rise in clothing consumption and production [45]. In Ontario, approximately 1.2 million people dispose their unwanted clothes into the waste bin at a rate of roughly 45,000 tons annually [46]. In the Metro Vancouver Regional District, an estimated 30,000 tons of textile waste are annually landfilled, accounting for 5% of the

annual total waste volume in 2016 [47]. In Toronto, a survey was conducted to determine if participants donated and/or disposed of their unwanted clothing [46]. According to the findings, 17% of participants consider "disposal" to be the most convenient (10%) and fastest (7%) method of getting rid of unwanted textile waste. In Manitoba, textile and carpet waste materials are under the Canadian Council of Ministers of the Environment (CCME) National Action Plan for EPR of the Waste Management Task Group [48]. Unwanted clothing items that could be donated are usually dropped off at city drop-off bins or collected by non-profit charitable organizations and municipal programs. Due to their poor condition, some donated textiles are frequently discarded in landfills [49].

## 4. Textile Reuse and Recycling

Generally, textile reuse and recycling could reduce environmental impact because it could potentially reduce virgin textile fiber production and avoid processes further downstream in the textile product life cycle. Moreover, textile reuse and recycling are more sustainable when compared to incineration and landfilling. However, reuse is considered more beneficial than recycling, mainly when sufficiently prolonging the reusing phase [50]. Textile reuse encompasses various means for extending the useful service life of textile products from the first owner to another [51]. This is commonly practiced by renting, trading, swapping, borrowing, and inheriting, facilitated by second-hand stores, garage sales, online and flea markets, and charities. On the other hand, textile recycling refers to reprocessing pre-consumer and post-consumer textile waste for use in new textile or non-textile products.

Textile recycling is typically classified as mechanical or chemical recycling. Mechanical recycling degrades waste into a decoration, construction, agricultural, and gardening use. Chemical recycling involves a process where polymers are depolymerized (polyester) or dissolved (cotton and viscose). Chemical recycling can produce fibers of equal quality compared to virgin materials [24,50]. The sorted textile waste could be chemically treated to extract resources such as protein-based fibers to produce wood panel adhesives; and cellulosic fibers for bioethanol production [27].

The textile recycling route can be classified based on the nature of the processes involved or the level of disassembly of the recovered materials [50]. Fabric recycling consists in recovering and reusing of a fabric into new products. Meanwhile, fiber recycling involves disassembling of fabric but preserving the original fibers. Polymer/oligomer recycling consists of disassembling of fibers while preserving the polymers or oligomers. Moreover, monomer recycling consists of disassembling of polymers or oligomers, while preserving the monomers [50].

Moreover, textile recycling can be classified into upcycling, downcycling, closed-loop, and open-loop recycling. If the product made from recycled material is of higher quality or value than the original product, it is termed 'upcycling'; the opposite of this is known as 'downcycling'. Closed-loop recycling involves recycling of a material from a product and reusing it in a more or less identical product. In contrast, open-loop recycling consists of recycling of a material from a product and reusing it in another product. Figure 6 shows the classification of various forms of reuse and recycling. The closed-loop recycling approach recovers the raw material used to produce a polymer product and then reprocess it into the same product of equivalent quality as that from the virgin material [50,52].

Furthermore, recycling technologies for fibers can be typically divided into primary, secondary, tertiary, and quaternary approaches. Primary approaches involve recycling industrial scraps. Secondary recycling involves the mechanical processing of a post-consumer product. Tertiary recycling involves pyrolysis and hydrolysis, converting plastic waste into chemicals, monomers, or fuels. Quaternary recycling refers to burning the fibrous solid waste and utilizing the heat generated [53].

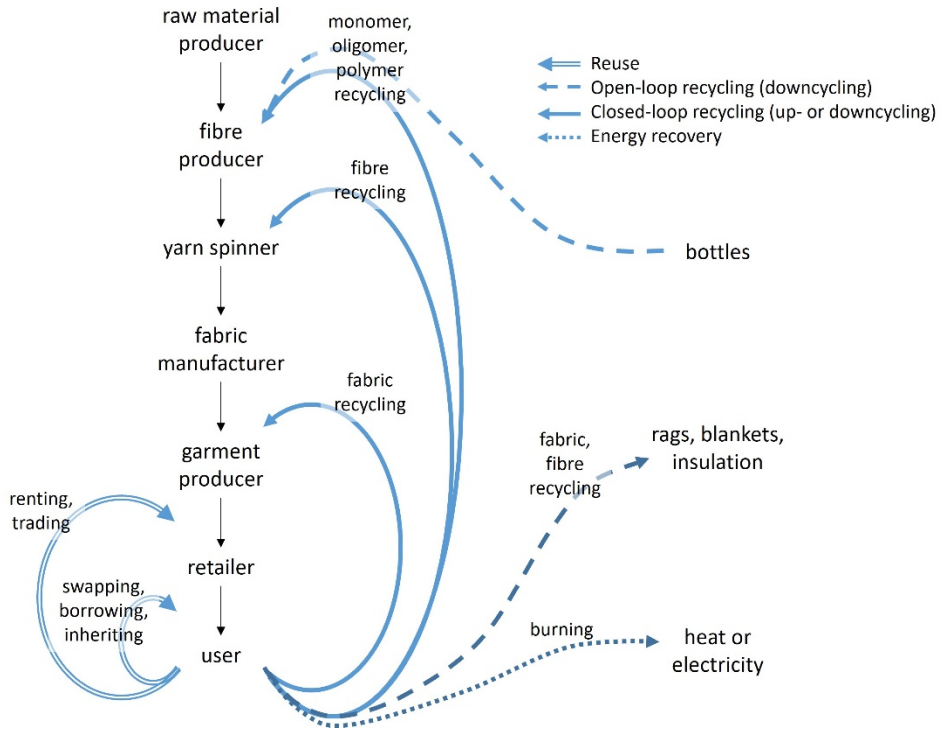


**Figure 6.** Classification of textile reuse and recycling routes, reprinted with permission from [50]. Copyright 2018 Elsevier.

## 5. Environmental Sustainability in Textile Recycling

Reuse and recycling of textile waste offers environmental sustainability. Upcycling and closed-loop recycling are the potential recycling routes that maximize conservation of resources such as raw materials, water, and energy, with minimal environmental impact [8]. Moreover, textile reuse and recycling reduce environmental impact compared to incineration and landfilling, and reuse is more beneficial than recycling [50]. Applying ecological footprint in a textile tailoring plant revealed that the resources category has the highest ecological footprint, followed by the energy consumed [54]. Resources recovery can provide significant environmental gains by replacing products from primary resources [55]. For every kilogram of virgin cotton displaced by second-hand clothing and polyester could save approximately 65 kWh and 95 kWh, respectively [56].

## 6. Textile Recycling and Recovery Technology

Nowadays, various technologies can be chosen to promote textile waste recycling and recovery. Technologies such as anaerobic digestion, fermentation, and composting are among the biotechnology available for textile waste. The following sections also discuss thermal recovery and conversion of textile waste into insulation/building materials.

### *6.1. Anaerobic Digestion of Textile Waste*

Anaerobic digestion (AD) is widely used to treat a biodegradable fraction of organic waste for biogas production. Cotton was characterized by more than 50% cellulose, a potential substrate for biological conversion (Table 1). Over the last decade, studies have been conducted on AD using cotton waste to produce methane-rich biogas. Cotton wastes (cotton stalks, cottonseed hull, and cotton oil cake) can be treated anaerobically to produce biogas [57]. Cotton waste from spinning mills is a potential substrate for AD [58]. The AD of medical cotton industry waste under thermophilic condition with the use of cattle manure as inoculum demonstrated an improved biogas yield of approximately 92% [59]. Pretreatment methods enhance the biodegradation of complex organic matter in AD systems, resulting in an increase in biogas quality and production and improved biosolids quality

in reduced production [60,61]. Various pre-treatment technologies mainly mechanical, thermal, chemical, biological, and their integration can be chosen to enhance the digestion process [60,62]. Pretreatment prior to AD of waste jeans (60% cotton, 40% polyester) and pure cotton waste substrates using 0.5 M $Na_2CO_3$ at 150 °C for 120 min generates a maximum methane yield of 328.9 and 361.1 mL $CH_4$/g VS, respectively [63]. Furthermore, a comparable maximum methane production rate of 80% was obtained using single-stage and two-stage digestions in batch reactors utilizing viscose/polyester or cotton/polyester textiles with 20 g/L cellulose loading [64]. Table 2 summarizes the optimum operating conditions using batch process of anaerobic digestion from the reviewed literature.

**Table 1.** Characteristics of cotton waste [58].

| Contents | Percentage |
|---|---|
| Cellulose | 54.00 |
| Non-cellulose | 16.00 |
| Ether extractive | 12.00 |
| Moisture | 8.80 |
| Ash | 7.20 |
| Metals and others | 3.20 |

**Table 2.** Optimum operating conditions for biogas production using cotton wastes

| Cotton Waste Stream | Pretreatment | Inoculum | Operating Temperature (°C) | Digestion Time (Days) | $CH_4$ Yield (mL/g VS) | $CH_4$ (%) | Reference |
|---|---|---|---|---|---|---|---|
| Cotton waste (cotton stalks, cottonseed hull, cotton oil cake) | - | Effluent from WWTP anaerobic digester | 35 ± 2 | 23 | 65 (cotton stalks); 86 (cotton seed hull); 78 (cotton oil cake) | 60 | [57] |
| Cotton waste from spinning mills | - | 5–7.5% cow dung/pig dung | 30–32 | 50 | - | 77 | [58] |
| Medical cotton waste | Alkaline ($Na_2CO_3$) | Cattle manure | 55 | 90 | 37.57 | 60–70 | [59] |
| Waste jeans (60% cotton) Cotton waste (100%) | 0.5 M $Na_2CO_3$ at 150 °C for 120 min | Effluent from municipal WWTP anaerobic digester | 37 | 40 | 328.9 (60% cotton); 361.08 (pure cotton) | - | [63] |
| Cotton textile waste (100% cotton) | 0.5 M $Na_2CO_3$ at 150 °C for 3 h | Digested sludge from municipal WWTP anaerobic digester | 37 | 15 | 306.73 | >50 | [65] |

### *6.2. Fermentation of Textile Waste for Ethanol Production*

Investigation of cotton gin waste as feedstock for ethanol production started in 1979 at Texas Tech University; however, limited studies investigated the efficacy of textile waste for ethanol production [66]. The effect of alkali pretreatment to enhance ethanol production was evaluated using polyester/cotton blend (polycotton) textile. The maximum ethanol yield by simultaneous saccharification and fermentation was 70% after the pretreatment with NaOH/urea at −20 °C, which was considered the most desirable [67]. Moreover, the cotton part of the waste blue jeans (40% polyester/60% cotton) was investigated for ethanol production, which involves the process of enzymatic hydrolysis and fermentation [63]. Enzymatic hydrolysis converts cellulose to fermentable sugars [58]. The effect of corona

pretreatment of non-mercerized and mercerized cotton fabrics enhanced the glucose and ethanol yields. The cotton fabric demonstrated its potential as an alternative feedstock for bioethanol production [68]. Table 3 summarizes the optimum operating conditions for ethanol production based on the reviewed literature.

**Table 3.** Optimum operating conditions for ethanol production using cotton wastes.

| Cotton Waste Stream | Pretreatment | Enzymatic Hydrolysis | Fermentation Condition | Glucose Yield | Ethanol Yield | Reference |
|---|---|---|---|---|---|---|
| Cotton part from polyester-cotton textile | NaOH/urea, −20 °C, 72 h | Cellulase and β-glucosidase enzyme, pH 4.8, 45 °C, 72 h | *S. cerevisiae*, 36 °C, 72 h | 91% | 70% | [67] |
| Bleached and mercerized cotton fabric (100% cellulose) | Corona pretreatment of mercerized cotton fabrics | Celluclast enzyme, 50 °C, 8 days | *S. cerevisiae* var *ellipsoideus*, pH 5, 30 °C, 100 rpm | 0.94 g/g | 0.9 g/L·h | [68] |
| Waste jeans (60% cotton) Cotton (pure) | 1 M $Na_2CO_3$, 150 °C, 120 min | Cellulase and β-glucosidase, 45 °C, 72 h, 120 rpm | *S. cerevisiae*, 36 °C, 72 h | 81.7% (60% cotton) 88% (pure cotton) | 59.5% (60% cotton) 69.4% (pure cotton) | [63] |

### *6.3. Composting of Textile Waste*

Composting is a natural phenomenon of biodegradation of organic waste, such as cotton waste, into a valuable soil supplement. Composting is a low technology, bio-oxidative process that reduces the volume of organic waste by up to 50% over the active phase of composting [66]. Composting utilized various microorganisms, including bacteria and fungi, to convert complex organic matter into simpler substances in the presence of air. Cotton waste poses a significant waste disposal problem nowadays, and composting was viewed as an alternative in preventing the direct landfill disposal of cotton trash. Composted and vermicomposted cotton trash could be an excellent long-term nutrient source [69].

Vermicomposting is a biotechnological composting process that uses earthworms to convert waste into compost with improved soil fertility that significantly exceeds conventional compost [69]. Using cotton waste substrate, the number of bacterial diversity in compost and vermicompost samples was similar. However, the vermicompost samples contain a rich density of bacterial isolates when compared with compost samples which produce better humus [70].

Vermicomposting of cotton textile waste in the form of willow waste from ginning factories was investigated. Willow waste is undesirable for textile application and is just disposed into landfill. The collected willow waste was mixed with cow dung slurry, cellulase, and amylase enzymes (isolated from cow dung), and an effective microorganism solution. The mixture was turned and sprinkled with water periodically. After 20 days, the waste was wholly decomposed, and earthworms were introduced. The vermicomposting process was ended when the waste mixture turned light brown or dark brown after 14 days. The resulting vermicompost was then used to grow plants in pots and revealed that the plants grown using the vermicompost made from willow waste had an excellent growth rate in root length, shoot length, and leaf area index compared to the control pot [71].

Furthermore, cotton gin waste cannot be directly reused on-farm due to farm hygiene risks, and composting of cotton gin waste is an accepted method [66]. Cotton gin waste was used as a bulking agent for pig manure composting under two different proportions of 4:3 and 3:4 of pig slurry:cotton gin waste [72]. This study concluded that the thermal properties of the bulking agent were responsible for the temperature development and aeration demand. The gaseous emissions were related to the organic matter degradation

process. The compost with the higher proportion of pig slurry (4:3) had greater organic matter humification and higher nutrient concentrations.

Furthermore, since the 1980s, the waste cotton substrate was utilized for oyster mushroom cultivation. More than 90% of oyster mushroom growers utilized waste cotton substrate for cultivation [73]. Cotton waste with fermented poplar sawdust exhibited the highest yield on fruit bodies of oyster mushroom, equivalent to 742 g per 4 kg of substrate [73]. A new cotton waste composting technology to cultivate oyster mushrooms shows a higher mushroom yield of 65.1% over substrate dry weight when compared to a traditional natural fermentation technology with a 43.6% yield [74]. The process involves adjusting cotton waste moisture content to 65%, after which it was pre-composted for two days by soaking in a lime solution. Then, the cotton substrate was sprayed with the previously prepared Ctec2 enzyme under optimal enzymatic activity conditions (pH 5, 50 °C, 60 h, and enzyme to substrate ratio of 0.45%) and then inoculated in pure culture of fungus. Then spawning, caring of the bed, and harvesting was conducted [74].

### *6.4. Fiber Regeneration from Textile Waste*

Since the 'export for reuse option' is no longer a sustainable option for second-hand clothing in many developing countries, virgin cotton fiber production demands the use of extensive resources. Fiber regeneration by recycling cotton waste garments is a closed-loop upcycling technology for cotton waste garments [75]. Fiber regeneration involves transforming the waste cotton fabrics into pulp, dissolving the pulp using a solvent, and spinning into fibers. The N-methylmorpholine N-oxide (NMMO) solvent can dissolve cellulose completely without any degradation and is environmentally safe to use. Pulp reclaimed from cotton-based waste garments can be blended with wood pulp to make fibers similar to lyocell [76].

Furthermore, phosphoric acid pretreatment was applied to waste textiles to recover polyester and glucose. The four pretreatment conditions investigated were the phosphoric acid concentration, pretreatment temperature, time, and the textiles to phosphoric acid ratio. The results showed that 100% polyester recovery was achieved with a maximum sugar recovery of 79.2% at the optimized conditions of 85% phosphoric acid at 50 °C for 7 h and the ratio of textiles and phosphoric acid of 1:15 [77]. The feasibility of cellulase production and textile hydrolysis using fungal cellulase vs. commercial cellulase via submerged fungal fermentation (SmF) using textile waste was investigated. The study demonstrated that glucose recovery yields of 41.6% and 44.6% were obtained using fungal cellulase and commercial cellulase, respectively. Thus, the proposed process has great potential in treating textile waste for the recovery of glucose and polyester as value-added products [52].

### *6.5. Building/Construction Material from Textile Waste*

Textile waste represents a source of raw materials for typical application in construction, such as insulation materials for noise and temperature and fillers or reinforcements of concrete [78]. The conversion of fibrous carpet waste into a value-added product as soil reinforcement demonstrated that fibrous inclusions derived from carpet wastes improve the shear strength of silty sands [79]. Moreover, textile reinforced concrete (TRC) is a composite concrete material that uses textile as reinforcement material used in various applications, including precast constructions, repair, rehabilitation, and structural strengthening of existing structures. This is innovated by the construction industry, which promotes sustainability in building material by utilizing waste from the textile industry. It combines fine-grained concrete and multi-axially oriented textiles which offers advantages such as thin size, good load-bearing capacity, resistance to corrosion, excellent ductility, no magnetic disturbances, and lightweight [80,81]. Furthermore, textile waste is used to produce thick ropes designed for slope protection against sliding and erosion. Scraps of insulating materials produced from poor quality wool and scraps of nonwoven produced from a blend of recycled fibers

were used to produce ropes. The results confirmed the usefulness of the technology for the protection of steep slopes [82].

### *6.6. Thermal Recovery*

Incineration with the thermal recovery of unwanted textiles not suited for recycling (carpets or textiles with unknown fibers) is considered a viable alternative to landfilling. Carpet fibers have a high calorific value that can reduce the need for fuels, and the resulting ash becomes raw material for cement [1]. The advantage of the incineration option is that it can handle the most significant part of unsorted textile waste, and energy can be recovered from combustion. However, burning textiles alone can cause irregular temperature behavior, ignition rate, and weight loss percentage in the ignition propagation stage. For this, textile waste should be mixed with waste cardboard upon incineration to maintain a uniform burning behavior of textiles [83]. Incineration of 1 ton of household textile waste can recover 15,800 MJ of energy, and 27 kg of ash is generated [84,85].

## 7. Textile Waste Management Challenges

The global increase in clothing consumption and production has resulted in a significant increase in textile waste generation, posing alarming challenges in many leading countries. Textile waste is recognized as the fastest-growing waste stream in MSW across the globe. However, waste collection and economically viable sorting infrastructure remain a challenge. Sorting of textile waste involves intensive time and labor and complications by arising from variations in fiber blends pose a significant challenge. Automation for sorting and innovations in textile recycling are growing interests [4]. Textile reuse, the most preferred option, suffers a shrinking market due to banning imported used clothing in some countries. Textile reuse and recycling to produce new products should be driven by economic incentives to make it feasible for the operating industry. Sustainable blended materials made from recycled fibers are innovative to reduce environmental impact. Further work on the characterization of the structure and properties of cellulosic fibers regenerated from cotton-based waste is essential. Moreover, recycling technologies to sustainably manage other textile waste, such as man-made cellulosic fiber (MMCF) and other fibers (polyamide, wool, rayon, silk, acrylic, etc.), need to be investigated. MMCFs are a group of fibers derived primarily from wood and in other sources of cellulose, which constitute the third most commonly used fiber in the world, behind polyester and cotton. MMCF accounts for approximately 6.4% of total fiber production, with an annual production equivalent of about 7.1 MT [11,86].

Moreover, developing non-conventional fibers—such as bast fibers—and a chemical-free binding technology promote sustainability. Natural fibers—such as bast fibers (among them hemp, flex, nettle, and jute)—can yield significant benefits due to a smaller environmental footprint when compared to conventional plant-based fibers. Innovations supporting the circular economy and closed-loop recycling systems include recycling technologies that can produce new fibers comparable to virgin fibers. Shifting from a current linear economy into a circular economy yields tremendous environmental benefits for the fashion industry while mitigating the effects of greater demand for garments due to a rising world population [34].

## 8. Conclusions

The global rise in population, industrial growth, and improved living standards have caused a global fiber consumption that generates an alarming amount of unwanted textiles. Economic and environmental sustainability should be incorporated into the long-term textile waste management program. Though the application of EPR policy in textile waste is still limited, it is considered essential in promoting a circular economy system. EPR makes the producers responsible for the overall textile waste management from the collection to the disposal at the end of the product's life cycle. Besides EPR, there is a holistic approach involving major stakeholders (industry, government, private agencies,

and consumers) who must work in unity to promote a dynamic circular system. The emerging economies in textile manufacturing should take the lead in shifting from a linear economy to a circular economy.

Textile reuse and recycling are more sustainable than incineration and landfilling, but reuse is more beneficial than recycling. For this, designing a textile product by prolonging the service life quality could promote reuse. In addition, it is essential to promote consumer awareness to foster an environmentally friendly consumption behavior on textile products. Leading economies should manage their textile waste in a closed-loop circular approach, mainly when exporting textile waste to developing countries is being outlawed. Various streams of textile recycling technologies are available and continue to innovate new ideas with biotechnology advancement. Applying holistic technologies, and not relying upon a single technology, to manage a complex textile waste is deemed essential.

**Author Contributions:** Conceptualization, Q.Y., J.P.J.-L.; Literature review, J.P.J.-L. and Q.Y.; Methodology, J.P.J.-L. and Q.Y.; Writing—original draft preparation, J.P.J.-L. and Q.Y.; Writing—review and editing, Q.Y., J.P.J.-L. and I.V.L.; Supervision, Q.Y.; Funding acquisition, Q.Y. All authors have read and agreed to the published version of the manuscript.

**Funding:** The research support was provided by the federal funds appropriated to the Graduate Enhancement of Tri-Council Stipends (GETS), the University of Manitoba and the Natural Sciences and Engineering Research Council of Canada (NSERC RGPIN-2014-05510).

**Conflicts of Interest:** The authors declare no conflict of interest. The funders had no role in the design of the study; in the collection, analyses, or interpretation of data; in the writing of the manuscript, or in the decision to publish the results.

## Abbreviations

AD, anaerobic digestion; CCME, Canadian Council of Ministers of the Environment; EC, European Council; EU, European Union; EPR, extended producer responsibility; LDCs, least developed countries; MMCF, man-made cellulosic fiber; MMT, million metric tons; MT, million tons; MSW, municipal solid waste; NMMO, N-Methylmorpholine N-oxide; SmF, submerged fungal fermentation; TRC, textile reinforced concrete; US, United States; VS, volatile solids; WTE, waste-to-energy.

## References

1. Wang, Y. Fiber and textile waste utilization. *Waste Biomass Valor.* **2010**, *1*, 135–143. [CrossRef]
2. Lin, S.D. Recycled fiber industry facing opportunities and challenges in the new situation. *Resour. Recycl.* **2012**, *11*, 44–47.
3. Claudio, L. Waste couture: Environmental Impact of the Clothing Industry. *Environ. Health Perspect.* **2007**, *115*, A448–A454. [CrossRef] [PubMed]
4. Bukhari, M.A.; Carrasco-Gallego, R.; Ponce-Cueto, E. Developing a national programme for textiles and clothing recovery. *Waste Manag. Res.* **2018**, *36*, 321–331. [CrossRef] [PubMed]
5. TTRI Taiwan Textile Research Institute. Low Carbon Intelligent Operations for Textile Industry in APEC Economies. 2013. Available online: https://www.apec.org/docs/default-source/Publications/2013/8/Low-Carbon-Intelligent-Operations-for-Textile-Industry-in-APEC-Economies---Project/TOC/Main-Report.pdf (accessed on 20 November 2021).
6. Athalye, A. Carbon footprint in textile processing. *Colourage* **2012**, *59*, 45–47.
7. Rana, S.; Pichandi, S.; Karunamoorthy, S.; Bhattacharyya, A.; Parveen, S.; Fangueiro, R. Carbon footprint of textile and clothing products. In *Handbook of Sustainable Apparel Production*; Subramanian, S.M., Ed.; CRC Press: Boca Raton, FL, USA, 2015; pp. 141–165. [CrossRef]
8. Chavan, R.B. Environmental sustainability through textile recycling. *J. Text. Sci. Eng.* **2014**. [CrossRef]
9. Ekstrom, K.M.; Salomonson, N. Reuse and recycling of clothing and textiles: A Network Approach. *J. Macromarketing* **2014**, *34*, 383–399. [CrossRef]
10. Ellen MacArthur Foundation. A New Textiles Economy: Redesigning Fashion's Future. 2017. Available online: https://www.ellenmacarthurfoundation.org/publications (accessed on 10 January 2021).
11. Textile Exchange. Preferred Fiber & Materials, Market Report. 2020. Available online: https://textileexchange.org/wp-content/uploads/2020/06/Textile-Exchange_Preferred-Fiber-Material-Market-Report_2020.pdf (accessed on 10 January 2021).
12. WTO (World Trade Organization). World Trade Statistical Review. 2018. Available online: https://www.wto.org/english/res_e/statis_e/wts2018_e/wts2018_e.pdf (accessed on 6 December 2019).

13. Statista. Production Volume of Textile Fibers Worldwide 1975–2017. 2018. Available online: https://www.statista.com/statistics/263154/worldwide-production-volume-of-textile-fibers-since-1975/ (accessed on 6 December 2019).
14. Textile World. Man-Made Fibers Continue to Grow. 2015. Available online: https://www.textileworld.com/textile-world/fiber-world/2015/02/man-made-fibers-continue-to-grow/ (accessed on 6 December 2019).
15. HIS Markit. Natural and Man-Made Fibers Overview. 2015. Available online: https://ihsmarkit.com/products/fibers-chemical-economics-handbook.html (accessed on 6 December 2019).
16. GFA & BCG (Global Fashion Agenda and the Boston Consulting Group). Pulse of the Fashion Industry. 2017. Available online: https://www.globalfashionagenda.com/publications/#pulseofthefashionindustryreport (accessed on 22 November 2018).
17. Caulfield, K. *Sources of Textile Waste in Australia*; Apical International Pty. Ltd.: Melbourne, Australia, 2009; Available online: https://studylib.net/doc/18791293/sources-of-textile-waste-in-australia (accessed on 22 November 2018).
18. Domina, T.; Koch, K. The textile waste lifecycle. *Cloth. Text. Res. J.* **1997**, *15*, 96–102. [CrossRef]
19. BIR (Bureau of International Recycling). Textiles 2014. Available online: http://www.bir.org/industry/textiles (accessed on 3 September 2018).
20. Akay, Ö.; Gündüz, S.; Gündüz, F.F. The factor affecting textile production amounts of leading countries in textile export dynamic panel data analysis. *Nicel Bilimler Derg.* **2020**, *2*, 1–13.
21. Zhang, M.; Kong, X.X.; Ramu, S.C. The transformation of the clothing industry in China. Economic Research Institute for ASEAN and East Asia (ERIA) Discussion Paper Series. 2015. Available online: https://www.eria.org/ERIA-DP-2015-12.pdf (accessed on 25 November 2018).
22. Pepermans, A. China as a Textile Giant Preserving its Leading Position in the World, and what it Means for the EU. *Taiwan. J. Political Sci.* **2019**, *80*, 63–108. Available online: http://ntupsr.s3.amazonaws.com/psr/wp-content/uploads/2019/06/03-4-Astrid-Pepermans.pdf (accessed on 10 January 2021).
23. Dudin, M.N.; Lyasnikov, N.V.; Kahramanovna, D.G.; Kuznecov, A.V. Chinese Textile Industry: Sustainable Development Challenges and Competitiveness issues in Economic Environment Dynamics. *Fibers Text. East. Eur.* **2015**, *23*, 14–18. [CrossRef]
24. Collective Responsibility. Unspoken Crisis: Mounting Textile Waste in China. 5 July 2018. Available online: https://www.coresponsibility.com/unspoken-crisis-mounting-textile-waste-in-china (accessed on 20 June 2019).
25. Xu, J.; Liu, Y.; Yang, L. A comparative study of the role of China and India in sustainable textile competition in the U.S. market under green trade barriers. *Sustainability* **2018**, *10*, 1348. [CrossRef]
26. Spuijbroek, M. Textile Waste in Mainland China. 2019. Available online: https://zakendoeninchina.org/wp-content/uploads/2019/08/report_Textile-Waste-in-Mainland-China_small.pdf (accessed on 10 January 2021).
27. EC (European Council). Circular Economy in Practice-Reducing Textile Waste. 2017. Available online: https://ec.europa.eu/easme/en/news/circular-economy-practice-reducing-textile-waste (accessed on 3 September 2018).
28. EC (European Council). Costs for Municipal Waste Management in the EU. 2002. Available online: https://ec.europa.eu/environment/waste/studies/pdf/eucostwaste.pdf (accessed on 4 September 2018).
29. EC (European Council). Directive 2008/98/EC of the European Parliament and the Council of 19 November 2008 on Waste and Repealing Certain Directives. European Commission: Brussels, Belgium. Available online: https://eur-lex.europa.eu/legal-content/EN/TXT/?uri=CELEX:32008L0098 (accessed on 4 September 2018).
30. European Parliament. Waste: Boost Recycling, Cut Landfilling and Curb Food Waste, Parliament Says. 2017. Available online: http://www.europarl.europa.eu/news/en/press-room/20170308IPR65671/waste-boost-recycling-cut-landfilling-and-curb-food-waste-parliament-says (accessed on 5 September 2018).
31. OECD (Organisation for Economic Cooperation and Development). Extended Producer Responsibility. A Guidance Manual for Governments. 2001. Available online: https://www.oecd-ilibrary.org/environment/extended-producer-responsibility_9789264189867-en (accessed on 5 September 2018).
32. Gupt, Y.; Sahay, S. Review of extended producer responsibility: A Case Study Approach. *Waste Manag. Res.* **2015**, *33*, 595–611. [CrossRef]
33. EC (European Council). Waste Management and Recycling: Council Adopts New Rules. 2018. Available online: https://www.consilium.europa.eu/en/press/press-releases/2018/05/22/waste-management-and-recycling-council-adopts-new-rules/# (accessed on 11 March 2019).
34. GFA & BCG (Global Fashion Agenda and the Boston Consulting Group). Pulse of the Fashion Industry. 2018. Available online: https://www.globalfashionagenda.com/publications/#pulseofthefashionindustryreport (accessed on 15 January 2021).
35. USEPA (United States Environmental Protection Agency). Advancing Sustainable Materials Management: 2015 Fact Sheet 2018. Available online: https://www.epa.gov/sites/default/files/2018-07/documents/2015_smm_msw_factsheet_07242018_fnl_508_002.pdf (accessed on 15 January 2021).
36. USEPA (United States Environmental Protection Agency). Advancing Sustainable Materials Management: 2018 Fact Sheet 2020. Available online: https://www.epa.gov/sites/default/files/2021-01/documents/2018_tables_and_figures_dec_2020_fnl_508.pdf (accessed on 10 February 2021).
37. CTR (Council for Textile Recycling). Available online: http://www.weardonaterecycle.org/ (accessed on 7 April 2018).
38. Wicker, A. Fast Fashion is Creating an Environmental Crisis. 2016. Available online: http://www.newsweek.com/2016/09/09/old-clothes-fashion-waste-crisis-494824.htm (accessed on 10 May 2018).

39. USEPA (United States Environmental Protection Agency). Advancing Sustainable Materials Management: 2014 Tables and Figures. 2016. Available online: https://www.epa.gov/sites/production/files/2016-11/documents/2014_smm_tablesfigures_508.pdf (accessed on 10 March 2019).
40. USEPA (United States Environmental Protection Agency). Facts and Figures about Materials, Waste and Recycling 2021. Textiles: Material-Specific Data, Summary Table and Graph. Available online: https://www.epa.gov/facts-and-figures-about-materials-waste-and-recycling/textiles-material-specific-data#TextilesTableandGraph (accessed on 15 January 2022).
41. Storry, K.; Mckenzie, A. Unravelling the Problem of Apparel Waste in the Greater Vancouver Area. 2018. Available online: https://businessinsurrey.com/wp-content/uploads/2018/05/UnravellingtheProblemofApparelWasteintheGreaterVancouverAreaMarch2 2018.pdf (accessed on 10 March 2019).
42. TWD (Textile Waste Diversion). The Potential for Textile Recycling in Canada. 2013. Available online: http://textilewastediversion.com/the-potential-for-textile-recycling-in-canada/ (accessed on 20 April 2018).
43. Marsales, C. Report to General Committee: Textile Recycling Smart Bin Program. City of Markham. 2016. Available online: http://www2.markham.ca/markham/ccbs/indexfile/Agendas/2016/General/gc160418/Textile%20Recycling%20Smart%20Bin%20Program.pdf (accessed on 20 April 2018).
44. Malilay-Pimentel, C.E. Reducing Textile Waste in Metro Vancouver Landfills. 2017. Available online: http://summit.sfu.ca/item/17761 (accessed on 25 April 2018).
45. WRW (Waste Reduction Week), Canada. Textiles Tuesday. 2017. Available online: http://wrwcanada.com/en/2017-theme-days/textiles-tuesday (accessed on 25 April 2018).
46. Weber, S. How Consumers Manage Textile Waste. Master's Thesis on Environmental Studies 2015, University of Waterloo, Waterloo, ON, Canada, 2015.
47. Tetra Tech. Metro Vancouver Waste Composition Monitoring Program. 2015. Available online: http://www.metrovancouver.org/services/solid-waste/SolidWastePublications/2015_Waste_Composition_Report.pdf (accessed on 20 April 2018).
48. Recycling and Waste Reduction-Association of Manitoba Municipalities. 2015. Available online: http://www.amm.mb.ca/download/.../Recycling%20and%20Waste%20Reduction.pdf (accessed on 10 May 2018).
49. Lyons, P. Textile Recycling Added to Eco Centre Services. Okotoks, Alberta, Canada. 2017. Available online: https://www.okotoks.ca/municipal-government/newsroom/news/textile-recycling-added-eco-centre-services-0 (accessed on 10 May 2018).
50. Sandin, G.; Peters, G.M. Environmental impact of textile reuse and recycling—A review. *J. Clean. Prod.* **2018**, *184*, 353–365. [CrossRef]
51. Fortuna, L.M.; Diyamandoglu, V. Optimization of greenhouse gas emissions in secondhand consumer product recovery through reuse platforms. *Waste Manag.* **2017**, *66*, 178–189. [CrossRef] [PubMed]
52. Wang, H.; Kaur, G.; Pensupa, N.; Uisan, K.; Du, C.; Yang, X.; Sze Ki Lin, C. Textile waste valorization using submerged filamentous fungal fermentation. *Process. Saf. Environ. Prot.* **2018**. [CrossRef]
53. Ignatyev, A.I.; Thielemans, W.; Vander Beke, B. Recycling of polymers: A review. *ChemSusChem* **2014**, *7*, 1579–1593. [CrossRef]
54. Herva, M.; Franco, A.; Ferreiro, S.; Alvarez, A.; Roca, E. An approach for the application of the ecological footprint as environmental indicator in the textile sector. *J. Hazard. Mater.* **2008**, *156*, 478–487. [CrossRef]
55. Zamani, B. Towards Understanding Sustainable Textile Waste Management: Environmental Impacts and Social Indicators. 2014. Available online: http://publications.lib.chalmers.se/records/fulltext/204502/204502.pdf (accessed on 24 April 2018).
56. Woolridge, A.C.; Ward, G.D.; Phillips, P.S.; Collins, M. Life cycle assessment for reuse/recycling of donated waste textiles compared to use of virgin material: An UK Energy Saving Perspective. *Resour. Conserv. Recycl.* **2006**, *46*, 94–103. [CrossRef]
57. Isci, A.; Demirer, G.N. Biogas production potential from cotton wastes. *Renew. Energy* **2007**, *32*, 750–757. [CrossRef]
58. Raj, C.S.; Arul, S.; Sendilvelan, S.; Saravanan, C.G. Biogas from Textile Cotton Waste—An Alternate Fuel for Diesel Engines. *Open Waste Manag. J.* **2009**, *2*, 1–5. [CrossRef]
59. Ismail, Z.Z.; Talib, A.R. Recycled medical cotton industry waste as a source of biogas recovery. *J. Clean. Prod.* **2016**, *112*, 4413–4418. [CrossRef]
60. Shrestha, B.; Hernandez, R.; Fortela, D.L.B.; Sharp, W.; Chistoserdov, A.; Gang, D.; Revellame, E.; Holmes, W.; Zappi, M.E. A review of pretreatment methods to enhance solids reduction during anaerobic digestion of municipal wastewater sludges and the resulting digester performance: Implications to Future Urban Biorefineries. *Appl. Sci.* **2020**, *10*, 9141. [CrossRef]
61. Ariunbaatar, J.; Panico, A.; Esposito, G.; Pirozzi, F.; Lens, P.N.L. Pretreatment methods to enhance anaerobic digestion of organic solid waste. *Appl. Energy* **2014**, *123*, 143–156. [CrossRef]
62. Pilli, S.; Pandey, A.K.; Katiyar, A.; Pandey, K.; Tyagi, R.D. Pre-treatment Technologies to Enhance Anaerobic Digestion. In *Sustainable Sewage Sludge Management and Resource Efficiency*; IntechOpen: London, UK, 2020. Available online: https://www.intechopen.com/chapters/72862 (accessed on 15 January 2022). [CrossRef]
63. Hasanzadeha, E.; Mirmohamadsadeghia, S.; Karimi, K. Enhancing energy production from waste textile by hydrolysis of synthetic parts. *Fuel* **2018**, *218*, 41–48. [CrossRef]
64. Jeihanipour, A.; Aslanzadeh, S.; Rajendran, K.; Balasubramanian, G.; Taherzadeh, M.J. High-rate biogas production from waste textiles using a two-stage process. *Renew. Energy* **2013**, *52*, 128–135. [CrossRef]
65. Juanga-Labayen, J.; Yanac, K.; Yuan, Q. Effect of substrate-to-inoculum ratio on anaerobic digestion of treated and untreated cotton textile waste. *Int. J. Environ. Sci. Technol.* **2021**, *18*, 287–296. [CrossRef]

66. Hamawand, I.; Sandell, G.; Pittaway, P.; Chakrabarty, S.; Yusaf, T.; Chen, G.; Seneweera, S.; Al-Lwayzy, S.; Bennett, J.; Hopf, J. Bioenergy from Cotton Industry Wastes: A Review and Potential. *Renew. Sustain. Energy Rev.* **2016**, *66*, 435–448. [CrossRef]
67. Gholamzad, E.; Karimi, K.; Masoomi, M. Effective conversion of waste polyester–cotton textile to ethanol and recovery of polyester by alkaline pretreatment. *Chem. Eng. J.* **2014**, *253*, 40–45. [CrossRef]
68. Nikoli, S.; Lazi, V.; Veljovi, D.; Mojovi, L. Production of bioethanol from pre-treated cotton fabrics and waste cotton materials. *Carbohydr. Polym.* **2017**. [CrossRef]
69. Mahitha, U.; Dhaarini Devi, G.; Akther Sabeena, M.; Shankar, C.; Kirubakaran, V. Fast Biodegradation of Waste Cotton Fibers from Yarn Industry using Microbes. *Procedia Environ. Sci.* **2016**, *35*, 925–929. [CrossRef]
70. Selvi, C.P.; Koilraj, A.J. Bacterial Diversity in Compost and Vermicompost of Cotton Waste at Courtallam, Nellai District in Tamilnadu, India. *Int. J. Curr. Microbiol. Appl. Sci.* **2015**, *4*, 582–585.
71. Aishwariya, S.; Amsamani, S. Evaluating the efficacy of compost evolved from bio-managing cotton textile waste. *J. Environ. Res. Dev.* **2012**, *6*, 941–952.
72. Santos, A.; Bustamante, M.A.; Tortosa, G.; Moral, R.; Bernal, M.P. Gaseous emissions and process development during composting of pig slurry: The Influence of the Proportion of Cotton Gin Waste. *J. Clean. Prod.* **2016**, *112*, 81–90. [CrossRef]
73. Oh, S.J.; Park, S.J.; Shin, P.G.; Yoo, Y.B.; Jhune, C.S. An improved compost using cotton waste and fermented sawdust for cultivation of oyster mushroom. *Mycobiology* **2004**, *32*, 115–118. [CrossRef]
74. Phuong, T.T. Development of a New Cotton Waste Composting Technology for Cultivation of Oyster Mushroom (Pleurotus Ostreatus). *ARPN J. Eng. Appl. Sci.* **2016**, *11*, 12607–12613.
75. Haule, L.V.; Carr, C.M.; Rigout, M. Preparation and physical properties of regenerated cellulose fibers from cotton waste garments. *J. Clean. Prod.* **2016**, *112*, 4445–4451. [CrossRef]
76. Woodings, C.R. The development of advanced cellulosic fibers. *Int. J. Biol. Macromol.* **1995**, *17*, 305–309. [CrossRef]
77. Shen, F.; Xiao, W.; Lin, L.; Yang, G.; Zhang, Y.; Deng, S. Enzymatic saccharification coupling with polyester recovery from cotton-based waste textiles by phosphoric acid pretreatment. *Bioresour. Technol.* **2018**, *130*, 248–255. [CrossRef]
78. Pichardo, P.P.; Martínez-Barrera, G.; Martínez-López, M.; Ureña-Núñez, F.; Ávila-Córdoba, L.I. Waste and Recycled Textiles as Reinforcements of Building Material. In *Natural and Artificial Fiber-Reinforced Composites as Renewable Sources*; 2017; Available online: https://www.intechopen.com/chapters/56947 (accessed on 3 September 2018).
79. Ghiassian, H.; Poorebrahim, G.; Gray, D.H. Soil Reinforcement with Recycled Carpet Wastes. *Waste Manag. Res.* **2004**, *22*, 108–114. [CrossRef]
80. Williams, N.; Lundgren, K.; Wallbaum, H.; Malaga, K. Sustainable potential of textile-reinforced concrete. *J. Mater. Civil. Eng.* **2015**, *27*, 1–12. Available online: http://ascelibrary.org/doi/pdf/10.1061/(ASCE)MT.1943-5533.0001160 (accessed on 15 January 2021). [CrossRef]
81. Anjana, E.A.; Shashikala, A.P. Sustainability of construction with textile reinforced concrete—A state of the art. In *Proceedings of the International Conference on Materials, Mechanics and Structures, Kerala, India, 14–15 July 2020*; IOP Conference Series; Materials Science and Engineering: Kerala, India, 2020. Available online: https://iopscience.iop.org/article/10.1088/1757-899X/936/1/012006/pdf (accessed on 15 January 2021).
82. Broda, J.; Przybyło, S.; Gawłowski, A.; Grzybowska-Pietras, J.; Sarna, E.; Rom, M.; Laszczak, R. Utilisation of textile wastes for the production of geotextiles designed for erosion protection. *J. Text. Inst.* **2018**, *110*, 435–444. [CrossRef]
83. Ryu, C.; Phan, A.N.; Yang, Y.; Sharifi, V.N.; Swithenbank, J. Ignition and burning rates of segregated waste combustion in packed bed. *Waste Manag.* **2007**, *27*, 802–810. [CrossRef] [PubMed]
84. Swedish EPA. Förbränningsanläggningar för Energiproduktion Inklusiverökgaskondensering, s.l.: Swedish Environmental Protection Agency 2005. Available online: https://www.naturvardsverket.se/globalassets/media/publikationer-pdf/8100/91-620-8196-9.pdf (accessed on 6 December 2018).
85. Youhanan, L. Environmental Assessment of Textile Material Recovery Techniques. Examining Textile Flows in Sweden. Master's Thesis, Royal Institute of Technology, Stockholm, Sweden, 2013. Available online: https://www.diva-portal.org/smash/get/diva2:630028/FULLTEXT01.pdf (accessed on 6 December 2018).
86. Hugill, R.; Ley, K.; Rademan, K. Coming Full Circle: Innovating towards Sustainable Man-Made Cellulosic Fibres. Available online: https://reports.fashionforgood.com/report/coming-full-circle-innovating-towards-sustainable-man-made-cellulosic-fibres/ (accessed on 15 January 2022).

MDPI
St. Alban-Anlage 66
4052 Basel
Switzerland
Tel. +41 61 683 77 34
Fax +41 61 302 89 18
www.mdpi.com

*Textiles* Editorial Office
E-mail: textiles@mdpi.com
www.mdpi.com/journal/textiles

MDPI
St. Alban-Anlage 66
4052 Basel
Switzerland

Tel: +41 61 683 77 34

www.mdpi.com


ISBN 978-3-0365-6081-6